AD-A076 012 ADVISORY GROUP FOR AEROSPACE RESEARCH AND DEVELOPMENT--ETC F/G 21/8.2
SOLID ROCKET MOTOR TECHNOLOGY.(U)
JUL 79
UNCLASSIFIED AGARD-CP-259 NL

1 OF 6
AD A076012

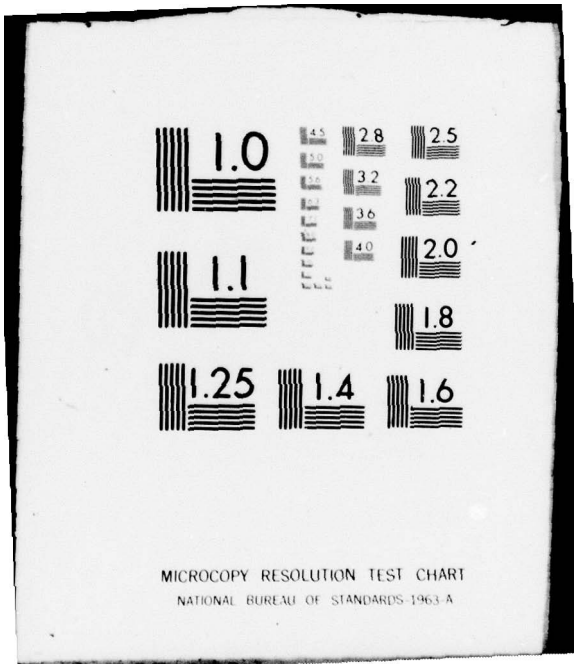
1.0
1.1
1.25
1.4
1.6
1.8
2.0
2.2
2.5
2.8
3.2
3.6
4.0
MICROCOPY RESOLUTION TEST CHART
NATIONAL BUREAU OF STANDARDS-1963-A

AGARD-CP-259

AGARD

ADVISORY GROUP FOR AEROSPACE RESEARCH & DEVELOPMENT

7 RUE ANCELLE 92200 NEUILLY SUR SEINE FRANCE

AGARD CONFERENCE PROCEEDINGS No. 259

Solid Rocket Motor Technology

NORTH ATLANTIC TREATY ORGANIZATION

DISTRIBUTION AND AVAILABILITY
ON BACK COVER

AGARD-CP-259

NORTH ATLANTIC TREATY ORGANIZATION

ADVISORY GROUP FOR AEROSPACE RESEARCH AND DEVELOPMENT

(ORGANISATION DU TRAITE DE L'ATLANTIQUE NORD)

12 526

9

AGARD Conference Proceedings No.259

6 SOLID ROCKET MOTOR TECHNOLOGY.

11 Jul 79

Papers presented at the 53rd Meeting of the AGARD Propulsion and Energetics Panel
held at the Old War School, Oslo, Norway, 2–5 April 1979.

THE MISSION OF AGARD

The mission of AGARD is to bring together the leading personalities of the NATO nations in the fields of science and technology relating to aerospace for the following purposes:

- Exchanging of scientific and technical information;
- Continuously stimulating advances in the aerospace sciences relevant to strengthening the common defence posture;
- Improving the co-operation among member nations in aerospace research and development;
- Providing scientific and technical advice and assistance to the North Atlantic Military Committee in the field of aerospace research and development;
- Rendering scientific and technical assistance, as requested, to other NATO bodies and to member nations in connection with research and development problems in the aerospace field;
- Providing assistance to member nations for the purpose of increasing their scientific and technical potential;
- Recommending effective ways for the member nations to use their research and development capabilities for the common benefit of the NATO community.

The highest authority within AGARD is the National Delegates Board consisting of officially appointed senior representatives from each member nation. The mission of AGARD is carried out through the Panels which are composed of experts appointed by the National Delegates, the Consultant and Exchange Programme and the Aerospace Applications Studies Programme. The results of AGARD work are reported to the member nations and the NATO Authorities through the AGARD series of publications of which this is one.

Participation in AGARD activities is by invitation only and is normally limited to citizens of the NATO nations.

Published July 1979

ISBN 92-835-0243-4

Printed by Technical Editing and Reproduction Ltd
Harford House, 7–9 Charlotte St, London, W1P 1HD

PROPULSION AND ENERGETICS PANEL

CHAIRMAN: Prof. Dr-Ing. G.Winterfeld
DFVLR, Institut für Antriebstechnik
D-5000 Köln 90, Germany

DEPUTY CHAIRMAN: Dr J.Dunham
NGTE
Pyestock, Farnborough, Hants GU14 OLS, UK

PROGRAMME COMMITTEE

HOST NATION COORDINATOR

Mr G.Kristofersen
Norwegian Defence Research Establishment
Division for Weapon and Equipment
P.O. Box 27, N-2007 Kjeller, Norway

PANEL EXECUTIVE

Dipl.-Ing. J.H.Krengel, D.I.C.

ACKNOWLEDGEMENT

The Propulsion and Energetics Panel wishes to express its thanks to the Norwegian National Delegates to AGARD for the invitation to hold its 53rd Meeting at the Old War School in Oslo, and for the personnel and facilities made available for this meeting.

CONTENTS

SESSION VII – TESTING AND INSTRUMENTATION

LES RECHERCHES DANS LE DOMAINE DES MOTEURS FUSÉES A PROPERGOLS SOLIDES (VUE D'ENSEMBLE)

par Marcel BARRÈRE

Office National d'Etudes et de Recherches Aérospatiales (ONERA)
92320 Châtillon (France)

◆

Résumé

Le but de cet exposé est de préciser les recherches qui intéressent actuellement les constructeurs de fusées en vue d'applications militaires.

Ces recherches portent principalement sur la combustion du propergol et sur les propriétés des produits brûlés avec leur impact sur les performances et la tenue des tuyères et des enveloppes.

Nous laissons de côté des problèmes importants liés aux propriétés mécaniques du bloc de poudre et aux matériaux constituant l'enveloppe et la tuyère, matériaux qui sont choisis en fonction de la mission du propulseur.

Les recherches sur la combustion sont divisées en deux parties suivant que le régime de fonctionnement du propulseur est permanent ou transitoire.

Dans l'optimisation d'un système de propulsion, la valeur de la vitesse de combustion joue un très grand rôle et plus particulièrement son évolution avec la pression et la température du bloc. Bien que de nombreuses recherches aient été consacrées à ce thème il reste encore de nombreux problèmes à résoudre pour étendre la gamme des propergols actuels. Quelques aspects des phénomènes de combustion lorsque la surface est balayée par un écoulement ou lorsque le propergol est soumis à des accélérations sont abordés.

La connaissance des lois qui régissent les conditions d'extinction est utile aussi bien aux constructeurs qu'aux chercheurs qui veulent avoir une idée plus précise des processus de combustion des propergols.

La propagation de la flamme dans les fissures et leur formation sont également analysées.

En régime transitoire, une large part de l'activité est consacrée à l'heure actuelle à l'évolution de la réponse du propergol à une fluctuation de pression et à une fluctuation de vitesse. Les théories linéarisées qui donnent cette fonction de transfert sont peu réalistes et le couplage avec la vitesse ne peut être abordé en utilisant les lois de vitesse de combustion érosive du régime permanent.

On dispose, à l'heure actuelle, de données relatives à la fonction de transfert du propergol ; il est encore difficile de prévoir les domaines de fonctionnement stable du propulseur car on ne dispose pas d'une méthode analytique pour prévoir les pertes en fonction de la taille du propulseur.

Sur l'incidence des produits de combustion (présence de particules) sur les performances et sur la tenue des tuyères, quelques aspects des recherches sont également évoqués.

RESEARCH IN THE FIELD OF SOLID PROPELLANT ROCKETS (A SURVEY)

Summary

The purpose of this paper is to review current research of interest at the present time to solid propellant rocket manufacturers for military applications.

The analysis presented deals mainly with the combustion of propellants and the nature of burned products, as well as their impact on performances and the behaviour of nozzles and casings.

This paper does not take into account the important problems of the mechanical properties of the propellant grain and of the nature of the materials used for the nozzle and casing of the rocket, which are chosen on the basis of the mission to be carried out.

Combustion research is divided into two parts : the steady and the unsteady regime of the combustion chamber.

The burning rate of the propellant plays an important role in the optimization of the propulsion system, in particular its level, its evolution with the pressure and its sensivity to the grain temperature. The influence of the gas velocity along the surface and acceleration effects are also dealt with.

Although a great deal of research has been carried out in this fiel, many problems still remain to be solved to extend the range of present propellants.

The knowledge of the laws which govern the propellant combustion pressure limit is important to both manufacturers and researchers who want to have a more precise insight on the combustion phenomena.

The flame propagation in cracks and their initiation are analyzed.

In the unsteady regime of combustion, a large part of the activity is devoted to the response of the propellant to pressure and velocity fluctuations. Experimental and theoretical works on the determination of the transfer function are dealt with. Linearized theories which give the transfer function are in some cases unrealistic and the coupling of the burning rate with the velocity is not well understood.

For some propellants the transfer function is known ; in spite of this, it is still difficult to predict the stable regime of the rocket motor, the losses evaluation for different sizes and geometries of the combustion chamber remaining inaccurate.

Some aspects of research on components (grain, liner, casing, nozzle) are given, in particular the effect of the nature of combustion products on their performance.

1 - INTRODUCTION [1]

Les recherches dans le domaine des propergols solides ont toujours été très actives. L'utilisation de ce type de propergol pour la propulsion par fusées a fait apparaître de nouveaux domaines d'applications civils et militaires et de 1948 à 1978 des recherches très importantes ont été menées un peu partout dans le monde. Devant cet accroissement d'activité, on pourrait croire que les principaux problèmes ont été résolus et qu'il ne reste que des études portant sur des actions de détails, plus particulièrement liées aux applications mais il n'en est rien car le nombre des missions ne cesse de croître et les contraintes imposées sont de plus en plus nombreuses et difficiles à réaliser. Si l'on examine la littérature spécialisée de ces cinq dernières années on note une baisse du potentiel "recherches" aux U.S.A., un accroissement en U.R.S.S. et au Japon, un maintien en Allemagne, au Royaume Uni et en France.

Nous nous proposons dans cet article de faire le point des activités dans ce domaine, en insistant plus particulièrement sur les sujets qui demandent encore un effort et, en fonction de futures applications, sur les nouveaux thèmes qu'il conviendrait d'aborder.

Nous allons suivre un plan classique en distinguant trois parties :

- la première est relative à la combustion du propergol en régime permanent. Dans l'optimisation d'un système de propulsion en vue d'une application donnée, la valeur de la vitesse de combustion joue un très grand rôle. Les recherches qui aboutissent à une meilleure détermination de ce paramètre sont abordées ;
- la deuxième partie traite du régime transitoire à l'allumage, à l'extinction ou durant le fonctionnement instable du propulseur ;
- la troisième partie concerne plus directement le propulseur :
  - . géométrie des blocs,
  - . écoulement interne dans le propulseur,
  - . érosion des tuyères.

Nous laissons de côté les problèmes importants qui sont liés aux propriétés mécaniques du bloc de poudre et aux matériaux constituant l'enveloppe et la tuyère, matériaux qui sont choisis en fonction de la mission du propulseur.

2 - RECHERCHES PORTANT SUR LA COMBUSTION EN REGIME PERMANENT

2.1 - Vitesse de combustion

On dispose à l'heure actuelle d'une large gamme de propergols permettant de couvrir un domaine de vitesse de combustion allant de quelques dixièmes de millimètre par seconde à plusieurs centimètres par seconde dans le domaine de pression utilisé.

La figure 1 donne l'ordre de grandeur des vitesses obtenues pour les trois types de propergols actuellement utilisés :

- propergols homogènes pour lesquels les atomes comburants et combustibles sont fixés sur la même molécule (double-base) ;
- propergols hétérogènes obtenus par mélange des substances comburantes et combustibles (composites) ;
- propergols hétérogènes obtenus par mélange de propergols homogènes et de substances comburantes ou combustibles (double-base composite).

Examinons tout d'abord les paramètres qui agissent sur la vitesse de combustion et dans quelle mesure peut-on les faire varier.

a) - Niveau de vitesse de combustion [2] [3] [4] [5]

Dans l'expression classique de la vitesse de combustion $v_b = a p^n$, nous allons plus particulièrement discuter de la valeur du niveau de vitesse de combustion a .

Pour fixer les idées considérons deux cas extrêmes d'application militaire, tout d'abord celui des propulseurs utilisés comme "boosters" à grande poussée et celui de petits propulseurs à court temps de combustion et à grande accélération.

Pour réaliser ces deux missions, on peut jouer sur trois paramètres :

a. la masse volumique, il faut choisir des propergols denses mais on est assez vite limité ;

b. la surface de combustion, on dispose à l'heure actuelle de géométries compliquées de bloc qui conduisent dans un volume donné, à une grande surface de combustion, mais ici encore on est limité par la tenue mécanique du bloc qui, en général, doit supporter de grandes accélérations, et, à l'allumage, des différences de pressions élevées, et qui doit posséder de bonnes propriétés au stockage ;

c. le niveau de la vitesse de combustion, c'est le paramètre sur lequel en définitive on peut agir mais qu'il est difficile de maitriser complètement.

Il existe au moins trois procédés pour agir sur a :

Le premier est lié au processus physique de transfert de chaleur à la surface et dans le solide ; la plupart des propergols sont constitués de substances plastiques et qui ont, malgré leur grande diversité, des propriétés thermiques équivalentes, pour fixer les idées la diffusivité thermique est de l'ordre de $10^{-3} cm^2 s^{-1}$. Comme cette diffusivité thermique conditionne en partie la valeur de a , il faut donc trouver des moyens pour l'améliorer, en utilisant par exemple des fils d'argent placés perpendiculairement à la surface de combustion. On peut égale-

ment choisir des substances qui,d'une part,augmentent l'énergie rayonnée par la flamme et, d'autre part,accroissent l'énergie absorbée par le propergol.

Le deuxième procédé consiste à utiliser dans les propergols hétérogènes des substances finement divisées (cristaux de perchlorate d'ammonium de granulométrie de l'ordre du micron par exemple).

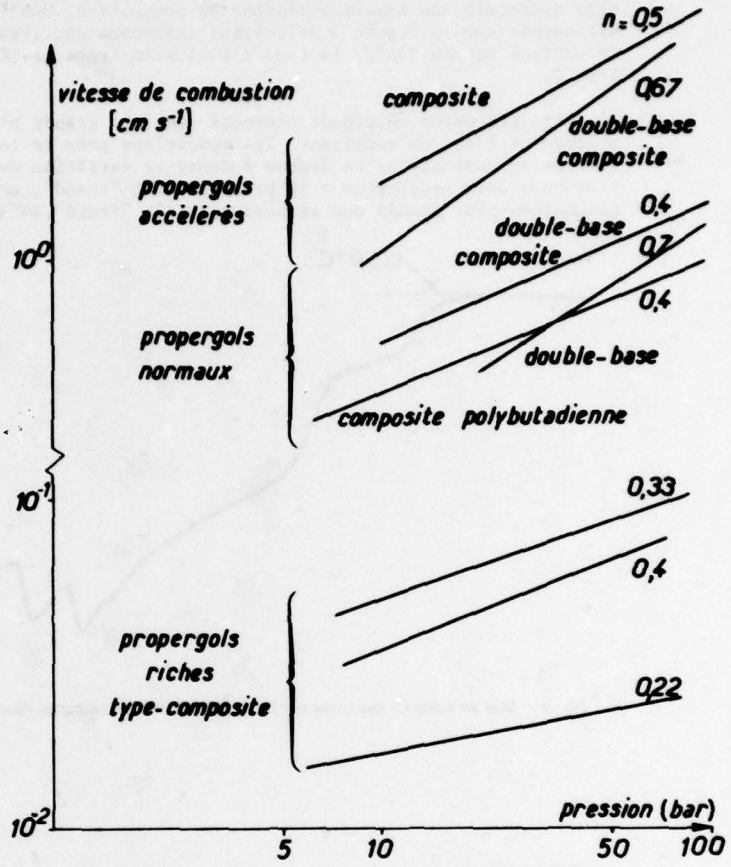

Fig. 1 – Domaine de vitesses de combustion actuellement utilisées.

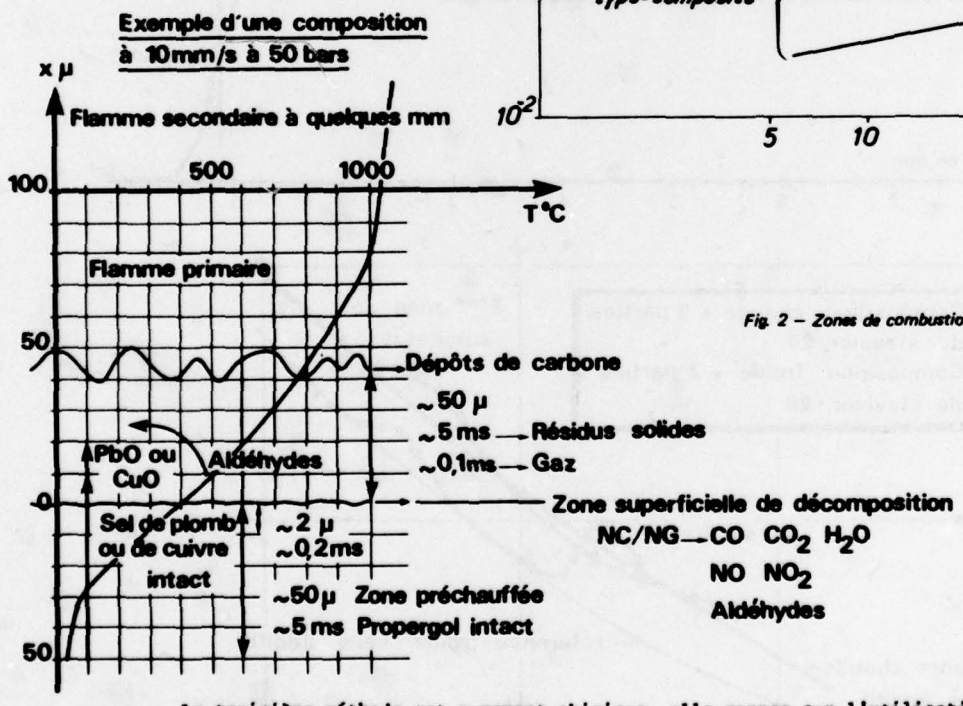

Fig. 2 – Zones de combustion propergols homogènes.

La troisième méthode est purement chimique, elle repose sur l'utilisation de composés endothermiques qui se détruisent facilement sous l'élévation de température ou de catalyseurs qui rendent plus rapides certaines réactions chimiques. Pour illustrer cette possibilité examinons le cas de propergols homogènes contenant certains catalyseurs. La structure de la flamme d'un propergol homogène évolue avec la pression et avec la nature du propergol, on peut néanmoins en donner une représentation comme celle indiquée sur la figure n°2 où le profil des températures est tracé en fonction de l'épaisseur traversée. Dans le solide on note tout d'abord une zone de préchauffage à l'intérieur de laquelle la température croît sans pour cela modifier de façon notable la composition du propergol ; dans l'exemple choisi la pression est de 50 bars, la vitesse de combustion de l'ordre de 1 cms^{-1}, la zone solide intéressée a une épaisseur de 50 μm ; à la surface du propergol on observe une zone superficielle de décomposition de la nitrocellulose et de la nitroglycérine avec formation de NO, NO_2, des aldehydes, des hydrocarbures, de l'hydrogène et des produits de combustion comme CO, CO_2, H_2O. Cette zone de dégradation comporte des résidus

solides, des dépôts de carbone et du gaz ; l'épaisseur de cette zone est de l'ordre de 50 µm ; plus au-dessus, apparait une flamme primaire correspondant à une oxydation exothermique des aldehydes par NO_2 avec formation de NO, CO, CO_2, H_2O, H_2 ; toujours en suivant l'écoulement se situe une zone d'induction, l'évolution des espèces est lente et les réactions chimiques peu importantes, la température est sensiblement constante ; une zone de combustion secondaire apparait ensuite conduisant à une combustion complète des espèces, cette zone est en général lumineuse, elle disparait aux basses pressions de combustion. Une évolution expérimentale de la température est donnée sur la figure 3 délimitant les zones décrites plus haut, dans ce cas la température de surface est de 340°C, la zone d'évolution lente de 1015°C et la zone de fin de combustion 1750°C.

Les processus chimiques tiennent donc une grande place dans la combustion des propergols homogènes et c'est en modifiant les conditions près de la surface que l'on pourra agir sur la vitesse de combustion. La figure 4 donne la variation de la vitesse de combustion avec la pression pour deux propergols : le propergol dit "chaud", correspondant à une énergie libérée par la combustion plus grande que le propergol dit "froid", et qui a une vitesse de combustion plus élevée.

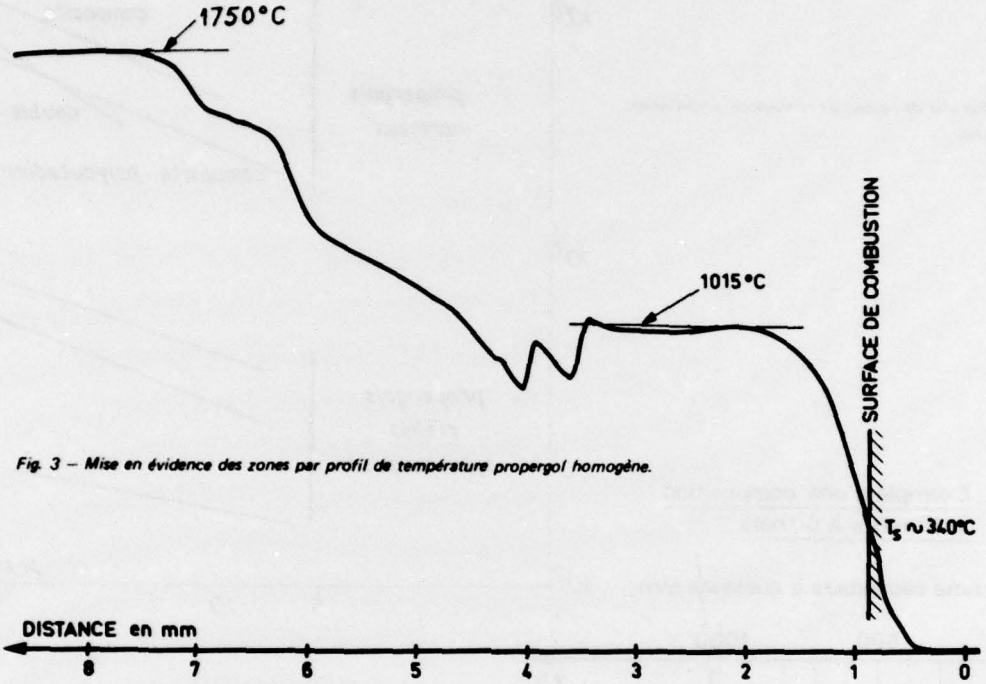

Fig. 3 – Mise en évidence des zones par profil de température propergol homogène.

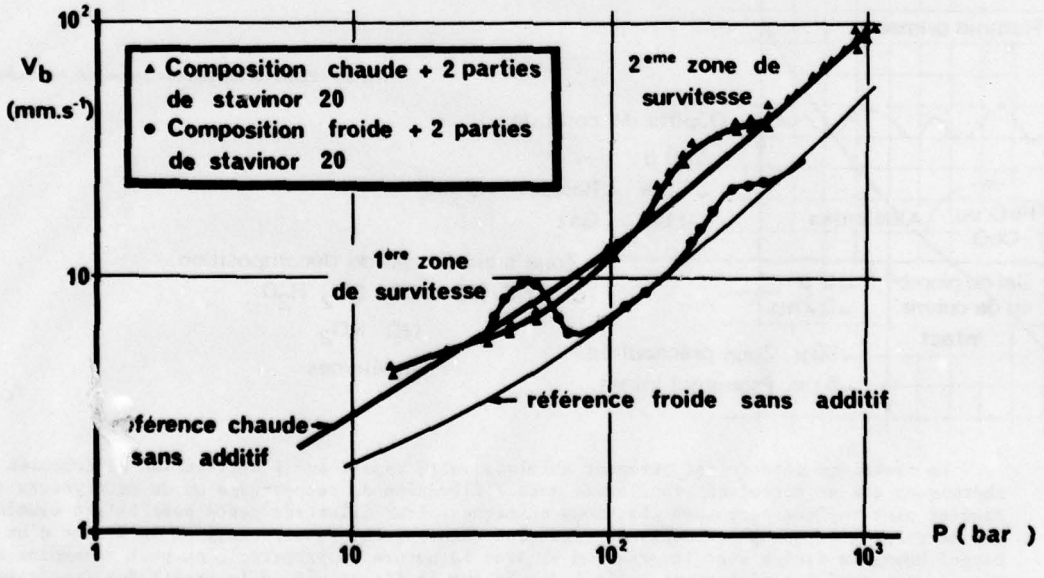

Fig. 4 – Vitesse de combustion en fonction de la pression et du pouvoir calorifique.

Sur cette même figure est portée l'influence de catalyseurs comme le stéarate de Plomb qui provoque dans des domaines de pression bien délimités des survitesses, un même propergol peut avoir en fonction de la pression plusieurs domaines de survitesse. Pour ces propergols le premier domaine de survitesse est dû à une libération plus grande d'énergie près de la surface, c'est-à-dire dans la flamme primaire, l'additif a pour effet de réduire plus activement NO en N_2, une

augmentation de la température en résulte, ce qui augmente le flux de chaleur transmis au solide. L'additif n'a aucun effet dans la phase solide. La flamme secondaire arrive alors près de la surface. Des espèces comme PbO, SnO possèdent un effet catalyseur sur les réactions exothermiques. Le noir de carbone a pour effet, comme l'indique la figure 5, de déplacer la zone de survitesse. On note également que les résidus de carbone sont plus abondants en présence d'additifs, ces résidus disparaissent à la fin de la zone de survitesse.

Avec les propergols composites ou hétérogènes les paramètres qui agissent sur la vitesse de combustion sont en plus des précédents, tout d'abord ceux qui sont liés à l'énergie mise en jeu par la combustion car le rapport de mélange peut aisément varier. Les lois régissant la vitesse de régression d'une substance sont de la forme $v_b = Be^{-T_A/T_s}$ où T_s est la température de surface, il faut donc connaitre cette loi pour tous les ingrédients composant un propergol hétérogène (Perchlorate d'ammonium, polyuréthane, nitrocellulose nitroglycérine par exemple). La figure 6 donne ces vitesses de régression, on peut donc voir qu'un propergol constitué de perchlorate d'ammonium et de polyuréthane aura de faibles vitesses de régression aux mélanges riches par suite de la diminution de la température de surface T_s et de la faible vitesse de régression du liant plastique qui est, dans ce cas, la substance prédominante. La figure 7 indique les variations de la vitesse de combustion en fonction du paramètre K = masse de Perchlorate d'ammonium/masse de polybutadiène ; pour un propergol normal ce rapport est de l'ordre de 5 et sur la figure présentée la combustion est encore possible pour des valeurs de K de l'ordre de 0,3 c'est-à-dire 17 fois plus petit. Ce type de propergol peut être utilisé comme générateur de gaz combustible dans les statofusées. La vitesse de combustion est faible de l'ordre de 0,1 mms^{-1} pour une pression de 10 bars. On peut augmenter la vitesse de combustion des propergols hétérogènes en utilisant des cristaux de perchlorate d'ammonium très fins de l'ordre du µm, en introduisant des additifs qui sont différents de ceux utilisés avec les propergols homogènes et en utilisant des liants oxygénés qui, comme l'indique la figure 6, ont des vitesses de régression plus élevées.

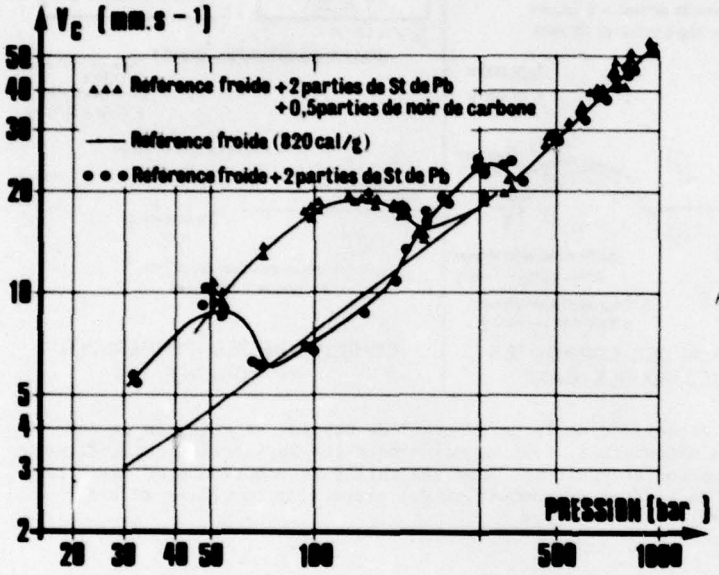

Fig. 5 – Vitesse de combustion en fonction de la pression avec effet de MESA.

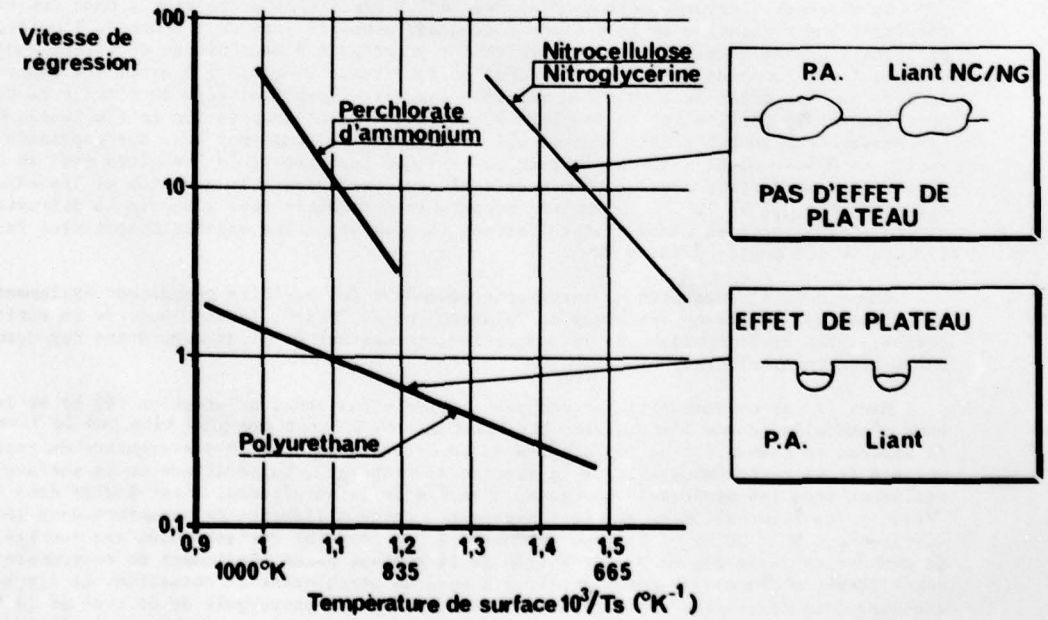

Fig. 6 – Lois vitesse de régression - température de surface des composants des propergols.

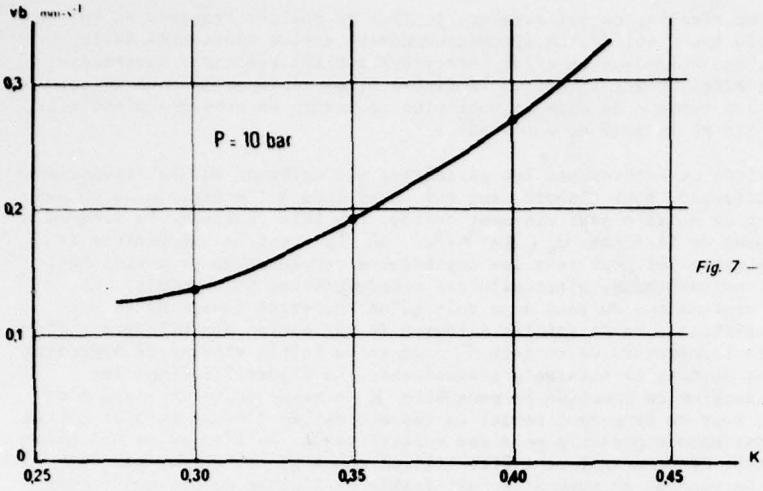

Fig. 7 – Influence du rapport K sur la vitesse de combustion.

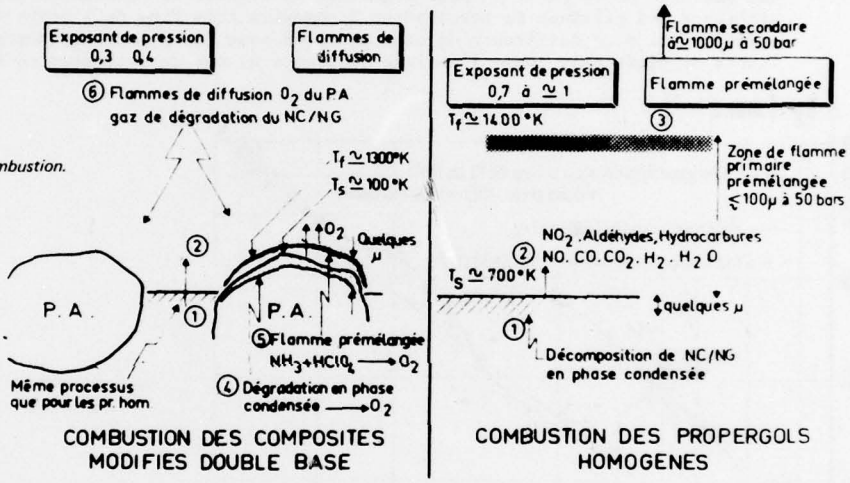

Fig. 8 – Différents types de régime de combustion.

Bien qu'on dispose à l'heure actuelle d'un large éventail de niveaux de vitesses de combustion des recherches sont encore nécessaires, tout au moins pour les applications militaires, pour les grandes vitesses de combustion et également pour une meilleure compréhension des paramètres qui agissent sur ce niveau de vitesse de combustion des propergols homogènes et hétérogènes dans une large gamme de pression.

b) - Exposant n de la pression [7]

Le choix de l'exposant est conditionné par la mission du propulseur : pour des missions nécessitant une modulation de la poussée l'exposant souhaité sera de l'ordre de l'unité, pour des missions à grande accélération on choisira des propergols à haut niveau de vitesse mais on placera le fonctionnement à la fin d'une zone de survitesse de manière à avoir des exposants voisins de zéro ou même négatifs ; pour des missions lanceurs l'exposant sera de l'ordre de 0,3 à 0,4 pour limiter en particulier le couplage entre fluctuations de pression et fluctuations de débit. Le constructeur souhaite donc trouver une large gamme de propergol avec des exposants pouvant varier de 0 à 1. D'une manière générale on sait que les propergols homogènes dont la combustion dépend fortement des processus chimiques sont très sensibles à la pression et les exposants se situent entre 0,7 et 1, quant aux propergols composites pour lesquels la diffusion des espèces comburantes et combustibles limitent la combustion, les exposants sont plus faibles et de l'ordre de $0,3 \div 0,4$ (Figure 8).

Comme nous l'avons noté au paragraphe précédent des additifs permettent également de jouer sur l'exposant en créant des zones de "plateau" ou de "Mesa", la structure de la surface du propergol, après arrêt brusque de la combustion, permettant de mieux comprendre ces domaines de combustion particuliers.

Dans le cas de composite par exemple il existe des zones de pression (68 b) où le perchlorate d'ammonium (comme l'indiquent les figures 6 et 9) régresse plus vite que le liant, la vitesse de combustion ne dépend plus de la pression mais de la distribution du rapport de mélange (comburant-combustible) à la surface du propergol. La structure de la surface change également pour les propergols homogènes à la fin de la survitesse, c'est-à-dire dans la zone de "Mesa" ; les figures 10A et 10B font apparaitre cette différence de structure dans la zone de survitesse (p = 30 b) et la zone de "Mesa" (p = 70 b) correspondant aux courbes de vitesse de combustion de la figure 5. Cet examen de la surface permet également de comprendre les exposants élevés obtenus avec des composites à base de perchlorate de potassium. La figure 11 donne quelques lois de vitesse de combustion obtenues avec des propergols de ce type et la figure 12 indique la structure de la surface après arrêt de la combustion, on observe la fusion du perchlo-

rate de potassium, donc une surface beaucoup plus lisse et donc une homogénéisation des gaz à la surface et une diminution de l'importance des processus de mélange par diffusion. Cet examen de la surface au microscope à balayage permet également de mieux comprendre le mécanisme de combustion des propergols composite-double base, cette structure est donnée sur la figure 13. La situation concernant l'exposant de la pression est résumée sur la figure 14 indiquant pour les différents types de propergol mentionnés plus haut la valeur de l'exposant n .

c) - Influence de la température initiale du bloc [8]

C'est un paramètre important qui limite l'utilisation des propergols solides, le but des recherches étant de réduire son effet. La vitesse de combustion peut être représentée pour traduire l'effet de la température initiale du bloc T_i par différentes lois, la plus classique étant $v_b = a p^n g(T_i)$ avec $g(T_i) = e^{\alpha(T_i - T_i^*)}$, T_i^* étant une température de référence et α le paramètre traduisant la sensibilité de la vitesse de combustion à la température T_i ; dans les études théoriques on utilise également des lois approchées linéaires $g(T_i) = 1 + \alpha(T_i - T_i^*)$. Si on admet une loi de régression d'Arrhenius $\alpha = \left(\frac{\partial \ln v_b}{\partial T_i}\right)_p = -\frac{T_{AS}}{T_{S^2}}$, il est donc très difficile d'éliminer cet effet. Il existe bien des catalyseurs qui diminuent la valeur de α mais sans plus ; comme la température d'activation des réactions de surface dépend de la nature du propergol, pour un propergol donné c'est aux faibles valeurs de T_s , donc aux faibles valeurs de la vitesse de combustion que la valeur de α est la plus élevée ; il est difficile dans cette situation de réduire l'influence de T_i . La figure 15 traduit cet effet, la valeur de α étant d'autant plus faible que la pression ou la vitesse de combustion (en mms^{-1}) est élevée. Dans les applications il est cependant possible de réduire le changement de la vitesse avec T_i en utilisant des propergols à exposant nul ou négatif. La figure 16 indique la différence de pression que l'on peut obtenir pour trois températures +50, +20, +31,5°C pour un propergol à exposant élevé et pour un propergol au voisinage de $n = 0$, la pression de chambre passe de 200 à 500 bars pour l'intervalle de pressions obtenu pour le premier propergol et de 295 à 325 bars pour le deuxième propergol à "mesa". Le constructeur peut donc, en jouant sur l'exposant de pression, réduire l'effet de la température initiale du bloc sur la performance de la fusée.

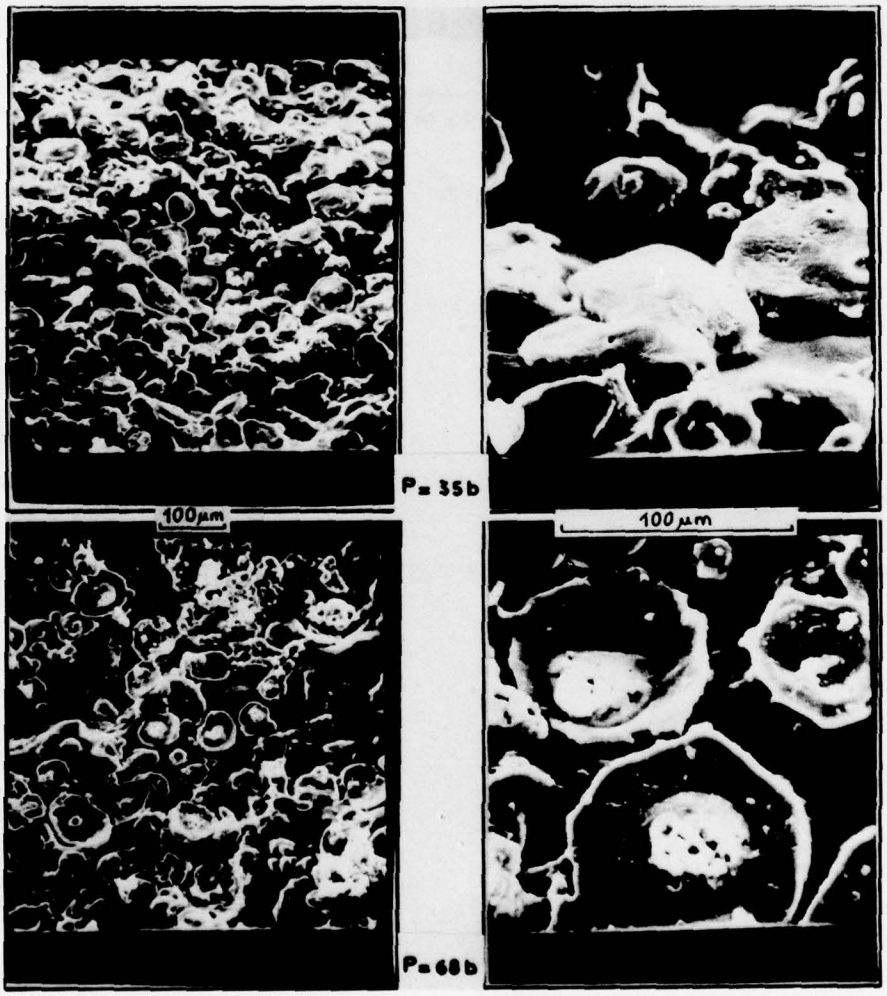

Fig. 9 – Structure de surface propergol
PA - Polyuréthane.
(72% de PA ; 90 µm, polyuréthane)

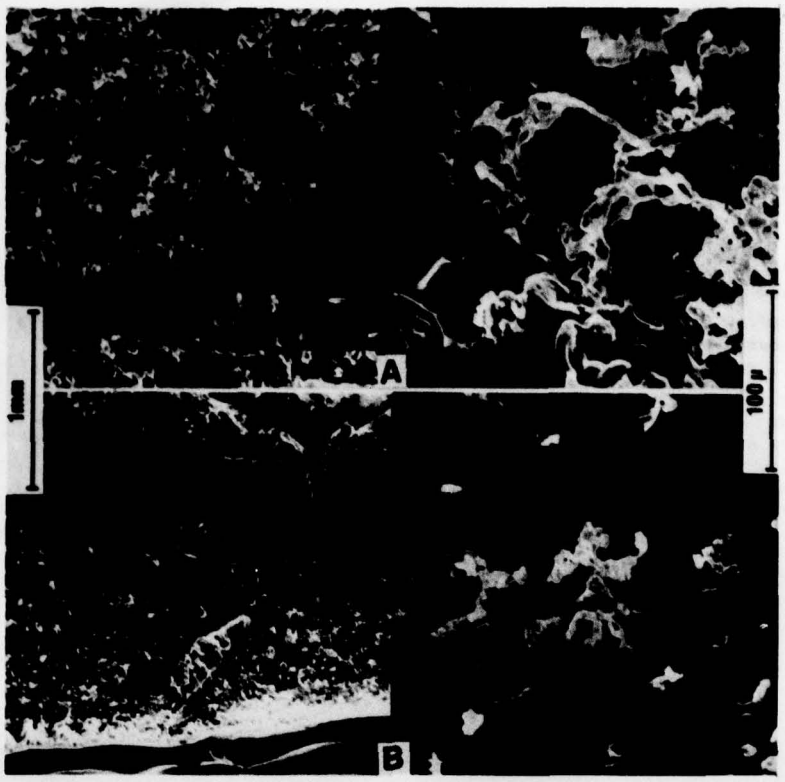

Fig. 10 – Surface des échantillons après extinction. Référence + 2 p de stéarate de plomb. A - 30 b, zone de survitesse ; B - 70 b, fin de l'effet MESA.

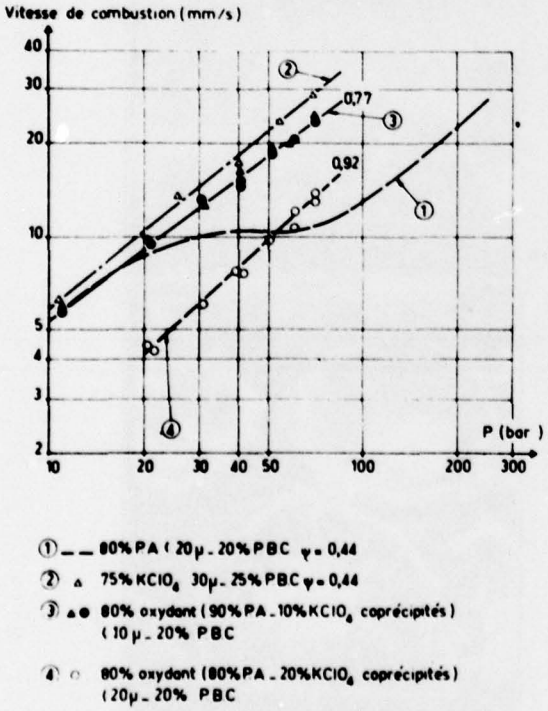

Fig. 11 – Sensibilité à la pression.

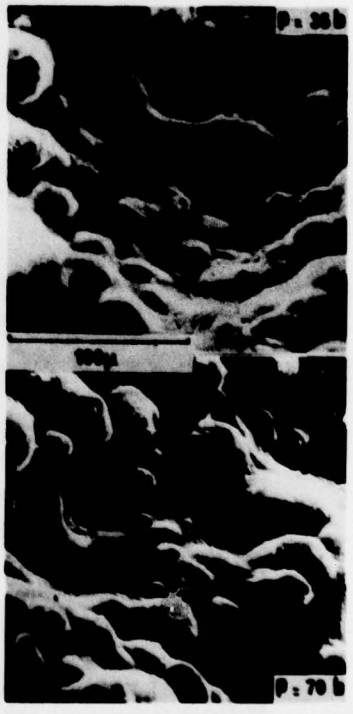

Fig. 12 – Structure de surface, propergol PK - PBC. 75% de PK, 30 µm, polybutadiène carboxylé.

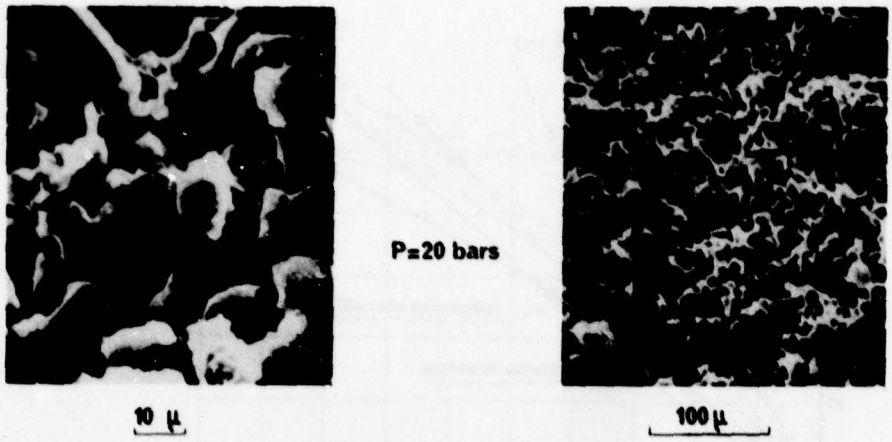

Fig. 13 – Structure de surface propergols composites modifiés double base, composition 30% PA 10 µm, liant ≃ 50% NC, ≃ 50% NG.

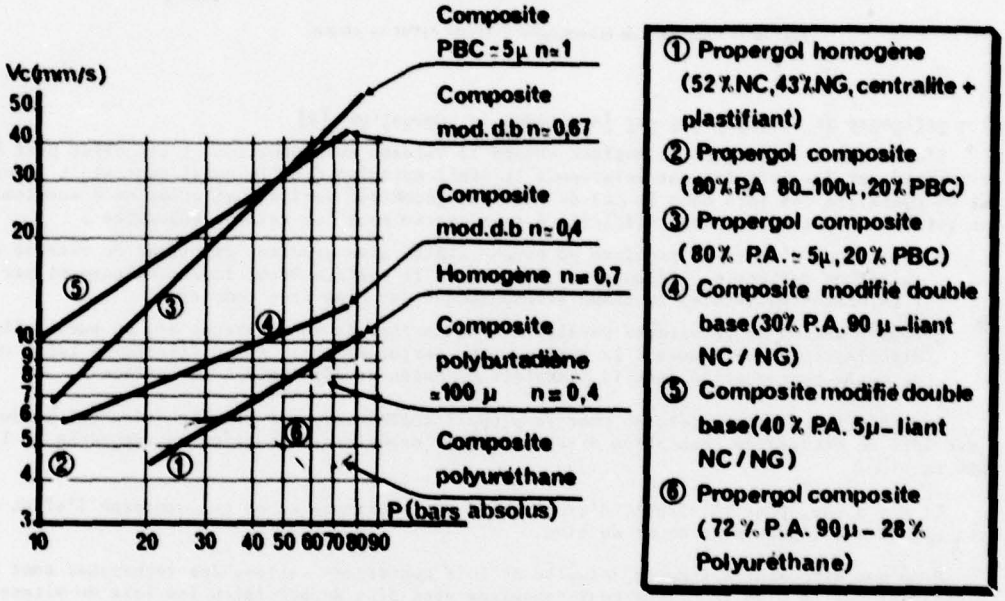

Fig. 14 – Vitesse de combustion de différents propergols.

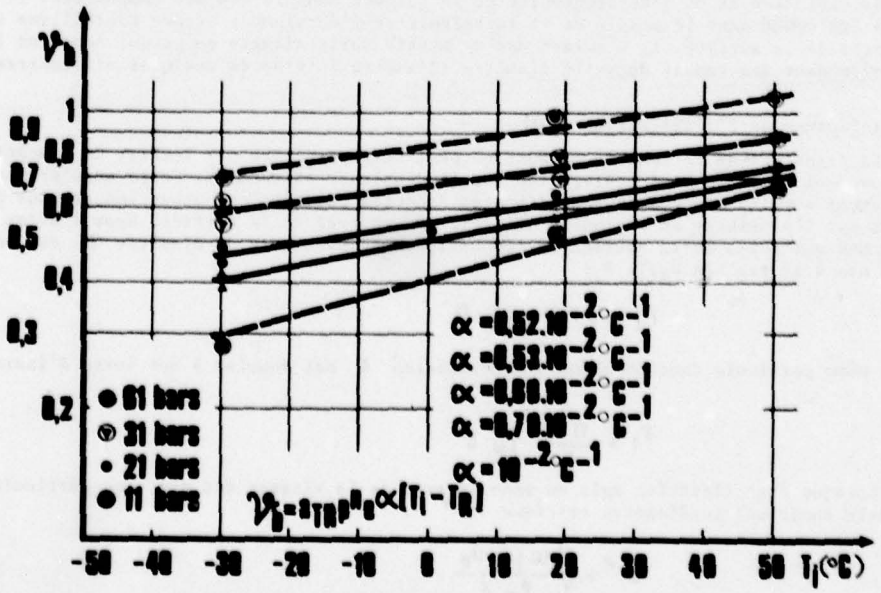

Fig. 15 – Influence de la température du bloc sur la vitesse de combustion.

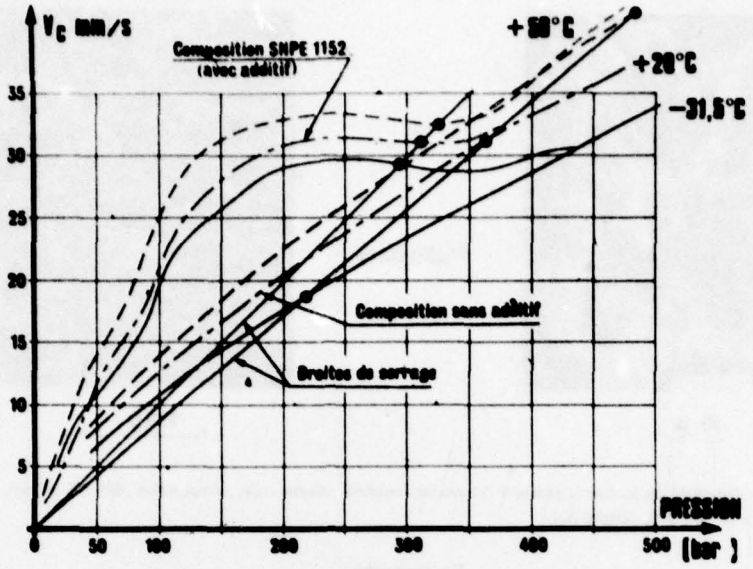

Fig. 16 – Réduction de la sensibilité à Ti par l'effet de plateau.

d) - Influence de l'écoulement sur la vitesse de combustion [9]

L'écoulement le long de la surface change la vitesse de combustion et cet effet peut être représenté par des lois faisant intervenir le débit unitaire dans le canal central. L'important est de connaître ces lois dans le cas de blocs de géométrie variée. Cet effet de l'écoulement de gaz parallèle à la surface est difficile à représenter pour les raisons suivantes :

- c'est tout d'abord un problème de couche limite avec gradient important de vitesse et injection pariétale, l'écoulement le long de la surface étant fourni uniquement par l'injection pariétale, le champ aérodynamique est donc très complexe ;
- sous l'action de la vitesse parallèle à la surface la zone gazeuse et, en particulier, la distribution des flammes à la surface, est perturbée et il est difficile de tenir compte de cette perturbation dans le transfert de masse et d'énergie à la surface.

Des théories élémentaires, et pour la plupart thermiques, ont été élaborées qui conduisent à des lois de vitesse de combustion assez près de l'expérience lorsqu'on se rapproche de l'extrémité du bloc.

Il n'y a pas, pour l'instant, d'explication satisfaisante en ce qui concerne l'effet d'érosion négative à l'extrémité amont du bloc.

Bien que disposant à l'heure actuelle de lois empiriques utiles, des recherches sont encore nécessaires sur le plan théorique pour connaitre avec plus de précision les lois de vitesse de combustion érosive en modélisant l'effet de la vitesse parallèle à la surface en tenant compte des réactions chimiques de surface dans le cas des propergols homogènes et des processus physiques de diffusion et de l'hétérogénéité de la surface dans le cas des composites. Il faut tenir compte également dans le modèle de la turbulence de l'écoulement et des tourbillons se développant près de la surface. Il n'existe pas de modèle satisfaisants en ce qui concerne l'effet d'érosion dans des canaux de petit diamètre (diamètre interne de quelques millimètres).

e) - Influence de l'accélération [10]

La structure de la zone de combustion peut être perturbée par l'effet de l'accélération due au mouvement de la fusée (accélération longitudinale ou azimutale). Cette accélération agit principalement sur les espèces denses présentes dans les produits de combustion et plus particulièrement sur l'aluminium et l'alumine qui se trouvent près de la surface. Sous l'effet de la vitesse des gaz issus de la surface en combustion, une particule de diamètre D est soumise à une force due à la traînée égale à :

$$F_T = 3\pi\mu_g v_g D$$

cette même particule dans un champ d'accélération γ est soumise à une force d'inertie F_I :

$$F_I = \frac{\pi D^3}{6} \rho_p \gamma$$

Lorsque l'accélération agit en sens inverse de la vitesse des gaz, les particules ayant un diamètre supérieur au diamètre critique D^* :

$$D^* = \sqrt{\frac{18 \mu_g v_g}{\rho_p \gamma}}$$

restent à la surface ; la vitesse des gaz pour une fraction massique Y_{Ac} d'aluminium est égale à :

$$v_g = (1 - Y_{Ac})\, \rho_p\, v_b / \rho_g$$

Pour fixer les idées lorsque δ est de l'ordre de l'accélération de la pesanteur D^* est de l'ordre de 100 à 300 μ.

Ces particules d'aluminium et d'alumine restant à la surface sont autant de points chauds locaux qui, accélérant le transfert thermique, provoquent localement des vitesses de combustion plus élevées, formant ainsi des puits dont la géométrie évolue au cours du temps ; l'effet moyen se traduit par une augmentation de la vitesse de combustion. Les lois donnant cette vitesse de combustion comparée à la vitesse de combustion sans accélération sont de la forme :

$$\frac{v_b}{v_{b_o}} = a \frac{Gr}{Re} \cos\theta + \left[\left(a \frac{Gr}{Re} \cos\theta \right)^2 + 0{,}28\, Gr^{1/2}\, S_c^{0{,}35} + 1 \right]^{1/2}$$

où θ est l'angle défini par le vecteur accélération et la normale à la surface du propergol, Gr , R_e , S_c les nombres de GRASHOF, de Reynolds et de SCHMIDT évalués dans le gaz.

L'effet combiné d'une accélération longitudinale et azimutale provoque un mouvement des particules à la surface qui modifie encore le transfert d'énergie à la surface et donc la vitesse de combustion ; il est difficile, en dehors de l'expérience, de pouvoir prédire cet effet combiné sur la vitesse de combustion.

Bien que l'effet de l'accélération soit important dans le cas des propergols solides métallisés, des accélérations de plus de 100 g peuvent également influencer la vitesse de combustion de propergols homogènes ou hétérogènes non métallisés.

2.2 - Pression limite d'allumage [11] [12]

L'étude de la pression limite d'allumage est intéressante pour deux raisons :

- une raison pratique tout d'abord ; à l'heure actuelle, pour augmenter la souplesse de fonctionnement des systèmes de propulsion à propergol solide, des techniques sont développées pour éteindre et rallumer le propulseur, l'extinction du propulseur ne peut être assurée en toute sécurité que si la pression dans le foyer est inférieure à la pression limite d'allumage ;
- une raison scientifique ensuite ; bien qu'on s'éloigne des conditions normales de combustion, il est important de connaître les lois qui définissent la pression limite pour définir le bilan énergétique à la limite d'extinction ainsi que pour valider les modèles mathématiques donnant les vitesses de combustion.

On peut concevoir un critère d'extinction basé sur la notion de débit limite critique $\dot{m}_L$. Une analyse théorique unidimensionnelle montre, en effet, que si l'on augmente les pertes de débit critique $\dot{m}_L$ varie peu de sorte que l'on peut admettre que pour $\dot{m} \leq \dot{m}_L$ il n'y a plus propagation de la flamme et le propergol s'éteint.

Ce critère a été vérifié expérimentalement de la manière suivante. La température initiale du bloc T_i a une grosse influence sur la pression limite d'extinction P_L . Dans le cas du perchlorate d'ammonium le débit unitaire $\dot{m} = \rho_p v_b$ est fonction de la température T_i en prenant en première approximation une loi $g(T_i)$ de la forme :

$$g(T_i) = 1 + \alpha T_i$$

On obtient comme condition donnant la pression limite p_L en fonction de T_i :

$$(1 + \alpha T_i) p_L^{0{,}5} = \dot{m}_L = \text{constante}$$

de sorte que :

$$p_L = \frac{K}{(1 + \alpha T_i)^2}$$

Cette loi est en accord avec les résultats expérimentaux (fig. 17). Une amélioration de la corrélation pourrait être obtenue en prenant pour $g(T_i)$ une loi plus conforme à la réalité.

On peut trouver un autre critère de condition limite à partir de la condition de propagation donnée par ZELDOVICH dans le cas d'un transfert unidimensionnel.

Le flux de chaleur q_s qui pénètre dans le solide est :

$$q_s = -\lambda_p \left(\frac{dT}{dx} \right)_{x=0} = \rho_p\, v_b\, C\, (T_s - T_i)$$

Il est possible d'exprimer T_i en fonction de v_b avec $g(T_i) = 1 + \alpha T_i$ on obtient la loi parabolique :

$$q_s = \rho_p C \left[T_s + \frac{1}{\alpha} \right] v_b - \frac{\rho_p C}{\alpha a p^n} v_b^2$$

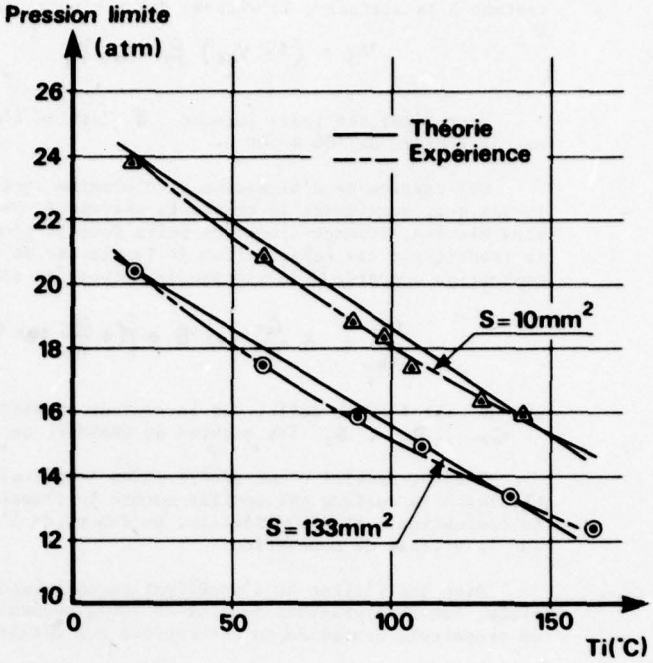

Fig. 17 – Effet de la température initiale sur la pression limite de combustion PA $\rho_p = 1{,}92$ g/cm³.

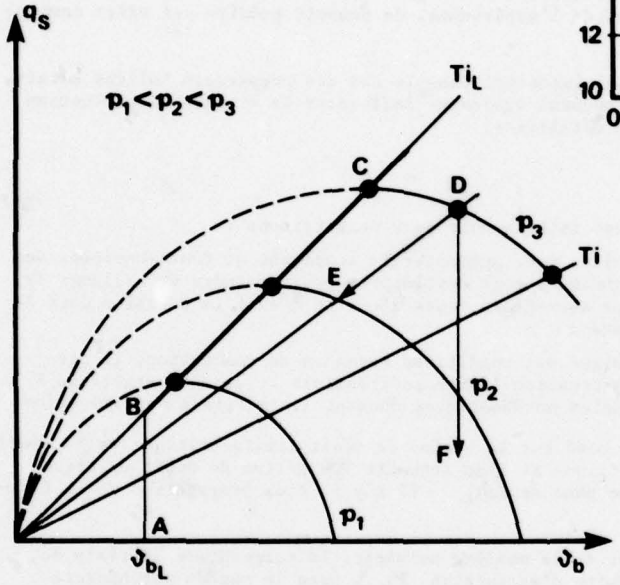

Fig. 18 – Conditions limites de propagation. Critère de Zeldovich.

T_s étant supposée constante, on obtient pour chaque pression une parabole telle que celles représentées sur la figure 11. Les maximums de v_b sont situés sur la droite $q_L = \frac{1}{2}\rho_p C v_b\left(\frac{1}{\alpha} + T_s\right)$ passant par l'origine. Cette droite correspond à une même valeur de T_i . Pour une même valeur de q_s on obtient donc deux valeurs de la vitesse de combustion : la valeur la plus faible n'a pas de réalité physique car le solide n'est pas suffisamment chauffé et la combustion ne peut se poursuivre. La valeur limite de propagation correspond donc au maximum de q_s ou encore à $\frac{\partial q_s}{\partial T_i} = 0$.

La condition s'écrit alors :

$$\left(\frac{\partial v_b}{\partial T_i}\right)_p (T_s - T_i) - v_b < 0$$

en posant $\left(\frac{\partial \ln v_b}{\partial T_i}\right)_p = \rho$ = constante, on obtient :

$$\alpha (T_s - T_i) < 1$$

La condition s'obtient en supposant $(T_s - T_i)$ constant. Le critère est un peu différent de celui basé sur le débit limite $m_L = \rho_p v_{bL}$ qui est plus restrictif comme l'indique la figure 18. Le critère du débit correspond à la portion AB et le critère de ZELDOVICH à la partie BC. Il faut également tenir compte de la variation de T_s qui est fonction de T_i de sorte que la nouvelle condition devient :

$$\alpha (T_s - T_i) + \left(\frac{\partial T_s}{\partial T_i}\right)_p < 1$$

Ce problème de la détermination de la pression limite d'extinction est d'une grande importance et n'a pas, pour l'instant, été abordé aussi bien sur le plan théorique qu'expérimental d'une manière très approfondie.

Pour conclure ce paragraphe nous ferons quatre remarques :

1/ dans le cas d'une dépressurisation lente on ne change pas le processus réactionnel et dans le plan de ZELDOVICH on se déplace suivant une droite passant par l'origine chemin DE et le processus réactionnel

est celui du régime permanent. Par contre, dans le cas d'une dépressurisation rapide on peut admettre que q_s est sensiblement constant : on se déplace suivant la droite DF, le processus réactionnel change et n'est plus celui du régime permanent. Cette influence sur la pression limite du dp/dt est indiquée sur la figure 19, elle augmente avec (dp/dt) ; les pressions limites d'allumage ou d'extinction dépendent donc des conditions de l'expérience ce qui peut expliquer les divergences observées dans les résultats ; certaines compositions sont très sensibles aux additifs, il faut donc être sûr de la composition chimique.

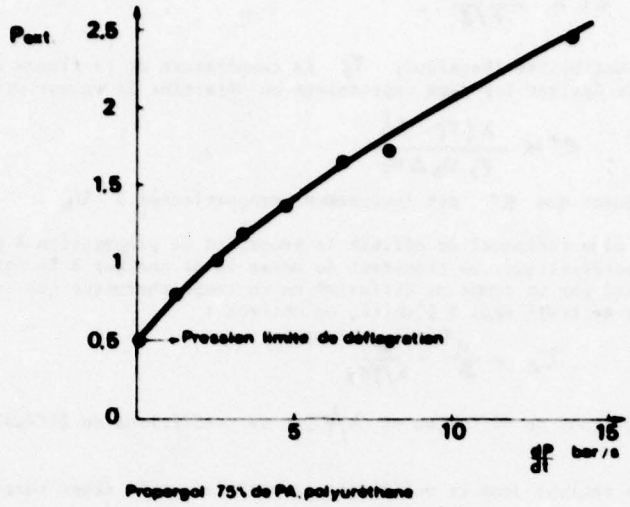

Fig. 19 – Extinction par dépressurisation.

2/ Les conditions d'extinction dans le cas d'un propergol composite peuvent dépendre du rapport de mélange local en particulier de la régression du perchlorate d'ammonium différente de celle du liant. La détermination de la pression limite doit tenir compte de ce rapport de mélange à l'extinction pouvant provoquer l'arrêt de la combustion.

3/ La recherche de propergols à pression limite d'allumage élevée est importante pour certaines applications où après extinction du bloc le rallumage est pratiquement exclu.

4/ Cette détermination de la pression limite de déflagration pourrait également se placer dans l'étude de la combustion en transitoire, comme elle est très près des conditions de vitesse de combustion en régime permanent nous avons préféré la faire figurer dans ce paragraphe.

2.3 - Propagation de la combustion dans les cavités [13] [14]

Par suite de défauts dans le bloc au cours de sa fabrication, sous l'effet de tension au moment de l'allumage ou pendant le stockage prolongé, des fissures peuvent apparaître qui modifient l'évolution de la combustion. Il est donc important pour le constructeur de pouvoir prédire les modifications apportées à la combustion par suite de la présence de ces fissures. T. GODAI a étudié en particulier la propagation de la flamme en considérant différentes géométries de fissures ; dans ce qui suit nous distinguerons deux cas :

- orifices à section circulaire percés dans le bloc, le canal étant fermé à une extrémité,
- canal ouvert aux deux extrémités (figure 20).

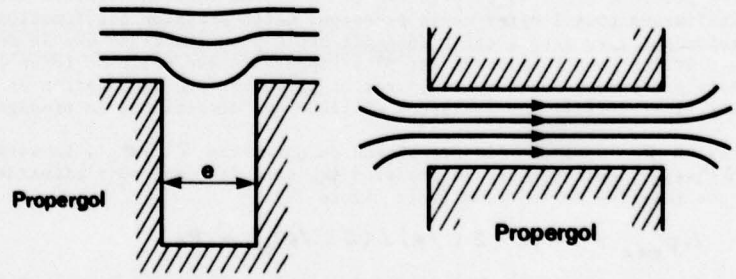

Fig. 20 – Propagation de la combustion dans des fissures.

a) - Canal fermé à une extrémité

Une telle configuration est représentée sur la figure 20a, lorsqu'on diminue le diamètre de l'orifice e ou l'épaisseur de la fente rectangulaire, on aboutit à un diamètre critique e^* au-dessous duquel il n'y a plus propagation de la flamme dans le canal. Ce diamètre ou épaisseur e^* est peu sensible à la température initiale du bloc, décroît lorsque la pression aug-

mente, et croît lorsque le pourcentage en aluminium augmente. On obtient une assez bonne corrélation lorsqu'on évalue e^* en fonction de la vitesse de combustion, e^* diminuant lorsque la vitesse de combustion augmente. T. GODAI a donné l'interprétation suivante : considérons une fissure de longueur L et d'épaisseur e, le taux d'énergie libérée par unité de surface est égal à $2L v_b \rho_p \Delta h_s$ où ρ_p est la masse volumique du propergol, Δh_s l'énergie libérée par unité de masse à la surface. La perte est proportionnelle au gradient de température à la surface et égale à :

$$2L\lambda \frac{T_f - T_s}{e/2} .$$

λ est la conductibilité thermique, T_f la température de la flamme et T_s la température à la surface. En égalant les deux expressions on détermine la valeur critique e^* de e :

$$e^* \propto \frac{\lambda (T_f - T_s)}{\rho_p v_b \Delta h_s}$$

cette relation indiquant que e^* est inversement proportionnel à v_b .

Il nous paraît plus rationnel de définir la propriété de propagation à partir de la considération de temps caractéristique. Le transfert de masse et de chaleur à la surface et provenant du gaz est caractérisé par un temps de diffusion ou un temps thermique qui lui est équivalent si on suppose le nombre de LEWIS égal à l'unité, on obtient :

$$\tau_g = \frac{e^2}{\mathcal{D}} = \frac{e^2}{\lambda/\rho c_p}$$

$\mathcal{D}$ étant le coefficient de diffusion et $\lambda/\rho c_p$ le coefficient de diffusivité thermique dans le gaz.

Le transfert de chaleur dans le solide est caractérisé par le temps thermique :

$$\tau_{th} = \frac{\lambda_p / \rho_p C}{v_b^2}$$

où λ_p est le coefficient de conductivité thermique dans le solide et C sa chaleur spécifique.

Il y aura propagation si le temps de diffusion est suffisamment long par rapport au temps thermique :

$$\tau_g > \tau_{th}$$

c'est-à-dire si $e^2/\mathcal{D}$ est suffisamment grand par rapport au temps thermique.

La valeur e^* peut être définie pour $\tau_g = \tau_{th}$ ou encore :

$$e^* \propto \frac{1}{v_b} \sqrt{\frac{nRT_f}{p}} \sqrt{\frac{\lambda_p \lambda}{\rho_p C C_p}}$$

On retrouve bien la corrélation de T. GODAI (fig. 21). Si le temps de diffusion n'est pas suffisant il n'y a pas de propagation possible.

Les résultats qualitatifs déduits de l'expérience sont retrouvés : l'épaisseur e^* est inversement proportionnelle à v_b , augmente avec T_f et varie peu avec la température initiale du bloc.

Un autre problème lié à la propagation de la flamme dans une fissure est celui de la propagation de la fissure sous l'effet de la pression. Cette pression est fonction de son épaisseur e et de sa profondeur L , sous l'effet du débit brûlé plus important que le débit sortant de la fissure, la pression dans la fissure est plus importante que celle du foyer ; cette pression peut être suffisante pour écarter les lèvres et provoquer une propagation de la fissure dans le bloc. On peut ainsi définir une épaisseur critique qui conditionne la propagation de la fissure.

La pression p_c dans une fissure dépend du paramètre $2L/e$. La surpression maximale $p_c - p_o = \Delta P_{max}$, entre p_c et la pression p_o dans la bombe où s'effectue la combustion est donnée par une relation de la forme (voir figure 22) :

$$\Delta p_{max} = 1{,}1\, p_o\, (2L/e) / (2L/e)_{cr} - p_o$$

en introduisant une valeur $(2L/e)$ critique pour laquelle $\Delta p_{max} = 0{,}1\, p_o$. Cette valeur de ΔP_{max} est supérieure à celle donnée par une théorie élémentaire :

$$\Delta P_{max} = (\rho_p v_b)^2 \cdot \frac{nRT}{p_o} \cdot \left(\frac{2L}{e}\right)^2$$

obtenue à partir du bilan de quantité de mouvement.

Sous l'effet de la pression le propergol peut se déformer de δ , e_o étant l'épaisseur initiale :

$$e = e_o + 2\delta$$

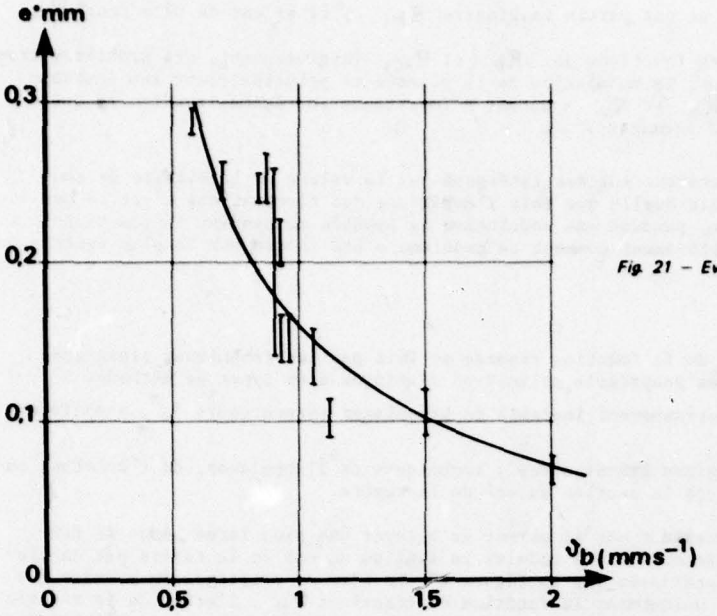

Fig. 21 – Evolution du diamètre critique avec la vitesse de combustion.

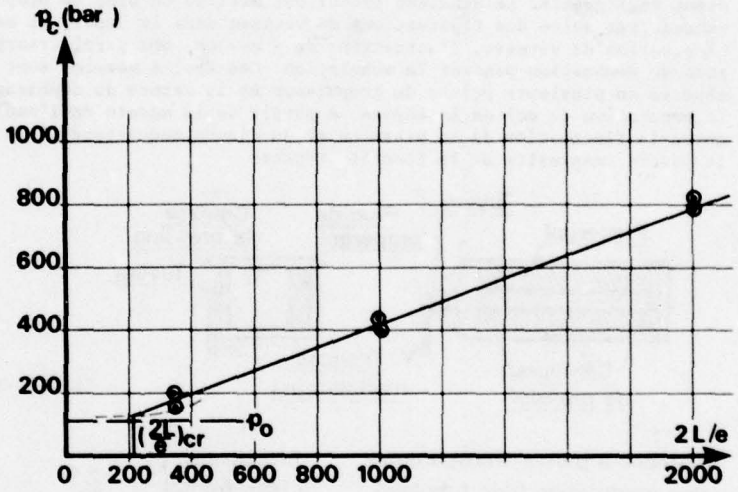

Fig. 22 – Evolution de la pression dans la fissure.

avec : $\delta = \Delta p_{max} \frac{L}{E}(1 - \nu)^2$

où E est le module d'élasticité et ν le coefficient de Poisson.

Si la déformation est suffisante la fissure peut se propager, il existe peu de résultats sur la propagation des fissures sous l'effet de contraintes durant un temps très court, il est nécessaire de tenir compte ici du facteur temps car l'excès de pression dans la fissure dû à la combustion dure un temps de l'ordre du centième de seconde.

b) - Canal ouvert aux deux extrémités

Dans cette configuration un écoulement gazeux peut alors s'établir à l'intérieur du canal, le transfert de masse et d'énergie à la surface du propergol se fait alors par convection et la propagation de la flamme dans le canal où la fissure est régie par les mêmes phénomènes qui conditionnent l'allumage d'un bloc de poudre (fig. 20b).

3 - RECHERCHES PORTANT SUR LA COMBUSTION EN REGIME TRANSITOIRE

3.1 - Fonction réponse de la surface du propergol en combustion [15] à [28]

En régime transitoire il est important de connaître la fluctuation de débit unitaire brûlé consécutive à une fluctuation de pression ou une fluctuation de l'écoulement parallèle à la surface. On pose pour le débit unitaire $\tilde{m} = \bar{m} + m'$, pour la pression $\tilde{p} = \bar{p} + p'$ et pour la vitesse $\tilde{u} = \bar{u} + u'$ faisant intervenir les grandeurs moyennes et fluctuantes. Sous une forme linéarisée, la fonction réponse, en séparant l'effet de la pression de l'effet de la vitesse, s'écrit :

$$\frac{m'}{\bar{m}} = R_p \frac{p'}{\bar{p}} + R_u \frac{u'}{\bar{u}}$$

R_p comportant une partie réelle R_{pr} et une partie imaginaire R_{pi}, il en est de même pour R_u.

Dans tout problème transitoire les fonctions de R_p et R_u interviennent, ces problèmes transitoires concernent l'allumage, l'extinction, la modulation de la poussée et principalement les instabilités de combustion ; la connaissance de R_p et R_u a autant d'importance en régime transitoire que celle de la vitesse de combustion en régime permanent.

D'une manière plus générale le constructeur est intéressé par la valeur de la vitesse de combustion en transitoire sous une forme valable quelle que soit l'amplitude des fluctuations c'est le cas pendant la phase d'allumage ou d'extinction, pendant une modulation de poussée ou pendant le fonctionnement instable du propulseur. Examinons brièvement comment ce problème a été abordé sur le plan expérimental et sur le plan théorique.

- Recherches expérimentales :

La détermination expérimentale de la fonction réponse se fait par les techniques classiques utilisées en instationnaire. Dans le cas des propergols solides on distingue deux types de méthodes :

- celles qui exploitent le fonctionnement instable du propulseur (propulseurs L^*, propulseurs en T, propulseurs réels),
- celles qui provoquent des régimes transitoires : techniques de l'impulseur, de l'échelon, ou de la modulation sinusoïdale de la section du col de la tuyère.

Le deuxième type est plus intéressant car il permet de balayer une plus large bande de fréquences ; une technique développée à l'ONERA consiste à moduler la section du col de la tuyère par un disque. Les deux propulseurs utilisés sont représentés sur la figure 23. Le bloc de propergol du premier est à combustion frontale de manière à évaluer uniquement la fonction de transfert R_p, l'effet de la vitesse étant négligeable. Le deuxième propulseur utilise un bloc de propergol tubulaire à combustion radiale. Dans ce cas, par suite des fluctuations de vitesse dans le canal, il est possible de voir l'effet du couplage fluctuation de vitesse, fluctuation de pression. Une paroi transparente (figure 24) permet d'observer la zone de combustion pendant la modulation. Les seules mesures sont des mesures de pression à court temps de réponse en plusieurs points du propulseur et la mesure du déphasage entre la fluctuation de pression et la modulation du col de la tuyère. A partir de la mesure de l'amplitude de la pression et du déphasage entre la fluctuation de la pression et du disque modulateur il est possible de déduire la partie réelle et la partie imaginaire de la fonction réponse.

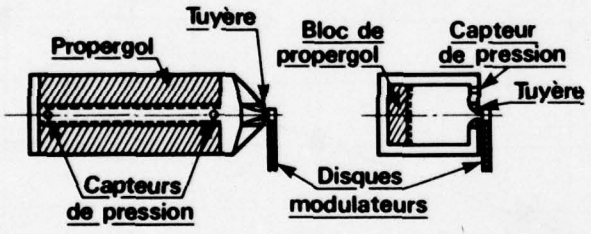

Fig. 23 – Propulseurs ONERA d'étude de la fonction de transfert.

Chambre à parois transparentes avec modulation bloc tubulaire

Propulseur à bloc frontal

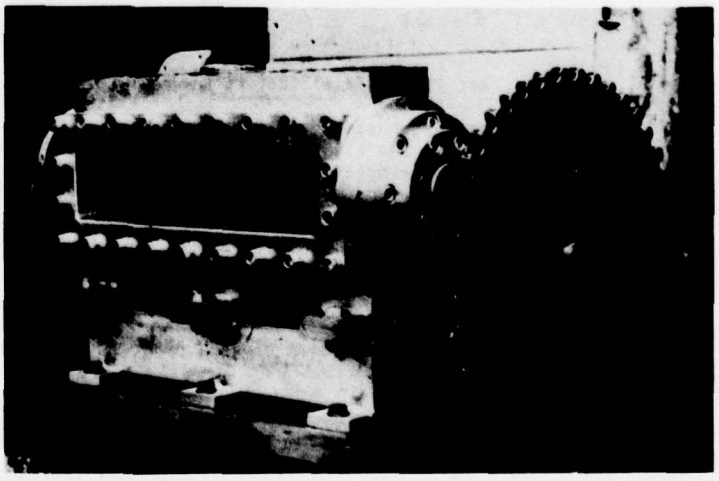

Fig. 24 – Propulseur à éjection modulée.

A côté de ces méthodes de mise en oeuvre et d'interprétation complexe, on dispose de techniques plus simples permettant d'avoir des données sur la vitesse de combustion en régime transitoire ; c'est le cas, par exemple, des propulseurs à temps de combustion court (quelques dizaines de millisecondes). Nous donnons sur la figure 25 une de ces techniques qui consiste à placer l'échantillon de propergol dans une bombe dans laquelle on peut faire varier le volume de l'échantillon et le volume mort. Cette bombe est équipée d'un transducteur ultrasonore pour mesurer en cours de combustion la vitesse de régression de l'échantillon, d'un capteur de pression à court temps de réponse, d'un système d'allumage de la surface du propergol et d'un système de mise en pression.

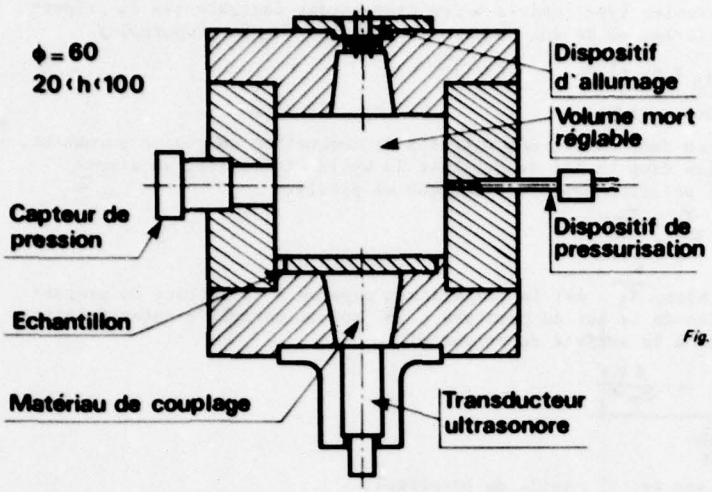

Fig. 25 – Dispositif d'étude de la vitesse de combustion des propergols homogènes : schéma.

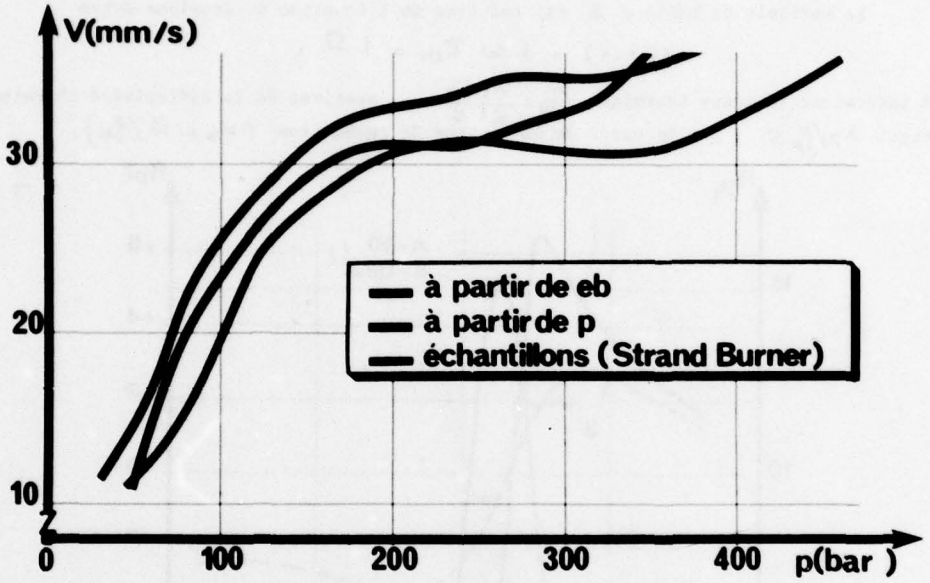

Fig. 26 – Vitesse de combustion des homogènes : comparaison des dépouillements (SD 1152, h = 100).

Après la mise à feu du propergol, la pression monte dans la bombe et la rapidité de cette montée dépend du volume mort. On détermine donc la vitesse de combustion en fonction de p et du dp/dt. Ces résultats sont portés sur la figure 26, la vitesse de combustion est donnée en fonction de la pression, on note une nette différence entre la vitesse de combustion mesurée en transitoire à partir de l'épaisseur de combustion e_b et celle déterminée en régime permanent (strand burner). En partant des équations du bilan de masse et du bilan d'énergie et de la mesure de la pression dans la bombe, on peut déterminer la vitesse de combustion en transitoire, cette mesure est différente de celle obtenue à partir de e_b montrant les difficultés d'interprétation.

Toutes ces techniques de mesure de la vitesse en transitoire aboutissent à des relations de la forme :

$$v_b = v_{b_0} \left(1 + b \frac{\lambda_p}{\rho_p C v_{b_0}^2} \frac{d \ln p}{dt}\right)$$

b est un paramètre caractéristique du propergol et dépend de l'exposant n de la pression, $\frac{\lambda_p}{\rho_p C}$ est la diffusivité thermique du propergol et v_{b_0} la vitesse de combustion du régime permanent. Les lois de ce type, quoique approchées, sont très utiles pour l'étude du fonctionnement en transitoire.

- <u>Recherches théoriques</u> :

Elles portent sur deux types d'analyse :

a) - une description aussi précise que possible des étapes de combustion suivie d'une linéarisation des équations instationnaires décrivant ces étapes ;

b) - une étude non linéaire du transfert de chaleur dans le solide en faisant l'hypothèse que, dans le gaz, la réponse est suffisamment courte pour qu'il soit possible d'utiliser les résultats du régime permanent.

- L'ensemble des théories du premier type conduit à des expressions équivalentes du propergol qui peuvent être mises sous la forme, en ce qui concerne la réponse R_p du propergol :

$$R_p = \frac{n\,AB + n_s(\Delta - 1)}{\Delta + \frac{A}{\Delta} - (A+1) + AB}$$

où n est l'exposant de la pression dans la loi des vitesses de combustion du régime permanent,
n_s est l'exposant de la pression dans la loi de pyrolyse du solide (comburant et liant)
A est un paramètre qui est en relation avec la cinétique de pyrolyse

$$A = \left(1 - \frac{T_i}{\overline{T_s}}\right) \frac{T_{AS}}{\overline{T_S}}$$

T_i est la température du bloc, $\overline{T_s}$ est la température moyenne à la surface du propergol, T_{AS} la température d'activation de la loi de pyrolyse ; B est un paramètre caractéristique de l'énergie Δh_s mise en jeu à la surface du propergol :

$$B = \frac{\frac{C_p}{C} - \frac{T_i}{\overline{T_s}} - \frac{\Delta h_s}{c_p \overline{T_s}}}{1 - \frac{T_i}{\overline{T_s}}}$$

C_p est la chaleur spécifique du gaz et C celle du propergol.

La variable de Laplace Δ est solution de l'équation du deuxième degré

$$\Delta(\Delta - 1) = i\,\omega\,\tau_{th} = i\,\Omega$$

où intervient le temps thermique $\tau_{th} = \frac{\lambda_p \rho_p}{\overline{m}^2 C}$ quotient de la diffusivité thermique du propergol $\lambda_p / \rho_p C$ par le carré de la vitesse de combustion ($v_b = \overline{m} / \rho_p$).

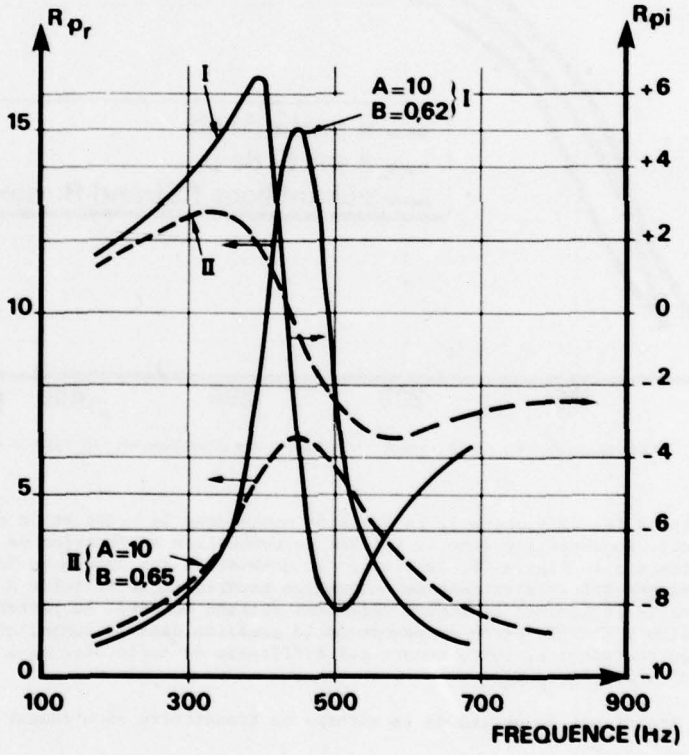

Fig. 27 – Variations de Rp_r et Rp_i avec la fréquence.

La figure 27 donne les variations de la partie réelle et imaginaire de R_p en fonction de la fréquence $N = \omega/2\pi$ pour une valeur de $A = 10$ et pour deux valeurs de B ($B = 0{,}62$ et $0{,}65$). On observe un maximum pour la partie réelle correspondant à la fréquence pour laquelle le propergol possède le maximum de sensibilité. Cette application souligne l'importance de B sur ce maximum.

- Le deuxième type est basé sur une méthode due à ZELDOVITCH. La vitesse de combustion est fonction, en régime permanent, des trois paramètres principaux : la pression p_o, la température initiale du bloc T_i et l'effet d'érosion E°,

$$v_b^\circ = v_b^\circ(p^\circ, T_i, E^\circ) \quad ;$$

il en est de même de la température de surface T_s° et de la température de fin de combustion T_f° fonctions des mêmes paramètres ; ces trois fonctions (v_b°, T_s° , T_f°) conduisent à définir 9 paramètres traduisant leur sensibilité aux variables p° , T_i , ε . La température de surface peut être liée à la vitesse de combustion par une loi type Arrhenius qui est supposée valable en régime instationnaire $\rho_p v_b^\circ = B \exp(-T_{AS} / T_s^\circ)$ ce qui a pour effet d'éliminer une équation. Le terme d'érosion E° dépend du débit unitaire $\rho^\circ u^\circ$ des gaz dans le canal central et du coefficient de frottement à la surface C_f fonction du nombre de Reynolds local :

$$E^\circ = \frac{\rho^\circ u^\circ}{\rho_p v_b^\circ} \; C_f^{\circ\, 1/2}$$

La température initiale T_i qui est un paramètre du propergol peut être éliminée en faisant intervenir le bilan d'énergie à la surface ; en régime permanent T_i est égal à :

$$T_i = T_s^\circ - \frac{\lambda_p}{\rho_p C v_b^\circ} f^\circ$$

où f° est le gradient de température dans le solide en régime permanent.

Nous pouvons construire un système de trois fonctions v_b°, T_s° , T_f° fonctions de trois paramètres p° , f° , E° qui se situent dans le gaz ou à la surface du propergol, donc utilisables en régime instationnaire.

En effet la méthode de ZELDOVITCH consiste à admettre que le gaz répond instantanément à toute perturbation, dans cette zone il est donc possible d'utiliser toutes les données du régime permanent, seule reste instationnaire l'équation de propagation de la chaleur dans le solide qui est de la forme :

$$\rho_p C \left(\frac{\partial T}{\partial t} + v_b \frac{\partial T}{\partial y} \right) = \frac{\partial}{\partial y} \left(\lambda_p \frac{\partial T}{\partial y} + q_R \right)$$

la direction y étant perpendiculaire à la surface et q_R étant le flux rayonné ; les conditions limites à la surface sont la température, T_s fonction du temps ainsi que le gradient f de la température ($\left(\frac{\partial T}{\partial y}\right)_s = f$). La démarche est alors la suivante, la vitesse de combustion en régime permanent est de la forme : $v_b = f(p)\, g(T_i)\, h(\varepsilon)$ avec $h(\varepsilon)$ par exemple $h = \frac{\rho u}{\rho_p} C_f^{1/4} \frac{1 + C_1(E - E_s)}{E}$ de sorte que :

$$T_i = \tilde{g}\left(\frac{v_b}{f(p)\, h(\varepsilon)} \right)$$

si on admet de plus que la vitesse de combustion et la température de surface sont liées par la condition d'Arrhenius les conditions aux limites s'écrivent :

$$\begin{cases} f = \dfrac{\rho_p C v_b}{\lambda_p} \left[\dfrac{T_{AS}}{\log_e \frac{B}{v_b}} - \tilde{g}\left(\dfrac{v_b}{f(p)\, h(\varepsilon)} \right) \right] = \varphi(v_b, p, \varepsilon) \\ T_s = \dfrac{T_{AS}}{\log_e \frac{B}{v_b}} = \psi(v_b) \end{cases}$$

Nous plaçant à la surface du solide avec des fluctuations connues de $p(t)$ et $E(t)$, l'intégration de l'équation de propagation de la chaleur conduit à la détermination de $v_b(t)$. La figure 28 indique les variations dans le temps de la vitesse de combustion en fonction de fluctuations sinusoïdales de la pression pour deux niveaux d'amplitude 1% et 10%. Ces quelques remarques traduisent l'orientation des recherches avec d'une part le développement de théories linéaires décrivant de mieux en mieux l'évolution de la combustion et d'autre part l'élaboration de théorie non linéaire portant sur des modèles simplifiés. La connaissance de la fonction réponse du propergol va nous permettre d'aborder les problèmes du régime transitoire.

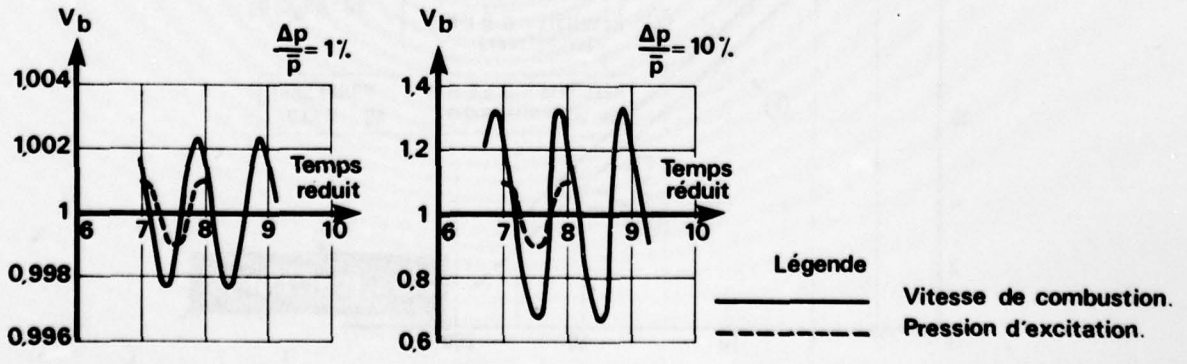

Fig. 28 – Réponse à une évolution sinusoïdale de la pression.

3.2 - Allumage du propulseur [1]

Le régime transitoire de l'allumage peut être analysé par des techniques analogues à celles que nous venons de décrire et il est possible d'utiliser la fonction réponse du propulseur lorsque tout le bloc est allumé ; il reste à étudier la phase avant l'allumage complet de la surface ; il faut en effet, au moyen d'un dispositif d'allumage, remplir le canal de gaz chauds, transmettre de l'énergie à la surface du propergol par convection et rayonnement. Ce dispositif d'allumage étant placé à l'extrémité du propulseur il faut tenir compte de la répartition dans le temps et l'espace du flux de chaleur transmis à la surface à partir de laquelle on peut admettre que le propergol est allumé et émet des gaz chauds à la température de fin de combustion.

Cette analyse a permis de calculer les courbes de montée en pression et de définir correctement le dispositif d'allumage caractérisé par le débit de produits de combustion émis et son temps de fonctionnement.

Examinons quelques problèmes particuliers de l'allumage.

a) Les délais d'allumage de la plupart des propergols sont inversement proportionnels au carré du flux incident, cette loi a été vérifiée par de nombreuses expériences ; la figure 29 indique par exemple les résultats obtenus sur un propergol composite jusqu'à des flux de 50 cal.cm^{-2}s^{-1}, les flux étant mesurés sur des échantillons ou sur des blocs réels. Ce résultat indique l'importance du débit de l'allumeur sur les délais d'allumage et permet de préciser ce débit. De cette manière l'allumeur peut être caractérisé par le débit correspondant au délai choisi et par le temps de fonctionnement de l'allumeur suffisant pour remplir la cavité, couvrir toute la surface du propergol et assurer un allumage complet de toute la surface.

b) Bien que des progrès substantiels ont été réalisés et qu'une modélisation correcte du processus soit actuellement possible, l'allumage des petits propulseurs pose encore quelques problèmes. Ce type de propulseurs est représenté sur la figure 30a ; ils sont caractérisés par de grandes surfaces de comcombustion pour un volume donné et des temps de combustion courts ; le bloc est constitué par un fagot de tubes de quelques millimètres de diamètre interne ou par des lamelles très rapprochées. Les courbes de pression obtenues sont données sur la figure 30b pour les blocs tubulaires et les blocs lamellaires ; ce type de bloc ne fonctionne pratiquement qu'en régime transitoire. Pour diverses raisons l'allumeur est placé côté tuyère et la complexité des problèmes provient de ce que la surface de propergol à initier est grande par rapport au débit de l'allumeur et qu'il est difficile de prévoir la progression des jets chauds et donc la progression de l'allumage qui conditionne l'évolution du débit dans le temps.

Comme les canaux sont étroits (quelques millimètres) les effets des couches limites sont prépondérants, ces effets ont lieu en écoulement transitoire avec pénétration du jet chaud de l'allumeur dans une direction puis établissement de l'écoulement de gaz de combustion du propergol dans une direction opposée. Pour décrire un peu mieux l'écoulement et analyser les mécanismes prépondérants, on utilise des propulseurs à voyant comme celui qui est représenté sur la figure 31, la progression de la combustion est étudiée dans un canal de 3 mm, le propulseur est équipé de capteurs de pression, de photodiodes et de fluxmètres.

Comme ces propulseurs sont de petites dimensions leur mise au point est effectuée en multipliant le nombre d'essais, il serait préférable d'améliorer les modèles de prédiction de l'évolution de la pression par des recherches analytiques plus poussées.

c) Nous avons vu que pendant la phase d'allumage il était possible d'utiliser la vitesse de combustion du régime transitoire, une autre difficulté provient de ce qu'il faut tenir compte également de la chaleur introduite dans le propergol pendant la phase d'initiation de la combustion, c'est un problème analogue à celui traité au paragraphe 3.2 mais qui se complique ici par son caractère tridimensionnel avec comme conditions aux limites une distribution dans le temps et l'espace du flux de chaleur apporté à la surface du propergol par le jet issu de l'allumeur.

d) Nous laissonsde côté tous les problèmes spécifiques qui apparaissent dans la définition de l'allumeur et dans la recherche pour chaque application de l'allumeur optimal.

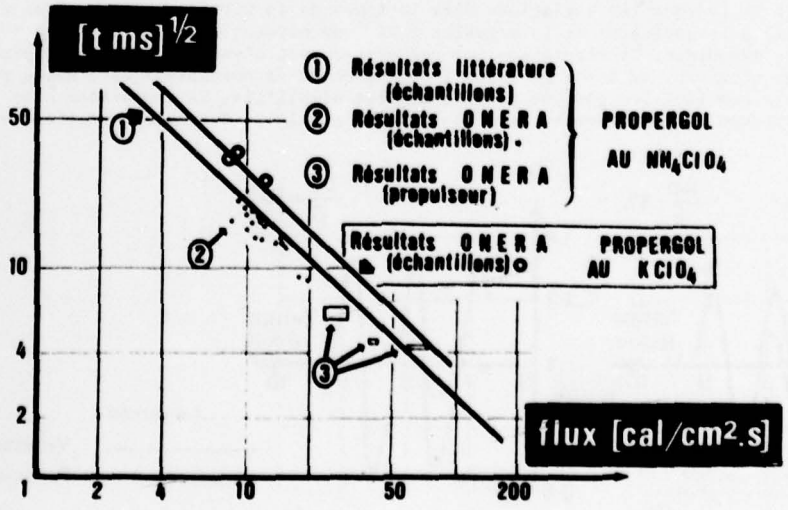

Fig. 29 – Allumage par jet de gaz chaud.

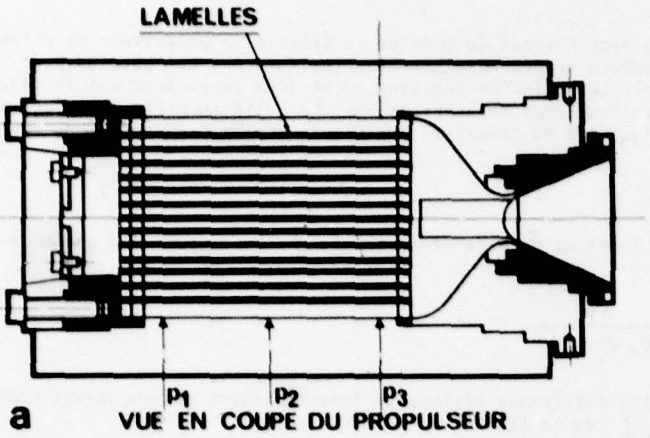

Fig. 30 — Chargements à court temps de combustion.
a - propulseur lamellaire $K_2 = 6$;
b - résultats expérimentaux.

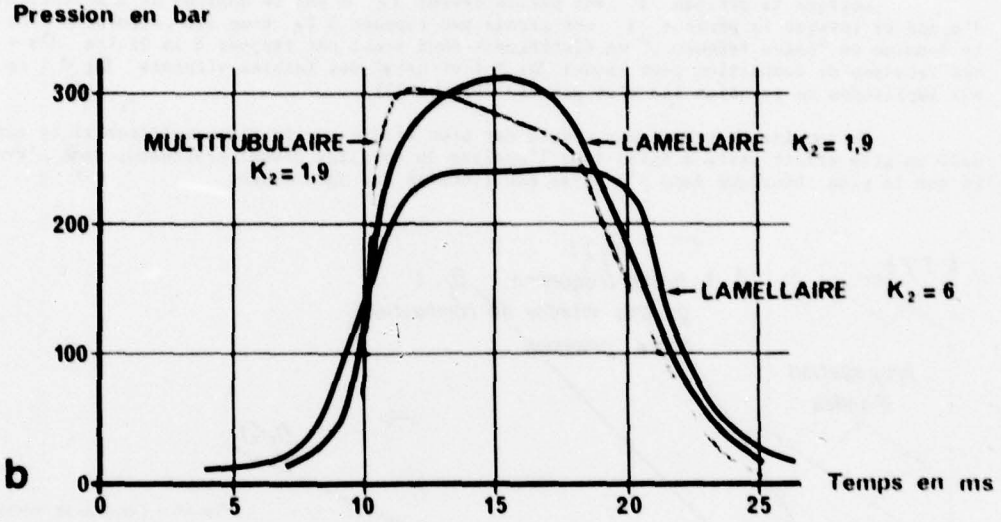

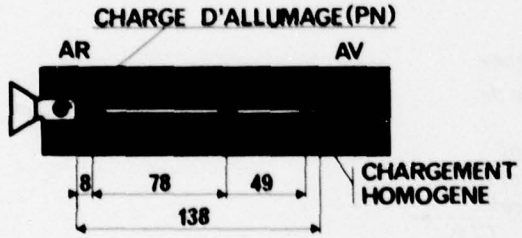

Fig. 31 — Propulseur d'étude de l'allumage d'un chargement tubulaire.

3.3 - Extinction du propulseur [29] [30]

Nous avons déjà abordé ce problème au niveau de l'échantillon dans le paragraphe consacré aux pressions limites. L'extinction du propulseur peut être obtenue par une dépressurisation rapide réalisée par agrandissement du col ou extinction d'une partie de la surface de combustion par injection d'eau.

Ce problème de l'extinction du propulseur peut être abordé dans sa première phase en introduisant la fonction réponse donnée au § 3.1. On note cependant des phénomènes complexes pendant la phase d'extinction comme, dans le cas des propergols composites, une augmentation de la luminosité à la surface pendant la dépressurisation due à l'hétérogénéité du propergol et également une variation locale du rapport de mélange, la loi du débit de pyrolyse du liant variant en fonction du temps d'une manière différente de celle du perchlorate d'ammonium. Il est difficile dans l'état actuel de nos connaissances de tenir compte de ces phénomènes mais ce problème sera abordé plus en détail au cours des prochaines séances.

3.4 - Propulseur modulé [31]

Nous avons vu qu'il était possible au banc d'essai de moduler le débit d'un propulseur en faisant varier périodiquement la section du col de la tuyère et des résultats intéressants ont été obtenus pour déterminer la fonction de transfert du propergol. Le régime de fonctionnement d'un propulseur modulé dépend du paramètre de DAMKOHLER défini par le rapport d'un temps caractéristique t_c lié au temps de séjour des gaz brûlés dans le foyer à un temps thermique t_{th} lié au transfert thermique dans le propergol. t_c est la constante de temps du foyer :

$$t_c = \frac{1}{\gamma} \frac{M^\circ}{\dot{m}_{b^\circ}}$$

où M° est la masse des gaz contenus dans le foyer et $\dot{m}_{b^\circ}$ le débit brûlé. γ le rapport des chaleurs spécifiques. Le temps thermique t_{th} est égal à :

$$t_{th} = \frac{\lambda_p}{\rho_p C \, v_{b^\circ}^2}$$

La période de modulation étant T, les différents régimes de fonctionnement du propulseur modulé peuvent être décrits dans le plan $[T/t_{th}, T/t_c]$ de la figure 32.

Lorsque la période T est petite devant t_c c'est le domaine de l'acoustique avec propagation d'ondes et lorsque la période T est grande par rapport à t_c tous les paramètres sont en phase, c'est le domaine de "basse fréquence" en distinguant deux zones par rapport à la droite $D_I = 1$ celui des grandes vitesses de combustion pour lequel $D_I > 1$ et celui des faibles vitesses $D_I < 1$ ce dernier conduisant aux amplitudes de pression les plus grandes (figure 33).

Ce domaine de propulseur modulé est bien étudié sur le plan expérimental et sur le plan théorique mais un gros effort reste à faire dans l'analyse du couplage pression-vitesse, dans l'évaluation des pertes et sur le plan théorique dans l'analyse non linéaire des phénomènes.

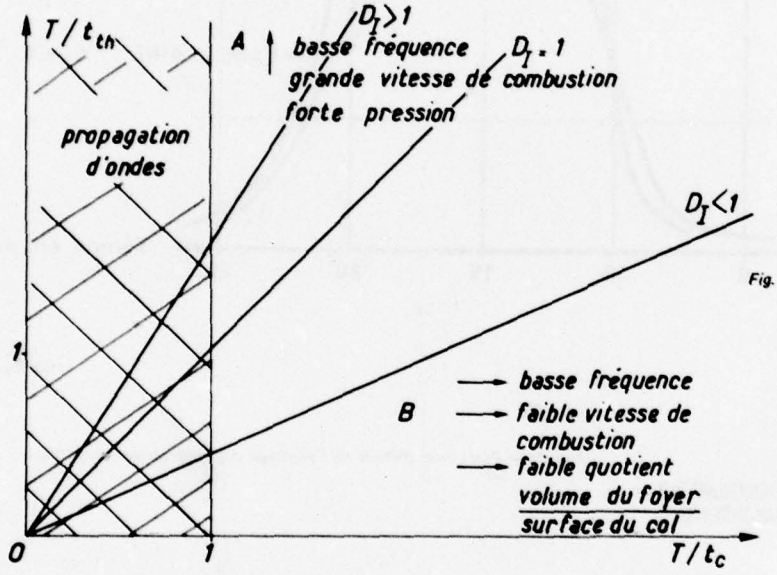

Fig. 32 – Domaine de fonctionnement du propulseur modulé.

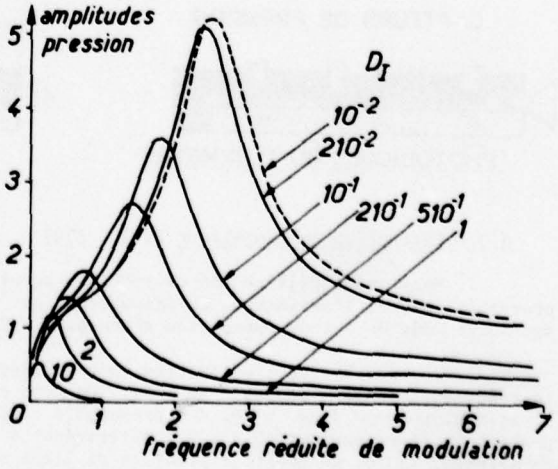

Fig. 33 – Influence du paramètre de Damköhler sur l'amplitude des fluctuations de pression.

3.5 - Instabilités de combustion [32] [33]

L'objectif des recherches dans ce domaine est de pouvoir prévoir sur plan, les domaines de fonctionnement instable du propulseur ; bien que les travaux présentés aux paragraphes 3.1 et 3.4 constituent une voie prometteuse pour atteindre cet objectif on ne peut encore conclure en toute certitude. Il est possible d'avoir pour un propergol la réponse à des fluctuations de pression et de vitesse ; on connait, pour ce propergol, le domaine de fréquence où des instabilités sont à craindre ; on connait également dans le domaine acoustique les fréquences caractéristiques du propulseur pendant tout son fonctionnement ; dans le domaine dit "de basse fréquence" on peut déterminer s'il y a possibilité d'amplification ou d'amortissement ; on sait dans certains cas prévoir l'effet d'échelle et retrouver en partant d'essais à échelle réduite les domaines instables du propulseur à échelle grandeur et évaluer les fréquences ; mais on ne peut, dans l'état actuel de nos connaissances, que donner des tendances. Une des difficultés découle d'une imprécision dans l'évaluation des gains et des pertes et comme le domaine d'instabilité est défini par la différence entre gains et pertes, ce domaine est donc extrêmement flou. Mais des progrès constants sont faits, dans la précision des mesures, dans le raffinement des modèles, aussi est-il permis d'espérer atteindre l'objectif précisé au début de ce paragraphe.

4 - RECHERCHES PORTANT SUR LES COMPOSANTS DU PROPULSEUR

Ces recherches sont très nombreuses et très importantes, nous retiendrons seulement quatre sujets.

4.1 - Combustion sous contrainte

Un des composants du propulseur est la liaison plastique protectrice qui se situe entre l'enveloppe et le bloc de propergol. Sous l'effet des déformations de l'enveloppe des fissures peuvent apparaître entre le propergol et l'inhibiteur ou entre l'inhibiteur et l'enveloppe. La mise au point d'un inhibiteur efficace est souvent délicate et sa tenue doit être déterminée dans des conditions voisines de l'utilisation c'est-à-dire après déformation du support. Des chambres à parois transparentes ont été mises au point comme indiqué sur la figure 34, le support, l'inhibiteur et le propergol étant déformés pendant le tir. A l'aide d'une technique cinématographique la progression de la combustion, la formation de fissures, la pénétration de la combustion peuvent être analysées.

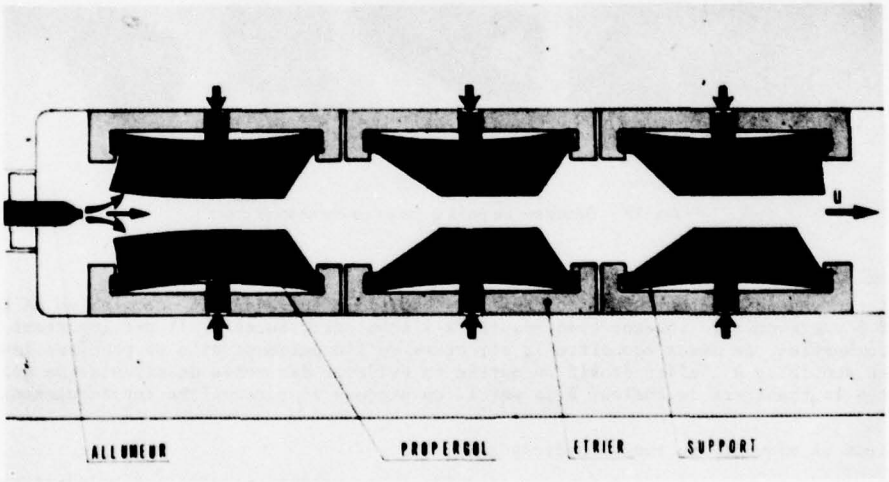

Fig. 34 – Combustion sous contrainte.

4.2 - Géométrie des blocs

Depuis trois décennies de recherches dans ce domaine on pourrait croire que tout a été dit, il n'en est rien car de nouvelles applications apparaissent avec des recherches de compromis souvent contradictoires. Pour la majorité des applications le constructeur recherche :

- une loi de combustion optimale pour la mission,
- un bon coefficient de remplissage,
- une fin de combustion qui permette de diminuer l'épaisseur de l'inhibiteur,
- une grande surface de combustion,
- un effet dû à l'érosion, minimal,
- une géométrie facilitant l'allumage du propergol,
- une bonne tenue au stockage,
- une réalisation aisée du bloc,
- une géométrie conduisant à une bonne tenue durant la montée en pression dans le propulseur et dans la phase d'accélération,
- une organisation de l'écoulement interne conduisant à un écoulement homogène à l'entrée de la tuyère,
- une géométrie tendant à amortir les instabilités de combustion,

et pour certaines applications on souhaite :

- réaliser des géométries de bloc avec une tuyère intégrée dans le bloc,
- utiliser des blocs à double composition avec des poudres froides près de la sortie tuyère pour améliorer la tenue du col ou pour tenter de réduire la signature infra-rouge ou des compositions avec des vitesses de combustion différentes,
- concevoir des blocs permettant de réaliser des propulseurs sans tuyère.

La conception d'une géométrie de bloc est donc un problème de recherche de compromis et de nombreuses études sont encore possibles dans ce domaine. Nous citons deux exemples de recherche de ce compromis : le premier est l'utilisation d'un bloc lamellaire qui permet d'obtenir des lois de combustion avec montée et descente en pression symétrique (figure 30a), le deuxième est la conception de blocs à grande surface de combustion en partant de lanières de propergols comportant une série de fentes (figure 35).

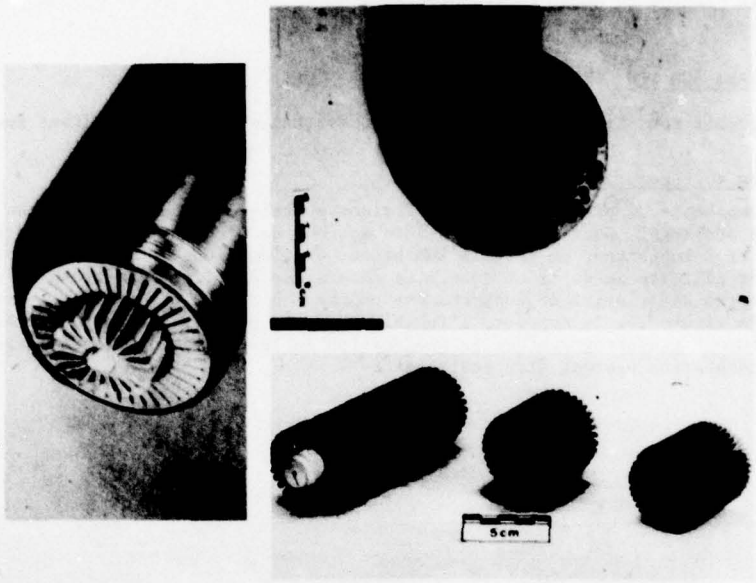

Fig. 35 – Géométrie de blocs à temps de combustion court.

4.3 - Aérodynamique interne

La recherche du compromis pour concevoir le bloc le mieux adapté à une mission ne conduit pas nécessairement à une géométrie interne bien adaptée à l'écoulement interne. Il est important, sans tenir compte de la combustion, de mieux connaître la structure de l'écoulement afin de préciser les zones de survitesse plus sensibles à l'effet érosif ou mettre en évidence des zones de circulation qui peuvent localement augmenter le transfert de chaleur à la paroi. On dispose pour connaître cet écoulement de plusieurs méthodes :

- étude de maquette au tunnel hydrodynamique,
- essais dans une conduite à froid reproduisant les conditions d'injection pariétale,
- méthodes analytiques donnant les lignes de courant, le profil des vitesses et des pressions à la surface pour des géométries de canal interne complexes comme celle qui est indiquée sur la figure 36. Cette étude est intéressante dans le cas de tuyère intégrée comme celle tracée sur la figure 37.

Ces méthodes sont couramment utilisées et suffisent pour la plupart des applications actuellement envisagées.

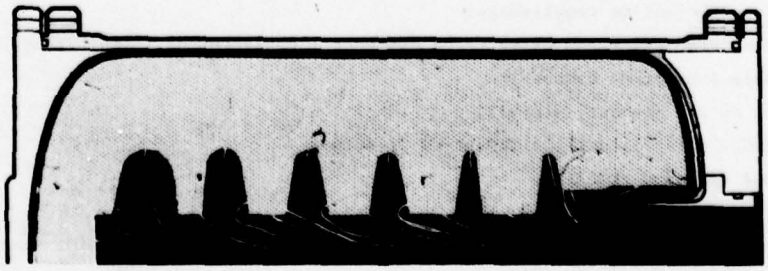

Fig. 36 – Lignes de courant dans un chargement usiné.

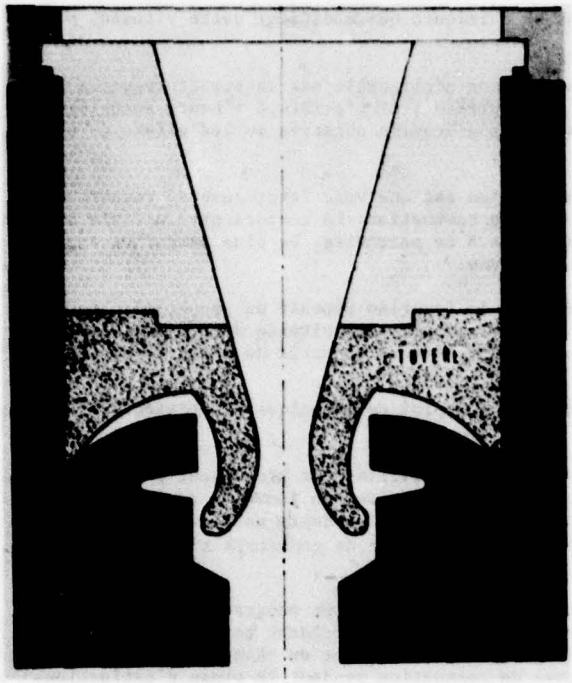

Fig. 37 – Ecoulement autour d'une tuyère intégrée.

4.4 - Performance des tuyères [34] [35]

Les principales recherches portant sur ce composant se rattachent :

- à la perte de performance due à la présence de particules dans les produits de combustion,
- aux pertes de performance découlant de l'érosion de la tuyère (érosion globale sur toute la surface, augmentation du diamètre du col par exemple) et de l'érosion locale qui intervient à des jonctions de matériaux,
- à la perte de performance due à l'intégration de la tuyère dans le bloc,
- au gain de performance possible grâce à l'utilisation de divergent déployable, solution intéressante pour certaines missions,
- à la mise au point de systèmes légers d'orientation de la tuyère,
- à la mise au point de systèmes utilisant des multituyères.

Les recherches portant sur ces thèmes sont toujours actuelles et de nombreux laboratoires travaillent encore sur l'étude des jets contenant des particules à partir des techniques de diagnostic utilisant les lasers ; les problèmes d'ablation de la tuyère par suite de la diversité des produits de combustion et de l'utilisation de graphite sont surtout abordés sous les deux aspects thermiques et chimiques, avec le graphite des réactions chimiques de surface apparaissent qui contribuent à l'ablation. C'est vers une meilleure compréhension de ces phénomènes et une meilleure modélisation que s'orientent les recherches.

5 - CONCLUSION

Nous voudrions pour conclure cet exposé insister sur quelques points importants et indiquer quelques voies de recherche.

1/ Dans cet exposé nous n'avons pas mentionné l'aspect énergétique du propergol qui pourtant est un point important de la performance du propulseur, on cherche en effet des formules de poudre d'impulsion spécifique et de masse volumique élevées. Cet oubli tient à plusieurs facteurs : tout d'abord les progrès réalisés sur l'impulsion spécifique en utilisant de nouvelles compositions sont faibles en comparaison avec la somme de travail effectué, de bonnes performances ont été obtenues avec des liants oxygénés, mais ces propergols ne sont pas opérationnels sur le plan militaire et utilisables en toute sécurité ; il existe donc un compromis entre performance et sécurité ; certaines compositions à impulsion spécifique élevée conduisent à des produits de combustion contenant des particules, il existe donc un autre compromis entre performance et discrétion (propergol sans fumée) ; les propergols solides à haute performance comportent en général des substances endothermiques qui risquent d'évoluer au cours du temps, un autre compromis apparait donc entre performance et vieillissement. Bien qu'à l'heure actuelle un gros effort soit fait pour concevoir de nouveaux propergols répondant à un certain nombre de critères, l'aspect énergétique n'est pas nécessairement le plus important.

2/ Dans la littérature spécialisée des modèles théoriques de combustion de propergols homogène ou hétérogène en régime permanent sont périodiquement exposés. Ces modèles progressent et décrivent de plus près les processus chimiques en ce qui concerne les propergols homogènes et tiennent mieux compte des hétérogénéités et du caractère tridimensionnel de la zone de combustion dans le cas des propergols hétérogènes ; ils donnent correctement les lois de vitesse de combustion en fonction de la pression. Nous n'avons pas parlé de cette activité de recherches car il nous semble que toutes ces théories comportent de très nombreux paramètres ajustables et nous avons préféré insister sur les recherches expérimentales portant sur l'aspect

analytique des phénomènes et sur les paramètres physiques et chimiques qui modifient cette vitesse, point important pour le constructeur.

3/ L'écoulement parallèle à la surface a une action non négligeable sur la structure de la zone de combustion et sur le transfert de masse et d'énergie à la surface ; il n'existe, à l'heure actuelle, aucun modèle qui prédise d'une manière satisfaisante les effets d'érosion négative ou les effets de seuil, ainsi que l'influence de la pression.

4/ La détermination des pressions limites de combustion est une voie fructueuse de recherche, cette étude doit permettre de mieux connaître les mécanismes de combustion. La température initiale du bloc joue un très grand rôle, la pression limite étant très sensible à ce paramètre. De plus certaines applications nécessitent l'emploi de propergols à pression limite élevée.

5/ La détermination par l'analyse et l'expérience de la fonction réponse du propergol est une part importante de l'étude des phénomènes transitoires. Le couplage pression-vitesse doit retenir l'attention des chercheurs, ainsi que la détermination de cette fonction réponse à partir de théories non linéaires.

La partie expérimentale pourra progresser grâce à l'emploi de techniques plus précises pour déterminer la fonction réponse.

6/ Un progrès sensible sur la prévision des domaines de stabilité d'un propulseur pourra intervenir lorsqu'on aura une idée plus précise des pertes et de leurs variations en fonction de la géométrie du bloc et de la tuyère ainsi que de la taille du propulseur. Des modèles en cours donnant le fonctionnement du propulseur en régime instationnaire ont fourni dans le cas de bloc de geométrie simple, des résultats intéressants.

7/ Les problèmes d'allumage et d'extinction du propulseur ne pourront progresser que lorsqu'on pourra décrire d'une manière plus précise les mécanismes complexes qui se succèdent pendant la phase d'allumage et d'extinction : évolution correcte du débit brûlé à chaque instant et en chaque point du bloc du propergol pendant la phase d'allumage, structure de la zone de combustion pendant la phase d'extinction.

8/ La mise au point de composants : enveloppe, tuyère, bloc, inhibiteur, repose avant tout sur l'avancement des recherches dans le domaine des matériaux, nous pensons, devant la diversité des applications que des recherches sont encore nécessaires pour améliorer les performances des tuyères et arriver à une géométrie optimale du bloc.

Bien qu'un progrès sensible ait été obtenu durant ces dernières années, un long parcours reste encore à faire pour une maîtrise complète de la combustion des propergols solides aussi bien en régime permanent que transitoire.

BIBLIOGRAPHIE

[1] - WILLIAMS, F.A., BARRERE, M. and HUANG, N.C.
Fundamental Aspects of Solid Propellants Rockets,
AGARDograph n° 116, (1969).

[2] - KUBOTA, N., OHLEMILLER, T.J., CAVENY, L.H. and SUMMERFIELD, M.
The Mechanism of Super-rate Burning of Catalyzed Double Base Propellants
AMS Report p. 1087, Princeton University, 1973 ; Fifteenth Symposium (International) on Combustion, p. 529, The Combustion Institute, 1975 ; AIAA J. 12, p. 1709, 1974.

[3] - LENGELLE, G., BRULARD, J. and MOUTET, H.
Combustion Mechanisms of composite solid propellants.
Sixteenth Symposium (International) on Combustion, p. 1257, The Combustion Institute.

[4] - BAKHMAN, N.N. and BELYAEV, A.F.
Combustion of Heterogeneous Condensed Systems.
Institute of Chemical Physics, Moscow. RPE Translation n° 19, 1967.

[5] - HEWKIN, D.J., HICKS, J.A., POWLING, J. and WATTS, H.
Combustion Science and Technology 2, p. 307, 1971 ; Internationale Jahrestagung, p. 35, Institut für Chemische Raketentriebe, 1974.

[6] - LENGELLE, G., DUTERQUE, J., VERDIER, C., BIZOT, A., TRUBERT, J.F.
Combustion Mechanism of Double Base Solid Propellants.
17ème Symposium International sur la Combustion LEEDS (G.B.) 20-25 août 1978.

[7] - STEINZ, J.A., STANG, P.L., SUMMERFIELD, M.
The Burning Mechanism of Ammonium Perchlorate Based Composite Solid Propellants.
Princeton University AMS Report n° 830, Février 1967.

[8] - COHEN-NIR, E.
Temperature Sensitivity of the Burning Rate of Composite Solid Propellant.
Combustion Science et Technology, 9, 183 (1974).

[9] - VILYUNOV, V.N. and DVORYASHIN, A.A. (1971a)
An experimental investigation of the erosive burning effect.
Fizika Goreniya (1), 45-51.

[10] - TOHRU MITANI, TAKASHI NIIOKA
An analytical Model of Solid Propellant Combustion in an Acceleration Field.
Combustion Science and Technology, 1977, vol. 15, n° 3 et 4.

[11] - STEINTZ, J.A. and SELZER, H.
Depressurization Extinguishment of Composite Solid Propellant.
Combustion Science and Technology 3, 25 (1971).

[12] - SUMMERFIELD, M. and CAVENY, L.N. (1971)
Theory of dynamic extinguishment of solid propellants with special reference to non steady heat.
J. Spacecraft and Rockets 8 (3).

[13] - BELAYEV, M.K., SUKOYAN, M.K., KOROTKOV, A.I., SULIMOV, A.A.
Consequences of the Penetration of Combustion into an individual Pore.
Combustion, Explosion and Shock Waves, vol. 6, n°2, April-June 1970.

[14] - BECKWITH, S.W., WANG, D.T.
Crack Propagation in Double-base Propellants.

[15] - LENGELLE, G., KUENTZMANN, P. and RENDOLET, C.
Response of a solid propellant to pressure oscillations.
AIAA SAE Propulsion Conference (October 1974), San Diego, Cal., U.S.A.

[16] - CULICK, F.E.C.
A review of calculations for unsteady burning of a solid propellant.
AIAA Journal, vol. 6, n°12 (December 1968), p. 2241.

[17] - BARRERE, M.
Response to a transient regime of the combustion surface of an heterogeneous solid propellant.
Acta Astronautica, vol. 15 (1970), p. 633-640.

[18] - KRIER H., T'IEN, J.S., SIRIGNANO, W.A. and SUMMERFIELD, M.
Non steady burning phenomena of solid propellants : theory and experiments.
AIAA Journal, vol. 6, n° 2 (February 1968), p. 278.

[19] - NOVIKOV S.S. and RYAZANTSEV Yu S.
The interaction of acoustic waves with the burning surface of condensed systems.
Traduction AFSC AD 700 687 (1970).

[20] - RYAZANTSEV Yu. and TULSKIKH V.E.
Calculation of acoustic admittance at the burning surface.
Acta Astronautica, vol. 3, n° 3-4 (March-April 1976), P. 171.

[21] - GOSTINTSEV Yu. A
Relationship between a phenomenological model of the unsteady state combustion of a powder and a model of a granular diffusion flame.
Combustion, Explosion and Shock Waves, vol. 9, n°6 (November-December 1973), p. 759.

[22] - KUENTZMANN, P. et NADAUD, L.
Réponse des propergols solides aux oscillations de pression et de vitesse.
Combustion Science and Technology, vol. 11 (1975), p. 119.

[23] - NOVOZHILOV, B.V.
Combustion instationnaire des propergols solides.
Editions La Science, Moscou (1973).

[24] - ZELDOVICH, Ja. B., LEJPUNSKIJ, O.I. et LIBROVICH, V.B.
Théorie de la combustion instationnaire des propergols solides.
Editions Nauka, Moscou (1975).

[25] - ROMANOV, O. Ya
Integral equations in the theory of unsteady combustion of powder.
Combustion, Explosion and Shock Waves, vol. 11, n°3 (May-June 1975), p. 319.

[26] - KUENTZMANN, P.
Modèles de Combustion Instationnaire des Propergols Solides Composites.
La Recherche Aérospatiale n° 1978-2, pp. 77-93.

[27] - VILYUNOV, V.N. and RUDNEV, A.P. (1971b)
Influence of erosion on combustion stability in solid-propellant rocket chambers.
Fizika Goreniya (4), 483-488.

[28] - BARRERE, M., NADAUD, L. and LHUILLIER, J.N. (1974)
ONERA and SNPE work on solid propellant combustion instability.
J. Spacecraft and Rockets, 11 (1), 33-40.

[29] - TURK, S.L., BATTISTA, R.A., KUO, K.K., CAVENY, L.H. and SUMMERFIELD, M.
Dynamic responses of solid rockets during rapid pressure change.
Journal of Spacecraft and Rockets, vol. 10, n°2 (February 1973), p. 137.

[30] - KRIER, H.
Model of Transient Ignition to Self-Sustained Burning.
Combustion Science and Technology 5-69 (1972).

[31] - BARRERE, M.
Analyse du fonctionnement d'un propulseur à éjection modulée.
Acta Astronautica vol. 5, pp. 851-875.

[32] - KOOKER, D.E.
Numerical solution of axial mode instability problems in solid propellant rocket motors.
Ph.D. Thesis 1974 Georgia Institute of Technology, and : KOOKER D.E. and ZINN B.T. - Triggering axial instabilities in solid rockets : numerical predictions - AIAA Paper 73-1298 (1973).

[33] - LEVINE, J.N. and CULICK, F.E.C.
Nonlinear analysis of solid rocket combustion instability
Technical Report AFRPL-TR 74-45 (October 1974)
and : LEVINE J.N. and CULICK F.E.C. - Numerical Analysis of nonlinear longitudinal instability in metalized propellant solid rocket motors - Technical Report AFRPL-TR 72-88 (July 1972).

[34] - BAETZ, J.G.
Advanced Carbon-Carbon materials for Solid Rocket Nozzles
AIAA paper n° 74-1057 - AIAA/SAE 10th Propulsion Conference, San Diego 1974.

[35] - KLAGER, K.
The Interaction of the efflux of Solid Propellants with nozzle materials.
Propellants and Explosives, vol. 2, n°3, juin 1977

SOLID ROCKET MOTOR DESIGN AUTOMATION TECHNOLOGY

W. G. Haymes
J. E. Williamson
S. E. McClendon
W. T. Brooks
Hercules Incorporated
McGregor, Texas, USA 76657

SUMMARY

This paper presents a status of Solid Rocket Motor Design Automation Technology. The total scope is reviewed, from initial preliminary design techniques to optimize rocket motor performance, mass, and envelope characteristics to those procedures used in final design activity. The latter include internal ballistics and grain design; combustion stability prediction; structural, thermal, and mass property analyses; and the like. Direction of current work in the United States of America is outlined.

INTRODUCTION

During the past 25 years, significant progress has been made in all areas of solid rocket technology. These areas include propellant chemistry and compositions, insulation materials, understanding of propellant structural behavior, thermal analyses, and performance predictions. Certainly, one area in which the most significant advancement, and which is the key to the progress made in most of the areas noted, has been made is design automation.

Availability of the digital computer has given solid rocket motor designers and analysts a capability hardly imagined 25 years ago. Indeed, its appearance and capabilities are the basis for much of the advancement made in solid rocket motor technology. Today, it is possible to select an optimum rocket motor design and detail it using computer methods entirely.

In the United States of American (USA), design automation methods are now used to various degrees by Government and industrial scientists and engineers. Government organizations sponsor activities to improve existing computer programs and to develop new ones. Industrial concerns do the same to improve their capabilities and competitive positions.

The intent of this paper is to survey the status of design automation technology in the USA. Accordingly, in the following sections the total scope is reviewed, from initial preliminary design techniques to optimize rocket motor performance, mass, and envelope characteristics to those procedures used in final design activity. The latter include internal ballistics and grain design; combustion stability prediction; as well as structural, thermal, and mass property analyses.

MOTOR OPTIMIZATION/PRELIMINARY DESIGN

As recently as the early 1960s, nearly all analyses for solid propellant rocket motor design were performed manually, utilizing slide rules or mechanical calculators for most computations. As a result, the analyses were extremely time-consuming and by necessity limited in scope. Rocket motor design involved much art, as well as science, and depended to a great extent on the experience and intuition of the analyst.

The proliferation of increasingly larger and faster digital computers during the mid 1960s permitted the automation of these previously manual operations and the development of computer programs to perform computations in minutes or seconds that were literally impossible to perform manually. Thousands of iterations can be made on various design parameters, such as motor weight, envelope, chamber pressure, etc., to examine every conceivable combination of available parameters to arrive at the optimum motor design for the intended mission.

In recent years, these early computer programs have been continuously improved to take advantage of the latest advances in computer technology; such as interactive time-sharing systems, computer-generated plotting and drafting, larger storage capability, and faster access times. As a result, the design of solid propellant rocket motors has transitioned into what is presently a science that can be performed with fewer people in less time and that results in a better, more reliable product than was previously possible.

When a new motor is to be designed, the specification usually places limits on motor characteristics such as the physical envelope, motor weight, total impulse, thrust-vs-time envelope, etc. In the preliminary design, it is desirable to be able to quickly and accurately evaluate the effects of a large number of variables such as chamber pressure, expansion area ratio, mass fraction, case/nozzle materials, and physical dimensions on specified motor characteristics. This type of study of a large number of parameters can readily be accomplished with the high-speed digital computers of today. Most solid rocket activities in the USA have been computer programs that accomplish this to one degree or another.

To illustrate this type of program and its capability, the Solid Rocket Motor Optimization Computer Program used by Hercules will be briefly described. The central portion of the optimization computer program is an automated solid rocket design routine. This routine receives inputs from which a particular solid rocket configuration can be defined; such as diameter, thrust schedule, total impulse, propellant properties, inert material properties, nozzle parameters, chamber pressure, etc. The design routine then constructs solid rocket motors incorporating the input parameters. The description of the motor necessary to achieve the input design criterion requirement is determined by the program.

Motor design criteria are selected from options such as:

- Fixed total impulse
- Fixed propellant weight
- Fixed length
- Fixed ideal velocity increment
- Fixed trajectory performance

When the fixed criteria are met, information concerning the particular motor design is printed out. Data for the design are also stored within the machine. This procedure is continued until an array of input parameters has been scanned that includes motor diameter, nozzle expansion ratio, chamber pressure, and thrust schedule. All the resulting designs are compared and the motor that meets the optimization criteria is selected. Optimization criteria include:

- Maximum total impulse
- Minimum weight
- Minimum length
- Maximum trajectory performance (burnout velocity, range, etc.)

Mathematical models within the program have been refined such that motor gross weights are consistently predicted to within 1% of that determined from detail board design layout.

Figure 1 illustrates the role of the optimization computer program in the motor design evaluation cycle.

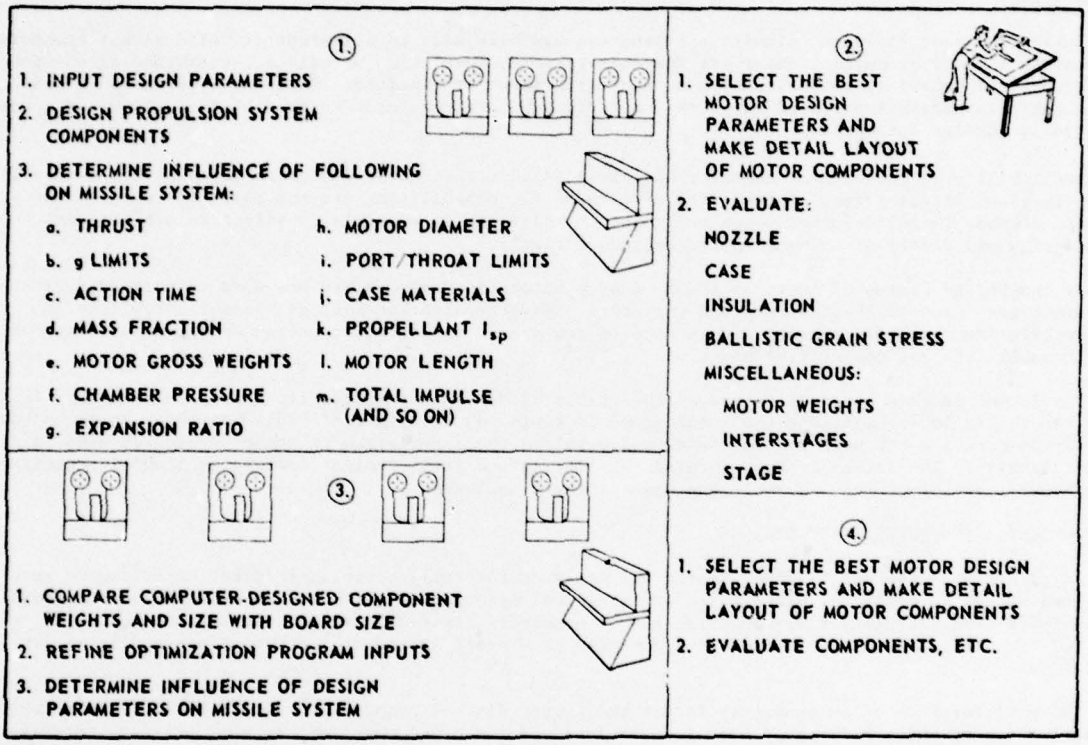

Figure 1. Motor Design Evaluation Cycle

If desired, a lifting point mass trajectory is flown for each motor to evaluate its flight performance. The program uses a building block approach to permit all likely missile maneuvers in an arbitrary order to achieve the required trajectory. A typical printout is shown in Fig. 2. The motor description is divided into four print-out columns. The first column tabulates ballistic and trajectory performance data; these data include both input and computer values. The second column contains the overall and detailed individual component weights. The third and fourth columns delineate case and insulation thicknesses, port area, volumetric loading, and nozzle dimensions. An outline of a rocket motor is printed out, along with the major overall dimensions, that allows rapid assessment of these data.

By cross-plotting the data received from an array of design parameters, it is not only possible to define the optimum solution, but also to determine the sensitivity of the system to the constraints imposed and the variables considered. This is illustrated in Fig. 3(a), which is a typical plot constructed from an array of design parameters for a particular propulsion system. Shown, on a fixed total impulse basis, is motor length versus weight with chamber pressure and nozzle expansion ratio as parameters; also fixed are thrust and motor diameter. The problem here was to determine the chamber pressure and expansion ratio at which weight is at a minimum within a 77.0-inch length constraint. The optimum condition identified as "Design Point" is a pressure of 750 psi and an expansion ratio of approximately 15.

Another example of optimizing the chamber pressure and nozzle expansion ratio is shown in Fig. 3(b). Plotted, on a fixed length basis, is total impulse versus motor weight with pressure and expansion ratio as parameters. The objective is to determine the minimum weight at which the desired total impulse of 23,000 lb-sec is delivered. Pressure and expansion ratio at which this occurs are 1100 psi and 5, respectively.

```
                                BALLISTIC MODE FIXED LENGTH

                          BOOST      SUSTAIN
ALTITUDE (FEET)       .5000E+0E      .0
ITOT (LB SEC)         .5713E+0E      .0

CHAMBER PC (AVG)  =       1CCO.          0.
  INITIAL         =       1CCC.          0.
  FINAL           =       1000.          0.
  PMM             =       1304.          0.
THRUST (AVG)-LBS  =      20CCO.          0.
  INITIAL   (TI)  =      20CCO.          0.
  FINAL     (TF)  =      20CCO.          0.
TF/TI RATIO       =      1.CCC         0.0
THRUST/WT (INIT)  =       8.23         0.0

ACTION TIME SEC.  =      28.5E         0.0

SPECIFIC IMPULSE
  REF   (1000 PSI)=     248.8C       248.80
  DELIVERED (SP)  =     275.27         0.0
  COMPOSITE       =     273.56         0.0
W DOT             =      72.6E         0.0

GRAIN IS STRESS LIMITED
CASE ALLOWABLE=  180000.
STAGING RATIO =   1.000
DVB ACHIEVED  =   17301.
DVB REQUIRED  =      0.
DVBI          =   17301.
G LIMIT       =      0.
TIME TO TARGET=     0.0
    TRAJECTORY
B.O. ALT. = N/A
VELOCITY  = N/A
MAX Q     = N/A
MAX MN    = N/A
MAX ACC   = N/A
GAMMA     = N/A
DRAG LOSS = N/A
GRAV LOSS = N/A

PAYLOAD WEIGHT          =      0.0
GROSS MOTOR WT.         =   2429.0
TOTAL INERT WEIGHT      =    353.7
CASE WEIGHT             =    265.6
  CYLINDRICAL           =    183.9
  AFT HEAD              =     19.0
  FWD HEAD              =     55.1
  NOZZLE  BOSS          =      3.8
  IGN.  BOSS            =      3.8
NOZZLE                  =     32.0
BLAST TUBE              =      0.0
INTERNAL  INSULATION    =     42.1
  CYLINDRICAL SECT.     =     15.2
  AFT  HD               =      8.3
  FWD  HD               =      5.6
  LINER                 =     12.9
IVC  SYSTEM             =      0.0
  FLUID                 =      0.0
  INERTS                =      0.0
EXTERNAL  INSULATION    =      0.0
RCATTAILCR FAIRING)     =      0.0
MOTOR MISC WEIGHT       =     14.0
PROPELLANT (TOTAL)      =   2075.3
  BOOST                 =   2075.3
  SUSTAIN               =      0.0
  TOTAL EFFECTIVE       =   2075.3
  SLIVER                =      0.0
  PROP. IN CYLINDER     =   1884.7
    POUNDS / INCH       =     25.2
  PROP. IN HEADS        =    190.6

MOTOR EMPTY WEIGHT)     =    340.8
STAGE MISC. WEIGHT      =      0.0
INTERSTAGE  (FWD)       =      0.0

MISSILE WT. AT IGN.     =   2429.0
MISSILE WT. AT B.O.     =    340.8

CASE TC  =  0.114   EXP RATIO  =   15.7
HEAD TC  =  0.109   ORIGINAL E =   40.0
TIIC AVG =  0.060   THROAT AREA=   11.8
TIIAF AVG=  0.300   P/T RATIO  =    2.0
TIIFF AVG=  0.200   HALF ANGLE =   15.0
PORT AREA=   53.5   ET FLOW DIA=    0.0
VOL LD-P =  0.860   LENGTH I S =    0.0
VOL LD-PI=  0.885   TKNESS I S =    0.0
                    STAGE MF   =  0.854
                    MOTOR MF   =  0.854

BLAST TUBE OD=   0.0
PERCENT LOSS =   0.0
CONE ANGLE   =   0.0
BURNING RATE =  0.268
GRAIN DESIGN W/F = 0.65C

                X   24.0   X
            X-  .  ..  .  -------
                |  .      .      |
                |  .---TP---.    |  6.0
                |  .      .      |
                |  .      .      |
                |  .      .      |
                |  .  H   .      |
                |  .  E   .      |
                |  .  R   .      |
                |  .  C   .      |
                |  .  U   .      |  74.9
                |  .  L   .      |
                |  .  E   .      |
                |  .  S   .      |
          106.0 |  .      .      |
                |  .      .      |
                |  .      .      |
                |  .      .      |
                |  .---TP---.    |
                |  .      .      |  6.0
                |  .      .      |
                |  ..    ..      |  1.9
                |  .      .      |
                |  .      .      |  17.2
                |  .      .      |
                |  .      .      |
            X-  .  ..  .  -------
                X  15.4  X
```

Figure 2. Sample Motor Optimization Program Printout

DETAILED MOTOR DESIGN

The motor optimization/preliminary design procedure previously discussed provides the designers with the basis and starting point for detailed design definition. The detailed design of the rocket motor requires a significant amount of interaction and iteration among several technical disciplines; including ballistic and mechanical design and ballistic, structural, and thermal analyses. This interaction is depicted in Fig. 4.

The computer analysis for preliminary design establishes ballistic performance requirements as input to the grain design analysis; and weight, envelope, and maximum pressure requirements as input to the mechanical design function and related analyses. A variety of computer codes are routinely used in grain design from the process of selecting and dimensioning the grain configuration to structural analysis and ballistic performance predictions. Several other sophisticated computer codes are used in analysis of component parts, such as finite element structural and finite difference heat transfer computer codes. Finally, a combustion stability prediction can be accomplished on the completed motor design with the aid of a series of computer codes. Also, if important, characteristics of the exhaust plume can be similarly determined. These programs are discussed in the following paragraphs.

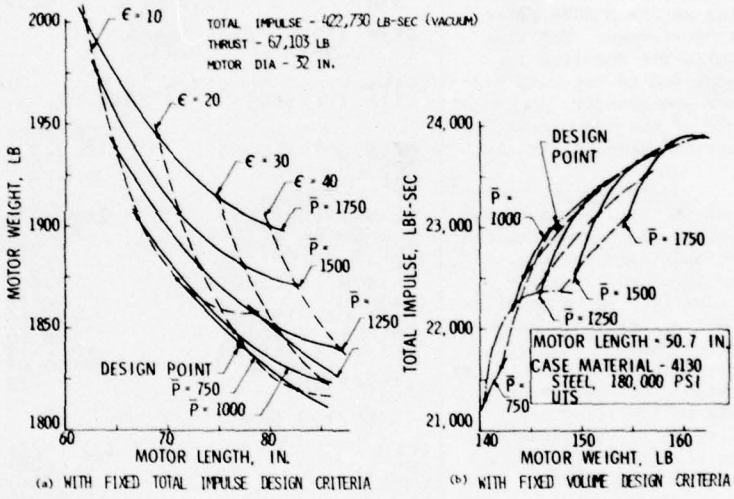

Figure 3. Optimization of Motor Design

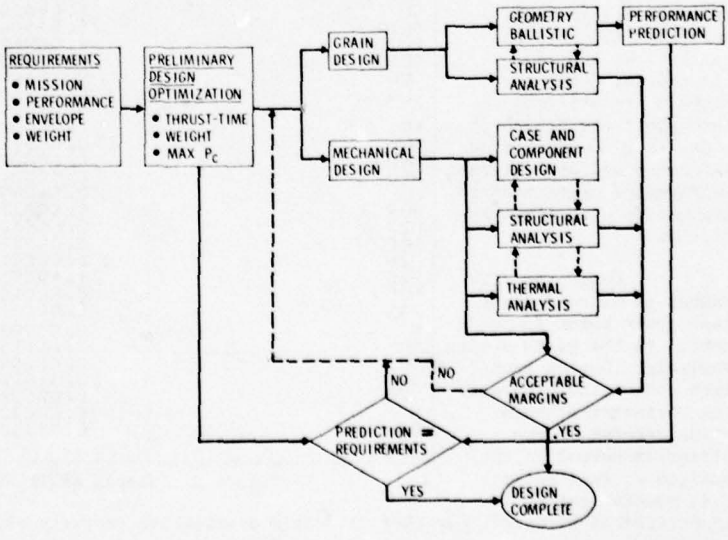

Figure 4. Solid Propellant Motor Design Sequence

Propellant Thermochemistry. Propellant thermochemistry computer programs are used in solid propellant rocket motor design to determine available combustion energy of the propellant and chemical composition of the exhaust gas. Generally, the Gibbs free-energy minimization

technique is used and a one-dimensional, perfect thrust chamber assumed to calculate theoretical thermodynamic properties of the system. The program output provides propellant thermodynamic properties (specific impulse, combustion temperature, ratio of specific heats, molecular weight, etc.) to the internal ballistics designer for use in motor performance prediction. Chemical composition of the exhaust gas is utilized as input for exhaust plume smoke prediction, which depends on energy changes and chemical recombinations that occur as the effluent mixes with the atmosphere.

Among the many codes used by industry for theoretical performance predictions are the NASA One-Dimensional Equilibrium Program (Ref 1); the JANNAF ODK Program, a 1-dimensional kinetic performance program; and the AFRPL Performance Program. These programs calculate theoretical performance. Also available is the fully automated Solid Performance Program (SPP) developed under AFRPL Contract (Ref 2), which computes the deviations from theoretical performance to be expected for a given solid rocket motor design. This program treats the following losses: 2-dimensional/2-phase (coupled), combustion efficiency, kinetics, nozzle erosion, boundary layer, and submergence. In addition, several companies have their own proprietary programs for computing propellant thermochemical characteristics.

Hercules utilizes the AFRPL Performance Program and the SPP for calculations. For most applications, the AFRPL program is used, in view of its efficiency and input simplicity. SPP is used when a sufficient data base is not available from similar configurations to empirically determine efficiencies.

The AFRPL Performance Program is completely general and can compute both equilibrium and frozen expansion performance parameters for any propellant for which the necessary propellant and reaction-product thermodynamic data are available. Ions can be included, if desired. The nozzle can be expanded to specified exit pressures, specified area ratios, or a mixture of both. Input to the program is straightforward, with the various operations available (e.g., air augmentation, detonation, optimization, frozen) indicated by 3-letter code names. Execution does not destroy the stored data, so parameters that do not change between cases need not be re-entered. Output data include verification of input propellant data; overall propellant density; and thermodynamic and performance variables at each exit point.

This program is used on an IBM 370-168 computer and requires 208K bytes core storage. Two tape units are required in addition to the card reader and printer. A sample of the computer printout is shown in Fig. 5.

Grain Design. Advances in grain design technology and computer-aided methods have greatly enhanced motor design capability in terms of both accuracy and man-hour efficiency. Techniques have been developed to the extent that performance within specified limits frequently is demonstrated by the first firing for design verification.

Three general areas of analysis are involved in grain design: (1) geometry; (2) internal ballistics; and (3) structures. Computer methods are utilized throughout the design process, from configuration selection and analysis and performance prediction to combustion stability prediction.

Geometry. The manner in which a propellant grain burns is fundamental to the grain design analysis. During propellant combustion, the burning perimeter at each point recedes in the direction normal to the surface at that point; this generalization is identified as Piobert's Law (Ref 3). This distinctive property of a solid rocket grain makes grain design readily amenable to computer methods and design automation. If the initial configuration (perimeter and port area) can be described mathematically, the burning perimeter as a function of web burned can be

PROPELLANT	HF	DENSITY	WEIGHT	MOLES	VOLUME
NH4C LO4	-70.6900	1.9500	86.0000	0.7320	44.1026
BIND	12.3400	0.9200	14.0000	0.1399	15.2174

GRAM ATOMS /100 GRAMS
C 0.9864 CL 0.7320 H 4.4182 N 0.7440 O 2.9580

ENTHALPY = -50.01724 DENSITY =1.686
CSTAR (FT/SEC)= 5057.676

	CHAMBER	THR(SHIFT)	EXH(SHIFT)
PRESSURE (PSIA)	1000.000	569.457	14.696
EPSILON	0.0	1.000	8.534
ISP	0.0	105.280	249.641
ISP (VACUUM)	0.0	194.799	269.407
TEMPERATURE(K)	2980.374	2753.075	1447.520
MOLECULAR WEIGHT	25.122	25.255	25.422
MOLES GAS/100G	3.981	3.960	3.934
CF	0.0	0.670	1.588
PEAE/M (SECONDS)	0.0	89.519	19.715
GAMMA	1.218	1.219	1.248
HEAT CAP (CAL)	44.266	43.849	39.334
ENTROPY (CAL)	241.714	241.714	241.714
ENTHALPY (KCAL)	-50.017	-62.750	-121.639
DENSITY (G/CC)	6.989840-03	4.331950-03	2.140310-04
ITERATIONS	18	3	10

GRAMS/100 GRAMS

CCLO	0.00211	0.00097	0.00000
CHN	0.00003	0.00002	0.00000
CHNO	0.00004	0.00002	0.00000
CHO	0.00045	0.00020	0.00000
CH2O	0.00005	0.00003	0.00000
CO	16.34038	15.86717	11.72916
CO2	17.73630	18.48195	24.98356
CL	1.09830	0.69097	0.00058
CLH	25.54564	25.97058	26.68819
CLHO	0.00948	0.00421	0.00000
CLNO	0.00005	0.00001	0.00000
CLO	0.00304	0.00092	0.00000
CL2	0.01356	0.00738	0.00000
H	0.01995	0.01228	0.00001
HN	0.00001	0.00000	0.00000
HNO	0.00012	0.00004	0.00000
HNO2	0.00001	0.00000	0.00000
HNO2	0.00001	0.00000	0.00000
HO	0.54699	0.27676	0.00002
HO2	0.00023	0.00006	0.00000
H2	0.61832	0.61897	0.88540
HCOOH	0.00029	0.00016	0.00000
H2N	0.00011	0.00005	0.00000
H2O	27.49093	27.59391	25.29189
H2O2	0.00018	0.00006	0.00000
H3N	0.00021	0.00015	0.00006
N	0.00003	0.00001	0.00000
NO	0.11115	0.04704	0.00000
NO2	0.00004	0.00001	0.00000
N2	10.36914	10.39924	10.42120
N2O	0.00002	0.00001	0.00000
O	0.02072	0.00665	0.00000
O2	0.08332	0.02710	0.00000

SECONDS = 0.0

Figure 5. Sample AFRPL Performance Program Printout

modeled for complete ballistic analysis on the computer--for general evaluation of the configuration and for calculation of burning surfaces.

Applicable grain configurations are identified through evaluation of web fraction and volumetric loading requirements. Each applicable grain configuration is then evaluated primarily for its burning surface characteristics and for sliver in configurations such as the star. This evaluation ranges in complexity from simple manual calculations for the circular-ported cylinder to computer methods for more complex configurations.

Several computer analyses of the star configuration that can be used for this purpose have been reduced to graphical analysis and reported in the literature. One such analysis sponsored by AFRPL is available in Reference 4. A computer program for the star analysis used by Hercules determines and tabulates the most neutral-burning star with the required volumetric loading for every combination of the seven (six dimensionless) variables of the star. A sample computer run is shown in Fig. 6. This computer analysis greatly simplifies tradeoffs between sliver and burning neutrality and ensures the designer of an optimum design.

STAR GRAIN DESIGNS WITH MINIMUM RATIO MAX/(WEB AVG) PERIMETER AND VOLUMETRIC LOADING = 0.85

RADII: R1/R = 0.05 , R2/R = 0.05 MINIMUM ETA = 5 DEGREES

5 STAR POINTS

(w/R) WEB FRACTION	(Perimeter Ratio) MIN PMAX/PAVG	SLIVER FRACT	(ξ) XI, DEG.	(η) ETA, DEG.
0.3	1.06064	0.15421	29.3105	24.6151
0.31	1.04145	0.159045	30.1464	26.7433
0.32	1.02239	0.163215	30.9427	28.9183
0.33	1.00431	0.166117	31.6603	31.0361
0.34	1.00457	0.155814	31.4955	31.0032
0.35	1.00761	0.14461	31.1976	30.6509
0.36	1.01248	0.133321	30.8149	30.1014
0.37	1.01892	0.122194	30.362	29.3914
0.38	1.02682	0.11137	29.847	28.5478
0.39	1.03603	0.100909	29.2737	27.5698
0.4	1.04642	9.08605E-2	28.6439	26.4621
0.41	1.05786	8.13644E-2	27.9697	25.2703
0.42	1.07038	7.23807E-2	27.2463	23.9773
0.43	1.08377	6.39764E-2	26.4811	22.604
0.44	1.09812	5.60833E-2	25.6639	21.1259
0.45	1.11314	4.87959E-2	24.8079	19.5786

6 STAR POINTS

WEB FRACTION	MIN PMAX/PAVG	SLIVER FRACT	XI, DEG.	ETA, DEG.
0.3	1.04936	0.167519	28.3687	28.0545
0.31	1.03106	0.171242	29.0813	30.2142
0.32	1.01332	0.173984	29.7396	32.3448
0.33	1.00419	0.169956	30	33.4518
0.34	1.00562	0.15891	29.8005	33.2857
0.35	1.00929	0.147322	29.5002	32.8459
0.36	1.01447	0.135902	29.1388	32.2596
0.37	1.02117	0.124604	28.7111	31.4953
0.38	1.02921	0.1137	28.2347	30.6086
0.39	1.03851	0.103151	27.7042	29.5839
0.4	1.04893	9.31223E-2	27.1326	28.4591
0.41	1.06045	8.35393E-2	26.5114	27.2105
0.42	1.07287	7.45378E-2	25.8536	25.8761
0.43	1.08633	0.066054	25.1508	24.4466
0.44	1.10056	5.81022E-2	24.4058	22.8853
0.45	1.11549	5.07379E-2	23.6232	21.2522

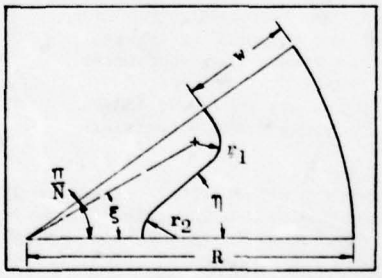

Figure 6. Sample Star Optimization Program Output

Computer codes are used extensively to calculate burning perimeters, surfaces, and port areas for input to performance prediction. These programs are either 2- or 3-dimensional codes, are easily modeled, and are usually prepared by individual companies in the format most suitable for each. Two of the most common 2-dimensional cross-sections that are programmed for computer solution are the star and slotted cylinder. An example computer run of a Hercules program for a slotted cross section is shown in Fig. 7. Inputs to all 2-dimensional codes are the independent variables that define the configuration and constants that control options.

Perhaps the most significant advancement that has been made in grain design analytical methods in recent years is development by Hercules under U. S. Army sponsorship of a generalized 3-dimensional grain geometry computer program (Ref 5). This computer program is capable of calculating burning surfaces and other geometrical features for virtually any grain design. The geometry is generalized to the extent that the shape can be described by a combination of intersections of cones, spheres, cylinders, and right triangular prisms (Fig. 8). This is sufficient for analytical definition of essentially any practical configuration, many of which could not be evaluated with closed-analytic methods.

Performance. Most computer programs that predict performance consider mass addition of combustion products to the chamber in increments along the flow channel. In so doing, pressure drop, loss in stagnation pressure, and other factors that influence net thrust can be treated in order to obtain an accurate thrust calculation. Erosive burning is usually considered to account for the significant effect of gas velocity on burn rate based on one of the many erosive burn rate models that have been proposed. /A comprehensive survey of erosive burning theories in Reference 6 contains a detailed list of models that have been proposed; one frequently used is the Lenoir-Robillard model (Ref 7)./

Several computer programs for performance prediction are referenced in the literature (Ref 8). The most recent computer program for performance prediction is the one developed under contract to AFRPL noted previously (Ref 2). This code, known as SPP, will calculate theoretical propellant properties, grain geometry, and internal flow and nozzle losses, as well as thrust and pressure with time; the program is presently being revised under AFRPL sponsorship to improve its capability.

ONE-DIMENSIONAL SLOTTED GRAIN CIRCULAR BORE OPTION FOR SLOTTED GRAIN

OUTSIDE RADIUS R1= 5 SLOT DEPTH R2= 4.5
HALF SLOT WIDTH R3= 0.25 INSIDE RADIUS R4= 1.25
NUMBER SLOTS N= 3

WEB IS R1-R4= 3.75

WEB	PERIMETER	PORT AREA	END AREA
0	26.8515	9.71584	68.824
0.25	28.0934	16.5815	61.9584
0.5	29.4268	23.77	54.7698
0.6	27.2478	26.5637	51.9761
0.7	26.3923	29.2436	49.2962
0.8	25.6915	31.8471	46.6927
0.9	25.051	34.3839	44.1559
1	24.4383	36.8582	41.6816
1.25	22.9437	42.7806	35.7592
1.5	21.4368	48.3289	30.2109
1.75	19.882	53.4949	25.0449
2	18.2635	58.2646	20.2752
2.25	16.5719	62.6206	15.9192
2.5	14.7976	66.5438	11.996
2.75	12.9047	70.0093	8.53049
3	10.87	72.9844	5.55546
3.25	8.66775	75.4304	3.10943
3.5	6.26181	77.3013	1.23851
3.75	0	78.5398	-8.9407E-8

PERIMETER-WEB INTEGRAL = 68.3944
GRAIN CROSS SECTION = 68.824
RATIO INTEGRAL/CROSS SECTION = 0.993758

Figure 7. Sample Slotted Grain Program Output

A typical computer program is one used at Hercules (Ref 9), called JCBALL. In this program, pressure and thrust histories are calculated considering the effects of mass addition, port area change, and burn rate variation under quasi-steady-state flow conditions. The burn rate theory used is a modification of the Lenoir and Robillard theory. The governing gas dynamic differential equations are solved by a finite difference technique. The grain may, in accordance with the technique, be considered to be comprised of nodes or elements of finite length. Pressure, mass flow rate, Mach number, velocity, temperature, and web burned are determined at each node along the grain length for each time increment. The resulting thrust, pressure and thrust impulse, throat diameter, exit diameter, amount of propellant burned, thrust coefficient, and delivered specific impulse are determined for each time increment. Inputs to the code include propellant properties; nozzle throat and exit diameters versus time; perimeter versus web; port area versus web; and wetted perimeter versus web, which may be varied independently for each node. Inputs and outputs are illustrated in Fig. 9.

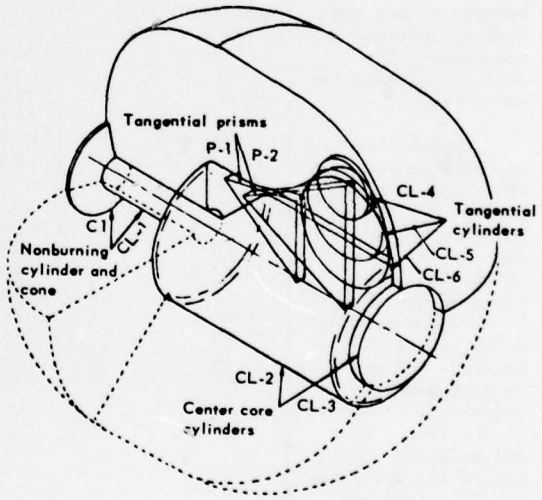

Figure 8. Simulation of Grain Configuration using Basic Geometric Shapes

An example computer run with partial output for JCBALL is presented in Fig. 10. The example grain design is a 5-point star having a volumetric loading fraction of 0.85 and web fraction of 0.40. The star angles are dimensioned such that it is the most neutral-burning 5-point star with that web fraction (from Fig. 6). Outputs include the fundamental quantities of pressure, thrust, and time. Appropriate quantities are integrated with time; these are thrust, pressure, and propellant weight. Burn rate and other quantities useful in ballistic analysis are also included in the output. Motor weight and center of gravity with time are optional outputs.

Grain - Structural Analysis. Before the advent of the large, high-speed digital computers in the early 1960s, grain structural analyses were restricted to closed-form solutions of simple cylindrical geometries, such as described in Reference 10, or photoelastic analyses as described in Reference 11.

With the capability provided by the digital computer it became feasible to apply finite element methods to grain structural analysis. Today many finite element structural analysis codes are available, such as TEXGAP-2D and TEXGAP-3D (both sponsored by the U. S. Air Force Rocket Propulsion Laboratory), AMG320-033 (sponsored by the U. S. Army Missile Command), SAP-IV (developed by the University of California), and NASTRAN (sponsored by the National Space and Aeronautics Association). Normally one of the

2-dimensional codes is utilized because of the excessive cost and time required for a 3-dimensional finite element analysis.

The primary finite element code utilized at Hercules is typical of the 2-dimensional codes. APSA (Fig. 11), the Hercules Finite Element Axisymmetric and Planar Structural Analysis Code, is utilized with orthotropic, temperature-dependent material properties. This program has been developed by Hercules partially under company-funded IR&D effort and partially under NASA and AFRPL sponsorship (Ref 12).

The basic framework of the APSA program comes from the SAAS I program (Ref 13, 14). A double-precision version of this program was released as Reference 15. This code was supplemented with plane stress and generalized plane strain programs and a plot program in 1968. The APSA program combines the three versions into one program and contains numerous improvements developed over the last several years. The most recent version was released in April 1974 (Ref 16).

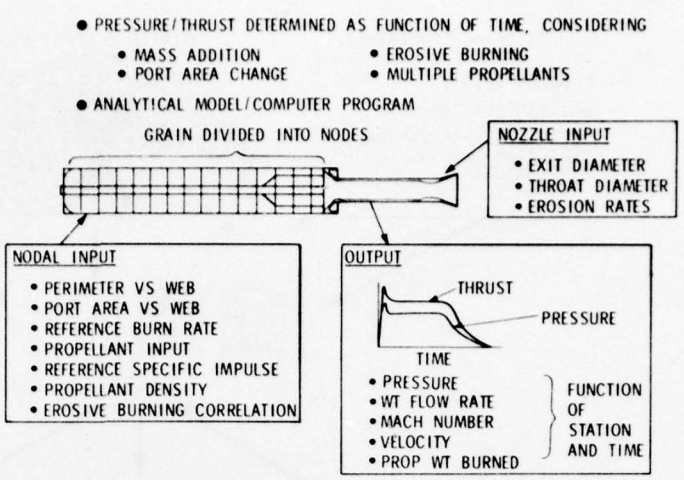

Figure 9. Generalized Internal Ballistic Analysis

OUTPUT

TIME SURF	PSTAG FWD/AFT	PSTAT FWD/AFT	THRUST IMPULSE	WDOT PROP WT	PRES IMP FWD/AFT	BURN RATE FWD/AFT	WEB FWD/AFT	THROAT DIA EXIT DIA	CF THD ISP DEL
0.0 1233.7	1967.6 1932.5	1967.6 1882.6	11057.8 0.0	43.31 0.0	0.0 0.0	0.4759 0.7997	0.0 0.0	2.1540 6.0920	1.5703 255.4612
0.042 1237.1	1876.4 1846.8	1876.2 1814.7	10553.3 458.5	41.41 1.80	81.5 80.2	0.4669 0.7247	0.0200 0.0323	2.1544 6.0920	1.5675 254.6958
0.086 1240.4	1807.4 1782.2	1807.2 1755.8	10173.6 905.7	39.98 3.55	161.0 158.5	0.4599 0.6696	0.0400 0.0624	2.1549 6.0920	1.5653 254.4365
0.129 1243.6	1755.1 1732.8	1754.8 1710.1	9883.9 1344.4	38.90 5.28	239.6 235.4	0.4546 0.6277	0.0600 0.0907	2.1553 6.0920	1.5634 254.0648
0.174 1246.8	1716.1 1696.3	1715.9 1676.4	9670.5 1776.5	38.08 6.98	315.7 311.1	0.4505 0.5951	0.0800 0.1177	2.1557 6.0920	1.5620 253.7762
0.218 1249.9	1684.1 1666.3	1683.9 1648.7	9496.3 2203.5	37.43 8.66	391.4 386.1	0.4471 0.5690	0.1000 0.1437	2.1562 6.0920	1.5608 253.5304
0.263 1253.0	1658.9 1642.6	1658.7 1626.6	9358.8 2626.5	36.93 10.33	466.4 460.3	0.4444 0.5477	0.1200 0.1687	2.1566 6.0920	1.5597 253.3297
0.308 1256.0	1638.7 1623.8	1638.5 1609.4	9250.8 3046.2	36.53 11.99	540.8 534.0	0.4423 0.5303	0.1400 0.1930	2.1571 6.0920	1.5585 253.1659
0.353 1259.1	1624.7 1611.0	1624.6 1597.7	9178.3 3463.6	36.24 13.63	614.7 607.2	0.4408 0.5161	0.1600 0.2187	2.1575 6.0920	1.5583 253.0513
0.399 1262.1	1612.4 1599.9	1612.3 1587.9	9116.0 3879.3	36.01 15.26	688.3 680.2	0.4394 0.5040	0.1800 0.2399	2.1580 6.0920	1.5578 252.9496
0.444 1264.9	1602.2 1590.7	1602.1 1579.7	9064.8 4293.6	35.82 16.91	761.5 752.9	0.4363 0.4938	0.2000 0.2626	2.1584 6.0920	1.5574 252.8635
0.490 1267.0	1593.1 1582.3	1593.0 1571.9	9018.1 4706.6	35.65 18.55	834.5 825.4	0.4373 0.4850	0.2200 0.2850	2.1585 6.0920	1.5570 252.7840

Figure 10. Sample JCBALL Program Printout

Input to the program consists principally of material properties, geometric configuration in the form of a finite element mesh, and the loading conditions. Program output consists of all input data and the following calculated information:

- Nodal Point Displacements
- Hoop Stress
- Radial (x) Stress
- Axial (y) Stress
- Shear Stress (xy)
- Maximum Principal Stress
- Minimum Stress
- Maximum Shear Stress
- N-Stress
- S-Stress
- Shear Stress (NS)
- Element Centroid
- Hoop Strain
- Radial (x) Strain
- Axial (y) Strain
- Shear Strain (xy)
- Maximum Principal Strain
- Minimum Strain
- Angle of Maximum Stress
- N-Strain
- S-Strain
- Shear Strain (NS)

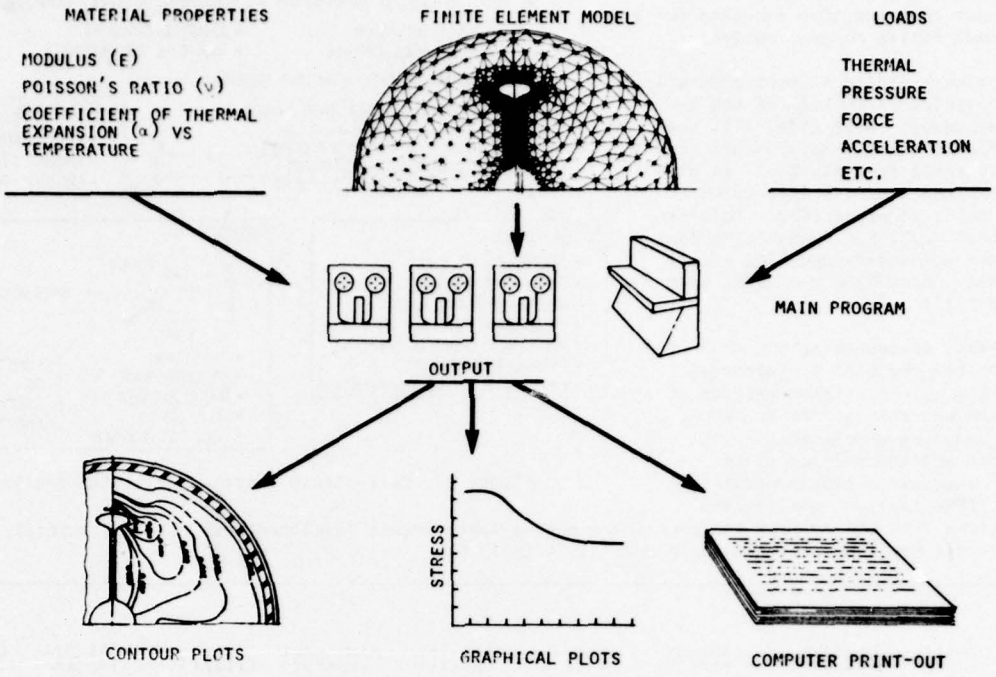

Figure 11. APSA Finite Element Stress Analysis Program

In addition to the printed output described above, automated plot routines are available to obtain grid plots, isoplots and graphical plots of both input data and calculated results. Examples of these plots are shown in Fig. 12 and 13.

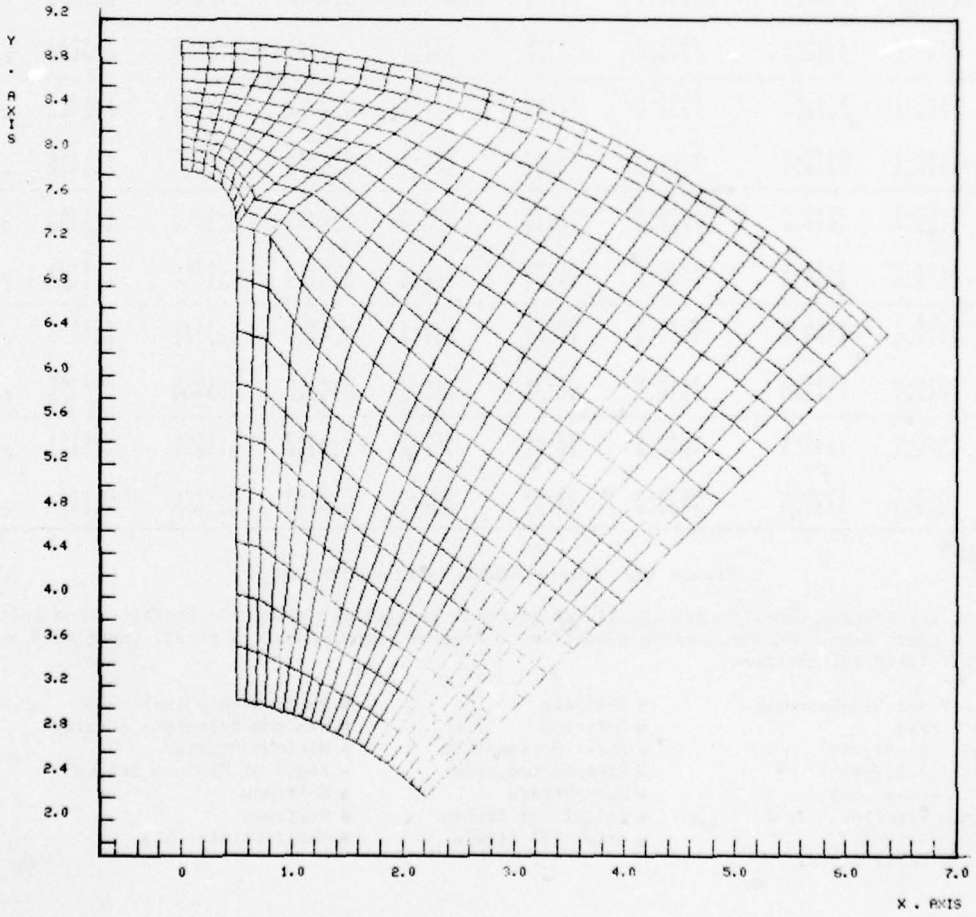

Figure 12. Sample Computer Graphic Plot of Plane Strain Finite Element Model

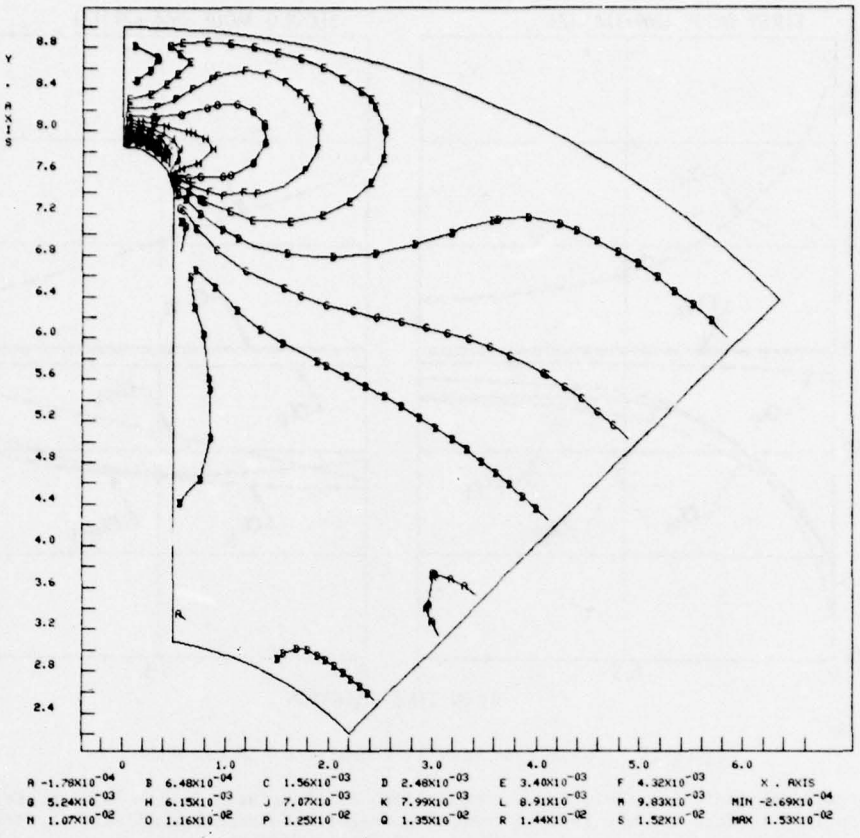

Figure 13. Sample Computer Graphic Plot of Isostrain Contours

Combustion Stability. The increasing demand for solid rocket motors with reduced or minimum-smoke exhaust plumes has increased the probability of encountering combustion instability. Even in motors having aluminized propellant, the risk of combustion instability is ever-present. An increased understanding of the mechanisms and theoretical aspects of combustion instability and advances in computer methods have made possible analytical methods for predicting the margin of stability of a solid rocket motor. All major solid rocket companies in the USA have their own proprietary computer codes for combustion stability prediction. Hercules has had an operational stability code for several years; this is used in conjunction with the NASTRAN finite element code that performs all acoustic mode calculations.

Significant recent accomplishments in this area have been sponsored by the AFRPL. Two stability codes have been developed, based on extensive industry participation under AFRPL sponsorship (Ref 17). One is a longitudinal mode program that calculates both acoustic modes and stability integrals. The other is a 3-dimensional code that, like the Hercules code, is used in conjunction with NASTRAN. This version treats both transverse and longitudinal acoustic modes.

The grain cavity is modeled by line numbers that correspond to segments of the cavity. Each segment is described in terms of its length, port area, and burning surface area. The burn rate of the propellant and distribution of particles in the gas stream for each line are listed separately. If the segment contains non-burning areas, these can be shown for purposes of calculating viscous damping. Nozzle admittance functions and various response functions complete the input data. Outputs include the combustion alpha and damping integrals for the various elements labeled and interpolated values of response functions applicable to the integral, the total linear alpha, and a summation of products of integrals and response functions.

The example stability analysis corresponds to one point in the burn duration. Typically, analyses are made at three or more points in time and results are plotted versus time. A typical plot showing the individual stability elements and net stability prediction versus time is presented in Fig. 14.

Although not developed to the degree that performance prediction has been developed, stability predictions provide an excellent means for ranking motor designs on the basis of combustion stability. If the propellant response function is well defined from substantial T-burner data and if nozzle damping values are well established, the stability prediction has reasonable merit.

Component Thermal Analysis. Since the thermal design of a solid propellant rocket motor is intimately related to the structural design, many thermal analysis programs are designed for use in combination with a structural analysis program. Examples of such programs are THVINC (U. S. Air Force/University of California); TEXGAP-2D (U. S. Air Force/University of Texas); and NASTRAN (NASA). For most rocket design activities these or programs with similar capability developed privately are utilized. The thermal analysis program ORTHEAT utilized in combination with a modified version of APSA at Hercules is typical of these programs.

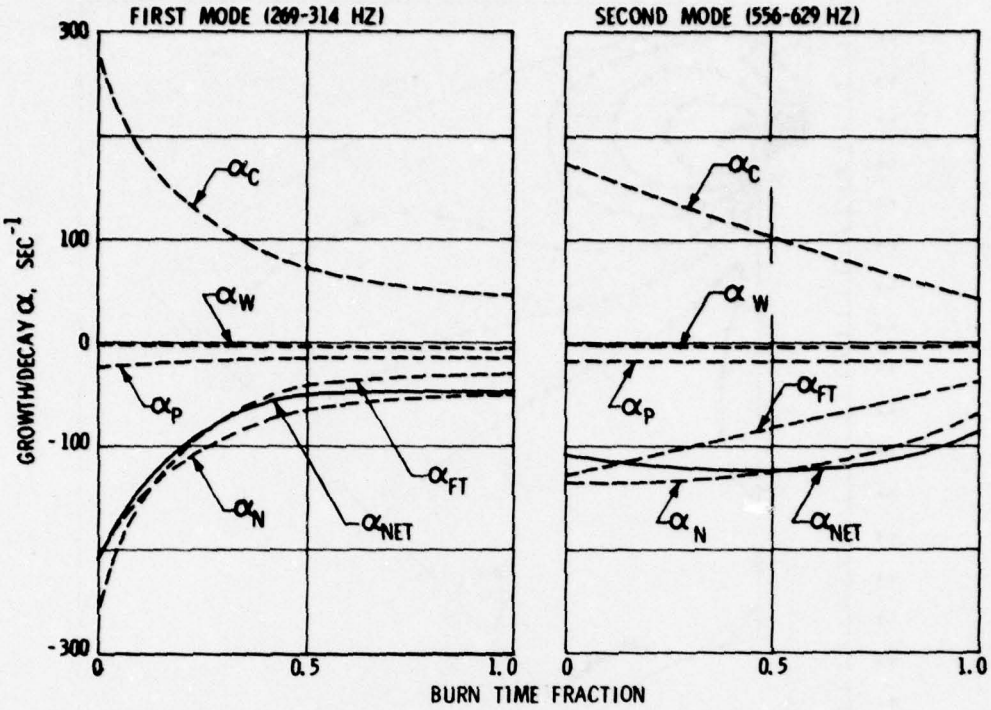

Figure 14. Combustion Stability Analysis - Axial Mode

Thermal-structural analysis (i.e., for thermally induced structural loads) is completely dependent on the analyst's ability to describe the induced thermal gradient. Currently available structural and thermal analytical techniques are sufficiently sophisticated that optimization of a design is limited only by the available data on material properties and time.

The 2-dimensional plane and axisymmetric finite element stress analysis and 2-dimensional plane and axisymmetric finite difference thermal analyses utilize analytical models that are very similar (Fig. 15). These two analyses may be formulated such that: (1) a single congruent set of data is required to describe the geometry; (2) the output of the thermal analysis is directly usable by the stress analysis; and (3) the thermal analysis can be conducted economically.

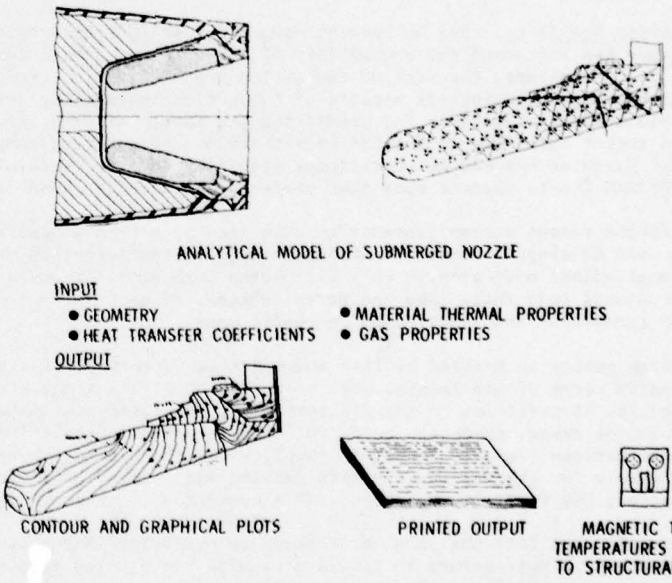

Figure 15. Component Thermal Analysis

In ORTHEAT the finite difference method is applied to the solution of the 2-dimensional plane and axisymmetric heat transfer problem using a finite-element model. The continuous body is replaced by a system of ring or plane elements with triangular or quadrilateral cross sections. Since elements are of arbitrary shape and have different material properties the procedure can be applied to bodies composed of many different materials of complex geometry. Up to 1500 nodal points and elements may be used to define the finite element model. Program interpolation between input data points provides for efficient and economical usage. The program considers orthotropic temperature-dependent material properties for up to 15 different materials. Properties are tabularly input as functions of temperature. Up to eight temperatures may be used to define each material.

Applicable boundary conditions may be specified by several input options. Nine time-dependent forcing temperatures may be specified for use with the convective and radiative coefficients. Time-dependent convective coefficients and temperature-dependent radiative coefficients are input tabularly using up to 15 points to define each curve. Five convective and five radiative coefficient curves may be specified. Boundary conditions may be specified as convective only; radiative only; convective and radiative to the same or different forcing temperatures or internal flow (for axisymmetric only). Internal flow may be

either a function of pressure or weight flow rate as functions of time. Gas properties (ratio of specific heats, molecular weight, flame temperature, and gas emissivity) are input as tabular functions of time with 15 points available for defining each variable. Among internal flow boundaries, gas transport properties are calculated using 1-dimensional isentropic relations with area change. Thus, for each boundary element exposed to internal flow, a pressure, convective coefficient, and radiative coefficient are calculated. Additional pressure boundary conditions as functions of time may be input for future use with stress programs, if desired.

The program is also capable of handling internal heat generation as a function of either time or temperature. Five curves of each type are available with 15 defining points for each. Total heat flow rate across up to 10 different specified boundaries may be obtained. Linear extrapolation is used between tabular input data points.

Program outputs include: nodal point and element data; boundary elements with applied coefficients and forcing temperatures; tabular input data; temperature of each element; and boundary pressure for each specified output time. At these specified times the element temperatures and pressure boundary data may be printed out as shown in Fig. 16 and written on tape for future use with the structural analysis program. Ablation and char fronts are also determined. Typical results are shown in Fig. 17. In addition, automated plotting provides plots similar to those of Fig. 12 and 13.

TIME= 5.5550

TEMPERATURE(I)= (Element Temperature, deg F -- Element No. 440, 441, 442, etc.)

Element No. →0	1	2	3	4	5	6	7	8	9
440	70.487	114.255	1033.986	1135.673	1285.500	1435.242	1621.024	1820.706	130.607	72.542
450	70.057	70.000	70.000	70.000	70.000	4270.195	2134.467	125.609	70.630	70.003
460	70.000	70.000	70.018	71.207	103.367	110.309	116.214	127.868	139.533	152.812
470	72.476	70.112	70.001	70.000	70.000	70.000	70.000	4248.727	2078.754	128.969
480	70.724	70.004	70.000	70.000	70.000	70.419	70.398	70.527	70.659	70.831
490	71.125	71.835	70.060	70.001	70.000	70.000	70.000	70.000	70.000	4102.184
500	1814.742	124.805	70.741	70.005	70.000	70.000	70.002	70.177	70.261	70.346
510	70.435	70.342	70.665	70.000	70.000	70.000	70.000	70.000	70.000	70.000
520	4003.131	1596.632	122.367	70.784	70.006	70.000	70.000	70.001	70.129	70.172
530	70.225	70.283	70.344	70.397	70.000	70.000	70.000	70.000	70.000	70.000
540	70.010	4018.355	1600.874	126.730	70.928	70.009	70.000	70.000	70.001	70.096
550	70.124	70.160	70.201	70.241	70.259	70.165	70.000	70.000	70.000	70.000
560	70.000	70.000	70.000	4074.673	1633.086	124.414	71.188	70.014	70.000	70.000
570	70.001	70.068	70.047	70.112	70.141	70.170	70.161	70.159	70.000	70.000
580	70.000	70.000	70.000	70.000	70.000	3926.749	1564.922	142.231	71.637	70.025
590	70.008	70.012	70.021	70.049	70.367	70.090	70.116	70.148	70.169	70.000
600	70.000	70.000	70.000	70.000	70.000	70.000	3938.500	1530.234	144.852	71.768
610	70.029	70.001	70.009	70.012	70.019	70.031	70.040	70.046	70.046	70.106
620	70.000	70.000	70.000	70.000	70.000	70.000	70.000	4051.657	1740.895	159.963
630	72.248	70.040	70.000	70.000	70.315	70.018	70.021	70.022	70.023	70.000
640	70.000	70.000	70.000	70.000	70.000	3974.235	1679.059	167.578	74.803	70.058
650	70.000	70.000	70.011	70.012	70.012	70.013	70.013	70.000	70.000	70.000
660	70.000	70.000	4012.768	1695.382	189.273	74.498	70.114	70.001	70.000	70.000
670	70.003	70.003	70.003	70.003	70.000	70.000	70.000	4010.264	1852.248	184.143
680	73.419	70.109	70.001	70.000	70.301	70.001	70.001	70.001	70.000	70.000
690	70.000	4063.837	1878.102	174.713	72.686	70.050	70.000	70.000	70.000	70.000
700	70.000	70.000	70.000	70.000	3389.143	1620.067	179.871	73.790	70.096	70.001
710	70.000	70.000	70.030	70.000	70.333	70.000	70.000	3930.628	1627.565	214.435
720	70.430	70.250	70.005	70.000	70.000	70.000	70.000	70.000	70.000	70.000
730	3416.085	1721.946	276.079	84.245	70.749	70.029	70.000	70.000	70.000	70.000
740	70.000	70.000	70.000	3924.896	1716.466	306.129	89.627	71.238	70.153	70.000
750	70.000	70.000	70.000	70.000	70.000	70.000	3874.462	1684.116	294.695	87.952
760	71.147	70.000	70.000	70.000	70.000	70.000	70.000	70.000	3782.922	1693.166
770	265.979	85.548	70.985	70.000	70.000	70.000	70.000	70.000	70.000	70.000
780	3795.594	1502.926	272.098	86.570	71.388	70.000	70.000	70.000	70.000	70.000
790	74.000	70.000	3818.747	1698.897	295.614	88.092	72.235	70.000	70.000	70.000
800	70.000	70.000	70.030	70.000	3793.655	1667.011	297.957	89.470	71.337	70.000
810	70.000	70.000	70.000	70.000	70.000	70.000	3801.649	1676.508	293.513	89.153
820	71.160	70.000	70.000	70.000	70.000	70.000	70.000	70.000	3831.882	708.583
830	166.095	81.379	71.142	70.000	70.000	70.000	70.000	70.000	70.000	70.000
840	2970.742	704.469	169.487	81.835	71.224	70.000	70.000	70.000	70.000	70.000
850	70.000	70.000	3028.753	739.403	177.392	83.102	74.396	70.000	70.000	70.000
860	70.000	70.000	70.000	70.000	3085.869	780.343	190.601	85.575	71.758	70.000
870	70.000	70.000	70.000	70.000	70.000	70.000	3039.030	768.082	188.450	85.299

Figure 16. Sample Thermal Analysis Program Output

Multiple runs may be made by stacking data. To facilitate more economical running of multiple conditions for the same model, an option to store model geometry and input data on tape is provided. Subsequent runs require only inputting the desired changes.

Component Structural Analysis. For preliminary structural analysis of various components other than the propellant grain, traditional structural analytical techniques are normally utilized; these are available in a wide variety of handbooks and textbooks, such as Roark (Ref 18) and Timoshenko (Ref 19). Frequently these calculations are performed manually or with the aid of programmable hand calculators. For more detailed structural analyses the same finite element computer codes as discussed under Grain Design Structural Analysis are normally utilized. On occasion, 3-dimensional codes such as SAP IV or NASTRAN are used.

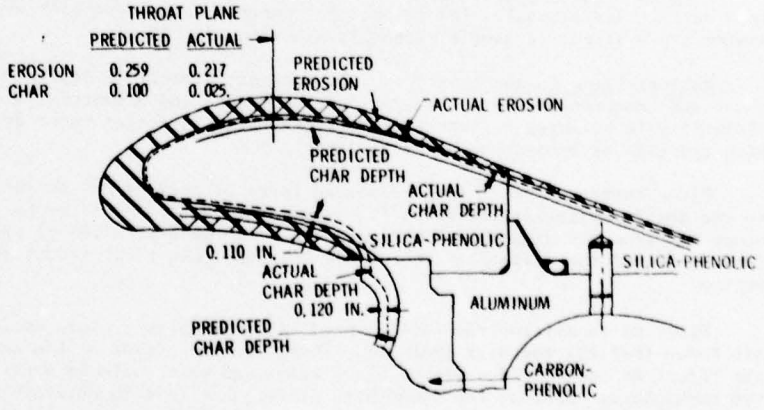

Figure 17. Predicted Char and Erosion

For thermal stress analyses, Hercules uses a modified version of its APSA finite element code. This accepts, as input, geometry and temperature data from tapes generated by the ORTHEAT thermal analysis code. The output is the same as previously described for APSA.

Mass Properties. Mass property characteristics of all components are critical in the design of a missile because of their influence on flight dynamics, guidance, and controls. Typically, for rocket motors, the specification for the propulsion section may place limits on loaded motor weight and on location of the longitudinal and radial center of gravity before, during, and after burning. Calculation of weights, centers of gravity, and moments of inertia of components and the techniques of combining these characteristics for several components to obtain the weight and center of gravity of the motor are not new. However, before development of high-speed digital computers, the manual techniques were tedious, time-consuming, and prone to error.

Most automated mass properties programs used today utilize the same geometrical techniques that have been used for years. They have simply been adapted to the computer to save time and reduce errors. A Hercules program (WTCG) is typical of those used for calculating mass properties of rocket motors and their components. The components are divided into segments, each of which is a standard geometrical shape whose dimensions, location and orientation are specified. Values of weight, center of gravity and moment of inertia are computed using standard formulas for each shape. The program then performs the calculations necessary to combine these results into a total weight, center of gravity, and moment of inertia for the part.

The general plan of the program, Fig. 18, requires that each component be resolved into a collection of standard shapes and that dimensional parameters defining each be submitted as input data. Separate subroutines then process the data for each entry; resulting in a weight, center of gravity, and three properly oriented inertia values for each with respect to a reference coordinate system. Input data for each entry consist of the dimensions defining the shape, the density of the material (material is removed), the location of a specified identifying point in the common reference system, and direction numbers indicating orientation of one or more of the principal axes of the shape with respect to the common axis system. A number identifying the particular shape must also be furnished with each entry.

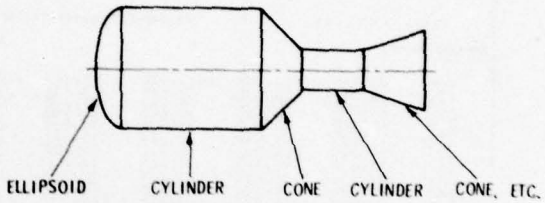

INPUT: DIMENSIONAL PARAMETERS OF COMPONENTS BASED ON 43 DIFFERENT STANDARD SHAPES
DENSITY AND LOCATION RELATIVE TO A REFERENCE POINT
ORIENTATION OF SHAPES RELATIVE TO COMMON AXIS SYSTEM

OUTPUT: WEIGHT, CENTER OF GRAVITY, MOMENT OF INERTIA FOR EACH INPUT SHAPE
WEIGHT, CENTER OF GRAVITY, MOMENT OF INERTIA FOR SPECIFIED GROUPS OF SHAPES
WEIGHT, CENTER OF GRAVITY, MOMENT OF INERTIA FOR ENTIRE SYSTEM

Figure 18. Mass Properties Program

The program contains subroutines for 43 different standard shapes. Within each subroutine the weight, center of gravity with respect to the common axis system, and moment of inertia with respect to the principal axes of the shape are calculated using standard formulas for the particular shape. Then, using the input direction numbers that describe the orientation of the shape, the moments of inertia about the center of gravity of the particular entry in the common reference system are calculated. After processing each separate entry the main program contains a complete set of weights, centers of gravity, and moments of inertia values for all elements.

Each of the formulas programmed represents an exact solution for the particular shape, thus the accuracy attained is limited only by the ingenuity used in representing the actual design with combinations of the available shapes.

Printed results consist of a list containing the weight, center of gravity, and moment of inertia for each entry. Additionally, the respective combined values for each of the subgroups and for the entire system are printed. A sample output is shown in Fig. 19.

Exhaust Plume Characteristics. Although not directly a design factor in the same sense as propellant grain and component design, associated performance, and structural and thermal analyses, exhaust plume visibility is becoming an important characteristic in rocket motor design, particularly with motors cast with reduced- or minimum-smoke propellants.

Plume characteristics are defined in terms of primary and secondary smoke, where primary smoke refers to the solid particulate effluent from the motor and secondary smoke to the condensation of species in the plume and from the atmosphere. Primary smoke can be controlled by propellant formulation, whereas secondary smoke and the visibility thereof depends on combustion product and atmospheric condition and interaction.

Programs to develop theoretical prediction of exhaust plume smoke are being developed by the U. S. Air Force (Ref 20) and Navy (Ref 21). These programs focus on the energy release from plume cooldown and the effect on condensation of the plume water, on water soluble species in the plume, and on moisture in the atmosphere. Because the atmosphere plays a key role in determining the secondary smoke formation, studies are now being directed toward better definition of the climate (Ref 22).

CONCLUDING STATEMENT

The availability of the digital computer in combination with development of finite element and finite difference methods over the last 25 years has drastically altered design methodology used in solid rocket motor design. As a result, the quality of design and the efficiency of the design operation have improved significantly.

RESULTS - INDIVIDUAL ENTRIES

GROUP	SHAPE		CENTER OF GRAVITY			MOMENTS OF INERTIA		
K	N	WEIGHT	XBAR	YBAR	ZBAR	DELTA X	DELTA Y	DELTA Z
1	1	0.222867685 01	81.58	0.0	0.0	0.166966435 02	0.109869265 02	0.109869265 02
1	1	0.689476975 00	93.00	0.0	0.0	0.466111665 01	0.236301335 01	0.236301335 01
1	109	0.472166155-01	79.73	0.0	0.0	0.373985705 00	0.191650395 00	0.191650395 00
1	114	0.139668825 01	79.20	0.0	0.0	0.198520515 02	0.109843755 02	0.109843755 02
1	107	0.429209545 01	72.49	0.0	0.0	0.916629275 02	0.699081575 02	0.699081575 02
1	1	0.361681825 02	32.49	0.0	0.0	0.892882815 03	0.131772095 05	0.131772095 05
1	1	0.100522525 01	2.70	0.0	0.0	0.247862095 02	0.126211625 02	0.126211625 02
2	1	0.618792835 00	9.40	0.0	0.0	0.133968545 01	0.681723545 00	0.681723545 00
2	114	0.192037775 01	1.32	0.0	0.0	0.941389475 01	0.511661825 01	0.511661825 01
2	159	0.448765565 01	3.45	0.0	0.0	0.940151375 02	0.472507935 02	0.472507935 02
2	109	0.491111745 00	2.00	0.0	0.0	0.107548525 02	0.538027305 01	0.538027305 01
2	109	0.367941865 00	2.01	0.0	0.0	0.729165655 01	0.366478225 01	0.366478225 01
3	1	0.312065845 01	5.94	0.0	0.0	0.697349665 03	0.344688625 03	0.344688625 03
3	109	0.504457965 00	1.92	0.0	0.0	0.116544195 02	0.582991795 01	0.582991795 01
3	109	0.111852695-01	80.07	0.0	0.0	0.106100685 00	0.533447775-01	0.533447775-01
3	109	0.322858815 00	80.80	0.0	0.0	0.199846545 01	0.599609385 00	0.599609385 00
3	108	0.384838365 00	79.18	0.0	0.0	0.198122055 01	0.101440435 01	0.101440435 01
3	1	0.817175565 00	80.79	0.0	0.0	0.398757085 01	0.236029155 01	0.236029155 01
3	109	0.293335145 00	82.44	0.0	0.0	0.149920565 01	0.794921885 00	0.794921885 00
3	1	0.979784195 00	81.16	0.0	0.0	0.639338835 01	0.403262335 01	0.403262335 01
3	1	0.874311035-01	83.13	0.0	0.0	0.529413105 00	0.268696135 00	0.268696135 00
4	109	0.201779015-01	78.70	0.0	0.0	0.343414555-01	0.177917485-01	0.177917485-01
4	1	0.144171545-01	78.98	0.0	0.0	0.236834515-01	0.118897675-01	0.118897675-01
4	1	0.454298475-01	78.17	0.0	0.0	0.225988455 00	0.113678345 00	0.113678345 00
4	1	0.556779405-01	78.70	0.0	0.0	0.111313585 00	0.582573125-01	0.582573125-01
4	109	0.773453715-01	79.42	0.0	0.0	0.153370665 00	0.810546885-01	0.810546885-01
4	109	0.157909995-01	78.25	0.0	0.0	0.556771765-01	0.274200445-01	0.274200445-01
4	1	0.563495345 00	78.15	0.0	0.0	0.172170165 01	0.994068675 00	0.994068675 00
4	108	0.264865165-01	80.00	0.0	0.0	0.729369935-01	0.367584235-01	0.367584235-01

RESULTS - SUB GROUPS

GROUP	WEIGHT	XBAR	YBAR	ZBAR	DELTA X	DELTA Y	DELTA Z
1	0.457954105 02	40.15	0.0	0.0	0.105006455 04	0.284508755 05	0.284508755 05
2	0.114910125 02	2.12	0.0	0.0	0.201544605 03	0.132833865 03	0.132833865 03
3	0.291369705 01	80.93	0.0	0.0	0.155650325 02	0.114687505 02	0.114687505 02
4	0.958615995 00	78.39	0.0	0.0	0.239601235 01	0.153125005 01	0.153125005 01

TOTAL

0	0.610585025 02	35.47	0.0	0.0	0.126956985 04	0.499828755 05	0.499828755 05

Figure 19. Sample Mass Properties Program Output

An attempt has been made in this paper to reflect current, typical capabilities in the area of design automation in the USA. Accordingly, examples have been used that are neither the most sophisticated nor the most limited in the various areas treated.

In the future, further progress certainly is indicated. Particularly, emphasis is expected in the areas of computer-generated graphics to aid the designer and analyst and in CAD/CAM (which utilizes the results of Computer Automated Design to produce design drawings of components and control tapes to drive the Computer Automated Machinery that fabricates the components).

REFERENCES

1. Gordon, S.; and B. J. McBride: "Computer Program for Calculation of Complex Chemical Equilibrium Compositions, Rocket Performance, Incident and Reflected Shocks and Chapman-Jouquet Detonations," NASA-SP-273, NASA Lewis Research Center, 1971.

2. Coats, D. E., et al: "A Computer Program for the Prediction of Solid Propellant Rocket Motor Performance," Report AFRPL-TR-75-36, Edwards Air Force Base, California, July 1975.

3. Huggett, C.: Combustion of Solid Propellants. High Speed Aerodynamics and Jet Propulsion, Vol. II-Combustion Processes, Sec. M, B. Lewis, R. N. Pease, and H. S. Taylor, eds., Princeton University Press, 1956.

4. Messner, A. M.: "Final Report. Integrated Structural and Ballistic Design Curves for Star-Perforated Propellant Grains," Report AFRPL-TR-70-106, Edwards Air Force Base, California, October 1970.

5. Peterson, E. G.; C. C. Nielsen; W. C. Johnson; K. S. Cook; and J. G. Barron: "Generalized Coordinate Grain Design and Internal Ballistics Evaluation Program," Preprint 68-490, ICRPG/AIAA 3rd Solid Propulsion Conference, Atlantic City, New Jersey, June 4-6, 1968.

6. Kuo, K. K. and M. K. Razdan: "Review of Erosive Burning of Solid Propellants," CPIA Publication 273, Vol. II, Johns Hopkins University, August 1975.

7. Robillard, G. and J. M. Lenoir: "The Development of a New Erosive Burning Law," Publ. 91, Jet Propulsion Lab., California Institute Technology, Padadena, California, April 1, 1957.

8. Brooks, W. T.: "Solid Propellant Grain Design and Internal Ballistics," Design Criteria Monograph, NASA SP-8076, Lewis Research Center, Cleveland, Ohio, March 1972.

9. Cunningham, J. M.: "Ballistic Performance Prediction for Solid Propellant Rocket Motors," Report R-4902-I, Hercules, Incorporated, McGregor, Texas, September 1975.

10. Williams, M. L., P. J. Blatz, and R. A. Schapery: "Fundamental Studies Relating to Systems Analysis of Solid Propellants, GALCIT SM 61-5," Thiokol Report No. 23-61, February 1961.

11. Fourney, M. E. and R. R. Parmerter: "Parametric Study of Rocket Grain Configuration by Photoelastic Analysis," Report AFRPL-TR-66-52, March 1966, Mathematical Sciences Corporation, Seattle, Washington.

12. Fulton, D.: "Investigation of Thermal Fatigue in Non-Tubular Regeneratively Cooled Thrust Chambers," Rockwell International Corporation, Canoga Park, California, Report AFRPL-TR-73-20, Volumes I and II, May 1973.

13. Wilson, E. L. and R. M. Jones: "Finite Element Stress Analysis of Axisymmetric Solids with Orthotropic, Temperature-Dependent Material Properties," Report TR-0158 (S3816-22)-1, The Aerospace Corporation, San Bernardino, California, September 1967.

14. Jones, R. M. and J. G. Crose: "SAAS II, Finite Element Stress Analysis of Axisymmetric Solids with Orthotropic, Temperature-Dependent Material Properties," Report TR-0200(S4980)-1, The Aerospace Corporation, San Bernardino, California, September 1968.

15. Minami, H. and S. Persselin: "Finite Element Stress Analysis of 2-D Structures with Orthotropic Temperature-Dependent Material Properties," Report SR8111-3002, Rockwell International Corporation, September 1968.

16. Newell, J. F. and S. F. Persselin: "Finite Element Axisymmetric and Planar Structural Analysis," Report SSME 74-1282, Rockwell International Corporation, April 1974.

17. Lovine, R. L.: "Standardized Stability Prediction Method for Solid Rocket Motors," Report AFRPL-TR-76-32, Edwards Air Force Base, California, May 1976.

18. Roark, R. J.: Formulas for Stress and Strain, McGraw-Hill Book Company, 1965.

19. Timoshenko, S.: Strength of Materials, D. Van Nostrand Company, Inc., 1965.

20. Hoshizaki, H., et al: "Plume Visibility Detection Study," 10th JANNAF Plume Technology Meeting, CPIA Publication 291, Volume II, September 1977.

21. Victor, A. C.: "Prediction of Rocket Exhaust Smoke Formation in Free Jets and Smoke Chambers," 1978 JANNAF Propulsion Meeting, CPIA Publication 293, February 1978.

22. Victor, A. C.: "A Proposed Standard Climate for Evaluating Rocket Exhaust Secondary Smoke Formation and Visibility," Naval Weapons Center Technical Memorandum 3638, Naval Weapons Center, China Lake, California, November 1978.

ACKNOWLEDGEMENTS

The authors wish to acknowledge the assistance of the following members of the Hercules-McGregor Research and Development Department in preparing the descriptions of the various computer codes: Messrs. D. K. Barrington and J. D. Burton and Ms. D. A. Browne.

DISCUSSION

H.F.R.Schöyer, Delft University of Technology, Ne

For the internal ballistic grain design you made your calculations by the method of successive approximations. However since you have large computers available it should be possible, after calculating the initial conditions for flow in the grain with mass addition, to determine the variation in time of all variables by solving non-linear algebraic equations. This would appear a simpler and more reliable means. Therefore why use the method of successive approximations?

Author's Reply

The successive approximation technique is used to couple the mass rate of gas produced by the grain to the mass rate of discharge permitted by the nozzle. This facilitates the determination of the initial condition and also the axial variation of pertinent parameters within the motor chamber. From an engineering viewpoint it is convenient and efficient to employ this process for the total operating time with the existing, available computer programme.

H.F.R.Schöyer, Ne

How do you allow for discontinuities in the grain such as the "moving slot" in a slotted tube grain design?

Author's Reply

Basically this is done by node definition. The approach is a quasi steady state approximation of a dynamic occurrence. Discontinuities or rather geometrical variations in the grain are accounted for by appropriate selection of grain nodes. The forward and aft grain planes defining node location remain fixed. Nodal description such as burning perimeter, surface area, port or flow area etc. are an input as a function of propellant web distance burned. Thus, as a function of incremental time and including propellant burning rate data, the geometrical variation of each node with time may be determined.

ALLUMAGE ET EXTINCTION DES PROPERGOLS SOLIDES

par Guy LENGELLÉ, Pierre MENTRÉ, Joël GUERNIGOU,
Alain BIZOT et Yves MAISONNEUVE

Office National d'Etudes et de Recherches Aérospatiales (ONERA)
92320 Châtillon (France)

Résumé

Les activités menées à l'ONERA sur l'inflammation et l'extinction portent à la fois sur le propergol lui-même et sur le chargement avec un dispositif d'allumage donné.

Les caractéristiques d'allumage des propergols composites et double base ont été étudiées en exposant des échantillons à un jet de gaz neutre produit par arc ainsi qu'aux produits issus d'un moteur à propergol contenant ou non de l'aluminium. Les moyens utilisés pour étudier l'inflammation sont les techniques de visualisation, la pyrométrie infrarouge, et les capteurs à ultra-sons qui effectuent un contrôle continu de l'épaiseur de l'échantillon. On observe que les lois d'inflammation restent les mêmes quel que soit le type d'échauffement (convection - conduction, impact de particules) et qu'elles sont contrôlées par les caractéristiques de dégradation des composants du propergol.

Les diverses techniques expérimentales utilisées dans des moteurs à échelle réduite pour étudier l'inflammation des propergols et la propagation de la flamme sont décrites, en particulier les fluxmètres.

Des exemples d'application de ces techniques à l'étude de l'allumage des moteurs, avec chargements de propergols composites ou double base, sont présentés.

Les études menées sur les caractéristiques d'extinction, limite de déflagration aux basses pressions et extinction par dépressurisation, de divers propergols composites révèlent l'influence des paramètres de la composition : taille des particules, nature du liant, et présence d'additifs.

IGNITION AND EXTINCTION OF SOLID PROPELLANTS

Summary

Activities carried out at ONERA on ignition and extinction are relative both to the propellant 'per se' and to the motor grain with a given type of igniter.

The ignition characteristics of composite and double base propellants have been investigated by exposing samples to arc generated neutral gas jet as well as to aluminized, or not, propellant motor exhaust. The means used to detect ignition are visualisation, I.R. pyrometer and ultrasonic transducers continuously monitoring the thickness of the sample. With the various types of heating (convection - conduction, particles impact) it is found that the ignition laws remain the same, controlled by the degradation characteristics of the propellant components.

The various experimental techniques used in scaled motors for the investigation of propellant ignition and of flame spreading are described, particularly fluxmeters.

Examples of applications of these techniques to the study of the ignition of motors, with composite as well as double base propellant grains, are presented.

The extinction characteristics, low pressure deflagration limit and extinction under depressurization, of various composite propellants have been studied revealing the influence of the composition parameters : particle size, nature of the binder, presence of additives.

1 - INTRODUCTION

De très nombreux travaux portant sur l'allumage des propergols solides composites et homogènes tant au niveau du propergol lui-même qu'à celui du propulseur se trouvent dans la littérature. Les références [1 - 9] représentent une sélection des travaux les plus significatifs, les références [3 , 6 , 7] et la référence [9] pouvant être consultées pour une liste exhaustive des études d'une part sur l'allumage du propergol et d'autre part sur l'ensemble du processus dans le propulseur. De nombreux travaux ont également été menés à l'ONERA, en particulier sur l'allumage et la mise en pression des propulseurs, références [10 - 13].

Ces travaux ont été poursuivis autant en ce qui concerne l'étude de l'allumage du propergol proprement dit que l'étude de la propagation de l'inflammation dans le moteur, avec dans ce dernier cas l'amélioration des moyens de détection déjà utilisés précédemment [11].

– *Ces travaux ont été effectués en partie sous contrats de la DRET (Direction des Recherches, Etudes et Techniques, Délégation Générale à l'Armement), de la SEP (Société Européenne de Propulsion) et de la SNPE (Société Nationale des Poudres et Explosifs).*

Un des buts de cette présentation est de faire la liaison entre l'allumage étudié au niveau de moyens de laboratoire et les phénomènes observés dans les propulseurs.

Les phénomènes relatifs à l'extinction, objet des références [18 , 19 , 20], sont également abordés, en particulier les paramètres de la composition qui influent sur la pression limite de combustion et les lois d'extinction en fonction d'une dépressurisation.

2 - CARACTERISTIQUES D'ALLUMAGE DES PROPERGOLS SOLIDES

Les études d'allumage au niveau d'échantillons ont été menées en exposant ceux-ci à des flux de chaleur obtenus par rayonnement, à partir d'un four [1], d'une image d'arc électrique [4 , 5 , 7], ou d'un faisceau laser à CO_2 [7], ou par convection, à partir d'une onde de choc [2].

Ces expériences ont été reprises et poursuivies à l'ONERA à l'aide de deux moyens d'apport de flux de chaleur nécessaire pour l'allumage. D'une part un jet de gaz chaud neutre (argon) produit dans un générateur à arc et d'autre part un jet de gaz issu d'un propulseur à échelle réduite chargé en propergol solide composite aluminisé ou non. Ce dernier moyen permet l'étude dans les conditions existant lors de l'allumage en propulseur, où le flux de chaleur reçu par la surface du propergol à allumer provient de la convection-conduction des gaz (gaz à caractère réducteur et pouvant éventuellement affecter le processus d'allumage), du rayonnement éventuel des gaz et particules et de l'impact possible des particules d'alumine.

L'utilisation de ces moyens permet d'obtenir des flux de chaleur dans une gamme importante (de 1 à 150 cal/cm^2s) (0,04 à 6 MW/m^2) et de simuler des délais d'allumage voisins (ou plus courts) de ceux observés en propulseur. Par ailleurs par la comparaison des résultats obtenus (ici et dans la littérature) dans différentes conditions d'apport de chaleur, de niveau de pression et d'atmosphère gazeuse, il doit être possible de conclure quant au caractère de généralité des lois d'allumage établies.

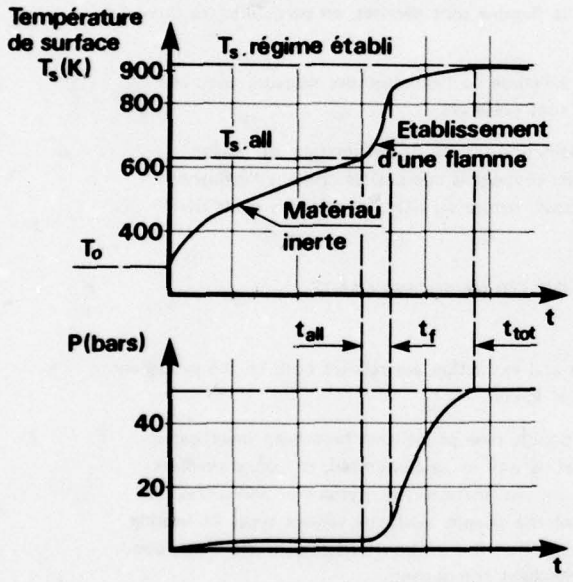

Fig. 1 – Evolution de la température de surface d'un propergol composite en cours d'allumage dans un propulseur.

La figure 1 permet de préciser les étapes de l'allumage. Lorsque la surface d'un propergol est exposée à un flux de chaleur une onde thermique s'y propage et sa température de surface T_s s'élève. Les réactions de dégradation du propergol sont tout d'abord lentes, T_s suivant une montée régulière en fonction du temps. Lorsque T_s atteint un niveau suffisant les réactions de dégradation, très sensibles à la température, deviennent importantes au voisinage de la surface, donnant lieu à un processus exothermique (soit en phase gazeuse, soit en phases condensée et gazeuse) qui vient s'ajouter au flux extérieur, la température de surface variant alors très rapidement et une flamme s'établissant. Parallèlement, au niveau du propulseur, le débit naissant issu du propulseur pressurise la chambre jusqu'à atteindre un régime de fonctionnement établi. Les délais d'allumage détectés ici sont t_{all} , le temps correspondant à l'amorce de réactions actives à la surface du propergol, et t_f le temps requis pour atteindre l'établissement d'une flamme. Le temps t_{tot} d'atteinte d'un régime établi dépend évidemment des caractéristiques du propulseur et de la réponse dynamique du propergol.

2.1 - Dispositifs utilisés

Un vue du générateur à arc est présentée sur la Figure 2. Ce générateur fonctionne avec des débits d'argon de quelques g/s, une pression d'arrêt de quelques bars et des températures de gaz jusqu'à 1500°C, ces dernières étant mesurées à l'aide d'un thermocouple platine-platine/rhodié introduit dans le jet en cours d'essai (son indication étant corrigée des pertes par rayonnement). La mesure du flux est obtenue à l'aide d'un fluxmètre capacitif en cuivre introduit pour quelques secondes dans le jet. L'échantillon est un cylindre de 5 mm de diamètre et de 3 mm de profondeur protégé latéralement dans une gaine isolante en durestos, introduit en point d'arrêt en environ 1 ms dans le jet par un verrin pneumatique.

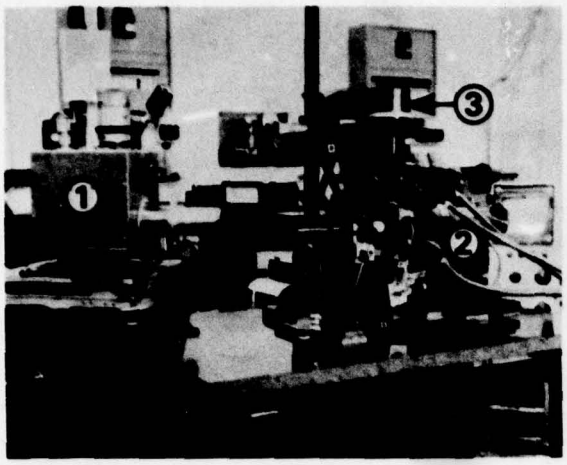

Vue d'ensemble du montage d'essai.

1. Pyromètre - 2. générateur à arc - 3. photomultiplicateur.

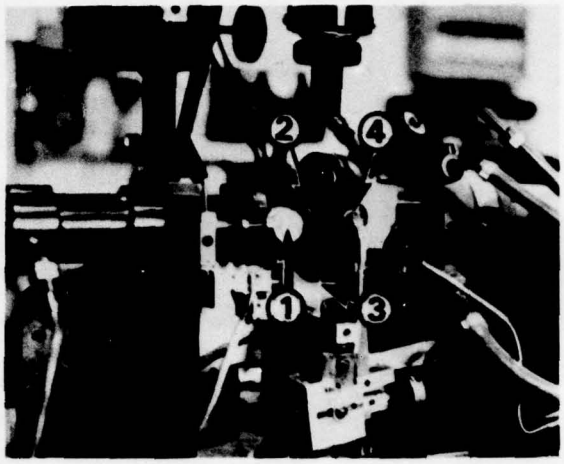

1. Porte échantillon - 2. tuyère - 3. thermocouple - 4. fluxmètre.

Fig. 2 – Dispositif d'allumage par jet de gaz chaud.

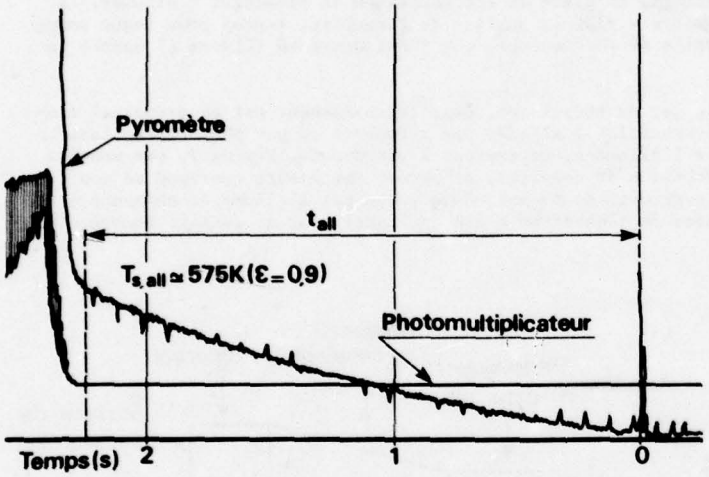

Fig. 3 – Détection de l'allumage et mesure de la température de surface d'un propergol solide composite.

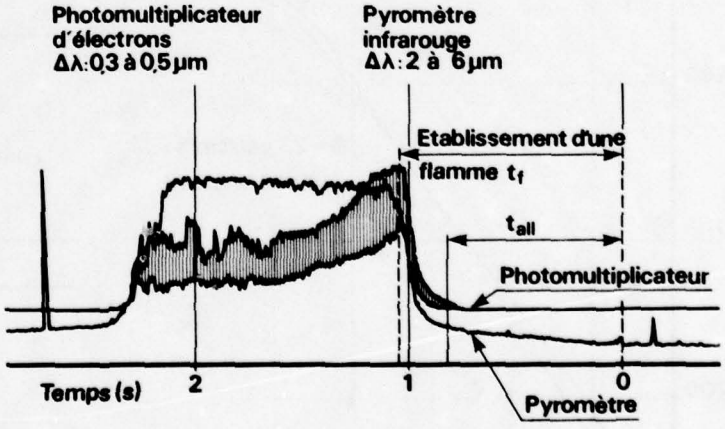

Fig. 4 – Détection de l'allumage d'un propergol solide composite.

La détection de l'allumage est obtenue grâce aux indications d'un pyromètre infra-rouge visant directement la surface de l'échantillon et d'un photomultiplicateur visant la zone au-dessus de la surface du propergol. On voit sur la figure 3 que, dans le cas d'un propergol composite, il est possible de détecter la montée régulière de la température de surface, puis sa déviation abrupte lorsque les réactions chimiques superficielles s'amorcent, avec en parallèle la réaction du photomultiplicateur à l'apparition d'une flamme, donnant ainsi une détermination claire du temps t_{all}. . Par la suite, Figure 4, il est possible de détecter l'établissement d'une flamme et l'atteinte d'un régime de combustion établie, correspondant au temps t_f existant pour les conditions de pression considérées. Dans le cas des propergols homogènes la flamme qui se développe au niveau de l'échantillon n'est pas suffisamment lumineuse pour donner un signal de photomultiplicateur utilisable et seule la lecture du pyromètre infra-rouge sert à la détection.

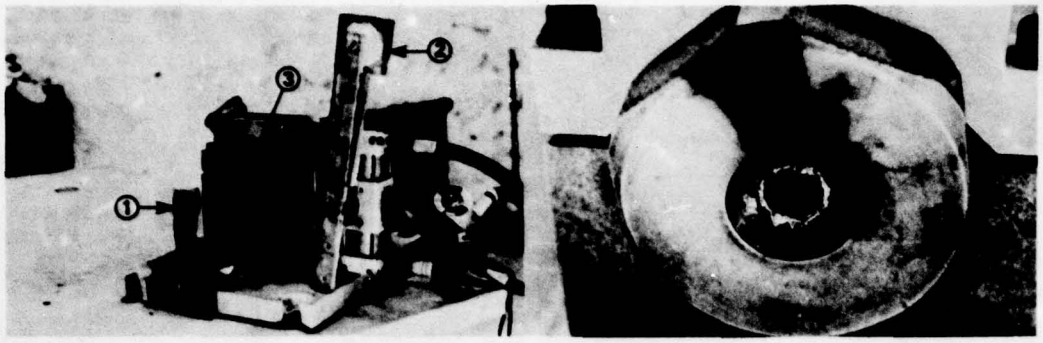

Fig. 5 – Vue du moteur pour essais d'allumage.

1. Mât porte échantillon - 2. protection - 3. tuyère.

Pour compléter les résultats obtenus avec le générateur à arc, des essais d'allumage ont été effectués par exposition d'échantillons dans le jet d'un petit propulseur à propergol PA-PBC ou PA-PBC-aluminium (Figure 5). L'échantillon monté sur un mât face à la tuyère du propulseur est, pendant la phase d'allumage de celui-ci, protégé par un écran qui se relève ensuite et le découvre en une fraction de milliseconde (au vu de films à environ 6000 i/s). En faisant varier la distance échantillon-tuyère il est possible de changer le flux de chaleur reçu. La mesure de ce flux est effectuée par fluxmètres capacitifs à pastille de cuivre monté, dans un essai répétitif, en place de l'échantillon de propergol à allumer. La bonne concordance entre la lecture d'un pyromètre visant la surface du fluxmètre, exposé pour cette comparaison dans le jet du générateur à arc, et celle du thermocouple qui y est incorporé (figure 6) montre la validité de la mesure.

Dans le cas de l'exposition dans le jet du propulseur, dont le chargement est en propergol aluminisé ou non, la visée de la surface de l'échantillon à allumer par pyromètre ou par photomultiplicateur est pratiquement impossible. Afin de détecter l'allumage, un capteur à ultra-sons, Figure 7, est monté à l'arrière de l'échantillon, protégé par un matériau de couplage, et permet une mesure continue de son épaisseur et en particulier une détermination précise du moment où le propergol s'allume et commence à régresser. Cette technique de mesure des vitesses de combustion a été appliquée pour un certain nombre d'études [14].

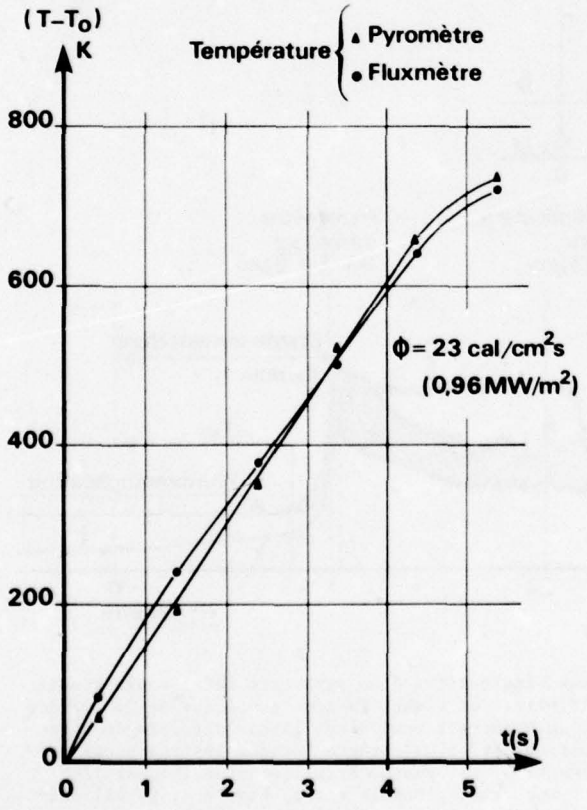

Fig. 6 – Etalonnage du fluxmètre exposé dans le générateur à arc.

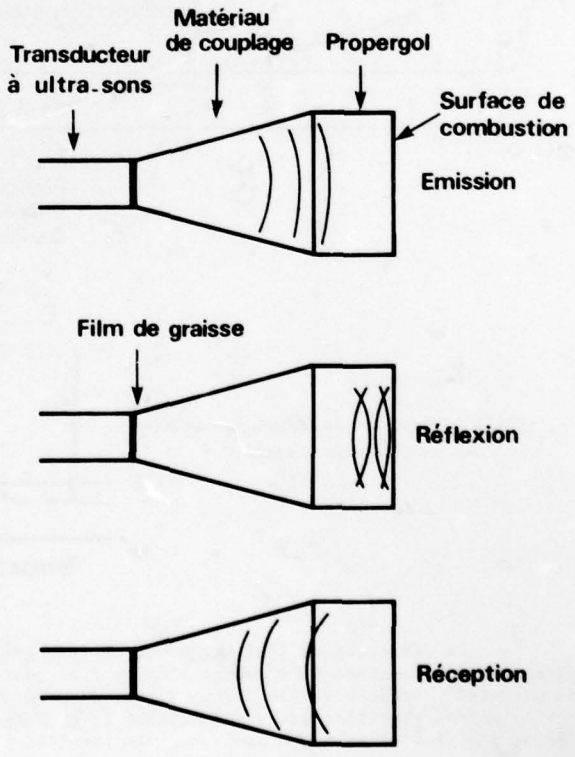

Fig. 7 – Schéma de principe de la mesure par ultra-sons.

2.2 - Résultats obtenus

Les résultats obtenus avec les dispositifs décrits ci-dessus, pour les propergols solides composites dans une large gamme de flux de chaleur et de conditions et pour les propergols solides double base dans des conditions plus restreintes, sont présentés sur la figure 8 et comparés aux résultats de la littérature. Les renseignements relatifs à ces différents résultats sont donnés ci-dessous.

Tableau des détails de la figure 8

1. Propergols composites au perchlorate d'ammonium

1.1 Courbe ⓪ Résultats de Baer et Ryan [1]

	Propergols A	B	C	F	G
P.A.	76 %	82 %	86 %	80 %	82 %
Liant	Polymère sulfuré 21 %	Polyuréthane 16 %	Caoutchouc Synth. 12%	PBAA 18 %	PBAA 18 %
Aluminium	2 %	2 %	0	0	0
Catalyseur (chromite de cuivre ou composés de Fe)	1 %	—	2 %	2 %	de 0 % à 4%

Echantillons exposés à un flux de rayonnement (1 à 13 cal/cm^{2}s), pression ambiante.

Résultats complémentaires de Baer et Ryan [1]
Propergol A de ci-dessus.

Flux de rayonnement (1 à 5 cal/cm^{2}s), pression de 0,2 à 11 bars. Aucune influence de la pression n'est détectée.

1.2 Courbe ⓪ Résultats de Baer et Ryan [2]

	Propergols F	U	CB
P.A.	40 % 15 µ 40 % 200 µ	75 % 15 µ	41 % 15 µ 41 % 200 µ
Liant	PBAA 18%	PBAA 23%	16 % noir de carbone (concrétion)
Catalyseur (C.C.)	2 %	2 %	2 %

Echantillons exposés à un flux de convection en tube à choc (20 à 150 cal/cm^{2}s). Atmosphère O_2 ou N_2, pression de 20 à 25 bars.

1.3 Résultats ONERA

a/ Propergol composite 82% de P.A. (granulométrie de 15 à 280 µm) - PBC, échantillon exposé dans le jet du générateur à arc (argon), figure 2.

⊖ indique le délai $t_{al.}$ et le délai t_f pour établissement d'une flamme, voir fig. 4.

b/ Même propergol composite 82 % de P.A.

◆ échantillon dans le jet du propulseur, fig. 5, à chargement non aluminisé (propergol 88 % de P.A.-PBC).

● échantillon dans le jet du propulseur à chargement aluminisé (propergol P.A.-PBC à 20 % d'aluminium).

c/ Propergol composite 65,4 % P.A., 18,2 % polyuréthane, 16,4 % aluminium.

1.2 Allumage dans un propulseur cylindrique à cavité étoilée, $L \approx 2$ m, allumeur chargé en propergol homogène, réf. [10]. Détermination des flux par fluxmètres de convection et des délais par fluxmètres de rayonnement incorporés dans le bloc de propergol à allumer. Déterminations assez incertaines.

3.4 Allumage dans un propulseur à surfaces planes, $L \approx 0,5$ m, allumeur chargé en propergol homogène, réf. [12].

2. Propergols homogènes nitrocellulose-nitroglycérine

2.1 Résultats ONERA

⊖ , ⊖ , Temps $t_{al.}$ et temps t_f d'établissement d'une flamme, sur échantillons respectivement de 820 cal./g et 1100 cal./g exposés dans le jet du générateur à arc, fig. 2.

2.2 Résultats de Suh [5]

Propergol M2 (1060 cal./g), échantillons exposés au flux de rayonnement d'une lampe à arc, flux $\leq$ 2 cal./cm^{2}s .

Courbe ⓪ , relation délai d'allumage-flux calculée en fonction d'une réaction de dégradation en phase condensée.

2.3 Résultats de De Luca, Princeton [7]

Courbe ④, propergol homogène n°8, échantillons exposés au flux de rayonnement d'une lampe à arc, flux $\leq$ 25 cal./cm^{2}s.

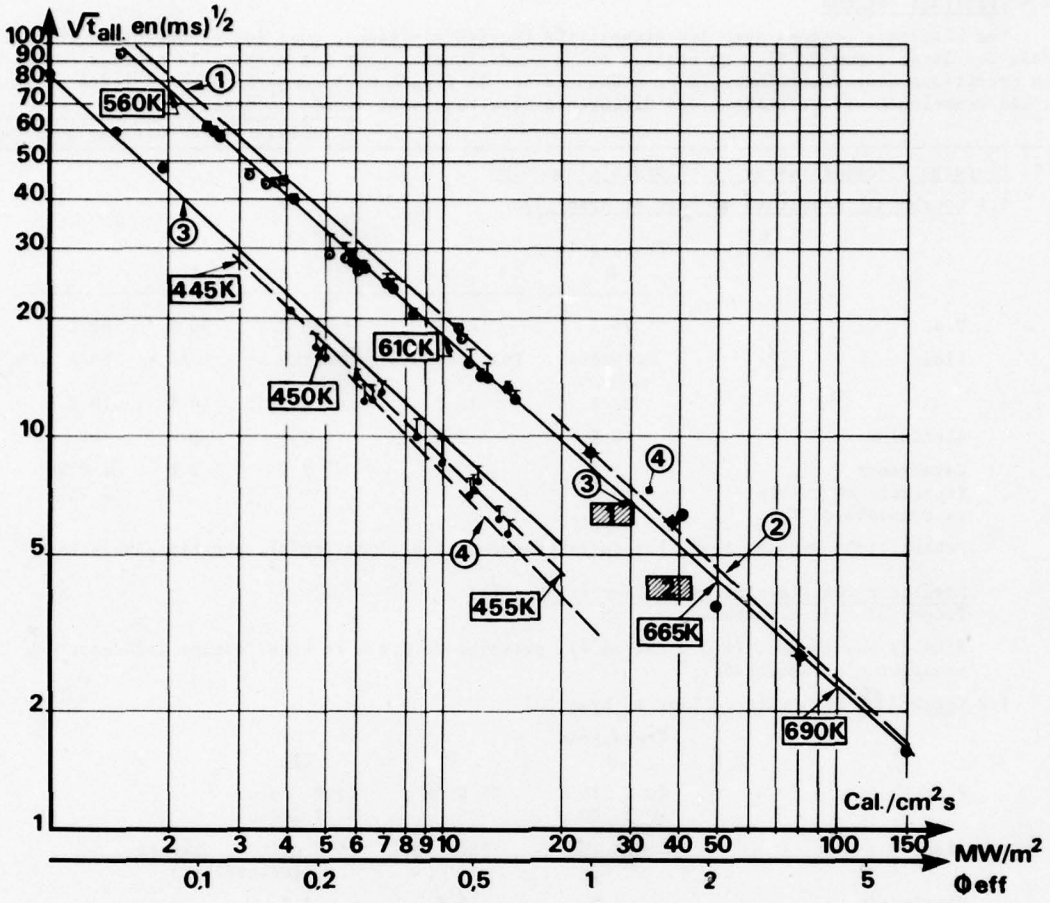

Fig. 8 – Lois d'allumage de différents propergols.

Pour ce qui est des propergols composites à base de perchlorate d'ammonium il ressort de la bonne concordance des résultats ONERA entre eux et avec ceux de Baer et Ryan [1 , 2] un certain nombre de conclusions importantes.

1/ Le mode d'apport du flux de chaleur n'a pas d'influence sur le délai d'allumage

Seul compte le niveau de flux reçu par le propergol, que ce flux soit apporté par rayonnement, par convection-conduction (de gaz neutres ou chimiquement réducteurs) ou avec participation d'impacts de particules d'alumine (expériences d'allumage en exposition directe dans le jet du propulseur à chargement aluminisé, fig. 5).

2/ Le niveau de pression et la nature des gaz, à flux de chaleur donné, n'intervient pas.

Cette conclusion ressort des résultats de Baer et Ryan [1 , 2] pour lesquels le niveau de pression varie de 0,2 à 25 bars et de ceux de l'ONERA où la pression d'arrêt des jets varie de quelques bars (générateur à arc) à plusieurs dizaines de bars (propulseur d'essai).

3/ La réaction de dégradation qui pilote l'allumage est caractéristique du perchlorate d'ammonium

Les propergols considérés comportent différents liants, polybutadiènes, polyuréthane (jusqu'à du noir de carbone non volatilisable à ces niveaux de température), des catalyseurs, de l'aluminium, et cependant la loi d'allumage reste unique. Il apparaît donc que c'est la dégradation intrinsèque du P.A. qui déclenche l'allumage.

Dans le cas des propergols homogènes le domaine des conditions d'allumage utilisées est moins vaste, cependant, de la concordance entre les résultats ONERA et ceux de Suh [5] et De Luca [7], des conclusions similaires à celles acquises pour les propergols composites ressortent. En particulier on note l'absence d'influence nette du niveau de pression (pression jusqu'à 20 bars pour la réf. [7], environ 50 millibars pour [5] et pression d'arrêt du jet d'arc de quelques bars pour les résultats ONERA). Par ailleurs on voit que les résultats ONERA obtenus pour des propergols de potentiel calorifique différents se confondent. Cela va dans le sens d'une réaction de dégradation en phase condensée dont les caractéristiques sont proches pour les composants nitrocellulose et nitroglycérine du propergol, comme également observé pour la combustion établie des propergols homogènes [16].

2.3 - Interprétation et corrélation des résultats, propergols homogènes

Les observations précédentes permettent de considérer que l'allumage (au sens de la première manifestation d'activité chimique à la surface du propergol, correspondant au délai $t_{all.}$ de la fig. 1) est dû à des réactions de dégradation en phase condensée. Dans le cas des propergols homogènes, Suh [5] a considéré l'élévation de température d'un propergol homogène soumis à un flux de rayonnement constant et subis-

sant une dégradation exothermique d'ordre zéro, le profil de température résultant alors du bilan :

$$(1) \qquad \rho c \frac{\partial T}{\partial t} - \lambda \frac{\partial^2 T}{\partial x^2} = \rho \varphi_s A \, e^{-E_p/RT},$$

où λ, ρ, c sont les conductivité, masse spécifique et chaleur spécifique, φ_s et A, E_p les chaleur de réaction et caractéristiques de dégradation du propergol. La forte sensibilité à la température de cette réaction de dégradation conduit à une évolution de température superficielle comme indiqué fig. 1. L'ajustement des paramètres de la description par le calcul pour obtenir l'accord avec les résultats expérimentaux conduit à :

$$\varphi_s \simeq 60 \text{ cal./g}, \quad A = 10^{17} \text{ s}^{-1} \quad \text{et} \quad E_p = 40\ 10^3 \text{ cal./mole},$$

correspondant à la courbe ③ de la fig. 8. On voit que cette description rend assez bien compte de l'ensemble des résultats relatifs aux propergols homogènes. Il est intéressant de noter que ces caractéristiques de dégradation en phase condensée permettent par ailleurs de bien rendre compte, voir fig. 3 de la réf. [16], des niveaux de température existant en combustion établie.

D'une manière simple, on peut caractériser l'allumage des propergols homogènes par la température superficielle à atteindre pour que se déclenchent des réactions exothermiques actives. On sait que, dans le cas le plus simple d'un flux extérieur constant Φ, la loi de montée en température superficielle en fonction du temps est :

$$(2) \qquad (T_s - T_o) = \frac{2}{\Gamma} \Phi \left(\frac{t}{\pi}\right)^{1/2}$$

où $\Gamma = (\rho c \lambda)^{1/2}$ est l'effusivité thermique. Cette loi permet de calculer, à flux donné, la température atteinte après le temps d'allumage observé expérimentalement (pour $\Gamma = 0{,}02$ cal./K cm^2 s$^{1/2}$, une valeur moyenne), que l'on voit sur la figure 8 être proche de 450K et assez peu évolutive avec le niveau de flux.

2.4 - Corrélation des résultats, propergols composites au perchlorate d'ammonium

Les températures superficielles atteintes en cours d'allumage des propergols composites au P.A. sont bien en dessous de la température estimée pour la fusion de celui-ci, au-delà de laquelle des réactions en phase condensée se produisent et jouent un rôle important pour la combustion établie [15]. Il apparaît que l'allumage correspond à des réactions superficielles de sublimation dissociative :

$$NH_4ClO_4 \longrightarrow NH_3 + HClO_4$$

Dans ce cas, et c'est ce que Baer et Ryan [1 , 2] ont considéré, l'évolution de la température résulte du bilan :

$$(3) \qquad \frac{\partial T}{\partial t} - \left(\frac{\lambda}{\rho c}\right) \frac{\partial^2 T}{\partial x^2} = 0$$

avec, dans le cas d'un flux extérieur Φ constant, la condition limite à la surface :

$$(4) \qquad \Phi + B e^{-E_p/RT_s} = -\lambda \left(\frac{\partial T}{\partial x}\right)_s ,$$

avec B en cal./cm^{2}s. Baer et Ryan [1 , 2] ont appliqué cette modélisation et ajusté les paramètres pour rendre compte des résultats expérimentaux. Il est en fait possible de corréler ces résultats de manière plus simple. Si l'on considère que l'allumage se produit lorsque le flux de chaleur produit à la surface par les réactions de décomposition (et la flamme correspondante) atteint la valeur du flux d'allumage on obtient la condition :

$$\Phi = B e^{-E_p/RT_s},$$

$$(5) \qquad T_{s\,all.} = \frac{E_p}{R} \left[\log\left(\frac{B}{\Phi}\right)\right]^{-1}.$$

Les températures atteintes en surface après le délai observé expérimentalement et pour le flux considéré peuvent être évaluées à partir de l'expression (2) (pour $\Gamma = 0{,}02$) ; elles sont reportées sur la figure 8. En appliquant la relation (5) en deux points de la courbe expérimentale on peut alors évaluer

$$B = 1.4\ 10^9 \qquad \text{et} \qquad E_p = 23 \text{ kcal./mole},$$

qui reportés dans (5) permettent de corréler la totalité de la courbe des résultats ONERA de 1 à 150cal/cm^{2}s.

On peut alors considérer la loi d'allumage des propergols composites, pour le cas le plus simple d'un flux constant, sous la forme, à partir des relations (2) et (5),

$$(6) \qquad (t_{all})^{1/2} = \frac{\Gamma}{2} \frac{\pi^{1/2}}{\Phi} \left[E_p/R \log\left(\frac{B}{\Phi}\right) - T_o \right],$$

correspondant à la droite tracée au travers des points ONERA de la figure 8. Si l'on exprime la pente de cette loi dans la représentation de la figure 8, on obtient :

$$(7) \qquad d \log (t_{all})^{1/2} \Big/ d \log \Phi = -1 + \frac{RT_o}{E_p} \frac{(T_{s\,all.})^2}{T_o (T_{s\,all.} - T_o)},$$

ou, pour une valeur moyenne $T_{sall} \simeq$ 650 K, une pente de $-1 + 4R^{o}T_{o}/E_{p}$, une relation très proche de celle trouvée en [1 , 2].

D'une manière plus simple, et de même que pour les propergols homogènes, on peut caractériser l'allumage des propergols composites à base de P.A. par une température superficielle à atteindre. On voit, figure 8, que de 560 K à 2 cal./cm²s elle atteint 690 K à 100 cal./cm²s.

3 - ALLUMAGE DES PROPERGOLS SOLIDES EN PROPULSEUR

Les essais sur échantillons de propergols composites et homogènes, soumis à des flux de chaleur variés (convection, impact de particules, rayonnement), ont montré que l'inflammation du propergol correspondait à une valeur critique (légèrement évolutive) de la température superficielle. Ce concept de température superficielle d'inflammation, souvent utilisé dans les études d'allumage [10] [8] [9], a été retenu pour l'étude de l'inflammation et de la propagation de la flamme des propergols solides en propulseurs.

Les évolutions de température superficielle du propergol sont déduites des réponses de fluxmètres à température superficielle disposés à la surface du chargement. Le principe de ces fluxmètres est basé sur la mesure de la température superficielle d'un élément calorimétrique isolant, assimilé à un milieu semi-infini durant toute la durée de la mesure. Les lois de la conduction appliquées à cet élément calorimétrique permettent de relier l'augmentation de température superficielle ΔT_s au flux de chaleur Φ pénétrant à sa surface, avec Γ' l'effusivité thermique de l'isolant (supposée constante),

$$\Delta T_s(t) = \frac{1}{\Gamma' \pi^{1/2}} \int_0^t \frac{\Phi(z)}{\sqrt{t-z}}\, dz \tag{8}$$

expression qui se réduit, dans le cas d'un flux constant, à l'éq. (2). En supposant l'égalité des flux de chaleur à la surface du propergol et du fluxmètre, on en déduit que leurs augmentations de température superficielle sont dans le rapport inverse des effusivités :

$$\frac{(\Delta T_s)_{prop.}}{(\Delta T_s)_{fluxm.}} = \frac{(\sqrt{\lambda \rho c})_{fluxm.}}{(\sqrt{\lambda \rho c})_{prop.}} \tag{9}$$

Les caractéristiques thermocinétiques du propergol sont déterminées par la méthode expérimentale de CLARK-KINGSTON.

Le flux de chaleur pénétrant à la surface du propergol sera déduit de l'évolution des températures superficielles mesurées par les fluxmètres à partir de la relation :

$$\Phi(t) = \frac{\Gamma'}{\pi^{1/2}} \int_0^t \frac{dT_s/dz}{\sqrt{t-z}}\, dz \tag{10}$$

3.1 - Description des fluxmètres (Figure 9)

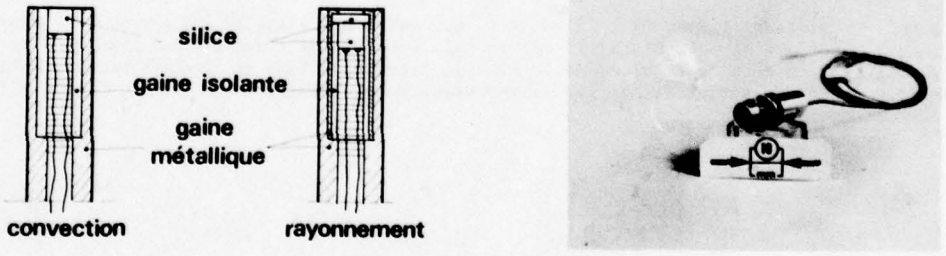

Fig. 9 – Fluxmètres.

- Fluxmètres totaux

L'élément calorimétrique est un cylindre de 4 mm de diamètre, de 4 mm de hauteur, en silice pure fondue. L'élément thermométrique est un film de platine, d'une épaisseur de l'ordre de 0,1 µ obtenu par un procédé de pulvérisation cathodique [17]. Les bornes de connexion sont réalisées par un dépôt de peinture à l'argent. Une gaine en durestos assure l'isolement thermique et électrique du fluxmètre.

Ces fluxmètres mesurent le flux de chaleur dû à la convection, à l'impact des particules et une partie du flux de rayonnement.

- Fluxmètres de rayonnement

Les fluxmètres de rayonnement utilisés sont réalisés suivant le même principe. Ils comportent en outre une mince couche absorbante, peu sélective, faite de noir de fumée avec liant organique. Un disque de silice permet, pendant toute la durée de la mesure, d'isoler l'élément sensible de l'écoulement.

La valeur du coefficient d'absorption qui est directement liée à l'épaisseur de la couche absorbante, est déterminée à partir de la réponse du fluxmètre à un flux de rayonnement périodique [11].

Le flux de chaleur dû à la convection et à l'impact des particules $\Phi_c(t)$ et le flux de rayonnement $\Phi_R(t)$ sont déduits du flux mesuré par le fluxmètre total $q(t)$ et par le fluxmètre de rayonnement $q'(t)$:

$$\Phi_c(t) = q(t) - \frac{a}{a'} q'(t) \quad , \quad \Phi_R(t) = \frac{1}{a'} q'(t) \quad , \tag{11}$$

en désignant par a et a' les coefficients d'absorption du fluxmètre total et du fluxmètre de rayonnement. L'expérience montre que ces coefficients ont pour valeurs moyennes :

$$a = 0{,}25 \quad ; \quad a' = 0{,}80 .$$

De même l'élévation de température superficielle $\Delta T_{sp}(t)$ du propergol est déduite de la réponse du fluxmètre total $\Delta T_{sc}(t)$ et du fluxmètre de rayonnement $\Delta T_{sR}(t)$ à partir de la relation:

$$\Delta T_{sp}(t) = \frac{\Gamma_{silice}}{\Gamma_{prop.}} \left[\Delta T_{sc}(t) + \frac{a_p - a}{a'} \Delta T_{sR}(t) \right] , \tag{12}$$

en désignant par a_p le coefficient d'absorption du propergol.

3.2 - Qualification en propulseur

Ces fluxmètres devant être utilisés comme détecteurs d'inflammation ont été qualifiés en propulseur à partir d'essais inerte et en combustion.

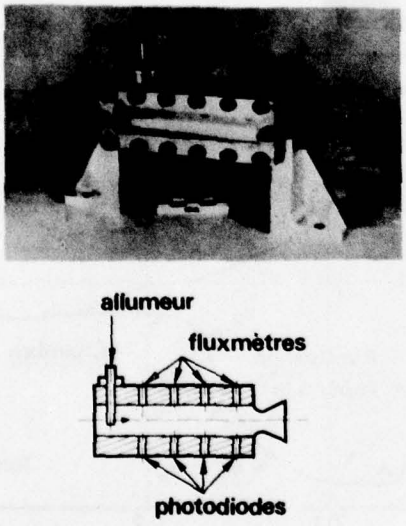

Fig. 10 – Montage de qualification.

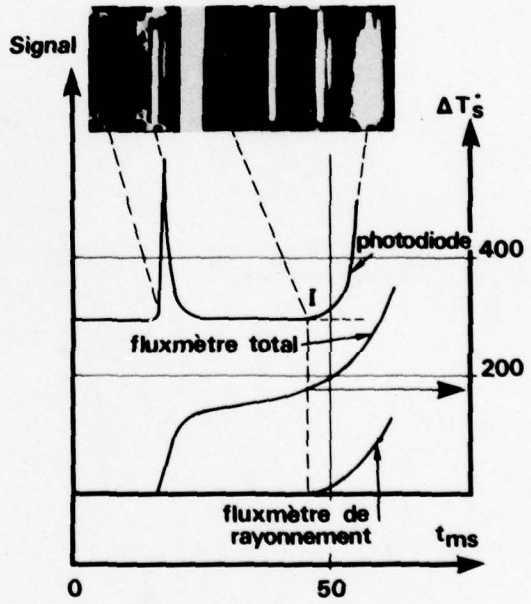

Fig. 11 – Corrélation des signaux des fluxmètres et des détecteurs d'inflammation.

Le dispositif expérimental utilisé est un propulseur bidimensionnel à voyant, spécialement instrumenté, muni d'un chargement constitué de 2 lamelles de propergol P.A.-polyuréthane-aluminium, l'allumeur du type roquette fonctionnant avec un propergol de même nature (figure 10). La visualisation de la combustion est effectuée au moyen d'une caméra rapide PHOTOSONICS, dont la cadence de prise de vue peut atteindre 1000 images/sec. L'inflammation du propergol est repérée à l'aide de photodiodes au silicium à court temps de réponse, dont le maximum de sensibilité se situe dans le proche infrarouge. Elles sont montées affleurantes à la surface du chargement en regard des fluxmètres à température superficielle. En comparant les réponses obtenues lors d'essais inerte et en combustion, on déduit l'instant correspondant à l'inflammation du propergol (Figure 11 : point I). Les visualisations effectuées lors de ces essais sont en bon accord avec les signaux délivrés par les photodiodes. A cet instant de l'inflammation, repéré par la photodiode, correspond une élévation de température superficielle ΔT_{sc} mesurée par le fluxmètre total de l'ordre de 175°C, celle indiquée par le fluxmètre de rayonnement étant négligeable. Compte tenu des valeurs des effusivités de la silice et du propergol, elle correspond pour le propergol à une température superficielle d'inflammation voisine de 620 K, valeur qui est en bon accord avec les résultats des mesures effectuées dans cette gamme de délais sur des échantillons de propergols composites, fig. 8.

Les essais en chargement inerte ont permis de contrôler la bonne tenue du film de platine soumis au jet de l'allumeur.

3.3 - Applications

Deux exemples d'application de cette méthodologie à l'étude des processus d'inflammation et de propagation de la flamme sont présentés. Ils concernent d'une part des propulseurs munis de blocs de propergol composite à cavité usinée où l'allumage est réalisé au moyen d'une petite roquette, et d'autre part des propulseurs à court temps de combustion munis de chargements de propergol homogène allumés par une composition pulvérulente. Pour ces types de propulseur la complexité de l'écoulement des gaz provenant de l'allumeur ne permet pas une approche théorique simple de l'inflammation.

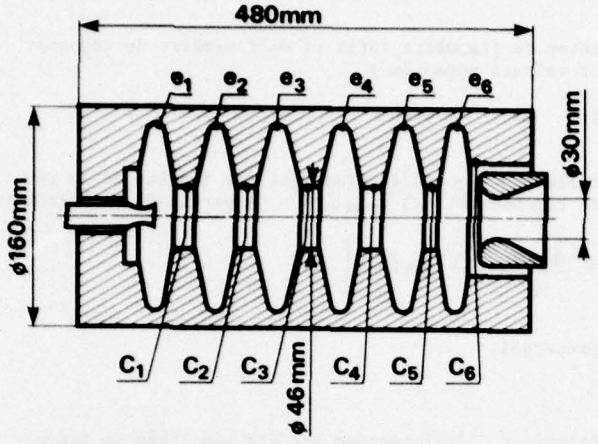

Fig. 12 – Propulseur à chargement usiné.

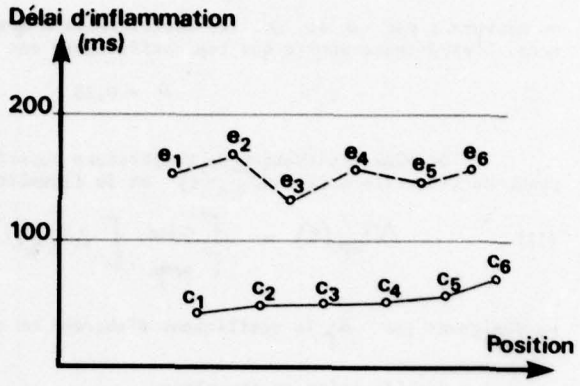

Fig. 13 – Inflammation d'un bloc usiné - Propergol composite.

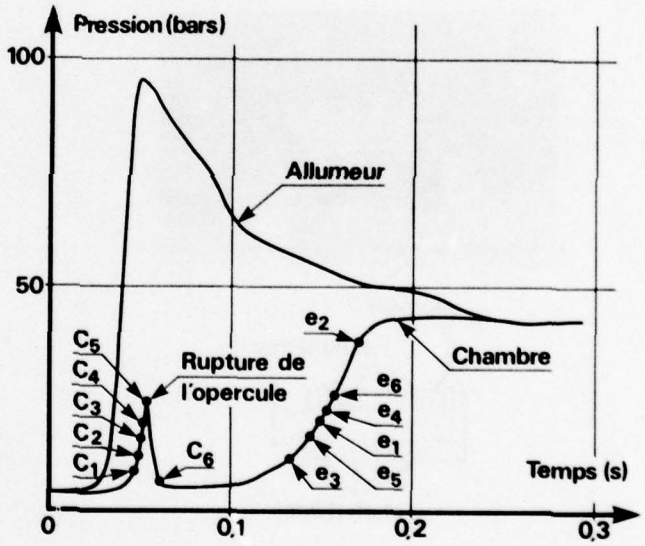

Fig. 14 – Evolution des pressions dans un propulseur à chargement usiné.

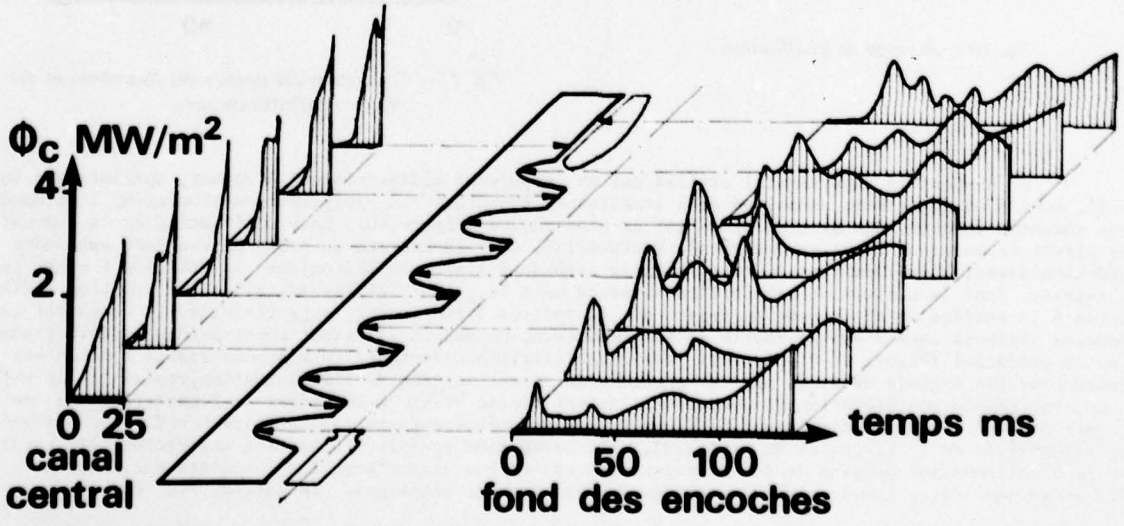

Fig. 15 – Cartographie des flux de chaleur à la surface d'un bloc usiné.

- Propergol composite

Le propulseur d'étude comporte un chargement cylindrique en propergol P.A.-polyuréthane-aluminium avec un canal central et 6 encoches également réparties (fig. 12). La tuyère, fortement intégrée, est munie d'un opercule dont la pression de rupture est voisine de 20 b. L'allumeur, disposé sur le fond avant, est une roquette utilisant un chargement de propergol de même nature que celui du propulseur, à surface dégressive, équipée d'une tuyère dont le diamètre au col est de 5,7 mm. Les pressions dans le propulseur et dans l'allumeur sont mesurées par des capteurs piézoélectriques KISTLER. Des fluxmètres totaux et de rayonnement sont disposés tout le long du canal central et dans le fond de chaque encoche.

Les délais d'inflammation le long du chargement ont été déterminés à partir de la réponse des fluxmètres totaux, celle relative aux fluxmètres de rayonnement étant négligeable, la température superficielle d'inflammation du propergol étant prise égale à 620 K. Les valeurs ainsi obtenues montrent que l'inflammation se produit presque simultanément dans tout le canal central et se propage ensuite lentement le long de chaque encoche (Fig. 13). L'évolution des pressions mesurées traduit bien ce phénomène (Fig. 14). La cartographie des flux, déduits des mesures de températures superficielles, met bien en évidence l'évolution différente des transferts de chaleur entre le canal central et le fond des cavités (fig. 15).

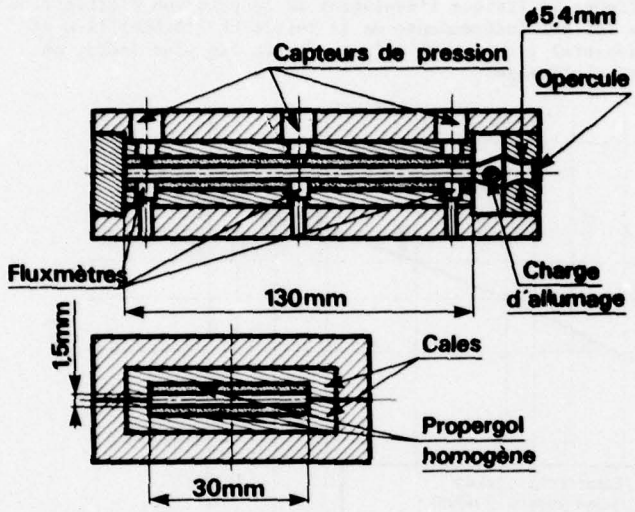

Fig. 16 – Propulseur à chargement lamellaire.

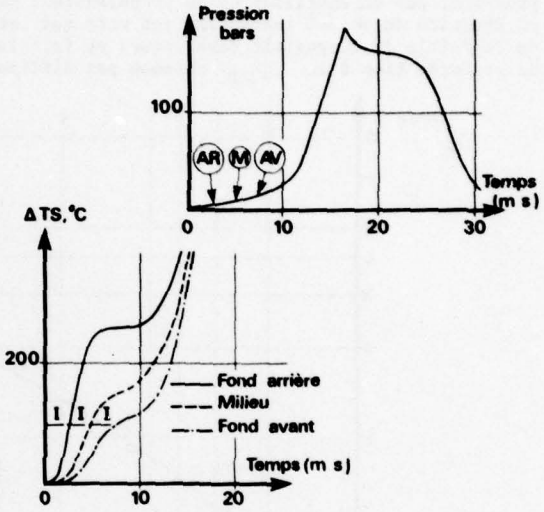

Fig. 17 – Inflammation d'un élément de chargement lamellaire - Propergol homogène.

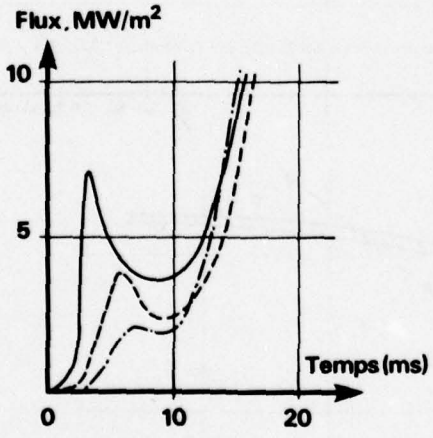

Fig. 18 – Répartition des flux de chaleur à la surface d'un élément lamellaire.

- Propergol homogène

Pour l'étude de l'inflammation des chargements lamellaires, un propulseur à chargement élémentaire, constitué de 2 lamelles de propergol double base extrudé, a été utilisé. Dans la tuyère, munie d'un obturateur dont la pression de rupture est voisine de 200 b, un allumeur constitué d'une petite charge de poudre noire est placé. Le long de la perforation sont disposés des capteurs de pression piézoélectriques KISTLER et des fluxmètres en regard (Fig. 16).

Comme pour l'étude des blocs usinés, les délais d'inflammation ont été déduits de la réponse des fluxmètres totaux, le flux de rayonnement mesuré étant négligeable, la température superficielle d'inflammation du propergol homogène étant prise égale à $\simeq$ 460 K. Les mesures effectuées montrent que l'inflammation débute sur le fond arrière et se propage très rapidement tout le long du chargement (fig. 17). Les évolutions de flux, déduites de ces mesures, sont présentées (fig. 18).

4 - CARACTERISTIQUES D'EXTINCTION DES PROPERGOLS SOLIDES

Il est important pour l'application des propulseurs modulés de connaître les paramètres qui conditionnent l'extinction d'un propergol, aussi bien sa pression limite intrinsèque, la "pression limite de déflagration" P_{LD}, que l'évolution de cette pression d'extinction en fonction de la vitesse de dépressurisation dp/dt . Les références [18 , 19 , 20] sont significatives des travaux que l'on trouve dans la littérature, les deux premières relatives à la P_{LD} et la troisième à l'extinction dynamique.

Dans le dispositif utilisé à l'ONERA, l'échantillon (5 x 5 x 20 mm) est placé dans une chambre d'environ 0,4 l, reliée par l'intermédiaire d'un col de taille ajustable et d'une électrovanne à une capacité de grande dimension ($\simeq$ 50 l), vidée au niveau désiré. Le fonctionnement s'effectue soit à pression constante (le volume total de l'enceinte étant suffisant pour que les gaz de combustion de l'échantillon ne modifie pas la pression affichée), soit, après allumage à quelques bars, en présence d'une chute de pression dp/dt (après ouverture de l'électrovanne et avec réglage par la taille du col). On peut alors obtenir la loi $V_c(p)$ à basse pression et la pression limite de déflagration P_{LD} , par difficulté d'allumage ou par dp/dt lent (un signal photodiode, indiquant la luminosité de la combustion, en parallèle avec le signal du capteur de pression permet de mesurer la pression instantanée à laquelle se produit l'extinction). La figure 19 montre un exemple d'évolution de la vitesse de combustion à basse pression et de la limite d'extinction atteinte (ces résultats sont raccordés à ceux obtenus par ailleurs à haute pression, sur échantillons et en propulseurs). La figure 20 indique l'évolution de la pression d'extinction en fonction du dp/dt instantané (on voit que cette loi est indépendante de la taille de l'échantillon et de la taille du dispositif dans lequel se fait la détente) ; on y voit qu'aux dp/dt les plus lents, on se raccorde bien à la P_{LD} obtenue par difficulté d'allumage.

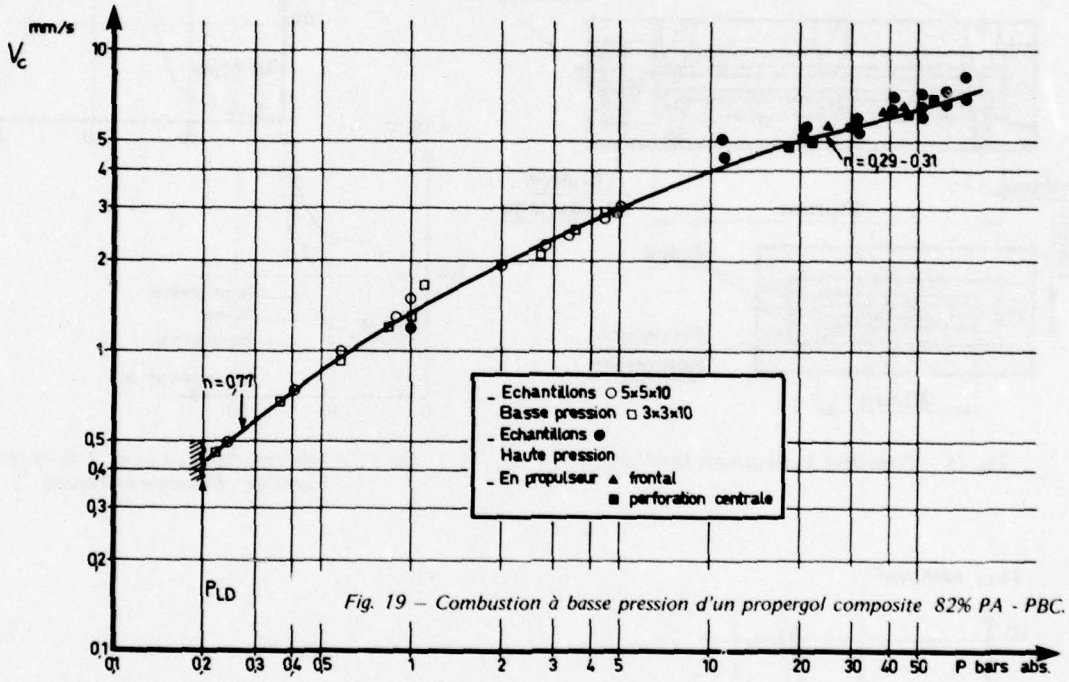

Fig. 19 – Combustion à basse pression d'un propergol composite 82% PA - PBC.

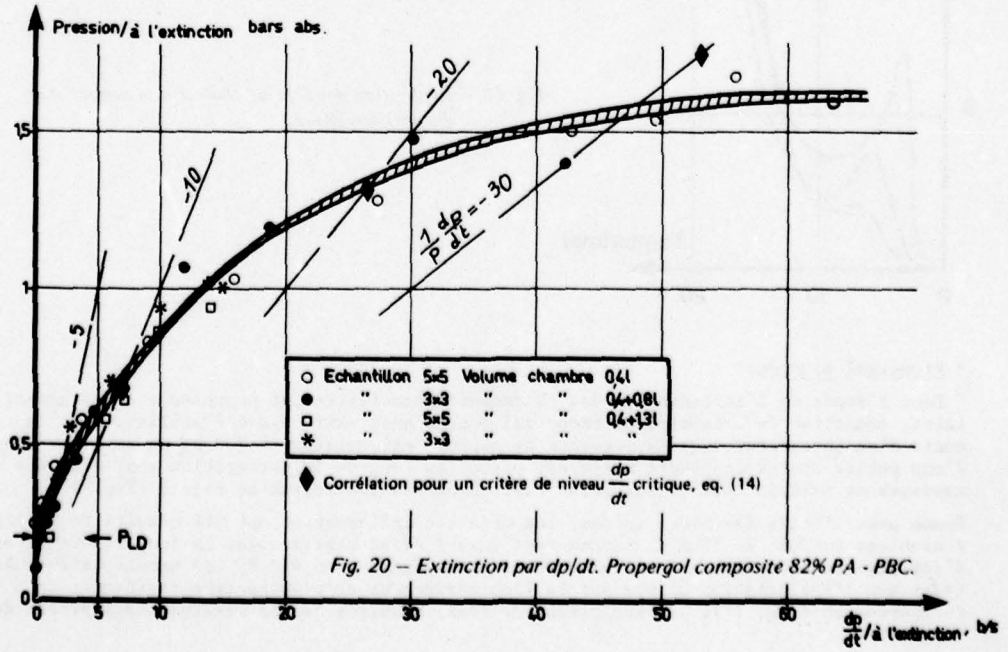

Fig. 20 – Extinction par dp/dt. Propergol composite 82% PA - PBC.

On sait qu'en régime dynamique une des relations les plus simples consiste à écrire la vitesse de combustion sous la forme :

(13) $$V_c = V_{c,0}(p)\left(1 + \psi \frac{d}{V_{c,0}^2} \frac{1}{p}\frac{dp}{dt}\right),$$

qui exprime que la vitesse s'écarte d'autant plus de la vitesse stationnaire $V_{c,0}(p)$ que le temps caractéristique de la dépressurisation $(d\log p/dt)^{-1}$ se rapproche du temps caractéristique de réponse du propergol, $d/V_{c,0}^2$ (avec d la diffusivité thermique), ψ étant un facteur constant de l'ordre de 1. Par ailleurs, on peut vouloir caractériser l'extinction par dépressurisation par un critère de niveau critique [19]

(14) $$\psi \frac{d}{V_{c,0}^2} \frac{d\log p}{dt} \geq c .$$

Dans le cas des expériences de la fig. 20 la chute de pression est pratiquement exponentielle et $d\log p/dt = -\alpha$ constant. L'équation (14) exprime alors qu'au cours d'une dépressurisation l'extinction se produira lorsqu'une pression telle que $\psi d\alpha \geq V_{c,0}^2$ sera atteinte. En appliquant ce critère aux résultats de la fig. 20 (et en ajustant les paramètres inconnus en un point à $\alpha = -10\ s^{-1}$), on obtient les points reportés qui rendent assez bien compte de la tendance observée.

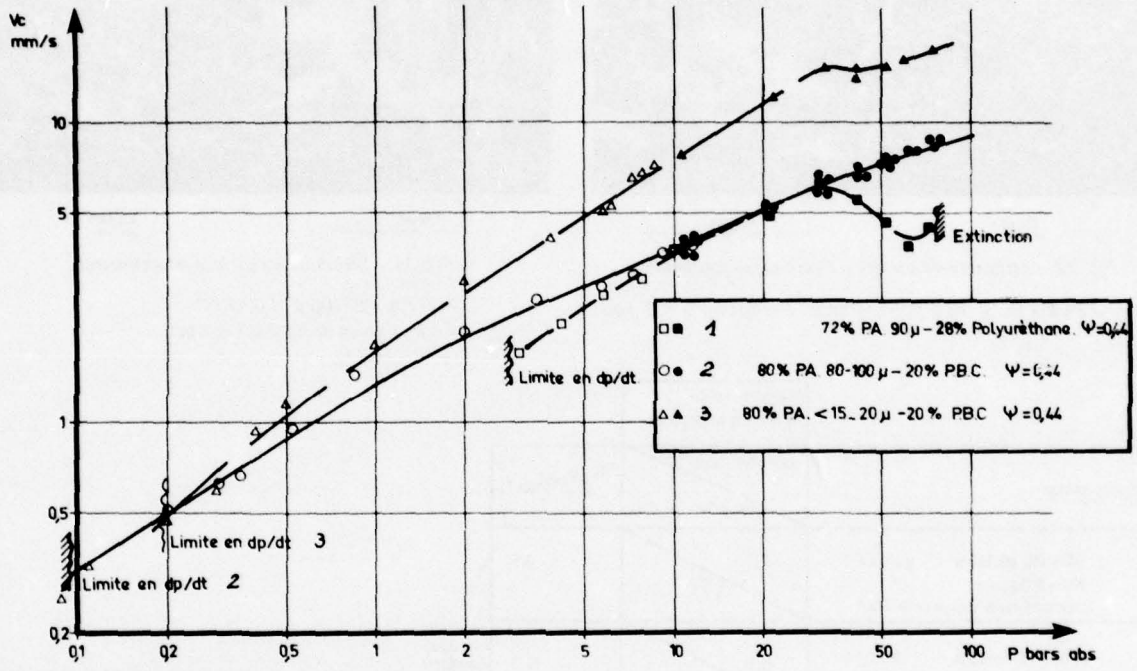

Fig. 21 – Combustion à basse pression et extinction.

La figure 21 rassemble quelques résultats obtenus. On y compare des propergols à même richesse soit au P.B.C. et granulométrie 100 µ ou 10 µ, soit au polyuréthane. On voit que l'influence de la granulométrie est très marquée au-delà de 1 bar, dans le domaine où la combustion est conditionnée par des flammes de diffusion [15], alors qu'à basse pression, lorsque la flamme se rapproche du régime prémélangé, elle ne se fait presque plus sentir. Par ailleurs, à granulométrie et richesse données, l'influence de la nature du liant est très marquée, n°2 au PBC à $p_{LD} \simeq 0{,}1$ b et composition 1 au polyuréthane à $p_{LD} \simeq 3$ bars. Cette différence est liée à des structures de surface très accentuées.

La figure 22 permet de voir que l'extinction des compositions au polyuréthane à p_{LD} élevée de 3 bars est liée à des structures de surface marquées, particules de P.A. très en relief par rapport au liant, avec la combustion du P.A. (le P.A. seul a, on le sait, une p_{LD} à 20 bars) moins soutenue par la contribution du flux de chaleur issu de la flamme principale O_2 du P.A./gaz du liant. La réf. [15] a montré que les lois de pyrolyse comparées P.A. et liant polyuréthane permettent d'expliquer ces structures de surface (on sait qu'à haute pression la structure s'inverse, particules de P.A. en dépression par rapport au liant conduisant à des combustions inefficaces et à l'effet de "mesa" observé vers 50 bars, fig. 21). Dans le cas des compositions P.A.-P.B.C., dont la p_{LD} est à 0,1 - 0,2 bar, les structures de surface sont plus harmonisées (fig. 23) (un réseau de carbone, filaments brillants blancs sur les photos, recouvre la surface proprement dite) et permettent de maintenir une combustion efficace jusqu'à très basse pression.

C'est à partir de résultats du type de ceux de la fig. 21 qu'a été élaboré le tableau de la fig. 24. On y voit que la granulométrie de l'oxydant a assez peu d'influence, tout au moins pour les compositions au P.B.C., que la nature du liant, P.B.C. → polyuréthane, est importante (par ailleurs, l'addition de quelques % d'additif métallique dans les compositions P.A.-P.U. relève le niveau général de vitesse et abaisse la p_{LD}). Dans le cas des compositions au polyuréthane à p_{LD} élevée, le remplacement par $KClO_4$ abaisse la p_{LD} probablement en harmonisant mieux les structures de surface oxydant-liant, voir [15]. Enfin, alors

que l'addition de $KClO_4$ au P.A. modifie fortement les lois $V_c(P)$ au-delà de 10 bars (exposant de pression modifié de 0,3 à 0,8 [15]), dans le régime piloté par les flammes de diffusion, à basse pression, dans le régime prémélangé, très peu d'influence est détectée.

Les résultats présentés ici sur la combustion à basse pression ne constituent pas un examen complet des possibilités d'augmenter la pression limite de combustion des propergols composites. Ils apportent des conclusions complémentaires (et en harmonie avec) de celles présentées en [15] sur la combustion à pression plus élevée, à savoir l'importance des structures de surface, les domaines respectifs de régime de flamme prémélangée ou de flammes de diffusion. Les réfs. [18 , 19] correspondent à des recherches plus systématiques pour augmenter la P_{LD} . On y trouve de même qu'ici que les liants oxygénés de type polyuréthane sont favorables à une P_{LD} élevée, et de plus que l'augmentation du % de liant permet d'accroître la P_{LD} , que la présence d'aluminium n'a pas une influence très marquée...

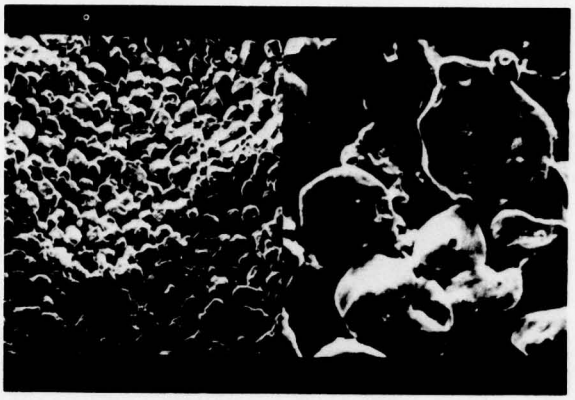

Fig. 22 – Structure de surface à l'extinction spontanée.

72% PA 90 µ 28% Polyuréthane Extinction à ≃ 3 bars

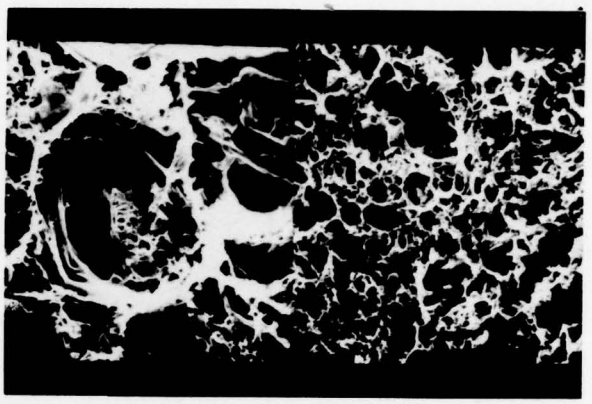

Fig. 23 – Structure de surface à l'extinction.

80% PA 80-100 µ 20% PBC
Extinction en dp/dt à 0,1-0,2 bar.

Composition	Pression limite de déflagration, bars : par dp/dt lent / par difficulté d'all.	V_c / P_{LD} mm/s	
80% P.A. 80.100 µ $\Psi = 0,44$ 20% P.B.C. Exposant de pression ≃ 0,3-0,4	0,1 / < 0,2	0,5	Granulométrie
80% P.A. <15-20 µ $\Psi = 0,44$ 20% P.B.C	0,2 / 0,1	0,3	Granulométrie
80% (90% P.A-10% $KClO_4$ copr.) <15-20µ 20% P.B.C. Exposant de pression ≃ 0,8	0,15 / 0,16	0,7	
72% P.A. 90µ-28% Polyuréthane $\Psi = 0,44$	3 / 3	1,8	Nature du liant
72% P.A. 90µ-28% P.U. +3% chromite de cuivre	0,8 / 1	0,8	
65% $KClO_4$ 30µ-35% PU $\Psi = 0,44$	— / 1,5	1,2	Nature de l'oxydant

Fig. 24 – Extinction des propergols composites.

5 - CONCLUSIONS

On a présenté les résultats d'études menées à l'ONERA sur l'allumage, au niveau du propergol et du propulseur, et l'extinction des propergols solides. On s'est efforcé de les intégrer dans ceux de la littérature afin d'en tirer des conclusions aussi générales que possible.

En ce qui concerne les caractéristiques d'allumage des propergols solides, on a montré qu'une loi unique délai d'allumage-flux de chaleur reçu existe, indépendamment du mode d'apport de chaleur (rayonnement, convection-conduction, impact de particules d'alumine), correspondant aux caractéristiques de dégradation en phase condensée du perchlorate d'ammonium (sans intervention directe de la nature du liant, de la

présence de catalyseurs, du niveau de pression...), dans le cas des propergols composites correspondants, et à celles des composants nitrocellulose, nitroglycérine,dans le cas des propergols homogènes. De la manière la plus simple cette loi d'allumage peut être caractérisée par une température superficielle à atteindre pour que se déclenchent activement les réactions conduisant à l'allumage, légèrement évolutive de 440 à 460 K pour les propergols homogènes, de 560 à 690 K pour les composites (pour une gamme de flux de chaleur de 1 à 150 cal./cm^2s, 0,04 à 5 MW/m^2, englobant largement les niveaux obtenus en propulseur).

Une méthodologie pour l'étude de l'inflammation des chargements de propulseurs, basée sur l'utilisation de fluxmètres à température superficielle, a été développée. Le délai d'allumage est déduit de l'évolution des températures superficielles mesurées par les fluxmètres, l'inflammation étant considérée correspondre à l'obtention des températures critiques à la surface du propergol mentionnées ci-dessus. Les processus d'inflammation et de propagation de la flamme ont été étudiés, à l'aide de cette méthodologie, dans le cas de propulseurs munis de chargements de propergols composite et homogène. Dans le but d'améliorer cette méthodologie, en cherchant notamment à reproduire les échanges thermiques à la surface du propergol et du fluxmètre, il est prévu d'utiliser de nouveaux éléments calorimétriques du type résine présentant des caractéristiques thermocinétiques proches de celles du propergol.

Les caractéristiques d'extinction des propergols solides composites ont été étudiées. On a vu que la pression limite de combustion d'un propergol peut être affectée pour certains paramètres de la composition, très particulièrement la nature du liant, les liants oxygénés du type polyuréthane étant favorables pour des pressions limites élevées (quelques bars par opposition à $\simeq$ 0,1 bar pour un liant polybutadiène). L'extinction dynamique, l'augmentation de la pression à laquelle le propergol s'éteint en fonction d'une dépressurisation, s'explique bien en tenant compte de la réponse instationnaire du propergol aux évolutions de pression.

RÉFÉRENCES

[1] - BAER, A.D. et RYAN, N.W.
Ignition of Composite Propellants by Low Radiant Fluxes.
AIAA Journal, vol. 3, n°5, p. 884, Mai 1965.

[2] - KELLER, J.A., BAER, A.D. et RYAN, N.W.
Ignition of Ammonium Perchlorate Composite Propellants by Convective Heating.
AIAA Journal, vol. 4, n°8, p. 1358, Août 1966.

[3] - PRICE, E.W., BRADLEY, H.H., DEHORITY, G.L. et IBIRICU, M.M.
Theory Ignition of Solid Propellants.
AIAA Journal, vol. 4, n°7, p. 1153, Juillet 1966.

[4] - INAMI, S.H., Mc CULLEY, L. et WISE, H.
Ignition Response of Solid Propellants to Radiation and Conduction.
Combustion and Flame, vol. 13, n°5, p. 531, Oct. 1969.

[5] - THOMPSON, C.L. et SUH, N.P.
The Interaction of Thermal Radiation and M2 Double-Base Solid Propellant.
Combustion Science and Technology, vol. 2, p. 59, 1970.

[6] - MERZHANOV, A.G. et AVERSON, A.E.
The Present State of the Thermal Ignition Theory : An Invited Review.
Combustion and Flame, vol. 16, n°1, p. 89, Février 1971.

[7] - DE LUCA, L., CAVENY, L.H., OHLEMILLER, T.J. et SUMMERFIELD, M.
Radiative Ignition of Double-Base Propellant : I - Some Formulation Effects.
II - Pre-ignition Events and Source Effects.
AIAA Journal, vol. 14, n°7, p. 940, Juillet 1976 ; vol. 14, n°8, p. 1111, août 1976.

[8] - DI LAURO, G.F., LINDEN, L.H., MOST, W.J. et SUMMERFIELD, M.
Theoretically Predicted Ignition Transients in Solid Propellants Rocket Motors.
Department of Aerospace and Mechanical Sciences, Report n°802, Princeton University, Juillet 1967.

[9] - PERETZ, A., KUO, K.K., CAVENY, L.H. et SUMMERFIELD, M.
The Starting Transient of Solid Propellant Rocket Motors with High Internal gas Velocities.
AIAA paper n° 72-1119, Nov.-Dec. 1972.

[10] - LARUE, P.
Dispositif expérimental d'étude de l'allumage d'un bloc de propergol solide de grandes dimensions.
La Recherche Aérospatiale, n°123, Mars-Avril 1968.

[11] - SCAGNETTI, M. et CRABOL, J.
Mesure des flux de chaleur pendant la phase d'allumage d'un propergol solide.
La Recherche Aérospatiale, n°123, Mars-Avril 1968.

[12] - LARUE, P. et NADAUD, L.
Processus d'allumage des propergols solides.
La Recherche Aérospatiale, n° 1972-6, Nov.-Déc. 1972.

[13] - BARRERE, M.
Allumage des petits propulseurs à poudre.
47th PEP-AGARD, CP n°194 (OTAN-Confidentiel), 1976.

[14] - KUENTZMANN, P., DEMARAIS, J.C et CAUTY, F.
Mesure de la vitesse de combustion des propergols solides par ultra-sons.
La Recherche Aérospatiale, n° 1979-1, Janv.-Fév. 1979.

[15] - LENGELLE, G., BRULARD, J. et MOUTET, H.
Combustion Mechanisms of Composite Solid Propellants.
16th Symposium (International) on Combustion, M.I.T., 1976.

[16] - LENGELLE, G., VERDIER, C., DUTERQUE, J., BIZOT, A. et TRUBERT, J.F.
Combustion Mechanisms of Double Base Solid Propellants.
17th Symposium (International) on Combustion, University of Leeds, 1978.

[17] - PICHOIR, R.
Application de la pulvérisation cathodique à l'amélioration des revêtements des superalliages.
La Recherche Aérospatiale, n° 1978-4, Juillet-Août 1978.

[18] - PETERSON, J.A., REED, R. et Mc DONALD, A.J.
Control of Pressure Deflagration Limits of Composite Solid Propellants.
AIAA Journal, vol. 5, n°4, p. 764, Av. 1967.

[19] - PARK, C.P., RYAN, N.W. et BAER, A.D.
Extinguishment of Composite Propellants at Low Pressures.
AIAA Paper n° 73-175, Janv. 1973.

[20] - STRAND, L.D.
Summary of a Study of the Low-Pressure Combustion of Solid Propellants.
Jet Propulsion Laboratory Technical Report 32-1242, Av. 1968.

IGNITION AND EXTINCTION OF SOLID ROCKET PROPELLANTS

by

L. DE LUCA, L. GALFETTI, and C. ZANOTTI
Centro di Studio per Ricerche sulla Propulsione
e sull'Energetica, Istituto di Macchine del Politecnico,
32 Piazza Leonardo da Vinci, 20133 Milano, Italy.

SUMMARY

Dynamic burning effects associated with ignition and extinction of solid rocket propellants are examined within the framework of a thermal theory of heterogeneous combustion and for quasi-steady gas phase. A nonlinear burning stability analysis was carried out via an integral method. This predicts that, for a given set of operating conditions, a well defined critical surface temperature exists below which extinction of a burning propellant necessarily follows independently on its past history. These critical surface temperature values define a lower dynamic stability boundary strictly depending on the propellant nature, but affected by the operating conditions. The analysis is based on an asymptotic stability criterion always valid for static (random disturbances) stability problems, but restricted to forcing functions levelling off in time for dynamic (external disturbances) stability. Under these circumstances, the lower dynamic stability boundary is independent on the nature of the transient (pressure or radiation driven),the shape in time of the forcing function (linear, exponential, parabolic, etc.) and the rate of change of the forcing function (even variable). The relevance of the lower dynamic stability boundary to ignition transients is discussed. While no experimental verification of the theory is yet available, computer simulated runs show a very good agreement with the analytical predictions.

LIST OF SYMBOLS

a = volume absorption coefficient, cm^{-1}
A_M = constant used in MTS flame model
B_M = constant used in MTS flame model
B_p = nondimensional depressurization rate coefficient
B_r = nondimensional deradiation rate coefficient
E = activation energy, cal/gmole
$f(\bar{\theta}_{i,s} - \theta_s)$ = static restoring function (see Eq. 3.13)
F_o = nondimensional radiant flux intensity impinging at the propellant surface
$g(\tau, \bar{\theta}_{i,s} - \theta_s)$ = nonautonomous function
H = nondimensional surface heat release
I = radiant flux intensity, cal/cm^2-s
I_o = radiant flux intensity impinging at the propellant surface, cal/cm^2-s
n = exponent in ballistic burning rate law; also: order of the approximating polynomial (see Eq. 3.4)
P = pressure, atm
$\mathcal{P}$ = nondimensional pressure
$\dot{q}$ = conductive energy flux, cal/cm^2-s
$\phi_{g,s}$ = nondimensional heat feedback from the gas phase
Q = nondimensional flame heat release
Q_f = flame heat release, cal/g
Q_s = surface heat release, cal/g
r = surface reflectivity
$\mathcal{R}$ = universal gas constant, cal/gmole-K
R = burning rate, cm/s
$\mathcal{R}$ = nondimensional burning rate
t = time, s
T = temperature, K
$\mathcal{T}$ = nondimensional temperature
u = nondimensional finite size disturbance of temperature
u_x = nondimensional finite size disturbance of thermal gradient
w = exponent in KTSS surface pyrolysis law
x = space variable, cm
X = nondimensional space variable

Greek Symbols

Δ = finite difference of a quantity evaluated between X=0 and X=-ξ
θ = nondimensional temperature
λ = thermal conductivity, cal/cm-s-K
ξ = nondimensional thickness of disturbance thermal layer
τ = nondimensional time

Subscripts and Superscripts

a = ambient
c = condensed phase
f = final or flame
g = gas
i = initial
m = minimum value for chemical reactions to occur (see Eq. 3.2)
s = surface

ref	= reference
—	= steady state or average value of a parameter
$-\infty$	= conditions far upstream

Abbreviations

AFSC	= Air Force System Command
AIAA	= American Institute of Aeronautics and Astronautics
AMS	= Aerospace and Mechanical Sciences Department
AP	= ammonium perchlorate
ARS	= American Rocket Society
CF	= Combustion and Flame
CPIA	= Chemical Propulsion Information Agency
CST	= Combustion Science and Technology
DB	= Double Base
FGV	= Combustion, Explosion and Shock Waves
FTD-MT	= Foreign Technology Division - Machine Translation
JETP	= Journal of Experimental and Theoretical Physics
JSR	= Journal of Spacecraft and Rockets
KTSS	= Krier-T'ien-Sirignano-Summerfield
MTS	= Merkle-Turk-Summerfield
NASA	= National Aeronautics and Space Administration
ODE	= ordinary differential equation
ONERA	= Office National d'Etudes et de Recherches Aérospatiales
PBAA	= polybutadiene-acrylic acid
PDE	= partial differential equation
PMTF	= Journal of Applied Mechanics and Technical Physics

Sec. 1 - INTRODUCTION

The purpose of this paper is to elucidate the dynamic burning effects associated with extinction and ignition of solid rocket propellants. An explanation of dynamic extinction valid under a broad variety of conditions, for pressure as well as radiation driven transients, is offered within the framework of a thermal model of heterogeneous combustion. Numerical calculations are given for an ammonium perchlorate (AP)-based composite solid propellant, but the basic concepts emerging from this investigation are expected to hold true for any condensed substance subjected to deflagration waves.

This study is based on a comprehensive combustion stability analysis (Refs. 1-2) developed in fully nonlinear conditions by means of an integral method. The method consists of evaluating the minimum burning rate (lower dynamic stability point), in function of pressure, under which extinction of the burning solid propellant necessarily occurs independently on its past history. This limiting burning rate is a property strictly dependent on the nature of the reacting substance; but it is affected by the operating conditions, such as pressure, ambient temperature, and heat exchange with the environment. It is shown that the analytical predictions of dynamic extinction are well verified by digital simulation both of depressurization and deradiation tests. Likewise, during an ignition transient, the dynamic burning following the external energy source cut-off is not allowed to fall below the lower dynamic stability point if ignition has to succeed.This point will be discussed in a more detailed way in Sec. 4.

This paper goes beyond previous works of the authors (Refs. 3-4) in that: (1) a generalized polynomial is used in order to implement the integral method, (2) ignition transients also are considered, (3) results from MTS and KTSS flame models are given, and (4) optical transparency of the condensed phase is examined. First, a literature survey is offered in Sec. 2. Then, an integral method with a generalized polynomial order is discussed (Sec. 3). Comparison between analytical predictions and computer simulated results is shown in Sec. 4. Conclusions and plans for future work (Sec. 5) will complete the paper.

Sec. 2 - A LITERATURE SURVEY

Although dynamic extinction might occur under a variety of conditions, due to the pioneering work of Ciepluch (Refs. 5-6) in 1961, only dynamic extinction by depressurization appears largely debated in the competent literature. For a critical review of papers offered until 1969, the reader might consult Merkle (Ref. 7). Contributions offered after this review (Refs. 8-20) are mostly of experimental nature. The theoretical understanding of dynamic extinction by depressurization is still little satisfactory. The erroneous application of the quasi-steady gas phase assumption, the strong limitations due to the use of linearized theories, and the empirical nature of several of the proposed extinction criteria are the most serious drawbacks in this area.

At least two excellent contributions should explicitely be mentioned. Merkle (Ref. 7) pointed out several mistakes commonly found in the literature, furnished a new unsteady flame model and recognized that dynamic extinction depends on the entire P(t) curve; but he did not formulate an extinction criterion. A paper by T'ien (Ref. 18), in 1974, is the only one aimed directly at establishing an extinction criterion for fast depressurization. T'ien argues that heat losses are the mechanism for both static and dynamic extinction of solid propellants; this view is not fully shared in this instance. However, T'ien concludes (Refs. 18-19) that for depressurization transients, if the instantaneous burning rate drops below the unstable burnig rate solution at the final pressure, extinction will

occur.A somewhat similar result has been found in this investigation (Refs. 1-4), but by a completely different approach.

The line of research evolved within the framework of Zeldovich method (Refs. 21-22) is of limited value. Istratov et al. (Ref. 23), in 1964, used an integral method in order to determine an approximate solution to the unsteady nonlinear energy equation in the condensed phase of a propellant burning with constant surface temperature. Extinction was assumed to occur when the surface thermal gradient on the condensed side exceeds a critical value corresponding to the static stability line. This is mistaken, since nothing can be said a priori about dynamic burning in a range of burning rate that is statically unstable. Novozhilov (Ref. 24), in 1967, improved the previous model by considering a variable surface temperature and recognizing that dynamic burning is allowed also in the range of parameters where statically stable solutions are not found. Extinction was then assumed to occur when the burning rate at the final pressure drops below a limiting value experimentally established in nonstationary burning conditions. This "ad hoc" criterion relies on very delicate experimental results.

The question of a possible early warning of extinction during a depressurization transient evaluated via the Zeldovich method was examined in a paper by the Princeton group (Ref. 25) in 1971. The possibility was checked that the crossing of the static stability boundary is sufficient to subsequently produce dynamic extinction. In our opinion the static stability boundary has only secondary relevance in a dynamic situation. Indeed, according to the same Princeton reference, "the dynamic conditions of extinguishment tend to shift the stability line" (p. 257 of Ref. 25). Further extensive work in this area (Ref. 26) failed to reach more significant conclusions. Finally Novozhilov (p. 216 of Ref. 27), in 1973, observed that this "question requires certain information about the properties of the system outside the area of smooth burning. Such information cannot be obtained from experiments on steady state combustion. For the calculation of unsteady conditions in the unstable region it is necessary to draw on certain schemes of combustion, which make it possible to predict the properties of propellants beyond the (static) stability limit". Further work by Soviet investigators (Refs. 28-34) offered fresh experimental information and theoretical considerations, but failed to define a physically sound extinction criterion.

Studies on dynamic extinction by deradiation and dynamic extinction associated with ignition overlap. A comprehensive literature survey was recently offered (Ref. 2). Experimental and theoretical studies were mainly conducted at Princeton (Refs. 2, 35-36) and in USSR (Refs. 37-40). An extinction criterion for opaque solid propellant subjected to fast deradiation was suggested by De Luca (Ref. 1), in 1975, within the framework of a general nonlinear combustion stability analysis. The Soviet work suffers the same deficiences mentioned above.

In this work, quantitative criteria for dynamic stability of burning propellants are defined by means of flame models. The integral method of Goodman (Ref. 41) is implemented in order to apply known mathematical methods to the resulting approximate ODE formulation of the problem. The same method has already been applied (Ref. 42) to droplet burning; somewhat simpler use has been made at Princeton (Refs. 43-44) on solid propellant rocket engines. The concept of using the simpler ODE formulation of the problem, instead of the PDE one, is relatively common in Soviet literature. However, the method of transformation is rather different; an interesting review of the mathematical problem was made by Gostintsev (Ref. 45).

The alternative approach based on asymptotic methods, mainly developed by Williams (a good summary is given in Ref. 46), has proven very successful in predicting ignition times for thermal runaway under different operating conditions. However, neither go/no-go nor deradiative extinction are considered in this otherwise excellent line of research. Therefore, this paper and Ref. 46 nicely complement each other.

Sec. 3 - THE LOWER DYNAMIC STABILITY BOUNDARY

Consider the physical system of Fig. 1 representing a strand of solid propellant subjected to a radiant flux impinging with instantaneous intensity $(1-r).I_o(t)$ at its surface, burning with instantaneous rate $R(t)$ in a closed vessel at instantaneous pressure $P(t)$ and fixed ambient temperature T_a. The following assumptions are made:

a) Entire Strand

1. Monodimensional.
2. Constant thermal, physical, and chemical properties.
3. Condensed and gas phases have identical specific heats.
4. At cold boundary, in thermal equilibrium with ambient.
5. Subjected to no external forces (e.g., acceleration).
6. No emission of radiation.

b) Condensed Phase

1. Semi-infinite slab.
2. Uniform and isotropic composition.
3. Adiabatic, except at the burning surface.
4. No chemical activity.
5. No radiation scattering.
6. No photochemical effects.

c) Interface Condensed/Gas

1. Infinitesimally thin plane surface.
2. One-step, irreversible gasification processes described by Arrhenius or KTSS (see Eqs. 3.2) pyrolysis.

d) Gas Phase

1. Semi-infinite columm of gas.
2. Mixture of thermally perfect gases of average molecular weight $\overline{m}$.
3. One-phase, laminar, nonviscous, and strongly subsonic flow.
4. Adiabatic, except at the burning surface.
5. No interaction with (external) radiation.
6. Quasi-steady, thermal flame models.

Under this set of assumptions, the evolution of burning rate in time of an opaque propellant is described by the following nondimensional equations (see Tables 1-2):

$$(3.1)\quad \begin{cases} \dfrac{\partial\theta}{\partial\tau} + \mathcal{R}\dfrac{\partial\theta}{\partial X} = \dfrac{\partial^2\theta}{\partial X^2} & X \leq 0, \tau \geq 0 \\ \theta(X, \tau = 0) = \bar{\theta}_i(x) & \\ \theta(X \to -\infty, \tau) = \theta_a & \\ \left(\dfrac{\partial\theta}{\partial X}\right)_{c,s} = \dfrac{\lambda_g}{\lambda_c}\left(\dfrac{\partial\theta}{\partial X}\right)_{g,s} - \mathcal{R}\cdot H + (1-r)F_o & \end{cases}$$

$$(3.2a)\quad \mathcal{R} = e^{\frac{-E_s}{\mathcal{R}T_{s,ref}}\left(\frac{1}{T_s}-1\right)} \qquad \text{Arrhenius pyrolysis}$$

$$(3.2b)\quad \mathcal{R} = (\theta_s - \theta_m)^w \qquad \text{KTSS pyrolysis}$$

where $\theta(X,\tau)$ is the unknown thermal profile in the condensed phase. The function

$$\dot{q}_{g,s}(\mathcal{P},\mathcal{R}) \equiv (\lambda_g/\lambda_c)\,(\partial\theta/\partial X)_{g,s}$$

describes the nondimensional heat feedback from the gas phase to the burning surface. This function must be assigned by means of an appropriate unsteady flame model.

No general method exists for studying the stability properties of the strongly nonlinear PDE describing the condensed phase thermal profile (Eq. 3.1) subjected to finite disturbances. Since rigorous methods of investigation have been established for the case of ODE, the stability analysis requires re-formulating the problem of Eqs. 3.1 - 3.2 in terms of an ODE. For this purpose, a new nondimensional variable is defined

$$(3.3)\quad u(X,\tau) \equiv \bar{\theta}_i(X) - \theta(X,\tau)$$

describing the finite temperature disturbance propagating inside the condensed phase and superimposed on the initial known steady thermal profile $\bar{\theta}_i(X)$ after the action of some perturbation. It is assumed that the disturbance temperature has a finite penetration depth $\xi(\tau)$ and within this layer its dependence on the space variable may be approximated by a polynomial (Ref. 41):

$$(3.4)\quad u(X,\tau) = K_o(\tau) + K_1(\tau)\cdot X + K_2(\tau)\cdot X^2 + K_3(\tau)\cdot X^3 \ldots K_n(\tau)\cdot X^n$$

This implies that the time history of the disturbance temperature is restricted to profiles monotonically decaying in space. The above n+1 coefficients $K_i(\tau)$ are determined from n+1 boundary conditions (on the finite penetration depth) expressing the energy balance at the hot boundary of the penetration depth and that no disturbance, up to the n-1 derivative, is felt at the cold end of the penetration depth. Under these circumstances, the following disturbance temperature profile is obtained:

$$(3.5)\quad u(X,\tau) = u_s\left(1 + \frac{X}{\xi(\tau)}\right)^n \qquad 0 \leq |X| \leq \xi(\tau)$$

where $u_s(\tau)$ is the unknown disturbance surface temperature. The history of the penetration depth is described by

$$(3.6)\quad \xi(\tau) = n\,\frac{u_s}{(u_x)_{c,s}}$$

where $(u_x)_{c,s}$ is the surface thermal gradient disturbance, at the condensed phase side, defined by

$$(3.7)\quad (u_x)_{c,s} \equiv \left(\frac{\partial u}{\partial X}\right)_{c,s} = \frac{\lambda_g}{\lambda_c}\left(\frac{\partial u}{\partial X}\right)_{g,s} - H\,(\bar{\mathcal{R}}_i - \mathcal{R}) + (1-r)\,(F_{o,i} - F_o)$$

The space dependence of the PDE of Eq. 3.1 can now be eliminated by integration from X=0 to $X=\xi(\tau)$ and taking into account the approximate disturbance temperature profile of Eq. 3.5. First the PDE has to be re-written in terms of the new nondimensional variable $u(X,\tau)$ defined by Eq. 3.3. After some manipulation, the integration gives the following differential expression

$$(3.8) \qquad \frac{d}{d\tau}\frac{u^2_s}{(u_x)_{c,s}} = -\frac{n+1}{n}\left[\mathcal{R}u_s - (u_x)_{c,s} - \mathcal{R}\cdot\Delta(\bar{\theta}_i) + \Delta\left(\frac{d\bar{\theta}_i}{dX}\right)\right]$$

where

$$(3.9) \qquad \Delta(\bar{\theta}_i) \equiv \bar{\theta}_i(X=0) - \bar{\theta}_i(X=-\xi)$$

$$(3.10) \qquad \Delta\left[\frac{d\bar{\theta}_i}{dX}\right] \equiv \frac{d\bar{\theta}_i}{dX}(X=0) - \frac{d\bar{\theta}_i}{dX}(X=-\xi)$$

are known quantities. The time derivative of the surface thermal gradient disturbance, at the condensed phase side, may be written as

$$(3.11) \qquad \frac{d(u_x)_{c,s}}{d\tau} = \frac{du_s}{d\tau}\left[\frac{\lambda_g}{\lambda_c}\left(\frac{\partial(u_x)_{g,s}}{\partial u_s}\right)_{\mathcal{P}} + H\frac{d\mathcal{R}}{du_s}\right] + \frac{\lambda_g}{\lambda_c}\frac{d\mathcal{P}}{d\tau}\left(\frac{\partial(u_x)_{g,s}}{\partial\mathcal{P}}\right)_{u_s} - (1-r)\frac{dF_o}{d\tau}$$

which can be evaluated once a flame model has been chosen and the external laws $\mathcal{P}(\tau)$ and $F_o(\tau)$ have been assigned.

Upon substituting the above relationship into Eq. 3.8, the following approximate ODE formulation of the problem is obtained:

$$(3.12) \qquad \begin{cases} \dfrac{d\theta_s}{d\tau} = +\dfrac{n+1}{2n}\dfrac{(u_x)_{c,s}}{u_s}\dfrac{\mathcal{R}u_s - (u_x)_{c,s} - \mathcal{R}\Delta(\bar{\theta}_i) + \Delta\left(\dfrac{d\bar{\theta}_i}{dX}\right)}{1-\dfrac{1}{2}\dfrac{u_s}{(u_x)_{c,s}}\left[\dfrac{\partial(u_x)_{c,s}}{\partial u_s}\right]_{F_o,\mathcal{P}}} \\ \qquad - \dfrac{\dfrac{d\mathcal{P}}{d\tau}\left[\dfrac{\partial(u_x)_{c,s}}{\partial\mathcal{P}}\right]_{F_o,u_s} - (1-r)\dfrac{dF_o}{d\tau}}{2\dfrac{(u_x)_{c,s}}{u_s} - \left[\dfrac{\partial(u_x)_{c,s}}{\partial u_s}\right]_{F_o,\mathcal{P}}} \\ \theta_s(\tau=o) = \text{given} \end{cases}$$

The above nonlinear ODE describes the instantaneous response of the system to a finite size departure of the surface temperature from the initial stationary value due not only to intrinsic perturbation sources acting on the system (static stability), but also to any arbitrary but externally assigned monotonical change in time of controlling parameters such as pressure and radiant flux (dynamic stability).

A system is defined asymptotically stable if

$$\theta(X,\tau\to\infty) = \bar{\theta}(X)$$

where $\bar{\theta}(X)$ is the initial steady thermal profile (static stability) or the final wanted steady thermal profile associated with a given transition of the external parameters (dynamic stability). Whenever no time derivative of the forcing function is acting on the system, i.e. $\mathcal{P}$= const and F_o=const, the PDE problem of Eq. 3.1 may be re-formulated as

$$(3.13) \qquad \frac{d\theta_s}{d\tau} = f(\bar{\theta}_{i,s} - \theta_s)$$

where the nonlinear algebraic function $f(u_s) \equiv f(\bar{\theta}_{i,s} - \theta_s)$, called the static restoring function, is given by the first term on the right-hand side of Eq. 3.12. The zeroes of the static restoring function are, in principle, equilibrium points of Eq. 3.13. Therefore, studying the asymptotic stability of the original PDE problem (Eq. 3.1) is reduced to analyzing the nature of the zeroes of an algebraic function. This simplified point of view is always valid in the case of static stability, while in the case of dynamic stability it helps only if the forcing functions level off.

In order to evaluate the static restoring function, a flame model and a specific polyno-

mial order have to be chosen. While a certain variety of unsteady flame models is available (an excellent review was recently offered by Kuo in Ref. 47), their use still is a matter of personal belief. In this research MTS and KTSS (both linearized and nonlinearized versions) flame models are implemented ; others will be considered in the near future. For example,according to MTS model the nondimensional heat feedback is

$$(3.14) \qquad \dot{q}_{g,s}(\mathcal{P},\mathcal{R}) = Q\mathcal{R}\left[\frac{\sqrt{\tau'_{ki}}}{\sqrt{\tau'_{re}}}\, e^{-\mathcal{R}^2\tau'_{re}} + \frac{\sqrt{\tau'_{di}}}{\sqrt{\tau'_{re}}}\, \frac{1 - e^{-\mathcal{R}^2\tau'_{re}}}{\mathcal{R}^2\tau'_{re}}\right]$$

where

$$(3.15) \qquad \sqrt{\tau'_{ki}} = A_M\, \frac{T_f}{\mathcal{P}}\, e^{\frac{E_f}{2\mathcal{R}T_{f,ref}}\left[\frac{1}{T_f} - 1\right]}$$

is a nondimensional kinetic time parameter;

$$(3.16) \qquad \sqrt{\tau'_{di}} = B_M\, \frac{(T_f)^{5/6}}{(T_s)^{7/8}(\mathcal{P})^{3/3}}$$

is a nondimensional diffusion time parameter;

$$(3.17) \qquad \sqrt{\tau'_{re}} = \sqrt{\tau'_{di}} + \sqrt{\tau'_{ki}}$$

is a nondimensional reaction time parameter. For details,consult Ref. 4.

As to the order of the approximating polynomial, a cubic law was chosen to represent the space distribution of the disturbance thermal profile. This choice was suggested by a large body of literature on heat transfer problems (e.g., Ref. 41) and by similar solid propellant rocket problems (Refs. 43-44). However, there is no a priori guarantee that this is the best choice. The choice has to be verified (for example, consult Ref. 4). A sketch of $f(\bar{\theta}_{i,s} - \theta_s)$ is shown in Fig. 2.

Sec. 4 - RESULTS FROM COMPUTER SIMULATED TESTS

For a standard set of parameters (T_a = 300 K,Q_s = - 158.2 cal/g, adiabatic propellant), the values of surface temperature for which the restoring function is zero in function of pressure are summarized in Tab. 3. Three equilibrium points are found: two are stable and correspond to steady reacting (root A) and unreacting (root C) configurations, the last one (root B) is unstable. The B-root, at the final operating pressure, represents that ultimate surface temperature beyond which a burning solid propellant necessarily extinguishes. For increasing pressure, the surface temperature associated with the B-root increases slightly. In the diagram of Fig. 3, burning rate is plotted vs pressure; the locus of B-roots defines the lower dynamic stability boundary. This separates the entire plane in two regions: dynamically stable above the boundary and dynamically unstable under. All transients, except ignition, are represented by trajectories starting in the dynamically stable region (at the given initial pressure and radiant flux corresponding to root A). If the process is dynamically stable, the trajectory never falls below the lower dynamic stability boundary. If the trajectory reaches even momentarily the lower dynamic boundary, necessarily dynamic extinction follows and the trajectory ends at the trivial zero burning rate solution (corresponding to root C). This is indipendent on the past history of the propellant at the instant of the boundary crossing.

Dynamic extinction can be interpreted as a consequence of an unstable energy coupling of the condensed phase to the gas phase at the burning surface. For burning rates below the lower dynamic stability boundary, the energy absorbed in the condensed phase always overcomes the sum of energy releases in gas phase and at the burning surface. This implies that the burning rate decreases more and more, until extinction finally occurs.

Ignition transients start in the dynamically unstable region (root C) and have to rise roughly above the lower dynamic stability boundary for the deflagration wave to be self-sustained (minimum energy input for ignition as a static requirement). Following then the external source cut-off,if in the meanwhile a steady burning configuration has been reached, the trajectory is not allowed to fall below the same lower dynamic stability boundary in order to be dynamically stable (maximum energy input for ignition or maximum cut-off rate as dynamic requirement).

The above predictions are made on a purely analytical basis. Go/no-go computer simulated tests have been run in order to check the theory. These tests were performed by integrating the full set of governing equations based on the PDE of Eq. 3.1. Purpose of the runs is to show that for a composite solid propellant a lower dynamic stability boundary may be constructed independently on the nature of the transient (pressure or radiation driven), the time shape of the forcing function (linear, parabolic, exponential, etc.), and its rate of change. The numerical values obtained in this way are summarized in Tab. 4 and compare very well with those expected by analyzing the nonlinear algebraic static restoring function associated with the approximate ODE of Eq. 3.12.

In particular, notice that the predictions are well respected even for deradiation runs

with optically transparent condensed phase (Fig. 4). The reason for this is that, after the decrease of the radiant flux intensity down to zero, the optical transparency of the condensed phase is no longer relevant. This dynamic extinction test was obtained, by deradiation, implementing the MTS flame model. Obviously, in no way dynamic extinction could be obtained, either by deradiation or depressurization, implementing the KTSS linearized flame model.

Several go/no-go ignition transients were also performed. A significative example obtained with the MTS flame model is shown in Fig. 5.The two runs plotted in this figure are identical, except a negligibly faster cut-off of the external radiant source for the extinguished case. The minor dynamic effects associated with the cut-off of the external radiant source are not enough, for the ignited case, to lead the instantaneous surface temperature (or burning rate) below the corresponding critical value. Under the specific operating conditions of Fig. 5, the lower dynamic limit is seen to constitute a rather accurate boundary both for the static (minimum energy) and dynamic (smooth energy source cut-off) ignition requirements. This, however, cannot be generalized. Indeed the lower dynamic limit was evaluated for an initially steadily burning propellant. The exact connection, if any, between ignition and lower dynamic limit has yet to be investigated. On the other hand, in the case of dynamic extinction of steadily overdriven burning rates associated with ignition transients, the lower dynamic limit is expected to be fully valid.

Sec. 5 - CONCLUSIONS AND SUGGESTIONS

It is felt that conclusive evidence has been offered for:(1) the existence of a minimum value of burning rate below which extinction of burning propellants necessarily follows and ignition transients are dynamically unstable;(2) the capability of the proposed theory to predict this critical value; and (3) the validity of the approach both for MTS and KTSS (linearized and nonlinearized) flame models. Although figures are given only for a composite solid propellant, the above facts are expected to hold true for any condensed, chemically reacting substance.

Remark that the predictive power of the proposed theory is well verified for depressurization and deradiation computer simulated tests. While dynamic extinction due to fast depressurization or deradiation (including ignition transients) is well confirmed experimentally, so far no attempt has been made to compare the theory proposed in this paper directly with experimental results. However, work in this direction is currently in progress. Remark also that the ignition transients were computed by assuming a quasi-steady gas phase history from the very beginning of the propellant warming up. Obviously, although common, this is not a rigorous procedure. However, an accurate description of the incipient flame should not be of particular importance for the overall propellant ignition transient.

As to the theoretical approach, the delicate assumption of a polynomial space dependence of the disturbance thermal profile has to be further investigated. Likewise, other unsteady flame models shall be tested and compared. In particular, more appropriate modelling is required in the low burning rate region. At any rate, the most significant result is felt to be the validity of the nonlinear burning stability analysis through the use of the static restoring function. In perspective, this suggests that other intriguing aspects of unsteady burning of solid propellants may be clarified (for example, see Refs.4 and 48). Yet, the lack of experimental verification still requires a word of caution against the full validity of the proposed model.

It is stressed that the use of a flame model is essential in the theoretical developments presented in Sec. 3. Notice that no attempt is being made to propose new flame models;rather a method is offered to judge how good any unsteady flame model is. Likewise, no attempt is being made to model the steady flame structure of solid propellants; this is supposed to be assigned in terms of burning rate and flame temperature vs pressure. It is also stressed that, although heat loss from the system is an important aspect of the problem as rightly pointed out by T'ien (Ref.18), the basic reason for dynamic extinction is the thermal inertia of the condensed phase which is a most important heat sink. However, in qualitative agreement with this work, T'ien found that the critical condition for dynamic extinction by depressurization is fixed by the (statically) unstable root at the final pressure. It is finally stressed that any interaction combustion/fluid-dynamics (for example, in a rocket combustion chamber) is out of the scope of this investigation.

In conclusion, a nonlinear algebraic function can be defined that contains all basic properties of equilibrium and asymptotic (both static and dynamic) stability of burning solid propellants, even for finite size disturbances, provided that the external forcing terms level off in time. This function, called static restoring function, strictly depends on the nature of the propellant (including its flame) but is affected by the operating conditions (pressure, ambient temperature and heat exchange with surroundings). In particular, the statically unstable burning rate associated with the restoring function defines a critical border for decelerating (extinction) as well as accelerating (steadily overdriven ignition) deflagration waves.

REFERENCES

1. De Luca, L. "Nonlinear Stability Analysis of Solid Propellant Combustion", II Symposium (International) on Dynamics of Chemical Reactions, University of Padova (Italy), 15-17 December 1975, pp. 245-256.

2. De Luca, L. "Solid Propellant Ignition and Other Unsteady Combustion Phenomena Induced by Radiation", Ph.D. Thesis, Princeton University, AMS Report No. 1192-T, 15 November 1976.

3. De Luca, L., Galfetti, L., Zanotti, C. "Dynamic Extinction of Composite Solid Propellants", Israel Journal of Technology, Vol. 16, No. 6, pp. 159-168, 1978.

4. De Luca, L., Coghe, A., Reggiori, A. "The Dynamics of Solid Propellant Combustion", 1st Annual Technical Report, European Research Office, November 1978.

5. Ciepluch, C.C. "Effect of Rapid Pressure Decay on Solid Propellant Combustion", ARS J., Vol. 31, pp. 1584-1586, 1961.

6. Ciepluch, C.C. "Effect of Composition of Solid Propellants During a Rapid Pressure Decrease", NASA TN D-1559, 1962.

7. Merkle, C.L., Turk, S.L., Summerfield, M. "Extinguishment of Solid Propellants by Rapid Depressurization", Princeton University, AMS Report No. 880, 1969.

8. Jensen, G.E., Brown, R.S. "An Experimental Investigation of Rapid Depressurization Extinguishment", 6th ICRPG Combustion Conference, CPIA Publication No. 192, pp. 411-423, 1969.

9. Wooldridge, C.E., Marxman G.A. "A Comparison between Theoretical and Experimental Extinction Behavior of Solid Propellant", AIAA Preprint 70-666, 1970.

10. Coates, R.L., Horton, M.D. "Predicted Effects of Motor Parameters on Solid Propellant Extinguishment", JSR, Vol. 7, No. 12, pp. 1468-1470, 1970.

11. Coates, R.L., Horton, M.D. "Further Evaluation of a Simplified Theoretical Model for Solid Propellant Extinguishment", 7th JANNAF Meeting, CPIA Publication No. 204, pp. 369-377, 1971.

12. Steinz, J.A., Selzer, H. "Depressurization Extinguishment of Composite Solid Propellants: Flame Structure, Surface Characteristics, and Restart Capability", CST, Vol. 3, pp. 25-36, 1971.

13. Steinz, J.A., Selzer, H. "Depressurization Extinguishment for Various Starting Pressures and Solid Propellant Types", AIAA Paper No. 71-631, 1971.

14. Baer, A.D., Ryan, N.W., Schulz, E.B. "Spectra and Temperature of Propellant Flame During Depressurization", AIAA J., Vol. 9, No. 5, pp. 869-875, 1971.

15. Park, C.P., Ryan, N.W., Baer, A.D. "Extinguishment of Composite Propellants at Low Pressures", AIAA Paper No. 73-175, 1973.

16. Selzer, H. "Depressurization Extinguishment of Composite Solid Propellants: Influence of Composition and Catalysts", AIAA J., Vol. 11, No. 9, pp. 1221-1222, 1973.

17. Mongia, H.C. Ambs, L.L. "A Model for the Combustion and Extinction of Composite Solid Propellants During Depressurization", CF, Vol. 22, pp. 59-69, 1974. See also Comments, CF, Vol. 23, pp. 401-402, 1974.

18. T'ien, J.S. "A Theoretical Criterion for Dynamic Extinction of Solid Propellants by Fast Depressurization", CST, Vol. 9, pp. 37-39, 1974.

19. Baliga, B.R., T'ien J.S. "Unsteady Effects on Low-Pressure Extinction Limit of Solid Propellants", AIAA J., Vol. 13, No. 12, pp. 1653-1656, 1975.

20. Suhas, H.K., Bose, T.K. "A Mathematical Model to Predict Transient Burning Rate and Pressure Decay Rates for Extinction of Composite Propellants", CF, Vol. 28, pp.145-153, 1977. See also Comments, CF, Vol. 31, pp. 329-332, 1978.

21. Zel'dovich, Ya.B. "On the Theory of Combustion of Powder and Explosives", Zh. Eksperim. i Teor. Fiz., Vol. 12, No. 11-12, pp. 498-524, 1942.

22. Zel'dovich, Ya.B. "The Burning Velocity of Powder Under Variable Pressure", PMTF, Vol. 5, No. 3, pp. 126-130, 1964.

23. Istratov, A.G., Librovich, V.B., Novozhilov, B.V. "An Approximate Method in the Theory of Unsteady Burning Velocity of Powder", PMTF, Vol. 5, No. 3, p. 139, 1964. Translation AFSC No. FTD-MT-64-319, pp. 233-242.

24. Novozhilov, B.V. "Nonstationary Burning of Powders Having a Variable Surface Temperature", PMTF, Vol. 8, No. 1, pp. 54-63, 1967. Translation AFSC No.FTD-MT-24-376-68.

25. Summerfield , M., Caveny, L.H., Battista, R.A., Kubota, N., Gostintsev, Yu.A., Isoda,H "Theory of Dynamic Extinguishment of Solid Propellants with Special Reference to Non-Steady Heat Feedback Law", JSR, Vol. 8, No. 3, pp. 251-258, 1971.

26. Battista, R.A., Caveny, L.H., Summerfield, M. "Nonsteady Combustion of Solid Propellants", Princeton University, AMS Report No. 1049, 1972.

27. Novozhilov, B.V. "Nonstationary Combustion of Solid Rocket Fuels", 1973. Translation AFSC No. FTD-MT-24-317-74.

28. Frost, V.A. "Extinction of a Powder with a Change in Pressure", PMTF, Vol.13, No. 5, pp. 113-118, 1972.

29. Frost, V.A., Yumashev, V.L. "Study of the Extinction of Gunpowder in the Combustion Model with a Variable Surface Temperature", PMTF, Vol. 14, No. 3, pp. 92-100, 1973.

30. Frost, V.A., Yumashev, V.L. "Extinction of a Solid Propellant Accompanying a Fall in Pressure as a Loss of Combustion Stability", FGV, Vol. 12, No. 4, pp.548-555, 1976.

31. Assovskii, I.G., Istratov, A.G., Leipunskii, O.I. "Extinction of a Propellant with a Pressure Drop", FGV, Vol. 13, No. 2, pp. 200-205, 1977.

32. Zemskikh, V.I., Istratov, A.G., Leipunskii, O.I., Marshakov, V.N. "Three Characteristic Ballistic Powder Combustion Modes with a Pressure Drop", FGV, Vol. 13, No. 1, pp. 14-19, 1977.

33. Librovich, V. "Non-Steady Burning Processes for Powder and Solid Propellants", XII International Symposium on Space Technology and Science, Tokyo, pp. 585-590, 1977.

34. Ivashchenko, Y.S., Komarov, A.S. "Extinction of a Ballasted Powder due to Pressure Drop", FGV, Vol. 14, No. 1, pp. 151-153, 1978.

35. Ohlemiller, T.J. Caveny, L.H., De Luca, L., Summerfield, M. "Dynamics Effects on Ignitability Limits on Solid Propellants Subjected to Radiative Heating", XIV Symposium (International) on Combustion, pp. 1297-1307, 1973.

36. De Luca, L., Caveny, L.H., Ohlemiller, T.J., Summerfield, M. "Radiative Ignition of Double Base Propellants: II. Preignition Events and Source Effects", AIAA Journal, Vol. 14, No. 8, pp. 1111-1117, 1976.

37. Khlevnoi, S.S. "Quenching of Explosives Following Interruption of the Igniting Light Flux", FGV, Vol. 7, No. 2, pp. 178-188, 1971.

38. Mikheev, V.F., Levashov, Yu.V. "Experimental Study of Critical Conditions During the Ignition and Combustion of Powder", FGV, Vol. 9, No. 4, pp. 506-510, 1973.

39. Assovskii, I.G. "Transient Combustion of Powder Subjected to Intense Light", FGV, Vol. 9, No. 6, pp. 874-883, 1973.

40. Gostintsev, Yu.A. "Extinction of a Steady-State Burning Powder by a Pulse of Thermal Radiation", FGV, Vol. 10, No. 5, pp. 764-767, 1974.

41. Goodman, T.R. "Application of Integral Methods to Transient Nonlinear Heat Transfer", Advances in Heat Transfer, Vol. 1, Academic Press, pp. 51-122, 1964.

42. Peters, N. "Theory of Heterogeneous Combustion Instabilities of Spherical Particles", XV Symposium (International) on Combustion, pp. 363-375, 1975.

43. Kuo, K.K., "Theory of Flame Front Propagation in Porous Propellant Charges under Confinement", Ph.D. Thesis, Princeton University, 1971.

44. Peretz, A., Caveny, L.H., Kuo, K.K., Summerfield, M. "The Starting Transient of Solid Propellant Rocket Motors with High Internal Gas Velocities", Princeton University, AMS Report No. 1100, 1973.

45. Gostintsev, Ya.A. "Method of Reduction to Ordinary Differential Equations in Problems of the Nonstationary Burning of Solid Propellants", FGV, Vol.3, No.3, pp.355-361, 1967.

46. Niioka, T., and Williams, F.A. "Relationship between Theory and Experiment for Radiant Ignition of Solids", XVII Symposium (International) on Combustion, Leeds (England), 20-25 August 1978.

47. Kuo, K.K., Coates, G.R. "Review of Dynamic Burning of Solid Propellants in Gun and Rocket Propulsion Systems", XVI (International) Symposium on Combustion, pp.1177-1192, 1977.

48. De Luca, L. "Self-Sustained Oscillatory Combustion of Solid Rocket Propellants", The Propulsion and Energetics Panel of AGARD, 53rd Meeting, Symposium on Solid Rocket Motor Technology, Oslo (Norway), 2-5 April 1979.

ACKNOWLEDGEMENTS

Project jointly supported by European Research Office and Centro di Studio per Ricerche sulla Propulsione e sulla Energetica under Grant Agreement No. DAERO 78-G-029.

TABLE 1

Definition of nondimensional variables

$\mathcal{P} = P/P_{ref}$		pressure
$\mathcal{R} = R/R_{ref}$		burning rate
$X = x/x_{ref}$		distance
$\tau = t/t_{ref}$		time
$H = Q_s/Q_{ref}$		surface heat release
$Q = Q_f/Q_{ref}$		gas heat release
$F_o = I_o/I_{ref}$		external radiant flux intensity
$\dot{q} = \dot{q}/I_{ref}$		conductive heat flux
$T = T_{(\ )}/T_{(\ ),ref}$		temperature, e.g. $T_f = T_f/T_{f,ref}$
$\theta_{(\ )} = \frac{T_{(\ )} - T_{ref}}{T_{s,ref} - T_{ref}}$		temperature, e.g. $\theta_s = \frac{T_s - T_{ref}}{T_{s,ref} - T_{ref}}$

TABLE 2

Properties of solid composite propellant AP/PBAA
No. 941 used as datum case in this study

ASSUMED OR MEASURED PROPERTIES		
Crystalline transition heat, Q_{cr}	+ 2.000 E+01	cal/g of AP (+endoth.)
AP vaporization heat, $Q_{v,AP}$	+ 5.260 E+02	cal/g of AP
AP decomposition heat, $Q_{A/PA}$	- 8.000 E+02	cal/g of AP
Binder vaporization heat, $Q_{v,B}$	+ 2.250 E+02	cal/g of binder
AP content, p	+ 8.000 E+01	%
Ballistic exponent, n	+ 4.600 E-01	
KTSS pyrolysis law power, w	+ 6.000 E+00	
Surface activation energy, E_s	+ 1.600 E+04	cal/gmole
Flame activation energy, E_f	+ 2.000 E+04	cal/gmole
Condensed phase density, ρ_c	+ 1.540 E+00	g/cm^3
Condensed phase specific heat, C_c	+ 3.300 E-01	cal/g-K
Condensed phase thermal diffusivity, α_c	+ 1.400 E-03	cm^2/s
Gas phase specific heat, C_g	+ 3.300 E-01	cal/g-K
Gas phase thermal conductivity, λ_g	+ 1.000 E-04	cal/cm-K-s
Average products molecular weight, $\bar{m}$	+ 2.600 E+01	g/gmole
Reflectivity of propellant surface, r	+ 0.000 E+00	%
Optical scattering coefficient, s	+ 0.000 E+00	%
Minimum surface temp. for reactions, T_m	+ 3.000 E+02	K
Matching surface temp. for pyrolysis, T_k	+ 4.050 E+02	K
EVALUATED PROPERTIES		
Cond. phase thermal conductivity, λ_c	+ 7.120 E-04	cal/cm-K-s
Refer. frequency factor, $A_{s,ref}$	+ 2.705 E+03	cm/s
Surface gasification heat, Q_s	- 1.582 E+02	cal/g
Chemical time constant, A_M	+ 3.380 E-01	
Diffusion time constant, B_M	+ 2.350 E+00	
Adiabatic flame temperature, $T_f(P)$	+ $T_{f,ref}$ - (50/68)·(P_{ref} - P)	
REFERENCE PROPERTIES		
Pressure, P_{ref}	+ 6.800 E+01	atm
Temperature, T_{ref}	+ 3.000 E+02	K
Burning Rate, $R_{ref} = R(P_{ref})$	+ 8.370 E-01	cm/s
Surface temperature, $T_{s,ref} = T_s(P_{ref})$	+ 1.000 E+03	K
Flame temperature, $T_{f,ref} = T_f(P_{ref})$	+ 2.430 E+03	K
Distance, $x_{ref} = \alpha_c/R_{ref}$	+ 1.673 E-03	cm
Time, $t_{ref} = \alpha_c/R^2_{ref}$	+ 1.998 E-03	s
Heat, $Q_{ref} = C_c(T_{s,ref} - T_{ref})$	+ 2.310 E+02	cal/g
Energy flux, $I_{ref} = \rho_c C_c R_{ref}(T_{s,ref} - T_{ref})$	+ 2.978 E+02	cal/cm^2-s

TABLE 3

Surface temperature and burning rate associated with roots A and B in the pressure range 10 to 60 atm. Root A (steady reacting solution) is indipendent on the order of the approximating polynomial, while root B (unsteady reacting solution) does depend. Nonlinear static restoring function evaluated for standard conditions (T_a=300K,Q_s= - 158.2 cal/g, adiabatic burning).

Pressure	MTS flame						KTSS nonlin. flame			
P,atm	θ_s(A)	$\Re$(A)	θ_s(B)	$\Re$(B)	θ_s(B)	$\Re$(B)	θ_s(A)	$\Re$(A)	θ_s(B)	$\Re$(B)
			n = 2		n = 3				n = 3	
10	0.860	0.415	0.667	0.084	0.618	0.052	0.866	0.414	0.571	0.035
20	0.909	0.575	0.691	0.107	0.646	0.070	0.910	0.570	0.610	0.051
30	0.937	0.687	0.709	0.126	0.663	0.083	0.939	0.686	0.633	0.065
40	0.957	0.775	0.719	0.138	0.674	0.093	0.960	0.783	0.651	0.076
50	0.972	0.849	0.729	0.151	0.684	0.101	0.977	0.868	0.664	0.086
60	0.984	0.913	0.737	0.161	0.692	0.108	0.990	0.944	0.675	0.095

TABLE 4

Computer simulated go/no-go transient tests showing agreement with the predicted lower dynamic boundary and strong dependence of dynamic extinction on the initial conditions. All runs performed for adiabatic strands with T_a = 300 K and Q_s = - 158.2 cal/g.

Pressure (*) P,atm	Forcing Law	B_p or B_r	Flame Model	Observed dynamic limit $\Re$	Observed dynamic limit θ_s	Predicted dynamic limit (n = 3) $\Re$	Predicted dynamic limit (n = 3) θ_s
10	linear deradiation,opaque	100	MTS	0.058	0.627	0.052	0.618
10	bilinear derad., opaque	100/20	MTS	0.057	0.626	0.052	0.618
10	parabolic derad.,opaque	640	MTS	0.056	0.625	0.052	0.618
10	exponential derad.,opaque	5	MTS	0.058	0.627	0.052	0.618
10	exponential derad.,opaque	10	MTS	0.053	0.619	0.052	0.618
10	exponential derad., a = 2000 cm^{-1}	10	MTS	0.048	0.610	0.052	0.618
10	exponential derad., a = 1000 cm^{-1}	10	MTS	0.052	0.618	0.052	0.618
10	exponential derad., a = 500 cm^{-1}	10	MTS	0.053	0.620	0.052	0.618
10	exponential depress.	10	MTS	0.051	0.615	0.052	0.618
10	exponential depress.	3.336	MTS	0.054	0.621	0.052	0.618
20	linear deradiation,opaque	200	MTS	0.076	0.655	0.071	0.647
20	exponential derad.,opaque	10	MTS	0.072	0.649	0.071	0.647
20	exponential derad.,opaque	10	KTSS nonlin.	0.070	0.642	0.051	0.610
20	linear deradiation, a = 2000 cm^{-1}	500	MTS	0.080	0.660	0.071	0.647
30	exponential derad.opaque	10	MTS	0.102	0.685	0.083	0.663
40	exponential derad.,opaque	10	MTS	0.123	0.706	0.093	0.674

(*) final pressure in the case of depressurization transients.

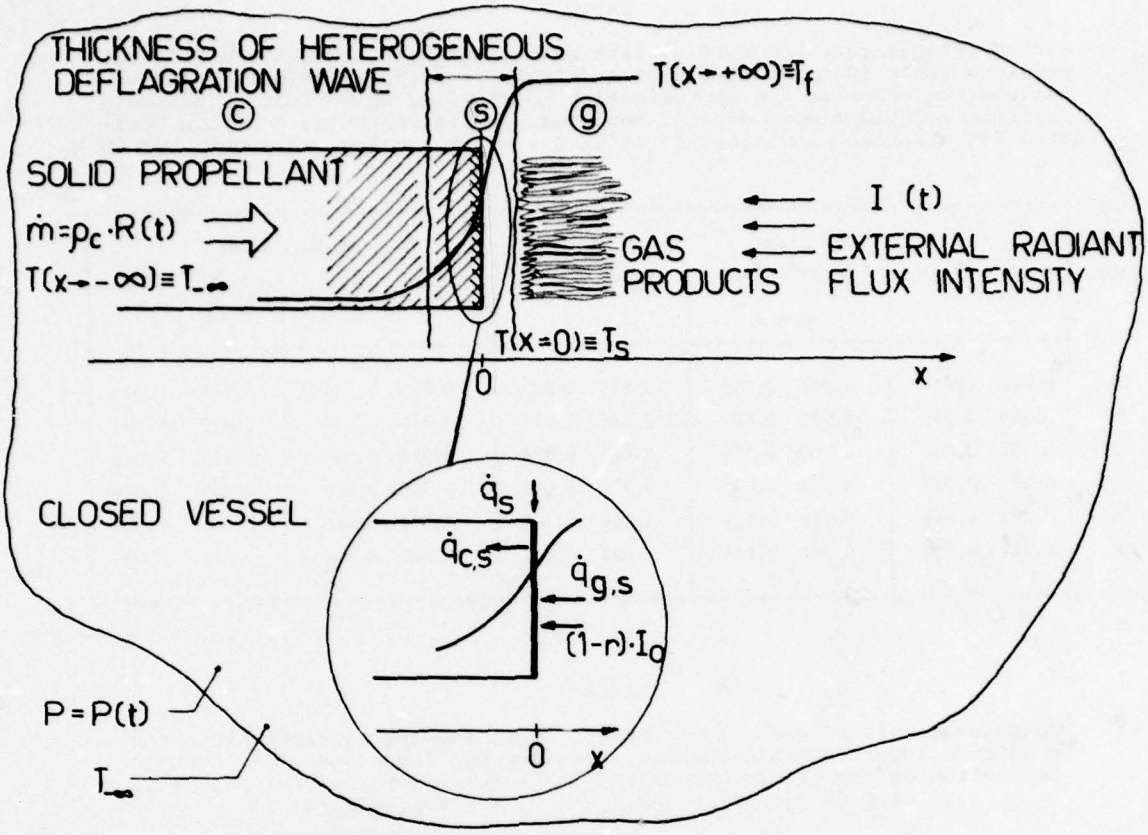

Fig. 1a - Schematic diagram of the physical problem.
1b - Schematic diagram of energy balance at the surface.

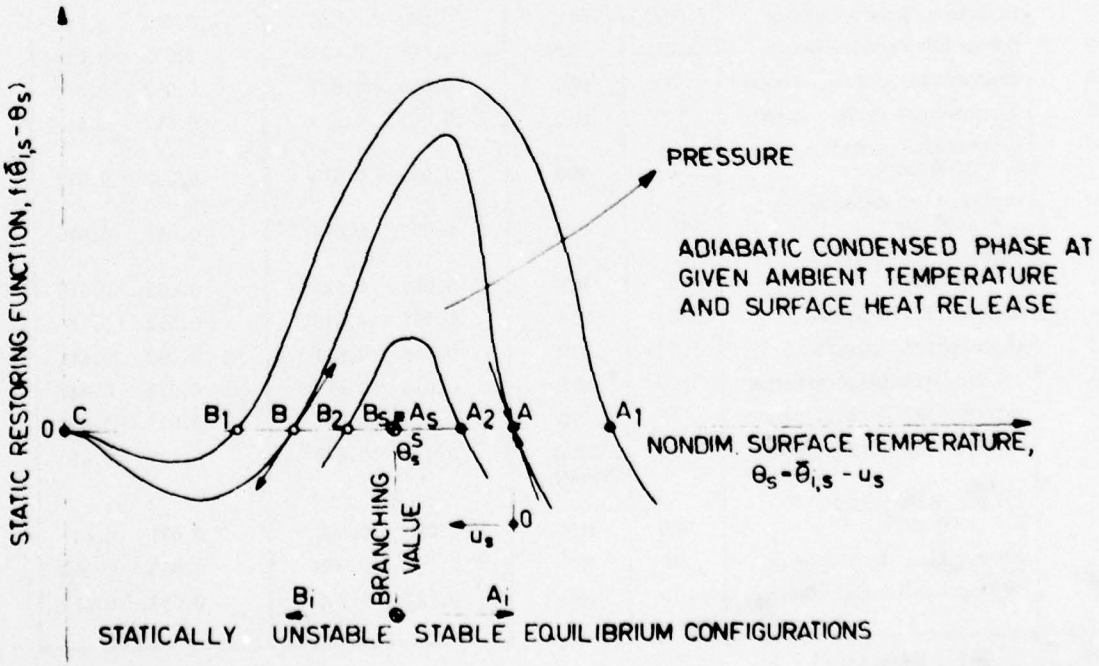

Fig. 2 - Qualitative skectch of the static restoring function, for different pressure values, illustrating the existence of three equilibrium configurations: A_i and B_i (for the reacting mode), C (for the unreacting mode). Roots B_i are statically unstable. MTS and KTSS nonlinearized flames.

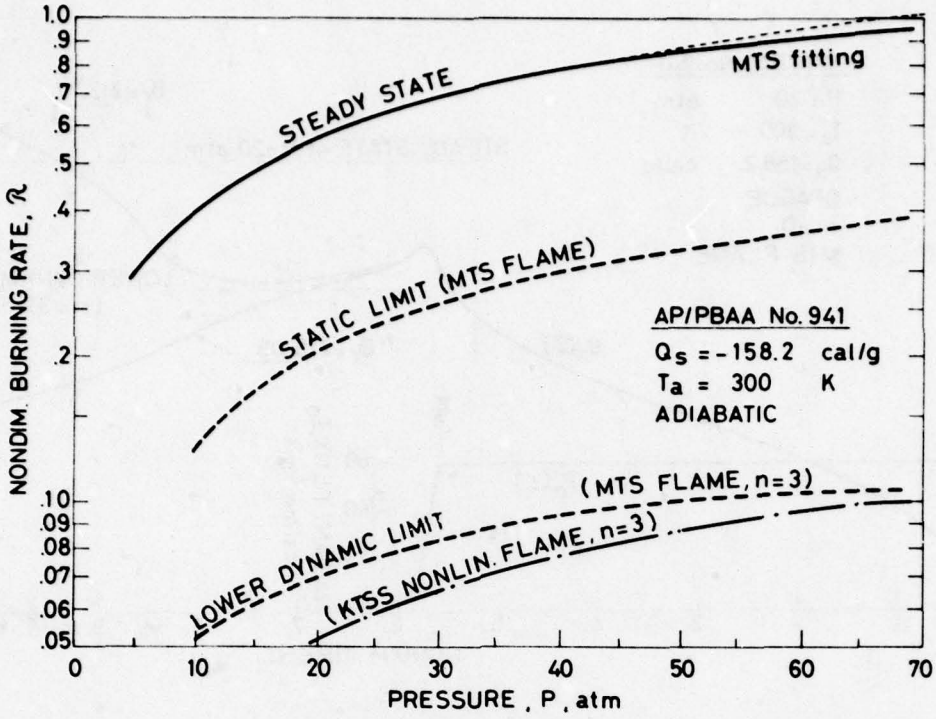

Fig. 3 - Static and dynamic (n = 3) stability boundaries on a burning rate vs pressure plot. MTS and KTSS nonlinearized flames.

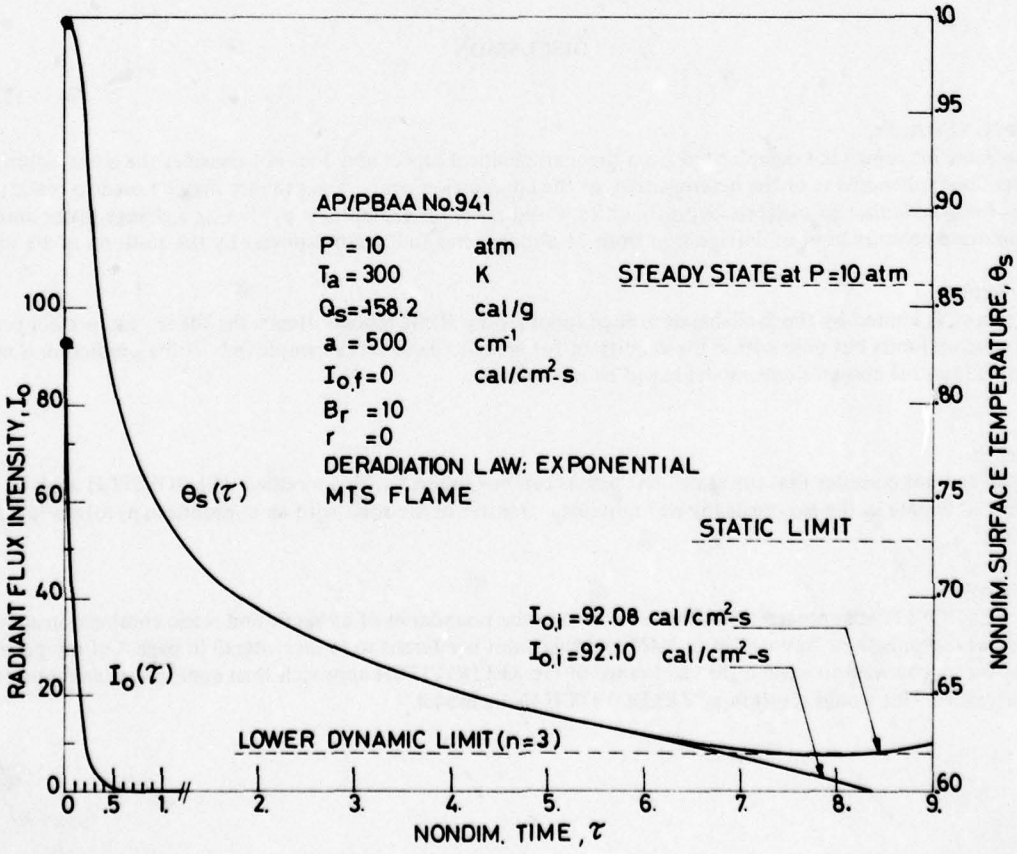

Fig. 4 - Dynamic extinction following exponential deradiation, at 10 atm of pressure, of a solid propellant with transparent condensed phase.

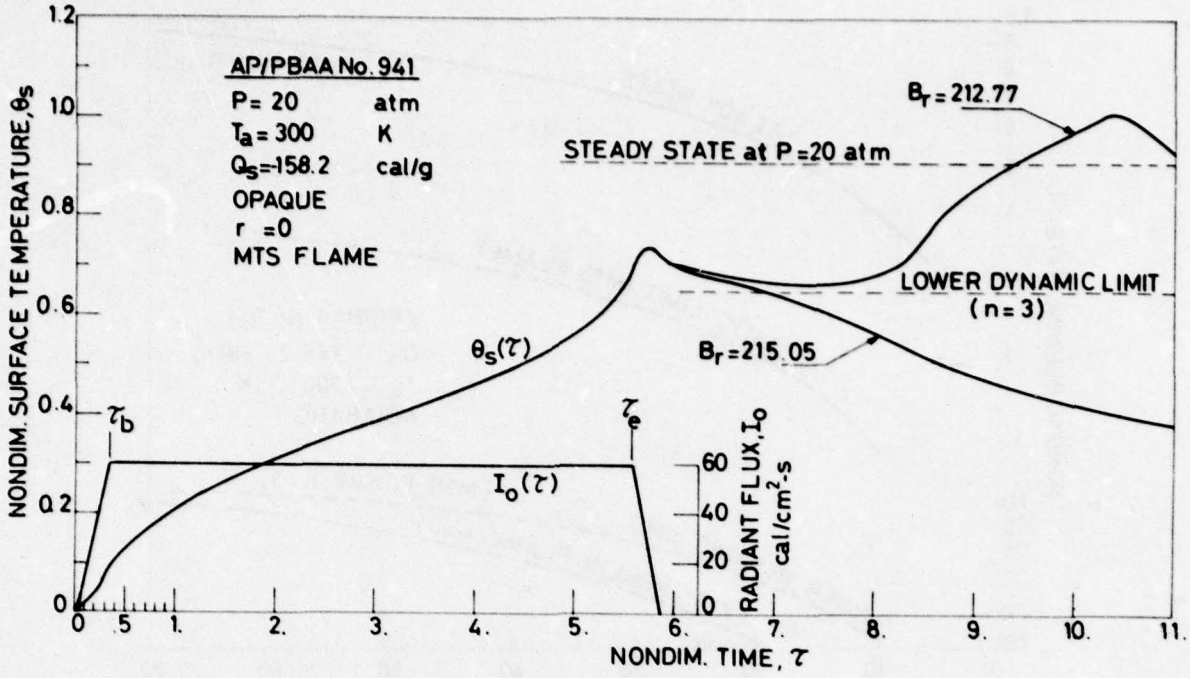

Fig. 5 - Radiative ignition transients, at 20 atm of pressure, of a solid propellant with opaque condensed phase showing occurrence of dynamic extinction.

DISCUSSION

M.Barrere, ONERA, Fr

Your model is somewhat complicated from the mathematical aspect and does not consider the combustion as a three dimensional phenomena or the heterogeneity of the combustion zone. Your theory may be used to make predictions for double base propellants but difficulties would arise, for example, in predicting a change in the ammonium perchlorate pressure limit of deflagration from 21 atmospheres to 0.5 atmospheres by the addition of 1% catalyst.

Author's Reply

My theory is limited by the available or utilised quasi steady flame model. Hence the theory can predict pressure deflagration limits but only within the validity of the specific flame model employed. If the prediction is not verified then the chosen flame model has to be rejected.

M.Barrere, Fr

Would you not consider that the same conclusions can be obtained with a modfied ZELDOVITCH analysis using steady state data in the gas, unsteady and non-linear transfer in the solid with an appropriate pyrolysis law at the surface?

Author's Reply

The ZELDOVITCH approach is unable to discrimate the boundaries of dynamic and static combustion stability. This was recognised by Novozhilov in 1973 and this point is referred to in more detail in page 2 of my paper. However, if you wish to extend the valid range of the ZELDOVITCH approach then appropriate assumptions have to be made. This would result in a "ZELDOVITCH flame model."

SOLID PROPELLANT SPECIFIC IMPULSE PREDICTION

by
Ellis M. Landsbaum and Manuel P. Salinas
The Aerospace Corporation
2350 E. El Segundo Blvd.
El Segundo, California 90245

ABSTRACT

The methods for the theoretical prediction of delivered specific impulse are relatively well-known. They involve computing the losses due to two-phase flow, divergence, boundary layer, kinetics, nozzle submergence and combustion efficiency. The largest computed loss in typical aluminized solid propellants is the two-phase flow loss; this computation also has the largest uncertainty because the particle size and distribution are not known precisely. In this paper, a correlation of mean particle diameter versus throat diameter from experimental data was used with the solid rocket performance prediction program (SPP) to predict the propellant specific impulse of a number of motors. These predictions are compared to the experimental values. The results indicate that the specific impulse efficiency appears to be an inherent property of the propellant. In addition, the experimental specific impulse and specific impulse efficiency were statistically correlated against throat diameter and expansion ratio for propellants of similar oxidizer and aluminum content. These correlations are as accurate as the longer, more expensive, theoretical analysis. In addition to specific impulse prediction, the equations are useful in optimization of motor design.

NOMENCLATURE

AP	Ammonium perchlorate
Al	Aluminum
ASUB	Inlet area ratio
c^*	Characteristic velocity, ft/sec
D_t	Throat diameter, in.
D_p	Particle diameter, μm
F	Thrust, lb
I_{sp}	Specific impulse, sec
L^*	Characteristic length, in.
L_n	Nozzle length, throat to exit, in.
P	Pressure, psi
r	Radius
R_d	Radius of curvature, downstream, nondimensional (R/R_t)
R_t	Throat radius, in.
R_u	Radius of curvature, upstream, nondimensional (R/R_t)
R	Correlation coefficient
S	Submergence fraction
TBL	Turbulent boundary layer, Eq. (7)
U	Velocity
$\dot{w}$	Weight flow, lb/sec
δ^*	Displacement thickness
ϵ	Expansion ratio
η	Efficiency
θ	Momentum thickness
θ_i	Initial divergence angle, deg
θ_e	Exit angle, deg
ξ	Condensed phase, moles/100 gm
ρ	Gas density

Subscripts

c	Combustion
d	Delivered
k	Kinetic
o	Overall, measured
s	Submergence
2D2ϕ	Two-dimensional two-phase

Superscript

o	Ideal

INTRODUCTION

It is highly desirable to be able to accurately predict the delivered specific impulse of solid propellants in rocket motors. This would assist in preventing unduly optimistic or conservative motor designs, in selecting solid propellants, in determining optimum motor parameters, and in selecting competing designs or alternatives. The methodology of solid rocket motor performance prediction is relatively well-known; Cohen, et al. (Ref. 1) recently made an excellent review of the subject and assessed the accuracy of the predictions. In addition to specific impulse, he also considered ignition transients, peak pressures, tail-off, extinguishment, and the prediction of pressure-time traces. This paper will discuss only the prediction of delivered specific impulse.

Although there have been a large number of papers concerned with methodology, discussion of loss mechanisms, development of equations and computer program, and the experimental determination of necessary data such as particle size, kinetic rates, drag coefficients, and heat transfer coefficients, there have been very few papers that have compared experimental specific impulse measurements to analytical predictions. The first paper on that subject appears to be that of Kliegel and Nickerson (Ref. 2), who utilized the first program developed to calculate two-phase flow losses. The analysis estimated boundary layer and divergence losses, and was compared to experimental measurements on test motors designed to determine the adequacy of the analysis. The results were good. Additional studies comparing the predicted and experimental specific impulse have only appeared recently (Refs. 3 through 6). The predictive capability of these later studies is excellent with a maximum error of 0.6 percent. The motors analyzed were primarily small test motors containing double-base propellants with four full-scale motors analyzed (Ref. 4). Composite propellants were studied in small test motors (Ref. 5) with low expansion ratios (< 10). Unfortunately, the programs utilized are not generally available. It is not clear how applicable Daines' (Ref. 4) technique is to the range of composite propellants, motor and nozzle designs found in space motors--a large class of motors of considerable importance. A space motor is usually a motor of medium pressure, long burn time, and high expansion ratio. One study (Ref. 7) has utilized empirical prediction techniques for these motors.

This study had two objectives, the first being to determine how well one could predict specific impulse, a priori. The second and more important objective was to determine how well one might predict motor performance if a limited amount of data were available on a motor of similar size or a near-identical motor with a different expansion ratio. These data are usually available because the conservatism of space systems usually dictates the use of proven technology. This study was to be accomplished by predicting the performance of a large sample of space motors for which the necessary information was available. The mechanics of the study were minimized by the availability of SPP--a solid performance prediction program recently developed under sponsorship of the Air Force Rocket Propulsion Laboratory (Ref. 8). The following section gives a brief description of SPP. In subsequent sections, the motors are described and the results of the analysis presented. The experimental data is analyzed with a multivariable regression analysis, and equations giving delivered specific impulse and overall motor efficiency as a function of motor and propellant parameters are presented.

DESCRIPTION OF SPP

A solid rocket motor performance prediction program (SPP) was developed under Air Force Rocket Propulsion Laboratory sponsorship (Ref. 8). SPP predicts delivered specific impulse based on the ideal value of specific impulse and losses in specific impulse due to the effects of two-phase flow, divergence, kinetics, boundary layer, submergence, and inefficient combustion. The program also has a general three-dimensional grain design capability and can predict mass flow, pressure and thrust as a function of time, given the appropriate grain and motor dimensions and propellant ballistic properties. This portion of the program will not be further discussed. A brief description of the specific impulse prediction portion of the program will be offered to enable a better understanding and evaluation of the results to be presented later.

The delivered specific impulse is calculated using the following equation:

$$I_{spd} = I^{o}_{sp}\, \eta_{2D2\phi} \eta_k \eta_s \eta_c - \Delta TBL \qquad (1)$$

The terms are defined in the nomenclature. The I^o_{sp} is the ideal vacuum specific impulse (ODE, one-dimensional equilibrium) calculated purely from thermodynamic data assuming one-dimensional flow, chemical equilibrium between species and phases, thermal and velocity equilibrium between condensed gaseous phases and adiabatic isentropic flow. The program contains routines (subprograms) to calculate each of the efficiencies or losses in Eq. (1). Each of these routines will be described below.

The two-phase, two-dimensional flow routine calculates combined two-phase and divergence efficiency ($\eta_{2D2\phi}$), and is based on the following assumptions and restrictions. The gas is an ideal gas with constant specific heats in the liquid and solid phase. Energy exchange between gas and particles occurs only by convection, and the only forces on the particles are viscous drag forces. The particle volume is negligible, and the internal temperature is uniform. The heat of condensation is accounted for. As many as nine particle groups of different diameters and weight fractions can be entered. The nozzle convergent section must be conical and less than 45 deg. The upstream and downstream radius of curvature at the throat can be different, but must be greater than 0.5 (normalized to the throat radii). There are five options for the exit cone: conical, parabolic, circular arc, and either a spline fit or straight tabular input. This routine calculates a two-dimensional, two-phase specific impulse, $I_{sp}(2D2\phi)$. It also calculates an ideal specific impulse, $I^o_{sp}(2D2\phi, R.E.)$, using the same assumptions as in the ODE with the added restrictions of the two-dimensional, two-phase program. The two-dimensional, two-phase efficiency is then calculated from the following equation:

$$\eta_{2D2\phi} = I_{sp}(2D2\phi) \Big/ I^o_{sp}(2D2\phi, R.E.) \tag{2}$$

This efficiency contains both the two-phase and divergence losses, and no attempt is made to separate them.

The kinetic efficiency (η_k) can be determined either by calculation or with an empirical equation. Both methods are described below. The kinetic loss calculation is one-dimensional. The same assumptions are made about the particles (condensed phase) as in the two-dimensional, two-phase portion of the program. Additionally, it is assumed that the particles are in thermal and velocity equilibrium with the gas. The gas can have a maximum of 150 distinct chemical reactions and 40 individual species. The maximum suggested for the C, H, O, N, Cl, Al system is 28 species and 73 reactions. Each reaction and the kinetic data must be input to the program so, typically, far less reactions are used. The program calculates a specific impulse, $I_{sp}(k)$, allowing for the effects of the kinetic reactions. It also calculates an ideal specific impulse, $I^o_{sp}(k, R.E.)$, using the assumptions of ODE and the additional assumptions about particle equilibrium used in the kinetic calculation. The gas species are allowed to vary according to equilibrium requirements, so one should input sufficient information to cover the major species and reactions. The specific impulse efficiency is then calculated from the ratio of these two specific impulses as follows:

$$\eta_k = I_{sp}(k) \Big/ I^o_{sp}(k, R.E.) \tag{3}$$

The results to be discussed later did not determine a kinetic efficiency by calculation but, instead, used the empirical formula. The empirical loss is based on the difference between frozen composition (ODF) and equilibrium specific impulse with a pressure correction. The equation is

$$\eta_k = 1 - 0.333 \left[1 - \frac{I^o_{sp}\,(ODF)}{I^o_{sp}\,(ODE)} \right] \frac{200}{P}, \quad P \geq 200 \tag{4}$$

Later, the differences between calculated and empirical kinetic efficiencies will be discussed.

A semiempirical equation for submergence loss is provided within SPP. The equation is

$$\eta_s = 1 - 0.000684 [P\xi / ASUB]^{0.8} S^{0.4} D_t^{-0.2} \tag{5}$$

A complex empirical equation for combustion efficiency as a function of propellant composition and burn rate is provided. The calculations described herein assumed 100 percent combustion efficiency; therefore, the efficiency function is not presented. It is probably better to base an estimate of the combustion efficiency on experimental information or experience, if available, than to use that provided by SPP which, in addition to its complexity, may not be particularly accurate.

The boundary layer loss (ΔTBL) is calculated from the turbulent boundary layer (TBL) routine. This is an integral method that uses the boundary layer edge conditions from the two-dimensional, two-phase flow program. Although it is considered inaccurate for heat transfer calculations, particularly at the throat region, it appears to be sufficiently accurate for the thrust loss calculation considering the small loss. The thrust loss is determined from the momentum deficit in the boundary layer at the nozzle exit plane from the following:

$$\Delta F_{BL} = 2\pi r \rho U^2 \theta \cos\theta_e \left[1 - \frac{\delta^* P}{\theta \rho U^2} \right] \tag{6}$$

Specific impulse losses are determined by dividing the thrust loss by the mass flow from the two-dimensional, two-phase routine.

$$\Delta TBL = \Delta F_{BL}/\dot{w}_{2D2\phi} \tag{7}$$

MOTOR DATA AND ANALYSIS METHOD

Sufficient information was obtained from motor manufacturers to allow the analysis of the 30 motors listed in Table I. The motors are numbered to allow easy comparison with the results given in Table II and for ease of discussion. The propellant information indicates the type of binder and weight percent of ammonium perchlorate and aluminum, while the nozzle type shows whether it is conical, parabolic, (circular) arc, or wall, indicating that a wall table was used for some other type of contour. ASUB is the ratio of the inlet nozzle area to the initial throat area. The inlet area was based on the nose of the convergent section of the nozzle; analysis shows that large changes in this value only affect the submergence efficiency. The radii of curvature at the throat are those for the initial contour. The initial deflection angle downstream of the throat is θ_i, while θ_e is the exit angle determined by the routine and is discussed below. Nozzle length is the initial nozzle length from throat to exit plane, submergence is the submerged length of the nozzle divided by the grain length, and throat diameter is the average of the initial and final throat diameters. The average expansion ratio is based on the initial exit area and the throat area calculated from the average throat diameter. The average pressure is that over web burn when there is a sharp tail-off. If there is no obvious web burnout, then the average pressure over action time is given. Action time is the time between pressures that are ten percent of maximum chamber pressure.

Using the initial radius of curvature (R_d) with the average throat radius results in slight differences between the analyzed and original nozzle contours. The conical nozzles analyzed become slightly shorter than the original. The nozzle length of the circular arc and parabolic contours was fixed, as was θ_i; the result is a slightly smaller exit angle than the original contour. The nozzles with tabulated wall contours had to be adjusted slightly to allow a smooth transition from the circular arc to the contour. These slight alterations in contour should have a negligible effect on the calculated specific impulse. This was considered preferable to using the initial contour and trying to correct the calculated specific impulse for the change in expansion ratio and also for the effect of the change in throat diameter on the particle size.

This analysis used a mean particle diameter that was a function of throat diameter only, as shown in Fig. 1. This is the result of some early work of Delaney on the measurement of mean particle diameters. His final correlation (Ref. 9) is also shown in the figure. The earlier correlation was used because of previous analyses that indicated its use in the predecessor programs to SPP gave predicted specific impulses that agreed rather well with experimental values for a number of motors. The correlation in the SPP is also shown in Fig. 1, and the equation is given below:

$$D_p = 0.454\, P^{1/3} \xi^{1/3} [1 - \exp(0.0004 L^*)] (1 + 0.045\, D_t) \tag{8}$$

This correlation was not used because of the smaller particle size it predicts. Only a single particle size was used, as analyses have indicated that there is a negligible effect of using multiple particle sizes. Multiple particle sizes are primarily of interest in studying possible impingement. A particle density of 168 lb/ft^3 (2.69 g/cm^3) was used, equivalent to a temperature of 4600°R (2556°K). With single particles, very few of the particles ever solidify, and this is a representative particle density. Some interaction between the particle density and particle size on the results of the calculation is recognized. An inlet angle of 30 deg was used which will normally not result in impingement with SPP. Therefore, impingement losses were not considered.

ANALYSIS RESULTS AND DISCUSSION

The results of the analysis are presented in Table II. The theoretical (ODE) vacuum specific impulse, I^o_{sp}, was calculated under the conditions ($\bar{\epsilon}$, $\bar{P}$) given in Table I. This calculation is made at a propellant temperature of 25°C. The delivered specific impulse is the experimental measurement made at simulated altitude conditions and corrected to vacuum conditions, and is the total impulse delivered by the motor divided by the loaded propellant weight. The data are reported at a variety of propellant temperatures near ambient. The correction for temperature is so small, approximately 0.015 sec/°F, that it can be neglected. The predicted specific impulse is calculated as previously described. The error in the prediction, ΔI_{sp} (predicted specific impulse minus delivered specific impulse) is given. The overall efficiency (η_o) is delivered specific impulse divided by the theoretical one-dimensional value. The remaining columns are the efficiencies and boundary layer loss calculated by the program.

A plot of the predicted versus delivered specific impulse is shown in Fig. 2. It will be noted immediately that one tends to overpredict the specific impulse. A gross underprediction is made for the Hercules' motors with double-base propellant. If average values for the nozzles of these motors had been available instead of the initial conditions used, the errors would have been larger. Most of the ensuing discussion will neglect these two motors because they contain double-base propellants, and their experimental results ($I_{sp\ del}$, η_o) are statistically different from the other motors containing composite propellants.

The average error (ΔI_{sp}) for the 28 composite propellant motors in Table II is 1.1 sec. The standard deviation is 2.3 sec--undesirably high. Possible causes of the error will be discussed later. These results are clearly less accurate than desirable. There is another question that requires examination. Given firing data, how well can one predict the performance of a higher expansion ratio nozzle or

of a similar motor from the same family? In these cases, the analysis provides much better results. Compare motor 27 with 28 and motor 12 with 13, where identical motors were fired with different expansion ratios. Given the results of the firing of the low expansion ratio motor and applying the bias between the predicted and experimental values of specific impulse for that motor to the prediction of the high expansion ratio motor, very accurate results are obtained. Thus, given the results of motor 12, one would have predicted motor 13 within 0.1 sec and, given the results of motor 27, one would have predicted motor 28 within 0.3 sec. The results for the Minuteman motors with extendable exit cones (EEC) are less accurate. However, cones were not extended over the full duration of the firings, and there were some minor problems with the cones that may have reduced the specific impulse slightly. Therefore, this procedure can be considered to be very accurate.

Noting how similar the biases are for similar motors, one finds relatively good agreement. Thus, motors 4 and 5 are similar, as are motors 15, 16 and 18 and motors 20, 21 and 22; within each group biases are quite similar. The worst spread of biases within each group is 2 sec. This would indicate that with data from one motor, one should be able to predict a similar motor within 2 sec. A larger view may also be taken of the group of motors, and one finds that the Thiokol CTPB propellant motors are grouped closely as are the UT-CSD PBAN motors. The Aerojet motors can be divided into two groups--low and high pressure motors, and each group has a relatively small spread in bias. It thus appears that, given data for a single motor, one can predict similar motors within approximately 2 sec.

A limited number of kinetic efficiencies were calculated to compare with the empirical values [Eq. (4)]. They only included 11 gaseous species (H, OH, H_2O, O, O_2, H_2, CO_2, CO, N, N_2, NO), eight recombination reactions and 15 binary exchange reactions. This limited analysis indicates that the empirical kinetic equation underestimated the loss at the higher pressures (greater than 300 psi) by approximately 0.5 percent. It also appears that a better pressure correlation in Eq. (4) would be 300/P, rather than 200/P. The boundary layer routine was run with an adiabatic wall. If a colder wall had been used, representative of the nozzle temperature, the boundary layer loss would have increased slightly. These corrections would reduce the bias from 1.1 sec to approximately -1 sec. Impingement was not considered in the analysis but, reportedly, all of the motors have negligible impingement except for motor 14 for which a preliminary estimate is that the loss due to the impingement is approximately only 1 sec.

It is unlikely that the errors in the specific impulse predictions are due to errors in the submergence, kinetics or boundary layer losses as the motors and propellants are too similar to allow much variation in these losses. The errors must be due to the assumption of 100 percent combustion efficiency or to the particle correlation used. A measure of combustion efficiency would be the c^* efficiency. Although specific impulse measurements are readily available, c^* measurements are not typically reported. An attempt will be made to obtain this information to see if the accuracy of the prediction is improved. The introduction of a pressure term into the particle size correlation, such as in Eq. (8), would probably improve the analysis. This is best illustrated by considering the Aerojet space motors where introduction of particle size as a function of pressure would reduce the error between the low-pressure and high-pressure motors. The particle size may also be dependent upon the propellant properties, as evidenced by the high efficiency of the Hercules' double-base motors. Motors 11 and 24, identical except for the propellants, and with a difference in efficiency of 0.6 percent, may also be compared. However, motor 24 has had only a single altitude firing. The only method for predicting particle size other than the correlation discussed herein is the method of Bartlett and Delaney (Ref. 10) utilized by Daines (Ref. 4). We have not yet tried this technique. It is doubtful that this technique would result in sufficiently different particle sizes, given the similarity of the propellants and the limitation of the program to conical inlets. The particle size may be a complex function of propellant properties and motor conditions not readily identified. Inclusion of measured c^* efficiencies in the analysis may indicate the extent to which particle size prediction is in error.

STATISTICAL ANALYSIS

The experimental data in the motors containing composite propellants were statistically analyzed with a multivariable least squares regression analysis to determine if useful correlations for preliminary estimates or optimization programs could be developed. The equations used and the results obtained are given in Table III. Note some minor changes in the nomenclature at the bottom of the table. The angle used in the divergence efficiency was previously used by Kirschner (Ref. 7). This type of equation was used because earlier studies of two-phase flow with the one-dimensional analysis showed these losses could be correlated by an equation of this form. The submergence was entered as $1 - S$ to prevent mathematical difficulties with zero submergence. Motor 19 was eliminated on some analyses because it was a large outlier in the efficiency correlation. Motor 19 contains the only propellant with substantial iron oxide, has the lowest expansion ratio of any of the motors, and had only one test firing.

The correlations of delivered specific impulse appear suitable for preliminary estimates with an error (1σ) of approximately 2.0 sec (0.70 percent), depending on which equation is used. The correlation coefficient R is > 0.9, indicating the validity of the correlation. The choice of equation should depend on the regime of expansion ratios being considered. The coefficients of the equations were examined with a student "t" test to determine the probability of accepting the hypothesis that the coefficients are equal to zero. The analysis was then repeated, eliminating those variables where there was a probability greater than five percent that the coefficients could be zero. This eliminated most of the variables and did not change the error (σ). The implications of this result are discussed below.

A better correlation of specific impulse could probably be developed by including variables for binder weight percent and type. However, since ideal values (ODE) of specific impulse are relatively easy to calculate, it appears to be more desirable to consider overall efficiency. The results of correlating overall efficiency (η_o) are presented in Table III, with and without motor 19, and, as previously discussed, with some variables eliminated. Eliminating motor 19 reduces σ in the efficiency correlation, although it did not do so in the specific impulse correlation. The error (1σ) without motor 19 has been reduced to 0.38 percent, a very acceptable figure. The statistical analysis reduces the error by more

than 50 percent since otherwise the variation (1σ) in η_o is 1.04 percent. The mean of η_o is 0.9172. Statistical analysis of efficiency resulted in a smaller error in prediction than the more exact calculation which had 1σ error of 2.1 sec (0.72 percent). The developed equations are admirably suited for preliminary analysis and optimization studies.

The elimination of pressure as a significant variable does not agree with previous comments on its probable effect on particle size. In a real motor, the increase in particle size due to pressure may be compensated for by the increasing drag. The effect may be more apparent in the calculation than in the motor. The low significance of submergence losses suggested that the analytical treatment and the experiments upon which the analysis was based should be thoroughly reviewed. Programs capable of analyzing subsonic, two-phase flow with submerged nozzles are presently being developed. Depending upon the results of the analysis, further experimental studies may be desirable to investigate the effects of submergence.

SUMMARY

Data were obtained on a large number of space motors, and delivered specific impulse predictions were made and compared to the experimental values. The calculations were made with the recently developed computer program, SPP. The error was not as small as would be desirable. The result was an average bias of 1.1 sec and a standard deviation of 2.1 sec. Prediction of specific impulse of a motor from experimental data on a similar motor is more accurate. The prediction of specific impulse for a high expansion ratio using the data for the same motor with a lower expansion ratio is very accurate.

Delivered specific impulse and specific impulse overall efficiencies were correlated against the variables of throat diameter, expansion ratio, chamber pressure, aluminum content, submergence, and divergence efficiency. The error for the delivered specific impulse correlation was approximately the same as that for the detailed analysis. The correlation of efficiency (η_o) was much better with an error (1σ) of only 0.38 percent. Not all independent variables were statistically significant, particularly submergence. This indicates that the submergence loss analysis and the data it was based upon deserve further evaluation. The statistical correlations developed are very useful for preliminary estimates and motor optimizations.

REFERENCES

1. Cohen, N.S., D.P. Harry III, C.F. Price, D.E. Coats, J.N. Levine and G.R. Nickerson, "Solid Rocket Performance Prediction Techniques," AIAA Paper No. 74-1200, AIAA/SAE 10th Propulsion Conference, San Diego, Calif., Oct. 1974.

2. Kliegel, J.R. and G.R. Nickerson, "Flow of Gas-Particle Mixtures in Axially Symmetric Nozzles," Progress in Astronautics and Rocketry, 6: Detonation and Two-Phase Flow, Academic Press, New York, 1962, pp. 173-194.

3. Daines, W.L., T.A. Boardman, R.K. Lund and R. Abel, "Effect of Aluminum Oxide Impingement on Specific Impulse of Solid Propellant Rocket Motors," AIAA Paper No. 76-145, AIAA/SAE 12th Propulsion Conference, July 1976.

4. Daines, W.L., J.L. Mayberry, R.K. Lund and R. Abel, "Prediction of Thrust Losses Occurring in Solid-Propellant Rocket Motors," AIAA Paper No. 74-1201, AIAA/SAE 10th Propulsion Conference, Oct. 1974.

5. Daines, W.L. and D.L. Boyd, "Effect of Aluminum Concentration in Propellant on Performance of Rocket Motors," AIAA Paper No. 75-1277, AIAA/SAE 11th Propulsion Conference, Sept. 1975.

6. Lavery, J.R., R. Abel, R.K. Lund and W.L. Daines, "Experimental Investigation of the Effects of Internal Nozzle Contouring on Nozzle Performance," JANNAF Propulsion Meeting, 1974 (CPIA Pub. No. 260), III, Pt. 2, Oct. 1974, pp. 623-643.

7. Kirschner, T.J., Jr., "Prediction of Delivered Specific Impulse Using Empirical Techniques," JANNAF Propulsion Meeting, 1975 (CPIA Pub. No. 266), III, Oct. 1975, pp. 115-134.

8. Coats, D.E., J.N. Levine, G.R. Nickerson, T.J. Tyson, N.S. Cohen, D.P. Harry III and C.F. Price, "A Computer Program for the Prediction of Solid Propellant Rocket Motor Performance," AFRPL-TR-75-36, Vol. I, July 1975.

9. "Solid Rocket Motor Performance Analysis and Prediction," NASA SP-8039, May 1971, p. 24.

10. Bartlett, R.W. and L.J. Delaney, "Effect of Liquid Surface Tension on Maximum Particle Size in Two-Phase Flow," Pyrodynamics, 4, 1966, pp. 337-341.

TABLE I. MOTOR DATA

Motor No.	Mfg.	Mfg. No.	Propellant			Nozzle							Sub, %	$\overline{D}_t$ (in.)	$\overline{\epsilon}$	$\overline{P}$ (psia)
			Binder	% AP	% Al	Type	ASUB	R_d	R_u	θ_i (deg)	θ_e (deg)	L_n (in.)				
1	Aerojet	SVM-1	CTPB	73	15	parabola	3.30	2.0	2	27	16.8	15.0	3	2.32	33.3	377
2		SVM-2	CTPB	73	15	parabola	2.65	1.7	2	27	16.1	16.4	24	2.75	28.0	322
3		SVM-4A	CTPB	73	15	wall	3.61	2	2	25	16.5	25.1	0	3.43	40.0	731
4		SVM-5	CTPB	73	15	parabola	3.55	0.9	1	27	15.6	15.3	24	2.61	26.8	515
5		SVM-6	CTPB	73	15	parabola	4.64	1	1	31	14.9	24.6	0	2.84	54.0	602
6		SVM-7	CTPB	73	15	parabola	2.64	1.4	2.1	31.5	14.3	28.3	24	3.27	51.2	612
7		MM III, st. 2	CTPB	73	15	parabola	2.42	1	2	26.7	16.7	52.6	14	9.63	24.8	443
8		MM III, st. 3	CTPB	73	15	arc	2.42	2	1	29	13.6	35.1	29	6.98	23.6	507
9		MM III, st. 3 W/EEC(ASPC)	CTPB	73	15	wall	2.42	2	1	29	17	54.0	29	6.98	42.7	507
10		MM III, st. 3 W/EEC(HPC)	CTPB	73	15	wall	2.42	2	1	29	20	76.0	29	6.98	87.9	523
11	UT-CSD	FW-4	PBAN	68	16.4	conical	2.70	2	2	20	20	19.9	9	2.41	47.3	683
12		FW-5	PBAN	68	16.4	conical	2.80	1.7	2	19.9	19.9	19.2	9	2.12	55.6	670
13		FW-5A	PBAN	68	16.4	conical	2.80	1.7	2	19.7	19.7	26.2	9	2.10	96.9	733
14		IUS	HTPB	68	18	arc	3.48	1.0	2	27	15	44.8	38	7.09	33.1	549
15	Thiokol	364-3	CTPB	70	16	wall	2.85	0.86	2	24.5	14.1	28.8	45	3.36	51.2	568
16		364-4	CTPB	70	16	wall	2.29	0.78	2	23.3	13.6	27.2	43	4.36	29.8	545
17		364-11	CTPB	72	16	wall	2.31	0.89	2	23.9	14	27.9	26	4.24	32.1	547
18		364-19	CTPB	70	16	wall	2.48	0.81	2	23.7	12.8	27.8	31	3.82	39.3	588
19		442-1 (a)	CTPB	69	16	conical	1.92	1	2	20	20	13.2	40	2.99	17.5	642
20		479	CTPB	70	16	wall	2.53	1.1	2.1	23.7	14.2	13.0	26	1.44	55.0	788
21		521	CTPB	70	16	wall	3.07	0.85	2	24.3	13.9	16.8	19	1.93	50.7	645
22		604	CTPB	70	16	wall	3.72	0.5	1	26.7	14.1	17.1	10	2.50	35.4	485
23		616	CTPB	72	16	wall	2.87	1	1	24.5	14.8	21.8	18	2.82	46.0	465
24		640	CTPB	70	16	conical	4.87	2	2	19.9	19.9	19.9	9	2.49	47.0	676
25		714-1	HTPB	71	18	wall	2.61	1	2	24	14.6	34.4	26	3.57	54.6	609
26		714-2	HTPB	59	20	wall	2.76	0.91	2	24	14.6	34.6	27	3.32	74.7	723
27	Lockheed	Y41-4	PBAA	69	16	conical	4.89	2	2	15	15	15.0	21	1.35	40.2	367
28		Y41-7	PBAA	69	16	conical	4.89	2	2	15	15	30.0	21	1.36	149.3	356
29	Hercules	258-E6 (b)	Double Base	7	19	conical	2.45	2	2	18	18	20.0	6	3.16	25.1	454
30		259-A6 (b)	Double Base	7	19	conical	1.65	2	2	15	15	41.1	6	6.67	17.9	344

(a) Contains 1% Fe_2O_3 (b) Initial nozzle dimensions

TABLE II. PERFORMANCE DATA

Motor No.	I^{o}_{sp}	$I_{sp\ del}$	$I_{sp\ pred}$	ΔI_{sp}	η_o	$\eta_{2D2\phi}$	η_s	η_k	ΔTBL
1	312.0	288.3	286.4	-1.9	0.9240	0.9339	0.9978	0.9923	2.2
2	308.7	284.0	283.4	-0.6	0.9200	0.9375	0.9950	0.9910	2.0
3	315.6	289.7	290.9	+1.2	0.9179	0.9303	1.0	0.9964	1.7
4	308.4	281.2	285.1	+3.9	0.9118	0.9409	0.9941	0.9949	1.8
5	320.2	293.2	297.8	+4.6	0.9157	0.9415	1.0	0.9953	2.2
6	319.4	293.6	295.6	+2.0	0.9192	0.9443	0.9917	0.9954	2.1
7	306.8	287.6	286.7	-0.9	0.9374	0.9486	0.9956	0.9940	1.3
8	306.0	284.7	284.5	-0.2	0.9305	0.9464	0.9929	0.9949	1.6
9	316.4	293.0	294.8	+1.8	0.9260	0.9492	0.9929	0.9944	1.7
10	327.0	300.3	301.6	+1.3	0.9183	0.9400	0.9927	0.9942	1.7
11	315.8	286.2	289.2	+3.0	0.9063	0.9310	0.9934	0.9962	1.7
12	318.2	286.5	291.1	+4.6	0.9004	0.9304	0.9934	0.9960	1.9
13	325.8	293.1	297.8	+4.7	0.8996	0.9309	0.9929	0.9962	2.1
14	312.3	287.7	289.1	+1.4	0.9212	0.9418	0.9929	0.9950	1.5
15	317.1	290.7	291.5	+0.8	0.9168	0.9393	0.9902	0.9953	2.0
16	308.5	284.6	284.4	-0.2	0.9225	0.9416	0.9895	0.9954	1.6
17	311.1	289.5	287.9	-1.6	0.9306	0.9441	0.9914	0.9950	1.8
18	313.0	288.9	288.3	-0.6	0.9230	0.9397	0.9906	0.9956	1.8
19	294.9	272.8	271.1	-1.7	0.9251	0.9339	0.9855	0.9966	1.2
20	318.3	290;0	290.2	+0.2	0.9111	0.9347	0.9867	0.9968	2.4
21	317.0	288.6	290.8	+2.2	0.9104	0.9361	0.9919	0.9960	2.3
22	311.3	285.9	286.6	+0.7	0.9184	0.9361	0.9960	0.9946	2.1
23	317.1	290.2	290.9	+0.7	0.9152	0.9359	0.9941	0.9936	2.2
24	315.9	288.3	289.7	+1.4	0.9126	0.9318	0.9936	0.9962	1.7
25	324.8	296.8	298.1	+1.3	0.9138	0.9385	0.9904	0.9949	2.3
26	329.7	298.1	301.6	+3.5	0.9042	0.9364	0.9887	0.9955	2.3
27	309.7	282.7	283.5	+0.8	0.9128	0.9345	0.9960	0.9931	2.7
28	325.7	294.3	294.8	+0.5	0.9036	0.9255	0.9961	0.9923	3.1
29	298.9	281.7	276.2	-5.5	0.9425	0.9370	0.9960	0.9956	1.5
30	292.6	281.4	273.9	-7.5	0.9617	0.9500	0.9962	0.9942	1.4

TABLE III. STATISTICAL ANALYSIS

$$Y = [a + b\,\ell n\,\overline{D}_t + c\,\ell n\overline{\epsilon} + d\,\ell n\,\overline{P} + e\,\ell n\,Al + f\,\ell n(1-S)]\,\eta_{div}$$

Y	a	b	c	d	e	f	σ	R	Remarks
I_{sp} (del)	232.9	6.61	11.70	2.151	0.504	7.40	2.03	0.948	All Data
I_{sp} (del)	244.6	6.66	11.94	-----	-----	7.36	2.01	0.944	All Data
I_{sp} (del)	231.6	6.35	11.26	2.59	0.264	6.48	2.03	0.934	Without Motor 19
I_{sp} (del)	245.6	6.51	11.68	-----	-----	6.82	2.04	0.927	Without Motor 19
η_o	0.8882	0.0111	- 0.00805	-0.000217	-0.0377	0.00289	0.00436	0.909	All Data
η_o	0.8811	0.0108	- 0.00785	-----	-0.0402	-----	0.00419	0.908	All Data
η_o	0.8972	0.0129	- 0.00508	-0.00312	-0.0361	0.00904	0.00348	0.939	Without Motor 19
η_o	0.8598	0.0117	- 0.00520	-----	-0.0455	-----	0.00360	0.928	Without Motor 19

Notes:

1. $\eta_{div} = 0.5 + 0.5\cos\beta$, $\beta = (\overline{\theta} + 2\theta_e)/3$, $\tan\overline{\theta} = \overline{D}_t[\overline{\epsilon}^{-0.5} - 1]/2L_n$
2. Al is weight fraction Al, S is fractional submergence
3. All motors are only composite propellant motors.

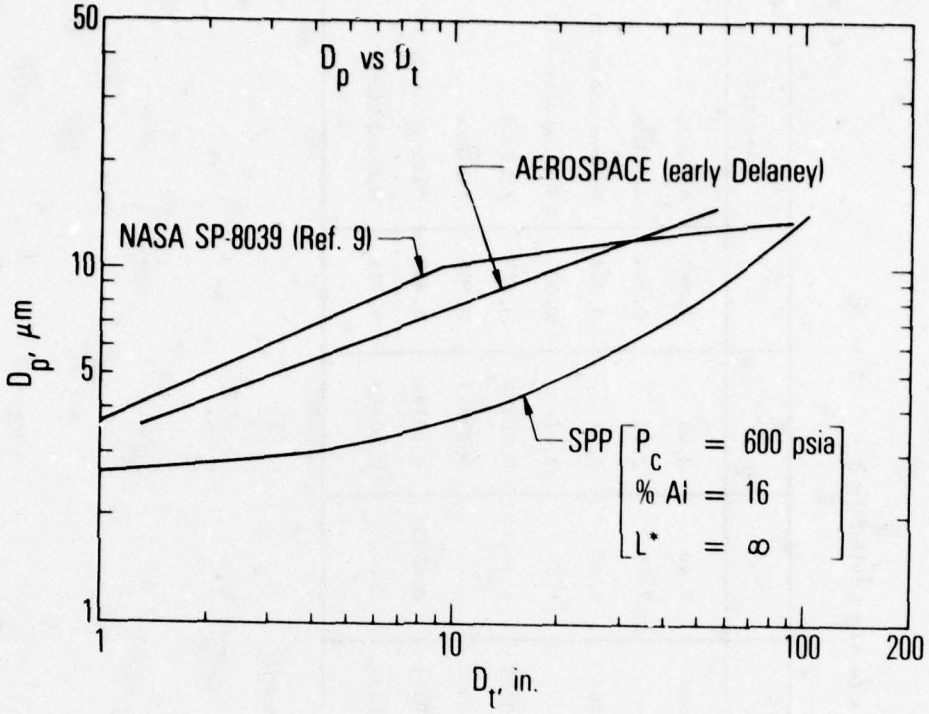

Fig. 1. D_p versus D_t

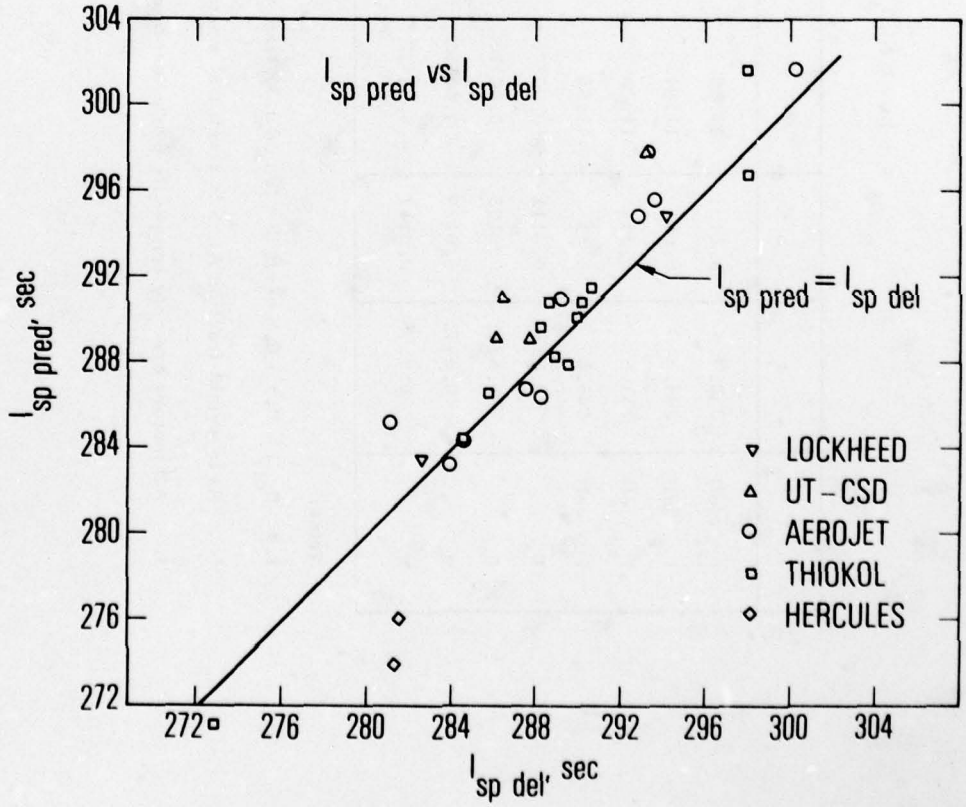

Fig. 2. $I_{sp\ pred}$ versus $I_{sp\ del}$

DISCUSSION

P.Kuentzmann, ONERA, Fr

What significance do you attach to the average diameter of the particles. It is most probable the particle sizes vary between the combustion chamber and the exit plane of the nozzle. This is influenced by a number of parameters such as pressure, scale etc.

Universal curves (DP-DT) relating particle size to nozzle throat were presented by you. Were these established on an experimental basis and can you elaborate?

Author's Reply

All three curves presented were founded on experimental data but the data base for each curve was different. The early work actually used cloud sampling techniques, whereby the exhaust clouds from flight test vehicles were sampled and the particle size distribution determined.

As such it was the particle sizes ejected from the nozzle, which were taken. The sizes inside the rocket chamber can, of course, be significantly larger than outside the motor, i.e. the mass mean diameter.

A SIMPLE METHOD TO ESTIMATE THE INFLUENCE OF A SMALL VARIATION IN THE THROAT AREA ON THE PERFORMANCE OF SOLID ROCKETS

by
H.F.R. Schöyer
Consultant National Defense Organization,
TNO Prins Maurits Laboratory,
Technological Research,
Lange Kleiweg 137, P.O. Box 45, 2280 AA Rijswijk
The Netherlands.
Senior Faculty Member, Delft University of Technology,
Department of Aerospace Engineering,
Kluyverweg 1, 2629 HS Delft,
The Netherlands.

SUMMARY

During surveillance tests of operational solid rocket motors, one will usually find (small) discrepancies between measured and nominal rocket performances. One cause may be erosion of the nozzle throat or a deviation from the nominal throat diameter. As the nozzle throat area determines the equilibrium pressure of the rocket motor, this directly affects the performance of the missile. If a computer program for the calculation of rocket performances is available, one may calculate the rocket performances for different throat areas to obtain a trend. With the technique presented here, a rapid estimate of this trend is obtained, which also shows the mutual dependence of motor parameters. Calculations are easily made with a small "calculator". A rapid insight in what may be expected from a small deviation in throat diameter is obtained. The method is based on linearization of the mean ballistic variables with respect to the variation in throat area. The variation of the thrust, specific impulse, burning time, mass flow and total impulse are predicted. These predictions are compared with predictions by a computer program for the internal ballistics of solid rocket motors and show good agreement.

LIST OF SYMBOLS

Latin alphabet

A_e	exit surface area	p_a	ambient pressure
A_t	throat surface area	p_c	chamber pressure
a	constant in burning rate law	p_e	exhaust pressure
F	thrust	R	gas constant
g_o	standard surface gravity	r	burning rate
I_{sp}	specific impulse	S_b	burning surface area
I_{tot}	total impulse	T_c	combustion temperature
m	mass flow	t	time
M_b	propellant mass	t_b	burning time
n	burning rate exponent	w	web thickness
p	pressure ratio		

Greek alphabet

Γ	Vandenkerckhove function	ρ_b	density of propellant
γ	ratio of specific heats	ρ_c	density of combustion products
λ	Malina correction factor		

Indices and superscripts

$( )_c$	chamber	$( )_p$	pressure
$( )^e$	exit	$( )_t$	throat
$( )_i$	impulse	$( )'$	perturbed quantity

INTRODUCTION

During static surveillance testing of operational rocket motors it is sometimes observed that the performance deviates from the expected nominal performance. One of the problems for the laboratory performing these surveillance tests, is to determine the cause for this deviation. In many cases, there will not be one single effect leading to these deviations, but there will be many combined effects leading to discrepancies between the observed and expected performance. To name a few of these effects: aging of the propellant, production inaccuracies, deformation of the propellant grain, debonding, and nozzle erosion. If the nozzle throat surface area, either due to production inaccuracies, or due to erosion deviates from its nominal size, this will affect the rocket performance. While performing tests with a particular operational missile from the Royal Netherlans Airforce, there was the suspicion that such deviations, caused by production inaccuracies, were present. It was found that the nozzle throat diameter was somewhat larger than its nominal value. To find out whether these deviations would lead to the observed deviations in the performance of the motor, this effect has been analyzed(1). It was found that the problem could be analyzed by linearizing the governing equations for the internal ballistics of the rocket motor. This allows for a quick look analysis, without the use of more sophisticated hardware and software, such as electronic computers and computer programs.
Such computer programs are not always available, and usually, a subroutine or procedure, describing the variation of the burning surface area is not available and has to be written for the specific rocket motor. This is always time consuming. The present method allows a very quick estimate of the variation in the performance and can be made by hand with the help of an electronic pocket calculator. Especially if it is not

clear whether the observed deviations are caused by a deviation in the nozzle throat area, or by other effects the method eliminates a possible unnecessary computer calculation.

ROCKET PERFORMANCE AND NOZZLE THROAT AREA

During a static test, one usually determines the Thrust, F, the Chamber Pressure, p_c, the Specific and Total Impulse, I_{sp} and I_{tot}, and the Burning Time, t_b.
All these parameters depend more or less on the throat area A_t. If the nozzle throat area deviates from its nominal value, these performance parameters will also deviate from their nominal values. In the following we will determine the effect of a small deviation, A_t', such that $A_t'/A_t \ll 1$, on these performance parameters.

The thrust of a solid rocketmotor may be written as[2]

$$F = \lambda \rho_b r S_b \sqrt{\frac{2\gamma}{\gamma-1} RT_c \left[1 - (p_e/p_c)^{\frac{\gamma-1}{\gamma}}\right]} + (p_e - p_a) A_e \tag{1}$$

where r stands for the propellant burning rate, p_e is the exhaust pressure, p_c represents the chamber pressure, p_a the atmospheric pressure, while A_e stands for the nozzle exhaust surface area. The Malina correction factor, λ, accounts for divergence losses.
As we will often encounter the pressure ratio p_e/p_c, we will for brevity write:

$$p = p_e/p_c, \text{ with } p < 1 \tag{2}$$

The expansion and pressure ratio are related by De Saint Venant's Equation[2]:

$$A_e/A_t = \Gamma / \{p^{\frac{1}{\gamma}} \sqrt{\frac{2\gamma}{\gamma-1}\left[1 - p^{\frac{\gamma-1}{\gamma}}\right]}\} \tag{3}$$

We will assume a small deviation A_t' in the nozzle throat area A_t, but not in the exit area A_e. Due to this deviation A_t' a deviation p' in the pressure ratio p will result. However, this is composed of deviations in both the chamber pressure, p_c, and in the exit pressure, p_e:

$$\frac{p'}{p} = \frac{p_e'}{p_e} - \frac{p_c'}{p_c} \tag{4}$$

Linearization of Eq. (3) for these deviations yields:

$$\frac{p'}{p} = \frac{\gamma\left(1 - p^{\frac{\gamma-1}{\gamma}}\right)}{1 - \frac{\gamma+1}{2} p^{\frac{\gamma-1}{\gamma}}} \frac{A_t'}{A_t} \tag{5}$$

This equation relates the variation in the pressure ratio and the variation in the nozzle throat area. Let us now consider the variations of the ballistic variables, chamber pressure, mass flow, thrust, specific impulse, burning time and total impulse, due to the deviation of the throat area.

Chamber Pressure

The chamber pressure of a solid rocket motor results of a balance between the mass production at the burning surface, S_b, of the propellant and the mass efflux through the nozzle:

$$\rho_b S_b a p_c^n = \Gamma p_c A_t / \sqrt{RT_c} \tag{6}$$

where use is made of a standard burning rate law:

$$r = a p_c^n$$

Linearizing Eq. (6) for small deviations p_c' and A_t':

$$p_c'/p_c = \frac{-1}{1-n} A_t'/A_t \tag{7}$$

Mass Flow

The mass flow m is given by[2]

$$m = \Gamma p_c A_t/\sqrt{RT_c} \tag{8}$$

In the same way as above, one finds for the variation in the mass flow due to a deviation in the nozzle throat area:

$$\frac{m'}{m} = \frac{p_c'}{p_c} + \frac{A_t'}{A_t} = \frac{-n}{1-n} \frac{A_t'}{A_t} \tag{9}$$

Thrust

The thrust of a rocket motor consists of two parts, the impulse thrust, F_i:

$$F_i = \lambda m V_e,$$

and the pressure thrust F_p:

$$F_p = (p_e - p_a)\, A_e.$$

For many rockets the expansion is near to ideal, i.e. $p_e \approx p_a$ and the pressure thrust may be neglected with respect to the impulse thrust. For some military rockets, anti-tank rockets, small air-launched rockets etc., this is not the case, as the nozzle is kept short. In such cases the pressure thrust is not negligible, though it is smaller than the impulse thrust. Hence,

$$F\,(1 + F'/F) = F_i + F_i' + F_p + F_p' \tag{10}$$

Linearizing this equation yields

$$\frac{F'}{F} = \left(\frac{F_i'}{F_i} + \frac{F_p'}{F_i}\right)\left(1 - \frac{F_p}{F_i}\right) \tag{11}$$

where

$$F_p/F_i = \frac{p\,\frac{A_e}{A_t}\left(1 - \frac{p_a}{p_e}\right)}{\lambda\,\Gamma\sqrt{\frac{2\gamma}{\gamma-1}\left(1 - p^{\frac{\gamma-1}{\gamma}}\right)}}$$

Now F_i is given by the first term at the right hand side of Eq. (1), which yields after linearization:

$$\frac{F_i'}{F_i} = n\,\frac{p_c'}{p_c} - \frac{\gamma-1}{2\gamma}\,\frac{p'}{p}\,\frac{p^{\frac{\gamma-1}{\gamma}}}{1 - p^{\frac{\gamma-1}{\gamma}}}$$

and after substitution of the Eqs (5) and (7) we obtain the variation of the impulse thrust:

$$\frac{F_i'}{F_i} = -\left[\frac{n}{1-n} + \frac{\frac{\gamma-1}{2}\,p^{\frac{\gamma-1}{\gamma}}}{1 - \frac{\gamma+1}{2}\,p^{\frac{\gamma-1}{\gamma}}}\right]\frac{A_t'}{A_t}\,. \tag{12}$$

For the ratio of the variation of the pressure thrust to the impulse thrust, we find

$$\frac{F_p'}{F_i} = \frac{A_e\,p_e'}{\lambda\,m\,V_e} = p\,\frac{A_e}{A_t}\,\frac{p_e'}{p_e}\,\frac{1}{\lambda\,\Gamma\sqrt{\frac{2\gamma}{\gamma-1}\left[1 - p^{\frac{\gamma-1}{\gamma}}\right]}}$$

which, with the help of the Eqs (4), (5) and (7) may be written as

$$\frac{F_p'}{F_i} = p\,\frac{A_e}{A_t}\left\{\frac{\left(1 - p^{\frac{\gamma-1}{\gamma}}\right)\gamma}{1 - \frac{\gamma+1}{2}\,p^{\frac{\gamma-1}{\gamma}}} - \frac{1}{1-n}\right\}\frac{A_t'/A_t}{\lambda\,\Gamma\sqrt{\frac{2\gamma}{\gamma-1}\left[1 - p^{\frac{\gamma-1}{\gamma}}\right]}} \tag{13}$$

and the deviation of the thrust is found by adding the Eqs (12) and (13) and multiplying the result with $1 - F_p/F_i$, according to Eq. (11).

Specific Impulse

The specific impulse may be defined as[2]

$I_{sp} = F/(m\,g_o)$, which yields

$$I_{sp}'/I_{sp} = F'/F - m'/m, \tag{14}$$

where F'/F is found according to the Eqs. (11), (12) and (13) and m'/m is given by Eq. (9).

Burning Time

The burning time of a solid rocket is given by

$$\int_0^{t_b} r\,dt = w,$$

where w stands for the web thickness. If the throat area deviates from its nominal value, the chamber pressure, and hence the burning rate, will deviate from its nominal value. For this reason the burning time will differ from the nominal burning time. This may be expressed as

$$\int_0^{t_b+t_b'} (r + r')\,dt = w$$

or equivalentely

$$\int_0^{t_b+t_b'} r\left(1 + n\frac{p_c'}{p_c}\right) dt = \left(1 - \frac{n}{1-n}\frac{A_t'}{A_t}\right) \int_0^{t_b} r\, dt + \int_{t_b}^{t_b+t_b'} r \left(1 - \frac{n}{1-n}\frac{A_t'}{A_t}\right) dt = w$$

Linearization of this equation yields

$$w \left(1 - \frac{n}{1-n}\frac{A_t'}{A_t}\right) + \bar{r}(t_b) \left(1 - \frac{n}{1-n}\frac{A_t'}{A_t}\right) t_b' = w, \text{ or}$$

$$t_b' = \frac{n\, w}{1-n}\frac{A_t'}{A_t} \Big/ \left\{\left(1 - \frac{n}{1-n}\frac{A_t'}{A_t}\right) r\,(t_b)\right\} \tag{15}$$

where $r(t_b)$ stands for the burning rate at the nominal burning time t_b.

Total Impulse

The total impulse may be determined in two different ways:
According to its definition, we have

$$I_{tot} = \int_0^{t_b} F\, dt \quad \text{, this leads to}$$

$$\frac{I_{tot}'}{I_{tot}} = \frac{F'}{F} + \frac{t_b'}{t_b} \tag{16}$$

Now this last equation may not be very accurate. Therefore recall that if the thrust decreases, the burning time increases. Therefore, F'/F and t_b'/t_b will have an opposite sign, and the total impulse is numerically determined from the difference of two numbers which are of the same order, which may be rather inaccurate. Another way of estimating I_{tot}'/I_{tot} circumvents this numerical inaccuracy more or less. Therefore recall that the specific impulse may also be written as[2]:

$$I_{sp} = \frac{\int_0^{t_b} F\, dt}{M_b\, g_o} = \frac{I_{tot}}{M_b\, g_o}$$

this immediately yields

$$\frac{I_{tot}'}{I_{tot}} = \frac{I_{sp}'}{I_{sp}} \tag{17}$$

The equations (11) through (17) now immediately allow a rapid estimate of the variation of the important rocket parameters due to a variation of the nozzle throat area.

RESULTS

The variations in rocket performance parameters now may be calculated according to the method outlined in the previous paragraph. The variations in Thrust, Specific Impulse, Burning Time, Mass Flow and Total Impulse have been calculated for variations in the throat area of -10%, -5%,5% and 10% for two typical military rockets.
Some (nominal) values of the parameters are presented in Table 4.1 for these two missiles.
To check the accuracy, the results of these linearized calculations are compared with the results obtained by computer calculations.
This computer program[3] makes detailed calculations of the internal ballistics of the rocket motor. It accounts for the specific variation in the burning surface, as the shape and dimensions of the grain are input variables of the computer program. The equations, governing the internal ballistics are integrated with small time steps. Finally the mean values for the performance parameters are determined by averaging their instantaneous values. The results of both calculations are presented in the Tables 4.2 and 4.3, and in the figures 1 and 2.

Comparing the computer calculations with the results of the calculations according to the present linearized approximations, shows a fairly good agreement. The discrepancies between both calculations are small and the tendencies are the same. With a 10% variation in the nozzle throat area the discrepancies are largest but quite acceptable. The prediction in the variation in the burning time is fairly well in agreement with the computer predictions. Equation (15) shows that the variation in burning time is not proportional with the variation in the throat area. This is in good agreement with the computer results, though the effect is over-estimated by the present linear approximation. The variations in F, I_{sp}, I_{tot} and m are fairly well predicted.

Table 4.1 Some Nominal Values for Two Typical Military Missiles

	Missiles	
Performance	A	B
Thrust (kN)	8,504	3,677
Specific Impulse (s)	197,8	198,5
Total Impulse (kN.s)	17,35	6,04
Burning Time (s)	2,04	1,644
Mean Chamber Pressure (MPa)	10,93	8,43
Mean Exit Pressure (MPa)	0,284	0,384
Pressure Ratio, p_e/p_c	0,026	0,0456
Geometric Properties		
Expansion Ratio, A_e/A_t	5,356	3,67
Web thickness (mm)	14,6	18
Malina Correction Factor λ	0,9896	0,9945
Propellant and Combustion Products		
Ratio of Specific Heats, γ	1,25	1,24
Combustion Temperature (K)	1800	1950
Molar Mass (g/mol)	22,7	23,25
Density of Propellant kg/m^3	1550	1550
Burning Rate Exponent, n	0,68	-0,195
Burning Rate Near Extinction (mm/s)	6,98	10,48

Table 4.2 Results of the Present Theory in Comparison with Results of Detailed Computer Calculations for Missile A

A'_t/A_t	-0,1		-0,05		+0,05		+0,1	
	present theory	computer results	present theory	computer results	present theory	computer results	present theory	computer results
F'/F	0,229	0,270	0,115	0,124	-0,115	-0,105	-0,229	-0,196
I_{sp}'/I_{sp}	0,0168	0,0153	0,0084	0,0077	-0,0084	-0,0077	-0,0168	-0,0155
t_b' (s)	-0,367	-0,409	-0,201	-0,211	0,249	0,223	0,564	0,458
m'/m	0,213	0,251	0,106	0,115	-0,106	-0,099	-0,213	-0,184
I_{tot}'/I_{tot}	0,0168	0,0153	0,0084	0,0077	-0,0084	-0,0077	-0,0168	-0,0154

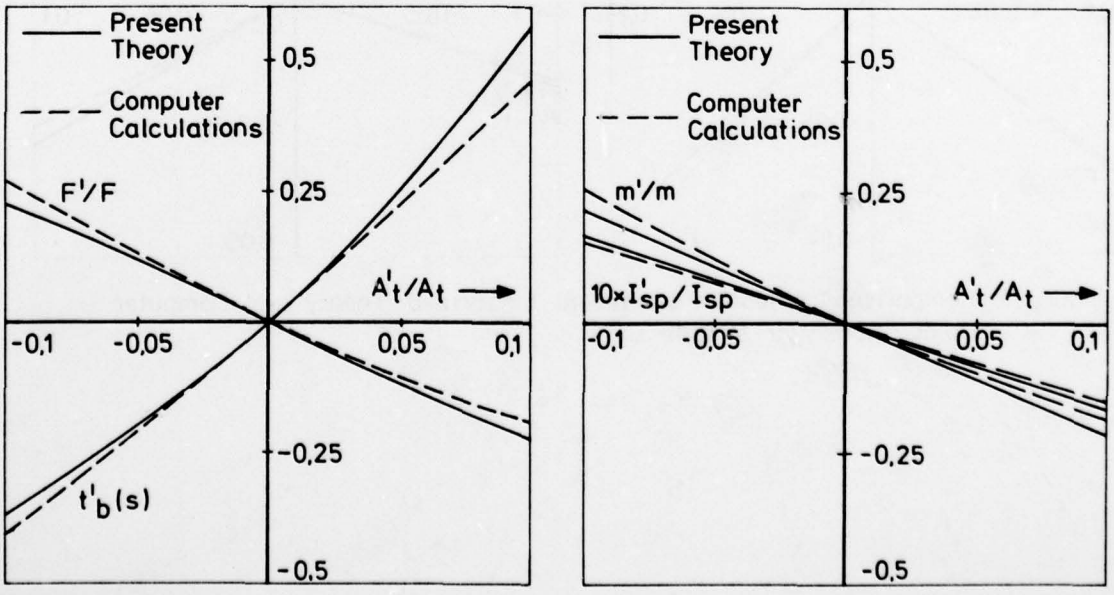

Figure 1: Comparison of Results of Present Linearized Theory and Computer Calculations, for Missile A.

AD-A076 012 ADVISORY GROUP FOR AEROSPACE RESEARCH AND DEVELOPMENT--ETC F/G 21/8.2
SOLID ROCKET MOTOR TECHNOLOGY.(U)
JUL 79
UNCLASSIFIED AGARD-CP-259 NL

2 OF 6
AD
A076012

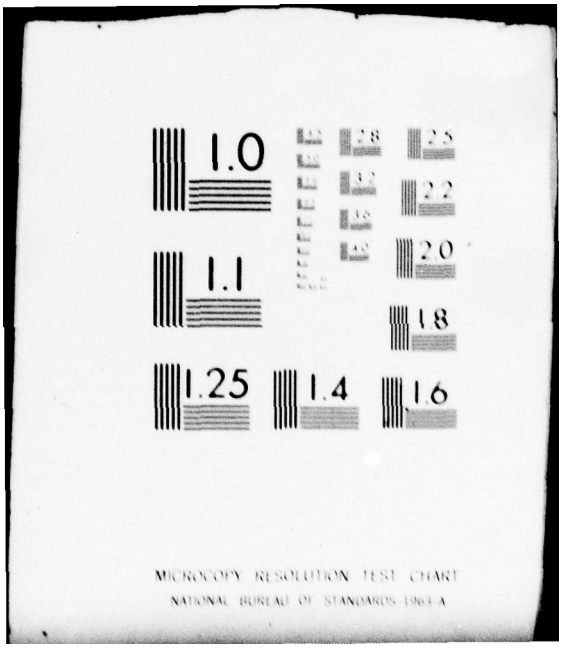
1.0
1.1
1.25
1.4
1.6
2.2
2.0
1.8
MICROCOPY RESOLUTION TEST CHART
NATIONAL BUREAU OF STANDARDS 1963-A

Table 4.3

Results of the Present Theory in Comparison With Results of Detailed Computer Calculations for Missile B

A_t'/A_t	-0,1		-0,05		0,05		0,1	
	present theory	computer results	present theory	computer results	present theory	computer results	present theory	computer results
F'/F	-0,0075	-0,0065	-0,0037	-0,0033	0,0037	0,0027	0,0075	0,0052
I_{sp}'/I_{sp}	0,0088	0,0107	0,0044	0,0033	-0,0044	-0,0051	-0,0088	-0,0101
t_b' (s)	0,028	0,029	0,014	0,014	-0,014	-0,013	-0,028	-0,025
m'/m	-0,0163	-0,0170	-0,0082	-0,0079	0,0082	0,0079	0,0163	0,0159
I_{tot}'/I_{tot}	0,0088	0,0108	0,0044	0,0053	-0,0044	-0,0051	-0,0088	-0,0101

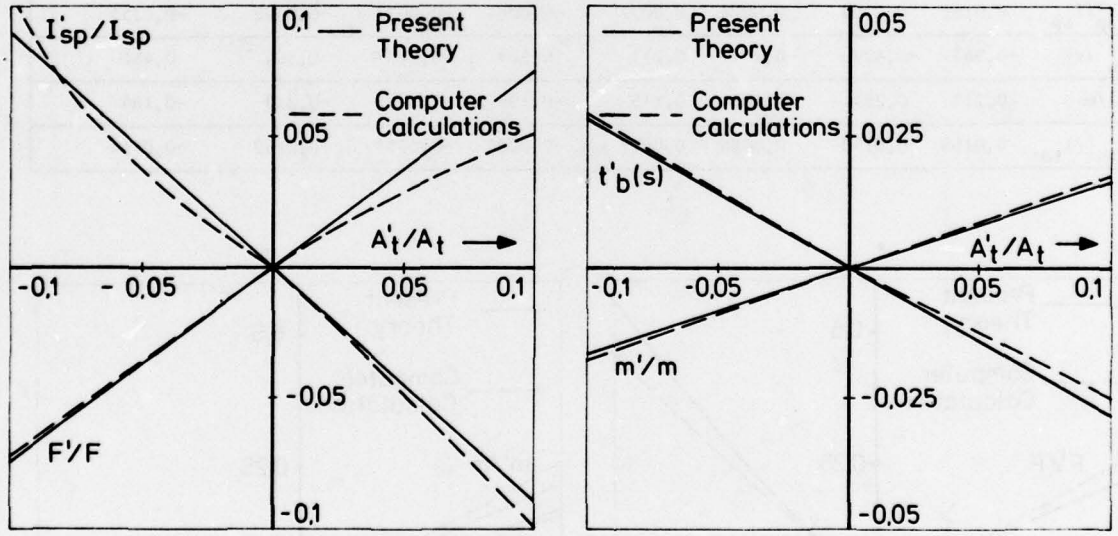

Figure 2: Comparison of Results of Present Linearized Theory and Computer Calculations, for Missile B.

CONCLUSIONS

The present method allows for a rapid determination of the variation of the performance of solid rocket motors, such as used in operational missiles, due to a deviation in the nozzle throat area. If this deviation is solely due to production inaccuracies, the present method gives results which are immediately applicable. If the deviation is caused by erosion, one should average out the erosion effect; one could for example assume a gradual increase in the nozzle throat diameter, and estimate a variation in the performance, based on a mean throat diameter.

The method is based on a linearization of the ballistic equations for the motor. The results of this calculation are in good agreement with a much more detailed computer analysis. A big advantage is that estimates based on this method may be made quickly with a small calculator.

REFERENCES

1. H.F.R. Schöyer, Report for the Prins Maurits Laboratory, Rijswijk, The Influence of a Change in the Throat Surface Area on the Performance of Solid Propellant Rocket Motors (in Dutch), 1978, TRHS-3.

2. J.W. Cornelisse, H.F.R. Schöyer and K.F. Wakker, Rocket Propulsion and Spaceflight Dynamics, London/San Francisco, 1979, Chapters 5 and 9.

3. F. Bebelaar and H.F.R. Schöyer, Delft University of Technology, Dept. of Aerospace Engineering, A Simple Computer Program for the Calculation of Stationary Rocket Performances and Internal Ballistics of Solid Propellant Rocket Motors, RAPIB. (in Dutch), 1977, Memorandum M-285.

INTERNAL BALLISTIC PROBLEMS OF HIGHLY ACCELERATED SOLID PROPELLANT ROCKETS

by

Walter Helmut Diesinger
Dynamit Nobel AG, ES-FG
Waltherstrasse 80
D-5000 Köln 80
Germany

SUMMARY

Standard internal ballistics of solid propellant rockets need an appropriate environment defined by limited rotation, external acceleration and thrust levels.

Remarkable deviation from these constraints cause severe modifications of the well known internal ballistics of solid propellant rockets.

The author describes some phenomena and problems of internal ballistics in a highly accelerated environment and shows how the engineer should overcome them for optimum design.

NOTATIONS

A_b	area of propellant burning surface (m^2)
A_r	reference area (m^2)
A_t	nozzle throat area (m^2)
a_c	thrust chamber stagnation speed of sound of exhaust gases (m/s)
a_r	radial acceleration (m/s^2)
a_x	axial acceleration (m/s^2)
c^*	characteristic exhaust velocity (m/s)
c_F	*nozzle thrust coefficient* (-)
F, $\bar{F}$	thrust, average thrust (N)
I_{spd}	delivered specific impulse (m/s)
K_n	ratio of burning surface area A_b to nozzle throat area A_t (-)
m	mass (kg)
$\dot{m}_p$	propellant mass flow rate (kg/s)
p_c	thrust chamber stagnation pressure (MPa)
r	burning rate (m/s) or radius (m)
r_t	nozzle throat radius (m)
r_w	inner radius of combustion chamber wall (m)
r_o	burning rate for $a_x = 1$ g (m/s)
T_c	thrust chamber stagnation temperature of exhaust gases (K)
t_a	action time (s)
$\bar{t}_r$	mean residence time (s)
V_c	thrust chamber free volume (m^3)
$V_{c,tot}$	thrust chamber total volume (m^3)
V_l	volumetric loading fraction (-), $V_l = V_p/V_{c,tot}$
V_p	initial propellant volume (m^3)
w	web thickness (m)
ε	nozzle contraction ratio (-), $\varepsilon = (r_w/r_t)^2$
ρ_c	thrust chamber stagnation mass density of exhaust gases (kg/m^3)
ρ_p	propellant mass density (kg/m^3)
σ	tensile stress (Pa)
ω	angular velocity (rad/s)

1. INTRODUCTION

In solid propellant rocketry the internal ballistic characteristics are strongly influenced by the propellant parameters. These are defined by specific impulse, burning rate, mass density, tensile strength, composition of the exhaust products. They are mainly sensitive to temperature, pressure and acceleration.

In this paper some information upon the state-of-the-art in the field of internal ballistics in a much more than 1 g acceleration environment is given. Furthermore it is shown how problems arising with high acceleration may be solved.

2. ACCELERATION LEVEL AND STANDARD INTERNAL BALLISTICS

Before reviewing some problems of internal ballistics caused by high acceleration I should define the conditions for standard internal ballistics which are prevailing in most solid fuel rockets.

These rockets have the following characteristics:

i) The periods of ignition delay as well as pressure rise and drop in the thrust chamber are short compared to burn, web or action time.

ii) In the caliber range of .1 through .5 m the maximum axial acceleration level when using radial burner grains does not exceed $a_x \approx 1000\ m/s^2$, since the thrust per cross section area is limited to about $F/A_T \leq 3.7$ MPa. This level declines with larger calibers, mainly because of mechanical similarity rules and the limited burning rates of current solid propellants.

iii) The rocket does not rotate about its longitudinal axis or rotation is only induced to balance thrust vector deviations. In this case the angular velocity is limited to about $\omega \leq 100$ rad/s at the end of the burning time.

iv) Additional environmental conditions for the grain are fulfilled such as limited temperature range, radiation and vibration level or moisture content.

This environment usually admits standard internal ballistics and allows to assume

i) near stationary internal ballistic data during most of the action time,

ii) negligible influence of acceleration and rotation on propellant and nozzle properties,

iii) sufficient strength of the solid propellant to withstand dynamic loads,

iv) tolerable additional environmental conditions.

Deviations from these constraints need an appropriate design to overcome the arising problems.

It is evident that the margins of standard ballistics cannot be defined clearly, since they are influenced by a set of design parameters such as size, shape of the grain, type and ingredients of the propellant.

3. ACCELERATION SENSITIVITY OF SOLID PROPELLANTS

The phenomena appearing when solid propellants are burning in an acceleration field are well known (refs. 1 through 4) and need not to be described in detail. For design considerations it is important to remind that doublebase solid propellants are less sensitive to acceleration than composite-doublebase or composite propellants, since mass densities of propellant and exhaust gases are homogeneous.

Solid propellants under acceleration show enhanced burning rate. This effect is intensified by metal additives. The increase of burning rate is attributed to molten metal or metal oxide particles. They are retained against the grain surface by the acceleration vector and cause a higher heat transfer into the propellant. They may even dip into the grain and increase the effective burning rate still more by building local conical burning surfaces.

This model explains, why

- slow burning propellants show greater acceleration sensitivity than fast burning propellants,
- the acceleration dependence is intensified when portion and particle size of metal additives are increased,
- the burning rate sensitivity is a maximum when the acceleration vector is perpendicular to the burning surface.

Fig. 1 shows the effects of acceleration direction and particle size on burning rate for a 16 % aluminium PBAA composite propellant.

The major observations from these figures are:

i) The burning rate augmentation is almost negligible at orientation angles of the acceleration vector less than 75° with respect to the propellant surface.

ii) A propellant with the smaller aluminium particle size has less burning rate augmentation than others. This is also true for other particles, in general the oxidizer (AP).

These results show that standard internal ballistics is very little influenced by self propelled axial acceleration because of the limited thrust factor F/A_r and the orientation of the acceleration vector.

Problems may arise even with slowly spinning standard internal burner grains at the end of the burning time because the radial acceleration ($a_r = r \cdot \omega^2$) turns the total acceleration vector to higher orientation angles. However, rotation tests without axial acceleration often overestimate the effect of spin since the orientation of the acceleration vector is not correctly simulated.

4. SHORT ACTION-TIME ROCKETS

As can be derived from fig. 1 the axial acceleration level may also create an internal ballistic problem, when thrust to cross section area levels of largely more than $F/A_r = 4.$ MPa must be verified (recoilless weapons, reusable boosters and other applications). Grains designed for this special type of rockets should have burning surfaces A_b parallel to the acceleration vector if composite or composite-doublebase propellants are used.

Equ. 1 illustrates that high values of F/A_r can only be achieved by an appropriate grain design because the performances of propellant and nozzle are limited.

$$(1) \qquad \frac{F}{A_r} = \frac{A_b}{A_r} \cdot \rho_p \cdot r \cdot c^* \cdot c_F$$

thrust factor — grain design — propellant performance — nozzle performance

A large burning surface area A_b compared to the reference area A_r (e. g. cross section) or the total chamber volume $V_{c,tot}$ will result in a short action time t_a and need a small web thickness w.

By using a cluster of internal/external burning tubes or perforated grains the thrust factor may be pushed up to $F/A_r = 25.$ MPa. Grains of these types are rather simple, but total impulse, thrust trace and burning time are not enough reproducible for many applications. Variations of these data are due to crashes of the tubes or slivers towards the end of the burning time, when the wall thicknesses cannot any more withstand the dynamic loads. Therefore, to get better reproducibility the propellant must be supported.

Fig. 2 shows grain designs (refs. 5 through 9) for high thrust short action time rockets or gas generators (ref. 7: $\bar{F} = 215$ kN, $t_a \approx 245$ ms; ref. 9: $\bar{F} = 100$ kN, $t_a \approx 22$ ms; ref. 8: $\bar{F} = 280$ kN, $t_a \approx 5$ ms). They are characterized by small values of web thickness w and volumetric loading fraction V_l, whereas the free volume V_c of the combustion chamber is large. These are the reasons for internal ballistic problems:

i) The average residence time of the exhaust products is short because $\bar{t}_r \sim V_c/A_b$. This is another reason to select a propellant which does not deliver two-phase exhaust products (specific impulse efficiency, ref. 10).

ii) The action time t_a is not long compared to the time intervals of ignition delay, pressure rise and drop in the thrust chamber. Therefore, the igniter should be powerful and carefully designed to ensure instantaneous ignition of the whole grain surface. Thus the igniter charge mass flow may considerably influence the thrust and pressure traces.

iii) The powerful igniter and the transient character of the action time will result in pressure and velocity inhomogenities in the thrust chamber. Therefore, flow areas should be larger than usual, to prevent casual erosive burning. Moreover, the supporting structure should have holes to balance pressure deviations.

Fig. 3 shows a short action time solid propellant rocket with three foil grains and three toroidal igniters. These are fitted with spray heads blowing the ignition gases between the foil spaces to garantee uniform and instantaneous ignition.

The left side of fig. 4 shows a foil grain with radial holes. Propellant sheets are bonded on both sides of a supporting steel mesh by means of ethyl cellulose. The grain is fixed in a resin mounting. After burn out the support remains as shown on the right side of this figure.

All short action time grains presented make use of conventional propellants and forming processes. An additional increase of the thrust to cross area factor is feasible

with porous grains or fast burning rates in thin propellant films. By these means the thrust factor may be pushed up into the order of magnitude of F/A_r = 45. MPa. More can only be achieved by high pressure gases within barrels.

5. ROCKET ASSISTED FIN STABILIZED SHELLS

The base pressure upon shells within the barrel is equivalent to the thrust factor defined before. This pressure is up to about F/A_r = 70. MPa for small recoilless arms (Davis gun) and F/A_r = 500. MPa for shells. Solid propellant rockets applied to these shells serve as sustainers to increase the range or to accomplish special ballistic data. In fin stabilized shells they are stressed in two different phases. The first one is characterized by extreme axial acceleration (6000 g up to 60000 g). In general the ignition of the grain is at least initiated during this phase. In the second phase the rocket is in action and in a standard ballistic environment. Therefore, the internal ballistic characteristics and problems are primarily created by the design needs of phase 1.

The grain is the most critical part of the rocket since the acceleration induced compressive stresses may attain 10 to 100 times the ultimate strength even compared to increased values observed with short time stresses in viscoelastic media.

Simply shaped radial burner grains or supported configurations as mentioned above may endure short time maximum acceleration levels from about 6000 g to 15000 g if they are small, since bendung moments and stresses are largely dependent upon the size of the grain, of course. At still higher acceleration levels the grain should be conceived to be a slurry or a fluid and supported accordingly.

Usually the ignition of the grain is done by the barrel gases. Since the design pressure levels of barrel and rocket are largely different a nozzle closure with a properly dimensioned chocking orifice should be used to prevent unduly high pressure in the thrust chamber as well as an imperfect or uneven ignition. The latter is important to prevent lateral center of gravity deviations which may influence the external ballistic properties of the shell.

The shell must withstand the dynamic loads as a result of the extreme axial acceleration level and, consequently, is largely overdimensioned during the second phase. Thus the rocket may be run at high chamber pressure p_c with the potential of high burning rate r and delivered specific impulse I_{spd}. Moreover, the shell is a heat sink and thermal problems may not be expected. On the other side, heat transfer and the poor efficiency of small nozzles cause specific impulse losses which may even overcompensate the advantage of a high chamber pressure p_c. Theoretical predictions of the thrust and pressure traces based only on the propellant data are largely modified in practice by these influences.

Fig. 5, left side, shows a hydrodynamically supported grain for extreme axial acceleration as depicted before. The inverse front burner grain is only submitted to compressive stress.

When combined extreme axial/radial acceleration of more than about 20000 g acts upon the grain a conical surface must be designed to compensate for the centrifugal forces (right side of fig. 5). The spin induced radial acceleration is not confined to the short axial acceleration phase but continues during the whole flight time of the shell. In the axial acceleration range up to about 20000 g internal tube burner grains are the best choice if they are designed to withstand the barrel phase (ref. 12). Since the radial acceleration field is prevailing during the free flight the internal tube burner grain is also hydrodynamically supported in this phase.

Stress problems of the internal tube burner grain in the barrel may be removed by filling the initial thrust chamber free volume V_c with a liquid having the same mass density as the propellant. This is rather complicated and creates new problems (shelf life, sealing, ignition).

6. SWIRLING FLOW AND NOZZLE PERFORMANCE

It is well known (refs. 14 through 17) that the performance of a spinning solid propellant rocket differs significantly from the performance of the same motor under static conditions. I shall first give a short description of the spin effects which cause the internal ballistic problems to be solved. The spin effects can be separated into two categories,

i) the effects of acceleration on the combustion process which have been discussed already,

ii) the effects of the rotating flow on the chamber and nozzle flowfields.

Early investigations of rotating flows in nozzles have been limited primarily to two types of velocity distribution in the swirling flow:

i) The free, irrotational or potential vortex defined by a tangential velocity decreasing inversely with the radial distance from the axis of rotation. This vortex pattern had been attributed to internal burner grains.

ii) The forced or solid body vortex has a tangential velocity increasing with the radial distance. This vortex is more likely for end burning grains.

In a real nozzle flow, a Rankine combined vortex, i. e. a forced vortex core with an outer free vortex, can be assumed because of viscous flow effects.

Theoretical investigations predict and tests have verified that the mass flow $\dot{m}_D$ through a nozzle is reduced by vorticity when the thrust chamber stagnation pressure p_c remains constant. A common solid propellant with a positiv pressure exponent consequently burns at a higher chamber pressure p_c and a shorter action time t_a. A free vortex has a greater influence on nozzle choking than a forced vortex. This means, that internal ballistic problems arising with swirling flow may be reduced by stimulating the formation of the solid core within the Rankine combined vortex.

Due to the inhomogenities of the flow, pressure, acceleration and stress fields the burning rate r of the grain is dependent on the radial distance from the axis of rotation.

Tests have shown (refs. 16 and 18) that motors incorporating end burning or radial burning grains are subjected to severe centerline coning of the propellant surface or the structure of the forward closure, respectively, when the spin rate exceeds a critical value. May be that the rotating solid body core of the Rankine combined vortex acts like a thermal drill.

Fig. 6, left side, shows the path of a gas particle Δm from the point of formation to the nozzle throat. The conservation of the angular momentum causes the special spiral pattern of the path.

The increase of the angular velocity ω inversely with the square of the radial distance from the axis of rotation is only valid for inviscid flows, of course.

The chart in fig. 6 shows results from tests (ref. 15) for two nozzle contraction ratios ε. If the stagnation pressure p_c and the speed of sound a_c of the gases as well as the chamber wall radius r_w are assumed to be constant the diagram shows the propellant mass flow rate $\dot{m}_D$ through the nozzle as a function of the angular velocity ω. It is obvious that nozzle choking is more pronounced for a nozzle contraction ratio of $\varepsilon = 215$ than for $\varepsilon = 77.4$. This applies only for moderate angular velocities ω. For higher values choking is less pronounced for $\varepsilon = 215$ than for $\varepsilon = 77.4$. This can be attributed to the more intensive sheer flow for $\varepsilon = 215$ and thus a larger radius of the solid body rotation core.

7. ROCKET ASSISTED SPIN STABILIZED SHELLS

Solid propellant rockets applied to spin stabilized shells are stressed by the spin in addition to the environment of fin stabilized shells. Unfortunately, the hydrodynamic support described before is not consistent for the transmission of angular momentum from the shell to the grain. It should be proved in any special case whether the arising sheer stresses will be tolerable. If not, additional radial supports are needed.

Phase 2 is characterized by stationary radial loads because of rotation and nozzle choking. The propellant should not deliver two phase exhaust products to avoid additional burning rate augmentation. Moreover, sedimentation of solid particles may increase heat transfer and burn out mass.

Swirling flow may create local erosive burning and a high heat transfer rate near the axis of rotation. The effective nozzle throat is reduced and the specific impulse efficiency will be comparatively small. Transfer of angular momentum from the gas to the shell will ease the problems of spin induced nozzle choking but may effect flight dynamics. Because of these rather complicated internal ballistic phenomena the design for and the prediction of specified pressure and thrust traces is limited (e. g. ref. 19).

Fig. 7 (ref. 13) represents the design of a range limited, spin stabilized training projectile (caliber 105 mm), which is lighter than the live subcaliber ammunition. The solid propellant thruster has to compensate for the increased influence of the aerodynamic drag thus ensuring the ballistic data of the live ammunition in the training range.

The training projectile consists of the forward cone, the solid propellant rocket forward closure, case, grain, blast tube and nozzle. The sabbot at the rear part of the figure has a central choking orifice for the barrel gases to ignite the grain. The cross-shaped coupling between shell and sabbot is needed to spin up the projectile.

8. REFERENCES

1. Landau; Cegielski: Ballistic Behavior of Solid Propellant Grains under High Acceleration. J. Spacecraft, vol. 2, no. 3, pp. 358-362.

2. Northam: Effects of the Acceleration Vector on Transient Burning Rate Augmentation of a Aluminazed Solid Propellant. AIAA Paper 70-126 (1970).

3. Glick; Hodge; Caveny: Effect of Acceleration on the Burning Rate of Composite Propellants. AIAA Paper 67-470 (1967).

4. Anderson; Reichenbach: An Investigation of the Effect of Acceleration on the Burning Rate of Composite Propellants. AIAA Journal, vol. 6 (1968), no. 2, pp. 271-277.

5. Iwanciow; Chase: Supported Grain Design for High Acceleration Rocket Motor. US Patent 3,664,135, May 23, 1972.

6. Fink: Grain Support for Solid Propellant Rocket Motor. US Patent 3,371,628, May 8, 1973.

7. Dilchert: Feststofftreibsatz mit kurzer Brennzeit für Raketentriebwerke. Offenlegungsschrift DT 1 808 111, 11. Juni 1970.

8. Ramont; Jean; Pradelle; Pierre; Massay: Feststofftreibsatz kurzer Brennzeit und Verfahren zu dessen Herstellung. Deutsche Patentanmeldung 2 034 550, 8. 4. 1971.

9. Cantey; Campbell: Foilac Motor Development for High-thrust Short-action-time Rocket Propulsion. AIAA Paper 70-1385.

10. Anon.: Solid Rocket Motor Performance Analysis and Prediction. NASA SP-8039, May 1971.

11. Northam; Lucy: On the Effects of Acceleration upon Solid Rocket Performance. NASA Langley Research Center, Hampton, Virginia. AIAA Paper 68-530.

12. Anon.: Waffentechnisches Handbuch. Rheinmetall GmbH, Düsseldorf, Germany 1977.

13. Diesinger; Homburg: Training Projectile. US Patent 4,133,265, Jan. 9, 1979.

14. Mager: Approximate Solution of Isentropic Swirling Flow through a Nozzle. ARS Journal, vol. 31, no. 8, Aug. 1961, pp. 1140-1148.

15. Norton; Farquhar; Hoffman: An Analytical and Experimental Investigation of Swirling Flow in Nozzles. AIAA Journal, vol. 7, no. 10, Oct. 1969, pp. 1992-2000.

16. Broddner: Effects of High Spin on the Internal Ballistics of a Solid Propellant Rocket Motor. Astronautica Acta, vol. 15, pp. 191-197.

17. Hsu; De Joode: Inviscid Swirling Flow through a Choked Nozzle. AIAA Journal, vol. 11, no. 11, Nov. 1973, pp. 1564-1565.

18. Jay; Ernst; Klein: Rotationsstand zur Untersuchung des Abbrandverhaltens schnell drehender Treibsätze. RT 520/75, ISL, 1975.

19. Nelson: An Interior Ballistic Model for a Spinning Rocket Motor. AGARD Conference Proceedings no. 194 on Small Solid Propellant Rockets for Field Use, 1976.

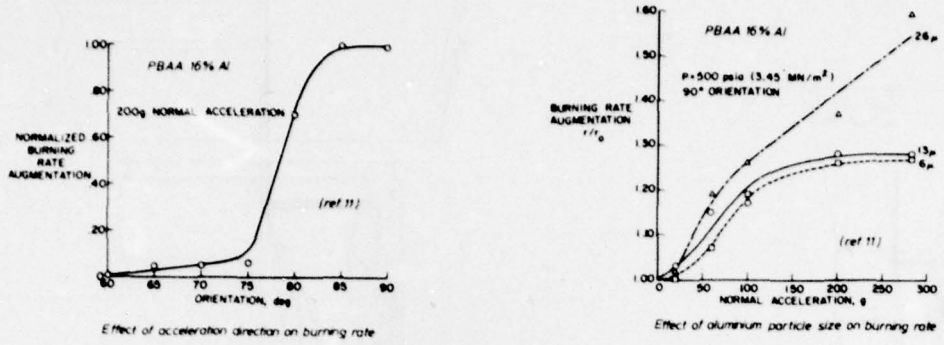

Fig. 1 Acceleration influence on an aluminized composite propellant

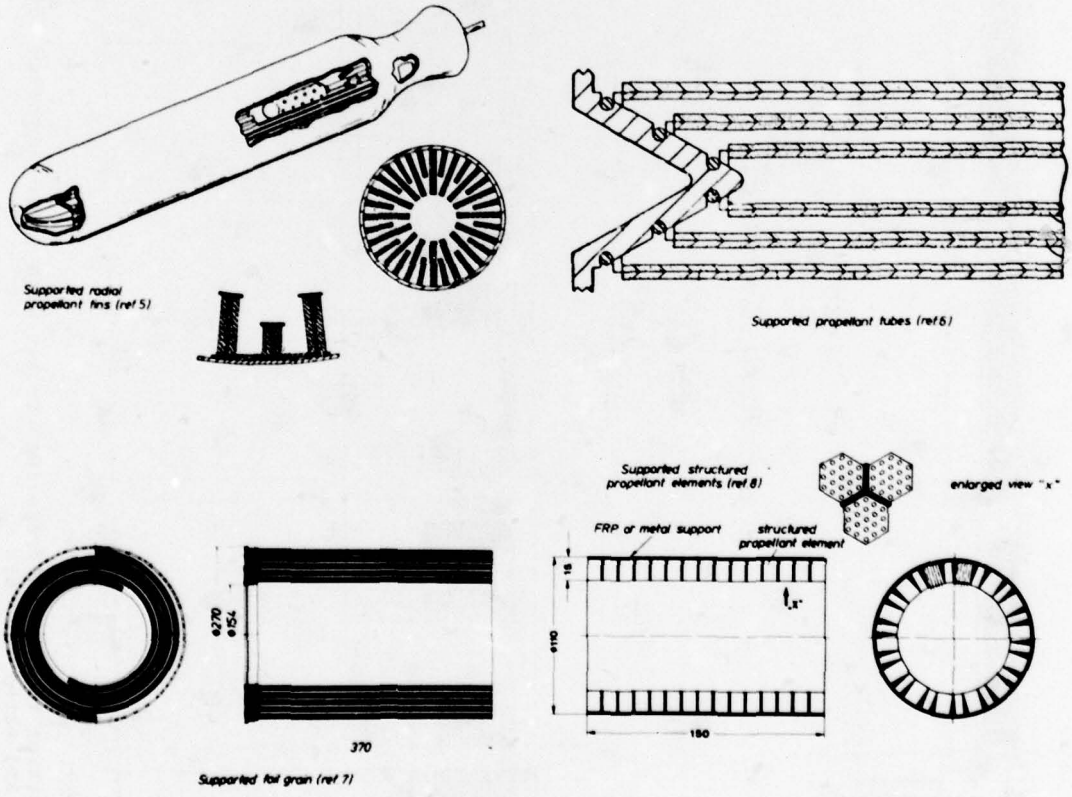

Fig. 2 Supported grains for high thrust and short action time

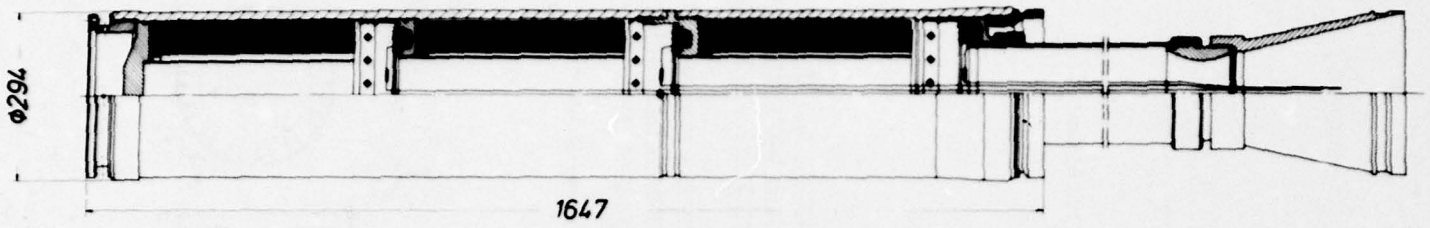

$\bar{F} = 343\,kN$, $t_a \approx 190\,ms$

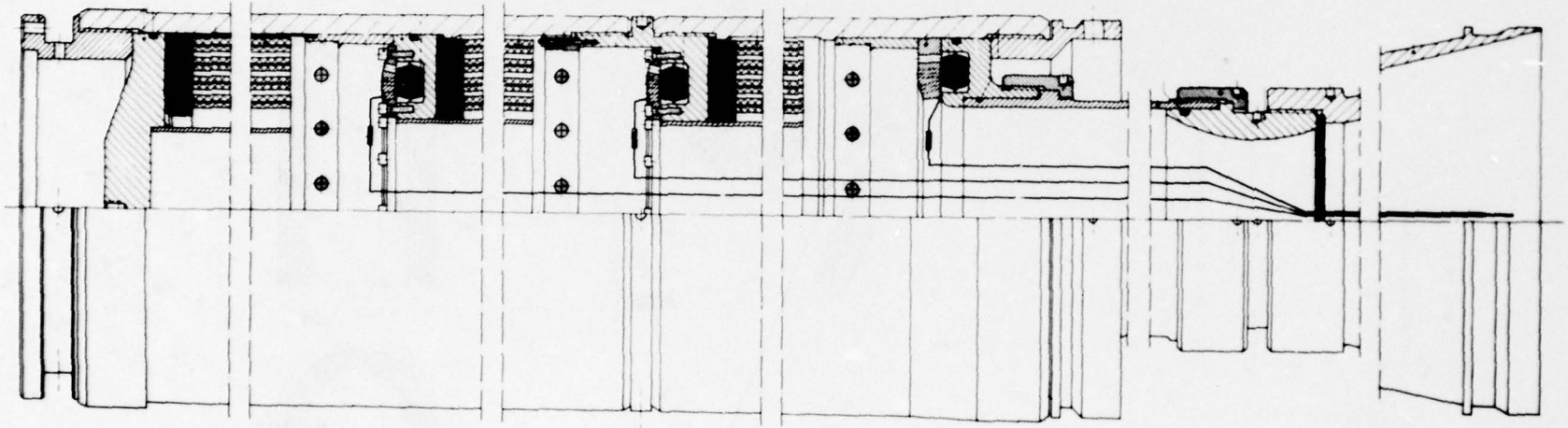

Fig. 3 Short action time solid propellant rocket with three supported foil grains and three igniters

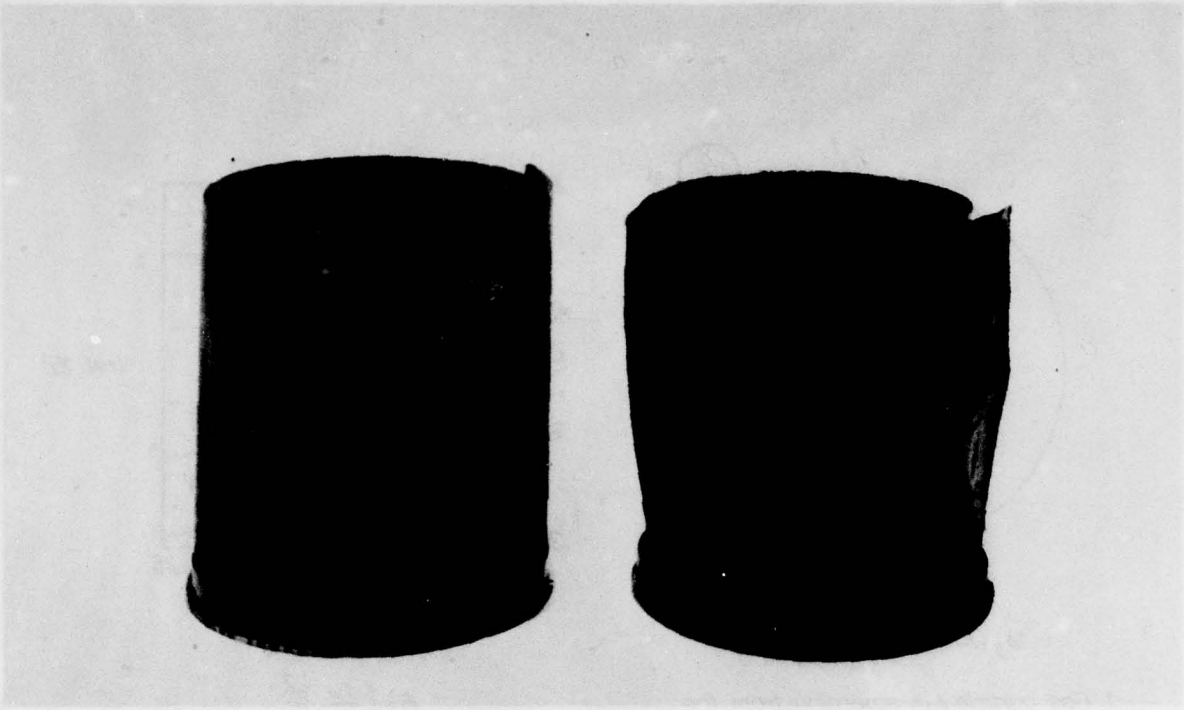

Fig. 4 Foil grain with holes to balance pressure deviations

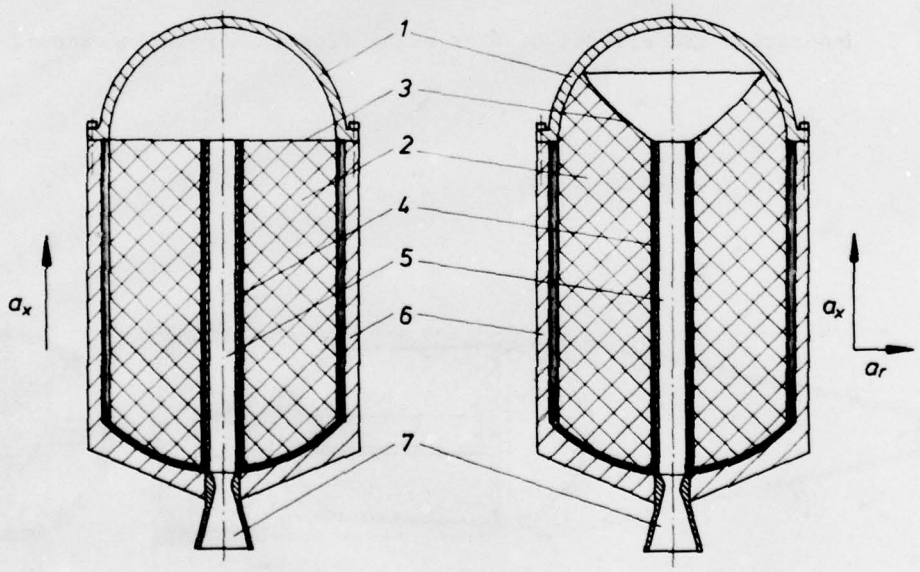

1. Forward closure
2. Propellant grain
3. Initial burning surface
4. Inhibitor
5. Blast tube
6. Supporting shell (case)
7. Nozzle

Fig. 5 Hydrodynamically supported grains for extreme acceleration (ref. 13)

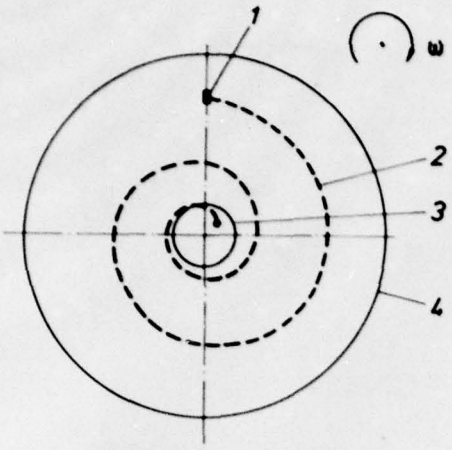

$\omega_1 (\Delta m) = \omega (case)$

$\omega_3 (\Delta m) = \omega_1 (\Delta m) \cdot \left(\frac{r_1}{r_3}\right)^2$

1. Gas particle Δm emerging from the burning surface
2. Path of Δm
3. Nozzle throat
4. Case

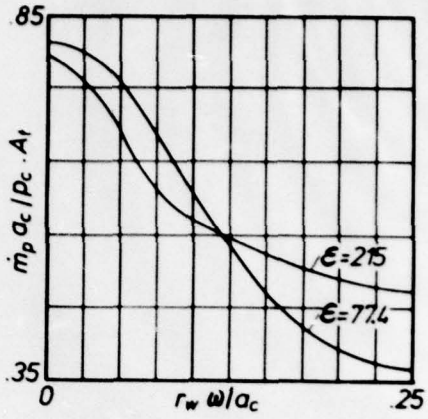

(ref. 15)

$r_w = r_4$; $r_t = r_3$

$\varepsilon = \left(\frac{r_w}{r_t}\right)^2$

Fig. 6 Generation and effects of a swirling flow in a rotating thrust chamber

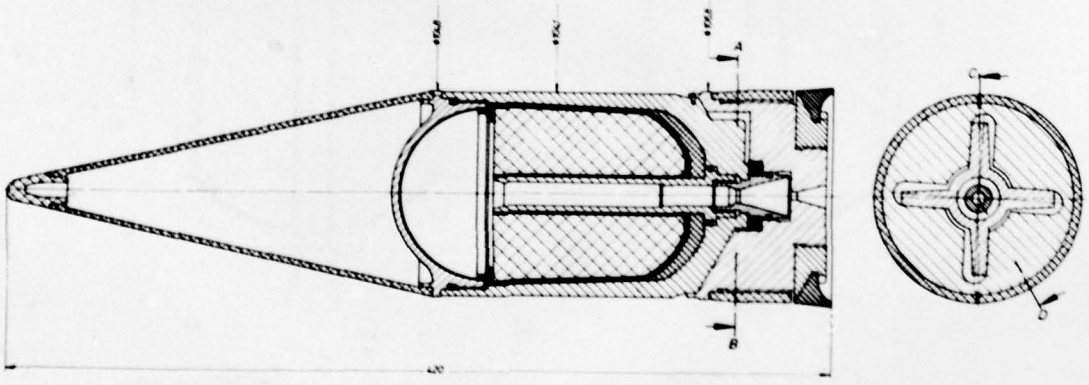

Fig. 7 Range limited, spin stabilized training projectile

DISCUSSION

M.Barrere, ONERA, Fr

Did you consider the case of aluminised propellant? In particular did you consider the losses due to the presence of aluminium oxide particles in the gas phase? For example the particle size increase with rotation, the velocity lag of the particles and the general rotating effect in a two phase flow are noteworthy.

Author's Reply

We did not consider an aluminium loaded propellant but confined ourselves to an ammonium perchlorate filled double base propellant in order to avoid problems you have pointed out.

PROPELLANT IGNITER DEVELOPMENT PROBLEMS

by

Hans Florin
Dynamit Nobel AG, ES-Z
D-5210 Troisdorf
Germany

SUMMARY

Design description of igniters for propelling charges. The light artillery rocket and anti-submarine training rocket serve as examples of the electric and internal ballistics data of igniters.

Special attention will be paid to the corresponding safety requirements. The mechanical and electrostatic safety is covered in connection with the general environmental compatibility.

In conclusion, there is a report on some EMC tests of igniters.

1. INTRODUCTION

This presentation describes the development problems with igniters of solid propellants using the Light Artillery Rocket and Anti-Submarine Training Rocket as examples.

The Light Artillery Rocket - hereinafter referred to as LAR - is used in the "110 SF rocket launcher" weapon system, a development by the Federal Republic of Germany. This weapon system is capable of launching various rockets to engage area targets.

The design of the rocket motor is shown in Fig. 1. It does not show all details, but only the major items which are of interest in this connection.
The motor casing (1) is made of glass-fibre-reinforced plastic. The propelling charge (2) is a double-base solid propellant and structured as a star configuration propellant. The solid propellant is retained by means of a spring (3). The igniter (4) is located in the front section of the rocket motor opposite the nozzle side.

The Anti-Submarine Training Rocket - hereinafter abbreviated as ASTR - is used to represent the "375 mm Anti-Submarine Rocket", which is in the inventory of the German Navy. The ASTR training rocket, like the operational rocket, must be capable of being fired at two different ranges, e. g. 1020 m and 1660 m, and leave a colour mark in the water of the target area.

Fig. 2 shows the design of the rocket motor in its essential components. The complete rocket motor is composed of an outer motor, main motor (1) and inner motor, the auxiliary motor (2). The combustion chambers are formed by two concentrically arranged metal tubes. The propelling charge (3) of the main motor consists of a tubular foil-type propellant. The propelling charge (4) of the auxiliary motor is designed as a star configuration propellant. Both propelling charges consist of double-based solid propellant.

For the short range, the rocket is propelled only by the main motor and for the long range by both motors. Accordingly, each motor is ignited by a separate igniter.
The two identical igniters (5) are located in line along the axis of the rocket motor front section opposite the nozzle side. The flash of the front igniter for the main motor passes through oblique ports (6) and into the outer annular combustion chamber.

2. GENERAL REQUIREMENTS FOR IGNITERS

The development of igniters is still an empirical matter. In spite of the different requirements, there are, however, some fundamental principles which must be taken into consideration when defining propellant igniters.

For ignition, the temperature of the propellant surface must be increased above the spontaneous ignition temperature. This heating is accomplished by means of heat transfer through convection, by radiation and impact of the hot particles onto the surface. During ignition time, the combustion chamber pressure must be increased beyond the minimum pressure necessary for stable burning.

Furthermore, the time sequence must be taken into consideration. A certain period of time is required for ignition, during which the outer heating must be continued because heat transfer will otherwise remove more heat from the propellant surface than is supplied by exothermic reactions.

For optimum ignition, the proper interaction of "temperature" and "pressure" as well as the time sequence are of significance.

Fig. 3 illustrates the conditions of the ignition process by means of the combustion chamber gas pressure which is plotted as a function of time.

In Fig. 3a, the gas pressure is sufficiently high, but the effective period too short. Fig. 3c shows the opposite situation with sufficiently long effective period but insuf-

ficient gas pressure.

In curves 1, 2 and 3 of Fig. 3b, the effective periods are long enough and the gas pressure is high enough such that the propellant can be ignited.
The solid lines more or less indicate the gas pressure generated by the igniter alone, while the dotted lines represent the overall gas pressure including the portions applied by the propelling charge.

In curve 1, the ignition is too quick, thereby leading to an undesirable pressure peak, whereas the ignition in curve 3 is too slow, which results in an unstable situation and consequently hangfires, "sputtering" or possibly failures-to-fire.

Curve 2 represents the ideal case of a steady pressure transition to the stable situation.

Fig. 4 once more shows the ideal case in order to define the terms used. The ignition response time is the duration between application of the electrical ignition voltage and the achievement of 10 % of the maximum gas pressure in the combustion chamber or a ballistic pressure vessel.

The ignition time is defined as the duration of the pressure rise from 10 % to 90 % of the maximum gas pressure in the combustion chamber or the ballistic pressure vessel.
This ignition time is reciprocally contained in the rate of the pressure rise, a quantity often used in the definition of the propellant igniters.

3. LAR PROPELLANT IGNITERS

The LAR propellant igniter must ignite a star configuration propellant. For propellants with lateral burning, it is expedient to place the igniter in the front section of the combustion chamber in order to cover the propelling charge with the hot combustion products.
Consequently, the igniter was located opposite the nozzle side (see Fig. 1).
The spontaneous ignition temperature of the double-base propellant used is comparatively low such that the ignition is not particularly difficult as far as reaching the necessary temperature is concerned. Because of the high pressure limit of double-base propellants, gas pressures of more than 30 bar will, however, be necessary.

For a scheduled combustion chamber pressure of appr. 100 bar, the ignition pressure should be in the order of appr. 30 to 45 bar.

For a rocket of this size, an ignition time of appr. 40 ms - as defined in Fig. 4 - seems to be appropriate. This requires a rate of pressure increase of appr. 1000 bar/s.
Thus, the requirements for this new igniter were defined with the following data (see Fig. 5):

ignition temperature	:	$> 2000^{o}$ k (if possible)
ignition pressure	:	appr. 30 to 45 bar
rate of pressure rise	:	appr. 1000 bar/s
ignition response time	:	$\leq$ 60 ms

Fig. 6 shows a photography of the igniter used for this purpose. Its design is shown in Figs. 7a, 7b and 7c. It consists of the metal can (1), an axial opening for the cable passage from the rocket head to the rocket tail section.

The igniter surface facing the propelling charge for the most part consists of a plastic disc of polyethylene (2), which is ejected by the gas pressure developed during the ignition and allows the ignition flash to reach the propelling charge.
Fig. 7b shows the other design areas. Two primary igniters (3) are retained in this position by a metal clamp (6) with the effect of a spring.
The two electric primary igniters are connected in parallel through cable terminal connectors (4). The largest part of the interior volume is taken up by the pyrotechnic igniter mixture (5). The igniter mixture is spring-mounted in a dense packing by means of a polyethylene foam disc (7) such that the individual pellets (5) of the igniter mixture cannot move in the can.

The design of the primary igniter is shown in Fig. 8. A pyrotechnic igniter mixture (2) with an axial port (5) is located in the lower section of a completely sealed aluminum cap (1). An electric squib (3), which is welded to the electrical leads is located above the igniter mixture.
The primary igniter is sealed tightly by crimping the metal capsule over a plastic plug (4). The axial port (5) in the igniter mixture causes the bottom of the primary igniter to tear up immediately after ignition of the squib. The ignition response time of the primary igniter is therefore practically determined by the squib alone.

4. INTERNAL BALLISTIC DATA AND MECHANICAL ENVIRONMENTAL COMPATIBILITY

The most important characteristics of a propellant igniter are its internal ballistics parameters. They are especially determined by the pyrotechnic igniter mixture.

Based on earlier experience, the following composition was used during the development of the propellant igniter for the LAR (see Fig. 9, upper part):

Pb_3O_4 43 %

$KClO_4$	17 %
Si	26 %
nitrocellulose (binder)	13 %
polyethylene (casing)	1 %

Pb_3O_4, $KClO_4$ and Si are processed with nitrocellulose as a binder to form a granular material.
In order to achieve the proper burning rate and the resulting pressure increase rate, a grain size of 2.5 to 5 mm diameter had to be chosen.
To increase the abrasion resistance, these grains were provided with a polyethylene coating such that grain configuration is maintained even after the mechanical environmental loads of the Jolt, 5 Foot Drop, 40 Foot Drop and transportation-vibration tests, a condition that is required to ensure uniformity of the internal ballistics parameters.

The lower part of Fig. 9 shows some important thermodynamic parameters of the igniter mixture. The values have been calculated in accordance with the chemical equilibrium thermodynamics method.
Typical values of the parameters obtained with this igniter mixture in the ballistic pressure vessel are shown in the following Fig. 10 for extreme temperatures. The mean values determined from a large number of measurements are shown as spread bars.
The propellant igniter with this mixture was initially able to withstand the aforementioned mechanical environmental loads such that it was possible to start manufacturing. However, certain incidents cast doubts on the handling safety and required renewed tests concerning the mechanical strength. Surprisingly, these tests showed that the specific design of the rocket, e. g. retention of the propelling charge by means of a spring, was a mechanical source of danger. As a result of this design (see Fig. 1), the retaining spring was severely compressed by the inertia of the propellant mass when the rocket or rocket motor dropped with the nose down. The air surrounding the igniter is then compressed to such a degree that the can is indented and there is a danger of mechanical ignition of the igniter mixture. It took very comprehensive tests in order to first determine to what extent the igniter mixture used was in fact the cause of unintentional ignitions as a result of its friction and impact sensitivity, although it had proved successful in the preceding qualification test using the normal sampling sizes.

The probability of an unintentional ignition of the propellant igniters was measured in a mechanical drop test from 80 cm height in the tup.
In fact, 21.000 (!) drop tests were performed and the ignition rate determined was 1.5 °/oo.

On the one hand, the ignition rate is so small that it could have been discovered only coincidentally during the development and final qualification tests; on the other hand, it had to be considered as being too high from a safety point of view.
Initially, attempts were made to reduce the sensitivity to friction and impact of this igniter mixture. This handling safety obtained in this manner was demonstrated in drop tests with rocket motors fitted with propellant dummies, because this was the easier method to simulate realistic conditions.
6000 (!) drop tests with rocket motors from a height of 80 cm were performed without any unintentional ignition.
Furthermore, drop tests were performed with rocket motors packed in containers from heights of up to 5 m without any unintentional ignitions.
In order to determine the statistical reliability of this handling safety, the probability of ignition as a function of dropping height was also determined in drop tests with propellant igniters. Fig. 11 shows the comparison between the igniter mixtures without graphite (measured values shown as circles) and with graphite (measured values are shown as crosses).
In this diagram, a standardized Gaussian distribution is shown with the curve. The ignition rate of the conventional igniter mixture approximately reflects the Gaussian distribution, whereas the ignition rate for the graphite-coated mixture considerably deviated from the Gaussian distribution. While it is recognizable that the graphite-coated mixture has a distinctly better handling safety because there is no Gaussian distribution, no statistically reliable safety value can be given for 0.8 m dropping height. The reason for the non-Gaussian distribution however was not studied and a decision was made in favour of a completely different igniter mixture.
This mixture consists of amorphous boron and potassium nitrate with the proportions shown in Fig. 12. The binder is a mixture of Adiprene (a plasto-elastic intermediate plastic product of linear polyurethane) and Moca (3.3' - diamino - 4.4' - dichlorine - diphenylmethane).
The igniter mixture manufactured from these substances has a completely different structure and consists of pressed pellets of a height and diameter of appr. 3.5 mm.
In manufacturing this igniter mixture, boron and potassium nitrate are processed with the binder to form a more or less granular material. This material is prehardened, brought to a specific grain size of 0.15 - 1 mm by grinding and screening and subsequently pressed into pellets at high pressure.

Fig. 13 shows the calculated thermodynamic parameters of this igniter mixture.
For comparison, the data of the earlier igniter mixture are listed again.

The combustion temperature and particularly the absolute enthalpy for the B/KNO_3 igniter mixture are higher than with the $Si/Pb_3O_4/KClO_4$ igniter mixture. The calculated values are quite accurate. A spectroscopic measurement of the combustion temperature showed that the values were in close agreement.

In the ballistic pressure vessel, the two igniter mixtures have considerable differences.

At a charge density of 0.02 g/cm^3 (2.8 g in 140 ml), the maximum pressures for B/KNO_3 are appr. 60 bar as against appr. 30 bar with $Si/Pb_3O_4/KClO_4$. The difference between the igniter mixtures is also evidenced by relative quickness in Fig. 14 which shows the advantages of the B/KNO_3 igniter mixture.

A valuable, even if only qualitative,insight into the burning processes of both mixtures is provided by a film of the igniter flash with unrestrained burning of the propellant igniters. The following series (Figs. 15 - 18) shows sections of the process photographed at 5000 frames per second after 20 ms, 80 ms, 200 ms, 320 ms counting from the application of the electric inition voltage.
The beginning of the expanding flash (after 20 ms) is earlier in the case of the B/KNO_3 mixture. After 80 ms, the flash has expanded to a considerably greater extent and has almost reached the size of the full flash pattern of the $Si/Pb_3O_4/KClO_4$ igniter mixture. After 200 ms, B/KNO_3 has fully ignited and from this point onwards, the degressive effect is stronger than with $Si/Pb_3O_4/KClO_4$, which is in conformance with the degressive behaviour of the terminal phase as already shown in the relative quickness.

The purpose of this igniter mixture was to improve the mechanical handling safety. The pellets therefore had to be made as abrasion- and break-proof as possible, while at the same time the previous internal ballistics parameters were of course not to be degraded but, if possible, improved. This optimization required very extensive studies, in which the influencing factors of the

igniter mixture
charge quantity
binder content
pellet size
grain size of components

as well as the thermal and mechanical environmental influences had to be determined.

Within the scope of this paper, only extracts of the most important test results can be given.

Because of the absolute enthalpy of the boron/potassium nitrate igniter mixture, which has been increased by a factor of 1.6, and the double amount of the maximum pressures achieved in the ballistic pressure vessel, it was possible to use a charge quantity reduced to below 20 g as against 32 g previously. In order to substantiate the expected theoretical values, the ignition response times, maximum pressures and rates of pressure increase were measured as a function of the charge quantity of the igniters. The following Figs. 19 - 21 show the test results. They show the spread zones in which the individual test data are located. The red and blue limiting lines at the same time represent the temperature dependence, with the red lines marking the limit values at appr. 50° C and the blue lines the limit values at appr. -30° C.

For comparison, the values of the previous $Si/Pb_3O_4/KClO_4$ igniter mixture have again been plotted in these diagrams. The ignition response time (see Fig. 19) of the new igniter mixture is considerably shorter and, even at the minimum quantity of 12 g, below the response of the old igniter mixture.
The maximum pressures (see Fig. 20) are about twice as high and therefore require a considerable reduction in the original charge quantity from 32 g to values below 20 g.

The rates of pressure increase are higher by a factor of appr. 1.7. The optimization of the charge quantity between 12 and 20 g should be obtained from a combination of these three diagrams in Fig. 22. The ignition response time is sufficiently good, even at the minimum charge. Perfect ignition at -40° C was demonstrated with the minimum quantity. A maximum ignition pressure should not be too low because of the relatively high pressure limit of the double-base propellant and should not be too high either,because of the pressure peaks that are liable to happen. In order to keep the ignition as steady as possible, the rate of pressure increase should not be considerably below 1000 bar/s. This resulted in the optimum charge quantity of 16 g for boron/potassium nitrate.

The optimization of the binder content was of great importance. Due to the absolutely necessary handling safety, the objective was to achieve a high binder content to ensure resistance to abrasion and pressure without degrading the ballistic parameters of the igniter mixtures. These measurements were made with 2.8 g igniter mixture each in a small test pressure vessel. The values obtained in this pressure vessel are standardized relative to the conditions in the test pressure vessel to measure propellant igniters as shown in Fig. 23 such that they are comparable with the values shown earlier.
The most important parameters are again summarized in a diagram. Furthermore, this diagram shows the influences of the fine grain portion recycled in the manufacturing process.

Since the fine grain portion must also be used for economical considerations, the binder content could not be increased beyond 5.6 %, above all because of the ignition response time. Since the influence is less below 5.6 % and, on the other hand, this content ensures good abrasion and pressure resistance of the igniter pellets, the optimum had

been reached.

Finally, Fig. 24 also illustrates the dependence of the pellet size for a constant cross-section and variable height of 2.5 to 3.5 mm.

The measurement of the ballistics data was made with 18 g igniter mixture in the neighbourhood of the expected optimum charge quantity at the extreme temperatures of -30^{o} C and $+50^{o}$ C.
The measurements in the ballistic pressure vessel were complemented by test stand measurements in the rocket motor.

In the case of the LAR rocket motor igniter, the boron/potassium nitrate igniter mixture proved very favourable as to its mechanical resistance to environmental influences.

The ballistics data measured after the shock, tumbling and vibration tests hardly differ from the values shown earlier.

A great deal of importance was attached to the demonstration of adequate handling safety. The fulfilment of this requirement was demonstrated in the drop tests from 12 m height.

The drop tests were conducted with propellant igniters in falling tups and, because of the special design characteristic described above, in rocket motors with propellant dummies. At 12 m dropping height, no ignition occurred. The determination of handling safety with statistical reliability by measuring the ignition rate as a function of dropping height was not possible because of the limited height of the tup. However, an improvement in the handling safety is clearly demonstrated even without this reliability measurement when making a comparison with the $Si/Pb_3O_4/KClO_4$ igniter mixture which has an ignition rate of 85 % at 6 m dropping height.

5. ASTR PROPELLANT IGNITER

After the presentation, we now return to the propellant igniter of the anti-submarine training rocket.
Because of the lateral burning of the propelling charges of both the main and auxiliary motor, both propellant igniters are located in the front section of the motor (see Fig. 2).
The ignition of the double-base propellant is a little more difficult for the outer main motor, because of the complicated passage of the ignition flash through the oblique ports. The peculiarity of the ignition of this rocket propellant was the requirement that both motors, if possible, should be ignited simultaneously with identical propellant igniters. The ignition response time, because of the initially scheduled electronic nose fuse to initiate a detonating charge, was not to be below 15 ms.

Due to the concentrically arranged motors, the propellant igniter had to be of a slender configuration as shown in Fig. 25. Fig. 26 shows the interior structure.
Because of the axial cable passage, the propellant igniter essentially consists of two concentric aluminum sleeves (1). In the lower section, a symmetrical annular arrangement accomodates four squibs (2) which are located in a plastic mount (3). The igniter mixture (4) which is covered by a celluloid cover (5) is located above the squibs. The four squibs are arranged in pairs and connected in parallel and in series and their connections are axially routed outward via supply lines (I shall discuss details in connection with the electrical parameters).
For the development, the same empirical method was used as described earlier in connection with the LAR propellant igniter. A number of different igniter mixtures were subjected to preliminary tests and in this particular case, the B/KNO_3- and $Si/Pb_3O_4/KClO_4$ mixtures described earlier proved most successful. However, I do not want to go into details at this point, because the tests did not reveal any new information. Since the ignition response time of boron/potassium nitrate is too rapid for this type of rocket, a silicon-lead oxide potassium perchlorate igniter mixture was used in the composition shown in Fig. 9. However, because of the fact that the ignition of both motors should be as steady as possible, a grain size of 0.5 to 1 mm as against the LAR mixture of 2.5 to 5 mm was necessary. Both motors are easy to ignite with a quantity of 10 g of this mixture. The time difference in the ignition of both motors is appr. 30 % of the ignition response time, which is about 40 - 60 ms for the main motor and appr. 26 - 35 ms for the auxiliary motor.
The ignition response time difference of both motors is only 4 % of the burning time of the main and auxiliary motor. This igniter mixture which did not prove sufficient handling safety in the LAR propellant igniter proved very reliable in the ASTR propellant igniter during the mechanical environmental tests. Drop tests were performed with igniters installed in rocket motors and it should be noted that not only the 1.5 m drop test required by MIL-STD 331 but also the 14 m drop test beyond the MIL-STD requirement was passed without any problem.
This is particularly due to the fact, that both igniters are mechanically protected within a solid mounting element, where they do not suffer any mechanical damage even under extreme loads.

6. ELECTRICAL PROPERTIES

Let us now take a look at the electrical parameters of the propellant igniters. The electrical parameters determine the electrical reliability on the one hand and safety against electric stray currents, electrostatic discharges and electromagnetic radiation, on the other hand.

Fig. 27 lists the electrical parameters of both propellant igniters.

Relatively sensitive bridgewire fuseheads with a bridgewire resistance of 1.2 to 1.4 are used in both cases as primary elements.
The electric ignition currents of the LAR and ASTR firing control units are considerably higher than the all-fire currents listed. The probabilities of ignition are above 99.9999 %.
Due to the parallel connection, the stray current safety of 0.46 A is too high that unintentional ignition can be excluded under the prevailing conditions.

7. ELECTROSTATIC SAFETY

In order to evaluate the electrostatic safety, Fig. 28 shows the different theoretically possible types of discharge for an electrostatic discharge from the housing of the propellant igniter to the electric leads.

The design as such establishes a direct connection from the housing of the propellant igniter to the housing of the primary igniter. Nevertheless, it is theoretically conceivable that igniter mixture or at least abraded igniter mixture may get between both housings as a result of mechanical environmental influences such that spark breakdown through the igniter mixture cannot be excluded.
In the initially used primary igniter (see upper primary igniter in Fig. 28), in addition to the discharge onto the electric leads to the squib, there is also a theoretical possibility, although remote, of a spark breakdown through the squib head.

The electrostatic sensitivity is therefore determined by
the sensitivity of the igniter mixture (1)
the sensitivity of the igniting mixture of the squib (2)
and the sensitivity across the glow bridgewire of the squib (3).

In this connection, it should be noted whether the discharge passes through the open ends of the electric leads - (a) and (b) - or through the short-circuited ends of the electric leads (c).
Fig. 29 represents the individual sensitivity levels in the form of "no-fire" energy levels. In this representation, the requirement of MIL-STD 332 is met at the same time. The greatest electrostatic sensitivity obviously occurs in the event of a spark breakdown through the squib head. By shrinking a plastic hose over the squib head (see lower primary igniter in Fig. 28), this type of discharge has been avoided completely. In this manner, the electrostatic safety of the LAR propellant igniter was increased well beyond the requirements of MIL-STD 322.

In the case of the ASTR propellant igniter, the conditions concerning electrostatic safety, are quite different. The propellant igniter has a nominal spark gap (6). As a result of the deep embedding of the squib (2) in the plastic mount (3), the electric breakdown voltage from the outer sleeve (1) across the igniter mixture (4) onto the squibs (2) is considerably higher than the breakdown voltage at the nominal spark gap.

The electrostatic safety is therefore solely determined by the electrostatic sensitivity of the squibs through the electrical heating of the glow bridgewires.
Fig. 30 shows the sensitivity levels in the form of the "no-fire" thresholds.
The ASTR igniter thus also is electrostatically safe beyond the requirements of MIL-STD 322.

8. ELECTROMAGNETIC COMPATIBILITY

Finally, a few observations on the important characteristic of electromagnetic compatibility.
As shown in Fig. 1, the propellant igniter of the LAR motor receives its electrical ignition energy through relatively long lines of appr. 1 m in length. Since these lines are not shielded and the motor casing consists of plastic material, it is actually possible that high-frequency energy from the electromagnetic field of the radar is able to reach these lines with little attenuation and cause electric currents. However, in actual practice, this condition prevails only for the short period of time of reloading the rocket from the metallic transport and storage container into the rocket launcher.

To assess the level of danger during the period of loading, measurements of the probability of ignition were performed only with rocket motors fitted with primary igniters within the close range (immediately in front of the antennas) with high-power high-frequency transmitters operating in the cw mode in the frequency range of 0.1 MHz to 2.5 GHz. The measurements were performed with different arrangements of the lead-in wires which are appr. 1 m long:

ends of wires : terminated at 50Ω
ends of wires : short-circuited
ends of wires : open with 50Ω termination

With the first two arrangements, even the maximum achievable field strength in the aforementioned frequency range was not able to trigger any unintentional ignitions. Ignitions were caused only in the range of 100 - 200 MHz with open leads. In actual practice, however, the condition of open leads exists only for an extremely short period of time, but then the rocket is in the launcher and the leads are shielded by the metallic jacket of the launcher. Therefore, these measurements allow the conclusion that unintentional firing of the LAR is practically impossible under the existing conditions.

firing of the LAR is practically impossible under the existing conditions.

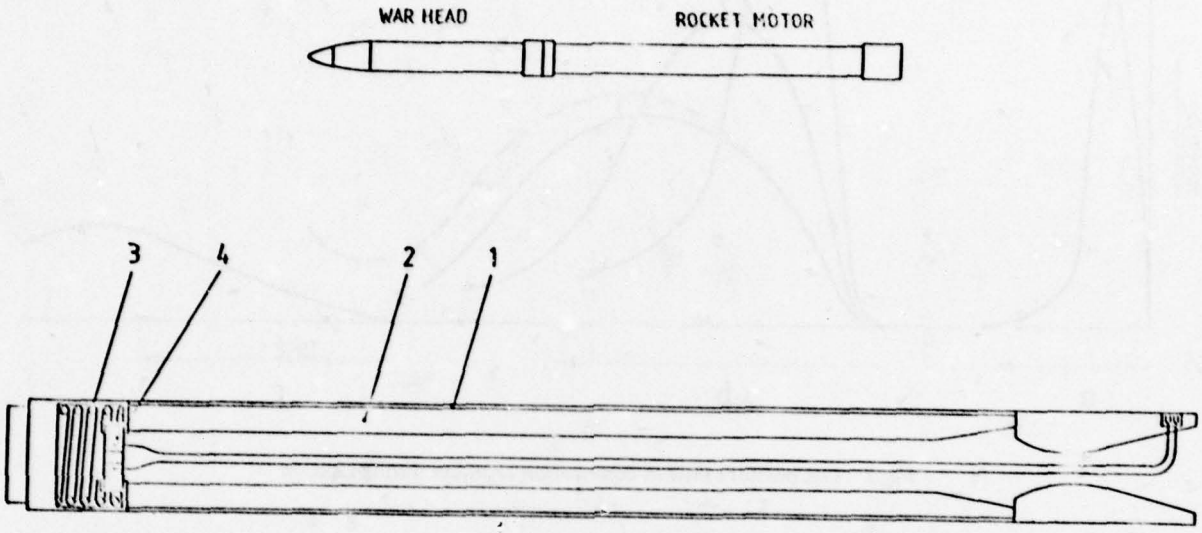

Fig.1 Light artillery rocket

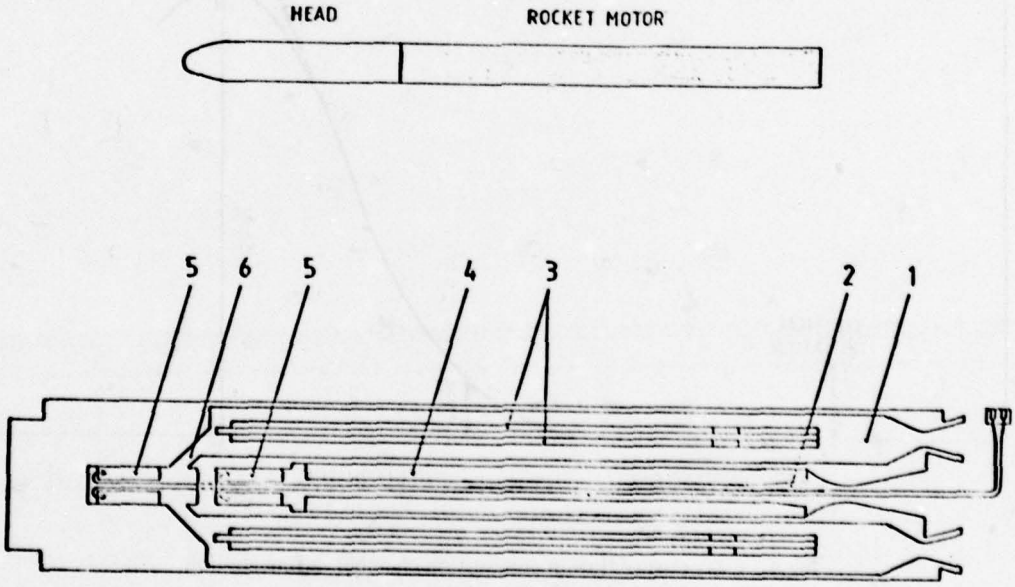

Fig.2 Anti-submarine training rocket

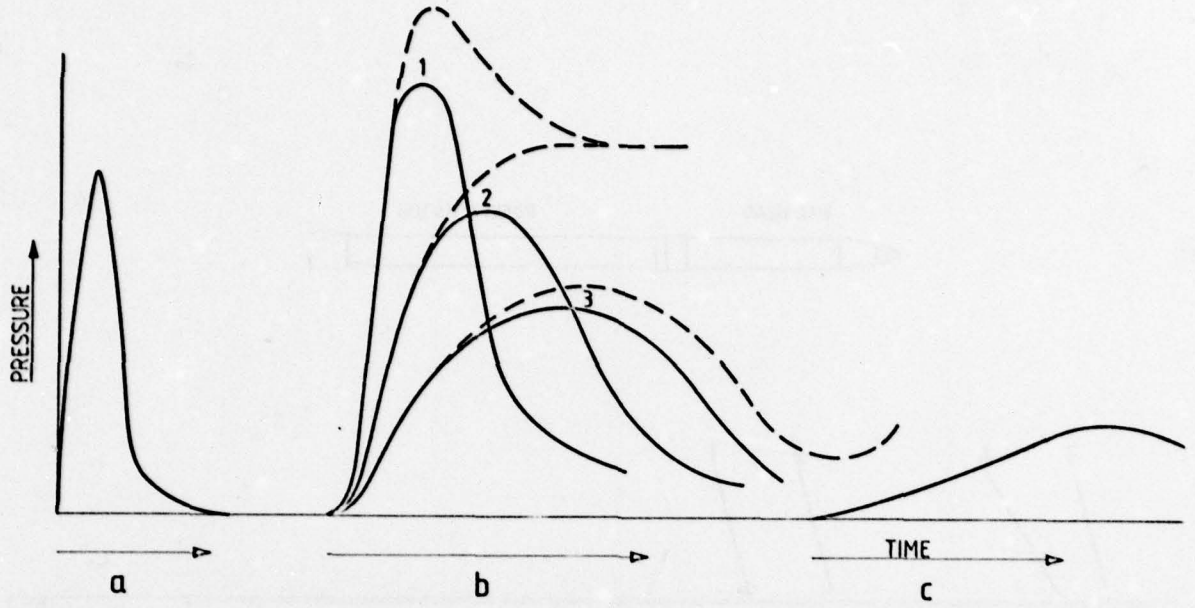

Fig.3 Gas pressure flow in combustion chamber during ignition

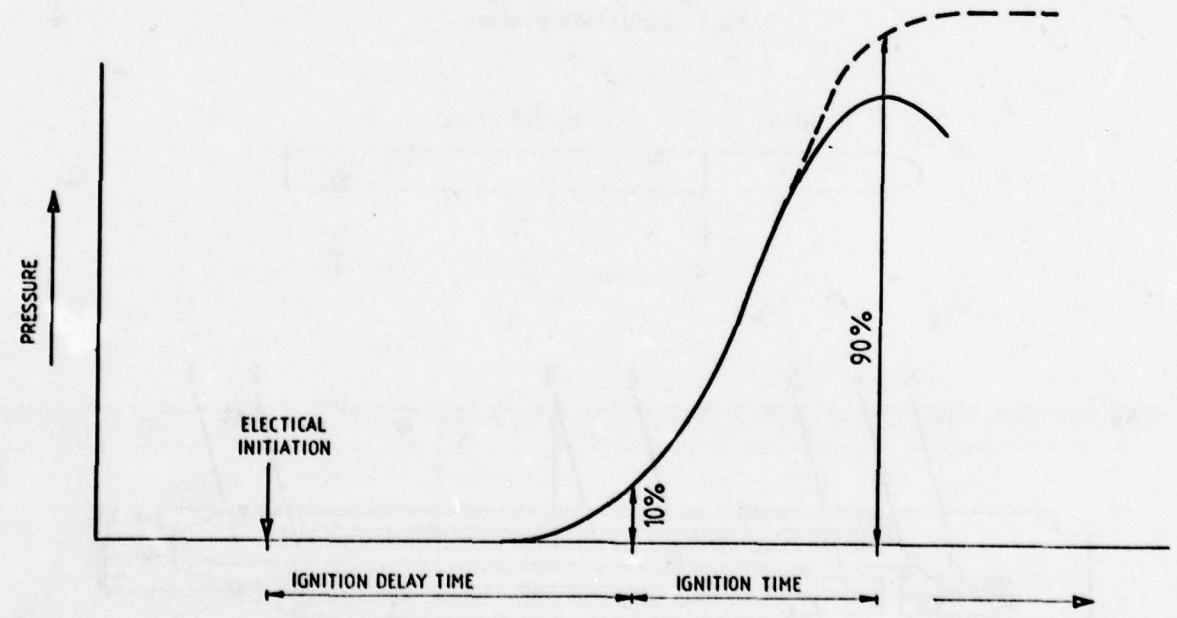

Fig.4 Gas pressure flow in combustion chamber during ignition

IGNITION TEMPERATURE	: > 2000°K
IGNITION PRESSURE	: ~ 30-45 bar
RATE OF PRESSURE INCREASE	: ~ 1000 bar/s
IGNITION DELAY TIME	: ≦ 60 ms

Fig.5 LAR-propellant igniter requirements

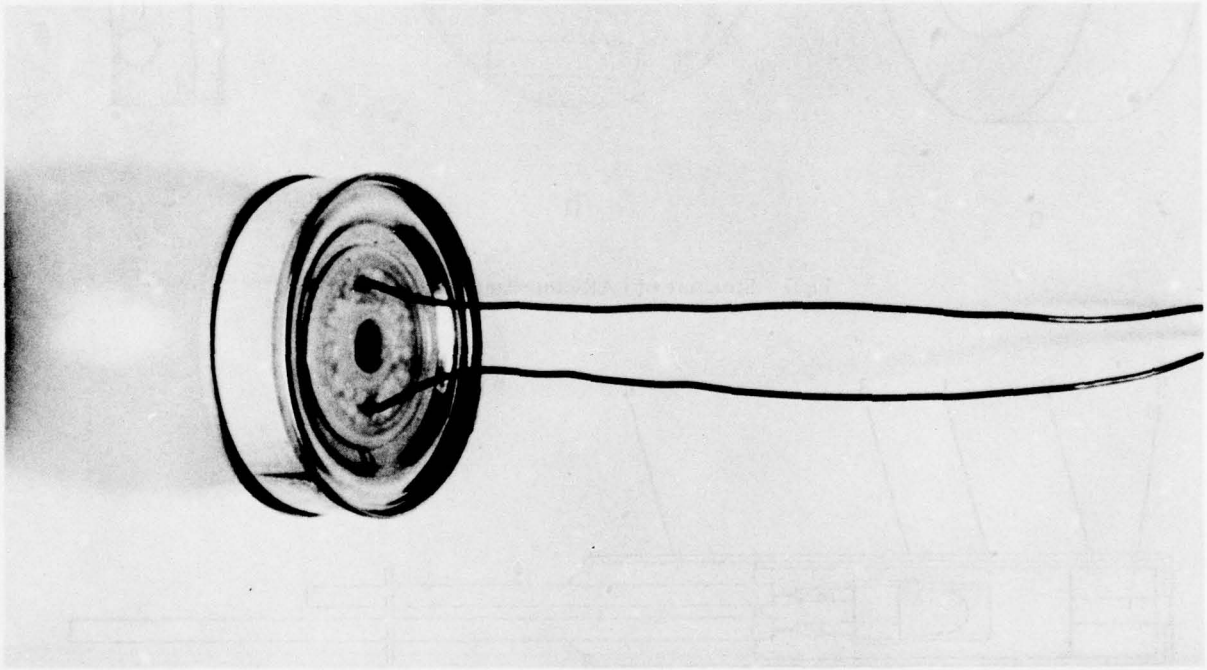

Fig.6 Photograph of LAR-propellant charge igniter

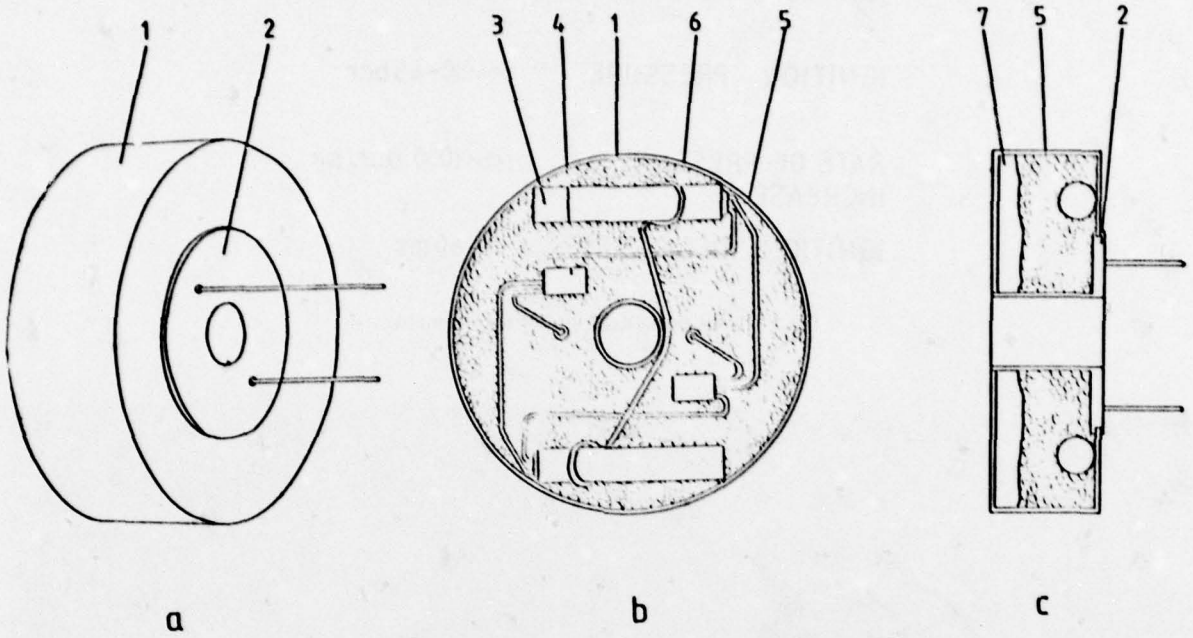

Fig.7 Structure of LAR-propellant igniter

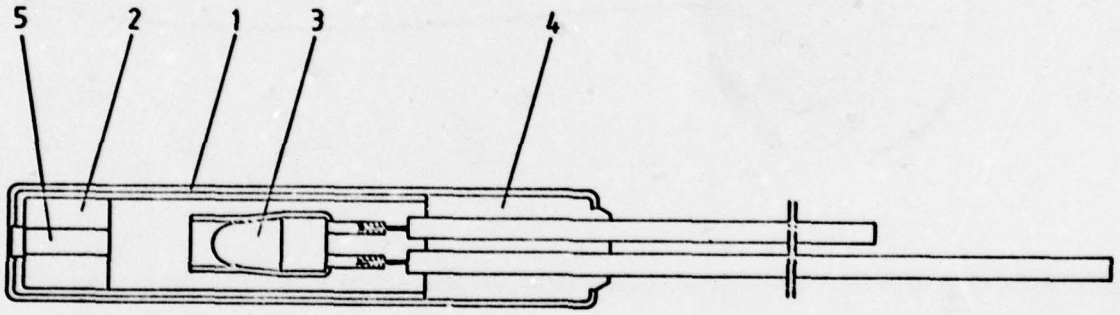

Fig.8 Primary igniter

COMPOSITION

Si	:	26 %
Pb_3O_4	:	43 %
$KClO_4$	:	17 %
NITROCELLULOSE LACQUER (BINDING AGENT)	:	13 %
POLYETHYLENE (COVER)	:	1 %

THERMODYNAMIC PARAMETERS

COMBUSTION TEMPERATURE	:	2250°K
MEAN MOLARE WEIGHT	:	56,3 g/Mol
PERCENTAGE OF CONDENSED REACTION PRODUCTS	:	20 %
ENTHALPIE	:	18.250 cal / 100 g

Fig.9 Composition of $Si/Pb_3O_4/KClO_4$-igniting charge mixture and thermodynamic parameters

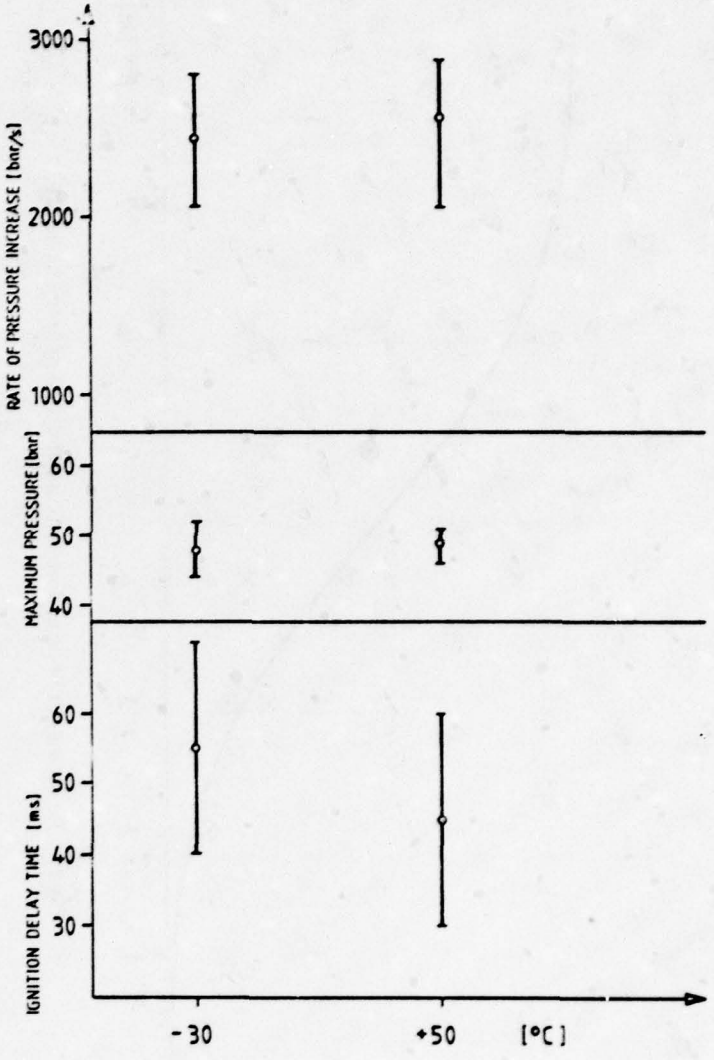

Fig.10 Ignition delay time, maximum pressure and rate of pressure increase of $Si/Pb_3O_4/KClO_4$-ignition charge mixture (LAR)

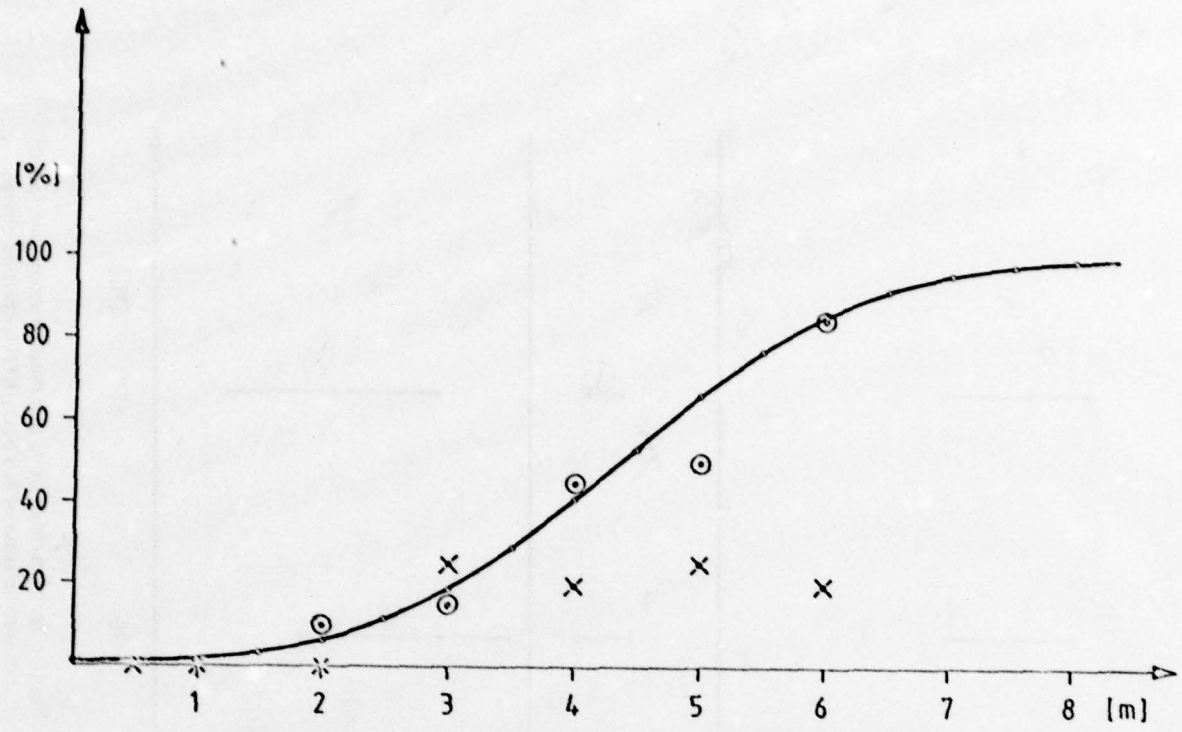

Fig.11 Probability of firing in drop tests as a function of dropping height

COMPOSITION

B(AMORPHOUS)	:	23,7 %
KNO_3	:	70,7 %
BINDING AGENT	:	5,6 %

BINDING AGENT: MIXTURE OF ADIPRENE (POLYURETHAN) AND MOCA (3,3' DIAMINO-4,4' DICHLORINE-DIPHENYL-METHANE)

Fig.12 Composition of B/KNO_3 ignition charge mixture (LAR)

	B/KNO_3	$Si/Pb_3O_4/KClO_4$
COMBUSTION TEMPERATURE	2440 °K	2250°K
MEAN MOLARE WEIGHT	37,2 g /Mol	56,3 g/Mol
PERCENTAGE OF CONDENSED REACTION PRODUCTS	25 °/o	20°/o
ENTHALPIE	29.860 $\frac{cal}{100g}$	18.250 $\frac{cal}{100g}$

Fig. 13 Thermodynamic parameters of B/KNO_3 - and $Si/Pb_3O_4/KClO_4$ -ignition charge mixture

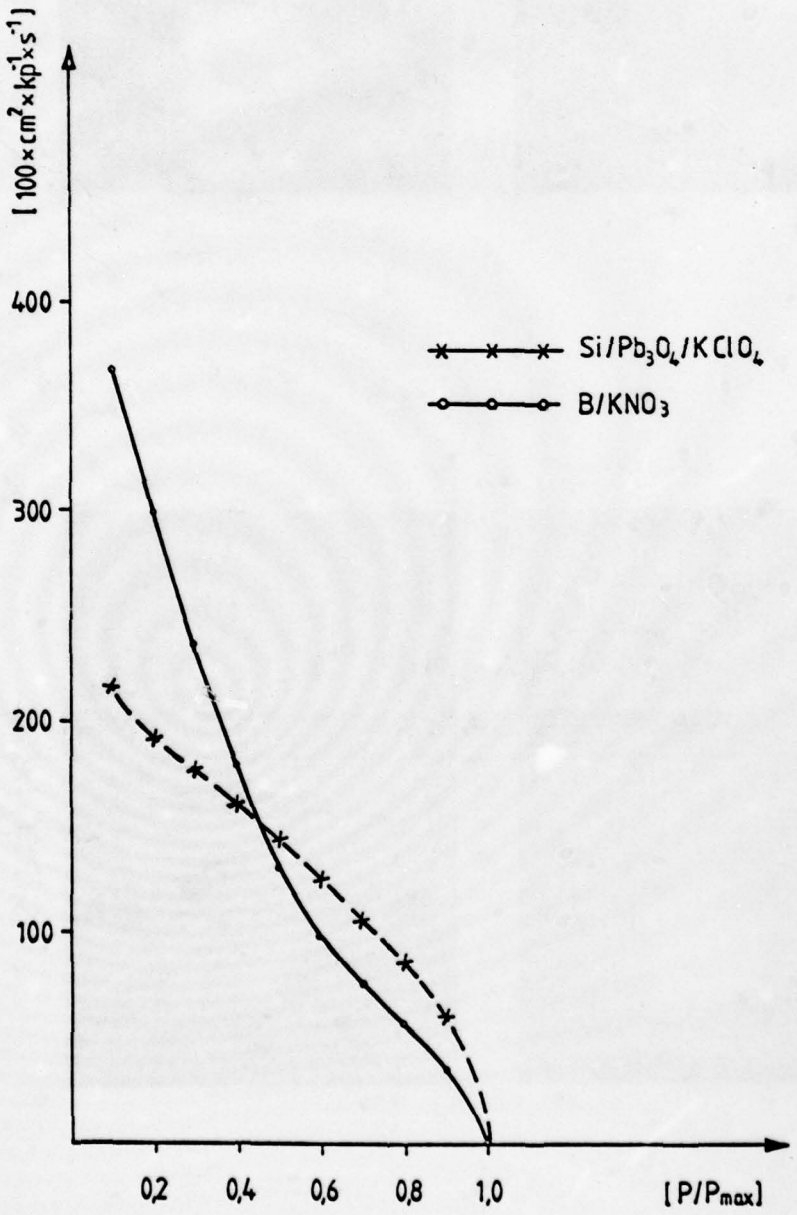

Fig. 14 Relative quickness plotted against P/P_{max}

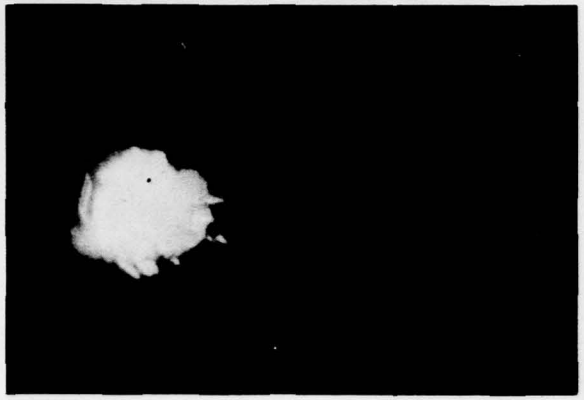

B/KNO_3

$Si/Pb_3O_4/KClO_4$

Fig.15 Flash pattern of the ignition with unrestrained burning 20 ms after electrical initiation

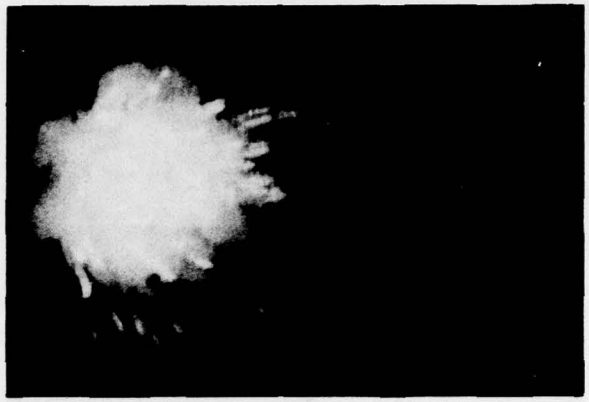

B/KNO_3

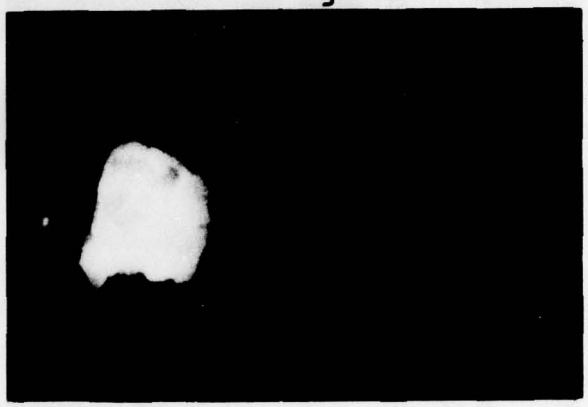

$Si/Pb_3O_4/KClO_4$

Fig.16 Flash pattern of the ignition with unrestrained burning 80 ms after electrical initiation

B/KNO_3

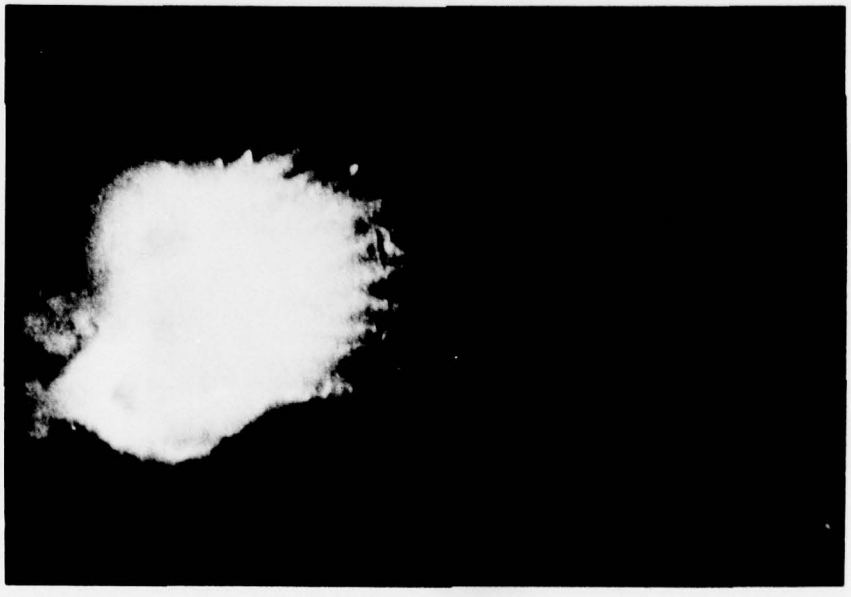

$Si/Pb_3O_4/KClO_4$

Fig. 17 Flash pattern of the ignition with unrestrained burning 200 ms after electrical initiation

B/KNO_3

Si/Pb_3O_4/$KClO_4$

Fig.18 Flash pattern of the ignition with unrestrained burning – 320 ms after electrical initiation

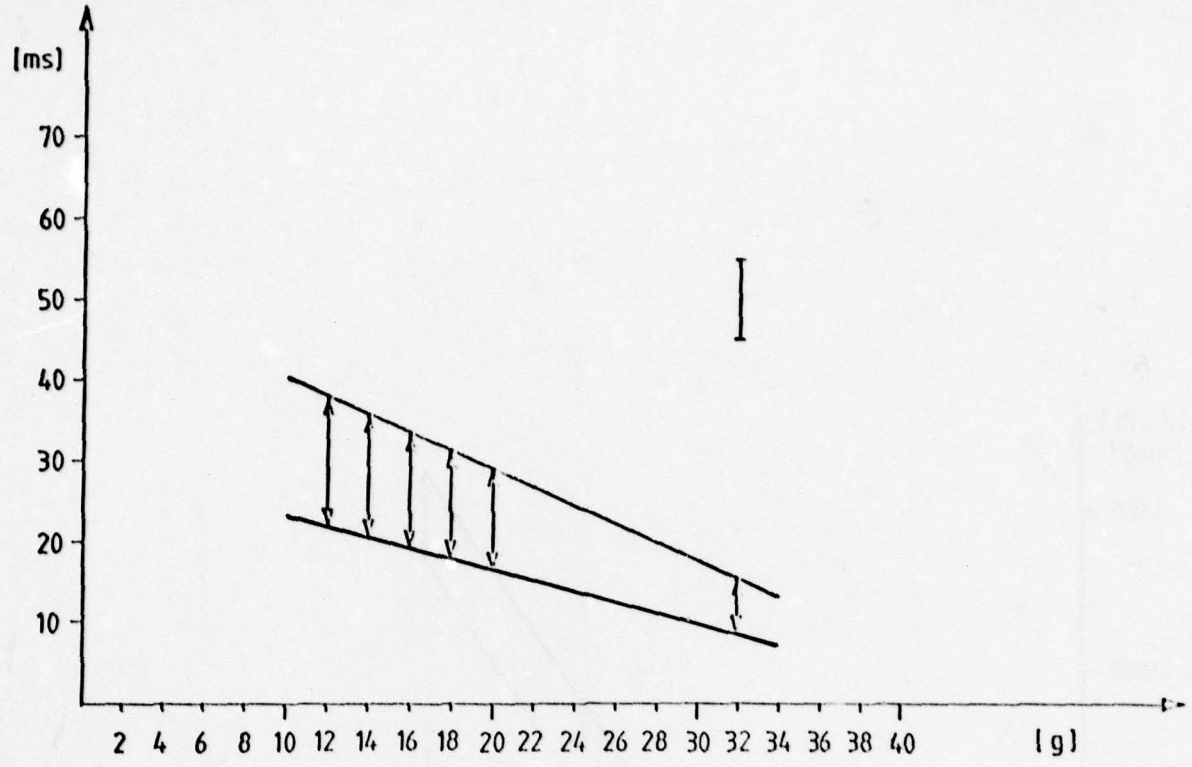

Fig.19 Ignition delay time as a function of charge weight

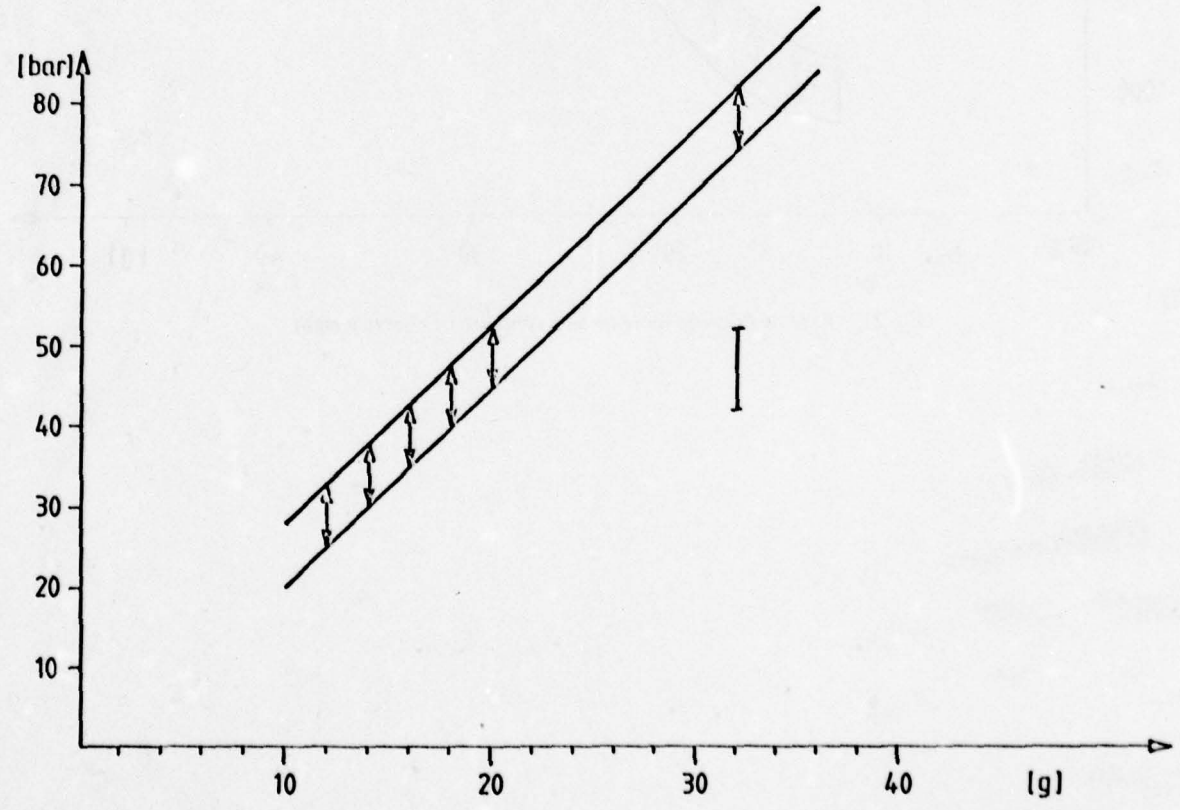

Fig.20 Maximum pressure as a function of charge weight

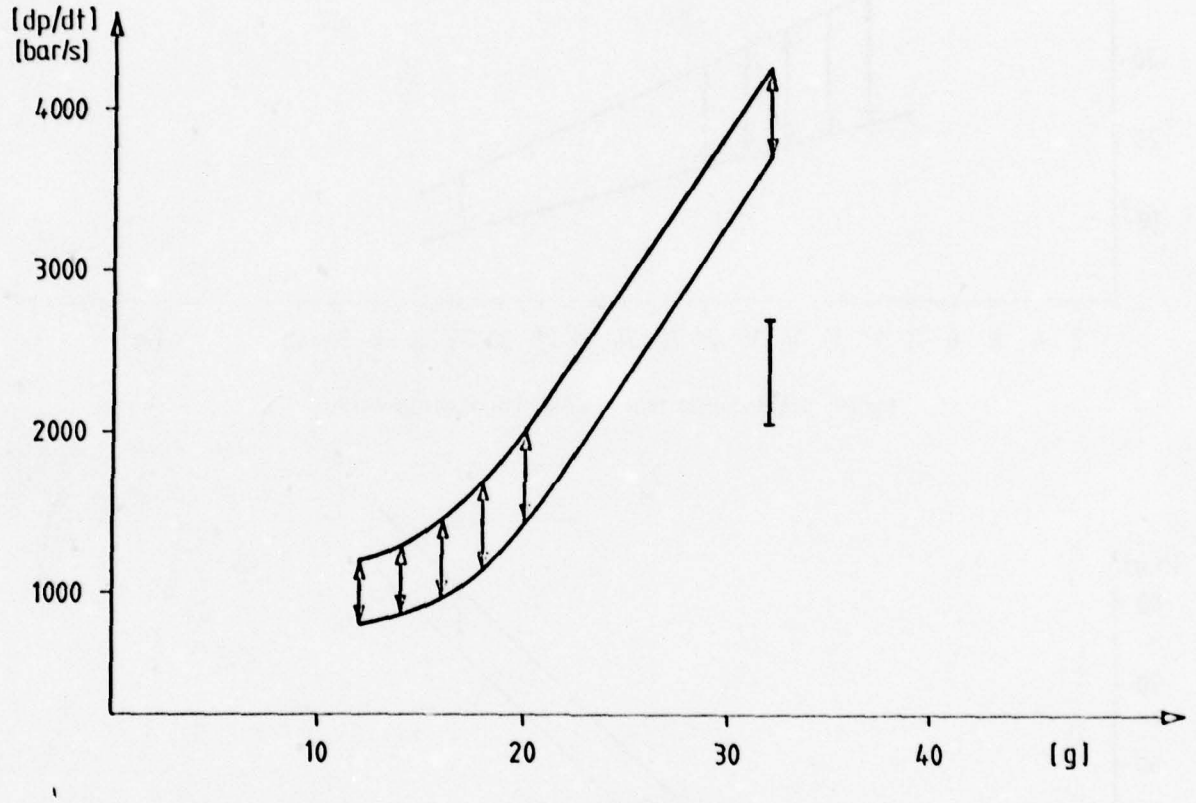

Fig. 21 Rate of pressure increase as a function of charge weight

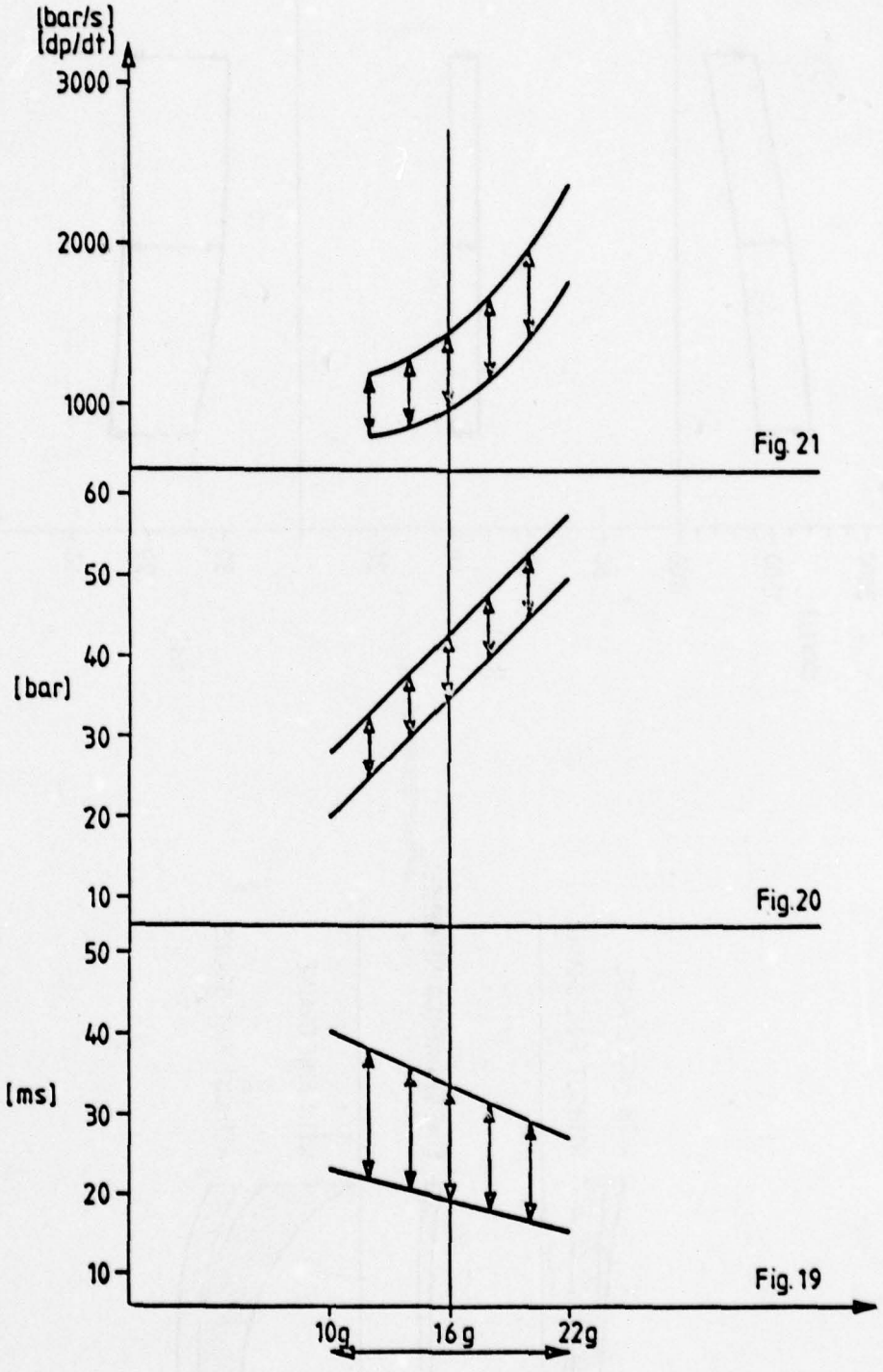

Fig.22 Ignition delay time, maximum pressure and rate of pressure increase as a function of charge weight

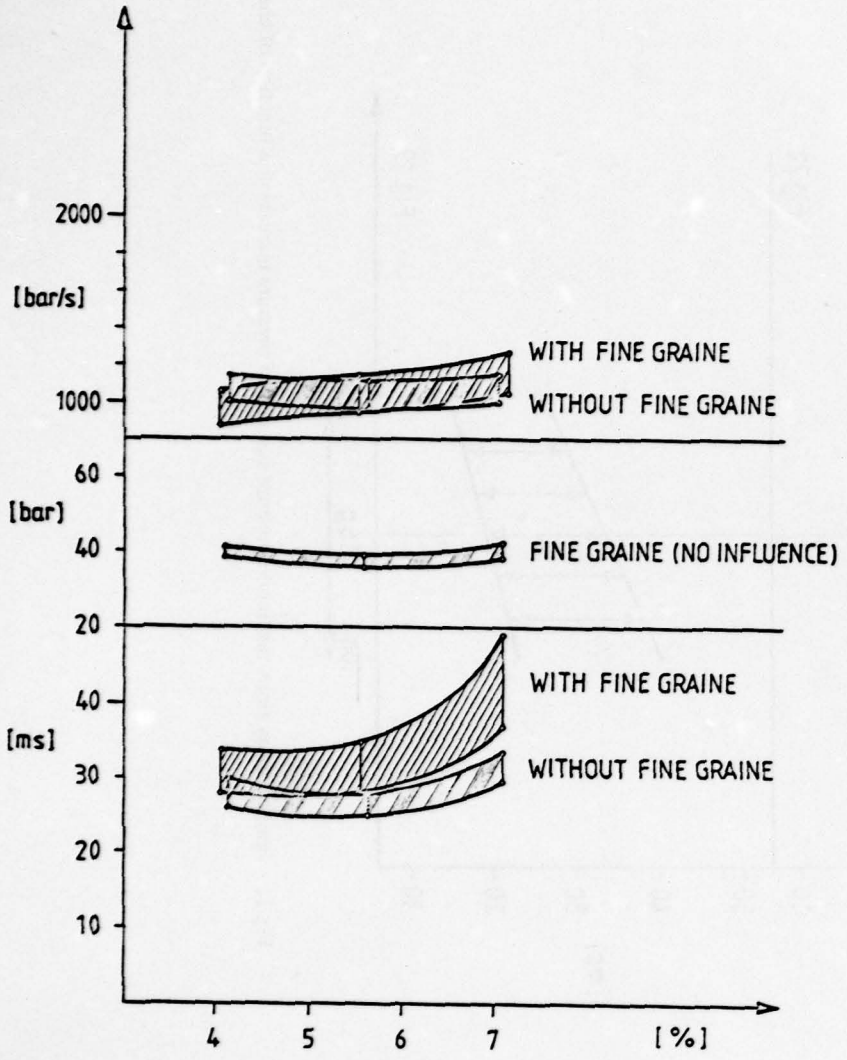

Fig.23 Ignition delay time, maximum pressure and rate of pressure increase as a function of binder-percentage, ignition charge mixture with and without fine graine

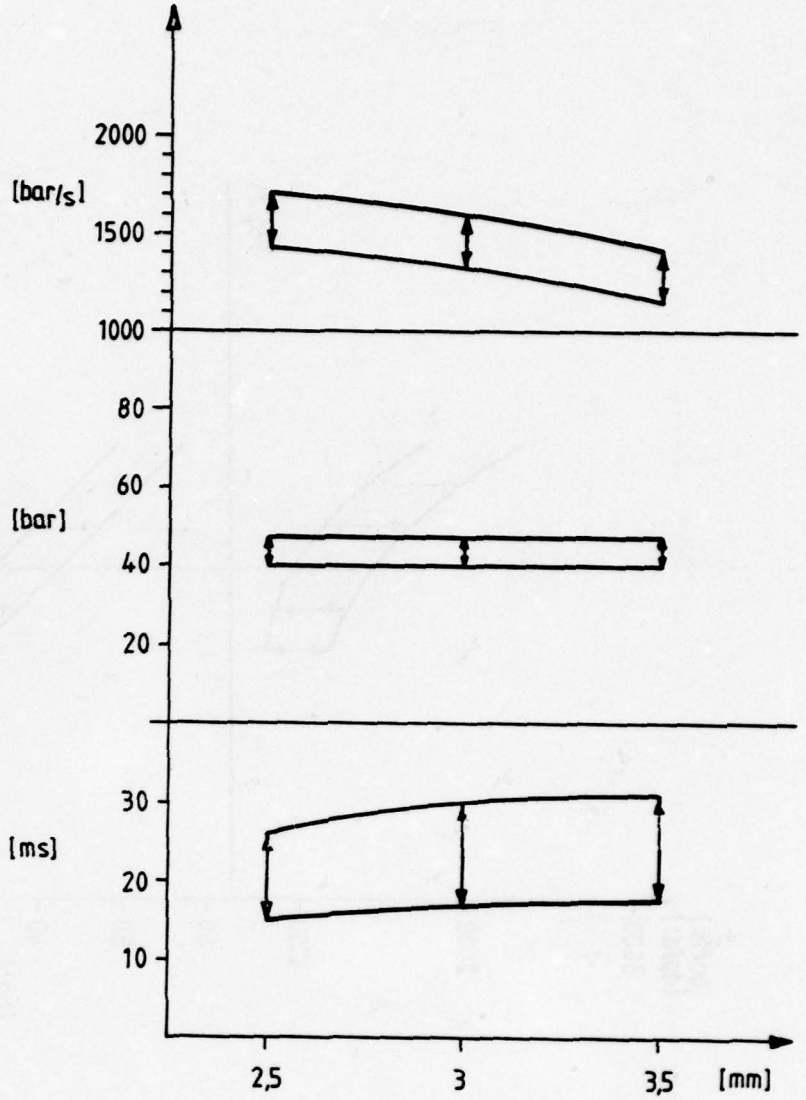

Fig.24 Ignition delay time, maximum pressure and rate of pressure increase as a function of pellet size (pellet height)

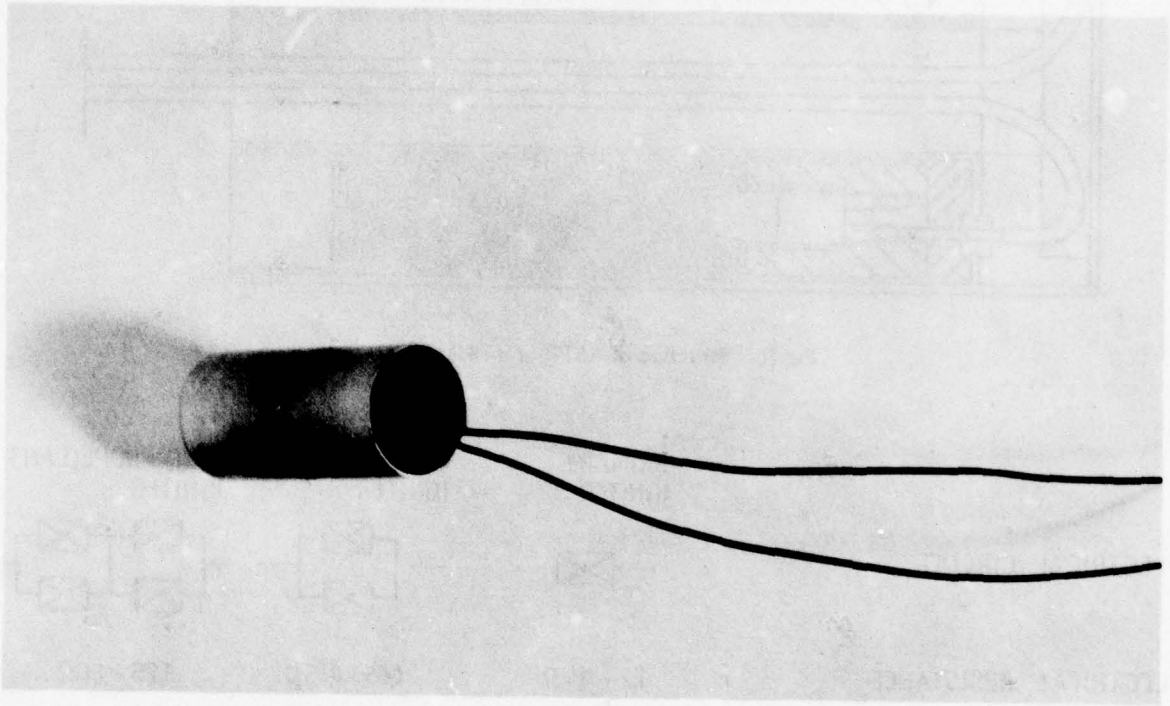

Fig.25 Photograph of ASTR-propellant charge igniter

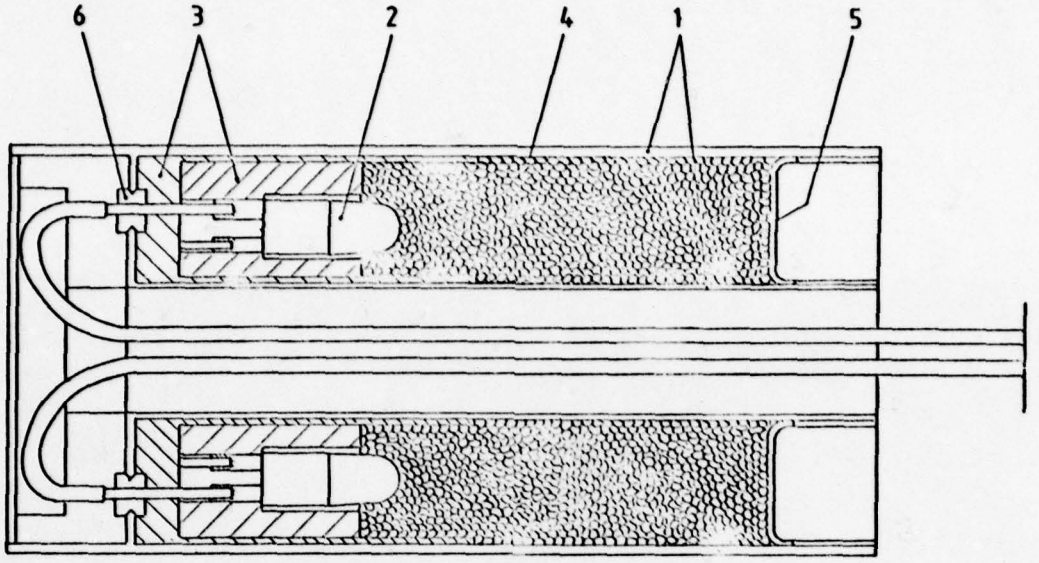

Fig.26 Structure of ASTR-propellant igniter

	PRIMARY IGNITER	LAR-PROPELLANT IGNITER	ASTR-PROPELLANT IGNITER
ELECTRICAL CIRCUIT		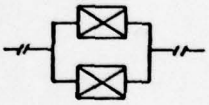	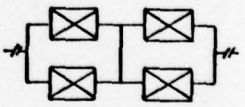
ELECTRICAL RESISTANCE	1,2 - 1,4 Ω	0,65 - 0,95 Ω	1,25 - 1,6 Ω
ALL FIRE CURRENT (99,9999% PROBABILITY)	0,35 amp.	0,76 amp.	0,76 amp.
NO FIRE CURRENT (0,0001% PROBABILITY)	0,25 amp.	0,46 amp.	0,46 amp
PROBABILITY OF IGNITION WITH LAR- OR ASTR- FIRING CURRENT	>99,9999%	≫99,9999 %	≫99,9999 %

Fig.27 Electrical properties of LAR- and ASTR-propellant igniter

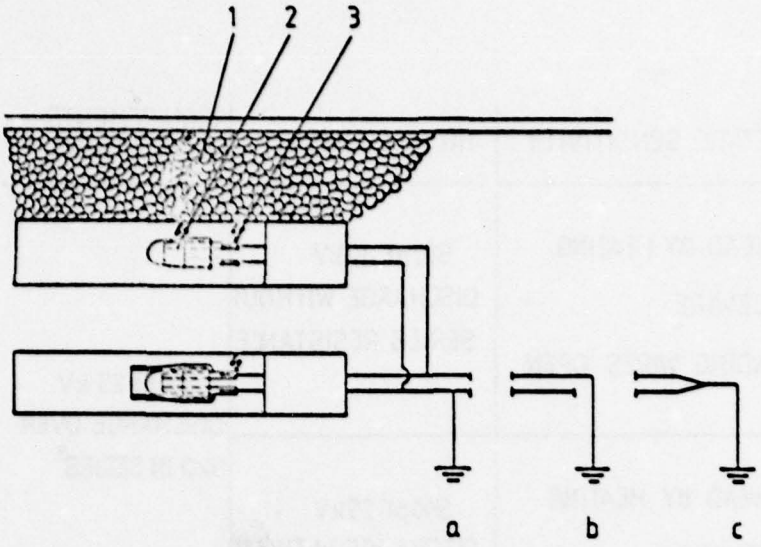

1 ELECTROSTATIC SENSITIVITY OF IGNITION CHARGE MIXTURE

2 ELECTROSTATIC SENSITIVITY OF FLASHING COMPOSITION OF FUSEHEAD

3 ELECTROSTATIC SENSITIVITY OF FUSEHEAD BY HEATING OF BRIDGEWIRE

Figure 28

ELECTROSTATIC SENSITIVITY	NO FIRE ENERGIE	REQUIREMENTS OF MIL-STD 322
OF B/KNO_3-IGNITION CHARGE MIXTURE	1000 pF 30 kV DISCHARGE OVER 1Ω IN SERIES	500 pF 25 kV DISCHARGE OVER 5 kΩ IN SERIES
OF FLASHING COMPOSITION OF FUSEHEAD	500 pF 11 kV DISCHARGE OVER 5 kΩ IN SERIES	
OF FUSEHEAD BY HEATING OF BRIDGE-WIRE WITH LEADING WIRES OPEN	500 pF 10 kV DISCHARGE WITHOUT SERIES RESISTANCE	
OF FUSEHEAD BY HEATING OF BRIDGE-WIRE WITH LEADING WIRES CLOSED	500 pF 25 kV DISCHARGE WITHOUT SERIES RESISTANCE	

Fig. 29 Electrostatic sensitivity of LAR-igniter and requirements of MIL-STD 322

ELECTROSTATIC SENSITIVITY	NO FIRE ENERGY	REQUIREMENTS OF MIL-STD 322
OF FUSEHEAD BY HEATING OF BRIDGEWIRE WITH LEADING WIRES OPEN	500 pF 10 kV DISCHARGE WITHOUT SERIES RESISTANCE	500 pF 25 kV DISCHARGE OVER 5 kΩ IN SERIES
OF FUSEHEAD BY HEATING OF BRIDGEWIRE WITH LEADING WIRES CLOSED	500 pF 25 kV DISCHARGE WITHOUT SERIES RESISTANCE	

Fig.30 Electrostatic sensitivity of ASTR-igniter and requirements of MIL-STD 322

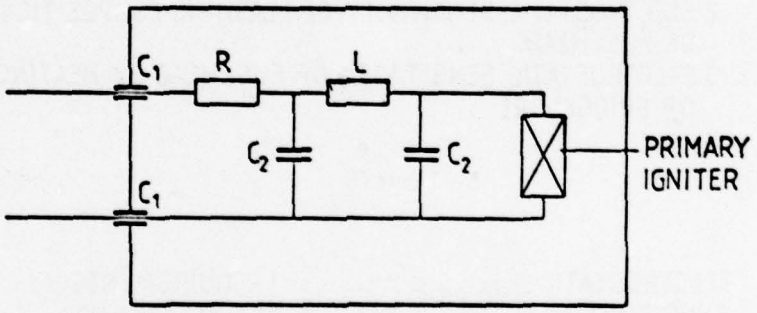

C_1 CERAMIC BUSHING CONDENSERS

C_2 CERAMIC CONDENSERS

R LEADING WIRE RESISTANCE OF HIGH INDUCTIVITY

L COIL ON FERRITE CORE

Fig.31 EMC-circuit for igniter for LAR, 2nd generation

SOME MEASUREMENTS OF IGNITION DELAY AND HEAT TRANSFER WITH PYROGEN IGNITERS

by

A.R. Hall, G.R. Southern and D. Sutton

Procurement Executive, Ministry of Defence
Propellants, Explosives and Rocket Motor Establishment
Westcott, Aylesbury
Buckinghamshire HP18 ONZ, UK

SUMMARY

To elucidate design principles for single orifice pyrogens charged with propellant, and fired axially in small motors, measurements have been made of ignition delay and the corresponding heat flux with a range of these units. Ignition delays were inferred from pressure-time records of both pyrogen and main motor and mean heat fluxes were calculated from the total temperature rise of copper capsules set in dummy motor charges. The motor ignition delay, t_{ig}, the mass rate of pyrogen discharge, $\dot{m}$, and the mean heat flux, $\dot{Q}$, were correlated as follows: (i) approximately $t_{ig} \propto \dot{m}^{-1.5}$, (ii) $\dot{Q} \propto \dot{m}^{0.8}$ and (iii) $t_{ig} \propto \dot{Q}^{-1.8}$. Hence $\dot{m}t_{ig} \propto \dot{m}^{-0.5}$ and $\dot{Q}t_{ig} \propto \dot{Q}^{-0.8}$. Comparison of igniters at the same values of $\dot{m}$ revealed that (a) ignition delays tended to be longer if igniter products contained a condensed phase, and (b) pyrogens performed as well as pyrotechnics.

1. INTRODUCTION

In the development of solid propellant rocket motors the design of a satisfactory igniter is often more difficult than that of any other component. The present authors believe that this situation can be remedied more readily by developing the pyrogen, i.e. a nozzled charge of propellant and thus essentially a miniature rocket motor, rather than the pyrotechnic igniter.

1.1 Ignition of Solid Propellant

The mechanism of ignition of a solid propellant is complex and the details obscure, but the broad features and principal factors are clear.

When the temperature of a propellant surface has been raised by the igniter heat to a particular level exothermic propellant reactions begin to contribute significantly to its further rise. (These reactions vary among propellant types and may occur in the condensed phase, the gas phase, or at the surface, or combinations of these.) Because chemical reaction rates vary exponentially with temperature the propellant self-heating rate responds similarly and can cause rapid rise in temperature, leading abruptly to a runaway condition[1]. Thus although the notion of a single 'ignition temperature', constant for all conditions for a particular propellant, is not valid the general concept remains broadly useful. However, the distinction also remains between an essentially thermal induction period and the subsequent chemical induction period which culminates in ignition.

The energy required by a propellant for ignition has been found to depend chiefly on the following factors[2,3]:-

1) type of propellant,
2) initial temperature of propellant,
3) rate of delivery of energy to the propellant, and
4) ambient pressure.

1.2 Igniters

Probably the most common type of igniter used with solid propellant motors is a pyrotechnic device. However, the design and testing of such devices remain largely empirical, so each new project demands much experimental work to ensure that its igniter meets all the requirements. Pyrotechnic igniter products are invariably very smoky and produce considerable flash.

Because a pyrogen is essentially a rocket motor as regards its internal ballistics, its burning performance can be predetermined and is reproducible, and scaling of rate and duration is both rational and simple. These clear cut principles offer attractive scope for its development, in contrast to that of the pyrotechnic igniter, especially as it can be made relatively smokeless if a double-base propellant is used.

The most precise method for designing an igniter would be the matching of the heat flux it provided at the surface of the motor charge with the ignition energy requirement of the propellant at the pressure induced by the igniter. Unfortunately the formulation of a comprehensive theoretical model for this heat transfer is unlikely in the foreseeable future[4]: even apart from the complexity of calculations involving simultaneous processes there is a lack of understanding of the complex flow patterns, etc. In these circumstances it is necessary to seek empirical, or semi-empirical correlations[5]. The present work aims to contribute to this by relating the igniter action of pyrogens to their mass rates of efflux and heat transfer performance. It is usually believed that with pyrogens operating in all but wide motor conduits the heat is transferred predominantly by convection[4,6]. However, the role played by particulate matter in general is being evaluated[7].

2. EXPERIMENTAL

2.1 Motors

Two solid propellant motors (I and II), 127 mm dia and 300 mm long, with star centre charge designs depicted in Fig. 1, were used. Motor I was filled with a plastic composite (I) and II with either a plastic composite (IIa) or a rubbery composite (IIb) whose compositions are given in Table 1. The motors were nozzled with graphite chokes of 22 mm and 30 mm dia respectively. All firings recorded here were made at ambient pressure and 25°C.

2.2 Ignition Delay Measurement

The pressures in both pyrogen and main motor were recorded with transducers coupled closely to their respective chambers, the small recesses being primed with a carbon-filled self-curing silicone rubber (Dow Corning Silastic 732 RTV) for heat insulation. High frequency galvanometers were used to ensure greater fidelity in the recording of the ignition transient.

The ignition delay was taken as the interval from the instant of pressure rise in the pyrogen to the moment when the main motor pressure had increased by 10% of its final rise, as illustrated in Fig. 2. This definition is something of a compromise. The moment of first appearance of propellant flame would be a more fundamental stage (and more difficult to determine) but would be less closely related to the practical ignition of the motor[8]. Many rocket igniters provide mass burning rates of the order of 10% of the motor rate. In such cases the motor charge is taking over from the igniter the task of completing the spread of ignition when the motor mass burning rate, and thus the motor pressure, has reached 10% of its final value.

The pressure-time history of the pyrogen was generally also integrated and recorded throughout its operation (Fig. 2) in order to obtain mean pressures for (a) the overall burning time, and (b) the burning period up to the ignition of the motor. Knowing the former pressure, and the pyrogen charge mass and its burning time, the discharge coefficient of the propellant may be obtained. From the latter pressure the mean discharge rate of the pyrogen up to that point may then be calculated.

2.3 Pyrogens

The pyrogen charges, whose compositions are given in Table 1, were contained in short metal cylinders 20 to 25 mm dia) with a single plain orifice at one end which directed the efflux down the axis of the main motor conduit, the exit plane of the jet being only slightly proud of the motor head end plate. To obtain a range of mass flow rates the choke diameters were varied between 3 mm and 10 mm, except for the platonized double-base propellant (D) for which the length of the loose extruded charge was altered. The Mg-PTFE-Viton (E) was also used in the form of a loose grain, as a small cylindrical pellet inhibited at the ends and with a single axial perforation. All the other propellants were formed as annular charges bonded to the tube wall. All the fillings thus had a near neutral burning character; usually they were of 10 g and were ignited with ½ g of Mg-$KClO_4$ powder.

Some ignition delays were measured with 10 g and 15 g charges of standard igniter pyrotechnics, viz powdered Mg-KNO_3 (flame temperature at 6.9 MNm^{-2}, T_f, 3260 K) and pelleted B-KNO_3 (T_f = 3100 K) under different degrees of confinement.

2.4 Heat Transfer from Pyrogens

Mean rates of heat transfer from pyrogens operating in a dummy motor with an inert charge (ICI Silcoset 105) cast in the shape of Motor I filling (Fig. 1) were determined from the total temperature rise of "surface calorimeters", i.e. copper capsules of known heat capacity mounted flush in the surface of the dummy charge. The capsules were shaped as spools to restrict the area of contact with the charge, and so reduce heat exchange, and carried a thermocouple. Heat transfer measurement with such a gauge is subject to many errors, particularly where the response time is lengthy, as in the present case (a few seconds). The results must thus be regarded as approximate, pending confirmation by the successful application of gauges which measure instantaneous heat flux.

3. RESULTS

3.1 Ignition Delays

3.1.1 Pyrogens

Ignition delay is plotted logarithmically against pyrogen mass discharge rate for Motor I (plastic composite) in Figs. 3 and 4 and for Motor II in Fig. 5 (cast composite) and Fig. 6 (plastic composite). The dotted line in Fig. 4 reproduces the line drawn in Fig. 3. (When results are available over a wider range of motors it will be more informative to have the abscissa units in mass flow rate per unit area of conduit cross-section.)

For all these plots the data are reasonably well correlated with a straight line for each pyrogen propellant for delays down to about 0.01 sec; for shorter delays the data are more scattered but suggest that the delay becomes less sensitive, if not insensitive, to the pyrogen discharge rate.

With Motor I the slopes are - 1.6 (pyrogen propellant A), - 1.4 (B), - 1.4 (C), - 1.5 (E) and - 1.4 (F). With Motor IIa the slope is - 1.2 (A) and with IIb it is - 1.5 (F). The points to date with the double-base pyrogen (D) in Figs. 4 and 6 are too few for graphing.

The pressures generated by the pyrogens in the motors, before ignition, ranged up to 1 MNm^{-2}.

3.1.2 Pyrotechnics

With pyrotechnics the mass burning rate and the ignition delay could not be established as satisfactorily as with the pyrogens. The results are therefore displayed as large circles in Figs. 4, 5 and 6; the particular pyrotechnics are not specified in the Figs. as only a general comparison of the two classes of igniter is sought here. No significant difference in igniting power is apparent.

The shortest ignition delays were achieved with Mg-PTFE-Viton grain burned as a choked charge.

3.1.3 Effect of ambient temperature

The effect of ambient temperature on ignition delay is being examined by firings at $-40^{o}C$ and $+60^{o}C$ as well as at ambient temperature. Provisionally it is judged that the lengthening of the delay as the temperature is reduced is primarily due to the effect of the lowering of the burning rate of the pyrogen.

3.2 Heat Transfer

The heat flux peaked some two thirds of the distance down the conduit. Apart from these peaks the difference in heat flux between the tip (T) and base (B) of the star (Fig. 1) was rarely more than 25% and the variation down the conduit was much less than this, with the exception of the area adjacent to the head end where the flux was always lowest.

In view of this near uniformity of flux it appeared justifiable to use the mean value here, particularly as the achievement of 10% of full Motor I pressure corresponds to the ignition of about half of the charge area[8].

Measurements have been made with propellants A, B and D. A and B were selected as they gave the least deposit. (The thicker the deposit the less accurately does the present technique measure the heat flux during the ignition delay.) Fig. 7 gives the plot of log mean heat flux, $\dot{Q}$, against log igniter mass efflux, $\dot{m}$,. $\dot{Q}$ varies as $\dot{m}$ to the power 0.84 for propellant A and 0.82 for B. The points for D are more scattered but $\dot{Q}$ is generally some 25% lower than A and B.

The results in Figs. 4 and 7 provide the data for a log plot of ignition delay, t_{ig}, against $\dot{Q}$. In Fig. 8 values of t_{ig} for both A and B over the range 0.1 sec to 0.01 sec are well correlated with $\dot{Q}$ on a single straight line (slope - 1.8). (Corresponding values for D cannot be plotted here until a graph for D can be drawn in Fig. 4.)

The product of $\dot{Q}$ and t_{ig} reveals the propellant ignition energy, Q_{ig}. The log plot of Q_{ig} vs $\dot{Q}$, is a reasonably straight line of slope approximately-0.8, with a suggestion of a deflexion, or even an inversion, of slope when $\dot{Q}$ rises above about 4 MNm^{-2} (100 cal cm^{-2} sec^{-1}) - see Fig. 9.

4. DISCUSSION

4.1 Ignition Delays

4.1.1 General

If the straight line relationship revealed in all the log plots of motor ignition delay, t_{ig}, with the pyrogen mass flow rate, $\dot{m}$, noted first by Beyer et al[9], holds at all generally it should prove a highly practical one in developing such an igniter for any specific task. All but one of the present plots are close to

$$t_{ig} \propto \dot{m}^{-1.5} \quad . \tag{1}$$

The product of $\dot{m}$ and t_{ig} discloses the quantity of igniter, m_{ig}, expended up to the moment of motor ignition, so

$$m_{ig} \propto \dot{m}^{-0.5} \quad . \tag{2}$$

4.1.2 Effect of condensed phase in igniter products

The presence of a solid or liquid in igniter products could affect heat transfer in three main ways:

1) Any deposition on the propellant would initially enhance the heat transfer rate.

2) After transient heat conduction any deposit would then act as a thermal insulant.

3) The gas velocity, and hence the convective heat transfer, for a given mass flow rate would be lower the greater the proportion of condensed phase[8]. (The pressure induced in the motor would similarly be lower - an effect which can increase propellant ignition energy[3,9,10].)

Propellant A (Table 1) was expressly formulated to be free of any solid product. (It was the absence of catalyst that made it inconvenient to extend the rate of pyrogen efflux to give a better overlap with the other propellants.) In contrast C and F were aluminized composites whose products contained some 17% of solid matter. In spite of the fact that their theoretical combustion temperatures were higher than that of A by 270 K and 520 K respectively, they gave longer ignition delays (in Motor I) then did A (Fig. 4) for a given total mass flow rate. It appears that the effect of these higher temperatures on the heat flux was offset by such factors as (2) and (3) above. (Heat transfer considerations call for the adoption of mass rate of flow of gas only for the abscissae units of such plots as Figs. 3 to 6. In Fig. 3 the line for C and F would then be displaced by some 17% to lower flow rates, a move which would align it closely with the plot for A.)

Significant build-up of deposit (in the absence of condensation) under igniter action probably requires appreciable adhesion between deposit and propellant surface. Under heating double-base propellants soften more readily than composites so particles may adhere more readily.

With Motor IIa two points for pyrogen propellant F fall at shorter ignition delays than corresponding points for A (Fig. 5). As propellant F is identical with that of the motor it may be that there is an advantage in such pairings, other things being equal.

Paradoxically the products of the most efficient igniter material tested, viz Mg-PTFE-Viton, consist almost entirely of condensable vapour, the only permanent gas (HF) being formed from the very small amount of hydrogen in the Viton. Condensation (of Mg and MgF_2 in this case), as distinct from impingement of particles, may thus achieve more effective heat transfer than purely convective flow.

4.1.3 Pyrotechnics

The calorimetric values of non-metallized propellants are typically only one half to two thirds of those of standard igniter pyrotechnics. Nevertheless no appreciable difference in igniting power is apparent at similar mass rates of burning.

The superior heating power of the pyrotechnics is no doubt counterbalanced to some extent by the factors discussed in the preceding section. Moreover the difference in heating power is not reflected to the same extent in the difference in their theoretical flame temperatures. However, there is evidence that some of the pyrotechnic escapes from the motor before combustion is complete.

4.2 Heat Transfer

4.2.1 Thermal model

Before considering the experimental results in detail it is useful to define the temperature history of the surface of a sample receiving heat at a constant rate, $\dot{Q}$. Neglecting heat losses, phase change and self-heating

$$T_s - T_o = \frac{2\dot{Q}}{k}\left(\frac{kt}{\pi\rho c}\right)^{\frac{1}{2}} \quad . \tag{3}$$

where the surface temperature is initially T_o rising to T_s after time t; k is the thermal conductivity, ρ is the density and c is the specific heat of the sample (Ref. 11).

The simplest model of ignition of a propellant is that based on the concept of an ignition temperature, such that when the propellant surface reaches this level ignition follows virtually instantaneously. We see from the above expression that if this model of ignition is strictly obeyed then the ignition delay time t_{ig} is related to the constant heat flux $\dot{Q}$ by

$$t_{ig} \propto \dot{Q}^{-2} \tag{4}$$

and a log plot of t_{ig} against $\dot{Q}$ should be a straight line with a gradient of - 2. Furthermore the ignition energy

$$Q_{ig} = \dot{Q}t_{ig} \tag{5}$$

should be inversely proportional to the heat flux.

4.2.2 Heat transfer with pyrogen mass flow

In Fig. 8 the straight line log plot of t_{ig} against $\dot{Q}$ has a slope not of - 2 but of - 1.8. (Correspondingly Q_{ig} varies not as $\dot{Q}^{-1}$ but as $\dot{Q}^{-0.8}$ - see Fig. 9.) A gradient of less than - 2 implies that the calculated surface temperature at the time of ignition increases with the applied heat flux. This continuous increase in the temperature at which rapid reaction occurs as the heating rate is increased may be associated with the chemical induction period referred to in the Introduction. Alternatively the slope may have been modified because the definition of ignition delay here includes a 'filling time' for the motor pressure to rise by 10% of its final increase.

Studies of the ignition of propellant by radiant energy have already detailed this sort of relationship between ignition delay and heat flux[2,3,9,10], and have shown that at values of $\dot{Q}$ above about 4 mWm^{-2} (100 cal cm^{-2} s^{-1}) the ignition energy, Q_{ig}, tends to become constant or even to increase at around atmospheric pressure. There is perhaps a suggestion of the latter in Fig. 9. At high values of $\dot{Q}$ the ignition energy also becomes sensitive to pressure.

For the two pyrogens examined (propellants A and B) the rate of heat transfer was found to be a function of the mass flow rate

$$\dot{Q} \propto \dot{m}^{0.8} \tag{6}$$

in line with other igniter work[12,13]. This is the classical relationship for convective heat transfer in cylindrical pipes with turbulent flow[14]. For strict application of the simple thermal model described above, for which

$$t_{ig} \propto \dot{Q}^{-2}$$

we would thus expect

$$t_{ig} \propto \dot{m}^{-1.6} \quad . \tag{7}$$

As the slopes found (Figs. 3 to 6) ranged from - 1.6 to - 1.4 (with one exception) the deviation from the model seems small enough to permit its continued use as a guide in the development of pyrogens. Certainly the results confirm the overriding importance of heat transfer (convective with smaller diameter motors) in the performance of rocket igniters. They also suggest that the present heat transfer measurements are not too inaccurate; what errors occur are thus presumably either of second order, or else they tend to offset each other.

The fact that the rate of heat transfer to the motor charge varies as $\dot{m}^{0.8}$ means that the proportion of igniter heat which is lost in the efflux from the motor varies as $\dot{m}^{0.2}$. Heat transfer measurements revealed that at a pyrogen mass flow rate of 0.15 kg s^{-1} in Motor I some 50% of the igniter heat is so 'lost'. This heat, of course, has still played an important role in maintaining gas pressure in the motor and thus lowering the ignition energy required and therefore enhancing the rate of flame spread over the charge surface.

4.2.3 Double-base pyrogen

The lower rates of heat transfer noted so far with double-base pyrogens, at mass burning rates up to 0.2 kg s^{-1}, explain the longer ignition delays with these igniters. These results are disappointing insofar as double-base propellant would be required for a smokeless pyrogen; the cause is probably the adhesive deposit which propellant D produced.

5. CONCLUSIONS

(These conclusions refer to ignition of composite propellant charges in small motors by pyrogens with a single axial jet. Their wider application has yet to be tested. Moreover those involving heat transfer are based on data which are both more limited and approximate.)

1) Motor ignition delay, t_{ig}, is a function of the mass discharge rate of the pyrogen, $\dot{m}$, and is generally close to

$$t_{ig} \propto \dot{m}^{-1.5}$$

for ignition delays between 0.01 and 0.10 seconds.

The product $\dot{m}t_{ig}$, i.e. the quantity of igniter charge expended up to the moment of ignition, varies as $\dot{m}^{-0.5}$.

2) The mean rate of heat transfer to the motor charge, $\dot{Q}$, is a function of $\dot{m}$:

$$\dot{Q} \propto \dot{m}^{0.8} \quad .$$

3) The ignition delay is thus a function of the rate of heat transfer. Approximately

$$t_{ig} \propto \dot{Q}^{-1.8} \quad .$$

The product $\dot{Q}t_{ig}$, i.e. the ignition energy of the propellant, thus varies as $\dot{Q}^{-0.8}$.

4) The presence of a condensed phase in the products of the igniter tends to impair its performance when comparisons are made at the same mass rate of burning.

5) Pyrogens with propellant charges perform as well as pyrotechnic igniters with the exception of the Mg-PTFE-Viton composition when burned as a choked charge.

6. REFERENCES

1. Price, E.W., Bradley, Jr, H.H., Dehority, G.L. and Ibiricu, M.M., 'Theory of Ignition of Solid Propellant', AIAA Journal, Vol. 4, July 1966, pp.1153-1181.

2. Beyer, R.B. and Fishman, N., 'Solid Propellant Ignition Studies with High Flux Radiant Energy as a Thermal Source', pp.673-692 of 'Solid Propellant Rocket Research', ARS Progress in Aeronautics and Rocketry, M. Summerfield (ed.), New York, Academic Press, 1960.

3. Sutton, D. and Wellings, P.C., PERME, Ministry of Defence, UK, 'The Ignition of Solid Propellants by Radiant Energy', 1966, RPE Technical Report No. 66/4.

4. Falkner, C.E. and Miller, C.L., Technology Incorporated, 'Analytical Igniter Design for Solid Propellant Rocket Motors', 1970, Tech. Report AFRPL-TR-70-69.

5. Jensen, G.E., Brown, R.S., Cose, D.A. and Anderson, R., 'Ignition and Ignition Propagation', AIAA Second Propulsion Joint Conference, Colorado Springs, 13-17 June 1966, Paper No. 66-677.

6. National Aeronautics and Space Administration, USA, 'Solid Rocket Motor Igniters', 1951, NASA SP-8051.

7. Smith, I.E. and Siddiqui, K.M., 'The Measurement of Igniter Heat Flux in Solid Propellant Rocket Motors', Paper No. 20, Propulsion and Energetics Panel, 47th (A) Meeting, Porz-Wahn, Germany, May 1976.

8. Hall, A.R. and Southern, G.R., 'Ignition of 127 mm Solid Propellant Motors by Pyrogens with and without Solid Particles', AIAA/SAE 14th Joint Propulsion Conference, Las Vegas, Nevada, July 25-27, 1978.

9. Beyer, R.B., Anderson, R., MacLaren, R.O. and Corcoran, W.J., United Technology Center, Sunnyvale, California, 'Ignition of Solid Propellant Motors under Vacuum', 1965, Final Report UTC-2079-FR.

10. DeLuca, L., Ohlemiller, T.J., Caveny, L.H. and Summerfield, M., 'Radiative Ignition of Double-Base Propellants: II Pre-ignition Events and Source Effects', AIAA Journal, Vol. 14, August 1976, pp.111-1117.

11. Carslaw, H.S. and Jaeger, J.C., 'Conduction of Heat in Solids', Oxford University Press, 1959, p.75.

12. Allan, D.S., Bastress, E.K. and Smith, K.A., 'Heat Transfer Processes during Ignition of Solid Propellant Motors', J. Spacecraft, Vol. 4, January 1967, pp.95-100.

13. Peleg, I. and Manheimer-Timnat, Y., 'A Study of Solid Propellant Rocket Motor Ignition', Israel Jour. Technology, Vol. 6 (1-2), 1968, pp.32-45.

14. McAdams, W.H., 'Heat Transmission', New York and London, McGraw-Hill, 1942, p.167.

Acknowledgements

The authors are grateful to numerous colleagues at PERME (Waltham Abbey and Westcott) for filling motors and igniters, etc.

TABLE 1

Propellant Ingredients

Composite Propellants

	Motors			Pyrogens			
Propellant	I	IIa	IIb	A	B	C	F
Ingredient	per cent, by weight						
Ammonium perchlorate	57	71	68	86	84.5	72.5	71
Ammonium picrate	30						
Polyisobutene, etc	11		13		12.5	12.5	
HTPB rubber		13		10.7			13
Isodecyl pelargonate				3			
Bonding agent				0.3			
Wetting agent	1		1		1	1	
Aluminium		15	18			12	15
Ferric oxide		1					1
Copper chromate					2	2	
Titanium dioxide	1						
Theoretical flame temperature, K, at 6.9 MNm^{-2}				2900	2740	3170	3420
Graph plot symbol				o	0	X	□

Pyrogen double base propellant (D)		Pyrogen composition (E)	
NC	53	Magnesium	55
NG	42	PTFE	40
DBP	2.8	Viton	5
Lead stannate	3		
2-NDPA	2		
Wax	0.075		
Theoretical flame temperature, K, at 6.9 MNm^{-2}	2860		2940
Graph plot symbol	+		Δ

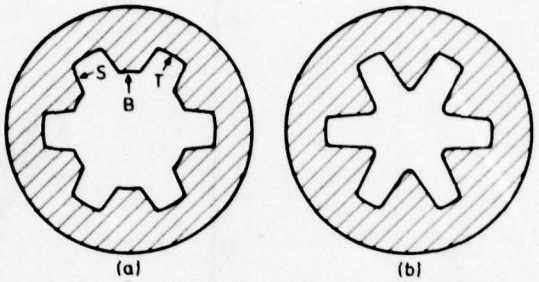

	(a)	(b)
Motor	I	IIa and IIb
Propellant	I	IIa and IIb
Conduit Perimeter, mm	333	366
" Area, mm²	4200	3170
Restriction ratio	271	160

Fig. 1 Propellant charge shapes

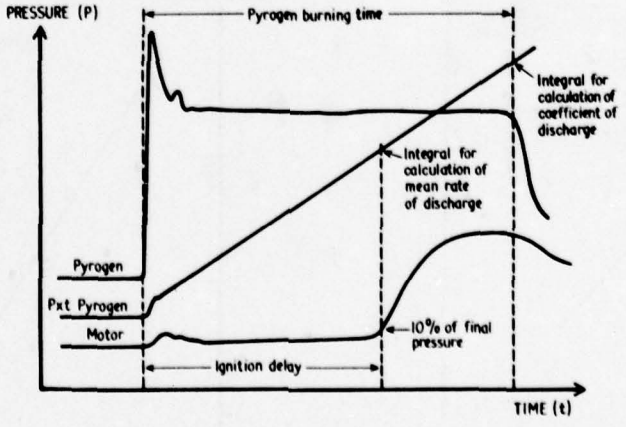

Fig. 2 Pressure-time record of pyrogen ignition of solid propellant motors

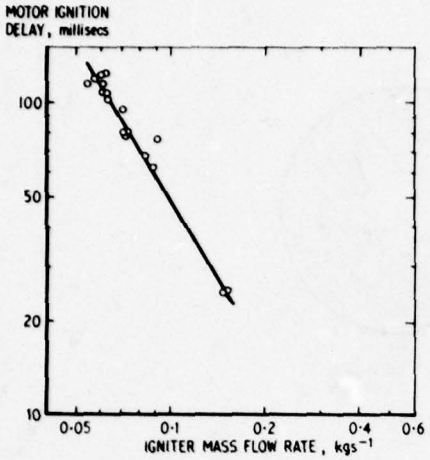

Fig. 3 Variation of motor I ignition delays with particle-free pyrogen mass flux (Propellant A, table 1)

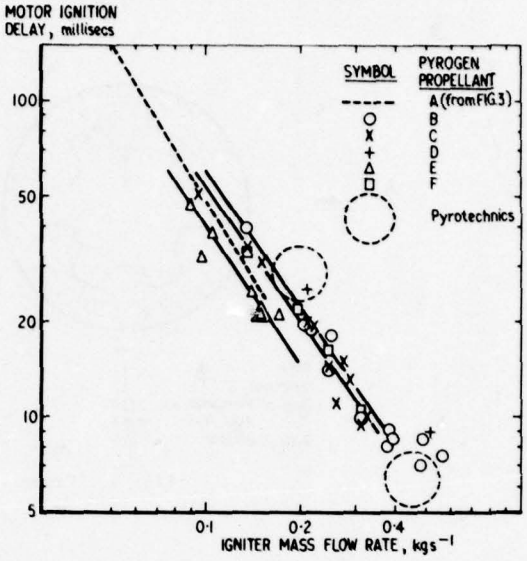

Fig. 4 Variation of motor I ignition delay with igniter mass flux

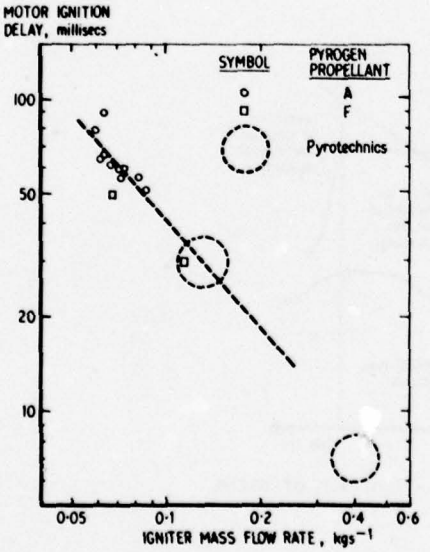

Fig. 5 Variation of motor IIa ignition delay with igniter mass flux

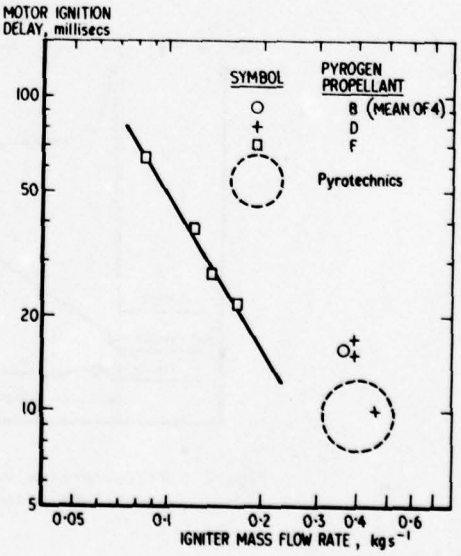

Fig. 6 Variation of motor IIb ignition delay with igniter mass flux

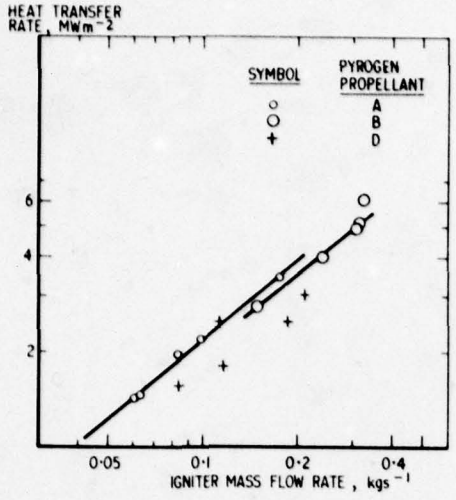

Fig. 7 Variation of heat flux to motor I with pyrogen mass flux

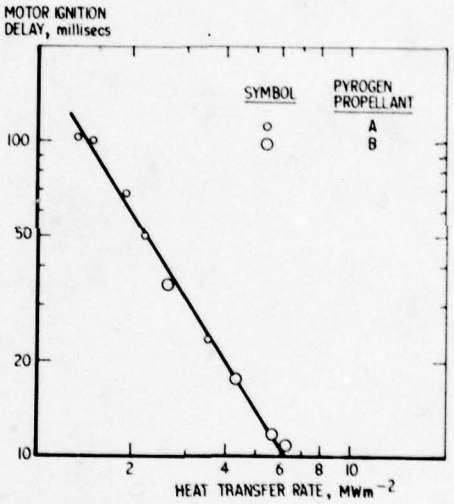

Fig. 8 Variation of motor I ignition delay with heat flux from pyrogens

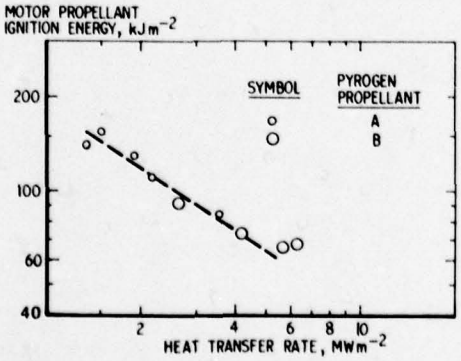

Fig. 9 Variation of motor I ignition energy with heat flux from pyrogens

BOUNDARY LAYER MODELS OF EROSIVE BURNING

by
R.C.Parkinson and P.D.Penny
Solid Propellant Motors Division
PERME Westcott,
Aylesbury, Bucks., U.K.

SUMMARY

Erosive burning occurs when free stream convection modifies the rate of heat transfer from the combustion zone to the surface of the propellant. Analysis of a wide range of rocket motors firings indicates that erosive burning can be correlated by a boundary layer "blow off" criterion. A momentum integral boundary layer theory can be used to predict the boundary layer re-attachment point in a rocket motor conduit, with acceleration of the combustion gases in the conduit as an important modifying force. Consideration of the energy balance in the boundary layer then provides a means of relating boundary layer thickness with burning rate including both normal and erosive burning effects. The ratio of the laminar sub-layer thickness to the combustion zone thickness is expected to be the controlling term in the energy integral.

NOMENCLATURE

A_c - conduit cross-sectional area
E^c - constant in $C_{f,o}$ equation
f - mass fraction of ammonium perchlorate in propellant
h - height of flame zone above surface of propellant
H_s - enthalpy of gas at main stream temperature
H_w^s - enthalpy of gas at propellant surface temperature
k_w - burning rate constant
m - exponent in $C_{f,o}$ equation
n - exponent in burning rate equation
p - pressure
P - burning surface perimeter
q_w - heat transfer rate to the propellant surface
r_b - local propellant burning rate
T_{FL} - apparent surface temperature of propellant
T_s - temperature in free stream
T_w^s - temperature at propellant surface
u_w - gas velocity
U - auxilliary function in boundary layer integration procedure
x - distance downstream
y - distance normal to surface
y_L - laminar sub-layer thickness

δ_2 - boundary layer momentum thickness
Λ^2 - auxilliary function in boundary layer integration procedure
μ - viscosity
ρ - density
χ - T_w/T_s
Ψ - $C_f/C_{f,o}^s$

ΔH - chemical energy release by combustion
ΔH^e - enthalpy rise in combustion gas between surface and free stream
ΔH^g - enthalpy rise in solid propellant between bulk and surface
ΔH^p - heat of combustion of ammonium perchlorate
$\Delta H_{c,AP}$ - heat of degradation of ammonium perchlorate in condensed phase
$\Delta H_{d,AP}$ - heat of sublimation of ammonium perchlorate
$\Delta H_{d,B}^s$ - heat of degradation of binder

Non-dimensional numbers

b - $2F/C_{f,o}$
C_f - skin friction coefficient
$C_{f,o}$ - skin friction coefficient without blowing at the same value of Re_2
F - blowing rate $(\rho u)_w/(\rho u)_s$
K - acceleration number
Ma - Mach number
Pr - Prandtl number
Re_2 - momentum thickness Reynolds number
Re^x - Reynolds number based on length along flow
St^x - Stanton number

1. INTRODUCTION

Erosive burning occurs when free stream convection modifies the rate of heat transfer from the combustion zone to the surface of the propellant. It will lead to pressure peaks in the early phases of burning in a rocket motor, and to non-uniform burning over the surface of the charge. In many instances it represents a natural limit for the designer of a rocket motor, and accurate definition of the conditions under which it occurs is important. There is a continuing interest at PERME Westcott in elucidating the nature of the phenomenon and in developing prediction techniques of use in real rocket motor designs. This paper represents a situation report on the current status of this work, following a previous paper presented at the 1978 AIAA Propulsion Conference (1). Some of the results presented will be common to both papers.

It seems apparent that erosive burning occurs due to the interaction between the boundary layer and the combustion zone, and it is possible to correlate experimental motor firings using the non-dimensional group associated with "blow-off" of transpired boundary layers (see Fig.1 and Section 2):

$$F\,Re_x^{0.2}$$

Here F is the ratio of the mass-flux from the burning surface to the mass-flux along the wall in the free stream $(\rho u)_w/(\rho u)_g$, and is called the "blowing rate". Re_x is the Reynolds number based on length along the surface. The widely used correlation of Lenoir and Robillard (2) can be written in terms of this group:

$$r_b = k\,p^n + r_b\left\{.0288\,Pr^{-.67}\frac{\Delta H_g}{\Delta H_p}\,\frac{\exp(-53\,F)}{F\,Re_x^{0.2}}\right\}$$

where ΔH_g and ΔH_p are the enthalpy rise of the propellant in the solid and the gas as it progresses to combustion. The equation is known to overpredict the burning rate in large motors (see Section 3), and the suspicion remains that the exponential term should also carry an Re_x factor.

The major theoretical difficulty with the Lenoir and Robillard theory is that it assumes that the convective heat transfer to the propellant surface can be added to the already existing transfer of heat from the combustion zone (largely conduction). In reality the heat transferred to the surface will depend only on the temperature gradient in the gas close to the surface, and the effects of convection and conduction must interact. The height of the combustion zone above the propellant surface, for example, may be expected to increase if the burning rate increases.

A succesful theory of erosive burning must therefore cope with the following problems:

(i) It must integrate the heat transfer modes of normal burning and erosive burning into a single variable describing boundary layer interactions.
(ii) It must explain the effectiveness of an $F\,Re_x^{.2}$ correlation in relating the behaviour of motors with quite different axial flow conditions.
(iii) It must give similar correlations against $F\,Re_x^{.2}$ for double base and composite propellant motors.
(iv) It must explain the fact that increasing the motor conditioning temperature increases the degree of erosive burning taking place (an observation which does not follow directly from the $F\,Re_x^{.2}$ relation).
(v) It is desirable if the same theory could also explain possible "negative erosion" effects which are sometimes reported on the threshold of the positive erosive burning region.

2. EXPERIMENTAL EVIDENCE

A large number of experimental motor firings investigating erosive burning effects have been carried out over the years at PERME Westcott. Typically these motors have been designed with a flat theoretical pressure-time curve, and erosive burning has appeared as an initial pressure peak. The ratio of the maximum to the minimum pressure during the main part of the firing will then provide a measure of the extent of erosive burning. This can be correlated with a value of $F\,Re_x^{.2}$ for a point at the nozzle end of the charge at the point of initial peak pressure, as in Fig. 1.

The data shown in Fig.1 cover operating pressures from 5 MPa to 75 MPa, conduit-to-throat area ratios from 1.1 to 4, propellant burning rates at 7 MPa from 8 mm/s to 36 mm/s (for composite propellants), 10 separate charge designs (conduit shapes), both platonized double base and plastic composite propellant types, and a range of Reynolds number (Re_x) from 6 to 500 million. Considering the diverse range of data and inevitable uncertainties in the experimental outputs the correlation is remarkably good. A theoretical curve showing the predictions of the Lenoir and Robillard equation (2) for a family of motors with a typical mid-range value of Re_x = 10 million and typical propellant properties has also been shown.

Erosive burning appears to reach serious proportions when $F\,Re_x^{.2}$ is less than about 0.3. However, Hacker (3) showed that for an isothermal, flat-plate boundary layer with blowing the skin friction coefficient (and hence, we would expect, convective heat transfer) became zero when

$$F\,Re_x^{0.2} \simeq 0.08$$

This difference in value suggests that, while a blown boundary layer correlation may be valid, it is necessary to demonstrate that the different constants arise out of the differences in flow conditions (temperature gradients, accelerated flow) found in rocket motors. It also suggests that the only valid experimental environment for studying erosive burning is in a rocket motor where the correct flow conditions exist.

Particular studies have been carried out on four composite propellant motors. The main characteristics are shown in Table 1. Three are conventional star centre charge motors covering a total impulse range of 26000 : 1, and are of greatest use in demonstrating the need for a Reynolds number term to achieve a satisfactory correlation. The analysis of this motor data is given in section 3. The fourth motor was an experimental short burning time motor with the propellant in thin vanes separated by narrow gaps, about 1.5 mm wide. These motors showed quite distinctive erosive burning behaviour.

For a short burning time motor the whole of the pressure time curve forms a transient region, which makes analysis of erosive burning effects difficult. Analysis was achieved by using the pressure-time curve to calculate the product of burning surface area and burning rate ($S\,r_b$), and to relate the ratio of this to the theoretical prediction to the propellant thickness burned on the basis of non-erosive burning. The evidence from these analyses was that parts of the charge began to burn out well in advance of the rest of the charge - implying the effects of erosive burning. The burn-out point could be related to $F\,Re_x^{-.2}$ (see Fig 2), but the required extent of erosive burning enhancement would be well above that found in conventional motors. The conclusion is that boundary layer interaction in the narrow gaps modifies the erosive burning effect. This is consistent with the thicknesses calculated in section 5.1.

3. LENOIR AND ROBILLARD PREDICTIONS

Although there are theoretical objections to the theory of Lenoir and Robillard (2) the equation is known to provide moderately accurate results and allows a simple basis for constructing a pressure-time prediction program for real rocket motors. The equation adds convective heat transfer to the already existing transfer of heat from the combustion zone without reference to the effect that this may have on the temperature gradient in the gas close to the surface.

A way of introducing intereaction into this equation is to allow the enhanced burning rate to modify ΔH_p, the enthalpy rise of the propellant as it progresses towards combustion. This may be done by using the method of Lengelle, Kuentzmann and Rendolet (4) to evaluate ΔH_p during the calculation of the burning rate r_b.

Lengelle et al consider the change of enthalpy between the combustion products at an apparent surface temperature (T_{FL}) as "seen" by the main flame, and the propellant at its conditioning temperatire (T_p) to be

$$H_p = C_p (T_{FL} - T_p) + 0.3 f (\Delta H_{c,AP} + \Delta H_{s,AP})$$

$$+ 0.7f \Delta H_{d,AP} + (1 - f) \Delta H_{d,B}$$

where f is the mass fraction of the ammonium perchlorate in the propellant, $\Delta H_{c,AP}$, $\Delta H_{s,AP}$ and $\Delta H_{d,AP}$ are the heats of combustion, sublimation and degradation in the condensed phase of the ammonium perchlorate respectively, and $\Delta H_{d,B}$ is the heat of degradation of the binder in the condensed phase. The value of the specific heat of the propellant Cp can be taken at the propellant bulk temperature.

The inclusion of the propellant conditioning temperature and the ammonium perchlorate solids fraction in the term for ΔHp means that these are modifying influences on the erosive burning function calculated in Lenoir and Robillard's equation. In fact it is tempting to generalize still further by observing the similarity between the average surface temperature and the melting point of aluminium, and to suggest that f should be the solids fraction rather than the ammonium perchlorate fraction in aluminised propellants.

The modified Lenoir and Robillard expression has been tested by comparing the predicted and measured results for the first three motors described in Section 2.

The Thrush motor is about 1.6 m long, and contains a non-aluminized composite propellant charge. The experimental and predicted pressure-time curves are shown in Fig. 3. The match between the erosive burning program and the experimental results are very good in the first half of the firing, and the discrepancy in the second half is almost certainly due to nozzle throat erosion, not allowed for in the program.

The Stonechat motor is 5.3m long and 0.9m in diameter, and contains an aluminized composite propellant charge. As can be seen from Fig 4 the modified expression overpredicts the early erosive burning but closely follows the measured pressure-time curve later in the firing. The divergence between experiment and theory in the early part of the firing could be compensated for by modifying the exponential term in Lenoir and Robillard's expression to include a Reynolds number effect. The effect of making this substitution is also shown in the figure.

The Imp XVIII motor, by contrast, is only 158 mm long and 36 mm in diameter. This also contains an aluminised composite propellant charge. The comparison between experiment and prediction is shown in Fig 5. The results can be expected to show an additional initial peak as a consequence of the relative size of the igniter. Once again the general correlation is good.

Finally, as we noted in the introduction, an important requirement of an erosive burning model is that it should explain the fact that increasing the motor firing temperature increases the degree of erosive burning taking place. Lenoir and Robillard's original expression would tend to predict a decrease in the erosive burning since F would remain constant, and Re_x would increase slightly. The inclusion of Lengelle's expression for ΔHp alters this by allowing the propellant temperature to directly affect the value of ΔHp which in turn is modified by the interpolation calculation for burning rate. An example of this effect is shown in Fig 6. Here the enhancement in burning rate at a given

position on the propellant charge has been plotted against the propellant temperature for various $F\,Re_x^{.2}$ values at +25°C. As can be seen the modified expression predicts more enhancement at higher conditioning temperatures.

The effect of the AP (or solids) fraction is more difficult to evaluate. Increasing the fraction for a given burning rate and a given pressure increases the enhancement. However in a real motor the rise in propellant density associated with the rise in solids fraction would cause an increase in pressure and therefore a rise in Re_x. Also the change in solids fraction may alter the original n, exponent or steady burning rate of the propellant. Therefore, as yet, we have not investigated the implications of this extra term.

5. BLOWN BOUNDARY LAYER THEORY

5.1 Momentum Integral Development

The boundary layer conditions close to the surface of a burning solid rocket motor charge will be influenced by at least three important conditions. First, the surface is evolving gas at a rate sufficient under many conditions to effectively detach the shear layer from the surface. Secondly, there will be large temperature gradients in the gas close to the propellant surface, and finally there will be a large longitudinal acceleration of the main stream, possibly including compressibility effects.

The momentum integral equation for the development of a boundary layer of this sort under arbitrary compressible conditions may be written as

$$\frac{d\,Re_2}{d\,Re_x} + (1 + H_{12})\,K\,Re_2 = \frac{C_f}{2} + F$$

where Re_2 and Re_x are the Reynolds numbers based on momentum thickness and flow length respectively, H_{12} is the shape factor between displacement and momentum thickness, Ma is the Mach number, C_f the skin friction coefficient, and K is an acceleration number for the free-stream

$$K = \frac{\mu}{\rho u^2}\frac{du}{dx}$$

If the blowing rate F is sufficiently high the skin friction coefficient C_f will fall effectively to zero. In a normal rocket motor with a constant conduit cross-sectional area A_c and a burning surface area varying as Px where P is the charge perimeter,

$$K\,Re_2 \simeq \frac{\delta_2}{x}$$

and

$$F = \frac{A_c}{Px}$$

so that

$$\frac{d\,\delta_2}{dx} = \left(\frac{A_c}{P} - (2 + H_{12} - M_a^2)\,\delta_2\right)\frac{1}{x}$$

The momentum thickness will start very large because of the flow distortion and high blowing rate near the motor head-end (Fig 6), but will decay towards an asymptotic value

$$\delta_2 \rightarrow \frac{A_c}{(2 + H_{12} - M_a^2)\,P}$$

as x becomes large. The decay is fairly rapid (see Fig 7 for example) and the limiting value will generally have been approached to within 10% long before erosive burning effects appear. For the short burning time motor described in section 2 this limiting value of δ_2 would be about 0.5 mm, which is comparable with the gaps between opposing vanes. In this instance therefore the assumed boundary layer profile will be distorted towards Couette flow and we would expect our boundary layer correlation to break down, as observed.

Kutateladze and Leont'ev (5) treat blown boundary layers by comparing the skin friction coefficient to that without blowing ($C_{f,o}$), but at the same momentum thickness Reynolds number Re_2. In effect they compare the distortion to the velocity profile caused by blowing. Defining the ratios

$$\Psi \equiv C_f/C_{f,o}$$

and

$$b \equiv 2F/C_{f,o}$$

the right hand side of the momentum integral equation can be written as

$$\frac{C_f}{2} + F = (\Psi + b)\,\frac{C_{f,o}}{2}$$

For a non-isothermal boundary layer such as we are concerned with in a rocket motor, Kutateladze and Leont'ev suggest that

$$\Psi = \frac{4\,(1 - b/b_{cr})^2}{(\gamma^{\frac{1}{2}} + 1)^2}$$

where b_{cr} is a critical value of b at which blow-off occurs

$$b_{cr} = \frac{1}{1-\gamma}\left[\ln\left\{\frac{1 + (1-\gamma)^{\frac{1}{2}}}{1 - (1-\gamma)^{\frac{1}{2}}}\right\}\right]^2 \qquad \gamma \leq 1$$

where $\gamma = T_w/T_s$

It seems unlikely that C_f does fall to zero at b_{cr} as suggested by Kutateladze and Leont'ev, as d^2u/dy^2 would then be negative at $y = 0$, which would imply recirculation. Rather it seems probable that C_f falls asymptotically to zero at large values of b (6), and b_{cr} serves only as a scaling factor. The temperature gradient has a significant effect on b_{cr}, however. For isothermal conditions $b_{cr} = 4$. For $\psi = 0.25$, b_{cr} is 9.25. Because combustion takes place deep within the boundary layer we might suspect the non-isothermal correction to be excessive. It is, however, in accord with our erosive burning experience.

If we use the simple correlation for $C_{f,o}$

$$C_{f,o} = E\,Re_2^{-m}$$

where $E = 0.0252$ and $m = 0.25$ for a 1/7th power law, when while C_f is close to zero and the boundary layer thickness has its asymptotic value δ_2^*

$$b = \frac{2A_c}{Px} \cdot \frac{1}{E}\left(\frac{r_b \rho}{\mu}\frac{Px}{A_c}\delta_2^*\right)^m$$

$$= \text{Const.}\; x^{m-1}$$

As we progress down the conduit, b therefore decreases until at about b_{cr} skin friction and erosive burning effects begin to be important.

The method proposed by Kutateladze and Leont'ev allows the momentum integral equation to be integrated, since the right hand side of the equation is a simple function of Re_2. Assuming $Re_2 = 0$ when $Re_x = 0$

$$Re_2 = U^{\frac{1}{1+m}}$$

where

$$U = (1+m)\exp(-\Lambda)\int_{Re_x} \frac{E}{2}(1+\Psi)\exp(\Lambda)\,d\,Re_x$$

and

$$\Lambda = (1+m)\int_{Re_x}(1 + H_{12})\,K\,d\,Re_x$$

We now know the momentum thickness and the skin friction coefficient. What is required is to relate this to the modification of the burning rate behaviour.

5.2 Energy Balance Equation

Let us now consider the energy balance in a section of the boundary layer including the effect of raising the gas evolved at the wall from the wall enthalpy (H_w) to the enthalpy at the combustion temperature (H_s) and the subsequent release of chemical energy ($^w\Delta H_e$). Heat is transferred to the wall at a rate q_w, which is used to "evaporate" further solid propellant. The energy balance is then

$$\frac{d}{dx}\left[\int_o^\infty \rho u\,(H_s - H)\,dy\right] + (\rho u)_w\,(H_s - H_w) + q_w$$

$$- (\rho u)_w\,\Delta He = 0$$

The terms in this equation represent, in order,

- the rate of change of longitudinal energy convection
- heat used in warming gas from the wall
- heat transferred to the wall, and
- heat liberated by combustion.

Now by definition of the burning rate

$$(\rho u)_w = r_b \rho_p$$

where ρ_p is the propellant density, and we are assuming

$$r_b = \frac{qw}{\rho_p \Delta Hp}$$

where ΔHp is the energy required to convert unit mass of the propellant into gas at the wall temperature.

If we make the energy balance non-dimensional, we have

$$\frac{-1}{(\rho u)_s} \frac{d}{dx} \left[\int_o^\infty \rho u \left(\frac{H_s - H}{H_s - H_w} \right) dy \right]$$

$$= F \left[1 - \frac{\Delta He}{H_s - H_w} \right] + St$$

but $$St = \frac{r_b \rho_p}{(\rho u)_s} \frac{\Delta Hp}{H_s - H_w} = F \frac{\Delta Hp}{H_s - H_w}$$

so that

$$F \left[\frac{\Delta H_e - H_s + H_w - \Delta H_p}{H_s - H_w} \right] = \frac{1}{(\rho u)_s} \frac{d}{dx} \left[\int_o^\infty \rho u \left(\frac{H_s - H}{H_s - H_w} \right) dy \right]$$

Since $F = \frac{r_b \rho}{(\rho u)_s}$

the burning rate will be proportional to

$$\frac{d}{dx} \left[\int_o^\infty \rho u \left(\frac{H_s - H}{H_s - H_w} \right) dy \right]$$

which is a function of the boundary layer development. This has now solved the problem of integrating erosive and non-erosive burning heat transfer components. In addition, the left-hand term of the energy balance equation provides a description of the enthalpy rise characteristics of the propellant, and will be susceptible to analysis by Lengellé's method, as in section 3. What we must now do is to show that this reduces to the non-erosive burning case when $C_f = 0$.

5.3 Non-erosive burning case

In the absence of erosive burning the propellant combustion zone is within the laminar region of the boundary layer, and in a simple model we can assume that heat transfer to the surface takes place by conduction from the combustion zone at a height h above the surface. Indeed, if we assume that the combustion zone is located by a simple time delay mechanism from the point at which gas is formed at the surface a square root law for the variation of burning rate with pressure results. As a typical example, the Thrush propellant described in Ref 1, with a burning rate of 12.4 mm/sec at 10 MPa, has a theoretical combustion zone height of 0.0105 mm. In this model, while the combustion zone remains undisturbed

$$\frac{H_s - H}{H_s - H_w} \simeq \frac{h - y}{h} \qquad y < h$$

The mass-flux distribution (ρu) will depend on the main stream value $(\rho u)_s$ and the ratio (y/δ_2) if we assume that the boundary layer profiles are all essentially similar when the boundary layer is fully blown ($du/dy = 0$ when $y = 0$).

That is

$$\frac{(\rho u)}{(\rho u)_s} = f\left(\frac{y}{\delta_2} \right)$$

so that

$$\frac{d}{dx} \left[\int_o^\infty \rho u \left(\frac{H_s - H}{H_s - H_w} \right) dy \right] = \frac{d}{dx} \left[(\rho u)_s \int_o^h f\left(\frac{y}{\delta_2} \right) \left(\frac{h - y}{h} \right) dy \right]$$

But $(\rho u)_s = \frac{Ix}{A_c} (r_b \rho)$, and we have shown in section 5.1

that the momentum thickness rapidly tends towards an asymptotic value, so that the expression is essentially constant except very close to the head-end.

5.4 Erosive burning case

If boundary layer re-attachment occurs, the assumptions made in section 5.3 about the values in the energy integral will be modified. The most immediate factor is that δ_2 will no longer be constant but will begin to increase. If $f(y/\delta_2)$ remains more or less the same shape then the integral (and hence the burning rate) will actually fall. However, the existence of skin friction implies that $du/dy \neq 0$

at $y = 0$, increasing $f(y/\delta_2)$ for a given value of y/δ_2. The third modification will occur if boundary layer turbulence interacts with the flame zone, leading to a spreading of the $(H_e - H)$ curve, also increasing the integral. Particularly in this last case the important factor will be the relative size of the boundary layer laminar sub-layer and the combustion zone height.

To establish the thickness of the laminar sub-layer in proportion to δ_2 we can investigate the characteristics of the unblown turbulent boundary layer. Here the edge of the laminar sub-layer occurs when

$$y_L^+ = \frac{y_L u_\tau \rho}{\mu} \simeq 10$$

On the same basis

$$\delta_2^+ = 0.0064\, Re_x^{0.7}$$

so that

$$\frac{y_L}{\delta_2} \simeq 1260\, Re_x^{-0.7}$$

Now the start of erosive burning is when

$$b = \frac{2F}{C_{f,o}} < b_{cr}$$

at which point δ_2 will have reached its asymptotic value

$$\delta_2 = \frac{Ac}{P(2 + H_{12} - M_a^2)}$$

Since also

$$F = \frac{Ac}{Px}$$

and

$$C_{f,o} = E\, Re_2^{-m}$$

the critical value of x can be found as

$$x = \left[\frac{2Ac}{b_{cr} P} \cdot \frac{1}{E} \left(\frac{r_b \rho}{2 + H_{12} - M_a^2} \right)^m \right]^{\frac{1}{1-m}}$$

and the laminar sub-layer thickness as

$$y_L = 1260 \left(\frac{P}{A_c} \right)^{0.167} \left(\frac{\mu}{r_b \rho} \right)^{1.167} \left(\frac{E\, b_{cr}}{2} \right)^{1.87} \frac{1}{(2 + H_{12} - M_a^2)^{.53}}$$

for $m = 0.25$. For larger motors this equation suggests that y_L becomes smaller, so that turbulent interaction between boundary layer and combustion zone are more likely.

As a comparison we can use this equation to estimate y_L for the Thrush motor described earlier, where $Ac/P = 10$ mm, and $b_{cr} \sim 9.25$. At the point of boundary layer re-attachment the equation estimates $y_L = 0.005$ mm compared with a combustion zone thickness of 0.01 mm. These are very comparable. We must remember, however, that the equation is based on un-blown boundary layer theory, and therefore is only an approximate estimate.

Further work is now required to finally elucidate the relationship between y_L and the energy integral to complete an integrated erosive burning boundary layer theory.

6. CONCLUSION

Evidence from experimental firings continues to support the idea that erosive burning is a boundary layer phenomenon, occurring when the normally detached boundary layer re-attaches under the influence of the increasing axial mass-flux down the rocket motor conduit. Normal burning in this situation occurs because the velocity profiles in the combustion zone close to the propellant surface remain similar until re-attachment occurs.

Use of the flame zone model of Lengellé *et al* (4) allows the Lenoir and Robillard prediction (2) to be used to give realistic pressure-time curves and to give the correct variation of erosive burning with propellant conditioning temperature. A more advanced model is being developed which uses a momentum integral method to predict the re-attachment properties of the boundary layer, and an energy flux integral to predict the burning rate directly from the boundary layer characteristics. This will allow a fully integrated approach to be taken to the problem of propellant combustion in rocket motors.

REFERENCES

1. R C Parkinson & P D Penny "A Transpired Boundary Layer Model of Erosive Burning" AIAA Paper 78-980 AIAA/SAE 14th Joint Propulsion Conference, Las Vegas, July 25-27, 1978

2. J M Lenoir & G Robillard "A Method to Predict the Effects of Erosive Burning in Rocket Motors." 6th Symposium on Combustion (1957)

3. D S Hacker "Empirical Prediction of Turbulent Boundary Layer Instability along a Flat Plate with Constant Mass Addition At the Wall" Jet Propulsion 26, (1956), p.786

4. G Lengellé, P Kuentzmann & C Rendolet "Response of a Solid Propellant to Pressure Oscillations" AIAA Paper 74-1209 AIAA/SAE 10th Propulsion Conference, San Diego, Oct 1974

5. S S Kutateladze & A I Leont'ev Turbulent Boundary Layers in Compressible Gases, Trans.D.B. Spalding (Edward Arnold, London, 1964)

6. W M Kays "Heat Transfer to the Transpired Turbulent Boundary Layer" Int. J. Heat Mass Transfer 15, (1972) P.1023.

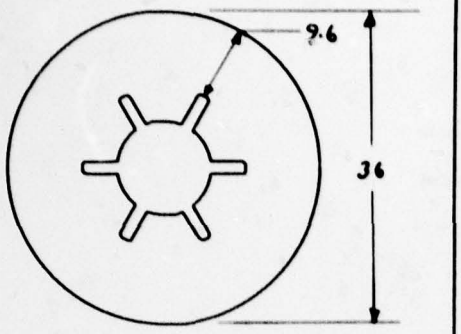

IMP XVIII	CD 81
Overall Length	156 mm
Charge Length	129 mm
Throat Diameter	9.5 mm
Peak Pressure at 20°C	4.0 MPa
Initial S/A	85
Initial A_c/A^*	2.46
Approximate F Re_x^{*2}	0.22

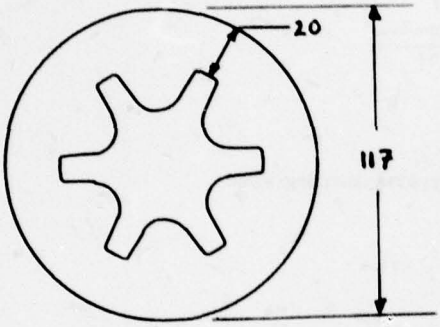

THRUSH	CD 36
Overall Length	1645 mm
Charge Length	1360 mm
Throat Diameter	42.2 mm
Peak Pressure at 20°C	12.4 MPa
Initial S/A	179.5
Initial A_c/A^*	1.76
Approximate F Re_x^{*2}	0.23

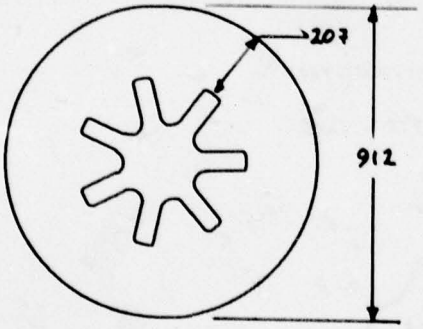

STONECHAT	CD 162
Overall Length	5317 mm
Charge Length	4597 mm
Throat Diameter	241 mm
Peak Pressure at 20°C	4.7 MPa
Initial S/A	120
Initial A_c/A^*	2.05
Approximate F Re_x^{*2}	0.33

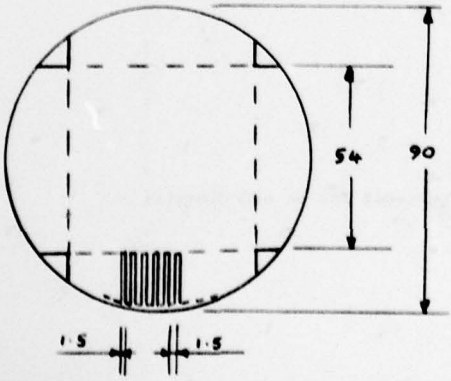

EXPERIMENTAL SHORT BURNING TIME MOTOR	
Charge Length	80 - 160 mm
Initial S/A	38 - 76
Initial A_c/A^*	3.4 - 1.4
F Re_x^{*2} range	0.74 - 0.43

Table 1: Experimental Motor Characteristics

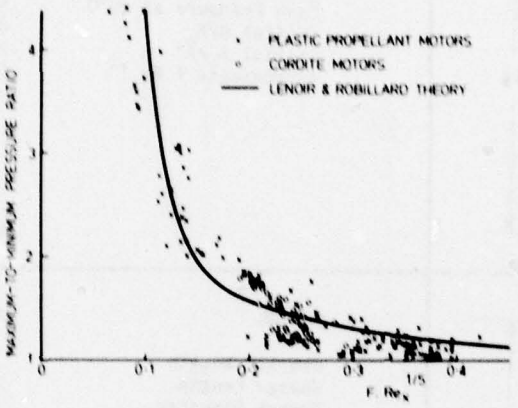

Fig.1 Correlation of peak pressure due to erosive burning with blow-off function.

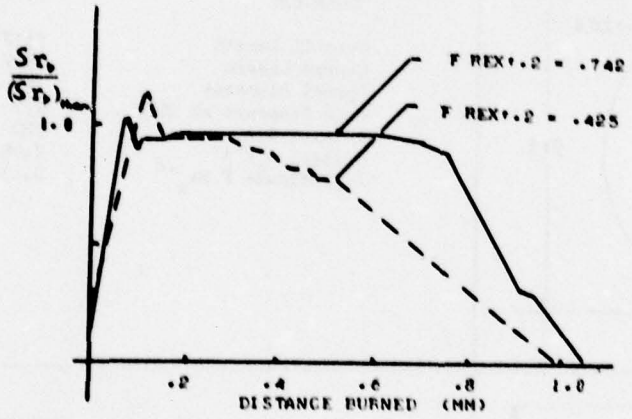

Fig.2 Effect of erosive burning on charge burn-out for an experimental short burning time motor.

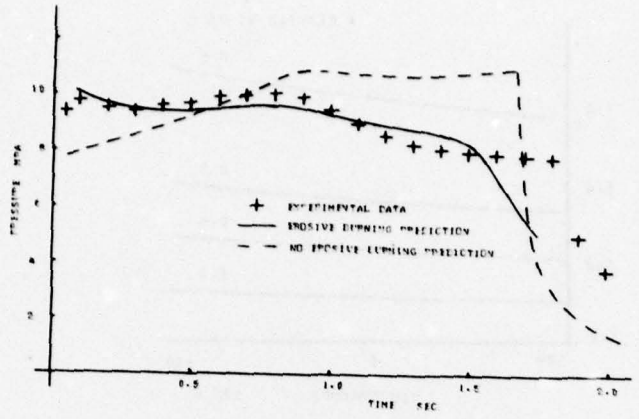

Fig.3 Comparison of pressure-time predictions with and without erosive burning with experimental results for Thrush motor

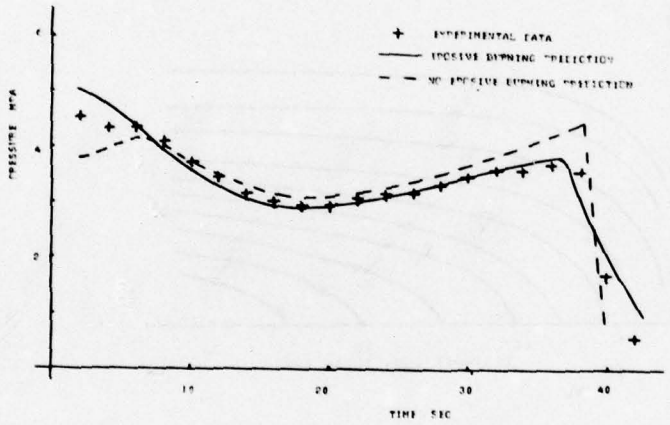

Fig.4 Comparison of pressure-time predictions with and without erosive burning with experimental results for Stonechat motor

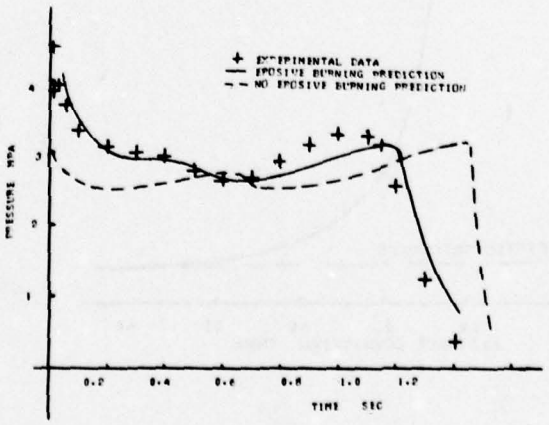

Fig.5 Comparison of pressure-time predictions with and without erosive burning with experimental results for Imp XVIII motor

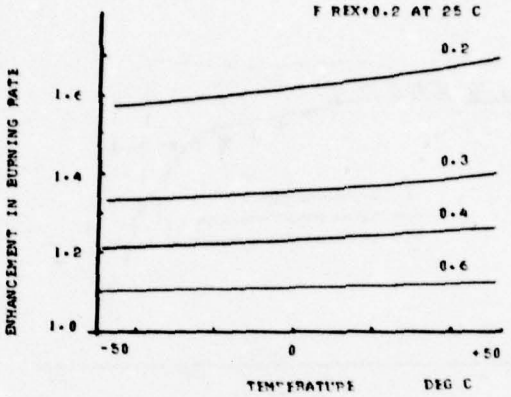

Fig.6 Effect of propellant bulk temperature on erosive burning enhancement using the combustion model of Lengelle et. al. (4)

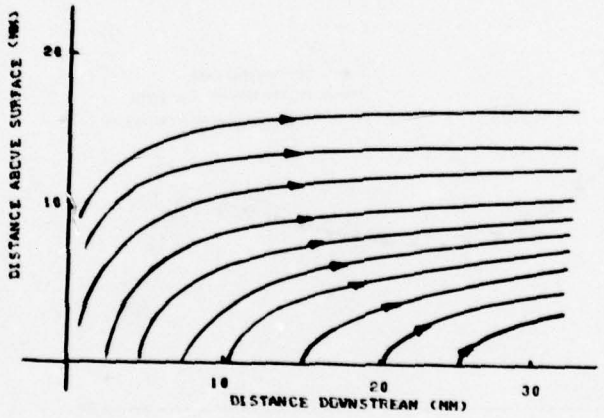

Fig.7 Calculated flow streamlines at head-end of Thrush motor

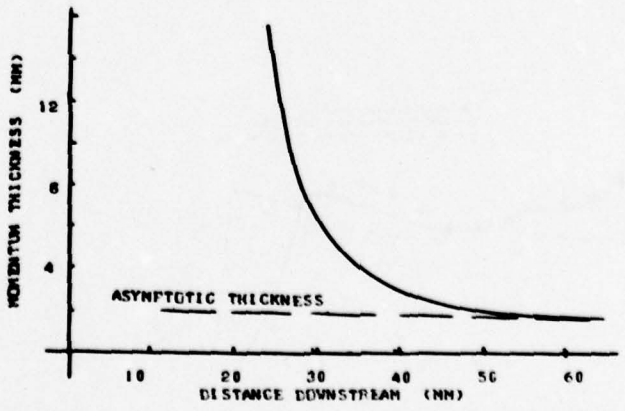

Fig.8 Development of boundary layer momentum thickness for head-end of Thrush charge.

DISCUSSION

M.Barrere, ONERA, Fr

Your approach is an excellent one to try and solve this complicated problem of erosive burning. However the combustion in the boundary layer is very complicated because it is not truly laminar near the surface. The boundary layer is often destroyed by pockets of flow and so whilst it may be described as steady, it is also unsteady. It is complex with respect to heterogeneity in composition and velocity with intermittency and heterogeneity of surface etc.

It may be possible to use mean values as you have done but why don't you use the heat transfer coefficient of Spalding when considering the friction coefficient with and without injection? Isn't Spalding's approach sufficient to describe the 'blowing effect'.

Author's Reply

The advantage of a momentum integral boundary layer approach is that it is not sensitive to the detailed integral structure of the boundary layer. It averages out many of these effects. We do need to know something about the structure in the combustion zone, but even here we can average out effects by the energy convection integral.

By Spalding's approach I presume you mean the simple correlation of the reduction in Stanton number with blowing rather than the more recent differential boundary layer method espoused by Spalding. The Stanton number reduction approach takes similarity assumptions which are not necessarily valid with rocket motors. This is particularly so with high longitudinal accelerations and the large temperature gradients in the boundary layer. We are attempting to avoid making this sort of assumption or needing arbitrary constants in the final formulation.

COMPOSITE PROPELLANT BURN RATE MODELING

Norman S. Cohen
Norman Cohen Professional Services
Redlands, California

SUMMARY

The current status of the steady-state combustion modeling of composite solid propellants is reviewed. Emphasis is placed upon revisions of original Beckstead-Derr-Price (BDP) model premises as applicable to simple monomodal AP propellants. Extensions to more complicated propellants (multimodal, etc.) are discussed also. Typifying results are presented which show parametric trends and comparisons with data. Areas of agreement and disagreement, deficiencies and continuing developments are pointed out.

NOMENCLATURE

A	Kinetics prefactor
A_{fh}	Average flame height factor
b	Characteristic diffusion flame dimension
c	A dimensionless characteristic length
c_p	Propellant specific heat (c_g is for the gas)
C	Various floating parameter constants
D_o	Oxidizer particle size
D'	Diameter intercepted by a plane through a sphere
$\bar{D}_m$	Mean diameter of the $m^{\underline{th}}$ mode
d	Distance regressed from the top of an oxidizer particle
$\mathcal{D}$	Diffusion coefficient
E	Activation energy
F_{Di}	Log normal distribution function
F_m	Modal weight fraction of all modes
h^m	Distance from planar surface to point of particle regression
$J(\ )$	Bessel function
k	Rate constant
m	Mass flux
m_{ign}	Power in particle ignition delay law
$\mathcal{M}$	Molecular weight
O/F	Local oxidizer/fuel ratio
P	Pressure
Q	Heat release
r	Burning rate
$\bar{r}$	Time-averaged burning rate for tracking models
R	Gas constant
S	Surface area
S_{oxAP}	Portion of AP surface assigned to stoichiometric AP flame reaction
t	Time
T	Temperature
u_{ign}	Power in particle ignition delay law
v	Gas velocity
X^*	Flame height
Y	Mole fraction in decomposition products
α	Weight fraction of ingredient in propellant
α^*	Weight fraction in pseudopropellant
β	Fraction of reactants
γ	Fraction of energy from primary flame that heats oxidizer
δ	Interstitial spacing
δ	With a subscript, reaction order
η	Burke-Schumann dimensionless height above surface
η'	Lumped parameter, Eq. (B-7a)
ϕ_i	Root of Bessel function
Φ	Stoichiometric oxidizer/fuel ratio
Φ_M	Stoichiometric molar oxidizer/fuel ratio
λ	Thermal conductivity
ν	Ratio of stoichiometric oxidizer/fuel ratio to local oxidizer/fuel ratio
ψ	Dimensionless characteristic length, Eq. (GC-7d)
ρ	Density
σ_m	Modal standard deviation of size distribution
ξ	Burke-Schumann dimensionless radial position
ξ^*	Dimensionless flame height
ζ	Volume fraction of ingredient in propellant
ζ^*	Volume fraction in pseudopropellant

SUBSCRIPTS

AP	Associated with oxidizer monopropellant flame
AP'	Effective value at monopropellant flame
c	Catalyst
D	Associated with final flame
DB	Double-base binder
f	Binder, or referring to binder characteristics
F	Associated with diffusion flame
FF	Associated with final flame
i	$i^{\underline{th}}$ particle size
j	$j^{\underline{th}}$ oxidizer (or particle size when calculating separate surface temperatures)
m	Associated with melting (or $m^{\underline{th}}$ mode)
o	Initial condition (or total surface)
ox	Oxidizer, or referring to oxidizer
p	Propellant as a whole
P	Planar
PD, PF, PDF	Associated with primary flame (diffusion, reaction, total)
s	Surface
ss	Associated with subsurface reactions
T	Total
v	Associated with a vaporization process
fPF	Example of combined subscript: fraction of binder associated with primary flame reaction

PREFACE

Most modern solid propellants are "composite" in the sense that powders (also known as fillers or solids) are included in a polymerized medium. On the scale of the fillers, the combustion is a three-dimensional, unsteady process with a complexity of sequences and interactions. Yet the aggregate propellant sample, which is large compared to a filler particle, burns at a measurable "steady-state" isobaric rate on the macroscopic scale. This fact forms the basis for the statistical averaging concept which is the common denominator of the models to be discussed. Work has emphasized ammonium perchlorate (AP) oxidizer-polymeric fuel binder composites because they have been of greatest general interest. However, the methodology is adaptable to composites generally, and recent work has been addressing more complicated propellants.

The statistical combustion modeling originated with Hermance.[1,2] Basically, the macroscopic propellant is represented by addressing the behavior of a statistical particle and its environment on the microscopic scale. Assumptions and approximations are made to convert the unsteady, three-dimensional process to a steady, one-dimensional model. A subsequent effort produced the Beckstead-Derr-Price (BDP) model,[3-5] which furnishes the baseline for this paper. The BDP model corrected the shortcomings of the Hermance model, incorporating updated experimental knowledge into the Hermance statistical framework. It was shown that a multiple flame structure was a satisfactory alternative to the unsupported Hermance interfacial reaction mechanism in explaining the shape of the burning rate-pressure curve as well as a number of other combustion properties.[3,4] At this juncture, the model was limited to monomodal AP in hydrocarbon binders. Subsequently, Cohen and co-workers,[6-8] and Beckstead,[9,10] extended the model to encompass more complicated propellants in the same basic statistical framework. The ability to do this, given a poor state of knowledge of ingredient interactions, and the proper method to be used, are controversial and unresolved questions.

Glick[11-13] objected to the statistical aspects of the BDP model and, together with Condon,[14] incorporated the BDP multiple flame model into a new statistical formalism. The new formalism purported to correct inconsistencies in the BDP approach, and better represent the time and dimension-dependent features of the combustion on the microscopic scale. At the same time, the formalism was derived for multimodal powders. The method is referred to as the "petit ensemble" model. A detailed summary has recently been published by Condon and Osborn.[15]

Another branch of the statistical modeling is being developed by King.[16] The formalism is more closely related to that of Glick, but is presently limited to monomodal AP propellants. The significant aspect of King's work is his attention to detail in describing the condensed phase and flame processes.

Another approach to statistical modeling has been published by Strahle.[17] Strahle calculated the statistically probable paths of burning through a packed bed of particles representing a composite propellant. Without the benefit of any particular combustion process model, but just from burnthrough times and the statistics, he argued that important features of composite propellant burning (such as the particle size effect) can be demonstrated. For purposes of steady-state modeling, it appears that Strahle's view is adequately represented by the averaging methods of Hermance or BDP and their offspring. For nonsteady phenomena, however, Strahle's view may have additional significance.[18]

The paper will concentrate on the modeling efforts of Beckstead, Cohen et al., Glick & Condon, and King. Discussions will be limited to the major equations (given in the Appendix) and the similar or differing ideas and assumptions behind them, organized in terms of the common elements of these models. The reader is referred to the source materials and their authors for derivations and additional details. Typical results and comparisons with data will be shown to demonstrate the state-of-the-art and support recommendations for continuing work.

THE BASIC PHYSICAL MODEL

The BDP view of an AP particle and its environment, photographed at an instant of time during burning, is shown in Fig. 1. This general representation has been adopted by the various modelers. AP is both a monopropellant and an oxidizer; the surrounding binder was limited to the inert fuel polymer type. The flame structure consists of a premixed monopropellant flame, a primary diffusion flame involving portions of the AP and binder decomposition products, and a final diffusion flame involving the remaining fuel products plus remaining oxidizing species following the monopropellant combustion. Each of these flames furnishes energy to the surface by conduction. In the case of the AP flame, a one-dimensional heat transfer from a flame sheet is a reasonable approximation. In the case of the diffusion flames, which are columnar in nature, the heat transfer would be three-dimensional but approximations are made to convert the problem to one that is effectively one-dimensional. The contribution of each flame to the surface heating depends upon the multiple flame geometry. These allocations, referred to as "competing flame" effects, are perhaps the key feature of this theory. Two additional energy terms are derived from the surface: the heat of decomposition of the binder (endothermic) and the heat of decomposition of the AP (net exothermic). Heterogeneous surface reactions, the key feature of the Hermance model, are not included. All of the energy terms combine to raise the temperature of the solid from its initial bulk temperature to the surface temperature. A uniform surface temperature is assumed, and thermal properties are taken to be constant average values. The uniform surface temperature is recognized to be a poor assumption, but the limited way that the binder enters into the

model renders it of minor importance.

The model focuses upon calculation of the AP surface temperature, and its burning rate as an Arrhenius function of the surface temperature. The binder is assumed to follow along in accordance with continuity to preserve the propellant formulation. The localized burning rate at the time of the photograph is then the total mass flux divided by the propellant density. Assuming a representative particle at a representative time, this burning rate is the propellant burning rate.

In order to apply continuity and implement some of the constitutive relations in the multiple flame model, something must be known about the surface structure: specifically, exposed ingredient surface areas and characteristic dimensions. It is known that AP particles may protrude above the adjacent binder plane or be recessed into that plane, depending mainly upon the pressure. Thus the surface is bumpy, because of the AP, as illustrated in Fig. 1. The binder is taken to be a planar surface. The surface is given an idealized representation to try to capture the essence of the problem in a tractable way.

The BDP idealization of the surface, again followed by others in general terms, is shown in Fig. 2. This figure depicts the geometric relationship of an AP particle to the burning surface. The propellant is viewed as a packed bed of spherical particles, with binder filling the interstitial spacings. The burning surface is a random planar cut through this packed bed. Half of the particles are cut below their centerline and half above. The statistical average diameter of intersection has been computed[19] to be $\sqrt{2/3}\ D_o$. BDP, Beckstead and Cohen, et al. use this statistical average as the representative particle configuration. In Fig. 2, the intersection is shown above the particle centerline and the intersection diameter is the statistical average D'. The burning surface of the AP is assumed to be a spherical segment. The position of this segment at the time of the photograph is given by how far the AP burns from the top (accounting for ignition delay) in the time that it takes the binder to regress from the top (first exposure of the particle) to the plane of intersection. If the AP is able to outrace the binder, the spherical segment would be dished down rather than up. The same analysis is applied to the particle cut below its centerline, and computation of the surface structure becomes a matter of geometry accounting for both particle groups. The parameter b is a characteristic dimension used in the diffusion flame analysis. Here, then, is one approach for averaging out the microscopic time-dependency of the combustion.

Glick & Condon, and King, have taken a different approach to the time-dependency. They go to the trouble of computing the surface and flame geometries as a function of time for discrete time steps as the plane moves down from the top of the particle to the bottom. There is no statistical average D', but a D' which varies with time. This procedure is illustrated by Fig. 3. The propellant burning rate is not represented by the single photographed state described above, but rather as the time average of an integrated motion picture. The method has intuitive appeal because it more closely resembles the way that propellants actually burn. However, comparisons of results between the two methods show such little difference that the BDP statistical averaging method can be deemed a good approximation after all.

ANALYSES FOR MONOMODAL AP/INERT BINDER PROPELLANTS

Continuity Relations

The continuity relations are given by Eqs. (1). Cohen retains the original BDP expression. Glick & Condon argue that m_T should be associated with the total planar surface rather than the total actual surface. They reason that propellant burning rate is with reference to a plane of regression. BDP believed that mass is derived from a total surface, so attempting to extract a single "burning rate" from the behavior of a two-component system in this way requires use of the total actual surface. Hermance used the planar surface, and King concurs; Beckstead follows BDP. The point has not been resolved, and does not make much difference in computed results. Beckstead, with active binder propellants in mind (to be discussed later), no longer requires the binder to follow the oxidizer to preserve the formulation. Thus, $m_f S_f$ needs to be computed separately. This raises interpretation problems to be discussed later. King, also, separates the oxidizer and binder components because he feels that forcing the formulation to be preserved here leads to inconsistencies elsewhere in the model.

As noted earlier, the foregoing equations in the King and Glick & Condon models apply at each of several states in the history of the burning particle. Thus, the additional step of Eqs. (1a) is required. A difference in method is apparent. One numerically approximates a time integral, whereas the other averages the mass flows over all of the increments. King discussed a number of possible averaging methods,[16] but reported results based on the equation shown while admitting the assumption that each increment is weighted equally even though the times differ. Another problem is raised by the fact that particle burn-out generally occurs prior to the time that the binder plane would have reached the bottom of the particle. King refers to this problem as the "end game", and ties it to the averaging question. Glick & Condon exclude the post-consumption increments from the summation with the interpretation that residual material is dispensed with (fills empty pockets, forms a char or is blown away). King includes the post-consumption increments in the averaging as increments having zero mass flow, but expresses uncertainty about it. In order to resolve this problem, it appears necessary to expand the scope of tracking to accommodate more particles. This is not likely to happen because of the effort required and because the credibility of the model and its results does not hinge upon this issue.

All of the models use the same ingredient decomposition relations, Eqs. (2a) and (2b).

Surface Area Relations

Cohen and Beckstead follow BDP in expressing S_{ox}/S_o, but account for the two sets of particle groups[6] (see Eqs. (3-5)). Glick & Condon apply the same geometric analysis, but written in general terms to cover the general plane of intersection. If S_{ox} is normalized by S_o rather than S_p, Eq. (GC-3) would become identical to Eq. (B-3) for $D' = \sqrt{2/3}\, D_o$ and one overall h ($h_p = h_N$). Thus the analyses are consistent when viewed on a common basis. Glick & Condon also follow the BDP particle ignition delay for purposes of computing d_{ox} and h.

King concurs with Glick & Condon, but with two exceptions, (see Eq. (K-3)). King does not impose an ignition delay so the AP has a head start relative to the other models. Consensus would hold this omission to be error, but it does not seem to have an important bearing on the results for AP propellants. Second, King computes S_p as a function of d_f by tracking a burn path through a closest packing particle array in the direction in which the lattice spacing is minimum.[20] He does this to begin to account for the overlapping layers of particles existing in highly loaded propellants, but S_p (and its two components, which are also computed) then becomes a complicated function of oxidizer volume fraction, particle size and planar location. Since the planar areas are functions of geometry only, they can be generated as external inputs to the iterative portions of the problem. S_{ox}, of course, remains coupled into the problem.

A consequence of the tracking approach is a considerable shift in instantaneous O/F ratio. Glick & Condon assume a constant ζ_{ox} and O/F ratio in the course of tracking to avoid the problem, but King is disturbed about resulting inconsistency between model geometry and mass flow contributions. This problem seems to be but another consequence of a tracking approach that does not go far enough.

Characteristic Surface Dimension

Cohen follows BDP as to the characteristic surface dimension, b (see Eqs. (C-6) and C-6a)). δ is computed by summing all of the D' along the line of intersection, subtracting that total from the total length, and dividing by the total number of particles along the line. It is the width of binder between each particle along that line. Half the width, plus half of D', is the dimension b. Note that Eq. (C-6a) can compute positive values of δ for ζ_{ox} in excess of 0.9 even though a packed bed of unimodal spheres could never even approach that volume fraction. The reason is that the statistical plane of intersection is away from the equator, so there is room for δ to be squeezed artifically. Clearly, this approach should not be used for monomodal propellants wherein α_{ox} exceeds about 70% (for AP and typical binders). BDP never violated that limitation, and continuing criticisms of the approach[13-15] are incorrect.

With multimodal propellants in mind, Glick & Condon adopted a different approach which has since been followed by Beckstead. Essentially, the fractional area of intersection of a plane through a packed bed of spheres is equal to the volume fraction of the spheres.[10,19] Stated another way, the fraction of planar surface occupied by oxidizer is ζ_{ox}.[13] Applying this principle to the single particle configuration yields Eq. (GC-6). From Beckstead's point of view, an interesting question is whether the intersection providing the statistical average planar area ratio is consistent with the intersection providing the statistical average D'. Glick[13] has plotted δ/D_o as derived from the two approaches, and the difference is roughly 20% for ζ_{ox} between 0.4 and 0.5. The BDP plane is located a bit further from the equator than the area distribution plane, so there is a small inconsistency in b in the direction of excess fuel. On the other hand, Eq. (GC-6) departs significantly from its premise for the general D' in the course of tracking. The approach takes on more significance for multimodal propellants; for monomodal propellants, it is still constrained by the practical upper limit for ζ_{ox}.

King adheres to the geometry existing at each increment of tracking, Eq. (K-6).

Flame Heights

The diffusion flame analysis has moved in several different directions from the original BDP version. All continue to be based, in one way or another, on the Burke-Schumann analysis[21] of a coaxial Bunsen-burner flame as modified by Williams.[22] Referring to Fig. 2, the analogy of the surface to the mouth of a coaxial Bunsen burner is evident. The inner oxidizer jet is of diameter D', and the outer fuel jet extends from D' to b.

King makes one preliminary change to accommodate the Burke-Schumann assumption that the gas jet velocities are equal. He assumes that the surface areas somehow adjust immediately in the gas phase to meet this requirement. Thus D' adjusts to a new value given by Eq. (K-6a). Implicit in BDP and the other models is that the velocities somehow adjust immediately to a value consistent with m_T/ρ_p to meet this requirement. One artificiality replaces another. It is possible to make too much of this issue because Burke-Schumann does not consider a concaved inner mouthpiece, a displaced inner mouthpiece or the presence of a competing monopropellant reaction inside the diffusion flame envelope. For this and other reasons, Beckstead and Cohen have essentially abandoned Burke-Schumann model calculations but have retained a key property of the solution for one limiting condition.

The Burke-Schumann analysis provides a series solution relating the axial and radial coordinates where mixedness is achieved relative to stoichiometry and the flame is located.

There are two possible solutions, one where the flame closes over the oxidizer jet and one where it bends over the fuel jet. The BDP model produces the former situation, which is consistent with the physical picture of Fig. 1, but wide swings in O/F ratio possible in other models (or other propellant types) can encounter the latter situation. The BDP model made two important simplifications to reduce computational time. First, it limited the calculation to the center of the oxidizer particle and assumed a parabolic flame shape to avoid calculating the entire flame shape. Second, it limited the calculation to the first term of the infinite series. Glick & Condon[15] have shown that this is not a good approximation, although it does provide a closed form expression for the flame height. In further studies of the properties of the solution, Beckstead[9] concluded that the limiting condition of a "short flame" was reasonably representative of the regime of interest. The expression for the diffusion length becomes Eq. (B-7). The factor A_{fh} converts the parabolic flame into an effective flame sheet for purposes of one-dimensional heat transfer to the surface. It represents that fractional height of the parabola, which, as a sheet, would average the parabola. C_{pD} is an optimized proportionality constant ("floating parameter"). Since η' remains fairly constant for a given propellant chemistry, and ϕ_1=3.83, Beckstead has considered making X^*_{pD} simply a constant times b in his more recent work.

Cohen has taken the same approach, but his expression for X^*_{pD} is Eq. (C-7). The placement of η' in the denominator rather than the numerator is an old error, but of little consequence because η' is fairly constant for a given propellant chemistry. Thus, the Cohen value for C_{pD} is different from the Beckstead value such that Eqs. (B-7) and (C-7) are essentially the same numerically. For AP propellants, the value of C_{pD} used by Cohen[23] has remained unchanged for nearly 10 years, so this "floating parameter" has become venerable.

Glick & Condon, and King, retain the formal analysis (see Eqs. (GC-7) and (K-7)). Since King and Glick & Condon anticipate wide variations in O/F ratio, both solution cases are contained. Approximately 10 terms of the series are carried. Glick & Condon follow BDP by calculating the peak location, $J_0(\phi_i\xi)$=1. King, to avoid a singularity at stoichiometric proportions, iterates for the point where only 90% of the mixedness is achieved.[24] To also avoid repetitive case-to-case computations, King[24] has parametrized his solution in the form of look-up correlations by running an extensive set of calculations externally to the combustion model. King also writes ν in terms of mole fractions rather than weight fractions, and accounts for portions used up in subsurface reactions not considered by the other models. King is the only one who accounts for changes in ν in the course of tracking, and who does not use an average flame height.

Glick & Condon follow BDP in expressing ϑ/ν (see Eq. (GC-7e)). King has a slightly different temperature-dependence for ϑ, and expresses ν in terms of the oxidizer characteristics (with the adjusted area) rather than in terms of m_T (see Eq. (K-7e)).

In all of the models, the diffusion flame height is the sum of the mixing height, X^*_{pD}, and the kinetics reaction distance X^*_{pF}. King expresses X^*_{pF} from an approximation of Zeldovich premixed flame theory. The others follow BDP, which used an approximation of von Kármán laminar flame theory. All of the models assume that the primary flame achieves the thermochemical flame temperature. King accounts for changes in the thermochemistry with O/F in the course of tracking. The AP monopropellant flame height is similarly expressed, see Eqs. (9). Beckstead has computed the effect of the final flame to be negligible in the surface energy balance because of its distant location (it is always furthest away, by model definition). Thus, he has removed it from the BDP surface energy balance, but keeps it in the model in order to properly compute T_{AP} by accounting for the heat transfer from the final flame to the AP flame. This process is consistent with the physical model, and is also accounted for by Glick and Condon. Cohen agrees that the final flame is negligible, but has retained it in the BDP surface energy balance. The Beckstead approach is the correct one because the final flame serves to heat the AP flame rather than superpose with the AP flame in heating the surface. However, the error is minor so long as the effect of the final flame is small. King omits the final flame completely. The final flame height is given by Eqs. (10). Taking the AP flame as the starting point for the mixing region of the final flame is consistent with the physical model. However, the computation of X^*_D may contain a serious conceptual error because it is computed in the same manner as X^*_{pD}, with the same characteristic dimensions. The characteristic dimensions should not be the same above the surface as they were at the surface. An argument can be made that they are smaller, which could have a significant impact upon high pressure results which are currently in error. The omission of a reaction distance for the final flame is of negligible effect. All of the flame heights are non-dimensionalized in accordance with one-dimensional heat transfer analysis in the gas phase, see Eq. (11). King uses m_T for the flames, which appears to be inconsistent with his definition of gas velocity. Beckstead, Cohen and Glick & Condon use m_T for the primary flame but m_{ox} for the other flames; although this may be consistent with the physical picture, it is no longer possible to interpret a consistency with the Burke-Schumann requirement of uniform velocity. Beckstead and Cohen avoid the issue to the extent that they evolve away from Burke-Schumann.

Energy Balance

The energy balance as written by BDP is followed by Cohen and Glick & Condon (see Eq. (C-12)). The flame terms are in the form of one-dimensional heat transfer analysis from a flame sheet. The superposition of the AP flame and the final flame is considered to be error. Glick and Condon properly feed the energy from the final flame back to the AP flame for purposes of Eq. (9a), but not here. For purposes of Eq. (9a), Eq. (9b) is used. The β_F term is an attempt to partition the AP reactants between the primary flame on the one hand and the sequence of the AP and final flames on the other hand. Since this could not be done in the diffusion analysis, it is done by projecting the flame areas on the planar surface of the AP. The AP and final flames project on the same inner circle,

the primary flame projects on the remaining outer annulus. Thus, the partitioning can be interpreted as one based upon geometric zones of energy influence[16] (a quasi two-dimensional effect), but it is meant to be based upon species. This is how the competing flame feature of the model becomes operative.

Beckstead now writes an energy balance for each oxidizer and binder.[10] This is done primarily with active binder propellants in mind, but is applicable to inert binders also. However, all of Beckstead's results (to be shown later) are based upon an earlier version[19] having the single energy balance. In keeping with the present discussion (simple propellants), the simpler version will be used here. The extended version and its problems will be deferred to later discussion. The simpler version can be written as Eq. (B-12). Beckstead now includes detailed species partitioning in expressing Q'_{AP}. For purposes of the present discussion, it can be obtained from Eqs. (9b) and (12a). All of the other Eq. (12) relations are the same. In this simpler version, $m_f S_f$ is not computed separately but follows the oxidizer to preserve the formulation.

King makes two changes from the BDP approach. First, there is a partitioning of surface energy terms to account for more surface processes. Second, the diffusion flame is taken to release its heat uniformly over the diffusion distance rather than singularly at the flame height. This method approximates distributed reactions. King also accounts for differences in specific heats, but a constant specific heat version will be shown here to facilitate comparison with the other models. The result is Eq. (K-12). The fraction of AP reacted in subsurface reactions, β_{oxss}, is determined by integrating the Arrhenius equation in a reactive layer but assuming a nonreactive thermal profile. This is error. The analysis for a thin reactive melt layer has been performed by Bowyer & Cohen.[25] The reactive layer thermal profile is nearly linear which is quite different from the exponential profile assumed by King. With β_{oxss} thus defined, β_{fss} is determined assuming that a stoichiometric amount of fuel reacts with the oxidizer in the subsurface reactions. Subsurface reactions involving both oxidizer and inert binder are not generally accepted. The β_f from the BDP model (but without A_{fh}) may be isolated in King's equation, but the overall competing flame partitioning is seen to be complicated by distributed heat release.

The foregoing equations are solved by a numerical iteration because surface temperature, surface areas, mass flux and flame heights are all interdependent.

Monopropellant Model Developments

Several recent models have been developed to describe the deflagration of the monopropellant powder ingredients (AP, HMX and RDX).[26,27] These models offer a potentially significant improvement to the composite propellant models because description of the monopropellant is a necessary part. The present treatment in the statistical models may be too simplified, although Beckstead[28] has argued that it is adequate. The new developments are more detailed, and address additional processes beneath the surface and in the gas phase. It has been suggested that comprehensive monopropellant models could conveniently be incorporated into the composite propellant models by parametrizing the monopropellant solutions. Thus, tables could be called for AP, HMX, etc. in the course of the propellant solution procedure. It would be analogous to what King has done with the Burke-Schumann diffusion model. The monopropellant modeling work is continuing.

EXTENSIONS TO MULTIMODAL AND ACTIVE BINDER PROPELLANTS

Glick & Condon

In the Glick & Condon view, there is no such thing as a unimodal propellant. This is, of course, true in the sense that no propellant is made with particles which are literally all of one size. Thus, they make a distinction between "monodisperse" (all sizes the same) and "polydisperse" (a distribution of sizes about some mean) in referring to any given "particle size" that is incorporated into a propellant. Similarly, the distinction is made for multimodal propellants which are monodisperse or polydisperse. The polydisperse propellant is subdivided into particle-binder pairs, one for each size, which are called "pseudopropellants". Glick & Condon obtain the propellant burning rate by summing the proportional contributions of each pseudopropellant to the mass flux. The procedural relation is given by Eq. (GC-14). The heart of theproblem is the monomodal model presented previously, which determines the mean state $\bar{m}_{Tj}$ of each size D_j. This is summed over all sizes in the m^{th} mode, each component being weighted in accordance with a log-normal size distribution function representing its proportional amount. The log-normal distribution is a very good representation of size distributions incorporated into propellants.[15,29] Results are then summed over all m modes for the j^{th} oxidizer, each mode weighted in accordance with its fraction of the total solids. For a monomodal AP propellant, j=1, m=1 and F_m=1. Lastly, results are summed over all j oxidizers. In this framework, a different model for a different oxidizer would be reflected in the method of calculating m_{Tj}. Glick & Condon have not, however, performed any computations for mixed oxidizer propellants.

The remaining task is to define ζ^*_{ox}, or the amount of binder to be allocated to oxidizer in each pseudopropellant. Glick & Condon argue that, considering the manner in which particles are packed and wetted in real propellants, the relation is not simply based on a weight proportion. One though might be to apportion based on particle surface area, considering wetting only, and this has been adopted by Beckstead in his current work. Glick & Condon prefer to leave it as a floating parameter particle size dependence. The result is Eq. (GC-15). ζ^*_{ox} replaces ζ_{ox} in all of the constitutive relations for m_{Tj}. It can be verified that $\zeta^*_{oxj}=\zeta_{oxj}$ for C_N=3, which would be the simple weight proportioning. C_N=2 corresponds to proportioning based on surface area (current Beckstead). Parametric results for an 87.4% AP/HTPB propellant are shown in Figure 4. Note that, for C_N<3,

fine sizes become fuel-rich and coarse sizes become oxidizer-rich. This is taken into account in the mixture ratio and thermochemistry of each size. Note also that it impacts the characteristic dimensions and other size-dependent aspects of the problem. As might be expected, the burning rate of each pseudopropellant is sensitive to the value of C_N (especially for the finer sizes).[13] The propellant burning rate becomes largely a question of the extent to which the finer sizes contribute. In any event, essentially all of the published results are for $C_N=3$, so $\zeta^*_{oxi}=\zeta_{oxi}$ anyway.

Probably the chief criticism of Glick & Condon here is that the gross propellant behavior cannot simply be a summation of uncoupled and non-interacting parts. Secondarily, there are implicit violations of formulation continuity because the contributions are not constrained to their proportions as formulated. The interpretation of inactive leftover material leaves something to be desired.

Beckstead and Cohen, et al. Methods

Beckstead and Cohen have two model versions, which might be called old version[6,9] and current version.[8,10] In each case, the distinguishing feature is the number of surface temperatures calculated. In the old version, only one surface temperature is calculated. Beckstead superposed up to three contributing diffusion flames (trimodal oxidizer) in a single energy balance. Essentially, Eq. (12) was expanded for three sets of competing flames with formulation continuity preserved completely. The characteristic dimension of each flame was calculated by assuming that the smallest particle is part of a higher density binder as far as the larger particles are concerned, and that the space occupied by larger particles is gone from a shrunken propellant volume as far as the smaller particles are concerned. Eq. (B-7) was used to compute each diffusion length. Cohen and Price with Derr calculated a single diffusion flame based on an average characteristic dimension for bimodal oxidizer. Cohen used the BDP method to calculate an average δ, which is open to question for multimodal packings because the particles are not all lined up as they are in the unimodal array. Since Cohen-Price-Derr calculated one surface temperature from a single energy balance, formulation continuity was preserved. With respect to surface structure, Cohen-Price-Derr superposed each contribution to S_{ox} according to volume fraction (the size-dependence is in t_{ign}, which Beckstead dismissed as having a negligible effect). Although these two models indicate ways of treating bimodal or trimodal oxidizer, through averaging and superposition, they are too simple and not physically satisfying. The new versions were aimed toward mixed oxidizer and active binder propellants, but could be applied to multimodal propellants also. Cohen and Price with Strand have published results with the new version,[8] but Beckstead has not as yet.

The new version continuity relations for a dual-oxidizer active binder propellant are given by Eqs. (B-14) and (C-14). The only difference between the two equations is that Beckstead calculates the planar binder area explicitly, from binder volume fraction, whereas Cohen-Price-Strand constrain the binder area to that remaining after the oxidizer areas are calculated. There is an inconsistency in Beckstead's method because the oxidizer surface is not generally planar. For inert binders, Cohen-Price-Strand preserve continuity as between binder and total oxidizer by replacing the binder term in analogous fashion to Eq. (C-1). For active binders, they assume that the binder burns with such independence that the binder burning rate (as a monopropellant) can be input directly for r_f. Beckstead calculates a separate surface temperature for the binder, and does not preserve either oxidizer-oxidizer or oxidizer-binder continuities, whether the binder is active or inert. Either way, the binder burning rate is a function of its surface temperature in accordance with Eq. (2b).

Cohen continues to calculate a δ by the BDP method, but now extends it to 4 particle sizes to accommodate two bimodal oxidizers. His intent was to use the old version model for each bimodal oxidizer, and the new version to couple the two oxidizers. Cohen uses this scheme for mixed nitramine propellants where the diffusion flame is less significant (see later), but does not recommend a 4-particle calculation in this way where AP is involved. The equation for δ is cumbersome[8] and will not be reproduced here. Given this δ, b for each oxidizer is 1/2 the sum of δ and the appropriate D'. Thus, there are two sets of multiple flames, one for each oxidizer, requiring two energy balances for two surface temperatures. The Beckstead b for each particle is now given by Eq. (B-6), but requires the proper ζ^*_{ox} in accordance with Glick's approach. Beckstead takes $C_N=2$ and obtains (by independent derivation) Eq. (B-15), which is consistent with Eq. (GC-15). The ζ^*_{oxj} is used to compute a diffusion flame temperature for each particle. The resulting drop in local flame temperature is significant and requires the insertion of another floating parameter to adjust the flame height. Cohen-Price-Strand, who do not use this approach, assume that the propellant flame temperature is applicable to both flames. An argument can be made for that assumption in the case of multimodal propellants, but it is not physically consistent or realistic for mixed oxidizer propellants.

The Cohen-Price-Strand energy balance for each oxidizer (or particle, when using this approach for bimodal propellants) is given by Eq. (C-16). The $(m_{ox}S_{ox})$ summation can be related to m_T through Eq. (C-14). For inert binder, it is simply $m_T S_o$ times the summation of α_{oxj}. Note that the energy balance and binder are apportioned in accordance with oxidizer mass flow. It is through this, the dependence of diffusion flame height on m_T, and the fact that m_T as computed for j=1 must equal that as computed for j=2, that the solution is said to be "coupled".

Beckstead's energy balance, following some manipulation is for each oxidizer (or size) given by Eq. (B-16). For the binder, it is Eq. (B-17). The elaborations stem from the desire to assign species and energy. Portions of the AP and binder go to the primary flame (β_F). A portion of the AP reacts stoichiometrically in the AP flame (β_{AP}). Remaining species go to the final flame. A portion of the primary flame heats the AP (γ), the remainder heats the binder; the assigned proportion is arbitrary. If the binder is active, there is another flame term which is treated like the AP flame (but with different kinetics constants). A detailed model of double-base propellant combustion is not used. The portion of binder species which do not go to the primary flame go to the "double-base" flame (β_{DB}). It is plausible that fuel species from an active binder can form a primary flame with the AP decomposition products, and there is experimental evidence for such interaction. Beckstead's solution, like Cohen's, is coupled but there are more terms to keep track of. Both have reported some difficulties with the iteration, which may be symptomatic of remaining inconsistencies. This is going to be a problem as the modeling gets more complicated, and merits careful attention.

Although the new versions are more physically appealing than the old ones, the violations of continuity continue to be disturbing. It may be necessary to provide additional terms or mechanisms to restore continuity in fact.

OTHER MODEL EXTENSIONS

Aluminized Propellants

Cohen, Glick & Condon and the old Beckstead version treat aluminum in a very simplified way. Its presence is accounted for in the computation of oxidizer volume fraction wherever that is used in the model. It is as though the binder were a higher density material. Second, the flame temperature used accounts for the thermochemistry of the aluminum. Thus the flame energy is increased. Third, a heat of fusion term is added to the energy balance since aluminum particles generally melt and agglomerate at the surface. The current Beckstead model is the first attempt to incorporate the details of aluminum behavior in a propellant combustion model. The model is described reasonably well in Ref. (10). Only a brief statement of what is done will be given here.

The aluminum occupies space as in the simple model. The heat of fusion term is added to the binder energy balance only, because the aluminum is in the binder. Rather than use a new thermochemical flame temperature to redefine Q_{PF} and Q_{FF}, new flame heat release terms are added to the oxidizer and binder energy balances. The other multiple flame thermochemistry remains as before, as though no aluminum were present. This approach is probably a better representation of how the aluminum contributes. The heat release terms represent a sum of contributions from "parent aluminum" (particles as formulated) and "agglomerated aluminum". Beckstead determines the fraction agglomerated, the agglomerate size, and the "flame height" for parent and agglomerated aluminum by combining theories of aluminum behavior, correlations of experimental data and calculations of particle motion off the surface. The essential result of this model is that aluminum burning occurs too far away from the surface to contribute anything significant to the surface energy balance. An exception would be fine parent particles which do not agglomerate, but that is a contradiction because fine particles are found to agglomerate quite extensively. The calculated ignition and burning distances are reasonable in the light of what is observed from motion pictures of burning propellants.

The simple and sophisticated models, and data in general, indicate that aluminum per se has a small effect upon burning rate. For most practical propellants, the effect appears to be rather one of removing oxidizer or binder or both to make room for the aluminum. Exceptions may be explained by surface interaction effects which lower burn rate, or circumstances whereby there are many fine particles burning to raise burn rate. The former is not addressed at all in the model, and the latter would require a more refined description of the aluminum behavior. Beckstead has made use of existing knowledge in a tractable way, and it is a good step forward.

Catalyzed Propellants

The models treat catalysts by modifying one or more of the kinetics constants contained. An optimization or calibration is performed in association with burning rate data to try to deduce the principal parameter affected. In this way, the model can help to discern the catalytic mechanism. Once the effect is deduced, the calibrated model is presumably applicable to other propellants in that class. The models do not describe a mechanism of catalysis per se, and would not be able to predict the effect of some new additive a priori. More cannot be done without detailed knowledge of catalytic processes in propellants.

Nitramine Propellants

The only published model of nitramine propellants in the BDP framework is that of Cohen, Price and Strand.[7,8] The model builds upon earlier BDP ideas and later experimental work.[23,30] The model modifications take note of the different surface and flame structures of nitramine propellants, and the different physical and chemical properties of nitramines, relative to AP propellants and AP. The nitramines of greatest interest are HMX (cyclotetramethylene tetranitramine) and the very similar RDX (cyclotrimethylene trinitramine). These nitramines are energetic monopropellants, and are fairly well balanced stoichiometrically such that they cannot really be called "oxidizers". Relative to AP, these nitramines have very low melting points and bulk melting of particles has been observed at low heating rates (low burning rates). At conventional rocket pressures, the propellant

surface is a planar melt consisting of the nitramine and binder which appears to have admixed with the nitramine at the particle peripheries.[23,30] At high pressure, above what has been identified as a particle size-dependent critical burn rate, the surface structure takes on a markedly different appearance.[23,30] Surface craters form, which are identified with combustion along paths of adjoining particles. It has been observed that, under these conditions, the nitramine particles are no longer melting. The flame structure consists of an active primary flame and the monopropellant flame. It is plausible that fuel binder decomposition products can react with some of the oxidizing species produced by nitramine decomposition to form a primary flame. However, a final flame is unlikely because there is nothing left to react the excess fuel. In the case of an active binder, even a primary flame is unlikely because both ingredients are stoichiometrically balanced and experiments have shown no interaction. Other physical, chemical and thermochemical constants required by the model will change relative to AP propellants. Only a synopsis of Cohen's method will be given here.

New expressions for S_{ox}/S_o are employed to describe the planar and cratered surface states. For the planar state, it is the particle volume fraction corrected by a floating parameter to attempt to account for the peripheral binder interference. For the cratered state, it is an exaggeration of the BDP model expression since h/D_o can exceed 1. It is not consistent as an expression of geometry, but it makes the essential point that S_{ox}/S_o approaches 1 so that the burning becomes dominated by the nitramine as shown by data. The change in the surface structure is deemed to occur at that burning rate (heating rate) where passage of the solid phase thermal wave across a spherical particle is too fast to heat the bulk particle to its melting point. The shift in the surface structure is the proposed mechanism for a major shift in pressure exponent observed with nitramine propellants.

The flame structure follows the BDP model, except that there is no final flame. Diffusion length floating parameters are adjusted from AP propellant values. For bimodal nitramine propellants calculated as j=1 (old version), b is computed using an average D' and δ. For j=2 (new version), each b is determined by δ and the respective D'. Unlike AP, it makes very little difference whether a bimodal propellant is calculated by the j=1 or j=2 method because the diffusion flame is relatively unimportant. For nitramine propellants, the diffusion flame temperature is much lower than the monopropellant flame temperature; the reverse is true with AP. With active binder, the diffusion flame is omitted. The weak diffusion flame is the proposed explanation for the small effect of particle size on burning rate. The major role of particle size on burning rate is to locate the region of the exponent shift, and to that extent there is a major effect on burning rate.

RESULTS

Monomodal Propellants

The BDP model standard cases were three AP/Polysulfide propellants. Two contained 70% AP, one of 20μ particle size and the other of 200μ. The third contained 60% of 20μ AP. The burning rate predictions were good for two of the cases, but on the low side for 200μ AP. Of equal importance, results for surface temperature, flame heights, surface structure, etc. (i.e., various internal details) were reasonable.

Glick & Condon[14] performed an interesting exercise on two of these cases to illustrate the individual effects of their proposed model modifications. Some of their results for one case are shown in Table 1 as the ratio of burning rate computed with the indicated modification to the BDP rate. The only significant change is by the use of time-averaging rather than the statistical average particle. But even here, the effect is limited principally to higher pressures and is not a large effect. Differences for the 200μ case were even smaller.[14]

Table 1. Effect of Modifications to BDP Model on Computed Burning Rates for an AP/Polysulfide Propellant (70% AP, 20μ); Ref. (14).

Pressure (psia)	Replace So with Sp (Eq. 1)	Eq. (B-6) for b	More terms in B-S series	Time-average method
52	1.000	0.991	1.000	0.981
93	1.006	0.988	1.006	0.976
165	1.004	0.972	1.004	0.943
294	1.003	0.953	1.006	0.896
520	1.005	0.934	1.007	0.852
932	1.046	0.964	1.014	0.796
1652	1.074	0.966	1.034	0.728

A comparison has also been made between the BDP model (as represented by Cohen) and King's model. This comparison would reflect the combined effects of the most elaborate departures from BDP. King[16] used three AP/HTPB propellants containing 73% AP; particle sizes were 5μ, 20μ and 200μ. Several important points were gleaned from this exercise, summarized by Figure 5. The striking observations are the gross underprediction of the 200μ case and the virtual identity of the two models for that case. Both models predict the other two cases reasonably well, but there are differences in the character of the curves produced. King's model is better as to general pressure exponent behavior, but BDP is better in picking up the inflection in slope which is attributed to the β_F shift (AP flame becoming controlling). King is able to improve his predictions as a whole by optimizing the kinetics of his subsurface reactions.[16] There is a large effect on the 200μ case, as shown, but only small effects on the other cases (not shown, in the interests of figure clarity). This is probably the most important point, and merits further discussion because it illustrates a latent deficiency in the BDP model.

Cohen's calculations showed that the β_F shift occurs at lower pressures as particle size increases. For 5μ, it occurred at about 100 atm (arguably in agreement with the data). For 20μ, it occurred at about 35 atm (in agreement with the data). For 200μ, according to the model, the β_F shift occurred below 10 atm. Thus, the entire regime is one of AP flame control. Predictions are good in regimes of diffusion flame control, but become poor in regimes of AP flame control (coarse AP or high pressure). King's optimization served to magnify a pressure-dependent AP heat release process. It is very important where AP fully takes over from the diffusion flame as the primary energy source (200μ), but of little importance otherwise (5μ and 20μ). In the BDP model, there is no sustaining pressure-dependent heat release term in the regime of AP control. The AP flame approaches a collapsed flame asymptote ($\xi^*_{AP} \to 0$), which is reflected completely by the predicted burn rate curve for 200μ. Q_{ox} is not pressure-dependent in the BDP model, but effectively becomes so in King's model with optimized constants.

This "latent" deficiency has not been noted before because circumstances have not encountered it or have masked it. Higher flame temperatures, multimodal sizes, and a restricted upper pressure all will promote diffusion flame control through most of the calculations. All of the multimodal calculations to be presented have this latent deficiency, but it is "dormant" for these reasons. King has proposed a correction, but it is not necessarily accurate. The advanced monopropellant models[27] incorporate related but better justified mechanisms that would produce a similar effect. Also, the final flame merits a reconsideration in the quantitative scheme, which could augment pressure-dependent heat feedback when $\beta_F < 1$. In any case, there is some unfinished business to resolve.

Multimodal Propellants

A statistical correlation of experimental data for trimodal AP propellants, by an effective average particle size, has been performed by Miller[31] and is shown in Figure 6. This correlation may be compared with parametric model results for the effect of monomodal particle size on burning rate. The model results, for Glick & Condon and Beckstead calculations at Miller's solids loading, are shown in Figure 7. Although the monomodal size cannot really be compared with the Miller average size, the ability of the models to show the qualitative mechanistic particle size effect is impressive. Condon also shows the effect of particle size distribution width or standard deviation for polydisperse monomodal sizes. This detail is but a small correction to the monodisperse results. Consistent with remarks pertaining to Table 1, the time averaging method departs from the BDP method results most significantly with finer sizes.

Another example of parametric results, for biomodal AP, is Beckstead's old version results shown in Figure 8. Condon[29] has made the same calculations, and the results are quite similar. These calculations typify what can be done with and learned from the models. Similar curves have been generated for pressure exponent and temperature sensitivity. Beckstead's pressure exponent results are shown in Figure 9. Note that there is an optimum fine size, and a stronger effect of fine size than coarse/fine ratio. The trends are qualitatively correct. Figures 10 and 11 demonstrate a remarkable quantitative agreement with Miller's rate and exponent data, respectively. Condon[29] performed the same calculations and showed similar agreement.

The modelers have noted that, in general, agreement with data is worst where there is a large difference between coarse and fine sizes. Cohen is attempting to resolve this problem by adding an interacting flame to the flame structure of a coarse particle adjacent to fine particles. Miller has endorsed the idea of interacting flame modeling because he sees particle size interactions running through his data correlations.[31] Cohen's work is not considered complete and has not been formally published.

Aluminized Propellants

Glick & Condon comparisons[32] with some of Miller's aluminized propellant rate data are shown in Figure 12. The agreement is good for some propellants and bad for others. A systematic problem appears to be those propellants having the widest spread between coarse and fine sizes in their respective subgroups. Those are the high points on Figure 12. Thus aluminum interactions are affecting the AP particle size interactions to a degree that the modeling must address them. The satisfactory predictions are consistent with the background of small effects of aluminum.

Beckstead[9] performed the same calculations with his old model and showed similar discrepancies. The general agreement between the Beckstead and Glick & Condon models as applied to Miller's propellants is remarkable in view of the differences in approach.

Nitramine Propellants

Results for two HMX propellants are shown in Figure 13. An attempt was made to approach monodisperse propellants by particle screening for each batch. Ordinarily, a given lot of HMX is quite polydisperse. The result, for the coarse HMX propellant, was an extraordinary exponent shift. The monodisperse model shows this as a discontinuity in the surface structure at the critical burn rate. The burn rate jumps to a value that is essentially the HMX rate. The slight exponent shift in the fine HMX propellant is the β_F shift. Rates do not jump as long as the surface remains planar. Approximately, the critical rate is inversely proportional to particle size. These data were used to calibrate the adjustable constants in the model. Upon calibration, the model was successfully applied to other monomodal HMX and RDX propellants.[7]

The latent deficiency discussed earlier does not show up in the HMX propellant calculations. This is perhaps due to the different kinetics and energetics, etc. constants of HMX and HMX propellants. Nevertheless, corrections for AP propellants should be carried over to nitramine propellants to the extent relevant.

Results for a series of biomodal HMX propellants are shown in Figure 14. Based upon examination of fine HMX particle size distributions, Cohen has split the fine component into two sizes. He has made an issue of HMX particle size quality control in connection with the exponent shift and hazards problems. Thus, the model has viewed these propellants as trimodal. Cohen and Price found that, for nitramine propellants, the j=1 and j=2 features of the model can be combined to calculate up to 4 particles. Although numerically unimportant, it is conceptually inconsistent. The predictions show the observed effect of changing coarse/fine ratio very well.

Active Binder Propellants

The effects of adding AP or HMX to an energetic double-base binder are shown in Figure 15. The key to these predictions is the treatment of the diffusion flame in Cohen's model. With AP, it is present such that the burning rate increases at low and intermediate pressures. The rate would also be noticeably particle-size dependent. The latent deficiency would not show up because the active binder takes over control at high pressures. With HMX, the diffusion flame is omitted such that the burning rate falls if the HMX rate is lower than the binder rate. The rate would not be noticeably particle-size dependent, except for exponent shift behavior at pressures higher than plotted here. As noted before, there is a need to incorporate a combustion model for the binder. With the current method, the prediction for the binder alone is a reproduction of input data.

Input Constants

Values of input constants used by Cohen are reported in Ref. (23). Values used by Glick & Condon are in Ref. (15). Values used by King are in Ref. (16). BDP model constants are in Ref. (3), and many of them are still used. Beckstead has not formally published his constants, but implies that he uses BDP values except where there are new adjustable parameters.

CONCLUDING REMARKS

Composite propellant burn rate modeling has developed to a point where it can and does make useful contributions to combustion research and practical propellant development. The models are able, at least qualitatively, to explain the burning rate characteristics of a wide variety of propellants of interest. However, deficiencies do remain and there is work yet to be done in order to improve the quantitative aspects and predictive capability in general.

In moving forward, a list of priority items may be presented as follows: restoration of the proper pressure-dependence for AP propellants where $\beta_F << 1$, by incorporating an improved monopropellant combustion model or other justifiable mechanism; accounting for component interactions, first without aluminum, but especially with aluminum as an eventuality; re-examination of the role of the final flame for AP propellants; completing a model for the active binder; and, last but not least, experimental work to obtain needed input values and improved understanding that would serve to replace adjustable parameters.

Certain elaborations which have more physical or intellectual appeal are going to cost computer program development and run times without appreciably changing the results. This is not a trivial matter as the extended modeling grows more complicated to address practical propellants. It does not appear necessary to go to the trouble of tracking and time-averaging individual particles. Nor does it seem necessary to detail the polydisperse nature of a given modal particle size. Nor does it seem necessary to solve the complete Burke-Schumann problem. On the other hand, apportionment of component masses and energies is necessary provided that it is done carefully and properly, with conservation preserved and component interactions accounted for; otherwise, the attempt will lead to inconsistencies, poor results and/or iteration problems.

REFERENCES

1. Hermance, C.E., "A Model of Composite Propellant Combustion Including Surface Heterogeneity and Heat Generation", AIAA Journal, Vol. 4, Sept. 1966, pp 1629-1637.

2. Hermance, C.E., "A Detailed Model of the Combustion of Composite Solid Propellants", Proceedings of the AIAA/ICRPG Second Solid Propulsion Conference, June 1967, pp 89-103.

3. Beckstead, M.W., Derr, R.L. and Price, C.F., "A Model of Composite Solid Propellant Combustion Based on Multiple Flames", AIAA Journal, Vol. 8, Dec. 1970, pp 2200-2207.

4. Beckstead, M.W., Derr, R.L. and Price, C.F., "The Combustion of Solid Monopropellants and Composite Propellants", Thirteenth Symposium (International) on Combustion, Combustion Institute, Pittsburgh, Pa., 1971, pp 1047-1056.

5. Hamann, R.J., "Three Solid Propellant Combustion Models, A Comparison and Some Applications to Non-Steady Cases", Memo M-215, Delft University of Technology, Delft, Netherlands, Apr 1974.

6. Cohen, N.S., Derr, R.L. and Price, C.F., "Extended Model of Solid Propellant Combustion Based on Multiple Flames", Proceedings of the Ninth JANNAF Combustion Meeting, CPIA Publication 231, Vol. II, Dec. 1972, pp 25-42.

7. Cohen, N.S. and Price, C.F., "Combustion of Nitramine Propellants", Journal of Spacecraft and Rockets, Vol. 12, Oct. 1975, pp 608-612.

8. Cohen, N.S., Price, C.F. and Strand, L.D., "Analytical Model of the Combustion of Multicomponent Solid Propellants", AIAA Paper 77-927, AIAA/SAE 13th Propulsion Conference, July 1977.

9. Beckstead, M.W., "Combustion Calculations for Composite Solid Propellants", Proceedings of the Thirteenth JANNAF Combustion Meeting, CPIA Publication 281, Vol. II, Dec. 1976, pp 299-312.

10. Beckstead, M.W., "A Model for Solid Propellant Combustion, "Proceedings of the Fourteenth JANNAF Combustion Meeting, CPIA Publication 292, Vol. I, Dec. 1977, pp 281-306.

11. Glick, R.L., "Statistical Analysis of Non-Metallized Composite Solid Propellant Combustion", Proceedings of the Tenth JANNAF Combustion Meeting, CPIA Publication 243, Vol. I, Dec. 1973, pp 157-184.

12. Glick, R.L., "On Statistical Analysis of Composite Solid Propellant Combustion", AIAA Journal, Vol. 12, Mar. 1974, pp 384-385.

13. Glick, R.L., "Steady-State Combustion of Non-Metallized Composite Solid Propellants", Report U-75-27, Thiokol Corporation, Huntsville, AL, July 1975.

14. Glick, R.L. and Condon, J.A., "Statistical Analysis of Polydisperse, Heterogeneous Propellant Combustion: Steady-State", Proceedings of the Thirteenth JANNAF Combustion Meeting, CPIA Publication 281, Vol. II, Dec. 1976, pp 313-345.

15. Condon, J.A. and Osborn, J.R., "The Effect of Oxidizer Particle Size Distribution on the Steady and Nonsteady Combustion of Composite Propellants", AFRPL-TR-78-17, Purdue University, School of Mechanical Engineering, W. Lafayette, IN, June 1978.

16. King, M.K., "Model for Steady State Combustion of Unimodal Composite Solid Propellants", AIAA Paper 78-216, AIAA 16th Aerospace Sciences Meeting, Jan. 1978.

17. Strahle, W.C., "Some Statistical Considerations in the Burning of Composite Propellants", AIAA Journal, Vol. 16, Aug. 1978, pp 843-847.

18. Lengelle, G. and Williams, F., "Simplified Model for Effect of Solid Heterogeneity On Oscillatory Combustion", Astronautica Acta 14, 97-118 (1968).

19. Blum, E.H. and Wilhelm, R.H., "A Statistical Geometric Approach to Random-Packed Beds", AIChE-Industrial Chemical Engineering Symposium Series, No. 4, London Institute of Chemical Engineers, 1965, pp 4:21-4:27.

20. King, M.K., "An Analytical and Experimental Study of the Erosive Burning of Composite Propellants", Part A, AFOSR-TR-78-0060, Atlantic Research Corp., Alexandria, VA, Nov. 1977.

21. Burke, S.P. and Schumann, T.E.W., "Diffusion Flames", Ind. and Eng. Chem., Vol. 20, Oct. 1928; see also First and Second Symposium on Combustion, Combustion Institute, Pittsburgh, PA, 1965, pp 2-11.

22. Williams, F.A., Combustion Theory, Addison-Wesley, 1965, pp 37-45.

23. Cohen, N.S. and Strand, L.D., "Nitramine Propellant Research", AFOSR-TR-76-1163, NASA TM-33-801, Jet Propulsion Laboratory, Pasadena, CA, Oct. 1976.

24. King, M.K., "An Analytical and Experimental Study of the Erosive Burning of Composite Propellants [etc.]", Report TR-PL-5763, Atlantic Research Corp., Alexandria, VA, Nov. 1976.

25. Cohen, N.S. and Bowyer, J.M., "Combustion Response Modeling for Composite Solid Propellants", AFRPL-TR-78-39, Jet Propulsion Laboratory, Pasadena, CA, June 1978.

26. Benreuven, M., et al., "Flame Zone and Subsurface Reaction Model for Deflagrating RDX", Sixteenth Symposium (International) on Combustion, Combustion Institute, Pittsburgh, PA, 1977, pp 1223-1233.

27. Price, C., Boggs, T. and Derr, R., "Modeling of Solid Monopropellant Deflagration", AIAA Paper 78-219, AIAA 16th Aerospace Sciences Meeting, Jan. 1978.

28. Beckstead, M.W. and McCarty, K.P., "Calculated Combustion Characteristics of Nitramine Monopropellants", Proceedings of the Thirteenth JANNAF Combustion Meeting, CPIA Publication 281, Vol. II, Dec. 1976, pp 57-68.

29. Renie, J.P., Condon, J.A. and Osborn, J.R., "Oxidizer Size Distribution Effects", Proceedings of the Fourteenth JANNAF Combustion Meeting, CPIA Publication 292, Vol. I, Dec. 1977, pp 325-339.

30. Cohen, N.S., "Combustion of Nitramine Propellants", Proceedings of the Eleventh JANNAF Combustion Meeting, CPIA Publication 261, Vol. I, Dec. 1974, pp 267-283.

31. Miller, R.R., et al., "Control of Solids Distribution in HTPB Propellants", AFRPL-TR-78-14, Hercules Inc., Allegheny Ballistics Laboratory, Cumberland, MD, April 1978.

32. Glick, R.L. and Condon, J.A., "Statistical Combustion Modeling - The Effect of Additives", Proceedings of the Fourteenth JANNAF Combustion Meeting, CPIA Publication 292, Vol. I, Dec. 1977, pp 341-378.

ACKNOWLEDGMENT

Support for this review was provided in part by the Air Force Office of Scientific Research through the National Aeronautics and Space Administration and the Jet Propulsion Laboratory, and in part by Norman Cohen Professional Services. The author acknowledges the cooperation of M.W. Beckstead, R.L. Glick and M.K. King in answering many questions regarding their models.

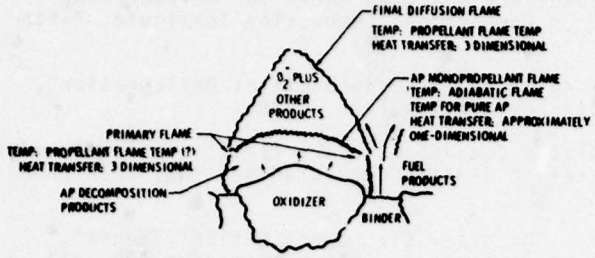

Fig. 1 BDP multiple flame structure, from Ref. (3)

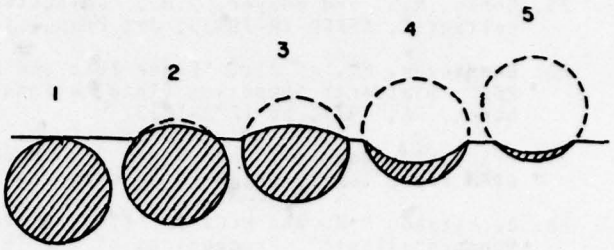

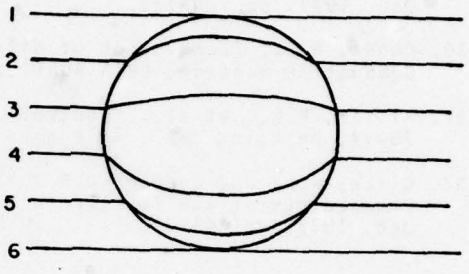

Fig. 3 The birth and consumption of an AP particle as viewed by Glick & Condon, from Ref. (15)

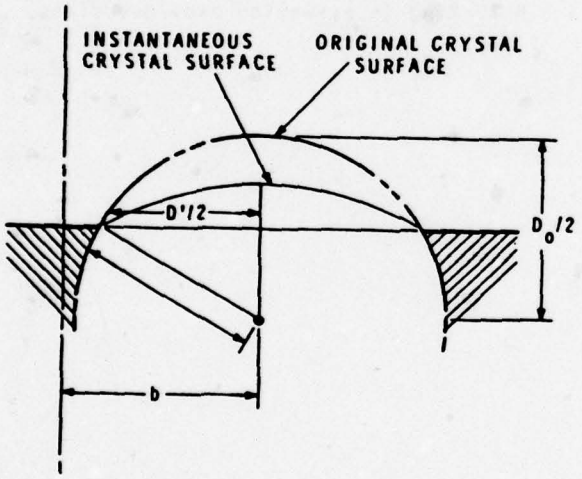

Fig. 2 BDP idealized surface structure, from Ref. (10)

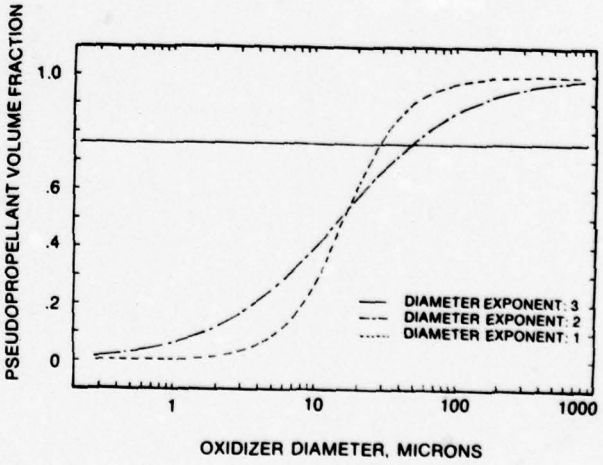

Fig. 4 Pseudopropellant oxidizer volume fraction as a function of particle size, from Ref. (15)

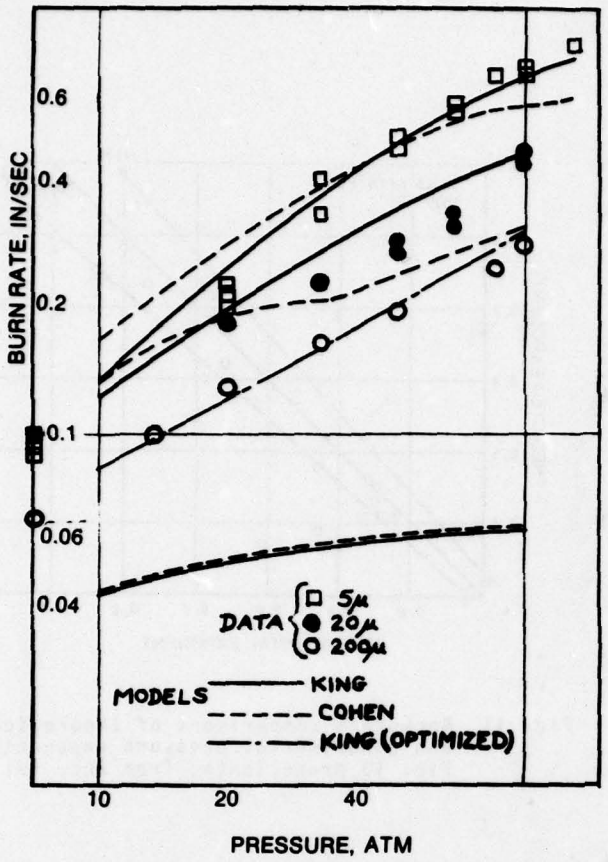

Fig. 5 Comparison of Cohen and King models for 73% AP (monomodal)/HTPB propellants

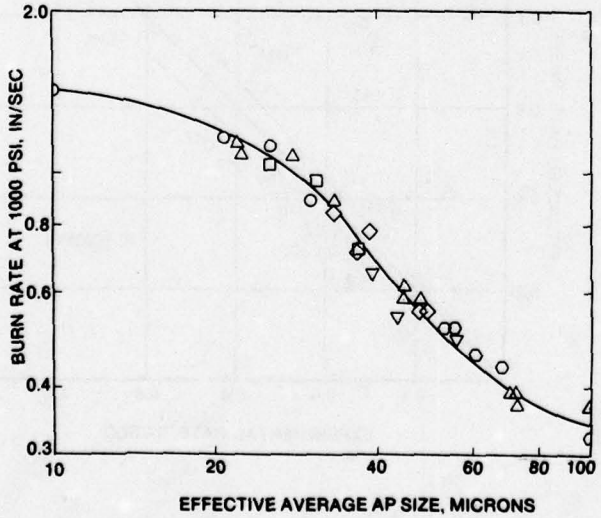

Fig. 6 Correlation of burn rate data by an effective AP average particle size, from Ref. (31)

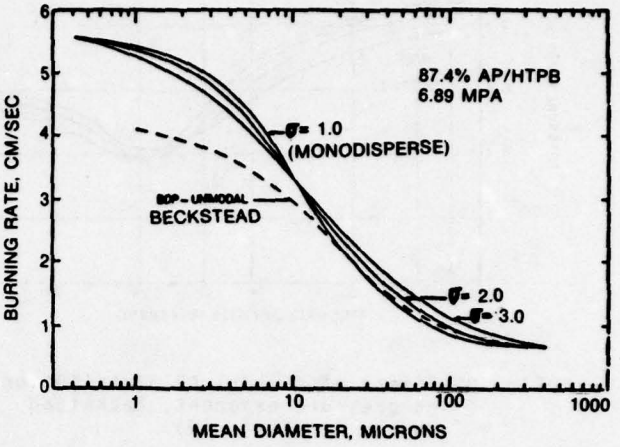

Fig. 7 Effect of monomodal AP size on burning rate, Beckstead (monodisperse) and Glick & Condon (polydisperse) models, from Ref. (29)

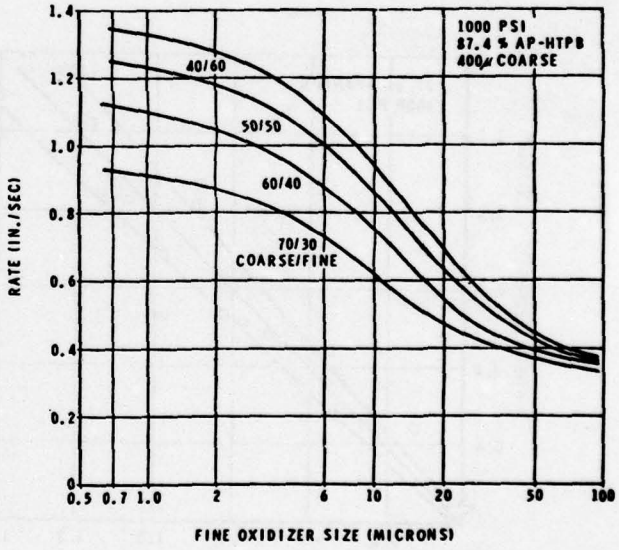

Fig. 8 Effect of bimodal AP distribution on burn rate, Beckstead model, from Ref. (9)

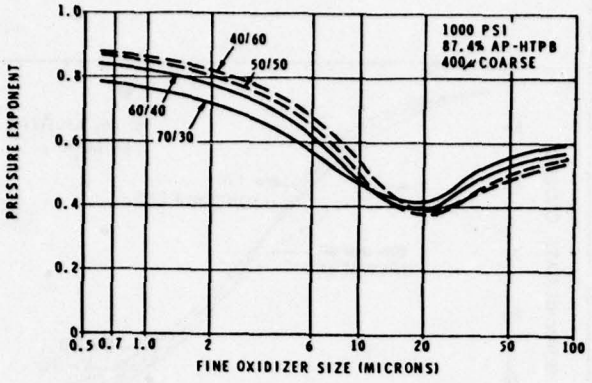

Fig. 9 Effect of bimodal AP distribution on pressure exponent, Beckstead model, from Ref. (9)

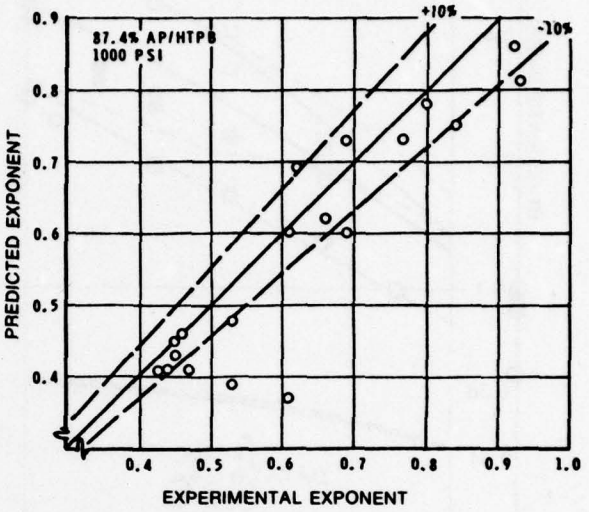

Fig. 11 Beckstead comparisons of theoretical and experimental pressure exponents, Fig. 10 propellants, from Ref. (9)

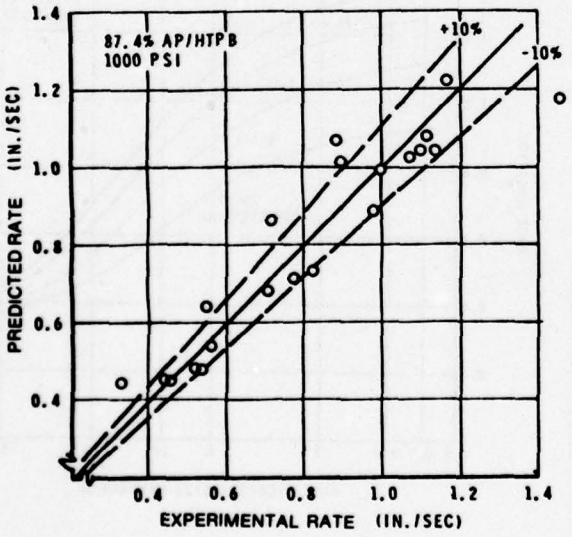

Fig. 10 Beckstead comparisons of theoretical and experimental burning rates, Ref. (31) trimodal propellants, from Ref. (9)

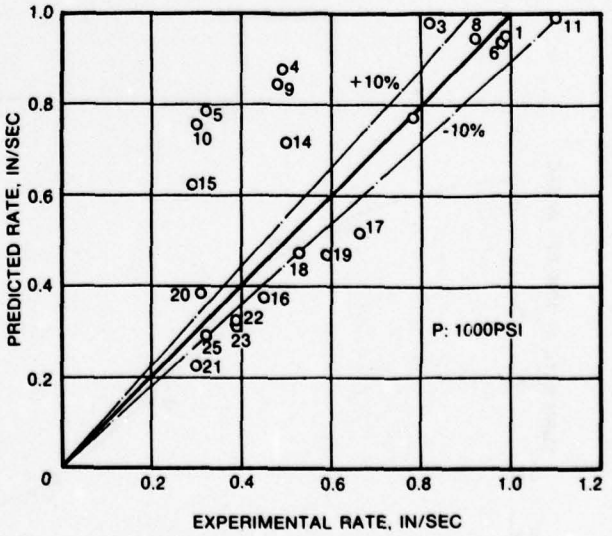

Fig. 12 Glick & Condon comparisons of theoretical and experimental burning rates, Ref. (31) aluminized propellants, from Ref. (32)

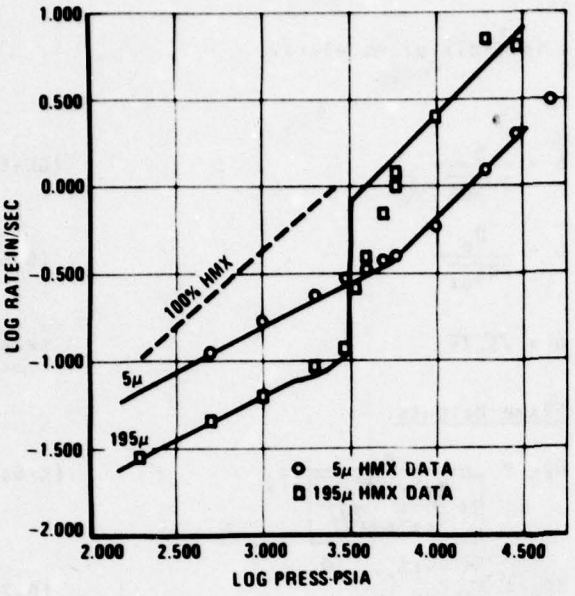

Fig. 13 Effect of monomodal HMX particle size on burning rate, 75% HMX/ HTPB, Cohen-Price model and data, from Ref. (7)

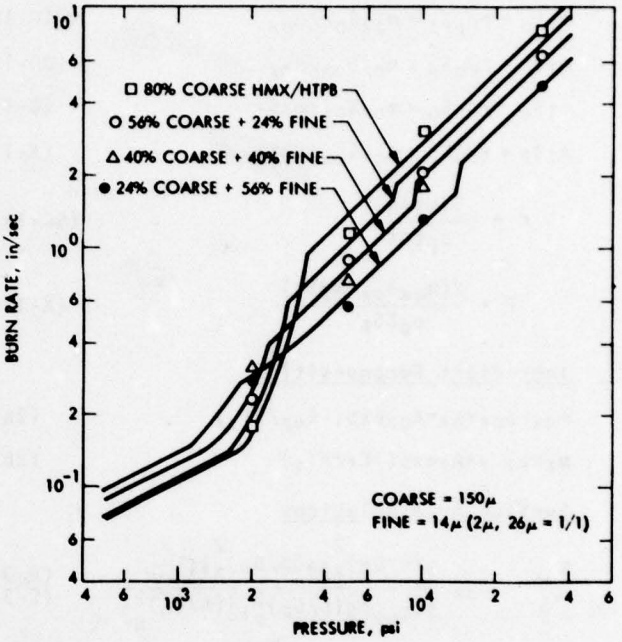

Fig. 14 Effect of bimodal HMX on burning rate, Cohen-Price-Strand model and data, from Ref. (8)

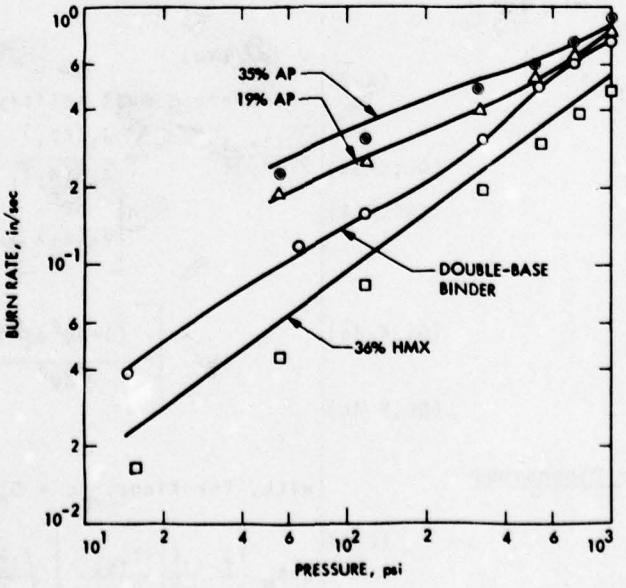

Fig. 15 Burning rates of AP and HMX active binder propellants, Cohen-Price-Strand model and data, from Ref. (8)

replaces another. It is possible to make too much of this issue because Burke-Schumann does not consider a concaved inner mouthpiece, a displaced inner mouthpiece or the presence of a competing monopropellant reaction inside the diffusion flame envelope. For this and other reasons, Beckstead and Cohen have essentially abandoned Burke-Schumann model calculations but have retained a key property of the solution for one limiting condition.

The Burke-Schumann analysis provides a series solution relating the axial and radial coordinates where mixedness is achieved relative to stoichiometry and the flame is located.

APPENDIX

Equations

Numbering system includes initials of modelers.

Continuity Relations

$$m_T S_o = r\rho_p S_o = m_{ox} S_{ox}/\alpha_{ox} \quad (C\text{-}1)$$

$$m_T S_p = r\rho_p S_p = m_{ox} S_{ox}/\alpha_{ox} \quad (GC\text{-}1)$$

$$m_T S_o = r\rho_p S_o = m_{ox} S_{ox} + m_f S_f \quad (B\text{-}1)$$

$$m_T S_p = r\rho_p S_p = m_{ox} S_{ox} + m_f S_f \quad (K\text{-}1)$$

$$\bar{r} = \frac{\Sigma(m_T \Delta t)}{\rho_p \Sigma \Delta t} \quad (GC\text{-}1a)$$

$$\bar{r} = \frac{\Sigma(m_{ox} S_{ox} + m_f S_f)}{\rho_p \Sigma S_p} \quad (K\text{-}1a)$$

Ingredient Decomposition

$$m_{ox} = \rho_{ox} r_{ox} = A_{ox} \exp(-E_{ox}/RT_s) \quad (2a)$$

$$m_f = \rho_f r_f = A_f \exp(-E_f/RT_s) \quad (2b)$$

Surface Area Relations

$$\frac{S_{ox}}{S_o} = \zeta_{ox} \frac{3(h/D_o)_p^2 + 3(h/D_o)_N^2 + 1}{1 + \zeta_{ox}[3(h/D_o)_p^2 + 3(h/D_o)_N^2]} \quad (B\text{-}3),\ (C\text{-}3)$$

$$\left(\frac{h}{D_o}\right)_{PN} = \frac{1}{2}\left(1 \pm \frac{1}{\sqrt{3}}\right)\left(1 - \frac{r_{ox}}{r_f}\right) + r_{ox}\frac{t_{ign}}{D_o} \quad (B\text{-}4),\ (C\text{-}4)$$

$$t_{ign} = \frac{C_{ign} D_o^{u_{ign}+1}}{p^{m_{ign}}} \quad (B,C,GC\text{-}5)$$

$$S_{ox}/S_p = (S_{ox}/S_o)(S_o/S_p) = \frac{h^2 + (\frac{D'}{2})^2}{(\frac{D'}{2})^2 \frac{1}{\zeta_{ox}}} \quad (GC\text{-}3)$$

$$S_{ox}/S_p = \frac{h^2 + (\frac{D'}{2})^2}{S_p(\zeta_{ox}, D_o, d_f)} \quad (K\text{-}3)$$

$$D' = 2[d_f D_o - D_f^2]^{1/2} \quad (GC,K\text{-}3a)$$

$$h = d_{ox} - d_f \quad (GC,K\text{-}4)$$

$$d_{ox} = \begin{cases} 0 & (t \le t_{ign}) \\ \frac{1}{\rho_{ox}} \Sigma (m_{ox} \Delta t) & \end{cases} \quad (GC,K\text{-}4a)$$

$$d_f = \frac{1}{\rho_f} \Sigma (m_f \Delta t) \quad (GC,K\text{-}4b)$$

Characteristic Surface Dimensions

$$b = \frac{D_o}{\sqrt{6}}\left(1 + \sqrt{3/2}\,\frac{\delta}{D_o}\right) \quad (C\text{-}6)$$

$$\frac{\delta}{D_o} = \left(\frac{\pi}{6\zeta_{ox}}\right)^{1/3} - \sqrt{2/3} \quad (C\text{-}6a)$$

$$b = \frac{D'}{2\sqrt{\zeta_{ox}}} \quad (GC\text{-}6)$$

$$b = \frac{D_o}{\sqrt{6\zeta_{ox}}} \quad (B\text{-}6)$$

$$b = \sqrt{S_p/\pi} \quad (K\text{-}6)$$

Flame Heights

$$D'_{PD} = \frac{b}{\left[1 + \frac{m_f S_f}{m_{ox} S_{ox}} \frac{\mathcal{M}_{ox}}{\mathcal{M}_f}\right]^{1/2}} \quad (K\text{-}6a)$$

$$X^*_{PD} = A_{fh} C_{PD} \frac{\eta' b}{\phi_1} \quad (B\text{-}7)$$

$$\eta' = \ln\left[\frac{2(1+\nu)cJ_1(c\phi_1)}{(\nu - (1+\nu)c^2)\phi_1 J_o^2(\phi_1)}\right] \quad (B,C\text{-}7a)$$

$$c = D'/2b \quad (B,C,GC\text{-}7b)$$

$$\nu = \phi(1-\alpha_{ox})/\alpha_{ox} \quad (B,C,GC\text{-}7c)$$

$$X^*_{PD} = A_{fh} C_{PD} \frac{b}{\eta' \phi_1} \quad (C\text{-}7)$$

$$X^*_{PD} = A_{fh} \frac{\eta b}{\psi} \quad (GC\text{-}7)$$

$$X^*_{PD} = \frac{\eta b}{\psi} \quad (K\text{-}7)$$

$$\psi = \mathcal{D}/(vb) \quad (GC,K\text{-}7d)$$

and where η must satisfy:

$$\frac{\nu - (1+\nu)c^2}{2(1+\nu)c} = \sum_1^\infty \frac{J_1(c\phi_i)}{\left[\begin{matrix} J_o^2(\phi_i) \\ \text{or} \\ J_o(\phi_i) \end{matrix}\right]} J_o(\phi_i \xi) \exp\left[-\frac{(1+4\psi^2\phi_i^2)^{1/2} - 1}{2\psi^2}\eta\right] \quad (GC,K\text{-}7a)$$

with, for King: $c = D'_{PD}/2b$ (K-7b)

$$\nu = \phi_M \frac{Y_f}{Y_{ox}} \frac{(1 - Y_{fss})}{(1 - Y_{oxss})}\left[\left(\frac{b}{D'_{PD}}\right)^2 - 1\right] \quad (K\text{-}7c)$$

Eq. (C-12)). The flame terms are in the form of one-dimensional heat transfer analysis from a flame sheet. The superposition of the AP flame and the final flame is considered to be error. Glick and Condon properly feed the energy from the final flame back to the AP flame for purposes of Eq. (9a), but not here. For purposes of Eq. (9a), Eq. (9b) is used. The β_F term is an attempt to partition the AP reactants between the primary flame on the one hand and the sequence of the AP and final flames on the other hand. Since this could not be done in the diffusion analysis, it is done by projecting the flame areas on the planar surface of the AP. The AP and final flames project on the same inner circle,

$$\mathcal{D}/v = \frac{\mathcal{D}_o T_s^{1.5} \mathcal{M}_{ox}}{RT_s m_{ox}} \frac{\pi D'^2_{PD}}{S_{ox}} \quad \text{(K-7e)}$$

$$\mathcal{D}/v = \frac{\mathcal{D}_o T_s^{1.75} \mathcal{M}_p}{RT_s m_T} \quad \text{(GC-7e)}$$

$$X^*_{PF} = \frac{(1+\nu)^2}{\nu} \frac{RT_s}{\mathcal{M}_{ox}} T_F^2 \frac{S_{ox}}{\pi D'^2_{PD}} \frac{m_{ox}}{k_{PF} P^{\delta PF}} \quad \text{(K-8)}$$

$$X^*_{PF} = \frac{m_T}{k_{PF} P^{\delta PF}} \quad \text{(B,C,GC-8)}$$

with $k_{PF} = A_{PF} \exp(-E_{PF}/RT_F)$ (8a)

$$X^*_{AP} = \frac{RT_s}{\mathcal{M}_{ox}} \frac{S_{ox}}{\pi D'^2_{PD}} \frac{m_{ox}}{k_{AP} P^{\delta PF}} \quad \text{(K-9)}$$

$$X^*_{AP} = \frac{m_{ox}}{k_{AP} P^{\delta AP}} \quad \text{(B,C,GC-9)}$$

with $k_{AP} = A_{AP} \exp(-E_{AP}/RT_{AP})$ (9a)

$$X^*_{FF} = X^*_{AP} + X^*_D \quad \text{(B,C,GC-10)}$$

$$\xi^* = \frac{mc_g}{\lambda} X^* \quad \text{(11)}$$

Energy Balance

$$m_T c_p (T_s - T_o) = -\alpha_{ox} m_T Q_{ox} - (1-\alpha_{ox}) m_T Q_f + \beta_F m_T Q_{PF} e^{-\xi^* PDF} + (1-\beta_F)\alpha_{ox} m_T \left[Q_{AP} e^{-\xi^* AP} + Q_{FF} e^{-\xi^* FF} \right] \quad \text{(C,GC-12)}$$

with

$$Q_{AP} = c_p (T_{AP} - T_o) + Q_{ox} \quad \text{(B,C,GC-12a)}$$

$$\alpha_{ox} Q_{FF} = c_p (T_F - T_o) - \alpha_{ox} c_p (T_{AP} - T_o) + (1-\alpha_{ox}) Q_f \quad \text{(B,C,GC-12c)}$$

$$Q_{PF} = c_p (T_F - T_o) + \alpha_{ox} Q_{ox} + (1-\alpha_{ox}) Q_f \quad \text{(B,C,GC-12b)}$$

and

$$\beta_F = \frac{X^*_{AP} - X^*_{PF}}{X^*_{PD}} A_{fh} \quad \text{(B,C,GC-13)}$$

$$T_{AP}' = T_F - \frac{Q_{FF}}{c_p} \left[1 - e^{-(\xi^*_{FF} - \xi^*_{AP})} \right] \quad \text{(B,GC-9b)}$$

$$m_T c_p (T_s - T_o) = -\alpha_{ox} m_T Q_{ox} - (1-\alpha_{ox}) m_T Q_f + \beta_F m_T Q_{PF} e^{-\xi^* PDF} + (1-\beta_F)\alpha_{ox} m_T Q_{AP}' e^{-\xi^* AP} \quad \text{(B-12)}$$

$$m_T c_p (T_s - T_o) = -m_{ox} \frac{S_{ox}}{S_p} \left[\beta_{oxss} Q_{ox} + (1-\beta_{oxss}) Q_{vox} + Q_{mox} \right] - m_f \frac{S_f}{S_p} \left[(1-\beta_{fss}) Q_{vf} + Q_{mf} \right] + m_T c_p (T_F - T_s) \frac{e^{\xi^* PDF}}{\xi^*_{PD} e^{(\xi^* PDF)} - (e^{\xi^* PD} - 1)} + m_T \frac{Soxp}{S_p} Q_{AP} (1-\beta_{oxss})(1-\beta_F) \frac{\xi^*_{PD} e^{(\xi^*_{PDF} - \xi^*_{AP})} - (e^{\xi^*_{PD}} - 1)}{\xi^*_{PD} e^{\xi^*_{PDF}} - (e^{\xi^*_{PD}} - 1)} \quad \text{(K-12)}$$

Model Extensions

$$\bar{r} = \sum_j \frac{1}{\rho_{ox_j}} \left[\sum_{\bar{m}} \left(\sum_i \frac{\bar{m}_{T_i}}{\zeta^*_{ox_i}} F_{D_i} \Delta D_i \right)_m F_m \right]_j \quad \text{(GC-14)}$$

$$\text{with } F_{D_i} = \frac{1}{\sqrt{2\pi}\,\sigma_m} \exp\left[-1/2 \left(\frac{\ln D_i - \ln \bar{D}_m}{\sigma_m} \right)^2 \right] \quad \text{(GC-14a)}$$

$$\zeta^*_{ox_i} = \left[1 + \frac{D_i^{C_N - 3} \zeta_f}{\sum D_i^{C_N - 3} \zeta_{ox_i}} \right]^{-1} \quad \text{(GC-15)}$$

particles are packed and wetted in real propellants, the relation is not simply based on a weight proportion. One though might be to apportion based on particle surface area, considering wetting only, and this has been adopted by Beckstead in his current work. Glick & Condon prefer to leave it as a floating parameter particle size dependence. The result is Eq. (GC-15). ζ^*_{ox} replaces ζ_{ox} in all of the constitutive relations for $\dot{m}_{Tj}$. It can be verified that $\zeta^*_{oxi}=\zeta_{oxi}$ for $C_N=3$, which would be the simple weight proportioning. $C_N=2$ corresponds to proportioning based on surface area (current Beckstead). Parametric results for an 87.4% AP/HTPB propellant are shown in Figure 4. Note that, for $C_N<3$,

$$m_T = \sum_j m_{ox_j} \frac{S_{ox_j}}{S_o} + \left(1-\sum_j \frac{S_{ox_j}}{S_o}\right) \rho_f r_f \qquad \text{(C-14)}$$

$$m_T = \sum_j m_{ox_j} \frac{S_{oxj}}{S_o} + m_f \frac{S_f}{S_o} \qquad \text{(B-14)}$$

$$\zeta^*_{oxj} = \left[1 + \frac{\zeta_f/D_j}{\sum \frac{\zeta_{oxj}}{D_j}}\right]^{-1} \qquad \text{(B-15)}$$

$$\frac{(\dot{m}_{ox}S_{ox})_j}{\Sigma(\dot{m}_{ox}S_{ox})_j}\, \dot{m}_T c_p (T_{sj}-T_o) = -\frac{(\dot{m}_{ox}S_{ox})}{S_o} Q_{oxj} - \left[\dot{m}_T - \sum \frac{(\dot{m}_{ox}S_{ox})_j}{S_o}\right] \frac{(\dot{m}_{ox}S_{ox})_j}{\Sigma(\dot{m}_{ox}S_{ox})_j} Q_f$$
$$+ \frac{(\dot{m}_{ox}S_{ox})_j}{S_o} (1-\beta_{F_j}) \left[Q_{AP_j} e^{-\xi^*_{APj}} + Q_{FFj} e^{-\xi^*_{FFj}}\right] \qquad \text{(C-16)}$$
$$+ \frac{(\dot{m}_{ox}S_{ox})_j}{\Sigma(\dot{m}_{ox}S_{ox})_j} \dot{m}_T \beta_{F_j} Q_{PF_j} e^{-\xi^*_{PDFj}}$$

$$T_{soxj} = T_o - \frac{Q_{oxj}}{c_p} + \gamma_j \beta_{F_j} \left(1+\frac{1}{(O/F)_j}\right) \frac{Q_{PFj}}{c_p} e^{\xi^*_{PFj}} + (1-\beta_{F_j}) \frac{Q'_{APj}}{c_p} e^{-\xi^*_{APj}} \qquad \text{(B-16)}$$

with

$$Q'_{APj} = Q_{APj} + \left[(1-\beta_{F_j})\left(1+\frac{1}{(O/F)_j}\right) - \beta_{APj}\right] \frac{Q_{FFj}}{c_p} e^{-(\xi^*_{FFj} - \xi^*_{APj})} \qquad \text{(B-16a)}$$

$$(O/F)_j = \frac{\dot{m}_{ox_j}S_{ox_j}}{\dot{m}_{fj}S_{fj}} = \frac{D_j}{\alpha_f} \sum \frac{\alpha_{ox_j}}{D_j} \qquad \text{(B-16b)}$$

$$\beta_{F_j} = \frac{\dot{m}_{fj}S_{fPFj}}{\dot{m}_{fj}S_{fj}} = \frac{\dot{m}_{ox_j}S_{oxPFj}}{\dot{m}_{ox_j}S_{ox_j}} = \text{Eq. (13)} \qquad \text{(B-16c)}$$

$$\beta_{AP_j} = \frac{\dot{m}_{ox_j}S_{oxAPj}}{\dot{m}_{ox_j}S_{ox_j}} = 0.34\text{(chemistry)} \qquad \text{(B-16d)}$$

$$\gamma_j = 2/3\text{(assumed)} \qquad \text{(B-16e)}$$

$$T_{sf} = T_o - \frac{Q_f}{c_p} + \sum \left[(1-\gamma_j)\beta_{F_j} \frac{\alpha_{ox_j}}{\alpha_f} \left(1+\frac{1}{(O/F)_j}\right) \frac{Q_{PFj}}{c_p} e^{-\xi^*_{PDFj}}\right] + \beta_{DB} \frac{Q_{DB}}{c_p} e^{\xi^*_{DB}} \qquad \text{(B-17)}$$

---

relate to m_T through Eq. (C-14). For inert binder, it is simply $m_T S_o$ times the summation of α_{oxj}. Note that the energy balance and binder are apportioned in accordance with oxidizer mass flow. It is through this, the dependence of diffusion flame height on m_T, and the fact that m_T as computed for j=1 must equal that as computed for j=2, that the solution is said to be "coupled".

DISCUSSION

H.F.R.Schöyer, Delft University, Ne

You were talking of the steady state combustion subject whereas a good combustion model has to take into account the non-steady state behaviour such as the response or admittance function. You have been working in this area also and could you comment?

Secondly the multiple flames model of Belkstead, Derr, Price (BDP) all emphasise the gas phase. However a group of people have emphasised the importance of the solid phase reactions at the burning surface. Could you comment on this?

Author's Reply

My paper is restricted to steady-state combustion models. They cannot in themselves predict response function, but can be used in the development of a non-steady behaviour model. For example Hermann has perturbed the BDP model to derive an expression for the response function. G.Lick and Condon have used the BDP model to apply a technique suggested by Zeldovich and Novozhilov to calculate response function. Dr de Luca, in his paper, noted that one could select a model for the gas phase in performing transient analysis. I believe that it is necessary to account specifically for the effects of AP particle size in future analytical developments to calculate response function. In doing so, there may be important effects of the solid phase, as suggested by Lengellé and Williams in 1968, which are not necessary to consider in steady-state but which do have significance in the non-steady behaviour.

With regard to your second question the multiple flame models do consider condensed phase reactions but at present are more or less deficient in the way they do so. The condensed phase reactions derive from the AP and improved models of AP monopropellant combustion are being developed which will describe them better. The monopropellant combustion is, of course, a necessary ingredient of the composite propellant combustion. Models which have emphasised condensed phase reactions, using a simple model for the flame, have proven to be inadequate. The preferred approach, would be to incorporate a description of the condensed phase in the multiple flame model.

EROSIVE AND TRANSIENT BURNING EFFECTS ON PERFORMANCE PREDICTION ACCURACY OF TACTICAL ROCKETS *

by
H.P. Sauerwein
A. Lampert
R.H. Schmucker

Bayern - Chemie
Solid Rocket Company
P.O. Box 220
8012 Ottobrunn
West-Germany

SUMMARY

Performance prediction of solid rockets requires, besides modelling of the internal flow field and the steady state burning rate obtained from Crawford and standard engine data, the inclusion of erosive burning and transient effects. Performance reexamination of rockets with high volumetric loading is practicable by the most common theory established by J.H. Lenoir and G. Robillard. A new erosive burning model, first developed by M.K. King, makes performance prediction without additional empirical parameters possible. A sensitivity analysis which uses the data of small tactical rockets shows the effects of the various geometric and ballistic parameters and the variation of pressure and thrust history due to transient effects.

1. INTRODUCTION

The continuously growing performance requirements for solid rocket motors necessitate, besides other means, an increase in volumetric loading fraction so that in case of an internal-burning grain configuration the port to throat area ratio approaches unity. As a consequence, the near surface flame structure is modified by the gas flow parallel to the burning surface such that an enhancement of the burning rate occurs. This alternation of the ballistic characteristics compared to the pure pressure sensitive behaviour is commonly described as erosive burning.

The phenomenon of erosive burning, firstly identified by Muraour (Ref.11) more than 50 years ago, is especially pronounced during the first proportion of the motor operation and results in an excessive initial chamber pressure when using the undisturbed burning rate as basis. To account for this effect, the designer of a solid rocket requires an appropriate method which allows an accurate ballistic prediction without additional experimental data.

In the past several interrelationships for the prediction of erosive burning were published. These were based either on pure empirical results, simplified semiempirical methods or the integration of the conservation equations including the Navier-Stokes-equations for turbulent flow with transpiration. In almost all cases, the methods are applied to the evaluation of laboratory burners rather than for a comparison with actual motor firings. The comparison as presented in a few available reports does not show a completely satisfactory agreement between theory and experiment (Ref.3,13).

In the latter case, small deviations in burning rate during the first portion of the firing compared to theory may run up to significant discrepancies in geometric grain shape during latter portion of the burning time, so that large differences in thrust or pressure are noticed. Therefore the integrating effect of the burning surface regression represents an excellent criterion for the evaluation of the ballistic performance prediction methods.

From an engineering standpoint, a simple relationship for prediction of erosive burning is highly desirable in order to facilitate the design calculations and the performance of sensitivity studies. Consequently, this analysis is based upon two engineering methods, one of which is commonly used, to establish the prediction accuracy and sensitivity. In addition, transient burning effects are included to evaluate its importance. The comparison relates to two tactical solid rocket motors of a few seconds burning time and 0.1 m to 0.2 m diameter.

2. EROSIVE AND TRANSIENT BURNING EFFECTS ON INTERNAL BALLISTICS

The ballistic performance of a solid rocket motor with a selected grain geometry and propellant is mainly affected by

- burning surface-to-throat area ratio
- grain temperature
- throat area-to-grain port area ratio
- free combustion chamber volume-to-throat area ratio (L*)
- free combustion chamber volume-to-burning area ratio.

The first two aspects describe the pressure and temperature sensitive burning, the third characterizes erosive effects and the latter two account for transient burning.

The alternation of the steady state burning rate obtained by strands and standardized small scale propellant grains due to the above mentioned effects is taken into consideration simply by

*This work was sponsored by Ministry of Defense / Government Procurement Agency, Federal Republic of Germany.

(1) $$r = r_0 + r_{er} + r_{tr}$$

where r_0, r_{er} and r_{tr} describe the steady state, erosive and transient burning rate. Of these, in case of a small tactical rocket motor, r_{er} plays the most important role on pressure sensitive ballistic performance modification, while r_{tr} may only contribute during ignition and, even to a lesser extent, tail-off transients.

In Fig. 1, for an assessment of the erosive effects, the burning rate of a highly aluminized hydroxy-terminated polybutadiene (HTPB)-composite is presented. With increasing port Mach-number the fraction of erosive burning increases so that an enhancement of the burning rate occurs near the throat resulting in an initial chamber pressure increase and a subsequent extended tail-off. In Fig. 2 this characteristic thrust-time history is presented.

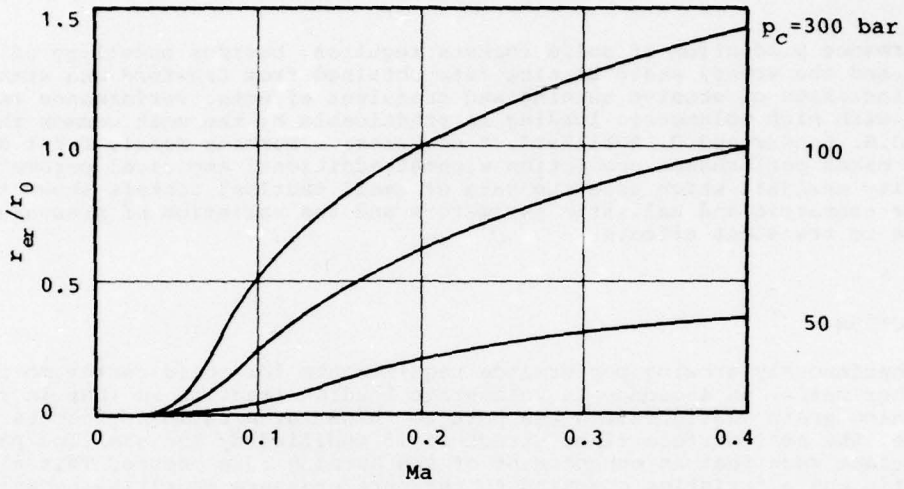

Fig. 1 Mach-number dependence of burning rate augmentation (Predicted data of HTPB-composite with 18% Al)

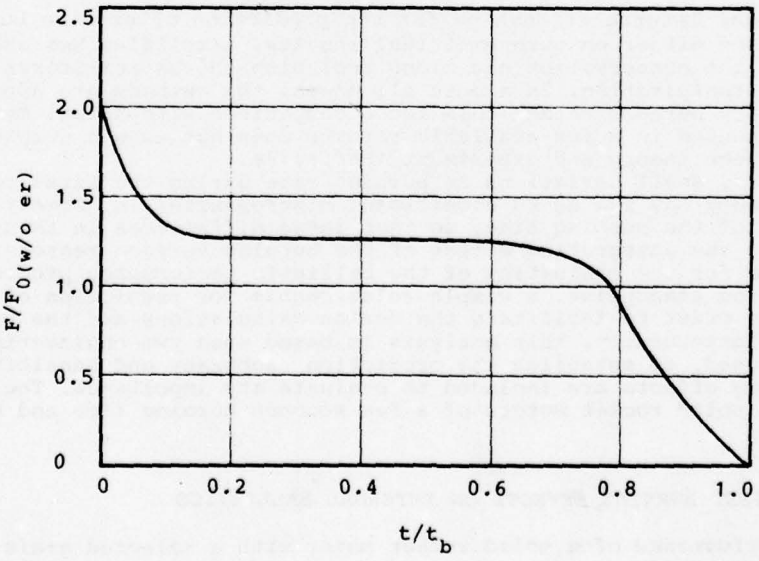

Fig. 2 Thrust-time history, normalized with non-erosive prediction

3. BURNING RATE MODELLING

Using the experimental strand and/or standardized propellant grain data as basis, the deviations due to erosion and high pressure gradients have to be modelled.

3.1 Erosive Burning

Several erosive burning models have been published which can be classified according to their sophisication. A review on the former models is given by Barrère (Ref.1); the more recent ones are characterized by King (Ref.7).

The consideration of erosive burning for performance prediction of an actual motor requires an engineering type model. Of the various laws the equation developed by Lenoir and Robillard (L&R) (Ref.9) in 1957 is commonly used (Ref.3,4,6). Besides this model which is based on heat transfer modifications due to gas flow requiring the experimental determinations of two parameters, a new model, developed by King (Ref.7) on the basis of a two-flame structure, is availible which is directly applicable without any empirical parameters. Both models will be used and compared for a performance prediction analysis. A discussion of the physical background of these models is given in Ref. 5.

3.1.1 Lenoir and Robillard Burning Model

The L&R-erosive burning model is based upon the general heat transfer equation for a flat plate with zero pressure gradient and a turbulent boundary layer with transpiration. The disturbance of the normal boundary layer profile by mass addition, is accounted for by an exponential factor, relating the normal and cross flow mass flux. With G as local port mass flux, the local axial position l and the propellant density, this erosive burning law is written

$$r_{er} = k_{LR,1} G^{0.8} l^{-0.2} \exp(-k_{LR,2} \rho_{pr} r/G). \tag{2}$$

The two constants $k_{LR,1 \text{ and } 2}$ comprise gas and propellant properties, both must be established from motor firings for selected propellants with erosive burning effects. Evaluation of firings at various temperatures indicate that the temperature sensitivity of these constants is negligible (Ref.2).

Although the physical basics of this model are criticized (Ref.7), by proper selection of the two constants a rather satisfying approximation of an experimental thrust/pressure-time history can be achieved.

3.1.2 King's Erosive Burning Model

This model is based upon a two-flame model, an ammonium perchlorate deflagration mono-propellant flame and a columnar diffusion flame resulting from mixing and combustion of the binder pyrolysis and deflagration products. Describing the velocity vector angle at the burning surface with θ and the local pressure with p_c, the equation for the burning rate is written

$$r_0 + r_{er} = k_{K,1} p_c \left(1 + \frac{k_{K,2}}{1 + k_{K,3} \sin\theta \; p_c^2}\right)^{0.5} \tag{3}$$

The constants $k_{K,1...3}$ may be evaluated by a regression analysis of test data without erosive effects. Thus Eq.(3) represents a prediction method which does not depend on empirical constants so that pre-test predictions rather than post-test predictions are possible.

The determination of θ follows from the data of Mickley and Davis (Ref.10), which relate the transpiration and crossflow velocity at a certain location within the boundary layer. Fig. 3 presents an example of the tendency of θ.

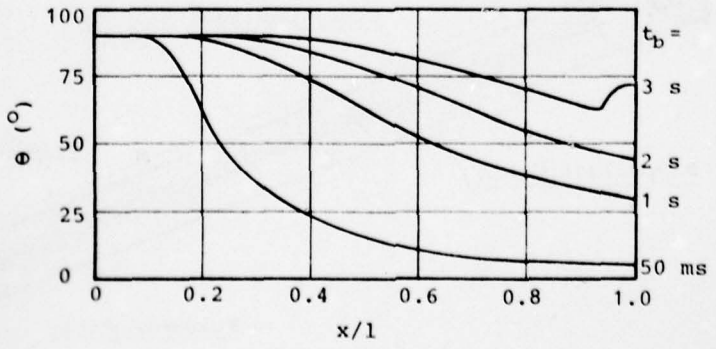

Fig. 3 Velocity vector angle versus dimensionless length of a tactical rocket motor of 0.11 m diameter at various burning times

3.2 Transient Burning

Transient burning effects result from propellant heating and flame spreading during ignition and pressure gradients with respect to time. Neglecting the first two phenomena - it is assumed that they happen prior to the burst of the diaphragm - only the pressure change has to be considered.

The determination of rapid pressure changes per unit time necessitates the evaluation of the non-steady conservation equation and the effect of pressure gradients on the burning rate.

According to the thermal wave-theory by Paul et al (Ref.12) and von Elbe (Ref.15) the transient burning rate may be written as

$$r_{tr} = \frac{k_{tr}\, n\, a_h\, \dot{p}_c}{(r_0 + r_{er})^2\, p_c} \tag{4}$$

where n describes the burning rate exponent, a_h the thermal diffusibility of the propellant and k_{tr} the transient burning rate constant.

4. COMPARISON AND PREDICTION ACCURACY EVALUATION OF BURNING RATE MODELS

The prediction accuracy of the burning rate models for ballistic performance evaluation is determined by a comparison of test results of typical motors with the respective pretest predictions. For simplification reasons, a separate analysis of the ignition transient and the quasisteady operation is performed.

4.1 Description of Reference Engines

The characterization of the models is based upon two tactical rocket motors, one of 0.11 m and one of 0.175 m diameter. In Table 1 the important data are listed. The propellants are HTPB-composites with different aluminum loadings and oxidizers. In Fig. 4 and 5, cross sectional drawings of the engines are presented, Fig. 6 compares the two grain geometries.

		0.11m-rocket	0.175m-rocket
Length of grain	[m]	1.141	1.357
Diameter of grain	[m]	0.11	0.175
Volumetric loading fraction	[-]	0.9	0.9
Port-to-throat area ratio	[-]	0.64	0.70
Burning-to-throat area ratio	[-]	219	144
Propellant mass	[kg]	16.3	47.6
Propellant type		HTPB - composite	
Oxidizer	[%]	67	65
Al	[%]	18	19
Binder	[%]	15	16
Combustion temperature	[K]	3235	3313

Table 1 : Data of Reference Engines

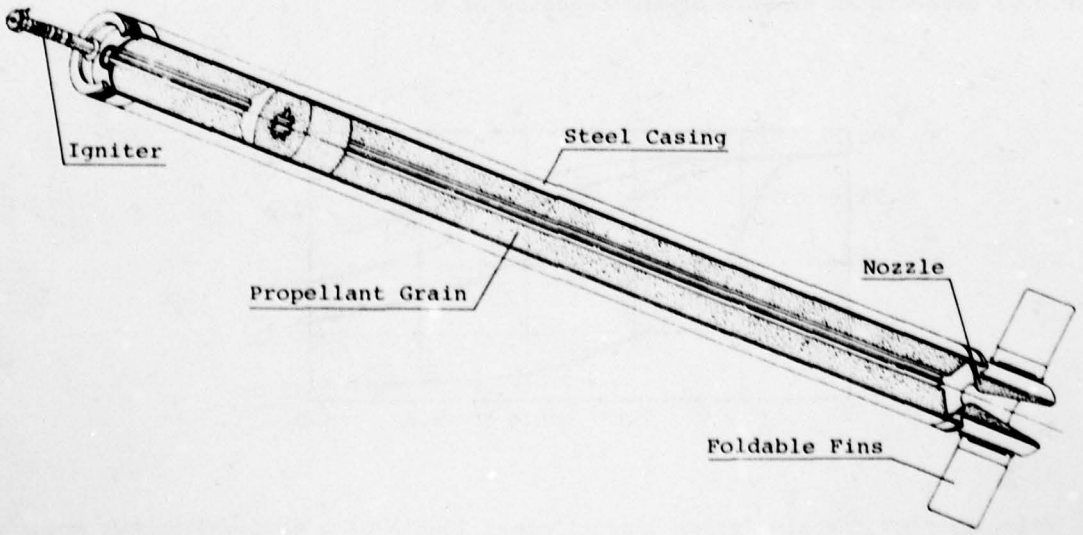

Fig. 4 Sectional view of 0.11 m tactical rocket

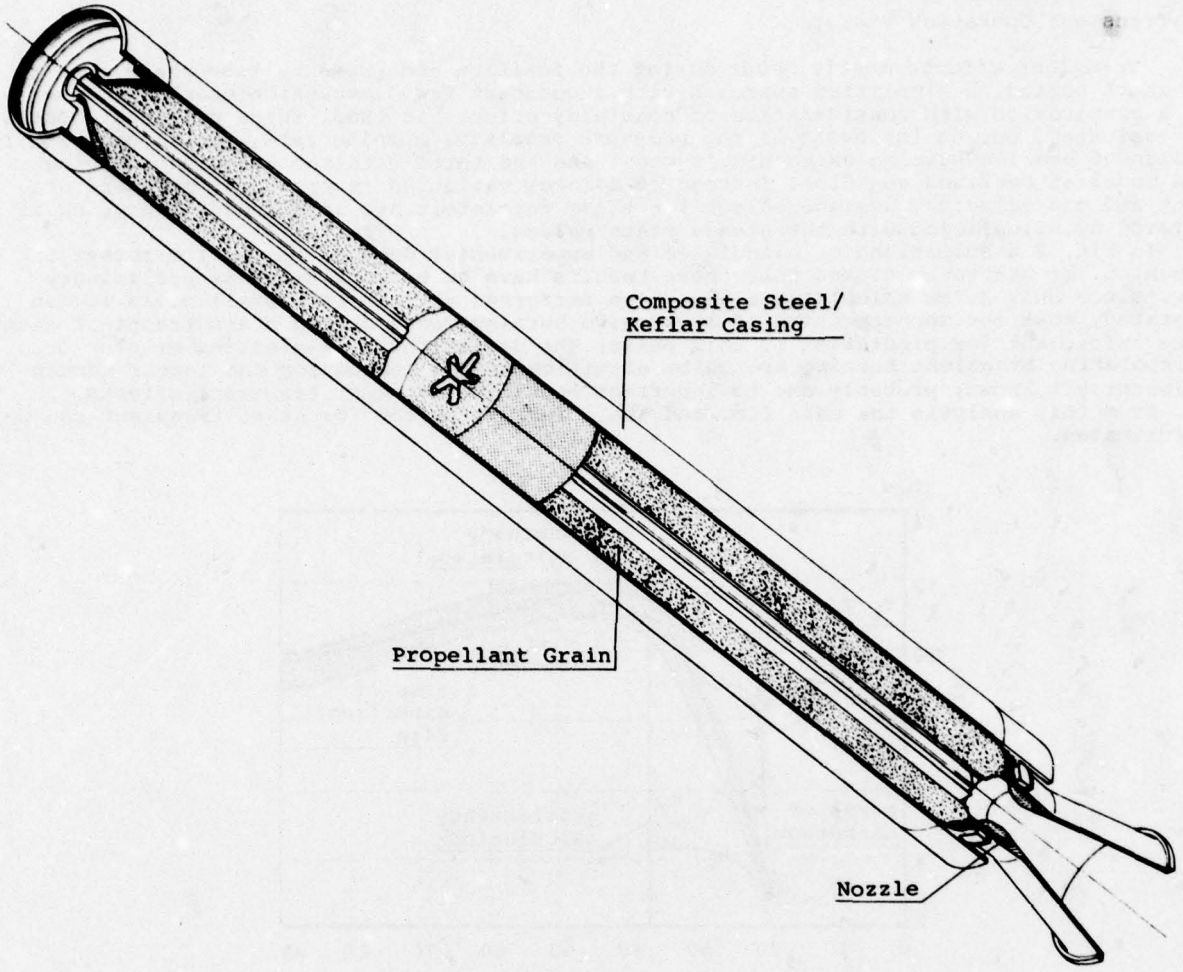

Fig. 5 Sectional view of 0.175 m tactical rocket

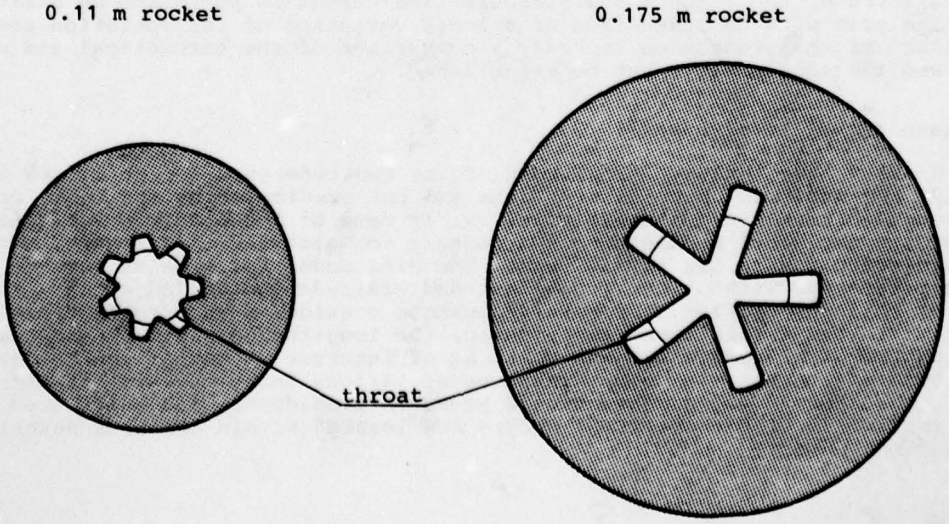

Fig. 6 Grain port configurations

4.2 Transient Operation Phase

Transient effects mostly occur during the ignition and pressure rise phase. Due to the short period, a simplified approach with a constant free combustion chamber volume and a computation with consideration of nonsteady effects is used. Three different models are evaluated, one on the basis of the pressure sensitive burning rate, the second with inclusion of erosive burning using King's model and the third with the transient burning rate model of Paul and von Elbe. Instead of a local variation in pressure, pressure gradient and gas velocity, average values for these parameters are introduced. Averaging is achieved by normalizing with the steady state values.

In Fig. 7 a comparison of calculated and experimental data of the 0.11 m-rocket is presented. It has to be stated that these results have to be considered as preliminary ones, since only a few calculations have been performed yet. On this small basis it can be stated, that the incorporation of an erosive burning model during start transient seems to be sufficient for prediction of this phase; the deviations by neglecting erosion or incorporating transient burning are quite significant. The reason for the latter tendency is not yet known; probably due to incorrect modelling of start transient effects.

From this analysis the mass flow and the effective period for start transient can be approximated.

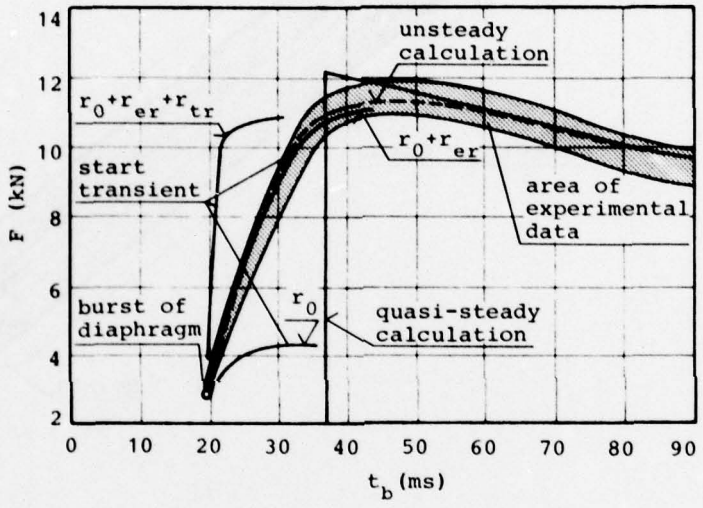

Fig. 7 Ignition transient of a 0.11 m motor

4.3 Quasi-steady Operation

The calculation of the thrust- and pressure-time-curves is performed on basis of a quasi-steady analysis with consideration of a local variation of the operation parameters. For an evaluation of the prediction accuracy a comparison of the theoretical and experimental trend and the sensitivity must be established.

4.3.1 Comparison of Ballistic Data

In Fig. 8 and 9, the thrust time history of the two reference rocket motors is presented. Obviously, the agreement between test data and the prediction on the basis of the two models for erosive burning is quite satisfactory. In case of the Lenoir & Robillard-model, a variation of the empirical parameters is necessary to match the test result. Even so, there is some discrepancy in the thrust peaks. The King model for erosive burning leads directly to a prediction without any propellant and grain-dependent "adjusting" parameter; in the light of this supposition, the results must be considered as excellant ones.

In addition to the thrust-time-relationship, the longitudinal axis dependence of the pressure during the high erosive burning phase is of interest. A comparison between test results of a 0.11 m - rocket, in which pressures at various locations are established by using strain gages (Ref.8) and a conventional pressure transducer, and calculated tendency is presented in Fig. 10. The theoretical curves are located within the area described by the measurement inaccuracy.

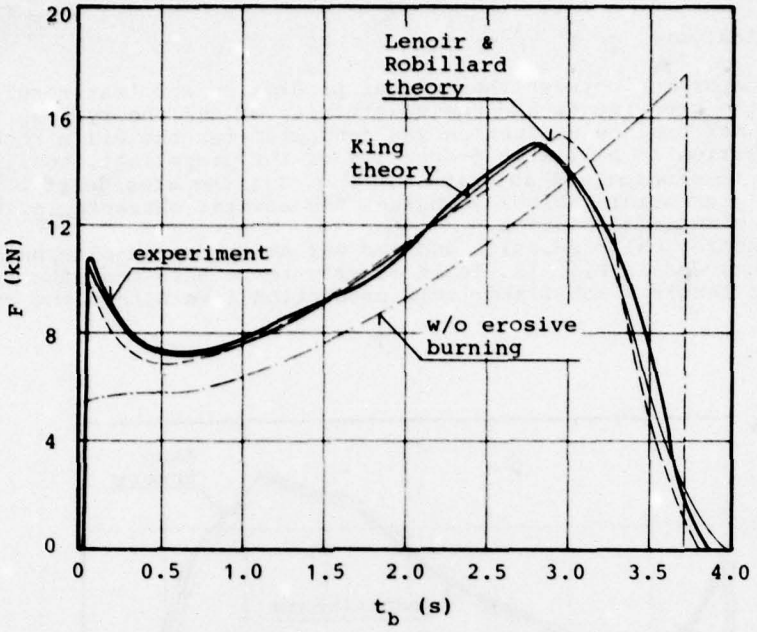

Fig. 8 Thrust-time curve for the 0.11 m rocket

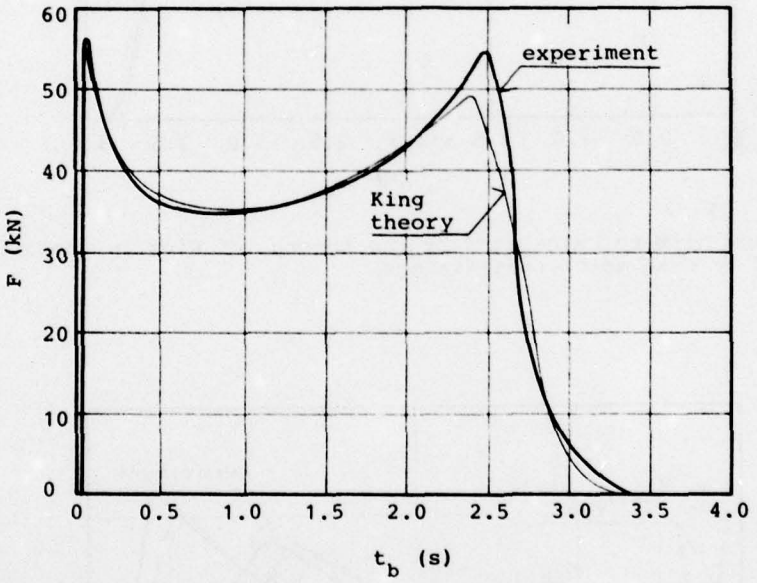

Fig. 9 Thrust-time curve for the 0.175 m rocket

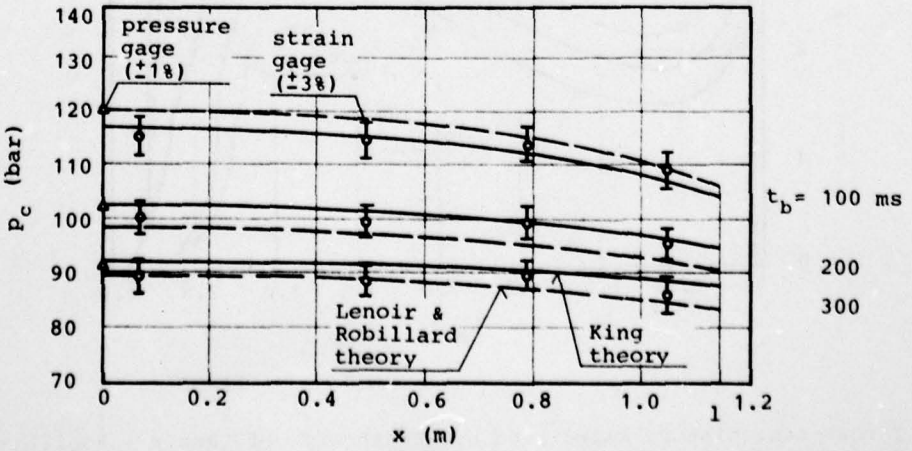

Fig. 10 Pressure variation along axis of 0.11 m rocket during high erosive burning phase

4.3.2 Sensitivity Analysis

A realistic comparison between theoretical prediction and test results must include the dispersion of the experiments and the sensitivity of the theory.

A statistical performance evaluation was conducted for the 0.11m rocket to establish the effects of variation in ballistic properties of the propellant, nozzle geometry and the alteration due to erosion and ablation. In Fig. 11, the area described by a large number of tests is presented; Table 2 comprises the several characteristic performance parameters and its standard deviation.

The nominal theoretical prediction and the variation due to alternation of the empirical constants is included in Fig. 12. It is clearly to be seen that the King approach is superior to that of Lenoir & Robillard; this prediction lies within the experimental inaccuracy.

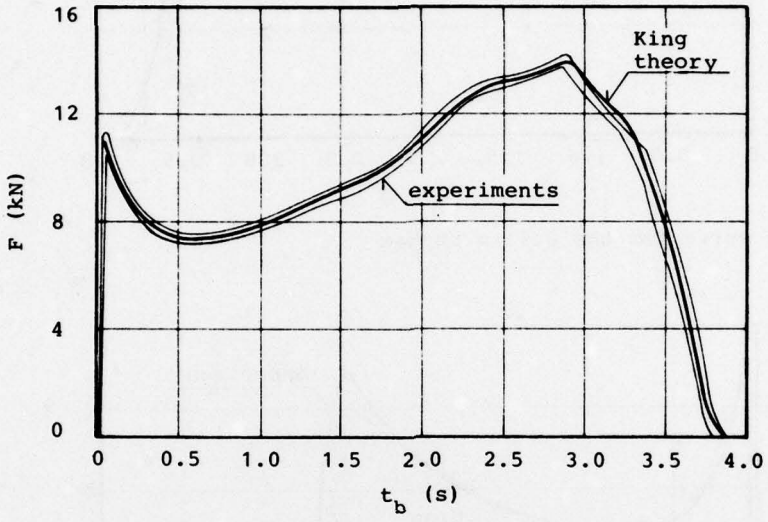

Fig. 11 Thrust-time history calculated by the theory of King in comparison to the area described by some motor test-firings

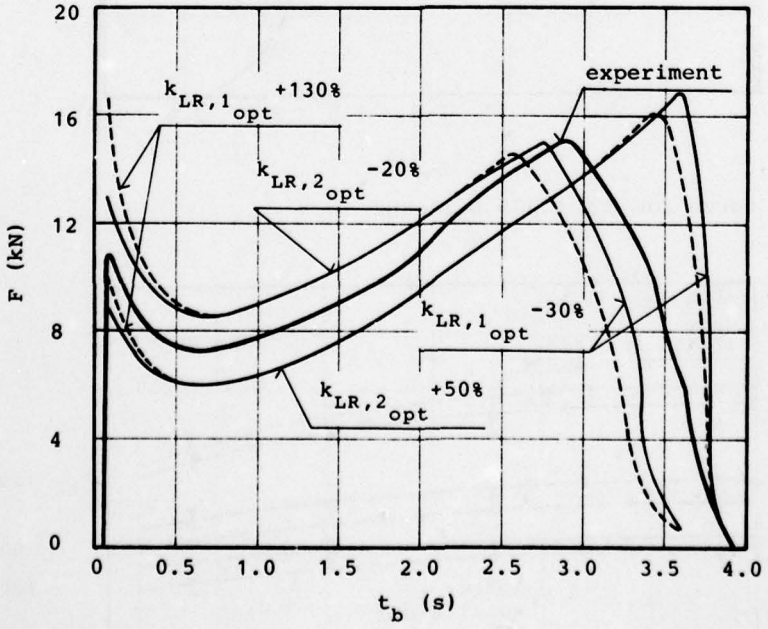

Fig. 12 Thrust-time history calculated by the thoery of Lenoir & Robillard and the variation due to alternation of the empirical constants

		Test		Computation	
		average of 15 measurements	max. relative deviation [%]		relative deviation [%]
Thrust (average)	[N]	10 170	2.9	10 034	1.2
Thrust (max.)	[N]	13 971	2.6	13 900	0.5
Total Impulse	[Ns]	36 468	1.0	36 022	1.2
Specific Impulse (average)	[m/s]	2 238	0.6	2 247	0.4
Burning Time	[s]	3.586	2.8	3.590	0.1

Table 2 : Comparison of theoretical and experimental performance parameters of 0.11 m rocket (data of a 15 unit lot).

Therefore it can be concluded that for composite propellants the erosive burning theory, firstly developed by M. King, represents an excellent method for pre-test prediction of ballistic performance. The results obtained according to Lenoir and Robillard are of similar yet slightly lower accuracy, but the empiricaly determined parameters yield too much scatter for pre-test predictions.

5. CONCLUSIONS

The increasing performance requirements for tactical rockets result, due to improved volumetric loading fractions, in enhanced erosive effects which might cause pressure peaks of a factor of more than two compared to a pure pressure sensitive ballistic analysis. To predict the thrust and pressure-time history of a rocket motor, a suitable erosive burning model is necessary. From an engineering standpoint a simple and easily usable burning model is highly desirable. Of the various available models the method presented by Lenoird and Robillard and King are well usable since these are easily incorporated into internal ballistic procedures. Of these the approach as described by Lenoird and Robillard is commonly used; but the physical background of this model which does not agree with all experimental tendencies and the application by fitting two parameters to experimental data make this method less qualified. King's model which is based on alteration of the flame structure due to crossflow seems to be a very well usable tool for internal ballistic predictions due to accurate matching of experimental data and the lack of empirical constants (a detailed physical comparison of both models is given in Ref. 14). During ignition transient effects play also an important role, but the transient burning rate as predicted by Paul and Von Elbe seems not to describe the test data with sufficient accuracy; for performance prediction of tactical motors with a few seconds burning time, the transient effects can be neglected.

Future work will require additional comparison with test data of high loaded rockets and the modelling of the propellant surface curvature effect, the so called root/valley-tip erosion; this phenomenon may cause the deviations in thrust and pressure peak at the end of burning time in calculations.

ACKNOWLEDGEMENT

The authors gratefully acknowledge the many helpful discussions and suggestions of Mr. MRat H. Walder and Mr. ORR O. Wolf of the German Ministry of Defence, Department RÜ VII 3, Mr. RDir Dr. J.K. Weis and ORR H. Falkenburg of the Government Procurement Office, Department WM IV 3.

REFERENCES

[1] Barrere, M., Williams, F.A., Huang, N.C., "Fundamental Aspects of Solid Propellant Rockets", AGARDograph No. 116, AGARD, 1969.

[2] Block, W., "Gasdynamische Erosion einschließlich Versuchsauswertung", Germany, Ottobrunn, Bayern Chemie GmbH, May 1977, TN H31-12/77.

[3] Coats, D.E., Levine, J.N., Nickerson, G.R., Tyson, T.J., Cohen, N.S., Harry III, D.P., Price, C.F., "A Computer Program for the Prediction of Solid Propellant Rocket Motor Performance", Vol. I, Final Report, Air Force Rocket Propulsion Laboratory, July 1975, Paper No. AFRPL - TL - 75 - 36.

[4] Cohen, N.S., Harry III, D.P., Price, C.F., Coats, D.E., Levine, J.N., Nickerson, G.R., "Solid Rocket Performance Prediction Techniques", AIAA/SAF 10th Propulsion Conference, San Diego, California, October 1974, AIAA Paper No. 74 - 1200.

[5] Condon, J.A., Osborn, J.R., "The Effect of Oxidizer Particle Size Distribution on the Steady and Nonsteady Combustion of Composite Propellants", Final Report, Air Force Rocket Propulsion Laboratory, June 1978, Paper No. AFRPL-TR-78-17.

[6] King, M., A Modification of the Composite Propellant Erosive Burning Model of Lenoir and Robillard", Combustion and Flame, Vol. 24, No. 2/75, pp. 365-368.

[7] King, M., "Erosive Burning of Composite Propellants", 13th JANNAF Combustion Meeting, Monterey, Calif., Sept., 1976, CPIA Publication 281, Vol. II, p. 407.

[8] Lampert, A., "Experimentelle Bestimmung von Drücken in Flugtriebwerken durch Dehnungsmessung", Germany, Ottobrunn, Bayern Chemie GmbH, Feb. 1979, TN H3-6/79.

[9] Lenoir, J.M., and Robillard, G., "A Mathematical Method to Predict the Effects of Erosive Burning in Solid Propellant Rockets", Sixth Symposium (International) on Combustion, 663 Reinhold Publishing Corp., New York, 1957, pp.663-667.

[10] Mickley, H.S., and Davis, R.S., "Momentum Transfer for Flow over a Flat Plate with Blowing", NACA Technical Note 4017, November, 1957.

[11] Muraour, H., "Note sur la vitesse de combustion des poudres colloidales en fonction de la pression et de la temperatur des gaz emis", Bull. soc. chim, 9, France, 1924, 511.

[12] Paul, B.E., Lovine,R.L., Foug, L.Y., "A Ballistic Explanation of the Ignition Pressure Peak", AIAA Solid Propellant Rocket Conference, Palo Alto, California, Jan. 1964, AIAA Reprint No- 64-121.

[13] Parkinson, R.C., Penny, P.D., "A Transpired Boundary Layer Model of Erosive Burning", AIAA/SAE 14th Joint Propulsion Conference, Las Vegas, July, 1978, AIAA Paper 78-980.

[14] Sauerwein, H.P., "Ein kritischer Vergleich der Abbranmodelle von Lenoir & Robillard und King", Germany, Ottobrunn, Bayern Chemie GmbH, in preparation.

[15] Von Elbe, G., "Theory of Solid Propellant Ignition and Response to Pressure Transients", Bulletin of the Interagency Solid Propulsion Meeting, Seattle, Wash., July 1963, CPIA Publ. 13, AD 338667.

DISCUSSION

R.C.Parkinson, PERME, Westcott, UK

I would like to make the comment that King's theory for erosive burning assumes a "flame bending" mechanism with the assumption that the flame zone occurs at a fixed flow distance. Taking the more reasonable assumption that the flame zone is determined by a mixing time, which describes non erosive burning better, King's theory will not give any erosive burning at all. That King's theory does work is probably because he takes account of the changes in velocity profile adjacent to the burning surface. This aspect is dealt with in my paper (Paper No.10).

It is probable, however, that the theory cannot be extrapolated indefinitely from known experience and must be treated with caution.

Author's Reply

Your comment notes the good agreement between known experimental evidence and the predictions by King's theory. In addition to the data I have given some more experimental evidence, with different grain sizes and geometry has been obtained but not yet published. Again good agreement between theory and experiment is obtained. These suggest that King's approach is a very good predictive tool for internal ballistic performance.

M.Barrere, ONERA, Fr

Why don't you replace the flow angle θ by the friction coefficient C_f, since they are approximately the same. For the determination of θ you use the data of Mickley and Davis in which the injection mass flow rate from the surface is small in comparison to the main mass flow rate along the surface, approximately 1/1000. Therefore why not determine the erosive factor from the local friction coefficient C_f?

Author's Reply

Significant erosive burning occurs at the aft end of the propellant grain. Here the injection mass flow rate is very small in comparison to the main flow rate. This is exactly the case in the Mickley-Davis experiments and it is therefore convenient and appropriate to use the flow angle θ . I see no advantage in changing to another empirical approach such as the use of C_f and an erosion factor.

L.Caveny, Princeton University, US

You stated that your transient burning results were not wholly satisfactory. If you use something as simple as the Von Elbe model for the transient process then you must take account of the involvement of the thermal wave and condensed phase. Following this the ZELDOVICH approach for modelling the transients of the flame may be useful.

Author's Reply

We used this burning rate model because it is utilised in the "solid Rocket Performance Prediction" method of the Rocket Propulsion Laboratory (RPL). We attempted to determine the transient burning rate effect on ignition transients.

Comment by H.F.R.Schöyer, Delft University, Ne

The Von Elbe model, first presented 16 years ago, is attractive from an engineering viewpoint because of it's simplicity. However caution is required in applying it to transient burning. It does not predict the time lag between a variation in pressure and the consequential variation in burning rate.

ALUMINUM COMBUSTION UNDER ROCKET MOTOR CONDITIONS*

Leonard H. Caveny and Alon Gany
Princeton University
Princeton, New Jersey 08544, USA

SUMMARY

Combustion processes of aluminum particles emitted from the surface of solid propellants were studied under rocket motor, cross-flow conditions as well as strand burning conditions. High-speed, color photographs (~5,000 fr/s) were taken of Al_2O_3 agglomerates forming on the surface, moving along the surface, entering the flow field, and breaking-up in nozzles. Experiments were conducted for cross-flow velocities as high as 30 m/s and pressures between 2 and 10 MPa. Data were obtained for a double-base propellant with up to 13% Al.

Agglomerate size distributions were obtained by direct measurements from the films. Analysis of size distributions of the agglomerates leaving the surface reveals that the following parameters decrease with increasing pressure: collision frequency on the surface, the agglomerate stay time on the surface, and mean agglomerate size. Increasing the cross-flow velocity decreases the mean agglomerate size. However, chamber pressure has the most pronounced effect on agglomerate size. The propellants which contain the large aluminum particles (e.g., 50 vs. 6 μm) burn without the aluminum igniting or agglomerating on the surface. A model was developed that accounts for accumulation of aluminum particles in a mobile surface layer, retention of particles by surface tension forces, and ignition on the surface. The model correlates the data and is the basis for a methodology for selecting an aluminum particle size range to obtain the minimum agglomerate size. Photographs of the agglomerate breakup processes in a converging nozzle were used to obtain data on breakup as a function of agglomerate size and two-phase flow velocities. The minimum agglomerate size for breakup was correlated in terms of the ratio of shear forces to surface tension forces.

INTRODUCTION

Recent investigations at Princeton University examined three aspects of aluminum combustion in solid propellant and solid propellant rocket motors: (a) formation of Al/Al_2O_3 agglomerates during propellant combustion (1), (b) the influence of cross-flow on agglomerate formation (2), and (c) agglomerate break-up under shear flow conditions (3). This paper summarizes and unifies the results which appeared in three papers (i.e., Refs. 1-3).

The original aluminum particles added to solid propellants, burn either as single particles or form agglomerates which may contain hundreds or even thousands of the original aluminum particles. In general, smaller agglomerate masses lead to higher combustion efficiencies, less slag retention, and lower two-phase flow losses as the combustion products accelerate through the rocket nozzle. Also, the desired range of agglomerate mass and size required to defeat a particular mode of acoustic instability is very dependent on the frequencies of the undesired oscillations. Thus, control and knowledge of agglomerate size is often an important consideration in propellant and rocket motor development programs.

Experimental studies of burning aluminized propellants and propellant ingredients in quiescent atmospheres, e.g., Refs. 4-9, reveal some of the details of the processes taking place at the burning surface. A large amount of valuable information about the behavior of aluminized propellants was summarized, for example, by Pokhil, Frolov, et al. (10,11) and Micheli and Schmidt (12). Rocket motor studies (13) have shown that important propellant performance increases can be obtained by improving combustion efficiencies of propellants containing high loadings of aluminum. It has been hypothesized that the two-phase flow processes in the nozzle produce breakup of sufficiently large agglomerates and thereby permit improved combustion efficiencies to be achieved. However, until recently, direct observations of agglomerate breakup under rocket motor nozzle flow conditions had not been made.

Conclusions with respect to agglomerate size, combustion efficiency, and slag formation must be limited to particular propellant types burning in particular rocket motors. Accordingly, generalizations are avoided in this paper. The primary contribution of the paper is that it illustrates three distinct processes that affect agglomerate size. In many situations, a combustion analyst must consider all three aspects during the selection of a propellant formulation, rocket motor internal geometry, and acceleration field.

*Based on research performed under AFOSR GRANT 76-3104 issued by Air Force Office of Scientific Research.

EXPERIMENTAL APPROACH

High-speed color movies (between 2000 and 5000 fr/s) were taken of propellants burning as strands and burning in a 7 cm long window motor, which used two propellant slabs 0.6 cm wide. Photographing the burning of aluminized propellants in a rocket motor flow field presented several problems not encountered during the photography of strands burning in a quiescent atmosphere. Firstly, the transparency of the windows in the motor (adjacent to the burning propellant and converging nozzle) must be maintained. For low flow conditions, this was accomplished by using polymethylmethacrylate windows which ablate slightly, thereby removing the deposits which would normally build up on glass or quartz windows. Under high flow conditions, deposits did not build up on tempered glass. Secondly, under typical motor conditions, the number of emitting Al/Al_2O_3 agglomerates is so great that an individual particle in the continuum cannot be examined. Furthermore, since the photographic depth of field is less than about 0.3 cm, photographing thick agglomerate clouds obscured the details of the agglomerates within the region of sharp focus. This depth of field and discrimination situation was overcome by photographing the flame zone above thin strips of aluminized propellant cast between sections of non-aluminized propellant. In this manner, combustion processes of individual agglomerates could be visualized. In the field of view of the photography ($\sim$8 mm along the flow axis), there was little opportunity for the parallel gas streams (from the aluminized and non-aluminized propellants) to mix; the local environment of the burning aluminum (near the propellant surface) was approximately the same as it would have been if the entire propellant charge had been aluminized.

The experimental apparatus is shown schematically in Fig. (1). Two configurations for observing the burning surface were used. In the first configuration, a side view was obtained and the propellants slabs were cast directly onto the window, and the initial port passage was usually set to be 2 mm. In the second configuration, the view normal-to-the-propellant surface was obtained and the propellant (viewed by the camera) was not bonded to the window. The location of the portion of the propellant which was aluminized was varied to obtain the desired cross-flow conditions.

The plastisol double-base propellants described in Ref. (14) was used. The formulation for the basic non-aluminized propellant is 53.7% nitrocellulose (NC), 39.3% trimethylolethane trinitrate (TMETN), and 7.0% triethylene glycol dinitrate. The aluminized propellants used in the experiments are the basic propellant with aluminum contents as high as 13%. Two size ranges of aluminum powders were used: 6 and 50 μm. The basic propellant has been characterized by a wide variety of combustion and ignition studies.

MODELING THE AGGLOMERATE FORMATION DURING PROPELLANT COMBUSTION

Two sets of photographs illustrate two important observations. Figure (2) shows the strong dependency of burning rate (and pressure) on agglomerate size. Figure (3) shows that agglomeration can increase markedly as aluminum particle size is decreased.

Aluminum particles brought into close contact and maintained under appropriate heating conditions will agglomerate. An adhesion process starts at a temperature of about 700 K [Refs. (4) and (5)], below the aluminum melting point (933 K). At the aluminum melting temperature, the adhesion process is enhanced by the formation of "welding bridges" among the particles, consisting of molten aluminum flowing through cracks in the oxide shells. The oxide shells remain solid and retard fast oxidation and self-sustained combustion of the particles. According to Ref. (10), ignition can take place (in a propellant combustion gas environment) when the particles achieve a temperature of about 1300 to 1500 K. Merging of the adjacent particles is accomplished when they reach the Al_2O_3 melting point (2300 K); then, large agglomerates with spheroid shapes are formed.

Reference (1) reported additional data relating to aluminized propellant combustion and unified in the form of a model the previous observations which have been made concerning the agglomeration mechanism, ignition, and ejection processes. The propellants which are of interest in this study are those in which the condensed phase granularity is generally less than that of the aluminum particles. The class of propellants in which condensed phase granularity significantly affects agglomeration was the subject of the Crump Pocket Model (6).

Outline of the Physical Model

While the overall combustion process of the propellant appears to be steady, the processes associated with the microscale are very unsteady. The influences on an individual aluminum particle are indicated on Fig. (4). The model which considers the scale of the individual aluminum particle can be summarized as follows:

1. A thin mobile layer which consists of intermediated decomposition and melt products (referred to as the reaction layer) exists at the surface. This layer is the site of several processes.
2. Initial heating, and, in some cases, accumulation of the particles takes place in the reaction layer.
3. Before merging, individual particles are heated separately. Individual particles exposed to intense heating will ignite first.
4. Agglomeration requires a certain minimum of particle accumulation (and close contact) prior to ignition and/or ejection from the surface.

5. Agglomerate size is related to the amount of accumulation before ignition or ejection.

6. Whether agglomeration and/or ignition of particles will take place on the surface depends on the relationship between the characteristic times of accumulation and ignition and on forces acting on the particles.

The existence of adhesion and surface tension forces are apparent from observing high-speed movies of burning aluminized propellants. Knowing the nature of the surface layer (i.e., molten) supports the interpretation of these observations. Other investigators recognize the surface adhesion [Refs. (5) and (6)] and are attempting to gain more information on it.

The first heating and, in some situations, accumulation of the metal particles can take place in the surface reaction layer, where the effects of the outer flow are minor. The reaction layer thickness can be approximated from the solution of the heat conduction equation in the condensed phase and data for NC double-base propellant (14).

The conditions for accumulation in the reaction layer are the following: (1) the particles are smaller than the reaction layer thickness, (2) the surface tension overcomes the forces acting against it (e.g., drag), and (3) either no ignition or delayed ignition of the particles in the reaction layer occurs. The condition for retaining an individual particle in the reaction layer (condition 2) is obtained from the balance between the surface tension force and the drag force resulting from the penetration of the retained particle into the mobile material at a speed equal to the burning rate.

Due to the surface tension, the regressing surface will retain particles as the surface regresses, while only the top of each particle may be exposed to the gaseous flame environment. Moving with the regressing surface, each particle will encounter other particles; this process forms a dense packing of particles in the mobile reaction layer. Additional accumulation will result in the forcing of the accumulate into the gaseous flame zone [see Fig (5)].

Heating and flow effects are much more intense above the surface than in the decomposition layer. Final agglomerate size, ignition process, and ejection from the surface are all affected by the conditions on the surface. When accumulates (or particles) are protruding from the condensed phase, their leading edge is fully exposed to surface heat flux conditions. The characteristic times for melting and ignition (t_{ig}) become much shorter than when they are in the decomposition layer. When the particles on the top of the accumulate ignite, the flame spreads over the accumulate and additional heat is provided for melting and merging of the particles; thus, a large burning agglomerate may be formed. A time for minimum accumulation ($t_{ac,min}$) that can lead to agglomeration is taken as the time to accumulate one densely-packed particle layer.

Observations Based on the Proposed Model

The model provides a means to examine the behavior of aluminum in double-base or other homogeneous propellants. A complex dependence of surface processes on various factors can be drawn. Different effects can be interpreted by the relationship among the various characteristic times. The potential of the model is demonstrated in this summary by the examination of a few parameters. Figure (6) shows the dependence of agglomeration, ignition, and ejection processes on the aluminum particle size. This figure was drawn for a propellant which contains 13% aluminum burning at 7.6 MPa. It demonstrates the domains in which the particle behavior is changed from agglomeration and ignition on the surface to ejection of unignited individual particles.

According to the outline of the model, agglomeration will not take place if individual particles ignite prior to sufficient accumulation. Applying this statement to particles smaller than the decomposition layer thickness, a nondimensional number $N_{ag} \equiv t_{ig}/t_{ac,min}$ can be used as a criterion for agglomeration. Agglomeration degree will increase for $N_{ag} > 1$ and decrease (sharply) for $N_{ag} < 1$.

Figure (7) illustrates the agreement between the calculated and experimental results as a function of particle size and pressure.

The model explains the known trend of decreasing average agglomerate size with increasing burning rate (and pressure). The reduction in reaction layer thickness with increasing burning rate leads to a smaller degree of accumulation and, thus, smaller agglomerates. Other factors such as increased surface heating rate with increased pressure lead to more rapid ignition and, thus, shorter stay times on the surface at higher pressures. The four agglomeration and ignition zones described in Figure (6) shift toward smaller particle sizes as pressure increases. Thus, smaller particles are necessary for agglomeration at higher pressures.

VISUALIZATION OF AGGLOMERATE FORMATIONS UNDER CROSS-FLOW CONDITIONS

The emphasis of this portion of the research is on photographing and interpreting the burning of aluminized propellants under cross-flow conditions similar to those that exist in rocket motors. High-speed photographs were taken of agglomerates forming on the surface, moving along the surface and entering the flow field, and the agglomerates burning (and undergoing further agglomeration) in the flow field. Several laboratories (most notably the work at the Naval Weapons Center, China Lake, CA, USA), have obtained high resolution

photographs of aluminized propellants burning as strands in quiescent atmospheres. These photographs revealed information about metal burning processes isolated from the shearing forces of high-speed flow. However, to answer the questions that have been raised concerning metal agglomerate particle size and combustion efficiency, the results obtained in quiescent atmospheres must be complemented by results obtained under cross-flow conditions. Other investigators [e.g., (10), (12), (13)] have studied how formulation, pressure, and port geometry affect the size distribution of metal agglomerates under rocket motor conditions, but those investigations were not concerned with visualizing the combustion processes that produced the agglomerates.

Volume fluxes of the agglomerates leaving the surface were obtained over the full range of the test conditions and were used to calculate accumulated volume versus particle size. For the range of cross-flow effects considered, the most prominent influence on the agglomerate size is chamber pressure. Actually, the combined effects of both the pressure and the burning rate can not be separated. Figure (8) summarizes the results obtained for several cross-flow conditions for pressures between 3.7 and 7.5 MPa; prominent changes occur in many of the parameters. The average agglomerate size (of the larger particle distribution) decreases from $\sim$ 650 μm at 3.7 MPa to $\sim$ 220 μm at 7.5 MPa. The stay time of the agglomerates on the burning surface changes from 40 - 100 ms to 5 - 9 ms; the frequency of collisions decreases from $\sim$ 70 to $\sim$ 4 per 100 particles leaving the surface, and the number flux increases tremendously from 250 to 12,000 particles/cm^2-s.

Similar trends were found by Pokhil, et al. (10), although their agglomerate sizes are smaller than in this investigation. The Ref. (10) results were obtained from small rocket motors fired in a particle collection combustor.

Port flow velocity affects the stay time of the agglomerates on the surface in several ways: (1) by pushing the agglomerates along the surface and destabilizing them and (2) by aerodynamic lifting due to the concave shape of the agglomerates. The movement along the surface appears to weaken the adhesion force to the surface and shorten the stay time on the surface. In the low speed region, the lifting force is relatively small while the drag is comparable to the weight of the particles. Therefore, in the low speed region, the cross-flow effects depend on the geometry; when this flow acts against the weight, it may even enhance the agglomeration process by slowing the movement of the agglomerates and stabilizing the adhesion to the surface. Higher flow velocities shorten the stay time of the agglomerates on the surface and result in smaller agglomerates.

Other Observations

As stated before, the aluminum particle size is an important factor in the agglomeration and combustion processes. Two regimes were observed. When the 6 μm aluminum powder is used, the particles are usually ignited on the surface and form large spherical burning agglomerates which remain on the burning surface, (e.g., for as long as 100 ms at 3.7 MPa) and then enter the gas flow. The 50 μm powders neither ignite on the surface nor form agglomerates on the surface; they move on the surface due to the cross-flow of the gas and, then, abruptly leave the surface unignited. Ignition occurs in the gas stream and the diameter of the burning particles appears to be the same size as the original aluminum powder.

AGGLOMERATE BREAKUP UNDER SHEARFLOW CONDITIONS

Observations and calculations based on a combustion model of Al/Al_2O_3 agglomerates (10) indicate that only a fraction of the Al in large (e.g., 400 to 800 μm) agglomerates has time to burn inside the chamber of high performance, moderate-size motors. Taking into account the unburned Al, a reduction in the motor performance compared with the theoretical would occur.

The results of Ref. (3) revealed that at sufficiently high two-phase flow lags, agglomerates begin to be deformed and then suddenly (within $\sim$ 0.2 ms) break up. The result is a large number of much smaller agglomerates. On the films, it is seen as a sudden expansion of the flame. Each film sequence reveals a variety of events, e.g., breakup of the larger agglomerates, smaller agglomerates passing through the nozzle without breaking up, medium size agglomerates deforming but not breaking up, agglomerates colliding with the wall and being deflected (with or without breakup), and agglomerates adhering to the wall.

Figure (9) is a typical sequence of a relatively large agglomerate being accelerated and breaking up after it has been subjected to the maximum two-phase flow lag which occurred at the throat. Direct projection of the original high-speed sequences reveal more detail than the prints.

The Weber number, which is the ratio of inertial forces to surface tension forces, was found to be a good correlation parameter. The surface tension of Al_2O_3 at 2300 K is $\sim$ 0.7 N/m and the surface tension of aluminum is $\sim$ 0.9 N/m in the temperature range of 970 to 1020 K. The surface tension of Al_2O_3 was used in the calculations. It is known that for low Weber numbers, droplets are spherical. They tend to distort when the Weber number exceeds about 4. The distortion increases with increasing We until breakup occurs in the range of We = 12 to 20.

The particle paths of over 70 agglomerates were measured on a frame-to-frame basis and used to calculate the agglomerate velocities. The gas velocity through the nozzle was calculated taking into account the flow area restriction due to the agglomerates. The Weber number was calculated along the direction of flow and usually achieved its maximum value at the beginning of the parallel-sided throat. Figure (10) illustrates this process for an agglomerate which did not break up.

Figure (11) summarizes results obtained from four tests and demonstrates that agglomerate breakup usually occurs when a critical Weber number of approximately 28 is exceeded. Thus, the observed critical Weber number is close to the maximum values observed in less hostile environments for carefully characterized liquids. Because of the uncertainty in the agglomerate diameter and composition, the calculated Weber numbers are probably systematically high.

Rocket motor performance conclusions cannot be based only on the dimensions of agglomerates leaving the propellant surface; the important effect of the accelerating flow field on the moving agglomerates must be considered also, and agglomerate breakup criteria are required. If agglomerate breakup results in sufficiently small droplets and if the nozzle is sufficiently long, the agglomerates can burn completely inside the nozzle, and, hence, the motor efficiency increases.

CONCLUSION

The experiments described in this paper permit the visualization of the combustion, agglomeration, and break-up processes of aluminum particles and agglomerates emitted from the propellant surface under quiescent and cross-flow conditions. Quantitative measurements of the agglomerate distribution under various conditions are an important result of the investigations.

The analytical studies provide a framework for interpreting and anticipating how propellant formulation and internal flow fields will affect the aluminum combustion and agglomeration processes.

REFERENCES

1. Gany, A. and Caveny, L. H., "Agglomeration and Ignition Mechanism of Aluminum Particles in Solid Propellants," accepted for publication in Proceedings of 17th International Symposium on Combustion, August 1978.

2. Gany, A., Caveny, L. H. and Summerfield, M., "Aluminized Solid Propellants Burning in a Rocket Motor Flow Field," AIAA Journal, Vol. 16, No. 7, July 1978, pp. 736-739.

3. Caveny, L. H. and Gany, A., "Breakup of Al/Al_2O_3 Agglomerates in Accelerating Flow Fields," AIAA Paper 79-0300, AIAA Aerospace Sciences Meeting, January 1979.

4. Kraentle, K. J., Personal Communication, September 1978.

5. Price, E. W., Sigman, R. K., and Sambamurthi, J. K., "Behavior of Aluminum in Solid Propellant Combustion" 1977, Georgia Institute of Technology, Atlanta, GA, USA, 1977.

6. Crump, J. E., Prentice, J. L., and Kraeutle, K. J., "Role of Scanning Electron Microscope in the Study of Solid Propellant Combustion: II. Behavior of Metal Additives," Combustion Science and Technology, Vol. 1, 1969, pp. 205-223.

7. Derr, R. L., Churchill, H. L., and Fleming, R. W., Lockheed Propulsion Company, Personal Communication, 1974.

8. Kraeutle, K. J., "Applications of Particle Size Analysis in Combustion Research," AIAA Paper No. 77-978, July 1977, American Institute of Aeronautics and Astronautics, New York, NY.

9. Barrere, M. "Recent Experimental Results onthe Combustion of Aluminum and Other Metals." Proceedings of AGARD Meeting on the Reactions of Gases and Solids, October, 1969.

10. Pokhil, P. F., Belyayev, A. F., Frolov, Yu. V., Logachev, V. S., and Korotkov, A. I., "Combustion of Powdered Metals in Active Media," Nauka, Moscow 1972.

11. Gladun, V. D., Frolov, Yu. V., Kashporov, L. Ya., Shakhidzhanov, E. S., and Borisov, A. A., "Nature of Agglomeration During Combustion of Highly Metallized Condensed Systems," USSR National Academy of Sciences (Preprint) 1977.

AD-A076 012 ADVISORY GROUP FOR AEROSPACE RESEARCH AND DEVELOPMENT--ETC F/G 21/8.2
SOLID ROCKET MOTOR TECHNOLOGY.(U)
JUL 79
UNCLASSIFIED AGARD-CP-259 NL

3 OF 6
AD
A076012

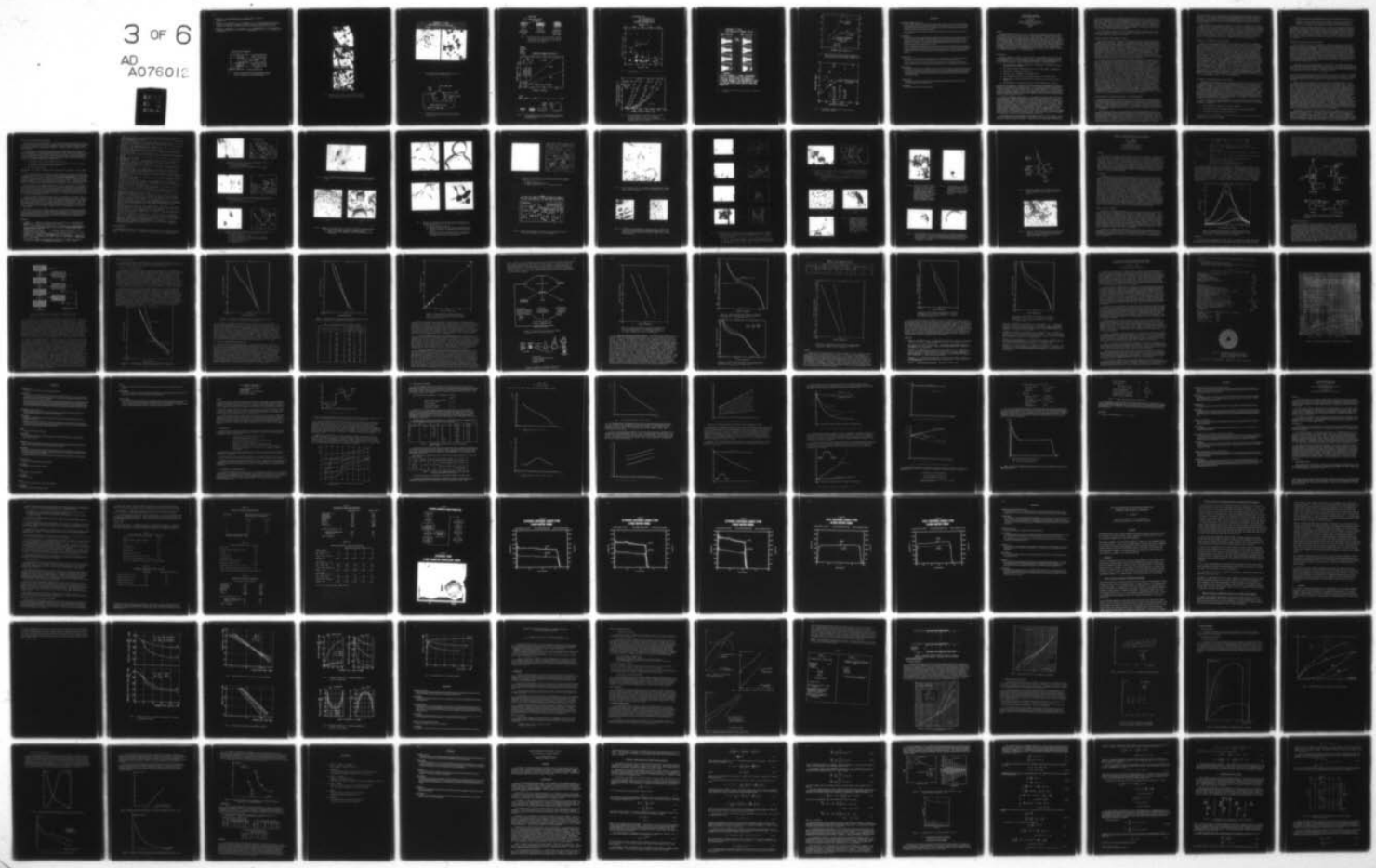

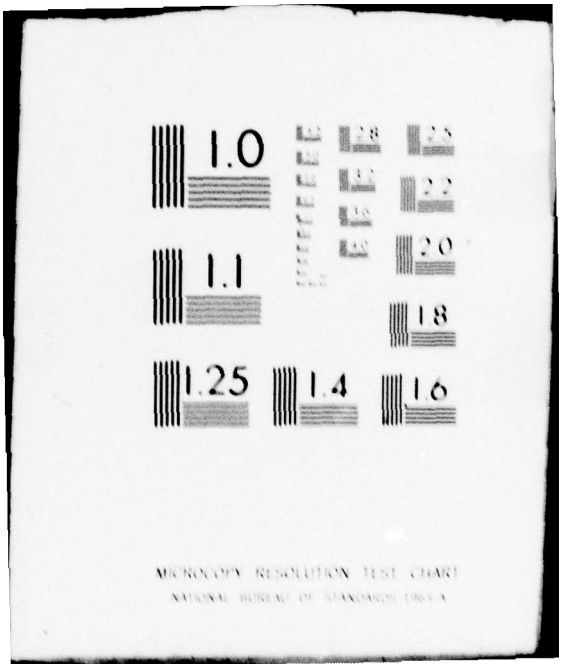
1.0
1.1
1.25
1.4
1.6
2.0
2.2
2.5
2.8
3.2
3.6
4.0
4.5
5.0
5.6
6.3
7.1
8.0
9.0
10.0
11.0
12.5
14.0
16.0
18
MICROCOPY RESOLUTION TEST CHART
NATIONAL BUREAU OF STANDARDS 1963-A

12. Micheli, P. L., and Schmidt, W. G., Aerojet Solid Propulsion Company, Sacramento, CA, Personal Communication, December 1977.

13. Geisler, R. L., Kinkead, S. A., and Beckman, C. W., "The Relationship between Solid Propellant Formulation Variables and Motor Performance," AIAA Paper No. 75-1199, October 1975, American Institute of Aeronautics and Astronautics, New York, NY.

14. Kubota, N., Ohlemiller, T. J., Caveny, L. H., and Summerfield, M., "Site and Mode of Platonizers in Double Base Propellants," AIAA Journal, Vol. 12, No. 12, December 1974 pp. 1709-1714.

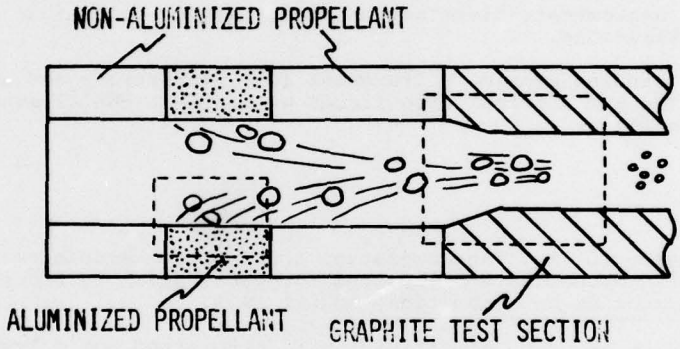

Fig. 1 Diagram of windowed rocket motor showing photographic field of view for agglomerates in cross-flow and agglomerate breakup experiments.

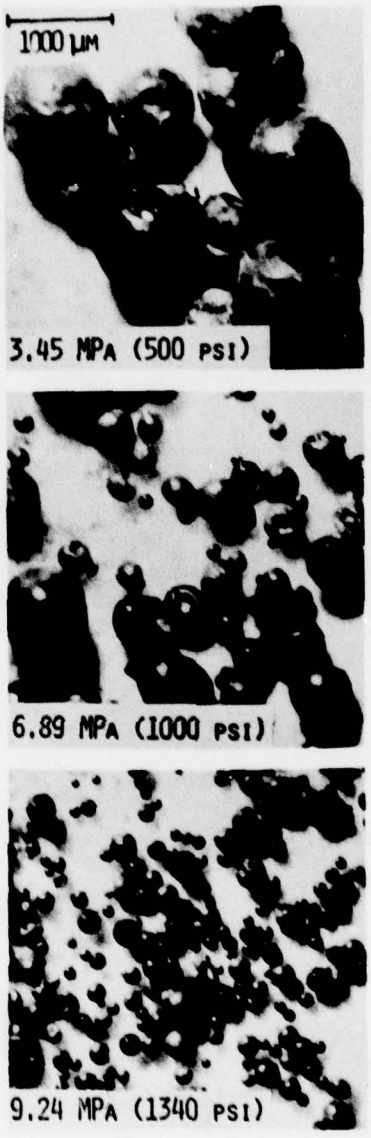

Fig. 2 Agglomerates collected from strands give qualitative measure of the decrease in agglomerate size with increasing burning rate and pressure.

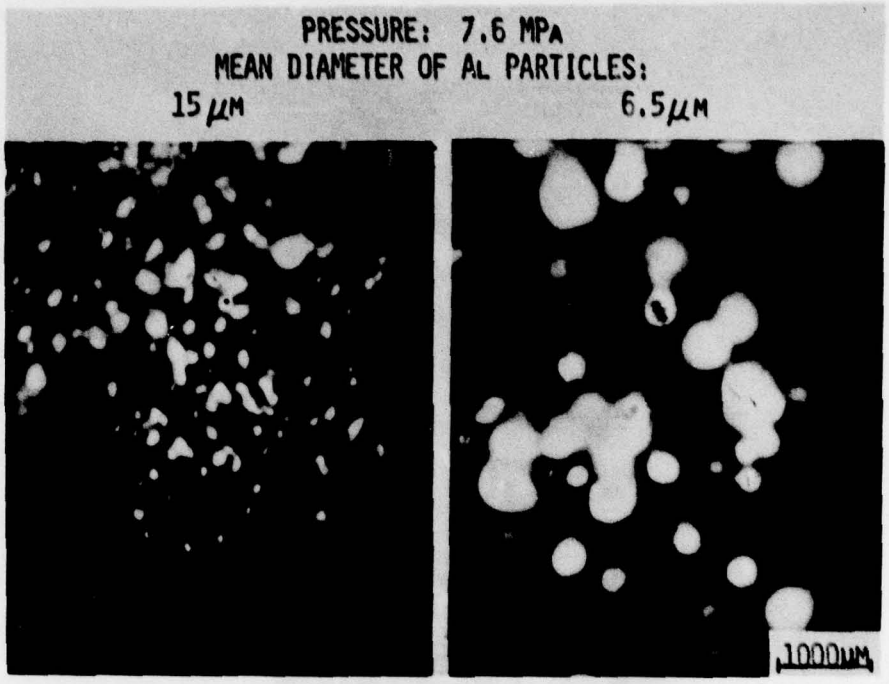

Fig. 3 Agglomerate size increases when Al particle size is decreased below threshold size.

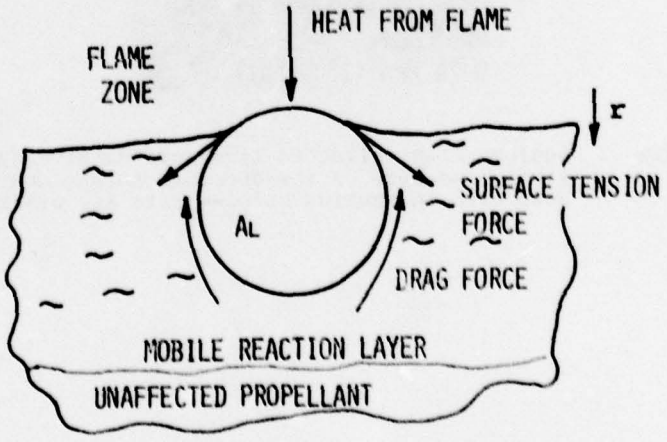

Fig. 4 Aluminum particle being heated by flame and retained in mobile reaction layer by surface tension force.

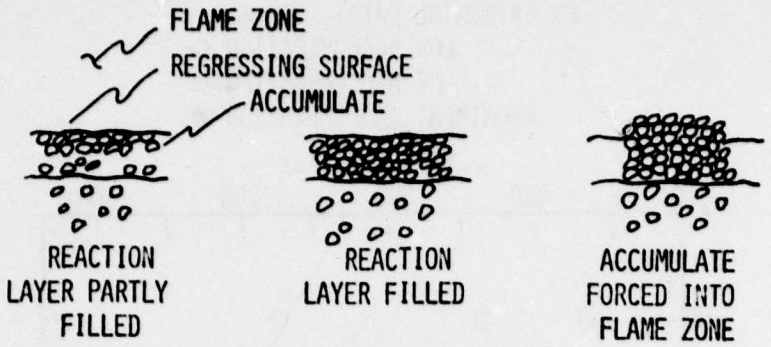

Fig. 5 Accumulation process in the mobile reaction layer showing how regression of the surface concentrates the aluminum particles and exposes them to the flame.

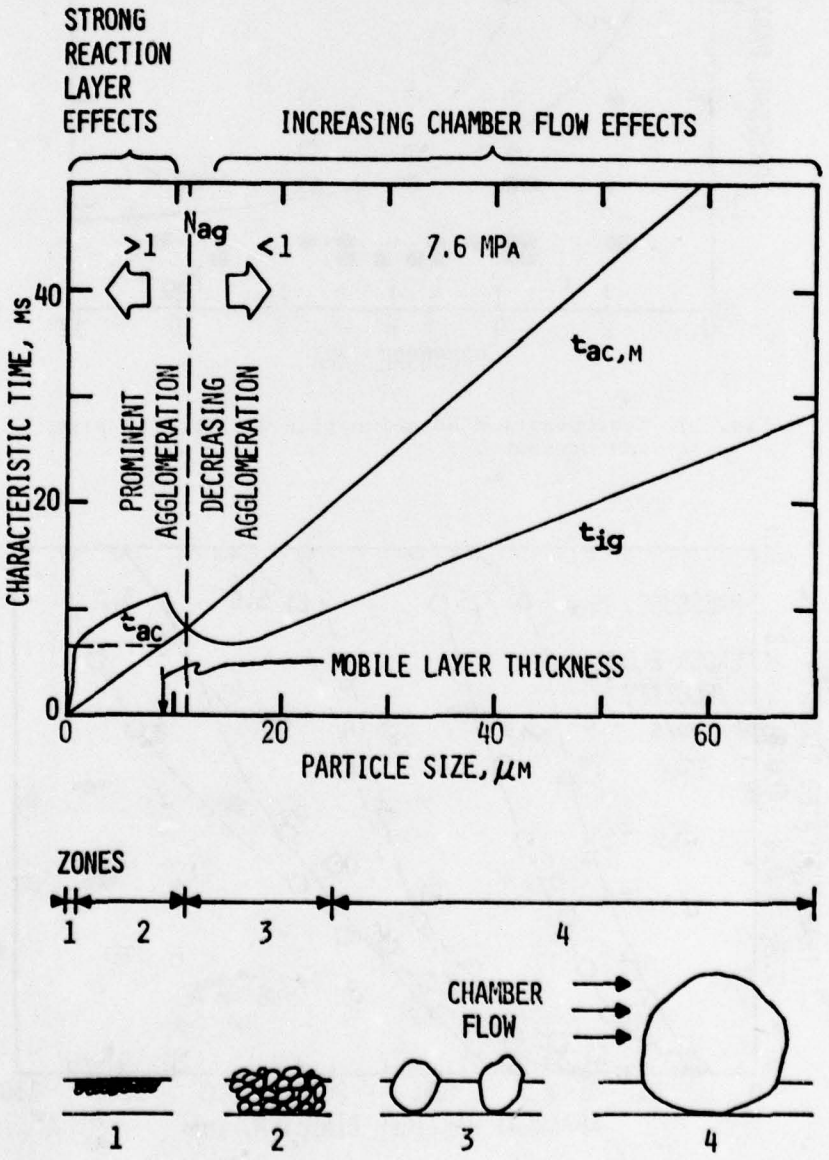

Fig. 6 Characteristic times of accumulation and ignition of aluminum particles affect the agglomeration characteristics.

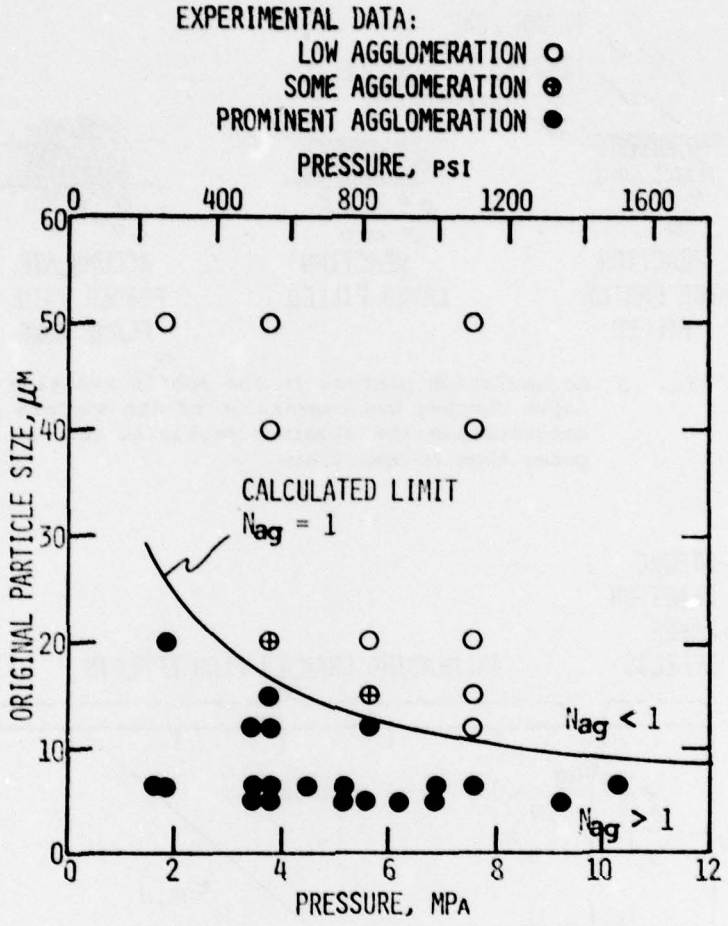

Fig. 7 Agglomeration as a function of particle size and pressure.

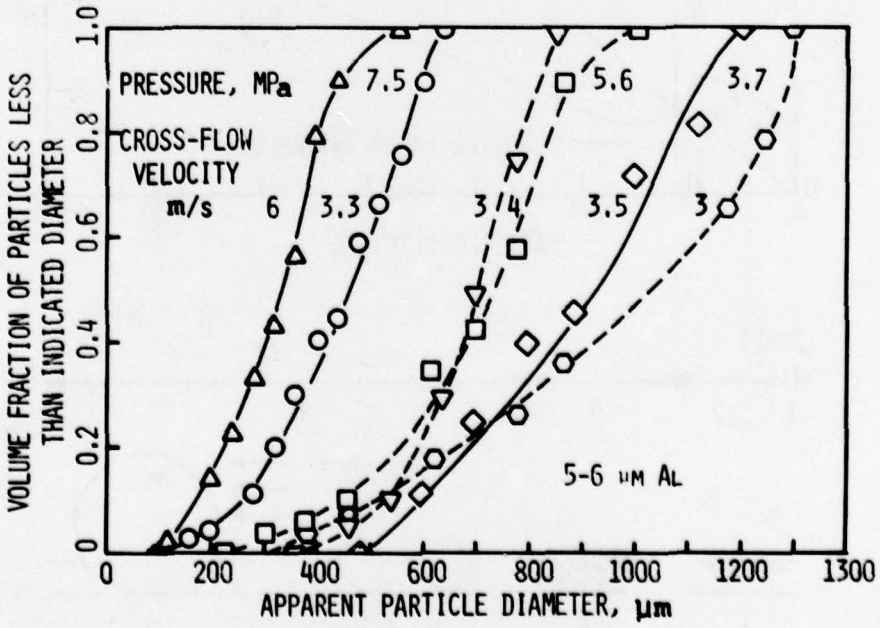

Fig. 8 Volume distribution of agglomerates for a range of motor pressures. Note: (1) decrease of agglomerate size with increasing pressure; (2) some tendency of decreasing particle size with increasing port flow velocity.

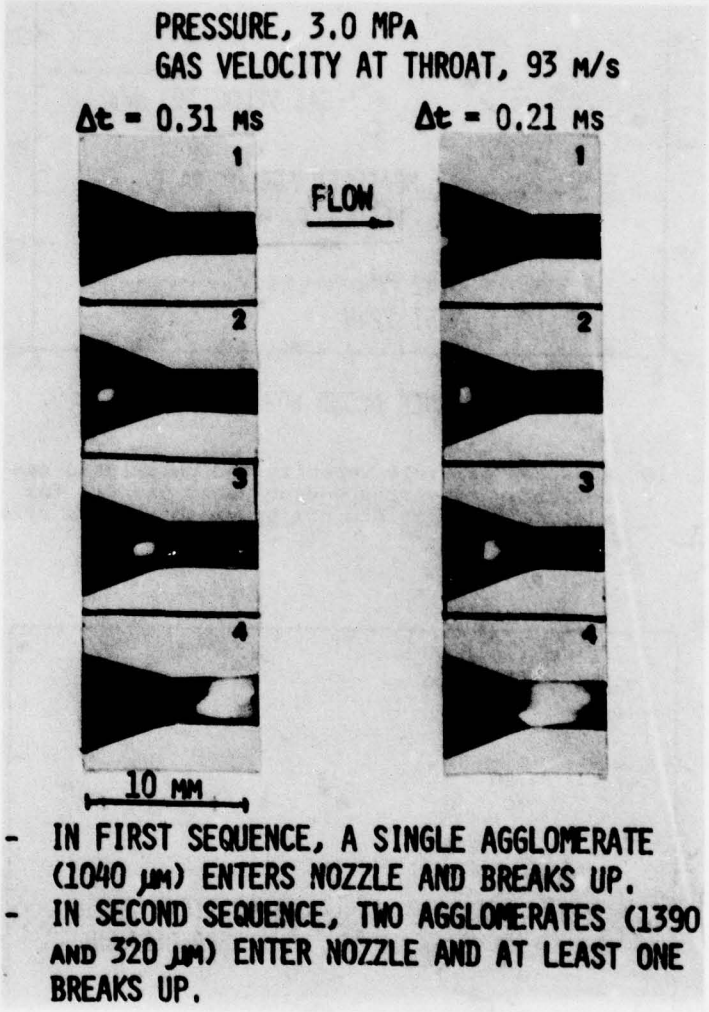

Fig. 9 Agglomerates breaking up in subsonic converging nozzle.

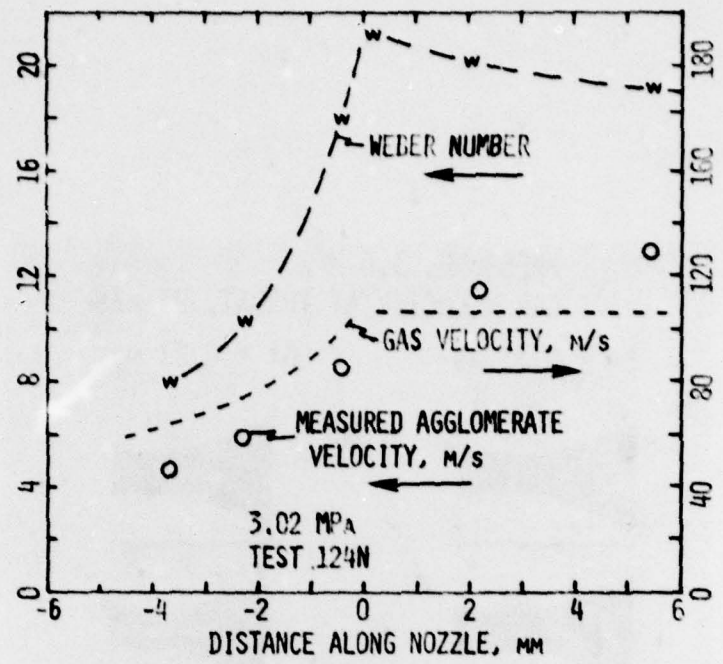

Fig. 10 Measured particle velocity and calculated gas velocity and corresponding Weber numbers for agglomerate that did not break up (580 μm size).

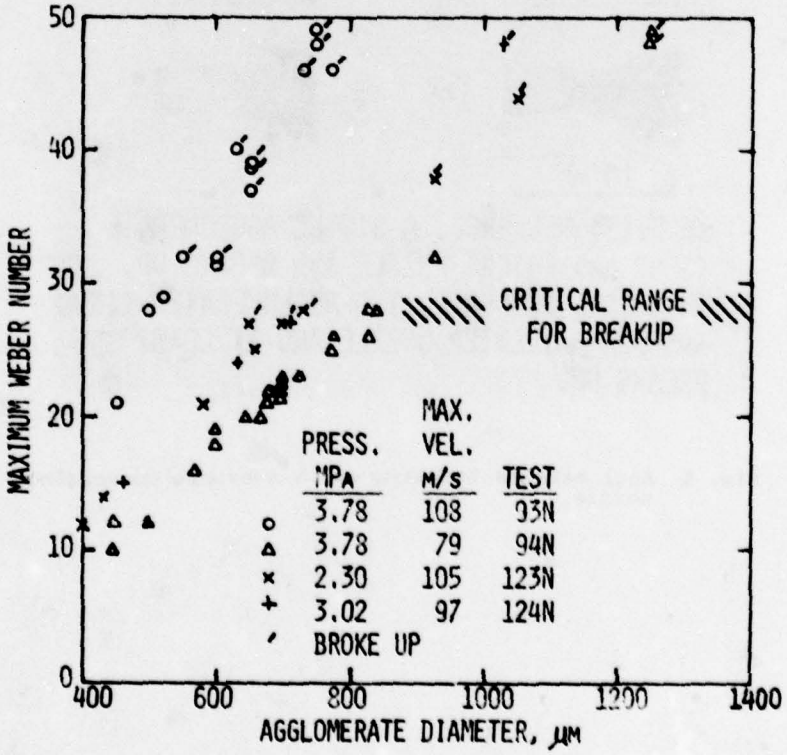

Fig. 11 Agglomerate breakup occurs at sufficiently high Weber numbers.

DISCUSSION

R.C.Parkinson, PERME, Westcott, UK

You have considered agglomerate break-up under the acceleration conditions at the entry to the nozzle. However the acceleration of gas in the motor conduit is comparable to the accelerations in the rocket nozzle. In particular, particles injected into the conduit gas stream by propellant very close to the downstream end of the charge must accelerate up to the main stream velocity very quickly.

Have you any observations of the relative mechanics of agglomerate break-up under acceleration in the conduit and in the nozzle?

Author's Reply

This question is pertinent to various internal motor geometries, for example the ejection of a stream from a slot into the main flow stream. Experiments at Princeton University with a 50 cm window motor had mean port flow velocities as high as 200 m/s. Only in rare instances were phenomena similar to break-up observed. The 2 phase flow lag was of the order of 10–20 m/s and in the experiments presented in the paper of the order 50–100 m/s. The latter is more like the converging section of a nozzle.

Diameters of agglomerates entering the port flow decreased with increasing distance along the port and agglomerate break-up of the type shown in Figure 9 was not observed. The decrease in size was similar to that shown in Figure 8. Thus the compensating effects were similar to the trends described in my paper. As the crossflow velocity increases, particle break-up was not observed in the port since the smaller agglomerates had correspondingly lower Weber numbers.

J.D.Berard, SNPE

You have shown that you can define a critical particle size for aluminium filler in the propellant with respect to agglomeration. Smaller particles result in agglomeration on the surface whilst larger particles do not.

This may perhaps be related to the acoustic response for a given frequency for aluminised propellants which is known for SNPE work to be at a maximum of 10 microns aluminium size at 70 atmospheres. Can you comment?

Author's Reply

In the presentation the plot for 70 atmospheres was shown. We have in fact produced plots over a range of pressures. In general at lower pressures the mobile layer becomes thicker and can accumulate larger agglomerates. However we have not tried to relate the type of particle or agglomerate to acoustic instability effects. We have been looking at very large particle sizes of the order of several hundred microns whereas much smaller particles are involved in gas phase particle damping.

J.D.Berard, SNPE

My question was not related to particle damping and small/large particle influence but rather to the acoustic response or admittance of the burning surface.

Author's Reply

We have not tried to relate our work to this aspect.

COMBUSTION OF ALUMINUM IN SOLID PROPELLANT FLAMES

by
E. W. Price
Professor
School of Aerospace Engineering
Georgia Institute of Technology
Atlanta, Georgia
30332
U.S.A.

SUMMARY

Powdered aluminum is used as a fuel in solid rocket propellants because the chemical equilibrium calculations show that it provides increased specific impulse (some other positive and negative contributions are also important). However, the process by which aluminum particles proceed to final combustion products is exceedingly complex, and dependent on motor operating conditions, details of propellant variables, and even of the aluminum powder. The paper describes the behavior of aluminum in the combustion zone, the mechanisms causing this behavior, and the significance to motor performance, with particular emphasis on ammonium perchlorate-hydrocarbon binder-aluminum propellants. The features of aluminum behavior involve retention, concentration, sintering and coalescence of most particles on the propellant burning surface. This is followed by detachment and ignition of the agglomerate material, burning in the combustor cavity with formation of a characteristic population of oxide droplets in a diameter distribution with most droplets $0.1 < D < 50$ micrometers.

INTRODUCTION

Powdered aluminum is used as a fuel ingredient in heterogeneous solid rocket propellants [1,2] because it is a dense, energetic fuel. Unlike other ingredients, it does not decompose or vaporize at the propellant burning surface, and has condensed phase reaction products. As a result it exhibits novel behavior in the combustion zone, not all of which is desirable. Some of the practical effects of aluminum include:

1. Increased specific impulse and density of propellants (in appropriate formulations and motor designs);
2. Only modest change in propellant burning rate in most types of propellants;
3. Suppression of combustion instability;
4. Erosion of motor components by aluminum oxide;
5. Poor combustion efficiency at low motor pressures or in small motors;
6. Reduced nozzle thrust efficiency due to thermal and velocity lag of oxide droplets;
7. Novel aspects of the exhaust plume due to large aluminum oxide content.

Of these various effects of aluminum, all are susceptible to some measure of control, modification or compromise, a fact that has led to fundamental studies of the detailed behavior of aluminum in the combustion zone. It is this detailed behavior that will be described here, along with related studies of aluminum behavior in controlled laboratory environments. It should perhaps be stressed that the effects 1-7 cannot be determined by conventional chemical equilibrium, combustion and heat transfer calculations because of analytical difficulties and insufficient information about aluminum behavior and oxide product characteristics.

To set the discussion in perspective, it is helpful to describe some of the more gross aspects of aluminum behavior that are applicable in varying degree to all aluminized propellants. Combustion photography shows that aluminum particles (typically 15-40 μm diameter) tend to accumulate on the burning surface (Figure 1). When the concentration of aluminum in the propellant is greater than about 8% by weight, the particles are concentrated on the surface until they become connected to each other. These clumps of particles (referred to here as "accumulates") leave the burning surface collectively, either as clumps or as burning droplets (Figures 2, 3). Depending on propellant variables and pressure, the assemblages of particles usually involve several of the original aluminum particles--typically 100 to 1000, and sometimes up to 10^6. Coalescence of a clump of particles into a large droplet (referred to here as an "agglomerate"), whether on the burning surface or later, is an event that is indistinguishable from ignition. At a distance of 1000 micrometers from the burning surface all accumulates have been converted to burning agglomerates (Figure 4).

The actual details are observed to differ among propellants, but virtually all conform to the above qualified description. Depending on the size of agglomerates, the pressure, combustor volume and combustor flow velocity, the combustion of aluminum may

be distributed throughout the combustor and even beyond the nozzle. The details are still often speculative, as is the information on size distribution of the oxide droplet population. Some inferences can be made about these processes, but simulation of motor conditions is difficult in systematic laboratory testing where observation of the process is feasible. Evidence of the behavior in motors can be inferred from effects on specific impulse, exhaust plume characteristics and combustor stability. However, motor tests are not amenable to systematic control of variables, unequivocal interpretation of results, or economically acceptable systematic studies, so efforts continue to characterize behavior from laboratory scale tests.

In the following, the nature of aluminum powder response to heating, and factors conducive to aluminum accumulation on the burning surface are examined first, followed by a description of the behavior of the accumulated aluminum upon continued exposure to the high temperature regions of the flame.

ALUMINUM PROPERTIES AND RESPONSE TO HEATING

Much of the behavior of aluminum in the combustion process is due simply to the characteristics of aluminum. Aluminum is highly reactive in most oxidizing atmospheres, including oxygen, air, water vapor and carbon dioxide. However, aluminum objects are protected from reaction by formation of an oxide film on the surface that is an effective barrier to diffusion of oxidizing species[3]. This is true of the ingredient particles of aluminum in a propellant, which consequently are reluctant to ignite on the propellant burning surface. Likewise, the aluminum does not vaporize, its boiling point being roughly three times the temperature of the propellant burning surface. On the other hand, the melting point of aluminum is in the same range as temperatures on the surface[4-6], and one may expect this to be manifested in the aluminum behavior. Specifically, the coefficient of thermal expansion of the metal is greater than that of the oxide, leading to stressing the oxide "skin" during heating. Further, the aluminum expands 6% by volume upon melting. Thus the protective property of the oxide is jeopardized during heating, and especially at the aluminum melting point.

In order to observe how aluminum powder behaves during heating, studies have been made of its behavior in various laboratory experiments amenable to control of test conditions and observation of microscopic behavior. A useful method for illustration is the hot stage microscope, which permits observation during heating, and provides a sample for microscopic and other study after a controlled heating experience[7-8]. This technique was used to illustrate response to heating, as illustrated by Figure 5, which shows aluminum powder after heating to 1275°K on a sapphire disc. The powder heated in oxygen looks much like the unheated powder (detailed examination shows the particles to be sintered together). The powder heated in argon has largely agglomerated, leaving a residue of oxide skins from the original particles (the pictures were taken at room temperature after the test, using a scanning electron microscope). When tests are run on dispersed particles, the effect of the aluminum expansion and contraction is evident in the form of wrinkles in the oxide skin (Figure 6b) and "warts" formed by aluminum forced through flaws in the oxide skin (Figure 6c). Such warts are accompanied by collapsed regions of the parent particle, reflecting the volume of aluminum frozen into the wart during cooling. Some particles drain from the oxide skin onto the sapphire plate, leaving empty oxide shells (recognizable in an optical microscope). The importance of surface forces and the nature of the oxide skin are revealed in tests on platinum surfaces (Figure 6d), where the aluminum drains into a conical configuration, leaving the collapsed skin at the tip of the cone. Continuing studies show that the behavior of aluminum powders and particles depend on source of the powder, but difficulties in determining and controlling the relevant details of the original particles and conducting systematic testing have prevented a complete understanding or control of aluminum behavior in laboratory testing and propellants. Commercial powders differ conspicuously according to manufacturer, and specifications used in purchase are usually limited to some rough specification on size distribution and purity.

BINDER RESPONSE TO HEATING AND IMPORTANCE TO ALUMINUM BEHAVIOR

Composite propellants contain from 10 to 60% by volume of binder material, with hydrocarbon polymer binders normally being used at the 10-20% level. On the microscopic scale, the aluminum particles of the propellant are immersed in the binder, and hence are reached by the receding propellant surface while in a decomposing binder environment (Figure 7). Since accumulation of aluminum on the surface is observed to be an important factor in the overall aluminum behavior, it is relevant to note the nature of binder at the temperatures present near the burning surface where this aluminum accumulation also takes place.

Observations of binder in various combustion and heating experiments[8-11] in the absence of aluminum show that decomposition involves an intermediate melt phase at temperatures in the same range as the aluminum melting point, which also is the range of reported propellant burning surfaces. Such conditions provide the opportunity for aluminum particles to be retained and concentrated in (or on) the surface layer, with binder residue serving as an adhesive. Figure 8[8] shows the results of visual observations of binder behavior during the relatively slow heating of a hot stage microscope (10°C/sec). These results show binders as molten to tar-like residues at temperatures from about

675°K up to 975°K or so.* Similar tests on 50/50 binder/aluminum samples[12] show the aluminum particles emerging as interconnected assemblages with substantial agglomeration (Figure 9). Thus one sees in the controlled heating experiments the same kind of aluminum particle concentration, adhesion and agglomeration in binder that is observed on the propellant during burning. In the propellant combustion zone, the processes continue until disruptive conditions develop locally and cause the aluminum to detach from the surface.

While considering the role of the binder, it is worthy of note that the aluminum is usually present in the propellant as particles that are fine compared to the oxidizer, and hence occurs in a spatial array of the binder. Thus it initially reaches the surface in a pattern characteristic of the binder distribution (Figure 10), and must accumulate for a protracted time (order of the burning time of the larger oxidizer particles) before it loses this pattern. In other words, the departing aggregates of particles will be characteristic fragments of this pattern unless accumulation is protracted. As will be seen, longer retention times do occur under many practical conditions. Then one must look beyond the binder retention of aluminum and spatial distribution of the aluminum in the propellant microstructure to understand such accumulation behavior.

COMBUSTION OF ALUMINUM WITH SOLID OXIDIZERS

While it is not surprising that aluminum particles do not burn in an atmosphere of hydrocarbon binder pyrolysis products, one is tempted to expect that the particles would burn well in the pyrolysis products of an oxidizer. That speculation is generally valid, but combustion does not occur without particle ignition, and we have noted that aluminum is resistant to ignition because of the protective nature of the oxide skin. There is much speculation in the literature about definition of ignition of aluminum particles[13-15], and it seems clear that they can survive as oxide-coated droplets to temperatures as high as the 1200°K estimated for ammonium perchlorate flames. By the same token it is no surprise that dry-pressed solid samples of ammonium perchlorate-aluminum powder mixtures do not burn well, and can burn without igniting the aluminum (Figure 11)[16-18]. Perhaps more of a surprise, aluminum accumulates on the surface as an interconnected array of particles, manifesting an adhesive process between the surface and the aluminum. Finally, the accumulation of aluminum (or some part of it) can break away and concurrently inflame propagatively and agglomerate (Figure 11b), indicating that ignition can occur in the dynamics of an accumulation even when the individual particles have not ignited. Indeed, it is significant that when the aluminum and ammonium perchlorate particles in the sample are of equal size so that aluminum particles encounter each other only infrequently, little or no surface accumulation occurs and aluminum particles fail to ignite (Figure 11c). Retention of aluminum, when it does occur, is probably aided by some surface forces due to the fluid film observed on the oxidizer surface, but in this case direct cohesion between aluminum particles is apparently necessary for prolonged retention. Thus in summary, the presence of the oxidizer deflagration does not precipitate detachment or ignition of aluminum particles, and may even aid in retention of the aluminum. Further, aluminum particles can sinter together in the absence of binder residue as an adhesive, much as in the case noted earlier of dry aluminum powders heated in an oxidizing atmosphere.

DETACHMENT OF ALUMINUM FROM THE BURNING SURFACE

Accumulation and detachment of aluminum occur in a variety of ways, and as a result of conditions too varied to discuss fully. Detachment may occur as single particles, as undermined fragments of the original aluminum distribution in the microstructure, as extensive filigrees of loosely interconnected material (Figure 2), as large sintered fragments, or as molten agglomerates (Figure 3). In a given propellant, the disorder of the microstructure assures a variety of behavior from a single burning surface. In normal propellants, ignition of the aluminum occurs on or near the propellant surface. If it occurs on the burning surface, the event is typically abrupt and concurrent with agglomeration, with detachment from the surface usually following immediately. Under unfavorable conditions (low pressure, low O/F ratio, unusually high aluminum content), the ignition and detachment are less abrupt (Figure 12), the spread of inflamation and the process of agglomeration on the burning surface are resolvable in combustion photography, and lead to very large agglomerates.

While the factors governing detachment are too varied and poorly evaluated to describe or exploit fully, it seems clear that the following are key factors in detachment of accumulated aluminum:

1. Transitions in the underlying surface to oxidizer.
2. The "blowing" force of pyrolysis products from the underlying surface.
3. Proximity of neighboring aluminum particles.

---

* Samples ignite at 875°K in oxygen.

4. Progressive changes in accumulated material due to "prolonged exposure" to the adjoining high temperature diffusion flame of binder and oxidizer products.

5. Proximity of the diffusion flame and its effect on ignition of accumulated material. (Fine oxidizer, burning rate catalysts and high pressure all act in this way to produce earlier ignition of aluminum, smaller agglomerates.)

The importance of the diffusion flame (Figure 11d) lies in its provision of temperatures high enough to break down the protective oxide, at least locally, somewhere in an accumulated mass of aluminum. Once this occurs in an oxidizing environment, the aluminum oxidation provides enough heat to assure inflamation of surrounding parts of the accumulation. The breakdown of oxide brings the aluminum surface tension forces into play, and the accumulate coalesces as it inflames. This is illustrated in Figures 12 and 13, where Figure 13 shows accumulates that were quenched in liquid nitrogen at the moment that surface tension was spheroidizing the molten aluminum[16]. Unmelted material was still present.

COMBUSTION OF ALUMINUM AND NATURE OF PRODUCTS

It was noted earlier that the formation of a protective oxide film on the aluminum surface is the principal barrier to ignition of an otherwise highly reactive metal. Ignition of aluminum is consequently a difficult event to define because it is determined by the irreversible breakdown of this oxide film under the existing state of the aluminum accumulation and environment. In propellant combustion, the aluminum accumulate is an array of droplets contained and held together by the sintered oxide "shells" (Figure 14), and mechanical breakdown may be the initiating step of ignition. However, ignition is not assured until local melt-down of the protective oxide at about 2300°K. Because the liquid oxide and aluminum are not miscible, when the oxide does melt, it tends to retract from the aluminum surface, with a corresponding abrupt rise in aluminum reaction rate and rising temperature. This quickly establishes a detached flame over the aluminum surface, fueled by evaporating aluminum and readily recognized by the trail of aluminum oxide smoke formed in the flame and carried away by the surrounding gas flow (visible in Figures 3, 4, 12, 15).

Although the time required may depend on many factors, the burning agglomerate apparently becomes a molten aluminum droplet with an oxide lobe (Figure 3, 16) similar to those observed in laboratory studies of single particles in controlled atmospheres[12,19-22]. While the literature is not consistent, it appears that burning time of the droplets can be estimated by the classical droplet burning rate law[2,23-25]

$$\tau = kD_o^n \qquad (1)$$

In contrast to simple diffusion-controlled theory, the value of n is about 1.75 (values from 1.5 to 2.0 in the literature). For n = 1.75, a value of k of 0.5 x 10^{-5} sec/$(\mu m)^{1/n}$ will yield approximately correct burning times under rocket motor conditions. A 150 μm agglomerate requires about 0.03 seconds to burn, and may travel 1 m in the motor in that time.

The progress of agglomerate combustion is illustrated schematically, along with approximate temperatures in Figure 17. The brightness of the flame (Figure 3, 4) is due primarily to the high-temperature oxide droplets in the detached flame. Roughly 30% of the oxide ends up in these "smoke" droplets, that range up to about 2 μm in diameter. The profusion of fine oxide smoke is so great in propellant combustion that it has been difficult to observe directly any but the early phases of agglomerate combustion. This has left the balance of the combustion open to considerable speculation. However, the balance of the oxide is in the lobes on the aluminum droplets, each of which produces one or more "residual" oxide droplets in the size range 5-50 μm (Figure 18). The size of these residual oxide droplets is dependent on the agglomerate size, an important issue in combustion instability in the 100-1000 Hz frequency range[26]. Regarding the amount and size of the residual oxide droplets, there is controversy as to how much of the oxide is formed before and during ignition, and whether further surface oxide is formed by surface reaction and/or smoke oxide diffusion to the surface during burning. Also the question is raised as to whether or not the oxide lobe is dispersed during burning or possibly at burnout. Such behavior is observed in laboratory experiments under idealized conditions[19-21,23,27]. In response to these speculations, single droplet experiments establish beyond doubt that oxide can accumulate during burning[28], and recent tests of droplet burning in propellant atmospheres indicate that dispersal of oxide from the surface during burning or at burnout was not conspicuous enough to cause visible deflections in the path of the burning droplet.

Summarizing the combustion phase of aluminum behavior, agglomerates of 1 to 10^6 original aluminum particles burn while moving out in the flow field, with burning times approximated by Equation (1). The droplet is oxidized primarily by H_2O and CO_2, to yield H_2, CO and liquid Al_2O_3. Most of the oxide is formed in the high temperature, luminous flame envelope around the droplet, and is a smoke consisting of droplets less than 2 μm in diameter. The balance of the oxide is found in the form of lobes on the aluminum droplets and eventually gives a component of the oxide droplet population mostly in the 5-50 μm diameter range (sizes dependent on original aluminum agglomerate sizes).

EFFECT OF THE ROCKET MOTOR ENVIRONMENT

Observations of aluminum behavior in actual rocket motor environments are difficult to make, and are sure to be different in some degree from laboratory experiments (because of gas flow, radiation field, and scale effects). However, behavior in motors can be inferred qualitatively by mechanistic arguments, laboratory tests, and observations of motor behavior.

Just as flow in the motor affects burning rate of propellants (erosive burning), so one would expect it to affect aluminum accumulation [29,30]. Usually it appears to reduce accumulation, and agglomerate droplet size. Of course this effect would be expected to vary with location in the motor and time during burning, in a manner analagous to erosive burning. In those regions of the motor where flow velocities are high, the size of the aluminum agglomerates is reduced, and their burning times correspondingly reduced. This modifies the droplet burning field

1) in the motor (which affects combustion stability);

2) in the nozzle (which affects nozzle erosion, two-phase flow loss of thrust, and combustion efficiency-related thrust loss);

3) and in the exhaust plume.

Such effects are observed in marginal motor designs that are conducive to heavy agglomeration.

In the case of combustor stability, any motor conditions that affect aluminum combustion can be important, but the effects related to combustion dynamics cannot presently be characterized. It is safe to assume that the spacewise nonuniformity of these effects resulting from the flow field is important, although not considered in most stability analyses [31]. One effect that has been evaluated is the reduction of residual oxide droplet size accompanying flow-induced reduction of agglomerate size [31]. Since these oxide droplets are in a size range that damps oscillatory behavior in the 100-1000 Hz frequency range [26], flow-induced stability effects may be anticipated in that frequency range.

Another important environmental condition in motors is acceleration. The principal effect is observed in spin stabilized motors, where the aluminum tends to accumulate excessively on the burning surface. This in turn affects (increases) burning rate and motor pressure, and can lead to aluminum accumulation in the motor, low combustion efficiency, nozzle slagging, etc. The basic combustion aspects of this behavior are illustrated in laboratory scale experiments [32,33], where it is shown that aluminum and oxide can continue to accumulate on the burning surface with enhanced propellant burning rates and reduced aluminum combustion rate.

A number of papers have appeared that dealt with the question of droplet size in the motor, nozzle and jet, based on droplet growth or disruption in the flow. The present discussion does not address this point, or discount the mechanisms involved. However, it should be noted that the initial oxide droplet size distribution is both wide and complex, and determined by the aluminum agglomeration and combustion. Since combustion-generated droplet size distributions do not appear to have been used as the initial distribution in the papers on droplet growth and disruption, it is not yet possible to explain the observed exhaust plume particle size distributions by reference to those papers.

Relative to the future, it seems likely that increasing understanding can provide for control of agglomeration, combustion dynamics and particle size of residual oxide droplets. Analytical modeling of steady and unsteady combustion of aluminized propellants is probably warranted now on the basis of accumulated understanding. Because of the complex behavior of aluminum, it will continue to be difficult to forecast behavior in new, novel propellant formulations.

REFERENCES

1. Glassman, I., "Combustion of Metals: Physical Considerations," ARS Progress in Rocketry, Vol. 1, New York, Academic Press, 1960.
2. Pokhil, P. F., Belyayev, A. F., Frolov, Yu. V., Logachev, V. S., and Korotkov, A. I., "Combustion of Powdered Metals in Active Media," Gorenyi Poroshkovbraznykh Metalov v Actionykh Shredakh, 1972; see also Air Force Systems Command Report FTD-MT-24-551-73, 1973.
3. Kubaschewski, O. and Hopkins, B. E., Oxidation of Metals and Alloys, 2nd Ed., London, Butterworths, 1962.
4. Beckstead, M. W. and Hightower, J. D., "Surface Temperature of Deflagrating Ammonium Perchlorate Crystals," AIAA Journal, Vol. 5, No. 10, 1967.
5. Sabadell, A. J., Wenograd, J., and Summerfield, M., "Measurements of Temperature Profiles through Solid Propellant Flames Using Fine Thermocouples," AIAA Journal, Vol. 3, No. 9, 1965.
6. Zenin, A. A., "Structure of Temperature Distribution in Steady-State Burning of a Ballistic Powder," Fizika Goreniya I Vzryva, Vol. 2, No. 3, 1966.

7. Crump, J. E., Prentice, J. L., and Kraeutle, "Role of Scanning Electron Microscope in the Study of Solid Propellant Combustion: II. Behavior of Metal Additives, Combustion Science and Technology, Vol. 1, 1969; see also same title, Naval Weapons Center, NWC-TP-5142.
8. Price, E. W. and Sigman, R. K., Air Force Office of Scientific Research, "Behavior of Aluminum in Solid Propellant Combustion," 1976, AFOSR-TR-77-0050.
9. Fleming, R. W., Derr, R. L., and Cohen, N. S., "Role of Binder in Solid Propellant Combustion," AIAA Journal, Vol. 12, No. 2, 1974.
10. Madorsky, S. L., Thermal Degradation of Organic Polymers, New York, Interscience Publishers, 1964.
11. Varney, M. A., Georgia Institute of Technology, "An Experimental Investigation of the Burning Mechanisms of Ammonium Perchlorate Composite Solid Propellants," Ph.D. Thesis, 1970.
12. Price, E. W., Sigman, R. K., and Sambamurthi, J. K., Air Force Office of Scientific Research, "Behavior of Aluminum in Solid Propellant Combustion," 1977, AFOSR-TR-78-0468.
13. Mellor, A. M. and Glassman, I., "A Physical Criterion for Metal Ignition," Pyrodynamics, Vol. 3, 1965.
14. Derevyaga, M. E., Stesik, L. N., and Fedorin, E. A., "Ignition and Combustion of Aluminum and Zinc in Air," Fizika Goreniya I Vzryva, Vol. 13, No. 6, 1977.
15. Breiter, A. L., Mal'tsev, V. M., and Popov, E. I., "Models of Metal Ignition," Fizika Goreniya I Vzryva, Vol. 13, No. 4, 1977.
16. Hubbartt, J. E., Price, E. W., Strahle, W. C., and Zinn, B. T., Air Force Office of Scientific Research, "Rocket Research at Georgia Tech," 1978, AFOSR report number unassigned.
17. Cohen Nir, E., "Combustion of Powdered Metals in Contact with a Solid Oxidizer (Ammonium Perchlorate)," Thirteenth Symposium (International) on Combustion, Pittsburgh, The Combustion Institute, 1971.
18. Price, E. W., Rice, D. W., and Crump, J. E., Naval Ordnance Test Station (Naval Weapons Center), "Low-Frequency Combustion Instability of Solid Rocket Propellants," 1964, NOTS-TP-3524.
19. Christensen, H. C., Knipe, R. H., and Gordon, A. S., "Survey of Aluminum Particle Combustion," Pyrodynamics, Vol. 3, 1965; see also same title, Combustion Institute Preprint No. 64-19, 1964.
20. Gordon, A. S., Drew, C. M., Prentice, J. L., and Knipe, R. H., "Techniques for the Study of the Combustion of Metals," AIAA Journal, Vol. 6, No. 4, 1960.
21. Brulard, Jean, Recherche Aerospatiale, "Contributions to the Study of the Combustion of Aluminum Particles," 1967, No. 118.
22. Prentice, J. L., ed., Naval Weapons Center, "Metal Particle Combustion, Progress Report, 1 July 1965 - 1 May 1967," 1968, NWC-TP-4435.
23. Belyayev, A. F., Frolov, Yu. V., and Korotkov, A. I., "Combustion and Ignition of Particles of Finely Dispersed Aluminum," Fizika Goreniya I Vzryva, Vol. 4, No. 3, 1968.
24. Davis, A., "Solid Propellants: The Combustion of Particles of Metal Ingredients," Combustion and Flame, Vol. 4, No. 12, 1963.
25. Hartman, K. O., "Combustion Kinetics of Aluminum Particles in Propellant Flames," preprint of the Western States Section Meeting, The Combustion Institute, 1971.
26. Dehority, G. L., Naval Weapons Center, "Parametric Study of Particulate Damping Based on the Model of Temkin and Dobbins," 1970, NWC-TP-5002.
27. Macek, A., Friedman, R., and Semple, J. M., "Techniques for the Study of Combustion of Beryllium and Aluminum Particles," AIAA Progress in Astronautics and Aeronautics, Vol. 15, Heterogeneous Combustion, New York, Academic Press, 1964.
28. Prentice, J. L., Naval Weapons Center, "Aluminum Droplet Combustion," 1974, NWC-TP-5569.
29. Dehority, G. L. and Price, E. W., Naval Weapons Center, "Axial Mode, Intermediate Frequency Combustion Instability in Solid Propellant Rockets," 1974, NWC-TP-5654; see also paper by Kraeutle, Mathes, and Derr in this meeting.
30. Gany, A., Caveny, L. H., and Summerfield, M., "Aluminized Solid Propellants Burning in Rocket Motor Flow Field," AIAA Journal, Vol. 16, No. 7, 1978; see also paper by Caveny in this meeting.
31. Eisel, J. L., Price, E. W., and Brown, B. G., "Pressure, Velocity and Geometry Effect on Al_2O_3 Produced during Aluminized Propellant Combustion," AIAA Journal, Vol. 13, No. 7, 1975; see also paper by Kraeutle, Mathes, and Derr in this meeting.
32. Cowles, D., and Netzer, D., "The Effect of Acceleration on Composite Propellant Combustion," Combustion Science and Technology, Vol. 3, 1971.
33. Willoughby, P. G., Crowe, C. T., and Baker, K. L., "A Photographic and Analytic Study of Composite Propellant Combustion in an Acceleration Field," Journal of Spacecraft and Rockets, Vol. 8, No. 4, 1971.

ACKNOWLEDGEMENTS

References and figures are for illustrative purposes only, as space does not allow complete coverage of past work. Illustrations are from work of R. K. Sigman, sponsored by U. S. AFOSR, and from work of the author's associates while at the Naval Weapons Center.

Fig. 1. Concentration of aluminum on the burning surface (taken from motion picture: width corresponds to 2.5 mm).
(1) Front face of sample.
(2) Back edge of burning surface.
(3) Burning agglomerate falling in front of sample.

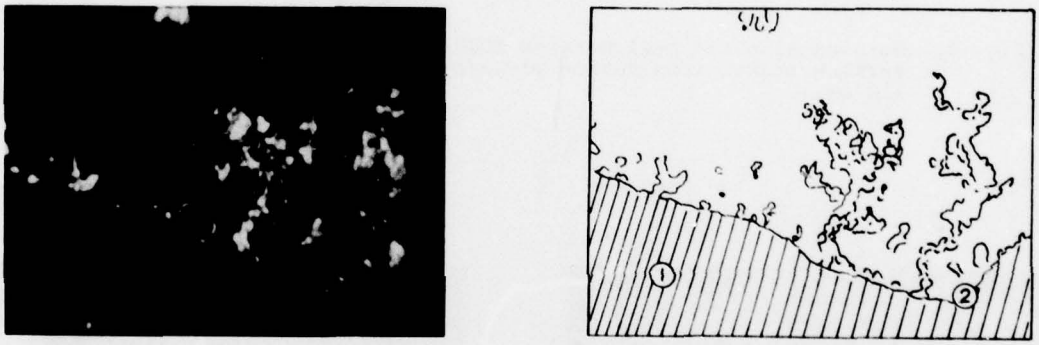

Fig. 2. Aluminum "accumulates" attached loosely to the burning surface (taken from motion picture: width corresponds to 2.5 mm).
(1) Front face of sample.
(2) Burning surface viewed edge-on.

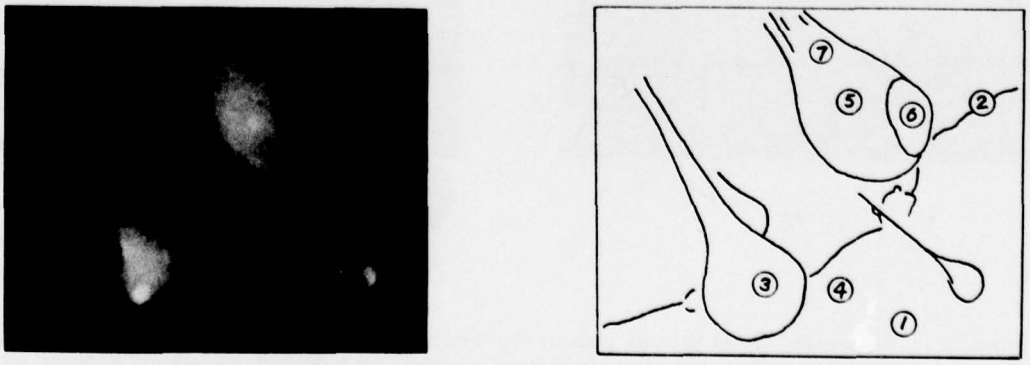

Fig. 3. Aluminum agglomerates leaving the burning surface (taken from motion picture: width of picture corresponds to 1.5 mm).
(1) Burning surface.
(2) Back edge of burning surface.
(3) Burning agglomerate, oxide not fully retracted.
(4) Shadow of droplet cast by external illumination.
(5) Burning agglomerate, with
(6) Retracted oxide lobe.
(7) Flame trail.

Fig. 4. Burning aluminum agglomerates 1000 μm above the propellant burning surface (taken from motion picture: width of picture corresponds to 5.0 mm).

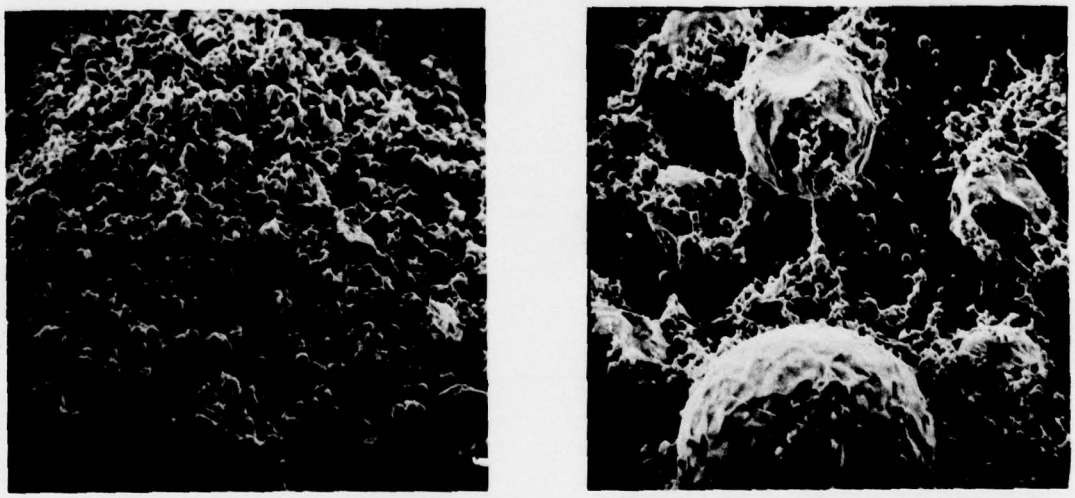

(a) (b)

Fig. 5. Response of aluminum powder to heating to 1275°K as revealed by examination after cooling (picture widths correspond to about 0.6 mm):
a) Heated in an oxygen atmosphere, showing sintering.
b) Heated in an argon atmosphere, showing agglomeration, and oxide debris.

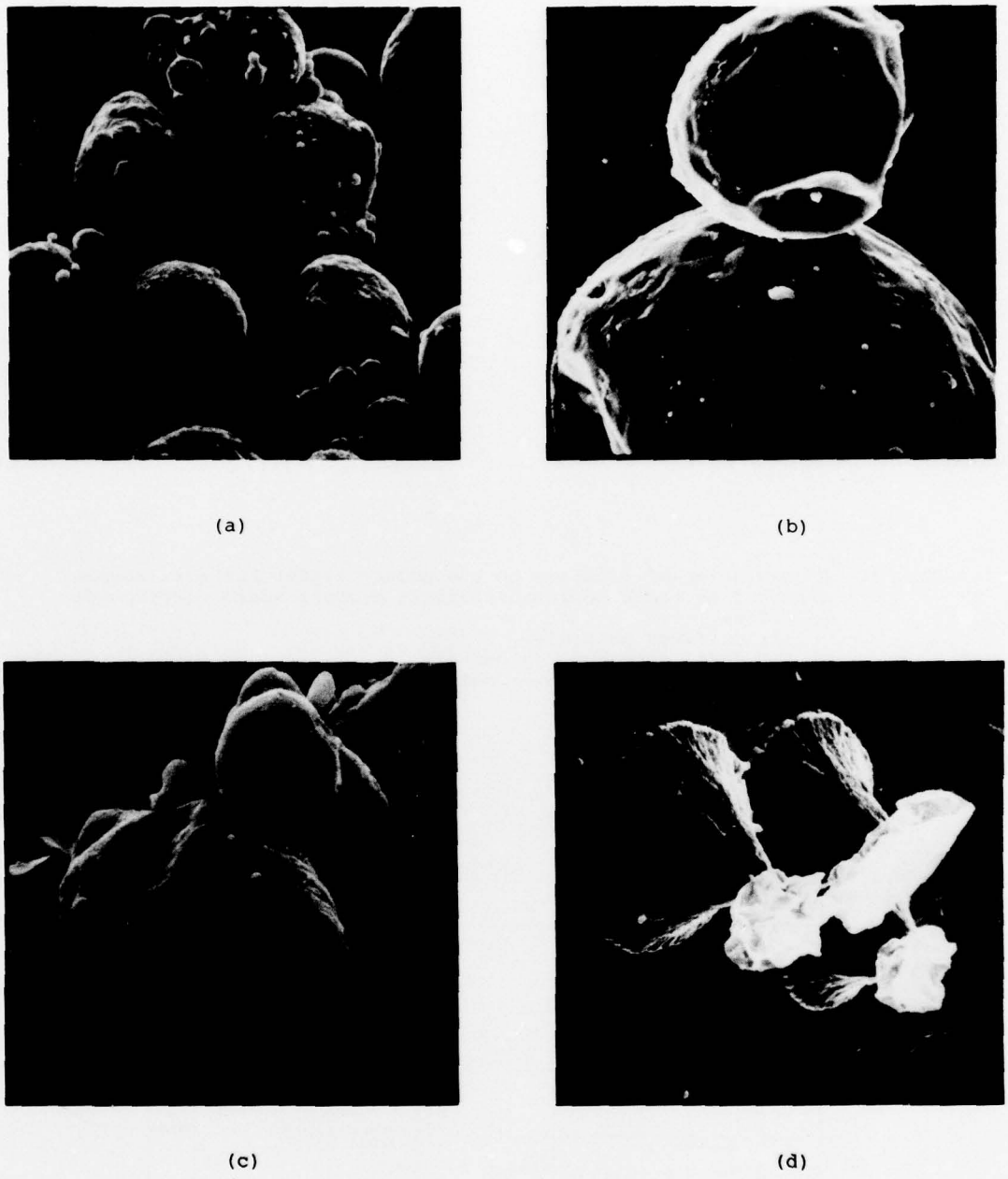

(a) (b)

(c) (d)

Fig. 6. Response of individual aluminum particles to heating, as revealed by examination after cooling (H-30 Al, average particle diameter 30 μm):
a) Typical unheated particles.
b) Wrinkled surface of particle heated to 1035°K in air.
c) Particle with "wart" of aluminum extruded through the oxide skin, illustrating expansion of the metal upon melting.
d) Particles heated on a platinum surface, illustrating importance of surface tension (which has evacuated the oxide skin: picture is right-side up).

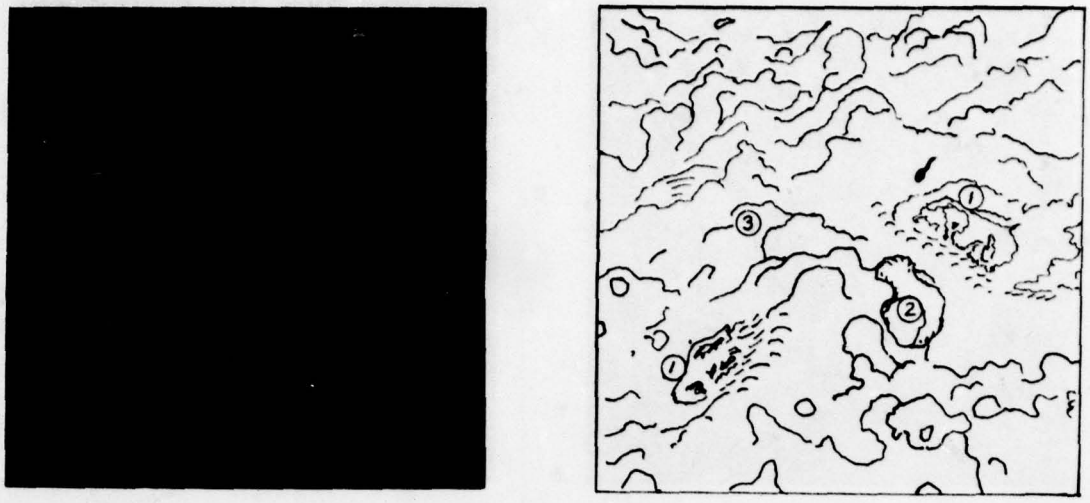

Fig. 7. Accumulation of aluminum on the molten binder surface (sample quenched by rapid depressurization: picture width corresponds to 0.5 mm).
(1) Oxidizer particle.
(2) Small aluminum agglomerate.
(3) Binder residue over edge of oxidizer particle.

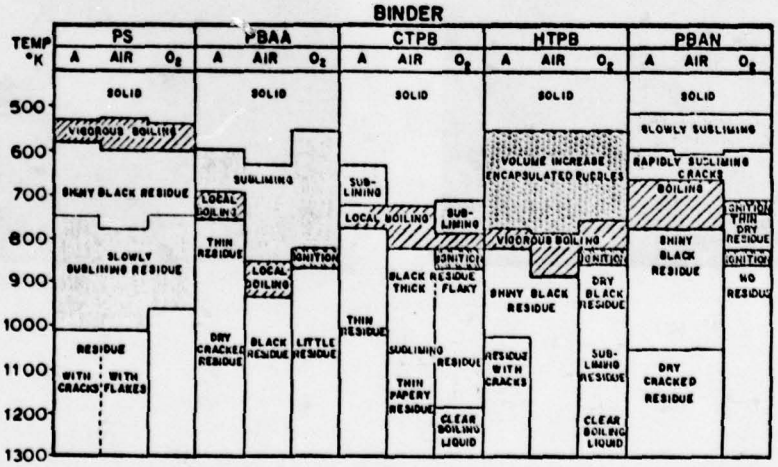

Fig. 8. Summary of observations of behavior of five binders heated in a hot stage microscope, in various atmospheres.

Fig. 9. Residue from heating a 50/50 sample of aluminum powder in CTPB binder, showing particle adhesion and agglomeration. Heating was to 1275°K in oxygen.

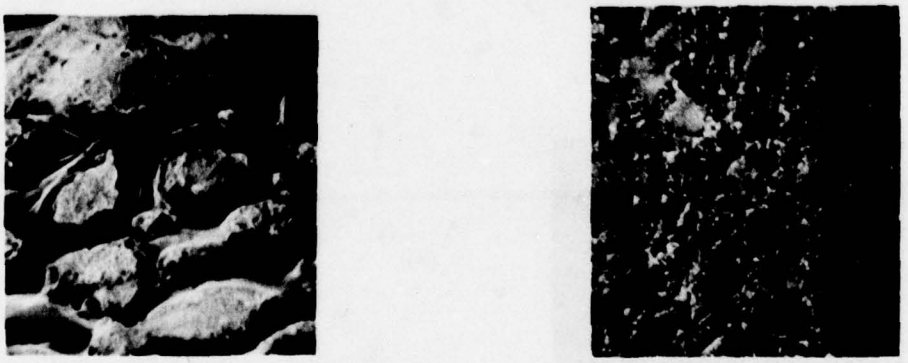

Fig. 10. Accumulation of aluminum on a burning surface in binder areas around the oxidizer particles (sample quenched by burnout on a heat-sink metal plate: picture width corresponds to 1.0 mm). Left side is a non-aluminized propellant, right side an aluminized propellant.

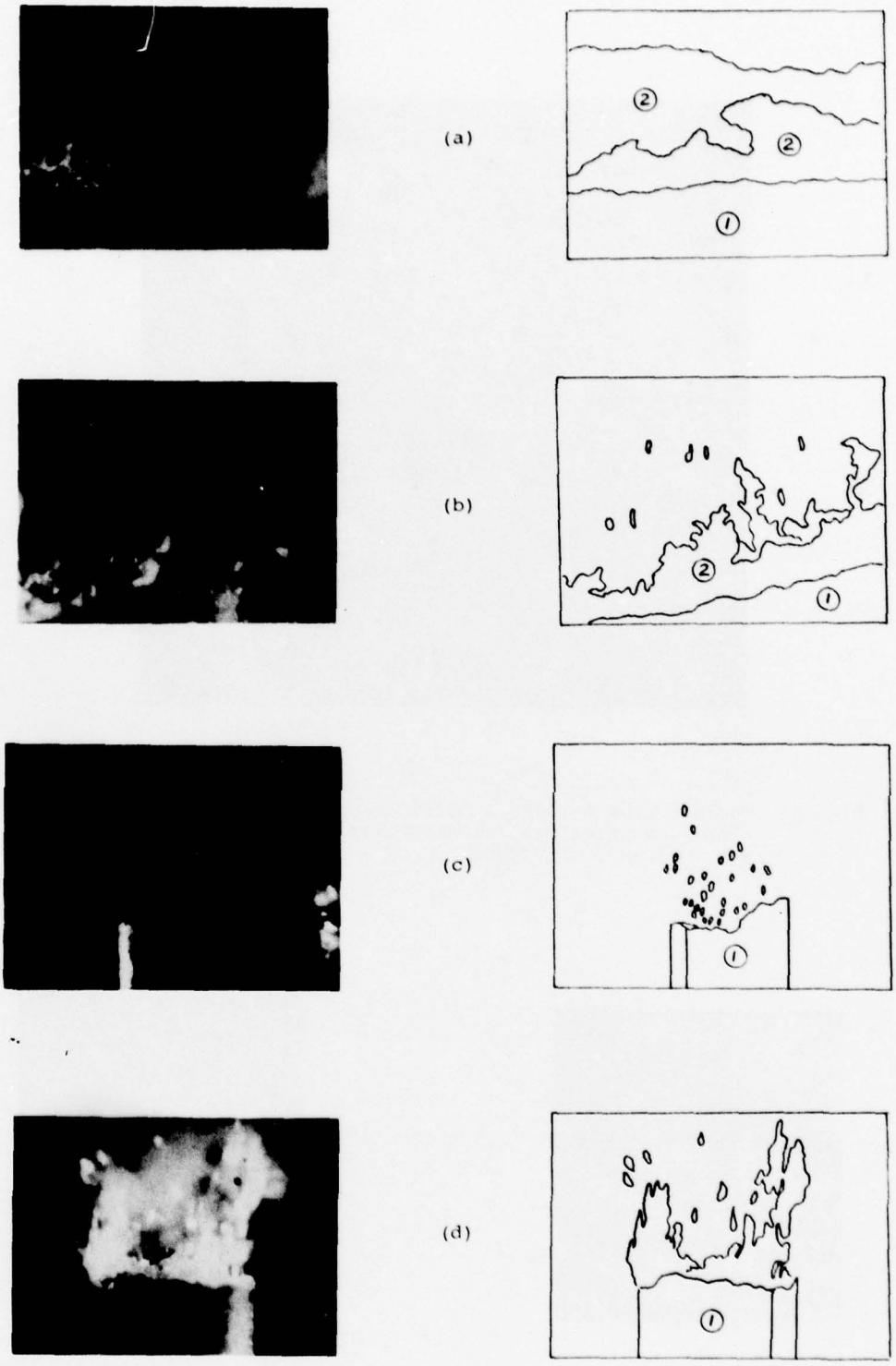

Fig. 11. Accumulation of aluminum on the burning surface of dry-pressed samples of AP-Al mixtures (85%, 100 μm AP; N_2 atmosphere, pressure 5.5 MPa; (1) indicates the front non-burning face of the sample, (2) indicates accumulated aluminum).
a) 15%, 35 μm Al, picture width is 5 mm; no aluminum combustion.
b) 15%, 35 μm Al, picture width is 5 mm; sporadic aluminum combustion.
c) 15%, 95 μm Al, picture width is 20 mm; no acculation or ignition of aluminum.
d) 11%, 35 μm Al, 4% wax, picture width is 12 mm.

Fig. 12. Inflamation of relatively large areas of accumulated aluminum under unfavorable local ignition conditions can be gradual with appreciable combustion on the surface (this is an extreme case to illustrate behavior; photography as in Fig. 1).
(1) Growing agglomerate on burning surface, oxide not retracted, but agglomerate apparently reacting.
(2) Agglomerate on the burning surface with oxide partially retracted.
(3) Inclination of burning surface.

(a) (b)

(c)

Fig. 13. Accumulates of aluminum quenched while in the process of conversion to agglomerate droplets. Obtained by combustion of an aluminized propellant in liquid nitrogen at atmospheric pressure (picture widths correspond to 11, 1.1 and 0.5 mm respectively for parts a, b, and c).

Fig. 14. Oxide shell fragment from an accumulate that was captured in liquid nitrogen before agglomerating, and then acid-etched to remove aluminum. The sample shows shells of original particles and "tubes" between particles from which connecting aluminum is removed (sample burned at atmospheric pressure: picture width corresponds to 240 μm).

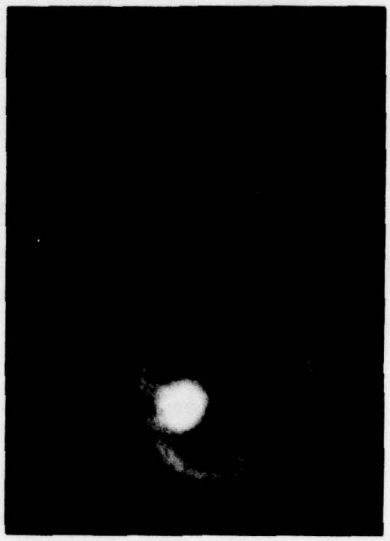

Fig. 15. Illustrations of the smoke trails developing as an agglomerate forms on or near the burning surface (taken from motion picture: width of picture corresponds to 750 μm).

Fig. 16. Aluminum agglomerates showing oxide lobes. The burning agglomerates were quenched in alcohol (atmospheric pressure, several cm from the burning surface), and then acid-etched to show internal details. The oxide shell is presumed to have formed after quench (picture width corresponds to 1.3 mm).

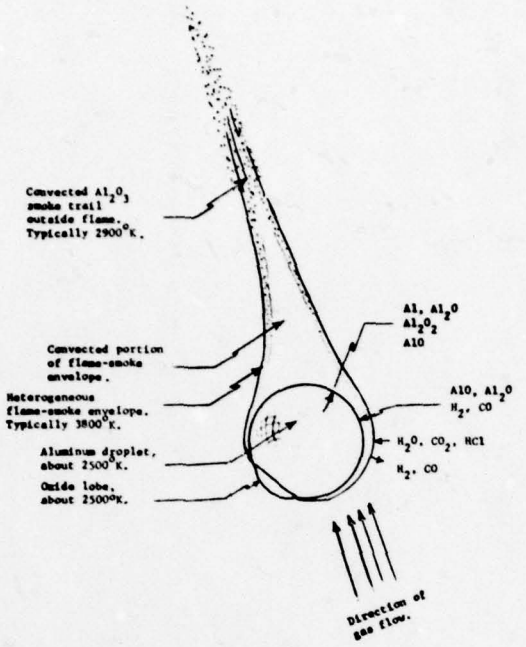

Fig. 17. Schematic representation of the burning of an aluminum agglomerate in a propellant environment (analogous to results shown in Fig. 3, 4, and 16).

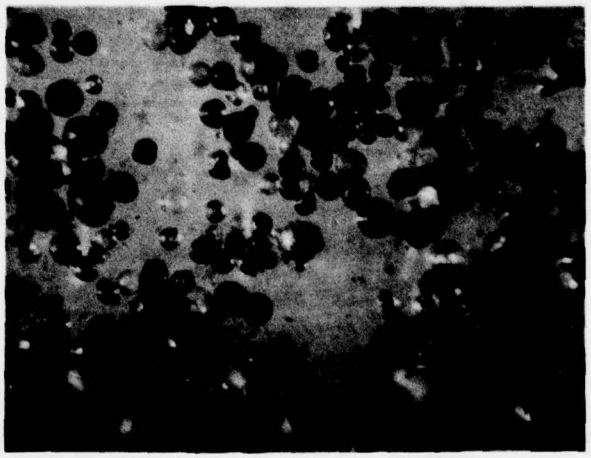

Fig. 18. Residual oxide droplets evolved from oxide lobes (Fig. 3, 16, 17) and collected by percolating propellant products through ethanol (picture width corresponds to 450 μm).

THE ROLE OF PARTICULATE DAMPING IN THE CONTROL OF COMBUSTION INSTABILITY BY ALUMINUM COMBUSTION

Karl J. Kraeutle
H. B. Mathes
Ronald L. Derr
Code 388
Aerothermochemistry Division
Naval Weapons Center
China Lake, California 93555
United States of America

SUMMARY

The combustion of aluminized propellants results in the formation of aluminum oxide particles which can attenuate acoustic oscillations caused by combustion instability. This paper summarizes methods used to minimize the risk of combustion instability in rocket motors by tailoring the oxide particle production. A brief discussion of particulate damping theory is given. Damping measurement with the T-burner and the procedure of damping calculation presently in use at the Naval Weapons Center are presented. The importance of particle size analysis for damping calculations is discussed. Particle size analysis methods are described which consider the peculiarities of combustion residues. Examples of size distributions and damping calculations are given. The results show that the theory adequately describes damping by aluminum oxide particles and that damping calculations supply information necessary for tailoring of aluminum oxide particle sizes toward increased damping.

INTRODUCTION

Aluminum used as a fuel in solid propellant formulations is known to go through a complex combustion process during propellant burning. This process results in the release of large amounts of energy and the formation of condensed phase reaction products in the form of aluminum oxide droplets. Under certain conditions, the condensed matter can attenuate acoustic oscillations related to combustion instability and prevent their build-up to dangerous amplitudes. The potential contribution of aluminum burning to the stabilization of oscillatory combustion was studied for many years. The work concentrated on the measurement of acoustic damping with specially designed combustors such as the T-burner, and on the theoretical treatment of what is known as particle damping. The connection between theory and experiment did not obtain the necessary attention for some time and the theory was applied mainly to predict trends in damping rather than absolute values. Agreement between theoretical and measured damping is essential to determine proper particle sizes for effective damping at given frequencies of instability. The verification of theory of particulate damping is, therefore, an important part of the work reported here. After the optimum particle sizes have been established, the propellant designer must formulate aluminized propellants whose particulate combustion products yield these particle sizes under given combustion conditions (e.g., pressure and burn rate). This very difficult task requires a thorough knowledge of the many aspects of aluminum combustion and their dependence on the formidable number of ingredient, propellant, and combustion parameters. Despite the impressive amount of work in the general field of aluminum combustion, information concerning the formation of particulate aluminum oxide is rather scarce and began to accumulate only in recent years. Some of our own studies in this area will be discussed in the paper.

THEORY OF PARTICLE DAMPING

The analysis of Temkin and Dobbins (Ref. 1) was used in this work as an approach to the calculation of the damping of acoustic waves by condensed phase particles. Their model assumed that the condensed phase consisted of spheres of uniform diameter. Solutions of the conservation equations were obtained by specifying the drag force for the viscous attenuation, according to Stoke's law, and the heat transfer term for the thermal attenuation. Because of the wide range of particle sizes found in combustion residues, the model had to be adapted to the more realistic case of a particle size distribution. In this modification, the conservation equations for the condensed phase were the sums of conservation equations written for each assumed particle diameter. The more complicated solution was then obtained by the technique of Temkin and Dobbins. The calculated spatial damping coefficient was converted to a temporal damping coefficient by multiplying by the damped speed of sound which was evaluated as part of the analysis. A computer program was set up for this type of calculation.

At present, the damping model developed by Culick (Ref. 2) is employed. He combined gas and solid conservation equations and thus derived equations which involved properties of the gas-solid mixture. In this new form, the theory can be used to calculate damping for a particle cloud which has an aribtrary particle size distribution. Culick's damping equation for a particle distribution composed of n discrete diameters may be expressed as

$$\alpha_p = -1/2 \frac{\bar{C}_m}{1 + \bar{C}_m} \sum_{i=1}^{n} \left(\frac{\omega^2 \tau_{di}}{1 + (\omega \tau_{di})^2} + (\bar{\gamma} - 1) \frac{C}{\bar{C}_p} \frac{\omega^2 \tau_{ti}}{1 + (\omega \tau_{ti})^2} \right) X_i \qquad (1)$$

α_p	Damping of particles with arbitrary size distribution
$\bar{C}_m$	Mass ratio of entire condensed phase to gas per unit volume of mixture
ω	Angular frequency
$\tau_{di} = 2R_i^2 \rho_s / 9\mu$	Dynamic relaxation time of particles with radius, R_i, and density, ρ_s
$\tau_{ti} = 3CPr\tau_{di} / 2C_p$	Thermal relaxation time of particles with radius, R_i, and specific heat, C
$\bar{\gamma}$	Ratio of specific heats of gas/condensed phase mixture
C	Specific heat of condensed phase
$\bar{C}_p$	Specific heat of gas/condensed phase mixture
X_i	Mass fraction of particles with radius, R_i

In this equation, τ_{di} and τ_{ti} are evaluated for the ith particle diameter. $\bar{\gamma}$ and $\bar{C}_p$ are evaluated for the total two-phase system. A computer program was written to calculate particle damping by means of this equation. It is advantageous to examine the sensitivity of damping to particle size and frequency of oscillation before the equation is applied to experiments discussed in this paper. Figure 1 shows the damping rates of spherical aluminum oxide particles which have a log-normal size distribution as a function of mean diameter, of width σ of distribution, and of frequency. The concentration of particles was held constant. The curves indicate the particle sizes for maximum damping at various frequencies and the approximate size range (≈1-50 μm) in which most of the damping is contributed. Therefore, particularly careful analysis of combustion residue is necessary in this size range in order to prevent serious errors in damping calculations.

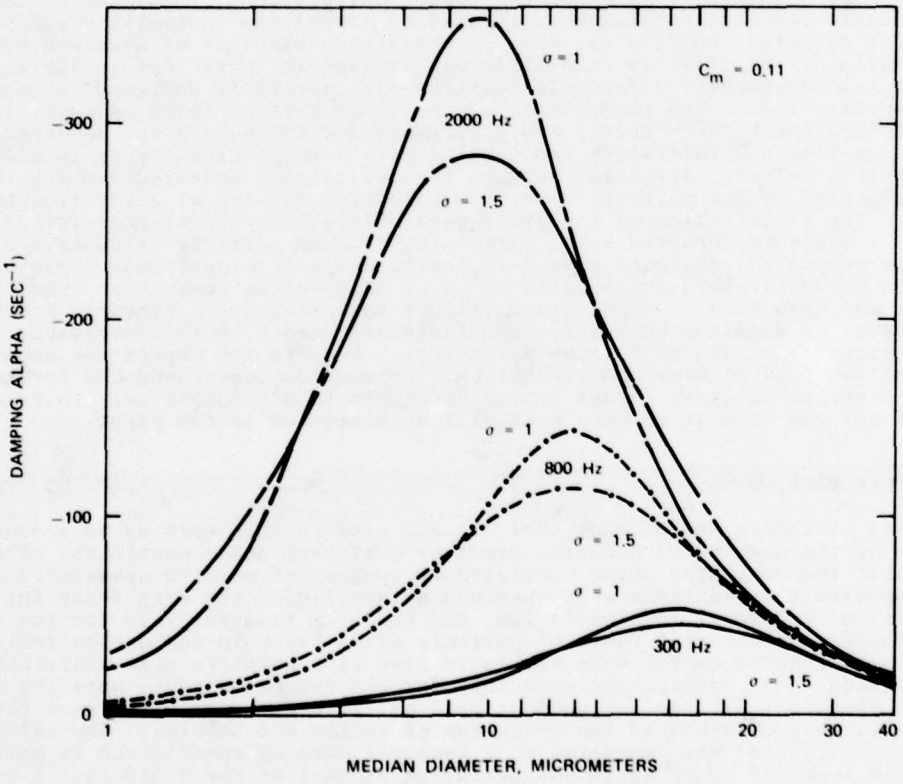

Figure 1. Damping Rates of Spherical Aluminum Oxide Particles With Log-Normal Mass Distributions as Function of Median Diameter and Width σ (Standard Deviation) of Distributions. Concentration C_m = 0.11 of particles was held constant.

EXPERIMENTS

The experiments were conducted in three steps: propellant procurement, propellant testing in a variety of combustors, and data reduction. Propellants used in the tests were composite modified double-base and composite formulations. The combustion experi-

ments were made in different burners as shown in Figure 2. Window bomb firings were particularly useful to examine qualitative aspects of combustion by high-speed photography and by residue collection and analysis. Much information on aluminum agglomeration, for example, was obtained from these tests. T-burner firings were employed primarily to measure the damping coefficients of the propellants. Frequently, residue collections were conducted after T-burner runs to supply the material for size analysis. These size data were then used to calculate damping rates or to study the effect of pipe length and gravity on particle fall-out and particle size characteristics (Ref. 3). The remaining two combustors were designed as particle collectors to improve the low collection efficiencies after T-burner tests. The pipe burner usually showed 95-100% residue collection as compared to 80-90% of the tank collector. Particle collection was accomplished by rinsing and brushing the burner walls with ethanol. After removal of the ethanol and vacuum drying, a sample was ready for size analysis. Accurate measurement of particle size distributions was critical for the entire process. Since it had to be adapted to the type of residues at hand, a detailed description of the methods is given (Ref. 4).

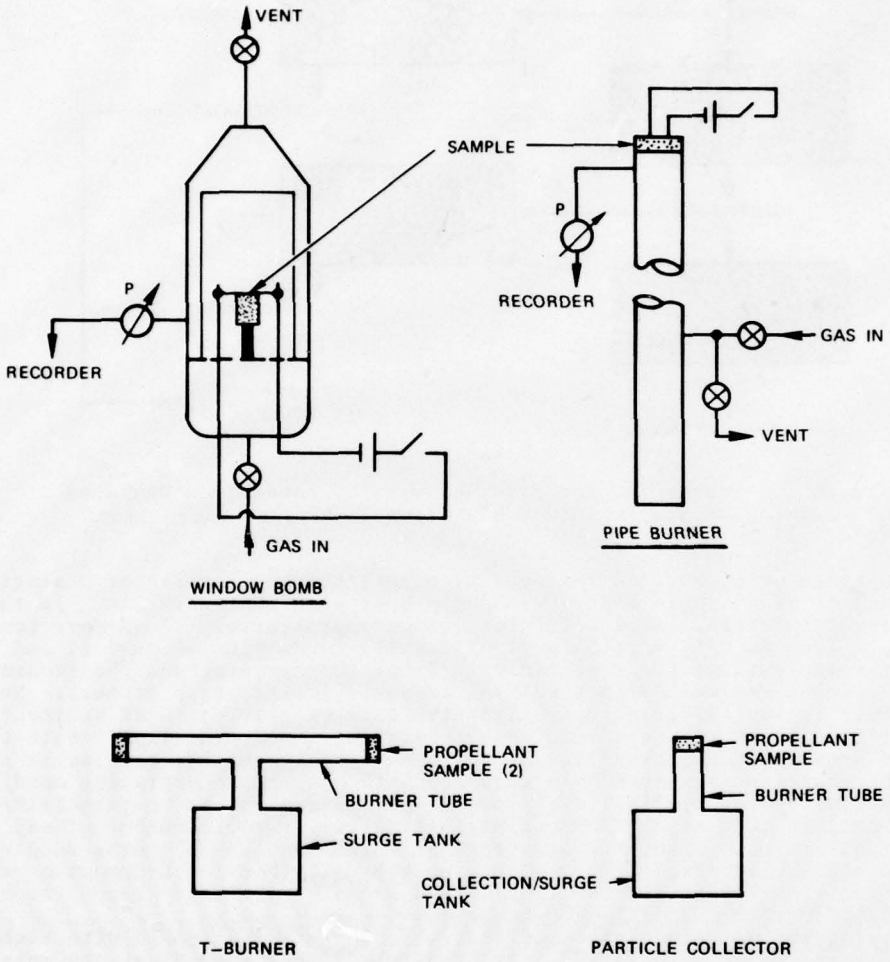

Figure 2. Types of Burners Used for the Combustion of Propellants and for the Collection of Combustion Residues.

PARTICLE SIZE ANALYSIS

Size distributions of residues from the combustion of aluminized propellants cover a range of at least four orders of magnitude. A typical sample contains not only smoke particles with diameters well below 1 μm, but also large particles of more than 100 μm which develop mainly by condensed phase oxidation. Frequently, measured size data exhibit certain types of distributions like normal or log-normal distributions. This is not the case with the combustion residues in question because the activity of more than one combustion mechanism leads to composite size distributions which only rarely show one of the common types. Thus, size analysis has to cover the whole size range in small enough increments to register the size pecularities of a given sample. The sizes of the most effective dampers often fall into the transition region between size populations as will be shown later. This region has to be analyzed carefully in order to make meaningful damping calculations. Finally, the overwhelming number of smoke particles and the importance of the much fewer larger particles for damping led to the use of the following size analysis procedure (Figure 3).

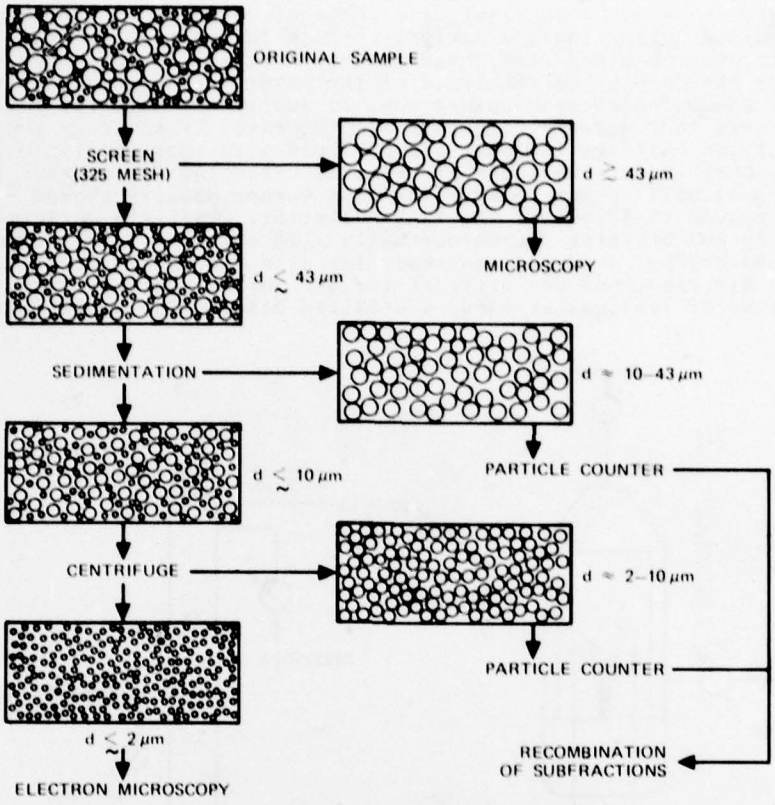

Figure 3. Scheme for the Size Analysis of Combustion Residues by Division of Sample Into Subfractions. (Figure taken from Ref. 4.)

The size range of combustion residues precludes the application of a single size analysis method or of a single method without proper sample preparation. In the first step of sample preparation, large particles (above approximately 43 μm) are removed by wet screening. They do not contribute significantly to damping (Figure 1) and cause problems in the analysis of finer particles. Prior to screening and the separations that follow, samples are well dispersed by ultrasonic treatment in ethanol. Next, the remaining sample is subdivided at approximately 10 μm by gravitational sedimentation. Finally, particles below 1 μm are removed by centrifugal sedimentation. Both types of sedimentation are based on Stokes' law and care must be taken that the law is applicable (Ref. 5). The equation may serve as a good guide to choose the operating conditions for the sedimentations, however, final experimental parameters should be established for the equipment at hand by test separations, especially with regard to number of sedimentations per subdivision. Also, the diameters at which samples are being subdivided should not be considered fixed. They should be kept flexible to accommodate requirements of the individual particle counting method and of exploratory type size analyses.

After drying and weighing, the size analysis proper is performed with each of the subfractions. For damping calculations, it usually suffices to analyze the intermediate size fractions from about 1 to 43 μm. This is accomplished at the Naval Weapons Center with a commercial high-speed counter. The method is based on the change of electrical current on passage of a particle through an orifice. The instrument counts individual particles at a high rate and, by virtue of calibration, associates each current pulse with a particle size. Since combustion residues are spherical, the true diameters are recorded. However, care must be taken to thoroughly disperse the particles in the carrier liquid and to keep the particle concentration low enough to prevent simultaneous passage of particles through the sensing orifice. The concentration requirement can jeopardize the counting of large particles if the distribution is wide (many small particles versus few large particles). Also, the counter memory may be saturated by the count of many small particles before enough large particles have been registered. The above described sample preparation by subdivision solved these problems successfully. Between 50,000 and 100,000 particles of each subfraction are usually counted. Numerical data can then be printed out in the form of cumulative number or mass distributions. Subsequently, the mass distributions of the individual subfractions are recombined by computer into a total mass distribution from which the computer takes data to calculate damping according to Eq. (1). Applying only the first part of the computer program, numerical or graphical presentation of complete size analyses may be obtained. In the following section of the paper, results are presented which reflect on the validity of the theory of particle damping followed by a discussion of possibilities to tailor the damping behavior of an aluminized propellant.

RESULTS AND DISCUSSION

The control of combustion instability by tailoring aluminum combustion depends on the validity of the theory in the selection of proper particle sizes and on the ability to produce aluminum oxide particles which have the selected diameters.

I. Validity of the Damping Theory

The validity of the damping theory was tested by comparison of calculated and measured damping rates (Ref. 6 and 7). Agreement between both was considered sufficient to apply the theory to particle damping studies and to unstable motors. The measured damping rates were obtained from T-burner firings of a variety of propellants. The damping rate calculations were made according to Eq. (1) with measured size data as input. Strictly speaking, the calculations were not purely theoretical since they contained particle size analysis as an experimental element. This situation is not expected to change in the near future because of the great difficulties in the theoretical treatment of the size characteristics of aluminum combustion products. The results of three pairs of propellants are presented. Propellants A and B of the first pair contained aluminum for which only the yield, but not the size distribution, of residues could be estimated. Both were of the same composition except for the particle size of the ingredient aluminum (average size 7.7 μm for Propellant A, 17 μm for Propellant B).

Propellants C and D were prepared to gain control of the size distribution and concentration of particles. They contained 5% (Propellant C) and 10% (Propellant D) nonspherical abrasive aluminum oxide. During combustion, the nonspherical particles became spherical and agglomerated (Figure 4). Size analysis of postfiring particles was necessary in this case to obtain size data for the damping calculations. The last two propellants were mixed with 5% of carefully prepared spherical aluminum oxide with mean diameters of 6.8 μm (Propellant E) and 14.8 μm (Propellant F). The size distributions of the particles are shown in Figures 5 and 6. The mean diameters of the narrow size distributions were chosen to obtain maximum damping at 300 and 1800 Hz (low and high frequencies of T-burner testing). Agglomeration again increased the size of ingredient particles during firing (Figures 5 and 6) and consequently reduced the difference between damping at 300 Hz and 1800 Hz. It is interesting to note that the increase of agglomeration with decrease of particle size is also observed for the preignition agglomeration of aluminum particles (see section II.A).

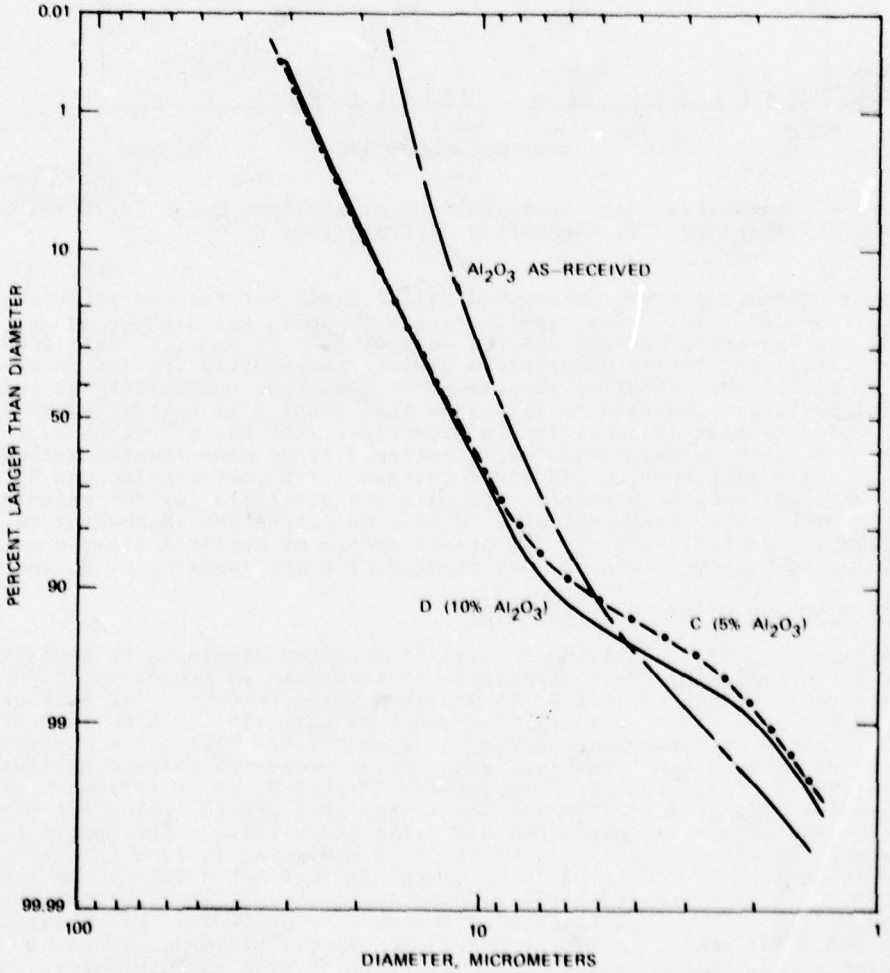

Figure 4. Cumulative Mass Distributions of Aluminum Oxide Particles Before (— · —) and After Firing of Propellants C (-.-.-) and D (—).

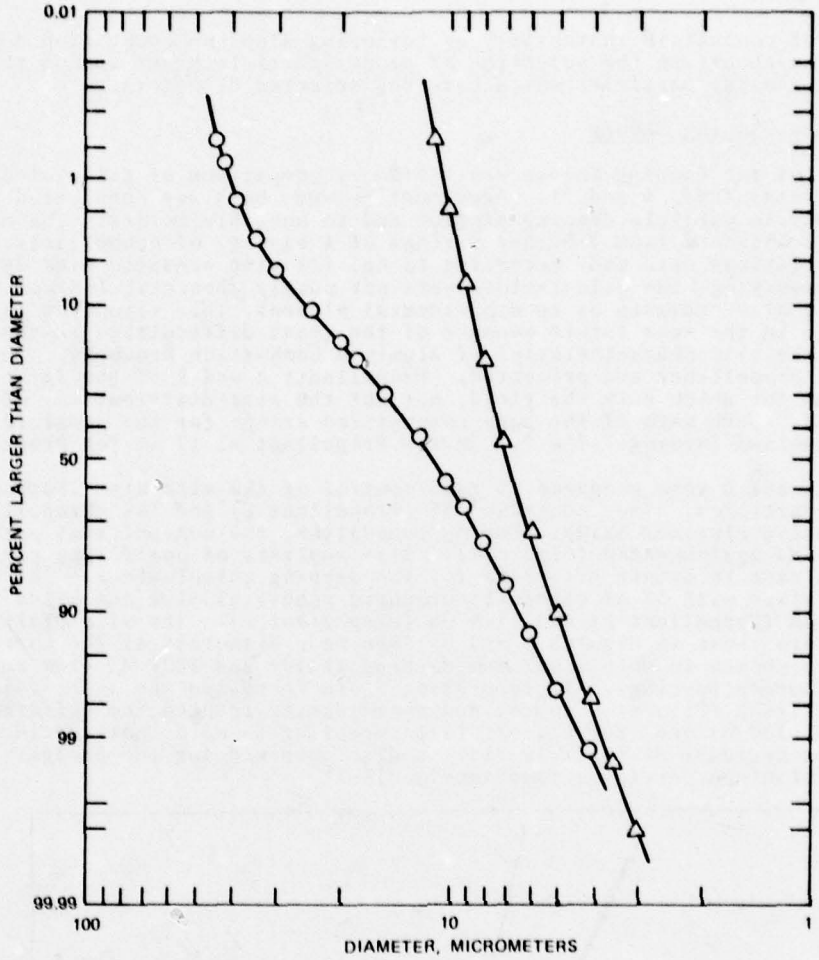

Figure 5. Cumulative Mass Distributions of Aluminum Oxide Particles Before (Δ) and After (o) Combustion of Propellant E.

The results of damping measurements and calculations for the six propellants are shown in Table 1 and Figure 7. The line in Figure 7, which has a slope of one, indicates that the agreement between the two sets of data is astonishingly good. These results fully support the theory of particle damping and justify its use in predicting the particle sizes for the effective abatement of combustion instability at known frequencies of instability. The results also show that damping is approximately proportional to the concentration of particles in accordance with Eq. (1) if $\bar{C}_m << 1$ (Propellants C and D). T-burner measurements were confirmed as an experimental method sensitive to particle size distribution and their changes. T-burner results can be predicted by the theory only if relevant particle size data are available for the calculations. This is important when refractory material is used as propellant ingredient to generate the cloud of damping particles, since the proper choice of particle size is not possible without knowledge of agglomeration as demonstrated by Propellants C, D, E, and F.

II. Control of Aluminum Oxide Particle Size

After confirmation of the damping theory, it appeared promising to investigate practicable ways to tailor particle damping by intervention in processes which control the transition from aluminum ingredient to aluminum oxide product. The goal of such an effort would be the generation of a maximum number of particles with optimum size for damping at a predicted or measured frequency of instability. This is a formidable task in view of complex preignition, ignition, and burning processes which constitute aluminum combustion and the large number of parameters (Figure 8) which influence aluminum combustion behavior. It is therefore not surprising that general rules for the size characteristics of aluminum oxide residue are still unavailable. The apparent shortcoming is somewhat balanced by the possibilities of modifying residue formation (Figure 8). Measures to achieve desirable particle sizes are best taken during the first stages of propellant design. The prospects for success are much smaller if one tries to improve existing propellant systems which have instability problems. Modifications of aluminum combustion may change important propellant specifications such as burn rate and specific impulse which, in most cases, is undesirable or even unacceptable.

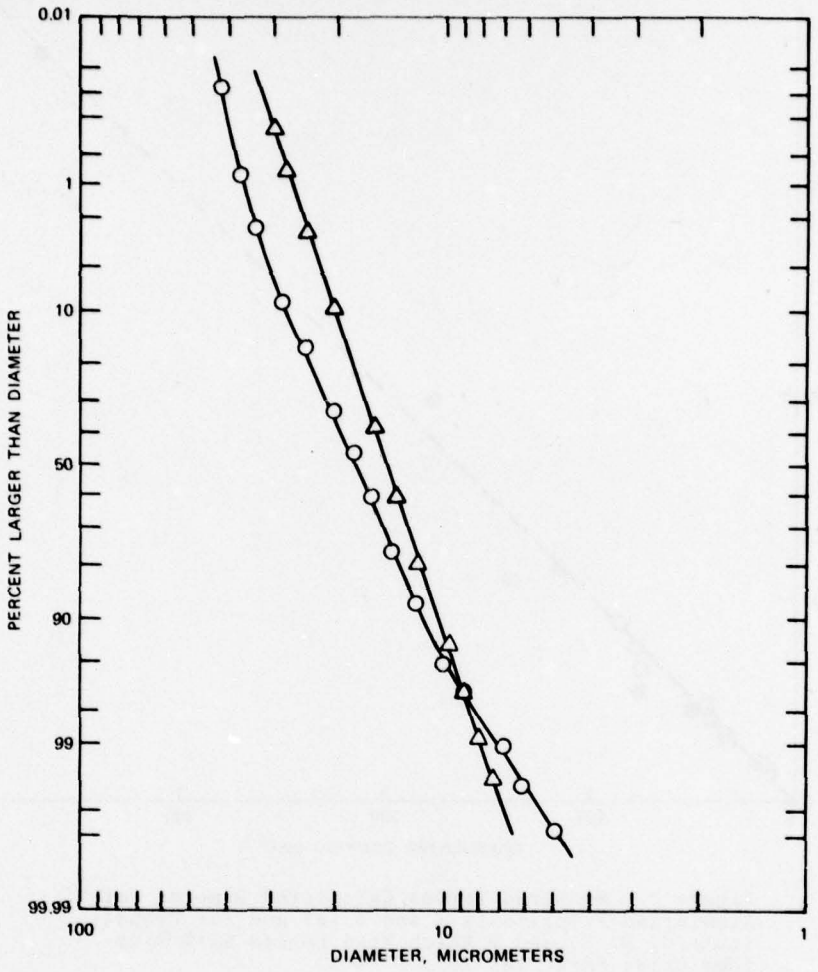

Figure 6. Cumulative Mass Distributions of Aluminum Oxide Particles Before (Δ) and After (o) Combustion of Propellant F.

TABLE I. Measured and Calculated Damping Alphas

Propellant	Frequency, Hz	Damping α (sec^{-1})	
		Measured	Calculated
A	291	-46	-49
	641	-115	-116
	1927	-364	-367
B	322	-55	-76
	802	-196	-176
	2037	-396	-384
C	268	-19	-15
	696	-40	-41
	1814	-64	-75
D	283	-33	-34
	732	-88	-85
	1824	-109	-139
E	255	-15	-13
	724	-48	-42
	1782	-76	-77
F	266	-20	-18
	676	-30	-32
	1735	-44	-41

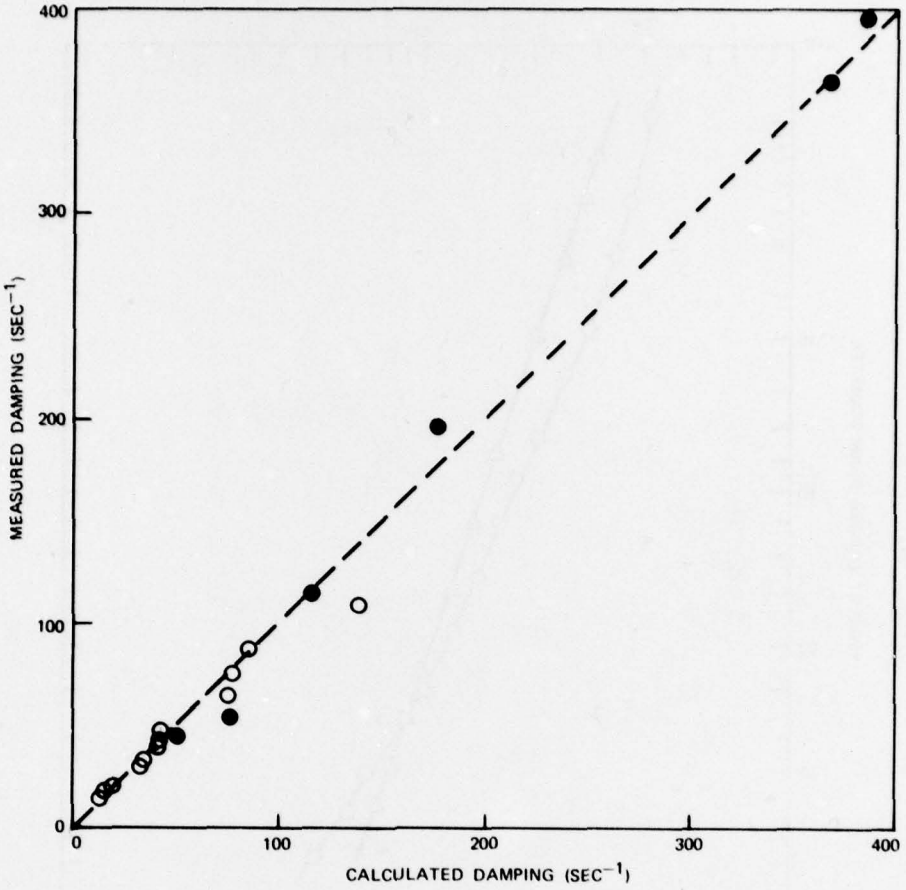

Figure 7. Measured Versus Calculated Damping for Aluminized Propellants A and B (●) and for Propellants C, D, E, and F Which Were Loaded With Aluminum Oxide Particles (o).

Generally, two processes are considered for aluminum oxide formation, namely, oxidation in the condensed phase which adds to oxide present on as-received aluminum, and vapor phase oxidation. The first process leads to coarse residue whereas the second mechanism is responsible for fine smoke as outlined in Figure 9. This results in the usual bimodality of residue size distributions. Shedding and collision of particles which have not obtained much attention to date should also be mentioned here because of their possible influence on the overall residue size characteristics. In the following, the influence of some of the parameters listed in Figure 8 on the process of aluminum combustion and oxide particle formation as shown in Figure 9 will be discussed and related to particle damping where data are available.

A. Effect of Aluminum Particle Size on Residue Formation. Propellant grade aluminum powder is available in a variety of sizes which makes it relatively easy to use aluminum particle size as a propellant parameter. The appreciable influence of aluminum agglomeration, residue formation, and damping characteristics is clearly demonstrated by data in Figures 10 and 11 and Tables I and II. The fine aluminum of Propellant A agglomerated heavily (Figure 10), and produced more coarse and fine residue than Propellant B which contained coarse aluminum (Table II). More important, Propellant B contributed more residue in the size range of effective damping (Figure 11) and consequently it exhibited a better damping performance (Table I) than Propellant A. It follows that aluminum particle size is indeed a useful parameter for tailoring damping.

B. Effect of Aluminum and Oxidizer Concentration on Residue Formation. Three experimental propellants A-217, A-218, and A-219 were mixed to study the effect of aluminum concentration on residue formation (Ref. 8). The propellants were formulated to give good aluminum combustion under laboratory conditions and a low degree of aluminum agglomeration. Unfortunately, variations of ingredient concentrations always affect more than one ingredient which may cause problems of interpretation. The aluminum and oxidizer concentrations were 20% and 55% in A-217, 10% and 65% in A-218, and 5% and 70% in A-219. The mean diameter of the aluminum was 40 μm. Residues from the propellants were collected and analyzed after firings in the pipe burner (Figure 2). The results are shown in Figure 12. Despite reduced agglomeration at low aluminum loading, a surprising increase of coarse residue with decrease of aluminum concentration was found. An explanation may be offered based on high-speed photography which indicated high flame density and temperature at high aluminum concentration. Hot flames seem to favor evaporation or boiling-off of aluminum at the expense of chemical reaction in the condensed

phase. Lowering of flame temperature and density would make the condensed phase reaction more competitive and increase the share of course residue. In the limit, negligible evaporation would therefore lead to mostly coarse residue (as in hot stage tests or similar experiments). Increased damping by virtue of a more favorable particle size distribution in the case of A-219 has to be judged against a relatively low damping because of small $\bar{C}_m$ in Eq. (1). Additional tests will have to show if properties of the non-aluminized flame or of the aluminum flame have more effect on residue particle sizes and hence on damping.

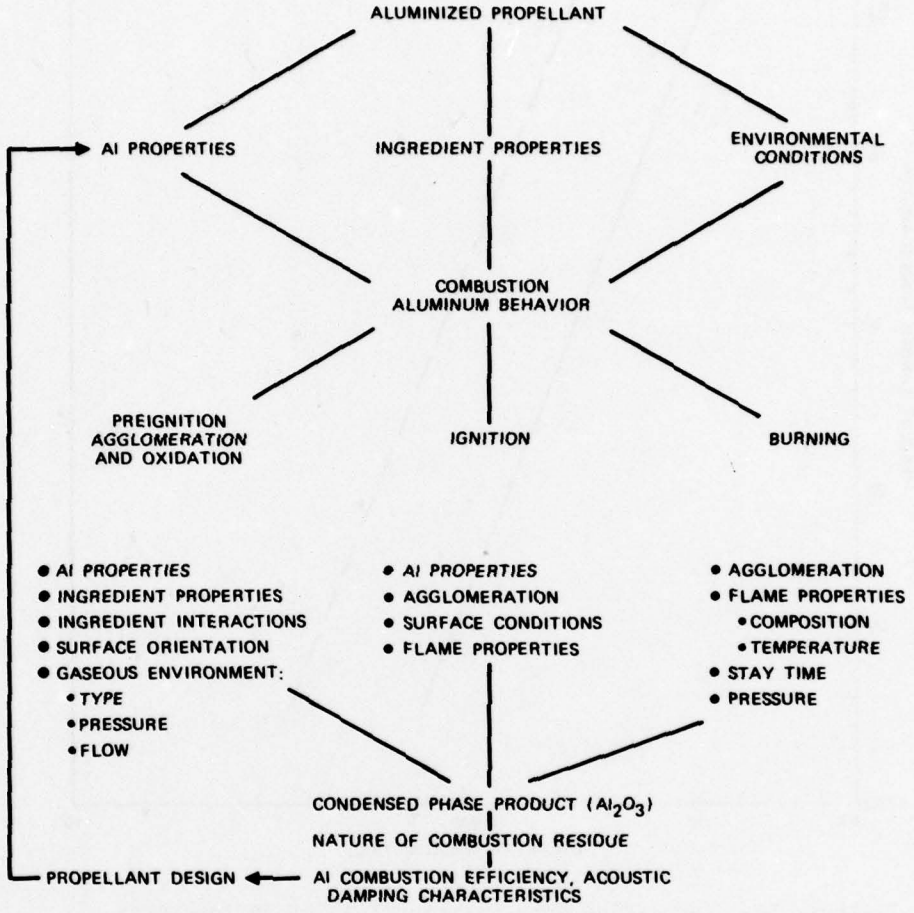

Figure 8. Scheme for the Tailoring of Damping by Modification of Aluminum Combustion.

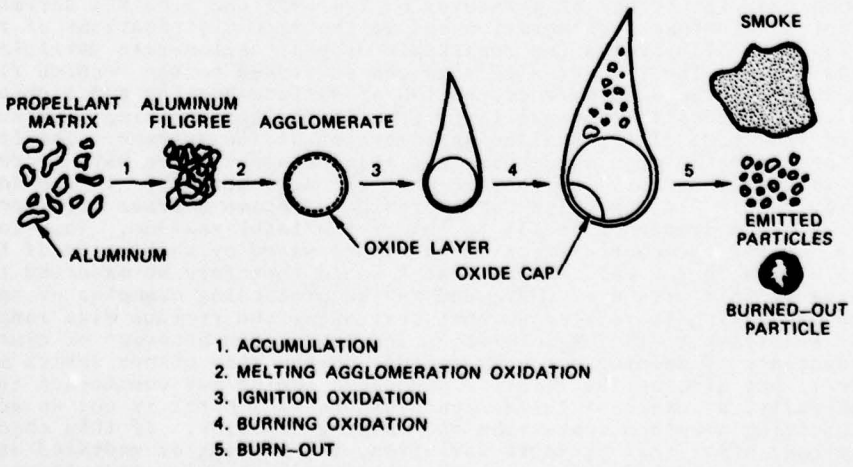

Figure 9. Sequence of Important Processes of Aluminum Combustion and Residue Formation.

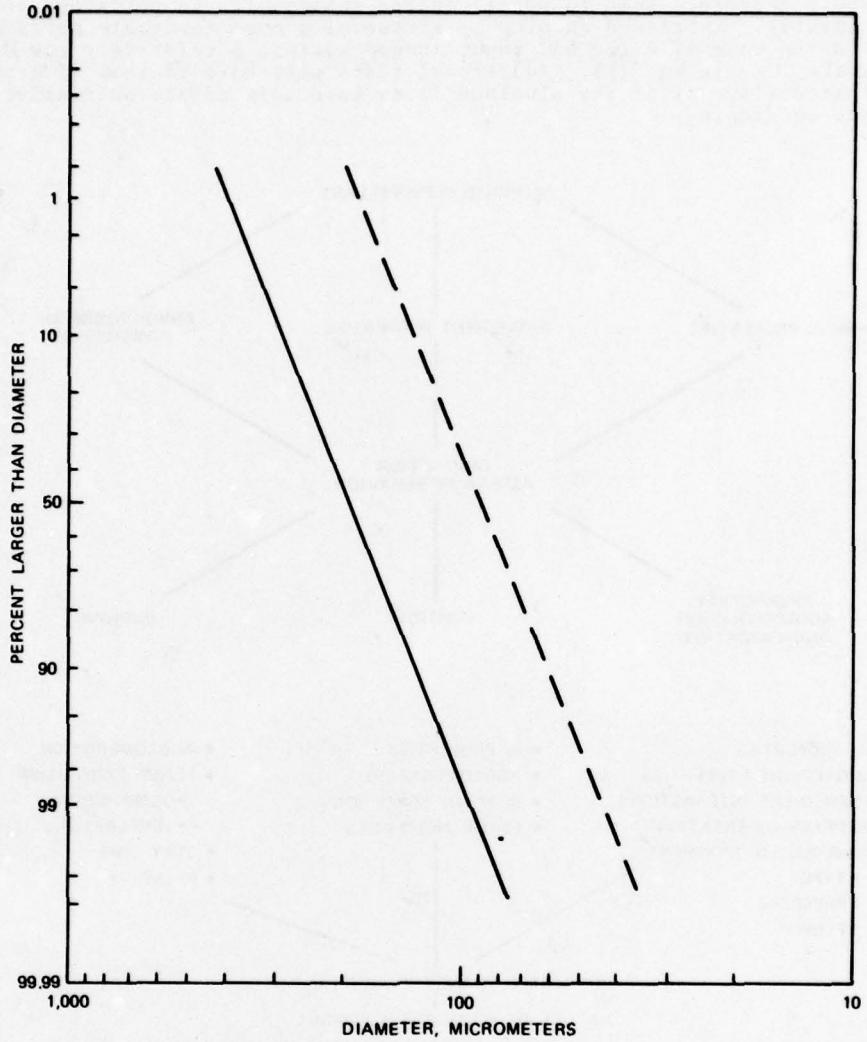

Figure 10. Cumulative Mass Distributions of Agglomerates Which Have Been Collected After Burning Propellant A (——) and Propellant B (– – –) in Nitrogen at a Pressure of 2.5 MPa. Firings were made in a window bomb.

C. Effect of Pressure on Residue Formation. The combustion of Propellant A in the window bomb and pipe burner at pressures of 1.47 MPa and 5.61 MPa serves to show the pressure effect on aluminum agglomeration and on the size distributions of residues (Ref. 9). Figure 13 illustrates the remarkable drop of agglomerate particle size with increase of pressure. The reduction in size can be linked to the reduced flame stand-off from the surface, the ensuing acceleration of surface heating and aluminum ignition, the decrease in volume of the thermal layer from which agglomerating aluminum originates, and to reduced stay-time of the smaller agglomerates at the surface. The large particles of residues from the pipe burner firings also became smaller with increasing pressure (Figure 14) and thus followed the trend of the agglomerates. In the important size range of approximately 2-43 μm, pipe burner residues became coarser with pressure (Figure 15) and the yield dropped from 23% to 19% of the total residue. This loss in yield and a similar one for the coarse fraction was compensated by an 8% gain of the smoke fraction at 5.61 MPa ($d \leq 2$ μm). Propellant A would therefore be expected to have reduced damping at this pressure. Here and in the preceeding examples of sections A and B, the change of damping is related to that section of the residue size range ($d \geq 2$ μm) which is most sensitive to the agglomeration and combustion behavior of aluminum. The increase or decrease of damping not only depends on the size change (which may have a positive effect) but also on the relative abundance (which may counteract the size effect). Generally, a change of the design pressure of a motor is not an acceptable method for improving aluminum combustion and damping behavior. If this objective is pursued by methods other than pressure variation, the testing of modified damping should be conducted at the specified working pressure of the particular propellant.

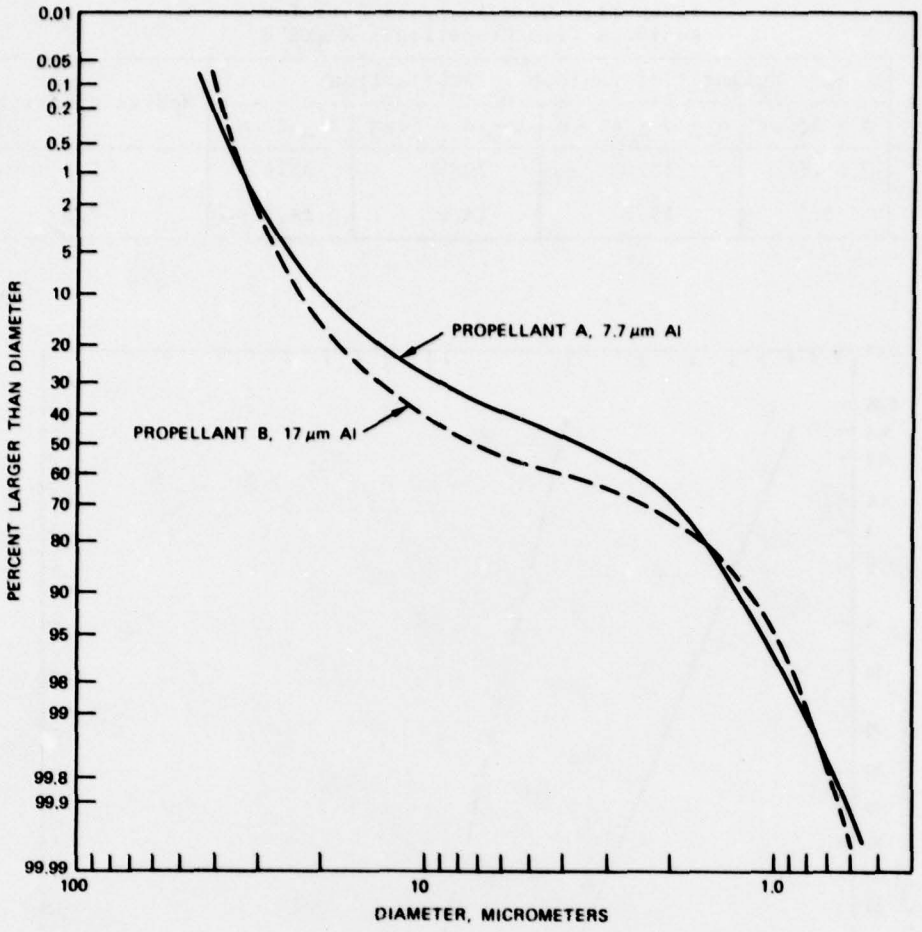

Figure 11. Cumulative Mass Distributions of Residues Which Have Been Collected After T-Burner Firings of Propellant A (——) and Propellant B (– – –).

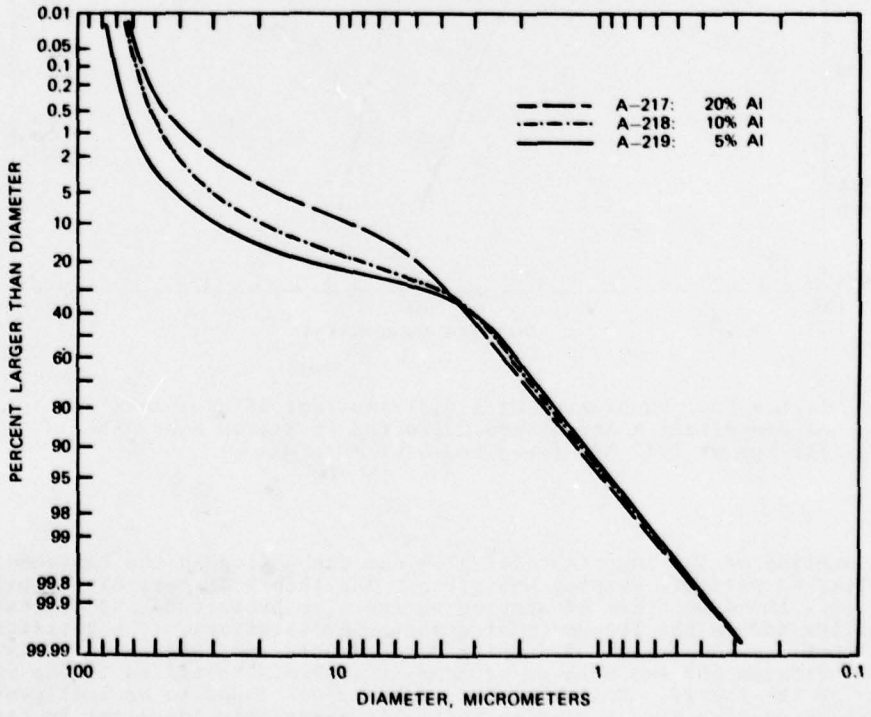

Figure 12. Cumulative Mass Distributions of Residues from Propellants A-217, A-218, and A-219. Firings were made in pipe burner at a pressure of 2.5 MPa Argon.

TABLE II. Size Analysis Data for Residues from Propellants A and B

Propellant	Weight % of residue in subfraction				Median diameter, μm
	$d \geq 43$ μm	$6 \leq d \leq 43$ μm	$2 \leq d \leq 6$ μm	$d \leq 2$ μm	
A	11.1	33.0	20.9	35.0	3.7
B	5.5	55.5	14.9	24.1	7.5

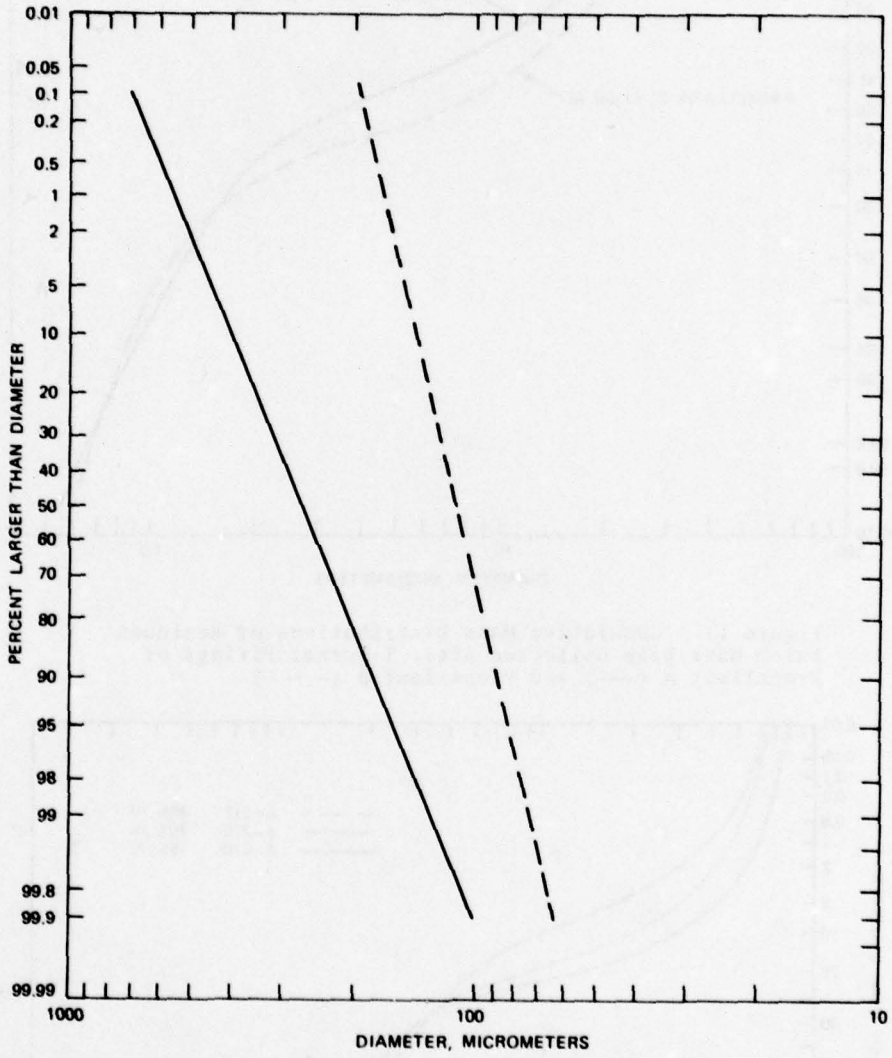

Figure 13. Cumulative Mass Distributions of Agglomerates of Propellant A Which Were Collected in Window Bomb After Firings at 1.47 MPa (——) and 5.61 MPa (– – –).

SUMMARY

A short outline of the importance of aluminum combustion in the abatement of combustion instability by particle damping was given. The theory of particle damping was discussed to show the dependence of damping on the size properties and concentration of damping particles and on the frequency of acoustic oscillations. The verification of the damping theory by comparison of damping measurements and calculations was described. Good agreement between the two methods of damping analysis testified to the validity and applicability of the theory. Reliable size analysis was found to be indispensible for the assessment of damping by calculation. This is especially important in cases where it is necessary or advantageous to employ damping calculation instead of damping measurement. The procedure of size analysis was presented in detail with consideration of the size characteristics of combustion residues.

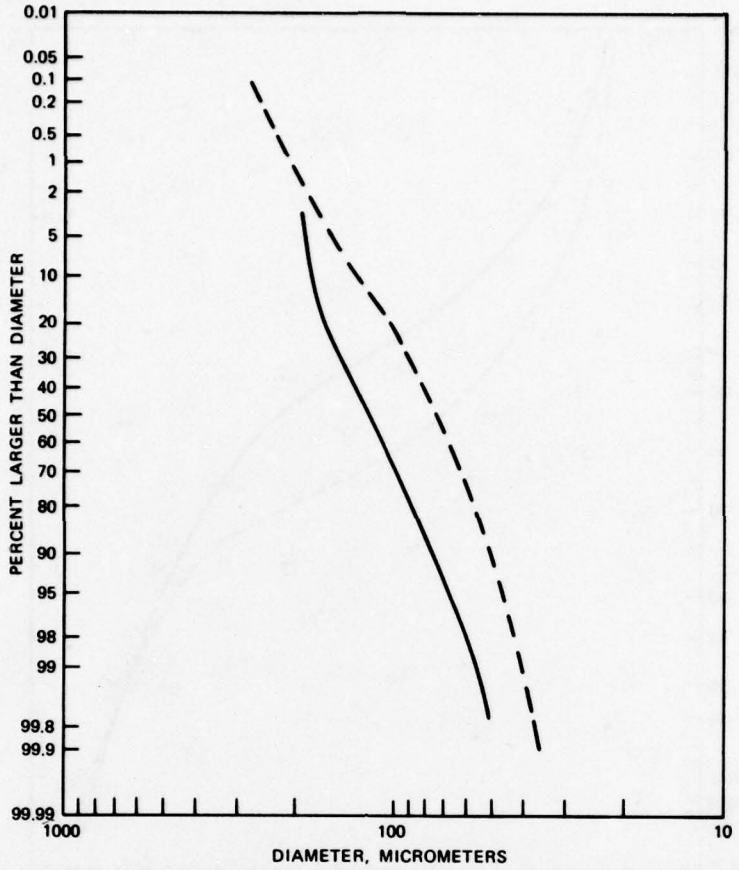

Figure 14. Cumulative Mass Distributions of Residues With Diameters d $\geq$ 43 μm of Propellant A. Firings Were Made in a Pipe Burner at Pressures of 1.47 MPa (——) and 5.61 MPa (– – –).

The full benefit of particle damping is realized if aluminum combustion can be directed towards the production of residue particles of proper size. Widely applicable and effective methods to achieve this goal are not available at present because of the many parameters which control aluminum combustion and residue formation. The effect of some of the parameters on the size properties of residues was shown. The low abundance of residue in the transition region between fine smoke and coarse residue became evident. The smoke forming combustion mechanism was dominant for all aluminized propellants. Tailoring of particle damping, therefore, will have to concentrate on reduction of the yield of smoke in favor of condensed phase oxidation to fill up the intermediate size interval. At the same time, aluminum agglomeration should be reduced or eliminated to take advantage of a proper choice of the sizes of aluminum particles. Much basic research will be required to accomplish these objectives.

REFERENCES

1. Temkin, S. and Dobbins, R. A. "Attenuation and Dispersion of Sound by Particulate-Relaxation Processes," J Acous Soc Amer, Vol. 40, No. 2 (May 1966), pp. 317-24.

2. Air Force Rocket Propulsion Laboratory. T-Burner Testing of Metallized Solid Propellants, by F. E. C. Culick. Edwards, CA, AFRPL, October 1974. (AFRPL-TR-74-28, publication UNCLASSIFIED.)

3. Mathes, H. B., Kraeutle, K. J., Dehority, G. L., and Derr, R. L. "Combustion Instability Studies Using Metallized Solid Propellants: Part III, Characteristics of Particulate Metal Oxide Residues in T-Burners," in 12th JANNAF Combustion Meeting, Volume II. Chemical Propulsion Information Agency, Laurel, MD, December 1975. (CPIA Pub. 273, publication UNCLASSIFIED.)

4. Kraeutle, K. J. "Particle Size Analysis of Aluminized Propellants," presented at AIAA/SAE 13th Joint Propulsion Conference, 10-13 July 1977. (AIAA Preprint No. 77-978, UNCLASSIFIED.)

5. Herdan, G. Small Particle Statistics. Butterworth, London, 1960.

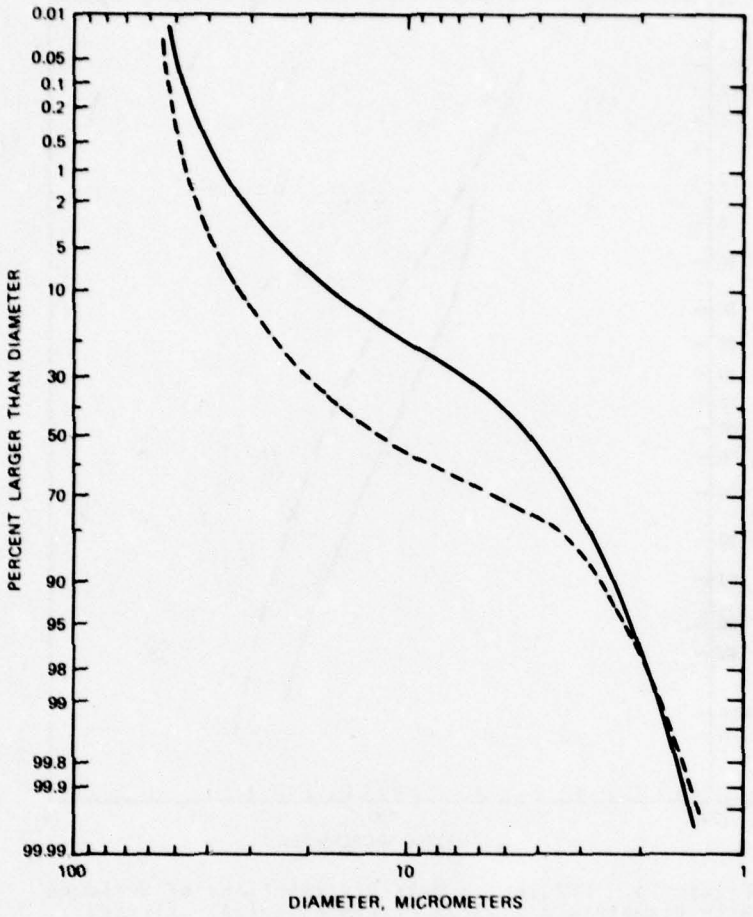

Figure 15. Cumulative Mass Distributions of Residues With Diameters $2 \lesssim d \lesssim 43$ μm of Propellant A. Firings were made in a pipe burner at pressures of 1.47 MPa (——) and 5.61 MPa (– – –).

6. Derr, R. L., Kraeutle, K. J., Mathes, H. B., and Dehority, G. L. "Combustion Instability Studies Using Metallized Solid Propellants: Part I, Experimental Verification of Particle Damping Theory," in 12th JANNAF Combustion Meeting, Volume II. Chemical Propulsion Information Agency, Laurel, MD, December 1975. (CPIA Pub. 273, publication UNCLASSIFIED.)

7. Kraeutle, K. J., Derr, R. L., Mathes, H. B., and Dehority, G. L. "Combustion Instability Studies Using Metallized Solid Propellants: Additional Experimental Evidence for the Validity of Particle Damping Theory," in 13th JANNAF Combustion Meeting, Volume II. Chemical Propulsion Information Agency, Laurel, MD, December 1976. (CPIA Pub. 281, publication UNCLASSIFIED.)

8. Kraeutle, K. J. and Atwood, A. I. "Distinct Size Classes of Aluminum Oxide Particles Produced During Combustion of Aluminized Propellants," presented at the 15th JANNAF Combustion Meeting, Newport, RI, 11-15 September 1978.

9. Kraeutle, K. J., and Bradley, H. H. "Combustion of Aluminized Propellants: The Influence of Pressure and Propellant Composition on Formation of Aluminum Combustion Residue," in 14th JANNAF Combustion Meeting, Volume I. Chemical Propulsion Information Agency, Laurel, MD, December 1977. (CPIA Pub. 292, publication UNCLASSIFIED.)

PLASTIC SCREEN STRUCTURED SMOKELESS PROPELLANTS FOR RECOILLESS GUNS AND VERY SHORT BURNING ROCKETS

by Albert T. Camp

Naval Ordnance Station, Indian Head, MD 20640

Retention of propellant in recoilless guns or extremely short burning rockets has long been a challenging problem. During the 1964 to 1970 time period the Lockheed Propulsion Company performed in-house and Army (MICOM) sponsored work directed at the use of aluminum foil as a supportive substrate for various propellants. Both double-base and composite types were tried. The principal problem encountered was overcoming faulty bonding of propellant to the aluminum foil. Army in-house efforts at ARRADCOM, (both Ballistic Research Laboratory and Picatinny Arsenal) and at the Radford Army Ammunition Plant in recent years have been aimed at using aluminum screen or plastic screen substrates. In these tests solventless M-8 double-base propellant sheet was rolled onto the screen. Bonding was again a major problem, as was the necessary welding of thin sheets applied to both sides of the screen.

In the present work plastic screen, typically Saran (polyvinylidene chloride) or polypropylene of about 16 meshes per inch, supplied by Chicopee Manufacturing Company of Cornelia, Georgia, has been used in combination with an acetone-based lacquer of a specially formulated, plateau burning double-base propellant. Generically similar to the well-known High Energy N-12 formulation[1] developed at NWC, China Lake in the mid fifties, this new formulation has a higher plateau burning rate of 1.5 inches/sec (38 mm/sec) from 3,000 to 5,000 psi (≈200 to 350 atmospheres) and also a higher heat of explosion of about 1100 cal/g. It is applied to the screen substrate as a 20 percent solution in acetone by a multiple dipping operation. Drying times between dips vary from 1 to 4 hours or longer but do not appear very critical to success. Drying time after the final dip is at least three days at room temperature under a chemical hood to achieve essentially constant weight. Typically from two to eight dips are employed to build up the desired propellant thickness for burning times ranging from 3 to 15 milliseconds.

To ensure that adequate bonding of propellant to and through the screen was being obtained, burning rate strands were prepared by cutting strips of 3mm width from screen that had first been dipped twice in the lacquer and dried. Subsequent dipping served to build up the desired 3mm thickness for reliable strand burning. Strands were inhibited in accordance with MIL Std 286B procedures for double-base propellant and burned at pressures from 1000 to 5000 psi. No evidence of flash-down was seen with strands so prepared although strands cut directly from 3mm thick screen-structured sheets, without any further dipping, did show flash-down burning at the higher pressures. This was apparently the result of damage to the bond between plastic and propellant caused by cutting the strands.

Although applications exist for simple scrolls, discs, and strips of screen-structured propellant, the greatest benefit is expected to derive from the use of preformed, bonded cylinders of corrugated and laminated screen. In this way 150 to 300 axial cells of propellant can be formed in an integral structure of 2.5 to 3.5-inch diameter at low cost. The result is a readily available, cartridge-loaded, smokeless propellant charge with very high burning surface, capable of producing 10 to 40 thousand pounds of thrust for a few milliseconds. Such charges should have great utility in a variety of applications. Ignition delay time is expected to be one millisecond or less with a head end igniter.

Figure 1 is a sketch of an end view of such a cylindrical structure of corrugated screen prior to dipping in propellant lacquer. In actual practice, the structure would be convolute-wrapped rather than the concentric rings shown. Figure 2 is a photograph of an early model of a completed propellant charge. Figure 3 is a logarithmic plot of strand burning rate of the NOSIH AA-15 propellant from 1000 to 5000 psi and at 70°F (21°C). Strands were also burned at -40°C and 60°C between 3000 and 5000 psi to allow calculation of the temperature coefficient shown in Figure 3 and in Table 1.

Table 1 also shows the formulation and properties of NOSIH AA-15 propellant prepared by normal solventless procedures used in the U.S.A. Films of the propellant cast from acetone lacquer on mercury typically have 70°F tensile properties of about 2000 psi with at least 50% elongation at rupture. Films formed by dipping screen into the same lacquer are stronger and exhibit higher modulus as would be expected.

Propellant properties obtained from dried lacquer films prepared by dissolving water-damp (12% H_2O) unrolled propellant paste in acetone are much the same as those shown for the solventless sheet stock. Thus it appears that rolling is not essential to the formation of high quality propellant lacquer. It is helpful in the development of the best ballistic and mechanical properties, but either differential rolling or even-speed rolling is probably sufficient to assure optimum properties.

In conclusion it appears that a low cost technique exists for structuring and retaining a very high surface, thin-web smokeless propellant charge with plateau burning characteristics and competitive specific impulse. The propellant should be utilized at pressures of about 4,000 psi (70°F) to take maximum advantage of its properties. Its low slope characteristics down to 1000 psi should make it attractive for recoilless

applications where the pressure at the muzzle may have decayed to this level.

Reference
1. U. S. Patent 3,138,499 of June 23, 1964
Nitrocellulose Gas Producing Charges Containing Copper and Lead Salts and Aluminum, A. T. Camp and F. G. Crescenzo.

Table 1

Formulation and Properties of NOSIH AA-15 Propellant

Nitrocellulose (12.6% Nitrogen, linters)	49.0%
Nitroglycerin	42.0
2-Nitrodiphenylamine	2.0
Di-normal-propyl adipate	1.5
Normal lead beta-resorcylate	2.5
Monobasic cupric beta-resorcylate	2.5
Carbon black	0.5
	100.0
Moisture	0.2
Heat of Explosion (cal/g)	1100
Burning Rate, inches/second at 3000 psi	1.5
Pressure Exponent (3000 to 5000 psi) 70°F	0.2
Temperature Coefficient (%/°F @ 4000 psi -40 to 140°F)	0.15
Density, pounds per cubic inch	0.058
Specific impulse 1000/14.7 psia (frozen) pound-seconds/pound mass	235
Specific impulse @ 4000 with ϵ = 4.0 (frozen) lb sec/lb mass	215
Range of 70°F pressure over which π_k is less than 0.2%°F, psia	~1000 to 4500
Discharge coefficient, C_D (lbm/lbf-sec x 10^3)	6.60
Taliani Stability, mm Hg/min at 100mm pressure	0.75
Heat capacity of gases at constant volume cal/g·°F	0.342
Moles of gas per gram of propellant	0.0384
Density of gas at 4000 psia and 2850°K, lb/in^3	0.00084
Adiabatic flame temperature, °K:	
Isochoric T_v	3480
Isobaric T_p	2869

Composition of Gases at 2850°K and 4000 psi, mole percent	
Hydrogen (H_2)	8.49
Steam (H_2O)	25.37
Carbon monoxide (CO)	36.15
Carbon dioxide (CO_2)	15.64
Nitrogen (N_2)	13.20
Gamma C_p/C_v (frozen)	1.24

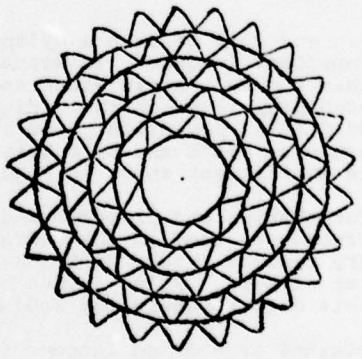

Figure 1. End View of Corrugated, Laminated Cylinder of Plastic Screen Suitable for 2.5-inch (64mm) Inside Diameter Rocket or Gun Tube

Note: Figure 2. In preparation. Copies will be brought to meeting.

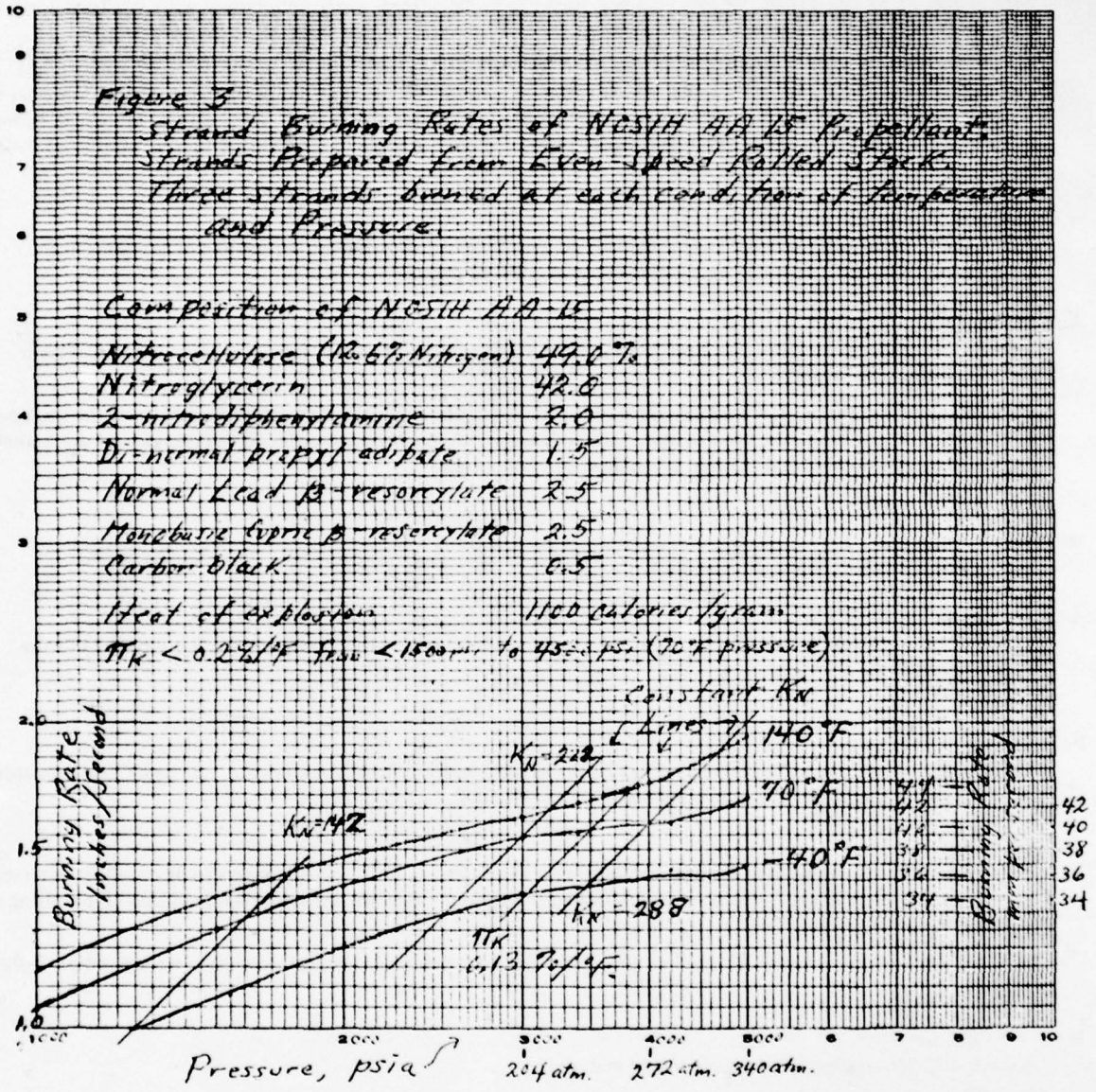

Figure 3. Strand Burning Rates of NOSIH AA 15 Propellant

DISCUSSION

B.P.Plantif, SNPE

What range of burning thickness can be obtained by this process?

Author's Reply

I have no specific information available but as a guide if you take the burning time of 15 m/s in the example and a burning rate of 37 mm/s then the web thickness used can be calculated. Only preliminary work has been done and the limits of the system have not been established.

We see the concept as most applicable and practical for applications with burning times of 3 to 10 milliseconds. These times correspond from 2 to about 6 dips of the screen in lacquer. By the time 6 dips of 20% propellant lacquer (in acetone) have been applied, the coating surface has nearly lost the screen pattern. This pattern is retained, however, fairly well through 4 dips and is advantageous for increasing the burning surface and degree of neutrality of surface.

W.H.Diesinger, Dynamit Nobel AG, Ge

Can you give some information on the specific impulse efficiency, allowing for the cooling of the gases in the combustion chambers? Also can you comment on the igniter design?

Author's Reply

With regard to specific impulse, we have no information yet since we have not fired charges in motors. This is planned in the near future.

With regard to the igniter, Al Camp envisages two different types of igniter. One igniter would be at the head end but the second type would be tubular igniter running down the centre of the wafer. The latter would simultaneously pressurise every assembly and ignite everything at the same time.

Mr Weyl

Do you use the plastic screen for the discs?

Author's Reply

Yes. The plastic screen is sliced by a cutter and propellant is subsequently deposited on it. Following this the separator ridges are glued on.

P.Spadetta, It

What could be the expected behaviour of a grain made with the described type of propellant under environmental stresses, such as temperature shock, mechanical shock, vibrations, ageing, etc. . ?

Author's Reply

We have a lot to determine in these respects, but bonding of propellant to screen appears to be excellent in strand burning tests "down-screen". No flash-down problems observed. We have not temperature cycled before firing nor have we fired charges under high acceleration.

Principal applications now are in recoilless guns with stationary propellant charge, minimum stresses on propellant.

R.Lo, DFVLR, Ge

Is there sufficient oxygen to burn the screen material?

Author's Reply

Calorimeter tests seem to indicate affirmatively.

R.Lo, Ge

What weight % is the screen material?

Author's Reply

Variable, 10 to 20%.

R.Lo, Ge

If it does not burn completely, does it cause smoke formation?

Author's Reply

Probably a fine dust if not combusted completely.

R.Lo, Ge

What is the loading density that can be achieved (in terms of energy per unit volume as compared with other charges).

Author's Reply

Stacked discs would appear to provide very competitive loading density. Corrugated structures probably less so, but the avoidance of any loss of propellant would seem to justify this deficiency.

Author's Comment

The work described in the paper is still at a very early stage of application. Both current applications are in recoilless guns. Tests are expected to take place in May. The advantages we see for recoilless guns are a very favorable pressure exponent and temperature coefficient compared with typical smokeless gun and rocket propellants, and the retention of propellant throughout burning. We expect ignition delay to be very short also.

GAS GENERATOR PROPELLANTS FOR AIR-TO-AIR MISSILES

R.A.H.STRECKER AND D.LINDE
BAYERN-CHEMIE
Gesellschaft fuer Flugchemische
Antriebe mbH
8261 ASCHAU, GERMANY

SUMMARY

The application of composite propellant technology for the power source of new weapon systems has increased steadily during the last few years. Especially for guided missiles, composite gas generators are considered as the optimum solution with respect to weight, reliability and cost effectiveness. In order to comply with the requirements of low burning rates, composite propellants with ammonium nitrate (AN) as the oxidizer are normally used.

Different crystal lattices as a function of temperature have been an inherent weakness of AN which ultimately change the density, the mechanical properties and therefore the burning rates of AN-propellants. In order to overcome these problems, the incorporation of metal ions into the crystal lattice is sometimes used.

Preferably nickel in small amounts very effectively stabilizes and shifts these phase changes to higher temperatures, thus leading to propellants, which can easily withstand temperature cycling between -54°C and +72°C up to 150 cycles. Developments and investigations with respect to achievable burning rates, ageing behavior and environmental loading capacities produced a family of gas generator propellants with an HTPB-binder system, suitable for use under severe environmental conditions such as air-to-air missile applications.

I. INTRODUCTION

The application of composite propellant technology for the power source of new weapon systems has increased steadily during the last few years. Hereby the following specific requirements have to be fulfilled.

- Operational range between -54°C and +72°C
- Combustion temperatures $\leq$ 1500 K
- Low soot and solid content of the combustion gases
- Non-corrosive combustion gases
- Mechanical stability toward environmental loading
- Stability of ballistic properties toward environmental loading
- Burning rates between 0,7 - 3 mm/s at 70 to 100 bar at ambient temperature.

Conventional composite propellants based on AP are not acceptable because the combustion temperatures are too high, the combustion gases are corrosive and the required burning rates are not achievable.

Single or double base propellants are sometimes used. However, here also is the achievement of the low burning rates, the low gas temperatures and low soot content a major problem.

Gasgenerator propellants based on ammonium nitrate are considered as the optimum solution with respect to weight, reliability and cost effectiveness. Polymers such as polybutadienes, polyesters, polyethers and polysulfides are used, each polymer having his advantage and disadvantage.

II. POLYMORPHISM OF AMMONIUM NITRATE

An inherent weakness of ammonium nitrate is its polymorphism, leading to seven different modifications in the temperature range between -180 and +180°C. Hygroscopicity of ammonium nitrate and its polymorphism cause a distinct caking tendency and permanent volume expansions and contractions whereby the phase change from modifications IV to III at 33 - 37°C accompanied with a volume increase of approximately 4 % is especially disturbing for practical applications.

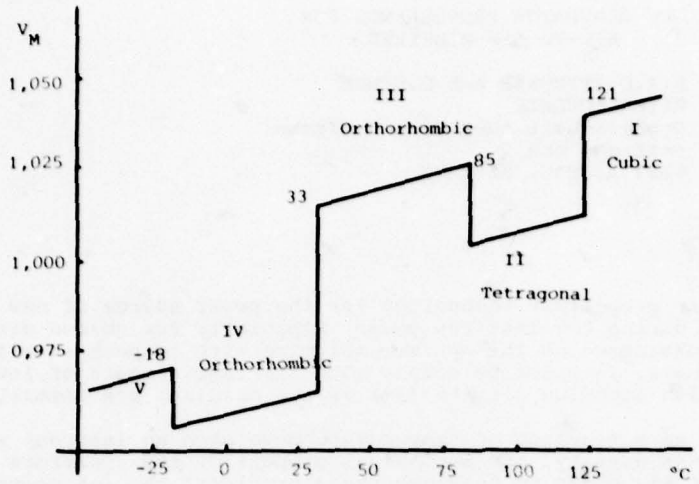

Fig. 1 Polymorphism of ammonium nitrate

Fig. 1 shows the polymorphism of ammonium nitrate within the temperature range of -25°C to +125°C, illustrating very clearly the large increase in volume at 33°C.

It has to be pointed out however, that parameters such as direction of temperature sweep, cooling or heating rate, crystal size and water content of the samples influence the phase-change temperatures, thus leading to different temperature quotations in the literature. In order to circumvent these disturbing properties of ammonium nitrate, extensive studies have been carried out including surface treatment and incorporation of impurity ions into the crystal lattice. Surface treatment alone naturally is not preventing the volume expansion during the phase change of modification IV to III and can improve the fluidity only. Proper selection of impurity ions, however, can prevent the volume expansion during phase change and improve the fluidity, this means introduce some anticaking properties as well.

Especially the incorporation of diamin complexes of nickel, copper and zinc, investigated by W.ENGEL (1), produced a satisfying phase stabilization and improvement of the fluidity even at relatively small amounts of impurity ions. Fig. 2 shows the volume expansion curves versus temperature of ammonium nitrate, stabilized with various amounts of nickel oxide, clearly illustrating the shifting and stabilizing effect of this impurity ion. For demonstration purpose only, the curves are shifted along the y-axis and are therefore not documenting an absolute value of the specific volumina.

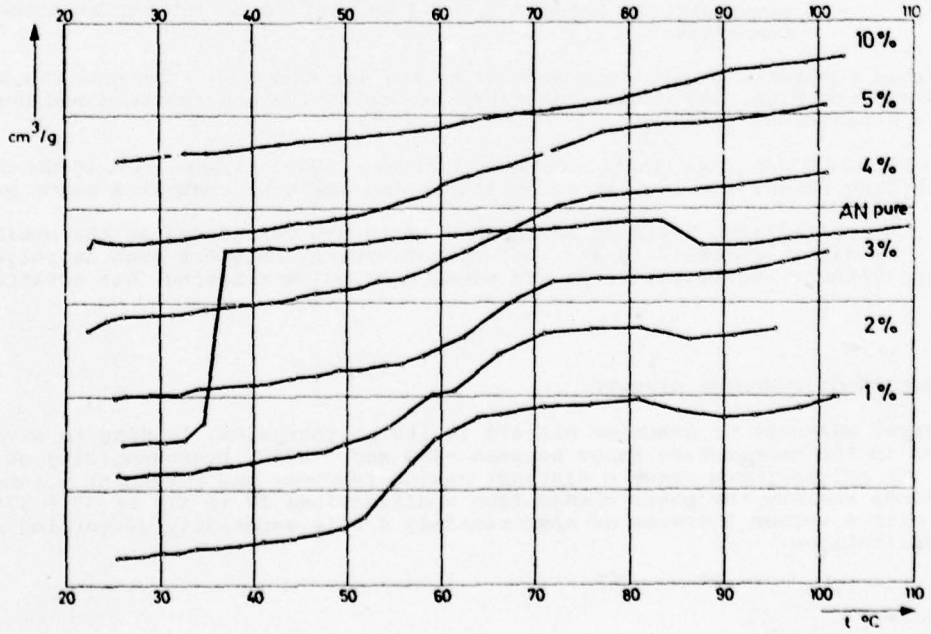

Fig. 2 Volume expansion curves of ammonium nitrate, stabilized with nickel oxide

III. PROPELLANT DEVELOPMENT

A lot of parameters have to be considered in selecting the proper binder for a propellant development. Availability, price, physical and mechanical properties play an important role and finally led to the selection of hydroxylterminated polybutadiene (HTPB), even though oxygen containing polymers such as polyethers and polyesters seem to be more favourable in view of the required low soot content, because of the possibility to work with a lower solid filler content.

The gas generator propellants are formulated as follows:

	weight %
ammonium nitrate, stabilized with 3 % NiO (ANS)	76 - 83
cooling agents	0 - 5
ballistic modifiers	0 - 3
HTPB-binder system	17 - 19

Manufacturing of the propellants takes place according to the usual composite technology, i.e. processing under climatized conditions, vacuum mixing with vertical mixers, yielding propellants which are easily castable. The compositions are cast at ambient temperature and cured at 40 - 50°C. The curing time ranges from 3 to 10 days, depending on the formulation. As can be concluded from the above mentioned general formulation, a whole family of gas generator propellants can be formulated. This family was designated "NB 410".

Thermodynamical properties and composition of combustion gases at chamber conditions for a NB 410 propellant with 82 % ANS can be seen from table 1.

				Vol.-%	weight %
Isp (70/1)	Ns/kg	2016	H_2O	27,855	23,60
T_c	K	1406	H_2	23,616	2,24
T_e	K	794	CO	3,268	4,31
		1,147	CO_2	16,942	35,08
$\bar{M}$		21,43	N_2	21,215	27,96
c*	m/s	1209	CH_4	6,380	4,80
			NH_3	0,017	0,01
			Ni (s)	0,703	1,93
			rest	0,004	0,07

Table 1 Thermodynamical properties of a NB 410 propellant with 82 % ANS

The required criterias for gas generator propellants such as combustion temperature, non-corrosivity of combustion gases and sootlessness are guaranteed with this formulation. Only 1.93 % by weight of nickel is obtained as solid component in the combustion gases. No damaging effects however could be detected, when experiments with a connected servo motor were carried out.

The change in gas composition after a shifting equilibrium expansion to 20 bar can be seen in table 2.

T (K)	1000	800	600	550	500	380	360	300
C (s)	-	-	-	3,11	15,09	55,45	147,1	148,14
Ni (s)	19,36	19,36	19,36	-	-	-	-	-
NiO (s)	-	-		24,60	24,60	24,60	24,60	24,60
H_2O (l)	-	-	-	-	-	-	539,95	546,91

Table 2 Composition of condensed phases in g/kg propellant at various temperatures and 20 bar.

At 550 K, some soot can be expected, while nickel changes to nickel oxide.

The uniaxial mechanical properties are presented as master curves in fig. 3 - 5. Superposition of the values for different temperatures and cross head speeds were obtained by application of the WLF-equation using a temperature shift factor

$$a_T = \frac{5.54\ (T - 298)}{162.6 + T - 298}$$

and an effective gauge lenght of 68.6 mm of the JANAF A sample.

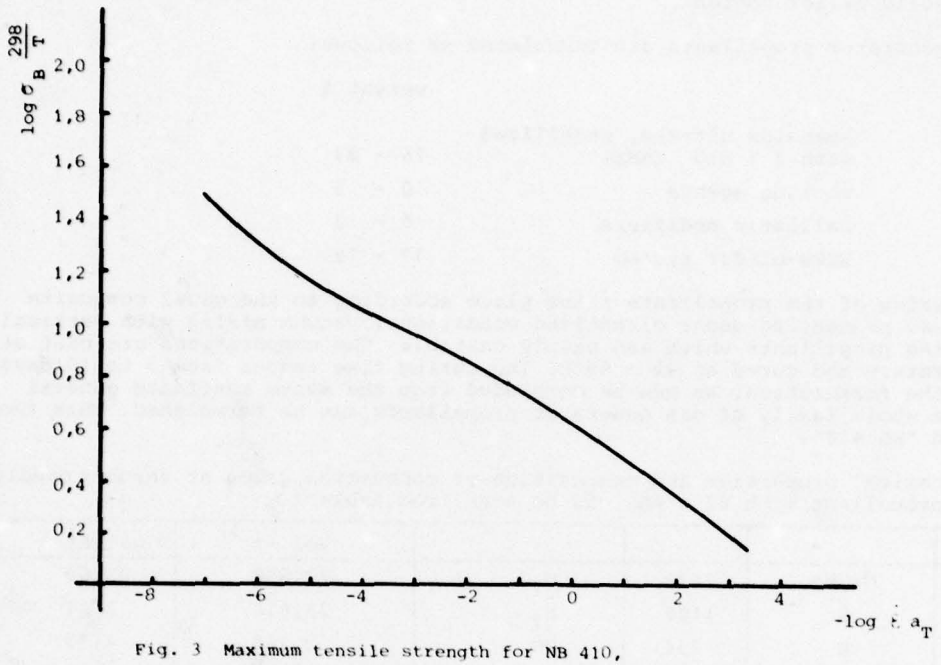

Fig. 3 Maximum tensile strength for NB 410, reduced to 298 K

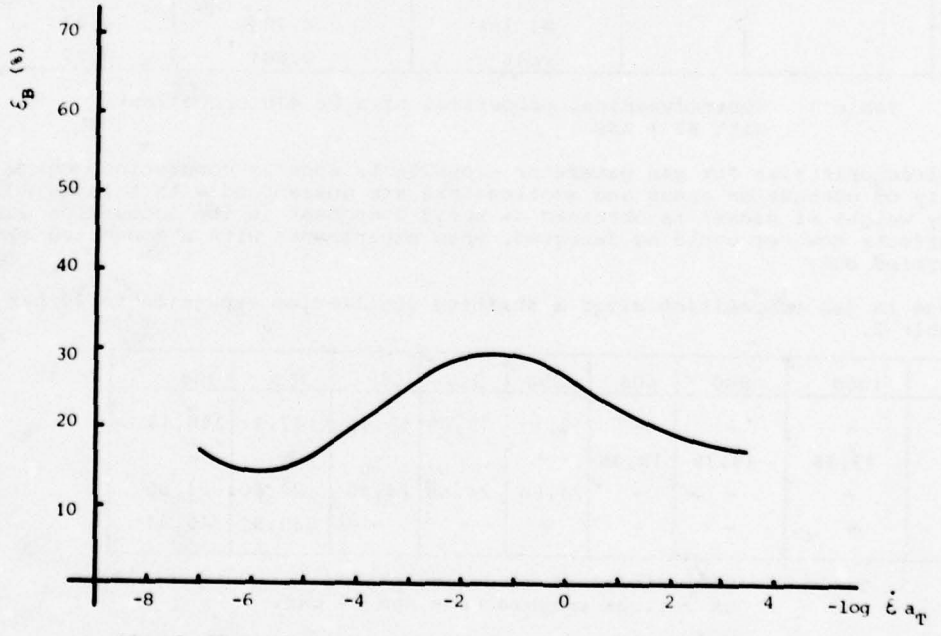

Fig. 4 Elongation at maximum tensile strength of NB 410, reduced to 298 K

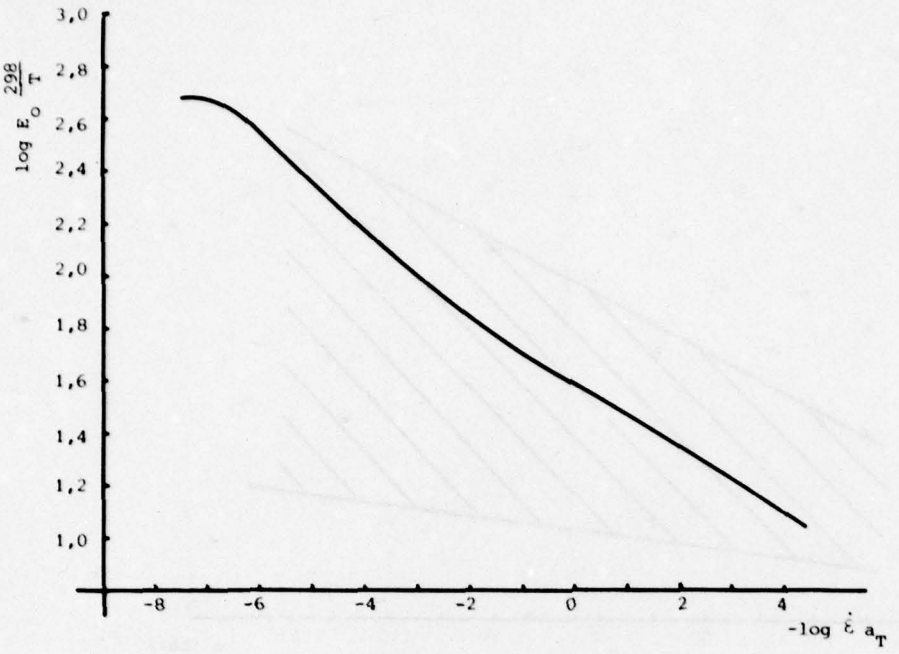

Fig. 5 YOUNG'S Modulus of NB 410, reduced to 298 K

The determination of the burning rate at various temperatures was carried out by means of endburners with a diameter of 36 mm and a lenght of 70 mm. Special care has to be taken in order to ignite ammonium nitrate propellants at low temperatures, where sometimes great difficulties are encountered. It was noted, however, that within the temperature range of -54 to +72°C ANS propellants are much easier to ignite than propellants with regular AN.

In fig. 6 the burning characteristic of one particular propellant, namely NB 410 213, is shown at various temperatures, while in fig. 7 the burning rate range at 20°C of the complete NB 410 family, including the whole array of formulations, is illustrated. It can be seen, that burning rates at 70 bar and 20°C below 1 mm/s are difficult to obtain. The reason for the increased burning rate is most likely the incorporation of nickel which also acts as burning rate modifier.

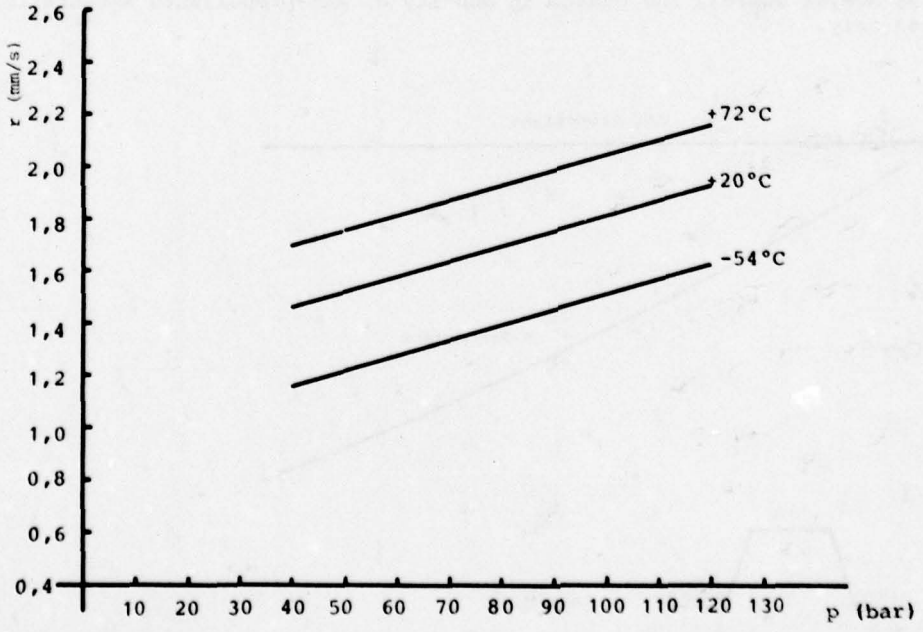

Fig. 6 Burning rate of NB 410 213

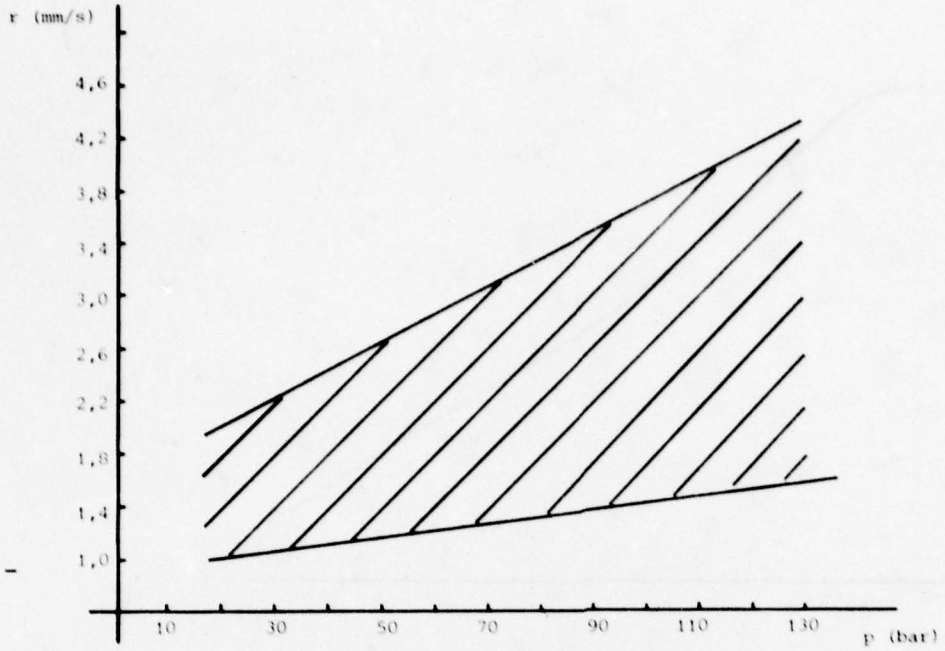

Fig. 7: Range of burning rates of ANS-propellants at 20°C

IV. COMPARISON OF AMMONIUM NITRATE PROPELLANTS AFTER ENVIRONMENTAL TESTING

The transition of unstabilized ammonium nitrate from modification IV to III at 33°C, accompanied with a substantial increase in volume leads to a restricted applicability of these propellants. Jumping this phase transition point several times causes a separation of the oxidizer particles from the binder matrix, also called dewetting, entailing a significant alteration of physical, mechanical and ballistic properties. The enormous improvement by using phase stabilized ammonium nitrate is demonstrated in a direct comparsion of AN and ANS propellants in fig. 8 - 10. Both types of propellant have been submitted to an environmental simulation program, crossing the critical transition temperature twice per cycle. Within the test programm of 125 cycles, samples were withdrawn for investigations every 25 cycles.

In fig. 8 the change in density after temperature cycling is shown for both types of propellant. It is noticeable that the density of AN-propellants decreases by 15 % already after 25 cycles whereas the change in density of ANS-propellants amounts to 2 % after 125 cycles only.

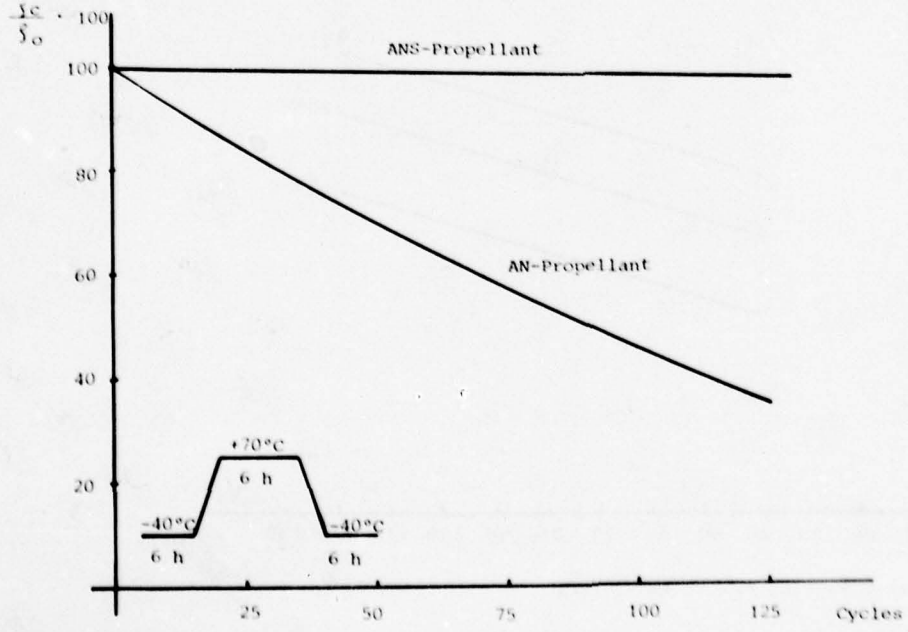

Fig. 8 Change of density after temperature cycling

Running parallel with the decrease in density, a tremendous deterioration of mechanical properties with increasing numbers of cycles can be observed. Concurrently, the tensile strength and the elongation is declining with AN-propellants while contrary ANS-propellants show hardly any effect even after 125 cycles (fig. 9).

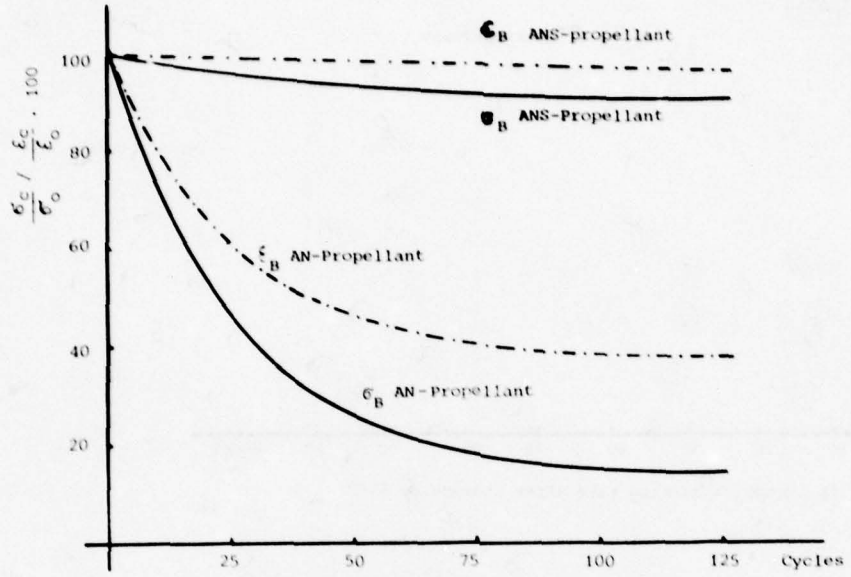

Fig. 9 Change of mechanical properties after temperature cycling

Guaranteeing the ballistic properties after environmental simulation is the decisive factor for the usability of propellants. It can be seen in fig. 10, that at most AN-propellants can be submitted to an environmental simulation of 25 cycles if an increase in burning rate of 8 % is acceptable. Using phase stabilized ammonium nitrate however, a much better constancy of the burning rate can be achieved, because an increase of only 3 % was observed after 125 cycles.

Long term storage behavior at elevated temperatures of AN/ANS-propellants (fig.11,12), where no crossover of the transition temperature takes place, is identical for both types of propellants. Storage of ANS-propellants at 50°C up to 72 weeks did not change the burning rate. The same behavior was found with AN-propellants, where the storage was terminated after 24 weeks.

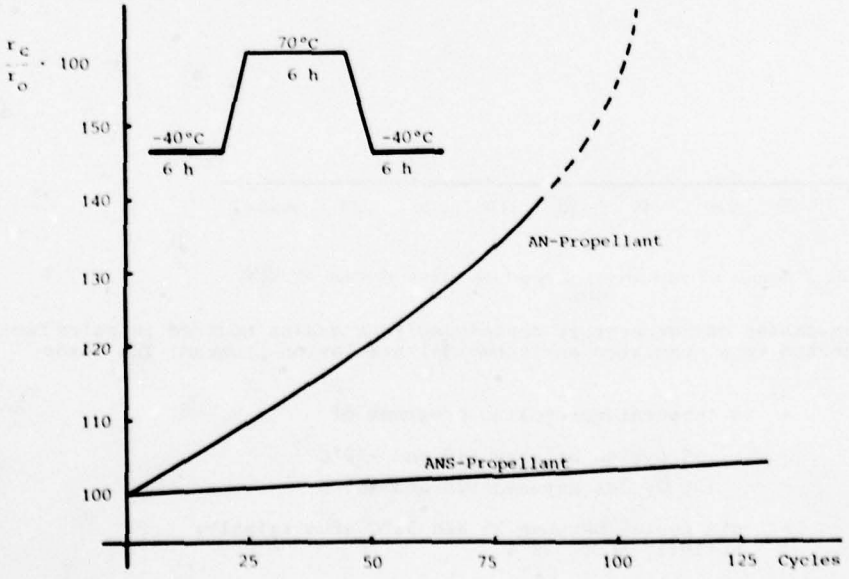

Fig. 10 Change of burning rate after temperature cycling

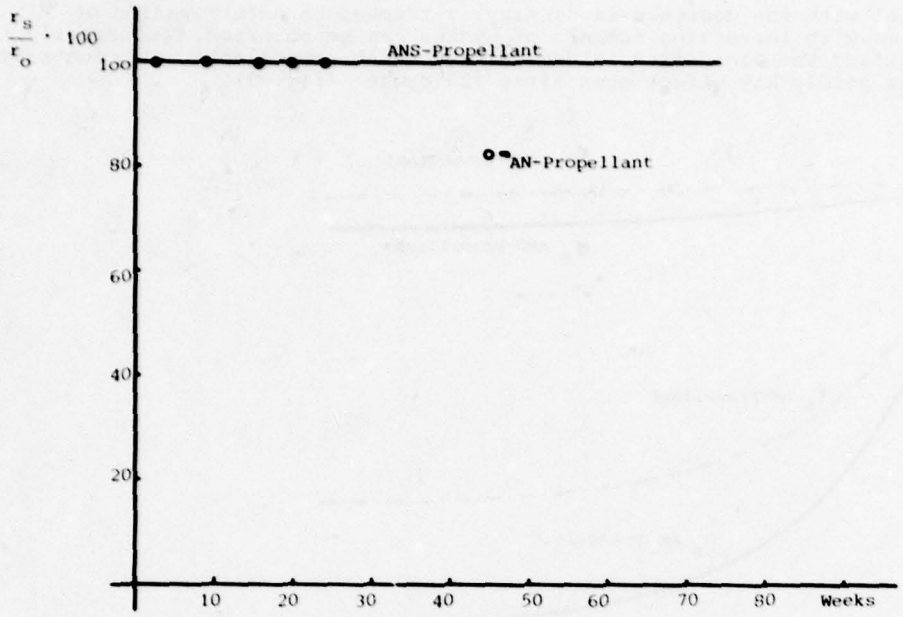

Fig.11 Change of burning rate after storage at 50°C

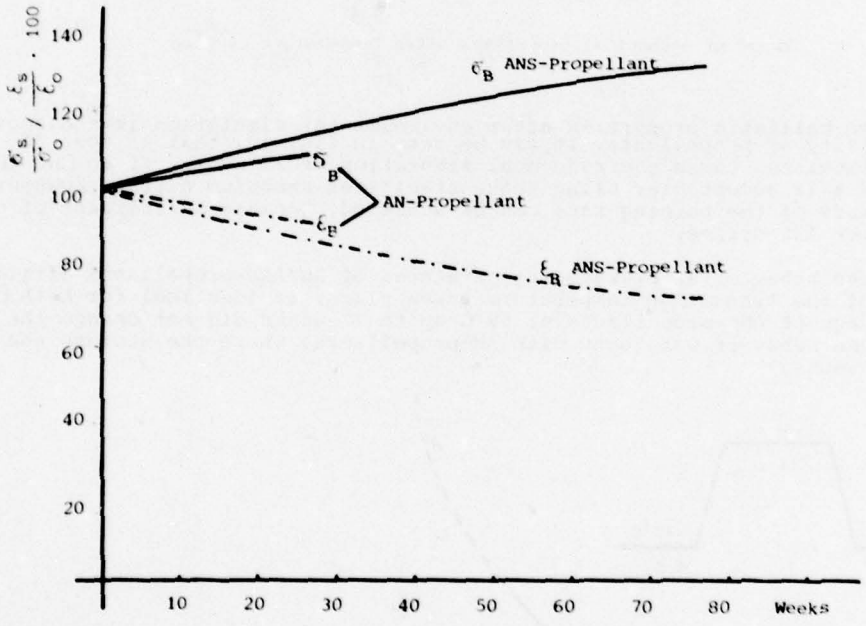

Fig. 12 Change of mechanical properties after storage at 50°C

A completely assembled gas generator, containing four grains mounted in pairs facing each other was subjected to a cumulated environmental simulation program. The loads consisted of:

- a temperature cycling programm of

  50 cycles between -40 and +50°C

  100 cycles between +20 and +50°C

- six cycles between 25 and 55°C at a relative humidity above 90 %

- random vibration at -40 and +65°C

frequency range	20 - 20 000 Hz
test axis	x, y and z
duration	1 h/axis

- bump test

number of shocks	2000/axis
test axis	±x, ±y and ±z
total number of shocks	12 000
shock frequency	1 - 3 shocks/s
duration	6 ms
acceleration	50 g

In fig. 13 the pressure/time-traces of gas generators with NB 410-propellants can be seen, of which one has been subjected to the above mentioned cumulated environmental simulation program. Both traces are identical except for a slight increase of pressure during the ignition phase at the gas generator after simulation, generated by the starter grain which consisted of a regular ammonium perchlorate propellant. It can be safely concluded, however, from these data, that the NB 410-propellants have satisfactorily endured the inflicted loadings.

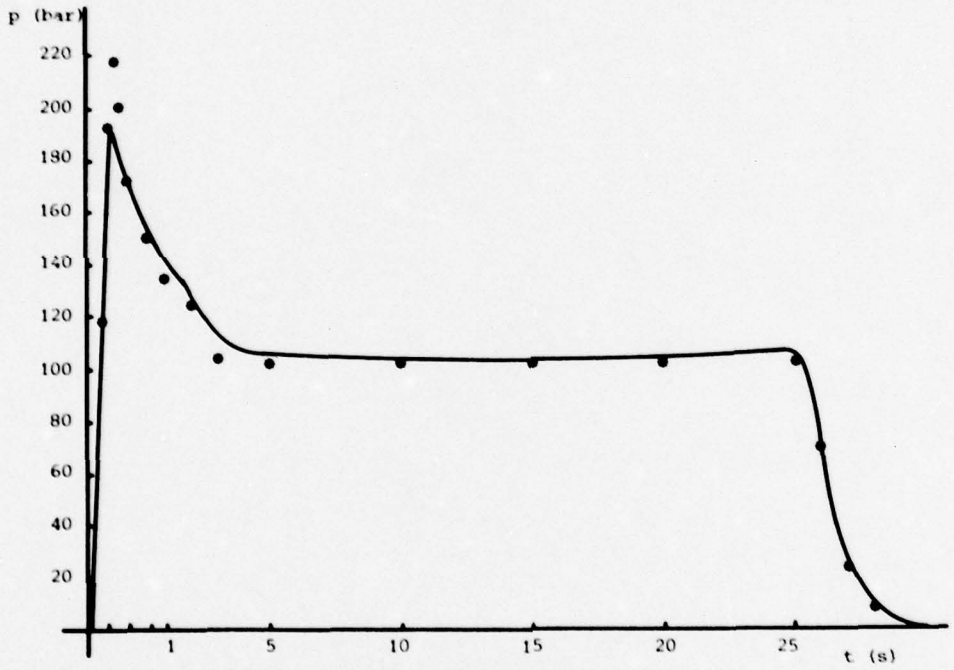

Fig. 13: Pressure/time-traces of NB 410-gasgenerators
— without environmental simulation
● after environmental simulation

After conclusion of propellant development, NB 410 206 was examined by an official governmental institution (BICT). The data listed in table 3 represent an excerpt out of these BICT reports.

Heat of explosion	J/g	3242
weight loss at		
363 K after 18 days	%	none
348 K after 34 days	%	none
ignition temperature	K	488 - 501
friction sensitivity by BAM		no reaction
impact sensitivity by BAM	J	25
detonation wave sensibility		none

Table 3 Safety and propellant data of NB 410 206

In conclusion, it can be stated, that NB 410-propellants are representative of gas generator propellants which are superior to propellants containing unstabilized ammonium nitrate. These NB 410-propellants are especially suited for applications where systems are exposed to a large temperature range and frequent temperature cycling such as air-to-air missiles.

References:

(1) W.ENGEL, EXPLOSIVSTOFFE No. 1, 9 - 13, 1973

DISCUSSION

G.Kristofersen, Norwegian Defence Research Establishment, No

My question concerns the nickel or solid particles in general in the combustion gases from your propellant. Gas generators are as a rule used with downstream servo mechanisms which contain filters and valves. Have you any experience of blockages of these components?

Author's Reply

The gas generator system was equipped with a filter of 80 micron mesh size. Hardly any clogging or specifically only a pressure difference of 3–4 bar before and after the filter has been observed. The valves must be properly designed in order to insure correct action.

G.Kristofersen, No

Is the burning rate affected by acceleration conditions? The solid particles could be important in this respect.

Author's Reply

Acceleration tests have been carried out with several types of propellants. No problems arise, when uncatalyzed propellants are used, i.e. the phase stabilized ammonium nitrate causes no problems. Proper selection of burning rate modifiers however is absolutely necessary in order to prevent an increased burning rate during acceleration tests.

N.Seiden, N.O.S. Indian Head

Can you tell us about your experience of igniting these gas generators with igniters using other than ammonium perchlorate propellants.

Author's Reply

The propellants can also be ignited with Boron/Potassium nitrate pyrotechnics. Success at all temperatures was obtained during development.

Mr Lanteri-Minet, Service Techniques des Poudres et Explosifs, SNPE

To obtain easier ignition would it not be possible to use polysulphide binder cured with paraquinone dioxide? This would permit a reduced ammonium nitrate filler level and hence a cooler flame. This binder would also provide higher burning rates than with HTPB. Thus a cooler flame (1 200°K) at the same burning rate is achieved.

Author's Reply

Polysulfides have been used at an earlier stage of development. This binder, however, was found to be incompatible because of the formation of liquid or solid nickel-sulfide as a combustion product which caused a lot of problems, especially to the valves.

O.Blichner, Norwegian Defence Research Establishment, No

In your Figure 13 the initial peak pressure is approximately 100% higher than the operational pressure. Did this result from a performance at an ambient temperature of 15°C? If so, what peak pressures can be expected at higher ambient temperatures?

Author's Reply

The experiment was carried out at ambient temperature of 20°C. The reason for the high ignition pressure, originating from the AP-starter grain is that no gas distributing ring was connected to the gas generator in this experiment. The completely assembled gas generator system would yield an ignition pressure of 120 bar at ambient temperature and 160 bar at +65°C.

NEW BINDER SYSTEM FOR COMPOSITE SOLID PROPELLANTS

Carl Gotzmer R-21
Naval Surface Weapons Center, White Oak
Silver Spring, MD

Nat Seiden PM1
Naval Ordnance Station, Indian Head, MD

ABSTRACT

A new binder system that has many unique properties has been developed for application with both castable and extrudable composite solid propellants. The binder system consists of a low acrylonitrile type carboxy-terminated-polybutadiene-acrylonitrile liquid copolymer (CTBN) which is crosslinked with di- and tri—epoxides. A dual epoxide crosslinking system is employed to permit broad adjustment of propellant modulus for various applications.

Castable and extrudable composite rocket propellants based on B.F. Goodrich's CTBN (1300 x 15) polymer have been developed and fired successfully in several motor sizes at typical service temperatures. This binder system provides the propellants with relative insensitivity to atmospheric moisture during processing and a generous pot life. Propellant costs are fully competitive with those of carboxy- or hydroxy—terminated polybutadiene binder propellants.

Although these propellants were developed for low smoke properties (high AP, very low Al and other particulate - producing additives), formulations with high solids loading (~90% of combined AP and Al) appear feasible with adequate mechanical properties and extrudability for cartridge loaded charges.

INTRODUCTION

A new binder system was developed for composite solid rocket propellants* that has many unique properties. The binder system consists of low acrylonitrile content carboxyl-terminated polybutadiene-acrylonitrile liquid copolymer (CTBN) which is crosslinked with di- and tri-epoxides.

The "Improved Binders for Propellants Application" is a NAVSEA program that is concerned with the development of improved binder systems for new propellants that can be scaled-up for use in future Navy rocket motors. The primary goal of the program was to develop a propellant binder with better propellant aging characteristics and physical properties than existing binder systems. However, other considerations such as good propellant processing properties, a potential for high solids loading, low primary smoke, and good resistance to atmospheric moisture during processing were guidelines in achieving the main objectives. Successful completion of the program would yield improved performance and lower costs through improved propulsion systems reliability and service life.

One such approach for achieving the objective is to avoid the commonly used urethane (HTPB-Isocyanate) or carboxyl-aziridinyl (CTBN-MAPO) type binder systems and utilize mercapto-epoxide or carboxyl-epoxide type curing systems. Beginning in 1972 a mercaptan terminated butadiene-acrylonitrile (MTBN) liquid copolymer was characterized and investigated for use as a propellant binder utilizing epoxide crosslinking agents. Important information was gained in these studies with respect to (1) regulating crosslink density via dual epoxide crosslinking systems and (2) binder-filler interaction of the nitrile groups in the backbone of the copolymer with ammonium perchlorate. Presently, carboxyl-terminated butadiene-acrylonitrile (CTBN) liquid copolymer utilizing the crosslink system developed during the MTBN studies is under investigation as a propellant binder.

DISCUSSION

MTBN BINDER SYSTEM

Previous work in this laboratory included the investigation of MTBN copolymer for use as a propellant binder. The copolymer was commercially available and manufactured by the B.F. Goodrich Chemical Company under the designation Hycar MTBN (1300 x 10). Characteristics of MTBN copolymer are listed in Table I.

* The new binder system was developed with funds provided by the Naval Sea Systems Command under project SEA-SF131332307 "Improved Binders for Propellant Application" and monitored by J.W. Murrin and R.F. Cassel. The program was carried out by the Propellants Chemistry Branch, NSWC, Code CR21 of Indian Head, Maryland. Patents have been applied for covering the binder system.

MTBN copolymer was cured with a dual epoxy resin system employing an organometallic catalyst. The dual epoxides provided control over the crosslink density of the binder system. Selection of the epoxides was based on the following criteria:

(a) Ability to act as reactive diluent (lower overall binder system viscosity).
(b) Suppression of Tg (function as internal plasticizer).
(c) Physical properties achieved (attainment of maximum work to produce rupture).
(d) Chain extension.

Processing of composite propellant was not hampered by the high MTBN viscosity because of the considerable drop in viscosity observed when MTBN was mixed with the two low viscosity epoxides.

Negligible differences between maximum and break values of the mechanical properties were found for MTBN propellants crosslinked with two epoxides and containing up to 30% plasticizer. Table II lists mechanical properties of propellant aged in dry air for 30 days at 176°F (80°C).

Excellent pot life (Table III) was demonstrated at 82 to 89% solids loading for MTBN propellants when a mixed antioxidant was employed such as alkylated diphenylamine and polybutylated bisphenol A. Such propellants attained complete cures after 7 days at 170°F (77°C).

Three important conclusions reached during the MTBN binder study were applied to the CTBN propellant development in the latter part of this program.

(1) The functionality (1.7) of MTBN copolymer was lower than desired. A functionality of 2.0 or greater would be needed to eliminate dangling polymer chains and improve the mechanical properties of the cured polymer network.
(2) MTBN copolymer molecular weight was lower than desired. To develop the necessary strain properties an increase in molecular weight from 1700 to 3000 would be desirable and could be brought about (without drastically increasing the viscosity of the copolymer) by correspondingly decreasing the nitrile content of the copolymer.
(3) The nitrile content (24%) of MTBN copolymer was found to be too high with respect to achieving good physical properties at -65°F (-54°C). Acceptable physical properties at -40°F (-40°C) could only be attained through the use of glass transition temperature depressants such as linear polyether di-epoxides or ester type plasticizers.

The above mentioned conclusions revealed during the investigation of MTBN copolymer were advantageously combined into the development of the present-day CTBN (1300 x 15) propellant discussed in the remainder of this paper.

CTBN BINDER SYSTEM

It is important to note that the CTBN copolymer discussed in the paper was originally a development product of B.F. Goodrich Chemical Company until late 1976 (CTBN 1300 x 15 is presently commercially available). It is not the same copolymer as the related commercial products CTBN (1300 x 8) and CTBN (1300 x 13) which have higher nitrile contents and viscosities.

The CTBN under investigation is a low acrylonitrile type designated CTBN (1300 x 15), the properties of which are listed in Table IV. Reaction of the epoxides with CTBN is analogous to MTBN in that the concentration of the epoxides can be used to control the functionality of the final crosslinked network. Thermally stable propellants have been prepared with moduli ranging from 400 to 4000 psi (at ambient temperature) at solids loadings in the range of 83% to 88%. Manipulation of the di- and tri-epoxide and epoxide/COOH equivalence ratios to control crosslink density of the binder system permits broad adjustment of propellant physical properties.

Table V shows how the propellant modulus may be varied by manipulating the di-/tri-epoxide ratio. Other influences on modulus such as solids loading, epoxide equivalence and the effect of a plasticizer were studied. Formulation "A" in Table VI, at low solids loading results in a high modulus, whereas formulation "B" at high solids loading exhibits a low modulus. The changes in propellant properties resulted from the use of a plasticizer and the inversion of the di-/tri-epoxide ratio. Table VII lists the results of typical aging tests conducted in dry air of a propellant formulation containing 85% solids.

The improved mechanical performance of CTBN over that of MTBN copolymer as a propellant binder can be attributed to the increased molecular weight, higher functionality and lower acrylonitrile content of CTBN (1300 x 15).

PROPELLANT GRAIN PROCESSING AND MOTOR FIRINGS*

The attainment of high moduli in composite propellants utilizing the new CTBN (1300 x 15) binder system has stimulated interest in use for cartridge loaded application. The initial application concerned the replacement of an extruded double base propellant in a 5-inch diameter JATO motor. Processing of the grain was carried out in standard production equipment, per the flow chart in Figure 1. Defect-free grains were produced in this manner as shown in Figure 2.

Eight motor firings have been conducted to-date over an operational temperature range of -40°F (-40°C) to +140°F (+60°C). Reproducibility of both impulse and thrust-time profile has been excellent. Traces of the motor firings are illustrated in Figure 3.

In addition, six loaded motors were aged at +140°F (+60°C); three for 45 days and three for 90 days. Dimensional changes of the grains due to aging were negligible.

The second application involved a 10-inch diameter motor. In this case the propellant was cast into a mold and permitted to cure. The propellant grain was then removed, cut to length and inhibited on both ends. Traces of static motor firings at 0°F (-18°C) and +140°F (+60°C) are shown in Figure 4. All motor firings to-date, in both programs, have been successful.

FUTURE PLANS

(U) The military utility of CTBN propellants is currently being explored. Current work in other areas includes: extruded rocket and gun propellants, extending propellants to 90% solids loading, case bonded applications and extending low temperature capability.

TABLE I

TYPICAL PROPERTIES OF HYCAR MTBN (1300 x 10)

EPHR, SH	0.103
Molecular Weight (number average)	1700
% SH	3.4
Functionality	1.7
% Acrylonitrile	24
Ash (percent)	0.1
Specific Gravity @ 25°C	0.93
Brookfield Viscosity @ 27°C, poise	350
Glass transition temperature, °C (by DSC)	-49

(Not to be construed as manufacturer's specifications)

TABLE II

MECHANCIAL PROPERTIES OF MTBN; MIX 7869

	Original Properties	After 30 days @ 80°C and twice cycled to 25°C
Tensile @ Max stress, psi	104	106
Elongation @ Max stress, %	19.6	19.7
Tensile @ Rupture, psi	102	106
Elongation @ Rupture, %	20.7	19.7

Strain rate 0.7407 in/in/min JANNAF DIECUT

* Funding for this effort has been provided by the Naval Air Systems Command under the direction of Casimir Orzechowski and Florian Hocke. The program was carried out by the Engineering, Pilot Operations and the Ordnance Departments at the Naval Ordnance Station, Indian Head, MD

TABLE III

TYPICAL POT LIFE OF MTBN PROPELLANTS

Time (hrs)	Brookfield Viscosity @ 130°F (54°C), 5rpm, Spindle "E" (Kilopoise)	
	Mix 7966	Mix 9085
1	12.4	15.0
2	13.2	15.8
3	14.8	16.4
4	16.0	17.6
19	24.0	26.0

Mix 7966 contained 86% solids
Mix 9085 contained 89% solids

TABLE IV

TYPICAL PROPERTIES OF CTBN (1300 x 15)

EPHR, COOH	0.053
Molecular weight (number average)	3600
% COOH	2.47
Functionality	1.9
% Acrylonitrile	10
Heat Loss, 2 hours @ 130°C, %	1.0
Specific Gravity @ 25°C	0.928
Brookfield viscosity @ 27°C, poise	500
Glass transition temperature, °C (by DSC)	-68

(Not to be construed as manufacturer's specifications)

TABLE V

ADJUSTMENT OF PROPELLANT PROPERTIES

(at constant solids loading)

CTBN (1300 x 15)	12.30	12.30
Di-Epoxide	0.77	0.67
Tri-Epoxide	0.39	0.49
Anti oxidant	0.36	0.37
Opacifier	0.10	0.10
Aluminum	1.0	1.0
AP	85.0	85.0
Catalyst	0.08	0.07
	100.0	100.0
Physical Properties @ 25°C		
Tensile @ Rupture, psi	172	285
Elongation @ Rupture,%	44	25
Molulus, psi	1053	2034
Shore A hardness	69	83

TABLE VI

ADJUSTMENT OF PROPELLANT PROPERTIES

	FORMULATION "A"	FORMULATION "B"
CTBN (1300 x 15)	14.22	8.74
Di-Epoxide	0.71	0.53
Tri-Epoxide	0.99	0.28
Anti Oxidant	0.62	0.50
Opacifier	0.50	--
Inerts	0.90	0.20
Aluminum	2.0	22.0
AP	80.0	66.0
Catalyst	0.06	0.06
Plasticizer	--	1.69
	100.0	100.0
Physical Properties @ 25°C		
Tensile @ Rupture, psi	265	100
Elongation @ Rupture,%	9	40
Molulus, psi	4270	410
Shore A Hardness	90	50

TABLE VII

PHYSICAL PROPERTIES OF AGED CTBN PROPELLANT

	Days heated at 170°F (77°C) in air				
	7	14	35	56	84
-40°F (-40°C)					
max. stress, psi	872	859	763	830	830
strain @ max. stress, %	9	8	8	8	9
Modulus, psi	17;634	19,538	15,735	17,179	16,549
77°F (25°C)					
max. stress, psi	286	280	291	297	279
strain @ max, stress, %	16	16	16	17	17
Modulus, psi	2,443	2,726	2,558	2,588	2,152
140°F (60°C)					
max. stress, psi	209	205	197	206	202
strain @ max. stress, %	17	15	14	15	17
Modulus, psi	1,690	1,894	1,893	1,902	1,624

Strain rate 0.7407 in/in/min JANNAF DIECUT

FIGURE 1

EXTRUDED COMPOSITE GRAIN PRODUCTION

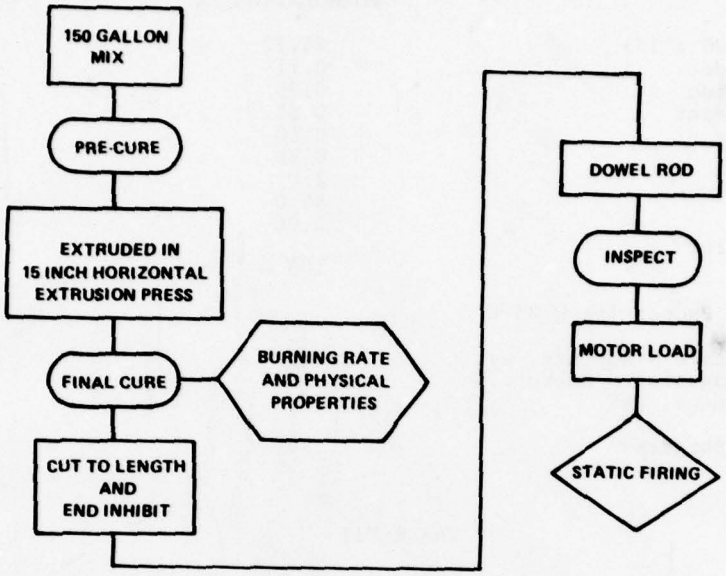

FIGURE 2

EXTRUDED CTBN

5-INCH DIAMETER PROPELLANT GRAIN

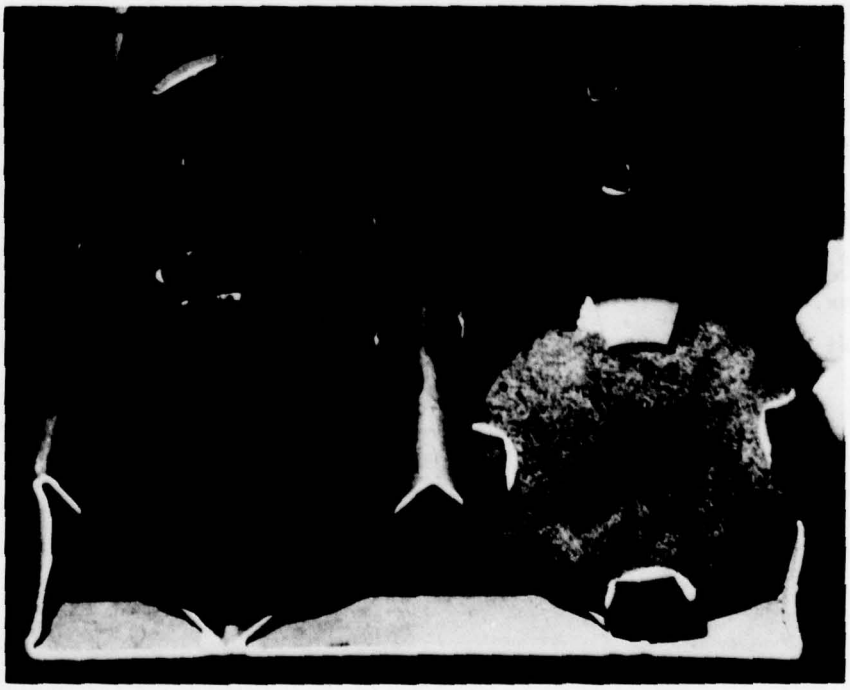

AFT FOWARD

FIGURE 3A

EXTRUDED CARTRIDGE LOADED CTBN 5-INCH MOTOR FIRING

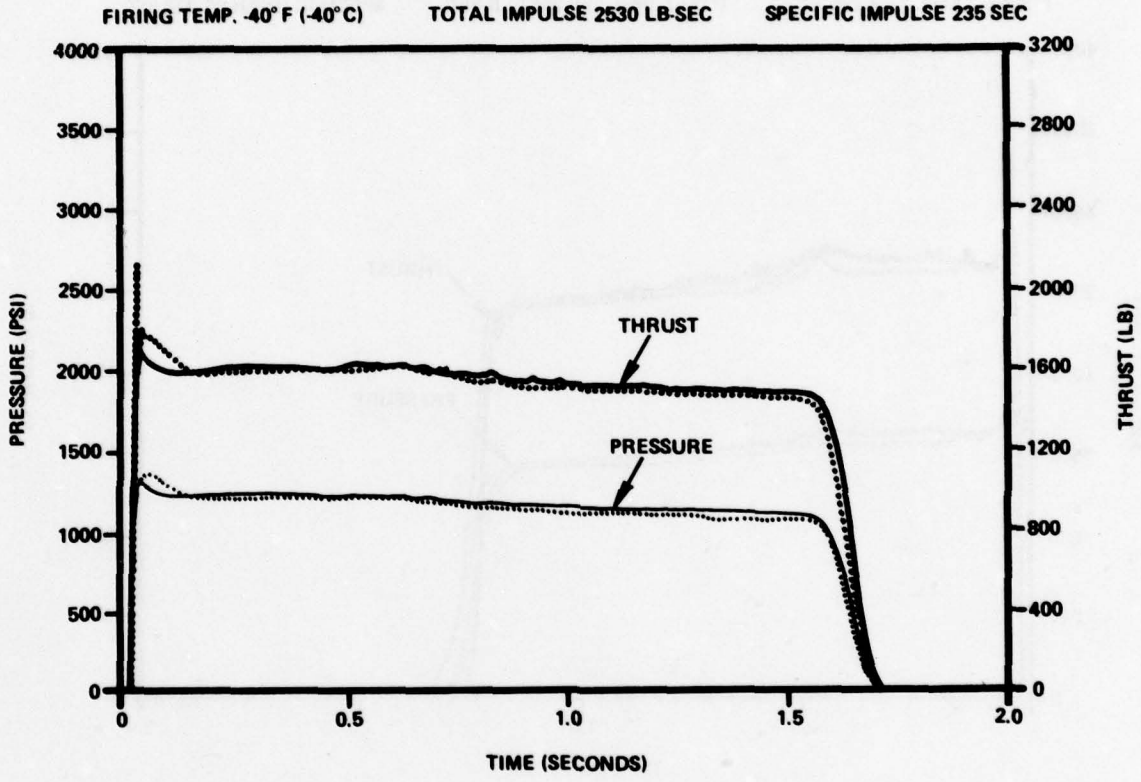

FIGURE 3B

EXTRUDED CARTRIDGE LOADED CTBN 5-INCH MOTOR FIRING

FIRING TEMP. 77° F (25° C) TOTAL IMPULSE 2567 LB-SEC SPECIFIC IMPULSE 238 SEC

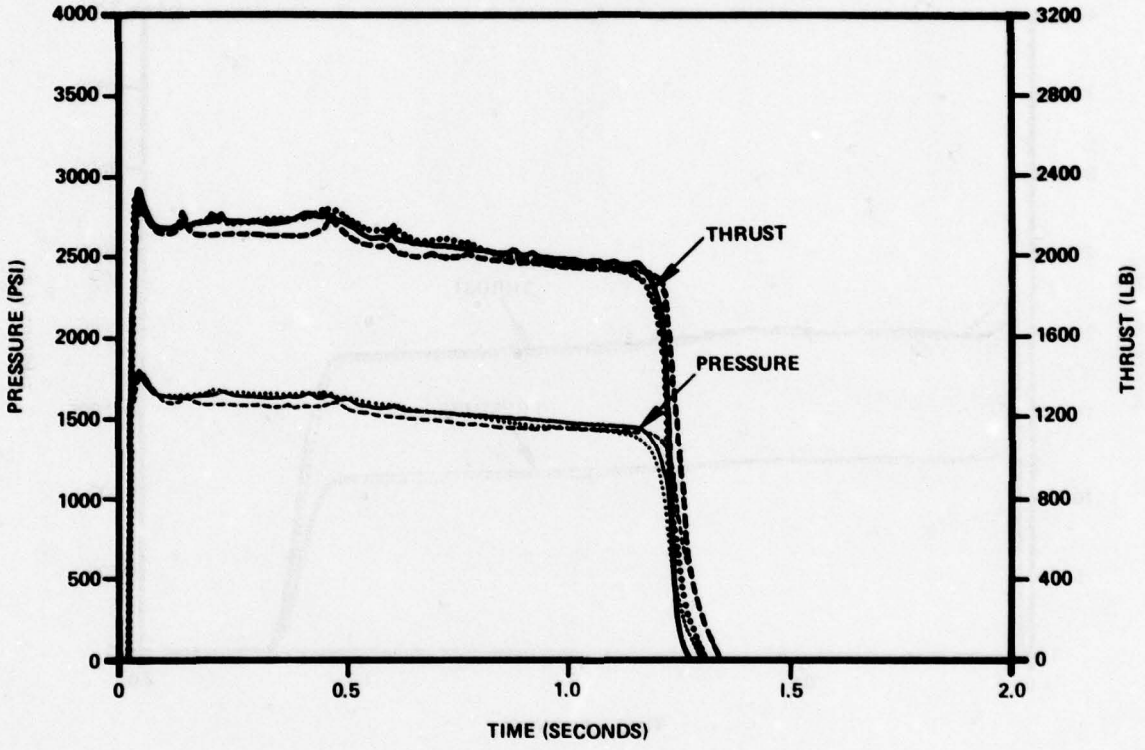

FIGURE 3C

EXTRUDED CARTRIDGE LOADED CTBN 5-INCH MOTOR FIRING

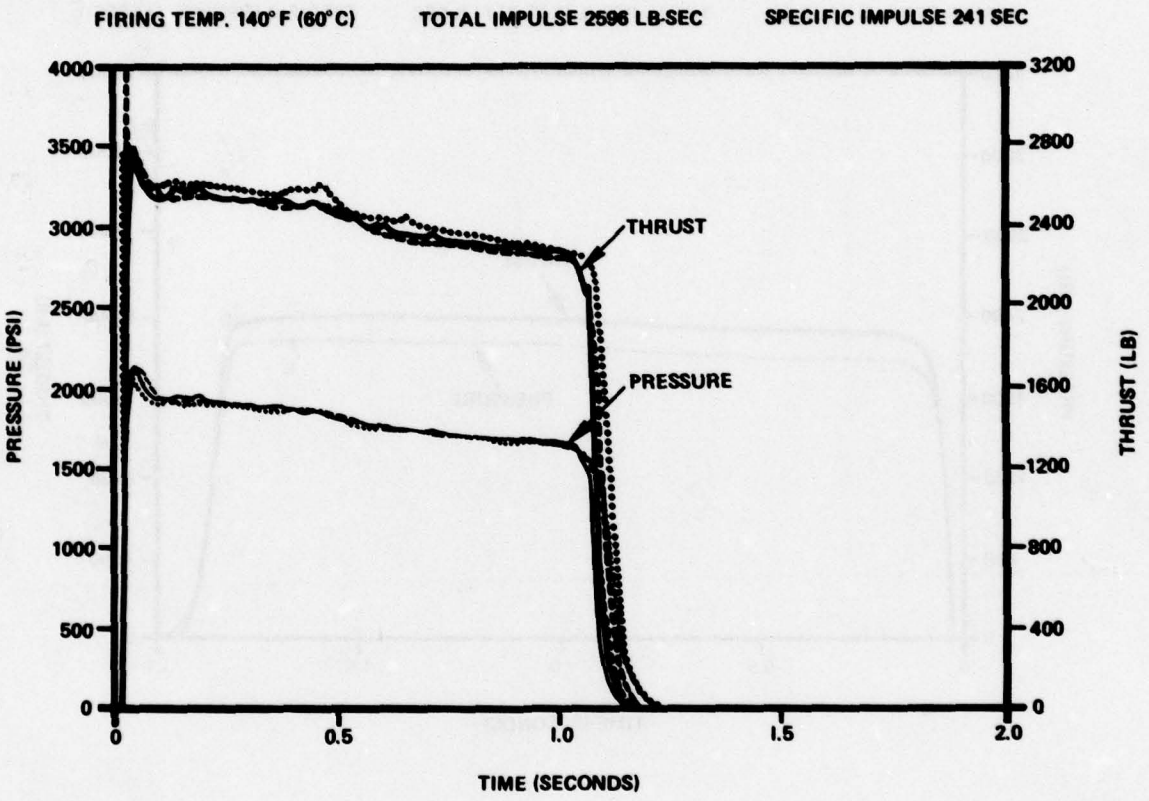

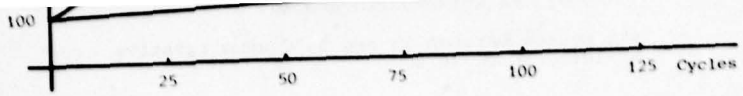

Fig. 10 Change of burning rate after temperature cycling

FIGURE 4A

CAST CARTRIDGE LOADED CTBN 10-INCH MOTOR FIRING

FIRING TEMP. 0° F (-18° C) TOTAL IMPULSE 25,911 LB-SEC SPECIFIC IMPULSE 237 SEC

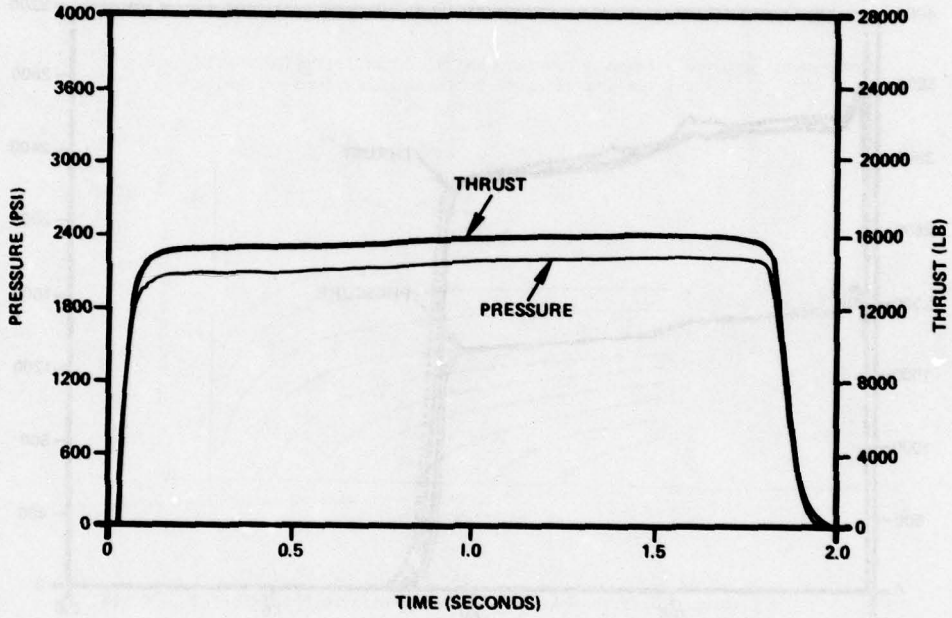

FIGURE 4B

CAST CARTRIDGE LOADED CTBN 10-INCH MOTOR FIRING

FIRING TEMP. 140° F (60° C) TOTAL IMPULSE 26,285 LB-SEC SPECIFIC IMPULSE 242 SEC

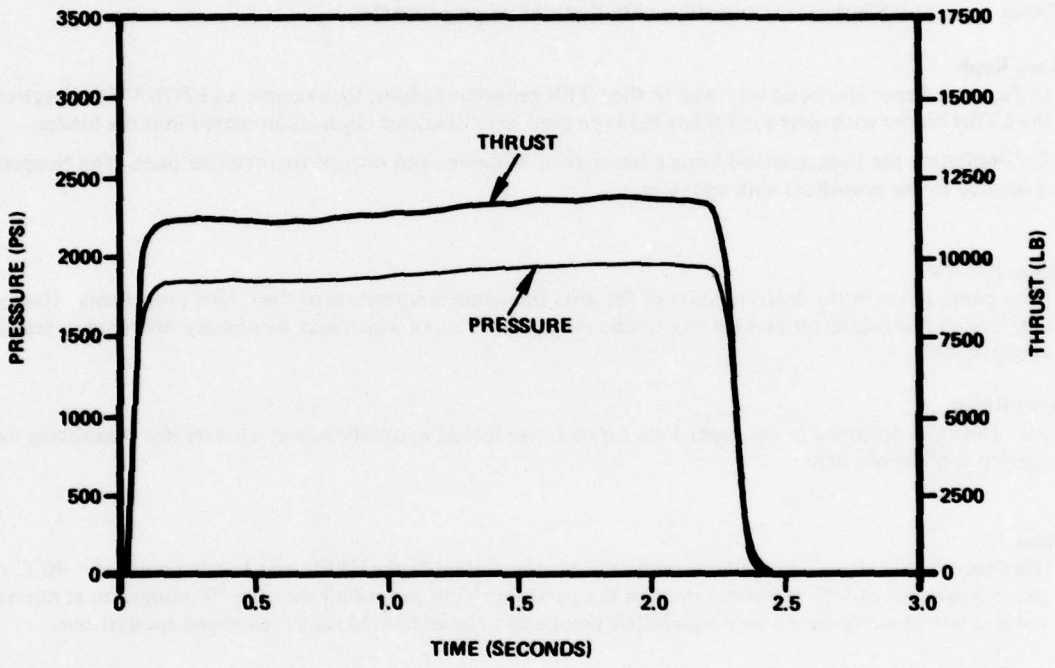

DISCUSSION

K.Klager, Aerojet, Solid Propulsion Company

In your Tables 6 and 7 you show a propellant formulation A which appears to show a deterioration in strain capability from 25% to 16% over 7 days. What are your comments on the ageing properties of these propellants?

Author's Reply

The formulation A has not been optimised for bonding agent content. Subsequent work indicates we need twice as much of this agent to stabilise the properties of this formulation. The bonding agent is a tri-functional epoxide which has a tertiary amine group in the molecule. This amine group forms a quaternary ammonium salt with the AP crystal surface. The presence of plasticiser such as in formulation B Table 5 has also been shown to be beneficial in ageing aspects.

P.Spadetta, SNIA Viscosa

What types of inhibition are compatible with this kind of propellant?

Author's Reply

Di-functional epoxides bond very well to the CTBN propellant grains, for example an EPON828/V40 system. Also the CTBN binder with inert solid fillers has been used with fiberglass cloth incorporated into the binder.

End inhibition has been achieved using a laminate of Neoprene and silicone foam rubber pads. The Neoprene face is bonded to the propellant with epoxides.

W.Klöhn, ICT, Ge

Your paper refers to the determination of the glass transition temperature of the CTBN propellants. Have you also determined this parameter by high rate tensile testing (i.e. 2 m/s), which may be of more relevance in practical applications?

Author's Reply

No. The units described in the paper were for cartridge loaded applications and we were not considering the case-bonded applications here.

W.Klöhn, Ge

Our experience with such propellants with 16% Nitrite content in the CTBN gave brittle points of $-40°C$ whilst good elongations of 50% at normal ambient temperature. Your propellant showing 9% elongation at normal ambient would surely have a very high brittle point and so be of limited use in case-bond applications.

Author's Reply

Your nitrile content in the polymer of 16% is very high. We have found that 10% is the maximum for good low temperature strain capability and some good results were obtained in such a case for a special application. In the latter case the CTBN with 10% nitrile had to be specially produced by the manufacturer. Normally we use CTBN of nitrile contents of 18% and 28%.

THE AGEING BEHAVIOUR OF SOLID ROCKET PROPELLANTS REGARDING THEIR MECHANICAL PROPERTIES

D. SCHMITT

Institut für Chemie der Treib- und Explosivstoffe
D-7507 Pfinztal-Berghausen, der Fraunhofer-Gesellschaft

SUMMARY

Mechanical properties, such as tensile strength and deformation properties measured under identical test conditions as a function of storage conditions, characterize the ageing process and, in this way, the physico-mechanical life of solid rocket propellants.

During ageing strength as well as deformation properties of double base solid propellants decrease. As in chemical lifetime, a relation can be established between the ageing time and the temperature. With increasing time composite solid propellants lose their visco-elastic properties, i.e., their strength increases as their deformation properties decrease. This process is accelerated with rising temperature. In addition, it has been shown that the condition of the surface of the propellant charge has an influence on the mechanical behaviour.

1. Introduction

Knowing the ageing behaviour and, hence, the life of solid propellants is of great interest both in technical and in economic respects. The present life expectancy and the future reliability of a solid rocket propellant are directly related to the state of the ageing process at a given moment. Ageing processes in a propellant, in turn, depend on the chemical composition, the shape of the propellant, the surface-to-mass ratio (web thickness), and on environmental conditions. Basically, two domains must be considered: the chemical life and the physical life. These two domains are interconnected and have to be considered together, if the all-over lifetime is to be discussed.

2. Storage at Elevated Temperatures and Mechanical Properties

Characteristic parameters are needed to describe the state of ageing of solid propellants. To obtain information at short notice on the probable lifetime, the studies which have to be undertaken must be comparatively short, i.e., they must be carried out under enforced or accelerated conditions. However, such studies are meaningful only if they allow a relation to be found between natural and accelerated artificial ageing. To establish such relations, solid propellant samples were stored over prolonged periods of time, i.e., in the temperature range between 20 ^{o}C and 80 ^{o}C, and the results obtained at various temperature levels were compared and extrapolated to the service temperatures.

Also the mechanical properties of the material under study can be used to determine the state of ageing. In practice, the tensile strength and the strain at break are characteristic parameters used for this purpose, both obtained from the stress-strain diagram of uni-axial tensile tests. To prove changes in these two mechanical properties they are determined before and after temperature loading under the following uniform test conditions: crosshead rate V = 50 mm/min, test tempera-

3. Influence of Ageing on the Mechanical Properties of Double Base Solid Propellants

To study the influence of ageing on the mechanical properties of double base solid propellants, tensile specimens of various types of propellants were stored at temperatures T = +50 °C, +65 °C and +80 °C where by the storage time decreased as the temperature increased. Fig. 1 shows the results of long term storage at 65 °C for a type A and a type B propellant. Type A has with 4518 J/g a higher heat of explosion where as the type B propellant with 3584 J/g has a lower heat of explosion. The mechanical properties were determined at intervals of two months over a total storage time of 24 months. Plotted over the storage time we see the tensile strength and the strain at break, relative to their values at the start of the test (the so-called zero values). The diagram is a typical representation of the behaviour of double base solid propellants. The mechanical properties change significantly already after the first few months of storage. Although the absolute values vary with propellant type, the same trends in the mechanical behaviour are observed: At first, both the tensile strength and the breaking strain decrease rapidly with storage time. Later, between the sixth and the fifteenth month they level off. The final value is only between 60 % and 20 % of the initial value and, in some cases, may even drop to zero.

At the two other storage temperatures similar changes in mechanical properties were found provided that different timescales are taken into account. The total storage time at 80 °C was three months, the samples were examined at weekly intervals. At 50 °C storage temperature the studies extended over a period of six years; samples were taken every six months.

A relation can be established between the results obtained for storage at different temperatures, which permits the extrapolation to the service temperatures. For this purpose the propellant was arbitrarily assumed to have satisfactory mechanical properties as long as the tensile strength and the breaking strain, were above 80 % of the initial values. The propellant was defined to have reached the end of its mechanical life, when either mechanical parameter dropped below this level. Depending on the use and the requirements of the propellant, that limit may be shifted upwards or downwards.

In Fig. 2 the storage temperatures are plotted against the logarithm of the time where both the tensile strength and the strain at break drop below the 80 % level. This points fall on a straight line which can be extrapolated to the service temperatures.

This representation of the results is analogous to that employed to determine the chemical life. An example for that is given Fig. 3.

Extrapolation to temperatures below 30 °C leads to extremely long mechanical lifetimes of double base solid propellants. However, these mechanical lifetimes are valid only if the propellant is stored constantly at this particular temperature, without any change, and is not subject to any other environmental effects. Since this is unlikely to apply in practice, corresponding allowances must be made. Any environmental load like transport or change of temperature alters the progress of ageing and, by this way, the lifetime.

4. Influence of Ageing on the Mechanical Properties of a Composite Solid Propellant

In composite solid propellants special attention must be paid to physical ageing. In contrast to double base solid propellants, they exhibit only insignificant chemical ageing phenomena. A few examples will show how storage at elevated temperatures, and constant loads at various temperatures, affect the mechanical properties of various composite propellants.

For this purpose, tensile specimens were stored in a dry atmosphere for up to eight weeks at temperatures between T = +20 °C and +80 °C and examined for their mechanical properties. The observed trends are straight forward: with increasing storage time and rising temperature the tensile strength increases, whereas the breaking strain decreases. Fig. 4 shows that large changes may be observed like a factor of 3 for strength and a factor of 0.2 for strain. This diagram is a plot of the relative tensile strength and the relative strain at break over storage time. The storage temperature was chosen as parameter. With increasing time, i.e., with progressing age, the material continues to cure; this process is accelerated at elevated temperatures. Corresponding observations are made if the material embrittles.

Ageing of composite propellants under the influence of temperature is also a function of the size and shape of the material. The results described above were obtained during temperature storage of tensile test specimens, i.e., in samples of relatively low thickness. They allow the ageing process to occur much faster than in propellant blocks of greater thickness. In samples of greater thickness the ageing phenomena occuring in the outer layers are similar to those encountered in the tensile test specimens. In contrast no profound changes in the mechanical properties are observed in the center of the block even at higher temperatures and prolonged storage periods. This is evident from Fig. 5 in which the values of the relative tensile strength and the relative breaking strain are plotted against the thickness of the layer. Thus ageing is found to proceed more slowly when going from the outer layer to the center of the block. However, the surface properties play a decisive role during mechanical loading of the propellant. If a crack is produced on the surface by an external load such as the pressure buildup during firing, this crack will propagate to the interior, irrespective of the prevailing mechanical conditions in the interior of the propellant charge.

As a consequence, special attention must be paid to surface ageing and its influence on lifetime. This aspect is most important in connection with the ageing of composite propellants because it is connected with embrittlement phenomena in the material. Moreover, changing mechanical properties from the outside to the inside may cause cracking as a result of the increased occurrence of internal stresses.

In a number of test series composite propellants were examined with regard to their creep behaviour under uni-axial steady state tensile stresses. Fig. 6 shows the change in strain versus time with the temperature as a parameter under constant stress load conditions. The main results found in these experiments are that the influence of temperature dominates and that it causes embrittlement of the material. The influence of the temperature cancels out the influence of the constant load and, with increasing time, a reversal change in strain results like the one at T = 20 °C.

5. Conclusions

It is possible to simulate the ageing behaviour of solid propellants. For this purpose, propellant samples are aged at elevated temperatures. For double base solid propellants it is possible to establish a relation between the time and the temperature with respect to mechanical properties. The relation allows to extrapolate the results obtained at elevated temperatures to service temperatures.

In composite propellants ageing results in a change of the visco-elastic properties which manifests itself like the embrittlement of a material: strength increases as deformation properties decrease. This change in mechanical properties decreases from the outside to the inside. However, since the surface condition determines the mechanical behaviour of the material, particular attention must be given to surface ageing.

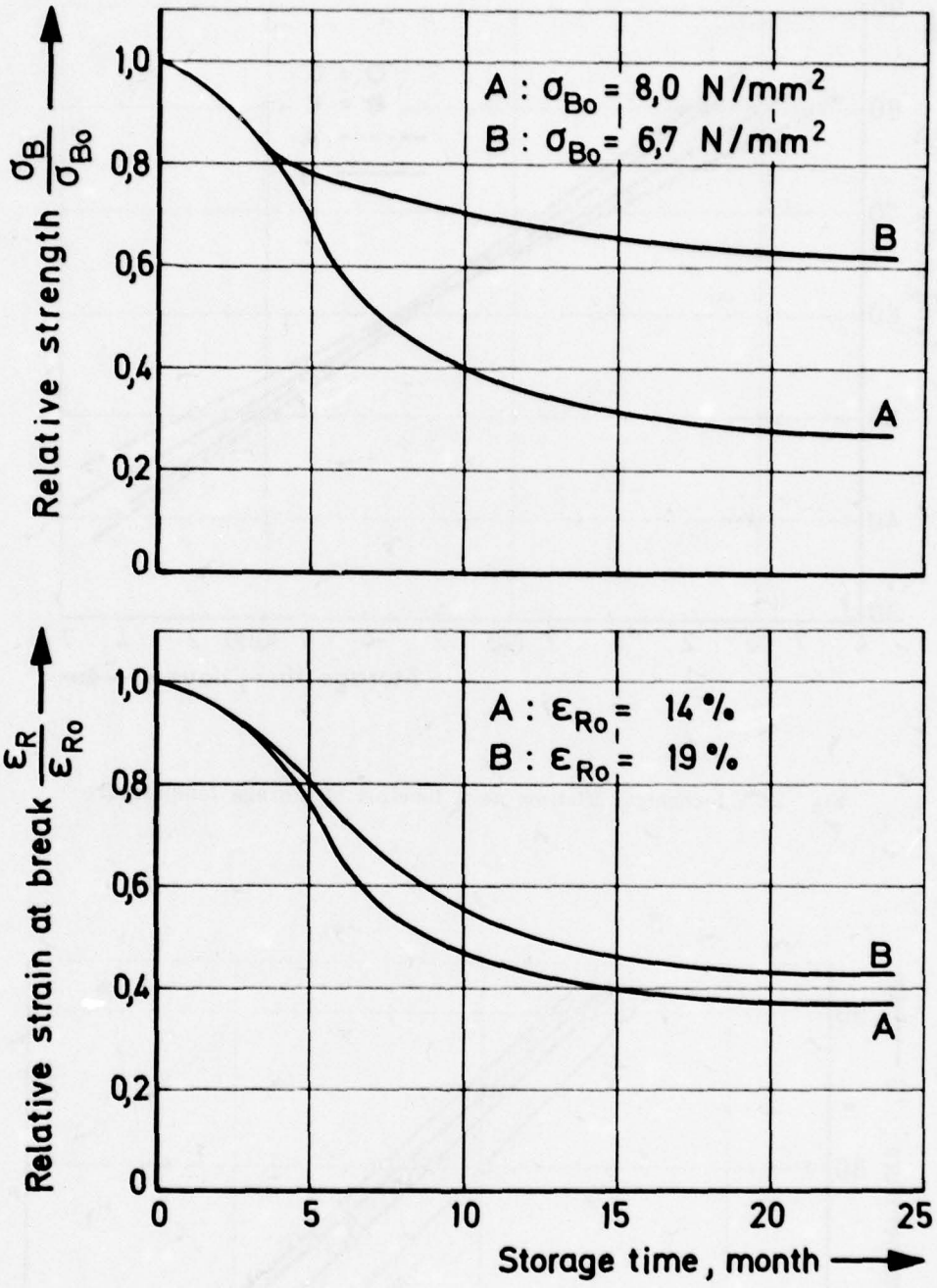

Fig. 1 Mechanical properties of double base propellants as a function of storage time at 65 °C

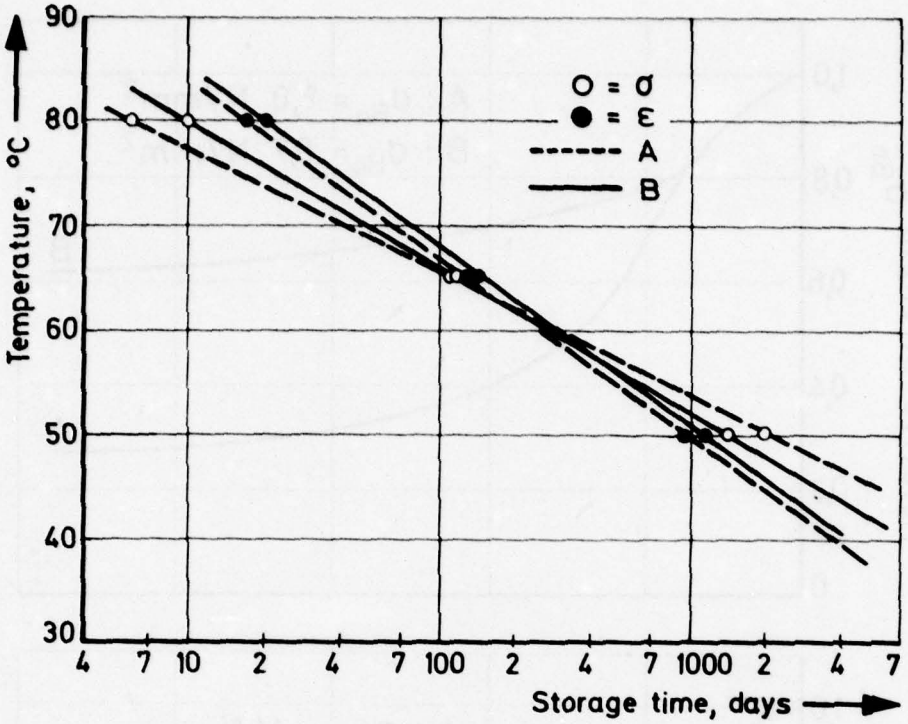

Fig. 2 Mechanical lifetime as a function of storage temperature

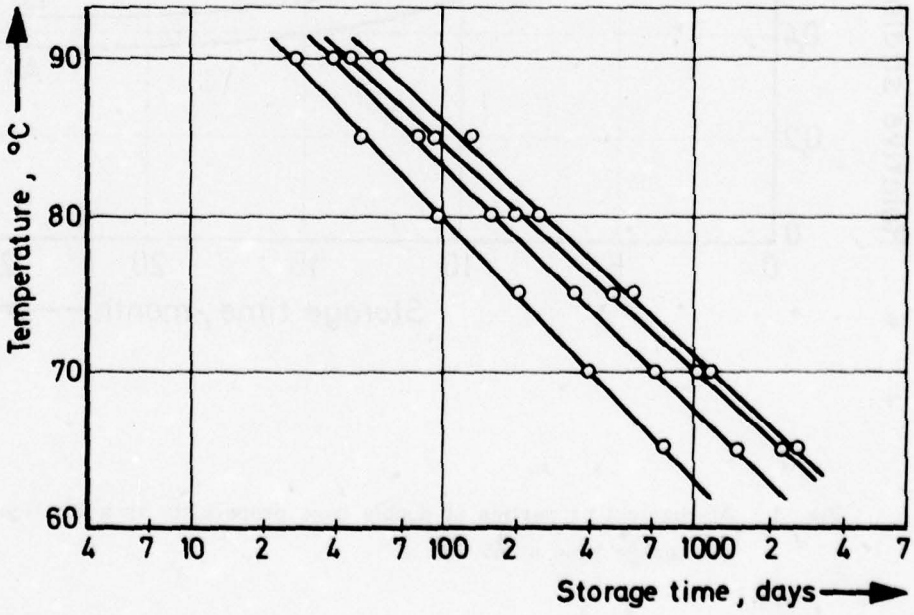

Fig. 3 Autocatalysis of propellants with different stabilizers

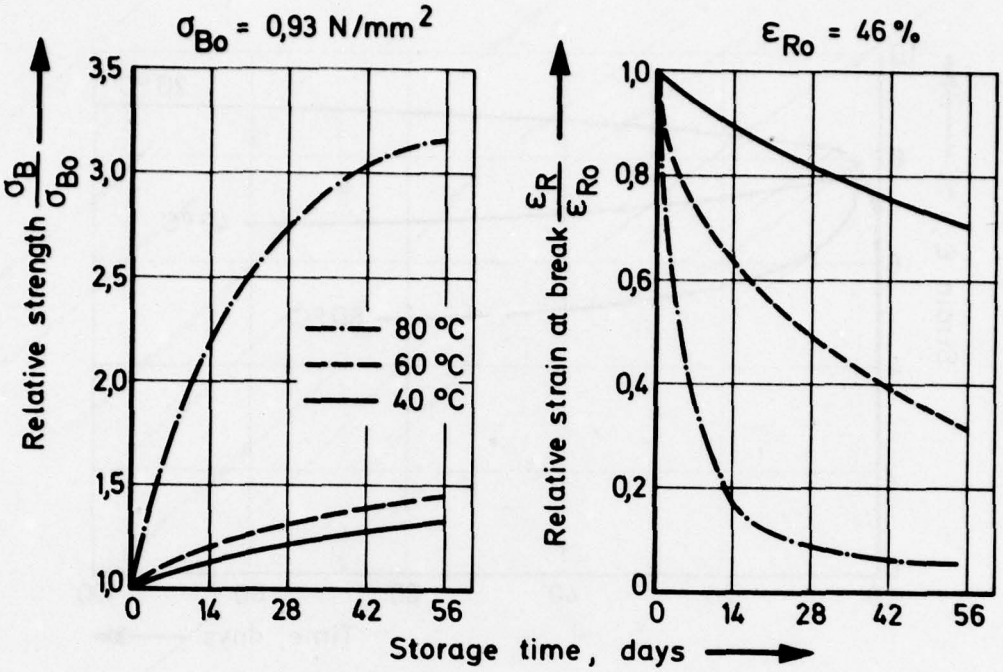

Fig. 4 Mechanical properties of a composite propellant as a function of storage time

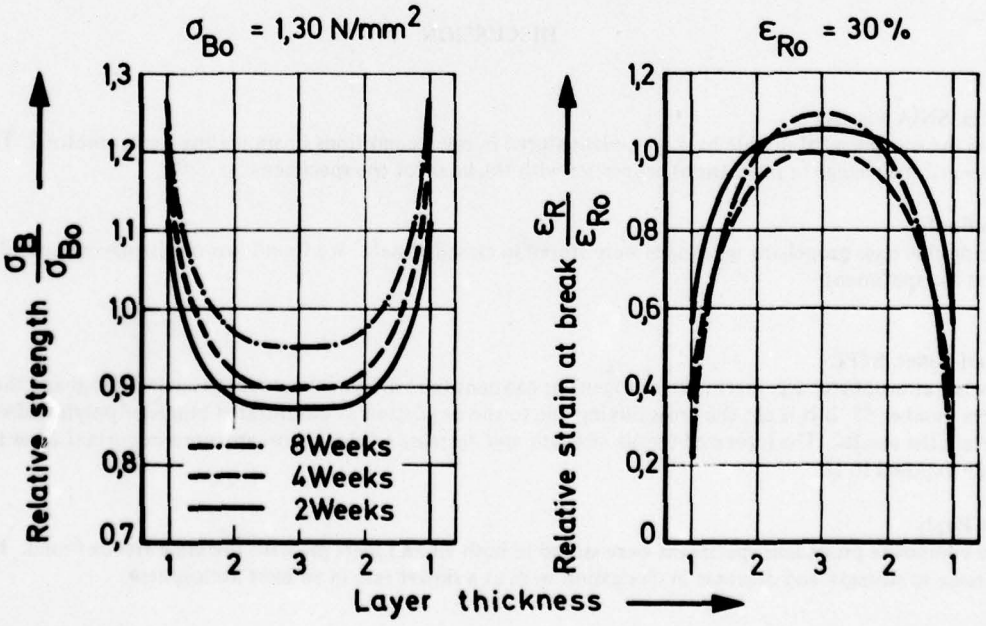

Fig. 5 Mechanical properties of a composite propellant as a function of layer thickness

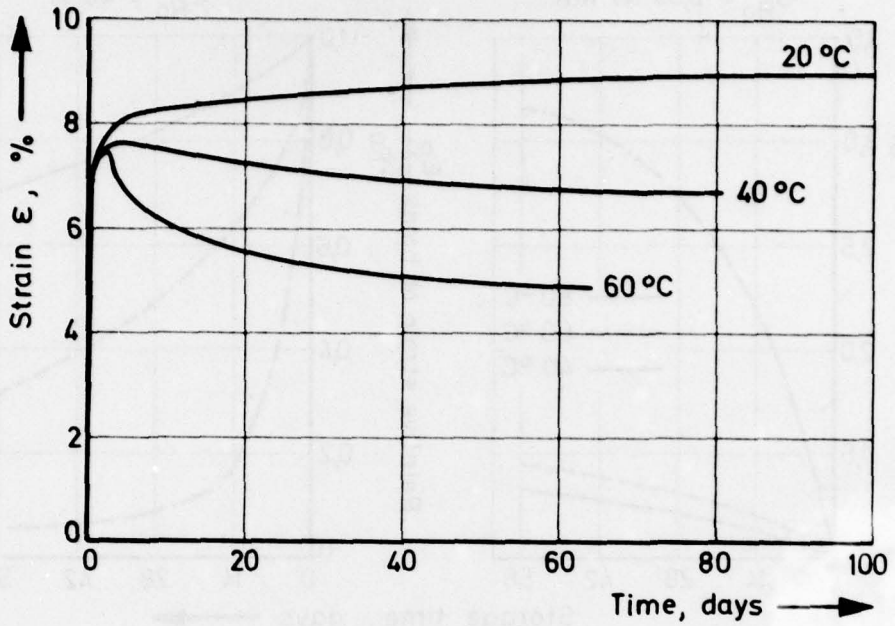

Fig. 6 Creep behaviour of a composite propellant

DISCUSSION

P.Spadetta, SNIA Viscosa

Were the specimens of double base propellant stored in open conditions or simulating rocket motors? This could influence the change of mechanical properties with thickness of the specimens.

Author's Reply

The double base propellant specimens were stored in closed vessels. We found loss of nitroglycerine and plasticiser from the specimens.

Mr Lanteri-Minet, STPE

In what atmosphere; e.g. inert (like nitrogen) or oxydant (air) did you conduct the ageing test giving the result of curve number 5? If it is air, the cross linking due to the oxydation of unsaturated bonds of polybutadienne would explain the results. The increased tensile strength and decrease of elongation are more important close to the surface when exposed to air.

Author's Reply

The composite propellant specimens were stored in both air and inert gas with the same trends found. However the increase in strength and decrease in elongation were at a slower rate in an inert atmosphere.

K.Klager, Aerojet, Solid Propulsion Company

Did you take humidity into account in your ageing tests?

Author's Reply

The influence of humidity was not examined. During the total storage period the relative humidity was less than 5%.

AMELIORATION DES PROPRIETES BALISTIQUES ET DES PROPRIETES MECANIQUES TOUS TEMPS DES PROPERGOLS SANS FUMEE

A. DAVENAS S.N.P.E. - DIRECTION TECHNIQUE AUTOPROPULSION
Centre de Recherches du Bouchet B.P. n° 2 - 91710 VERT-LE-PETIT - FRANCE

Depuis une vingtaine d'années on utilise couramment dans les propulseurs d'engins tactiques des propergols double-base moulés. Ces propergols ont un module d'élasticité élevé et un comportement vitreux en température et des performances balistiques : densité et impulsion spécifique limitées.
Pour augmenter les performances des propergols sans fumée il était donc nécessaire :
- d'augmenter leurs performances balistiques,
- de modifier les propriétés mécaniques de façon à leur conférer un comportement élastique dans un large domaine de température. Le propergol se prête alors à des chargements moulés-collés qui permettent un coefficient de remplissage plus élevé du propulseur.

Ce but a été atteint par la mise au point de propergols chargés aux nitramines (hexogène ou octogène) dont le liant est énergétique et réticulé.

Dans cette communication on expose des résultats fondamentaux sur l'influence de l'octogène ou de l'hexogène ainsi que l'effet du taux de plastifiant énergétique et de la réticulation sur les caractéristiques thermodynamiques, cinétiques et mécaniques du propergol. Une comparaison est effectuée avec les propriétés des propergols composites à liant hydrocarboné et octogène. On présente ensuite quelques caractéristiques des propergols mis au point à la suite de ces études et dégage des perspectives d'améliorations ultérieures.

1. INTRODUCTION

Depuis une vingtaine d'années on utilise des propergols sans fumée dans les chargements de missiles tactiques, particulièrement pour des missions où la fumée apporte soit une gêne pour le guidage depuis le poste de tir soit un risque de repérage du poste de tir ou du missile ("discrètion"). Ces propergols sont généralement des propergols double-base extrudés ou double-base moulés. Dans les deux cas, même si le procédé de fabrication très différent induit certaines différences de propriétés on retrouve des caractéristiques communes.

Du point de vue composition il s'agit d'un mélange de nitrocellulose et de plastifiants énergétiques (presque toujours la nitroglycérine) ou inertes dans lequel sont intimement dispersés des stabilisants et des modificateurs balistiques. L'homogénéité du mélange nitrocellulose-plastifiant est obtenue par un ensemble de processus chimiques de solvatation caractérisé globalement par le terme de "gélatinisation".

Les propriétés balistiques de ces produits sont limitées : la masse spécifique dépasse difficilement 1,60 et l'impulsion spécifique calculée (détente en équilibre 70 bars/1 bar) 240 secondes pour les double-base moulés.

Ces matériaux ont un module élastique élevé à température ambiante et à froid et un comportement vitreux aux basses températures, c'est-à-dire en particulier une capacité d'allongement très faible et un comportement non linéaire. Leur utilisation privilégiée est donc celle de blocs libres où leur module élevé permet de bien supporter la mise en pression d'allumage (ainsi d'ailleurs que les accélérations élevées). Leur utilisation en chargements moulés-collés à coefficient de remplissage intéressant n'est possible que par le biais de dispositifs complexes permettant de soulager les contraintes à froid.

On constate que ces produits ont par rapport aux propergols composites à liant polybutadiène développés depuis une vingtaine d'années des propriétés mécaniques et énergétiques très inférieures. Il était donc nécessaire d'améliorer ces propriétés en gardant le caractère "sans fumée". Il convient cependant de conserver au maximum deux qualités importantes des propergols double-base traditionnels : une fabrication "rustique" conduisant à des coûts relativement faibles en série et des propriétés cinétiques intéressantes pour le fonctionnement tous temps : coefficient de température minime et exposant de pression très faible grâce à l'utilisation de modificateurs balistiques appropriés.

Objectifs du programme

Depuis plusieurs années, sous l'égide du STPE (Service Technique des Poudres et Explosifs) la SNPE a mis en oeuvre un programme de recherche sélection et développement de propergols sans fumée pour chargements moulés à performances énergétiques et mécaniques améliorées pour deux grands types d'application :

- chargements libres, surtout en combustion frontale,
- chargements moulés-collés.

Moyens d'atteindre les objectifs

1. Augmentation de l'énergie

Dans le but d'augmenter l'énergie du propergol deux actions ont été retenues : l'utilisation de composés énergétiques solides de densité élevée, l'augmentation des taux de plastifiants énergétiques, si l'on utilise le liant double-base.

Les composés énergétiques nouveaux doivent être organiques pour conduire dans la combustion à une formation minimale d'espèces condensées ou recondensables responsables de fumées. Deux corps ont principalement été retenus après une préétude, comme dans les autres pays : l'hexogène (RDX) et l'octogène (HMX). Ces nitramines ont en effet une masse spécifique et une enthalpie de formation intéressantes ainsi qu'une stabilité chimique et une compatibilité très satisfaisantes vis-à-vis des "ingrédients" utilisés couramment dans les propergols solides. Par contre du fait de leur balance en oxygène nulle on les emploie au mieux avec des systèmes de liants relativement oxygénés particulièrement du type nitrocellulose-plastifiant nitré ou nitraté. L'incorporation de nitramines dans des liants très peu oxygénés tels que les liants polybutadiènesne conduit du point de vue thermodynamique à des performances intéressantes que pour des taux de ce liant faibles ou pour des nitramines plus oxygénées que l'hexogène ou l'octogène. On trouvera à la figure 1 une illustration de l'influence de l'oxygénation du système liant-composé énergétique sur l'impulsion spécifique pour deux liants et deux nitramines typiques :

- un liant peu oxygéné : polybutadiène
- un liant relativement oxygéné : polyester
- une nitramine peu oxygénée : octogène ou tétraméthylène tétranitramine
- une nitramine oxygénée : tétranitroglycoluryle (ce dernier composé est décrit dans le brevet de la référence (1)).

La performance maximale est obtenue :

- soit avec les systèmes à l'octogène à taux de liant très faible (plus faible avec polybutadiène qu'avec polyester) difficilement accessibles dans l'état actuel de la technique,
- soit avec des systèmes relativement oxygénés dans la zône plus accessible de 88 à 90 % de taux de charge massique (la masse spécifique de l'octogène est de 1,90, celle du tétranitroglycoluryle de 1,98) par des couples octogène-liant polyester ou polybutadiène-tétranitroglycoluryle.

2. Modification des propriétés mécaniques

Pour l'utilisation en bloc libre on recherche souvent des modules élastiques élevés, et l'emploi du liant double-base classique ou de liants de propergols composites se prête à ces applications. Pour l'utilisation en chargement moulé-collé il convient avant tout d'augmenter les allongements à basse température et ceci suppose l'emploi de liants élastiques à froid. La tenue à chaud sera alors obtenue par une réticulation du polymère empêchant son fluage. Si la densité de pontage n'est pas trop élevée elle modifiera peu les propriétés d'allongement à froid. On utilisera donc les liants de propergols composites ou on modifiera les liants double-base pour les rendre élastiques à basse température.

Plan de la recherche

Compte-tenu de l'analyse précédente nous avons décidé de porter notre effort dans un premier temps sur l'utilisation de nitramines relativement classiques : hexogène ou octogène et de liants de propergols composites classiques ou de liants double-base modifiés pour développer une première génération de propergols. Ultérieurement des nitramines plus nouvelles telles que le tétranitroglycoluryle peuvent, comme nous l'avons vu, être envisagées, seules celles-ci permettant d'espérer sérieusement concurrencer les liants énergétiques avec des liants du type hydrocarboné. Compte-tenu des difficultés de développement d'une matière première nouvelle il convient de toutes façons d'abord de bien cerner les possibilités et les limites des nitramines bien connues. Nous examinerons donc successivement les performances thermodynamiques et les caractéristiques cinétiques et mécaniques des propergols à l'hexogène ou à l'octogène, soit de type composite, soit de type double-base composite.

2. PERFORMANCES THERMODYNAMIQUES

Les deux systèmes étudiés : composite ou double-base composite présentent la particularité que l'impulsion spécifique et la masse spécifique augmentent régulièrement avec le taux d'octogène ou d'hexogène. Nous nous bornerons donc à examiner les résultats de calculs d'impulsion spécifique volumique Isp x ρ. L'impulsion spécifique est calculée à l'aide d'un programme analogue au programme NASA LEWIS SP 273 de Mac Bride et Gordon pour une détente en équilibre 70 bars à 1 bar. Bien que ce programme ne soit pas exempt de toute imperfection il a le mérite d'être utilisé couramment dans divers pays -à notre connaissance au moins les USA et la RFA- ce qui permet des comparaisons aisées. Par ailleurs l'intérêt de comparer des performances théoriques est de s'abstraire des conditions de mesure standard très variables selon les pays. Enfin nos comparaisons ont essentiellement un but de classement relatif des diverses solutions.

Les figures 2 et 3 nous indiquent les résultats de calcul pour les systèmes considérés. Les performances réellement accessibles ne peuvent être cernées que par la considération des limites technologiques du procédé de fabrication du point de vue taux de charge massique.

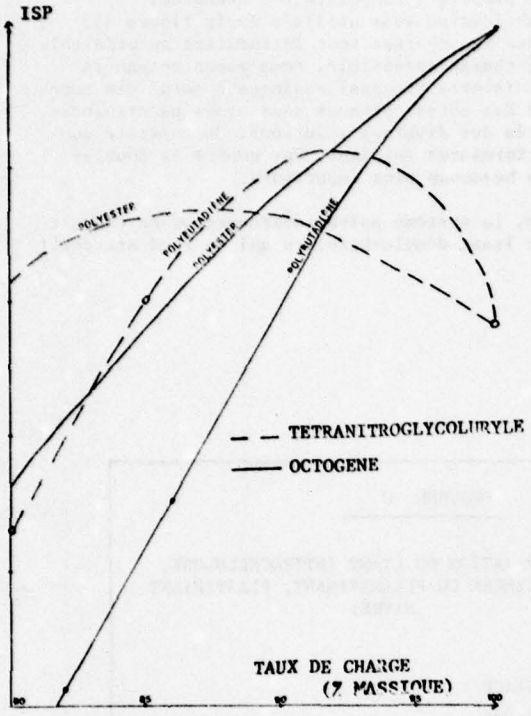

FIGURE 1 : INFLUENCE DU TAUX DE CHARGE SUR L'IMPULSION SPECIFIQUE

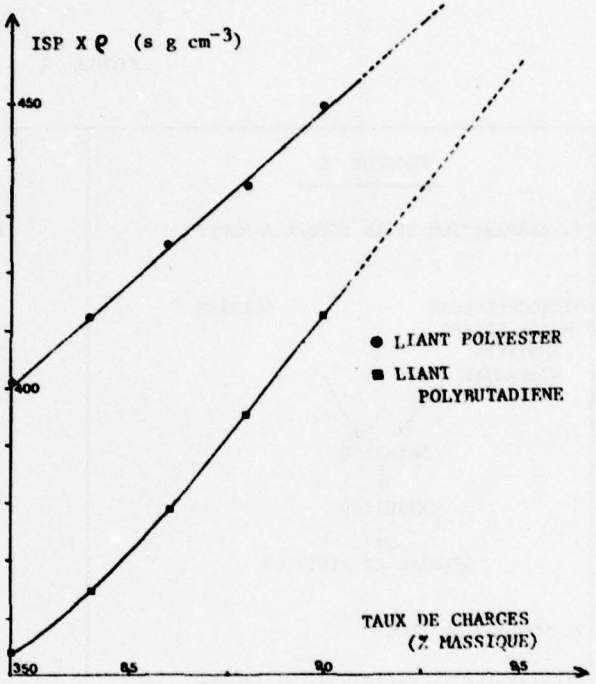

FIGURE 2 : IMPULSION VOLUMIQUE EN FONCTION DU TAUX DE CHARGES (HMX)

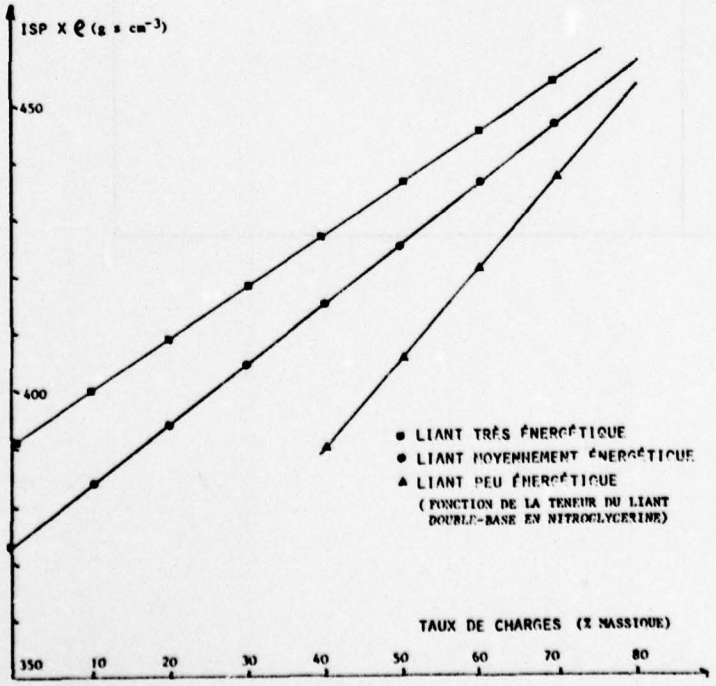

FIGURE 3 : IMPULSION VOLUMIQUE EN FONCTION DU TAUX DE CHARGES (HMX)

Sur la base d'études expérimentales nous avons retenu une limite de 90 % en liant polybutadiène et de 86 % en liant polyester pour la possibilité de couler un propergol composite à l'octogène.
Pour le propergol double-base composite deux procédés de fabrication sont utilisés (voir figure 4).
Pour le procédé E (casting powder process) dans lequel toutes les charges sont introduites au préalable dans une poudre à mouler ce qui limite fortement le taux de charge accessible, nous avons retenu la limite de 50 % pour le propergol terminé. Pour le procédé G (slurry process) analogue à celui des composites ou la limite de faisabilité est liée à la viscosité des pâtes obtenues nous avons pu atteindre 80 %. Dans ces conditions la figure 5 résume les possibilités des diverses solutions. On constate que la solution composite et la solution E conduisent à des performances voisines. Par contre la double-base composite G laisse espérer des niveaux de performances beaucoup plus importants.

Remarque : Pour des impulsions spécifiques pas trop élevées, le système polybutadiène-octogène conduit cependant à des températures de chambre plus faibles que le liant double-base, ce qui le rend attractif pour des applications de générateur de gaz.

FIGURE 4

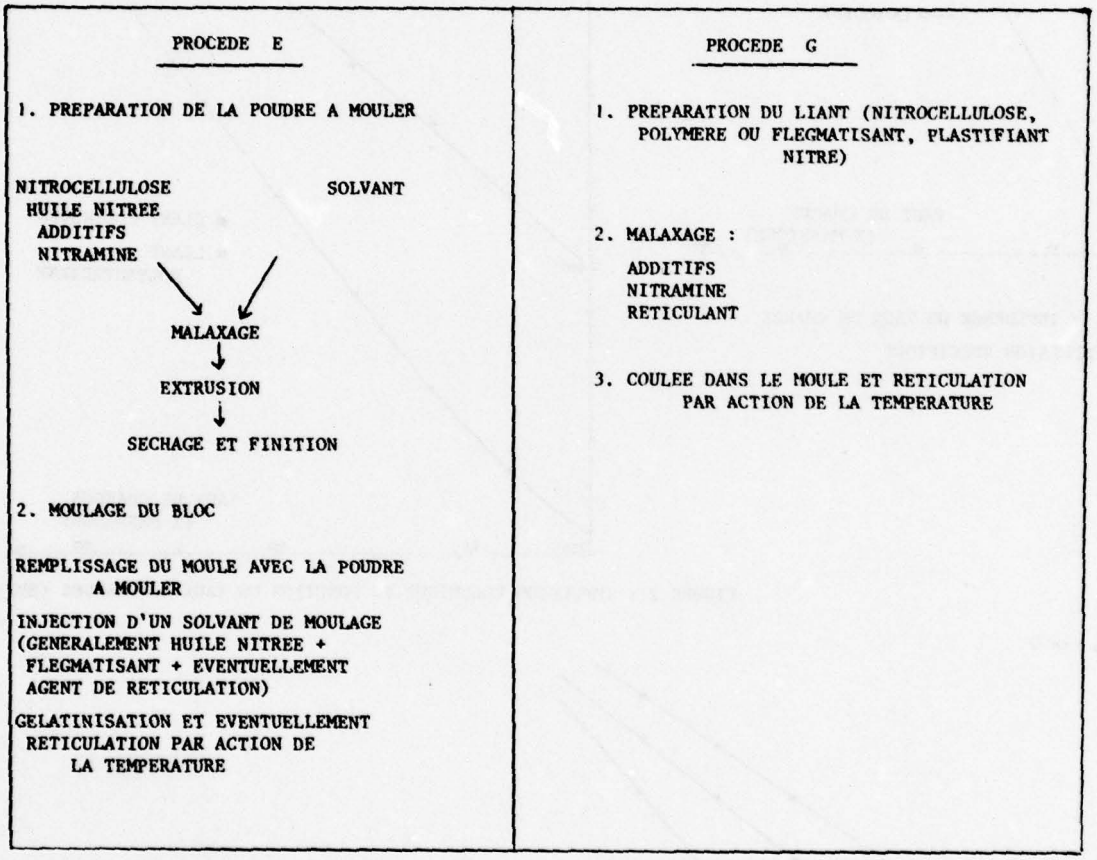

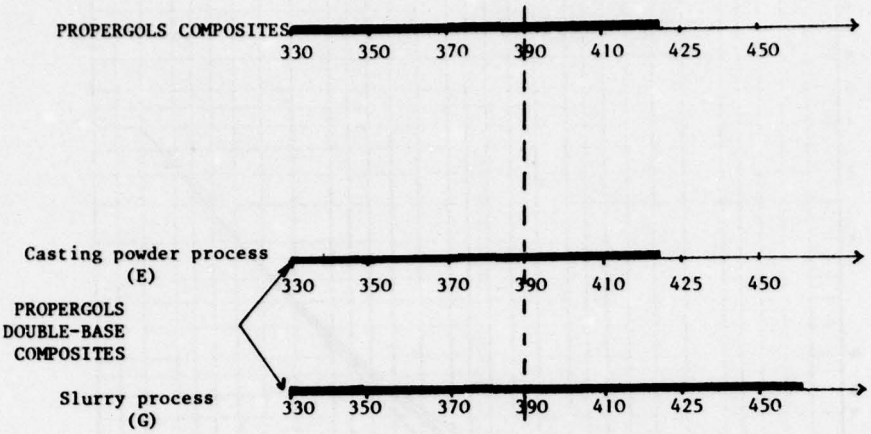

FIGURE 5 : PERFORMANCES THEORIQUES ACCESSIBLES (impulsion volumique)
COMPARAISON PROPERGOLS COMPOSITES - PROPERGOLS DOUBLE-BASE COMPOSITES

3. CARACTERISTIQUES CINETIQUES

1. Propergols composites

La figure 6 représente l'évolution de la vitesse de combustion en fonction de la pression pour un propergol à liant polybutadiène et une seule granulométrie d'octogène, sans aucun modificateur balistique. On retrouve un comportement mis en évidence par de nombreux auteurs dont le premier à notre connaissance fut Zimmer-Galler (2) : la vitesse de combustion aux pressions moyennes est faible. A une pression d'autant plus basse que la granulométrie de l'octogène est élevée on assiste à une modification du mécanisme de combustion généralement attribuée à un chargement d'état de surface du propergol en combustion. A basse pression la surface est en fusion, alors qu'à haute pression la nitramine brûle plus vite que le liant "inactif", formant une surface "cratérisée" (3). L'exposant de pression voisin de 0,7 à basse pression passe ensuite à des valeurs supérieures à 1. Pour un propergol formulé avec plusieurs granulométries la zône de transition devient continue (figure 7) et aux taux de charge de 86 % un fonctionnement correct en propulseur ne peut être obtenu au-dessous de 100 bars dans le cas présenté. Il est toutefois possible de modifier un peu la forme de la courbe au-dessous de 100 bars par des additifs sans que nous ayons réussi à obtenir une véritable "platonisation" (figure 7).

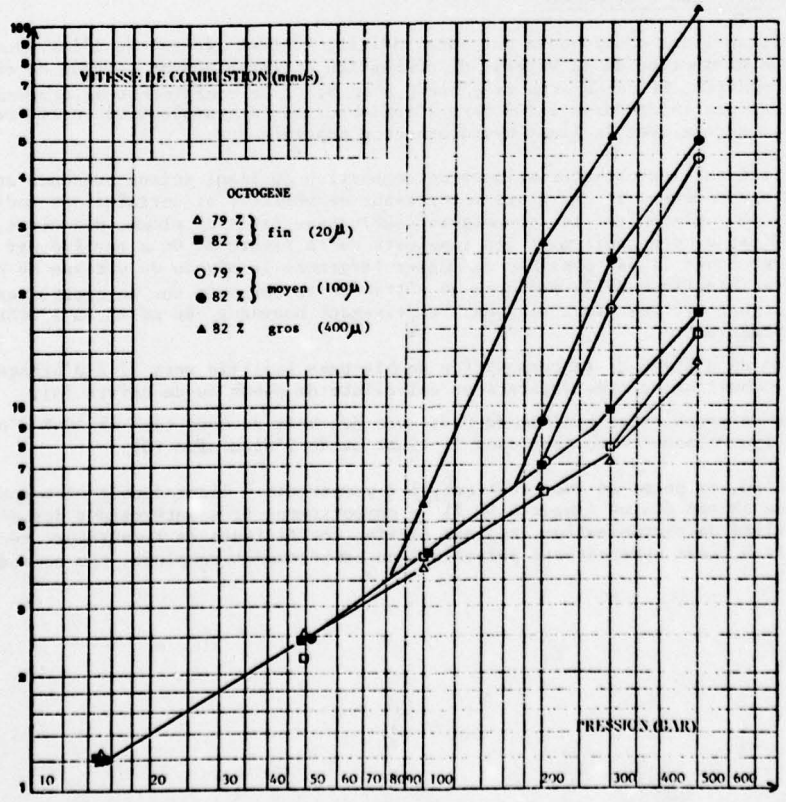

FIGURE 6 : INFLUENCE DE LA GRANULOMETRIE DE LA CHARGE
(une seule granulométrie)

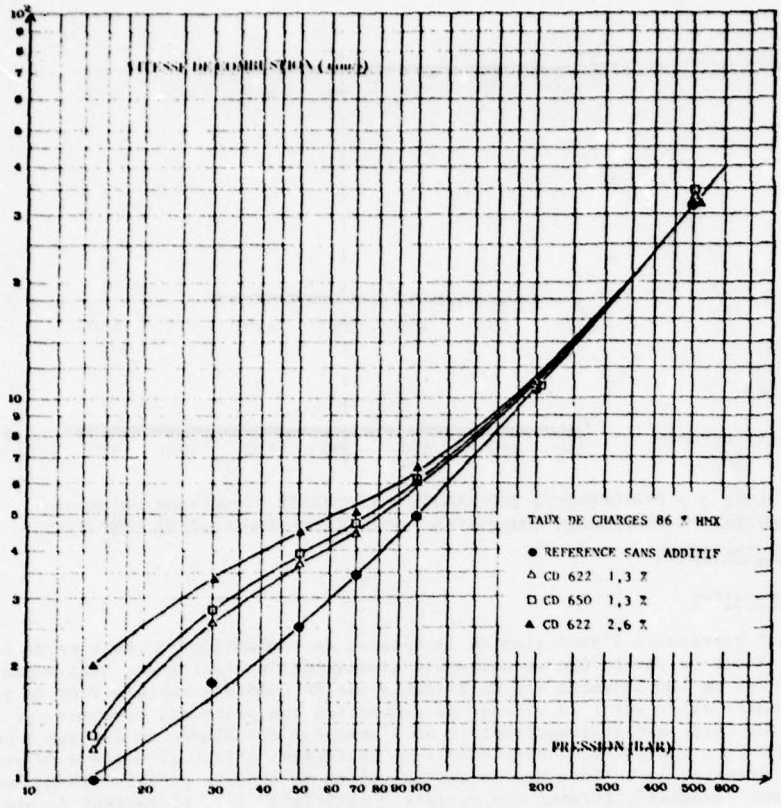

FIGURE 7 : MODIFICATION DE LA LOI V(P) INCORPORATION DE CATALYSEURS

2. Propergols double-base composites

Par rapport au liant double-base pur sans additif, l'effet général de l'introduction d'hexogène ou d'octogène est une diminution de la vitesse de combustion croissante avec le taux de charge. L'exposant de pression est peu modifié, il reste compris entre 0,6 et 0,8 , le coefficient de température est diminué. Dans la zône des pressions inférieures à 300 bars l'influence de la granulométrie n'est pas significative et la discontinuité observée avec le liant hydrocarboné n'apparait pas.

Il semble ici que les caractéristiques de combustion du liant soient prépondérantes, du moins pour des taux de charge modérés. Il est alors intéressant de vérifier si certains des modificateurs balistiques utilisés pour platoniser les propergols double-base (sels de plomb, de cuivre, complexes, etc...) restent efficaces. C'est ce que confirment les résultats de la figure 8. On a vérifié par ailleurs que pour un taux de charge donné il est possible de régler largement le niveau de vitesse de combustion au plateau. Enfin l'effet bénéfique de la présence de nitramine se retrouve sur le coefficient de température à divers serrages (figure 9). Ces résultats sont relativement nouveaux. En effet la littérature mentionne pour ce domaine de pression :

- soit la disparition du plateau de la composition double-base initiale vers 27 % d'octogène avec des modificateurs de combustion du type stéarate ou salycilate de plomb ou de cuivre (4),
- soit des exposants de pression au minimum de 0,45 avec des sels du même type et 40 % d'octogène mais avec en plus un polyuréthanne renforçant dans le liant et de l'aluminium (5).

En conclusion, du point de vue cinétique, les propergols à liant double-base conservent dans le domaine de taux de charge évalué (jusqu'à 50 %) le comportement très intéressant des double-base classiques : possibilité de platonisation, réglage facile, coefficients de température réduits. Par contre les propergols à liant hydrocarboné présentent un comportement complexe, peu commode pour l'utilisateur.

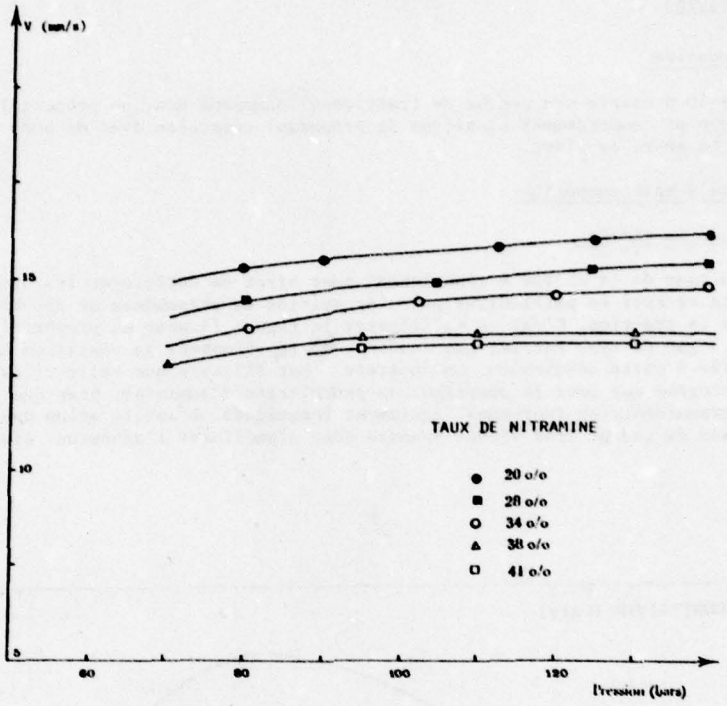

FIGURE 8 : MODIFICATION DE LA LOI V(P) INCORPORATION D'ADDITIFS RALISTIQUES

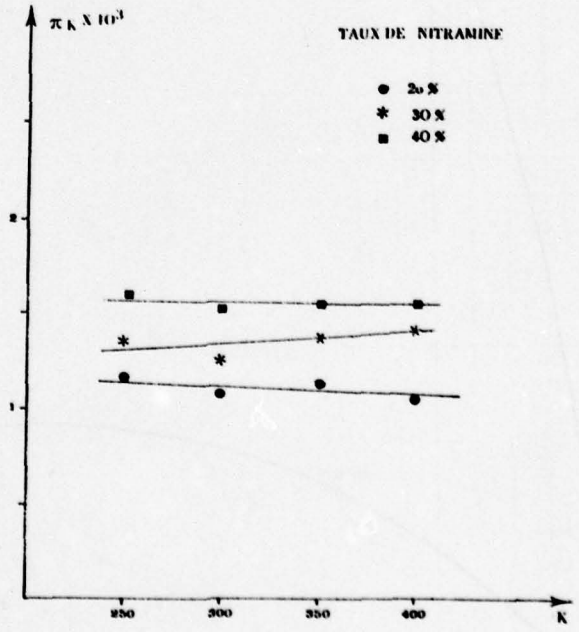

FIGURE 9 : EVOLUTION DES COEFFICIENTS DE TEMPERATURE
EN FONCTION DU SERRAGE A DIFFERENTS TAUX DE CHARGES

4. PROPRIETES MECANIQUES

1. Propergol composite

La figure 10 présente une courbe de traction-allongement pour un propergol polybutadiène-octogène. On retrouve un comportement classique de propergol composite avec de bons allongements à froid, typiques de ce genre de liant.

2. Propergol double base composite

a) Influence de la charge

L'introduction de la charge a globalement pour effet de détériorer les propriétés mécaniques du liant double-base et ceci en particulier par l'apparition de phénomènes de décohésion entre la charge et le liant lors de la traction. C'est ce qu'illustre la figure 11 pour un propergol tractionné à 20° sur un dilatomètre à gaz de type Farris. Les courbes $\frac{\Delta V}{V}$ représentent la variation de volume en traction de l'éprouvette, liée à cette décohésion. On constate par ailleurs que celle-ci est plus grande pour le propergol à l'octogène que pour le propergol au perchlorate d'ammonium, bien que les liants soient identiques et les granulométries (moyennes) également identiques. L'amélioration des propriétés mécaniques surtout pour les taux de charge très élevés suppose donc d améliorer l'adhésion liant-charge de ces systèmes.

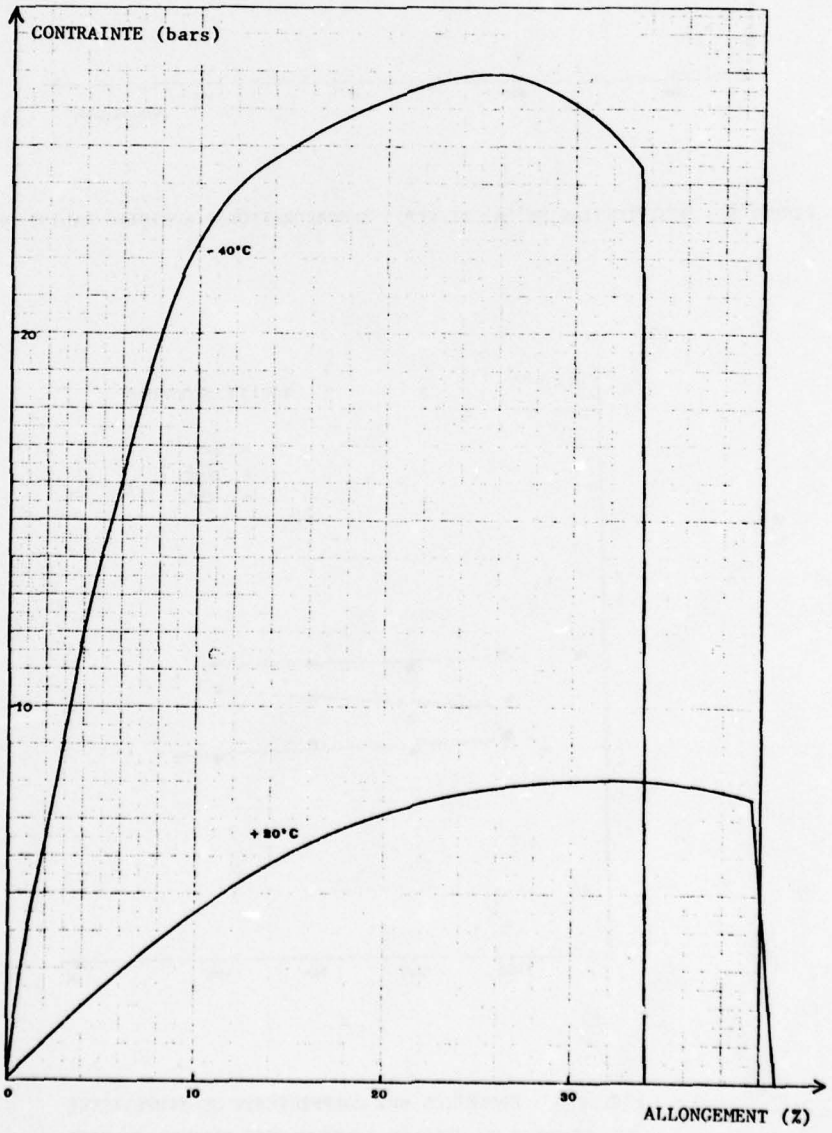

FIGURE 10 : PROPRIETES MECANIQUES D'UN PROPERGOL COMPOSITE A L'OCTOGENE

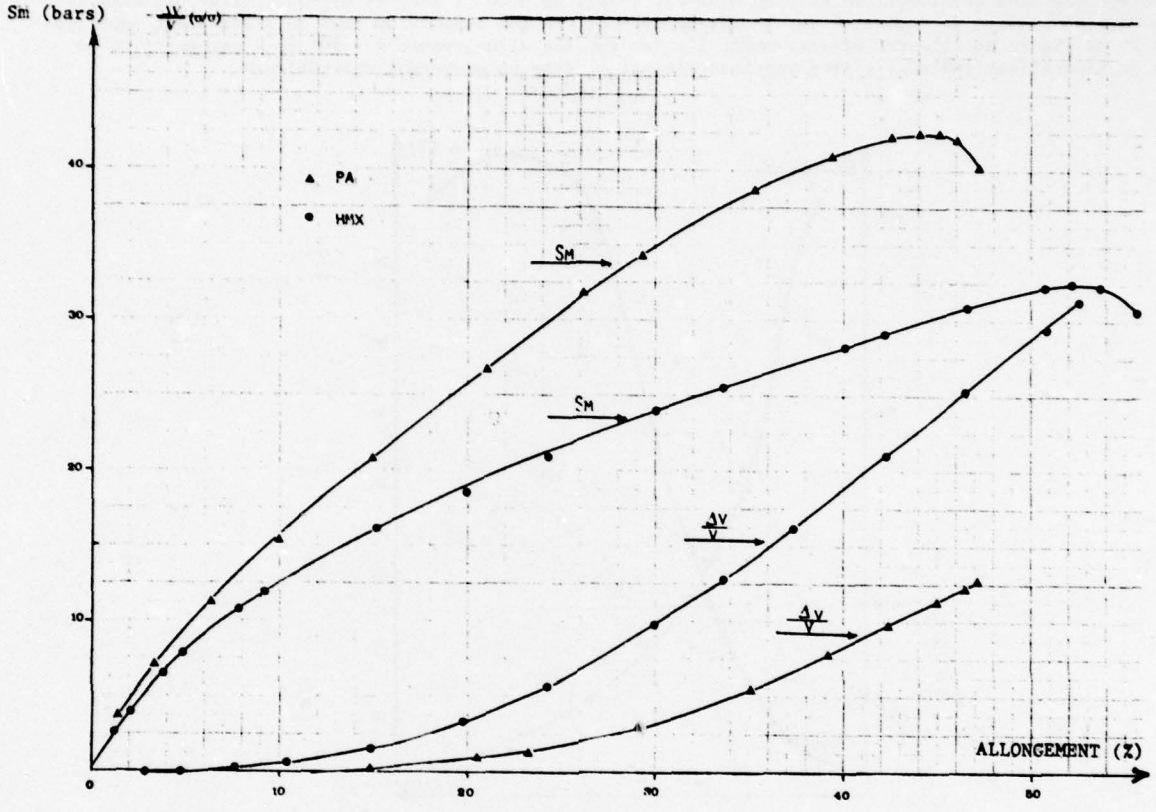

FIGURE 11 : PROPRIETES MECANIQUES DES PROPERGOLS DOUBLE-BASE COMPOSITES

b) Propriétés à basse température

Les propergols double-base classiques sont en général vitreux à basse température et ont donc des capacités d'allongement très faibles, de quelques pour cents (figure 12). Le passage du domaine caoutchoutique au domaine vitreux peut être repéré par le point de transition vitreuse (Tg) du matériau. La figure 13 montre l'évolution de Tg mesuré par analyse thermique différentielle pour deux couples nitrocellulose-plastifiant énergétique. Le taux de plastifiant utilisé dans les double-base classiques est inférieur à 45 % et Tg est alors supérieur à - 40°. A titre de comparaison, Tg pour le liant polybutadiène que nous avons utilisé en composite est voisin de - 80 °. Avec la nitroglycérine par exemple il parait nécessaire de repousser Tg en-dessous de - 50° ce qui suppose un taux de plastifiant supérieur à 70 %. La figure 14 illustre effectivement l'effet sur les allongements à - 40° de l'augmentation du taux de plastifiant (mélange nitroglycérine-triacétine) dans un propergol non réticulé.

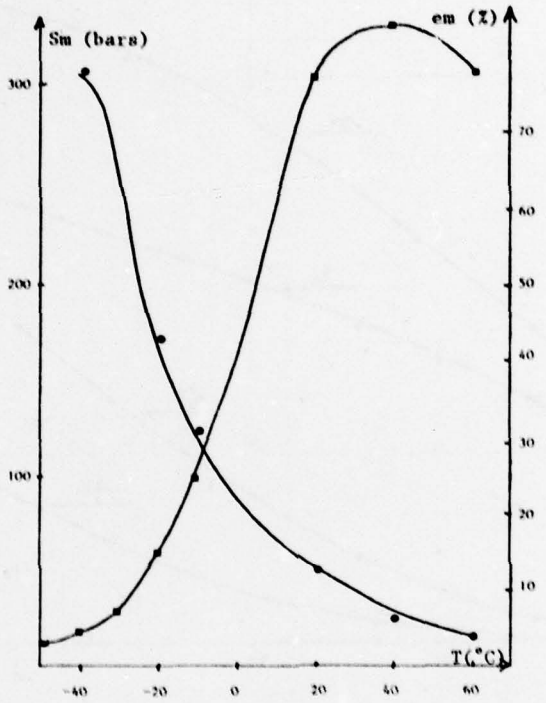

FIGURE 12 : PROPRIETES MECANIQUES EN TEMPERATURE POUR UN LIANT DOUBLE-BASE CLASSIQUE

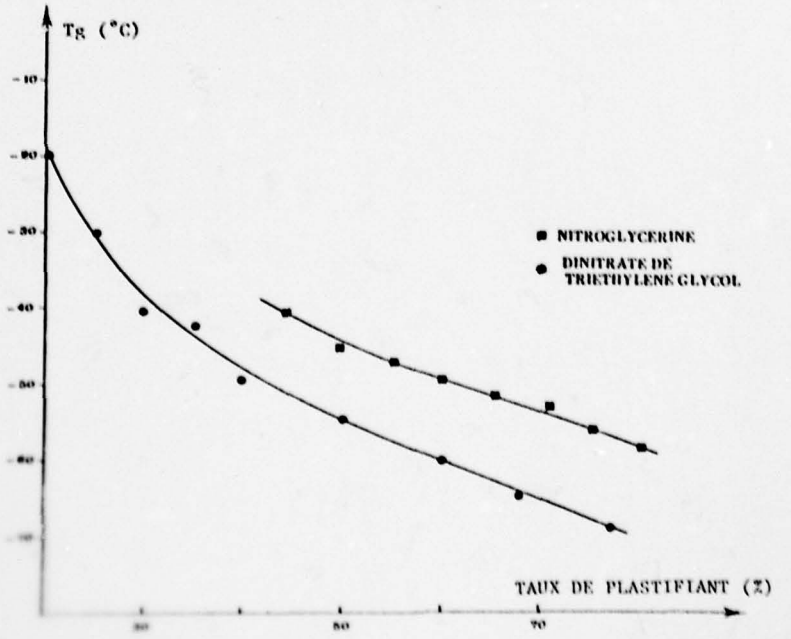

FIGURE 13 : EVOLUTION DE Tg EN FONCTION DU PLASTIFIANT

L'un des inconvénients de ces taux élevés de plastifiant est bien entendu la chute des propriétés mécaniques à chaud. La figure 15 montre ainsi l'évolution de la contrainte à allongement maximum mesurée à 60° pour des taux de plastifiant croissant. Le module subit une évolution tout à fait parallèle. Ceci est lié à la diminution des interactions entre les chaînes de nitrocellulose qui confèraient la cohésion du matériau. Il est possible de retrouver une cohésion comme dans le cas des propergols composites en utilisant les fonctions hydroxyles initiales de la cellulose non estérifiées, qui restent très nombreuses.

En réalité toutes les fonctions ne sont pas accessibles mais il suffirait qu'en moyenne deux par chaîne le soient pour pouvoir transformer cet ensemble de macromolécules en une seule macromolécule et un peu plus de deux pour former un réseau tridimensionnel. Comme il y a nettement plus de deux hydroxyles disponibles par chaîne, la réaction avec un diisocyanate devrait conduire à un optimum de propriétés mécaniques pour un rapport fonction isocyanate/fonctions hydroxyles de la nitrocellulose nettement inférieur à 1.

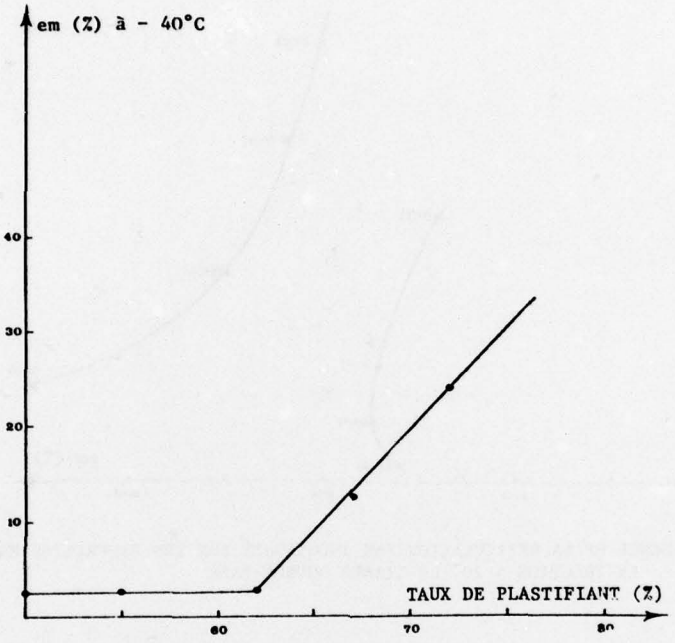

FIGURE 14 : INFLUENCE DU TAUX DE PLASTIFIANT SUR LES NIVEAUX D'ALLONGEMENTS EN TRACTION A - 40°C

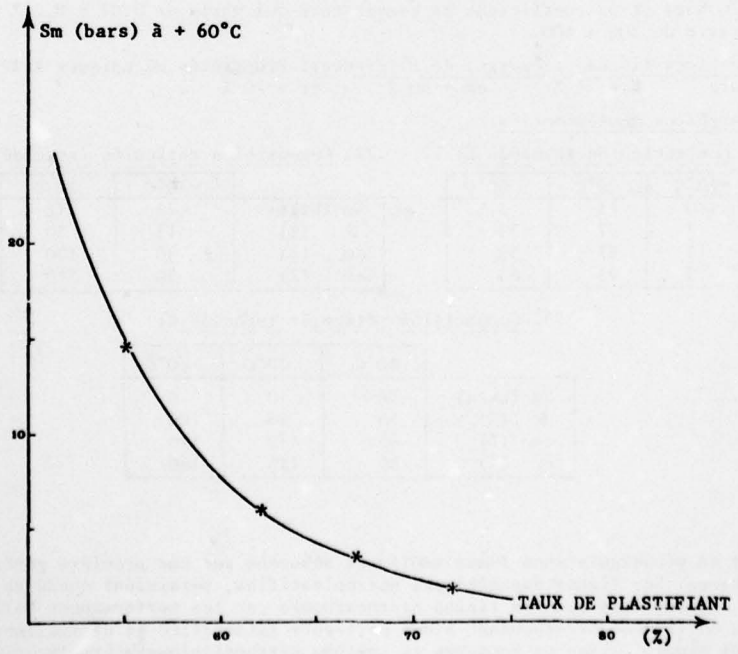

FIGURE 15 : INFLUENCE DU TAUX DE PLASTIFIANT SUR LA CONTRAINTE MAXIMUM EN TRACTION A + 60°C

La figure 16 représente dans un diagramme Sm, em pour diverses teneurs en plastifiant énergétiques l'effet très important de la réticulation sur les propriétés mécaniques du liant double-base. Naturellement dans ces systèmes la réaction de réticulation est un processus beaucoup plus complexe que dans les polymères classiques car il y a simultanément gonflement et gélatinisation de la nitrocellulose par le plastifiant et diffusion de l'isocyanate et réaction de celui-ci dans les parties gonflées plus "mobiles". Cette réticulation peut être effectuée tant dans le procédé G que dans le procédé E l'isocyanate étant alors généralement introduit en solution dans le solvant de moulage.

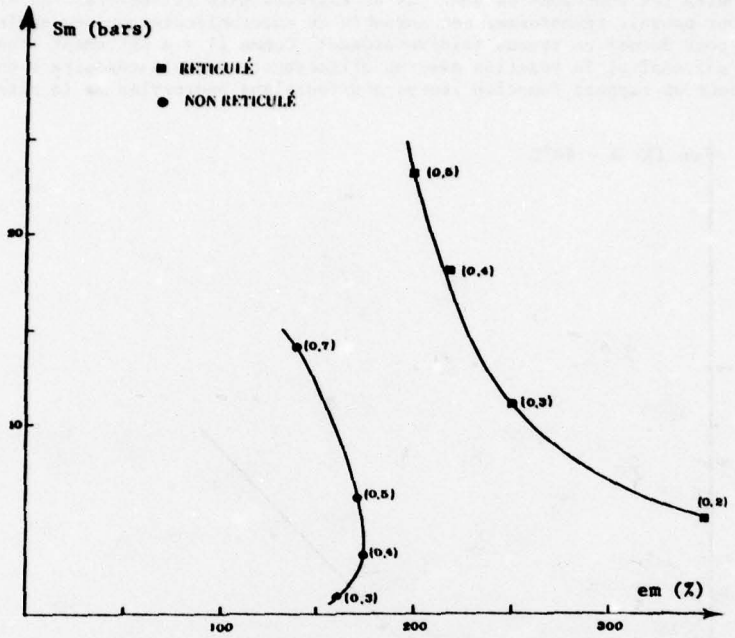

FIGURE 16 : INFLUENCE DE LA RETICULATION PAR ISOCYANATE SUR LES PROPRIETES MECANIQUES EN TRACTION A 20° DE LIANTS DOUBLE-BASE

5. APPLICATION

Nous illustrerons l'application de ces diverses considérations au réglage des propriétés mécaniques sur un propergol contenant 35 % d'hexogène et dont la masse spécifique et l'impulsion spécifique varieront légèrement autour de 1,65 et 245 s en fonction de la composition du liant (taux de nitroglycérine, de réticulant...). Le propergol de référence a un domaine de vitesse utilisable de 7 à 15 mm/s entre 50 et 120 bars et un coefficient de température qui varie de 0,02 à 0,2 % par degré Celsius lorsque le serrage K varie de 300 à 400.

1. Composition pour blocs libres (propergol de référence). Propriétés mécaniques à 20 °C
   Sm = 25 bars ε = 25 % em = 60 % er = 70 %

2. Compositions pour blocs moulés-collés

21. Composition non réticulée (procédé E)

	-40°C	20°C	60°C
Sm (bars)	160	15	3,5
ε (%)	7	57	39
em (%)	13	87	59
er (%)	13	91	63

22. Composition réticulée (procédé E)

	-40°C	20°C	60°C
Sm (bars)	70	12	5
ε (%)	12	50	60
em (%)	30	100	90
er (%)	30	110	100

23. Composition réticulée (procédé G)

	-40°C	20°C	60°C
Sm (bars)	50	10	6
ε (%)	15	90	100
em (%)	45	110	120
er (%)	45	115	130

CONCLUSION

La recherche de propergols sans fumée améliorés débouche sur une première génération utilisant de l'hexogène comme charge. Les liants énergétiques nitroplastifiés, paraissent conduire avec ces nitramines à des propergols plus intéressants que les liants hydrocarbonés car les performances balistiques sont obtenues pour des taux de liants correspondant à une meilleure faisabilité et de meilleures propriétés mécaniques du propergol final. Lorsqu'on conserve le système nitrocellulose-nitroglycérine comme base du liant il est possible jusqu'à au moins 50 % de nitramine de conserver un mécanisme de combustion du type double-base avec des exposants de pression et des coefficients de température très favorables. Enfin les propriétés mécaniques des double-base moulés classiques peuvent être considérablement améliorées par une plus grande plastification et une réticulation du liant les rendant aptes à des utilisations en chargement moulé-collé dans un large domaine de température.

BIBLIOGRAPHIE

(1) BOILEAU.J , EMEURY J.M et KEHREN J.P
Brevet français 73 27038 du 24 juillet 1973

(2) ZIMMER-GALLER R.
"Correlation between Deflagration Characteristics and Surface Properties of Nitramine-Based Propellants", AIAA Journal n° 11, Nov. 1968 p 2107

(3) COHEN N.S et PRICE C.F
"Combustion of Nitramine Propellants"
AIAA Paper 75-238, AIAA 13 th Aerospace Sciences Meeting, Pasadena, CA, Janv. 1975

(4) SUMI K. , KUBOTA N.
"Reduction of Plateau-Burning Effect of HMX Based CMDB Propellant,
Proc. Int. Symp. Space Technol. Sci. 11th, 1975, pp 157-166

(5) KLOHN W.
"High Energy Composite Double-Base Solid Propellants"
AGARD-PEP 47th Meeting Portz-Wahn, Mai 1976

(6) ALLABASHI J.C
"Cross-linked Nitrocellulose Propellant Formulation"
United States Patent 4,011,114 du 8 mars 1977

DISCUSSION

W.H.Klöhn, ICT, Ge

Your paper referred to two smokeless double base propellants, namely Type E based on the casting powder process and Type G the slurry process. What form did the nitrocellulose take in both processes?

Author's Reply

In Type E nitrocellulose of 12.5–12.6% N was incorporated into the powder by the classical means. In the Type G two forms of NC could be used. Firstly as in Type E except in the physical form of microspheres or fluid balls and secondly nitrocellulose of low DP directly dissolved in the nitric ester plasticiser.

W.H.Klöhn, Ge

You have used burning rate modifiers to change the pressure exponent of the nitramine filled double base propellants. How did you incorporate these modifiers?

Author's Reply

The results, shown in the paper, of the influence of nitramine filler level on burning rate platonisation were obtained from the classical casting powder process. The classical process is very good for platonisation, particularly the dispersion of the modifiers with the NC. I do not think the new processes such as fluid balls, polymer mix etc. can compare.

W.H.Klöhn, Ge

What kind of polymeric binder was preferred for the composite double base propellant? What binder was used for the composite propellant?

Author's Reply

In the case of the double base propellants we used compatible polymers especially polyesters. The composite propellants consisted of HTPB plus HMX filler.

SOME PROBLEMS OF NONLINEAR WAVES IN SOLID PROPELLANT ROCKET MOTORS

F. E. C. Culick
California Institute of Technology
Pasadena, California 91125

ABSTRACT

This paper is concerned with analyses of nonlinear waves in solid propellant rockets. Most attention is given to an approximate technique which inexpensively provides results which appear to be quite accurate at least up to amplitudes of ten percent. The connection with linear stability analysis is shown. Primarily to study nonlinear stability, or triggering, the method is extended to third order in the amplitude of wave motion; no explicit results have been obtained. Application of the approximate method to the behavior of pulses is described.

I. INTRODUCTION

It is now well-known that unsteady motions must be expected to occur sometime during the development of a solid propellant rocket motor. We refer here not to the inevitable ignition and extinction transients, or to random noise. Rather we mean wave motions which are in some manner related to the normal modes of oscillation in the chamber. A wave of this sort arises because of the enormous amount of energy available in a chamber having relatively low losses. The phenomenon is generically called combustion instability, although its existence does not rest on any unstable processes of combustion.

Many of the features of the general problem are in fact matters of acoustics. The essential requirement for the occurrence of combustion instability is the sensitivity of combustion processes to variables of the acoustic field, mainly pressure and velocity. This coupling constitutes a feedback loop and to an external observer measuring pressure, for example, the appearance of combustion instability may be interpreted as an unstable motion of a self-excited system.

Consequently, a small amplitude instability grows exponentially in time according to linear analysis. It will reach a limiting amplitude only if some sort of nonlinear processes are acting. The system may then execute a stable limit cycle. Questions of considerable practical importance concern determination of the conditions under which a limit cycle is attained; the character of the wave motion in the limit cycle; and especially how the limiting amplitude might be reduced.

The techniques described here are intended ultimately to produce approximate answers to those questions. In earlier work (references 1 and 2) we have been able to demonstrate the usefulness of the methods, and to show that the results are satisfactorily accurate under realistic conditions. However, the questions raised above remain unanswered, partly because only special cases have been examined.

In previous works, the stability of stationary or standing waves has been studied. The nonlinear acoustics has been treated only to second order in the wave amplitude. Here we obtain a few results for some special problems of pulse propagation. These are particularly relevant to certain instances of instabilities in motors when the unsteady motions have been induced by the ejection of a piece of material through the exhaust nozzle. That sort of problem is simulated in the laboratory by pulse testing, either by using explosive charges or by ejecting a small pellet. It is likely that pulse testing of motors may eventually become a standard procedure during development, to verify stability to finite disturbances. The analysis developed here is directly applicable.

Extension of the analysis to third order in the wave amplitude is a more fundamental matter. All of the calculations done to date with second order acoustics suggest that when it exists, the limit cycle - in particular the limiting amplitude - is independent of the initial conditions. Perhaps the most important consequence of this feature is that in its present state, the formulation of the acoustics does not contain truly nonlinear instability, or triggering. We mean by that term that a system which is stable to small disturbances may be unstable if the disturbance is sufficiently large. If the system has a single degree of freedom, then it is easy to show (reference 3) that triggering does not exist if the nonlinearities are of second order and monotonic in the amplitude. The numerical calculations have suggested that the result is true as well for a system having many degrees of freedom. For all the examples treated to date, the characteristics of the limit cycle are independent of the initial conditions. We develop here the equations to third order necessary to examine triggering. Thus the general analysis is now applicable to a wider range of practical problems.

There is another way of formally producing triggering, which will not be studied here. That is simply to include a destabilizing process which doesn't act unless the amplitude exceeds a specified level. Velocity coupling exhibits that sort of behavior in solid propellant motors. It can be incorporated within the analysis discussed here.

The results presented in this paper are of a general nature and are not directed to a particular motor. It is important to emphasize that all of this work involves expansion of the unsteady flow field in the normal modes of the chamber, and subsequent use of the method of averaging. Thus the behavior of pulses can be interpreted in terms of normal modes, a procedure which has certain

conceptual advantages and also provides a particularly easy means of incorporating empirical information. With the method of averaging, only first order ordinary differential equations must be solved. The calculations are therefore much less expensive than those done with second order equations not averaged.

II. GENERAL FORMULATION FOR SECOND ORDER ACOUSTICS

The nonlinear analysis we shall discuss here has been constructed to be a logical extension of the conventional linear stability analysis. Results for the stability of an arbitrary small amplitude disturbance can be obtained by treating the stability of the normal modes. That procedure not only simplifies the computations required but greatly promotes physical insight.

Practically all of our present understanding of the stability of linear motions in a solid propellant rocket motor is expressed in terms of normal modes. It is therefore obviously advantageous to extend that viewpoint to nonlinear behavior and to the propagation of pulses. In this section we review briefly the procedures developed in reference 2 for second order acoustics. Extension to higher order is described in the following section.

In the earlier work (reference 2), both the pressure and velocity fields were expressed as sums of average and fluctuating values: $p = p_o + p'$; $\vec{u} = \bar{\vec{u}} + \vec{u}'$. Eventually only terms of the order of squares of the fluctuations were retained in the conservation equations; we call that subject generally 'second-order acoustics'. Briefly the analysis is worked out in the following way. By suitable combination of the conservation an inhomogeneous wave equation can be deduced for the pressure disturbance;

$$\frac{1}{a^2}\frac{\partial^2 p'}{\partial t^2} - \nabla^2 p' = -h \tag{2.1}$$

This is accompanied by the inhomogeneous boundary condition

$$\hat{n}\cdot\nabla p' = -f \tag{2.2}$$

The functions h and f depend nonlinearly on both the pressure and velocity fluctuations. The pressure and velocity fields are now expressed as syntheses of the normal modes $\psi_i(\vec{r})$, each mode having a time-dependent amplitude $\eta_i(t)$:

$$\frac{p'}{p_o}(\vec{r},t) = \sum_{i=0}^{\infty} \eta_i(t)\psi_i(\vec{r}) \tag{2.3}$$

$$\vec{u}' = \sum_{i=1}^{\infty} \frac{\eta_i(t)}{\gamma k_i^2}\nabla\psi_i(\vec{r}) \tag{2.4}$$

The normal modes are those for a volume having the same shape as the combustion chamber, and enclosed by a rigid boundary. They satisfy the equation and boundary condition

$$\nabla^2\psi_i + k_i^2\psi_i = 0 \tag{2.5}$$

$$\hat{n}\cdot\nabla\psi_i = 0 \tag{2.6}$$

where k_i is the wavenumber for the ith mode. Term by term, (2.3) and (2.4) satisfy the classical linear acoustic equations without perturbations. To this order, then, we ignore entropy changes associated purely with the wave motions. Note also that (2.3) and (2.4) do <u>not</u> satisfy the actual boundary condition (2.2), and are therefore only approximations to the true fields. The error is small, because we assume always that the perturbations are small, and has small effect because of the spacial averaging described below.

The formal apparatus is constructed to provide means for calculating the amplitudes $\eta_i(t)$. In the case of linear motions, the amplitudes vary exponentially in time,

$$\eta_i(t) = \hat{\eta}_i e^{ia_o K_i t} \tag{2.7}$$

The main results are algebraic formulas for the complex wavenumber K_i of the ith mode, $K_i = (\Omega_i - i\alpha_i)/a_o$ where Ω_i is the angular frequency in the presence of perturbations, and α_i is the growth constant.

For nonlinear motions, the amplitudes must be determined as the solutions to nonlinear ordinary differential equations. First multiply (2.1) by ψ_n, the shape of the nth mode, and integrate over the volume of the chamber. After use of the boundary conditions (2.2) and (2.6) one finds

$$\int \psi_n \frac{\partial^2 p'}{\partial t^2}\, dV + \omega_n^2 \int \psi_n p' dV = -a_o^2 \int \psi_n k dV$$

$$- a_o^2 \oiint \psi_n f dS \tag{2.8}$$

Now substitute the expansion (2.3) for p' on the left hand side of the last equation. This produces the second order equation for η_n:

$$\ddot{\eta}_n + \omega_n^2 \eta_n = - \frac{a_o^2}{p_o E_n^2} \left\{ \int \psi_n h dV + \oiint \psi_n f dS \right\} \tag{2.9}$$

where

$$E_n^2 = \int \psi_n^2 dV \tag{2.10}$$

When h and f are nonlinear in the pressure or velocity, (2.9) represents a coupled set of nonlinear differential equations.

In the case of linear motions, the form (2.7) can be used for η_i, and substitution into (2.9) gives

$$- (\Omega_n - i\alpha_n)^2 + \omega_n^2 = - \frac{1}{p_o E_n^2} \left\{ \int \psi_n \frac{\hat{h}}{\hat{\eta}_n} dV + \oiint \psi_n \frac{\hat{f}}{\hat{\eta}_n} dS \right\}$$

The perturbations represented by $\hat{h}$ and $\hat{f}$ are small, so that α_n/ω_n is small and Ω_n, the frequency of the actual motion, is not much different from the unperturbed frequency ω_n. Thus the last equation gives the two formulas, extracted as the real and imaginary parts:

$$\Omega_n^2 = \omega_n^2 + \frac{1}{p_o E_n^2} \mathcal{R}e \left\{ \int \psi_n \frac{\hat{h}}{\hat{\eta}_n} dV + \oiint \psi_n \frac{\hat{f}}{\hat{\eta}_n} ds \right\} \tag{2.11}$$

$$\alpha_n = \frac{1}{2\omega_n p_o E_n^2} \mathcal{I}m \left\{ \int \psi_n \frac{\hat{h}}{\hat{\eta}_n} dV + \oiint \psi_n \frac{\hat{f}}{\hat{\eta}_n} dS \right\} \tag{2.12}$$

These two results are the basis for practically all contemporary calculations of linear stability. The effort lies in constructing the functions h and f, and in calculating the mode shapes ψ_n. There are of course values of Ω_n and α_n associated with each of the modes.

If the functions h and f are not linear, then the substitution of (2.7) is no help. Let F_n denote the right hand side of (2.9),

$$\ddot{\eta}_n + \omega_n^2 \eta_n = F_n \tag{2.13}$$

With the approximations (2.3) and (2.4), F_n is in general a function of all the η_i and $\dot{\eta}_i$. This coupled set of equations can be solved numerically, but at considerable expense. In reference 2 the method of averaging has been used to reduce the set of N second order equations to a set of 2N first order equations, when N modes are accounted for.

The basis for the development is the observation that practically all of the problems we shall be concerned with display oscillatory behavior having slowly varying amplitude and phase. Each of the amplitudes $\eta_n(t)$ may reasonably be assumed to have the form

$$\eta_n(t) = \mathcal{A}_n(t) \sin(\omega_n t + \varphi_n(t)) = A_n \sin \omega_n t + B_n \cos \omega_n t \tag{2.14}$$

The crucial assumption is that during some period τ of the order of the period of oscillation, the fractional changes are small; thus $\Delta\mathcal{A}_n/\mathcal{A}_n \ll 1$ in the interval $\Delta t = \tau$. But $\Delta\mathcal{A}_n = \dot{\mathcal{A}}_n \Delta t = \ddot{\mathcal{A}}_n \tau$. Thus the assumption implies:

$$\dot{\mathcal{A}}_n \tau,\ \dot{\varphi}_n \frac{\tau}{2\pi},\ \dot{A}_n \tau,\ \dot{B}_n \tau \ll 1 \tag{2.15}$$

With that assumption as the basis, equations can be deduced eventually for the amplitudes and phases. We shall work here with the functions A_n and B_n which are to be found as the solutions to the equations

$$\frac{dA_n}{dt} = \frac{1}{\omega_n \tau} \int_t^{t+\tau} F_n \cos \omega_n t' \, dt' \tag{2.16}$$

$$\frac{dB_n}{dt} = \frac{-1}{\omega_n \tau} \int_t^{t+\tau} F_n \sin \omega_n t' \, dt' \tag{2.17}$$

Here τ represents the interval of averaging. During that interval, A_n and B_n may be treated as constants when the integrals on the right hand sides are done.

In the special case of purely longitudinal oscillations, $\omega_n = n\omega_1$. Equations (2.16) and (2.17) may be simplified. Because the integrands are then periodic, and because τ may be taken to be the period of the fundamental mode, $\tau = \tau_1 = 2\pi/\omega_1$, we have

$$\frac{dA_n}{dt} = \frac{1}{2\pi n} \int_0^{2\pi/\omega_1} F_n \cos \omega_n t' \, dt' \tag{2.18}$$

$$\frac{dB_n}{dt} = \frac{-1}{2\pi n} \int_0^{2\pi/\omega_1} F_n \sin \omega_n t' \, dt' \tag{2.19}$$

It is these equations which are eventually solved to treat the problems in the remainder of this paper.

The major nonlinear effects we shall be concerned with here are those arising in the acoustics. They are purely fluid-mechanical and do not depend on the presence of combustion processes. In reference 2, the nonlinear acoustics was carried out to second order, leading to the form of F_n

$$F_n = -\sum_{i=1}^{\infty} [D_{ni}\dot{\eta}_i + E_{ni}\eta_i] - \sum_{i=1}^{\infty}\sum_{j=1}^{\infty} [A_{nij}\dot{\eta}_i\dot{\eta}_j + B_{nij}\eta_i\eta_j] \tag{2.20}$$

For the case of longitudinal modes, the equations (2.18) and (2.19) become

$$\frac{dA_n}{dt} = \alpha_n A_n + \theta_n B_n + \frac{\beta n}{2} \sum_{i=1}^{\infty} [A_i(A_{n-i} - A_{i-n} - A_{n+i}) - B_i(B_{n-i} + B_{i-n} + B_{n+i})] \tag{2.21}$$

$$\frac{dB_n}{dt} = \alpha_n B_n - \theta_n A_n + \frac{\beta n}{2} \sum_{i=1}^{\infty} [A_i(B_{n-i} + B_{i-n} - B_{n+i}) + B_i(A_{n-i} - A_{i-n} + A_{n+i})] \tag{2.22}$$

where $\beta = (\gamma+1)\omega_1/8\gamma$.

Note that the double series in (2.20) has become a single series for this case. The terms involving α_n and θ_n govern linear behavior: $\alpha_n = -D_{nn}/2$; $\theta_n = -E_{nn}/2\omega_n$. Clearly α_n is the growth constant defined earlier; it is quite easy to show by direct solution that $-\theta_n$ is the shift of frequency from that of the unperturbed normal mode (reference 2).

The nonlinear processes accounted for in (2.20) and (2.21) arise partly from variations in the speed of sound; partly from inertial effects, such as $\rho\, \partial\vec{u}/dt$; and partly from convective influences, such as those represented by the term $\rho\, \vec{u}\cdot\nabla\vec{u}$ in the momentum equation. It is a relatively straightforward matter to incorporate other nonlinear processes. For example, nonlinear attenuation due to gas/particle interactions has been discussed in reference 2. Some consequences of the second order nonlinearities will be encountered here when we examine the propagation of pulses in Section IV.

It is through the constants α_n, θ_n that connection is made with linear stability analysis. For example, the influences of surface combustion (the response function) and attenuation due to particles are contained in α_n and θ_n, in the form of integrals over the mode shapes. All results of linear analysis are accommodated by the technique described here; it is a straightforward matter to incorporate both numerical computations and experimental data for linear behavior.

To illustrate the sort of results which may be obtained, two examples from reference 2 will be quoted. The first is for the attenuation of a standing wave due to particles suspended in a gas; the mixture is contained in a box with no combustion or flow. Figure 2.1(a) shows the cycle-to-cycle attenuation constant, compared with an 'exact' numerical calculation. The mass fraction of particulate material is 0.36, the diameter of the particles is 2.5 microns, and the frequency is 800 Hertz. The evolution of the decay constant is due to the nonlinear generation of harmonics, as shown by the waveform in Figure 2.1(b).

The second example is for an unstable fundamental longitudinal mode in a cylindrical motor. In this case, the influences of the exhaust nozzle, combustion, the mean flow field, and particles were accounted for. Figure 2.2 shows the amplitudes of the first five harmonics as they develop from an initial disturbance having the shape of the fundamental mode. The instability ultimately executes a limit cycle in which the fundamental mode has amplitude slightly greater than 4% of the average pressure.

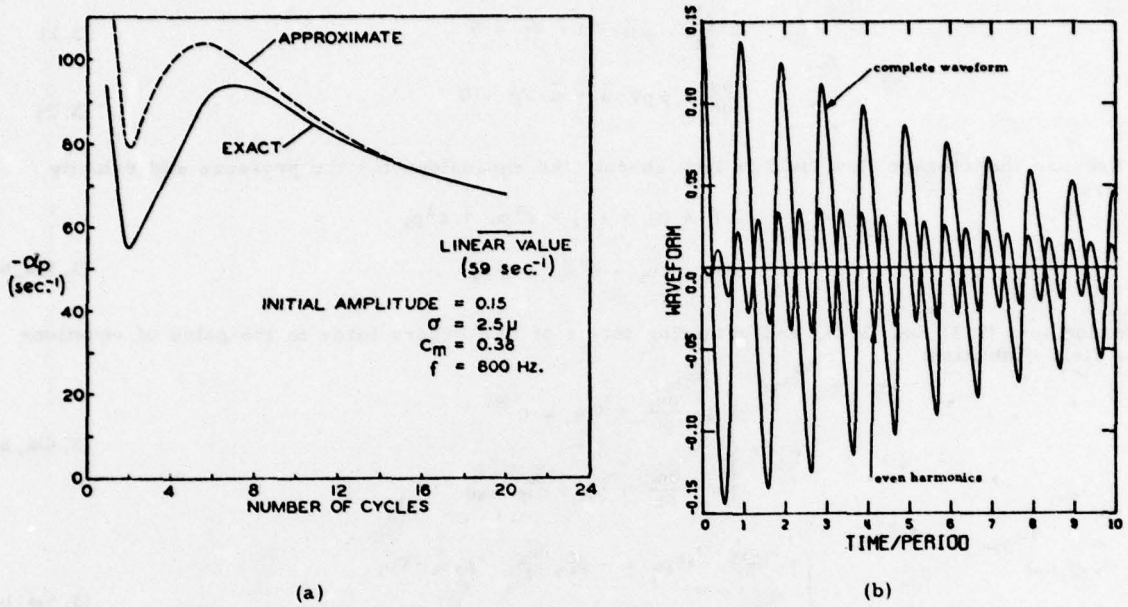

(a) (b)

Figure 2.1. Decay constant and waveform for attenuation by 2.5-micron particles at 800 Hz, $\Delta p(0)/p_0 = 0.15$.

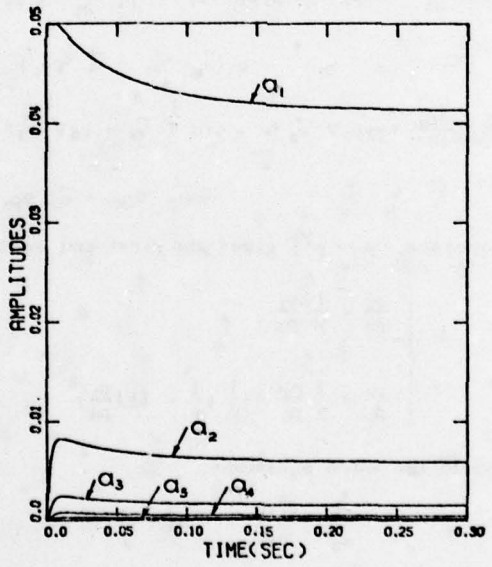

Figure 2.2. Amplitudes for an unstable oscillation in a motor.

III. REPRESENTATION OF NONLINEAR ACOUSTICS TO THIRD ORDER

Extension of the analysis to third order acoustics requires careful attention to ordering and closer consideration of the approximations. In the interest of facilitating practical calculations of stability for combustion chambers, and eventually parametric studies, we wish to produce formulas which involve the unperturbed classical modes. An enormous amount of labor is avoided if we need not apply the actual boundary conditions to obtain mode shapes.

An assumption implicit in the methods applied here is that the dominant nonlinear processes are the acoustics. Others, such as nonlinear viscous effects associated with gas/particle interactions occupy a lesser position and are accounted for later by introducing suitable terms in the forcing functions F_n, equation (2.13). To illustrate the techniques we shall therefore consider here only the acoustics, a tactic which permits us to treat the simpler equations for classical flows without combustion and mean flow:

$$\rho \frac{\partial \vec{u}}{\partial t} + \rho \vec{u} \cdot \nabla \vec{u} + \nabla p = 0 \tag{3.1}$$

$$\frac{\partial p}{\partial t} + \gamma p \nabla \cdot \vec{u} + \vec{u} \cdot \nabla p = 0 \tag{3.2}$$

Because the average flow field is now absent, the expansions for the pressure and velocity fields are

$$p = p_0 + \epsilon p_1 + \epsilon^2 p_2 + \epsilon^3 p_3$$

$$\vec{u} = \epsilon \vec{u}_1 + \epsilon^2 \vec{u}_2 + \epsilon^3 \vec{u}_3 \tag{3.3)a, b}$$

Substitution into (3.1) and (3.2), and gathering terms of like orders leads to the pairs of equations for the field quantities:

$$\begin{cases} \rho_0 \dfrac{\partial \vec{u}_1}{\partial t} + \nabla p_1 = 0 \\ \dfrac{\partial p_1}{\partial t} + \gamma p_0 \nabla \cdot \vec{u}_1 = 0 \end{cases} \tag{3.4)a, b}$$

$$\begin{cases} \rho_0 \dfrac{\partial \vec{u}_2}{\partial t} + \nabla p_2 = - \rho_1 \dfrac{\partial \vec{u}_1}{\partial t} - \rho_0 \vec{u}_1 \cdot \nabla \vec{u}_1 \\ \dfrac{\partial p_2}{\partial t} + \gamma p_0 \nabla \cdot \vec{u}_2 = - \gamma p_1 \nabla \cdot \vec{u}_1 - \vec{u}_1 \cdot \nabla p_1 \end{cases} \tag{3.5)a, b}$$

$$\begin{cases} \rho_0 \dfrac{\partial \vec{u}_3}{\partial t} + \nabla p_3 = - \rho_1 \vec{u}_1 \cdot \nabla \vec{u}_1 - \left(\rho_1 \dfrac{\partial \vec{u}_2}{\partial t} + \rho_2 \dfrac{\partial \vec{u}_2}{\partial t}\right) \\ \qquad - \rho_0 (\vec{u}_1 \cdot \nabla \vec{u}_2 + \vec{u}_2 \cdot \nabla \vec{u}_1) \\ \dfrac{\partial p_3}{\partial t} + \gamma p_0 \nabla \cdot \vec{u}_3 = - \gamma (p_1 \nabla \cdot \vec{u}_2 + p_2 \nabla \cdot \vec{u}_1) \\ \qquad - (\vec{u}_1 \cdot \nabla p_2 + \vec{u}_2 \cdot \nabla p_1) \end{cases} \tag{3.6)a, b}$$

The formula for isentropic processes, $p \sim \rho^\gamma$, gives the first and second order fluctuations of density:

$$\begin{cases} \dfrac{\rho_1}{\rho_0} = \dfrac{1}{\gamma} \dfrac{p_1}{p_0} \\ \dfrac{\rho_2}{\rho_0} = \dfrac{1}{\gamma} \dfrac{p_2}{p_0} + \dfrac{1}{2} \left(\dfrac{1}{\gamma} - 1\right) \left(\dfrac{p_1}{p_0}\right)^2 \end{cases} \tag{3.7)a, b}$$

The pairs (3.4) - (3.6) yield the wave equations:

$$\frac{1}{a_0^2} \frac{\partial^2 p_1}{\partial t^2} - \nabla^2 p_1 = 0 \tag{3.8}$$

$$\frac{1}{a_0^2} \frac{\partial^2 p_2}{\partial t^2} - \nabla^2 p_2 = \nabla \cdot \left(\rho_1 \frac{\partial \vec{u}_1}{\partial t} + \rho_0 \vec{u}_1 \cdot \nabla \vec{u}_1\right) - \frac{1}{a_0^2} \frac{\partial}{\partial t} (\gamma p_1 \nabla \cdot \vec{u}_1 + \vec{u}_1 \cdot \nabla p_1) \tag{3.9}$$

$$\begin{aligned} \frac{1}{a_0^2} \frac{\partial^2 p_3}{\partial t^2} - \nabla^2 p_3 = \nabla \cdot \Big[& \rho_1 \vec{u}_1 \cdot \nabla \vec{u}_1 + \left(\rho_1 \frac{\partial \vec{u}_2}{\partial t} + \rho_2 \frac{\partial \vec{u}_1}{\partial t}\right) \\ & + \rho_0 (\vec{u}_1 \cdot \nabla \vec{u}_2 + \vec{u}_2 \cdot \nabla \vec{u}_1) \Big] \\ & - \frac{1}{a_0^2} \frac{\partial}{\partial t} \left[\gamma (p_1 \nabla \cdot \vec{u}_2 + p_2 \nabla \cdot \vec{u}_1) + (\vec{u}_1 \cdot \nabla p_2 + \vec{u}_2 \cdot \nabla p_1)\right] \end{aligned} \tag{3.10}$$

where $a_o^2 = \gamma p_o/\rho_o$ is the speed of sound. Addition of (3.8) and (3.9) gives the wave equation for* $p' = p_1 + p_2$ used as the basis for the analysis to second order described in Section 2:

$$\frac{1}{a_o^2}\frac{\partial^2 p'}{\partial t^2} - \nabla^2 p' = \nabla\cdot\left(\rho_1\frac{\partial \vec{u}_1}{\partial t} + \rho_o \vec{u}_1\cdot\nabla\vec{u}_1\right)$$

$$- \frac{1}{a_o^2}\frac{\partial}{\partial t}\left(\gamma p_1 \nabla\cdot\vec{u}_1 + \vec{u}_1\cdot\nabla p_1\right) \qquad (3.11)$$

There is a corresponding expression for the boundary condition which we will not display here; these two results are equations (2.1) and (2.2); h is the right hand side of (3.11), if only the nonlinear acoustics is accounted for.

Only the first order (classical) acoustic quantities are required to evaluate the right hand side of (3.11). The formulas (2.3) and (2.4) satisfy (3.4)a,b exactly. Those two equations produce respectively the equations for η_i and ψ_i:

$$\ddot{\eta}_i + \omega_i^2\eta_i = 0\ ; \quad \nabla^2\psi_i + k_i^2\psi_i = 0 \qquad (3.12)$$

Thus, the use of (2.3) and (2.4) in the right hand side of (3.11) is rigorously correct according to the expansion procedure, but because p' on the left hand side is $p_1 + p_2$, (2.3) is only an approximation. As we noted earlier, the approximation works because of the spacial averaging [recall (2.8) and (2.9)] which incorporates the correct boundary condition (2.2).

The analysis to third order rests on the wave equation found by summing (3.8) - (3.10):

$$\frac{1}{a_o^2}\frac{\partial^2 p'}{\partial t^2} - \nabla^2 p' = \nabla\cdot\Big[\rho_1\frac{\partial\vec{u}_1}{\partial t} + \rho_o\vec{u}_1\cdot\nabla\vec{u}_1$$

$$+ \rho_1\vec{u}_1\cdot\nabla\vec{u}_1 + \left(\rho_1\frac{\partial\vec{u}_2}{\partial t} + \rho_2\frac{\partial\vec{u}_1}{\partial t}\right)$$

$$+ \rho_o(\vec{u}_1\cdot\nabla\vec{u}_2 + \vec{u}_2\cdot\nabla\vec{u}_1)\Big]$$

$$- \frac{1}{a_o^2}\frac{\partial}{\partial t}\Big[\gamma p_1\nabla\cdot\vec{u}_1 + \vec{u}_1\cdot\nabla p_1 \qquad (3.13)$$

$$+ \gamma(p_1\nabla\cdot\vec{u}_2 + p_2\nabla\cdot\vec{u}_1)$$

$$+ (\vec{u}_1\cdot\nabla p_2 + \vec{u}_2\cdot\nabla p_1)\Big]$$

We shall continue to use the form (2.1) as an approximation to p' on the left hand side of, with the idea that once again adequate corrections are introduced with the method of spatial averaging. To evaluate the right hand side, (2.1) and (2.2) are correctly used for p_1 and $\vec{u}_1$, but now we require formulas for p_2 and $\vec{u}_2$. At this point we assume again that the acoustical nonlinear processes dominate and seek particular solutions to (3.5)a,b; those solutions will subsequently be used even when additional processes are included.

Suitable solutions are

$$p_2 = \sum_{r,s=0}^{\infty}\left(P_{rs}\eta_r\eta_s + Q_{rs}\dot{\eta}_r\dot{\eta}_s\right)$$

$$\vec{u}_2 = \sum_{r,s=0}^{\infty}\left(\vec{U}_{rs}\eta_r\dot{\eta}_s + V_{rs}\dot{\eta}_r\eta_s\right) \qquad (3.14)a,b$$

Substitute (2.1), (2.2) and (3.14)a,b into (3.5)a,b, and assume that the coefficients of the time-dependent functions ($\eta_r\eta_s$, $\dot{\eta}_r\dot{\eta}_s$, etc.) must vanish term-by-term. With some effort, one may then deduce that

$$\vec{V}_{rs} = \vec{U}_{sr} \qquad (3.15)$$

and that $\vec{U}_{rs}$ must satisfy the differential equation

*We now set the ordering parameter $\epsilon = 1$.

$$\nabla(\nabla\cdot\vec{U}_{rs}) + (k_s^2 - k_r^2)\vec{U}_{rs} = \nabla\left(\frac{\gamma-1}{2\gamma^2}\,\psi_r\psi_s + \frac{a_o^2}{\gamma^2\omega_s^2}\,\nabla\psi_r\cdot\nabla\psi_s\right) \tag{3.16}$$

The functions P_{rs} and Q_{rs} are then given by the formulas

$$P_{rs} = \frac{p_o}{2}\,\psi_r\psi_s + \frac{\gamma p_o}{\omega_s^2 - \omega_r^2}\,\nabla\cdot(\omega_r^2\vec{V}_{rs} - \omega_s^2\vec{U}_{rs}) \tag{3.17}$$

$$Q_{rs} = \frac{p_o a_o^2}{\gamma\omega_r^2\omega_s^2}\,\nabla\psi_r\cdot\nabla\psi_s + \frac{\gamma p_o}{\omega_s^2 - \omega_r^2}\,\nabla\cdot(\vec{V}_{rs} - \vec{U}_{rs}) \tag{3.18}$$

Now (3.14)a,b are to be used in (3.13) when spacial and time-averaging are carried out according to the procedures outlined in Section 2. These steps involve a great deal of tedious effort. Note that the third order terms produce sums over three indices. For the case of longitudinal modes, the triple series become double series, corresponding to the simplification to single series in second order acoustics. Explicit results and numerical examples will be covered in subsequent publications.

IV. REPRESENTATION OF PULSES

For sometime there have been a few unanswered questions concerning the relationships between the normal modes of a chamber and discrete travelling disturbances. Such questions have been raised in practice by observations of the apparent development of a discrete wave out of a more familiar sort of unstable normal mode. There is also a great deal of interest in the evolution of the disturbances following generation of a pulse by external means. The two main techniques are based on use of a small explosive charge, or ejection of an inert pellet through the nozzle. Both problems can be treated with the same formal apparatus.

The basis for the calculation is best displayed for the simplest case of a pulse propagating in a closed tube containing gas at rest, with no combustion. As indicated in Figure 4.1, a single pulse within the chamber may be represented as the superposition of two infinitely long trains of pulses, one train moving to the left, and one to the right. At the instant for which the figure is drawn, the pulse A is about to cross the boundary z = 0 from right to left, and the pulse B is about to cross from left to right. This represents reflection of a leftward moving pulse at the end, z = 0, of the

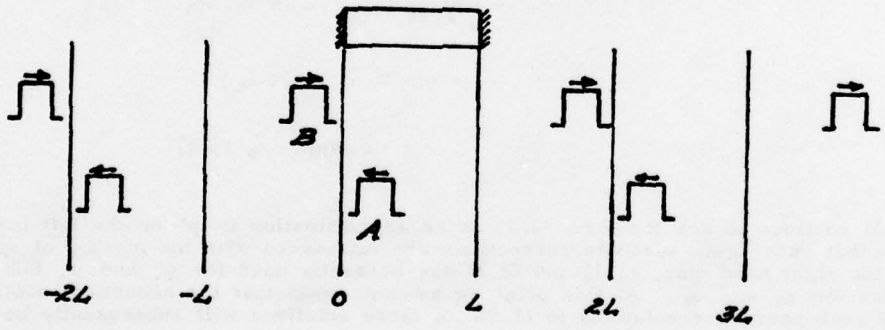

Figure 4.1. Superposition of two Pulse Trains to Represent Propagation of a Single Pulse in a Closed Tube.

tube. It is easy to deduce from the figure that during reflection the amplitude of the pulse is doubled near the reflecting boundary. Just before reflection, the real pulse within the chamber is represented by pulse A, and after reflection pulse B represents the real pulse. Note that pulses in each of the trains are separated by the distance 2L, twice the length of the chamber. Hence the wave system comprising the two wave trains had period 2L. This represents the pulse within the chamber travelling the distance 2L for a full cycle.

Under the conditions chosen here, the pressure pulse in the chamber must satisfy the homogeneous wave equation subject to the boundary condition for rigid walls at the ends

$$\frac{\partial^2 p'}{\partial z^2} - \frac{1}{a_o^2}\frac{\partial^2 p'}{\partial t^2} = 0 \tag{4.1}$$

$$\frac{\partial p'}{\partial z} = 0 \quad (z = 0, L) \tag{4.2}$$

The general solution of (4.1) may be written as the sum of rightward and leftward moving waves:

$$\frac{p'}{p_o} = f(z - at) + g(z + at) \qquad (4.3)$$

Figure (4.1) shows a special case of this solution. The train of pulses moving to the right is represented by f(z - at) and those moving to the left are contained in g(z + at). It is apparent that in order to satisfy the boundary conditions at the ends of the chamber having length L, the wave trains must have period 2L.

We shall be particularly concerned here with the wave motions subsequent to specified initial conditions. Note that the example shown in Figure (4.1) was constructed artificially; it is not immediately obvious what initial conditions will produce the wave motion. The simplest initial value problem is that for a pulse initially at rest:

$$\left.\begin{aligned} p'(z,0) &= p_o\, P(z) \\ \frac{\partial p'}{dt}\,(z,0) &= 0 \end{aligned}\right\} \quad (t = 0;\ 0 \le z \le L) \qquad (4.4)$$

For $t > 0$ such a pulse splits into <u>two</u> pulses, one moving to the left and one moving to the right. The solution can be represented as the superposition of two pulse trains as sketched in Figure 4.2. For this case the pulses in each of the trains have half the amplitude of the initial pulse.

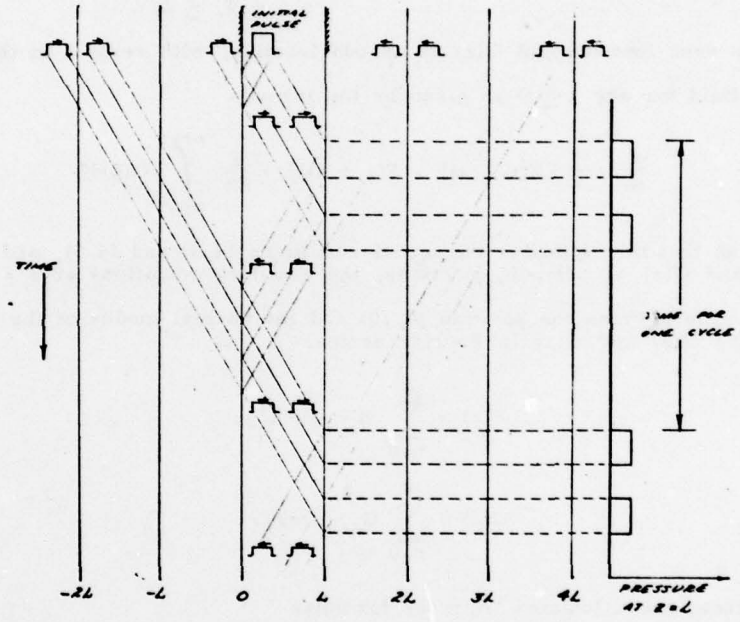

Figure 4.2. Propagation of Pulses Developed From a Stationary Initial Pulse in a Closed Tube.

Because the initial pulse splits, there are always two pulses in the chamber. Measurement of the pressure at one end produces a signal which is periodic, having period equal to the round trip time for <u>one</u> of the pulses. The fundamental frequency of the signal is the fundamental frequency of the chamber. In special symmetric cases, the signal may show a higher fundamental frequency. For example, if a symmetric pulse is introduced at the center of the chamber, then the fundamental frequency of the signal is the frequency of the second mode of the chamber.

The case of a single pulse, sketched in Figure 4.1, is the simplest to visualize, and constitutes a special case of the general initial value problem. In order to satisfy the boundary conditions, it is necessary, as Figure 4.1 illustrates, to use wave trains having period twice the length of the chamber. We wish to account for both the initial pulse shape, P(z), and its initial rate of change with time, Q(z); the initial conditions are

$$\frac{p'}{p_o}\,(z,0) = P(z) \qquad (4.4)$$

$$\frac{\partial}{\partial t}\,\frac{p'}{p_o}\,(z,0) = Q(z) \qquad (4.5)$$

AD-A076 012 ADVISORY GROUP FOR AEROSPACE RESEARCH AND DEVELOPMENT--ETC F/G 21/8.2
SOLID ROCKET MOTOR TECHNOLOGY.(U)
JUL 79
UNCLASSIFIED AGARD-CP-259 NL

4 OF 6
AD
A076012

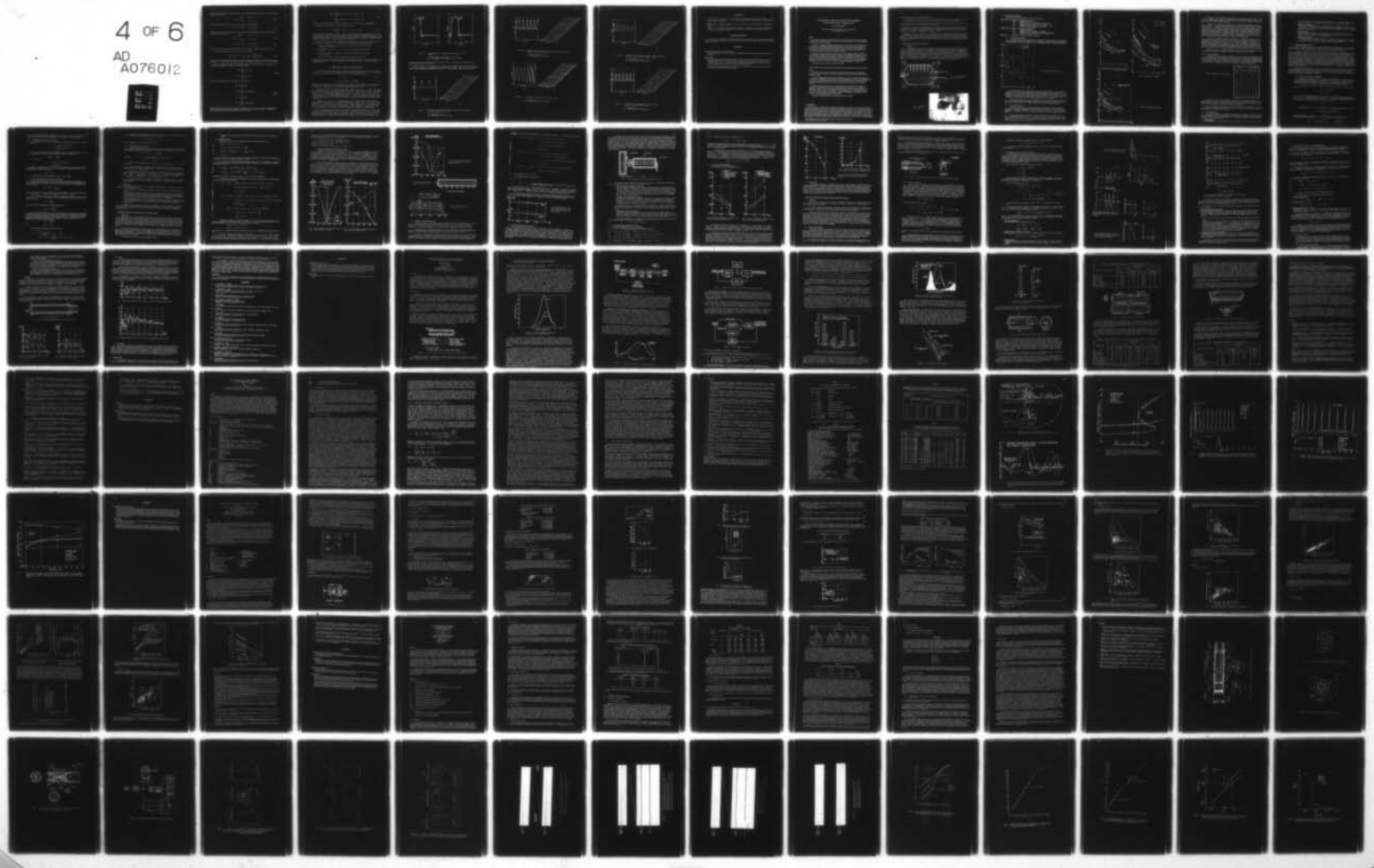

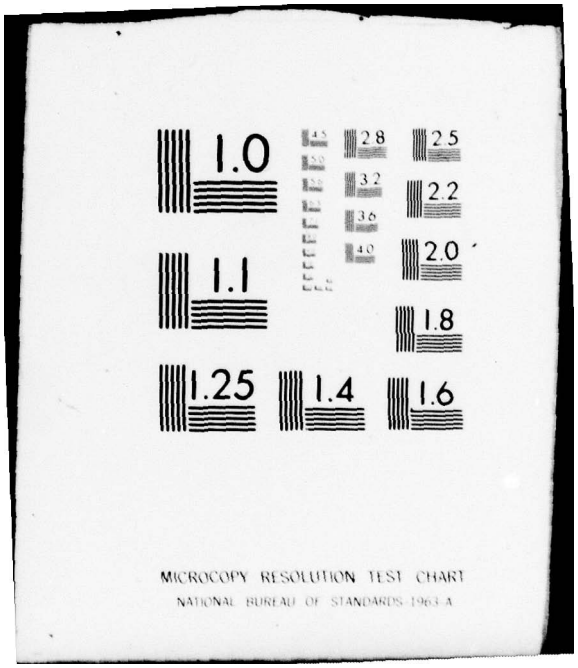
1.0
1.1
1.25
1.4
1.6
2.8
3.2
3.6
4.0
2.5
2.2
2.0
1.8
MICROCOPY RESOLUTION TEST CHART
NATIONAL BUREAU OF STANDARDS-1963-A

Define the function F(z) representing leftward and rightward moving pulse trains required to satisfy the initial shape (4.4):

$$F(z) = \begin{cases} P(z) & 0 \le z \le L \\ P(-z) & -L \le z \le 0 \end{cases} \tag{4.6}$$

Outside the region $-2L \le z \le 2L$, F(z) is periodic, having period 2L:

$$F(z + 2nL) = F(z) \qquad -2L \le z \le 2L, \quad n = \pm 1, \pm 2, \ldots \tag{4.7}$$

Similarly a function G(z) is defined to represent pulse trains required to satisfy the initial rate of change of the pressure field

$$G(z) = \begin{cases} Q(z) & 0 \le z \le L \\ -Q(-z) & -L \le z \le 0 \end{cases} \tag{4.8}$$

$$G(z + 2nL) = G(z) \qquad -2L \le z \le 2L, \quad n = \pm 1, \pm 2, \ldots \tag{4.9}$$

Note that F(z) is an even function and G(z) is an odd function, with respect to the origin z = 0.

The pressure field for any $t \ge 0$ is given by the formula

$$\frac{p'}{p_0} = \frac{1}{2}\left[F(z - at) + F(z + at)\right] + \frac{1}{2a}\int_{z-at}^{z+at} G(\xi)d\xi \tag{4.10}$$

It is easy to establish that this satisfies the initial conditions (4.4) and (4.5), and because of the definitions of F(z) and G(z) as periodic functions, the boundary conditions at z = 0, L are satisfied.

Now the connection between the solution (4.10) and the normal modes of the chamber is established by expanding F(z) and G(z) in Fourier series:

$$F(z) = \sum_{n=0}^{\infty} B_n \cos k_n z$$

$$G(z) = \sum_{n=0}^{\infty} C_n \cos k_n z \tag{4.11)a,b}$$

The Fourier coefficients are calculated from the formulas

$$B_0 = \frac{1}{L}\int_0^L P(z)dz$$

$$B_n = \frac{2}{L}\int_0^L \cos(k_n z)\, P(z)dz$$

$$C_0 = \frac{1}{L}\int_0^L Q(z)dz \tag{4.12 a,b,c,d}$$

$$C_n = \frac{2}{L}\int_0^L \cos(k_n z)\, Q(z)dz$$

The average values of the pulse and its rate of change are B_0 and C_0. In later calculations we shall be concerned only with the evolution of departures from the average values. Substitution of (4.11)a,b into (4.10) leads to the Fourier series for p'(z, t):

$$\frac{p'}{p_0} = \frac{1}{2}\sum_{n=0}^{\infty} B_n[\cos k_n(z - at) + \cos k_n(z + at)]$$

$$+ \frac{1}{2}\sum_{n=0}^{\infty} C_n \frac{1}{\omega_n}[\sin(z + at) - \sin k_n(z - at)] \qquad (4.13)$$

Because C_n has dimensions of frequency, the factor $\omega_n = ak_n$ makes C_n/ω_n dimensionless.

Expression of the functions in (4.13) leads to the form

$$\frac{p'}{p_0} = \sum_{n=0}^{\infty} [A_n \sin \omega_n t + B_n \cos \omega_n t] \cos k_n z \qquad (4.14)$$

in which A_n has been written for C_n/ω_n. This result is identical with the expansion (2.1), using (2.15) for $\eta_i(t)$. We have now made the connection with the stability and nonlinear analyses described in the preceding sections. For a pulse which propagates in a passive medium, with unchanging shape, the Fourier coefficients A_n and B_n are constant. For the problems arising in rocket motors, A_n and B_n vary with time according to equations (2.19) and (2.20).

Hence we have now a means for analyzing the behavior of an arbitrary pulse in terms of the normal modes of a chamber. The procedure may be summarized in the following steps.

1) The initial shape and rate of change of the pressure are specified, giving the functions $P(z)$ and $Q(z)$.

2) The initial values of B_n and $A_n = C_n/\omega_n$ are calculated from the formulas (4.12)a, b.

3) The time evolution is calculated by using the appropriate forms of equations (2.19) and (2.20).

4) The pressure field can then be calculated at any time by using (4.14).

In principle, any problem of pulse propagation can be handled in this way. Practical difficulties may arise in the treatment of a steep-fronted pulse requiring a large number of modes for a faithful representation.

V. SOME RESULTS FOR PULSE PROPAGATION

We shall consider here only cases of rectangular pulses with the initial pressure not changing in time. Thus $Q(z) = 0$ in (4.5), and the Fourier coefficients are given by (4.12)a, b. For a pulse having height Δ, and non-zero in the range $L_1 \leq z \leq L_2$, the coefficients are

$$B_0 = \Delta(L_2 - L_1) \qquad (5.1)$$

$$B_n = \frac{2\Delta}{n\pi}\left[\sin\left(n\pi \frac{L_2}{L}\right) - \sin\left(n\pi \frac{L_1}{L}\right)\right] \qquad (5.2)$$

Figures (5.1)a and (5.1)b show the approximations using 10, 30 and 50 modes for a pulse generated at one end of a chamber, $0 \leq z \leq .3L$, and for a pulse generated in the range $.1L \leq z \leq .4L$. The second case corresponds to the situation sketched above in Figure 4.2.

Equations (3.2) and (3.3) have been solved here, with the values of α_n, θ_n chosen to illustrate the propagation of pulses. No results have been obtained for the conditions in a motor. The simplest case is a small amplitude pulse with no losses: $\alpha_n = \theta_n = 0$. Figure 5.2(a) is the pressure at the head end ($z = 0$) for the pulse represented by ten modes, Figure 5.1(a), and $\Delta = 0.006$. Because only ten modes are used, ripples appear in the waveform. The pulse shape in the chamber is shown in Figure 5.2(b) for various times during three cycles. For the small amplitude of this pulse, the second order nonlinearities have no discernible effect on the pulse shape for the short time covered in this figure.

In contrast, the case $\Delta = 0.1$ is a large amplitude pulse, and the influence of nonlinearities appear already in the first cycle. The initial shape is that of Figure 5.1(a). Figure 5.3(a) is the waveform at $z = 0$, and Figure 5.3(b) shows the pulse shape at various times. For comparison, the waveform of a simple cosine, the fundamental mode, is shown in Figure 5.4. Note the steepening into a weak shock after three cycles. The generation of higher harmonics is evident, both in the waveform measured at $z = 0$ and in the shape of the pressure distribution, in the chamber.

One of the interesting and potentially useful features exhibited by pulses in motors is the change of shape due to different rates of decay for the modes. In Figure 5.5, the decay of a small amplitude pulse is shown. For this case, $\theta_n = 0$ and $\alpha_n = -40n$, in equations (3.2) and (3.3); again the initial pulse shape is the approximation for ten modes, Figure 5.1(a). After six cycles there are still substantial amounts of the first five harmonics but the next five are practically absent. The

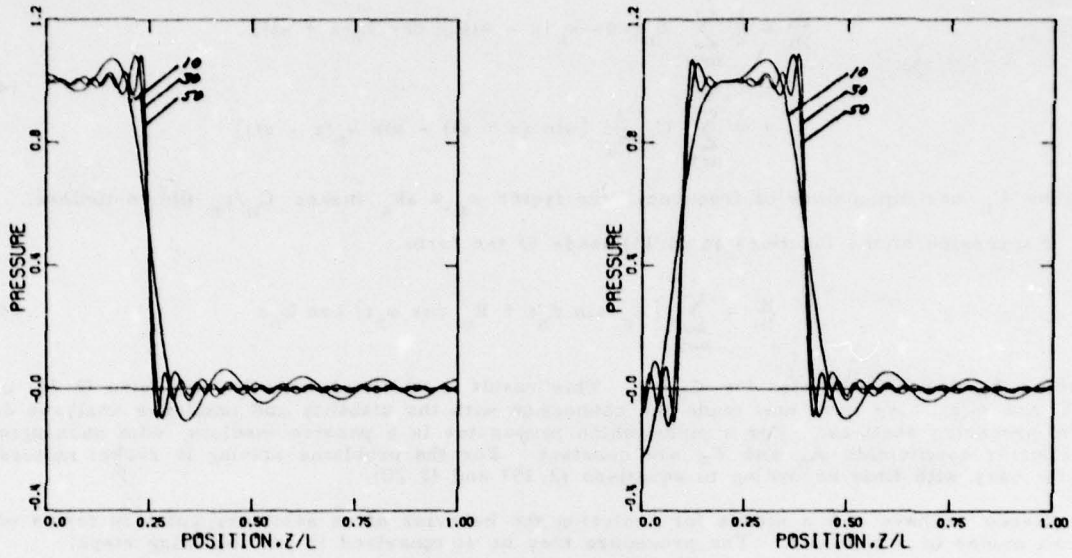

Figure 5.1. Approximations to a Rectangular Initial Pulse by 10, 30, 50 Modes.

(a) Pulse Initially in the Range $0 \leq z \leq .25L$
(b) Pulse Initially in the Range $0.1L \leq z \leq 0.4L$

average value of the pulse remains fixed at its initial value, so the pressure fluctuation does not become negative after several cycles.

Finally, in Figure 5.6 the behavior of a rectangular pulse initially displaced from one end is shown. The initial shape is the approximation with ten modes, Figure 5.1(b). This case corresponds to the perfect rectangular pulse sketched in Figure 4.2. The qualitative similarities are obvious.

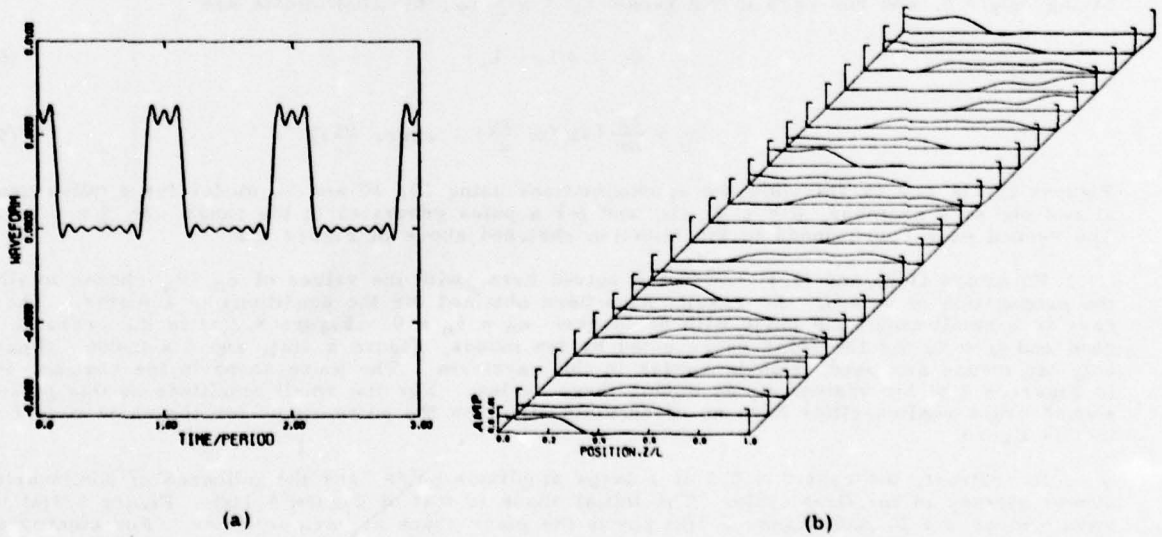

Figure 5.2. Propagation of a Rectangular Pulse Without Losses (10 modes): $p'(z,0) = 0.006p_o$; $0 \leq z \leq 0.3L$

(a) Waveform at $z = 0$
(b) Pulse Shapes for Three Cycles

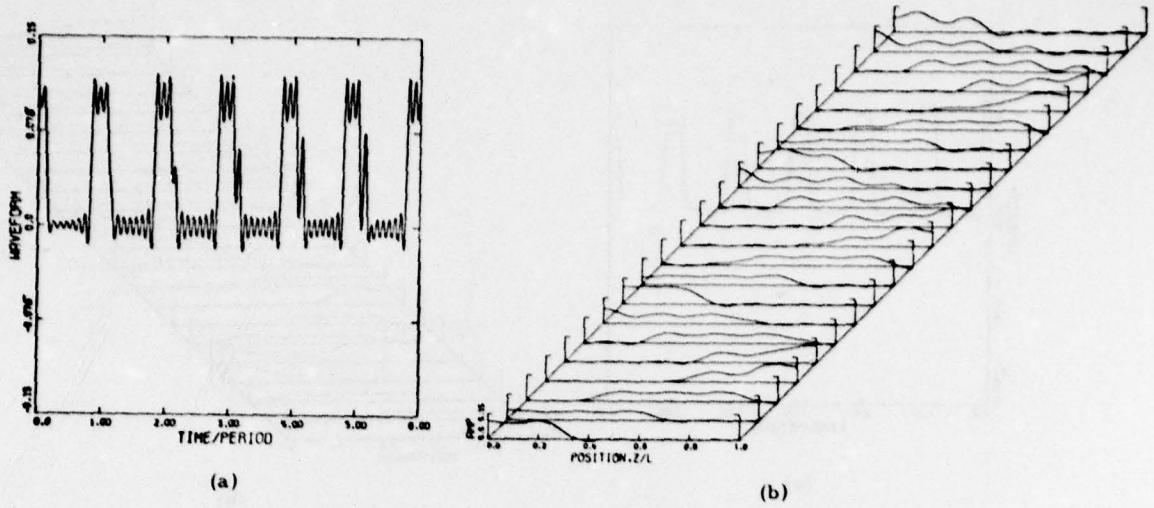

(a) (b)

Figure 5.3. Propagation of a Rectangular Pulse Without Losses (10 modes): $p'(z,0) = 0.01p_0$; $0 \leq z \leq 0.3L$

(a) Waveform at z = 0
(b) Pulse Shapes for Three Cycles

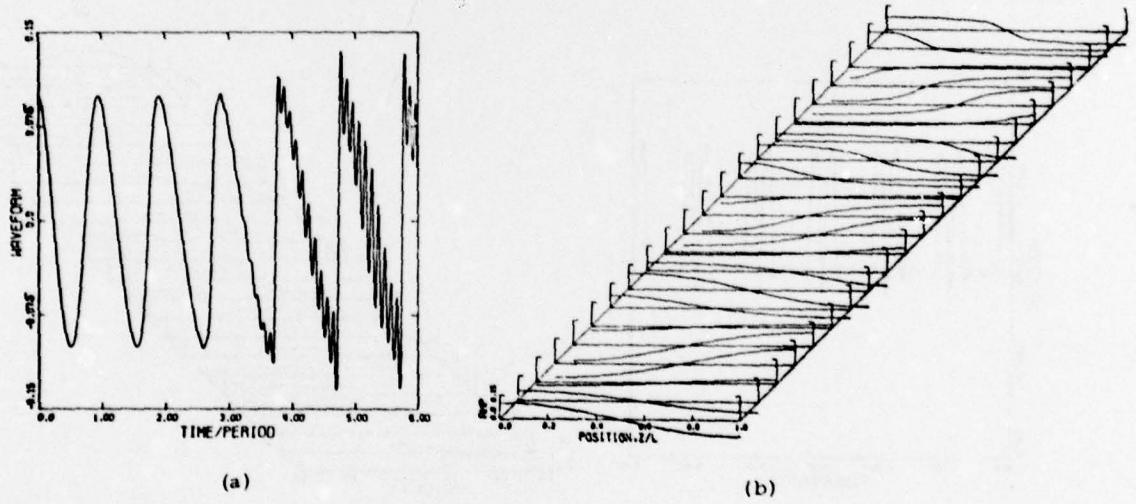

(a) (b)

Figure 5.4. Propagation of a Cosine Wave: $p'(0,0) = 0.01p_0$

(a) Waveform at z = 0
(b) Pulse Shapes for Three Cycles

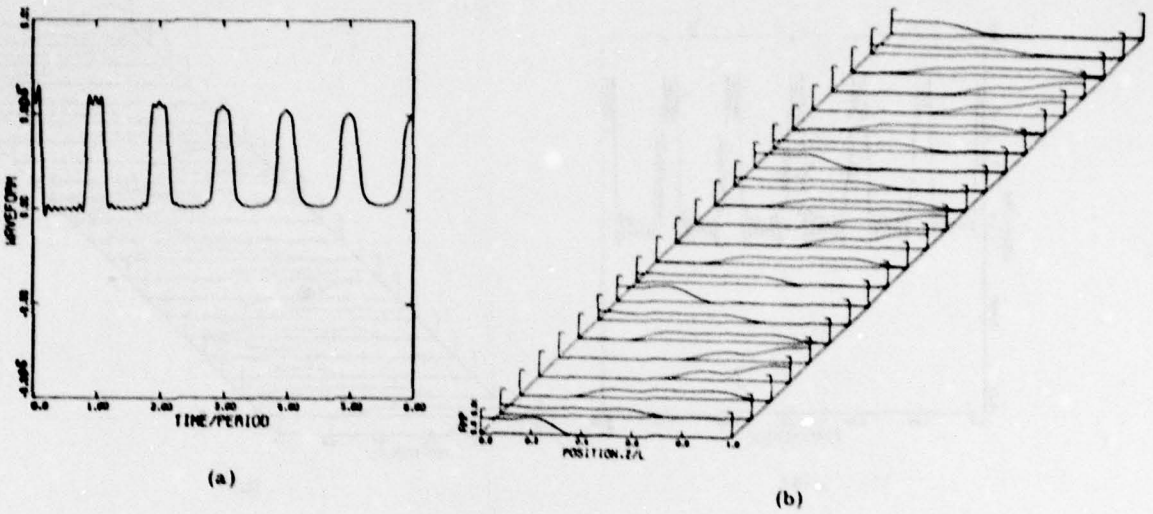

(a) (b)

Figure 5.5. Propagation of a Decaying Rectangular Pulse (10 modes): $p'(z,0) = 0.006p_0$, $0 \leq z \leq 0.3L$; $a_n = -40n$

(a) Waveform at $z = 0$
(b) Pulse Shapes for Three Cycles

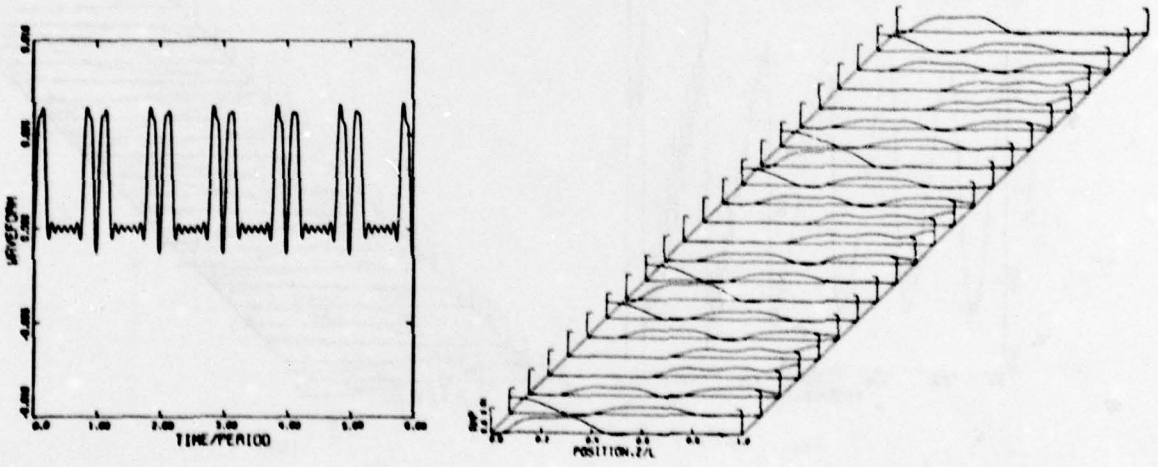

(a) (b)

Figure 5.6. Propagation of a Rectangular Pulse (10 modes): $p'(z,0) = 0.006p_0$, $0.1L \leq z \leq 0.4L$

(a) Waveform at $z = 0$
(b) Pulse Shapes for Three Cycles

REFERENCES

1. Culick, F. E. C. and Levine, J. N. "Comparison of Approximate and Numerical Analyses of Non-Linear Combustion Instability", AIAA 12th Aerospace Sciences Meeting, (1974), Washington, DC, AIAA Paper No. 74-201.

2. Culick, F. E. C. "Nonlinear Behavior of Acoustic Waves in Combustion Chambers", Acta Astronautica, V. 3 (1976) pp. 715-757.

3. Culick, F. E. C. "Research on Combustion Instability and Application to Solid Propellant Rocket Motors, II", AIAA/SAE 8th Joint Propulsion Specialist Conference, New Orleans, Louisiana (1972), AIAA Paper No. 72-1049.

ACKNOWLEDGEMENTS

This work was supported by the Aerothermochemistry Research Division, Naval Weapons Center, China Lake; and by the National Aeronautics and Space Administration under Jet Propulsion Laboratory Contract NAS 7-100.

DISCUSSION

L.De Luca, Instituto di Macchine del Politechnico, It

Can you comment on your important assumption of no coupling of the fluid dynamics with the combustion process in general?

Author's Reply

There is no question that the fluid dynamics dominate. What combustion does in particular modes is to wipe out the higher harmonic content. Modes appear as clean sinusoidal waves at amplitudes which shouldn't be clean according to classical acoustics. I believe the reason for that is primarily the influence of combustion which tends to drive lower frequencies and tends to extract energy from higher frequencies.

Combustion may be treated reasonably as a linear process for amplitudes up to 10% and tacks on to the non-linear processes which are dominated by the fluid mechanics.

ÉTUDES RÉCENTES A L'ONERA SUR LES INSTABILITÉS DE COMBUSTION DANS LES MOTEURS FUSÉES A PROPERGOL SOLIDE

par Paul KUENTZMANN

Office National d'Etudes et de Recherches Aérospatiales (ONERA)
92320 Châtillon (France)

◆

Résumé

Le problème des instabilités de combustion dans les moteurs à propergols solides est encore insuffisamment maitrisé. L'objet de cet article est de donner un aperçu des techniques expérimentales et numériques développées à l'ONERA pour faire face à ce problème.

Une étude de la similitude des instabilités de combustion a été conduite dans le cadre du développement de gros moteurs dont le chargement est géométriquement complexe et qui ont manifesté quelques instabilités. Le mauvais accord entre les caractéristiques des phénomènes observés et celles prévues par le calcul a amené à proposer la réalisation d'essais à échelle réduite. Cette technique purement expérimentale s'est avérée féconde ; les principaux résultats obtenus et les limites de la méthode seront donnés.

Des études de base sont poursuivies pour parvenir à une description complète et réaliste des instabilités longitudinales pour un chargement géométriquement simple. Deux voies complémentaires sont suivies : d'un côté et pour les études de stabilité, une meilleure utilisation des équations linéarisées décrivant la combustion du propergol et l'écoulement des produits de combustion est recherchée ; parallèlement et pour prévoir les niveaux d'instabilité, une technique numérique est développée prenant en compte le caractère non linéaire des phénomènes La première approche est aussi appliquée à la recherche du couplage pression-vitesse des propergols solides.

Cette synthèse permettra de préciser les orientations envisagées.

RECENT ONERA STUDIES ON COMBUSTION INSTABILITIES IN SOLID PROPELLANT ROCKET MOTORS

Summary

The problem created by combustion instabilities in solid propellant motors has not yet been sufficiently mastered. The purpose of this paper is to review the experimental and numerical techniques developed at ONERA to solve this problem.

A study on the similarity of combustion instabilities has been carried out on the occasion of the development of large size engines with geometrically complex grain, revealing some instabilities. In view of the poor agreement between the observed and predicted phenomena characteristics, it was proposed to conduct tests on a reduced scale. This purely experimental technique proved fruitful ; the main results obtained and the limitation of this method are presented.

Fundamental studies are being performed to achieve a complete and realistic description of longitudinal instabilities for a geometrically simple grain. Two complementary avenues are followed : on the one hand, for stability studies, a better use of the linearized equations describing the combustion of the propellant and the flow of combustion products, is sought ; on the other hand to predict instability levels, a numerical technique, taking into account the non linear nature of the phenomena, is developed. The first approach is also applied to the determination of the pressure-velocity coupling of solid propellants.

This synthesis will provide the means of better defining the trends contemplated.

1 - INTRODUCTION

Les instabilités de combustion des propulseurs à propergol solide restent un sujet de préoccupation. La complexité des phénomènes mis en jeu, l'incertitude des données disponibles et la limitation des moyens d'analyse existants rendent nécessaire la poursuite des recherches visant à prévoir la stabilité des propulseurs au stade de leur conception. L'évolution technologique des chargements qui présentent une forme de plus en plus complexe tend à accroître le fossé séparant les connaissances des réalisations et le développement d'un nouveau propulseur fait encore largement appel à l'empirisme. Cette situation n'a pas jusqu'à présent posé de problèmes importants car les comportements instables observés sont restés tolérables. Dans ce contexte l'activité que l'ONERA continue à consacrer aux instabilités de combustion est orientée schéma-

Travail effectué sous contrats de la Direction Technique des Engins, de la Société Européenne de Propulsion et de la Société Nationale des Poudres et Explosifs.

tiquement dans deux directions complémentaires :

- le développement de techniques globales permettant de répondre à court terme aux besoins industriels,
- des études de base à plus long terme en vue d'une meilleure compréhension des phénomènes.

Les travaux dont il sera fait état par la suite ne concernent que les instabilités de combustion à prédominance longitudinale et les propergols solides composites.

Le problème de la similitude des instabilités de combustion a été particulièrement étudié depuis quelques années en vue de créer un moyen expérimental peu coûteux susceptible d'apporter des informations sur la stabilité de chargements géométriquement complexes. L'ensemble des résultats obtenus sur un chargement axisymétrique sera présenté et commenté dans une première partie.

Les études de base sont consacrées à une meilleure description des phénomènes instationnaires au niveau de la combustion du propergol et au niveau de l'écoulement. Deux approches complémentaires sont mises en oeuvre : description des phénomènes par les équations linéarisées (recherche de la stabilité) et simulation numérique des phénomènes sans simplification des équations (recherche des niveaux d'instabilité). Quelques expériences réalisées dans des conditions simples sont menées en parallèle pour valider les moyens de calcul mis en place.

2 - SIMILITUDE DES INSTABILITES DE COMBUSTION

2.1 - Objectifs

Le chargement étudié est de type axisymétrique. Des instabilités de combustion ont été observées pendant les dix premières secondes de fonctionnement. Les fréquences mises en évidence par l'analyse des signaux de pression décroissent en fonction du temps et sont mal prévues par les calculs acoustiques classiques ou par des mesures réalisées sur des cavités à parois rigides représentatives [1]. L'insuccès des méthodes prévisionnelles disponibles a conduit à rechercher expérimentalement les modes potentiels d'instabilité au cours d'essais sur des chargements à échelle réduite. La figure 1 donne le schéma du propulseur à l'échelle 1/6ème expérimenté ; l'homothétie entre ce propulseur et le propulseur réel a été assurée précisément en ce qui concerne le chargement et la tuyère mais pas pour la structure (figure 2). Le propergol de référence pour le chargement étudié est un propergol composite aluminisé à liant polyuréthane.

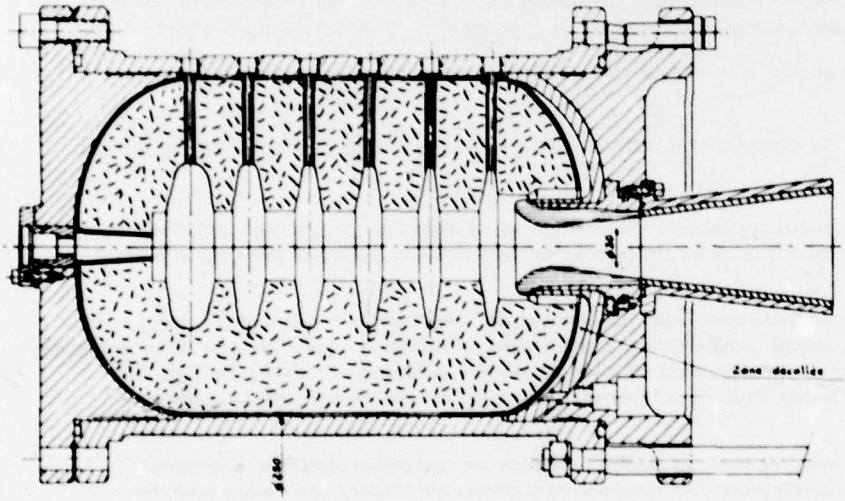

Fig. 1 – Schéma d'ensemble du propulseur à l'échelle 1/6.

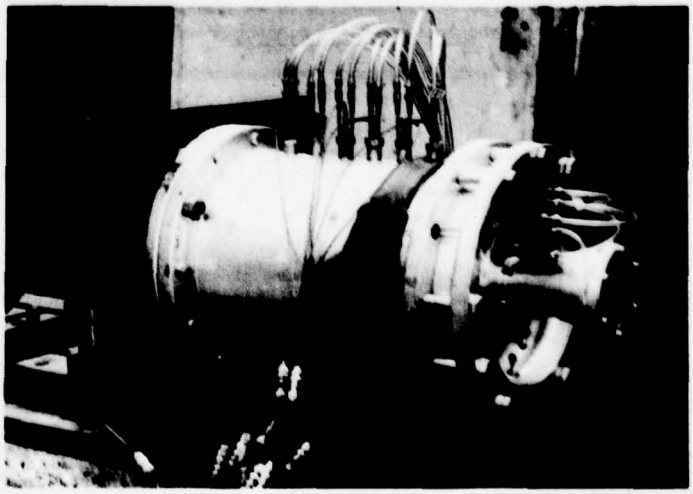

Fig. 2 – Vue générale du banc du propulseur.

2.2 - Résultats expérimenteux

Onze essais ont été effectués dans les conditions suivantes :

- Essais n°1 à 6 : premier lot du propergol de référence :
  - n°1 et 2 : géométrie nominale,
  - n°3 : modification de la zone décollée du fond arrière,
  - n°4 : modification de l'intégration de la tuyère,
  - n°5 : géométrie nominale, extinction du propulseur après 1 s,
  - n°6 : modification du convergent de la tuyère.
- Essais n°7 à 10 : second lot du propergol de référence :
  - n°7 : géométrie nominale,
  - n°8 : modification de la géométrie du chargement,
  - n°9 : augmentation de la pression moyenne de fonctionnement,
  - n°10 : introduction d'une zone décollée au fond avant.
- Essai n° 11 : changement de propergol, géométrie nominale.

2.2.1 - Observations générales

Tous les essais à échelle réduite ont été instables. L'analyse harmonique des signaux de pression indique l'existence de nombreux modes d'instabilité ; les principales fréquences identifiées décroissent en fonction du temps, ce qui a été également observé à l'échelle 1 (figure 3).

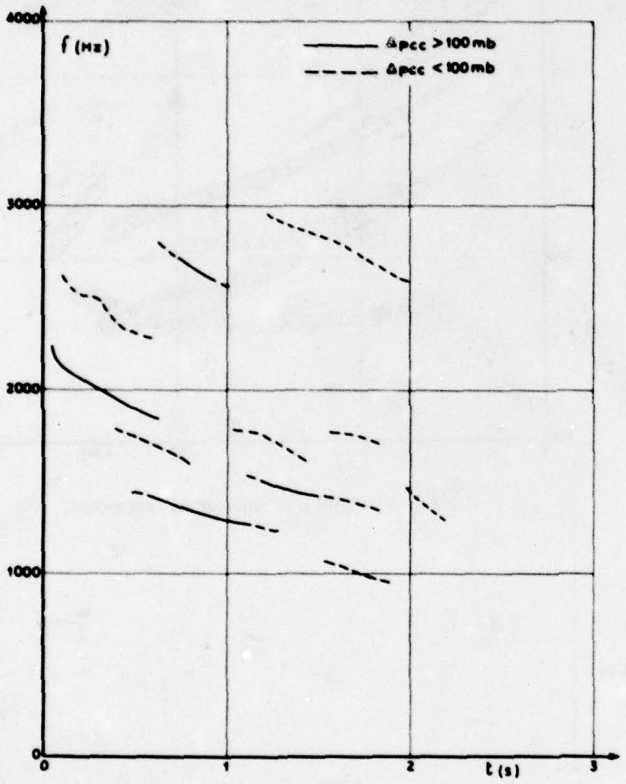

Fig. 3 – Exemple de résultats (essai No 1).

La reproductibilité est mauvaise même pour un lot donné de propergol : le niveau maximal d'instabilité est détecté à des instants et des fréquences différents lors des essais n°1, 2 et 5. L'influence du lot de propergol est manifeste puisque des fréquences non décelées au cours de la première série d'essais ont été systématiquement mises en évidence lors de la seconde. Les niveaux d'instabilité sont généralement renforcés dans les zones décollées ; la plus forte instabilité est apparue lors de l'essai n°9, avec un niveau maximal de 4,5 b crête à crête.

Les déphasages instantanés entre les composantes harmoniques des signaux de pression enregistrés en différents points de la chambre présentent pour certains modes des valeurs régulièrement réparties entre -180 et 180°, laissant présager une structure acoustique complexe.

2.2.2 - Etude des fréquences

La synthèse effectuée montre que les mêmes modes apparaissent au cours des différents essais, avec des niveaux toutefois variables. Des décalages de fréquence se manifestent lorsque la géométrie du propulseur est modifiée ; pour ces variations, on trouve par ordre d'influence croissante : la géométrie de la tuyère, l'importance des zones décollées et la géométrie du chargement.

Il a donc été possible de regrouper les résultats obtenus lors des essais n°1, 2, 4, 5, 6, 7 et 9 (propergol de référence ; $\Delta P_{cc} > 100$ mb) sur la figure 4. Les zones hachurées traduisent la légère dispersion des résultats ; l'identification des modes est conventionnelle : les chiffres 1, 2, 3, 4, 4', 4", 4"', 5 ... correspondent aux modes, les lettres a, b ... à la composante fondamentale, au premier harmonique...

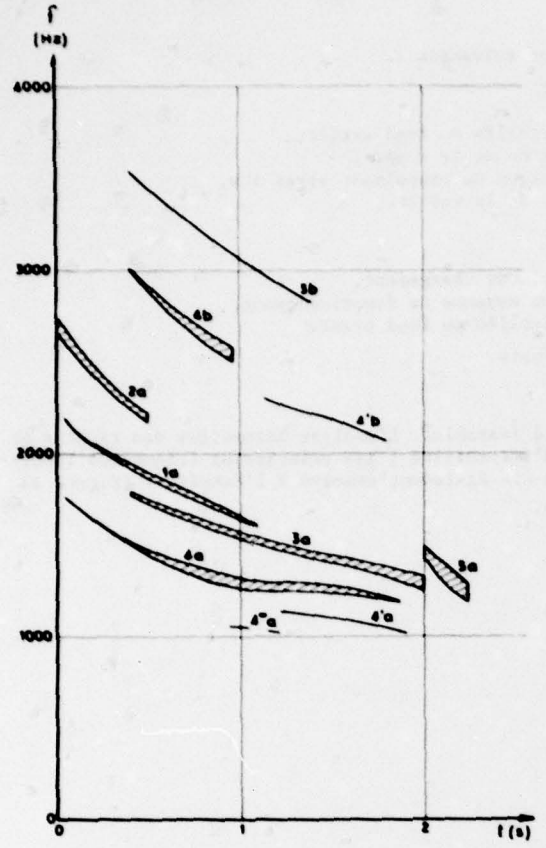

Fig. 4 – Récapitulation des principales fréquences observées (essais No 1, 2, 4, 5, 6, 7 et 9 ; propergol de référence).

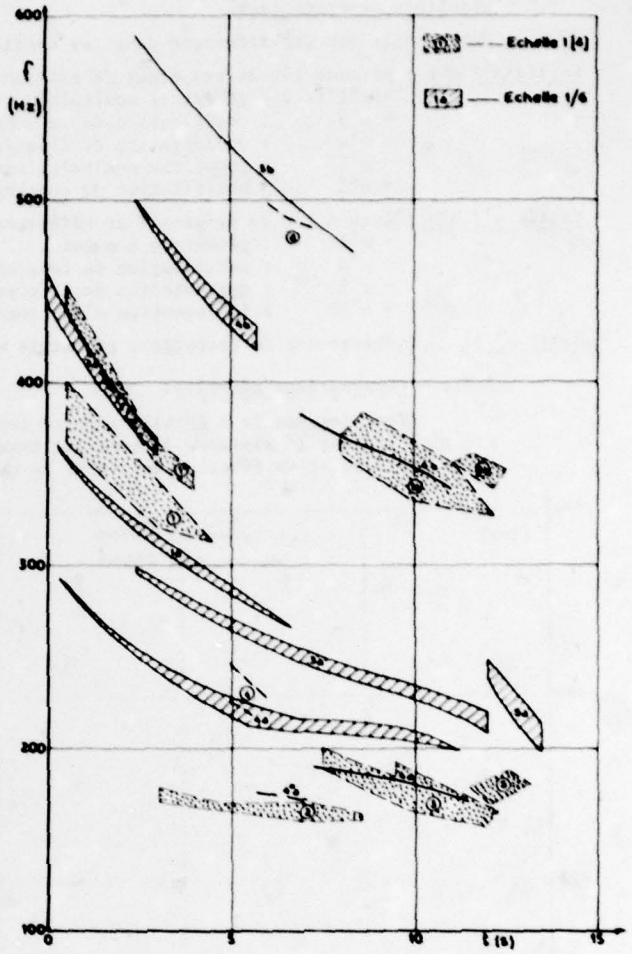

Fig. 5 – Effet d'échelle sur les fréquences.

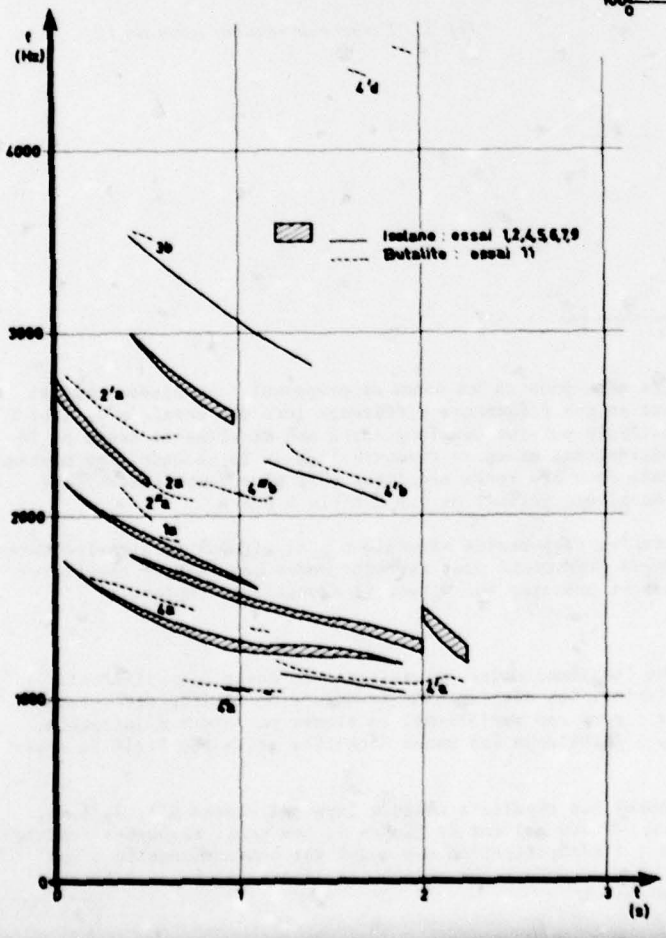

Fig. 6 – Influence d'un changement de propergol.

L'influence du lot de propergol s'est manifestée sur les modes de basse fréquence : alors que dans la première série d'essais, les modes 4''' a et 4'a n'étaient pas apparus, ils se sont au contraire systématiquement dégagés de la seconde série d'essais, avec un niveau assez important pour 4'a ($\Delta p_{..}$ = 0,7 b) lors de l'essai n°7.

L'influence de l'échelle sur les fréquences a été recherchée en ramenant à l'aide du facteur d'échelle les temps et les fréquences obtenus à l'échelle réduite aux valeurs correspondantes à échelle 1. La comparaison entre résultats à échelle 1 et à échelle 1/6ème est effectuée sur la figure 5 : les principales fréquences observées à échelle 1 peuvent être déduites, à de légers décalages près, des essais réalisés à échelle 1/6ème. Toutefois le changement d'échelle apparaît privilégier les modes de fréquence intermédiaire au détriment des modes de plus basse fréquence, pratiquement absents de la première série d'essai. Cet effet peut être attribué à l'incidence de l'échelle sur les pertes acoustiques ; c'est pourquoi en vue d'une prévision plus complète des modes potentiels d'instabilité, un essai complémentaire a été réalisé avec un propergol non métallisé permettant d'éliminer les pertes de nature biphasique.

Le choix de ce propergol a résulté d'un compromis : il fallait en effet maintenir la pression moyenne à un niveau comparable à celui des dix premiers essais et s'efforcer d'établir simplement une correspondance entre les différents résultats. Ce compromis a été réalisé : la pression moyenne n'a été inférieure que de 5 b dans la phase d'instabilité, l'évolution de la géométrie dans le temps a été très comparable et les valeurs voisines de la célérité du son (à l'équilibre thermodynamique et biphasique) ont permis d'obtenir des fréquences peu différentes. Au cours de cet essai, des instabilités se sont manifestées à haut niveau, y compris pour les modes de plus basse fréquence, à proximité immédiate des fréquences déjà identifiées (figure 6).

Les modes potentiels d'instabilité n'apparaissent donc pas dépendre du propergol utilisé, l'utilisation d'un propergol non métallisé permet de les déterminer plus facilement.

2.2.3 - Etude des amplitudes

La reproductibilité des essais et l'influence du lot de propergol rendent délicate l'identification des modes les plus instables. La synthèse des résultats obtenus fait cependant apparaître pour chaque mode un temps de combustion critique défini par l'obtention du maximum d'amplitude de pression en un point de la cavité. L'effet d'échelle sur ces temps critiques a été dégagé sur le tableau n°1, les temps critiques relatifs à l'échelle 1/6 étant ramenés à l'échelle 1 par le facteur d'échelle. L'accord entre les deux catégories de résultats est satisfaisant.

Tableau I – Effet d'échelle sur les temps critiques.

Echelle : 1		Echelle : 1/6	
Mode	t_c (s)	Mode	t_c (s)
①	1	1a	-
	2,5		3,3
②	6	4'''a	6
③	9	4'a	9
③b	10,5	4'b	8,4
④	5	4a	4,4
⑤	12	5a	12,8
⑥	6,5	3b	5,3

Des essais à échelle réduite permettent donc de définir les temps de combustion et donc les géométries pour lesquelles la stabilité du propulseur doit être étudiée en priorité ; une réelle économie de temps et d'argent peut découler de cette observation, en particulier si l'étude de la stabilité fait appel à des moyens de calcul sophistiqués.

En ce qui concerne les niveaux mêmes d'instabilité aux différentes échelles, il est seulement possible de constater qu'ils sont du même ordre de grandeur, la dispersion des résultats n'autorisant pas de conclusion plus précise.

2.2.4 - Etude paramétrique

Certains essais visaient à déterminer l'incidence sur la stabilité du propulseur de modifications destinées à améliorer son comportement instationnaire ou imposées par d'autres contraintes technologiques. Le faible nombre d'essais et la dispersion des résultats n'ont pas permis de conclusions nettes dans tous les cas :

a) - pression moyenne
une augmentation de la pression moyenne de 40% a été obtenue lors de l'essai n°9 par réduc-

tion de la section du col. Le niveau maximal d'instabilité a été fortement augmenté sur le mode 4a, atténué sur les autres modes. La même tendance a été observée à l'échelle 1 ;

b) - géométrie du chargement
la modification du chargement n°8 a consisté à réaliser des chanfreins à l'aval des gorges afin de limiter les survitesses de l'écoulement liées au contournement du profil. Cette modification semble avoir réduit les niveaux d'instabilité dans la période où le profil de combustion est le plus modifié ;

c) - zones décollées
les résultats sont contradictoires : la diminution de la zone décollée du fond arrière (essai n°3) s'est traduite par un accroissement du niveau maximal d'instabilité, l'introduction d'une zone décollée au fond avant également ;

d) - géométrie de la tuyère
il n'a pas été possible de dégager l'influence de l'intégration de la tuyère ou de la forme de son convergent, la réduction de l'intégration (essai n°4), l'augmentation de la longueur du convergent n'ont pas changé les instabilités de manière significative.

2.3 - Interprétation des résultats

Les essais réalisés ont fourni des informations intéressantes indépendamment de toute considération théorique sur la physique du phénomène. Il faut maintenant s'interroger sur les limites des essais à échelle réduite et tenter d'interpréter théoriquement certaines des observations faites.

La saturation des instabilités à un certain niveau d'amplitude est liée à des phénomènes non linéaires au niveau de la combustion et de l'écoulement des produits de combustion, phénomènes encore difficiles à prévoir surtout dans le cas de géométries complexes. Aussi le premier problème à résoudre est-il celui de la stabilité linéaire du propulseur c'est-à-dire de la réponse du propulseur à une petite perturbation à partir d'un état stationnaire. Les équations peuvent être alors grandement simplifiées (linéarisation) et leurs composantes instationnaires peuvent être traitées par les méthodes acoustiques classiques. Cette technique conduit, dans la mesure où le nombre de Mach de l'écoulement moyen reste faible, à assimiler les modes harmoniques d'instabilité aux modes acoustiques classiques (cavité fermée à parois rigides) et à exprimer l'amplification algébrique du phénomène global comme la somme des contributions apportées par chaque phénomène élémentaire (bilan acoustique) : réponse instationnaire de la surface de combustion, comportement instationnaire de la tuyère, amortissement viscoélastique dans le chargement, pertes biphasiques dans les produits de combustion...

Les fréquences observées ne sont pas en accord avec celles prévues par l'acoustique classique, ce qui laisse supposer une interaction assez forte entre l'écoulement moyen et l'écoulement instationnaire. Il n'a pas encore été possible d'expliquer précisément ces écarts et le problème reste ouvert. En dépit de cette difficulté nous nous appuierons sur la méthode du bilan acoustique pour estimer qualitativement l'influence de l'échelle sur la stabilité du propulseur.

2.3.1 - Réponse de la surface de combustion

La réponse du propergol de référence aux oscillations harmoniques de pression a été mesurée au propulseur à éjection modulée [2]. Le maximum de la partie réelle de la réponse se produit peu avant 1000 Hz aux pressions moyennes remontées, il est assez marqué et dépasse 6. Nous ne tiendrons pas compte pour simplifier du couplage pression vitesse cependant probable dans les zones de survitesse de l'écoulement en raison de l'observation d'une érosion moyenne.

La contribution de la surface de combustion au bilan acoustique s'écrit de façon classique [3] :

$$\alpha_c = \frac{\bar{a}}{\mathcal{E}} \frac{\iint_{S_b} \tilde{\varphi}_n^2 \left(A_b^{(r)} + \bar{M}_b\right) dS}{\iiint_V \tilde{\varphi}_n^2 \, dV}$$

Plutôt que l'admittance réduite A_b de la surface de combustion nous utiliserons ici les réponses R_{MP} (réponse en débit à la pression), R_{TP} (réponse en température à la pression) et $R_c = R_{MP} + R_{TP}$ (réponse globale à la pression), R_c étant mesurée directement au propulseur à éjection modulée. Entre A_b et R_c existe la relation :

$$R_c = 1 + \frac{A_b}{\delta \bar{M}_b} .$$

En admettant que $\bar{M}_b$ et R_c ne varient pas sur la surface de combustion, il vient :

$$\alpha_c = \frac{\bar{a} \bar{M}_b \left(\delta R_c^{(r)} - \delta + 1\right)}{\mathcal{E}} \frac{\iint_{S_b} \tilde{\varphi}_n^2 \, dS}{\iiint_V \tilde{\varphi}_n^2 \, dV}$$

Comparant maintenant les valeurs de α_c à l'échelle 1 (α_{c_1}) et à l'échelle λ (α_{c_λ}) pour les fréquences correspondantes f et f/λ et un même propergol, on aura donc :

$$\frac{\alpha_{c_\lambda}}{\alpha_{c_1}} = \frac{1}{\lambda} \frac{R_c^{(r)}\left(\frac{f}{\lambda}\right) - \frac{\alpha_1}{\delta}}{R_c^{(r)}(f) - \frac{\alpha_1}{\delta}} \simeq \frac{R^{(r)}\left(\frac{f}{\lambda}\right)}{\lambda \, R_c^{(r)}(f)}$$

Pour les essais à échelle réduite et compte tenu de la courbe $R_e^{(r)}(f)$, la contribution de la surface de combustion devrait être augmentée pour les modes de plus basse fréquence.

2.3.2 - Comportement instationnaire de la tuyère

La contribution de la tuyère au bilan acoustique s'exprime comme celle due à la surface de combustion :

$$\alpha_T = - \frac{\bar{a} \iint_{S_E} \tilde{\varphi}_n^2 \left(A_E^{(r)} + \bar{M}_E \right) dS}{\mathcal{E} \iiint_V \tilde{\varphi}_n^2 \, dV} .$$

Dans le cadre d'une étude monodimensionnelle de l'écoulement instationnaire de la tuyère, il est plus simple de substituer à A_E l'admittance réduite Y définie par :

$$Y = \frac{\tilde{u}/\bar{u}}{\tilde{p}/\bar{p}} = \frac{A_E}{\gamma \bar{M}_E} .$$

Il vient donc :

$$\alpha_T = - \frac{\bar{a} \bar{M}_E \left(1 + \gamma Y^{(r)} \right) \iint_{S_E} \tilde{\varphi}_n^2 \, dS}{2 \iiint_V \tilde{\varphi}_n^2 \, dV} .$$

Comme Y ne dépend pour une géométrie de tuyère donnée que de la fréquence réduite des oscillations (par exemple $\beta = \frac{\omega \ell}{\bar{a}}$, où ℓ est la longueur du convergent), le terme $1 + \gamma Y^{(r)}$ ne dépendra pas de l'échelle considérée :

$$\frac{\alpha_{T\lambda}}{\alpha_{T_1}} = \frac{1}{\lambda} .$$

L'amortissement de la tuyère augmente lorsque l'échelle diminue.

2.3.3 - Pertes biphasiques dans les produits de combustion

Dans le cadre d'hypothèses très simplifiées (particules sphériques très petites et de taille uniforme, hypothèse de Stokes pour la loi de traînée, transfert thermique négligé entre gaz et particules), il est possible de parvenir à une expression simple de l'amortissement dû aux particules [4] :

$$\alpha_p = - \frac{\omega K}{2} \cdot \frac{\omega \tau_u}{1 + (\omega \tau_u)^2} ,$$

où K est le rapport de la masse volumique de la phase condensée à celle du gaz (caractéristique du propergol) et τ_u la constante de relaxation en vitesse ($\tau_u = \frac{2 r_p^2 \rho_c}{9 \mu}$).

Pour une fréquence donnée, l'amortissement est maximal pour les particules dont le rayon est tel que : $\omega \tau_u = 1$. Une fréquence critique d'amortissement existe donc pour une taille donnée de particule :

$$f_c = \frac{9 \mu}{4 \pi r_p^2 \rho_c} ,$$

soit pour des valeurs raisonnables des paramètres physiques :

$$f_c \; (\text{Hz}) \simeq \frac{10\,000}{r_p^2 \; (\mu\text{m})} .$$

Une incertitude importante subsiste sur le rayon moyen des particules dans la chambre de combustion d'un propulseur et sur ses variations avec le temps de séjour moyen dans le propulseur. En fonction des résultats fragmentaires obtenus dans ce domaine [5], nous sommes conduits à estimer que la majorité des particules ont un rayon inférieur au micron, si bien que les fréquences observées doivent toujours être inférieures à la fréquence critique. L'expression de prend dans ces conditions la forme simplifiée :

$$\alpha_p \simeq - \frac{\omega^2 \tau_u K}{2} .$$

D'où :

$$\frac{\alpha_{p\lambda}}{\alpha_{p_1}} = \frac{1}{\lambda^2} .$$

Récapitulons les résultats dans une formule unique :

$$\alpha_1 = \alpha_{c_1} + \alpha_{T_1} + \alpha_{p_1} ,$$

$$\alpha_\lambda = \frac{1}{\lambda} \left[\frac{R_e^{(r)}\left(\frac{f}{\lambda}\right)}{R_e^{(r)}(f)} \alpha_{c_1} + \alpha_{T_1} + \frac{1}{\lambda} \alpha_{p_1} \right]$$

$$= \frac{1}{\lambda} \left[\alpha_1 + \alpha_{c_1} \left(\frac{R_e^{(r)}\left(\frac{f}{\lambda}\right)}{R_e^{(r)}(f)} - 1 \right) + \alpha_{p_1} \left(\frac{1}{\lambda} - 1 \right) \right] .$$

La différence de comportement au point de vue de la stabilité des essais à différentes échelles dépendra donc essentiellement du signe de la somme :

$$\Delta = \alpha_{c_1}\left(\frac{R_c^{(\sigma)}\left(\frac{f}{\lambda}\right)}{R_c^{(\sigma)}(f)} - 1\right) + \alpha_{p_1}\left(\frac{1}{\lambda} - 1\right) \quad , \alpha_{c_1} > 0 \, , \alpha_{p_1} < 0 \, ,$$

et par conséquent de la fréquence et du mode considéré.

2.3.4 - Application aux essais réalisés

La faible instabilité des essais à échelle réduite pour les modes de plus basse fréquence laisse supposer une augmentation de l'amortissement dû aux particules supérieure à celle de la contribution de la surface de combustion :

$$|\alpha_{p_1}|\left(\frac{1}{\lambda} - 1\right) > \alpha_{c_1}\left(\frac{R_c^{(\sigma)}\left(\frac{f}{\lambda}\right)}{R_c^{(\sigma)}(f)} - 1\right) \, ,$$

mais comme $\alpha_{c_1} > |\alpha_{p_1}|$ (mode instable échelle 1), on devrait avoir :

$$R_c^{(\sigma)}\left(\frac{f}{\lambda}\right) < \frac{1}{\lambda} R_c^{(\sigma)}(f) \, .$$

Cette inégalité n'est pas exclue en raison de la rapide décroissante de $R_c^{(\sigma)}$ après son maximum.

L'apparition des modes instables à haute fréquence aux deux échelles n'est par contre explicable que si l'on admet que l'amortissement dû aux particules croît beaucoup moins que ne le laisse supposer la formule proposée.

L'augmentation des instabilités de combustion de moyenne fréquence avec le changement de pression s'interprète correctement si l'on admet que $R_c^{(\sigma)}$ est fonction d'une fréquence réduite $\frac{\omega \, c_1 r}{\partial P_b}$: l'augmentation de pression équivaut à une diminution de la fréquence réduite et compte tenu des fréquences mises en jeu à une augmentation de $R_c^{(\sigma)}$.

Pour l'essai réalisé avec le propergol non métallisé, on vérifie bien que le changement d'échelle n'amortit pas les modes d'instabilité, compte tenu du changement de réponse pour le nouveau propergol.

2.4 - Conclusion

L'étude expérimentale conduite sur des chargements axisymétriques à petite échelle a permis de recueillir les enseignements suivants :

- pour des chargements géométriquement complexes, les calculs classiques de stabilité tombent en défaut,
- les modes potentiels d'instabilité et les profils de combustion pour lesquels le propulseur est le plus instable peuvent être déterminés par des essais à échelle réduite. Cette détermination est peu sensible au choix du propergol, à géométrie imposée, l'élimination de l'amortissement dû aux particules par le choix d'un propergol non métallisé est intéressante,
- la correspondance exacte entre essais à différentes échelles est difficile à établir en raison des incertitudes subsistant sur les données de base (réponse du propergol au couplage pression-vitesse, granulométrie des particules d'alumine) et sur la structure détaillée des modes d'instabilité.

Les essais à échelle réduite ne peuvent donc se substituer aux essais à échelle 1 ; ils constituent, dans l'arsenal des moyens mis à la disposition des constructeurs, une possibilité supplémentaire pour mieux cerner le problème des instabilités de combustion et réduire les coûts de développement de nouveaux propulseurs.

3 - ANALYSE DES INSTABILITES DE COMBUSTION DANS LE DOMAINE LINEAIRE

3.1 - Objectifs

L'utilisation de la forme linéarisée des équations de la mécanique des fluides reste l'approche la plus simple pour étudier la stabilité d'un propulseur. La méthode du bilan acoustique est, du moins dans sa forme élémentaire, limitée aux écoulements moyens à faible nombre de Mach, de telle sorte que la distorsion des modes acoustiques classiques reste faible. Cette méthode tombe en défaut lorsque les conditions du problème traité ne permettent pas de négliger l'interaction de l'acoustique avec l'écoulement moyen ; son insuccès pour des géométries axisymétriques complexes a été mentionné au chapitre précédent, un autre exemple est celui des moteurs sans tuyère puisque le nombre de Mach de l'écoulement moyen en sortie de canal atteint 1.

Pour surmonter cette difficulté, l'idée suivie est d'intégrer numériquement les équations linéarisées de base au lieu de rechercher des solutions analytiques approchées explicites. Cette démarche commencée il y a quelques années [6] a été reprise récemment. Elle n'a été appliquée jusqu'ici qu'à des problèmes simples se satisfaisant d'une description monodimensionnelle monophasique mais est a priori susceptible d'être généralisée à des écoulements bi ou tridimensionnels biphasiques. Les applications visées en priorité sont en effet les suivantes :

- propulseurs à perforation centrale faiblement évolutive,

- montages d'essai pour la mesure de la réponse des propergols solides au couplage pression-vitesse.

3.2 - Equations de base

Les équations de base sont les équations de bilan et l'équation d'état du gaz :

$$\begin{cases} \dfrac{\partial}{\partial t}(\rho A) + \dfrac{\partial}{\partial x}(\rho u A) = A m, \\ \dfrac{\partial}{\partial t}(\rho u A) + \dfrac{\partial}{\partial x}\left((p+\rho u^2)A\right) = p\dfrac{\partial A}{\partial x}, \\ \dfrac{\partial}{\partial t}(\rho h_t A) + \dfrac{\partial}{\partial x}(\rho u h_t A) = A\dfrac{\partial p}{\partial t} + A m h_{ip}, \\ p = \rho r T. \end{cases}$$

m est ici le débit de la surface de combustion par unité de longueur le long de l'axe du propulseur, h_{ip} l'enthalpie des produits de combustion injectés localement.

La résolution du problème stationnaire se ramène, dans la mesure où la température de flamme est indépendante de la pression, à deux équations différentielles ordinaires, par exemple pour la pression $\bar{p}$ et le nombre de Mach $\bar{M}$:

$$\begin{cases} (1-\bar{M}^2)\dfrac{d\bar{p}}{dx} = -2\bar{M}\sqrt{1+\frac{\gamma-1}{2}\bar{M}^2}\;\bar{m}\bar{a}_0 + \gamma\bar{p}\bar{M}^2\dfrac{1}{A}\dfrac{dA}{dx}, \\ (1-\bar{M}^2)\dfrac{d\bar{M}}{dx} = (1+\gamma\bar{M}^2)\sqrt{1+\frac{\gamma-1}{2}\bar{M}^2}\;\dfrac{\bar{m}\bar{a}_0}{\gamma\bar{p}} - \bar{M}\left(1+\frac{\gamma-1}{2}\bar{M}^2\right)\dfrac{1}{A}\dfrac{dA}{dx}. \end{cases}$$

L'écoulement stationnaire n'est pas isentropique en raison de l'injection latérale.

La linéarisation des équations instationnaires conduit après quelques calculs au système canonique suivant (oscillations naturelles) :

$$\begin{cases} (\bar{a}^2-\bar{u}^2)\dfrac{d\tilde{\varphi}}{dx} = \left[\dfrac{\gamma\bar{m}}{\bar{\rho}}\left(1+\frac{\gamma-1}{2}\bar{M}^2\right)\left(2-(2R_{MP}+R_{TP})\right)+(\gamma-1)\dfrac{d\bar{u}}{dx}+j\omega\right]\bar{u}\tilde{\varphi} \\ \qquad -\gamma\left[\dfrac{\bar{m}}{\bar{\rho}}\left(1+\frac{\gamma-1}{2}\bar{M}^2\right)(2R_{Mu}+R_{Tu})+2\dfrac{d\bar{u}}{dx}+j\omega\right]\bar{u}\tilde{\nu} \\ \qquad +(\gamma-1)\bar{u}\dfrac{d\bar{u}}{dx}\tilde{S}, \\ \gamma\bar{u}(\bar{a}^2-\bar{u}^2)\dfrac{d\tilde{\nu}}{dx} = \left[\gamma\dfrac{\bar{m}}{\bar{\rho}}\left((R_{MP}-1)(1+\gamma\bar{M}^2)+R_{TP}\left(1+\frac{\gamma-1}{2}\bar{M}^2\right)\right)-(\gamma-1)\bar{M}^2\dfrac{d\bar{u}}{dx}-j\omega\right]\bar{a}^2\tilde{\varphi} \\ \qquad +\gamma\left[\dfrac{\bar{m}}{\bar{\rho}}\left(\bar{M}^2-1+R_{Mu}(1+\gamma\bar{M}^2)+R_{Tu}\left(1+\frac{\gamma-1}{2}\bar{M}^2\right)\right)+2\bar{M}^2\dfrac{d\bar{u}}{dx}+\bar{M}^2 j\omega\right]\bar{a}^2\tilde{\nu} \\ \qquad -(\gamma-1)\bar{u}^2\dfrac{d\bar{u}}{dx}\tilde{S}, \\ \bar{u}\dfrac{d\tilde{S}}{dx} = \dfrac{\bar{m}}{\bar{\rho}}\left[-(1+\gamma\bar{M}^2)+\gamma R_{MP}\bar{M}^2+\dfrac{\gamma}{\gamma-1}R_{TP}\left(1+\frac{\gamma-1}{2}\bar{M}^2\right)\right]\tilde{\varphi} \\ \qquad +\gamma\dfrac{\bar{m}}{\bar{\rho}}\left[R_{Mu}\bar{M}^2+\dfrac{R_{Tu}}{\gamma-1}\left(1+\frac{\gamma-1}{2}\bar{M}^2\right)\right] \\ \qquad -\left(\dfrac{\bar{m}}{\bar{\rho}}+j\omega\right)\tilde{S}. \end{cases}$$

Ce système a été établi pour l'amplitude réduite $\tilde{\varphi}$ de pression, l'amplitude réduite $\tilde{\nu}$ de vitesse et l'amplitude de l'entropie réduite $\tilde{S}$. Le choix de $\tilde{\varphi}$ et $\tilde{\nu}$ s'impose pour expliciter le couplage instationnaire entre l'écoulement et la combustion ; nous avons posé :

$$\tilde{v_b}/\bar{v_b} = R_{MP}\tilde{\varphi} + R_{Mu}\tilde{\nu},$$
$$\tilde{T_f}/\bar{T_f} = R_{TP}\tilde{\varphi} + R_{Tu}\tilde{\nu},$$

l'utilisation de $\tilde{S}$ permettant en outre de simplifier les calculs et l'interprétation physique des résultats.

L'écoulement stationnaire intervient par les grandeurs $\bar{u}$, $\bar{a}$, $\bar{M}$, $\bar{m}$ et $\bar{\rho}$ et par la seule dérivée $\dfrac{d\bar{u}}{dx}$ qui peut être exprimée en fonction des grandeurs stationnaires. Ce jeu d'équations est valable aussi bien dans la chambre de combustion que dans la tuyère ($\bar{m} = 0$). Il doit être intégré avec les conditions limites implicitement contenues dans les équations : $\bar{M} = 0$ (fond avant du propulseur)

et $\bar{M} = 1$ (col de la tuyère) sont en effet des singularités pour lesquelles il faut assurer la continuité des solutions ; une dernière condition reste libre en raison du caractère homogène des équations, il est par exemple possible de choisir $\tilde{\varphi} = 1$ en un point.

Trois applications seront successivement étudiées :

- stabilité d'un propulseur classique géométriquement simple,
- stabilité d'un moteur sans tuyère,
- détermination du couplage pression-vitesse d'un propergol solide.

3.3 - Stabilité d'un propulseur géométriquement simple

La géométrie du propulseur est illustrée par la figure 23 ; le canal cylindrique est raccordé à une tuyère biconique et de rayon de courbure constant au col. La réponse en débit du propergol aux oscillations de pression est introduite sous forme analytique par une loi classique à deux paramètres n et β [7] ajustés pour retrouver un maximum réaliste de la partie réelle ; la réponse en température de flamme du propergol aux oscillations de pression se déduit de la réponse en débit ; le couplage pression-vitesse est négligé. Le problème mathématique à résoudre est donc un problème à valeur propre ω (complexe) ; il est résolu numériquement par approximations successives en intégrant simultanément le système différentiel en $\tilde{\varphi}$, $\tilde{v}$ et $\tilde{S}$ et le système adjoint.

Une application numérique a été effectuée pour une valeur modérée du nombre de Mach à l'entrée de la tuyère ($\bar{M}_e = 0{,}15$) dans le but de comparer cette méthode numérique à celle du bilan acoustique. L'accord est satisfaisant puisque le coefficient d'amplification est trouvé respectivement égal à $-58{,}8\ s^{-1}$ et $57{,}1\ s^{-1}$. Les figures 7, 8 et 9 donnent la répartition de $\tilde{\varphi}$, $\tilde{v}$ et $\tilde{S}$ dans la chambre et leur comparaison avec le mode acoustique classique. Ces résultats confirment la bonne approximation d'ensemble fournie par le mode acoustique classique lorsque le nombre de Mach de l'écoulement reste faible dans la chambre ; toutefois des écarts de déphasage supérieurs à 10° sont constatés au fond arrière. De tels écarts ne sont pas compatibles avec la recherche expérimentale des couplages pression et pression-vitesse (paragraphe 3.5) qui nécessite une description plus précise du champ de pression.

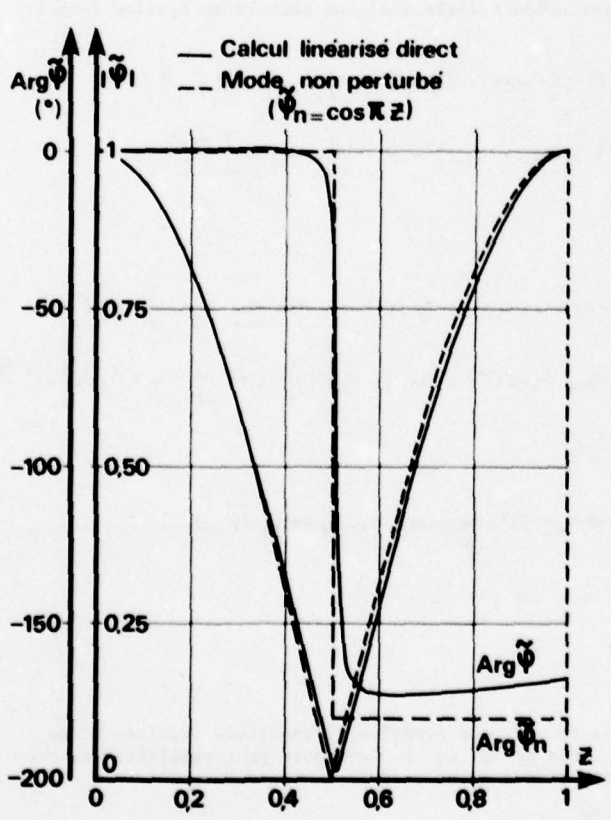

Fig. 7 – Etude de la stabilité d'un propulseur par intégration des équations linéarisées (amplitude de pression).

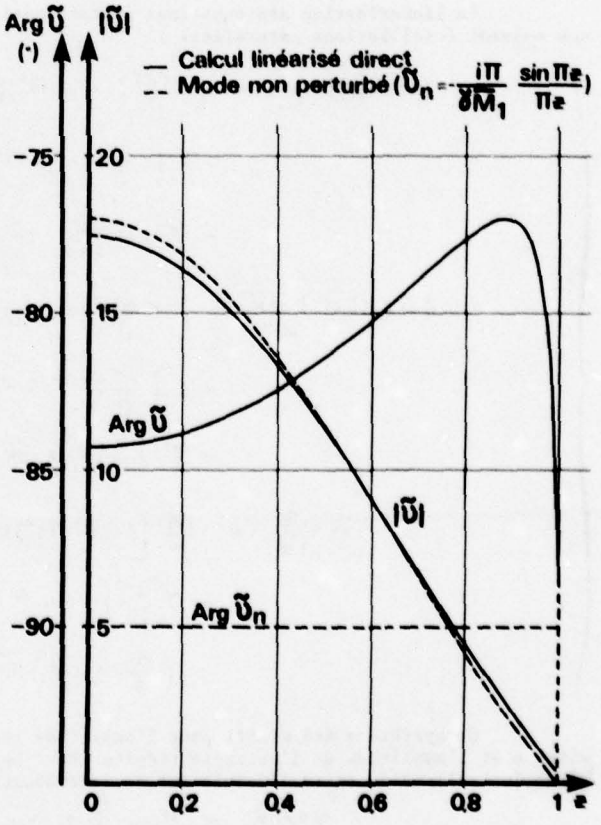

Fig. 8 – Etude de la stabilité d'un propulseur par intégration des équations linéarisées (amplitude de vitesse).

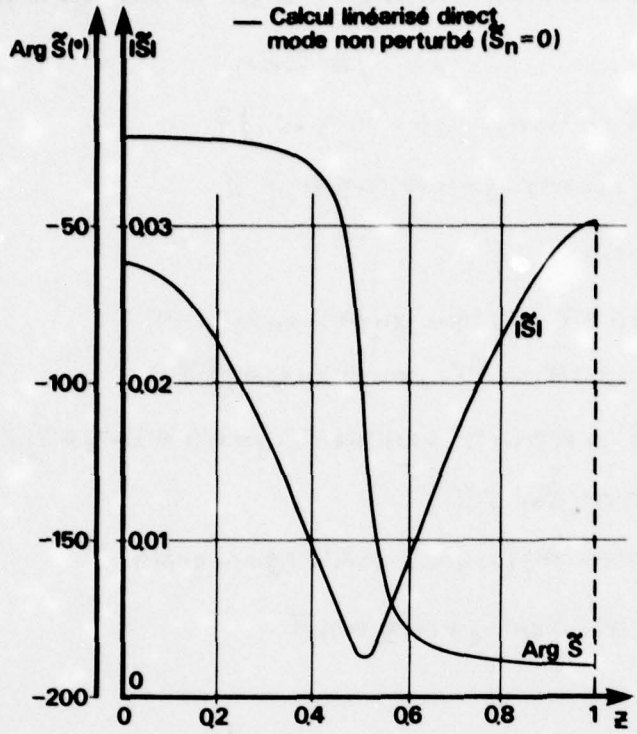

Fig. 9 – Etude de la stabilité d'un propulseur par intégration des équations linéarisées (amplitude d'entropie).

Fig. 10 – Application des équations linéarisées à un moteur sans tuyère.

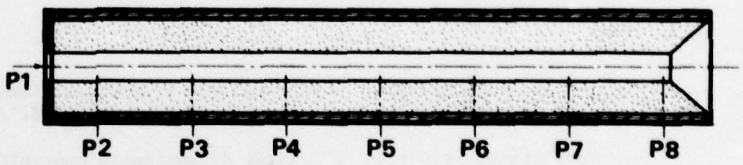

P1 à P8 prises de pression

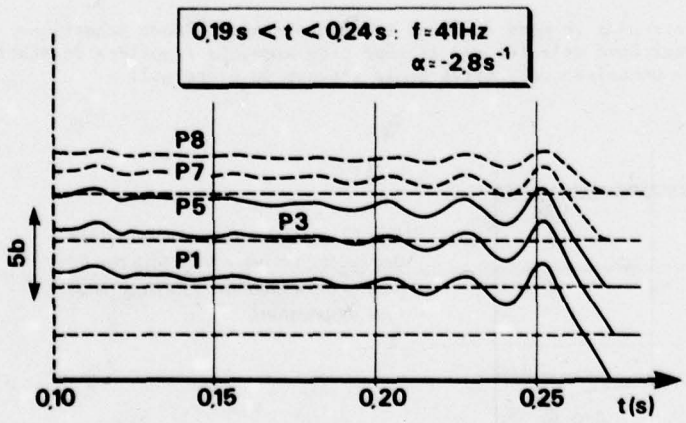

Fig. 11 – Instabilités basse fréquence sur un moteur sans tuyère.

3.4 - Stabilité d'un moteur sans tuyère

Le moteur sans tuyère est l'exemple type d'un couplage élevé entre l'écoulement moyen et l'acoustique. Le problème sera limité ici aux instabilités basse fréquence que nous considèrerons comme un cas particulier d'instabilité acoustique ; notre point de vue sera donc différent de celui adopté par Thrasher [8] qui assimile le phénomène à celui d'instabilités en volume dans un propulseur classique.

L'expérience montre que dans un propulseur sans tuyère (figure 10), les instabilités basse fréquence sont caractérisées par une amplitude réduite $\frac{\delta p}{p}$ de pression sensiblement constante dans le canal (figure 11). C'est cette particularité que nous avons tenté de retrouver par le calcul.

Dans un but de simplification, nous avons supposé le canal cylindrique et la vitesse stationnaire de combustion constante : la solution du problème stationnaire prend alors une forme explicite [9]. Seules les réponses en pression du propergol sont prises en compte, elles sont exprimées analytiquement. Un changement de variable permet alors de se ramener à trois équations différentielles ordinaires linéaires et

homogènes dont les coefficients ne dépendent que de la nouvelle variable $\bar{m}$ et qui sont donc plus faciles à intégrer :

$$
\left\{
\begin{aligned}
(1-\bar{M}^2)(1+\tfrac{\gamma-1}{2}\bar{M}^2)(1+\delta\bar{M}^2)^2\frac{d\tilde{\varphi}}{d\bar{M}} &= \bar{M}\Big[\delta\big(2(1-R_{MP})+R_{TP}\big)(1-\bar{M}^2)(1+\tfrac{\gamma-1}{2}\bar{M}^2)(1+\delta\bar{M}^2)\\
&\quad +(\delta-1)(1+\delta\bar{M}^2)^2+J\varpi(1-\bar{M}^2)(1+\tfrac{\gamma-1}{2}\bar{M}^2)\Big]\tilde{\varphi}\\
&\quad -\delta\bar{M}\Big[2(1+\delta\bar{M}^2)^2+J\varpi(1-\bar{M}^2)(1+\tfrac{\gamma-1}{2}\bar{M}^2)\Big]\tilde{v}\\
&\quad +(\delta-1)\bar{M}(1+\delta\bar{M}^2)^2\tilde{S}\ ,\\
\delta\bar{M}(1-\bar{M}^2)(1+\tfrac{\gamma-1}{2}\bar{M}^2)(1+\delta\bar{M}^2)^2\frac{d\tilde{v}}{d\bar{M}} &= \Big[\delta(1-\bar{M}^2)(1+\delta\bar{M}^2)\big((R_{MP}-1)(1+\delta\bar{M}^2)+R_{TP}(1+\tfrac{\gamma-1}{2}\bar{M}^2)\big)\\
&\quad -(\delta-1)\bar{M}^2(1+\delta\bar{M}^2)^2-J\varpi(1-\bar{M}^2)(1+\tfrac{\gamma-1}{2}\bar{M}^2)\Big]\tilde{\varphi}\\
&\quad +\delta\Big[-(1-\bar{M}^2)^2(1+\delta\bar{M}^2)+2\bar{M}^2(1+\delta\bar{M}^2)^2+J\varpi\bar{M}^2(1-\bar{M}^2)(1+\tfrac{\gamma-1}{2}\bar{M}^2)\Big]\tilde{v}\\
&\quad -(\delta-1)\bar{M}^2(1+\delta\bar{M}^2)^2\tilde{S}\ ,\\
\bar{M}(1+\tfrac{\gamma-1}{2}\bar{M}^2)(1+\delta\bar{M}^2)^2\frac{d\tilde{S}}{d\bar{M}} &= (1-\bar{M}^2)(1+\delta\bar{M}^2)\Big[-1+(R_{MP}-1)\delta\bar{M}^2+\frac{\delta R_{TP}}{\delta-1}(1+\tfrac{\gamma-1}{2}\bar{M}^2)\Big]\tilde{\varphi}\\
&\quad -(1-\bar{M}^2)\big(1+\delta\bar{M}^2+J\varpi(1+\tfrac{\gamma-1}{2}\bar{M}^2)\big)\tilde{S}\ .
\end{aligned}
\right.
$$

où est la fréquence réduite $\frac{\omega L}{a_0}\sqrt{2(\delta-1)}$.

Les conditions limites à respecter sont :

- $\bar{M} = 0$: $\tilde{\varphi}_0 = 1$,

- $= 1$: $\tilde{\varphi}_1 - \frac{\delta}{\delta-1}\tilde{v}_1 + \tilde{S}_1 = 0$, condition traduisant l'annulation de l'amplitude des oscillations du nombre de Mach en sortie de canal.

Pour chaque valeur de $\bar{p}_0$ fixée et partant d'une valeur ϖ approchée, on tend par approximations successives vers la valeur propre ϖ recherchée. La valeur de $\bar{p}_0$ conduisant à la stabilité est obtenue après quelques passages du programme de calcul. La figure 12 illustre les résultats obtenus à la stabilité pour la répartition de $\tilde{\varphi}$: l'amplitude de pression est bien sensiblement uniforme dans le canal.

Ce type de calcul permet donc de retrouver le mode de basse fréquence comme un mode acoustique d'ordre 0, les autres modes acoustiques peuvent être calculés par le même programme. La frontière de stabilité pour chaque mode dépend évidemment de la connaissance précise de la réponse du propergol.

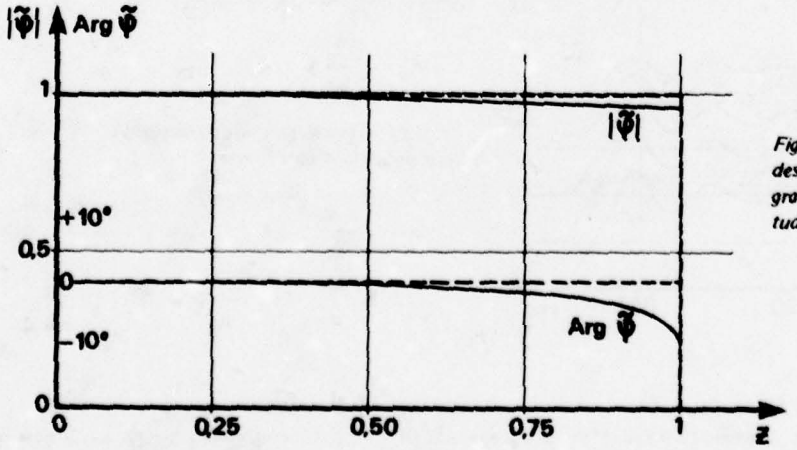

Fig. 12 – Moteur sans tuyère : étude des instabilités basse fréquence par intégration des équations linéarisées (amplitude de pression).

3.5 - Etude du couplage pression vitesse

Le problème du couplage pression vitesse, c'est-à-dire de l'action combinée sur la combustion du propergol des oscillations de la pression et de la vitesse de l'écoulement parallèlement à la surface, est d'une grande complexité puisqu'il s'agit de déterminer la modification apportée par l'écoulement au couplage pression, phénomène dont l'étude est déjà difficile. L'approche adoptée ici se situe dans le cadre des études de stabilité et de la description linéaire des phénomènes, l'interaction écoulement-combustion est donc envisagée comme le déplacement périodique d'un phénomène d'érosion, suivant en cela l'analyse présentée par Lengellé [10]. Cette approche exclut donc les phénomènes de caractère non linéaire susceptibles de se produire lorsque l'amplitude des oscillations de vitesse devient du même ordre de grandeur que la vitesse moyenne.

Un montage d'essai a été construit pour vérifier si la description qui a été donnée du phénomène est réaliste et tenter d'en quantifier les effets. Des conditions de fonctionnement susceptibles de créer un effet érosif mesurable et de privilégier les oscillations de vitesse par rapport aux oscillations de pression ont été donc recherchées. La solution retenue repose sur la création d'oscillations forcées, par la modulation du col de sortie, dans une chambre d'expérience bidimensionnelle elle-même alimentée par un générateur (figure 13) ; le découplage du générateur et de la chambre d'expérience par une tuyère amorcée permet d'atteindre des niveaux de modulation intéressants, de limiter les coûts de fabrication et de faciliter l'étude paramétrique (pression moyenne, fréquence). Les essais réalisés ont permis de mesurer l'érosion moyenne du propergol et la répartition de l'amplitude de pression dans la chambre [1] ; le travail récent a porté sur l'analyse du fonctionnement instationnaire du montage en vue de rechercher les paramètres de couplage.

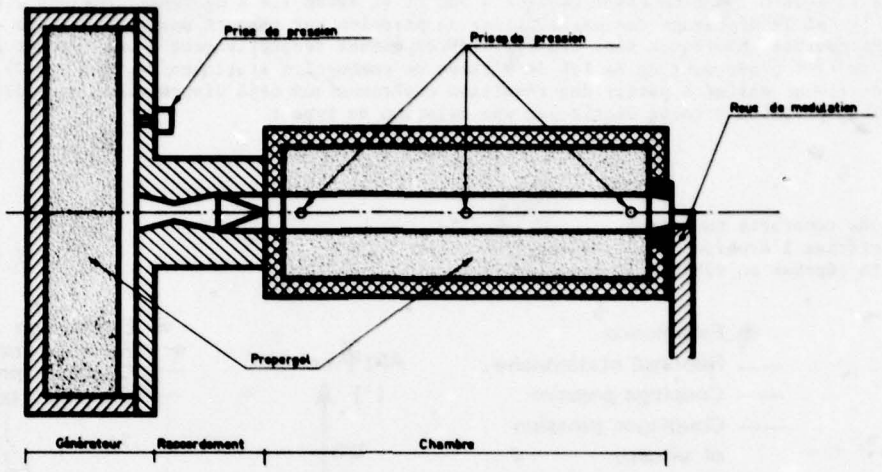

Fig. 13 – Schéma du montage destiné à l'étude du couplage pression-vitesse.

Les équations de base présentées précédemment sont utilisées, avec quelques modifications imposées par les conditions d'essai et portant sur les points suivants :

a) conditions limites à l'entrée de la chambre
dans les exemples précédemment traités, les conditions limites amont correspondaient à un fond avant rigide ; l'existence dans le montage étudié maintenant d'un générateur nécessite de reprendre l'examen de ces conditions. L'écoulement instationnaire dans la tuyère de raccordement est étudié par les équations de base en prenant pour origine la position moyenne du choc de recompression supposé plan et comme conditions limites en ce point celles résultant d'un choc oscillant [11]. Le calcul donne alors les relations existant à l'entrée de la chambre entre les différentes amplitudes $\tilde{\varphi}$, $\tilde{v}$ et $\tilde{s}$.

b) traitement des discontinuités de section
la combustion du chargement de la chambre d'expérience fait apparaître des discontinuités de section au fond avant et au fond arrière. Pour établir les relations entre les valeurs des amplitudes $\tilde{\varphi}$, $\tilde{v}$ et $\tilde{s}$ de part et d'autre des discontinuités, on a admis qu'une discontinuité est un canal divergent dont on fait tendre la longueur vers zéro ; cette démarche formellement simple est sans doute criticable.

L'évolution réelle de la surface de combustion du chargement de la chambre est déduite des films pris en cours d'essai ; le calcul de la section locale du canal, compte tenu de l'évolution de la surface de combustion et de l'ablation du hublot de visualisation est effectué à chaque instant.

c) conditions à l'aval de la chambre
le problème n'est plus ici de rechercher les valeurs propres de la fréquence complexe puisque la fréquence est imposée par la modulation mais de traduire complètement le comportement instationnaire de la tuyère. Les équations de base doivent donc être complétées pour tenir compte de la modulation du col que nous caractériserons par son amplitude réduite $\tilde{\sigma}_c$.

Il est possible de montrer que le comportement instationnaire de la tuyère conduit à une relation à vérifier dans son plan d'entrée pour les amplitudes $\tilde{\varphi}$, $\tilde{v}$, $\tilde{s}$ et $\tilde{\sigma}_c$:

$$\tilde{v} = Y\tilde{\varphi} + X\tilde{s} + W\tilde{\sigma}_c ,$$

où X est l'admittance réduite de la tuyère,
Y est définie comme coadmittance de la tuyère,
W traduit la réponse de la tuyère à la modulation.
Y , X et W sont calculées par intégration des équations suivantes :

$$\left\{\begin{aligned}
\gamma\bar{M}(1-\bar{M}^2)\left(1+\tfrac{\gamma-1}{2}\bar{M}^2\right)\frac{dY}{d\bar{M}} &= \gamma^2\bar{M}^2(2+F)Y^2+\gamma(3-\gamma)\bar{M}^2Y-\left(\tfrac{\gamma+1}{2}\bar{M}^2+F\right),\\
\gamma\bar{M}(1-\bar{M}^2)\left(1+\tfrac{\gamma-1}{2}\bar{M}^2\right)\frac{dX}{d\bar{M}} &= X\left[\gamma(2\bar{M}^2+F)+\gamma^2\bar{M}^2(2+F)Y\right]-\left(\tfrac{\gamma+1}{2}\bar{M}^2(1+\gamma Y)\right),\\
\gamma\bar{M}(1-\bar{M}^2)\left(1+\tfrac{\gamma-1}{2}\bar{M}^2\right)\frac{dW}{d\bar{M}} &= W\gamma\bar{M}^2(2+F)(1+\gamma Y)-\gamma L(1+\gamma\bar{M}^2Y) .
\end{aligned}\right.$$

où F est défini par : $F = \delta\,\bar{\omega}\sqrt{1+\tfrac{\gamma-1}{2}\bar{M}^2}\;\frac{d\bar{x}}{d\bar{M}}$ $\left(\bar{\omega}=\frac{\omega L}{a_0}\,,\ \bar{x}=\frac{x}{L}\right)$,

et où Ξ traduit l'effet local de la modulation du col :

$$\Xi = \frac{1}{\gamma_c}\left(\Gamma\gamma + \bar{M}\left(1+\frac{\gamma-1}{2}\bar{M}^2\right)\frac{\partial\tilde{\varphi}}{\partial\bar{M}}\right) .$$

L'ensemble des équations établies est intégré numériquement et donne les amplitudes $\tilde{\varphi}$, $\tilde{\nu}$ et $\tilde{\Sigma}$ en chaque point de la chambre. L'amplitude $\tilde{\varphi}$ est comparée aux valeurs mesurées, les amplitudes $\tilde{\nu}$ et $\tilde{\Sigma}$ permettent de préciser la physique du phénomène et de vérifier si les hypothèses de départ sont bien vérifiées ($|\tilde{\nu}| \ll 1$ en particulier).

La comparaison entre les résultats expérimentaux et ceux du calcul s'est avérée décevante. Les figures 14 et 15 donnent pour un essai réalisé à 500 Hz et après 1,4 s de fonctionnement l'amplitude de pression $|\tilde{\varphi}|$ et le déphasage des oscillations de pression par rapport aux oscillations de la section du col. Plusieurs courbes théoriques sont tracées, correspondant respectivement à une réponse stationnaire du propergol ($R_{MP} = 0$, exposant de la loi de vitesse de combustion stationnaire, $R_{TP} = 0$), au seul couplage pression (R_{MP} estimé à partir des résultats expérimentaux déjà disponibles, R_{TP} déduit de R_{MP}) et à un couplage pression vitesse décrit par une relation du type :

$$\frac{\tilde{v_b}}{\bar{v_b}} = (1+C\beta)\,R_{MP}\,\tilde{\varphi} + C\beta\,R_{TP}\,\tilde{\nu} ,$$

où C est une constante numérique,
β caractérise l'érosion stationnaire,
R_{MP} est la réponse en débit à la pression seule.

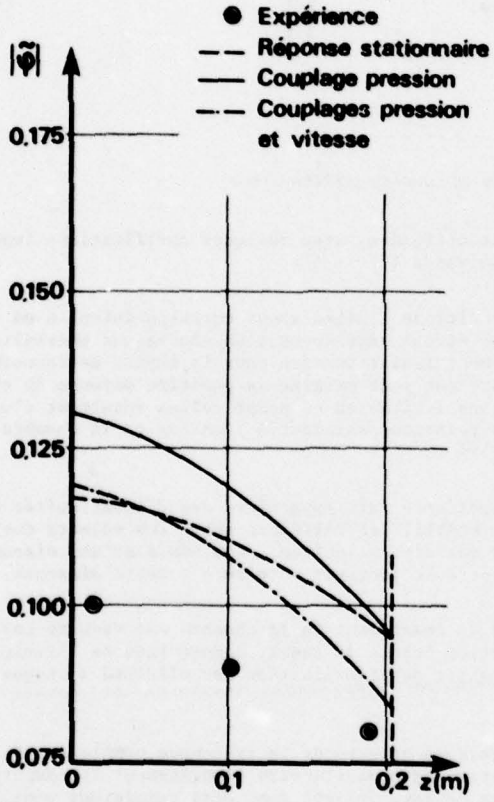

Fig. 14 – Analyse du fonctionnement du montage d'étude du couplage pression-vitesse (amplitude de pression).

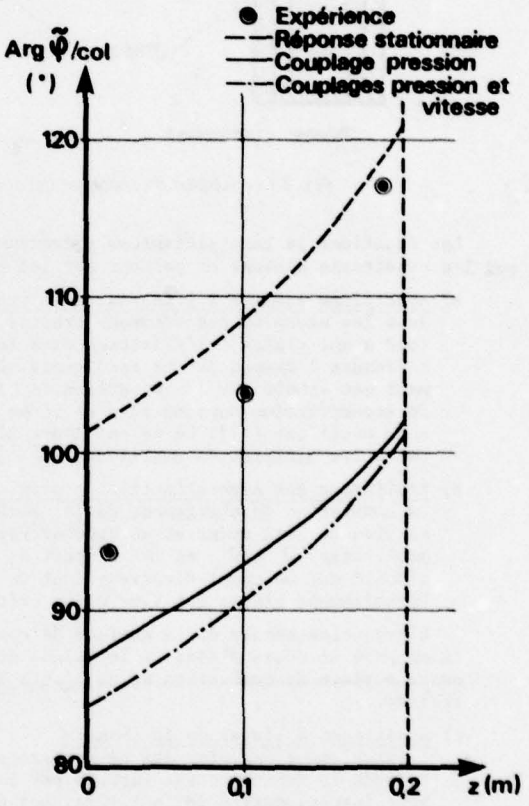

Fig. 15 – Analyse du fonctionnement du montage d'étude du couplage pression-vitesse (déphasage de pression).

Il apparaît nettement que la répartition de l'amplitude $|\tilde{\varphi}|$ et du déphasage $\mathrm{Arg}\,\tilde{\varphi}$ est mal prévue par le calcul et que dans ces conditions, il est impossible de déterminer à partir des mesures de pression le couplage pression (en l'absence d'érosion) et la contribution de l'écoulement (en présence d'érosion). Différentes observations semblent indiquer que le fonctionnement échappe à une description monodimensionnelle en particulier au niveau de l'entrée de la chambre.

Nous avons été conduits à rendre responsables des écarts constatés les conditions expérimentales plutôt que l'analyse du fonctionnement. C'est ce qu'ont confirmé des essais réalisés sans générateur et en l'absence de phénomène érosif. Sur les figures 16 et 17 sont comparées dans ces nouvelles conditions les prévisions théoriques et les mesures à 1000 Hz et après 1 s de fonctionnement ; pour éliminer l'influence du réglage de la modulation et du système de mesure associé, le module de l'amplitude de pression est ramené à sa valeur au fond avant où le déphasage est pris nul. Les écarts constatés sont plus réduits que dans les conditions expérimentales initiales. L'étude du couplage pression vitesse est donc réorientée en conséquence, le calcul servant à optimiser les caractéristiques du nouveau montage.

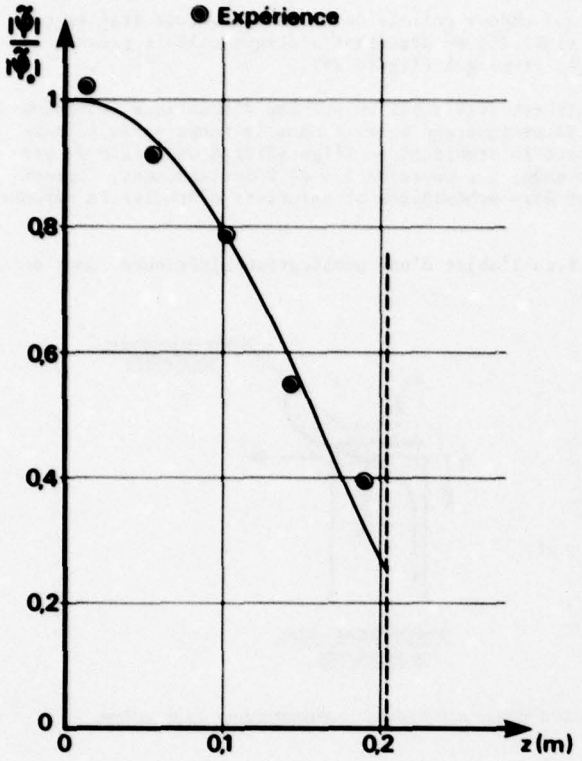

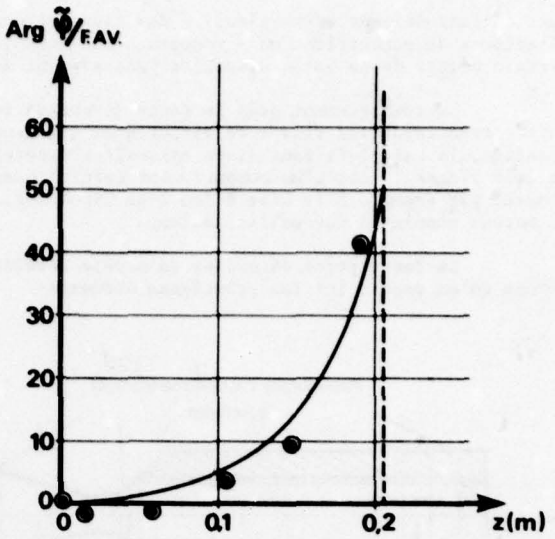

Fig. 17 – Analyse du fonctionnement du montage d'étude du couplage pression-vitesse sans générateur (déphasage de pression).

Fig. 16 – Analyse du fonctionnement du montage d'étude du couplage pression-vitesse sans générateur (amplitude de pression).

3.6 - Conclusion

Les équations linéarisées de la mécanique des fluides ont été utilisées pour modéliser le fonctionnement instationnaire de quelques propulseurs ou montages de géométrie simple. Au prix de calculs numériques peu coûteux, cette technique peut avantageusement remplacer les méthodes analytiques et globales plus classiques, lorsque le nombre de Mach de l'écoulement moyen est élevé ou lorsqu'une description précise de la structure stationnaire est recherchée. L'application des équations à un propulseur conventionnel ne soulève pas de problème, celle relative à un moteur sans tuyère est plus originale. La modélisation du montage d'étude de la combustion instationnaire des propergols a progressé mais le difficile problème du couplage pression-vitesse n'est pas encore résolu.

4 - ANALYSE DES INSTABILITES DE COMBUSTION DANS LE DOMAINE NON LINEAIRE

4.1 - Objectifs

Dans le cas des instabilités de combustion à prédominance longitudinale, la pression moyenne est peu affectée par les oscillations tant que leur amplitude relative ne dépasse pas approximativement 5%, limite rarement atteinte en pratique.

Le critère relatif au comportement d'un propulseur vis-à-vis des instabilités de combustion pourra donc être pour le constructeur plus l'amplitude maximale admissible des oscillations de pression que la stabilité absolue. La prévision des niveaux d'instabilité est donc d'un grand intérêt.

L'amplitude des oscillations de pression est limitée par des phénomènes de caractère non linéaire et le recours au calcul numérique est donc indispensable. Compte tenu de la dimension du problème, nous avons choisi d'étudier dans une première étape le comportement instationnaire non linéaire d'un chargement simple (perforation cylindrique, tuyère non intégrée) susceptible d'être décrit par des équations monodimensionnelles. Le travail est donc dans son approche du moins, analogue à ceux conduits par Levine et Culick d'une part [12], Kooker et Zinn d'autre part [13] ; quelques différences existent par contre au niveau de la modélisation des phénomènes et les techniques numériques utilisées. Un support expérimental constitué par quelques essais effectués dans les conditions retenues pour le calcul a été mis parallèlement en place. Cette première étape a permis de dégager les possibilités et les limites de ce type de simulation numérique, en vue de développements plus ambitieux.

4.2 - Description du modèle

Toute approche numérique d'un problème instationnaire impose une discrétisation spatiale et temporelle des équations décrivant les phénomènes mis en jeu. Nous avons recherché ici une technique numérique permettant de traiter de manière homogène les équations de l'écoulement et celles traduisant la combustion du propergol. La technique des volumes finis a été retenue en fonction de l'expérience acquise à l'ONERA pour la résolution de problèmes variés [14, 15] et de son caractère modulaire permettant de prendre facilement en compte des conditions limites quelconques, des changements aisés des modèles physico-chimiques choisis ou une amélioration des interpolations à l'intérieur de chaque volume élémentaire.

La chambre de combustion et la tuyère sont décomposées en un assemblage monodimensionnel de cellules dont l'évolution est contrôlée par les différents flux à leurs interfaces ; les mécanismes de com-

bustion introduisent en particulier des flux pariétaux sur chaque cellule de la chambre. Pour traiter ces mécanismes de combustion, on a recours à une technique similaire en associant à chaque cellule gazeuse un certain nombre de cellules disposées latéralement dans le propergol (figure 18).

Le comportement dans le temps de chaque cellule est décrit par un système d'équations instationnaires traduisant les bilans de différentes grandeurs. Ce système est intégré dans le temps après initialisation, le calcul faisant alors apparaître naturellement la stabilité ou l'instabilité naturelle du propulseur ; dans le cas d'un comportement naturellement stable, une perturbation du fonctionnement, correspondant par exemple à la mise à feu d'un impulseur, peut être schématisée et permettre d'étudier la réponse du moteur complet à une sollicitation.

La description détaillée du modèle développé fera l'objet d'une publication ultérieure, nous ne ferons qu'en donner ici les principaux éléments .

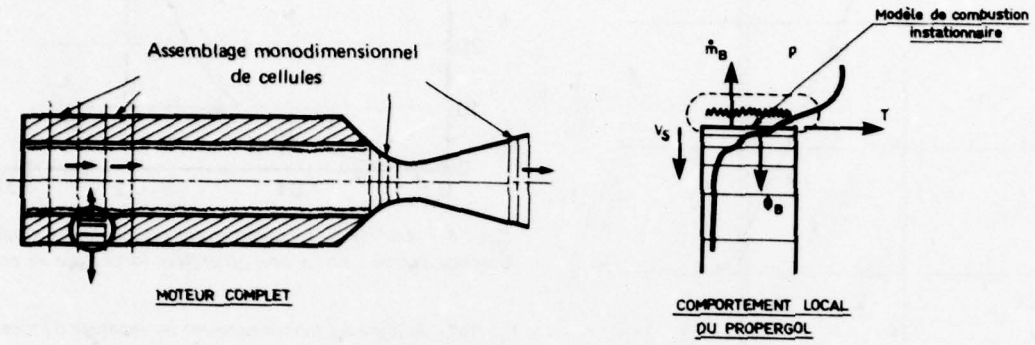

Fig. 18 – Analyse des instabilités de combustion dans le domaine non linéaire : schématisation du problème.

4.2.1 - Modèle de combustion

Le choix du modèle de combustion est ici primordial. L'exposé du modèle retenu a été fait dans la référence [16]. Il a été établi en vue de son utilisation systématique au niveau numérique et un certain nombre de simplifications se sont avérées nécessaires. Au point de vue de sa formulation, ce modèle ne présente pas d'originalité par rapport aux travaux parus antérieurement dans la littérature : il s'agit d'un modèle thermique, l'aspect instationnaire de la conduction de la chaleur étant rendu responsable du fait que la vitesse de combustion ne s'ajuste pas instantanément aux conditions locales de pression, et d'un modèle semi explicite , puisqu'il est fait à la fois appel à une description analytique des réactions de surface (loi d'Arrhénius) et aux données expérimentales stationnaires et instationnaires de combustion. Dans ces conditions on ramène le problème à l'intégration de l'équation de la chaleur dans un milieu semi infini :

$$\frac{\partial^2 T}{\partial x^2} + \frac{v_b}{a_p}\frac{\partial T}{\partial x} = \frac{\partial T}{\partial t}$$

avec les conditions initiale et limite :

$$\left.\begin{aligned} &t = 0 \;,\quad T = T_i + (\overline{T_s} - T_i)\exp\left(-\frac{v_b x}{a_p}\right) \;, \\ &t > 0 \;,\quad x \to \infty \;,\quad T \to T_i \\ &x = 0 \;,\quad -\lambda\frac{\partial T}{\partial x} = \rho\, v_b \left(T_s - \mathcal{A}(v_b, p(t))\right) \end{aligned}\right\} \qquad v_b = B_v \exp\left(-\frac{E_s}{R T_s}\right)$$

La fonction $\mathcal{A}(v_b, p(t))$ dépend de l'approche choisie pour estimer la densité de flux q_s^+ entrant dans le propergol vierge. Suivant l'approche proposée par Zeldovich, on peut admettre que la loi $q_s^+(v_b, p)$ peut être étendue du stationnaire à l'instationnaire ; l'expression exacte de $\mathcal{A}$ fait alors apparaître la loi de vitesse de combustion stationnaire en fonction de la pression et de la température initiale T_i . Il est également possible d'adopter la démarche des chercheurs de l'Université de Princeton (modèle KTSS) ; on suppose alors que la densité de flux reçu par la surface de combustion de la zone de flamme peut être exprimée par une loi universelle :

$$q_s^+ = \frac{\Phi(p)}{v_b}$$

où $\Phi(p)$ est déterminée à partir de la loi stationnaire à une température initiale de référence.

Nous avons tenté pour un propergol composite connu de recaler ces différents modèles par rapport aux données expérimentales disponibles afin de mettre en évidence les différences de comportement instationnaire qu'ils impliquent. Chaque modèle étudié possède ses propres limites liées au fait que les données expérimentales sont déterminées dans un domaine de température initiale ou de pression trop étroit. Pour des effets non linéaires peu prononcés, les deux modèles conduisent à des résultats proches.

La température instantanée de flamme se déduit de la vitesse instantanée :

$$T_f = \overline{T_{fa}} + \frac{c}{c_p}\left(\mathcal{A}(v_b, p(t)) - T_a \right)$$

Il est possible de ramener le problème ainsi posé à la résolution d'une équation intégrale non linéaire pour v_b.

4.2.2 - Traitement_numérique_du_modèle_de_combustion

La technique des volumes finis a été appliquée à la résolution du problème thermique associé au modèle de combustion. Parallèlement, la résolution numérique de l'équation intégrale qui en dérive a été effectuée ; plus lourde à mettre en oeuvre que la précédente mais plus précise, cette résolution a servi à valider les calculs effectués avec la technique des volumes finis dans le domaine non linéaire. La validation des calculs a également été faite par comparaison avec les calculs analytiques dans le domaine linéarisé : réponse à une oscillation harmonique de pression ou à une variation exponentielle de pression.

Pour se ramener à un domaine d'étude borné, nous posons :

$$\zeta = 1 - \exp\left(-\frac{\overline{v_b}\, x}{\alpha_p}\right),$$

et :

$$\tau = \frac{\overline{v_b}^2 t}{\alpha_p},$$

$$\Theta = \frac{T - T_a}{\overline{T_s} - T_a},$$

$$V = \frac{v_b}{\overline{v_b}}.$$

Ces changements ont pour effet d'adimensionner les différentes grandeurs, de dilater la zone voisine de la surface de combustion et de contracter la zone où la température tend vers sa valeur initiale, rendant ainsi les gradients plus homogènes.

L'équation à intégrer devient donc :

$$\left.\begin{aligned} &(1-\zeta)^2 \frac{\partial^2 \Theta}{\partial \zeta^2} + (V-1)(1-\zeta)\frac{\partial \Theta}{\partial \zeta} = \frac{\partial \Theta}{\partial \tau}, \\ &\tau = 0, \quad \Theta = 1-\zeta, \\ &\tau > 0, \quad \zeta = 1, \quad \Theta = 0, \\ &\zeta = 0, \quad \frac{\partial \Theta}{\partial \zeta} = -V\left(\Theta_s - \mathcal{G}(V,\tau)\right), \\ &\text{où} \quad \mathcal{G}(V,\tau) = \frac{\mathcal{A}\left(\overline{v_b} V,\, p\left(\frac{\alpha_p \tau}{\overline{v_b}^2}\right)\right) - T_a}{\overline{T_s} - T_a} \end{aligned}\right\} \quad V = \exp\left(\frac{-M(1-\Theta_s)}{\Theta_s + (1-\Theta)\Theta_s}\right)$$

Pour une instabilité de combustion, le profil $\Theta(\zeta,\tau)$ évolue autour de la droite $\Theta = 1-\zeta$.

Dans l'espace transformé, l'équation est discrétisée sur un nombre N de tranches d'épaisseur $\Delta\zeta$ égales (figure 19). L'intégration de l'équations aux dérivées partielles sur la tranche $\Delta\zeta$ considérée conduit formellement à l'équation :

$$\Delta\zeta \frac{\partial \hat{\Theta}}{\partial \tau} = \left[(V+1)(1-\zeta)\Theta + (1-\zeta)^2 \frac{\partial \Theta}{\partial \zeta} \right]_M^P + (V+1)\Delta\zeta\, \hat{\Theta},$$

où $\hat{\Theta}$ est la valeur moyenne de Θ dans la cellule, P et M les indices des intervalles amont et aval. Le problème est alors ramené à l'expression des valeurs d'interface en fonction des valeurs moyennes $\hat{\Theta}$ dans les différentes cellules :

a - cellules intermédiaires
on se satisfait d'interpolation linéaire du type :

$$\Theta_M = \frac{\hat{\Theta}^- + \hat{\Theta}}{2}, \quad \Theta_P = \frac{\hat{\Theta}^+ + \hat{\Theta}}{2},$$

$$\left(\frac{\partial \Theta}{\partial \zeta}\right)_M = \frac{\hat{\Theta} - \hat{\Theta}^-}{\Delta\zeta}, \quad \left(\frac{\partial \Theta}{\partial \zeta}\right)_P = \frac{\hat{\Theta}^+ - \hat{\Theta}}{\Delta\zeta}.$$

b - première cellule (surface de combustion)
une approximation parabolique du profil est utilisée en conjonction avec la condition limite :

$$V\left(\Theta_s - \mathcal{G}(V,\tau)\right) + \frac{6(\hat{\Theta}_1 - \Theta_s) + (\hat{\Theta}_2 - \hat{\Theta}_1)}{2\Delta\zeta} = 0.$$

c - dernière cellule
l'expérience a montré qu'un traitement particulier doit être réservé à cette cellule car le changement de variable effectué peut conduire à des valeurs $\left(\frac{\partial \Theta}{\partial \zeta}\right)_{\zeta=1}$ nulle, finie ou infinie.

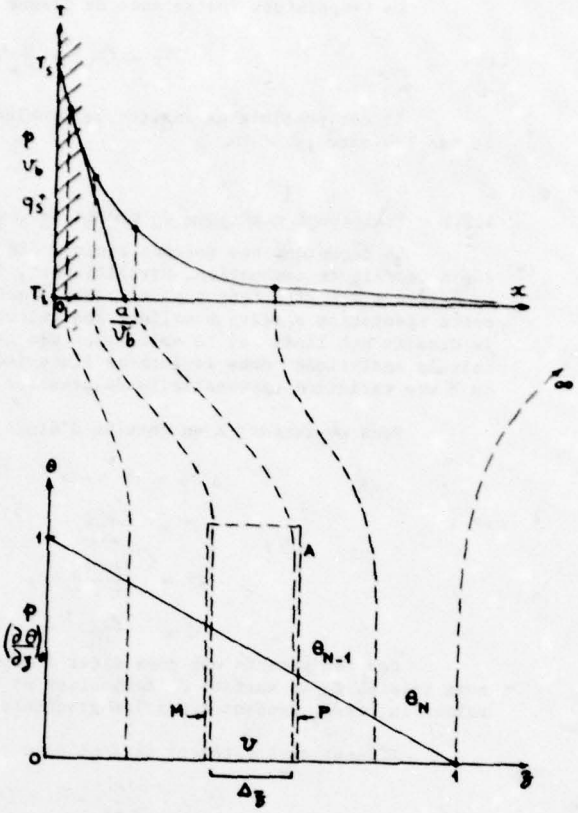

Fig. 19 – Traitement numérique du modèle de combustion : changement de variable.

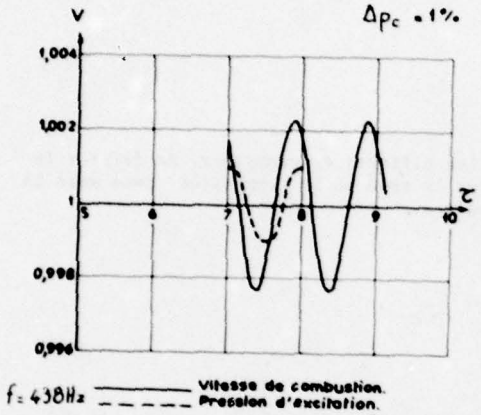

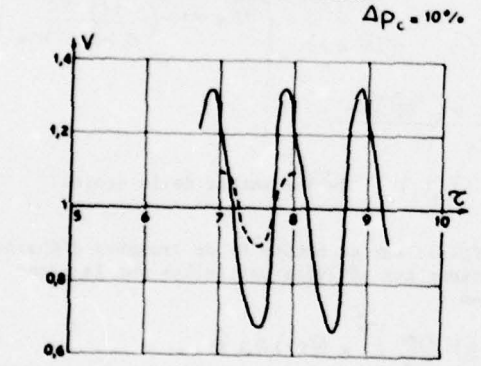

Fig. 20 – Réponse du modèle de combustion à une oscillation harmonique de pression : influence de l'amplitude.

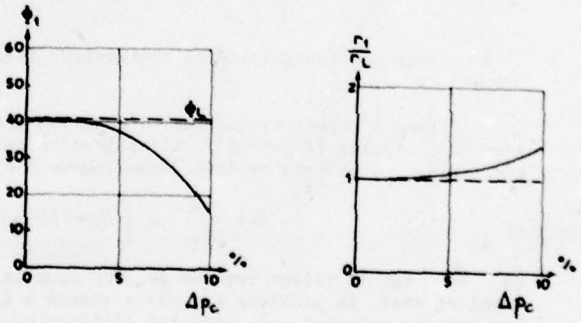

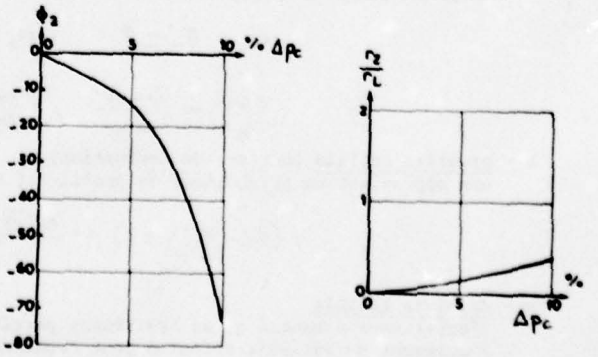

Fig. 21 – Réponse du modèle de combustion à une oscillation harmonique de pression : analyse de Fourier de la vitesse de combustion.

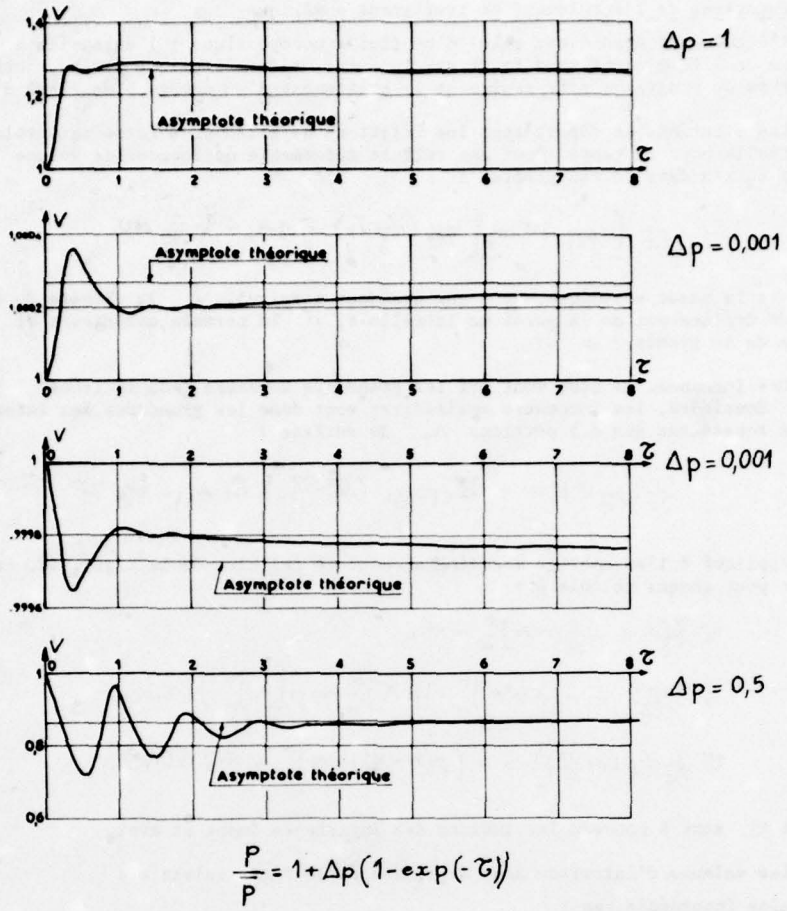

Fig. 22 – Réponse du modèle de pression à une croissance ou à une décroissance exponentielle de pression : influence de la variation Δp.

Les équations différentielles ainsi définies seront intégrées en même temps que les équations de l'écoulement. Il y a donc intérêt à limiter le nombre des cellules pour réduire le temps de calcul. L'objectif étant de pouvoir prendre précisément en compte des variations de pression de l'ordre de 1 %, nous avons été amenés à choisir $N = 10$.

Les figures 20, 21 et 22 illustrent les résultats obtenus dans le cas d'évolutions imposées de la pression :

1 - <u>évolution harmonique de la pression</u>
des oscillations de pression dont la fréquence physique variait de 400 à 4500 Hz et l'amplitude crête réduite de 1 % à 10 % ont été simulées. Après établissement de l'oscillation de vitesse de combustion, une analyse de Fourier est conduite pour mettre en évidence la non linéarité de réponse du propergol (distorsion de l'oscillation, augmentation de la vitesse moyenne) :

- Δp_c = 1%, les résultats de l'analyse linéaire sont retrouvés précisément même à haute fréquence,
- influence de Δp_c : la figure 20 illustre la distorsion de l'oscillation de vitesse de combustion pour une période réduite de 1 (f = 438 Hz) lorsque Δp_c passe de 1 % à 10 %. La figure 21 résume l'influence de Δp_c sur l'amplitude et le déphasage à 438 Hz de la composante harmonique fondamentale et de son premier harmonique ; les amplitudes sont ramenées à la valeur linéarisée. La non linéarité du phénomène se manifeste dès que Δp_c dépasse 2%, l'effet est encore plus marqué lorsque la fréquence correspond au maximum de la partie réelle de la réponse linéaire du propergol. Pour les fortes amplitudes Δp_c , le calcul indique la possibilité d'une extinction dynamique du propergol.

2 - <u>évolution exponentielle de la pression</u>
les résultats de l'analyse linéaire sont retrouvés pour une transition exponentielle entre deux niveaux de pression dont l'acart relatif est de 1 % ; les différences d'évolution de la vitesse instantanée sont marquées pour une augmentation de pression de 100% ou une diminution de 50% (figure 22).

Les résultats obtenus pour le traitement numérique du modèle de combustion sont apparus suffisamment intéressants au point de vue précision et temps de calcul pour que ce mode de traitement soit introduit dans le modèle complet.

4.2.3 - Equations de l'écoulement et traitement numérique

L'écoulement étudié est celui d'un fluide monophasique ; l'extension à une description biphasique de l'écoulement sera faite par la suite, elle n'implique pas a priori de modifications de structure du programme mais seulement le traitement d'un nombre plus élevé d'équations.

Les équations de départ sont les relations de bilan sous forme intégrale pour l'espace et différentielle pour le temps. Pour une cellule déformable quelconque de volume $\mathcal{V}$ et de surface A, on écrira dans le cas général :

$$\frac{\partial}{\partial t}\int_{\mathcal{V}} \rho g \, d\mathcal{V} + \int_A \rho g \,(\vec{v}-\vec{v}_p).\vec{n}\, dA = \int_{\mathcal{V}} \dot{w}_g \, d\mathcal{V} ,$$

où ρ est la masse volumique, g une grandeur massique, $\vec{v}$ la vitesse du fluide, $\vec{v}_p$ la vitesse de déplacement de la paroi de la cellule, $\vec{n}$ la normale extérieure et $\dot{w}_g$ la production volumique de la grandeur g.

Les inconnues de base sont ici les grandeurs moyennes (non indicées) à l'intérieur du volume $\mathcal{V}$ considéré, les inconnues auxiliaires sont donc les grandeurs aux interfaces (indice i) supposées constantes sur des portions A_i de surface :

$$\frac{\partial}{\partial t}(\rho g \mathcal{V}) = -\sum_i \rho_i g_i (\vec{v}_i-\vec{v}_{p_i}).\vec{n}_i A_i + \dot{w}_g \mathcal{V}$$

Appliqué à l'assemblage monodimensionnel de cellules de la figure 18, cette équation conduit donc pour chaque cellule à :

$$\begin{cases} \mathcal{V}\dfrac{\partial \rho}{\partial t} = -\left[\rho v A\right]_M^P + \dot{m}_b , \\ \mathcal{V}\dfrac{\partial (\rho v)}{\partial t} = -\left[\rho v^2 A\right]_M^P - \left[p A\right]_M^P + p\left[A\right]_M^P , \\ \mathcal{V}\dfrac{\partial}{\partial t}\left(\rho\left(e+\dfrac{v^2}{2}\right)\right) = -\left[\rho\left(h+\dfrac{v^2}{2}\right) v A\right]_M^P + \dot{m}_b h(T_f) . \end{cases}$$

où P et M sont à nouveau les indices des interfaces amont et aval.

Les valeurs d'interface sont exprimées de la façon suivante :

a - cellules intermédiaires :

$$\rho_M = \frac{\rho^- + \rho}{2} , \quad \rho_P = \frac{\rho^+ + \rho}{2} , \quad v_M = \frac{v^- + v}{2} \ldots$$

b - première cellule (fond avant) :

$$\rho_M = \rho , \quad v_M = 0 , \quad p_M = p + \rho\frac{v^2}{2} .$$

c - dernière cellule (sortie tuyère) :
extrapolation linéaire sur l'interface P à partir de la valeur interne et de la valeur sur l'interface M ; comme l'écoulement est supersonique dans cette région, le calcul est insensible à cette hypothèse.

Les équations relatives à l'écoulement et à la combustion sont regroupées au niveau d'une cellule (sauf pour la tuyère où ne subsistent que les équations de l'écoulement) : dans chaque tranche subsistent donc trois inconnues ρ, V et P pour la phase gazeuse, N inconnues Θ_i pour la phase solide et l'inconnue supplémentaire Θ_s liée à la température de surface du propergol. Chacune de ces inconnues y_i obéit à une équation différentielle ordinaire :

$$\frac{dy_i}{dt} = f_i(y_j, t)$$

L'intégration temporelle est effectuée après initialisation par une méthode d'intégration simultanée de Runge-Kutta du quatrième ordre. Le pas en temps est limité par des conditions de stabilité : critère de Fourier pour le problème thermique, critère de Current-Friedrich-Lévy pour le calcul de l'écoulement. Le second critère est plus pénalisant que le premier ; il s'est avéré possible de travailler avec deux pas en temps différents pour réduire le temps de calcul (Δt = 2 µs pour l'écoulement, Δt = 10 µs pour le problème thermique).

4.2.4 - Séquences du calcul

a - introduction des paramètres définissant le problème : géométrie du foyer (cylindrique circulaire) et de la tuyère (biconique à rayon de courbure constant au col), caractéristiques physiques du propergol, caractéristiques thermodynamiques du propergol et des produits de combustion, caractéristiques cinétiques du propergol (modèle de combustion), température initiale, nombres de cellules dans le foyer, la tuyère et le propergol ;

b - recherche du régime stationnaire
une initialisation des inconnues de base est réalisée par une approximation, du régime stationnaire. Le régime stationnaire exact est alors recherché par la méthode générale instationnaire, en gardant toutefois à la vitesse de combustion et à la tempéra-

ture de flamme leurs valeurs stationnaires. Une fois le régime stationnaire atteint (stabilité des grandeurs), les valeurs des inconnues de base qui seront utilisées par la suite sont mises en mémoire ;

c - étude de la stabilité naturelle du propulseur :
le calcul est repris en déterminant maintenant à chaque instant le profil thermique dans le propergol à chacune des positions considérées. Si le propulseur est naturellement instable, les grandeurs se mettent à osciller progressivement et le calcul est arrêté lorsque les oscillations sont stabilisées. Si le propulseur est naturellement stable, il n'y a aucune évolution des grandeurs à partir de leurs valeurs stationnaires ;

d - étude de l'amortissement du propergol :
dans le cas d'un fonctionnement naturellement stable, le calcul est destabilisé en simulant un débit supplémentaire dans la première cellule pendant un court instant de façon à schématiser par exemple la déflagration d'une charge pyrotechnique au fond avant. L'amortissement des perturbations du fonctionnement ainsi provoquées est calculé.

4.3 - Résultats

La mise au point du programme est acquise mais son exploitation n'a pas encore été faite systématiquement. Les résultats donnés le seront donc uniquement à titre indicatif. Les conditions d'applications correspondent au propulseur schématisé sur la figure 23 : la longueur initiale de la chambre est 600 mm, le diamètre initial 70 mm, le propergol est un composite non métallisé à liant polybutadiène, la chambre est décrite par 100 cellules, la tuyère par 40 cellules, le propergol par 100 x 10 cellules.

La figure 24 donne l'évolution dans le temps de la pression au fond avant (p_{AV}), au fond arrière (p_{AR}) et à la position 6 (p_6) pendant et après la destabilisation du propulseur qui s'est avéré naturellement stable dans la configuration géométrique initiale. La figure 25 donne les évolutions correspondantes de la vitesse de combustion au fond avant et dans la position 6. L'établissement du régime périodique est précédé par une phase complexe correspondant au transit de la perturbation du fond avant au fond arrière, à sa réflexion dans la tuyère puis à la composition des perturbations progressive et régressive.

Le fonctionnement du modèle apparaît pour l'instant sain, la seule difficulté pratique réside dans l'importance du temps de calcul (1 ms dans la phase d'instabilité correspond à 10 mn de calcul sur IRIS 80). Il est possible d'abaisser le temps de calcul en réduisant le nombre de cellules mais la précision du calcul en souffre.

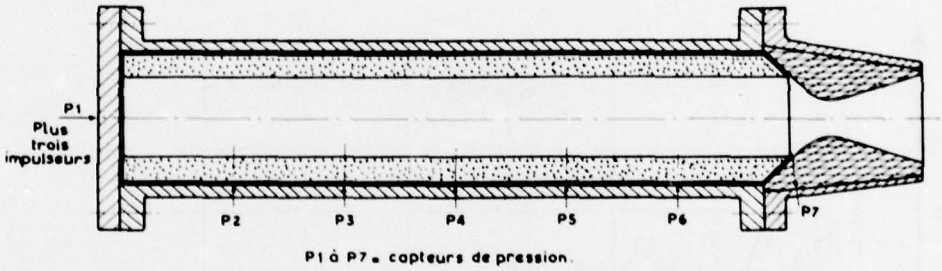

Fig. 23 – Schéma du propulseur étudié expérimentalement et simulé numériquement.

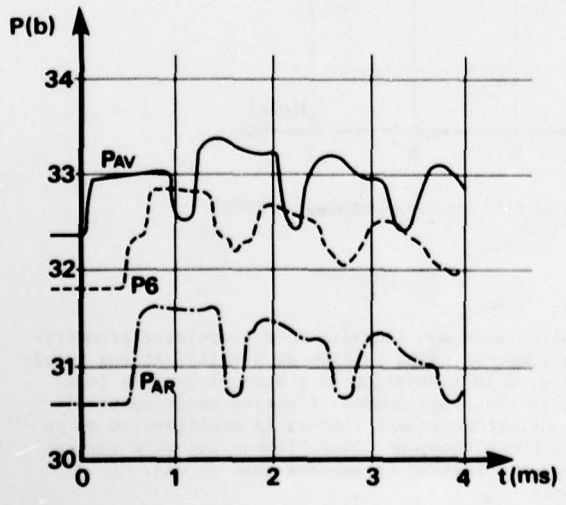

Fig. 24 – Réponse d'un propulseur stable à une excitation : calcul des évolutions de pression.

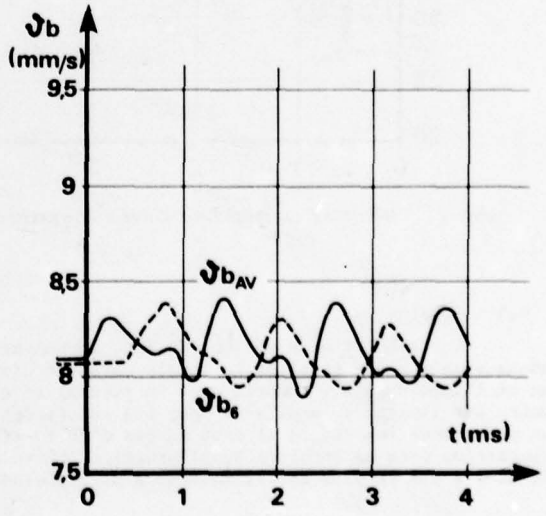

Fig. 25 – Réponse d'un propulseur stable à une excitation : calcul des évolutions de vitesse de combustion.

4.4 - Essais

Un certain nombre d'essais sont en cours de réalisation sur le propulseur schématisé sur la figure 23 en vue d'une comparaison théorie-expérience pour deux propergols respectivement non métallisé et métallisé. Le fonctionnement s'est avéré stable dans les deux cas, aussi a-t-on été conduit à destabiliser le propulseur par des impulseurs pyrotechniques. Les figures 26 et 27 illustrent les résultats obtenus après 1 s de fonctionnement pour les pressions relevées au fond avant et au fond arrière.

Les évolutions de pression mesurées sont assez comparables qualitativement pour les deux propergols en dépit d'une différence notable dans l'augmentation initiale de pression. Les oscillations de la pression au fond avant présentent un front de montée raide suivi d'une décroissance plus lente, le phénomène est moins masqué au fond avant. Des harmoniques apparaissent superposées à la fréquence fondamentale de chambre. L'amortissement des oscillations est rapide surtout dans le cas du propergol métallisé, après disparition des oscillations la pression n'est pas encore revenue à sa valeur stationnaire.

La comparaison entre l'expérience et le calcul sera faite dans les prochains mois ; certains ajustements sont nécessaires pour retrouver la phase initiale du phénomène, en particulier en ce qui concerne le fonctionnement de l'impulseur. Les courbes de la figure 24 d'une part, des figures 26 et 27 d'autre part ne peuvent être comparées.

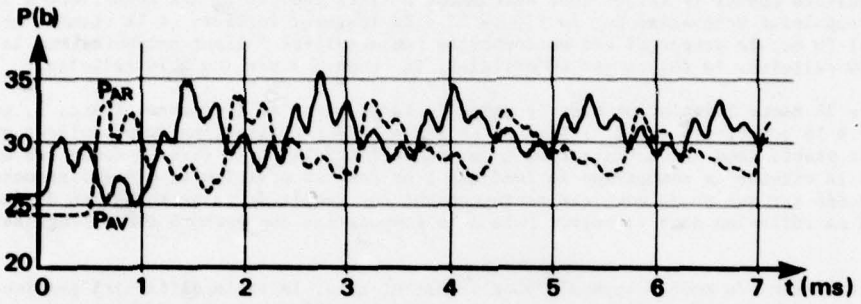

Fig. 26 – Réponse d'un propulseur stable à une excitation : mesure des pressions (propergol non métallisé).

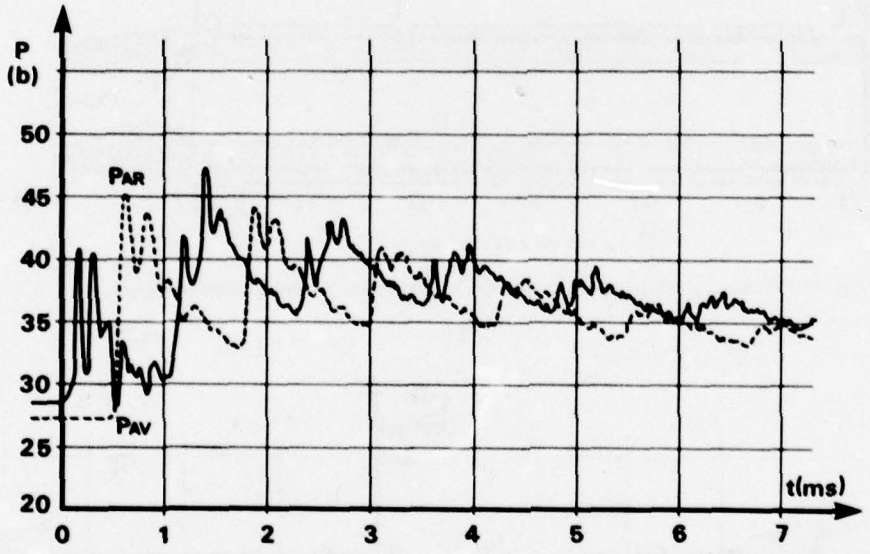

Fig. 27 – Réponse d'un propulseur stable à une excitation : mesure des pressions (propergol métallisé).

4.5 - Conclusion

Une simulation numérique du fonctionnement instationnaire non linéaire d'un propulseur géométriquement simple a été établie. Le modèle physique adopté ne comporte qu'un minimum de simplifications au niveau de l'écoulement (y compris dans la tuyère) et au niveau de la combustion du propergol traitée localement. Les limites du modèle ne sont pas encore dégagées. Le choix des données d'entrée revêt naturellement une grande importance et dans le cas d'un fonctionnement naturellement stable, la modélisation de la perturbation pose un problème supplémentaire. L'étude d'un fonctionnement naturellement instable semblerait donc a priori plus facile mais nous ne disposons pas pour l'instant de mesures dans ce cas.

5 - RECAPITULATION

Les problèmes rencontrés au cours du développement de propulseurs d'architecture compliquée sont encore peu accessibles à la modélisation. Une approche purement expérimentale de ce problème utilisant des

essais à échelle réduite a été étudiée ; elle offre la possibilité de déterminer les modes potentiels d'instabilité et les temps critiques de fonctionnement et donc de préciser le phénomène.

Parallèlement à cette étude expérimentale sont développées des méthodes à caractère semi analytique (domaine linéaire) ou numérique (domaine non linéaire) en vue de perfectionner les moyens prévisionnels. L'intégration numérique des équations linéarisées permet de traiter les interactions fortes entre l'acoustique et l'écoulement moyen comme dans le cas du propulseur sans tuyère ou de déterminer précisément la structure acoustique dans des conditions plus classiques ; l'application de cette technique à la recherche du couplage pression vitesse n'a pas conduit aux résultats escomptés en raison de difficultés d'ordre expérimental. L'analyse numérique complète du fonctionnement instationnaire d'un propulseur géométriquement simple a été réalisée et est en cours d'exploitation. L'extension de cette méthode à des chargement complexes peut être techniquement envisagée ; une optimisation de la méthode numérique devra être recherchée pour limiter le temps de calcul.

REMERCIEMENTS

Ce travail d'équipe a bénéficié du concours de Madame Duban et Monsieur Hirsinger (Analyse non linéaire des instabilités de combustion) et ceux de Monsieur Avalon et Monsieur Comas (Analyse linéaire des instabilités de combustion).

BIBLIOGRAPHIE

[1] - P. KUENTZMANN, G. LENGELLE
Recent research activity at ONERA on combustion instability and erosive burning.
Réunion conjointe AFOSR/AFRPL Lancaster (Californie, USA), 7-11 mars 1977.

[2] - P. KUENTZMANN, L. NADAUD
Réponse des propergols solides aux oscillations de pression et de vitesse.
Combustion, Science and Technology 1975, vol. 11, p. 119.

[3] - F.E.C. CULICK
Stability of three dimensional motions in a combustion chamber.
Combustion, Science and Technology 1975, vol. 10, p. 109.

[4] - F.A. WILLIAMS, M. BARRERE, N.C. HUANG
Fundamental aspects of solid propellant rockets.
AGARDograph 116, Technivision Services, 1969.

[5] - P. KUENTZMANN
Pertes d'impulsion spécifique dans les fusées à propergol solide. Note technique ONERA n° 151, 1973.

[6] - B. DEBOUT
Théorie linéaire d'un propulseur à propergol solide à éjection modulée. TP ONERA 1159, 1972.

[7] - F.E.C. CULICK
A review of calculations for unsteady burning of a solid propellant.
AIAA Journal, 1968, vol. 6, n°12, p. 2241.

[8] - D.I. THRASHER
Bulk mode instability of nozzleless rocket motor.
9ème conférence JANNAF sur la combustion, 1972.

[9] - E.W. PRICE
One dimensional steady flow with mass addition and the effect of combustion flow on rocket thrust.
ARS Journal, 1955, vol. 25, n°2, p. 61.

[10] - G. LENGELLE
Model describing the erosive combustion and velocity response of composite propellants.
AIAA Journal, 1975, vol. 13, n°3, p. 315.

[11] - P. CARRIERE
Petites perturbations instationnaires d'un écoulement monodimensionnel permanent.
La Recherche Aérospatiale, 1976, n°6, p. 307.

[12] - J.N. LEVINE, F.E.C. CULICK
Non linear analysis of solid rocket combustion instability.
Technical Report AFRPL-TR-74-45, october 1974.

[13] - D.E. KOOKER, B.T. ZINN
Triggering axial instabilities in solid rockets : numerical predictions. AIAA Paper 73-1298, 1973.

[14] - R. BORGHI, F. HIRSINGER, H. TICHTINSKY
Méthodes disponibles à l'ONERA pour le calcul des chambres de combustion.
Entropie, 1978, n°81, p. 3.

[15] - F. HIRSINGER, H. TICHTINSKY
Modélisation numérique de l'établissement d'une zone de combustion avec recirculation.
Congrès International sur les Méthodes Numériques dans les Sciences de l'Ingénieur (GAMNI), Paris (France), 27 novembre-1er décembre 1978.

[16] - P. KUENTZMANN
Modèles de combustion instationnaire des propergols solides composites.
La Recherche Aérospatiale, 1978, n°2, p. 77.

DISCUSSION

L.Caveny, Princeton University, US

When ONERA presented, to the open literature in 1973, their important contribution of modulated concepts this aroused considerable interest in the USA. When you compared the data to the analysis, I think you may be too severe on yourself in criticising the agreement obtained. In working with your test motor with losses of the type involved then you have another correction difficulty which will not be present in a real rocket motor. Therefore possibly your measurement of phase angle and amplitude would be a little better in the real case.

Author's Reply

I think that in order to arrive at essentially interesting results it is necessary to have a greater accuracy or precision in data.

APPLICATION OF COMBUSTION INSTABILITY RESEARCH TO SOLID PROPELLANT ROCKET MOTOR PROBLEMS

Ronald L. Derr
H. B. Mathes
James E. Crump
Code 388
Aerothermochemistry Division
Naval Weapons Center
China Lake, California 93555

ABSTRACT

Experimental and analytical tools for minimizing the risk of combustion instability in solid rocket motors are briefly reviewed. With this as an introduction, examples of practical application to motors are discussed. Both successful and unsuccessful examples are described for large and small rocket motors. Included are discussions of laboratory characterization of particle damping associated with a metallized propellant and optimization of particle damping to eliminate pressure oscillations in a tactical solid rocket motor. In addition, prediction of motor behavior and comparison with motor firing results are presented for solid rocket motors used in the NASA Space Shuttle system. The paper will conclude with a realistic assessment of the practical state-of-the-art of combustion instability technology.

INTRODUCTION

Combustion instability in a solid rocket motor is a result of pressure waves traveling in the motor cavity and becoming attuned to one or more natural acoustic frequencies associated with the cavity. The result is combustion pressure oscillations that could lead to one or more of the following problems affecting the performance of a rocket motor: (a) mechanical vibrations, (b) variations in the design thrust characteristics, and (c) catastrophic failure (e.g., case rupture).

In general, combustion instability is a natural phenomenon in solid rocket motors. Sources of pressure perturbations are always present (e.g., ejecta from the nozzle); however, if acoustic energy losses (damping) exceed acoustic energy gains (driving) in the motor, the resulting pressure oscillations will be damped and the motor will return to a stable mode of operation. If acoustic energy gains exceed losses, the amplitude of the pressure oscillations will increase with time and the potential for the aforementioned problems exists.

Considerable research has been conducted in past years to improve the understanding of combustion instability phenomena. Unfortunately, the complexity of the problem precludes a simple experiment or analysis that would provide solutions for all motor problems. However, progress has been made to the extent that corrective action can be recommended based on systematic laboratory tests and analysis. Figure 1 shows different types of acoustic energy gains and losses associated with a solid rocket motor. In general, the risk of combustion instability is minimized by minimizing acoustic energy gains and/or maximizing acoustic energy losses in the motor.

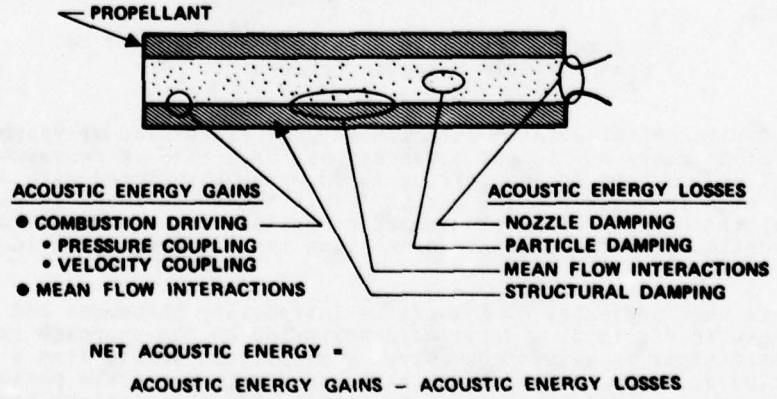

Figure 1. Acoustic Processes Associated With Solid Rocket Motors.

Combustion instability technology has evolved from not one, but numerous, research and development programs. Three aspects of this technology are listed to allow a partial review of advances made in recent years:

- o Maximizing acoustic energy losses (particle damping)
- o Minimizing acoustic energy gains (combustion driving)
- o Motor stability analysis

These topics are presented in terms of simple logic diagrams which are used in subsequent discussions dealing with motor applications.

Maximizing Acoustic Energy Losses (Particle Damping). Aluminum powder was first incorporated in propellants as an energetic additive. However, a bonus effect resulted from the formation of small droplets of aluminum oxide. These condensed phase products from aluminum combustion fill the motor cavity and provide appreciable damping of pressure oscillations. For a time, it was believed that all combustion instability problems in motors could be solved by simply adding aluminum powder to the solid propellant formulation. But this was a short-lived opinion (Ref. 1). It was found that the magnitude of damping is dependent upon droplet diameter and oscillation frequency (Ref. 2, 3, and 4), and the mean diameter of the droplets is not always the correct size to damp the prevailing frequency. Recent development in particle damping theory allows graphic examination of these dependencies (see Figure 2). Here the particle damping is expressed as the pressure amplitude rate of decay (sec^{-1}). It can be seen that if a motor exhibits pressures oscillations at a frequency of 2000 Hz, optimum particle damping would occur if the mean diameter of the particle cloud is approximately 6 μm. Similarly, for 4000 Hz, the optimum mean diameter would be approximately 4 μm. The fact that an optimum diameter exists for maximum damping at a given frequency is an important point. Of equal importance is the fact that aluminized propellants do not always provide droplets of an optimum size. Both of these facts bear on one motor example to be discussed later.

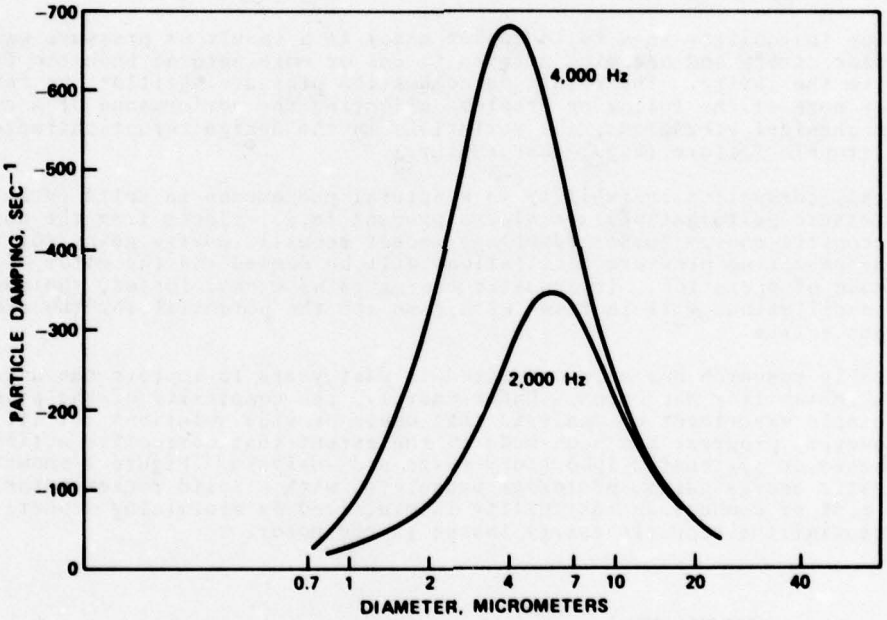

Figure 2. Particle Damping Dependency Upon Particle Size and Frequency.

With the above technical details established, the discussion of approach can be continued. In recent years sufficient advances have been made in research studies to allow development of a scheme for optimizing the damping associated with an aluminized solid propellant used in a given motor design. This scheme is shown in Figure 3 (Ref. 5 and 6). Briefly, the damping of an aluminized propellant is determined, and if calculated to be non-optimum, the propellant formulation is tailored to provide the optimum damping.

To appreciate the complexity of combustion instability phenomena and the simplicity of the scheme shown in Figure 3, a detailed description of the approach (as followed by the Naval Weapons Center) is warranted. Given a propellant sample from a motor that exhibits combustion pressure oscillations, high-speed motion picture photography studies are conducted in a pressurized window bomb to examine how the aluminum powder (propellant ingredient) behaves at and near the propellant surface during propellant combustion. Typical behavior is accumulation of the powder on the propellant surface, agglomeration of accumulates, and the formation of molten aluminum droplets that can have diameters ranging from 1 to 20 times the original powder diameter. These large droplets ignite and move into the gas stream. The droplets that produce damping are the products of combustion from these burning aluminum droplets. The important point here is that the diameters of droplets producing damping are not the same as the aluminum powder ingredient. Complex processes, dependent upon the propellant formulation, occur between the time the aluminum powder rests in the propellant interior and the time the aluminum oxide droplets form (Ref. 7, 8, and 9).

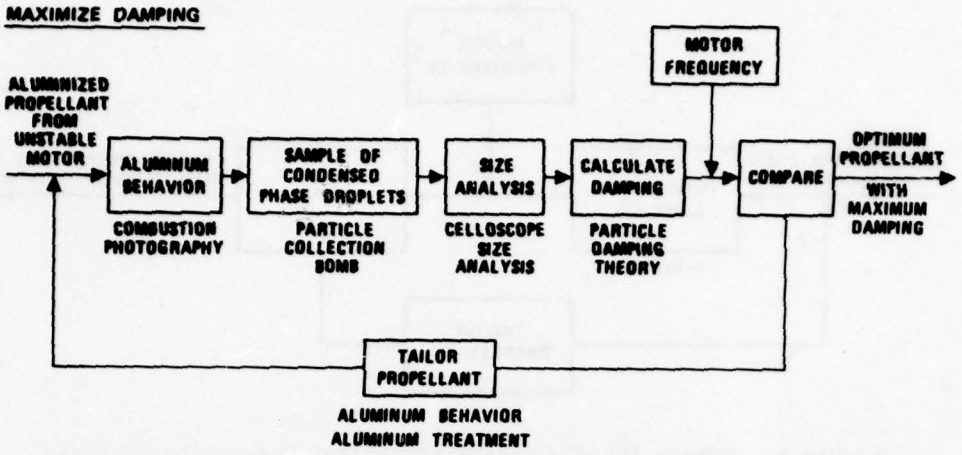

Figure 3. Scheme for Optimizing Damping for Aluminized Solid Propellants.

Following combustion photography tests, samples of the solid propellant are burned in a pressurized particle collection bomb (Ref. 10). In this test, the aluminum oxide droplets (condensed phase combustion products) are collected in quantities of approximately 2 g. Following removal of the collected sample from the bomb, the size distribution is measured in terms of the fraction of mass within a series of narrow size ranges (Ref. 11). Based on this size distribution, the damping expected in a motor can be calculated (Ref. 4). If the damping is not optimum for the pressure oscillation frequencies exhibited by the motor, the propellant formulation can be tailored (based on knowledge gained from the combustion photography study) and the entire process is repeated until a propellant with optimum particle damping is achieved.

Minimizing Acoustic Energy Gains (Combustion Driving). The burning propellant provides the acoustic energy gains that drive or sustain combustion instability in the motor cavity. As noted in Figure 1, these gains can arise from either pressure or velocity coupling between the acoustic wave and the burning surface. Efforts have been made to develop a theory that would allow calculation of the propellant response (Ref. 12 and 13); however, to date, theory is only adequate to correlate instability data and allow the propellant response to be inferred. For pressure coupling, the T-burner is the most accepted experimental tool for characterizing both nonmetallized and metallized solid propellants (Ref. 14 and 15). Other experimental methods, however, are available to measure the pressure coupled response (Ref. 16). Efforts to develop an experimental tool for measuring the velocity coupled response of a solid propellant are relatively recent compared to those of pressure coupled response (Ref. 16, 17, and 18).

The pressure and velocity coupled response are dependent upon both mean pressure and frequency. The pressure coupler response is peaked as shown in Figure 4. Accordingly, application of a scheme as shown in Figure 5 is appropriate for minimizing acoustic energy gains associated with a solid propellant. If the peak in the combustion response for the propellant is near one of the natural frequenices of the motor, the formulation of the propellant can be changed to shift the response characteristics. A similar procedure can be followed for the velocity coupled response.

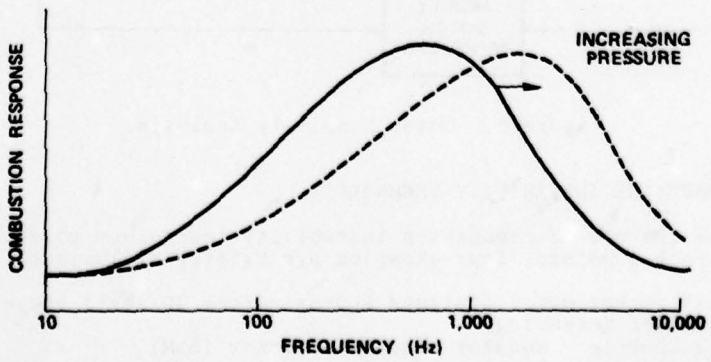

Figure 4. Combustion Response of a Solid Propellant.

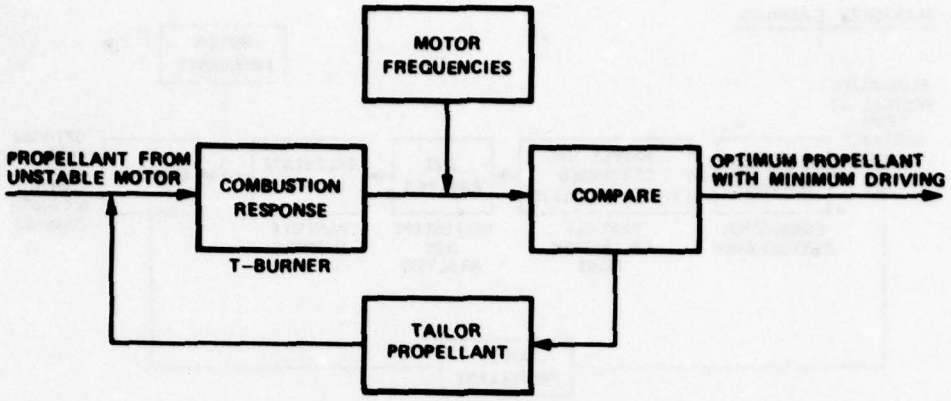

Figure 5. Scheme for Minimizing Propellant Combustion Response.

Motor Stability Analysis. The two preceding discussions have dealt with examples of maximizing acoustic energy losses and minimizing gains by modifying ingredients in the solid propellant. Changes in the motor geometry also can achieve these stabilizing effects. In recent years linearized stability analyses have been developed that compute the different acoustic energy gains and losses shown in Figure 1 (Ref. 19-22). The net acoustic energy gain (or loss) is then computed indicating whether pressure waves will be damped or amplified.

More recently, efforts have been directed toward the development analyses of nonlinear combustion instability in solid rocket motors (Ref. 23-26). As yet, these models are not in a stage for application to motor design; however, nonlinear effects (e.g., pulse triggering and limiting amplitude) are important to motor design.

A scheme for utilizing a motor stability analysis is shown in Figure 6. Here, the combustion response data (as determined from T-burner tests) and particle damping data (as determined from particle sizing) are input for the stability analysis. If the analysis shows the motor to be unstable, changes in motor geometry can be explored as well as changes to the propellant.

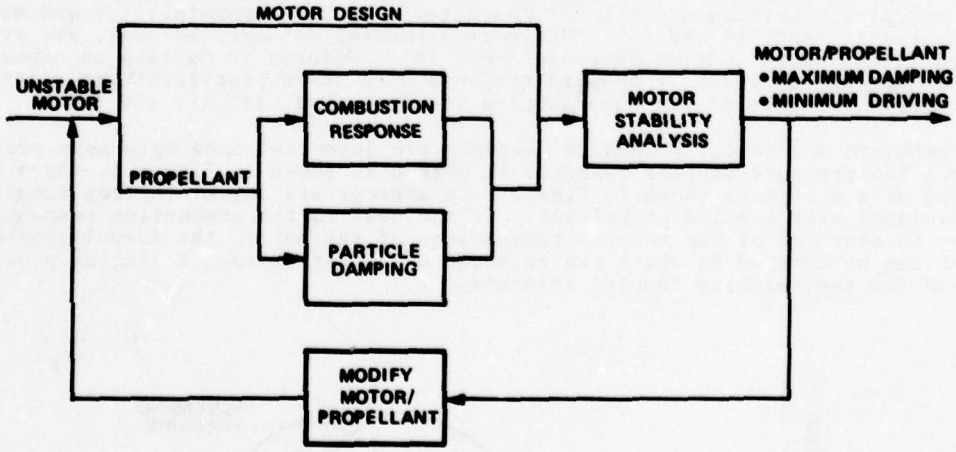

Figure 6. Motor Stability Analysis.

APPLICATION OF COMBUSTION INSTABILITY TECHNOLOGY

To demonstrate the use of combustion instability technology to minimize the risk of problems in solid rocket motors, four examples are briefly discussed:

1. a tactical rocket motor designed approximately 20 years ago without the benefit of the present technology
2. the space shuttle - booster separation motor (BSM)
3. the space shuttle - booster igniter
4. the space shuttle - booster.

Tactical Rocket Motor. This case is presented to contrast the technology of 20 years ago with that of today. The motor contains an aluminized double-base propellant.

In the development of this motor, the final propellant was selected from a screening program using subscale motors containing different propellants (primary variations were aluminum type and concentration). Data from these motor tests were pressure as a function of time. Pressure oscillations, if present, were rated as moderate or severe. From this screening approach, a propellant was selected for motor development. Since it is now known that acoustic energy gains and losses are dependent upon motor geometry, such an approach is judged to be inadequate and could yield misleading results. Perhaps the greatest problem is that the frequencies of oscillations in the subscale motor are different from those in the full-scale motor. Based on the crude subscale screening method, the following observations were made in a 1958 report:

- *the ability of aluminum to stabilize is not affected by size or configuration of propellant*
- *aluminum oxide is not promising for use as an additive in suppressing unstable burning.*

Both of these observations are incorrect. The first statement suggests that particle damping is independent of frequency. Extensive studies, both experimental and analytical, show otherwise (Ref. 4 and 6). In addition, studies have shown that the second statement has been shown to be incorrect in numerous low smoke solid rocket programs.

Based on the foregoing discussion, it is not surprising that combustion pressure oscillations have been present in this motor since it was first developed. Fortunately, problems associated with the instability have been limited to mechanical vibrations. Undoubtedly, a decision that these vibrations would not be deterimental to missile performance was made early in the missile development. The oscillations exist, however, and the potential for problems is present.

Recently, the technology described earlier in this paper was applied to the tactical rocket motor. Specifically, the scheme for examining particle damping (Figure 3) was applied to the metallized double-base propellant. Samples were burned at the motor pressure, collected, and the size distribution measured. Results of this measurement are shown as the open bars in Figure 7. It can be seen that the condensed phase products form the motor propellant are largely fine particles (diameters less than 2 μm) and coarse particles (diameters greater than 43 μm). The weight-fraction in the intermediate sizes (2 to 43 μm) is quite low. This was a surprising result. For comparison purposes, a more typical result is given in Figure 7 as solid bars. These data are for a conventional aluminized solid propellant.

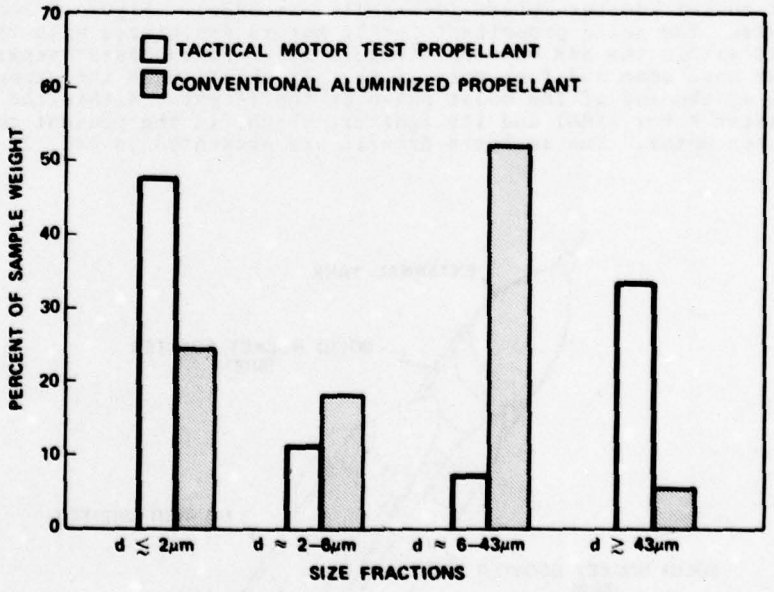

Figure 7. Particle Size Distribution for Tactical Motor Propellant and a Conventional Aluminized Propellant.

The significance of the size distribution data shown in Figure 7 is immediately realized when the frequencies of pressure oscillation in the motor are examined. Static motor tests with high frequency response pressure transducers mounted on the forward dome of the motor show that the frequencies of concern in the motor are in the range of 2000 to 4000 Hz. The question is: what is the damping effectiveness of the collected particles over this frequency range? The answer is shown clearly in Figure 8.

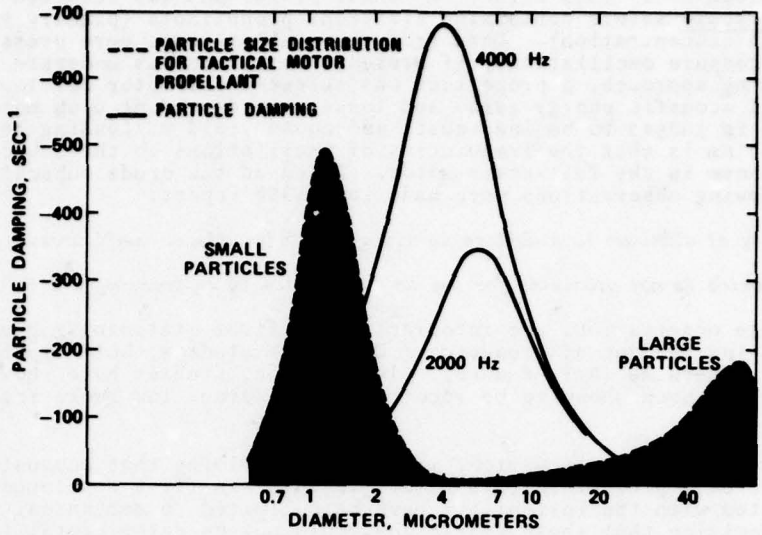

Figure 8. Comparison of Particle Size Distribution to Optimum Size for Damping in Motor.

Here, Figure 2 has been repeated with the size distribution of the particles superimposed as shaded area. As noted earlier, to effectively damp frequencies over the range of 2000 to 4000 Hz, particles in the 4 to 6 μm range are desired. However, the mass fraction of particles in this size range is essentially zero. Thus, the propellant damping is far from being optimum and it is not surprising that pressure oscillations prevail in the motor.

Space Shuttle Motors. The space shuttle solid rocket motors are presented here to demonstrate the application of motor stability analysis (Figure 6). Before continuing the topic of combustion instability, a brief description of the overall system is appropriate. The space shuttle consists of the orbiter, which carries the crew and cargo; the external tank, which contains liquid propellant for the orbiter's engines; and two solid propellant rocket booster motors (designated as SRBs). Figure 9 shows the Shuttle in the boost phase. The solid propellant rocket motors associated with the Space Shuttle are all contained within the SRB envelope (Figure 10). Four booster separation motors (BSMs) in the SRB nose cone and four more in the aft skirt, push the expended SRB away from the shuttle at the end of the boost phase of the flight. Within the SRB are the solid rocket booster motor (SRM) and its igniter, which, in the present context, is treated as a rocket motor. The analysis details are presented in Ref. 27-29.

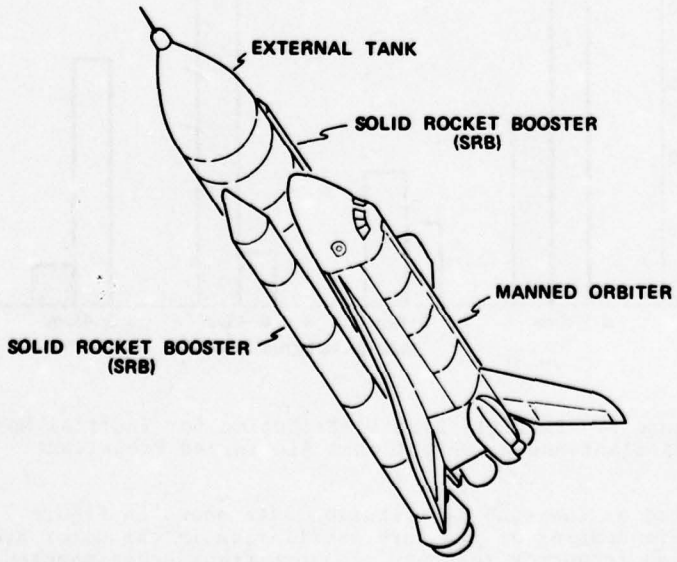

Figure 9. Space Shuttle During Launch.

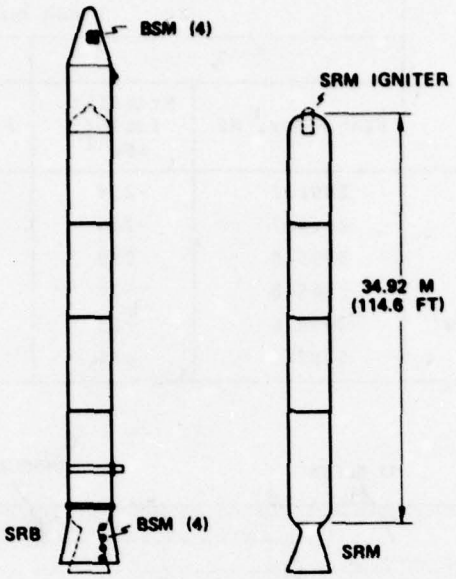

Figure 10. Solid Propellant Rocket Motors for the Space Shuttle.

The booster separation motor (BSM) is a medium size motor using a conventional HTPB ammonium perchlorate (AP) composite propellant with 2% powdered aluminum. Figure 11 presents pertinent design geometry details.

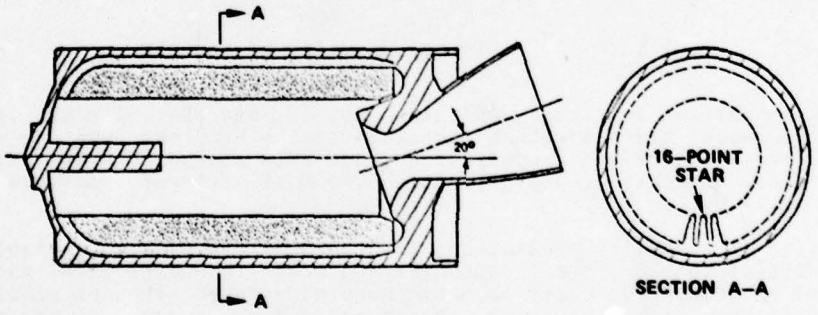

Figure 11. Booster Separation Motor (BSM) Geometry.

The results of the stability calculation using a linearized stability program, are shown in Table 1 for the 0% web burn and the 50% burn. The acoustic mode frequencies for which solutions are shown, cover the lower axial and transverse modes; T-burner propellant response tests were conducted over that frequency range. Over the indicated range of frequency, the pressure-coupled combustion burning term was destabilizing while the nozzle, particle damping, and mean flow terms were all stabilizing. The net result, assuming that the velocity-coupled combustion response is insignificant, was that the motor is stable. The axial modes are the most stable. The transverse modes are about an order of magnitude less stable than the axial modes, but are still stable according to the calculated results.

For the BSM, static test data show that there is no combustion instability behavior. Thus, the predicted results are in agreement with motor performance.

The solid rocket booster motor (SRM) is shown in Figure 12. The internal geometry is a combination of a forward slotted section, a long circular bore in the central portion of the motor, and an expanding conical aft section terminated by a short enlarged portion which surrounds a re-entrant (submerged) nozzle. The propellant is a conventional PBAN-AP composite propellant with 16% powdered aluminum.

Table 1. Motor Stability Analysis: Booster Separation Motor.

Acoustic wave structure	% Web burn			
	0		50	
	Frequency, Hz	Stability factor, sec^{-1}	Frequency, Hz	Stability factor sec^{-1}
First axial	1091.2	-254	1064.9	-205
Second axial	2128.7	-266	2105.3	-219
Third axial	3095.8	-279	3106.4	-234
First tangential	2365.5	-27	2045.9	-17
First tangential, first axial	2688.6	-23	2313.6	-30
Second tangential	3187.3	-54	3017.8	-30

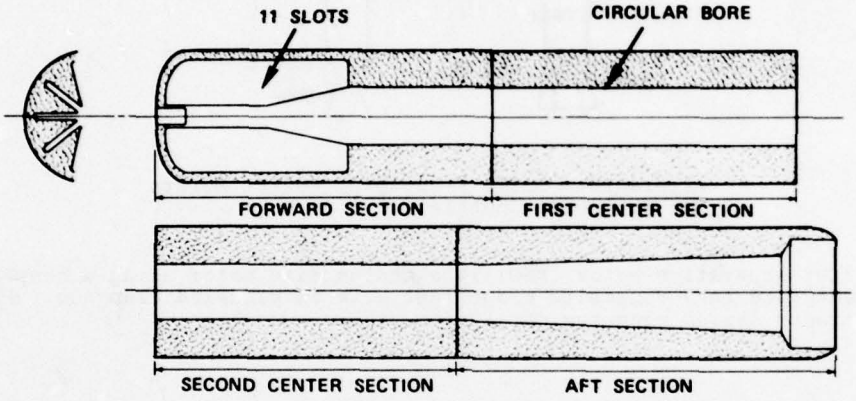

Figure 12. Internal Geometry of the SRM.

The SRM was analyzed for three web burns: 0, 45, and 80%. The two latter burns, respectively, represent times at which the slots in the head end burn out and a condition for which the port diameter and propellant surface area are both large. At burnout the SRM has an internal diameter of approximately 3.66 M (12 ft) and a forward dome to throat length of 35 M (115 ft).

A tabulation of stability predictions for the SRM is presented in Table 2. Because of the large size of the SRM, the frequencies and acoustic energy gains and losses are low compared to the BSM. For every acoustic mode considered, the net acoustic energy was calculated to show stable behavior. For axial modes, however, it was noted that nozzle damping diminished as the web was consumed. This trend is seen in the data of Table 2.

TABLE 2. Motor Stability Analysis for the Space Shuttle Booster Motor (SRM).

Acoustic wave structure	% Web burn					
	0		45		80	
	Frequency, Hz	Stability* factor, sec^{-1}	Frequency, Hz	Stability factor, sec^{-1}	Frequency, Hz	Stability factor, sec^{-1}
First axial	15.25	-9.87	13.98	-10.11	16.18	-9.33
Second axial	31.09	-11.42	29.89	-10.41	32.18	-10.00
Third axial	47.80	-13.89	47.03	-11.09	48.64	-10.77
First tangential	201.61	-3.52	186.31	-14.44	178.01	-13.37
First tangential, first axial	246.77	-24.70	189.09	-14.86	186.00	-14.25
Second tangential	218.42	-9.91	299.67	-28.18	291.2	-26.84

*Stability factor ≡ Net acoustic energy gains or losses.

Static test data for the SRM has verified the stability prediction for transverse modes. For axial modes, however, low amplitude (<2 psi) oscillations are observed late in burn. The presence of these oscillations at high percent web burned is consistent with the trends of the predicted net acoustic energy losses; however, the presence of oscillations suggests the stability analysis is overlooking a source of acoustic energy gains or overestimating some of the losses. It is suspected that combustion noise/aerodynamic effects could provide the necessary explanation. These pressure oscillations are not ignored because of their relatively small amplitude. The pressure rise acts across the fore end dome of the motor and creates a thrust perturbation which is approximately 30,000 lb (peak-to-peak) per psi (peak-to-peak) pressure perturbation. Thus, the 2 psi peak-to-peak oscillation (approximately 0.2% of mean chamber pressure) creates a 60,000 lb peak-to-peak thrust perturbation (approximately 3% of mean thrust).

The igniter for the space shuttle booster has dimensions comparable to those of a conventional tactical rocket motor.

The igniter geometry and the finite element grid used for zero web burn are shown in Figure 13. Internal dimensions of the igniter case include a nominal diameter of 42 cm (16.5 inches) and a nominal forward dome-to-throat distance of 84 cm (33 inches). The propellant is a PBAN-AP composition which contains 10% powdered aluminum.

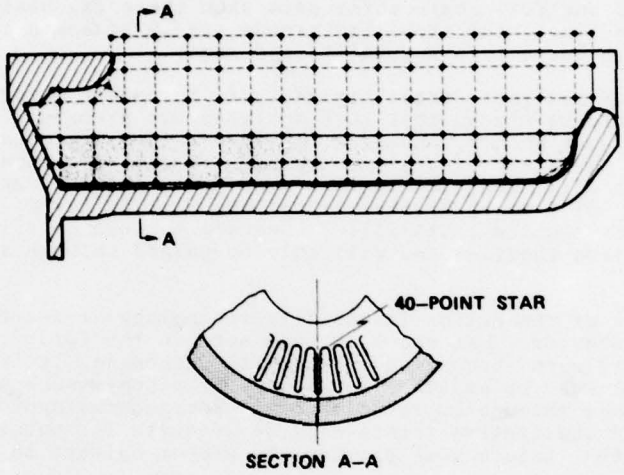

Figure 13. SRM Igniter Geometry and Finite Element Grid.

Stability predictions for the igniter at zero web are shown in Table 3. It can be seen that the motor is predicted to be stable in both axial and transverse modes.

Full-scale tests of the igniter, however, showed that the first tangential mode was unstable which is in contradiction to the stability prediction. In this case, therefore, the stability predictions for all modes analyzed in the igniter were correct except for the first tangential mode.

Design changes to the igniter have been made which result in shortening the propellant grain by removing propellant from the head end of the motor. Stability analyses for an igniter with propellant removed from the head end show that the removal improves the stability of the tangential mode. Full-scale firing tests have confirmed the predicted stability trend.

Table 3. Motor Stability Analysis: Booster Igniter.

Acoustic wave structure	% Web burn			
	0		100	
	Frequency, Hz	Stability factor, sec^{-1}	Frequency, Hz	Stability factor sec^{-1}
First axial	613	-499.9	613	-365.9
Second axial	1224	-490.5	1224	-356.5
Third axial	1837	-547.8	1837	-413.8
First tangential	1644	-175.2	...	...
First tangential, first axial	1843	-223.2	...	...
Second tangential	2444	-365.9	...	...

ASSESSMENT OF COMBUSTION INSTABILITY TECHNOLOGY

In the past 20 years, significant advances have been made in understanding fundamental combustion instability processes. These advances are reflected in an improved technology for minimizing the risk of combustion instability in solid rocket motors and the application of this technology to motor design.

Laboratory techniques and theoretical models have evolved to the point where solid propellant tailoring programs can usually be conducted at the laboratory level rather than through full-scale motor tests. In particular, schemes for developing propellants with improved particle damping and pressure-coupled response are available. There are deficiencies in the available laboratory techniques and theoretical models (for example, velocity-coupled response); however, the usefulness of these schemes is not dependent upon the quality of the laboratory test techniques alone. Rather, methods for tailoring propellants also must be available for achieving a desired change in combustion behavior. It is in this area where the schemes are weakest. This suggests, therefore, that future research studies require closer links between the combustion specialist and the chemist responsible for synthesis of ingredients and formulation of propellants.

By combining a linearized stability analysis with propellant response and damping data, the net acoustic energy gains or losses for a motor can be calculated. Comparisons between predicted and full-scale motor data show these calculations to be correct in a qualitative sense--i.e., the stability trends are in agreement; however, the predictions are not always correct in a quantitative sense.

The application of nonlinear stability analysis to rocket motor problems is relatively young. It could be argued that such analyses are premature since linear stability analysis has numerous weak points. However, there are too many motor problems that appear dependent upon nonlinear processes. Methods of analysis remain somewhat uncertain because terminology is still confused in this area. For example, are the processes associated with the driving of a steep frontal travelling wave different from those associated with nonlinear velocity-coupled instability? Answers to such questions go beyond the linear small perturbation theories and will only be gained through studies of nonlinear stability.

This brief review of combustion instability technology--research advances and applications to motor behavior--must end with some note on the future. Because of the complexities associated with combustion instability phenomena, it is doubtful if quantitative analysis will ever be possible. However, if schemes such as those presented here can be strengthened through improved theory, experimental approaches, and tailoring methods, prediction of qualitative trends will be adequate for motor design. It is, therefore, important that future work provide the proper balance in emphasis between these different areas.

REFERENCES

1. Director of Defense Research and Engineering. Instability of Combustion of Solid Propellants, by AdHoc Group on Solid-Propellant Instability of Combustion. Washington, D.C., June 1959. (Publication UNCLASSIFIED.)

2. Temkin, S., and Dobbins, R. A. "Attenuation and Dispersion of Sound by Particulate-Relaxation Processes," J Acoust Soc Amer, Vol. 40, No. 2 (1966), pp. 317-24.

3. Naval Weapons Center. A Parametric Study of Particulate Damping Based on the Model of Temkin and Dobbins, by G. L. Dehority. China Lake, CA, NWC, September 1970. (NWC TP 5002, publication UNCLASSIFIED.)

4. ------. Procedure for the Calculation of Particulate Damping of Acoustic Oscillations, by George L. Dehority and Karl J. Kraeutle. China Lake, CA, NWC, September 1976. (NWC TM 2889, publication UNCLASSIFIED.)

5. Derr, R. L., Kraeutle, K. J., and Mathes, H. B. "Combustion Instability Studies Using Metallized Solid Propellants: Part I, Experimental Verification of Particle Damping Theory," in 12th JANNAF Combustion Meeting, Volume II. Chemical Propulsion Information Agency, Laurel, MD, December 1975. (CPIA Pub. 273, publication UNCLASSIFIED.)

6. Kraeutle, K. J., Derr, R. L., Mathes, H. B., and Dehority, G. L. "Combustion Instability Studies Using Metallized Solid Propellants: Additional Experimental Evidence for the Validity of Particle Damping Theory," in 13th JANNAF Combustion Meeting, Volume II. Chemical Propulsion Information Agency, Laurel, MD, December 1976. (CPIA Pub. 281, publication UNCLASSIFIED.)

7. Price, E. W. "Summary Report on JANNAF Workshop on 'Behavior of Aluminum in Solid Propellant Combustion,'" in 13th JANNAF Combustion Meeting, Volume II. Chemical Propulsion Information Agency, Laurel, MD, December 1976. (CPIA Pub. 281, publication UNCLASSIFIED.)

8. Price, E. W. "Combustion of Aluminum in Solid Propellant Flames," to be presented at the AGARD 53rd Symposium on Solid Rocket Motor Technology, Oslo, Norway, 2-5 April 1979.

9. Kraeutle, Karl J., Mathes, H. B., and Derr, Ronald L. "The Role of Particulate Damping in the Control of Combustion Instability by Aluminum Combustion," to be presented at the AGARD 53rd Symposium on Solid Rocket Motor Technology, Oslo, Norway 2-5 April 1979.

10. Mathes, H. B., Kraeutle, K. J., Dehority, G. L., and Derr, R. L. "Combustion Instability Studies Using Metallized Solid Propellants: Part III, Characteristics of Particulate Metal Oxide Residues in T-Burners," in 12th JANNAF Combustion Meeting, Volume II. Chemical Propulsion Information Agency, Laurel, MD, December 1975. (CPIA Pub. 273, publication UNCLASSIFIED.)

11. Kraeutle, K. J. "Particle Size Analysis of Aluminized Propellants," presented at AIAA/SAE 13th Joint Propulsion Conference, 10-13 July 1977. (AIAA Preprint No. 77-978, UNCLASSIFIED.)

12. Culick, F. E. C. "A Review of Calculations for Unsteady Burning of a Solid Propellant," Amer. Inst. Aeronaut. Astronaut. J., Vol. 6 (Dec 1968), pp. 2241-2254.

13. Cohen, N., et al. "Combustion Response Modeling for Composite Solid Propellants," in 14th JANNAF Combustion Meeting, Volume I. Chemical Propulsion Information Agency, Laurel, MD, December 1977. (CPIA Pub. 292, publication UNCLASSIFIED.)

14. Chemical Propulsion Information Agency. T-Burner Manual, by Committee on Standardization of Combustion Instability Measurements ICRPG Working Group on Solid Propellant Combustion. Laurel, MD, CPIA, November 1969. (CPIA Pub. 191, publication UNCLASSIFIED.)

15. ------. T-Burner Testing of Metallized Solid Propellants, by F. E. C. Culick. Laurel, MD, CPIA, March 1976. (CPIA Pub. 275, publication UNCLASSIFIED.)

16. Brown, R. S. "Pressure and Velocity Response Function Measurements by the Rotating Valve Method," to be presented at the AGARD 53rd Symposium on Solid Rocket Motor Technology, Oslo, Norway, 2-5 April 1979.

17. Beckstead, M. W., et al. "A Technique for Evaluating Velocity Coupled Combustion Instability," in 10th JANNAF Combustion Meeting, Volume I. Chemical Propulsion Information Agency, Laurel, MD, December 1973. (CPIA Pub. 243, publication UNCLASSIFIED.)

18. Air Force Rocket Propulsion Laboratory. Investigation of Velocity Coupled Combustion Instability, by P. L. Micheli. Edwards, CA, AFRPL, January 1977. (AFRPL Report TR-76-100, publication UNCLASSIFIED.)

19. Naval Weapons Center. Interactions Between the Flow Field, Combustion, and Wave Motions in Rocket Motors, by F. E. C. Culick. China Lake, CA, NWC, June 1972. (NWC TP 5349, publication UNCLASSIFIED.)

20. Culick, F. E. C. "Stability of Three-Dimensional Motions in a Combustion Chamber," Combustion Science and Technology, Vol. 10 (1975), pp. 109-124.

21. Beckstead, M. W., Krashin, M., Butcher, A. G., and Pilcher, D. L. "Acoustic Stability Characterization of the TRIDENT I (C-4) Motors," in 11th JANNAF Combustion Meeting, Volume I. Chemical Propulsion Information Agency, Laurel, MD, September 1974. (CPIA Pub. 261, publication UNCLASSIFIED.)

22. Lovine, R. L. and Waugh, R. C. "Computer Programs for Solid Rocket Motor Stability Predictions," in 12th JANNAF Combustion Meeting, Volume II. Chemical Propulsion Information Agency, Laurel, MD, December 1975. (CPIA Pub. 273, publication UNCLASSIFIED.)

23. Air Force Rocket Propulsion Laboratory. Numerical Analysis of Nonlinear Longitudinal Combustion Instability in Metalized Propellant Solid Rocket Motors, Volumes I and II, by Jay N. Levine and F. E. C. Culick. Edwards, CA, AFRPL, July 1972. (AFRPL-TR-72-88, publication UNCLASSIFIED.)

24. Culick, F. E. C. Nonlinear Behavior of Acoustic Waves in Combustion Chambers. California Institute of Technology, Pasadena, CA, April 1975.

25. Culick, F. E. C., and Levine, J. N. "Comparison of Approximate and Numerical Analyses of Nonlinear Combustion Instability," presented at the AIAA 12th Aerospace Sciences Meeting, Washington, D.C., January 30-February 1, 1974. (AIAA Paper No. 74-201, UNCLASSIFIED.)

26. Culick, F. E. C. "Some Problems of Nonlinear Waves in Solid Propellant Rocket Motors," to be presented at the AGARD 53rd Symposium on Solid Rocket Motor Technology, Oslo, Norway, 2-5 April 1979.

27. Naval Weapons Center. Internal Acoustic Characteristics of the NASA Solid Propellant Booster Motor (SRM), by H. B. Mathes and C. J. Bicker. China Lake, CA, NWC, November 1976. (NWC TM 2822, publication UNCLASSIFIED.)

28. ------. Combustion Instability Testing of NASA BSM Propellant (UTP 19048) in the NWC T-Burner, by James E. Crump. China Lake, CA, NWC, August 1976. (NWC TM 2911, publication UNCLASSIFIED.)

29. Mathes, H. B. and Bicker, C. J. "Combustion Stability Predictions for Space Shuttle Solid Propellant Rocket Motors," in 13th JANNAF Combustion Meeting, Volume II. Chemical Propulsion Information Agency, Laurel, MD, December 1977. (CPIA Pub. 281, publication UNCLASSIFIED.)

DISCUSSION

M.Barrere, Fr

I agree in general with your conclusions but to predict instability in a rocket motor is difficult and it is important to evaluate all the losses which are a function of many parameters, in particular the scale effect. The damping effect of particles is only one part of the losses. Do you agree?

Author's Reply

I do not disagree. Particle damping was selected to illustrate the concept of developing a scheme to maximise acoustic energy losses in a solid rocket motor. Figure 1 illustrates that particle damping is only one of the losses involved.

It is important that we identify and understand all acoustic energy gains and losses so that we establish the means of determining magnitudes and optimising these through propellant formulation and motor design.

SELF-SUSTAINED OSCILLATORY COMBUSTION OF SOLID ROCKET PROPELLANTS

by
L. DE LUCA
Centro di Studio per Ricerche sulla Propulsione
e sull'Energetica, Istituto di Macchine del Politecnico,
32 piazza Leonardo da Vinci, 20133 Milano, Italy.

SUMMARY

Self-sustained oscillatory burning of solid rocket propellants is considered, within the framework of a thermal theory of heterogeneous combustion and for quasi-steady gas phase. A nonlinear burning stability analysis, carried out via an integral method, predicts the existence of three well defined static regimes: stationary, self-sustained oscillatory, and extinguished. The self-sustained oscillatory solution is related to large values of surface heat release; these values increase with pressure. The burning rate oscillations are of thermokinetic nature and feature characteristic spikes. The existence and the properties of these oscillations can be analytically predicted; they strictly depend on the operating conditions. Computer simulated runs show a very good agreement with the analytical expectations. Identical self-sustained oscillations were observed following different transients to the same final set of operating conditions. Frecuencies, increasing with pressure, of the order of 100 Hz were found at pressures of the order of 10 atm; amplitudes were found to decrease with pressure. The same basic features can be observed for different flame models.

LIST OF SYMBOLS

B_p = nondimensional pressurization rate coefficient
E = activation energy, cal/gmole
$f(\bar{\theta}_{i,s}-\theta_s)$ = static restoring function
I_o = radiant flux intensity impinging at the propellant surface, cal/cm^2-s
n = exponent in ballistic burning rate law; also: order of the approximating polynomial
P = pressure, atm
$\dot{q}$ = conductive energy flux, cal/cm^2-s
Q_f = flame heat release, cal/g
Q_s = surface heat release, cal/g
$\mathcal{R}$ = universal gas constant, cal/gmole-K
R = burning rate, cm/s
t = time, s
T = temperature, K
u = nondimensional finite size disturbance of temperature
u_x = nondimensional finite size disturbance of thermal gradient
x = space variable, cm
Δ = finite difference of a quantity evaluated between X=0 and X=-ξ
λ = thermal conductivity, cal/cm-s-K
ξ = nondimensional thickness of disturbance thermal layer

Subscripts and Superscripts

a = ambient
c = condensed phase
f = final or flame
g = gas
i = initial
s = surface
$-$ = steady state or average value of a parameter

Abbreviations

AFSC = Air Force System Command
AIAA = American Institute of Aeronautics and Astronautics
AMS = Aerospace and Mechanical Sciences Department
AP = ammonium perchlorate
ARS = American Rocket Society
CF = Combustion and Flame
CST = Combustion Science and Technology
DB = Double Base
FGV = Combustion, Explosion and Shock Waves
FTD-MT = Foreign Technology Division - Machine Translation
JETP = Journal of Experimental and Theoretical Physics
JSR = Journal of Spacecraft and Rockets
KTSS = Krier-T'ien-Sirignano-Summerfield
MTS = Merkle-Turk-Summerfield
NASA = National Aeronautics and Space Administration
ODE = ordinary differential equation
ONERA = Office National d'Etudes et de Recherches Aérospatiales

PBAA = polybutadiene-acrylic acid
PDE = partial differential equation
PMTF = Journal of Applied Mechanics and Technical Physics

Sec. 1 - INTRODUCTION

The purpose of this paper is to examine whether, and under which conditions, a burning solid rocket propellant may undergo self-sustained oscillatory combustion. The study is based on a comprehensive combustion stability analysis (Refs. 1-2) developed in fully nonlinear conditions by means of an integral method. This stability analysis allows, within the framework of a thermal model of heterogeneous combustion and for quasi-steady gas phase, to predict when the steady reacting solution becomes statically (i.e., intrinsically) unstable and which solution, under these circumstances, may occur. Numerical calculations are given for an ammonium perchlorate (AP)-based composite solid propellant (see Tabs. 1-2). However, within the limitations specified below, the basic concepts emerging from this investigation are expected to hold true for any condensed substance subjected to deflagration waves.

This paper goes beyond previous works of the writer (Refs. 3-4) in that: (1) it profits by the results from a less restrictive integral method obtained in the companion paper of Ref. 5, (2) both MTS and KTSS flame models are considered, and (3) results are interpreted in terms of bifurcation diagrams. A literature survey is offered in Sec. 2. Analytical predictions and computer simulated results are discussed in Sec. 3. Conclusions and suggestions for future work will close the paper in Sec. 4.

Sec. 2 - A LITERATURE SURVEY

The original work of Huffington (Refs. 6-8) on chuffing and oscillatory burning of cordite goes back to the beginning of the '50. Experimental results and a theoretical interpretation, in terms of condensed phase thermal explosion, were given for both phenomena. The proposed mechanism for oscillatory burning of cordite is the successive explosion, assisted by gas phase heat feedback, of discrete surface layers of decreasing thickness with increasing pressure. The Frank-Kamenetskii thermal explosion theory (Ref. 9) was extended to consider a monodimensional slab of decomposing explosive, enclosed between two parallel walls, with one surface (hot boundary) subjected to a constant rate of heat transfer while the other (cold boundary) is maintained at a constant temperature. For cordite this temperature was taken as the melting temperature (460 K); for other cases it was just the ambient temperature. The solution determines, for a given heat transfer rate to the burning surface, the critical slab thickness and surface temperature above which the volumetric decomposition develops to explosive rates. These critical values were found to depend on the dimensionless parameter $E_c/\alpha T_a$, being E_c the activation energy of the distributed exothermic reactions (assumed of Arrhenius type) in the condensed phase and T_a the cold boundary temperature. The theory was quite successful in predicting, at 20 atm, a thickness of layer burnt off in a single explosion of about 50 μm and a frequency of about 40 Hz. This theoretical approach, remarkable 25 years ago, suffers today the known limitations of the Frank-Kamenetskii type of theory.

A relatively large amount of work on oscillatory burning of several reactive materials, including DB and AP-based composite propellants, was performed by Soviet investigators. A good review, mostly focused on the theoretical aspects of this question, is contained in Novozhilov's monograph on solid propellant burning (Ref. 10). In particular, a numerical solution for the unsteady propagation of an exothermic reaction front in a gasless system (condensed phase energy equation coupled with a distributed chemical reaction rate term of Arrhenius type) was given in 1971 (Ref. 11). The rather vague mechanism invoked by the authors, to explain the oscillating combustion observed under a wide combination of the relevant parameters, relies on the "excess enthalpy" of the steadily propagating combustion front as compared with the enthalpy of the initial material. Librovich and Makhviladze (Ref. 12) took up this problem in 1974; they simplified the gasless system by considering a collapsed chemical layer separating the initial material from the combustion products. An analytical solution was found via an integral method (Fourier transform) and successfully compared with the previous numerical solution of Ref. 11. In both cases an increase of the activation energy was found to increase the period of the oscillating combustion rate and the amount of movement of the reaction front during one oscillation, but decrease the mean velocity. Frequencies were of the order of several 10 Hz. The oscillating mechanism, according to Librovich and Makhviladze, consists of a succession of fast burnup of unreacted but heated layers, each requiring a prolonged thermal time lag for the ignition to occur.

Experimental results on self-sustained oscillatory combustion of pure and metallized DB propellants, both in a strand burner and rocket combustion chamber, were published by Svetlichny et al. (Ref. 13) in 1971. In the pressure range 1-140 atm, combustion oscillations (revealed by radiation emission and electrical conductivity of the burning zone) up to several 10 Hz were detected. The authors qualitatively ascribe these oscillations to unstable thermal relaxation of the condensed phase heated layer.

However, according to the same authors (Ref. 13), self-sustained oscillatory burning of the same DB propellants at pressure less than 70 atm is due to incomplete combustion. This and other oscillating mechanism related to burning peculiarities (e.g., incomplete burning invoked in Ref. 13 and inhomogeneities of the combustion wave in Refs. 14-15) are out of the scope of this work. Oscillatory burning due to combustion/fluid-dynamics coupling (e.g., see Ref. 16) is also out of the scope of this work. In this paper self-sustained oscillatory burning of exclusively thermokinetic character is considered, for the wide

class of heterogeneous combustion systems. It will be shown that this type of oscillatory burning is mainly related to the presence of a strongly exothermic chemical reaction in the condensed phase (collapsed at the burning surface). Pressure will be seen to favor stability. The combustion frequency, of the order of several 10 to several 100 Hz, will be found to increase with pressure. The characteristic burning rate spikes associated with these oscillations intuitively confirm the physical mechanism suggested by Librovich and Makhviladze (Ref. 12).

First detailed analytical predictions and numerical results, for a model explicitely considering the heterogeneous burning of a solid propellant (quasi-steady MTS flame), were offered by De Luca (Refs. 2-3) in 1976. Recently, Kooker and Nelson (Ref. 17) numerically confirmed the existence of a self-sustained oscillatory burning regime for solid propellants (the quasi-steady KTSS linearized flame model was adopted). Peters (Ref. 18), in 1975, numerically observed self-sustained oscillations of heterogeneous burning of spherical particles by solving, via an integral method (polynomial space dependence of the relevant variables), the governing set of PDE's.

Sec. 3 - ANALYTICAL PREDICTIONS AND NUMERICAL RESULTS

Consider the physical system of Fig. 1 representing a strand of solid propellant subjected to a radiant flux impinging with instantaneous intensity $(1-r)\cdot I_o(t)$ at its surface, burning with instantaneous rate $R(t)$ in a closed vessel at instantaneous pressure $P(t)$ and fixed ambient temperature T_a. The following important assumptions are made: quasi-steady gas phase, optically opaque and chemically inert condensed phase, infinitesimally thin burning surface and irreversible gasification processes, specific heat constant throughout the deflagration wave. For a detailed list of assumptions, the reader might wish to consult Ref. 4. The assumption of quasi-steady gas phase might be open to criticism, as rightly pointed out by T'ien (Ref. 19). However, something has to be given up in order to reach meaningful conclusions in a nonlinear theory. In any event, one of the purposes of this study is to verify the self-consistency of the combined analytical and numerical approach.

It is shown in a companion paper (Ref. 5) that the equilibrium and asymptotic stability properties of the nonlinear system of Fig. 1 are enclosed in an algebraic function called the static restoring function. This function is determined by assuming a polynomial space dependence of the disturbance thermal profile in the PDE describing the condensed phase energy conservation. Upon integration of this PDE, the following approximate ODE is found for a given initial condition $\theta_s(\tau=o)\equiv\bar{\theta}_{i,s}$

$$(3.1)\qquad \frac{d\theta_s}{d\tau} = + \frac{n+1}{2n}\,\frac{(u_x)_{c,s}}{u_s}\,\frac{\Re\cdot u_s - (u_x)_{c,s} - \Re\cdot\Delta(\bar{\theta}_i) + \Delta\left(\frac{d\bar{\theta}_i}{dX}\right)}{1-\frac{1}{2}\,\frac{u_s}{(u_x)_{c,s}}\left[\frac{\partial (u_x)_{c,s}}{\partial u_s}\right]_{\mathcal{P},F_o}}$$

where n is the polynomial order to be chosen; $u_s\equiv\bar{\theta}_{i,s} - \theta_s(\tau)$ is the disturbance surface temperature and $(u_x)_{c,s}$ is the disturbance thermal gradient, at the condensed phase side, to be assigned by means of a flame model. The quantities

$$(3.2)\qquad \Delta(\bar{\theta}_i) \equiv \bar{\theta}_i(X=0) - \bar{\theta}_i(X=-\xi)$$

$$(3.3)\qquad \Delta\left[\frac{d\bar{\theta}_i}{dX}\right] \equiv \frac{d\bar{\theta}_i}{dX}(X=0) - \frac{d\bar{\theta}_i}{dX}(X=-\xi)$$

depend on the steady thermal profile $\bar{\theta}_i(X)$ prevailing at the initial conditions and the disturbance thermal layer thickness.

$$(3.4)\qquad \xi(\tau) = n\,\frac{\bar{\theta}_{i,s} - \theta_s(\tau)}{\left(\frac{d\bar{\theta}_i}{dX}\right)_{c,s} - \left(\frac{\partial\theta}{\partial X}\right)_{c,s}}\quad .$$

The static restoring function $f(\bar{\theta}_{i,s} - \theta_s)$ is given by the right hand side of Eq.3.1. It holds true, even for finite size disturbance, both for static (random disturbances) and dynamic (coupling with external disturbances) stability. Yet, in the case of dynamic stability, the validity of the approach is restricted to forcing functions levelling off in time. The general behavior of the static restoring function when the pressure is varied parametrically, at fixed ambient temperature and surface heat release, was discussed in Ref. 5. The behavior of the static restoring function when the surface heat release is varied parametrically, at fixed ambient temperature and pressure, is illustrated by the qualitative picture of Fig. 2. When the surface heat release is low enough (in a sense which will be better understood below), the system behaves according to curve CBA.

For increasing values of the surface heat release, it is found that the static restoring function is represented by curve $CB_1A_1D_1E$. This is surprising. It is immediately recognized that C is the stable equilibrium solution for the unreacting state (trivial solution).

Consider the steady state energy balance of the overall combustion wave: for each set of parameters, only one stationary solution exists for the reacting state. Let us call A this particular root. Root E_1, although stable according to Lyapunov, is a false equilibrium solution introduced by the approximate ODE formulation of the problem. The remaining roots B_1 and D_1 are both unstable equilibrium solutions for the reacting state.

For further increase of the surface heat release, A- and D-type roots respectively increase (moving to right) and decrease (moving to left) in the plot of Fig. 2, until coalescence and then crossing over occur with exchange of stability character. This important point will be discussed later. For further increasing of the surface heat release, B- and D-type roots disappear after coalescence, while both A_2 and E_2 roots cannot be stable reacting solutions (curve CA_2E_2 in Fig. 2). Under these circumstances, it follows that the only allowed solution is the trivial unreacting configuration represented by root C. Any attempt to produce a stationary combustion wave with a static restoring function of type CA_2E_2 will inevitably result in extinction. This type of extinction, however, should not be qualified as "dynamic".

Quantitative plot of the static restoring function $f(\bar{\theta}_{i,s} - \theta_s)$ vs the nondimensional surface temperature θ_s are given for the propellant AP/PBAA No. 941 (see Tab. 2). A quantitative plot requires the choice of a specific flame model and a specific order of the approximating polynomial. By applying different flame models to the same propellant, different stability properties are predicted: this offers a criterium for discriminating flame models. In this work MTS and KTSS flame models are implemented (e.g., consult Ref.4). As to the order of the approximating polynomial, n=3 has been shown to give accurate results (for details, consult Ref.4).

The values of the nontrivial roots A,B,D,E vs surface heat release (bifurcation diagram) are plotted at 30 atm of pressure in Fig. 3. This plot was obtained implementing the MTS flame model with n=3. It can be seen that: (1) the fundamental A root monotonically increases with $|Q_s|$; (2) B,D , and E roots all lie on the same curve; and (3) this S-shaped curve crosses the A- curve (bifurcation point). For $|Q_s|$ low enough, A and B are the only reacting roots; A defines the steady solution, while B defines the lower dynamic stability point (Ref. 2). For increasing $|Q_s|$, D and E roots branch off; A still is the steady solution, while B and D respectively define the lower and upper dynamic stability points (Refs. 2 - 3). For further increases of $|Q_s|$, A and D roots cross over and exchange their stability character; the steady solution, even in a static environment, is now self-sustained oscillatory burning, between D and E, around A. For $|Q_s|$ even larger, B - D roots coalesce ; under these circumstances there is no steady reacting solution.

Self-sustained oscillatory burning may only be found, at a given pressure, for Q_s values ranging between A - D roots coalescence and B - D roots coalescence. These particular intervals of Q_s values are plotted vs pressure in Tab.3.Both A-B roots and B-D roots coalescences occur at increasing $|Q_s|$ with increasing pressure. However, the extent of this critical $|Q_s|$ interval shows only minor increases with increasing pressure. The physical upper limit for $|Q_s|$ is also plotted in Tab. 3; this is defined by $|Q_s| = C_c(\bar{T}_f - T_a)$ being $C_c = C_g$ by assumption . The value $|Q_s| = C_c(\bar{T}_s - T_a)$, finally plotted in Tab. 3, represents the maximum amount of surface heat release allowed by KTSS nonlinearized flame model according to Eq. 2.3.10 of Ref. 4. No such a limitation exists for the MTS flame model.

It should be explicitely remarked that Q_s ranging within the values of Tab. 3 is a necessary but not sufficient condition for the occurence of self-sustained oscillatory burning. Dynamic extinction, due to decelerating deflagration waves or overstability (Ref. 3), is always an alternative to the self-sustained oscillatory burning. Even without external disturbances, the actual range of Q_s values for which self-sustained oscillatory burning may occur is narrower than indicated in Tab. 3. Indeed, in this oscillatory regime, the burning propellant bounces back and forth under the competing influence of D and E roots. For dynamic reasons the amplitude of these surface temperature oscillations has to be somewhat larger than $\theta_s(E) - \theta_s(D)$. This implies that, especially near B - D roots coalescence, extinction will somewhat shrink the Q_s range of self-sustained oscillatory burning.

The above analytical predictions were verified by digital simulations of transient burning tests obtained by integration of the full set of governing equations (for details, see Ref. 2). The pressurization runs from 10 to 30 atm shown in Fig. 4, for several values of Q_s , were computed implementing the MTS flame model. The results nicely confirm the existence of the three static burning regimes predicted by the bifurcation diagram of Fig.3. Remark that $|Q_s| = 180$ cal/g is less than the A - D roots coalescence value ($|Q_s| = 190$ cal/g), while $|Q_s| = 220$ cal/g is very close to the B - D roots coalescence value ($|Q_s| = 222$ cal/g). Compare with Tab. 3. Notice that for increasing $|Q_s|$, the same external forcing function gives more pronounced dynamic burning effects. For example, see the succession of the initial surface temperature peaks in Fig. 4 for the three indicated values of Q_s. Large values of $|Q_s|$ favor (dynamic) extinction due to overstability.

For $|Q_s| = 200$ cal/g the numerical solution of the pressurization test confirms that, after a certain transient, the combustion wave undergoes characteristic, sharp self-sustained oscillations around A root ($\theta_s = 0.99$) with peaks near E ($\theta_s = 1.61$) and D ($\theta_s = 0.94$) roots. This implies, under the specified set of operating conditions, the existence of a limit cycle. Being a limit cycle an overall property of the governing nonlinear PDE (condensed phase energy equation), once triggered this oscillatory behavior would not depend on the previous history of the system and in particular on its initial conditions, but just on the operating conditions. The frequency of these oscillations is expected to be somehow related to the thermal wave relaxation time in the condensed phase (at the final conditions of the pressurization test).

In order to check these anticipations, further computer simulated tests were performed. The results are summarized in Tab. 4. No self-sustained oscillatory regime was found for

several values of $|Q_s| \leq 180$ cal/g and $|Q_s| \geq 210$ cal/g. But for Q_s=-200 cal/g, after a few transient cycles, exactly the same oscillatory pattern was found for exponential pressurization tests from 10 to 30 atm with $B_p = 1$ or $B_p = 200$. Likewise, exactly the same self-sustained oscillatory pattern was found for exponential pressurization tests to 40 atm with $B_p = 200$ from $P_i = 10$, 20 and 30 atm. However, the amplitude and the period τ_p of the surface temperature oscillations decreased, for increasing final pressure, according to the values listed in Tab. 4. Exponential pressurization tests to 50 atm, with $B_p = 200$, from $P_i = 10$ or 40 atm confirmed this point. All this evidence neatly suggests that, for a propellant with the appropriate value of Q_s, the existence and the properties of the self-sustained oscillatory regime are uniquely defined by the final operating pressure (being all runs performed at fixed ambient temperature of 300 K and for adiabatic burning). In Tab. 4, for the reader's convenience , the values of $\theta_s(E)$, $\theta_s(D)$, and $\theta_s(A)$ are plotted for n=3. Likewise the values of thermal wave relaxation time in the condensed phase, $\tau_{th,c} = \mathcal{R}^{-2}$, are given. However, the exact meaning of this parameter in the present context is open to questions.

The previous computer simulated tests were obtained by implementing the MTS flame model. Pressurization tests with the KTSS nonlinearized flame model, from 10 to 30 atm with B_p=1, were also performed. Unfortunately, the value of Q_s = -200 cal/g falls outside the range of applicability of the KTSS nonlinearized flame at 10 atm; therefore no direct comparison with the MTS flame was possible. The same pressurization test was then attempted for Q_s=-180 cal/g. A self-sustained oscillatory regime was detected (τ_p=2.8), with the same general features observed with the MTS flame (see Fig. 5). A self-sustained oscillatory regime with the KTSS linearized flame was also recently detected by Kooker and Nelson (Ref. 17), who found $\tau_p = 1.36$ at 68 atm for $Q_s = 105.8$ cal/g (their H = 0.88).

The characteristics spikes, observed in all runs, of the burning rate oscillations physically suggest a succession of thermal "explosions" of surface layers (strongly heated by the intense heat source due to large Q_s values at the burning surface) followed by similarly fast burning rate decreased (due to the tight coupling condensed/gas phases at high burning rates) and slow thermal wave build-up (ignition lag).

A most significative way to summarize the findings of this investigation is shown in Fig. 6. This is a surface temperature vs pressure plot at constant Q_s (the standard burning rate vs pressure plot on logarithmic scale is inconvenient for graphical reasons). Root A corresponds to what is usually measured in a strand burner. However, for pressures less than A - D coalescence, A root becomes statically unstable and the solution is a self-sustained oscillatory burning peaking slightly above E and below D roots. For pressures less than B - D coalescence, in no way a reacting steady solution can be found. Therefore, for a given propellant, it can be concluded that pressure favors combustion stability. However, too large pressure might cause instability of the monodimensional heterogeneous deflagration wave (Ref. 20); but this is out of the range of validity of this study. On the other side, for decreasing pressures, the burning wave "jumps" abruptly from the usually steady configuration to a large amplitude self-sustained oscillations before getting fully extinguished. Exactly this same remark was made in Ref. 11 on a totally different basis. In view of this, experimental techniques (and the very concept of pressure deflagration limit) should be re-considered in this region of marginal burning.

Sec. 4 - CONCLUSIONS AND SUGGESTIONS

It is felt that conclusive evidence has been offered for: (1) the existence of a self-sustained oscillatory burning regime of a thermokinetic nature; (2) the fact that the properties of this oscillatory regime strictly depend on the final operating conditions; (3) the capability of the comprehensive nonlinear combustion stability analysis, developed by the author in Refs. 1-5, to predict the existence and the basic properties of this special regime by means of bifurcation diagrams; and (4) the applicability of the analysis to both MTS and KTSS (linearized and nonlinearized) flame models.

Although figures are given only for an AP-based composite solid rocket propellant, the above facts are expected to hold true for any condensed, chemically reacting substance that can be modelled within the framework of a thermal theory of heterogeneous combustion with quasi-steady gas phase. The behavior of the steady deflagration wave at low pressure is of particular interest;more sophisticated diagnostic techniques and pressure deflagration limit definitions are suggested.

The delicate assumption of a polynomial space dependence of the disturbance thermal profile has to be further investigated. Other quasi-steady flame models shall be tested and compared. But the quasi-steady gas phase assumption has to be properly qualified. Considering the importance of the surface heat release, the assumption of constant specific heat throughout the heterogeneous deflagration wave shall be dropped. Exact predictions of the oscillating burning period have yet to be proposed.

In conclusion, the static restoring function, defined in the framework of a nonlinear asymptotic stability of burning solid propellants, demonstrates the existence of three well defined static regimes: stationary, self-sustained oscillatory, and extinguished. The self-sustained oscillatory burning regime is associated with values of surface heat release increasing with pressure. Frequencies of the order of 100 Hz and large increases of surface temperature (up to 50%), at pressures of the order of 10 atm, were numerically observed for both MTS and KTSS quasi-steady flame models.

REFERENCES

1. De Luca, L. "Nonlinear Stability Analysis of Solid Propellant Combustion", II Symposium (International) on Dynamics of Chemical Reactions, University of Padova (Italy), 15-17 December 1975, pp. 245-256.

2. De Luca, L. "Solid Propellant Ignition and Other Unsteady Combustion Phenomena Induced by Radiation", Ph. D. Thesis, Princeton University, AMS Report No. 1192-T, 15 November 1976.

3. De Luca,L. "Instability of Heterogeneous Deflagration Waves", VI Symposium (International) on Detonation, San Diego (California) USA, 24-27 August 1976, pp. 281-289.

4. De Luca, L., Coghe, A., Reggiori, A. "The Dynamics of Solid Propellant Combustion", 1st Annual Technical Report, European Research Office, Grant No. DA-ERO 78-G-029, November 1978.

5. De Luca, L., Galfetti, L., Zanotti, C. "Ignition and Extinction of Solid Rocket Propellants", The Propulsion and Energetics Panel of AGARD, 53rd Meeting, Symposium on "Solid Rocket Motor Technology", Oslo (Norway),2-5 April 1979.

6. Huffington, J.D. "The Burning and Structure of Cordite", Trans. Faraday Soc., Vol.47, 1951, pp. 864-876.

7. Huffington, J.D. "The Unsteady Burning of Cordite", Trans. Faraday Soc., Vol. 50, 1954, pp. 942-952.

8. Clemmow, D.M., Huffington, J.D. "An Extension of the Theory of Thermal Explosion and its Application to the Oscillatory Burning of Explosives", Trans. Faraday Soc., Vol. 52, 1956, pp. 385-396.

9. Frank-Kamenetskii, D.A. "Diffusion and Heat Exchange in Chemical Kinetics", Princeton University Press, 1955, Chapters 6-9.

10. Novozhilov, B.V. "Nonstationary Combustion of Solid Rocket Fuels", 1973. Translation AFSC No. FTD-MT-24-317-74.

11. Shkadinskii, K.G., Khaikin, B.I., Merzhanov, A.G. "Propagation of a Pulsating Exothermic Reaction Front in the Condensed Phase", FGV, Vol. 7, No. 1, pp. 19-28,1971.

12. Librovich, V.B., Makhviladze, G.M. "One Limiting Scheme for the Propagation of a Pulsating Exothermic Reaction Front in a Condensed Medium", PMTF, Vol. 15, No. 6, 1974, pp. 107-116.

13. Svetlichnyi, I.B., Margolin A.D., Pokhil, P.F. "Low-Frequency Self-Oscillatory Processes in Propellant Combustion", FGV, Vol. 7, No. 2, 1971, pp. 188-194.

14. Ilyukhin, V.S., Mysov, V.G., Novikov, S.S. "Low-Frequency Nonacoustic Fluctuations During Combustion of Nitroglycerine Powder", FGV, Vol. 10, No. 3, 1974, pp. 334-337.

15. Ilyukhin, V.S., Margolin, A.D., Mysov, V.G., Novikov, S.S. "Role of Heterogeneneity Of Composite Solid Fuels in the Mechanism of Pulsating Burning", FGV, Vol. 11, No. 3, 1975, pp. 498-501.

16. Brulard, J., Kuentzmann, P., Kling, R. "Réponse d'un Propergol Solide à un Echelon de Pression", La Recherche Aérospatiale, No. 5, 1975, pp. 279-287. Also ONERA T.P. No. 1975-138.

17. Kooker, D.E., Nelson, C.W. "Numerical Solution of Solid Propellant Transient Combustion", J. Heat Transfer, on print.

18. Peters, N. "Theory of Heterogeneous Combustion Instabilities of Spherical Particles", XV Symposium (International) on Combustion, 1975, pp. 363-375.

19. T'ien, J.S. "Oscillatory Burning of Solid Propellants Including Gas Phase Time Lag", CST, Vol. 5, No. 2, 1972, pp. 47-54.

20. Strahle, W.C. "One-dimensional Stability of AP Deflagrations", AIAA J., Vol. 9, No. 4, 1971, pp. 565-569.

ACKNOWLEDGMENTS

The author wishes to thank Prof. C. Casci, director of the Istituto di Macchine del Politecnico, for constant encouragement and interest in this work; ing. G. Riva for help in numerical computation; and ing. L. Galfetti for help in the manuscript preparation. Project jointly supported by European Research Office and Centro di Studio per Ricerche sulla Propulsione e sulla Energetica under Grant Agreement No. DAERO 78-G-029.

TABLE 1

Definition of nondimensional variables

$\mathcal{P} = P/P_{ref}$		pressure
$\mathcal{R} = R/R_{ref}$		burning rate
$X = x/x_{ref}$		distance
$\tau = t/t_{ref}$		time
$H = Q_s/Q_{ref}$		surface heat release
$Q = Q_f/Q_{ref}$		gas heat release
$F_o = I_o/I_{ref}$		external radiant flux intensity
$\dot{q} = \dot{q}/I_{ref}$		conductive heat flux
$\mathcal{T} = T_{(\ )}/T_{(\ ),ref}$		temperature, e.g. $\mathcal{T}_f = T_f/T_{f,ref}$
$\theta_{(\ )} = \frac{T_{(\ )} - T_{ref}}{T_{s,ref} - T_{ref}}$		temperature, e.g. $\theta_s = \frac{T_s - T_{ref}}{T_{s,ref} - T_{ref}}$

TABLE 2

Properties of solid composite propellant AP/PBAA
No. 941 used as datum case in this study

ASSUMED OR MEASURED PROPERTIES		
Endoth.crystal.transition heat, Q_{cr}	20	cal/g of AP
Endoth.AP vaporiz. heat, $Q_{v,AP}$	526	cal/g of AP
Exoth. AP decomposition heat, $Q_{A/PA}$	800	cal/g of AP
Endoth. binder vapor. heat, $Q_{v,B}$	225	cal/g of binder
AP content, p	80	%
Ballistic exponent, n	0.46	
KTSS pyrolysis law power, w	6.00	
Surface activation energy, E_s	16000	cal/gmole
Flame activation energy, E_f	20000	cal/gmole
Condensed phase density, ρ_c	1.54	g/cm^3
Condensed phase specific heat, C_c	0.33	cal/g-K
Condensed phase thermal diffusivity, α_c	1.4×10^{-3}	cm^2/s
Gas phase specific heat, C_g	0.33	cal/g-K
Gas phase thermal conductivity, λ_g	1×10^{-4}	cal/cm-K-s
Average products molecular weight, $\overline{m}$	26	g/gmole
Reflectivity of propellant surface, r	0	%
Minimum surface temp. for reactions, T_m	300	K
Matching surface temp. for pyrolysis, T_k	405	K
EVALUATED PROPERTIES		
Cond.phase thermal conductivity, λ_c	7.12×10^{-4}	cal/cm-K-s
Refer. frequency factor, $A_{s,ref}$	2705	cm/s
Surface gasification heat, Q_s	-158.2	cal/g (+endoth.)
Chemical time constant, A_M	0.338	
Diffusion time constant, B_M	2.350	
REFERENCE PROPERTIES		
Pressure, P_{ref}	68	atm
Temperature, T_{ref}	300	K
Burning Rate, $R_{ref} = R\ (P_{ref})$	0.837	cm/s
Surface temperature, $T_{s,ref} = T_s(P_{ref})$	1000	K
Flame temperature, $T_{f,ref}$	2430	K
Distance, $x_{ref} = \alpha_c/R_{ref}$	1.673×10^{-3}	cm
Time, $t_{ref} = \alpha_c/R^2_{ref}$	1.998×10^{-3}	s
Heat, $Q_{ref} = C_c(T_{s,ref} - T_{ref})$	231	cal/g
Energy flux, $I_{ref} = \rho_c C_c R_{ref}(T_{s,ref} - T_{ref})$	297.8	cal/cm^2-s

TABLE 3

Maximum range of values of surface heat release, for which self-sustained oscillating combustion may occur, in function of pressure. Static restoring function evaluated for MTS flame with n=3 at standard conditions (T_a = 300K, adiabatic burning).

Pressure P, atm	Surface Heat Release, Q_s, cal/g			
	A-D roots coalescence	B-D roots coalescence	$\|Q_s\| = C_c(\bar{T}_f - T_a)$ at standard conditions	$\|Q_s\| = C_c(\bar{T}_s - T_a)$ at standard conditions
10	-168	-197	-688.4	-199.4
20	-182	-212	-691.2	-210.2
30	-190	-222	-693.7	-216.9
40	-195	-230	-696.0	-221.8
50	-200	-235	-698.5	-225.7
60	-205	-240	-700.9	-228.7

TABLE 4

Computer simulated transient tests showing agreement with analytical predictions of the bifurcation diagram (cf. Fig. 3). All runs performed for adiabatic burning and T_a = 300 K.

Q_s cal/g	flame model	P_i	P_f	forcing function	B_p	solution	$\theta_{s,max}$	$\theta_{s,min}$	τ_p	$\theta_s(E)$	$\theta_s(D)$	$\theta_s(A)$	$\tau_{th,c}$
-150	MTS	10	30	expon.	1	stationary	=	=	=	=	=	0.929	2.33
-158.2	MTS	10	30	expon.	1	stationary	=	=	=	=	=	0.937	2.11
-180	MTS	10	30	expon.	1	stationary	=	=	=	1.43	1.04	0.962	1.56
-190	MTS	10	30	expon.	1	(*) small damping	1.45	0.82	1.96	1.53	0.976	0.976	1.32
-200	MTS	10	30	expon.	1	oscillating	1.65	0.82	1.5	1.61	0.94	0.992	1.10
-210	MTS	10	30	expon.	1	extinction	=	=	=	1.68	0.90	1.011	0.88
-220	MTS	10	30	expon.	1	extinction	=	=	=	1.75	0.86	1.032	0.70
-230	MTS	10	30	expon.	1	extinction	=	=	=	1.81	=	1.057	0.54
-200	MTS	10	30	expon.	200	oscillating	1.65	0.82	1.5	1.61	0.94	0.992	1.10
-200	MTS	10	30	linear	40	oscillating	1.65	0.827	1.5	1.61	0.94	0.992	1.10
-200	MTS	10	40	expon.	200	oscillating	1.58	0.84	1.3	1.60	0.99	1.009	0.90
-200	MTS	20	40	expon.	200	oscillating	1.58	0.84	1.3	1.60	0.99	1.009	0.90
-200	MTS	30	40	expon.	200	oscillating	1.58	0.84	1.3	1.60	0.99	1.009	0.90
-200	MTS	10	50	expon.	200	oscillating	1.45	0.86	1.2	1.59	1.022	1.022	0.78
-200	MTS	40	50	expon.	200	oscillating	1.45	0.86	1.2	1.59	1.022	1.022	0.78

(*) values taken at the 7th cycle

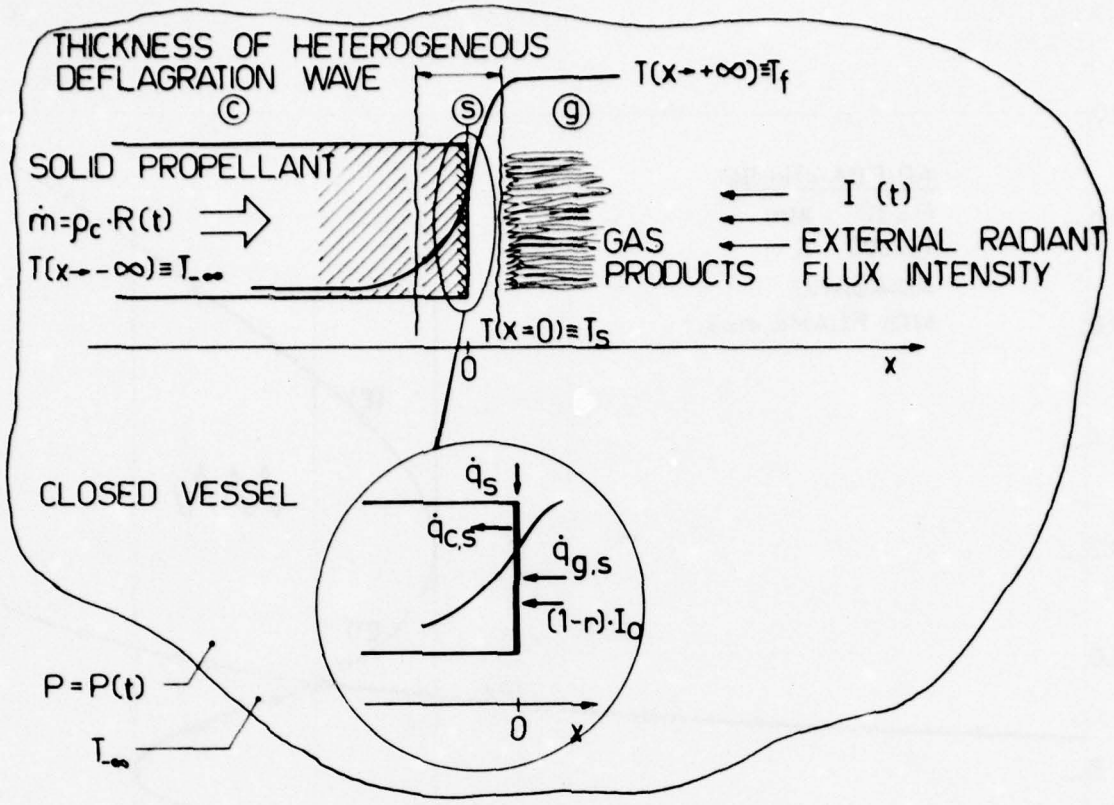

Fig. 1a - Schematic diagram of the physical problem.
1b - Schematic diagram of energy balance at the surface.

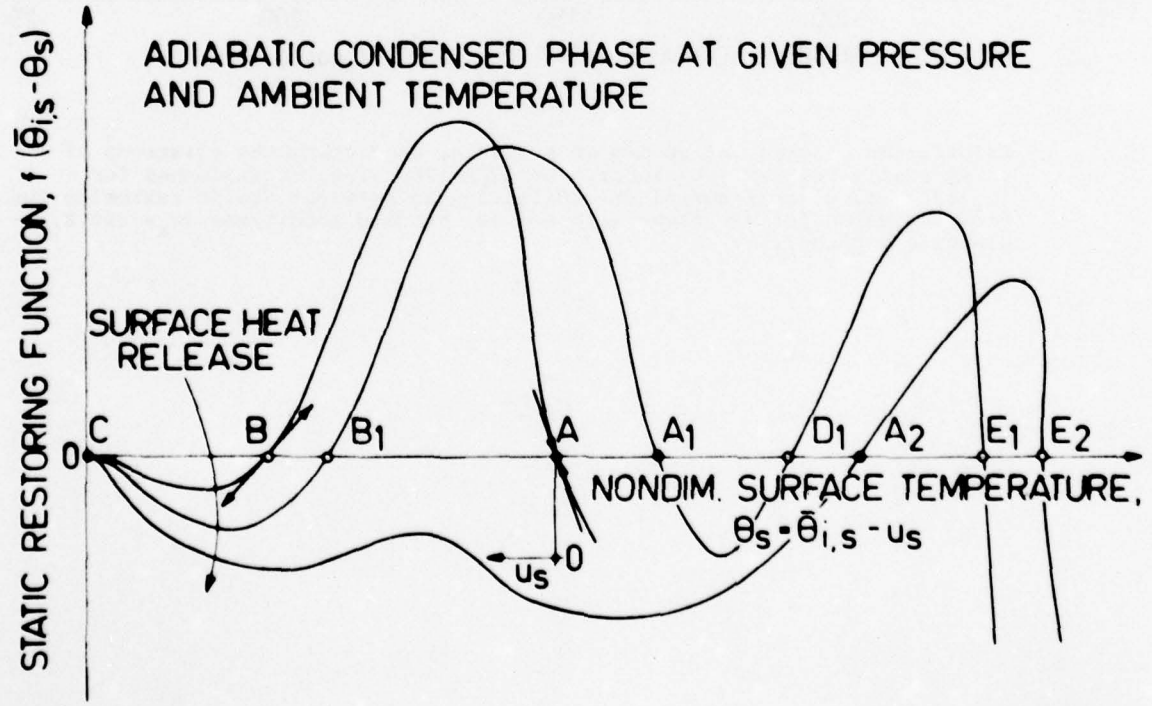

Fig. 2 - Qualitative sketch of the static restoring function, for increasing surface heat release, showing the appearance of a second pair of roots, D and E, for the reacting mode (upper dynamic instability). MTS and KTSS nonlinearized flames.

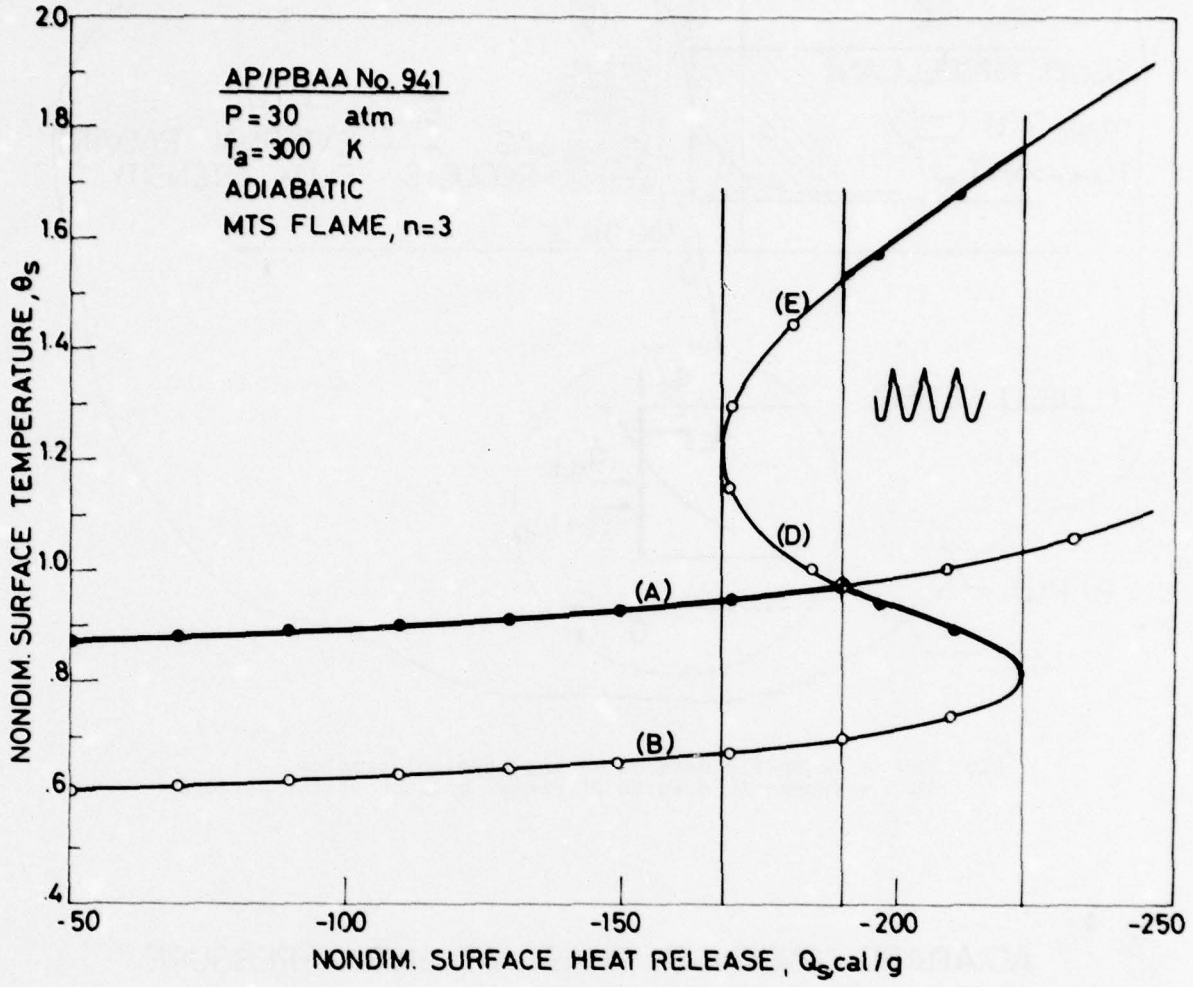

Fig. 3 - Bifurcation diagram, at 30 atm of pressure, predicting the existence of three static regimes (stationary for $|Q_s| \leq 190$ cal/g, extinguished for $|Q_s| \geq 222$ cal/g, self-sustained oscillating in between). Static restoring function evaluated for MTS flame with n=3 at standard conditions (T_a = 300 K, adiabatic burning).

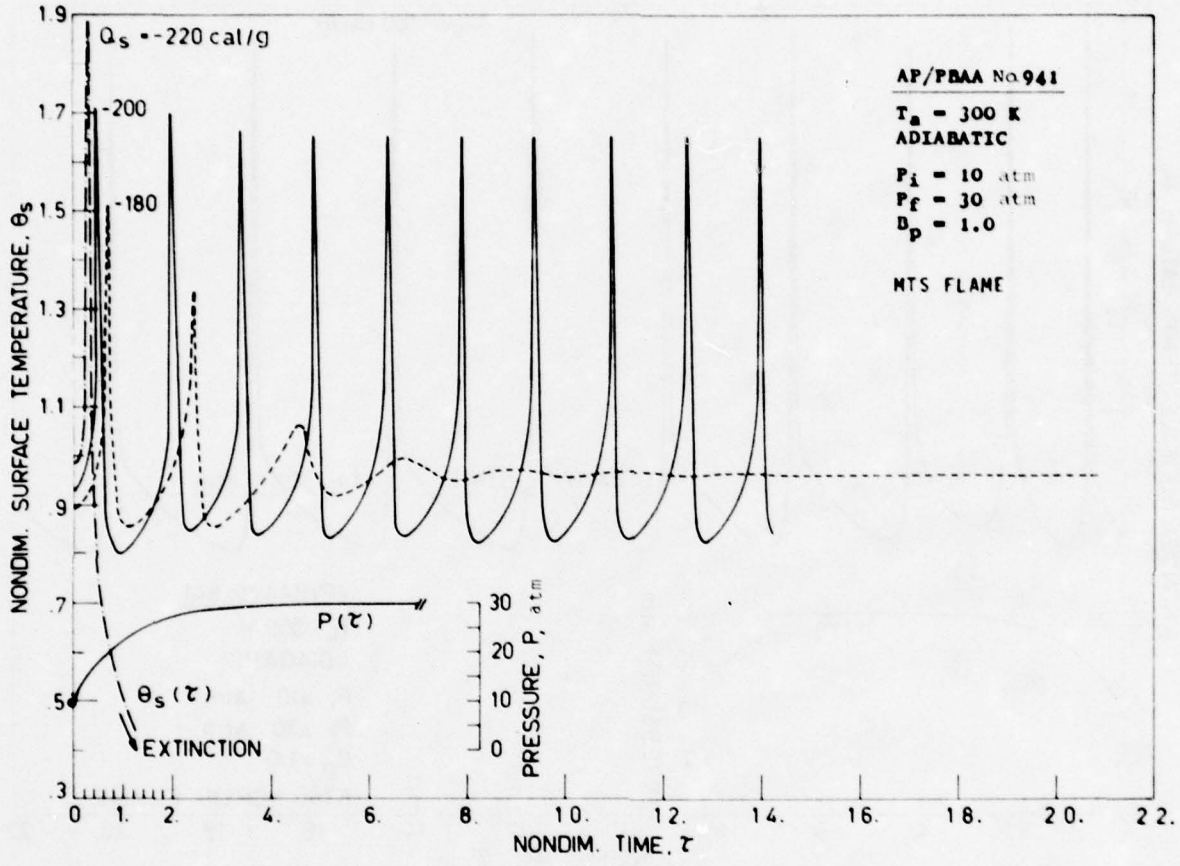

Fig. 4 - Computer simulated pressurization tests confirming the existence of three possible static regimes (stationary for Q_s = -180 cal/g, self-sustained oscillating for Q_s = -200 cal/g, extinguished for Q_s = -220 cal/g). MTS flame.

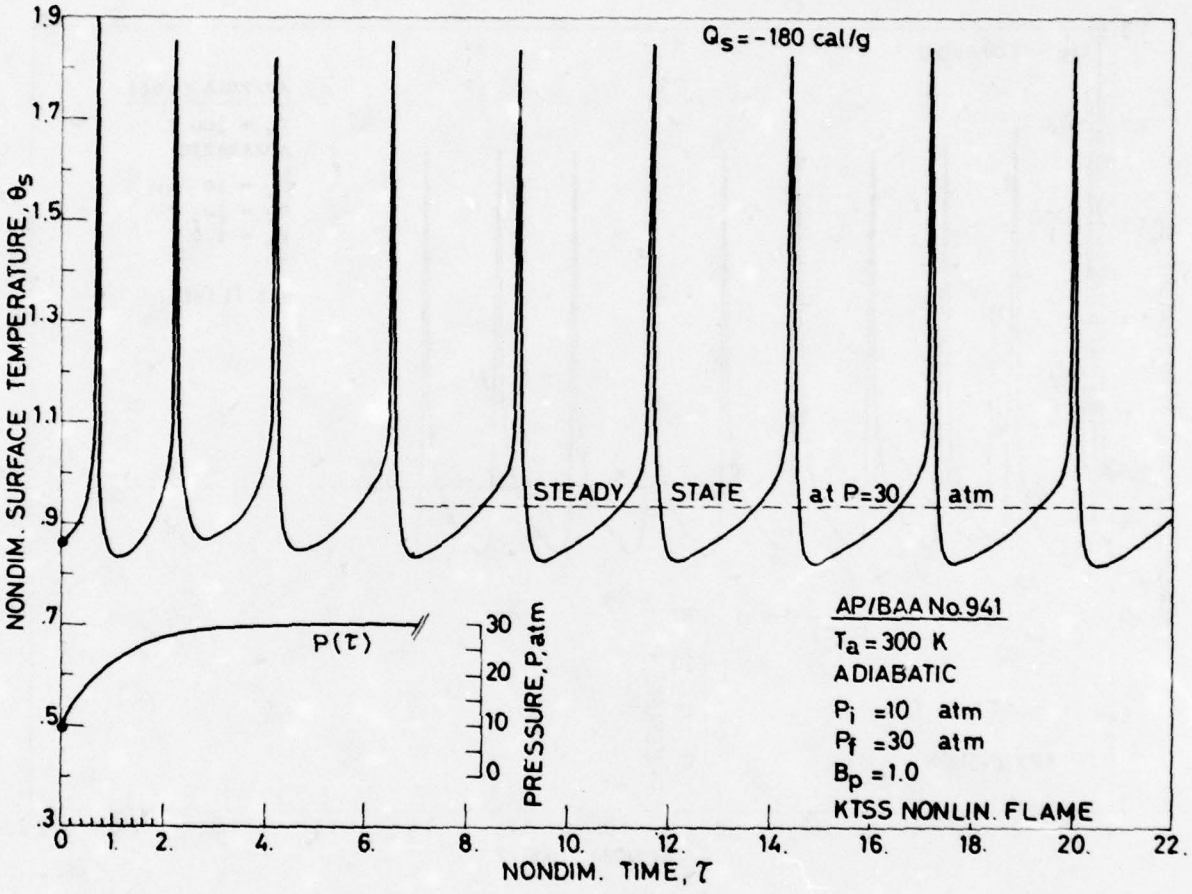

Fig. 5 - Computer simulated pressurization test confirming the occurence of self-sustained oscillatory burning for KTSS nonlinearized flame.

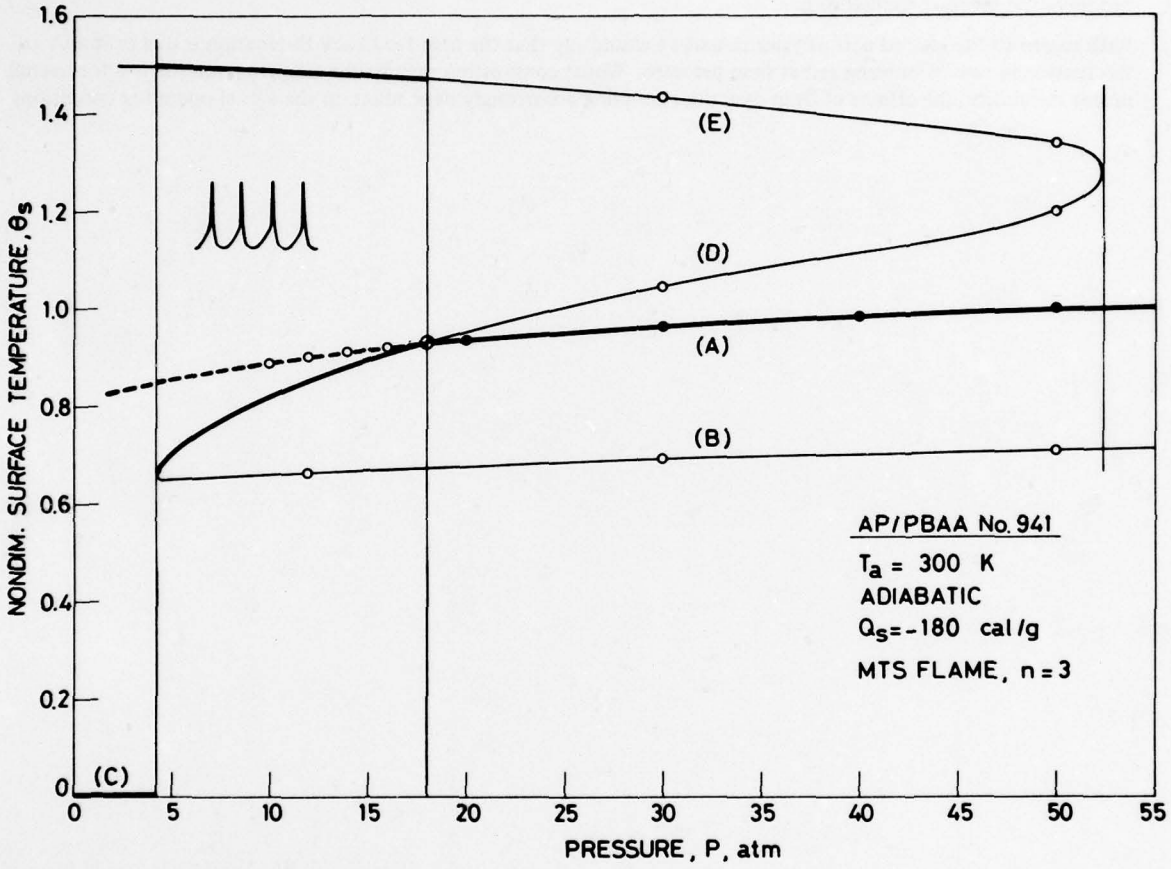

Fig. 6 - Upper and lower dynamic stability boundaries (MTS flame, n=3) on a surface temperature vs pressure plot, for Q_s = -180 cal/g, showing the existence of three static regimes (extinguished, self-sustained oscillatory, and stationary).

DISCUSSION

H.F.R.Schöyer, Delft University, Ne

In your model you have assumed a constant pressure. However fluctuations in surface temperature can occur due to variations of heat flux into the burning surface and the heat release in the substrate due to sub-surface reactions. In a real rocket motor the pressure will fluctuate out of phase with the surface temperature fluctuations and out of phase with burning rate fluctuations. The pressure oscillations will result in strong heat transfer oscillations, both conductive and convective. This is not accounted for in your model. Can you comment on how this would affect the instability in the motor?

Author's Reply

The first part of your remarks is correct. The model presented has no tight coupling with the environment that produces the pressure oscillations.

With regard to the second part of your remarks I would say that the heat feed back fluctuation is due primarily to fluctuation in rate of burning rather than pressure. Whilst combustion may be the triggering mechanism for overall motor instability, the effects of fluid-dynamics coupling are strongly dependant on the actual operating conditions.

LOW FREQUENCY OSCILLATORY COMBUSTION; EXPERIMENTS AND RESULTS

by
H.F.R. Schöyer
Delft University of Technology, Dept. of Aerospace Eng.
Kluyverweg 1, 2629 HS Delft
The Netherlands
Consultant National Defense Organization TNO,
Prins Maurits Laboratory, Technological Research,
Lange Kleiweg 137, P.O. Box 45, 2280 AA Rijswijk,
The Netherlands

SUMMARY

During the combustion of solid propellants in rocket motors, low frequency oscillations may occur as a result of the time lag between a pressure fluctuation and the resulting efflux of combustion products through the nozzle and the reaction of the propellant to the pressure fluctuation. The residence time of the combustion products is proportional to the characteristic length of the rocket motor. These oscillations are therefore called L^* oscillations.

Experiments have been carried out employing an L^*-burner with a 5 cm i.d. and one with a 10 cm i.d. Double base, as well as composite propellants have been tested. The results obtained with two burners of a different size, but with one type of propellant agree very well. There are noticeable differences between the oscillatory combustion of the double base and the composite propellant. Chuffing has frequently been observed with the double base propellants, while dp/dt extinguishment has been observed in the majority of cases of oscillatory combustion of the composite propellant. Both propellants display a relation between the frequency of the oscillations and the mean pressure. From the experiments, stability boundaries could be estimated for both types of propellants. In addition the imaginary part of the response function has been estimated for the composite propellant.

A computer program had been develloped and has been applied successfully for the digital data reduction of the experimental results. It is felt that the application of this data reduction program has largely improved the reliability of the results.

LIST OF SYMBOLS

A	constant	α	growth constant
B	constant	Γ	Vandenkerckhove function
C	proportionality constant	γ	ratio of specific heats
F	frequency	κ	thermal diffusivity
i	$\sqrt{-1}$	σ	standard deviation
L^*	characteristic length of the rocket motor, i.e. ratio of chamber volume to nozzle throat area	Ω	dimensionless frequency
m	mass flow per unit area	$( )_i'$	perturbed quantity
n	burning rate exponent	$( )_i$	imaginary part
p	pressure	$( )_r$	real part
p'	initial pressure amplitude	$( )_{cr}$	critical
R_o	propellant response function	$( )_{eff}$	effective
R_b	burning rate	$( )_d$	damping
r	variable defined in Eq. (7)		
T	combustion temperature		
T_c	(initial) propellant temperature		
T_i			

INTRODUCTION

Unstable combustion in solid rocket motors may manifest itself in various ways. If no stable equilibrium pressure can be reached, premature extinction or an explosion may occur. The classical stability condition to prevent this is a burning rate exponent smaller than unity, or more precise, $n < (\gamma + 1)/2\gamma$ [1]. In many cases, combustion instability manifests itself in (large) pressure fluctuations. Their occurrence may be explained by a time lag between the pressure fluctuation and the fluctuation in the mass production of the burning propellant. If this time lag equals a phase angle between $\pi/2$ and $3\pi/2$ the fluctuations of the mass production at the burning surface will amplify the pressure fluctuations. If the fluctuation in the amount of pyrolysis products at the burning surface is large in comparison to the pressure fluctuation the amplitude will grow rapidly.

If reliable, unsteady combustion models for solid propellants were available, the time lag between a pressure fluctuation and the fluctuation in the pyrolysis products could be predicted from such a model, like the growth of the pressure fluctuation.

Expressing the pressure fluctuation and the fluctuation in the mass flow from the burning surface as complex quantities, one may define a propellant response function [2]:

$$R_b = R_b^{(r)} + i\, R_b^{(i)} = \frac{m'/\bar{m}}{p'/\bar{p}} \qquad (1)$$

It will be evident, that in a rocket motor, or test device employing solid propellants, in which pressure oscillations occur, the amplitude history and frequency are related to this response function. This allows us to turn the problem around. If we deliberately generate these oscillations, we may deduce the response function from the frequency and growth in amplitude. This reponse function, if measured over the entire temperature, pressure and frequency ranges of interest, can be regarded as an additional

propellant characteristic and may be used to predict whether a rocket motor will display oscillatory burning or not. On the other hand knowledge of the response function may help to give us a better understanding of the combustion mechanism of solid propellants. Any good combustion model should at least correctly predict the burning rate and the propellant response function. Measuring the propellant response function therefore is both of practical interest in so far as it may help to design inherently stable solid rocket motors, and of more academic interest to get a better understanding of the combustion processes.

It is for these reasons that in many countries special test devices have been develloped and are used. The most common ones are the T-burner[3], the pulsed motor and the L^*-burner.

The T-burner is especially suited for experiments at higher frequencies.The pulsed motor[4], which has been develloped in France, should cover the entire frequency range. Variations of the pulsed motor have been develloped[5]; they should allow a more accurate data reduction.

The L^*-burner is suited for low frequency experiments; i.e. the oscillatory frequency, in general, will not exceed 300 to 400 s^{-1}. With our experiments we have concentrated on these low frequency oscillations in L^*-burners. The pressure oscillations that may occur in an L^*-burner are the result of the time lag in the resonse of the burning propellant to a pressure fluctuation and the characteristic time of the rocket motor, i.e. the time it takes for the combustion products to be exhausted from the combustion chamber. According to a simple linear acoustic analysis, the pressure fluctuations should be in phase at both ends of the combustion chamber[6].

During many of our test runs, we have measured the pressure at both ends of the combustion chamber, and we always noted that the pressure oscillations were perfectly in phase. This is illustrated in fig. 1.

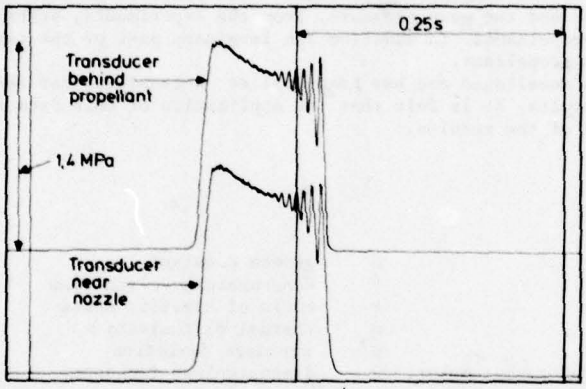

Fig. 1. Pressure during L^* oscillations. The pressure is measured at both ends of the chamber; the oscillations are in phase.

The frequency of this particular oscillation corresponds to roughly 170 s^{-1}. A critic may remark that this perhaps represents the second harmonic, as for the second harmonic the pressure at both ends of the chamber would also be in phase. The conditions for this specific testrun, shown in fig. 1, however, were such, that the second harmonic would require a frequency of ~ 200.000 s^{-1}.

We have used both double base and composite propellants. The appearance of the oscillatory pressure history differs significantly for these two types of propellant.

We have also spent considerable time in develloping a reliable ignition procedure.

We found that the ignition may have a profound influence on the accuracy and the history of oscillatory combustion; therefore, a reliable and repoducible ignition procedure is of prime importance.

INSTRUMENTATION

For the test runs two L^*-burners have been used; one with a 5 cm and one with a 10 cm internal diameter. A schematic of the L^*-burner is given in fig. 2.

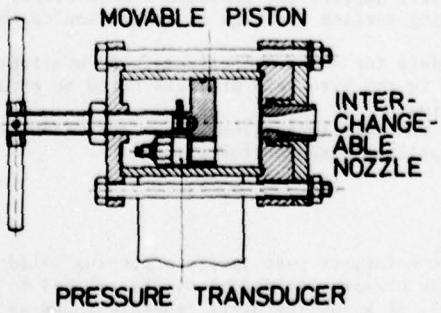

Fig. 2. Schematic of the L^*-burner

It consists of a cylindrical chamber with a piston at one end and a nozzle end plate, containing a nozzle, at the other side. Circular disks of propellant are bonded to the piston. Burning is restricted to the flat face of the propellant disk by inhibitor at the periphery of the disk. There is a large variety of nozzles, which allows us to select the equilibrium pressure for steady burning. This equilibrium pressure follows from [1]

$$P_c = (\rho_b \, a \sqrt{RT_c} \, K/\Gamma)^{\frac{1}{1-n}} \tag{2}$$

where the klemmung, K, stands for

$$K = S_b/A_t \tag{3}$$

The characteristic length of the L^*-burner follows from

$$L^* = L(D/D_t)^2 \tag{4}$$

i.e. the distance of the propellant surface to the nozzle times the square of the ratio of chamber- and throat-diameter. During a test run propellant is consumed, and the distance of the propellant to the nozzle increases. If a test run is to be carried out at a specific L^* range, one can adjust the distance of the propellant to the nozzle to the required value.
If should be noted that the characteristic length L^*, is directly related [7] to the characteristic time or residence time, τ^*, of the combustion products in the combustion chamber:

$$L^* = \tau^* \ldots \Gamma \sqrt{RT_c} \tag{5}$$

The pressure is measured by piezo-electric transducers at the nozzle end plate, and directly behind the propellant at the surface of the piston. That it is possible to measure the pressure through the propellant is due to the extremely high rigidity of the piezo-electric transducers, which hardly allows any deformation of the propellant. As can be seen from fig. 1 there is no loss of signal.

The pressure is recorded on an Ultra Violet oscillograph, with high frequency response galvanometers and an F.M. instrumentation tape recorder. This analogue signal is digitalized. A special data reduction program has been develloped [8, 9] by which the digital information is analyzed. The instantaneous L^* is estimated by integrating the mean burning rate. As the initial and final L^* values for a test run are known, the estimated L^* values are adjusted such that they match with the initial and final L^* values.

For the earlier test runs this refined numerical data reduction was not yet available, and data reduction was done "by hand". All data for experiments with double base propellants have been reduced "by hand"; the data reduction for all test runs with composite propellants has been done with help of the computer.

IGNITION

For operational rocket motors, a short ignition delay is of utmost importance. For experimental testruns, a short ignition delay time, though desirable, is not very important. The prime requirements for testruns with oscillatory combustion are:

- smooth ignition
- reproducible pressure histories during testruns.

Moreover, the ignition device should easily be applied.

We have experimented with many different ignition techniques, varying from pyrotechnic squibs, in combination with igniter mixtures, to a pyrotechnic paste which is ignited by a hot wire.
The squibs and many of the pyrotechnic mixtures often lead to irreproducible pressure spikes. We found that these pressure spikes may trigger oscillatory combustion, while a similar test run, in absence of a pressure spike yielded a rather smooth pressure history. This is illustrated by fig. 3, which shows the pressure history for two L^*-burner tests under similar conditions, with the exception that for testrun no. 303A, 1 g of ignition mixture was used while for testrun 303B, 2 g of ignition mixture was used.

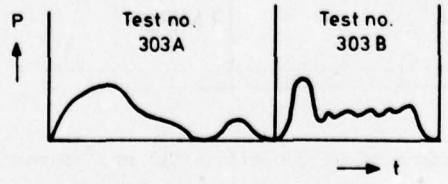

Fig. 3. Two L^* testruns under similar conditions. The ignition peak in testrun 303B caused oscillatory combustion.

This lead to ignition peaks of respectively 0,3 and 2,2 MPa. We atttribute the occurrence of oscillatory combustion to this difference in ignition pressures.
We finally arrived at a pyrotechnic lacquer which is pasted on one face of the propellant disks. The composition of this lacquer is presented in Table I. An electric wire is imbedded in the pyrotechnic lacquer. After its devellopment, this ignition technique has been used with all subsequent testruns. It has been found that this method provides us with a very good reproducibility and no need is felt for further improvements.

Table 1: Composition of successful pyrotechnic lacquer.

Potassium Nitrate	20% (by weight)
Blackpowder (meal)	10% (by weight)
Silicon	20% (by weight)
A solution of 75 g smokeless propellant PH 5179 in 1000 cm^3 acetone	50% (by weight)

Composition of Double base propellant PH 5179.

Cellulose Nitrate	52,7 % (by weight)
Glycerol Trinitrate	42,85% (by weight)
Centralite I (ethyl)	2 % (by weight)
Vaseline	0,45% (by weight)
Potassium Nitrate	1,5 % (by weight)
Graphite	0,15% (by weight)
Moist	0,35% (by weight)

EXPERIMENTS WITH DOUBLE BASE PROPELLANTS

Experiments with double base propellants employed JPN and ARP propellant. These experiments have been reported in detail by De Boer, Schöyer and Wolff[7, 10]. For JPN propellant, oscillatory combustion has only been observed in four testruns out of 66. The oscillations seemed to have been triggered by ignition peaks, and were not well reproducible. During 7 out of 60 testruns, oscillatory combustion of ARP propellant has been observed. There was no high ignition peak so that oscillations cannot have been triggered by such a peak.
Moreover, the phenomenon was well reproducible.

Experiments with ARP propellant.

The composition of ARP propellant is listed in Table 2.

Table 2: Composition of ARP propellant

Cellulose Nitrate	49,9% (by weight)
Glycerol Trinitrate	36,4% (by weight)
Triacetin	4 % (by weight)
Lead salts	4 % (by weight)
Additives	5,7% (by weight)

All testruns during which oscillations have been observed, have been ignited by the pyrotechnic lacquer and the ignition peaks have been low (between 0,2 MPa and 0,4 MPa). In all cases the ignition is followed by chuffs (between 4 and 81) before a definite pressure build-up occurs.

The oscillations, in general, start before equilibrium (mean) pressure is reached. It may be that the oscillatory nature of the combustion delays the moment at which equilibrium (mean) pressure is reached. A typical pressure history such as has been observed during oscillatory combustion of ARP propellant, is presented in fig. 4.

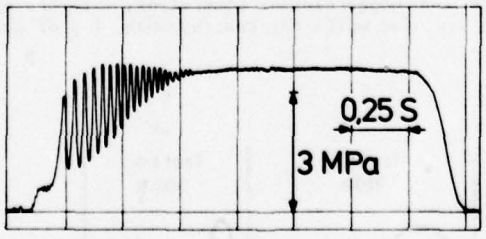

Fig. 4. L^* oscillations of ARP propellant (10 cm L^*-burner)

This particular experiment, has been conducted in the 10 cm L^*-burner.

Fig. 5 shows L^* oscillations during a testrun which has been carried out at about the same pressure and L^* ranges as the test run of fig. 4, but in the 5 cm L^*-burner. Though not exactly replicas of each other, the figures are very much alike and display many similar features, which have also been observed in other testruns[10]:

- After the initial pressure rise, the pressure levels off for a short period at about 0,5 MPa. At this low pressure level high frequency, small amplitude oscillations are seen.
- The low pressure level is followed by a rise in mean pressure upon which pressure oscillations with a rather large amplitude are visible.
- After equilibrium pressure is reached, the oscillations rapidly decay and steady burning results.

The observed dimensionless pressure amplitude and the frequency of the testrun of fig. 4 are shown in the figs. 6 and 7.

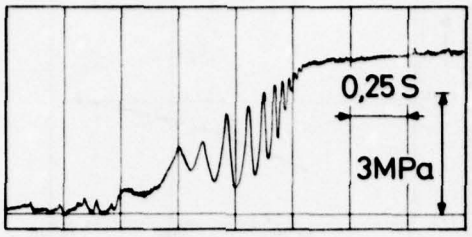

Fig. 5. L^* oscillations of ARP propellant (5 cm L^*-burner)

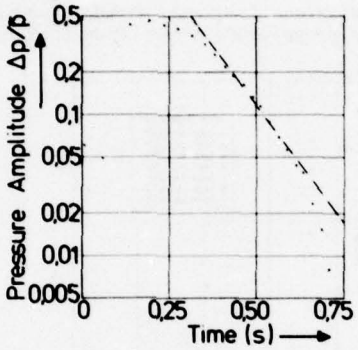

Fig. 6. Pressure amplitude during L^* oscillations of ARP propellant in the 10 cm L^*-burner

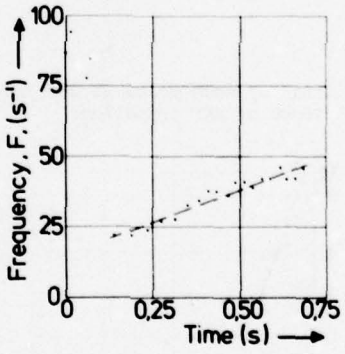

Fig. 7. Frequency during L^* oscillations of ARP propellant in the 10 cm L^*-burner

It can be seen from these figures, that at the very beginning the pressure amplitude is small and the frequency is high. Moreover, the pressure amplitude history, fig. 6, is seen to be more or less parabolic on the logarithmic scale, while the frequency, fig. 7, seems to increase about linearly with time. This last phenomenon has been observed during most cases of oscillatory combustion of ARP propellant.

During this particular testrun the frequency increases from ~22 s^{-1} to 46 s^{-1}. The mean pressure during the oscillations also increases. If one considers an oscillatory temperature profile in the burning propellant, this is associated with a dimensionless frequency[2] $\Omega = 2\pi F\kappa/r^2$. Such an oscillatory temperature profile may be caused by oscillatory heat transfer into the propellant, due to the pressure fluctuations. In fig. 8, for this particular test run, the dimensionless frequency has been plotted versus time. It is seen that the variation in this dimensionless frequency Ω is much smaller than the variation in the frequency F. While the frequency during this testrun increases with about 100 %, the dimensionless frequency only increases from ~0,12 to ~0,155 or ~30 %, which seems to confirm that heat transfer into the burning propellant is a prime rate controlling factor.

When combining all available data from the experiments with ARP propellant, it has been found that there is a strong correlation between the observed frequency and the mean pressure at which the oscillations take place. This is illustrated by fig. 9. There are two branches; high frequency oscillations at a low mean pressure and lower frequency oscillations at higher mean pressure levels. The figure suggests linear relationships between pressure and frequency. The same data are also plotted in fig. 10. This figure displays some interesting features: First of all we note that the high-frequency low-pressure branche has changed its slope from positive to negative, while Ω ranges from ~1 to 7,5.

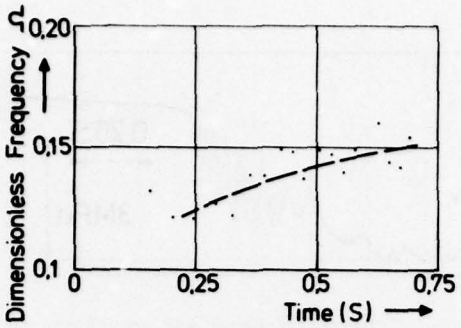

Fig. 8. Dimensionless frequency during L^* oscillations of ARP propellant in the 10 cm L^*-burner

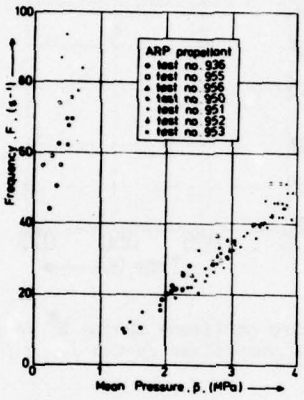

Fig 9. Correlation of mean pressure and frequency during oscillations of ARP propellant

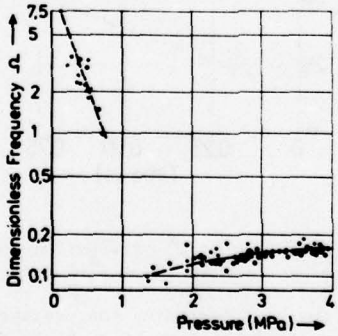

Fig. 10. Correlation of mean pressure and dimensionless frequency during oscillations of ARP propellant

The actual frequency F only ranges from ~40 s^{-1} to 90 s^{-1}. In the low frequency-high pressure branch, the dimensionless frequency ranges from ~0,08 to ~0,18, while the actual frequency range is from ~10 s^{-1} to 50 s^{-1}. This seems to imply that there are two different mechanisms taking place. The high-frequency oscillations take place at the low level pressure plateau, just after (re)ignition of the propellant. It could be argued, that the propellant is not yet fully ignited at this point and that flame spreading has something to do with it, but without more detailed information, it is not possible to draw any firm conclusion. The behavior of the low frequency oscillations at the higher pressure levels seems to confirm that indead oscillatory heat transfer into the propellant is one of the major factors in oscillatory combustion of double base propellants.

It has been tried to estimate the propellant growth constants by comparing the results of different experiments. Owing to the use of two L^* burners of different size, it has been possible to repeat experiments at about the same L^* and combustion pressure with different chamber volumes. In all cases, after

an initial growth, the amplitude of the oscillations decays rapidly. This decay may be attributed to various losses in the combustion chamber. If the losses depend on geometrical quantities a damping constant may be estimated.

It is assumed that the effective growth constant, α_{eff}, is the difference between the propellant growth constant and a damping constant:

$$\alpha_{eff} = \alpha - \alpha_d \tag{6}$$

If the damping is proportional to the chamber volume or the exposed wall surface area, then

$$\alpha_d = C.T \tag{7}$$

C is a proportionality constant, and T stands for the chamber volume or the exposed wall surface area. The propellant growth constant may be estimated from two, more or less similar tests 1 and 2:

$$\alpha = (\alpha_{eff_1} \cdot T_2 - \alpha_{eff_2} \cdot T_1)/(T_2 - T_1) \tag{8}$$

The best correlation is obtained if the damping is assumed proportional to the gas volume. The results are shown in Table 3. The values of the growth constants are of same order of magnitude as the growth constant, $\alpha = 5.7\ s^{-1}$, which has been observed during a testrun with a prolongued growth of the oscillations.

Table 3: Estimated ARP propellant growth constants

Frequency, $F(s^{-1})$	Growth constant $\alpha(s^{-1})$
~21	-2,84
~25	0,52
~30	1,38

The growth constant, α, versus the frequency, F, is shown in fig. 11.

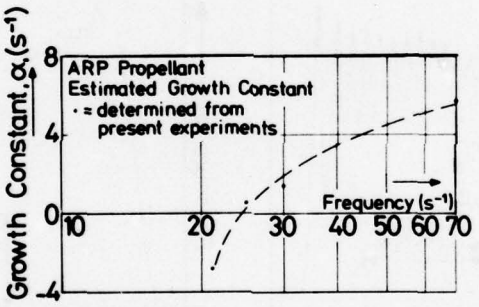

Fig. 11. Estimated Growth Constant for ARP propellant

Below ~25 Hz, $\alpha < 0$ which implies that any oscillation below this frequency is damped, even if there were no other damping mechanisms. According to fig. 11, above ~25 Hz the propellant will drive oscillations.

It has been observed - see figs.4 and 5 - that the oscillations decay with increasing time or increasing L^*. It seems logical to assume that past the point where the oscillations seem to disappear or merge with the noise, no (appreciable) oscillations will take place anymore. Therefore, Kumar[11] defines "the point where the pressure amplitude merges with the noise level in the time-inpendent combustion" as a locus of the stability boundary in the L^* - p plane. Such a stability boundary for ARP propellant is shown in fig. 12.

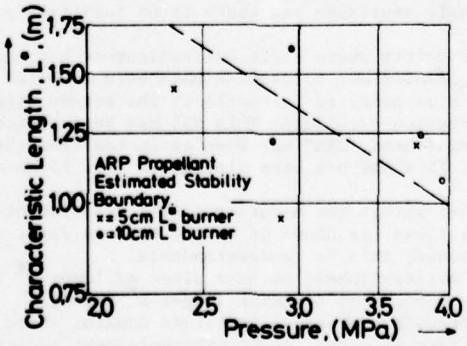

Fig. 12. Stability boundary of ARP propellant

Though the scatter is large, the scatter between the data of the 5 cm burner and the 10 cm burner is not larger than the scatter in the data of one type of burner. Moreover, it does not seem to be worse than observed in similar stability plots[11].

Chuffing has been observed in many cases, sometimes preceding oscillatory combustion, but many times only chuffing took place. Often more than 100 chuffs in succession have been counted. In those cases that oscillatory combustion was preceded by chuffing, it has been noted that this may be either by a few chuffs (4 to 6) or by a great many ones, 81.

Experiments with composite propellants

Experiments with composite propellants concentrated on a polyurethane propellant ANP-2608. The composition of the propellant is listed in Table 4.

Table 4: Composition of ANP-2608 propellant

AP	81,9 %	Wetting agents	0,21%
Polyurethane	12,44%	Catalyst	0,05%
Additives	2,10%	Antioxidant	0,20%
Plasticizer	3,10%	(percentages by weight)	

More than 60 testruns have been made; more than 30 of these showed oscillatory combustion. Frequently dp/dt extinguishment has been observed followed by reignition, so that more than 80 different pressure histories have been obtained. Chuffing was not very prominent. Experiments were carried out both in the 5 cm and 10 cm L^*-burner; the results agree very well. In the following, results of these experiments are presented. There are many similarities between the L^* oscillations of ANP-2608 composite propellant and ARP double base propellant but there are also noticeable differencies.

In the majority of cases the pressure histories which showed L^* oscillations displayed a (more or less regular) rise in pressure; shortly after which oscillations with a growing amplitude appeared, followed by dp/dt extinguishment. Often reignition took place and the sequence repeated itself. In some cases four successive repetitions have been observed. In 16 cases, after initially growing amplitudes, the amplitude levelled off and then decayed. In the figs. 13 and 14 typical pressure histories, as observed in the 5 cm and 10 cm burners are depicted.

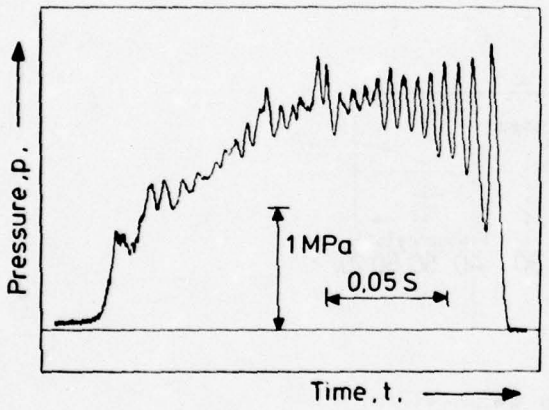

Fig. 13. L^* oscillations of ANP-2608 propellant (5 cm L^*-burner)

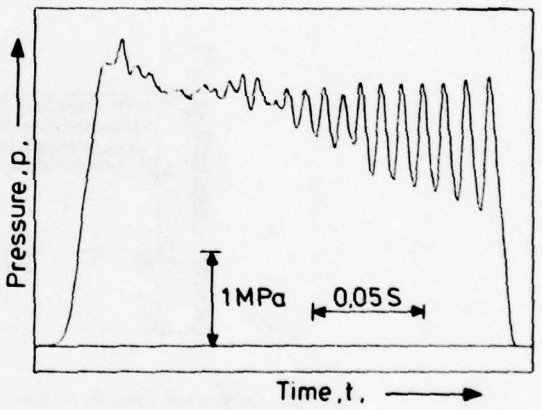

Fig. 14. L^* oscillations of ANP-2608 propellant (10 cm L^*-burner)

Fig. 13 shows a pressure history which has been obtained in the 5 cm L^*-burner. The mean pressure during oscillations ranges between 2 MPa and 1,8 MPa, while the L^* ranges between 0,22 m and 0,32 m. A pressure history as obtained with the 10 cm L^*-burner has been depicted in fig. 14. The mean pressure during the oscillations ranges between 1,2 MPa and 1,1 MPa while the L^* varies from 0,58 m to 0,64 m. The similarity is evident; the difference with the pressure histories for ARP propellant also is obvious. Oscillations here start with a small amplitude and there is no low-level pressure plateau with higher frequency oscillations.

From the experiments, the loci of points where dp/dt extinguishment has been observed, and the loci of points where the oscillation disappeared due to damping have been compiled. From the loci of points where the amplitude of the oscillation disappears in the noise of the steady signal a "mean boundary, MSB" has been estimated with a linear regression technique. This MSB has been plotted in fig. 15. In the same way a "mean boundary, for dp/dt extinguisment, MBE" has been estimated from the loci of points where dp/dt extinguishment has been observed. This MBE has been plotted in fig. 15 as a dashed line. It should be noted that:

1. the MSB and the MBE are parallel within the accuracy of the measurements
2. all loci for damping of oscillations lie above or on the MBE. As dp/dt extinguishment occurs in the case of rapidly growing amplitudes, this is understandable.
3. there is a tendency for dp/dt extinguishment to take place at lower L^* values, while damping of oscillations has the tendency to occur at somewhat larger L^* values.

Fig. 16 shows the region in the frequency-pressure amplitude domain, where L^* oscillations have been observed. Recall that in the majority of cases, dp/dt extinguishment occurred. So the dashed line in fig. 16 may be interpreted more or less as a dp/dt extinguishment boundary.

Of one assumes that dp/dt extinguishment takes place if the actual rate of change of the pressure becomes smaller than a certain critical value, i.e. dp/dt extinguishment occurs if $dp/dt < (dp/dt)_{cr}$ then, one may

easily show that there is a relation between the frequency, the pressure amplitude, and the critical rate of change of the pressure:

$$(dp/dt)_{cr} \approx -2\pi Fp' \tag{9}$$

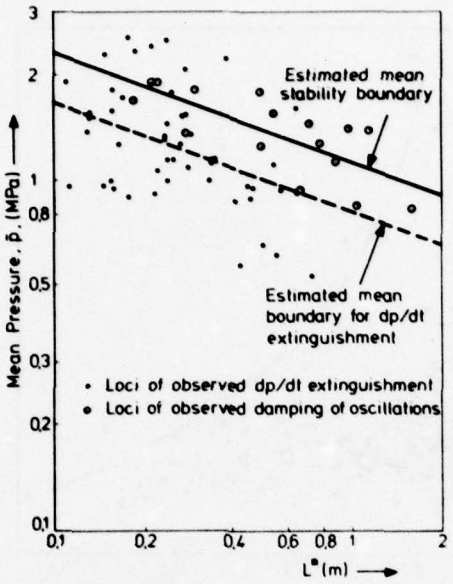

Fig. 15. Stability boundary for ANP-2608 propellant

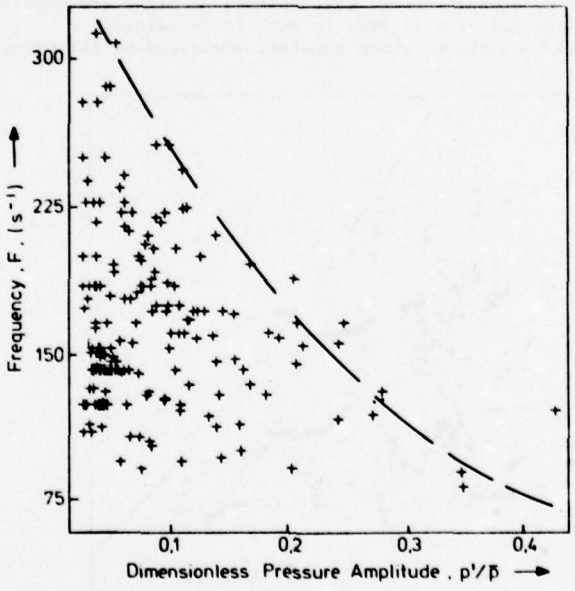

Fig. 16. Region where L^* oscillations have been observed in the $p'/\bar{p}$-F plane (ANP-2608)

The pressure fluctuation may be expressed as

$$p'(t) = p'_o e^{\alpha t} \cos(2\pi Ft) \tag{10}$$

and $p'_o e^{\alpha t} = p'$, the instantaneous pressure amplitude; this is the pressure amplitude that has been plotted in the figures.
The minimum value of dp/dt then equals

$$(dp/dt)_{min} = -2\pi Fp' \tag{11}$$

and as extinguishment is supposed to occur if $(dp/dt)_{min} \leq (dp/dt)_{cr}$, we find for the dp/dt extinguishment boundary,

$$F \approx -(dp/dt)_{cr}/(2\pi p') \qquad (12)$$

which is an hyperbola in the F-p' plane. This seems to be confirmed more or less by fig. 16, though in this figure the dimensionless amplitude $p'/\bar{p}$, instead of p' has been plotted. Fig. 17 shows the same data, but now in terms of the observed dimensionless frequency, Ω, versus the dimensionless pressure amplitude $p'/\bar{p}$.

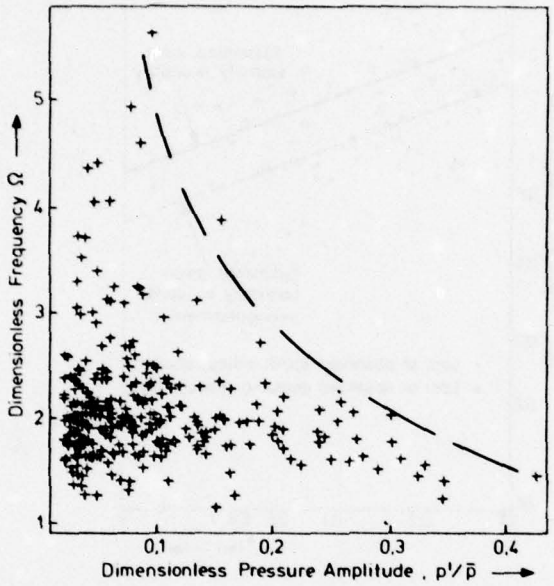

Fig. 17. Region where L^* oscillations have been observed in the $p'/\bar{p}$ - Ω plane (ANP-2608)

These figures also show, that at lower (dimensionless) frequencies, pressure fluctuations up to ~35% of the mean pressure may occur before extinguishment takes place. At higer frequencies, extinguishment has taken place, before the amplitudes had time to grow to such large values.
Fig. 18 shows the region in the L^* - $\bar{p}$ plane, where regular, sustained oscillations have been observed.

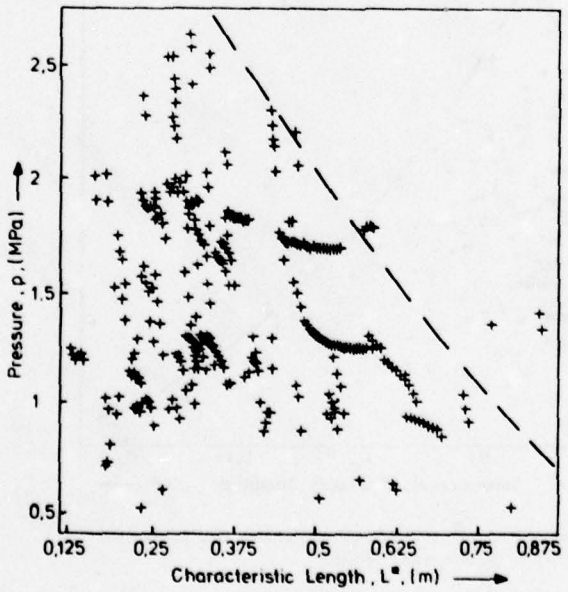

Fig. 18. Region in the L^* - $\bar{p}$ plane, where L^* oscillations have been observed. Some individual testruns are clearly recognizable (ANP-2608)

Some individual testruns are clearly visible in this figure. The dashed line indicates an estimated stability boundary in the $\bar{p}$ - L^* plane. The mean stability boundary of fig. 15 has been based on all observations, while the estimated stability boundary in fig. 18 is based on regular, sustained oscillations.

In addition it combines dp/dt extinguishment and decay of oscillations.
Fig. 19 shows the observed relation between the frequency and the characteristic length during oscillatory combustion.

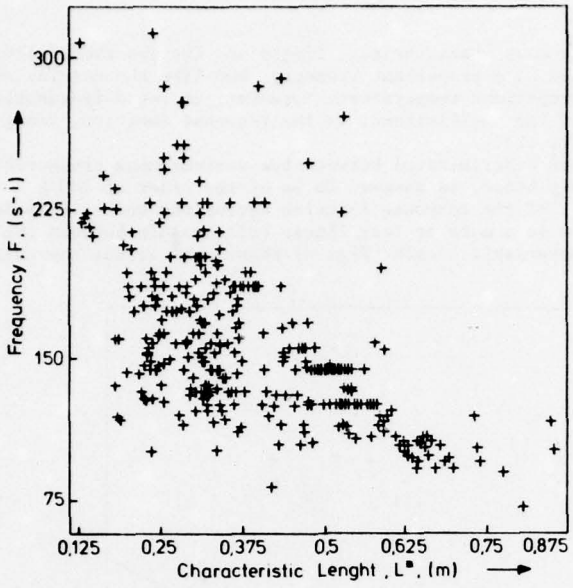

Fig. 19. Region in the L^*-F plane, where L^* oscillations have been observed (ANP-2608)

It is seen that the higher frequencies occur at lower L^* values. At high L^* values only low frequency oscillations have been observed.

It has been tried, to estimate from the available data, the imaginary part of the response function, R_b^i. This is possible, because in the L^*-burner, the response function determines the frequency of the oscillations. According to a linear acoustic analysis of oscillations in the solid rocket motor[6] the pressure fluctuation may be expressed as

$$p'(t) = p'_o \, e^{\frac{\gamma\Gamma}{L^*}\sqrt{RT_c}\left(R_b^r - \frac{\gamma+1}{2\gamma}\right)t} \cos\left(\frac{\gamma\Gamma}{L^*}\sqrt{RT_c}\, R_b^i t\right) \tag{13}$$

and also as

$$p'(t) = p'_o \, e^{\alpha t} \cos(2\pi F t) \tag{14}$$

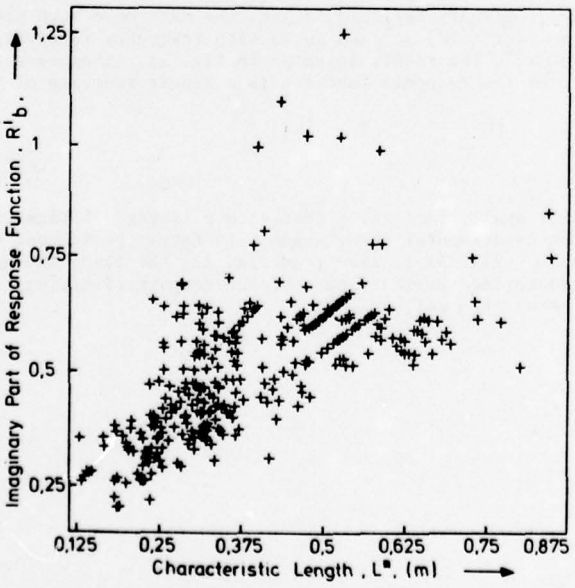

Fig. 20. The imaginary part of the response function, R_b^i, for ANP-2608, during L^*-burner tests, versus the instantaneous L^*

Hence, the imaginary part of the response function,

$$R_b^i = \frac{2\pi}{\gamma\Gamma\sqrt{RT_c}} F.L^* \quad , \tag{15}$$

may be deduced from the instantaneous characteristic length and the observed frequency of the oscillations. The response function is regarded as a propellant property, and like the burning rate it should depend on the mean pressure, and the propellant temperature. Moreover, it seems reasonable to assume that it also depends on the frequency of the oscillations, as the response function, among others, accounts for the phase-lag. So, $R_b = R_b\ (\bar{p}, T_i, F)$.
In reducing the data, we have not discriminated between the various mean pressures. The propellant temperature, though not precisely known, is assumed to be of the order of 300 K.
Fig. 20 shows the imaginary part of the response function versus the characteristic length, L^*. This figure seems to imply that there is a more or less linear relationship between the imaginary part of the response function and the characteristic length. Fig. 21 shows $\Omega.L^*$ versus the characteristic length.

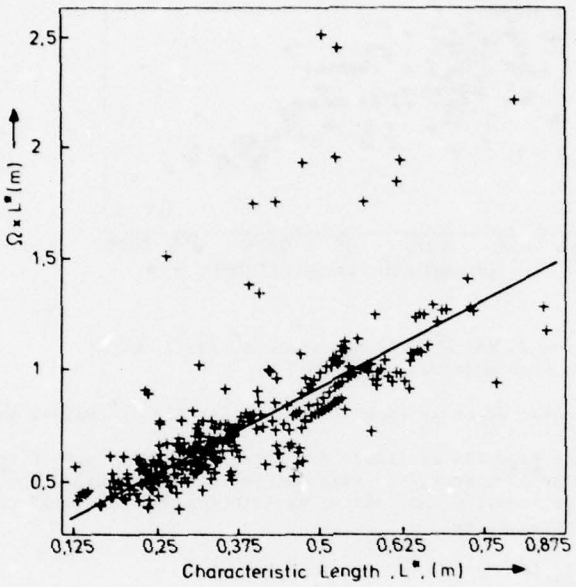

Fig. 21. The product of the dimensionless frequency and characteristic length, versus the characteristic length for ANP-2608

This figure is more or less equivalent with fig. 20, though now the dimensionless frequency, Ω, instead of the actual frequency, F, has been used. The scatter in the data, clearly is less, again underlining the importance of the heat transfer mechanism. The scatter may partly be explained perhaps by the fact that we have not discriminated for the mean pressure. To find out whether there is indeed relationship between the response function and the characteristic length, the data have been plotted in frequency bands: $\pm 50\ s^{-1} < F \leq 100\ s^{-1}$, $100\ s^{-1} \leq F < 125\ s^{-1}$ and so on with frequency intervals of $25\ s^{-1}$ up to $225\ s^{-1} \leq F < 250\ s^{-1}$ and $F \geq 250\ s^{-1}$. The result is shown in fig. 22. It appears that within these frequency bands, the imaginary part of the response function is a linear function of the characteristic length:

$$R_b^i = A + B.L^* \tag{16}$$

The variance in general was rather small, indicating that such a linear relation indeed is a reasonable mathematical approximation of the experimental observations. In fact, the largest variance $\sigma^2 = 0{,}0024$ while R_b^i ranges from 0 - 2,4. As is seen from fig. 22, the slope increases, with increasing frequency. We have tried to estimate the imaginary part of the response function from this figure. For this purpose, Eq. (16) may be written as:

$$R_b^i = A + B \cdot \frac{\gamma\Gamma\sqrt{RT_c}}{2\pi F} \cdot R_b^i$$

or

$$R_b^i = \frac{2\pi AF}{2\pi F - \gamma\Gamma\sqrt{RT_c}\,B} \tag{17}$$

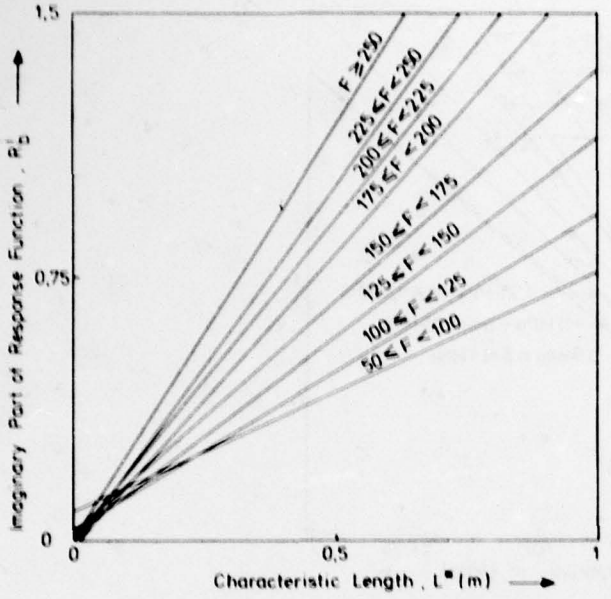

Fig. 22. The imaginary part of the response function as a function of characteristic length for various frequency-bands (ANP-2608)

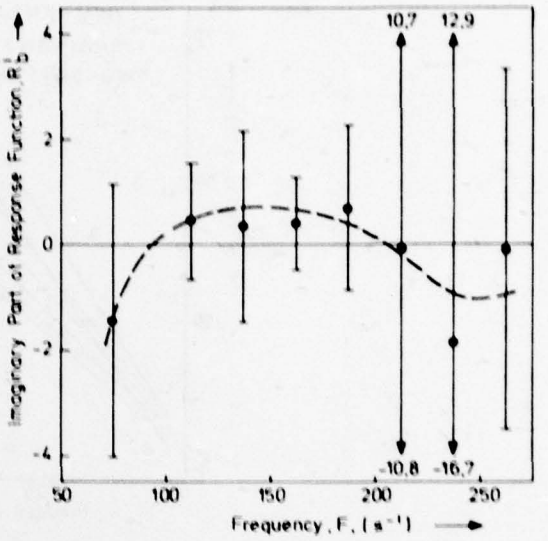

Fig. 23. Estimated imaginary part of the response function as a function of frequency. The vertical lines indicate the ± 3σ reliability interval (ANP-2608)

By substituting the mean value of the frequency, and taking the appropriate values for A and B, for the various bands, R_b' is estimated as a function of the frequency. The result is shown in fig. 23. Also shown is the ± 3σ reliability interval. Of course, $R_b' > 0$ is necessary, but this possibility lies within the ± 3σ interval. Especially for frequencies between 200 s^{-1} and 250 s^{-1}, the uncertainty is extremely large. This is mainly due to the very small values of the denominator in Eq. (17) for these cases. In the same way, the negative values of R_b' are caused by negative values of the denominator. The effect of the mean pressure has not been accounted for, while an average frequency has been used; better correlations may perhaps be obtained by using more refined, multidimensional regression techniques, which account for the pressure and frequency. Fig. 24 shows the imaginary part of the response function versus frequency but plotted in L^* bands of 10 cm. In general the slope of the lines increases with increasing values of L^*.

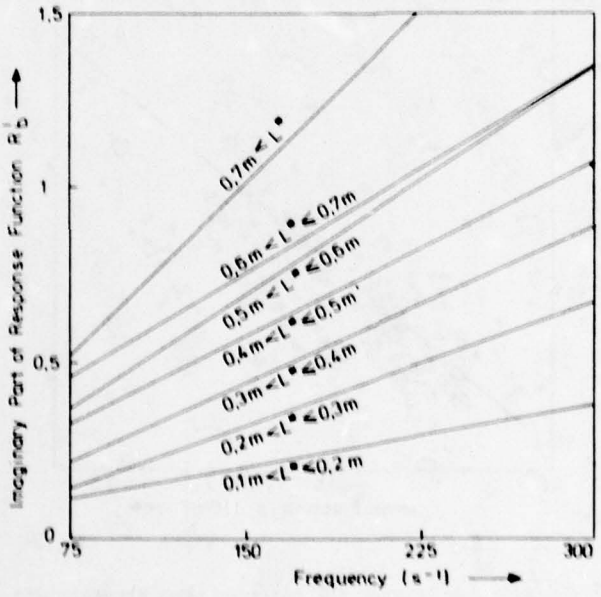

Fig. 24. The imaginary part of the response function versus frequency for various L^*-bands (ANP-2608)

Another interesting feature of these L^* oscillations is depicted in fig. 25.

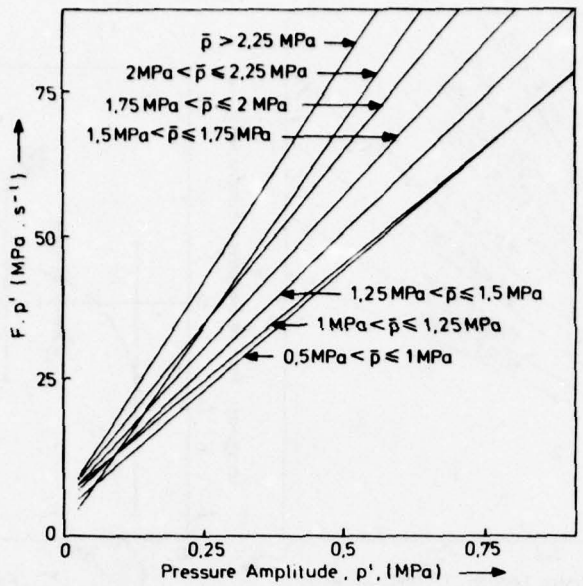

Fig. 25. The product of frequency and pressure amplitude versus pressure amplitude. The slope increases with mean pressure (ANP-2608)

This figure shows the product of frequency and pressure amplitude, versus pressure amplitude. One may not be surprised to see straight lines. The remarkable fact, however, is that the slope of these lines increases with increasing mean pressure. This again means a relationship between frequency and mean pressure.

$$F = A/p' + B(\bar{p}) \tag{18}$$

For ARP double base propellant, a relation between frequency and pressure had been observed (see fig. 9). A similar plot for ANP-2608, composite propellants indicates that here too, a relation must hold between the mean pressure and the frequency. However, the scatter is much larger, as is evident from fig. 26.

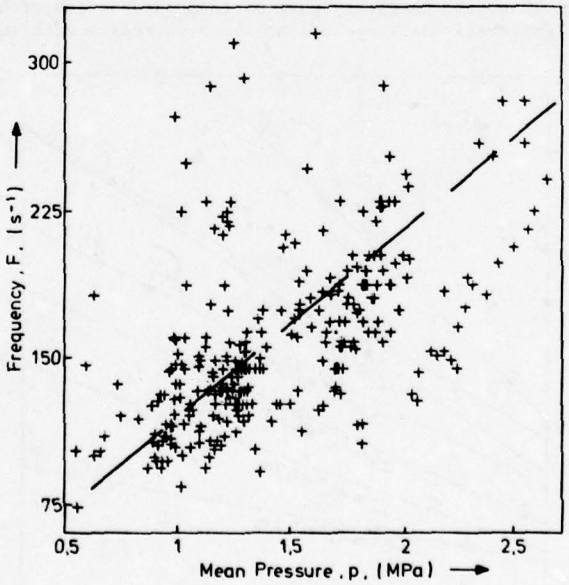

Fig. 26. The relation between the observed mean pressure and frequency during L-oscillations of ANP-2608 propellant*

It may well be, that if Eq. (18) is a valid description of a relation between the pressure and the frequency, the pressure amplitude has to be accounted for. This has not been done in fig. 26, which may account for the larger scatter.

Finally fig. 27 shows a relation between the product of the frequency and pressure amplitude versus the characteristic length for various intervals of the pressure ampltiude.

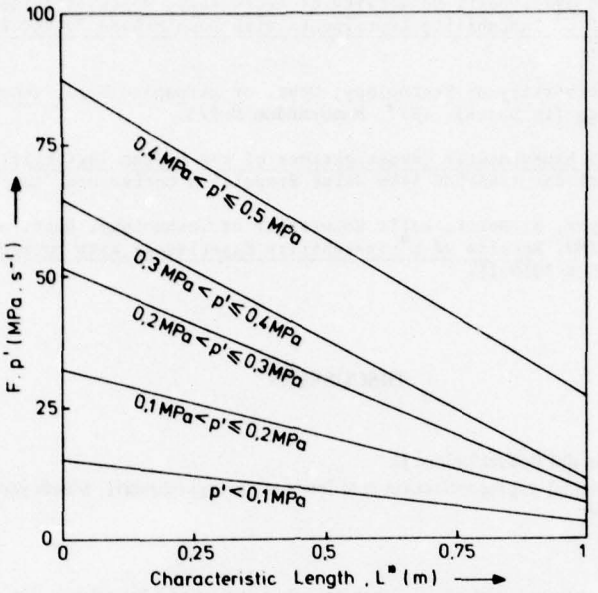

Fig. 27. The product of frequency and pressure amplitude versus L^* during L^* oscillations of ANP-2608 propellant, for various pressure amplitude bands

Except for pressure amplitudes between 0,4 and 0,5 MPa, all lines intercept the L^* axis somewhere between L^* = 1,17 m and L^* = 1,25 m, which seems to imply that above these values no L^* oscillations should be expected for ANP-2608.

CONCLUSIONS

- The L^*-burner is a suitable instrument for the investigation of low-frequency instability of solid rocket propellants.
- The size of the L^*-burners has no noticeable influence on the occurrence and type of L^* instability. Testruns in the 5 cm L^*-burner are reproducible in the 10 cm L^*-burner and vice versa. This gives confidence to apply information, obtained from the L^*-burner experiments to actual rocket motors.
- The imaginary part of the propellant response function may be estimated from experimental data, obtained with the L^*-burner.
- Both, ARP double base propellant and ANP-2608 composite propellant display a correlation between the mean pressure and the frequency during oscillations.
- The assumption that dp/dt extinguishment takes place if the rate of change of the pressure is smaller than a critical value, seems to be supported by experimental evidence.
- There is a pronounced difference in the observed amplitude histories during L^* instability of ARP-double base propellant and ANP-2608 composite propellant. For ARP double base propellant the amplitude decays continuously from an initially large value, while for ANP-2608 propellant the amplitude increases continuously in most cases, until dp/dt extinguishment takes place.
- L^* instability may be triggered by ignition peaks. The size of this peak may determine, among others, the type of the resulting L^* instability.
- It seems that below a mean pressure of 2,5 MPa no L^* instability will occur for ANP-2608 composite propellant if $L^* \gtrsim 1{,}25$ m.
- There is experimental evidence that the propellant response function depends on the frequency of the oscillations.
- Reliable and reproducible propellant ignition may be obtained by the combination of a pyrotechnic lacquer and an electric ignition wire. Ignition peaks are virtually eliminated by this technique.

REFERENCES

1. J.W. Cornelisse, H.F.R. Schöyer, K.F. Wakker, Rocket Propulsion and Spaceflight Dynamics, London/San Francisco, Pitman, 1979, Chapter 9.

2. E.W. Price and F.E.C. Culick, Combustion of Solid Rocket Propellants, AIAA Professional Study Series, New York, AIAA, 1968, Chapter 10.

3. An., Chemical Propulsion Information Agency, T-Burner Manuel, 1969, CPIA publication no. 191.

4. M. Barrère, L. Nadaud, and J.N. l'Huillier, ONERA and SNPE Recent Work on Solid Propellant Combustion Instability, J. Spacecraft and Rockets, vol. 11, no. 1, January 1974, pp 33-40.

5. R.S. Brown, United Technologies Corporation, Development and Evaluation of Rotating Valve Combustion Response Test Technique, 1976, AFRPL-TR-76-72.

6. H.F.R. Schöyer, Delft University of Technology, Dept. of Aerospace Eng., A One-Dimensional Analysis of Acoustic Pressure Fluctuations in a Simple Rocket Motor, 1978 Memorandum M-317.

7. R.S. de Boer and H.F.R. Schöyer, Delft University of Technology, Dept. of Aerospace Eng.,/Technological Laboratory TNO, Results of L* Instability Experiments with Double Base Rocket Propellants, 1976, Report LR-224/TL R 3050-I.

8. B.A.C. Ambrosius, Delft University of Technology, Dept. of Aerospace Eng., Computer Program for Data Reduction of L* Experiments (in Dutch), 1977, Memorandum M-275.

9. H.F.R. Schöyer, Results of Experimental Investigations of the L-Star Instability Phenomenon, AIAA-paper 78-1075, paper presented at the AIAA/SAE 14th Joint Propulsion Conference, Las Vegas, Nev., July, 1978.

10. R.S. de Boer, H.F.R. Schöyer, H. Wolff, Delft University of Technology, Dept. of Aerospace Eng./ Technological Laboratory TNO, Results of L*-Instability Experiments with Double Base Rocket Propellants II, 1977, Report LR-252/TL R 3050-II.

DISCUSSION

L. De Luca, Instituto di Macchine del Politechnico, It

Is it not the case that the critical depressurisation rate law for extinguishment, which you suggest, is dependent on the experimental conditions?

Author's Reply

The relationship, for dp/dt extinguishment, is an hypothesis put forward by others; for application to rocket motors in general. The experimental results are in agreement with the hypothesis. We have not observed differences in the results between L* burners of 5 cm and 10 cm internal diameter.

P.Kuentzmann, ONERA, Fr

You have assembled a large body of experimental data. I am curious to know why you chose to obtain this data from the imaginary part of the response function rather than the real part?

Author's Reply

The value of the imaginary part of the response function will determine whether L* oscillations will occur or not. This is the case even if the propellant growth constant is large. A good knowledge of R_b^r is mandatory in order to predict if oscillatory combustion will occur in a rocket motor or not.

It is my intention to determine the real part of the response function from this test data, in due course. However from the L* burner data one can obtain a gross growth constant, which is the difference between the propellant growth constant and losses, such as heat transfer and viscosity. These have not yet been calculated and hence no information on the real part of the response function is presently available.

NON LINEAR COMBUSTION INSTABILITY IN SOLID PROPELLANT ROCKET MOTORS - INFLUENCE OF GEOMETRY AND PROPELLANT FORMULATION

by
P.M. Hughes Defence Scientist
and
D.L. Smith Group Leader
Centre de Recherches pour la Défense
Defence Research Establishment
Valcartier
P.O. Box 880, Courcelette
Québec, Canada
G0A 1R0

SUMMARY

The characteristics of the longitudinal non linear (or steep-fronted shock) mode of instability are compared in a single size of motor for three different grain cross- sections (cylindrical, star and slotted tubular) and three propellant formulations. The formulations are all based on a hydroxy-terminated polybutadiene binder, contain no aluminum and vary only in the level of burning rate catalyst and oxidizer distribution. The test motors were 7 cm in diameter and 68.5 cm long, and were pulsed at various times during the firing with gunpowder charges to initiate instability.

The degree of instability is defined as the percentage increase in the time-average pressure during transition to unstable operation at a given stable operating pressure. It was found that the degree of instability decreased with increasing burning rate and was affected by the number of waves propagating. No correlation could be established between the strength of the unstable wave and either the formulation or grain cross-section. In the case of the slotted tubular motors a double wave form was always present. For the first time at D.R.E.V., a low level acoustic wave form was observed to transition naturally into a steep-fronted, shock-type wave-form.

The growth of the shock wave-form was studied from initiation to steady state and it was found that the growth rate generally increased with decreasing propellant burning rate. The growth mechanism tended to be a complicated one in the earlier stages of a particular firing (before expending 50% of its propellant mass); however, it can generally be stated that a pulse will grow at a faster rate in the later stages of a firing.

NOMENCLATURE

A_t - Nozzle throat area (cm^2)

c - Burning rate pressure coefficient ($cm\ s^{-1}\ kPa^{-n}$)

K_n - Restriction ratio, ratio of burning surface area to nozzle throat area

n - Burning rate pressure exponent

P_{ac} - Amplitude of the steep fronted wave (kPa)

P_{cs} - Average stable chamber pressure (kPa)

$\overline{P}_{cus}$ - Average unstable chamber pressure (kPa)

$\Delta\bar{p}$ - Amplitude of disturbance normalized to its final value

r^2 - Correlation coefficient for regression analysis

$\overline{r}_{6890}$ - Propellant burning rate at 6890 kPa ($cm.s^{-1}$)

$t_{a.3p}$ - 206.7 kPa (30 psi) action time (s)

t - Time (s)

$\bar{t}$ - Time relative to the initiation of the disturbance normalized to the time to fully grown

ϕ - Mass fraction of propellant expended

1.0 INTRODUCTION

There has always been a demand for the reduction or elimination of primary or particulate exhaust smoke in small tactical rocket motors. The response to this demand in recent years has been to remove the aluminum from the propellant formulation. However, it is known that removing the aluminum from the formulation reduces the particulate damping of both the longitudinal and transverse modes of combustion instability; "this increases both the probability of occurrence of instability and the severity, should

it occur" (1).

Extensive investigations of the occurrence of longitudinal mode instability with aluminized propellants were conducted at the Defence Research Establishment Valcartier during the 1960's (2, 3, 4, 5, 6, 7) with some preliminary work on nonaluminized formulations in the mid 1970's (1). These previous studies used the pulse technique (8) to initiate instability in full scale motors with the purpose of determining the influence of propellant composition, grain configuration, motor size and the initial grain temperature on such parameters as the transition pressure and the degree of instability. The degree of instability is defined as the percentage increase in pressure due to transition from stable to unstable operation. It was found that for a particular propellant system well defined behavioral trends could be established as the formulation and motor geometry were varied.

The work described herein covers a similar investigation into the characteristics of longitudinal instability in a series of solid propellant rocket motors. The test motors under investigation contained three nonaluminized hydroxy-terminated polybutadiene formulations having stable nonerosive burning rates of 1.064, 1.240 and 1.445 cm/s at 6.89 x 10^3 kPa and in three grain cross sections, i.e. cylindrical, star and slotted tubular.

2 0 EXPERIMENTAL TECHNIQUE

Nonlinear longitudinal combustion instability is characterized by the cyclical propagation of a strong gaseous compression wave along the internal cavity of the motor. The average levels of pressure and thrust rise above their normal values and, at the same time, high-intensity fluctuations in the pressure and thrust levels occur at the frequency of the oscillation.

An important aspect of this mode of instability is that the onset is governed by a highly nonlinear mechanism. Transition from stable to unstable operation occurs only if the motor is intrinsically capable of instability and if the flow is disturbed by a wave of appropriate magnitude. In the absence of an initiating disturbance, a motor capable of instability will operate stably; consequently, normal proof firings offer no guarantee that a motor design is inherently stable. Disturbances to the internal flow field can occur naturally, albeit in a random fashion, caused by ejection of small pieces of material through the nozzle. However, to overcome the experimental difficulties associated with random initiation, a pulse technique was developed which injects flow disturbances at preselected times during burning (8); it was established that naturally and artificially triggered motors behaved identically shortly after the initiation transient. In the present investigation, the triggering distrubances are generated by 0.5g black powder charges in pulse tubes located in the head end of the motor.

2.1 Motors Under Investigation

The test motors use a standard MK4 7 cm FFAR chamber with a 1.905 cm diameter hole drilled through the forward bulkhead for the pressure transducer and pulse tubes. The nozzle is a simple graphite cylinder with conical inlet and expansion sections. The throat size of each motor configuration was selected to produce a maximum stable operating pressure of approximately 1.24 x 10^4 kPa. The three grain cross-sections used in the tests were cylindrical, star and slotted tubular. The motor with the slotted tubular grain cross-section is shown in Figure 1 while the cylindrical and star cross-sections are shown in Figures 2 and 3 respectively. The case bonded grains are 6.35 cm in diameter and 71.196 cm long.

Ignition of the motor was achieved by means of a polyethelene bag containing 15 g of 2A BPN pellets placed near the head end and ignited with an S140 squib. This ignition system was used to deliver a smooth ignition curve.

The head end of the motor is shown in Figure 4. A piezoelectric pressure transducer (Kistler Model 701A) is positioned along the center line of the internal cavity; the pulse tubes are located on either side of the transducer.

2.2 Data Acquisition

The output of the pressure transducer is amplified and split to provide both a filtered (< 100 Hz) D.C. (or average) pressure signal and a high frequency A.C. coupled signal. The circuit is shown in Figure 5. The high frequency pressure signal is recorded on 35 mm ciné film and magnetic tape for subsequent analysis. The D.C. signal is digitized, recorded and analyzed to provide pressure-time and pressure integral-time information.

2.3 Pulse Sequencing

In order to characterize the unstable behavior of a particular combination of formulation and grain cross-section, four motors were fired. One motor was not pulsed in order to provide a stable baseline and to detect any naturally occurring transverse modes. The remaining three motors in each group were used to determine the earliest point at which a particular grain cross-section, propellant formulation could be driven unstable (i.e. the transition point). A pulsing scheme was set up for these motors in which the pairs of pulses were fired so as to bracket the transition point, the interval between the pulses being reduced on each successive motor (see Figure 6b). When a motor became unstable on the first pulse, the pulse size in the subsequent motor was reduced to 0.25 g and the motor was pulsed at the same time as its predecessor; thus an elementary appreciation of the effect of pulse size on transition was gained.

2.4 Propellant Formulations

The three propellant formulations tested were selected from reference 1 to span the range of mildly to violently unstable when used with the cylindrical grain cross-section. The formulations all use the

same hydroxy-terminated polybutadiene binder based on the R45HT prepolymer, a trimodal blend of ammonium perchlorate oxidizer and varying amounts of 1 μm spherical red iron oxide. None of the formulations contain aluminum. The compositions of the three formulations are shown in Table I.

TABLE I Formulation Composition

Formulation Code	Binder Level (%)	Catalyst Level (%)	Oxidizer Dist'n 400	200	17 μm
A	13	0.5	2	3	4
B	13	1.0	2	3	4
C	13	1.2	2	3	5

Table II lists the detailed breakdown of particle sizes in the oxidizer blends as a percentage by weight less than a specific diameter.

TABLE II Detailed Oxidizer Particle Size Distribution

Specific Diameter (μm)	Finer Than Specific Diameter (%)	
	Code A & B	Code C
589	100	100
417	92	93
297	77	79
210	67	70
149	53	57
105	45	50
74	41	47
53	38	45
32	33	38

The average diameter of the ground (17μm nominal) ammonium perchlorate is 10 to 12 μm.

The stable nonerosive burning rate for each formulation was determined by firing six 5.08 cm by 10.16 cm burning rate motors. The results are shown in Table III.

TABLE III Stable Nonerosive Burning Rate

Formulation C Code	$\bar{r}_{6890}$ (cm/s)	Coefficient (c)	Exponent (n)
A	1.064	0.031	0.401
B	1.240	0.050	0.363
C	1.445	0.054	0.371

The 5.08 cm by 10.16 cm motors and the full scale test motors were cast from the same batches of propellant.

3.0 EXPERIMENTAL RESULTS AND DISCUSSION

3.1 Initiation of Instability

3.1.1 Conditions at Initiation

The manner in which the three motors of each group (propellant grain cross-section) were pulsed was formulated so as to zero-in on the earliest transition point from stable to unstable operation. Tabulated values of time, average pressure (P_{ss}) and mass fraction consumed (ϕ) for the last stable, first unstable pulses are shown in Table IV. The trends indicated in Table IV are illustrated in figures 6 to 8 where the time average chamber pressure is plotted against ϕ. Figure 6 shows the variation of the stable motor chamber pressure with ϕ for the three propellant formulations in the star geometry. The portion of each curve labled $\bar{P}_{cus}$ is the unstable chamber pressure variation with ϕ, averaged over the three unstable firings. The small spikes on the stable curve show the occurrance of the pulsers which were damped. Figure 6a includes the variation of the chamber pressure when 2 unstable waves were generated in the motor. Figure 6b shows the pulse bracketting technique. Figures 7 and 8 shows the same information for the cylindrical and the slotted tubular cross-sections respectively. Figures 8b and c demonstrate the initial oscillation of these motors from stable to unstable operation.

It is thus shown that for a given geometry of motor can be driven unstable earlier in the firing (lower value of ϕ) if the burning rate of the propellant is reduced. It also appears that, for a given propellant formulation, the cylindrical configuration can be driven unstable earlier and at a lower chamber pressure than can the star.

TABLE IV

Internal Ballistics at Initiation

Grain Cross Section	Formulation	Last Stable Pulse			First Unstable Pulse		
		time (s)	ϕ	P_{cs} (kPa)	time (s)	ϕ	P_{cs} (kPa)
Cylindrical	A	0.252	0.131	7483	0.416	0.236	8461
	B	0.376	0.245	9074	0.553	0.404	10618
	C	0.328	0.260	9674	0.460	0.396	10907
Star	A	0.335	0.257	9901	0.463	0.357	10349
	B	0.506	0.450	10797	0.579	0.522	10914
	C	0.596	0.639	11403	0.596	0.643	11279
Slotted Tubular	A	0.253	0.131	10542	0.386	0.214	11534
	B	0.219	0.130	10700	0.319	0.191	11617
	C	0.391	0.292	12457	0.476	0.366	11830

3.1.2 Pulse Size

As was described earlier, the possibility of varying the size of the initiating disturbance was included in the pulsing scheme. After firing the second of the three pulsed motors of the slotted tubular-A, slotted tubular-B, and cylindrical-A configurations, the earliest transition point as discussed in the previous section, was determined. The remaining motor of each configuration was then pulsed at the same time but with only 0.25 g of charge in the pulse tubes. In the remaining series (slotted tubular-C etc.) all the motors were required to establish the transition point.

Both of the A propellant motors became unstable on the first pulse; whereas, the first pulse of the B propellant motor was damped out. The disturbance initiated by both the 0.5 g and 0.25 g charge in the cylindrical A configuration is shown in Figure 9a to grow at the same rate in roughly the same number of oscillations to approximately the same peak amplitude. The slotted tubular configurations tended to be much more difficult to compare due to the complicated growth mechanism discussed in another section; however, suffice it to say that the slotted tubular-A propellant combination was pulsed unstable at the same time with two different initiating pulse sizes.

That an inherently more unstable propellant formulation (propellant A) requires a smaller triggering pulse is in agreement with a similar observation made for polyurethane propellants in reference 2.

3.2 High Frequency Data Reduction

3.2.1 Instability Wave Traces

Both the wave strength data and the pulse growth information were gathered from the A.C.-coupled signal recorded on the ciné camera equipment. Typical traces used in the data reduction are shown in Figures 9a to 9d. These figures show the pressure measured at the head-end of the rocket motor, in the upper trace, as the steep fronted wave is reflected off the head end plate. The bottom trace is the same signal but amplified to a lesser degree. The middle trace is a time mark at 0.001 s intervals commencing at ignition.

From these traces the history of the peak to peak value of the wave in the chamber can be followed.

3.2.2 Wave Strength

The standard Rankine-Hugoniot relationship for the strength of the oscillating wave is approximated by the following relationship

$$\frac{P_{ac} + P_{cus}}{P_{cus}} \qquad (1)$$

as the pressure after the arrival of the shock at the head end tended to drift.

Throughout the unstable portion of the firings of the twenty-five rocket motors, no consistent relationship could be found between the strength of the wave as defined above and the burning rate or grain cross-section. However, the wave strength and average unstable pressure measured for this series of tests are shown in Table V. At the time of writing of this report, studies were under way to gain a further insight into the variation of wave strength and amplitude with ϕ or restriction ratio K_n.

TABLE V

Grain Cross-Section	Formulation					
	A		B		C	
	Wave Strength Range	$\bar{P}_{cus}$ Range (kPa)	Wave Strength Range	$\bar{P}_{cus}$ Range (kPa)	Wave Strength Range	$\bar{P}_{cus}$ Range (kPa)
Cylinder	1.65-1.51	9563-13835	1.62-1.49	11444-12939	1.60-1.42	11940-13560
Star	1.61-1.52	11637-13801	1.76-1.68	11858-12306	1.57-1.53	11837-11651
Slotted Tubular	1.53-1.45	10252-14827	1.35-1.31	10976-13704	1.15-1.41	11830-9660

3.2.3 Wave Phenomena

In all of the firings of the slotted tubular grain configuration a small amplitude (160 to 200 kPa) pressure perturbation developed at a frequency significantly lower than that of the oscillating shock wave (Fig. 9b, 9c). This small amplitude disturbance occurred much before the instability-initiating pulse and on two occasions transitioned naturally into the non-linear type of instability. This transition can be seen in Figures 9b and 9c where the small amplitude distrubance in the A propellant formulation appears to change form and grow into a fully-developed, steep-fronted wave in 17 and 18 head-end reflections respectively. The acoustic wave in Figure 9b has a frequency of about 716 Hz and an amplitude of 165 kPa before transition and becomes a steep fronted wave of 6563 kPa amplitude and 778 Hz frequency. In Figure 9c, a 177 kPa, 700 Hz acoustic wave becomes a 7097 kPa, 757 Hz steep-fronted shock wave. Conditions at transition are shown in Table VI. This phenomenon is reported for the first time as reference 2 states that "no instances of amplification from the noise level have been encountered" and reference (3) repeats this claim.

TABLE VI

Transition from Acoustic to Steep-Fronted Wave Forms

Motor No.	Figure No.	Time (s)	ϕ	P_{cs} (kPa)
5291	9b	0.903	0.548	11100
5292	9c	0.618	0.370	11775

During the unstable portion of the slotted tubular firings a secondary wave of lesser amplitude (1378 kPa as compared to 5512 kPa) coexisted with the primary steep-fronted wave (Figures 9b & 9c). This secondary wave arrived at the head end of the motor after the primary one and maintained somewhat the same frequency as the primary wave. This structure probably results from the interaction of the primary wave with the step change in the axial crossection (see Fig. 1) of this motor geometry. A partial reflection of the primary wave at the step change further reflects from the nozzle end of the motor and follows the primary shock towards the head end. This raises an interesting question - do these waves pass through each other or bounce off each other after reflections at either the nozzle or head ends? Evidence exists for both and the reply tends to depend on the strength of either or both waves. A strong wave will ignore a small one but will be reflected by an equally strong one. This is exemplified in the fact that in some cases the secondary wave remained small and not steep-fronted; whereas, in others the small and large waves tended to oscillate between 1378 kPa and 4134 kPa in amplitude but opposite in phase. In their oscillations the larger of the two waves would take on the steep-fronted role as its amplitude became sufficiently large and the other wave would consequently lose the steep-fronted form as it diminished.

3.2.4 Pulse Amplification

All of the motors which were pulsed into instability and the two motors which became unstable naturally displayed an exponential growth relationship from initiation to fully developed instability. Certain of the motors with the star or cylindrical cross-section and particularly those pulsed to instability early in the firing (before $\phi = 0.5$) tended to grow to the fully developed instability in a two step fashion. This can be seen in Figure 10, where the log of the height of the growing wave, normalized to its final value, is plotted against time, normalized to the total time from initiation to fully-developed instability. This figure is drawn for the cylindrical grain cross-section for the three propellant formulations pulsed at a ϕ value of about 0.3. These growth curves are shown to contrast drammatically with the same type of graph drawn for a cylindrical-B propellant motor pulsed into instability after expending 87% of its propellant ($\phi = 0.87$)(Fig. 11).

In the case of the slotted tubular cross-section the effect of the geometry tended to be much more extensive. During the growth of the pulse from initiation, the damping effect of the step change in axial cross-section resulted in the arrest of the growth of the wave and at times a reversal in the growth (Fig. 12). These growth reversals were much more prominent in the more stable or faster burning propellants to the extent that the time-averaged chamber pressure was shown to oscillate between the stable and unstable operating condition (Figures 8b and 8c). After these growth plateaus or reversals the wave grew at a much faster rate as indicated by the slope of the linear sections of the growth curves.

A regression analysis was applied to the growth information and in both situations, that is the multi-step and the single step growth, the data was found to correlate linearly with a correlation coefficient

(r^2) of 0.98 or better.

3.3 Degree of Instability

3.3.1 Definition of Degree of Instability

The degree of instability is defined as:

$$\frac{(\bar{P}_{cus} - P_{cs})}{P_{cs}} \qquad (2)$$

where $\bar{P}_{cus}$ is the time averaged unstable pressure corresponding to a given stable pressure P_{cs}. The degree of instability can be calculated from the linear regression of log K_n versus log P_{cs} and log K_n versus log $\bar{P}_{cus}$ as outlined in reference 9 and illustrated in Figure 13. However, this method is most easily applied to a much more extensive motor evaluation program where many more than thirty-six motors are fired and at a variety of stable operating pressures. It is in this way that the humping effect (3) can be avoided; however, for motors designed to develop a relatively constant K_n (such as the star), this method may be difficult to apply and implies a very accurate calculation of K_n^n.

The degree of instability can also be determined from the curves of P_{cs} and $\bar{P}_{cus}$ versus ϕ (mass fraction consumed). The mass fraction consumed (ϕ) is defined by the following relationship:

$$\frac{\int_0^t P_c A_t dt}{\int_0^{ta.3p} P_c A_t dt} \qquad (3)$$

The P_{cs} and $\bar{P}_{cus}$ used in equation 2 are the average values determined from the P-ϕ curves resulting from the four motor firings of any particular propellant formulation grain cross-section combination at a specified ϕ. The P-ϕ curves for the nine combinations of grain cross-section and formulation are shown in Figures 6 to 8.

3.3.2 Effect of Formulation

Smith et al (1) showed that for a nonaluminized propellant system in motors of the same size but restricted to the cylindrical grain cross-section the degree of instability is inversely dependent on burning rate. Figure 14 is the variation of degree of instability at 1.034×10^4 kPa with burning rate for a cylindrical grain cross-section, reproduced from reference (1) with the formulations A, B and C from this report included. It is evident that the three current formulations concur with the previously established trend.

The range of pressures at which the motors were to operate was higher for this report than that for the motors of reference (1). Also, the star and slotted tubular cross-section geometries are not as progressive burning as the cylinder and so it was not possible to find a $\bar{P}_{cus}$ at a stable P_{cs} of 1.034×10^4 kPa. Thus comparison of the various cross-sections in this study is much more meaningful if they are compared, with respect to degree of instability, at 1.102×10^4 kPa. The trend previously shown by Smith et al (1) is further born out in Figure 15 where the degree of instability at 1.102×10^4 kPa is shown plotted against burning rate for the nine combinations of grain cross-section and formulation. As can be seen in this figure, regardless of grain configuration, the degree of instability is inversely dependent on burning rate.

3.3.3 Effect of Grain Cross-section and Multiple Wave Systems

No consistent correlation could be found between degree of instability and grain cross-section for the star and cylindrical interior geometries.

In one of the unstable firings of the star-A configurations a dual wave system developed on initiation and supported a steep-fronted type of instability at about twice the frequency normally encountered in unstable operation. This phenomenon is shown in Figure 9d where the lower trace is the single wave fully-developed instability (7641 kPa and 730Hz) and the upper trace is the corresponding double wave system (7262 kPa and 1750 Hz) both at a ϕ of about 0.8.

The degree of instability resulting from this double wave propagating in the chamber is 44% higher than that in an equivalent motor with a single wave. This apparent jump in the degree of instability is shown in Figure 15. It is believed that this increase in degree of instability is due to the additional shock wave propagating in the combustion chamber since the actual amplitudes of the waves in both situations are approximately the same.

The slotted tubular grain cross-section has a substantially higher degree of instability than either the star or cylindrical configurations for the A and B formulations as can be seen in Figure 15. The reason for this observation is suspected as resulting from the above noted phenomenon. As was described in a previous section the interior geometry of the slotted tubular grain cross-section supported a dual wave system as shown in Figures 9b and 9c. It is believed that the inordinate increase in the degree of instability of the slotted tubular configuration over the cylindrical or star geometries is due to this dual wave-form.

Whereas the appearance of dual wave systems have been noted in the literature (ref. 2), they have only resulted in minor increases in the degree of instability and the appearance of the phenomena was the result of a second pulse initiation. The significance of the observation in this report is two-fold. First the multiple wave systems found in this study were all initiated from one disturbance and, in the case of the slotted tubular motors, the interior geometry further supported the multiple wave system. And finally, the multiple wave system can cause a significant increase in the degree of instability and is most pronounced in the slower burning rate propellants.

4.0 CONCLUSIONS

This study is restricted to a particular size of rocket motor and type of non-aluminized propellant system and thus the effects of scaling, binder variation or oxidizer type on the observations cited are unknown. The trends noted, however, conform to those indicated in the literature and are thus taken to be valid. The phenomenological observations are of significant interest, particularly in the area of acoustic - non-linear instability interaction.

It was shown that the pressure jump from stable to unstable operation, used in the calculation of degree of instability, can be determined from the P versus ϕ curve without a loss in the interpretation of the results. The degree of instability was calculated for this paper in the above manner and subsequently compared with respect to burning rate to the degree of instability of reference (1) for the same propellant system; the same trend resulted. This method of calculating the pressure jump is of particular utility when it is necessary to compare a series of propellant formulations in a motor with a small variation of K_n such as the star grain cross-section. In this situation the standard method of using the P versus K_n curves (outlined in reference 9) to determine the pressure jump may not be applicable; an accurate estimation of K_n would be necessary.

The degree of instability was found to vary inversely with burning rate for the three grain cross-sections. This is in agreement with previously published trends (ref. 1) for the same non-aluminized propellant system; however the results in this paper show that the trend holds true for a variety of internal grain geometries.

The degree of instability can be strongly influenced by the number of logitudinal waves propagating in the motor cavity particularly in the case of slower burning rate propellants. This is exemplified by the 44% increase in the degree of instability with the appearance of a double wave in the star configuration and the inordinately high degree of instability found with the slotted tubular grain cross-section motors. The significance of this result is that if the effect of the instability wave can be visualized as enhancing the combustion processes in the thin flame above the propellant surface, increasing the frequency that this disturbance occurs at any one position will thus increase its effect on the flame. The fact that it is the existence of the instability wave that increases the time average chamber pressure and not necessarily its strength is further exemplified by the result that no consistent correlation could be found between wave strength and burning rate. Since the degree of instability is shown to vary inversely with the burning rate of the propellant then the strength of the unstable wave may not vary in a consistent manner with degree of instability. The significance of the previous statement is that a larger amplitude instability wave (or a stronger wave) may not result in a larger pressure jump (or a higher degree of instability) when transitioning to instability. Furthermore it was shown that, whereas the amplitude of the instability wave was approximately the same for both the single and double wave form instability, the average pressure in the motor chamber increased overwhelmingly with the double wave form. Thus it can be stated that increasing the frequency of the instability wave by causing more waves to propagate in the chamber will have a much greater effect on the degree of instability than simply increasing the wave strength for any particular rocket motor.

It has been shown that irrespective of motor interior geometry the slower burning rate propellant is more susceptible to transition to non-linear instability earlier in the firing with a smaller pulse size and the pulse will grow at a faster rate than in the same motor with a faster burning propellant. The fact that the degree of instability is strongly dependent on the number of waves propagating in the chamber and not on their strength and that slower burning propellants are more easily pulsed to instability can be explained by the hypothesis that the shock type of instability is a surface-related or velocity-coupled phenomenon. Erosion effects, or velocity-coupled phenomena, are known to be more pronounced in slower-burning propellants (10). Further, it has been shown in the optical experiments of Brownlee et al (11) that, with the arrival of the shock, the gases streaming towards the nozzle can be made to slow down and even travel in the reverse direction at high velocities, depending on the direction of travel of the shock and the axial position viewed. In the light of the above observations it is understandable that a phenomenon which causes large fluctuations in gas velocity in a solid propellant rocket motor will have a more significant effect on a propellant which is more susceptible to erosive effects.

A study of the amplification of an initiating disturbance can prove to be an informative one as it is here that the feeding mechanisms versus the damping mechanisms can be directly observed. All of the grain cross-sections and all of the propellant formulations presented growth curves which showed distinct and different growth regimes. This is most apparent in the early stages of a particular firing and is evidenced by the change in slope of the pulse-amplitude-versus-time curves. The damping effect of the step change in the axial cross-section of the slotted-tubular configuration tends to have its greatest effect in propellants which are more inherently stable.

Keeping in mind the complicated nature of the growth mechanism of a disturbance, it can generally be stated that the growth rate is inversely proportional to the burning rate. Also a pulse will tend to grow faster if initiated later in a firing of a motor.

REFERENCES

1. Smith, D.L., Christie, F. and Clark, M.N., "Combustion Instability of Non-Aluminized Propellants - The Influence of Propellant Formulation" Paper No. 77-900 AIAA/SAE 13th Propulsion Conference July 1977.

2. Brownlee, W.G., "Nonlinear Axial Combustion Instability in Solid Propellant Rocket Motors", AIAA J., 2, 275--284 (1964).

3. Roberts, A.K. and Brownlee, W.G., "Longitudinal Combustion Instability: Some Empirical Results and Related Design Considerations", CPIA Publication No. 105, Vol. I, May 1966.

4. Roberts, A.K., "Longitudinal Combustion Instability of Propellants with High Solids Content", CARDE Technical Note 1737/66, UNCLASSIFIED.

5. Roberts, A.K., Bergman, W.A. and Brownlee, W.G., "Longitudinal Combustion Instability: Behaviour of Propellants with High Solids Content", CPIA Publication No. 138, Vol. I, February 1967.

6. Roberts, A.K., "Preliminary Data on Unstable Combustion in Aluminized Polybutadiene Rocket Motors", DREV Technical Note 1824/69, UNCLASSIFIED.

7. Roberts, A.K. and Brownlee, W.G., "Nonlinear Longitudinal Combustion Instability: The Influence of Propellant Composition", AIAA Paper No. 69-480 (AIAA 5th Propulsion Joint Specialist Conference, June 1969).

8. Morris, E.P., "A Pulse Technique for the Evaluation of Combustion Instability in Solid Propellant Rocket Motors", CAS J., 11, 329-333 (1965).

9. Roberts, A.K. and Brownlee, W.G., "Nonlinear Longitudinal Combustion Instability: Influence of Propellant Composition", AIAA J, 9, No. 1, 140.

10. Green, L., "Erosive Burning of Some Composite Solid Propellants" Jet Propulsion Journal of the American Rocket Society, Jan-Feb 1954, 24, No. 1, 9.

11. Brownlee, W.G. and Kimbell, G.H., "Optical Studies of Longitudinal Combustion Instability" DREV Report No. CARDE TN1708/66, May 1966.

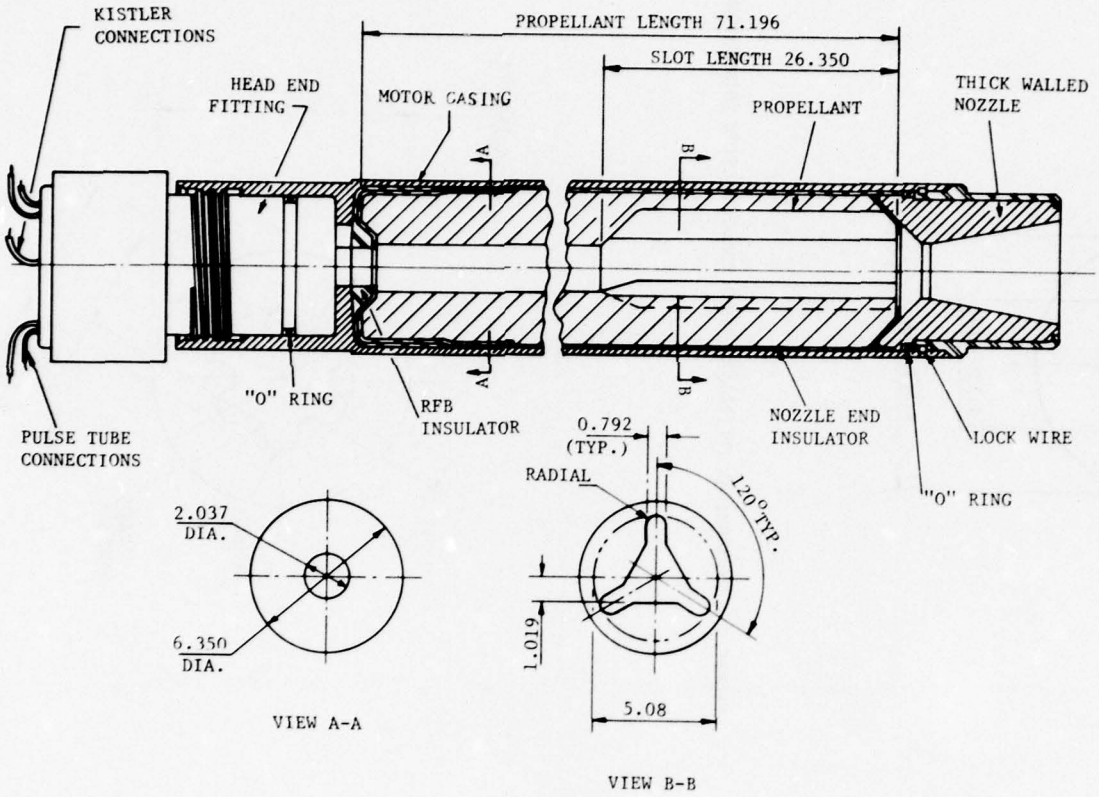

FIGURE 1 - THE TEST MOTOR WITH THE SLOTTED TUBULAR GRAIN CROSS-SECTION (DIMENSIONS IN cm)

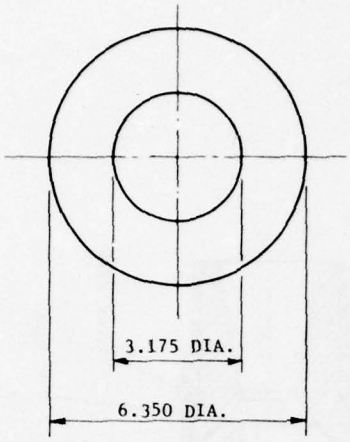

FIGURE 2 - CYLINDRICAL PROPELLANT GRAIN CROSS-SECTION (DIMENSIONS IN cm)

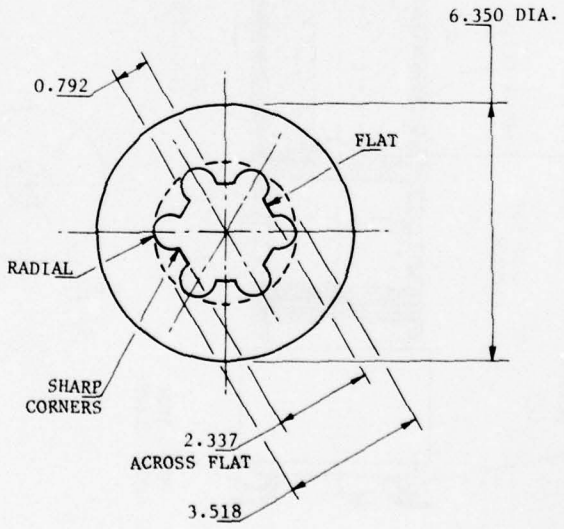

FIGURE 3 - STAR PROPELLANT GRAIN CROSS-SECTION (DIMENSIONS IN cm)

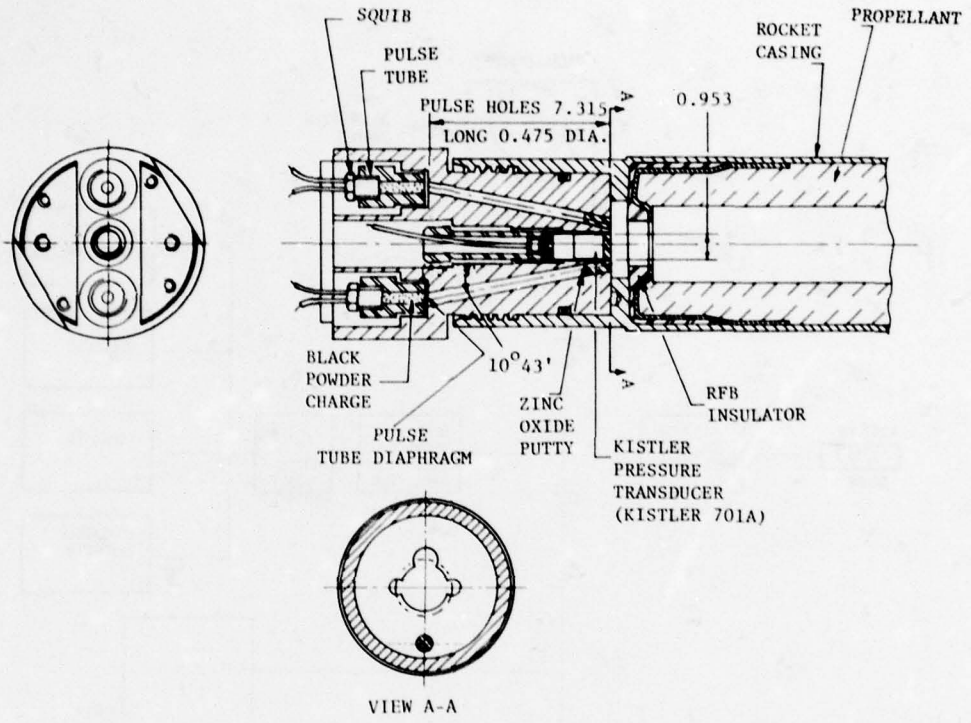

FIGURE 4 - THE HEAD END OF THE TEST MOTOR SHOWING THE TWO PULSE TUBES AND THE PIEZOELECTRIC PRESSURE TRANSDUCER (DIMENSIONS IN cm)

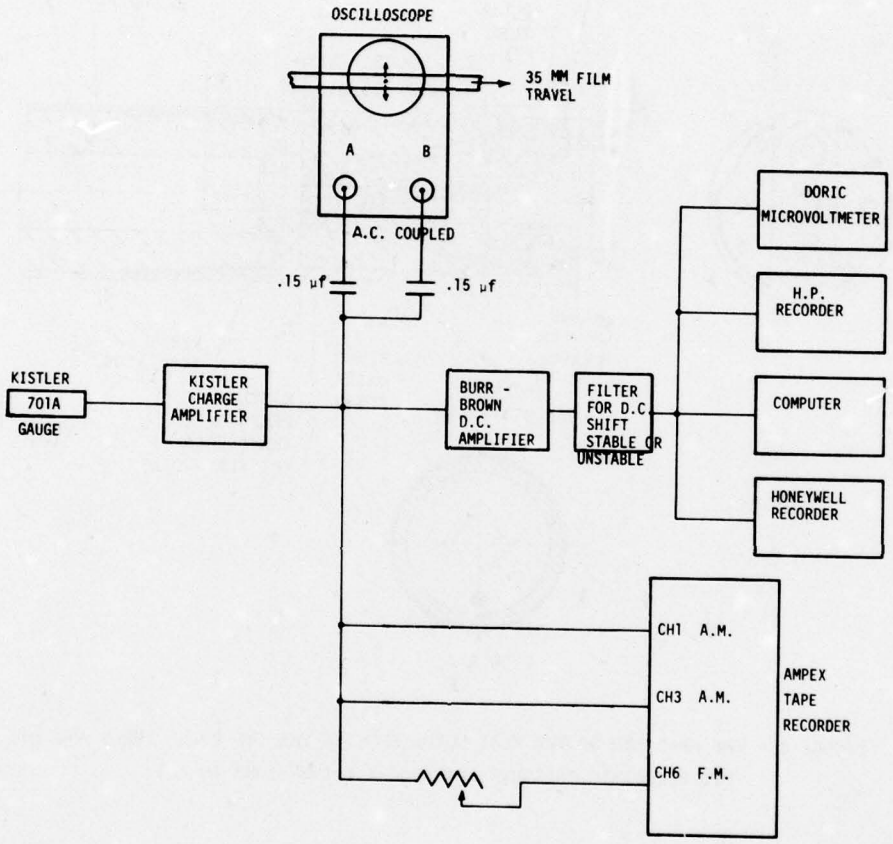

FIGURE 5 - CIRCUIT SCHEMATIC FOR UNSTABLE ROCKET MOTOR DATA GATHERING

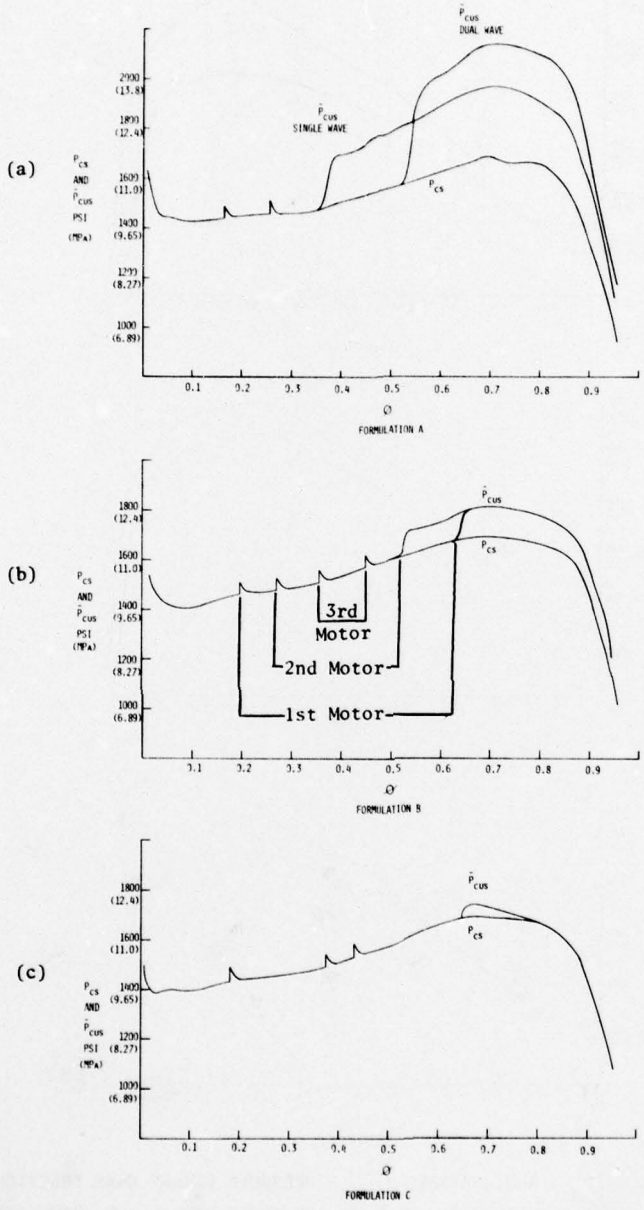

FIGURE 6a, b, c - STABLE (P_{cs}) AND UNSTABLE ($\bar{P}_{cus}$) PRESSURE VERSUS MASS FRACTION CONSUMED (ϕ) FOR THE STAR GRAIN CROSS-SECTION AND THE THREE PROPELLANT FORMULATIONS

6b, SHOWS PULSE BRACKETTING TECHNIQUE

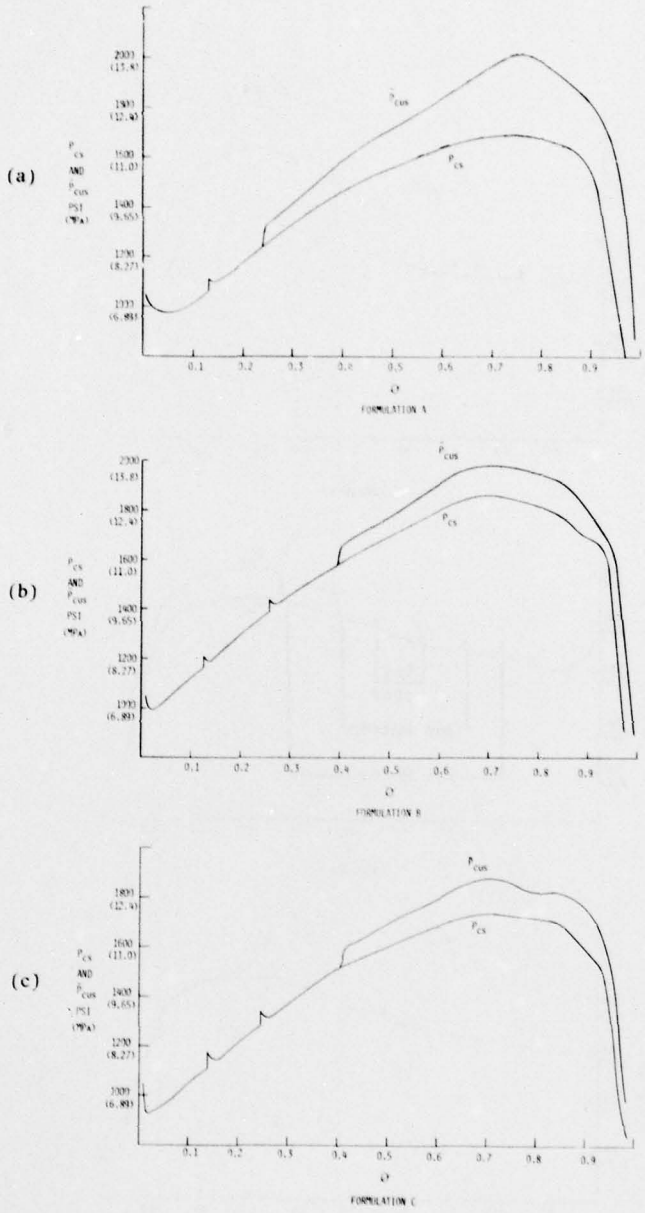

FIGURE 7a, b, c - STABLE (P_{cs}) AND UNSTABLE ($\bar{P}_{cus}$) PRESSURE VERSUS MASS FRACTION CONSUMED (ϕ) FOR THE CYLINDRICAL GRAIN CROSS-SECTION AND THREE PROPELLANT FORMULATIONS

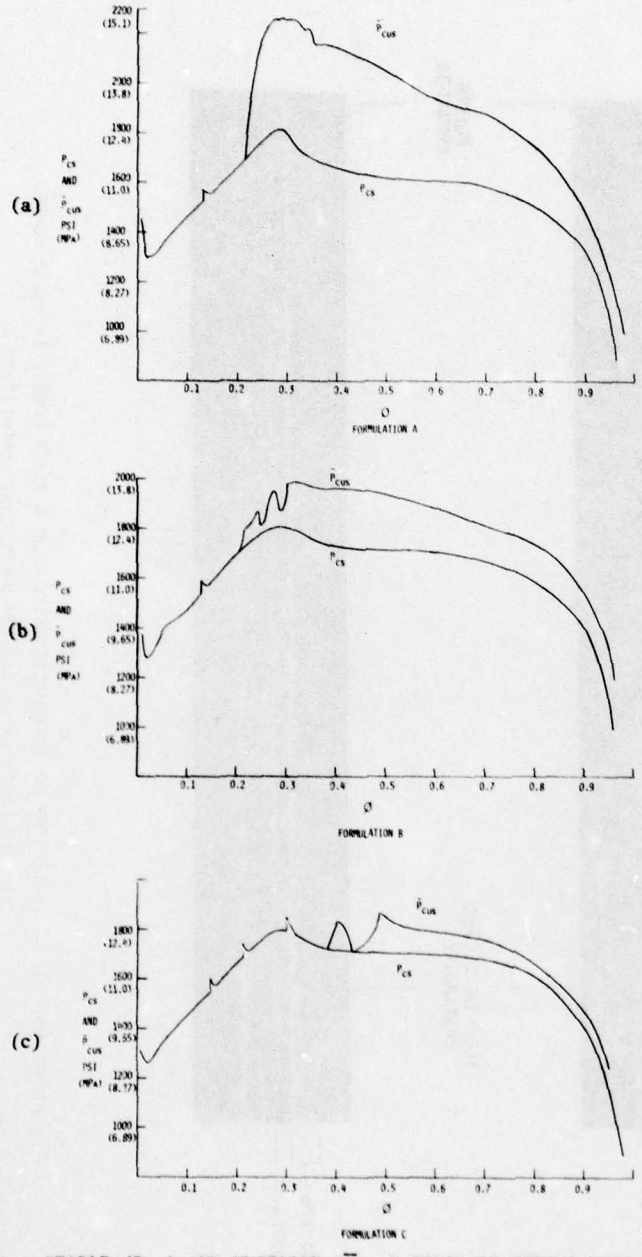

FIGURE 8a, b, c - STABLE (P_{cs}) AND UNSTABLE ($\bar{P}_{cus}$) PRESSURE VERSUS MASS FRACTION CONSUMED (ϕ) FOR THE SLOTTED TUBULAR GRAIN CROSS-SECTION AND THE THREE PROPELLANT FORMULATIONS

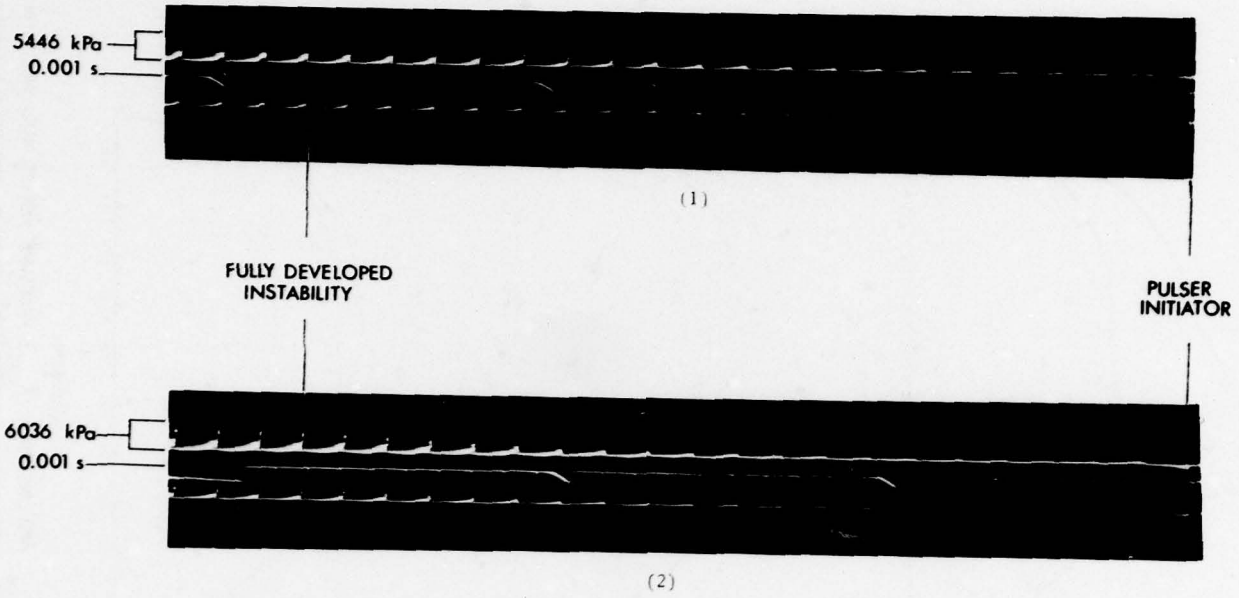

FIGURE 9a) 1 - INITIATION OF INSTABILITY WITH 0.25 g BLACK POWDER IN PULSE TUBES. CYLINDER GRAIN CROSS-SECTION PROPELLANT FORMULATION A.

2 - INITIATION OF INSTABILITY WITH 0.50 g BLACK POWDER IN PULSE TUBES. CYLINDER GRAIN CROSS-SECTION PROPELLANT FORMULATION A.

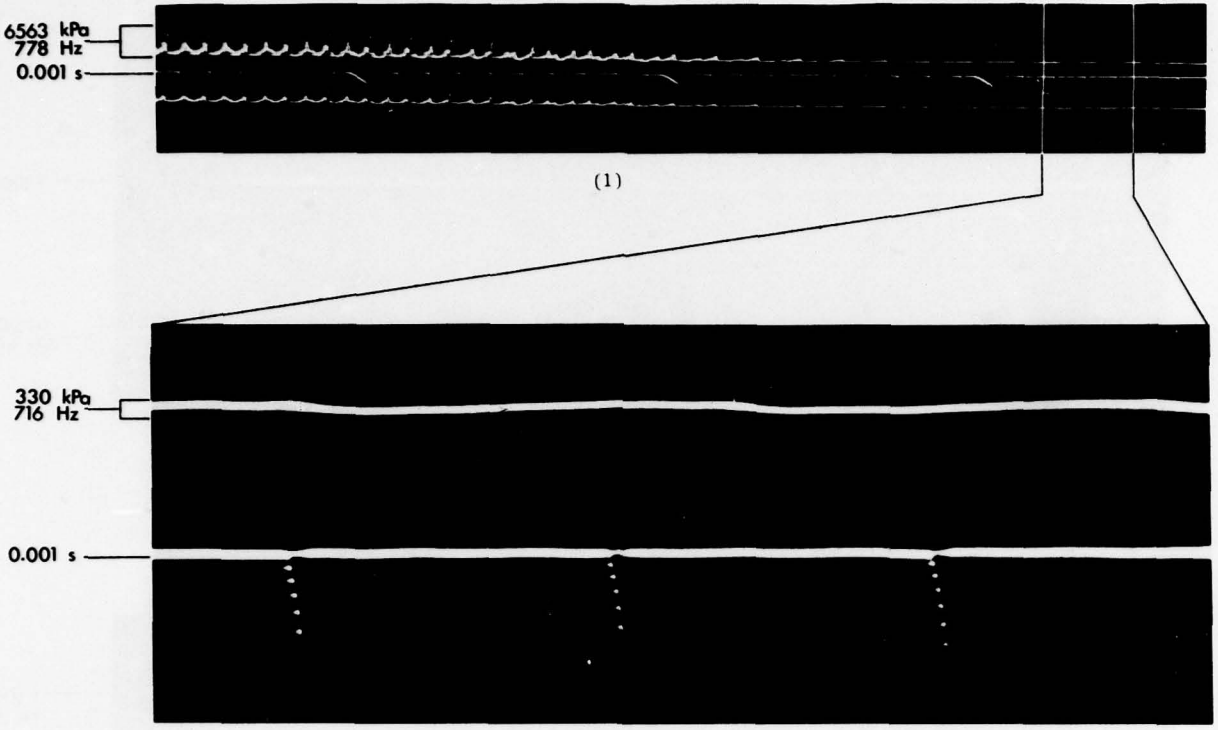

FIGURE 9b) 1 - NATURAL TRANSITION FROM ACOUSTIC (165 kPa AMPLITUDE, 716 Hz) TO STEEP FRONTED SHOCK (6563 kPa AMPLITUDE, 778 Hz). SECONDARY WAVE FORM ALSO VISIBLE. MOTOR 5291. *SLOTTED TUBULAR GRAIN CROSS-SECTION PROPELLANT FORMULATION A.*

2 - ENLARGED VIEW OF ACOUSTIC WAVE (330 kPa PEAK TO PEAK, 716 Hz)

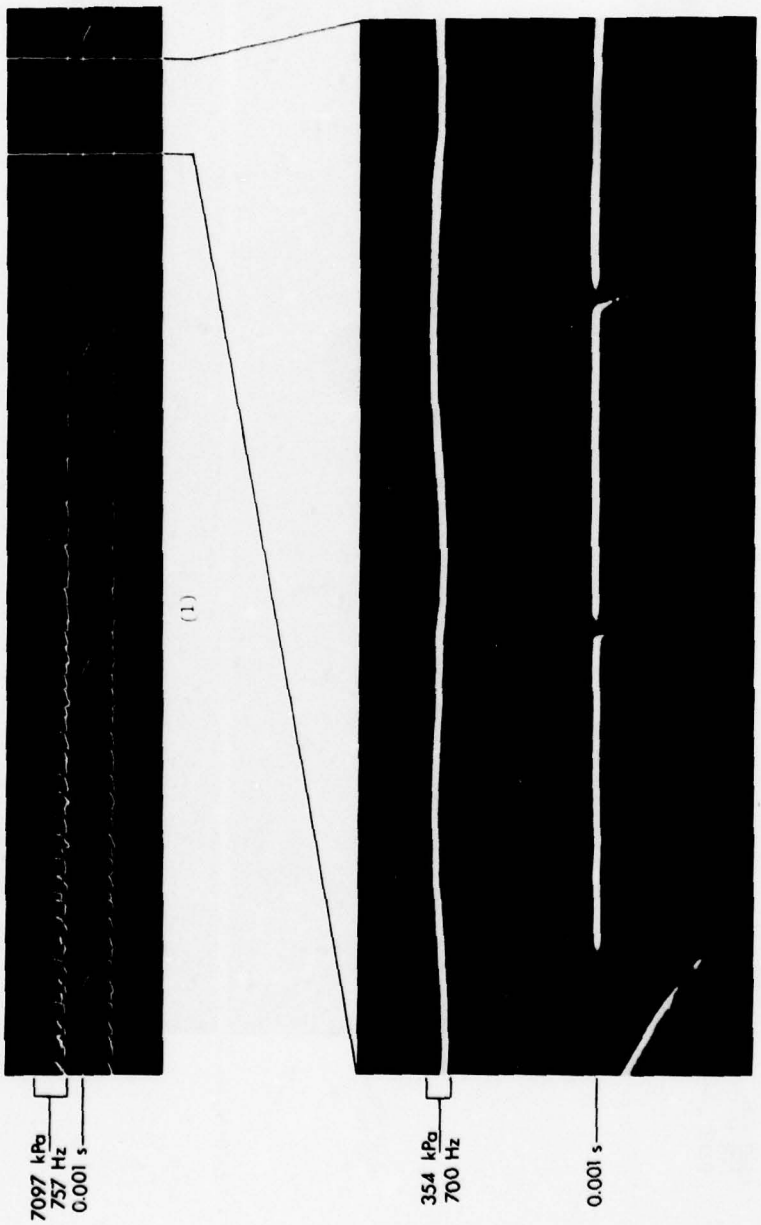

FIGURE 9c) 1 - NATURAL TRANSITION FROM ACOUSTIC (177 kPa AMPLITUDE, 700 Hz) TO STEEP FRONTED SHOCK (7097 kPa AMPLITUDE, 757 Hz). SECONDARY WAVE FORM ALSO VISIBLE. MOTOR 5292. SLOTTED TUBULAR GRAIN CROSS-SECTION PROPELLANT FORMULATION A.

2 - ENLARGED VIEW OF ACOUSTIC WAVE (354 kPa PEAK TO PEAK, 700 Hz)

(1)

(2)

FIGURE 9d) 1 - DUAL WAVE FORM FOUND IN THE STAR-A PROPELLANT COMBINATION. THIS PHOTO TAKEN AT $\Phi = 0.8$

2 - SINGLE WAVE FORM FOUND IN THE STAR-A PROPELLANT COMBINATION. THIS PHOTO TAKEN AT $\Phi = 0.8$

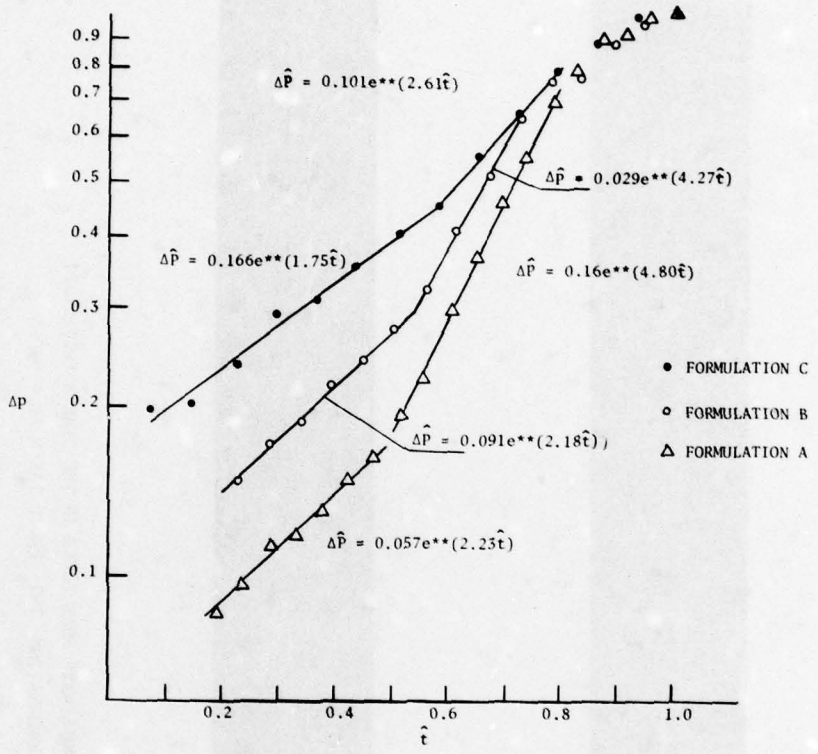

FIGURE 10 - NORMALIZED GROWTH CURVES OF A DISTURBANCE IN THE CYLINDRICAL GRAIN CROSS SECTION FOR THE THREE PROPELLANT FORMULATIONS (ϕ = 0.3)

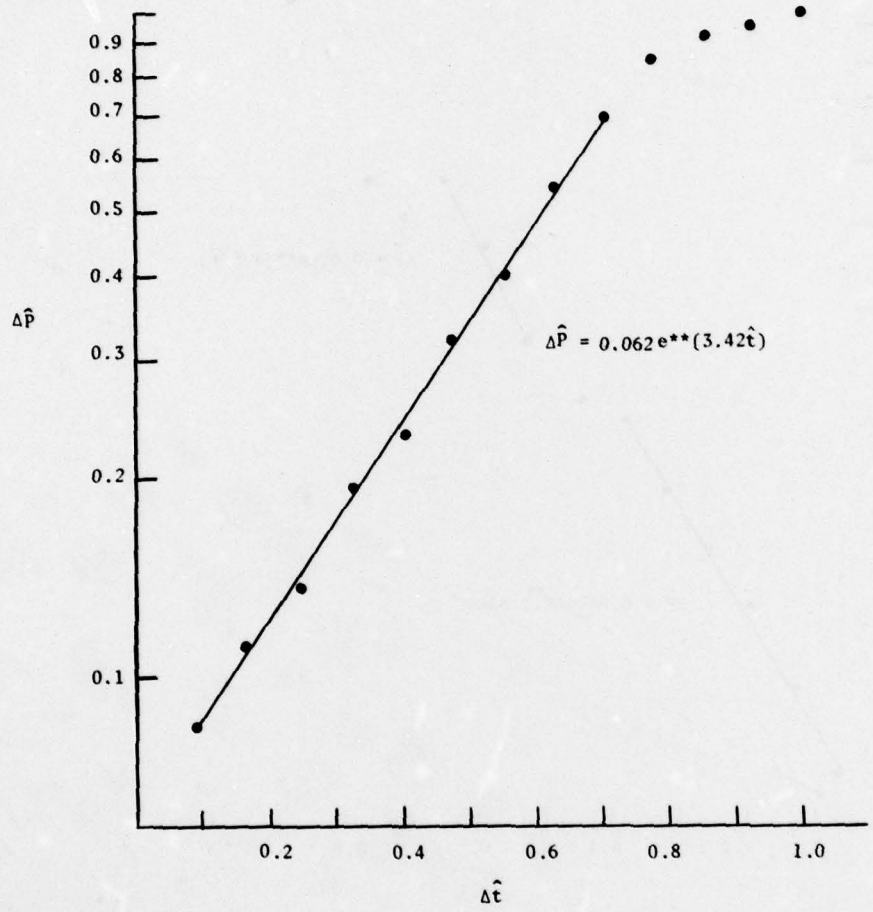

FIGURE 11 - NORMALIZED GROWTH CURVE OF DISTURBANCE IN THE CYLINDRICAL GRAIN CROSS-SECTION FOR PROPELLANT FORMULATION B (Φ = 0.87)

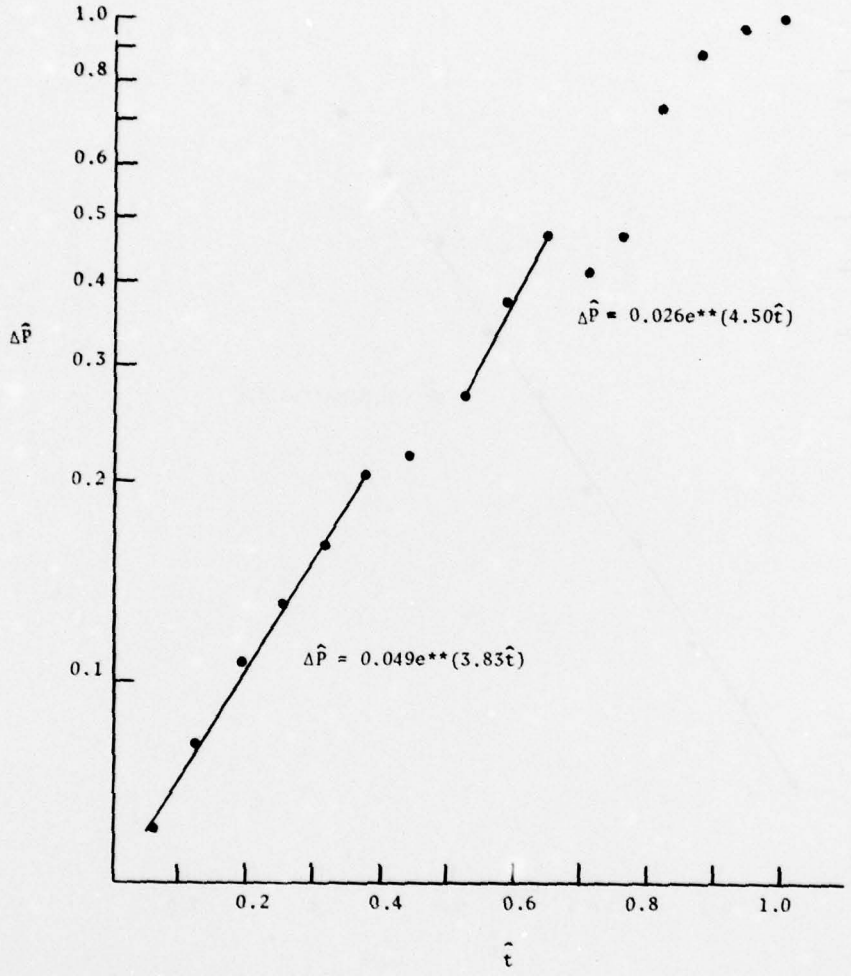

FIGURE 12 - NORMALIZED GROWTH CURVE OF A DISTURBANCE IN THE SLOTTED TUBULAR GRAIN CROSS SECTION AND PROPELLANT FORMULATION A (ϕ = 0.45)

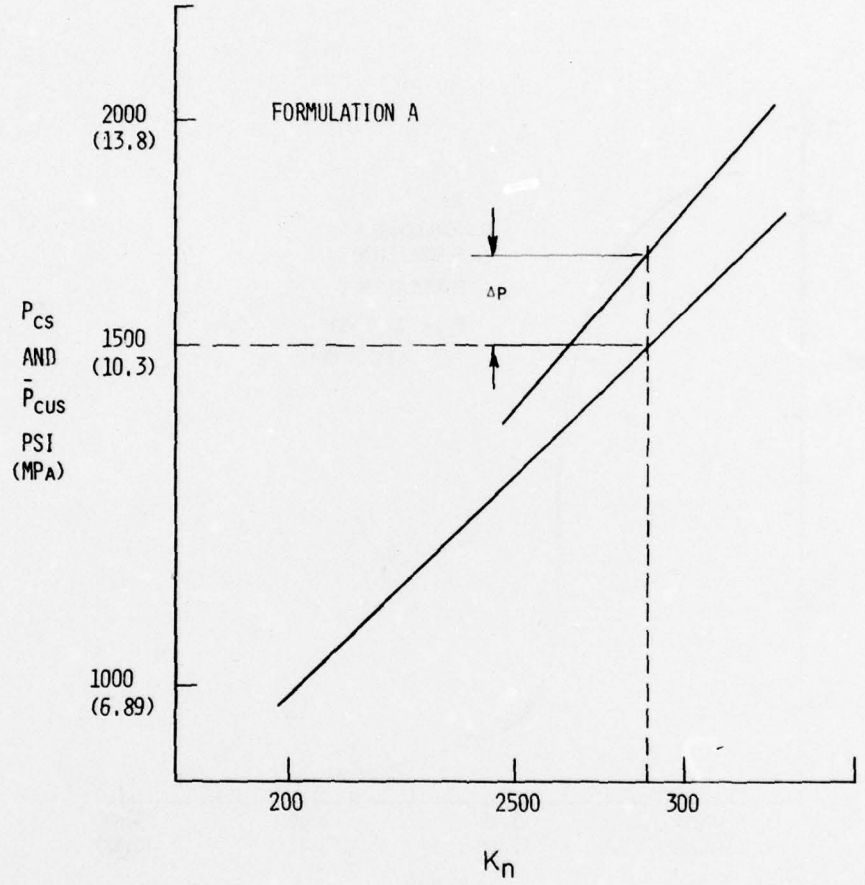

FIGURE 13 - PRESSURE VERSUS Kn FOR THE STABLE AND UNSTABLE FIRINGS OF THE CYLINDRICAL GRAIN CROSS SECTION MOTORS WITH THE A PROPELLANT FORMULATION

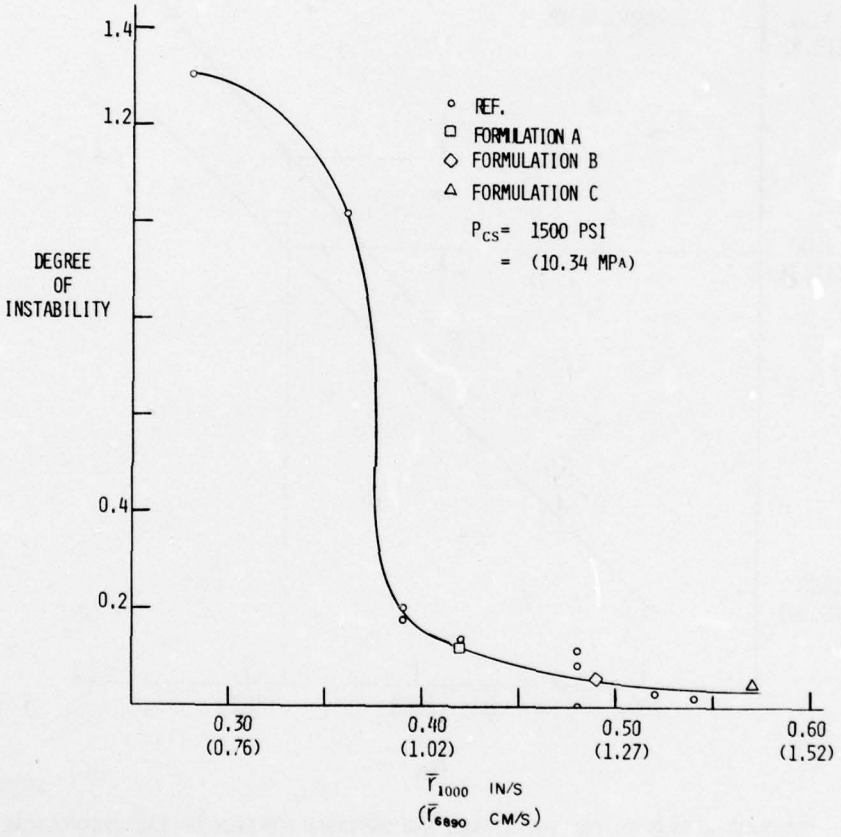

FIGURE 14 - THE DEGREE OF INSTABILITY AT 10335 kPa VERSUS BURNING RATE AT 6890 kPa FOR CYLINDRICAL GRAIN CROSS SECTION INCLUDING DATA FROM THIS STUDY

AD-A076 012 ADVISORY GROUP FOR AEROSPACE RESEARCH AND DEVELOPMENT--ETC F/G 21/8.2
SOLID ROCKET MOTOR TECHNOLOGY.(U)
JUL 79
UNCLASSIFIED AGARD-CP-259 NL

5 OF 6
AD
A076012

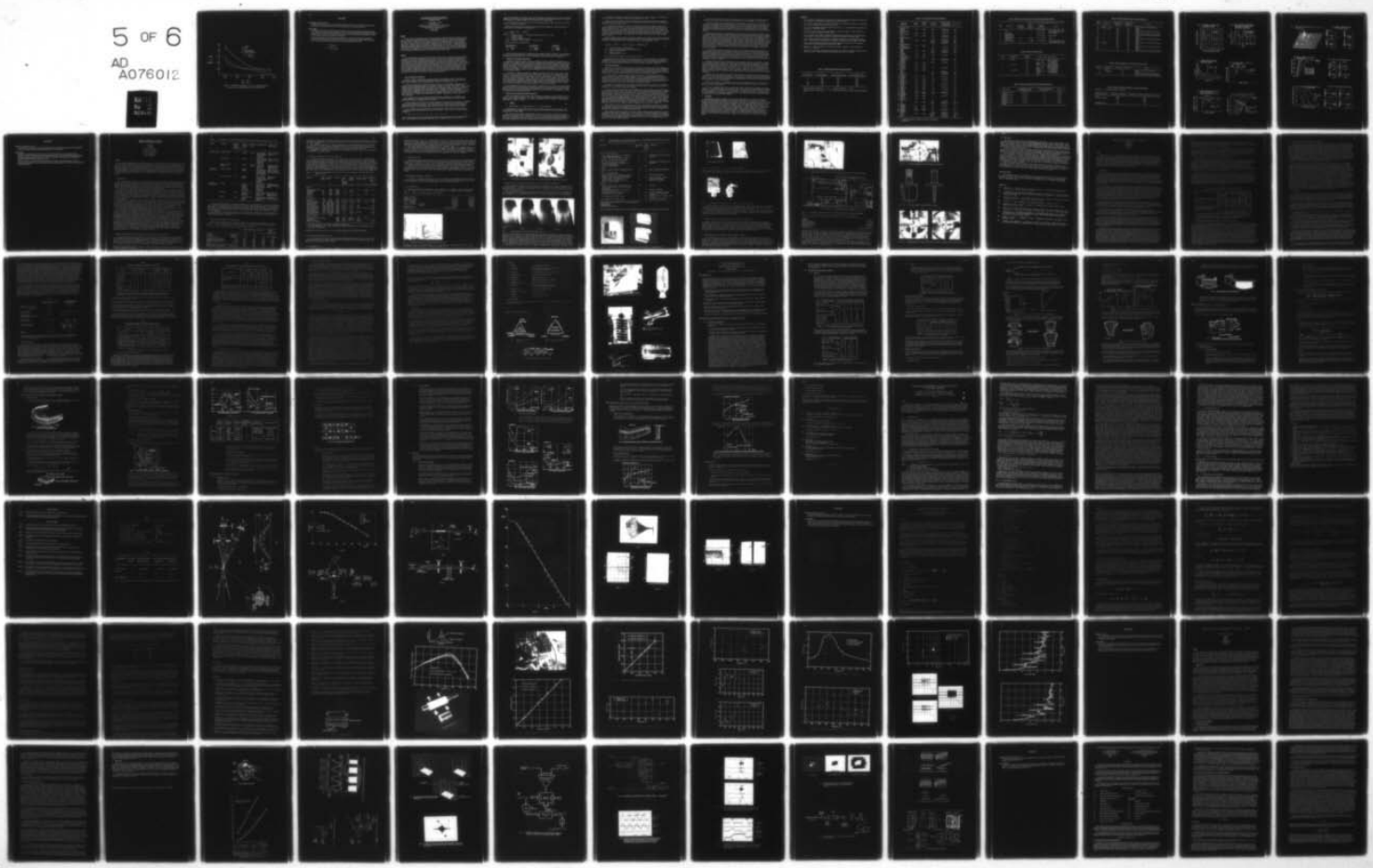

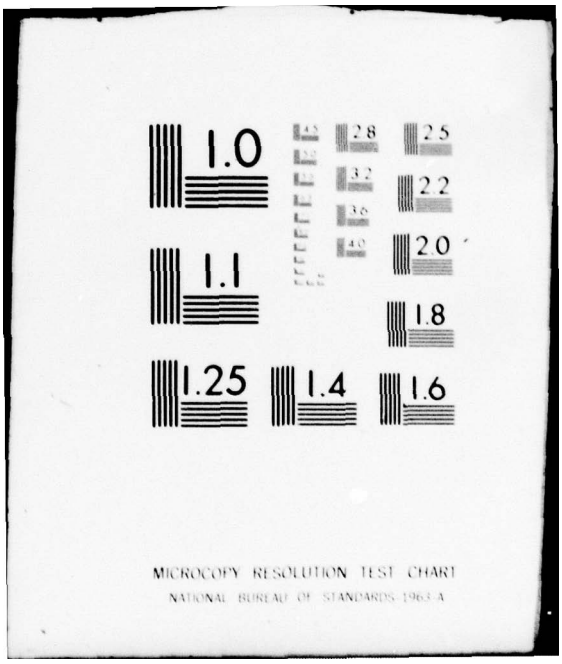
1.0
1.1
1.25
1.4
1.6
1.8
2.0
2.2
2.5
2.8
3.2
3.6
4.0
MICROCOPY RESOLUTION TEST CHART
NATIONAL BUREAU OF STANDARDS-1963-A

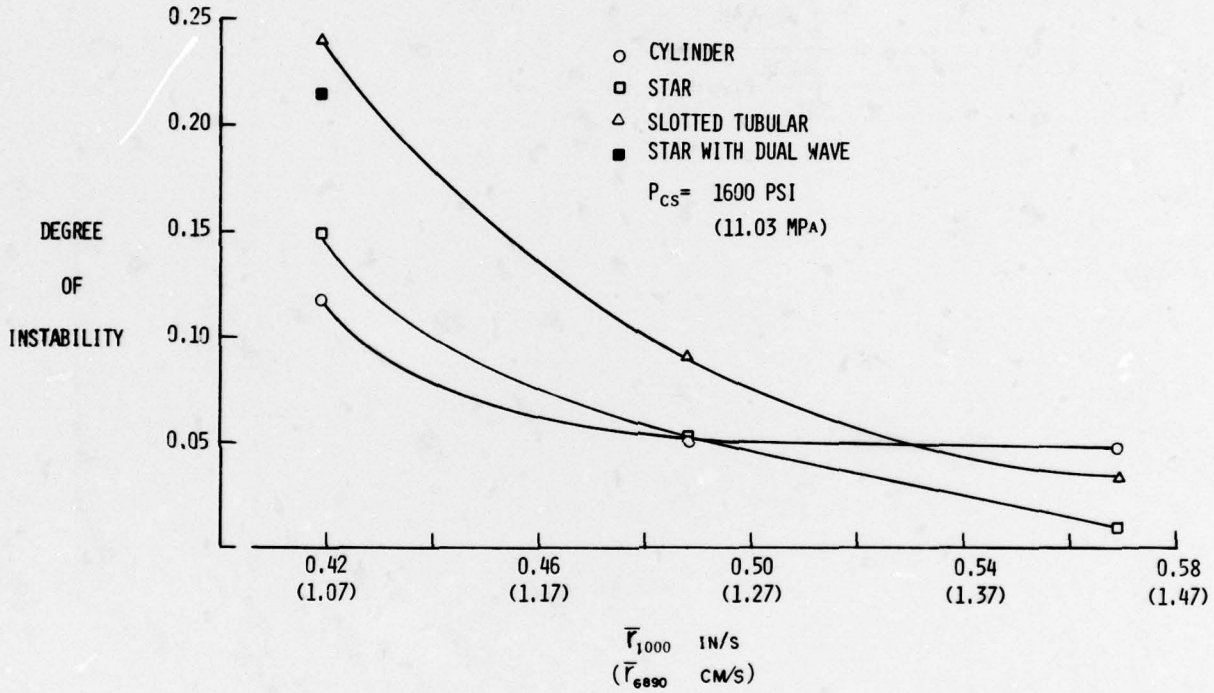

FIGURE 15 - THE DEGREE OF INSTABILITY AT 11024 kPa VERSUS BURNING RATE AT 6890 kPa FOR ALL THE GEOMETRIES AND ALL THE FORMULATIONS

DISCUSSION

W.H.Diesinger, Dynamit Nobel AG

My question concerns your Figures 6 and 8. Why did you plot the pressure as a function of mass fraction rather than burn time? Secondly how did you measure the mass fraction ϕ as a function of pressure?

Author's Reply

The reasons are detailed in our paper. The pressure change, for the degree of instability at the operating pressure of 10.34 MPa and 11.02 MPa, was determined from the curves of the pressure versus spent mass fraction. Therefore these curves had to be drawn for all 36 motor firings. These curves were thought useful to demonstrate the effects of burning rate and geometry on the transition to instability.

To answer the second part, I can say that the low frequency (i.e. < 100 Hz) pressure signal was digitalised at a maximum of 200 Hz and recorded during each of the 36 firings. Subsequent to the firings the data was analysed. The following integral relationship for the mass fraction of expended propellant was used.

$$\phi = \frac{\int_o^t P_c A_t \, dt}{\int_o^{ta.3P} P_c A_t \, dt} \quad .$$

THE SUPPRESSION OF COMBUSTION INSTABILITY BY PARTICULATE DAMPING IN SMOKELESS SOLID PROPELLANT MOTORS

by
G. I. Evans and P. K. Smith
IMI Summerfield
(Operated by IMI Kynoch Limited on behalf of the
Procurement Executive, Ministry of Defence)
Kidderminster Worcestershire
DY11 7RZ
United Kingdom

SUMMARY

Acoustic combustion instability can be a serious problem in smokeless CDB solid propellant rocket motors. Theroetical considerations predict that particulate damping can be employed as a means of overcoming combustion instability and that a specific density and size of particle gives optimum damping. To achieve the best control of the size density function in the combustion gases, it was considered that refractory particles which are unreactive during combustion should be used. The paper presents a theoretical treatment together with extensive experimental trials in a variety of representative motors. Experimental work shows that small quantities of refractory powder are very successful in suppressing combustion instability but that a wider range of particle sizes than is theoretically predicted proves to be effective. Manipulation of the size density function has been shown to be an effective means of achieving maximum combustion stability with minimum amounts of exhaust smoke.

PREFACE

This paper describes an approach to the practical resolution of the problem of acoustic combustion instability without sacrificing performance in smokeless rocket motors. The traditional methods of suppression used, based on an empirical approach, have a number of disadvantages as described later. In this paper the propellant formulation has been taken as the vehicle for solving the problem facing the rocket designer. In particular refractory additives in the propellant have been chosen to control the size density function of particulate matter in the gas phase for optimum damping of the acoustic frequency. At the same time the size density function is manipulated to give a size which preferably avoids the region of maximum scattering for visible light in the exhaust and so enhances smokelessness or alternatively utilises a high density particle, which for a given mass fraction of particles necessary for acoustic damping, minimises the number of particles/unit volume of exhaust gases and hence low smoke. The experimental work described has been confined to base grain CDB solid propellant smokeless rocket motors but the principles can be applied to other propellant systems.

1. Acoustic Combustion Instability

Acoustic instability occurs when the energy released by the combustion process is fed into the acoustic field in one or more of the resonant modes of the rocket chamber cavity. The phenomena has been studied intensively in the last 30 years and surveyed in the literature (ref 1-7).

In the rocket motor there are modes of acoustic oscillation of longitudinal, tangential, radial or combined types at frequencies determined by the specific system. These can manifest themselves in broadly two types of phenomena, namely "irregular" and "oscillatory" burning. The former is characterised by large deviations from the desired rocket pressure time relationship, these deviations often being of a similar order of magnitude to the mean pressure itself. "Irregular" burning is detected by low frequency pressure transducers used in the normal recording equipment for rocket test firings. "Oscillatory" burning is characterised by low amplitude, high frequency oscillations in an acoustic mode of the rocket motor cavity. Special high frequency sensitive pressure transducers are used to measure the latter phenomena.

It is believed that the onset of small amplitude oscillatory combustion is a precondition for irregular combustion. A particular mode oscillates with growing amplitude when the acoustic energy gains exceed the acoustic energy losses for that mode.

The most important gain factor is the acoustic response of the propellant surface which is influenced by the acoustic pressure and erosivity. The pressure response is usually the more significant for low amplitude oscillatory burning. However, when the acoustic velocity oscillations are large enough to produce flow reversal in the combustion chamber then the acoustic erosive response becomes important.

For an unstable motor a growth constant α can be defined as a measure of the rate at which the magnitude of the small amplitude acoustic oscillations increase. The net value of this growth constant is given by:-

$$\alpha = \alpha_b + \alpha_f + \alpha_n + \alpha_s + \alpha_p + \alpha_m + \alpha_v + \alpha_w + \alpha_H \qquad (1)$$

where α_b and α_f are gain factors arising from the acoustic pressure response and flow coupling respectively. The remainder are loss sources associated with the convergent section of the nozzle (α_n),

visco-elastic damping by the propellant (α_s), particle damping in the gas phase (α_p), molecular relaxation damping in the gas phase (α_R), volume losses due to the viscosity and thermal conductivity of the gases (α_v), damping by the exposed chamber wall (α_w), head end cavity damping (α_H).

The relationship in Eq.(1) applies to each of the individual modes of oscillation and all the components of α are frequency dependent.

Prediction criteria have been established for calculating the frequencies of quasi gas modes for a uniform cylindrical charge with a central conduit.

$$F_{lmn} = \left[\frac{Co}{2\Pi a} \beta^2_{mn} + \frac{\Pi a l}{L} \right]^{\frac{1}{2}} \qquad (2)$$

where F = Frequency and l mn = integral parameter indicating type of mode
a = Radius of conduit
L = Length of conduit
Co = Velocity of sound in the gas
β_{mn} = Solutions of equation $Jm'(\beta) = 0$ given in ref 7

Thus for the various acoustic modes:-

Pure Longitudinal (m = n = o)	Pure Tangential (l = n = o)	Pure Radial (l = m = o)
$F_{100} = \frac{Co\ 1}{2L}$	$F_{omo} = \frac{Co\ \beta mo}{2\Pi a}$	$F_{oon} = \frac{Co\ \beta on}{2\Pi a}$ (3)

From acoustical theory it may be inferred that the fundamental modes are dominant, with the higher harmonics of decreasing importance. Experience has shown that the modes most likely to be unstable in a solid propellant rocket motor are the first longitudinal and particularly the first tangential.

2. Suppression of Combustion Instability

Resonance rods have been used as baffles to interfere and prevent strong vortex systems being developed from the cumulative effects of acoustic streaming interactions between the combustion zones and flow field. The resonance rods are applicable to tangential modes in radial burners but as the burning surface recedes they clearly become less effective as baffles. Such rods are sometimes successful and sometimes unsuccessful. Their effectiveness is dependent on propellant composition, rod size and shape, acoustic mode and frequency. In addition other disadvantages arise associated with the weight penalty, interference with design, in particular igniter engineering, and erosion/combustion of the rod can give rise to significant smoke.

An alternative, slightly more effective, mechanical suppressor is the use of inert flaps. These consist of sheets of erosion resistant polymer based material cast radially into the propellant charge such that a portion protrudes continuously into the conduit. Again these act as baffles and are most effective at interrupting the flow field adjacent to the propellant surface. Hence they would appear to be most effective for tangential modes. Again these devices are not successful in all cases and their effectiveness is dependent on propellant composition, flap size/thickness and composition, number of flaps and angular spacing, mode type and frequency. Amongst the disadvantages of these devices are their contribution to exhaust smoke, volumetric replacement of propellant, increased cost and reduced motor reliability associated with fitting and bonding to the motor and propellant.

Further examination of the gain and loss factors, illustrated in Eq.(1), imply major design changes could be necessary to eliminate acoustic combustion instability in a given rocket motor. Moreover many gaps exist in the current understanding of the predictive criteria necessary for the designer. In this work the resolution of the practical problem is based on α_p, the loss factor due to particulate damping by manipulating the propellant composition.

3. Particle Acoustic Damping and Optical Properties

Dobbins and Temkin (ref 8) and Culick (ref 9) have shown that particles attenuate acoustic oscillations in rocket combustion chambers. The extent of attenuation depends on weight of particles per unit volume, particle radius and density. The following relationship gives the frequency at which maximum attenuation is caused by a particle:-

$$F = \frac{9V}{\Pi \rho' Do^2} \qquad (4)$$

V = gas viscosity, ρ = particle density, Do = particle diameter.

The gas viscosity is readily determined from the propellant composition and motor design. Thus from a knowledge of the frequency of the acoustic mode in the motor the particle size and density can be predicted for optimum damping.

With regard to rocket exhaust smoke properties, classical optical theory of particulate clouds enables us to relate the extinction coefficient of a particle to its particle diameter. This holds only for a dilute, monodisperse cloud of spherical particles but low smoke rocket motor exhaust presume by definition a dilute smoke cloud. Fig 1 shows a plot of extinction coefficient against particle size for an incident wavelength of 0.524 microns (visible light) and refractive index of particle (M) = 1.33.

Fig 2 shows the variation in light scattering coefficient for values of $\frac{2\Pi r}{\lambda}$ up to 30 established by the literature for incident wavelengths in the region 0.14μ to 3.0 μ.

Thus by choice of size/density function of particles for optimum acoustic instability damping a dilute particle cloud in the motor exhaust may be achieved whose optical properties for low smoke may be optimised by selecting particle size.

Fig 3 presents the optimum particle size for various particle densities against frequency of the acoustic mode derived from Eq.(4). In Table 1 the visible light extinction coefficient as related to particle diameter is given. For a given mass of particles per unit volume of gas, then obviously the greater the density for a given diameter the smaller the number of particles/unit volume and hence the lower the total scattering coefficient. The latter coefficient is given in column 4 of Table 1. Clearly in terms of low smoke results it is of marked advantage to select particles of high density to achieve acoustic instability suppression. The persistency of the smoke trail would also be less with higher density particles.

However, cognisance must be taken of the greater precision and control of particle size for acoustic instability damping with particles of higher density compared to lower density. This can be deduced from an equation for a dimensionless acoustic attenuation given by Dobbins and Temkin (ref 8).

$$Co\alpha/C_m W = (y/yo)^2/1 + (y/yo)^4 \quad \text{where } y/yo = \left(2W\rho' R^2/q_v \right)^{\frac{1}{2}} \qquad (5)$$

Co = Velocity of sound in undisturbed gas
α = Acoustic attenuation due to suspended particles
C_m = Mass fraction of particles
R = Radius of particle
W = Angular frequency = $2\Pi F$

Eq.(5) maximises at a numerical value of 0.5 when y/yo = 1.

By taking an acoustic frequency of 10 KHz then the data in Fig 4 can be obtained to illustrate the increasing sensitivity to particle size with increasing density. This size sensitivity becomes more pronounced at higher acoustic frequencies as illustrated in Fig 5. The latter figure was obtained from Eq.(5) by plotting the attenuation coefficient for silicon carbide at different frequencies.

4. Experimental Programme

Clearly in order to achieve the most efficient instability suppression by particulate damping and low exhaust smoke, a means of controlling the particle properties in the gas phase within the chamber and exhaust is required. This is best achieved by utilising refractory materials which are also unreactive in the combustion process. By incorporating such materials in the propellant and selecting the size and density prior to incorporation into the propellant, the desired effect may be achieved.

The incorporation of aluminium powder in propellant has been a long established expedient for acoustic instability suppression. In many instances it is not an acceptable means since it is not a refractory and is reactive. The propellant ballistic properties are affected but more importantly it produces a dense exhaust smoke. This arises since the aluminium combustion produces a wide distribution of metal/metal oxide particle sizes in the exhaust which straddles the region of maximum extinction coefficient together with a high value for number of particles/unit volume.

Typically a size distribution of 0.1-10μ with the largest proportion of particles in the submicron range is obtained. Similarly the wide distribution of particle sizes is not sufficiently selective in many cases for efficient particulate acoustic damping.

The main test vehicle used throughout this programme was the 150 mm diameter slotted radial charge fired in a heavyweight steel body. Fig 6 shows the theoretical radial and tangential modes of oscillation produced within the conduit and how these modes decay to lower frequencies as the charge burns. These decaying frequency chains were derived from Eq.(2). Charges fired in this configuration all showed severe combustion instability, high frequency analysis of the firings showing the lowest frequency transverse mode to possess the highest amplitude. Full frequency analysis of these firings was not possible due to the large DC signal changes associated with the fluctuating pressure. However, later firings with small amounts of particulate damping enabled full frequency analysis to be carried out. Fig 7 shows a pseudo three dimensional analysis of a firing using a low level of additive and it can be seen that the frequencies occurring are very similar to those predicted in Fig 6. It can also be seen that the highest amplitude occurs in the first tangential mode which appeared to be the case with no additive.

Table 2 shows the range of refractory materials which have been examined together with a comment on their suitability for use. This is based on stability tests on the additive in contact with propellant and microscopic examination of the powders which in some cases revealed the presence of aggregates which would make the particle size in the gas stream indeterminate.

Table 3 shows the effect in the main test vehicle of this different refractory material on an otherwise unstable propellant and a comparison of the effectiveness of the additive compared with mechanical suppressing devices. The size density function for the additive is tabulated together with the frequency at which it would produce maximum attenuation. This shows that the 3 μ silicon carbide would be expected to be effective at the frequency of the first tangential mode whereas the 4 μ molybdenum would not be effective except at much lower frequencies.

The results obtained agree with the theory showing the 3μ Silicon Carbide to suppress combustion instability as efficiently as the mechanical devices whereas the 4μ molybdenum was not effective.

3μ silicon carbide was incorporated into 3 different burning rate propellants at different levels to determine the amounts needed to give suppression. Table 4 gives the results obtained which show that the additive is successful in all three propellants but the level of additive needed to give stability varies with the propellant type with the expected result that the propellants which give the greatest instability without additive need the highest level of additive to promote stability. Fig 8 shows the pressure time records obtained from a series of firings with the type 3 propellant at different levels of additive.

As further test vehicles for the programme five different rocket motor designs were selected which in various propellant systems were known to give grossly irregular burning arising from acoustic combustion instability. The test vehicles are shown in Table 5 and Fig 9 together with the 1st tangential acoustic mode calculated from Eq.(3) and later verified experimentally to be the principle coupling mode. Also shown in Table 5 is the optimum damping frequency for 3μ silicon carbide which was incorporated at various levels in the propellant for all these motors. Firing results for these motors showed stability to be achieved in all cases. Two typical results are shown in Fig 10. These results were unexpected especially in the case of the 100 mm 8 slot radial charge where very high frequency oscillations just after ignition caused the instability whereas the 3μ silicon carbide would not be expected to become efficient until later in the firing. The results however showed that the additive was efficient even at the beginning of the firing and lead to the conclusion that the additive was perhaps not so frequency selective as had been anticipated.

A further demonstration that the additive was efficient at a range of frequencies outside that predicted by theory was obtained by incorporating a range of different sized silicon carbide powders into propellant and establishing the level needed to give stability for each size. The particle size distributions for these powders are shown in Fig 10 which illustrates that there is very little overlap between the different grades. Table 6 gives the results obtained from the different particle sizes and Fig 12 illustrates the pressure time records at two additive levels for the finest and coarsest grades. The results show that over the range of particle size examined, the mass fraction and not the size of particle determines the stability achieved.

Following the success of silicon carbide particles as combustion instability suppressors, a higher density refractory namely Zirconia was obtained in two different particle sizes which fall either side of the theoretically predicted optimum size. These powders were incorporated into propellant at the same levels which had been used for the silicon carbide particles. Table 6 gives the results obtained with the Zirconia powders and it can be seen that the size of particle does not effect the degree of stability obtained. The other significant result from Table 6 is that Zirconia and silicon carbide appear to be equally efficient at equal mass fraction. Work is underway to compare the smoke emissions from silicon carbide with Zirconia and it is expected that the higher density Zirconia particles will give better smoke performance.

A further series of firings was conducted in which aluminium was incorporated into the propellant at the same levels as silicon carbide and Zirconia. Table 7 gives the results of these firings and comparison of Table 7 with Table 6 shows that a proportionately higher amount of aluminium is needed to give the same degree of stability. Fig 13 shows the pressure time records obtained from firings of the three additives at the same level (1.4%) in the propellant.

Table 8 shows the effect of the propellant additive on rocket exhaust smoke and it can be seen that much lower levels of smoke are obtained with silicon carbide than aluminium as expected from the size distribution in the motor exhaust.

Work is now in progress using some of the much higher density powders such as Tungsten and Tantalum Carbide. It was originally thought that as shown in Fig 4, very tight particle size control for the high density powders might be necessary and that these would not be commercially obtainable. However, the work to date has suggested that this may not be a problem and if the results obtained with these powders show the mass fraction to be the dominating parameter then it is anticipated that acoustic combustion stability can be achieved with even lower smoke penalties.

5. Conclusion

The experimental evidence has shown that the acoustic modes present in a rocket motor chamber can be predicted with reasonable accuracy by the simple theoretical model. The theory does not predict whether the acoustic mode oscillations grow in amplitude, coupled with the burning process, to give unstable irregular burning, neither does it predict which modes of oscillation become dominant. However, in five different test vehicles the lowest frequency transverse mode (first tangential) has always proved to be the dominant mode. Knowing the frequency of the dominant mode, a suitable sized refractory particle can be chosen to eliminate acoustic instability and the experimental evidence suggests that the size needed may not be too precise but that the mass fraction appears to be of primary importance. One such refractory silicon carbide used in the amounts necessary to suppress grossly unstable motors produced results which showed only slight increases in smoke over non-suppressed rounds and gave results far superior to aluminium used at the same level. However, silicon carbide may not necessarily be the best material to use and higher density refractories appear to offer the possibility of even lower exhaust smokes.

References

1. R. W. Hart and F. T. McClure, Theory of Acoustic Instability in Solid Propellant Rocket Combustion - Tenth Symposium (International) on Combustion, pp. 1047-1065 (1964).

2. W. G. Berl, R. W. Hart and F. T. McClure, Solid Propellant Instability of Combustion - 1964 Status Report, Applied Physics Laboratory TS 371-8A (1964).

3. E. W. Price, Experimental Solid Rocket Combustion Instability - Tenth Symposium (International) on Combustion, pp. 1067-1082 (1964).

4. E. W. Price, Status of Solid Propellant Combustion Instability Research - Naval Ordnance Test Station, China Lake, California, TP 4275 (1967).

5. G.F.P. Trubridge and H. Badham, Experimental Studies of Unstable Combustion in Solid Propellant Rocket Engines - Combustion and Propulsion, Fifth AGARD Colloquium, pp. 497-530 (1962).

6. G.F.P. Trubridge, Review of Presentations on Combustion Instability in Solid Propellant Rocket Motors - Tenth Symposium (International) on Combustion, Summerfield Technical Report 64/27 (1964).

7. G.F.P. Trubridge, Prediction Criteria for Acoustic Combustion Instability in Solid Propellant Rocket Motors - Summerfield Technical Report 68/26 (1968).

8. Dobbins R. A., Temkin, Measurement of Particulate Acoustic Attenuation - AIAA Journal 1964 Vol 2, No. 6, 1106-1111.

9. Culick F.E.C. Stability of Longitudinal Oscillations with Pressure and Velocity Coupling in Solid Propellant Rocket - Combustion Science and Technology 1970, Vol 2, pp. 179-201.

Table 1 Smoke/Light Attenuation of Particle Clouds

1 Particle Density	2 Particle Diameter	3 Extinction Coefficient*	4 Corrected Coefficient**
2	2.5	2.8	1.4
3	2.2	2.2	0.71
5	1.0	4.0	0.8
7	0.8	3.5	0.5
18	0.52	1.6	0.03
18	1.0	4.0	0.22
2	1.0	4.0	2.0

Refractive index of particles = 1.3 Incident wavelength = 0.52 μ

(* Coefficient for single particle, ** Total coefficient for cloud of constant mass/unit volume of gas)

Table 2 List of Particulate Additives Examined

Additive Type/Grade	Density g/cm^3	Melting Point °C	Size Range Microns	Frequency Range for Maximum Attenuation KHz	Suitability
1. Boron Nitride					
SRG 325	2.27	3000	2-15	20.37-0.36	Yes
SHP 325			2-7	20.37-1.66	Yes
2. Boron Carbide					
G1200	2.52	2350	2-5	18.35-2.94	Yes
3. Calcium Oxide					
Std	2.92	2614	2-12	15.83-0.44	No A
Select			1-12	63.35-0.44	No A
4. Silicon Carbide					
F800			5-8	2.29-0.89	Yes
F1000	3.22	2700	3.5-5.5	4.69-1.89	Yes
F1200			2.5-3.5	9.19-4.69	Yes
F1500			1-2.5	57.45-9.19	Yes
5. Magnesium Oxide					
Maglite D	3.58	2852	-	-	No S
Darlington LT			4-10	3.23-0.52	No A
6. Aluminium Oxide					
MA95			3-8	5.17-0.73	Yes
MA250	3.97	2015	1-3	46.59-5.17	Yes
F1200			2.5-3.5	7.45-3.80	Yes
7. Titanium					
Boride	4.52	2900	5-25	1.63-0.07	Yes
8. Zirconium					
Orthosilicate	4.56	2550			
Opazon Extra			1-2.5	40.57-6.49	Yes
Superzon			1-2	40.57-10.14	Yes
9. Titanium					
Carbide	4.93	3140	2.5-20	6.00-0.09	Yes
10. Chromium					
Oxide	5.21	2266	-	-	No A
11. Titanium					
Nitride	5.22	2930	1-20	35.44-0.09	Yes
12. Zirconium					
Oxide	5.6	2715			
ZS2			1-4	33.03-2.06	No S
Zedox 5			1-4	33.03-2.06	Yes
Zedox 10			2-5	8.25-1.32	Yes
13. Zirconium					
Boride	6.09	3000	2-8	7.59-0.47	Yes
14. Chromium					
Boride	6.17	2760	4-12	1.87-0.21	Yes
15. Lanthanum					
Oxide	6.51	2315	4-12	1.77-0.19	Yes
16. Zirconium					
Carbide	6.73	3540	1-8	27.48-0.43	Yes
17. Cerium					
Oxide	7.13	2600	1-5	25.95-1.04	Yes
18. Neodymium					
Oxide	7.24	2272	5-20	1.02-0.06	Yes
19. Niobium					
Carbide	7.82	3500	1-10	23.65-0.24	Yes
20. Niobium	8.57	2468	4-35	1.35-0.02	Yes
21. Molybdenum					
Carbide	9.18	2687	1-5	20.15-0.81	No A
22. Hafnium					
Oxide	9.68	2768	-	-	Yes
23. Molybdenum					
4 μ			2-5	4.52-0.72	Yes
1-5 μ	10.22	2617	1-6	18.10-0.50	No SA
2 μ			0.5-3	72.41-2.01	No S
24. Tantalum					
Carbide	13.9	3880	1-5	13.31-0.53	Yes
25. Tungsten					
Carbide	15.63	2870	1-5	11.84-0.47	No A
26. Tantalum	16.60	2996	1-10	11.14-0.11	Yes
27. Tungsten					
WF 200			0.5-3.5	38.24-0.78	No SA
WF 150	19.35	3410	0.5-3.5	38.24-0.78	No SA
WP 80			1.5-11	4.24-0.08	Yes
WP 50			1.5-7	4.24-0.19	Yes

S - Stability Problems of Powders in Contact with Propellant
A - Aggregates

Table 3 Comparison of Various Acoustic Instability Suppression Systems

Test No	Suppressor	Additive Size Density Function	Frequency of max Attenuation	Frequency of 1st Tangential Mode	Results
		150 mm 4 slot Radial Normal Operating Pressure 40 bar/6 s			
1	None	-	-	10.4—4.0 KHz	Gross irregularity. 500 bar transducer destroyed.
2	Cruciform Resonance Rod	-	-	10.4—4.0 KHz	Fairly Stable
3	Hypalon Radial Resonance Flaps	-	-	10.4—4.0 KHz	Fairly Stable
4	1.4% Silicon Carbide 3 μ	2.9	6.4 KHz	10.4—4.0 KHz	Stable
5	1.4% Molybdenum 4 μ	16.3	1.13 KHz	10.4—4.0 KHz	Gross Irregularity. 500 bar transducer destroyed.

Table 4 Effect of Propellant Type

Type	Burning Rate mm/s	% Silicon Carbide	Acoustic Combustion Stability	
1	4 at 25 b	0	Highly Unstable	400% overpressure
		0.7	" "	250% overpressure
		1.4	Fairly Stable	No overpressure
		2.1	Stable	No overpressure
2	8 at 50 b	0	Highly Unstable	> 250% overpressure
		0.7	" "	200% overpressure
		1.4	Fairly Stable	10% overpressure
		2.1	Stable	No overpressure
3	24 at 120 b	0	Unstable	50% overpressure
		0.7	Fairly Stable	No overpressure
		1.4	Stable	No overpressure
		2.1	Stable	" "

Table 5 Effect of Silicon Carbide on Various Test Vehicles

	Motor Type	1st Tangential Acoustic Mode Frequency KHz	Optimum Damping Frequency 3μ SiC KHz	Results
1	150 mm dia 4 slot Radial L	10.4—4.0	6.4	Stable
2	150 mm dia 6 slot Radial L	8.0—4.0	6.4	Stable
3	127 mm dia 4 slot Radial C	23.4—5.0	6.4	Stable
4	100 mm dia 8 slot Radial L	33.0—6.1	6.4	Stable
5	195 mm dia 4 slot Radial C	8.4—3.1	6.4	Stable

Table 6 Effect of Different Particle Sized Refractories

Test No	Additive	Additive Size Micron	% Additive in Propellant	Results
1	None	-	0	Highly Unstable 50% overpressure
2	Silicon Carbide	6.5	2.1	Stable
3	" "	6.5	1.4	Stable
4	" "	6.5	0.7	Slight Instability giving lower pressure
5	" "	4.5	2.1	Stable
6	" "	4.5	1.4	Slight Initial Instability then Stable
7	" "	4.5	0.7	Slight Instability giving lower pressure
8	" "	3.0	2.1	Stable
9	" "	3.0	1.4	Stable
10	" "	3.0	0.7	Slight Instability giving lower pressure
11	" "	2.0	2.1	Stable
12	" "	2.0	1.4	Stable
13	" "	2.0	0.7	Slight Instability giving lower pressure
14	Zirconia	2.8	2.1	Stable
15	"	2.8	1.4	Stable
16	"	2.8	0.7	Slight Instability giving lower pressure
17	"	1.1	2.1	Stable
18	"	1.1	1.4	Stable
19	"	1.1	0.7	Slight Instability giving lower pressure

Table 7 Effect On Stability of Various Amounts of Aluminium

Test No	Additive	% Additive in Propellant	Results
1	None	0	Highly Unstable 50% overpressure
2	Aluminium	2.1	Stable
3	"	1.4	Slight Instability giving lower pressure
4	"	0.7	Instability causing slight overpressure

Table 8 Effect of Propellant Additives on Rocket Exhaust Smoke

Test Motor: 150 mm SCB burning for 30 seconds.

Additive Type/Size	% Additive in Propellant	Smoke/Light Attenuation Through Exhaust Axis dB
None	None	0.5
3μ Silicon Carbide	0.35	0.86
	0.7	0.88
	1.0	1.07
	1.4	1.25
Aluminium Powder	1.4	5.0

FIG. 1. ATTENUATION OF VISIBLE LIGHT BY PARTICLE CLOUDS.

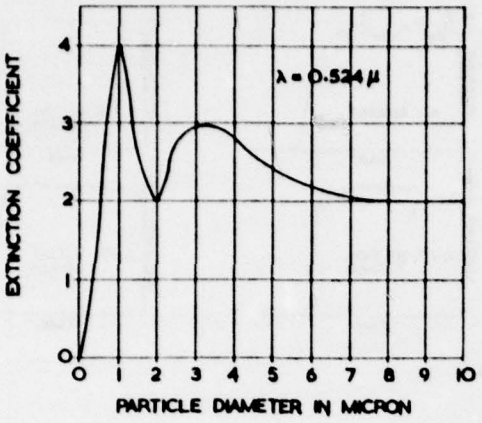

FIG. 2 LIGHT SCATTERING COEFFICIENT Ks DEPENDENCE ON PARTICLE SIZE AND INCIDENT WAVELENGTH.

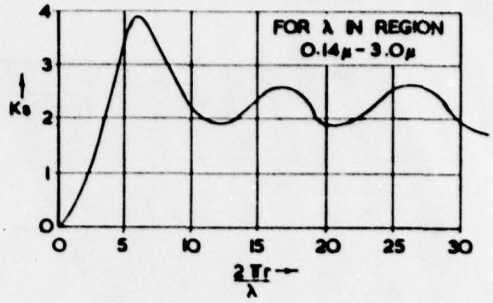

FIG. 3. OPTIMUM PARTICLE SIZE FOR ACOUSTIC ATTENUATION AGAINST FREQUENCY FOR VARIOUS PARTICLE DENSITIES.

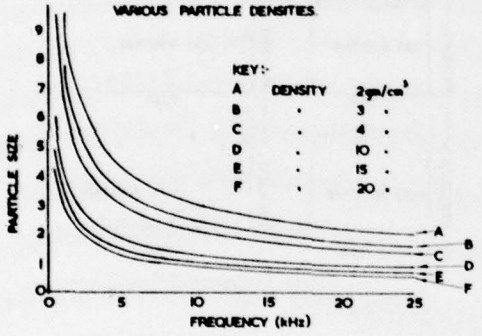

FIG. 4 ACOUSTIC DAMPING SENSITIVITY TO PARTICLE SIZE WITH INCREASING DENSITY

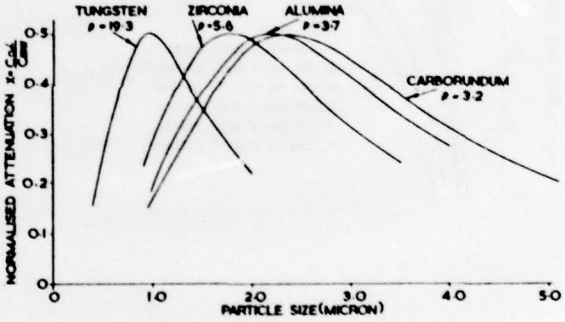

FIG. 5 ACOUSTIC DAMPING SENSITIVITY TO PARTICLE SIZE RANGE WITH HIGHER FREQUENCY.
NORMALISED ATTENUATION Vs PARTICLE SIZE

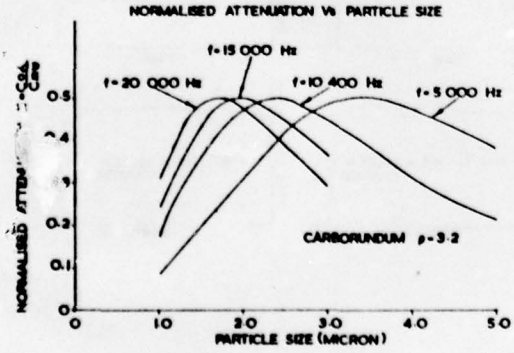

FIG. 6 150mm 4 SLOT RADIAL DECAY OF QUASI GAS MODES.

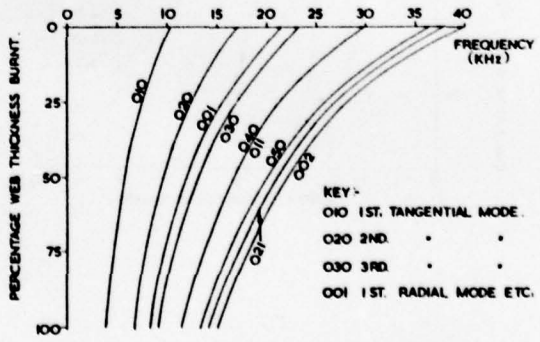

FIG 7 PSEUDO THREE DIMENSIONAL PLOT OF 150 mm 4 SLOT RADIAL FIRING

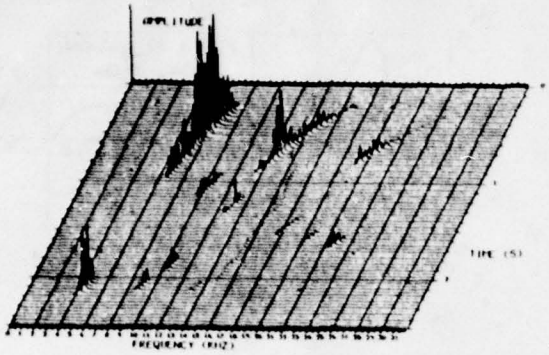

FIG. 8 NORMAL TEST FIRING LOW FREQUENCY SENSITIVE PRESSURE RECORDS.

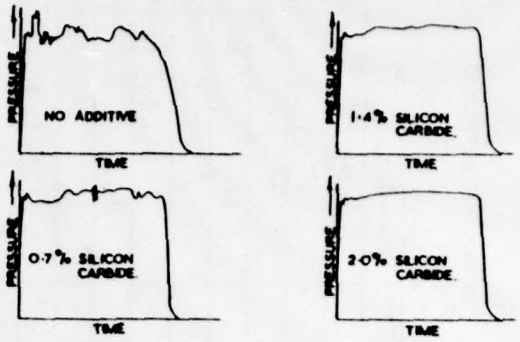

FIG. 9 DECAY OF 1st. TANGENTIAL QUASI-GAS MODES FOR VARIOUS MOTORS.

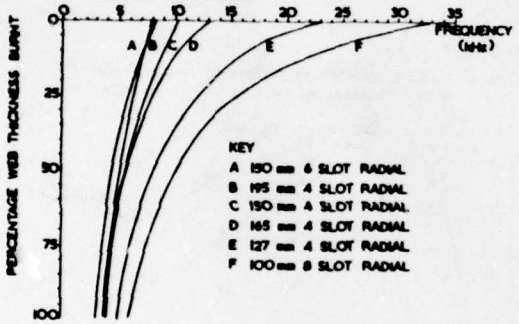

FIG. 10. EFFECT OF ADDITIVES ON UNSTABLE MOTORS.

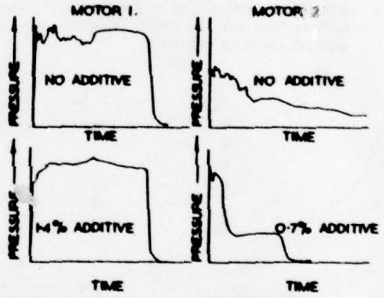

FIG. 11 PARTICLE SIZE DISTRIBUTION FOR VARYING SIZES OF SILICON CARBIDE.

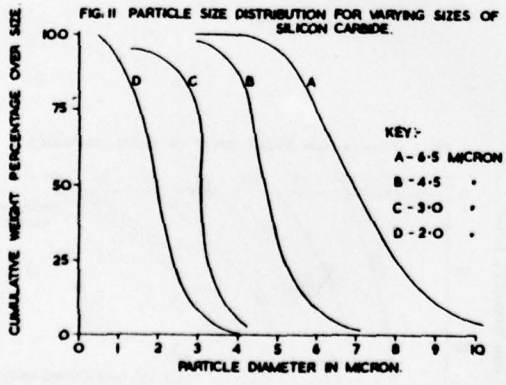

FIG. 12 EFFECT OF DIFFERENT PARTICLE SIZED SILICON CARBIDE.

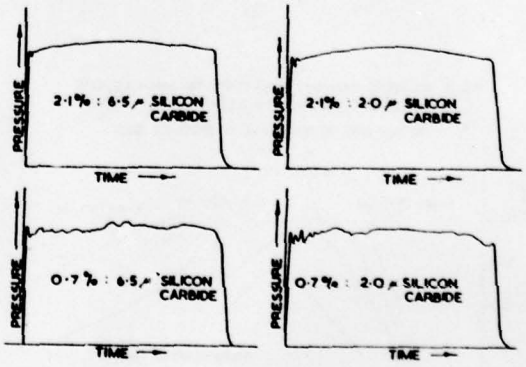

DISCUSSION

R.L.Derr, Naval Weapons Centre, US

Have you collected and measured the mass size distribution of solid combustion residue and have you compared this data to the mass size distribution of the solid particle additives to the propellant?

Author's Reply

Perhaps I should emphasise that the additives were very carefully examined prior to incorporation into the propellant. A variety of techniques were used to examine size and shape. For example following size measurement the additive sample was subjected to ultrasonic vibration and rechecked to ensure there was no susceptibility to aggregation or agglomeration in the additive to be used.

Samples of additive were collected from within the combustion chamber and the exhaust plume. These were examined microscopically and were found, particularly in the case of silicon carbide, to be identical in shape and size to the initial condition.

MATERIAL PROBLEMS IN JET VANE THRUST VECTOR CONTROL SYSTEMS*

by
D. Kampa
A. Weiß
R.H. Schmucker

Bayern - Chemie
Solid Rocket Company
P.O. Box 220
8012 Ottobrunn
West-Germany

SUMMARY

For highly manoeuverable tactical missiles, a thrust vector control system with high side forces is essential: of the various methods, jet vane systems offer maximum jet deflection angles, but high heat flux and particle erosion, especially at high angles of attack, lead to material problems which can only be overcome by careful material selection and proper shaping of the geometry by means of suitable heat transfer and flow field prediction procedures. For two different HTPB-composite propellants with low (1%) and high (16-18%) aluminum loading, materials are tested and the experimental results with respect to thermal resistance are applied for an experimental jet vane thrust vector control system.

1. INTRODUCTION

The realization of many present day and future missile missions necessitates an active control system. The control force and momentum generated by such a system are required to accomplish specified trajectory changes compared to the undisturbed vehicle motion due to gravity and atmospheric effects; in addition, this device has to balance external disturbances such as wind and pressure forces and missile inherent forces which are the result of a non-accurate missile arrangement and non-nominal operation.

Of the various means for active trajectory correction, a thrust vector control system represents the only principle independent of missile external forces so that this method is operative during every phase of the mission propelled phase. By this method, a thrust vector component normal to the main thrust axis is generated. In case of a solid rocket this can be realized by three different means, movable nozzle, secondary injection and mechanical jet deflection. Considering the chamber pressure of typical high-performance tactical missiles which amounts to approximately 15o to 200 bar, these systems can be classified as listed in Table 1.

Although such a comparison due to the subjective character of the valuation has to be examined with some caution, it appears that mechanical jet deflection devices are characterized by a low actuation torque, low response interval and, in case of a jet vane system, by a small installation envelope. The main aspect, the thrust vector angle capability, shows significant advantages compared to the other systems so that this method is especially attractive for high manoeuverability during the initial mission phase.

On the other hand, some disadvantages and problems are also connected with these systems,performance loss and material compatibility with exhaust jet.

Of the various mechanical jet deflector systems, jet vanes offer the possibility of roll control - in case of a single nozzle arrangement a jet vane device represents the only practical thrust vector control system to perform such a task - , ease of combination with an aerodynamic control mechanism and extreme thrust vector angle. In addition, by the arrangement character of the system, during the mission phase subsequent to the launch when aerodynamic forces are sufficient for control purposes a separation of this device is possible thus eliminating performance loss, actuation power and reducing inert weight.

Jet vane thrust vector control systems were firstly used almost 5o years ago by R.H. Goddard. More than two decades later, the experience gained by the developmental work and operational use during World War II was applied to rockets like Redstone, Sergeant and Pershing. Due to the material problems when using high energy aluminized propellants and the advance of other thrust vetor systems, jet vane devices were further studied only on a low effort level. New mission concepts and the above mentioned system capabilities presently result in a discussion of the application of jet vane thrust vector control systems especially for start phase trajectory control.

2. THERMAL AND MECHANICAL JET VANE LOAD EFFECTS ON MATERIAL SELECTION

The design of jet vanes requires the selection of a suitable material to withstand the thermal and mechanical loads and the proper shaping of the geometry in order to maximize the side thrust with minimum performance losses while maintaining the structural rigidity of the blades during operation. Both requirements closely interrelate but in opposite directions,since a material with a lower strength at elevated temperature results in a thicker vane and, hence, more unfavourable aerodynamic characteristics.

---

*This work was sponsered by the Ministry of Defense/Government Procurement Office of the Federal Republic of Germany.

Table 1 Comparison of Solid Rocket Motor Thrust Vector Control Systems (Ref. 1,6,9)

System	Method	Maximum thrust vector deflection (°)	Axial thrust loss (%)	Actuation torque	Disadvantage	Status and application
Movable nozzle	Flexible joint	15	Cosine	Large	Joint thermal protection and pivot point floatation.	State of the art; Polaris C3.
	Fluid bearing	25	Cosine	Low	Bearing thermal protection and pivot point floatation.	State of the art; Trident I (C4).
	Ball and socket/ gimbal	25	Cosine	Large/ Low	Sealing and erosion at splitline.	State of the art; Minuteman, anti-tank missiles.
Secondary injection	Liquid injection	4	Augmen-tation		Low thrust de-flection; high system weight; long term stor-age of liquid.	State of the art; Polaris, Minute-man, Titan, Sprint.
	Hot gas injection	7-12	Augmen-tation		Hot gas valve thermal loads; no precise veloc-ity control possible.	Experimental rockets.
Mechanical jet deflection	Jet vane	30	3-5% w/o actuation; propor-tional to 50-100% of side thrust.	Low	Thermal loads; limitation to short burning time or low-temperature propellant.	Operational for Pershing, Sergeant, Talos.
	Jetevator	20-30	0-10% w/o actuation; see above.	Low	System envelope; thermal loads see above.	Operational for Polaris A1, anti-tank missiles.
	Spoiler	1o-20	Proportional to side thrust.	Low	System envelope; thermal loads see above.	Operational for anti-tank missiles.

The aerodynamic design of the vane geometry can be performed with reasonable accuracy on the basis of supersonic flow theory with boundary layer correction (Ref. 5). Experiments show that the deviations between theoretical and test data are small (Ref. 2,3). Since the vane geometry is determined by the material properties and loads, the aerodynamic shape can only be varied within certain limits so that this part of the vane design is of secondary importance.

The behaviour of the vane material in the exhaust jet according to the mechanical and thermal properties can hardly be predicted with sufficient reliability necessitating an experimental material selection.

2.1 Propellant and Combustion Product Data

The kind of thermal loads is characterized by the energetic properties of the propellant and the thermodynamic gas data. In Table 2, for three different HTPB (hydroxyl-

Table 2 Data of HTPB-Composite and Double-Base Propellants

		HTPB-composite propellant			Double-base propellant
		A	B	C	
Aluminum	(weight-%)	18	16	1	0
Oxidizer	(weight-%)	66	68	83	48/41-Nc/Ng
Binder&catalyst	(weight-%)	16	16	16	11
Combustion temperature	(K)	3240	3230	2820	2640
Characteristic velocity	(m/s)	1453	1575	1509	1447
Specific impulse (70:1)	(s)	241	261	244	233
Density	(kg/m^3)	1820	1720	1680	1620
Nozzle exit gas temperature (70:1)	(K)	2020	1850	1315	1180
Solid particle fraction	(weight-%)	34	30	2	0

terminated polybutadien)-composite propellants with various aluminum loadings the respective data are presented; for comparison, the data of a conventional double-base propellant are also included.

The composite propellants A and B represent high energy compositions with aluminum fractions of 16 to 18%, the gas temperature exceeds 3200 K and the weight fraction of solid particles in the exhaust jet range from 30 to 34%. These data are typical for propellants imposing maximum thermal and erosive loads onto the vane material.

Composition C describes a propellant with negligible primary smoke, the gas temperature amounts to roughly 2800 K.

2.2 Physical Properties of Jet Vane Materials

To withstand such a high-temperature environment, a material with a corresponding high melting point must be selected. Three material types are available, metals, ceramics such as oxides, borides and carbides and graphite and carbon products; these can either be used as pure construction material or composite material when a base material of sufficient strength is covered by a thin layer of a thermal and erosive resistant material. Due to the high gas temperature, for practical purposes only materials with a melting point exceeding approximately 2500 K are applicable. In Table 3, the mechanical and thermal properties of various refractory material are presented. The thermal data of the ceramics depend very much on the compression of the base material, in case of graphite and carbon the

Table 3 Mechanical and Thermal Properties of Various Refractory Jet Vane Materials* (Ref. 4,7,8,9)

Material	Chem. symbol	Melting point (K)	Density	Linear coeff. of thermal expansion (10^{-6}/K)	Thermal conductivity (W/mK)	Tensile strength (N/mm²)	Specific heat (kJ/kgK)	Modulus of elasticity (10kN/mm²)
Metals								
High strength steel		1800	8000	7.1	25.1	1500	0.48	20
Molybdenum	Mo	2890	10200	5.3	142.0		0.25	
Tantalum	Ta	3270	16600	21.7	54.4		0.15	
Rhenium	Re	3440	20500					
Tungsten	W	3680	19300	4.6	125.0	800	0.14	41
Ceramics								
Boroncarbide	B_4C	2460	2500	3.1-6.5	29	350		45
Zircona	ZrO_2	2600	5800	5.0-11.6	1.7-2.7	190-300	0.42-0.75	16-20
Siliconcarbide	SiC	2300-2760	3200	5.0-5.9	41-100	860		39-48
Tungstencarbide	WC	2600-2780	15600	5.2-7.3	117-197	555	0.85	72
Boronnitride	BN	2400-3000	3450	13.3				
Titaniumboride	TiB_2	2850-2980	4500	4.6-7.4	29-54	600		37-42
Zirconiumboride	ZrB_2	2990-3060	6000	6.8-7.5	23-44	200		35
Titaniumcarbide	TiC	3090-3160	4900	3.4-7.7	25	240-400	0.56-0.80	32-46
Tantalumboride	TaB_2	3100-3150	12000	5.1-5.7	12-19			26
Hafniumboride	HfB_2	3200-3250	11000	5.4	58			
Zirconiumcarbide	ZrC	3330-3540	6500	6.7	20-42	280-400		35-38
Hafniumcarbide	HfC	3740-4040	12300	6.5	12-29			35-40
Carbon/Graphite **	C	3900						
Polycristalline graphite			1900	6.0	90	85	0.75	
Pyrolytic			2200	1/25	380/2-8	240		
Carbon/carbon			1700	0.7/6.5	250/100	60-150		2.5-3.5
Glass-like carbon			1500	2.7		90		3.0

* All values shown are for room-temperature properties.
** Typical properties, not design properties. Values separated by a slash apply to the two main orientations.

properties can be varied over a wide range by changing the processing methods.

2.3 Jet Vane Load Characteristics

The jet vane loads can be classified into thermal and mechanical loads; the former affect the structural integrity during the first several 100 ms of operation while the latter control the long term rigidity.

2.3.1 Thermal Load

Due to the initial temperature difference between exhaust gas and vane material a

nonsteady heating occurs. As a consequence of the heat transfer coefficient, which amounts due to the high gas velocity and the particle loading to an order of magnitude of several kW/m^2K, the surface temperature rises within a few 100 ms from ambient to nearly stagnation temperature. The temperature increase at the vane axis occurs, depending on the vane material and the blade thickness, approximately half a second later.

The large temperture differences within the material result in a thermal shock so that the tensions due to thermal expansion may destroy the blade. This thermal shock sensitivity, which can be roughly described by the product of modulus of elasticity, thermal expansion coefficient and temperature difference, divided by material strength represents an important criterion for the applicability of materials for jet vane systems.

2.3.2 Mechanical Load

Mechanical loads result from vane lift and drag. The combined load corresponds approximately to the attained side thrust so that at high angles of attack of the vane severe loads occur. Therefore, in spite of the unfavourable aerodynamic characteristics, for the realization of high thrust vector angles, relatively thick jet vane blades are required.

Abrasion by particles represents an important effect when large weight fractions of solid particles in the exhaust jet occur. Using sandblast experiments as basis, it can be concluded that particle density and material strength play an important role so that, especially shortly prior to the end of the burning time, significant material erosion may happen.

3. EXPERIMENTAL MATERIAL EVALUATION

To select a suitable material for a jet vane system, an experimental material evaluation program was performed. A portion of this test program was conducted in close cooperation with Messerschmitt-Bölkow-Blohm (MBB), material laboratory (Ref. 7).

3.1 Test Apparatus

Material testing was accomplished with a small 0.11 m diameter rocket. The relevant data are listed in Table 4; in Fig. 1, a photograph of the rocket at the test stand is

Table 4 Data of Jet Vane Material Test Engine

Length of grain		1.141 m	1.141 m
Diameter of grain		0.110 m	0.110 m
Propellant mass		16.3 kg	14.6 kg
Trust -	average	10,200 N	15,200 N
	maximum	14,000 N	25,800 N
Chamber pressure -	average	118 bar	144 bar
	maximum	153 bar	238 bar
Burning time		3.59 s	2.40 s
Propellant type		HTPB-composite A	B

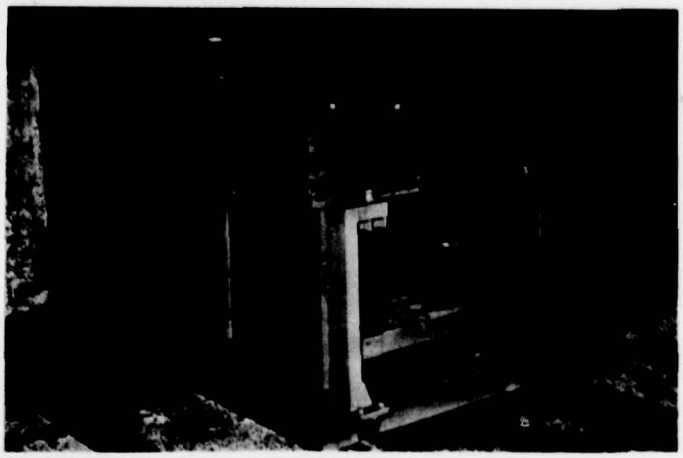

Fig. 1 Rocket Engine for Jet Vane Material Testing

presented. In Fig. 2, the arrangement of the vane material test specimen is to be seen; the blades penetrate roughly 3 cm into the exhaust jet.

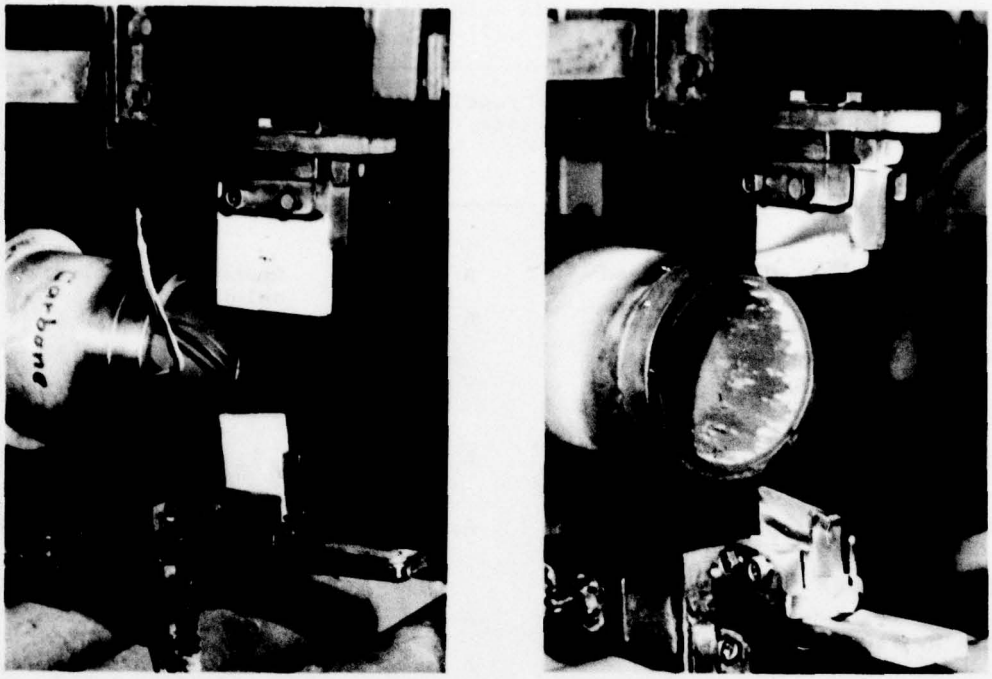

Fig. 2 Arrangement of Jet Vane Material Test Specimen Before and After Testing

3.2 Material Tests with Highly Aluminized (16-18%) Composite Propellant

Most emphasis was placed upon the material evaluation for a highly aluminized composite propellant. A number of tests using some of the materials listed in Table 3 were performed. These are classified in Table 5, which comprises also the respective test conditions and the results.

The test specimens made of pure ceramics, glass, composite ceramics and coated glass were destroyed due to inadequate thermal shock resistance. In Fig. 3, as an example for this phenomenon, the disintegration of a TiC jet vane is presented. Little improvement

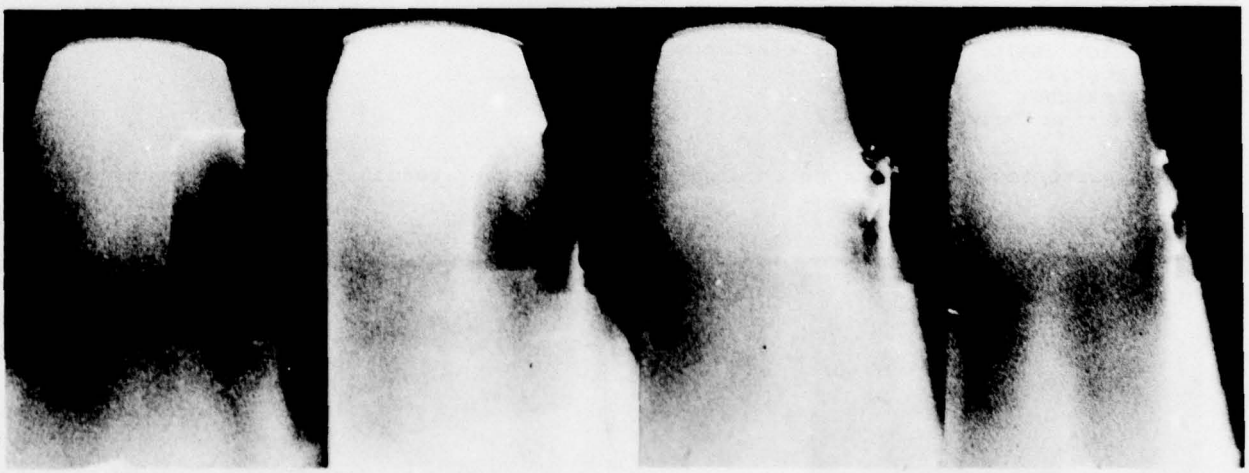

Operation time

20 ms 70 ms 260 ms 1500 ms

Fig. 3 Disintegration of TiC Jet Vane Material (Ref. 7)

seems to be possible (Ref. 7). Pure carbon and impregnated carbon were nearly completely destroyed. This results from the soft surface structure which cannot withstand the severe particle erosion load. Fig. 4 shows a jet vane before and after testing, made of glass-like carbon. Using a protective layer to improve the surface hardness, the efficiency depends on the compatibility between base material and the layer and, if necessary, the primer. Graphite coated with tungsten and a reinforced tip shows promising results; in all other cases, a separation of the layer with subsequent destruction of the base material occurred

The best results were obtained with pure tungsten. Here, only little erosion at the tip was measured, as seen in Fig. 5, in which a tungsten jet vane before and after test-

Table 5 Test Results of Jet Vane Materials with 16-18%-Aluminum HTPB Composite Propellant (Including the Results of Ref. 7)

Material	Propellant type	Angle of attack (°)	Results
Pure Ceramics and glas:			
ZrO_2, TiB_2, TiC, B_4C, SiC, compressed at elevated temperature.	A	0	Destroyed by thermal shock; ablated.
Glass, glass with polished surface.	B	0	
Composite ceramics and coated glass:			
TiC with Ni, TiC with Ni/Mo_2O, ZrB_2/SiC/C, Mo/ZrO_2, compressed at elevated temperature.	A	0	Destroyed by thermal shock; ablated.
Glass with ZrO_2-layer.	A	0	
Carbon:			
Carbon/carbon, carbon impregnated with SiC.	A,B	0	Nearly completely ablated.
Coated graphite/carbon:			
Graphite (R,E)* with W-layer; carbon/carbon with W, TaC, ZrO_2, SiC-layer.	A	0	Destroyed, ablated.
Graphite (EK 76**, SE 18, FE 49***) with W-layer, reinforced tip.	A	0	Little erosion; W-layer partially removed.
Graphite (Ellor 5890****) with W-layer, reinforced tip.	A	0	Negligible erosion.
Metals:			
High strength steel, coated with ZrO_2, Al_2O_3, spinel-layer; Mo, coated with ZrO_2-layer.	A,B	0	Ablated.
W with metallic binder (Ni, Cu) and carbonized surface.	A	0	Severely ablated.
W, sintered and as sheet metal; W coated with B, ZrO_2-layer	A	0,10	Nearly negligible erosion at tip; layer partially abrased.
W, coated with B-layer (20µ)	A	15,20	little erosion; severely distorred.
W, coated with B-layer (40µ)	A	15	Negligible distortion.

*R: rocket engine quality; E: electrode quality.
**Ringsdorff.
***Schunk&Ebe.
****Deutsche Carbone.

ing is presented. Deformations at high angles of attack result from severe heating and

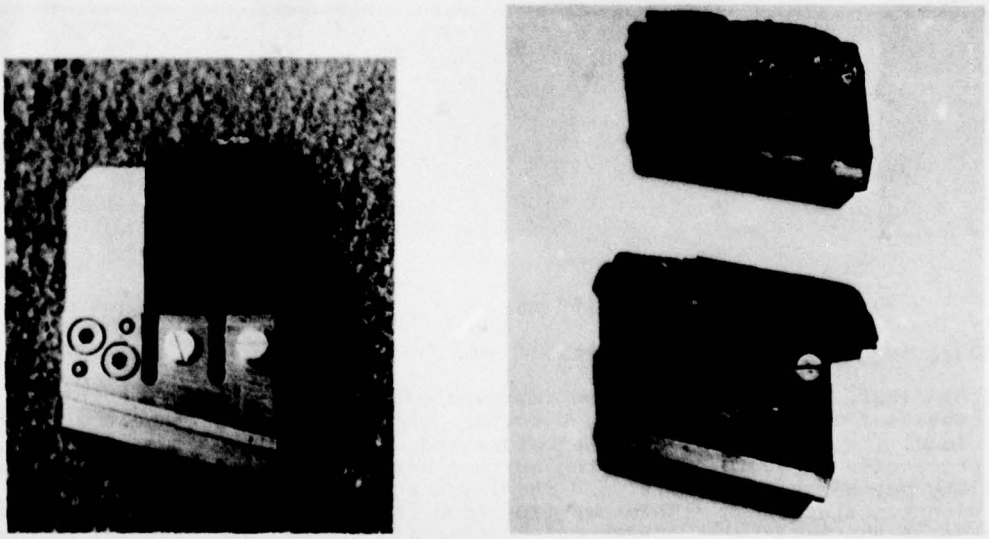

Fig. 4 Erosion and Ablation of Carbon (Glass-like Carbon) Jet Vane Material

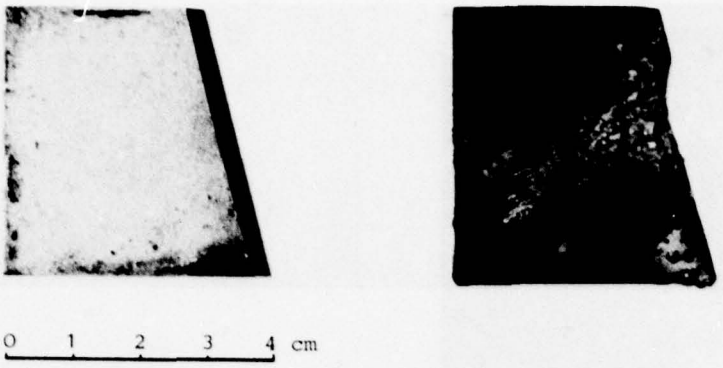

Fig. 5 Tungsten Jet Vane Before and After Testing

high aerodynamic loads, as shown in Fig. 6, and were avoided by using a protective layer so that the core temperature remains lower during the later part of operation.

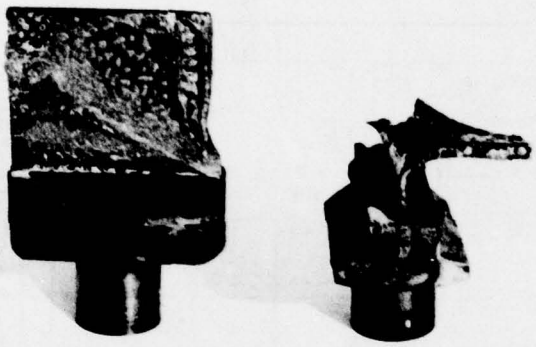

Fig. 6 Deformation of Tungsten Jet Vane at 15° Angle of Attack

The experiments indicate that pure tungsten coated with a thin layer of a low thermal conductivity material yields the best jet vane material. Sufficient mechanical strength can be achieved by designing the vane as beam of uniform rigidity.

Specifically selected graphite with a surface layer of tungsten and a reinforcement at the tip show promising results, at least at zero angle of attack, but the data currently available are not sufficient to allow further conclusions. Material brittleness may yield additional handling and operational problems.

3.3 Material Tests with Low Aluminized (18) Composite Propellant

Only a few tests with low aluminum loading composite propellant were performed. Molybdenum and tungsten did not show any erosion or ablation; carbon/carbon demonstrated little erosion at the tip. At high angles of attack, similar to the tests with high aluminum loading propellant, problems with material strength occured, necessitating proper vane geometry shaping and surface coatings to reduce the temperature rise at the blade core. A layer of zirconia was sufficient to resolve this problem. This material combination was applied for an experimental jet vane thrust vector control system.

4. EXPERIMENTAL JET VANE THRUST VECTOR CONTROL SYSTEM

For verification of the jet vane concept, an experimental engine with a jet vane thrust vector control system usind a propellant with low primary smoke, the composition C of Table 2, is presently being developed. In Fig.7, a photograph of the engine in the test-bench with the hot gas actuation system and the associated instrumentation is shown; Fig. 8 comprises a schematic cross sectional drawing of the nozzle and hot gas pipe with the jet vane arrangement and the actuation devices for fins and jet vanes. In Table 6, the important data of the engine are listed.

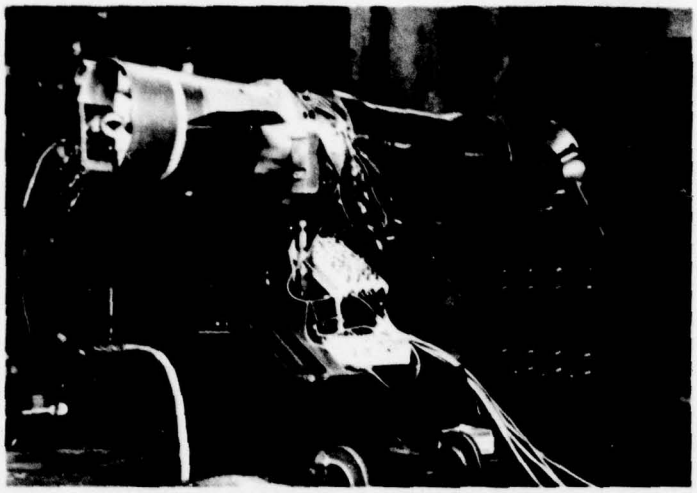

Fig. 7 Experimental Engine for Jet Vane Thrust Vector Control System Testing

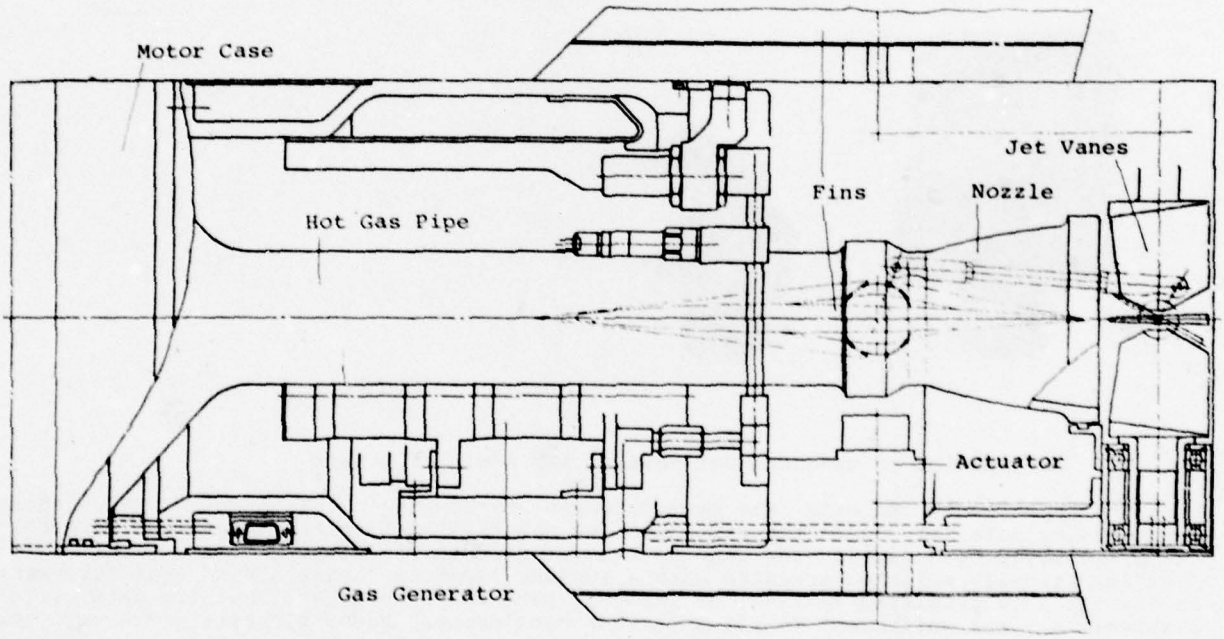

Fig. 8 Schematic Cross Section of Jet Vane and Actuation System Arrangement

Table 6 Data of Experimental Jet Vane Thrust Vector Control Engine

Diameter	0.24 m
Length	1.15 m
Propellant mass	25.7 kg
Thrust (average)	20,000 N
Pressure (average)	192 bar
Burning time	3.7 s
Propellant type	HTPB composite C

During the initial test program, a material and geometry evaluation was performed indicating that heat conduction into the vane bearing plays an important role on the strength of the vane. Fig. 9 shows an example of vane deformation with subsequent burning of the mounting support. This problem was overcome by proper shaping of vane and bearing and a coating layer. In Fig. 10, a drawing of the vane is presented; the size approximates 0.05 x 0.05 m. Another method for prevention of excessive heating of the blade, cooling by a small nitrogen mass flow, was also successfully tested.

In several operational tests, the jet vane thrust vector control system proved its reliability. In Fig. 11, the jet vanes before and after a test firing are shown. Little effect on the jet vane conditions is noticed deonstrating that this thrust vetor control system can be used for flight testing.

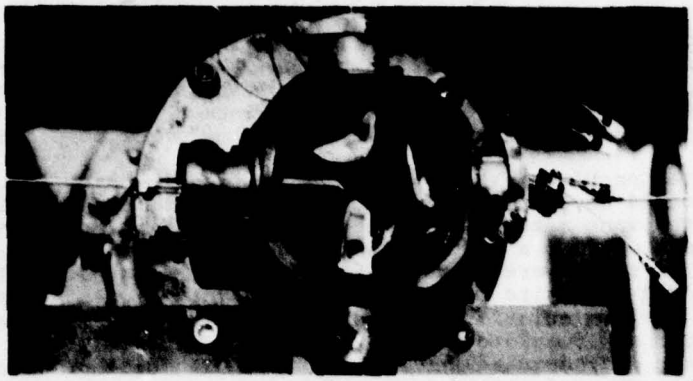

Fig. 9 Jet Vane Deformation at High Angle of Attack

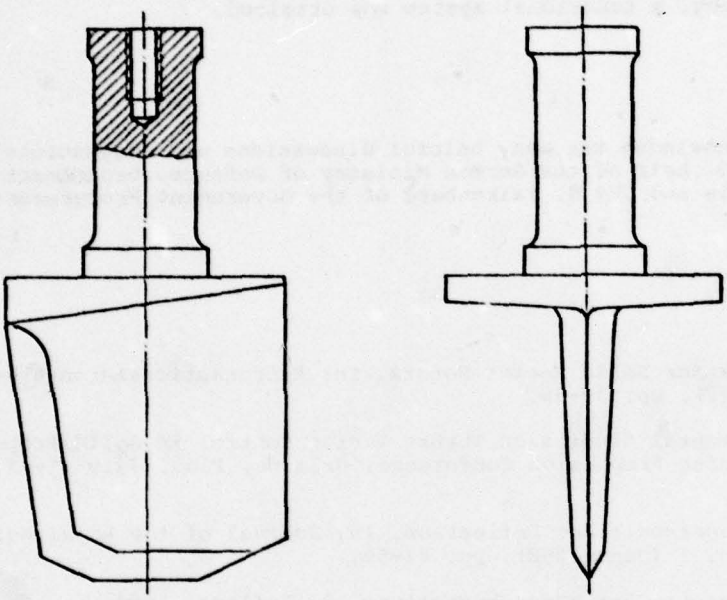

Fig. 10 Jet Vane Blade of Experimental System

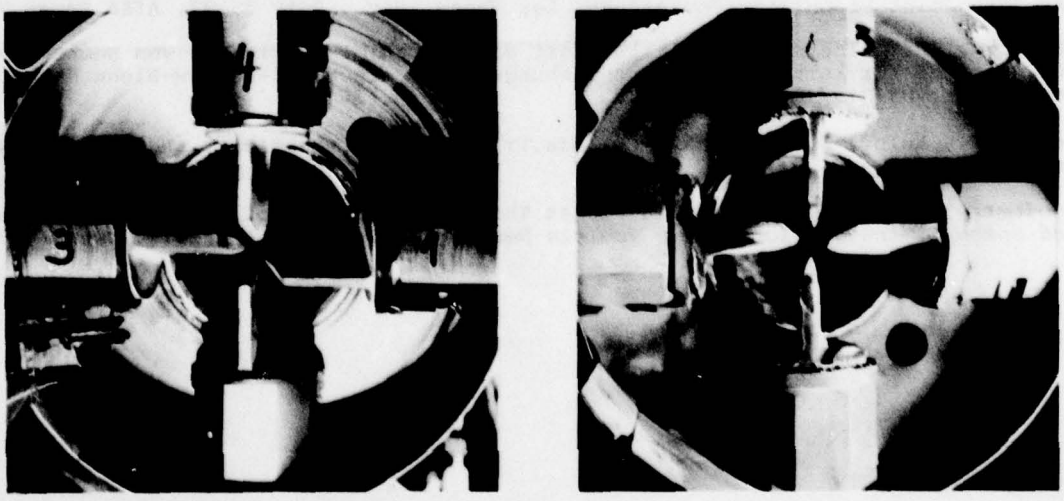

Fig. 11 Experimental Jet Vane Thrust Vector Control System Before and After Testing

5. CONCLUSION

For missions requiring high manoeuverablity during the initial flight phase, a jet vane thrust vector control system offers advantages compared to the other thrust vector systems available, which result from the possibility of roll control, high thrust vector angle, low actuation power, small installation envelope and ease of integration with the aerodynamic control system. In addition, a separation of the vane system after completion of the task is easily performed.

On the other hand, severe material problems exist, which result from the high temperature, high velocity and particle loaded environment, requiring an experimental material selection. To withstand these loads the vane material must show a high melting point, a sufficient strength at elevated temperature and a thermal shock sensitivity.

Five different refractory material types were studied using a highly aluminized HTPB-composite propellant. Of these, pure and composite ceramics exhibited insufficient thermal shock resistance, pure carbon showed extreme ablation and erosion. Specifically selected graphite, covered with a tungsten layer and reinforced by a tip of this material, performed well, but the data available are not adequate for systems' use. The best results were obtained with pure tungsten vanes, covered with a layer of low thermal conductivity. to maintain structural rigidity.

Tests with low aluminum loading propellants showed less severe problems so that molybdenum was sufficient. The results were applied to an experimental thrust vector control system with a low primary smoke HTPB composite propellant. By proper vane shaping, heat shielding and surface coating, a functional system was attained.

ACKNOWLEDGEMENT

The authors gratefully acknowledge the many helpful discussions und suggestions of Mr. MRat H. Walder and Mr. ORR O. Wolf of the German Ministry of Defence, Department RÜ VII 3, Mr. RDir Dr. J.K. Weis and ORR H. Falkenburg of the Government Procurement Office, Department WM IV 3.

REFERENCES

[1] Edwards, G.: The Outlook for Solid Rocket Motors. In: Astronautics&Aeronautics, Vol. 15, No. 9 (Sept. 1977), pp. 30-38.

[2] El-Sharkawy, A.: Experimental Studies on Thrust Vector Control in Solid Propellant Rockets. AIAA/SAE 13th Joint Propulsion Conference, Orlando, Fla., July 11-13, 1977, AIAA Paper 77-989.

[3] Fraser, R., Rowe, P.: Supersonic Jet Deflection. In: Journal of the Royal Aeronautical Society, Vol. 2, No. 1 (Jan. 1958), pp. 43-59.

[4] Grigull, U.: Die Grundgesetze der Wärmeübertragung. 3. Auflage, 1963.

[5] Krasnow, N. (Ed.): Rocket Aerodynamics. "Vysshavashkola" Press, Moskau, 1968, NASA TT-F-601, June 1971.

[6] Lloyd, R.: A Review of Thrust Vector Control Systems for Tactical Missiles. AIAA/SAE 14th Joint Propulsion Conference, Las Vegas, Nev., July 25-27, AIAA Paper 78-1071

[7] Meistring, R.: Thermische Belastbarkeit und Verschleißfestigkeit von Hochtemperaturkeramiken für kurzzeitige Beanspruchungen. Messerschmitt-Bölkow-Blohm GmbH, Bericht Nr. BB-315/78, Sept. 1978.

[8] Weast, R., Selby, S., Hodgeman, C. (Eds.): Handbook of Chemistry and Physics. 45th Edition, 1965.

[9] Woodberry, R., Zeamer, R.: Solid Rocket Thrust Vector Control. National Aeronautics and Space Adminustration, Space Vehicle Design Criteria, NASA SP-8114, Dec. 1974

COMPOSITES IN FUTURE MOTOR HARDWARE - A RESEARCH VIEW

by
N J Parratt
PERME
Waltham Abbey
Essex
UK

SUMMARY

Problems such as cost, inert weight, fire risk and development time compel designers of tactical motors to consider the use of composite materials to bear loads and to resist heat and erosion. This paper first traces the move from traditional materials to more recent concepts such as dual-function composites and integrated construction. It then reviews the question of whether in fact the best use is being made of available materials, particularly in reducing weight and cost together, and suggests how this might be done. It concludes that particularly in the construction of motor cases, significant improvements can be made immediately with only minor changes in design, if supported by adequate measurement and prediction of any deterioration. Innovative research is still necessary and worthwhile however, on composite materials for insulants and for end plates.

1 INTRODUCTION

There is renewed interest in the use of fibre reinforced composites in tactical motor hardware for several reasons. Glass fibre composites have been used for many years to produce motor cases quickly at relatively low cost, and they are also considered to provide reliable "leak before burst" behaviour in fires. However, these features are also available in steel strip wound laminates, and simple motor tubes made in this way show less dilation under pressure. Conversely GRP materials are more versatile in forming structural shapes and more tolerant of damage, but can also be more variable and need careful storage to prevent deterioration of their strength properties. However, they do also function as thermal insulants, and this illustrates the need to look at the total performance and cost requirements before making a decision.

In the last decade we have perhaps seen conventional solid propellant technology approach its natural limits, whereas in the materials area there has been significant progress, with the introduction of new fibres such as carbon and Kevlar, and at least some deeper understanding of the role of insulating materials. It is these material changes which lead one to suspect that the weight of certain types of hardware might indeed be halved, and that this will have a significant effect on motor designs of high inert weight and those systems designs which are performance-limited. If such gains are attainable consistently and at reasonable cost, then it is important to evaluate them quickly, if only to prevent an unfavourable technology gap from developing. One way of assessing the opportunities is to consider first the functions to be performed by the materials, how these may be combined and with what restrictions, then to see what this implies in terms of fabrication and cost, and finally to look at specific solutions which have proved fruitful, or should do so.

There are of course some useful simplifications which can be made from the start. In small, cigarette-burning motors, the weight and volume of erosion-insulation linings will be most important. For high aspect ratio motors, the mass of the ends is not very critical, and if they are radial burning, nor is that of the case insulation. Such a motor would be a good candidate for a lightweight motor tube, or for tolerating the increased chamber pressure associated with higher burning rates.

The orthodox view of motor hardware is that each material should have a single function, ie structure - insulation - erosion face, to which it is best suited, using the word erosion to describe all forms of surface attack other than by heat alone. This trilaminar arrangement stems from the use of strong, but thermally conducting alloys, with reduced strength at high temperatures, whose use is therefore limited to a few hundred degrees above room temperature.

The materials with maximum erosion resistance at temperatures around 3000 K are of necessity to be found in nozzle throat sections which must ideally maintain a constant bore during firing. Dense graphite and tungsten, both good thermal conductors, are the traditional materials here, and the analogy with their use in filament lamps is obvious, exemplifying the few materials which retain strength or indeed exist as solids as these temperatures. Silicon carbide is preferred under oxidising conditions, where the solid becomes coated with silica which in turn can evaporate as SiO. In an inert atmosphere SiC will decompose to silicon and carbon, since the partial pressure of silicon over SiC is several millimetres at 2500 K (1).

Insulants too are commonly subjected on one face to temperatures exceeding 2500 K, whether or not they are exposed directly to the combustion flame. To function effectively they must resist radiated and convected heat as well as conducted heat and thereby prevent serious rise in temperature of the structure, or the unburnt propellant. At least during ignition, they may be called upon to transmit the gas pressure to the structure, before high pressure gas has leaked behind them or into them. This requirement has obviously favoured the use as insulants of solids which are virtually impervious and only later degrade to a fine, porous and insulating layer which would not in itself resist a sharp change in gas pressure. Polymers of low stiffness have a disordered molecular structure which minimises heat transmission, and rubbers in particular provide mechanical accommodation between propellant and case. They are able to decompose, absorbing heat, to porous but fragile carbon chars which serve well as insulants at very high temperatures, but offer little resistance to erosion. Although rubbers and thermoplastics are the best insulators in the uncharred state, crosslinked phenolics provide a

slightly stronger and heavier char, and polyphenylenes a stronger one still. Mechanical stability is commonly maintained throughout decomposition by the introduction of a fibre network. This probably represents the first serious use of a fibre reinforced composite in the propulsion field if one neglects the cardboard tubes from which display rockets are constructed.

This one material - one function approach is illustrated in Figure 1 as a composition diagram. There is of course no reason why any one of these traditional materials should not be used for more than one purpose, but the result would be heavy and ineffective. Cardboard offers a strong hint that this need not always be so. The introduction of carbon fibre composites as lightweight structural materials exemplifies the way in which the materials picture has changed. Figure 2 illustrates the way intermediate compositions can now be used to serve more than one function.

2 COMBINED INSULATION AND STRUCTURE (ORGANIC MATRIX COMPOSITES)

Even in the presence of conducting fibres the thermal insulating properties of the organic matrix and its char are largely preserved in the direction perpendicular to the fibre plane of laminates and wound structures (2). However, fibres which are exactly in the plane of the ablating surface will be swept away by eroding gases, so the simple advantage is only one of insulation, not of erosion resistance. Specifically, the presence of carbon fibre tends to increase conductivity a little perpendicular to the fibres, and in the case of the high modulus graphite fibre, the composite conductivity parallel to the fibres approaches that of graphite itself. However, in the case of the oriented aromatic fibre Kevlar, which also has a high specific strength, the conductivity perpendicular to the fibre axis will be virtually that of a matrix polymer.

Although fabrication of insulation and structure together is attractive, there is no particular reason for using an expensive fibre like carbon, rather than glass for a purely insulating role unless a useful element of risk-sharing is involved. It is not unusual to provide say twice as much material for structure or for insulation as is needed on average and this of course allows for statistical variability in strength or thermal attack on the material. If these two risks are regarded as unrelated so far as the material is concerned, then they are very unlikely to occur together. Thus if similar materials are used for each purpose the total allowance for variability is smaller and the weight is reduced purely for this reason. A highly simplified form of this argument is presented in Table 1 for the case where structural and insulant safety margins are similar.

TABLE 1

OVERLAPPING RISKS OF CHARRING OR PURE MECHANICAL FAILURE

	Depth, in Standard Deviations				
	Structure			Insulation	
	0	1	2	3	4
(A) Mech failure probability	0.5	0.32	0.06	0.001	
(B) Probability of charring	0.001	0.06	0.32	0.5	
or	-	0.001	0.06	0.32	0.5
Risk of charring and mech functions being needed together (A x B)	0.0005	0.02	0.02	0.0005	-
or	-	0.00032	0.0036	0.00032	-

In considering these relative risks, it is interesting to note that whereas structural variability can sometimes be narrowed by proof-testing and NDT techniques, similar techniques are not in general use for testing the insulant function.

3 COMBINED STRUCTURE AND EROSION RESISTANCE (CARBON REINFORCED CARBON)

If the structure is strong at high temperatures, no insulation may be necessary. If it resists erosion, even better. Even though the absence of insulation increases heat loss, there are certain parts of motor hardware where these arguments can apply, notably to choke materials, which are probably strong enough structurally already but require ideally a higher capability to resist thermal strains, possibly to expansion cones and to thrust vector control vanes within the exhaust, but hardly to blast tubes which can overheat their surroundings, or to motor cases which might overheat the unburnt propellant in contact with them. The use of structure which is to run very hot locally also presents extra joining problems. In their present stage of development these materials are expensive to produce, variable in properties, and do not always match polymeric composites for strength or (generally) the best graphite chokes for oxidation resistance, although their resistance to thermal strain is an advantage. Their use has been demonstrated in both large and small motors and modification by converting both fibre and matrix to silicon carbide is improving oxidation resistance. This may be sufficient to permit a lightweight integral choke and expansion cone construction to be used on small, long burn motors, since expansion cones need not be very highly stressed. It is also feasible that for many motors, sufficiently durable components could be produced by heat-stabilising the polymer phase without infiltrating with more carbon. Perhaps the main potential here is the development of these less costly forms, supplemented where necessary by a densified surface.

4 EROSION AND INSULATION (CARBON-ORGANIC COMPOSITES)

Although the behaviour of polymeric motor insulants is quite complex, as a practical matter there is now no difficulty in providing pure insulants which are very efficient, and in which the reinforced char resists the temperature of a motor flame. This has been demonstrated with low conductivity carbon fibres in phenolics and in flexible insulants designed either for milling or casting. The real problem is to provide simultaneously adequate erosion resistance, insulation and sufficient strain to break, in compositions which are easily fabricated and compatible with other motor substances. Fibres such as asbestos, alumina, glass or silica all confer to chars some erosion resistance, but are unsuitable for use at the highest flame temperatures unless they form stable reaction products with the char. Glass and silica have the lowest axial conductivity at room temperature, but asbestos in particular contributes the least depth of charring in insulants such as moulding compound RA51. This may be because, at least in its dehydrated condition, it neither conducts nor functions as a "light pipe" for the near infra-red at elevated temperatures. However, the fact that it decomposes below 1000 K and melts below 2000 K does make such compositions very sensitive to changes of motor environment, and asbestos itself must be replaced as soon as an efficient and safe alternative can be found.

The polymers used must form coherent chars - at the high rates of decompositio required many polymers decompose entirely to volatile products or leave only a dusty char. The ra e of suitable polymers is extending, eg phenolics, nylon, polyphenylene resins, polyacrylonitrile and cellulose compositions, chlorinated polyethylenes, HTPB, etc. Taken overall, these changes have led to improvements in fabrication and mechanical properties more than in insulation behaviour, and the typical char depth for ten seconds exposure remains obstinately about one millimetre. These active and open forms of carbon in chars have little prospect of resisting for long the oxidation by propellant gases (CO_2, H_2O) flowing under high pressure at 3000 K, and some are too weak to resist the most severe cases of mechanical erosion, due to surface shear and to particle bombardment. Graphite moulding compounds and structured graphite-phenolic composites possessing comparatively high erosion resistance (3) but poor insulation have of course already been developed and used. The alternative is to examine how changes in the geometry of insulating and erosion-resisting phases may be used to advantage. A conducting erosion additive and an insulant can be combined in various ways, see Figure 3. A1 is the classical but inefficient moulding compound, while B contains the same ingredients arranged physically to form the correct barriers to erosion and heat flow. C is a preferred arrangement to prevent stripping of the separate layers. If erosion is very severe, then D is the only choice, but is also a risky one if the single erosion barrier breaks away. A2 is the moulding compound version of B, where the fibres or plates of A1 are equiaxial particles in A2, and only fibres of low conductivity pin the whole together. Simple calculation shows that the only conditions under which the conductivity of A1 may be made almost as small as B or D would be if the erosion element were small in volume concentration (less than 10%), or no more than five to ten times the conductivity of the insulating element.

5 CONSTRAINTS

To sum up, we cannot expect dual-function materials to perform each function quite as well as would two or more concentric layers selected for the purpose. However, there are advantages in overlapping the functions, especially when one function is a minor one, and it is also possible to fabricate two different layers together, thereby still saving fabrication cost. We might generalise by saying that integration of material and fabrication will tend primarily to save cost in the radial direction of a motor design, but could save both weight and cost in the axial direction.

Indeed, one of the more compelling arguments for use of fibre composite materials in structures generally is that they lend themselves to fabrication virtually in one piece, thereby saving both cost and weight. The asbestos-phenolic wing in Figure 4 weighed no more than an aluminium one, in spite of the superior properties of aluminium. This is common experience for large, lightly-loaded composite structures, but is not necessarily a reliable axiom for the highly-stressed parts of a motor. There are several reasons for this:

1 One piece construction can prevent optimum choice of material for each component - assuming there is no single optimum material.

2 The hardware cannot then be broken down into simple, reliable units which can gradually replace existing units. At least in the UK, the progressive improvement of material, design and fabrication of one piece, polar wound cases (Figure 5) has led to an artificially high scatter of research results and to too much reliance on proof-testing as a means of truncating variability.

3 Highly-stressed composites are often sensitive to small defects in their construction. Specifically motor cases which include wound ends are hitherto much more variable than simple tubes, which in turn are more variable than laboratory test specimens. Integral ends also make filling more difficult.

4 The winding of elaborate shapes is usually expensive both in fabrication time and in capital for machines and can be used to best effect only if the structural shape is allowed first priority in the systems design. Thus the skill is in selecting designs containing a few well-chosen joints.

The propellant, linings and structure must also strain together and so a practical limit is set by whichever is the least extensible. Propellants and rubbers lose their extensibility at low temperatures and with high loadings of fillers. In tubes of very thick wall, the hoop strain is largest on the inside surface, and star-centred charges in particular experience a high strain concentration hoopwise at the point of the star, which may restrict the possible hoop strain in the supporting case to 1-1.5%, and is one reason why glass is not commonly used at high strains as a reinforcement. However this need not prevent the <u>axial</u> strain in a case from being large, and fibreglass could be used efficiently here. Existing Kevlar or carbon fibre reinforced epoxies are unlikely to be used above 1.5% strain in any case.

If the stiffness of the insulating lining is low enough (about 0.4 GPa) then secondary (Poisson) strain in the insulant, due to the applied gas pressure, will accommodate the displacement of the case

under pressure. This will not necessarily suppress a local fracture of the insulant completely, but the risk of crack propagation or tearing is then much less, as it is if the insulant is very firmly bonded to the case. Where rigid insulant moulding compounds are used, eg in blast tubes, nozzles and expansion cones, there is a high risk of local fracture even at strain levels of 1%, and the best asbestos-phenolic mixes available will not be free of cracks above 0.5% hoop strain (4). Dynamic burst measurements on traditional rigid insulants suggest that cracks must have occurred quite commonly in the past (Figure 6) and were probably not catastrophic up to crack openings of 0.5 mm, since in the presence of asbestos, the cracks took a devious path around the fibres, but increased charring and erosion could still have occurred locally. Inspection shows that beyond 0.5 mm opening, optical and thermal radiation can pass directly down such a crack. Thermal strains in insulants are also large, due to the radial thermal gradient, ie even allowing that charring softens the majority of a lining, the dimensional difference due merely to a 250° rise is about 0.5% for a phenolic compound and 2% or so for a rubber lining. However, since the position of the outside of the lining is determined by the supporting structure, these strains are primarily compressive and at worst lead only to the shear failures (spalling) observed in ceramics and graphites. Little is known about the defect tolerance of moulding compounds in compression, but structured mouldings should certainly accommodate strains of this order.

With average tensile strain to break figures around 0.2%, the graphites used as thick sections to resist erosion in chokes and sometimes in entry linings are very sensitive to mechanical and thermal strain. Fortunately chokes are relatively small and any strain limitations reflected on supporting structure will therefore not contribute greatly to structure weight. A statistical approach to the design of these critical items has been given by Margetson (5). The expansion coefficient of random graphite is of course sufficiently low for it to be pre-stressed accidentally into compression by surrounding structure and insulant during cooling from a moulding or hot-bonding cycle. Table 2 summarises the strain limits discussed and highlights the need for erosion-resistant linings having a strain to break of one or two per cent.

TABLE 2

	Mechanical Strain Limits	Linear Expansion for 100° Temp Rise
Propellant strain axial	5 - 10%	about 1%
outer hoop with star centre	1 - 1.5%	
Rubbery Insulants	10% or more	0.2% to 2%, depending on fillers
Rigid Insulant (m/c) - wound, see composite structure	0.5% - 1%	0.1% to 0.4% " " "
Metal Structure	0.7% - 1% at yield	Steel 0.14% Aluminium 0.25%
Composite Structure	1% - 3%	Longitudinal Carbon*, - 0.01% Kevlar -0.01%* Glass +0.05% Epoxy 0.3 - 0.7%
Graphites	0.2% - 0.4%	0.04%

*Transverse fibre values are high, 0.27% for carbon, 0.6% for Kevlar, and planar constraint from the reinforcement causes large thickness expansion of matrix, up to 2% between 40 - 140°C. See reference 12.

6 COMPOSITE STRUCTURES

A useful insight into the value of composite construction can be obtained from comparison with metallic designs. A metallic pressure vessel is best made spherical, so that the metal is used efficiently to resist isotropic tension. When a cylindrical vessel is used, the ratio of hoop to axial stress increases to 2:1, placing the metal at a disadvantage for this shape. If oriented fibres are used to resist the stresses, however, the weight of structure needed to produce a vessel of given volume is theoretically the same, whether it be cylindrical or spherical. The structural weight per unit of contained volume also remains constant, independent of scale (in contrast to the weight of thermal insulation which depends on surface area). However, the reduced axial tension due to the large choke bore needed in very short burn motors also favours the use of composites, since hoop to axial load ratios can then be as high as 4:1, as in blast tubes and certain launch tubes.

If one accepts that the strength variation of composite structures may be about 10% of the mean, then allowing for scale effects and statistical risk, a design stress level about half the strength given in Table 3 below would need to be adopted. The choice of this stress level also confers some tolerance of small holes and local damage which is necessary in practice.

TABLE 3

MECHANICAL PROPERTIES OF UNIDIRECTIONAL COMPOSITES

Material	Modulus GPa	Elastic Limit %	SG	Specific Modulus GPa	Specific Strength GPa
Alloy Steel	210	0.7	7.8	26 (1)	0.18 (1)
Strip Steel	210	1	7.8	26 (1)	0.26 (0.7)
HTS CFRP	120	1.1	1.45	83 (0.31)	0.91 (0.2)
Super A CFRP (1977)	105	1.8	1.45	71 (0.37)	1.27 (0.15)
Kevlar RP	62	2	1.3	48 (0.55)	0.97 (0.19)
GRP	34	3	1.8	19 (1.35)	0.57 (0.32)
GRP/Super A in equal weights	76	1.8	1.6	48 (0.55)	0.86 (0.22)
(Plastic Propellant)	-	-	1.6 - 1.8		

Weights relative to steel are given in parentheses, assuming 50% fibre by volume in the composite, although 60% can often be attained in wound or moulded components.

The above approach leads to a comparison with metal structures given here in Table 4 which lends numeracy to several useful conclusions:

1 In principle the weight of blast tubes and cases can be markedly reduced - more than 50% - leaving ample opportunity for use of diluents of lower material cost, such as fibreglass or metal structure.

2 Careful attention to controlling variability will reduce both weight and material cost further, which is probably done most easily in hoop winding operations and least easily for wound ends, where misorientation and voidage together are difficult to eliminate.

3 Comparing possible diluents, fibreglass is unsuitable for use in stiffness-limited designs, where steel or light alloy would be a better choice, unless it is also to function as an insulant.

GRP should therefore be allowed to strain freely, but unless variability is reduced, it cannot compete where a metal could be used to take equiaxial stress. The weight difference is however small enough for other factors, such as ease of fabrication, to settle the issue. Theoretically, a hoop-wound GRP insulant could also be extended to shed some 20% of the weight of a metal case.

TABLE 4

RELATIVE MINIMUM WEIGHTS OF STRUCTURAL COMPONENTS, (Steel - 1)
ASSUMING DESIGN MAKES FULL AND PROPER USE OF MATERIAL

Assumptions	Blast Tube	End Plate	Cylindrical Case
Dominant stress	Hoop	Biaxial 1:1 approx	Biaxial 2:1
Designs limited by stiffness (up to 0.5% strain)	0.31 (HTS)	0.62 (HTS)	0.46 (HTS)
Limited to 50% of average strength by variability etc	0.3 (K/SA) 0.58 (G)	0.6 (K/SA) 1.16 (G)	0.45 (K/SA) 0.87 (G)
Hypothetical case, limited only by average strength	0.15 (K/SA) 0.3 (G)	0.3 (K/SA) 0.6 (G)	0.22 (K/SA) 0.45 (G)

Fibre type in parentheses
ie G - Glass, K - Kevlar 49, SA - Grafil Super A, HTS - Grafil HTS

6.1 A Combined Composite-Metallic Structure

Maximum hoop overwinding of metal tubes is the fabrication technique likely to yield most easily to close control in production and one which can utilise advances in composites and metal structure alike (eg flow-forming). Kevlar overwrapped pressure vessels have been introduced in the USA (6) and work by AERE Harwell shows that very consistent CFRP hoops can be wound (7), in this case of HTS-MY750 carbon epoxy. It also has the advantage for motor tubes of providing lightness but with fewer attachment problems, and lower material cost, see Table 5. In this Table, it is assumed that the best available metal structure is used to carry equal stress in the axial and hoop directions, but supplemented by an overwind to carry the remaining hoop stress. The hoop stress is taken to be only twice the axial stress in this example.

TABLE 5

WEIGHT BREAKDOWN OF POSSIBLE EQUIVALENT MOTOR TUBE CONSTRUCTIONS

Case Materials	Present		Long Term	
	Weight of Tube	Wt of Composite Used	Weight of Tube	Wt of Composite Used
All metal case	1.0	None	0.8	None
GRP - metal	0.8	0.3	0.7	0.3
			(higher strains of no use)	
Super A or Kevlar - metal	0.65	0.15	0.5	0.10
Best all-composite case	0.45	0.45	0.3	0.3

Thus when the cost of the reinforcement is the most critical part of the production cost, and the additional overwinding operation can be justified to save weight, this approach is the most promising. It becomes difficult to justify an all-composite case purely on weight-saving grounds, and the consumption of fibre is three times larger. Because of the thin gauges of steel required, high strength aluminium alloy would be a better choice for overwinding. Selection of a hot-curing resin would lead to detachment of the overwind, or unnecessary tensile stress in the alloy on cooling. This would need to be rectified by inflating the metal lining out to size it and leave it in compression, a form of proof-testing. Given sufficient consistency from the overwind, this treatment would also permit less overwind to be used.

6.2 All-Composite Cases

Accepting that GRP motor cases have been produced economically, then complete composite cases might be preferred to overwinding if fabrication costs were more important than fibre cost and attachment problems. Certainly it is desirable to exploit helical winding if one is to reduce the weight of a cylindrical pressure vessel below half the equivalent metal structure, to levels around a third, but with existing fibres this would involve hoop strains of 1.5%, normally regarded as excessive for the propellant. This level would be reached by eliminating all but the "inherent" variability of strength, ie misorientation and voidage occurring together can introduce very large errors, but the coefficient of variation of fully dense composite laminates is only about 5%. Some 2% of this is related to similar variations in stiffness, due to residual errors of fibre mass/unit area and of orientation. The alternative strategy, to leave component variability as it stands but to await further costly improvements in fibres, is even less likely to be fruitful. The specific stiffnesses of both Kevlar and carbon fibres are only about a factor of two below the theoretical limits for the molecular structures which they contain (8).

It is not efficient to operate glass fibre at only 1% strain - an all-glass case at this strain level would weigh 1.3 times a metal structure, whereas at 1.5% strain it is only 0.87 of metal. Thus the use of glass as a simple diluent in parallel with other fibres will only be successful with very carefully-made cylinders of small variability. However, with existing variability, one third of the reinforcement introduced as glass parallel to the axis would lead to a weight of 0.6 metal instead of the 0.45 for 100% of expensive reinforcement, if this step were justified by the extra complexity.

Unless a weight penalty is accepted, some hoop-wound fibre has also to be introduced on a simple composite tube to correct the strength after fibre orientations are adjusted to resist bending. In most motors, the resulting deflection will have two components, that due to pure bending, for which axial fibres are needed, and that due to shear where ideally $\pm 45^{\circ}$ orientation is needed. In practice the presence of a third fibre direction (triangulation) decreases the precision with which fibre orientations must be maintained. However, if great precision is available, then the possibility also exists of changing orientation under stress, provided only two directions are used. This effect is commonly observed when pressurising steel-braided rubber or plastic tubes, and could enable radial dilation to be replaced by zero dilation or indeed radial contraction. We also note that hoop overwound metal tubes will in general be less stiff than their metal counterparts, but continue to resist both shear and pure bending.

6.3 Composite End Plates and Closures

Reinforced plastics can in principle be shaped easily to form components such as these (9), although the use of systematically reinforced thermoplastics for the purpose has hitherto been neglected. This is surprising since they promise the most rapid fabrication of efficient structure. Where the weight and volume of such ends are of secondary importance, simple moulding compounds have of course been used for closures worked largely in compression or shear. Integral end plates incorporating closure, nozzle and expansion cone such as that illustrated in Figure 7 have saved weight not because the structural design in CFRP was particularly efficient, but largely because the number of joints was reduced. We have already noted that the proportion of weight saved by using composites for structures stressed in biaxial tension is smaller than elsewhere, and at high motor pressures it may not even be possible to maintain the simple membrane stress conditions in tension which are assumed. The design of joints which are strengthened rather than weakened by gas pressure also appears to have been ignored. Thus a good deal remains to be done in this area, at least for low aspect ratio motors, although conservatively stressed, but easily moulded parts can be introduced elsewhere.

7 PROGRESS IN EROSION RESISTANCE

We are able nowadays to provide any required level of resistance to erosion by appropriate dilution of the already high resistance of carbon and graphite, aided where necessary by surface coatings. Fortunately, the weight of the choke region in which erosion is most severe is not very critical, but control of magnitude and direction of thrust is then more important. Those regions of larger diameter, however, require more extensible linings if structural weight is not to become excessive, and thus it is the means by which erosion resistance is traded off which needs to be studied.

In the area of so-called rigid insulants we have already perhaps doubled the design strain of asbestos-phenolics, and also produced lighter moulding compounds of equivalent insulating value but higher erosion resistance. Similarly castable rubber insulants having the thermal performance of the more intractable milled rubbers have also been introduced. They all contain fibres and they all form chars, but our understanding of their erosion mechanisms is rather poor. Resistance to surface shearing and to chemical attack can in principle be reduced with increasing gas cross-section within a motor, because of reduced gas velocity and increased boundary layer thickness.

Droplet erosion, like rain erosion, will depend critically on the kinetic energy of the droplets, which controls the stagnation pressure of impact and is resisted by the work of fracture of the attacked material. The evidence is that it is volume porosity rather than internal surface area which limits the erosion resistance of commercial graphites. This suggests that what chemical attack there may be is quite superficial, but probably selective, leading to the undercutting and removal of the more inert particles which could therefore just as well have been attacked initially. Well-embedded fibres can resist this type of attack but will eventually be released by charring and attack on the matrix. Thus for short-burn motors discharging at high pressure, a polymeric matrix should be adequate, whereas in a long-burn motor, although more stagnant conditions might well occur within the fibres, they could suddenly be released by mechanical action on their increasingly exposed length. This argument favours the use of a coarse fibre with a matrix which has the same order of resistance to attack, although neither needs to be fully dense. Decisions of this type in turn influence the ease with which composite end plates can be made.

8 CHARRING AND PRE-CHARRING

Mathematical models of ablation have been largely confined to attempts to describe accurately what already exists (10,11) and perhaps cruder physical models offer more insight into what improvements can be made. In a simple solid suddenly heated on one face, the time taken for a given depth to rise to a given temperature increases with the square of the depth, and depends on α, the thermal diffusivity of the solid, which is the ratio of its thermal conductivity to its specific heat per unit volume, ie

$$d = (\alpha L)^{\frac{1}{2}} \quad \text{where } \alpha = \frac{k}{\rho c}$$

This expression recognises the fall in the temperature gradient as deeper layers have to be heated. In the case of a charring insulant, the heat must flow through the char to decompose the polymer. This latter process requires latent as well as specific heat and so attempts to minimise depth of charring have focused both on increasing the energy of decomposition or evaporation and on lowering the heat transfer through the char material. If the primary decomposition temperature of the polymer is chosen to be about the same as the safe working temperature of the structure, the conductivity of the polymer itself becomes irrelevant. If the polymer conductivity is significant and its decomposition temperature high, then it may function more as a fuse, tolerating heat fluxes up to a critical value, at which charring occurs and reduces the flow of heat permanently. The designer of new insulants must also consider the effect of radiation on surface temperature of his materials, even when they are protected by a cooler boundary layer. Unless the char proves an excellent reflector of red and infra-red, Stefan's Law indicates that its surface temperature must approach the flame temperature closely if it is to re-radiate most of the incident energy. The alternative assumption that the surface is appreciably cooler and the energy is merely absorbed in the insulant would lead to total decomposition of the insulant, at a rate many times faster than is in fact observed.

It is therefore suggested that there will be little useful effect from cooling of the surface and its boundary layer by decomposition products, although they may well suppress oxidation and certainly do absorb heat within the insulants. In the entry region and choke for example, the boundary layer itself is usually too thin to inhibit conductive heat flow from the combustion gases. Provided it is not eroded then, the thickening char layer must quickly become influential in controlling rate of charring. This leads to the concept of char penetration in Figure 8. Charring is first limited only by decomposition OA, then by diffusion OD and becomes progressively slower with time. The presence of a heat sink at the backface leads to an equilibrium in which charring stops, ie the heat flow through the char layer is equal to that between the char boundary and the backface. The char layer can be thought of as having at least two components of specific heat, that of the solid of which it is composed, and that of the decomposition products flowing through it. The latter will be high for light gases, and hydrogen is an excellent choice, but low for heavy molecular gases similar to solid matter. Further complications include for example, endothermic side reactions between gases and char, as in the water gas reaction. Thus even with perfect heat exchanging, the temperature gradient through the char layer itself is unlikely to be uniform, and even if all the latent heat of decomposition is taken up as remotely as possible at the charring boundary, the specific heat of the products is taken up less usefully throughout the char. However, this should not inhibit the measurement of families of charring curves such as Figure 8, the form of which will depend on the exposure conditions as well as on the material. A single curve enables an estimate to be made of when pre-charring would save some insulant weight. (It does not appear possible to save thickness in this way.)

Assume in the worst case that the solid char has trivial specific heat but has some mass and is efficient as an insulator. Consider first the use of a normal, uncharred insulant to match a burn

time t_B, which requires an insulant thickness illustrated by say point P on Figure 8. For simplicity let that thickness be unity. Then if a fraction p of that thickness is precharred, this would normally occur in a time t. However, the negligible specific heat in the char means that when a precharred insulant is fired from cold, an extra time equal to t must be provided at the end of a burn and this requires a maximum additional thickness of insulant Gt, where G is the slope of the tangent TT at P, the instantaneous charring rate, at time t. The total weight of this partially precharred assembly, relative to the original insulant is therefore

$$W = pR + (1 - p) + Gt$$

where R is the ratio charred/uncharred density, assuming unidirectional heat flow. For success, this expression is less than unity, ie $p(1 - R) - Gt$ is positive and passes through some stationary value at minimum weight, when

$$\frac{dW}{dp} = G\frac{dt}{dp} - (1 - R) = 0$$

Therefore the safe prechar depth is given by the value of p at which the charring rate $(\frac{dp}{dt})$ is $\frac{1}{1 - R}$ times greater than that at P. Where precharring is desirable for other reasons, such as dimensional stability or proof-testing, it is interesting to note the breakeven point $W = 1$ is given by the value of p at the intersection of the secant from the origin, parallel to this tangent. A corollary is that an artificial char should improve the weight efficiency of an insulant.

The polymer decomposition temperature is usually higher than the maximum structural service temperature, so if the charring depth and burn time are known, one would ideally like to minimise the sum of material eroded, material charred and material needed as simple, solid insulation. The critical value of total thickness is best illustrated by projecting back from P in Figure 8 for example, a thickness allowance for constant heat diffusion with the differing transmission times available prior to completion of burn. This is shown as the dashed line from P and illustrates a maximum thickness required. Conceptually, for times less than that of this maximum, charring largely overtakes normal diffusion, but for longer times the diffusing heat reaches the structure after burn is completed, when gas pressure is negligible.

9 CONCLUSIONS

1 There is a good deal of experience in the design and construction of GRP motor cases, dating in the UK from about 1952 (Figure 9). Composite materials research in the 1960's led in the 1970's to the manufacture of certain cases made of carbon or Kevlar-epoxy. These have proved both lighter and cheaper than the best maraging steel ones. However, because the material and structure are formed at the same time, too few cases have been made and assessed in these more advanced forms of construction to establish full design confidence. This is best done on small motors which are simple but realistic, and most directly rewarding when applied to high aspect ratio motors having short burn times.

2 When the behaviour of eroding, charring and insulating linings is analysed, there is potential for further research to reduce the weight and thickness of these items, notably on erosion-resistant linings of adequate strain capability and consistent thermal behaviour. Insufficient use is made of existing developments and this is partly related to the high cost of necessary firings and consequent lack of experience as well as the cost of introducing or modifying specifications. Clear agreement between designers about what constitutes a significant materials improvement is needed at this stage.

3 The choice of composite materials and designs for integral moulded end plates, which also save weight, is much influenced by both 1 and 2 above. This choice will vary greatly with the type of motor, ranging from thermoplastics to carbon reinforced carbon. The form of material adopted will similarly influence the design of efficient pressure joints and here again there is a need to establish more confidence.

4 It is concluded therefore that in spite of the need to improve performance of solid propellant motors, we are not making full use of available materials or knowledge in the hardware. When the various items of hardware are considered, it would be realistic to treat 40% reduction in weight as an attainable objective through use of composites, although there may be more efficient ways of interpreting such a change during the design of a complete system.

10 REFERENCES

1	Brown A	Unpublished MOD(PE) Review
2	Ziebland H	Polymer Engineering Composites, p 318-361 Applied Science Publishers 1977
3	Trigg T A	J Brit Interplanetary Soc 22 337-352 (1969)
4	Gooding R W et al	Proc ICCM II Publ AIME NY 1978
5	Margetson J	PERME Report TR 42 1977
6	Wesselski C L	AMMRC (Watertown, Mass) Report MS-67-2
7	Hitchon J W, Phillips D C	AERE (Harwell) Report 6758
8	Parratt N J	Fibre Reinforced Materials Technology Van Nostrand Reinhold 1972 21-27
9	Edwards H E et al	Proc ICCM II Publ AIME NY 1978
10	Parkinson R C, Ziebland H	AGARD AG-148-71, 115
11	Clark B L	J Heat Transfer Nov 1972, 347
12	Rogers K F et al	J Mat Sci 12 718-734 (1977)

11 ACKNOWLEDGEMENTS

Contributions and advice from many members of the research staff of PERME and of Bristol Aerojet Ltd are gratefully acknowledged.

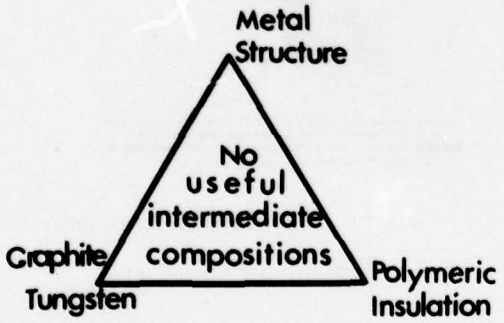

Fig 1 Traditional materials of construction

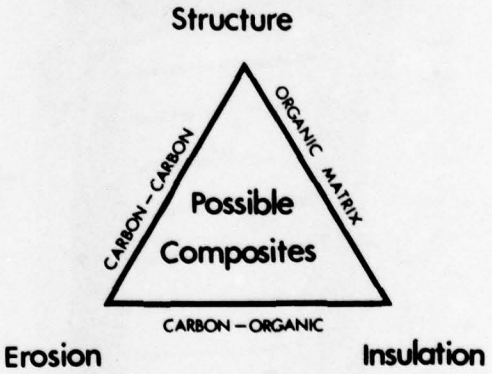

Fig 2 Influence of composites

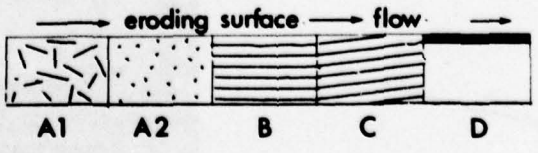

Fig 3 Combining erosion and insulation

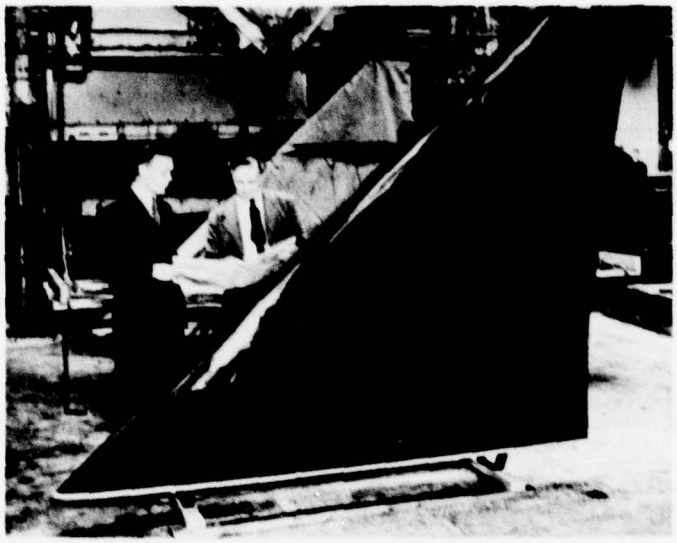

Fig 4 Asbestos-phenolic delta wing (1952)

Fig 5 Polar wound carbon-epoxy case (1971)

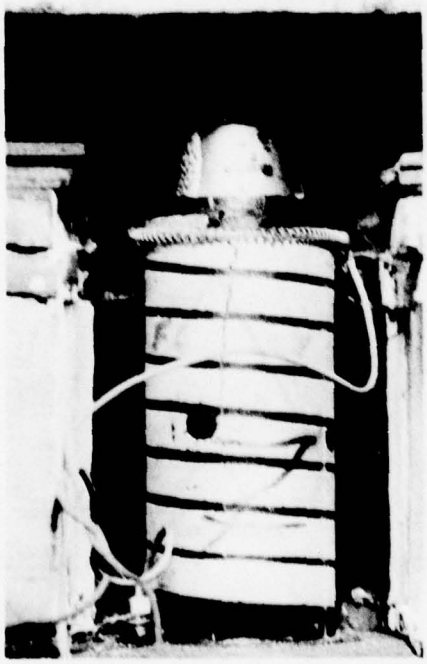

Fig 6 Dynamic burst of asbestos-phenolic blast tube

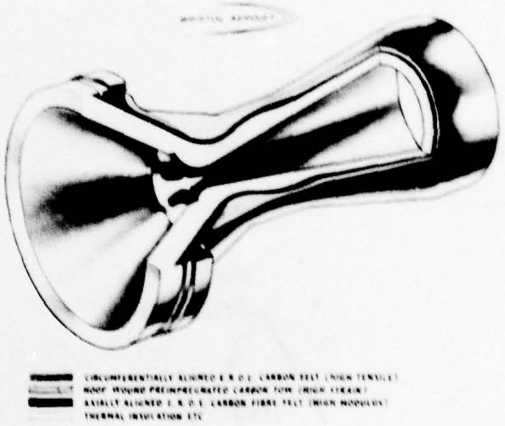

Fig 7 Composite end plate (1974)

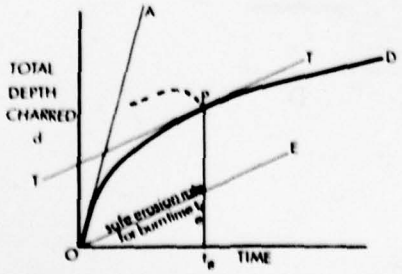

Fig 8 Charring - burn time curve

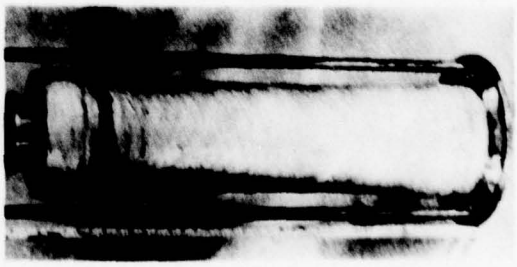

Fig 9 Prototype fibreglass case (1953)

PREDICTION DU COMPORTEMENT DES MATERIAUX PHENOLIQUES ABLATIFS

PROGRES RECENTS

Claude BONNET - SOCIETE EUROPEENNE DE PROPULSION - 33160 ST-MEDARD-EN-JALLES

1 INTRODUCTION -

Durant la dernière décennie, les métaux réfractaires et les graphites qui équipaient les tuyères des propulseurs à poudre ont été progressivement remplacés par des matériaux composites ablatifs. Ces derniers étaient essentiellement composés de renforts réfractaires (carbone, silice, amiante) et d'une résine se décomposant sous l'effet de la température tout en laissant un résidu important de carbone. Cette technique a permis d'alléger de façon considérable les tuyères et de pallier en grande partie la mauvaise résistance au choc thermique des graphites. Par contre, il a été pendant longtemps très difficile sinon impossible de prévoir le comportement en tir de ces tuyères pour les raisons suivantes :

1°) Les matériaux, et les pièces fabriquées avec ces matériaux, n'étaient pas reproductibles du fait de la nouveauté des techniques utilisées et de la sensibilité à l'environnement des matières premières.

2°) On ne disposait pas de méthodes d'analyse suffisamment performantes pour prévoir le comportement thermostructural des pièces de tuyère.

3°) Les caractéristiques de ces matériaux aux températures d'utilisation (2500 - 3000°C) n'étaient pas connues.

Les années 70 ont permis de réaliser des progrès importants dans l'utilisation de ces matériaux et les lignes qui suivent vont montrer les efforts accomplis pour :

- améliorer les méthodes de fabrication des matériaux composites ablatifs et des pièces et leur assurer une meilleure reproductibilité.
- mettre au point de nouvelles méthodes d'analyse et des programmes de calcul permettant de prédire avec une bonne précision le comportement mécanique et thermique des pièces de tuyère en tir.
- caractériser ces matériaux aux températures d'utilisation c'est-à-dire entre l'ambiante et 2500°C.

2 AMELIORATION DES METHODES DE FABRICATION DES COMPOSITES ABLATIFS -

2.1. - Description des matériaux :

La réalisation de tuyères de propulseurs à poudre nécessite l'utilisation de deux types de matériaux :

- au contact des gaz de poudre, un matériau conducteur de la chaleur permettant de transférer une partie de l'énergie calorifique,
- derrière le matériau conducteur, un matériau isolant absorbant les calories transférées et protégeant ainsi les parties structurales de la tuyère.

Les premiers matériaux utilisés furent des métaux réfractaires (tungstène par exemple) et du graphite. Mais ils présentaient deux inconvénients majeurs ; les uns sont très denses et alourdissent considérablement les tuyères ce qui diminue les performances des engins ; le graphite, quant à lui, résiste mal au choc thermique et ses propriétés mécaniques s'effondrent au-delà de 2000°C. Des études montrèrent alors qu'il était possible d'utiliser à leur place des matériaux ablatifs c'est-à-dire des matériaux se consommant sous l'action conjuguée de l'érosion mécanique et de la chaleur. En effet l'énergie nécessaire à échauffer puis pyrolyser le matériau ajoutée à l'énergie de réaction à la paroi permet d'évacuer une partie importante des calories (1). Encore faut-il que le résidu de ces réactions soit suffisamment important et suffisamment solide pour que l'intégrité de la tuyère soit assurée jusqu'à la fin du tir. Ce sont ces considérations qui ont conduit à l'utilisation de matériaux composites c'est-à-dire de matériaux constitués d'un renfort et d'une matrice. Le renfort est en général une fibre réfractaire dont le choix dépend de la conductibilité recherchée. Pour un matériau de veine, au contact des gaz, et qui doit être conducteur on utilise une fibre de carbone plus ou moins graphitée. Pour un matériau isolant on utilise une fibre de silice ou d'amiante. Dans tous les cas le renfort peut se présenter sous plusieurs formes : fibre coupée, tissu, mat, tricot. Le choix dépend des caractéristiques mécaniques recherchées. La matrice se doit de posséder un taux de carbone aussi élevé que possible de façon à déposer sur le renfort lors de la pyrolyse un coke solide. Pour ce faire, une résine phénolique est en général recommandée - Renfort et matrice sont associés lors de l'opération d'imprégnation et c'est l'imprégné obtenu qui est ensuite mis en forme et subit les opérations de "cuisson" au cours desquelles la résine durcit sous l'effet de la température et de la pression. Outre les caractéristiques intrinsèques de chaque composant, ces différentes opérations délicates et sensibles à l'environnement, conditionnent les caractéristiques du matériau final et par conséquent son comportement en tir.

Dans la suite de ce document nous avons retenu de décrire les trois matériaux qui sont les plus utilisés dans les tuyères. Tous trois utilisent la même résine phénolique mais diffèrent par la nature du renfort (tissu de carbone, de graphite ou de silice) et bien entendu par la composition.

2.2. - Caractéristiques des matières premières :

2.2.1. - Renforts :

Si l'on a choisi d'utiliser essentiellement un renfort sous forme de tissu c'est parce que ce dernier apporte au matériau une meilleure tenue mécanique avant et après pyrolyse de la résine. Il offre en outre la possibilité d'orienter les fibres par rapport aux sollicitations thermiques ou mécaniques dans la tuyère ce que ne permettent pas les fibres coupées ou les mats. C'est également pour cette raison que l'on a adopté un tissage satin plus déformable qu'un tissage toile. Le tissu de carbone utilisé résulte de la pyrolyse en atmosphère neutre d'un tissu de rayonne. Cette opération de carbonisation est délicate et la principale amélioration récemment apportée a consisté à l'effectuer en continu pour remplacer la carbonisation statique qui entraînait des différences de propriétés d'un lot à l'autre et à l'intérieur d'un même rouleau. On a ainsi amélioré la reproductibilité du matériau.

Le tissu de graphite résulte d'un traitement à haute température (environ 2500°C) du tissu de carbone ci-dessus. Ce traitement entraîne une modification de la structure atomique du carbone et par suite une augmentation de la conductibilité des fibres constituant le tissu. On trouvera dans le tableau de la figure 1 les valeurs moyennes des principales caractéristiques de ces tissus.

Caractéristiques		Tissu de Carbone	Tissu de Graphite
Masse spécifique	g/cm^3	1,85 - 1,95	1,45 - 1,50
Résistance traction chaîne	daN/cm	4 - 5	9 - 11
trame		3 - 4	9 - 11
Poids au m^2	g/m^2	280 - 290	250 - 270
Nombre de mailles/cm chaîne		20	21
trame		20	20
Taux de reprise d'humidité	%	4 - 6	0,2
Taux de carbone	%	96 - 98	> 99
Taux de cendre	%	0,2	< 0,1
Surface spécifique	m^2/g	50 - 100	1,3
Résistivité	Ω	0,6 - 0,7	0,4 - 0,5

Figure 1 : Caractéristiques moyennes des tissus de carbone et de graphite utilisés dans les matériaux ablatifs.

Ces deux tissus sont utilisés pour fabriquer des matériaux de veine conducteurs. Pour le matériau isolant on utilise plus volontiers un tissu de silice obtenu par traitement chimique puis thermique d'un tissu de verre. Les caractéristiques moyennes de ce tissu sont rassemblées dans le tableau de la figure 2.

Caractéristiques		Valeurs moyennes
Masse spécifique	g/cm^3	2,25
Résistance traction chaîne	daN/cm	10 - 11
trame		10 - 11
Poids au m^2	g/m^2	650 - 750
Nombre de mailles/cm chaîne		17 - 18
trame		14 - 15
Taux de silice	%	∿ 99
Taux de reprise d'humidité	%	0,5 - 1,5
Surface spécifique	m^2/g	∿ 70

Figure 2 : Caractéristiques moyennes du tissu de silice utilisé dans les matériaux isolants.

Ces tissus possèdent une bonne aptitude à l'imprégnation par les résines phénoliques sans traitement supplémentaire.

2.2.2. - Résine :

La recherche d'une résine à taux de coke élevé a conduit à développer une résine phénolique spéciale pour applications ablatives. Il était également nécessaire de prendre en compte les contraintes liées à l'élaboration du matériau imprégné (viscosité) et à sa mise en oeuvre (temps de gel) ce qui a conduit aux caractéristiques du tableau de la figure 3.

Caractéristiques		Valeurs moyennes
Masse volumique à 20°C	g/cm^3	1,18 - 1,19
Viscosité à 20°C	mpl	630
Temps de gel à 150°C	s	120 - 130
à 180°C	s	20 - 25
pH		7,5 - 7,6
Taux de coke	%	60 - 63

Figure 3 : Caractéristiques moyennes de la résine phénolique utilisée dans les matériaux ablatifs et isolants.

2.3. - Fabrication des préimprégnés :

L'opération d'imprégnation qui permet d'associer renfort et résine est une opération importante et délicate car c'est elle qui permet de déterminer le taux de résine et son degré de polymérisation, essentiels pour la mise en oeuvre du préimprégné et les caractéristiques du matériau final. Elle nécessite un contrôle soigné des paramètres d'imprégnation dont les principaux sont :

- la dilution du bain de résine,
- l'écartement des rouleaux permettant d'éliminer l'excès de résine déposée sur le tissu,
- les conditions de séchage : température du tunnel, vitesse de défilement du tissu imprégné dans le tunnel.

A la sortie de la machine les caractéristiques de l'imprégné sont contrôlées et les valeurs moyennes obtenues sont celles du tableau de la figure 4.

Caractéristiques	Carbone phénolique	Graphite phénolique	Silice phénolique
Taux de résine %	35 - 40	34 - 39	29 - 32
Taux de volatiles %	3 - 6	3 - 5,5	2 - 4
Indice de fluidité %	4 - 9	4 - 8	5 - 8
Indice Infra-rouge	0,63 - 0,73	0,58 - 0,70	0,65 - 0,90

Figure 4 : Caractéristiques moyennes des imprégnés phénoliques pour matériaux ablatifs et isolants.

Comme nous l'avons déjà indiqué ces propriétés sont très sensibles à l'environnement, la résine se trouvant alors dans un état de "semi polymérisation" assez instable.

Température et humidité peuvent faire varier de façon sensible en particulier la fluidité ce qui entraînera des hétérogénéités dans le matériau final. Il est donc prescrit de stocker ces imprégnés à basse température et dans des emballages étanches jusqu'à leur utilisation qui sera, elle aussi, soigneusement réglementée. Dans ces conditions la durée de vie des imprégnés est de plusieurs mois.

2.4. - Fabrication des pièces (2) :

Compte tenu de la sensibilité, ci-dessus mentionnée, des imprégnés aux conditions ambiantes, ils sont en général mis en oeuvre dans des ateliers à atmosphère contrôlée. Les deux principales techniques utilisées pour fabriquer les pièces des tuyères des propulseurs à poudre sont :

- le moulage à la presse de strates ou petits carreaux,
- le bobinage de ruban.

Le déroulement des opérations est schématisé figure 5.

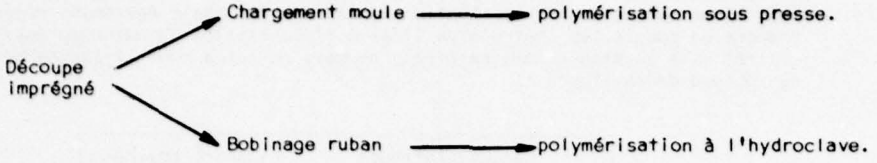

Figure 5 : Schéma de réalisation de pièces de tuyères en matériau composite ablatif.

Différents types de strates et de rubans sont utilisés en fonction du type de pièce à fabriquer. Pour effectuer la découpe, des techniques manuelles s'avèrent encore souvent les plus efficaces compte tenu du soin à apporter à la manipulation de l'imprégné.

Dans le moulage à la presse, le matériau est mis en forme et polymérisé en une seule opération de thermocompression. Les paramètres de moulage sont déterminés par les caractéristiques de fluage, et l'épaisseur de la pièce comme indiqué figure 6.

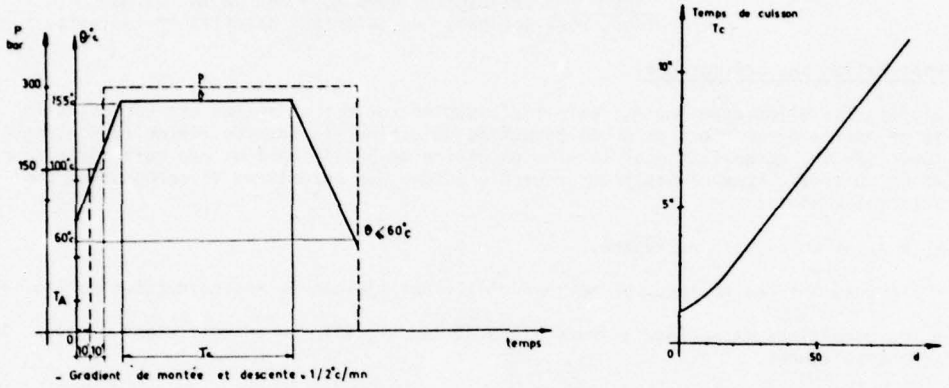

Figure 6 : Choix du cycle de polymérisation d'une ébauche moulée.

Par cette technique on réalise des pièces de différentes configurations pouvant atteindre une épaisseur de 100 mm et un poids de 30 kg (figure 7). On vérifie la qualité des pièces en mesurant leur densité et par un examen aux rayons X montrant l'orientation du renfort et les défauts éventuels.

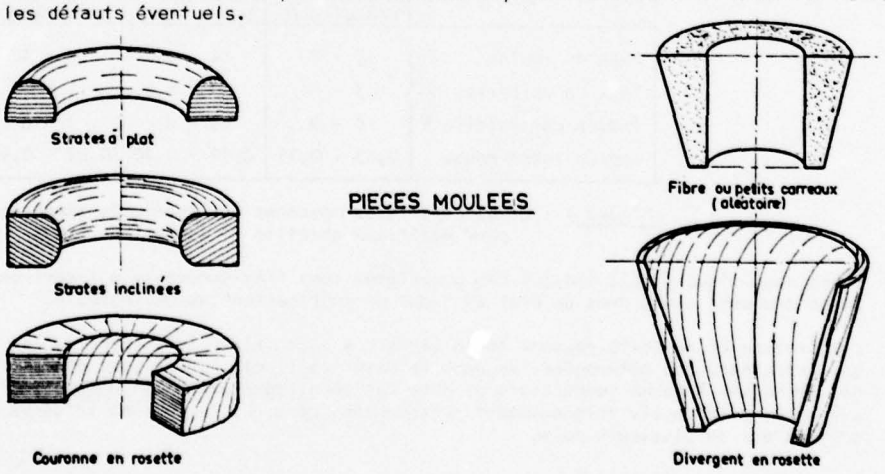

Figure 7 : Quelques configurations de pièces moulées.

La technique du bobinage est plus délicate et demande un imprégné dont les caractéristiques sont très constantes. Elle permet, par contre, d'orienter le ruban d'imprégné dans des directions variables par rapport à l'axe de la pièce donc par rapport au jet de gaz du propulseur d'où une meilleure adaptation aux sollicitations.

La réalisation d'une pièce bobinée s'effectue en deux étapes :

- Obtention d'une ébauche compacte par enroulement de ruban de tissu sur un mandrin.

- Polymérisation isostatique de la pièce en hydroclave.

La première opération s'effectue sur un tour à bobiner, les principaux paramètres étant

- température de chauffage de la résine,

- tension du ruban,

- pression du galet de compactage,

- température de refroidissement.

On obtient ainsi une ébauche dont la densité atteint couramment 95 % de la densité du composite polymérisé. Dans le cas du bobinage biais on est limité en particulier par le rapport : $\frac{\text{Diamètre extérieur}}{\text{Diamètre intérieur}} \leq 2{,}5$ pour éviter les plis dans la pièce.

Après bobinage les ébauches sont polymérisées en hydroclave. Cette "cuisson" nécessite une protection par tissus de drainage et membrane caoutchouc étanche. Comme pour la thermocompression les cycles de cuisson sont déterminés par le taux de fluage et l'épaisseur de la pièce comme indiqué figure 8.

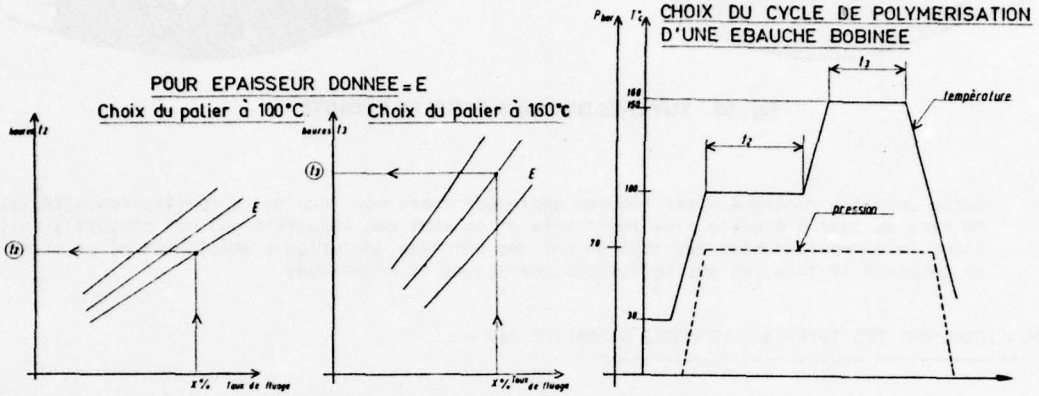

Figure 8 : Choix du cycle de polymérisation d'une ébauche bobinée.

Pression et température sont enregistrées en continu pour tous les cycles et depuis 1976 on réalise ainsi des divergents de tuyère bimatériaux (carbone - silice) avec plusieurs orientations différentes du ruban et dont le poids peut atteindre 140 kg (figure 9).

La densité, l'orientation des strates et l'absence de défauts lors de l'examen aux rayons X constituent également les critères de qualité des pièces bobinées.

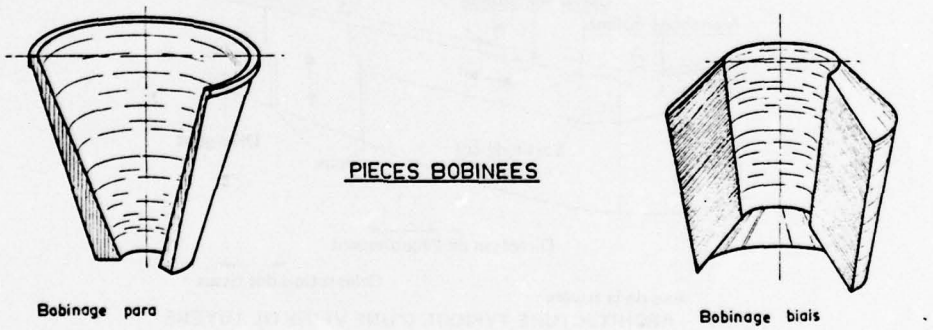

Figure 9 : Configurations de pièces bobinées.

Pour parvenir à la définition des meilleures techniques de mise en oeuvre, il a fallu évaluer différents types de matériaux. Pour ce faire on a réalisé une quinzaine de tirs au banc à échelle réduite. Des tuyères du type indiqué sur la figure 10 ont été montées sur des bombes de diamètre 390 et 800 mm chargées d'une poudre Isolane 36/9. Les matériaux à tester constituaient les cols et divergents de ces tuyères.

L'exploitation de ces tirs a consisté non seulement à mesurer l'érosion des matériaux en différents endroits de la tuyère mais également à mesurer les jeux résiduels entre pièces après tir. On en a déduit les principales conclusions suivantes :

- Le graphite phénolique a une meilleure tenue à l'ablation que le carbone phénolique par suite de sa meilleure conductibilité thermique.

- Pour un graphite phénolique et dans les zones à flux thermiques importants, l'orientation des strates dans le sens de l'écoulement des gaz est favorable à la tenue à l'ablation.

- L'examen des jeux résiduels montre que, pour un matériau donné, la tenue à l'ablation dépend de ses possibilités d'expansion en cours de dégradation. Ceci s'explique par la grande quantité de matières volatiles dégagée lors de la pyrolyse de la résine (3).

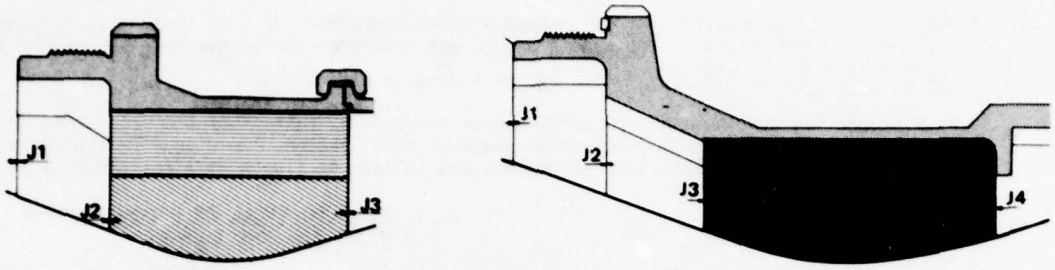

Fig : 10 TUYERES D'ESSAI A ECHELLE REDUITE

Cette dernière remarque s'est trouvée amplement confirmée lors de la réalisation ultérieure de tirs au banc à échelle plus importante et ce sont ces résultats qui ont conduit à envisager le dimensionnement des tuyères par des méthodes analytiques améliorées et en prenant en compte à la fois les sollicitations thermiques et mécaniques.

3 DIMENSIONNEMENT DES TUYERES - METHODES D'ANALYSE (4) -

Le dimensionnement par le calcul consiste à prédire aussi précisément que possible le comportement thermique et mécanique des différentes pièces composant une tuyère de façon à définir leur architecture (épaisseur des matériaux ablatifs et isolants, collages, dimensions des pièces métalliques, jeux ...).

La figure 11 présente un exemple du type d'assemblage étudié.

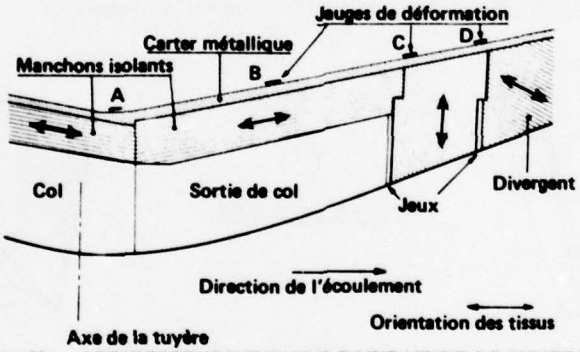

Fig : 11. ARCHITECTURE TYPIQUE D'UNE VEINE DE TUYERE

Le calcul apporte une aide importante à la conception et au dimensionnement de tels ensembles.

3.1. - Objectifs des calculs :

3.1.1. - Calculs thermiques :

Ces calculs ont deux objectifs principaux :

- Calcul de l'érosion en fonction du temps, et par suite dimensionnement de l'épaisseur des matériaux ablatifs.

- Calcul de la carte thermique dans l'épaisseur des matériaux en fonction du temps, et par suite dimensionnement de l'épaisseur des isolants. Cette épaisseur doit être telle que les parties structurales jouant un rôle mécanique (collages fonctionnels, pièces métalliques) restent à une température inférieure à une valeur donnée.

3.1.2. - Calculs mécaniques :

Une prévision des contraintes et des déformations de la tuyère au cours du tir est effectuée à l'aide des cartes thermiques précédemment calculées et compte tenu des efforts appliqués au matériel (pressions, réactions aux liaisons).

Ces sollicitations sont calculées :

- au sein des composites, dont on déduit le comportement à l'aide de critères adaptés à l'anisotropie ("contrainte maximale" dans certaines directions privilégiées, critère de Hill ...),
- au niveau des liaisons fonctionnelles (collages) où sont particulièrement étudiées les contraintes de traction et de cisaillement,
- au sein des pièces métalliques (critère de Von Mises) sur lesquelles sont généralement implantées des jauges de contrainte permettant de recouper les prévisions et les essais.

3.2. - Calcul du champ de températures dans une tuyère :

Le calcul du champ de température dans une tuyère pendant un tir passe par la résolution de l'équation de Fourrier qui peut s'écrire pour une géométrie de révolution :

$$\frac{\partial}{\partial x}\left(\lambda_x \frac{\partial T}{\partial x}\right) + \frac{\partial}{\partial y}\left(\lambda_y \frac{\partial T}{\partial y}\right) = \rho c_p \frac{\partial T}{\partial t} + P(T, t)$$

On voit donc apparaître les grandeurs physiques caractérisant la conduction dans un matériau orthotrope :

- la conductivité thermique suivant 2 directions,
- la chaleur spécifique,
- la masse volumique,

le terme P (T, t) représentant ici la pyrolyse du matériau phénolique.

L'écriture des conditions aux limites fait intervenir les échanges par rayonnement et convection entre la surface et les gaz de poudre, il faut donc connaître le pouvoir émissif du matériau de veine. Pour intégrer cette équation 2 codes distincts utilisant tous les deux la méthode des différences finies sont actuellement employés.

1) MABL 1 :

La schématisation utilisée dans ce programme n'est applicable qu'au cas d'un empilage comportant un matériau ablatif exposé aux gaz de poudre et un ou plusieurs matériaux inertes. La géométrie de l'ensemble est un cylindre de révolution.

L'empilage est décomposé en mailles élémentaires et le terme P (T, t) s'écrit :

$$P(T, t) = \frac{\partial}{\partial y}(x_{ig}\, h_g)_t$$

x_{ig} étant le débit de gaz produit dans la zone de pyrolyse et h_g leur enthalpie.

Pour calculer x_{ig} on admet que le matériau phénolique peut être représenté par un ou plusieurs corps dont les décompositions se produisent de façon indépendante en fonction de la température en suivant chacun une loi d'Arrhénius.

Les constantes de ces lois peuvent être déduites de mesures thermogravimétriques effectuées sur le matériau en laboratoire.

L'écriture des conditions aux limites côté surface chaude fait intervenir en plus de la convection et du rayonnement les réactions chimiques à l'équilibre entre surface et gaz de poudre. Ceci permet le calcul de l'ablation de la surface en fonction du temps.

2) BIDABL :

Ce code permet l'étude d'un massif bidimensionnel axisymétrique constitué de matériaux orthotropes. Il permet donc de traiter la zone convergent-col-entrée de divergent d'une tuyère.

Afin d'alléger les calculs la pyrolyse des matériaux phénoliques est représentée par une augmentation de la chaleur spécifique au moment de la dégradation. Cet accroissement apparent de chaleur spécifique a été obtenu à partir de calculs effectués à l'aide du code MABL 1 pour des échauffements semblables.

Les conditions aux limites sont traitées d'une façon analogue à celles de MABL 1 cependant les réactions gaz-paroi ne sont plus à l'équilibre mais sont pilotées par une cinétique suivant le schéma de Langmuir. Ceci permet de calculer avec une bonne précision le recul de la surface en fonction du temps pour les matériaux utilisés actuellement et de tracer la carte thermique d'une tuyère à un instant donné.

3.3. - Prévision des sollicitations mécaniques dans les pièces de tuyère :

3.3.1. - Méthode de calcul :

Les calculs sont généralement effectués par la méthode des éléments finis à l'aide du programme MARC (5). La figure 12 présente un exemple de maillage.

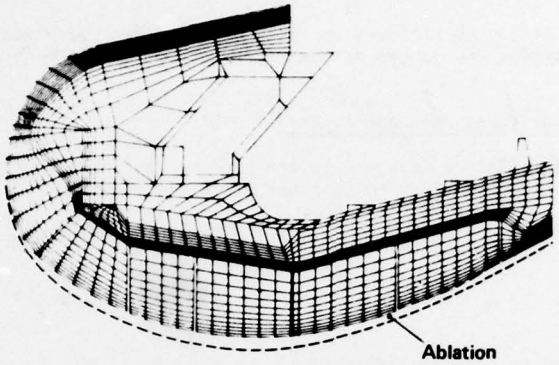

Fig : 12 MAILLAGE DE LA TUYERE POUR CALCUL THERMOMECANIQUE

Les calculs sont effectués à plusieurs instants de combustion en tenant compte de l'évolution du profil de veine avec l'ablation, et avec les hypothèses de l'élasticité linéaire en petites déformations. La géométrie et les charges étant supposées axisymétriques, le programme permet de modéliser l'évolution des jeux de dilatation séparant les pièces (avec possibilité de fermeture au cours du tir) et permet également de tenir compte des éventuels glissements de composants.

En ce qui concerne la modélisation des matériaux, un effort particulier a été accompli en liaison avec les résultats d'un important programme de caractérisation.

De façon générale, les calculs prennent en compte l'anisotropie des composites et la variation de leurs caractéristiques avec la température ; la modélisation des composites phénoliques est décrite de façon plus détaillée au paragraphe suivant.

3.3.2. - Caractéristiques des composites phénoliques utilisées dans les calculs :

L'évolution des caractéristiques de ces matériaux avec la température dépend de la façon dont se déroule la pyrolyse de la résine phénolique en cours de tir, c'est-à-dire en particulier des deux paramètres suivants :

- Quantité de gaz de pyrolyse produite par unité de temps, paramètre dépendant de la vitesse de chauffage.

- Pression des gaz de pyrolyse, paramètre dépendant de l'environnement de la pièce (possibilités d'évacuation des gaz de pyrolyse, état de contrainte).

On peut donc écrire : $C = f\left(T, \text{position}, \frac{dT}{dt}, \varepsilon\right)$

Soit $C = f(a, \quad b \quad , \quad c \quad , d)$ [1]

C est l'une quelconque des caractéristiques mécaniques du composite, que l'on peut considérer comme orthotrope :

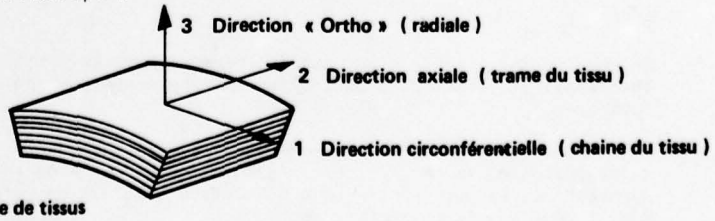

Avec cette hypothèse, le calcul exige la connaissance de 11 caractéristiques mécaniques :

. 3 modules d'Young E_1, E_2, E_3.

. 3 coefficients de Poisson ν_{12} (ou ν_{21}), ν_{13} (ou ν_{31}), ν_{23} (ou ν_{32}).

. 2 modules de cisaillement G_{31} et G_{32} compte tenu de l'axisymétrie du problème traité (G_{12} n'intervient pas).

. 3 coefficients de dilatation α_1, α_2 et α_3.

En pratique, les matériaux moulés peuvent être considérés comme monotropes (le plan 1-2 est isotrope, d'où 7 caractéristiques indépendantes seulement).

Nous examinons ci-après comment sont choisies ces caractéristiques, compte tenu des paramètres a, b, c, d de [1], en liaison avec les différents résultats de caractérisation.

a - Paramètre température T :

Pour chaque composite phénolique, chacune des caractéristiques est introduite dans les calculs sous forme d'une courbe C = F (T).

b - Paramètre "position du matériau dans la tuyère" :

L'expérience (étude de l'état des pièces de tuyère après tir, comparaison entre prévisions de calcul et essais) nous a conduit à séparer les composites phénoliques en deux groupes suivant la position occupée dans la tuyère. Dans chaque groupe il faut en outre distinguer les matériaux suivant leur renfort (graphite, carbone, silice) et suivant leur procédé de fabrication (bobinage, moulage).

Ces deux groupes sont les suivants :

. Groupe I : pièces de type "isolants" (exemple : manchons, figure11) montées sans jeux et pyrolysées sous compression biaxiale ou triaxiale.

. Groupe II : pièce de type "ablatifs" généralement séparées des autres composants par des jeux parallèles aux strates. La pyrolyse est dite "libre" (compression orthogonale aux strates nulle ou faible ; exemple : sortie de col, figure 11).

c - Paramètre vitesse de chauffage "$\frac{dT}{dt}$" :

La mesure classique de la dilatation des composites phénoliques met en évidence l'importance de la vitesse de chauffage, comme le montre la figure 13.

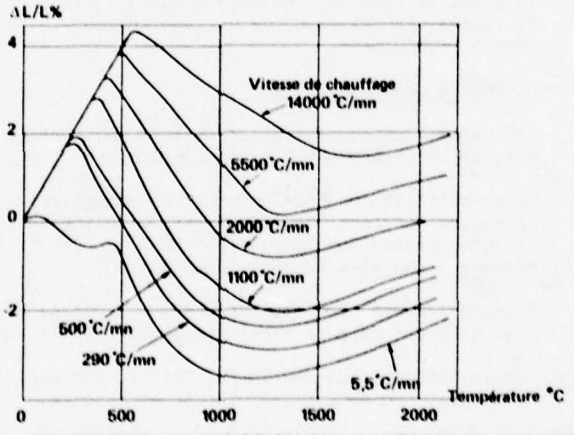

Fig 13 : DILATATION EN FONCTION DE LA VITESSE DE CHAUFFAGE

En réalité la dilatation mesurée aux vitesses de chauffage élevées est due à un gonflement de l'éprouvette consécutif à la génération rapide de gaz de pyrolyse de la résine entre les couches de tissus. Les valeurs α ainsi obtenues ne sont pas homogènes avec les valeurs correspondantes des modules qui sont mesurées sur éprouvettes chargées et stabilisées à la température de mesure après une étape de chauffage très lent.

Des caractéristiques (E_i, α_i) homogènes sont obtenues par caractérisation "sous charge" ("restrained thermal growth tests" (7)). Les valeurs obtenues, dont les figures 14 et 15 ci-après donnent des exemples, sont représentatives des caractéristiques des matériaux pyrolysés sous compression multi-axiale (groupe I).

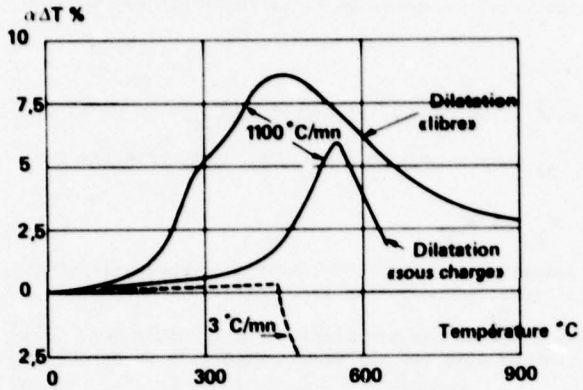

Fig 14 : DILATATION « LIBRE» ET «SOUS CHARGE» DU CARBONE PHENOLIQUE BOBINE

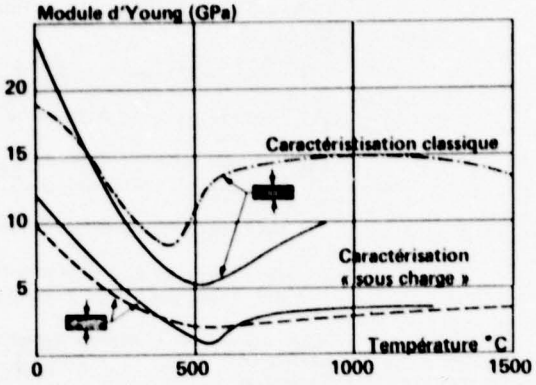

Fig : 15 MODULES D'ELASTICITE «LIBRE» ET«SOUS CHARGE» D'UN CARBONE PHENOLIQUE BOBINE

Finalement, les modélisations utilisées dans les calculs sont résumées dans le tableau suivant :

	RENFORT (TISSUS)	PROCEDE DE FABRICATION	MODELE DE CALCUL	NOMBRE DE CARACTERISTIQUES (COURBES C - f (T)	ORIGINE DES CARASTERISTIQUES	EXEMPLES DE PIECES
GROUPE I	Carbone	Bobinage	Orthotrope	11	Caractéristiques «sous charge » à la vitesse moyenne de pyrolyse de la pièce considérée	Manchon isolant - divergent
	Carbone	Moulage	Monotrope	7		Isolant moulé
	Carbone	moulage «petits carreaux»	Isotrope	3		Isolant moulé
	Silice	Bobinage	orthotrope	11		Manchon isolant
GROUPE II	Carbone	Moulage	Monotrope	7	Dilatation « libre »	Pièces ablatives de veine
	Graphite	Moulage	Monotrope	7		

Les calculs nécessitent donc théoriquement 46 courbes C = f (T) pour différentes vitesses de pyrolyse, dans la plage des vitesses rencontrées dans les pièces de tuyère. En pratique, on utilise surtout les courbes de caractéristiques mesurées à 1100°C/mn.

d - Paramètre déformation "ε" :

Les composites considérés présentent des courbes contrainte/déformation non linéaires, particulièrement à haute température.

La caractérisation "sous charge" ne permet pas d'obtenir ces courbes, les caractéristiques mesurées étant des valeurs "à l'origine" (elles sont obtenues par application, pendant un temps très court, de petits incréments de charge ; les déformations mécaniques restent très faibles).

Jusqu'à présent, les courbes σ / ε issues de caractérisation classique ne donnent lieu qu'à des calculs élastiques non linéaires comparatifs sur des pièces isolées.

Les besoins nécessaires aux calculs étant exprimés l'étape suivante a consisté à réaliser le programme de caractérisation nécessaire.

4 CARACTERISATION DES MATERIAUX PHENOLIQUES -

4.1. - Matériaux retenus :

Compte tenu du nombre élevé de caractéristiques à mesurer à différentes températures, il fallait choisir judicieusement les matériaux à caractériser. Ce choix s'est fait en fonction de l'utilisation dans les tuyères et des préoccupations du moment et on a retenu les quatre matériaux phénoliques suivants :

- Graphite phénolique moulé en strates entières.

- Carbone phénolique moulé en strates entières.

- Carbone phénolique bobiné parallèlement à l'axe de la pièce.

- Silice phénolique bobinée parallèlement à l'axe de la pièce.

Pour les quatre matériaux, les propriétés ont été étudiées, lorsque nécessaire, suivant les directions principales d'orthotropie du matériau soit :

- Parallèle aux strates ("para" = "with lamina") et perpendiculaire aux strates ("ortho" = "across lamina") pour les matériaux moulés.

- Circonférentielle (sens chaîne du tissu), axiale (sens trame du tissu) et radiale (perpendiculaire aux strates) pour les matériaux bobinés.

4.2. - Eprouvettes :

Les éprouvettes nécessaires à la réalisation des essais de caractérisation ont toutes été prélevées dans des ébauches fabriquées dans des conditions industrielles. C'est dire que les valeurs obtenues sont représentatives des caractéristiques des matériaux utilisés dans les tuyères des propulseurs.

Pour les essais aux températures supérieures à 400°C, il a fallu tenir compte de la dégradation de la résine et les ébauches d'éprouvettes ont subi une prépyrolyse suivant un cycle thermique bien défini et atteignant une température maximale de 2200°C. La figure 16 résume les différentes opérations subies par les ébauches et les éprouvettes avant essai.

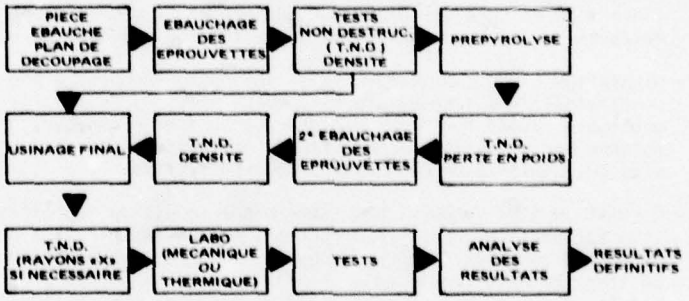

Fig : 16 CYCLE SUBI PAR LES EPROUVETTES

4.3. - Essais :

Les essais effectués devaient naturellement conduire à l'obtention de toutes les caractéristiques nécessaires au dimensionnement des tuyères et ce, en fonction de la température.

4.3.1. - Essais mécaniques :

- TRACTION : A l'ambiante et à température inférieure à 400°C on utilise une machine classique et les éprouvettes sont chauffées par effet JOULE. La vitesse de chauffe est de 1100°C s^{-1} et la vitesse de traction 1,3 mm mn^{-1}. La température est contrôlée par pyromètre optique et les déformations mesurées par pinces extensométriques. On enregistre la courbe contrainte-déformation qui permet de calculer le module d'élasticité et le coefficient de Poisson.

  A température élevée on doit assurer l'alignement de l'équipage par des paliers à gaz. La température est obtenue par un four en graphite et les déformations axiales et latérales sont mesurées par un système optique de poursuite de repères. On enregistre également les courbes contrainte-déformation.

- COMPRESSION : On utilise sensiblement les mêmes systèmes et les mêmes méthodes de mesure que pour les essais de traction.

- CISAILLEMENT : Pour la mesure de la résistance interlaminaire, on soumet une éprouvette double entaille à un effort de compression ; elle se rompt en cisaillement dans le plan défini par le fond des entailles. On obtient cet effort par un montage sur la machine de traction décrite ci-dessus.

  La mesure de la résistance translaminaire s'obtient par application d'un effort tranchant sur une éprouvette pré-entaillée au moyen d'un outillage adapté placé sur les machines de traction décrites ci-dessus.

  Des essais de torsion sont également réalisés et permettent de mesurer la résistance à rupture et le module interlaminaires d'une part, le module apparent de cisaillement duquel on déduit le module de cisaillement translaminaire d'autre part.

4.3.2. - Essais thermiques :

- CONDUCTIBILITE : Pour les températures d'essai comprises entre 60 et 800°C on utilise la méthode comparative qui consiste à faire circuler un flux de chaleur dans le sens axial d'une éprouvette cylindrique intercalée entre deux pièces de référence de conductivité connue, en négligeant les pertes radiales que l'on peut minimiser dans l'appareillage, on écrit la conservation du flux à travers les trois éléments. On obtient une précision de ± 3 %.

  Au-dessus de 1000°C on utilise la méthode du flux radial dont le principe est le suivant : un cylindre creux isolé à chacune de ses extrémités et chauffé sur sa surface latérale est traversé par un flux de chaleur que l'on mesure en faisant circuler à l'intérieur du cylindre un courant d'eau dont on mesure le débit et la variation de température. La précision de la mesure est estimée à ± 12 %.

  Pour les matériaux à faible conductibilité thermique c'est-à-dire le carbone phénolique bobiné vierge dans le sens radial et la silice phénolique bobinée entre l'ambiante et 800°C il a fallu utiliser des méthodes particulières dérivées de la méthode comparative.

- CHALEUR MASSIQUE : Entre la température ambiante et 550°C on utilise un calorimètre adiabatique (calorimètre classique) qui fournit la valeur de l'enthalpie en fonction de la température et par dérivation, la chaleur massique avec une précision de ± 3 %.

  Au-delà et jusqu'à 2200°C on utilise un calorimètre à glace. Sous l'effet de la chaleur dégagée par l'échantillon porté à une certaine température, l'état d'équilibre d'un mélange eau glace est déplacé et il s'ensuit une variation de volume retransmise à une colonne de mercure, la précision est de ± 5 %.

- DILATATION LIBRE : On mesure la variation de longueur d'une éprouvette placée dans un dilatomètre à tube de graphite. Deux vitesses de chauffe ont été utilisées : une lente (2,8°C mn^{-1}) obtenue grâce à un four classique, une rapide (1100°C mn^{-1}) obtenue par un système à induction. Les températures sont contrôlées par thermocouples puis au-delà de 800°C par pyromètre optique.

- DILATATION SOUS CHARGE : Pour déterminer la dilatation effective sous charge dont il a été parlé au chapitre précédent, deux types d'essais ont été réalisés : des essais de compression sous charge pour mesurer les modules d'élasticité E' en régime transitoire et les essais de dilatation sous charge proprement dits. Pour obtenir la valeur du module on réalise un essai de compression classique mais on charge périodiquement l'éprouvette pendant le chauffage et on enregistre les courbes effort-déformation.

  Pour mesurer la dilatation effective sous charge on utilise une machine de traction dont l'effort est transformé en un effort de compression par un outillage. L'éprouvette est chauffée par effet Joule ou micro-ondes. Un asservissement permet de conserver à peu près constante la longueur de l'éprouvette en la comprimant au fur et à mesure de sa dilatation. Une pince extensométrique mesure les déformations axiales, un thermocouple la température de l'éprouvette et une cellule l'effort exercé. On enregistre toutes ces données.

4.4. - Résultats :

On a déjà présenté, pour une meilleure compréhension, les résultats de dilatation au chapitre 3. Les quelques exemples traités ici sont ceux qui nous ont paru les plus significatifs et qui permettent de tirer une conclusion générale sur les caractéristiques des 3 composés phénoliques étudiés.

4.4.1. - Conductibilité thermique :

Cette valeur est essentielle pour le calcul du champ de température dans une tuyère. Les courbes présentées dans les figures 17 et 18 sont obtenues en prenant les points de mesure correspondant aux températures de précarbonisation pour lesquelles le matériau est stabilisé. On représente ainsi une conductibilité moyenne en régime transitoire, la conductibilité réelle étant difficile à déterminer entre 300 et 1000°C du fait de la pyrolyse de la résine.

On constate que la silice phénolique est de loin le matériau le plus isolant et que le graphite phénolique est plus conducteur que le carbone phénolique jusqu'à 300°C. L'écart tend à diminuer lorsque la température augmente.

Dans tous les cas la conductibilité du matériau "para" est plus élevée que celle du matériau "ortho", l'écart augmentant avec la température et étant d'autant plus grand que le matériau est plus conducteur. Cette dernière caractéristique conduira évidemment à orienter les strates perpendiculairement à l'axe d'une tuyère dans les zones les plus sollicitées.

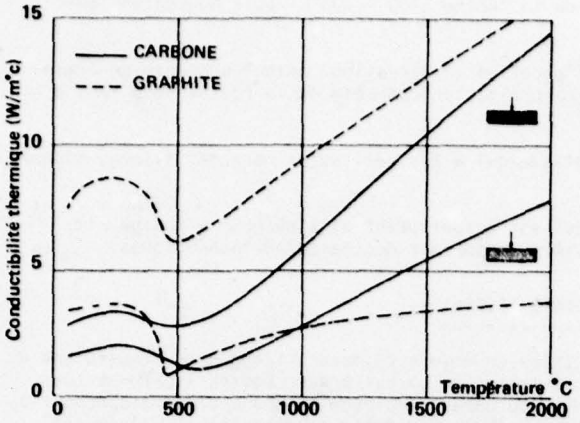

Fig :17 CONDUCTIBILITE DES CARBONES ET GRAPHITES PHENOLIQUES MOULES

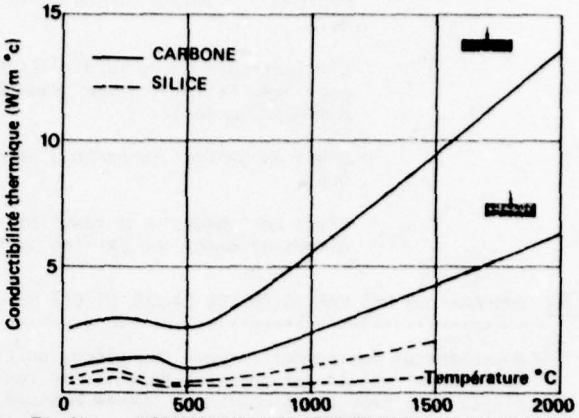

Fig :18 CONDUCTIBILITE THERMIQUE DES CARBONES ET SILICES PHENOLIQUES BOBINES

4.4.2. - Caractéristiques mécaniques :

Les essais effectués ont permis de tracer les courbes des caractéristiques exigées par le dimensionnement, en fonction de la température. Quelques exemples sont présentés sur les figures 19 - 20 et 21. Comme pour la conductibilité thermique, les parties de courbe correspondant au régime transitoire (pyrolyse de la résine entre 300 et 1000°C) ont été estimées d'après les mesures effectuées sur matériau prépyrolysé.

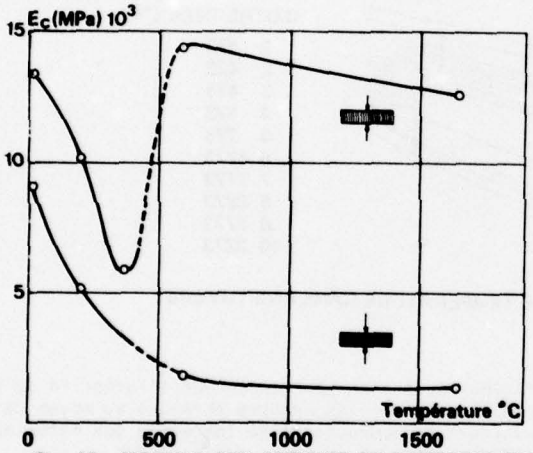

Fig : 19 MODULE D'ELASTICITE EN COMPRESSION DU GRAPHITE PHENOLIQUE MOULE

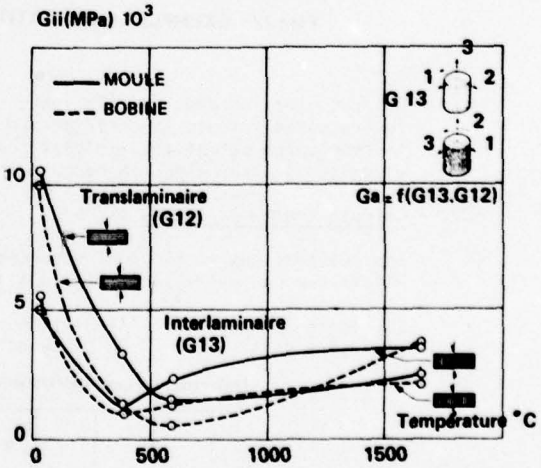

Fig :20 MODULE D'ELASTICITE EN CISAILLEMENT DU CARBONE PHENOLIQUE

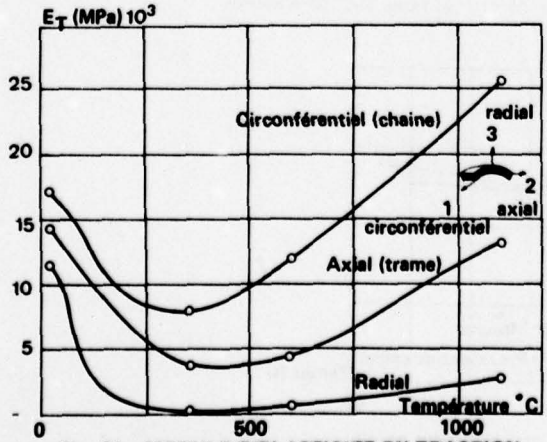

Fig : 21 MODULE D'ELASTICITE EN TRACTION DE LA SILICE PHENOLIQUE BOBINE

Tous les matériaux étudiés ont un comportement voisin : les caractéristiques chutent rapidement jusqu'à carbonisation de la résine (400 à 600°C) puis augmentent au-delà.

L'anisotropie entre la direction "para" et la direction "ortho" augmente généralement avec la température jusqu'à carbonisation complète de la résine puis tend à diminuer au-delà.

C'est en général le carbone phénolique qui a les meilleures caractéristiques mécaniques.

C'est cet ensemble de résultats qui est actuellement utilisé pour effectuer le dimensionnement des parties de tuyère comportant des matériaux phénoliques.

5 COMPARAISON DES PREVISIONS DE CALCUL ET DES RESULTATS D'ESSAI -

Moyennant un équipement correct des pièces sollicitées en moyens de mesure (jauges de température et de déformation) il est possible de comparer les prévisions de calcul à des résultats obtenus lors d'essais au banc des propulseurs. Cette méthode est couramment employée en phase de développement de nouveaux programmes et permet d'affiner peu à peu les résultats. Quelques exemples sont présentés ci-après.

5.1. - Répartition des températures :

Les méthodes de calcul présentées au chapitre 3 permettent non seulement de prévoir le recul de la surface de la veine par suite du phénomène d'ablation mais également de tracer une carte des isothermes dans la tuyère à chaque instant du tir comme le montre la figure 22.

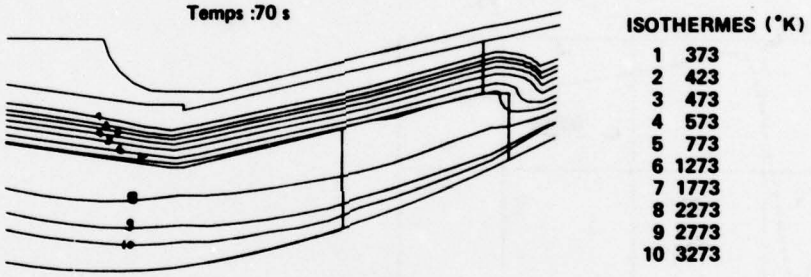

Fig : 22 EXEMPLE DE REPARTITION DE TEMPERATURE DANS UNE TUYERE

On peut ainsi en déduire l'épaisseur de matériau nécessaire pour conserver l'intégrité de la tuyère pendant toute la durée du tir. La comparaison avec les mesures obtenues au moyen de thermocouples permet ensuite d'affiner les valeurs de conductibilité thermique des matériaux et de réduire peu à peu la marge d'incertitude.

5.2. - Calculs thermomécaniques :

Les déformations en tir sont mesurées à l'aide de jauges de déformation collées sur le carter métallique de tuyère (voir figure 11), trois exemples sont présentés ci-après.

La figure 23 représente l'évolution avec le temps des déformations circonférentielles du carter de tuyère dans le cas où la pièce de sortie de col glisse sur le manchon.

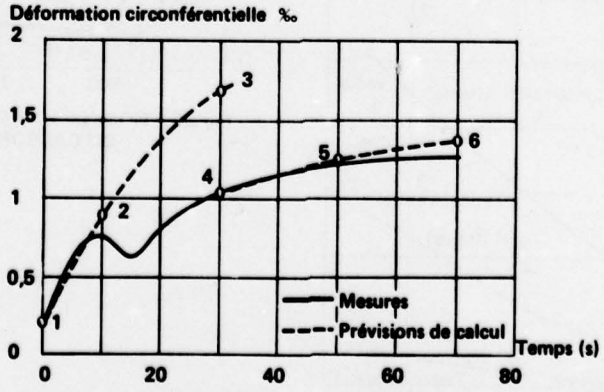

Fig : 23 COMPARAISON CALCUL/MESURE AVEC GLISSEMENT DE PIECE (JAUGE B)

Le glissement intervient aux environs du temps de tir 10 s ; les calculs notés 1, 2 et 3 sont effectués en supposant que les pièces restent rigidement liées. Les calculs notés 4, 5 et 6 modélisent le glissement. Dans ce cas, les déformations du carter au-delà du temps 15 s sont essentiellement dues au manchon isolant en carbone phénolique. La bonne corrélation entre calcul et essai valide la modélisation adoptée pour ce matériau (caractéristiques "sous charge").

La figure 24 représente l'évolution avec le temps des déformations circonférentielles du carter de tuyère dans le cas où la sortie de col reste dans sa position initiale.

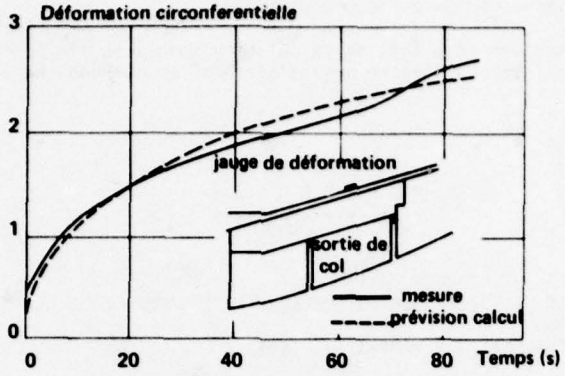

Fig : 24 COMPARAISON CALCUL/MESURE SANS GLISSEMENT DE PIECE

La figure 25 représente l'évolution axiale - le long d'une méridienne du carter de tuyère - des déformations circonférentielles au temps de combustion 70 s. La courbe des "déformations mesurées" est tracée à partir des mesures données par les jauges notées A, B, C, D (voir figure 12).

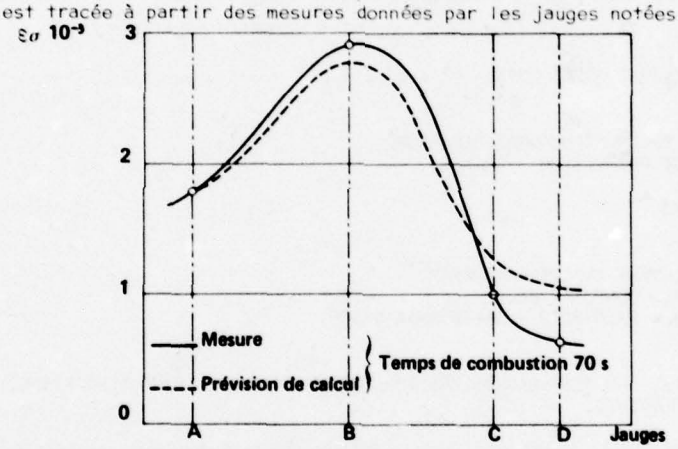

Fig : 25 EVOLUTION AXIALE DES DEFORMATIONS CIRCONFERENTIELLES DU CARTER

On constate sur cette dernière figure que le calcul recoupe correctement l'essai au niveau des jauges A et B (carbone phénolique en position d'isolant), mais que la corrélation est moins bonne au niveau de la jauge D (pièce ablative en carbone phénolique). Cet écart montre que l'utilisation des dilatations "libres" du matériau pour une telle pièce n'est pas entièrement satisfaisante.

6 CONCLUSION -

Les efforts accomplis depuis une dizaine d'années permettent de prédire désormais avec une bonne précision le comportement des pièces de tuyère en matériaux phénoliques pendant la durée d'un tir. Il a fallu pour cela :

- améliorer la qualité et la reproductibilité des matériaux en :
  - . préparant et contrôlant soigneusement les matières premières,
  - . définissant et contrôlant avec soin la mise en oeuvre en automatisant autant que possible les procédés.
- utiliser les nouvelles méthodes d'analyse par éléments finis et développer de nouveaux programmes de calcul : MABL 1 et BIDABL pour les calculs de champ thermique, MARC pour les sollicitations mécaniques.
- mesurer toutes les caractéristiques à introduire dans ces programmes et ce en fonction de la température pour quatre matériaux :

. un graphite phénolique moulé,

. un carbone phénolique moulé,

. un carbone phénolique bobiné,

. un silice phénolique bobiné.

Dans certains cas il s'est avéré nécessaire d'effectuer ces mesures en se rapprochant des conditions réelles de tir : dilatation sous charge par exemple.

La poursuite de la comparaison des résultats de calcul et d'essais en tir permet d'une part d'améliorer peu à peu l'architecture des tuyères, d'autre part d'affiner les méthodes de calcul et les valeurs de certaines caractéristiques.

REFERENCES

[1] S. KOHN - J.J. NICOLAS - G. TAGUET de l'ONERA :
CONTRIBUTION A L'ETUDE DE L'ABLATION DE QUELQUES MATERIAUX A BASE DE RESINE PHENOLIQUE.

LA RECHERCHE AEROSPATIALE N° 117 MARS-AVRIL 1967.

[2] C. DEVOUGE :
MISE EN OEUVRE DES MATERIAUX COMPOSITES.

COLLOQUE SUR LES MATERIAUX NOUVEAUX - ADERA - 20-22 AVRIL 1977.

[3] J. JAMET - R. JALIN - C. LE TOURNEUR - ONERA :
ETUDE EXPERIMENTALE DE LA DEGRADATION THERMIQUE D'UN MATERIAU ABLATABLE.

LA RECHERCHE AEROSPATIALE ANNEE 1973 - n° 4 p. 233.

[4] L. LEMOINE :
SOLID ROCKET NOZZLE THERMOSTRUCTURAL BEHAVIOR.
SOCIETE EUROPEENNE DE PROPULSION - FRANCE.

AIAA PAPER n° 75-1339.

[5] MARC-UNIVAC :
NON LINEAR FINITE ELEMENT ANALYSIS PROGRAM.
MARC ANALYSIS RESEARCH CORPORATION.
260, Sheridan Avenue - PALO-ALTO - CALIFORNIA 94306.

[6] DRIGGERS, G.W. :
DEFINING ENVIRONMENTAL AND TEST PARAMETERS FOR NOZZLE MATERIAL CHARACTERIZATION.
SOUTHERN RESEARCH INSTITUTE.

AIAA PAPER n° 75 1255.

[7] DRIGGERS, G.W. :
APPLICATION ORIENTED TESTING OF ROCKET NOZZLE MATERIALS.
SOUTHERN RESEARCH INSTITUTE.

AIAA PAPER n° 75 818.

GAS PHASE VELOCITY MEASUREMENTS IN SOLID ROCKET PROPELLANTS BY LASER DOPPLER ANEMOMETRY

by
A. COGHE, L. DE LUCA, G.L. SENSALARI and A. VOLPI
Centro di Studio per Ricerche sulla Propulsione e sull'Energetica (C.N.P.M.) - Istituto di Macchine, Politecnico, 32 piazza Leonardo da Vinci, 20133 Milano
Italy

SUMMARY

Laser-Doppler Anemometry is a convenient diagnostic technique for the gas flow field associated with a burning solid rocket propellant, because of the non perturbing nature of the measuring system, the good space and time resolution. Experimental results have been collected in the pressure range 1 - 10 atm for different propellants. A continuous velocity output is possible when a sufficiently large particle rate is available. The pressure and the condensed phase burning rate are simultaneously measured and related to the gas phase velocity.

Sec. 1 - INTRODUCTION

A Laser Doppler Velocimetry (LDV) technique has been used to perform velocity measurements in the gaseous region near the combustion surface of a burning solid rocket propellant. The main reason of this choice is the fact that the usual intrusive experimental techniques are of little help in a high temperature, reactive medium with large thermal gradients. Likewise, several laser-based optical techniques were developed to measure the condensed phase burning rate and the size of the particles carried away by the gas in the plume of the burning solid propellant. These same particles were used as scattering centers for the LDV measurements. The condensed phase burning rate (as well as the flame temperature, the condensed phase thermal profile and the instantaneous pressure) were also determined by other standard techniques. This would allow to cross-check the LDV results in the gas phase zone.

A steady state strand burner, with two symmetrical and opposite optical windows, was specifically designed for LDV experiments. The operating pressure range is 1 to 10 atm. The differential mode of operation was used for the LDV system, with observation in the forward direction. Measurements were made of the gas phase velocity component in the direction of the axis of the rod of solid propellant. A computerized data acquisition and processing system was also realized. The apparatus has been applied to a steadily burning solid propellant, with the purpose of exploring the possibility of future applications to unsteady situations. Reasonably good results were obtained, but some problems remain to be solved and more data are needed in order to cross-check the LDV results and to clarify the uncertainties so far encountered.

Sec. 2 - FUNDAMENTALS OF LASER DOPPLER VELOCIMETRY

The basic principle involved in LDV is the Doppler frequency shift of a monochromatic and coherent light beam scattered by micrometric particles suspended in a moving medium.

The Doppler frequency shift is normally resolved by heterodyning the scattered light with a reference beam on the surface of a photodetector (reference beam LDV). Alternatively, scattered waves coming from two incident beams can be heterodyned (differential LDV). The resulting light intensity, and hence the photocurrent, will be modulated at the Doppler frequency (Refs. 1-3)

$$f_D = 2\,U \sin(\beta/2)/\lambda \qquad (2.1)$$

where: U = the particle velocity component in the direction of the bisector of the illuminating cross-beams;
$k = 2\pi/\lambda$ is the wave vector;
λ = the wave lenght of the laser beam
β = the angle between the two cross-beams.

The main advantage of the differential LDV (see Fig. 1) is that it is quite simple to align and it is not sensitive to small vibrations. Moreover, the frequency is independent of the detection angle. A picture, which is often used to describe this system, is the so called "fringe model" that involves visualising a set of interference fringes produced by two incident laser beams in their cross region. The Doppler signal is produced by light scattered from particles crossing the intersection of the illuminating beams (probe volume), when the scattered light, collected through a receiving lens, reaches a photomultiplier. The probe volume is geometrically defined by the cross region of the two incident laser beams and it looks like an ellipsoid with the major axis perpendicular to the measured flow velocity component.

LDV techniques allow a direct measurement of velocity components (through the measurement of the Doppler frequency by an electronic signal processor) with a very sharp space resolution ($\cong 0.1$ mm^3) and without disturbing the flow. This is an important feature in reactive media. However, a sufficiently large number of scattering particles ($\geq 10^8$ m^{-3})

is required to obtain a continuous velocity information. The performance of an LDV system strongly depends on the size distribution and concentration of the particles scattering light into the photodetector. Particle concentration has to be high to obtain good time resolution of the velocity variation, while particle sizes have to be very small to follow spatial velocity gradients. In unsteady flows, the LDV chain of instruments must be treated as a transducer for which the transfer function is determined by the dynamics of tracer particles.

The capability of particles to follow the gas flow can be roughly estimated from the Bassett's general equation (Refs. 4 and 5). On the assumption that the particle density ρ_p is larger than the gas density ρ_g, the Bassett's equation reduces to

$$\frac{dU_p}{dt} = \frac{1}{\tau}(U_g - U_p) \tag{2.2}$$

where

$$\tau = \frac{(2\rho_p + \rho_g)d^2}{36\mu} \tag{2.3}$$

being U_p and U_g the particle and gas velocities;
d the particle diameter and
μ the gas viscosity.
The parameter τ has the meaning of a relaxation time for a particle of diameter d subjected to a spatial velocity gradient. The evaluation of τ necessitates the knowledge of the particle density and size distribution.

Parallel measurements of particle size and density are of the greatest importance in experiments where flow seeding with particles of known size is not feasible or it cannot be assumed "a priori" that ambient particles are adequately following the fluid flow. LDV systems can provide information on particle size from the correlation of particle diameter with the shape of the LDV signal.

It was shown (Refs. 6-9) that the single particle Doppler signal can be accurately predicted on the basis of the Mie scattering theory. The general expression of the Doppler photocurrent, produced by a single particle crossing the geometric center of the probe volume, is given by

$$i(t) = \frac{\eta I_o}{k}\left\{P(\vartheta,\varphi) + D(\vartheta,\varphi)\cos\left[\omega_D t - \Psi(\vartheta,\varphi)\right]\right\} \tag{2.4}$$

where η is the detector sensitivity,

$$\omega_D = 2\pi f_D$$

and the two incident beams are assumed to have equal intensities $I_{01} = I_{02} = I_0$. The term P represents the "pedestal" amplitude of the current (Fig. 2), while D represents the Doppler amplitude and Ψ determines the phase of the scattered intensity. P, D and Ψ are integral quantities, integrated over the collecting solid angle, Ω, of the receiving optics. They depend on the direction of detection (ϑ,φ), i.e. the axis of the collecting aperture, and are defined in terms of the complex amplitude functions given by the Mie theory (Refs. 10 - 12). The quantities P, D and Ψ depend only on the scattering properties and size of the particle (for a fixed LDV geometry), whereas the photocurrent is a time-varying function of the particle position in the probe volume. Indeed, a moving fringe pattern is seen by the detector due to two beam interference and particle motion.

The fringe contrast or Visibility is defined by

$$V = D/P \tag{2.5}$$

Visibility is an important parameter because its computed values can be easily compared with experimental ones. The exact dependence of V on particle diameter, d, can be numerically obtained through P and D evaluated by a computer code (Ref. 9) based on Mie scattering formula. A significative example obtained by this code is shown in Fig. 3. The Visibility curve vs particle diameter exhibits a quasi-linear behaviour, at least in the size range from 20μm to 80μm. Obviously, this result is only valid for the specific optical parameters selected:
- scattering in the forward direction ($\gamma = 0^\circ$);
- small cross-angle β;
- small collecting solid angle Ω.

Notice that the relation between Visibility and particle diameter is in this case independent from the refractive index (real or complex) of the particles. This is an important feature, because the refractive index is normally an unknown parameter. In conclusion this method could be used for particle sizing, or at least, for defining the upper bounds of particle size distribution, in conjunction with measurements of velocity and particle concentration.

Sec. 3 - EXPERIMENTAL SET-UP

LDV measurements were performed in a steady state strand burner, with two symmetrical and opposite optical windows, specifically designed for this purpose. In the final version of the experimental set-up (see Fig. 4), two thick lenses were mounted directly on the burner. Advantages of this configuration are:

1) maximum simlicity of the optical system;
2) possibility of utilising all of the small window aperture that is available;
3) minimum focal length of the lens L_1 and, therefore, reduced probe volume dimension.

The limitation due to the fixed position of the probe volume has not been a problem up to now, because we were only interested in the velocity profiles along the vertical axis in the plume of the solid propellant.

The differential LDV mode was chosen because of its higher signal to noise characteristics at moderate particle concentrations. Moreover, this type of LDV system is the best suited for individual realization velocimetry and parallel particle size analysis. It is not difficult to realize the situation in which the Doppler signal, that is available for processing, is produced by no more than one particle in the probe volume at a time. In fact, it is possible to adjust the probe volume dimensions, both in diameter and in length, by selecting the proper cross-beam angle β and the magnification of the light collecting system. Typical values relative to our experiments are given in Table 1.

The LDV system comprises a 5 mW,He-Ne laser and a beam splitter with variable beam separation allowing continuous variation of the cross-beam angle. The two incident parallel beams were directed toward the lens L_1, in such a way that one laser beam was centered on the lens axis. This beam is not diverted from its horizontal direction, but focused on the focal point (on the axis of the strand burner). The second beam is impinging on the lens L_1 at a distance h from the axis, and is deflected and focused on the same focal point. The crossing region defines the probe volume of the LDV system and the velocity component in the vertical direction can be measured. With the geometry of Fig. 4 the measured velocity component is not exactly the axial one; however the difference, of the order of $\sin(\beta/2)$, is not significant for small β. LDV experiments were performed by using as scattering centers the particles present in the plume of the burning solid propellant sample. No external seeding was used in order to avoid any disturbance of the combustion processes. Preliminary experiments showed that, generally, sufficiently high particles rates are found in the region near the burning surface.

Now, the experimental conditions are schematically described. Initially, the rod of solid propellant, centered on the axis of the burner, shuts out the two incident laser beams. When the rod burns, its surface goes down and at the instant t_o the horizontal beam is allowed to pass. After a delay Δt, the second beam is also passing and the scattered light with Doppler information is received by the photomultiplier. A triggering signal, coming out from the photodiode (P.D.) intercepting the horizontal beam, precisely defines the starting time t_o and the corresponding burning surface initial position. In fact, after proper calibration, it could be possible to assume $t = t_o$ when the burning surface is crossing the axis of the horizontal laser beam, with an error less than the transverse dimension of the probe volume. From this reference point, the axial position of the probe volume, with respect to the burning surface, can be inferred by comparison of the time delay and the measured burning rate.

It should be noted that the LDV geometry used here minimizes the dead zone thickness adjacent to the burning surface, whose extension depends on the system geometry and in particular the β angle and the propellant sample radius (see Fig. 5). In our case, the dead zone tickness is of the same order of the probe volume minor axis (see Table 1).

The receiving optics of the LDV system comprises: the lens L_2, fixed on the burner window, collecting the radiation scattered in the forward direction; the lens L_3 that is movable and focuses the scattered light on a 0.3 mm pinhole in front of a photomultiplier. This is equipped with an interferential optical filter, centered at 632.8 $\pm$ 1.0 nm (the laser wave-length), in order to reject flame emission. The photomultiplier signal is processed by an electronic counter processor (DISA mod. 55L90) that allows to work with variable particle concentrations and does not have dropout problems. Moreover, it has a large dynamic range and no slewrate limitations; it accepts individual signals and determines the correct Doppler frequency, hence, the particle velocity. Proper use of this instrument would require rejection of multiple particle signals, because of random phase fluctuations which will lead to incorrect velocity measurements (Ref. 15). This requirement can be generally satisfied by proper reduction of the probe dimensions. It should be noted at this regard that, although the probe volume has a very simple geometrical definition, it really depends on the receiving optics, the observation direction and the sensitivity of the photo-electronic system. Many of these parameters can be accurately changed in order to get the best compromise.

The time resolution of the LDV measurements depends on the particle rate, $\dot{n}$, hence on the particle concentration N, the mean particle axial velocity $\bar{U}$ and the probe volume cross-section S:

$$\dot{n} = \alpha N \bar{U} S \qquad (3.1)$$

where α is an efficiency factor taking into account the validation of particle signals from the counter processor. In our experiments with double-base propellants the time history of $\dot{n}$ was measured by a multiscaler. Many tests were made during preliminary velocity measurements and the mean values of $\dot{n}$ for different optical and electronic configurations of the LDV were determined in order to match the optical system to the mean particle concentration. Large fluctuation of $\dot{n}$ were found from 0 to a maximum value of about 1 KHz corresponding to a particle concentration of about 2×10^8 m^{-3} . With these experimental conditions the LDV cannot provide a continuous record of the gas velocity. Moreover, since the particles randomly cross the probe volume, they provide a randomly sampled time series of the fluctuating velocity. Time resolution can be limited by this characteristics. This is an important feature for unsteady situations and rapidily fluctuating flows. As far as steady state situation is concerned, the particle rate is more than adequate to perform velocity measurements by LDV. Present results are limited to this case.

The burning rate of the solid propellant was initially measured by standard techniques (Ref. 14). Later on, a new technique was developed based on the non perturbing laser system shown in Fig. 6. The beam of a 5 mW, He-Ne laser was enlarged by a beam expander passed through a variable diaphragm and directed on the sample of the solid propellant. The beam radius was chosen less than the solid propellant radius, therefore the whole beam is initially stopped. When the burning surface goes down, an increasing portion of the laser beam is transmitted and then collected on a photodiode by means of a focusing lens. A Centronic Quadrant Detector was used, since this kind of photodiode allows a linear relationship between the voltage output and the displacement of the burning surface. A calibration curve referring to an illuminating beam diameter of 3.5 mm is shown in Fig. 7. The ordinate is the photodiode voltage output and the abscissa is the solid sample displacement referred to an arbitrary position. The curve was obtained by means of a non burning sample of propellant displaced by a micrometer screw in steps of 0.2 mm. Obviously, accurate measurements of the solid propellant burning rate require that the burning surface remains flat and horizontal. The advantage of this technique is its non perturbing character and continuous output over the fixed spatial range. For example it points out any change of the burning rate during the LDV measurements.

Sec. 4 - EXPERIMENTAL RESULTS

A typical individual Doppler signal, after amplification and band-pass filtering, is shown in Fig. 8. Many of these signals were recovered in order to optimize the optical system and to define the effective probe volume dimension, by comparing the observed and the computed fringe number. With the experimental conditions summarized in Table 1, and the solid propellants used, generally no more than one particle at once was present in the probe volume. If the pass-band filtered Doppler signal, relative to each particle, satisfies a number of validation conditions, in terms of amplitude level and signal to noise ratio, the counter processor measures the Doppler frequency by means of a zero crossing method. The output is a velocity information that is retained until another particle gives a validated signal. By digital to analog conversion of the output of the Doppler counter processor, a voltage is obtained proportional to the velocity and the time history of the gas velocity can be stored on a magnetic tape recorder.

Data reduction was performed by a minicomputer, but is limited to a maximum data acquisition rate of about 2 KHz. Numerical data analyses by computer codes have been performed for the LDV measurements and are described in Ref. 16. The velocity time history, monitored by a storage Oscilloscope, looks like the lower trace of Fig. 9, in which each point corresponds to a single particle velocity measurement. Oscilloscope record is triggered by the photodiode signal (upper trace) and the time span corresponds to a displacement of less than 0.5 mm above the burning surface. The propellant is a noncatalyzed Double Base (DB) sample burning at a pressure of 5 atm.

In Fig. 10 the velocity trace of a sample of the same propellant (lower trace) is shown, but the record is covering a larger time interval. The upper trace, in this case, refers to the pressure, measured by means of a Kistler quartz transducer mod. 412, equipped with a Kistler Charge Amplifier mod. 5001. The pressure scale is 1 atm/div. It can be noted a slight time variation of the pressure from the initial value of 4 atm to a final value of 4.8 atm. At this point the velocity trace indicates the end of the burning rod of propellant. It can be noted that the mean velocity vs time is nearly constant, but a large dispersion (about 20%) characterises the velocity trace and similar behaviour was found in the other tests.

Fig. 11 refers to a test with an AP based composite propellant at a nearly constant pressure of 7.5 atm. For both propellants the condensed phase burning rate and the gas phase velocity agree satisfactorily. Indeed, a steady state mass balance gives for the expected gas flow velocity:

$$(4.1) \qquad U = \dot{m}/\rho_g = R\rho_c/\rho_g$$

being ρ_c and ρ_g the condensed phase and the gas phase densities, and R the condensed phase burning rate.

Comparison of the expected and measured values of U are reported in Table 2. The burning rate was measured both by standard fuse wire technique and the optical method previously described. Typical results (oscillographic records) obtained by this new technique are reported in Fig. 12. They refer to same samples of noncatalyzed DB propellant burning at about 7 atm and agree satisfactorily with standard results. With the AP based composite propellant some difficulties were encountered due to the higher level of the flame emission and consequently to the higher radiation background compared to the laser intensity.

Sec. 5 - CONCLUSIONS AND SUGGESTIONS

Data collected up to now suggest the possibility of LDV measurements in the gaseous region above the burning surface of a solid propellant. So far, only tests in a steady state situation at pressure up to 10 atm were performed, but experimental work is in further progress. Although only these preliminary results are presently available, some general aspects of LDV measurements can be inferred.

Some aspects of LDV results are not completely understood right now. The velocity measurements seem to show more complicated profiles than expected. In all runs a large velocity dispersion (up to 20%) was observed around the mean value. This is difficult to explain on the basis of fluidynamics considerations. In fact, comparison with shadograph

movies (5000 fr/s) at similar test conditions suggests a quasi-monodimensional laminar gas flow, unless of turbulence time scale well above the movie speed. The discrepancy with the presumed steady state laminar flame conditions is likely due to a polydisperse particle size distribution and the consequent difficulty for larger particles or agglomerates to follow accurately the gas flow. Indeed, the measured mean velocities, for both the DB and the AP propellants, seem to be below the values obtained by the measured burning rate of the condensed phase and the estimated flame temperature, assuming a quasi-steady state mass balance (see Table 2).

Particle size evaluation by means of electron microscope analysis seems to confirm this hypothesis, showing a wide particle size distribution up to diamaters well above 10 μm. However the particle capture could cause agglomeration and clustering. The same phenomena may also occur while particles are traveling and reacting in the gaseous stream.

Moreover, the precision of the LDV instrument itself could be questioned in this difficult application. In fact, rapid change in particle rate and particle size during the burning of the propellant sample cause difficulties in the selection of the operational conditions of the counter processor. A compromise must be chosen, with regard to the amplification and triggering levels that cannot be changed during the short time of a single test (about 5s).

To improve the LDV measurements reliability and to define the accuracy of this technique in this particular condition, a wide research program is starting, with improved LDV instrumentation comprising a higher power laser, a Bragg cell frequency shifter and a direct interface between the counter processor and the computer. With this instrumentation a systematic analysis of particle size distribution (by the Visibility method) can be also performed, in conjunction with measurements of velocity and particle concentration. This procedure would allow to take into account all these parameters in evaluating the correct gas flow velocity. In principle, usuful information could be obtained in unsteady situations as well.

REFERENCES

1. Durst, F., Melling, and Whitelaw, J.H., "Principles and Practice of Laser Doppler Anemometry", Academic Press, 1976.
2. Durrani, T.S., and Greated, C.A., "Laser Systems in Flow Measurements", Plenum Press, 1977.
3. Watrasiewicz, B.M., and Rudd, M.J., "Laser Doppler Measurements", Butterworths,1976.
4. Soo, S.L., "The Physics of Fluids", 18, 2, 1975.
5. Melling, A., and Whitelaw, J.H., Proceedings of the LDA Symposium, pp. 382-402, Copenhagen, 1975.
6. Adrian, R.J., and Orloff, K.L., Applied Optics, 16, 3, 1977.
7. Adrian, R.J., and Earley, W.L., Proceedings of the Minnesota Symposium on Laser Anemometry, pp. 426-454, Minneapolis, Minnesota, 1976.
8. Chu, W.P., and Robinson, D.M., Applied Optics, 16, 3 pp. 619-626, 1977.
9. Coghe, A., and Ghezzi, U., "LDA signal processing". Dynamic Flow Conference, Marseille, 1978.
10. Kerker, M., "The Scattering of Light", Academic Press, 1969.
11. Born, M., and Wolf, E., "Principles of Optics", Pergamon Press, 1975.
12. Van de Hulst, C.H., "Light Scattering by Small Particles", J., Wiley, 1957.
13. Farmer, W.M., "Measurement of Particle Size and Concentrations Using LDV Techniques", Dynamic Flow Conference, Baltimore, 1978.
14. De Luca, L., and Zanotti, C., "Measurement of Steady Solid Propellant Burning Rate and Data Processing", Technical Note, XXXII Congresso ATI, Roma, 1977.
15. George, W.K., Proceedings of the LDA Symposium, pp. 20-63, Copenhagen, 1975.
16. Coghe, A., Sensalari; G.L., and Volpi, A., C.N.P.M. NT/RT No. 305, Politecnico di Milano, 1978.
17. Bacholo, W.D., "Particle Field Measurements in Coal-Fired Systems", Dynamic Flow Conference, Baltimore, 1978.
18. Kubota, N., Ohlemiller, T.J., Caveny, L.H. and Summerfield, N. "The Mechanism of Super-Rate Burning of Catalyzed Double Base Propellants", Princeton University, AMS Report No. 1087, 1973.

ACKNOWLEDGMENTS

Project jointly supported by Consiglio Nazionale delle Ricerche (C.N.R.) and European Research Office under Grant Agreement No. DAERO 78-G-029.

LIST OF TABLES

LIST OF FIGURES

Table 1

Laser wavelength, λ	632.8 nm
Cross-angle, β	4.70°
Fringe spacing = $\lambda/(2 \sin(\beta/2))$	7.7 μm
Probe volume dimensions	$3 \times 0.15 \times 0.15$ mm^3
Fringe number (effective)	20
Collecting solid angle, Ω	$4^{\circ} - 6^{\circ}$
Dead zone thickness ($h = r \, tg\beta$)	0.25 mm (r = 3mm)

Table 2

PROPELLANT	PRESSURE (atm)	BURNING RATE (mean values)	GAS PHASE MEAN VELOCITY expected	measured
DB noncatalized	7	4.2 (mm/s)	3.7 (m/s)	3.2 (m/s)
	5	3.3 "	4.1 "	3.4 "
AP composite	7	3.5 "	6.1 "	5.7 "

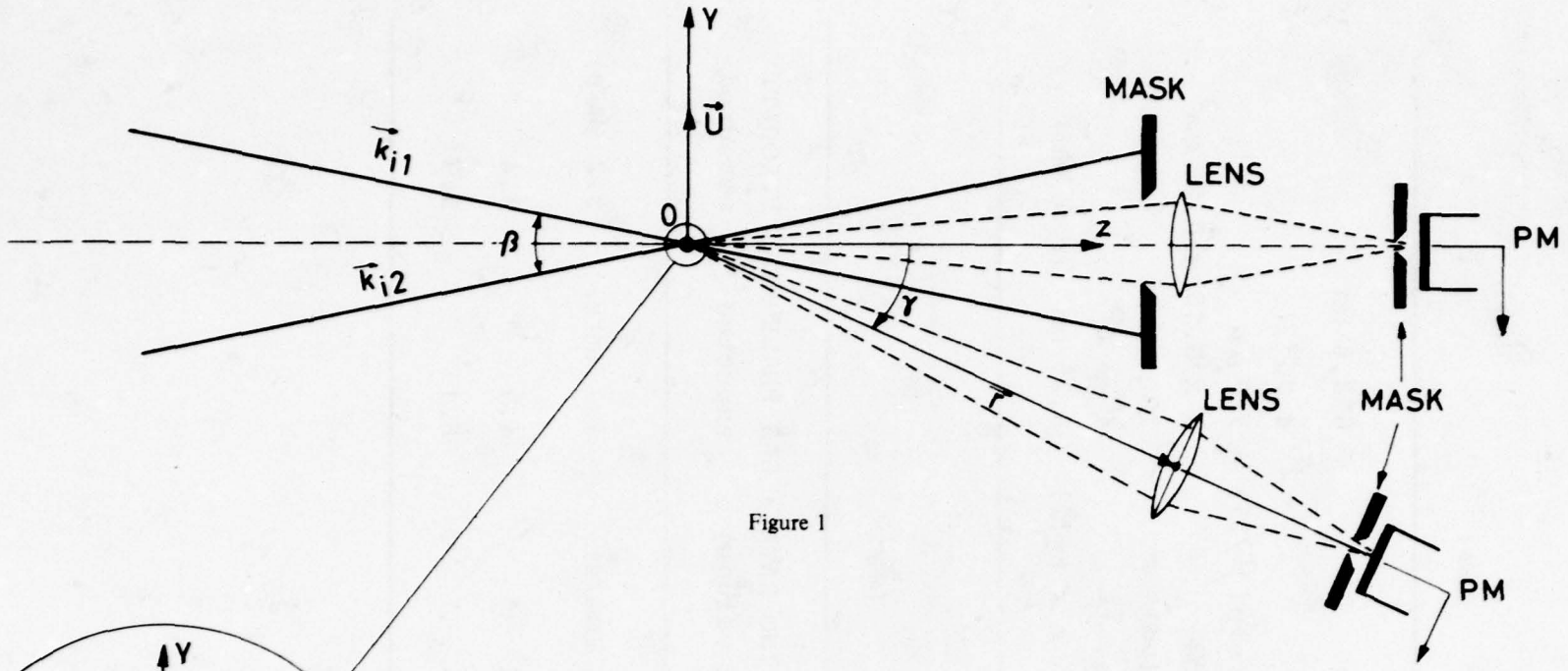

Figure 1

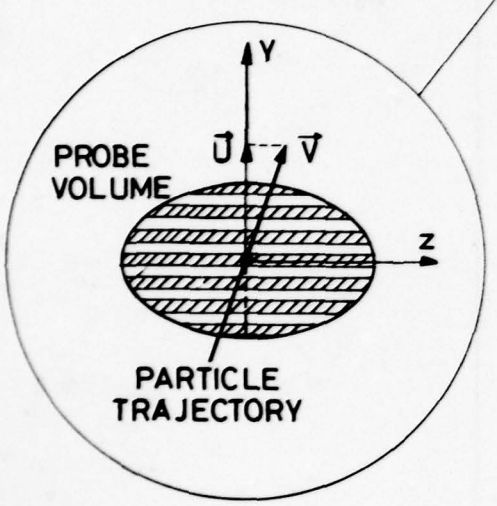

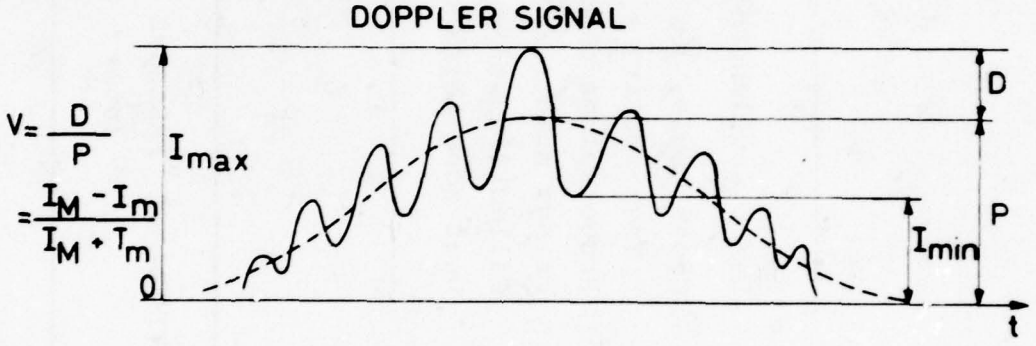

Figure 2

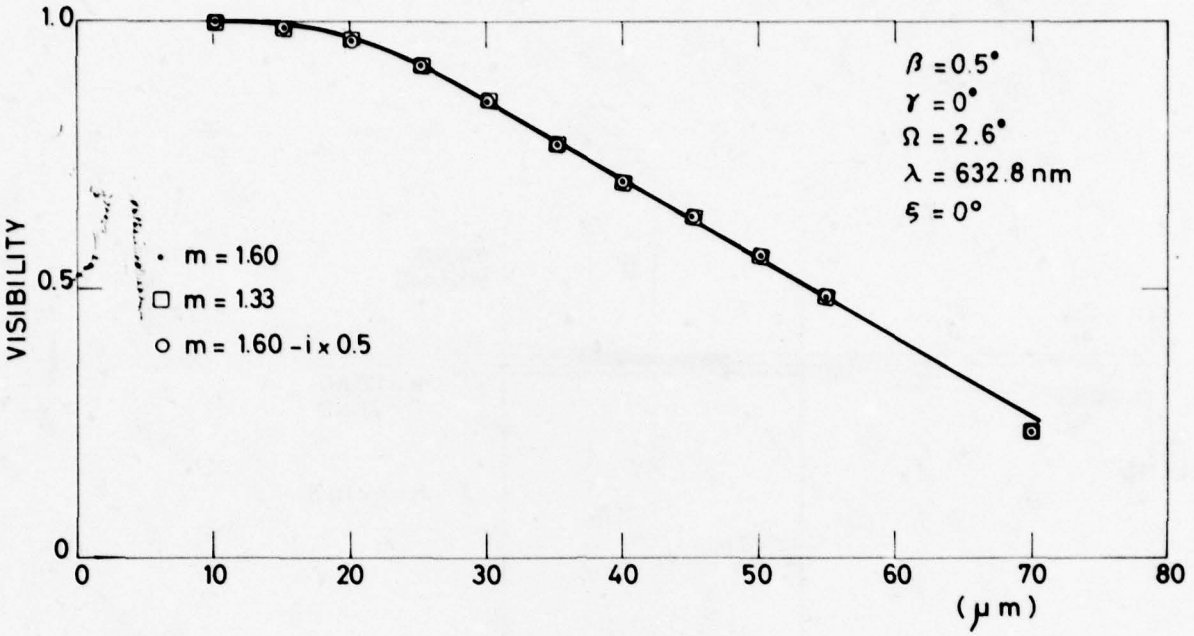

Figure 3

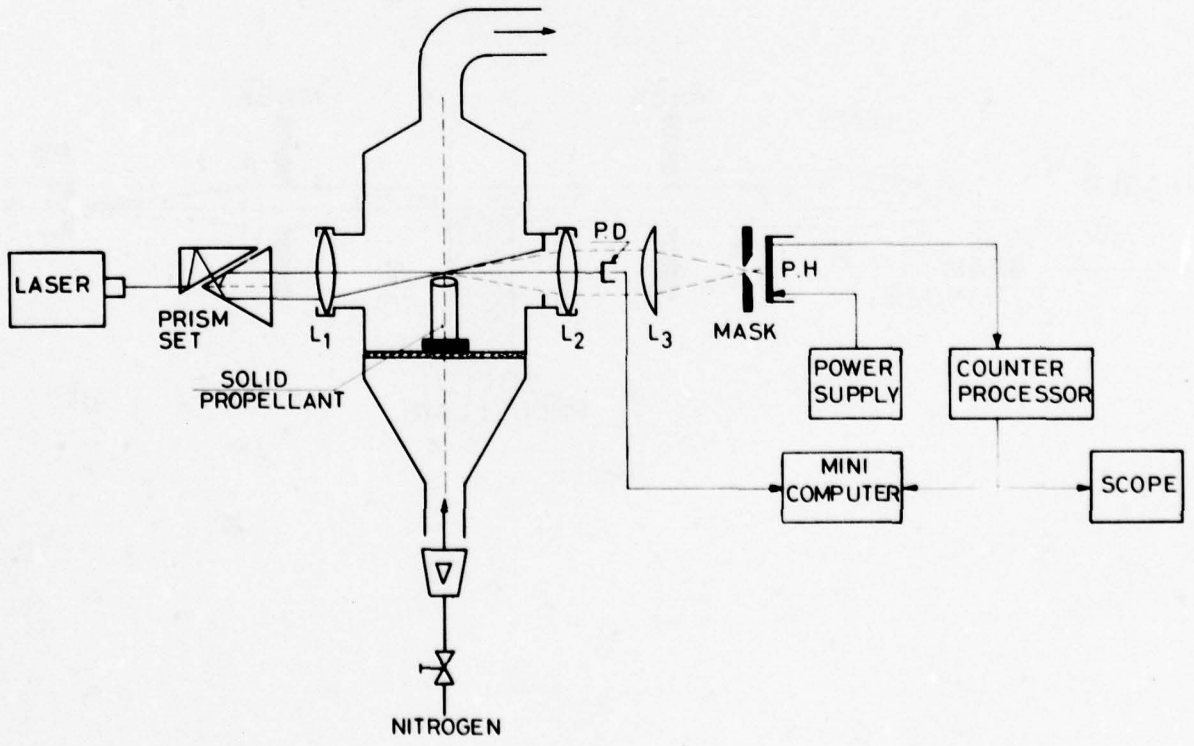

Figure 4

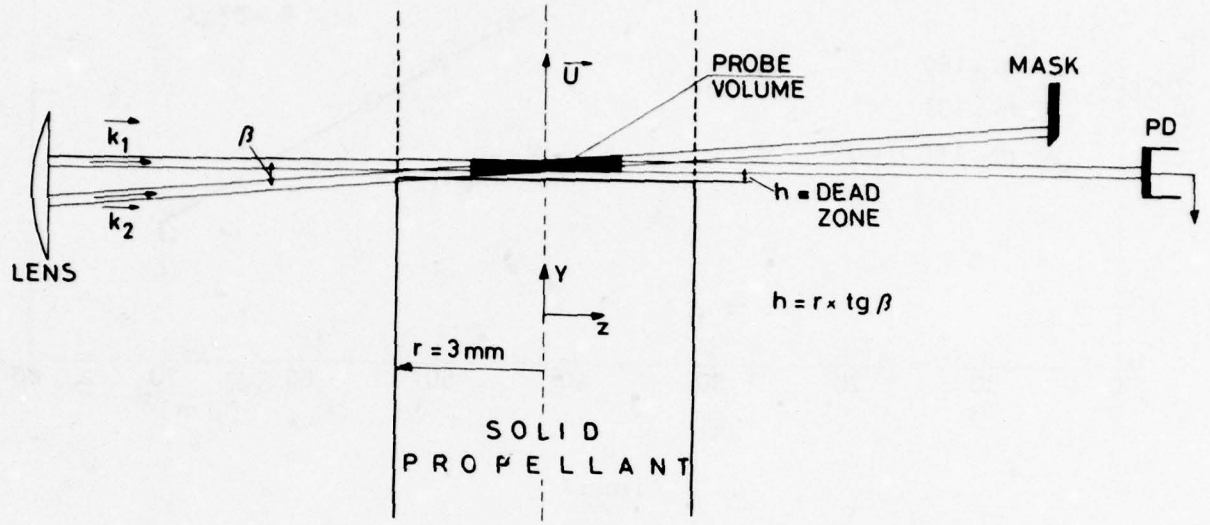

Figure 5

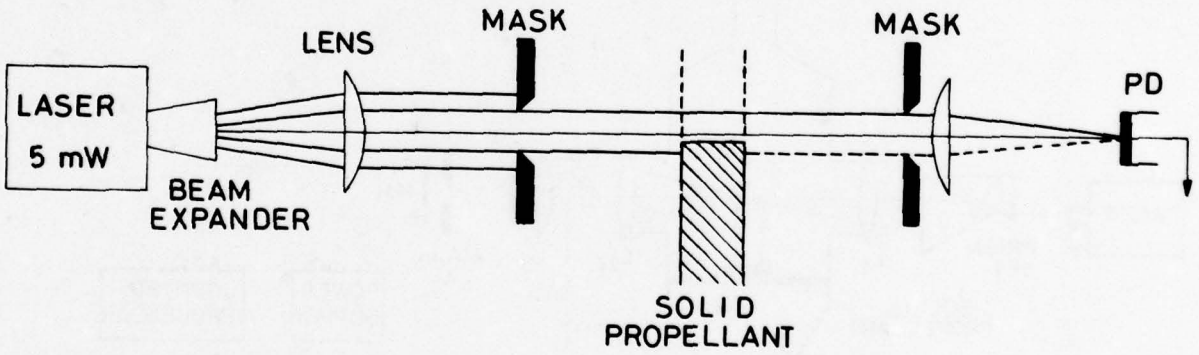

Figure 6

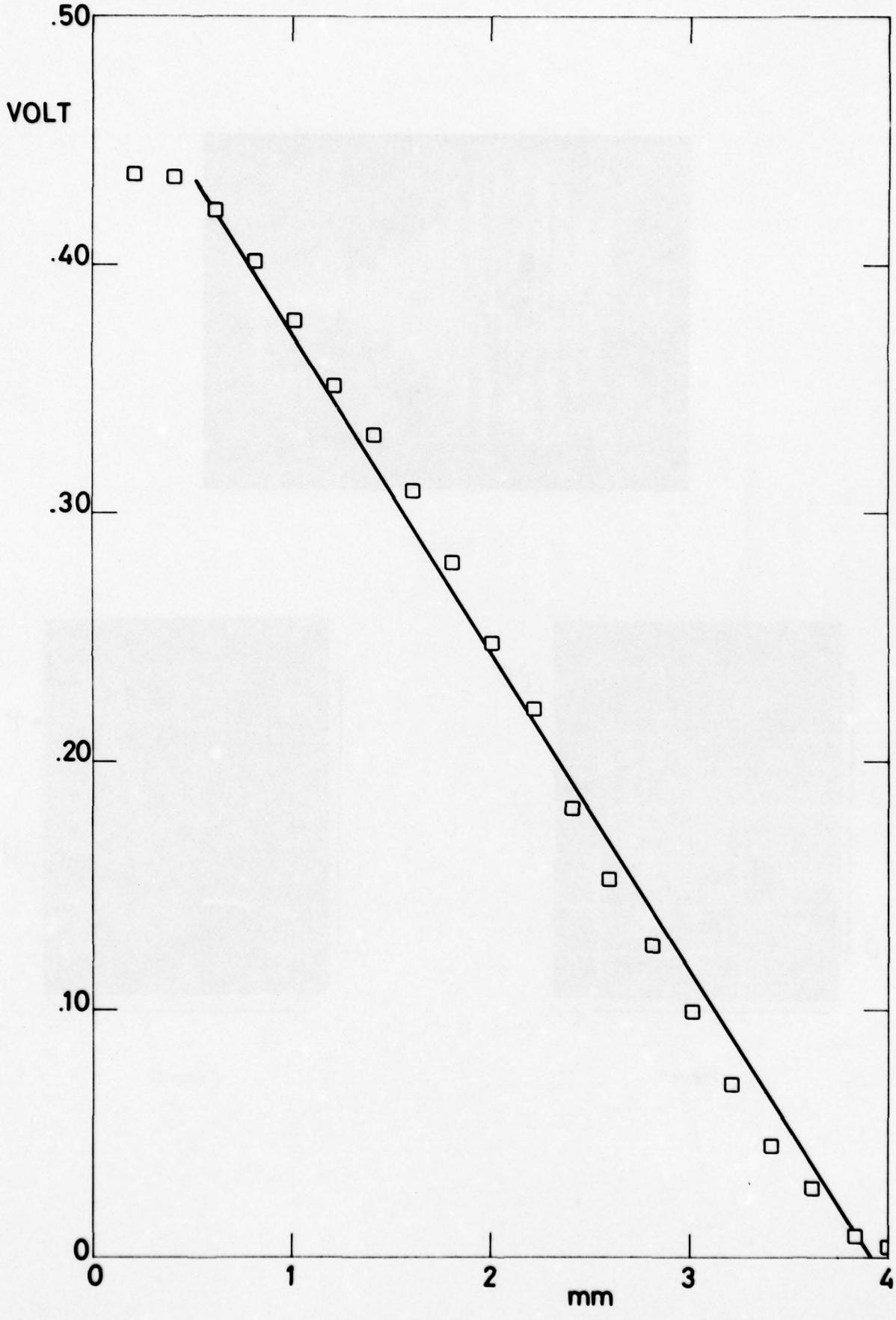

Figure 7

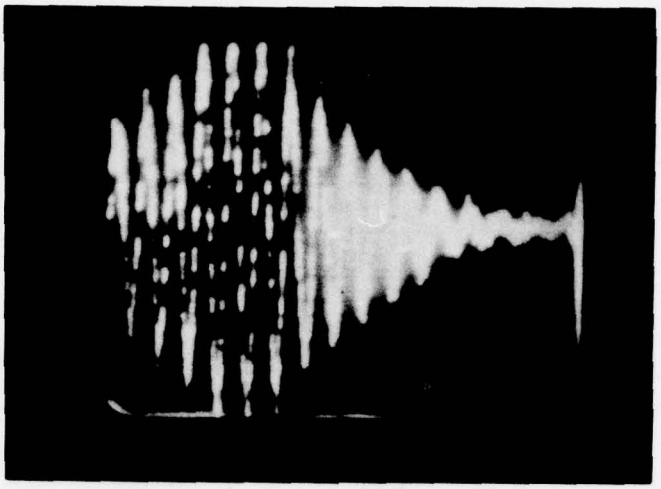

Figure 8

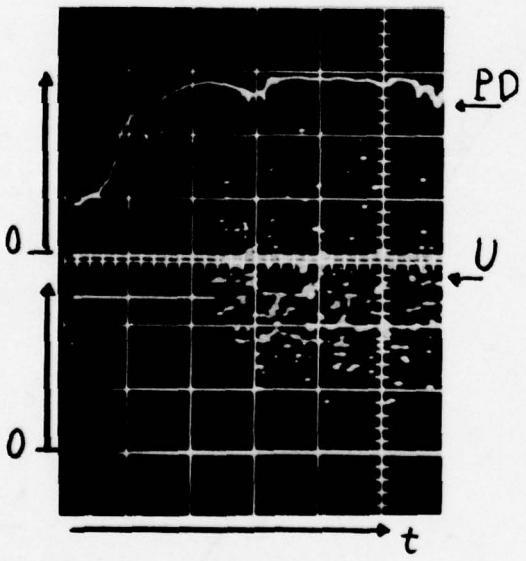

Figure 9

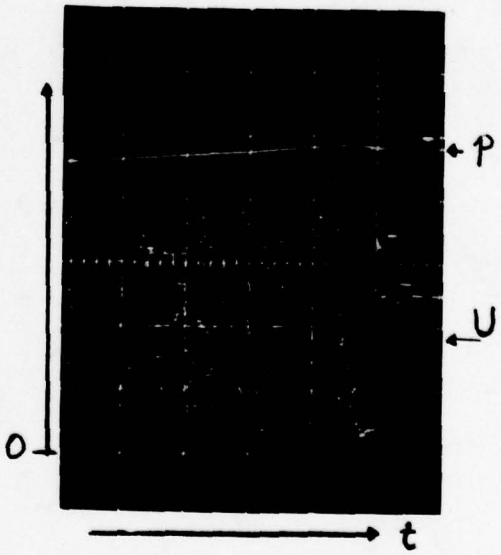

Figure 10

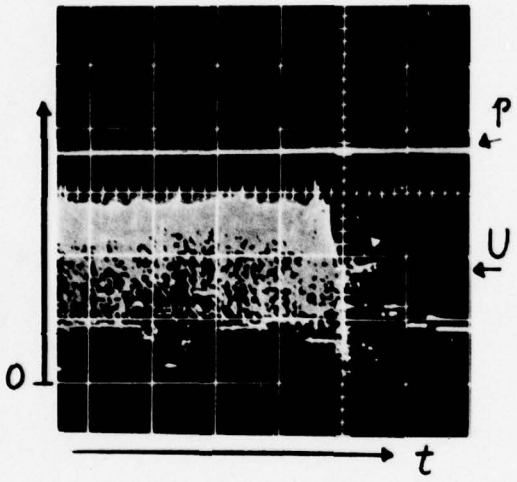

Figure 11

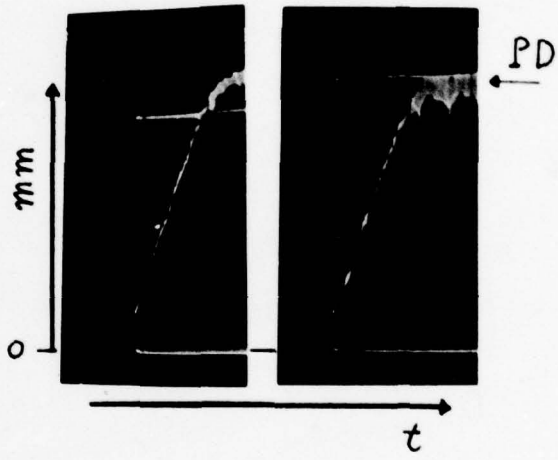

Figure 12

DISCUSSION

R.L.Derr, Naval Weapons Centre, US

What were the propellant formulations used in your experiments? Were they metallised? Would you agree that propellants seeded with particulates of known size would improve the experiments?

Author' Reply

In this study two types of propellant were examined, namely uncatalysed conventional double base and also an AP filled composite propellant. Neither of these propellants contained metal additives. We agree that propellants seeded with particles of known size and concentration could aid LDV measurements. However carbon and/or other particles present in the gas flow would also scatter light.

PRESSURE AND VELOCITY RESPONSE FUNCTION MEASUREMENTS BY THE ROTATING VALVE METHOD*

R. S. Brown and R. C. Waugh
Chemical Systems Division/United Technologies Corporation
Sunnyvale, California 94086

SUMMARY

Analytical and experimental studies have been conducted to develop and demonstrate the rotating valve method for measuring the pressure- and velocity-coupled response functions of solid propellants. The method is based on producing pressure or velocity oscillations in a small combustion chamber by varying the area of one or two secondary exhaust nozzles in a periodic manner. This is accomplished by using rotating valves as the secondary orifices. The valves operate concurrently with a primary nozzle which controls the steady-state pressure.

Analytical studies have developed an analytical solution of the transient mass, momentum, and energy equations. The equations include the effects of pressure coupling, linear and nonlinear velocity coupling, particle damping, flow turning, and nozzle losses. These analytical solutions agree with independently developed solutions for low frequency bulk mode conditions and for the frequency response characteristics at acoustic resonance.

These solutions show that at low frequency, pressure coupling dominates when one valve is used or where two valves are operated in phase. When two valves are operated 180° out of phase, velocity coupling dominates the response. Approximate solutions have been developed for both conditions to permit the direct derivation of response functions from experimental data.

An experimental apparatus was constructed and its performance compared with predictions under cold flow conditions. Excellent agreement was found between the measured and predicted pressure amplitudes and phase angles. Pressure-coupled combustion tests also show excellent agreement between response functions measured in the T-burner and in the rotating valve. Velocity-coupled tests show control of the phase angle between the two valves is important to ensure proper apparatus performance and elimination of modulation of the pressure amplitude. Additional testing and apparatus development are currently in progress.

LIST OF SYMBOLS

a sonic velocity

A acoustic admittance

C concentration of particulates, $C = 0.5\left(\frac{d\bar{M}}{dZ}\right)\left(Q + T + \frac{2d\bar{M}}{dZ}\right)$

C* characteristic velocity

d diameter

D integration constant in Eq. (5)

E integration constant in Eq. (5)

f frequency

F particle damping term ($F' = i\lambda C_m M'/(1 + i\lambda t_d)$)

i $\sqrt{-1}$

K Kummer's function[20]

L chamber length

M Mach number

N $N = -0.5\ Y\left(\frac{Q + d\bar{M}/dZ}{Q}\right) + \frac{\bar{X}_1}{2}\frac{d\bar{M}}{dZ}\left(Q + T + 2\frac{d\bar{M}}{dZ}\right)$

p pressure

*The primary support for this work was provided by the U.S. Air Force under contracts F04611-72-C-0007, F04611-74-C-0045 and F49620-77-C-0048.

q chamber perimeter

Q $Q = i\lambda\left(\frac{1 + C_m + i\lambda\tau_d}{1 + i\lambda\tau_d}\right) + \frac{2d\bar{M}}{dZ}$

Q f/Δf of filter in figure 15

r $r = (CZ - N)^2/C$

R response function

S area

T $T = i\lambda - A_b qL/S_c$

Y $Y = \left(R_b + \omega_r\right)_v \frac{\bar{M}}{|\bar{M}|} \frac{d\bar{M}}{dZ}$

Z dimensionless chamber length

Greek

α oscillation growth rate

γ specific heat ratio

ε acoustic pressure (p'/γp)

λ dimensionless frequency, $2\pi fL/a$

$\lambda'/T_r = \lambda/\frac{d\bar{M}}{dZ}$ in Eq. (8)

μ viscosity

ω dimensionless flame temperature oscillation

ψ dimensionless area, $S'/\bar{S}$

ρ density

σ flow turning parameter ($\sigma' = M'd\bar{M}/dZ$)

τ dimensionless time

τ_d particle damping parameter [$\tau_d = \bar{a}d_p^2\rho_p/(18\mu L)$]

$\bar{\chi}_1$ $\bar{S}_{vo}/(\bar{S}_{vo} + \bar{S}_{v1})$

Subscripts

o at Z = 0

1 at Z = 1

c chamber

v valve, velocity

b burning surface

m mass of condensed phase

d damping

p particle, pressure

Superscripts

− time average

' oscillating component

INTRODUCTION

The stability of the combustion pressure in a solid propellant rocket motor is determined by a delicate balance between the sources and losses of oscillatory energy. The primary sources of oscillatory energy are the flowfields in the combustion chamber (mean flow driving) and the dynamic combustion properties of the propellant (combustion response). Among the losses are the dynamic flow properties of the nozzle (nozzle damping), the drag losses of the particulate combustion products (particle damping), and the vibration characteristics of the propellant grain and motor case (structural damping). Each process must be characterized quantitatively to predict the overall stability of a specific propellant in a specified motor.

The responses of propellants to acoustic pressure and velocity oscillations have received particular attention because they constitute large energy sources and because they are the most difficult to characterize analytically. Several studies[1-4] have been conducted to develop methods for predicting the dynamic combustion response. Each of the resulting theoretical expressions contains a number of chemical and physical parameters that are difficult to determine independently. Thus, for the propellant formulator and the motor designer, these theoretical expressions have little value. Consequently, experimental methods have been sought to obtain the data required for predicting the stability of proposed motor designs.

The T-burner has been the primary experimental method for measuring the combustion response to pressure and velocity oscillations. Several studies[5-13] have been conducted to evaluate various methods of operating the T-burner. Several tests must be conducted to obtain a value of the combustion response at a specific frequency and pressure. In motor development programs, in which there are often several candidate formulations to be evaluated, a range of frequencies and several pressures to be considered, the T-burner is an expensive method for screening candidate propellants. In addition, there are theoretical uncertainties[14,15] in the equations used to derive the combustion response function from the T-burner data.

In view of these shortcomings, consideration was given to the development of alternative methods for characterizing the combustion response of solid propellants. This report summarizes the results of several programs conducted to explore the rotating valve method as an alternative approach for measuring the combustion response function.[16-18]

Description of the Rotating Valve Method

In the rotating valve method, a small rocket motor is test-fired using a conventional nozzle to control the combustion pressure. In addition, a secondary exhaust orifice is periodically opened and closed by a specially designed rotating valve to generate small amplitude pressure oscillations in the rocket motor. The frequency of oscillations is controlled by the rotational speed of the rotating valve. Thus, small amplitude pressure oscillations are generated in the motor at a selectable pressure and frequency. The amplitude and phase of these pressure oscillations relative to the exhaust area oscillations depend on the transient combustion properties of the propellant and the dynamic ballistics of the chamber. The general apparatus can have both a conventional nozzle and a rotating valve at each end of the motor, as shown in figure 1. Details of the experimental hardware and test procedures are presented elsewhere.[16-18]

Analytical Studies

To develop the relationship between the propellant combustion response characteristics and the dynamic chamber ballistics, consider the one-dimensional flow equations of the motor, in conjunction with the ideal gas law. After linearization and rearrangement one obtains[14]

$$\frac{\partial \varepsilon'}{\partial Z} + \frac{\partial M'}{\partial \tau} + \frac{\partial (\bar{M} \cdot M')}{\partial Z} + \sigma' - F' = 0 \qquad (1)$$

for the momentum equation and

$$\frac{\partial \varepsilon'}{\partial \tau} + \bar{M} \frac{\partial \varepsilon'}{\partial Z} + \frac{\partial M'}{\partial Z} = \frac{A_b q L}{S} \varepsilon' + \frac{\bar{M}_b q L}{S} (R_b + \omega_f)_v \frac{\bar{M} \cdot M'}{|\bar{M}|} \qquad (2)$$

for the energy equation. These equations were originally derived by Culick,[14] who was interested in calculating the change in the complex eigenvalue of a chamber to determine the stability of self-excited acoustic waves. Thus, his solution incorporates approximations that are valid only near resonant conditions. In this work, however, the primary interest is the burner response to nonresonant frequencies; hence, the approximations which are appropriate for resonant conditions are not valid in this development.

To obtain the solution for nonresonant conditions, Eqs. (1) and (2) can be combined to eliminate dM'/dZ by separating variables and replacing $\partial()/\partial\tau$ by $i\lambda()$. The result is then differentiated with respect to Z to yield

$$\frac{d^2\varepsilon'}{dZ^2} - \left[\bar{M}\left(T + Q + \frac{2d\bar{M}}{dZ}\right) + Y\left(\frac{Q + d\bar{M}/dZ}{Q}\right)\right]\frac{d\varepsilon'}{dZ} - T(Q + d\bar{M}/dZ)\varepsilon' = 0 \tag{3}$$

Note that Eq (3) is second order and has coefficients that are linear in the independent variable.

Equation (3) can be transformed to a Kummers equation[19] to yield

$$r\frac{d^2\varepsilon'}{dr^2} + \left(\frac{1}{2} - r\right)\frac{d\varepsilon'}{dr} - k\varepsilon' = 0 \tag{4}$$

The solution becomes

$$\varepsilon' = DK\left(k,\tfrac{1}{2},r\right) + Er^{1/2}K\left(k + \tfrac{1}{2},\tfrac{3}{2},r\right) \tag{5}$$

The two constants of integration can be evaluated from the nozzle flow equations at each end of the chamber. Assuming the nozzles and valves behave in a quasi-steady manner, one finds at Z = 0

$$QM'_o = \left(\frac{-d\varepsilon'}{dZ_o} + \bar{M}_o T\varepsilon'_o\right) = Q\bar{M}_o\left[0.5\varepsilon'_o(\gamma - 1) + \psi_o\right] \tag{6}$$

and at Z = 1

$$QM'_1 = \frac{-d\varepsilon'}{dZ_1} + \bar{M}_1 T\varepsilon'_1 = Q\bar{M}_1\left[0.5\varepsilon'_1(\gamma - 1) + \psi_1\right] \tag{7}$$

Because Y changes sign when the mean flow Mach number goes to zero, two sets of constants are required: one set for $0 < Z < \bar{X}_1$ and for $\bar{X}_1 < Z < 1$. The additional boundary conditions are obtained by requiring the oscillatory pressure and velocity to be continuous for $Z = \bar{X}_1$.

Thus, if the acoustic response, particle damping parameters, and chamber dimensions are known, the oscillating components of pressure and velocity can be predicted for any point in the chamber. Furthermore, these predictions can be made for any phase relationship between the two valves, simply by selecting the appropriate value of ψ_o and ψ_1. The significance of this flexibility will be apparent later.

Verification of Solution

The analytical solution of the equations described in the preceding paragraphs has been checked in several ways. First, at low frequencies, the equations should reduce analytically to the equations derived for the pressure-coupled rotating valve, assuming no velocity response and driving from only one valve. For low frequencies, the Kummer functions in Eq. (5) approach unity. Following through the resulting algebra leads to

$$\frac{A_b}{\gamma M_b} = R_p + \omega/\varepsilon - 1 = 0.5\left(\frac{\gamma - 1}{\gamma}\right) + \frac{i\lambda'}{\gamma T_r} + \frac{\psi}{\gamma\varepsilon} \tag{8}$$

This solution is identical to the results reported in reference 16 for one valve and also for both valves when operated in phase. Numerical calculations using appropriate inputs to model this case also yield identical results from Eq. (8). This is an important point since it provides a numerical verification of the computer programming in addition to the analytical verification.

Second, this model should predict the correct frequency response behavior when the combustor is driven at frequencies near the natural acoustic frequencies. In particular, one would expect that near resonance the pressure amplitude would exhibit the behavior shown in figure 2. Further, one would expect that the frequency difference at the

half-power amplitudes (i.e., 0.707 multiplied by the peak amplitudes) would be related to the overall system damping of the self-excited system by the expression

$$\frac{\alpha}{f} = \frac{\pi \Delta f}{f} \tag{9}$$

The left side can be evaluated independently from Culick's solutions, while the right side can be evaluated from numerical solutions of this model.

This comparison has been made in three cases. The first case contained only pressure coupling effects and used only one valve. The second and third cases incorporated both pressure and velocity coupling as well as particle damping effects with two valves operating in phase. In case two, the response functions were low (i.e., 0.2) while in case three, they were approximately an order of magnitude higher. The results are shown below.

TABLE 1. COMPUTED SYSTEM DAMPING ($-\alpha/f$)

Case	Culick Analysis	This Solution
1	0.112	0.117
2	0.155	0.156
3	0.102	0.108

The excellent agreement found between the two independent analyses further substantiates the solution presented in this paper. Examination of the numerical results shows that in all cases the amplitudes of the pressure at both ends of the burner are nearly equal, but are 180° out of phase, exactly as expected.

Application to Response Function Measurements

Studies of the analysis show that conditions where the frequency of the driver oscillations is low compared to the acoustic frequency are particularly attractive for response measurements. Under these conditions, the mass and energy balances dominate the behavior of the burner while momentum effects are relatively unimportant. This observation is independent of valve phasing. This eliminates particle damping and flow turning effects, which are two large sources of uncertainty in the T-burner, while retaining pressure- and velocity-coupling effects.

Further parametric studies show that pressure coupling dominates the burner behavior when one valve is used or when two valves are operated in phase with each other. The velocity response function has little effect on the oscillation under these conditions. Therefore, Eq. (8) is a valid approximation which can be used to derive pressure-coupled response functions from measured pressure oscillations. Pressure-coupled response functions reported later in this paper were, in fact, derived in this manner.

When two valves are operated 180° out of phase, velocity coupling dominates the burner behavior. There is little effect of the pressure-coupled response under these conditions. Further examination of the predicted behavior shows the pressure oscillations are approximately a linear function of axial position. Combining this approximation with the energy equation yields a first-order ordinary differential equation with the oscillatory Mach number as the dependent variable. After suitable manipulations, the solution becomes

$$(R + \omega_r)_v = \frac{T\varepsilon_o' + (2T + d\bar{M}/dZ)\chi_1(\varepsilon_1' - \varepsilon_o') + (M_1' - M_o')}{(d\bar{M}/dZ)M_1'(1 - 2\chi_1)} \tag{10}$$

The accuracy of this approximation has been examined numerically. The exact solution was used to predict oscillating pressures and velocities using a set of pressure and velocity response functions. These pressures and velocities were then used as inputs to Eq. (10), simulating experimental observations, to derive the velocity response. Figure 3 compares the derived and exact velocity response for a variety of particle-damping parameters. This comparison was made using the imaginary part of the response since this is a parameter used in motor stability predictions. It therefore appears that the approximate analysis provides a reasonably accurate solution at the lower frequencies for the conditions examined. This approximate solution also suggests a good method for estimating initial inputs if the complete analysis is required for data reduction purposes.

The formulation of the velocity coupling that was included in the analysis needs to be considered in further detail. The form incorporated in Eq. (2) is the classical linear form which is included in the Standard Stability Prediction Program.[21] This form also forms the basis for interpreting velocity-coupled T-burner data.[12, 13]

However, Culick[22] and Price[23, 24] have suggested that there may be an analog between velocity coupling and erosive burning. Specifically, this means there may be a minimum, or threshold, velocity which must be exceeded before there is coupling between the combustion and the velocity oscillations. Both Culick and Price have discussed the characteristics of this conceptual model in detail and have shown how the effects of flow reversal and the threshold velocity influence the coupling process.

Studies have been conducted to determine how the threshold and flow reversal effects would modify the predicted ballistics of the dual rotating valve experiment. The basic approach to incorporating these modifications into the analysis follows the methods used in the Standard Stability Predictions Program[21] and by Price and Dehority.[23, 24] The wave is decomposed into the appropriate Fourier coefficients. Parametric studies were then made to show how the time average burning rate shift, the fundamental components, and the second harmonic vary with mean flow velocity and velocity amplitude.

The most striking result from these calculations is the approximately linear variation of the fundamental component with mean flow for constant velocity amplitude. Calculations with the model described previously show the amplitude of oscillating velocity is nearly constant along the burner at low frequencies. Since the mean flow varies linearly with axial position, the fundamental component of velocity coupling also varies linearly with axial position.

Using this approximation, the parameters in Eq. (3) can be redefined and solutions can be obtained in terms of Kummer's functions. The details of this analysis are presented in reference 18 along with parametric studies of the expected burner response.

EXPERIMENTAL STUDIES

Apparatus Description

A dual rotating valve apparatus was designed and constructed under this program. The basic apparatus layout is shown schematically in figure 1. This arrangement provides the flexibility required to study both velocity-coupled and pressure-coupled configurations simply by changing the arrangement of holes in the graphite rotor sleeve.

Figure 4 shows the essential components in exploded view. The rotor with a graphite sleeve is shown, together with four graphite slots in their relative positions. The two slots on the upper left vent to the auxiliary chambers; those on the lower right vent to each end of the combustion chamber. A motor case loaded with propellant is also shown.

Figure 5 shows a photograph of the apparatus with a propellant grain being inserted into the combustion chamber. Kistler pressure transducers are located at each end of the grain to monitor the oscillating component of pressure. In addition, a Taber transducer monitors the average chamber pressure. The valve at each end of the chamber also has an auxiliary chamber that serves as a phase reference for each valve. Each is equipped with a Kistler and Taber transducer to monitor the oscillating pressure and the average chamber pressure. All the transducer outputs are recorded with an FM tape recorder and played back through appropriate filters and phase meters as described in references 16 and 17.

Cold Flow Tests

Cold flow tests were conducted as the first step in experimentally evaluating this method. In these studies, nitrogen was injected into the combustion chamber and the two auxiliary chambers (used as a phase reference) through individual sonic chokes. The discharge coefficients of all three exhaust nozzles were evaluated by calibration against a standard venturi flowmeter. Under these conditions, the response functions are zero and the analysis described in the previous section can be used to predict the ballistics of all three chambers.

The first series of tests was conducted using a rotor sleeve where the two rows of holes were in phase, i.e., the pressure-coupled configuration. Figure 6 shows the excellent agreement the predicted and observed amplitude in all three chambers. These tests were conducted at frequencies between 100 and 250 Hz using the clockwise-counterclockwise method of reference 17.

The corresponding phase comparison, shown in figure 7, used the oscillating pressure in the combustion chamber as a reference. Thus, excellent agreement was obtained between the predicted and observed phase differences. Additional cold flow tests reported in reference 16 substantiate the phase results. These results demonstrate that the operation of the apparatus is basically sound and that the analytical model can be used to derive response functions from experimental data.

Pressure-Coupled Response Tests

Combustion tests have been conducted with a single rotating valve to determine the pressure-coupled response function of several aluminized and nonaluminized propellants.

Concurrently, T-burner tests were also conducted to compare the two test methods. Comparisons for the aluminized formulations are shown in figures 8 through 12 while comparisons for nonaluminized formulations are shown in figures 13 and 14. Reasonable agreement between the rotating valve and T-burner response values was found for all propellants except propellant E. Table 2 shows the linear burning rate for each propellant at the combustion pressure corresponding to the response measurements.

TABLE 2. COMPARISON OF BURNING RATES

Propellant	Burning Rate (in./sec)
A	0.34
B	0.31
C	0.43
D	0.67
E	0.29
F	0.16
G	0.44

The measured c^* for each propellant was within 90% of the thermodynamically predicted value. Furthermore, the measured burning rate corresponded to the value measured independently using strands and small motors.

The discrepancy noted for propellant E has not been satisfactorily explained. This propellant had the lowest burning rate of the aluminized formulations tested. However, propellant F had a substantially lower burning rate but showed good agreement between the two test methods. Furthermore, propellant B had only a slightly higher burning rate than propellant E, but yielded excellent agreement. However, the T-burner data did show significant deviation from the expected linear relationship between the decay rate and area ratio for propellant E. Thus, it is not clear if the difficulty rests with the rotating valve or the T-burner. Extensive additional work would be required to resolve this discrepancy.

Barrere and co-workers[25-27] have independently developed an apparatus for pressure-coupled response function measurements using this basic approach. They also report good agreement between the rotating valve and T-burner results. In addition they have reported measurements of the imaginary part of the response function and have correlated both the real and imaginary parts in terms of combustion theory.

The combined results from all these studies show the approach to be technically sound and to offer a number of advantages. This method eliminates complications associated with particle damping and minimizes thermal losses. This is particularly advantageous at low frequencies where large corrections are required in the T-burner results.

Velocity-Coupled Response Tests

Combustion tests to evaluate this method for velocity response function measurements are currently in progress. The initial series of tests revealed significant modulation of the pressure amplitude. Figure 15 shows the oscillating pressures at each end of the motor and the mean chamber pressure vs. time. The time delay in the rise of P_c and the appearance of oscillations resulted from delays in the release of the Kistler grounding circuit. Results are shown for various filter settings (Q) at the fundamental frequency and for the second harmonic content.

The most notable observations are the large amplitude modulations in the oscillating pressure. By imposing the condition that $\partial\varepsilon/\partial t = i\lambda\varepsilon$, the analysis does not permit evaluation of the modulations. Further study revealed that the frequency of the modulations is every twenty cycles, which equals the number of holes around the rotor. Careful review of the machining tolerances showed these rotors had excessive variations in the spacing between holes. New rotors were machined to more exacting tolerances. Tests with these new rotors showed a substantial reduction in the magnitude of modulations. Thus, tolerance control is extremely important in these measurements.

Using the improved rotor, another series of combustion tests was conducted using propellant G. Power spectra analyses from two tests, both conducted at 300 Hz, are shown in Figures 16 and 17. These results were obtained using a Hewlett-Packard Model 3582A Spectrum Analyzer. The data shown in figure 16 were obtained using one steady-state nozzle while the data in figure 17 were obtained using identical steady-state nozzles at each end of the burner.

Several observations can be made. First, both figures show significant harmonic content. Analysis of the driver wave form[16] shows no driving of the even harmonics by the valve and only minimal (-36 dB) driving of the third harmonic. Thus, the harmonic content shown in figures 16 and 17 is produced by the burner and not by the rotating valve

driver. In the light of the analyses presented earlier in this paper, linear velocity coupling would not produce this frequency spectrum. However, the amplitude-dependent velocity coupling model also does not produce the relative harmonic magnitudes shown in both tests.[16]

The second observation derives from a comparison of Eq. (10) with these data. According to Eq. (10) testing with identical steady-state nozzles at each end (i.e., $\bar{x}_1 = 0.5$) should result in no pressure oscillations being generated. Obviously that is not the case in figure 17. Thus, the results to date cast doubt on the validity of the "linear" velocity coupling concept and thereby suggest that perhaps the amplitude-dependent velocity coupling model should receive further experimental and analytical study.

Another source of the high harmonic content could result from nonlinear flow effects. For example, the linearization of the momentum equation assumes the mean flow velocity is much larger than the Mach number of the oscillating flow at every axial position. Since there is mean flow from both ends of the burner, the mean flow Mach number is zero at some point along the axis ($Z = \bar{x}_1$). The oscillating flow Mach number is essentially constant along the axis. Hence, the assumption breaks down in the region where $\bar{M} = 0$. Eliminating this assumption introduces a nonlinear term that ultimately could contribute to the harmonic content. The counter argument to this point is that this flow nonlinearity enters through the momentum equation. At low frequencies, momentum effects are relatively unimportant; hence, nonlinearity should not be important. At this date, this point remains unresolved.

CONCLUSIONS

Analytical and experimental studies have demonstrated the applicability of the rotating valve method for measuring the pressure-coupled combustion response function of solid propellants. With one exception, good agreement has been obtained with T-burner results. For velocity-coupled response function measurements, progress has been made using the dual valve approach. However, more effort is needed to evaluate this approach properly and to understand the results available to date.

REFERENCES

1. Denison, M. R. and Baum, E., "A Simplified Model of Unstable Burning in Solid Rocket Propellants," ARS Journal, Vol. 3, No. 6, March 1961, pp. 1112-1121.

2. Friedly, J. C. and Peterson, E. E., "Influence of Combustion Parameters on Instability in Solid Propellant Motors: Part I - Development of Model and Linear Analysis," AIAA Journal, Vol. 4, No. 9, September 1966, pp. 1605-1610.

3. Culick, F. E. C., "A Review of Calculations for Unstable Burning of a Solid Propellant," AIAA Journal, Vol. 6, No. 12, December 1968, pp. 2241-2254.

4. Brown, R. S. and Muzzy, R. J., "Linear and Nonlinear Pressure Coupled Combustion Instability of Solid Propellants," AIAA Journal, Vol. 8, No. 8, August 1970, pp. 1492-1500.

5. Price, E. W., Mathes, H. B., Burn, D. E., and Brown, B. G., "Combustion Instability of Aluminized Propellants," Rept. NWC TP 5060, April 1971, Naval Weapons Center, China Lake, CA.

6. Beckstead, M. W. et al., "Variable Area T-Burner Investigation," Rept. AFRPL-TR-72-85, December 1972, Hercules, Inc., Magna, UT.

7. Peterson, J. A. et al., "Pressure Oscillation Investigation for Minuteman III," Rept. AFRPL-TR-72-98, January 1973, Thiokol Chemical Corp., Brigham City, UT.

8. Derr, R. L., "Development and Evaluation of Variable Area T-Burners," Rept. AFRPL-TR-72-97, November 1972, Lockheed Propulsion Company, Redlands, CA.

9. Micheli, P. L., "Evaluation of Pulsed T-Burner for Metallized Propellants," Rept. AFRPL-TR-72-54, September 1973, Aerojet Solid Propulsion Company, Sacramento, CA.

10. Wendelken, C. P., Chew T. J. C., and Weiss, R. R., "Combustion Instability Characteristics of Several Solid Propellant Rocket Propellants for Booster and Tactical Rocket Applications," presented at the 9th JANNAF Combustion Conference, Monterey, CA, September 11-15, 1972.

11. Andrepont, W. C. and Schoner, R. J., "The T-Burner Test Method for Determining the Combustion Response of Solid Propellants," AIAA Paper 72-1053, New Orleans, LA 1972.

12. Beckstead, M. W., and Butcher, A. G., "The Velocity Coupled T-Burner," AIAA Preprint No. 74-200 presented at 12th Aerospace Sciences Meeting, Washington, DC, 1974.

13. Micheli, P. L., "Investigation of Velocity Coupled Combustion Instability," AFRPL Report No. TR-76-100, Aerojet Solid Propulsion Company, 1977.

14. Culick, F. E. C., "The Stability of One Dimensional Motions in a Rocket Motor," Combustion Science and Technology, Volume 7, pp. 165-175, 1973.

15. Coates, R. L., "Application of Hart-McClure Analysis to Interpretation of T-Burner Data," presented at the Third AFRPL Workshop on Combustion Instability, Sacramento, CA, October 1971.

16. Brown, R. S., Erickson, J. E., and Babcock, W. R., "Combustion Instability Study of Solid Propellants," AFRPL Report No. TR-73-42, CSD, 1976.

17. Brown, R. W., "Development and Evaluation of Rotating Valve Combustion Response Test Techniques," AFRPL-TR-76-72, October 1976.

18. Brown, R. S., Waugh, R. C., and Kelly, V. L., "Rotating Valve for Velocity Coupling Combustion Response Studies," paper presented at 15th JANNAF Combustion Meeting, Newport, RI.

19. Murphy, G. M., "Ordinary Differential Equations and Their Solutions," Van Nostrand Reinhold Company, New York, pp. 323, 1960.

20. Abramowitz, M. and Stegun, I. A., "Handbook of Mathematical Functions with Formulas, Graphs, and Mathematical Tables," National Bureau of Standards Applied Mathematics Series No. 55, 1964.

21. Lovine, R. L., Dudley, D. P. and Waugh, R. C., "Standardized Stability Prediction Method for Solid Rocket Motors," AFRPL-TR-76-32, Aerojet Solid Propulsion Company, May 1976.

22. Culick, F. E. C., "Stability of Longitudinal Oscillations with Pressure and Velocity Coupling in a Solid Propellant Rocket," Combustion Science and Technology, Volume 2, pp. 179-201, 1970.

23. Price, E. W. and Dehority, G. L., "Velocity Coupled Axial Mode Combustion Instability in Solid Propellant Rocket Motors," ICRPG/AIAA Second Solid Propulsion Conference, June 1967, pp. 213-227.

24. Dehority, G. L. and Price, E. W., "Axial Mode, Intermediate Frequency Combustion Instability in Solid Propellant Rockets," Naval Weapons Center Report NWC-TP-5654, October 1974.

25. Barrere, M., Nadaud, L., and Lhuillier, J. N., "Survey of ONERA and SNPE Work on Combustion Instability in Solid Propellants," Journal of Spacecrafts and Rockets, Vol. 11, January 1974, pp. 33-40.

26. Kuentzmann, P. and Nadaud, L., "Reponse des Propergols Solides aux Oscillations de Pression et de Vitesse," Combustion Science and Technology, Vol. II, 1975, pp. 119-139.

27. Kuentzman, P. and Langelle, G., "Recent Research Activity at ONERA on Combustion Instability and Erosive Burning," paper presented at 1977 AFOSR/AFRPL Rocket Propulsion Meeting, Lancaster, CA, March 1977.

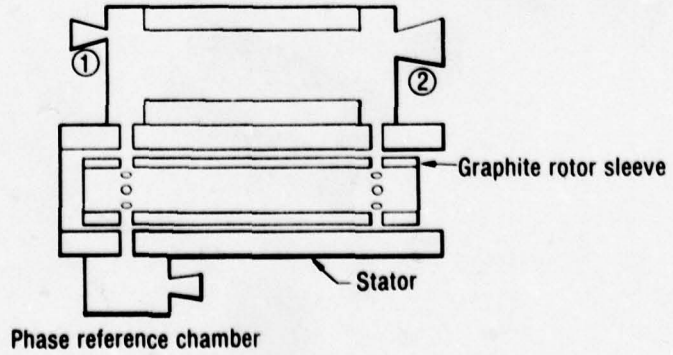

Figure 1. Apparatus Layout

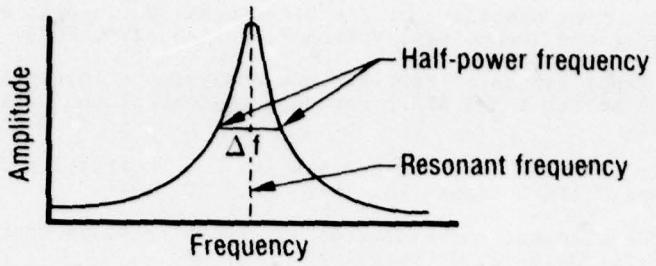

Figure 2. Dynamic Amplitude Response

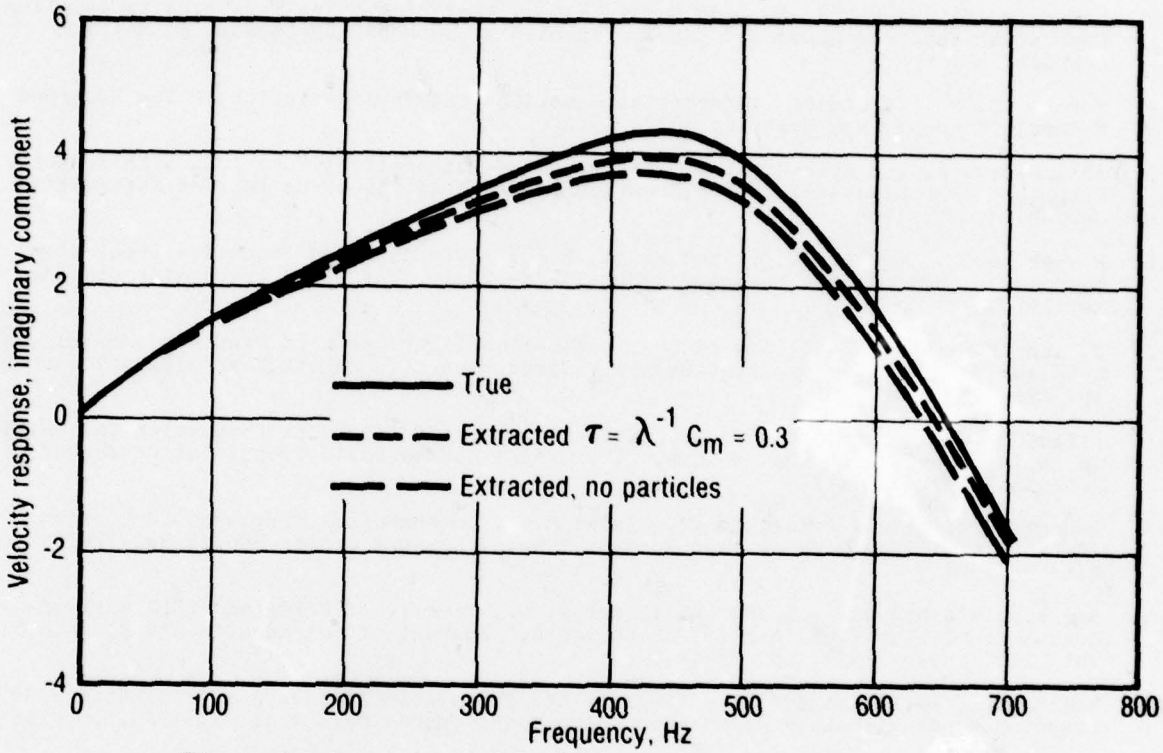

Figure 3. Comparison of Derived and Exact Velocity Response

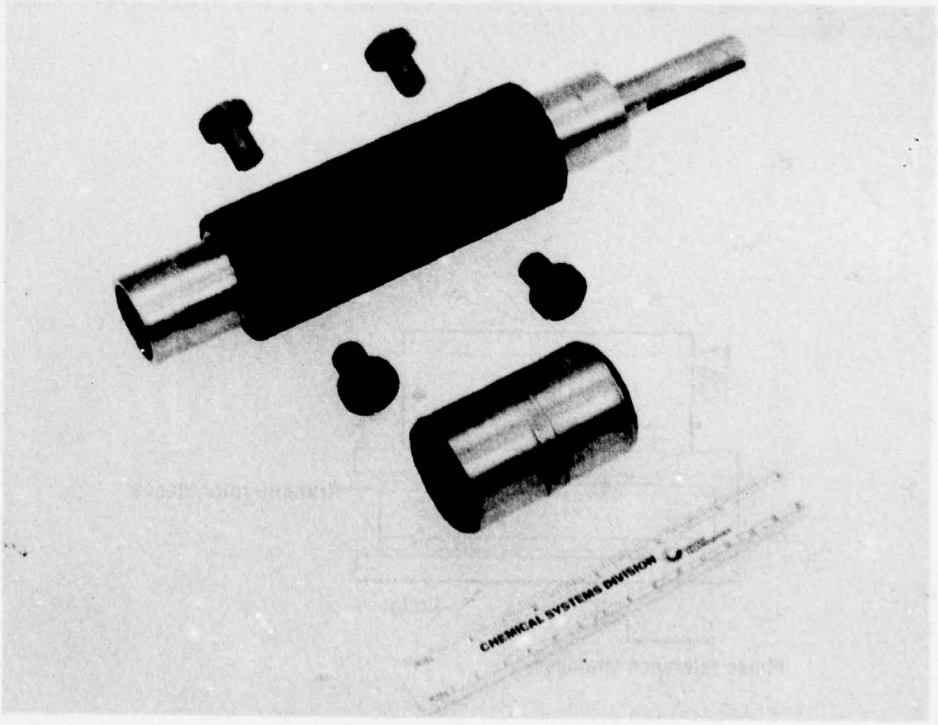

Figure 4. Dual Rotating Valve Components

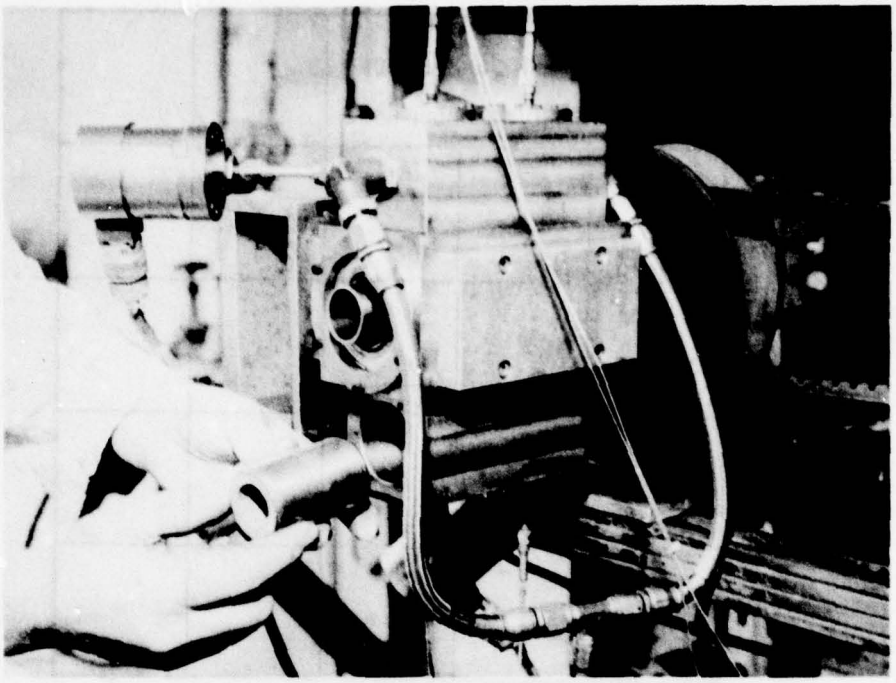

Figure 5. Propellant Grain and Valve Assembly

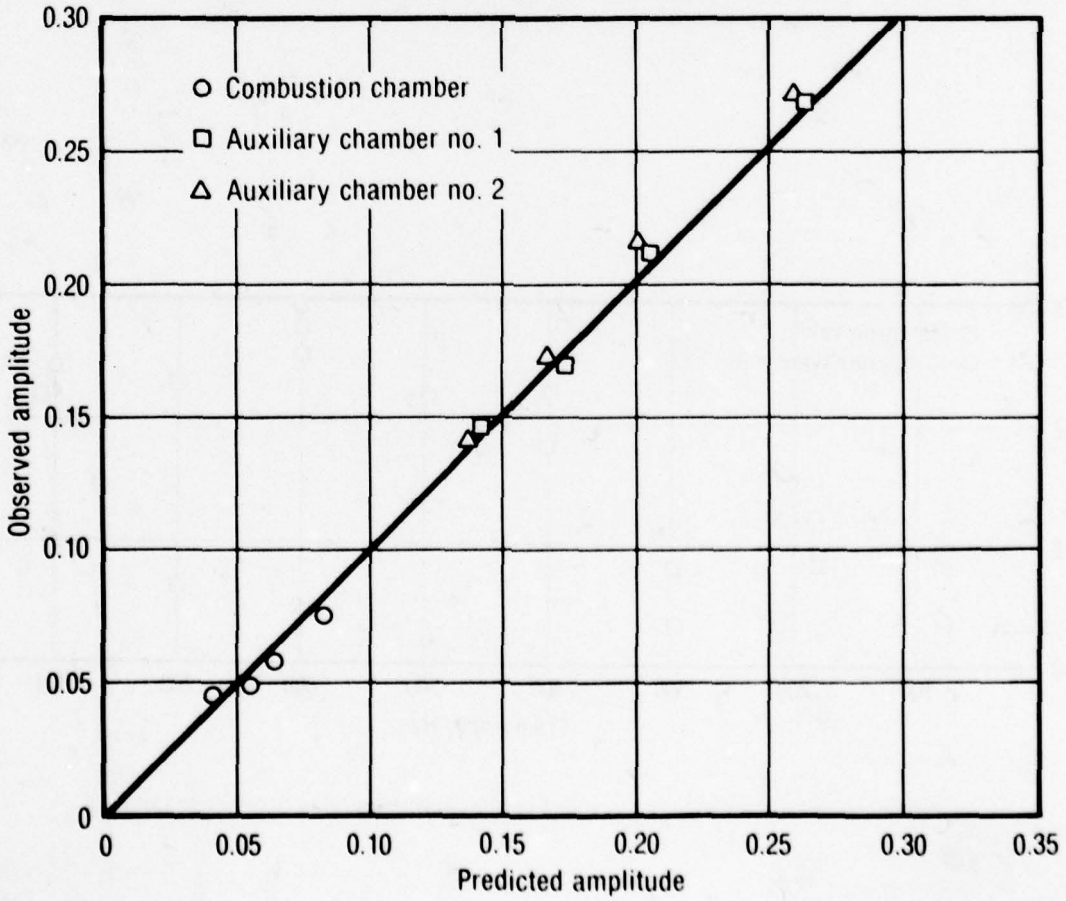

Figure 6. Cold Flow Amplitude Data Pressure Coupled Dual Valve Configuration

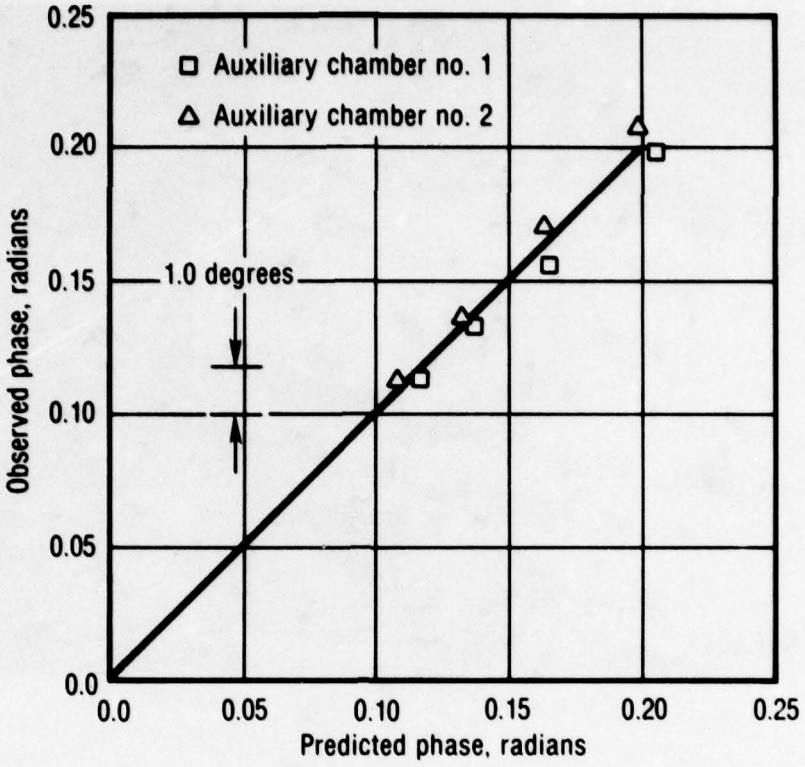

Figure 7. Cold Flow Phase Data Pressure Coupled Dual Valve Configuration Combustion Chamber as Reference

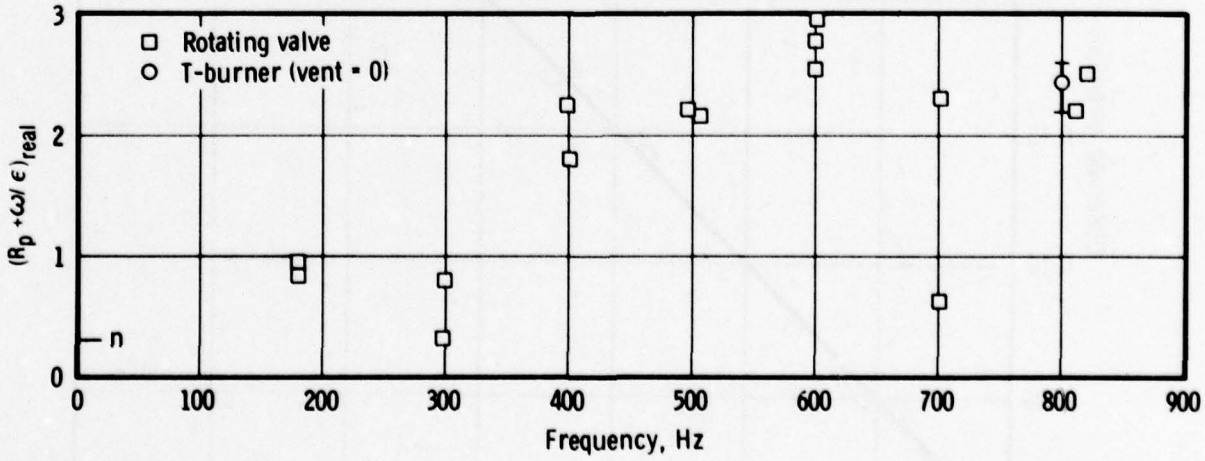

Figure 8. Pressure Coupled Combustion Response of Propellant A

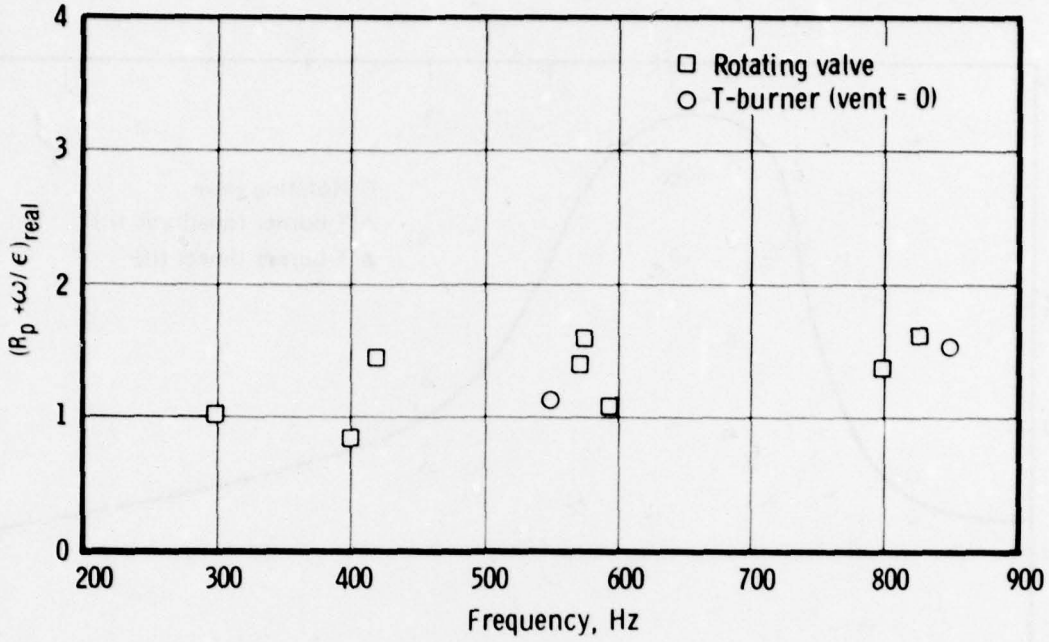

Figure 9. Pressure Coupled Combustion Response of Propellant B

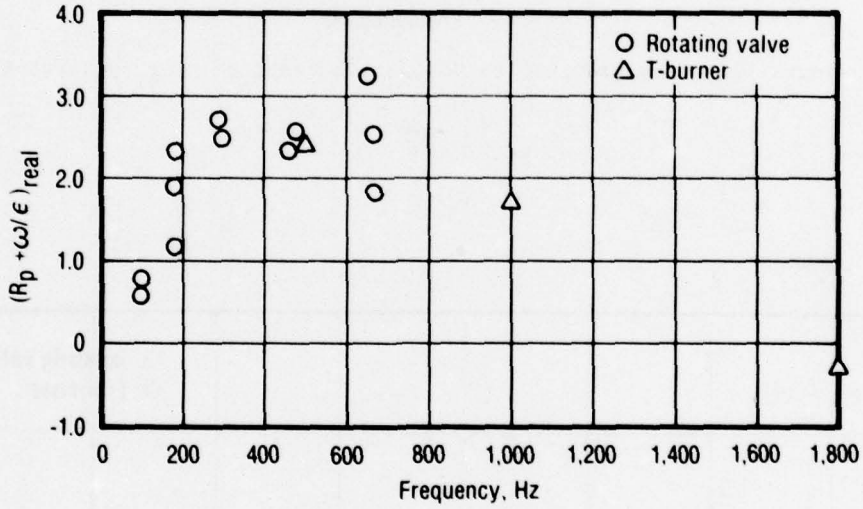

Figure 10. Pressure Coupled Combustion Response of Propellant C

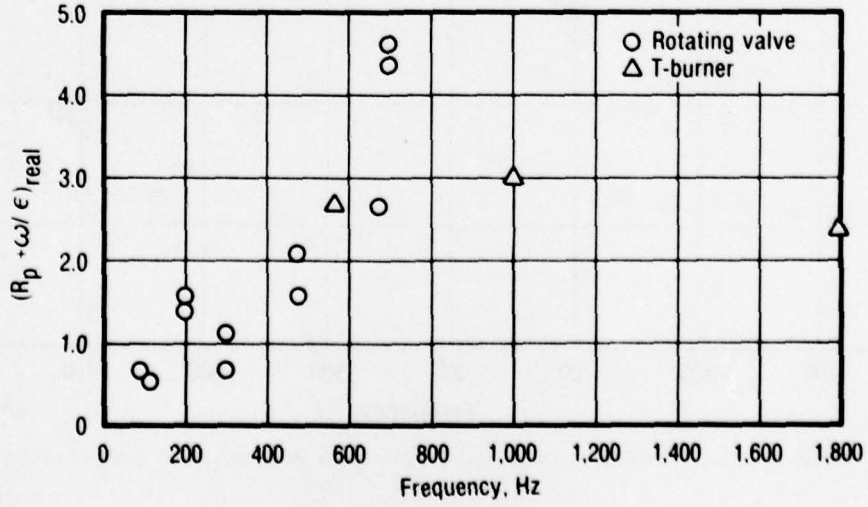

Figure 11. Pressure Coupled Combustion Response of Propellant D

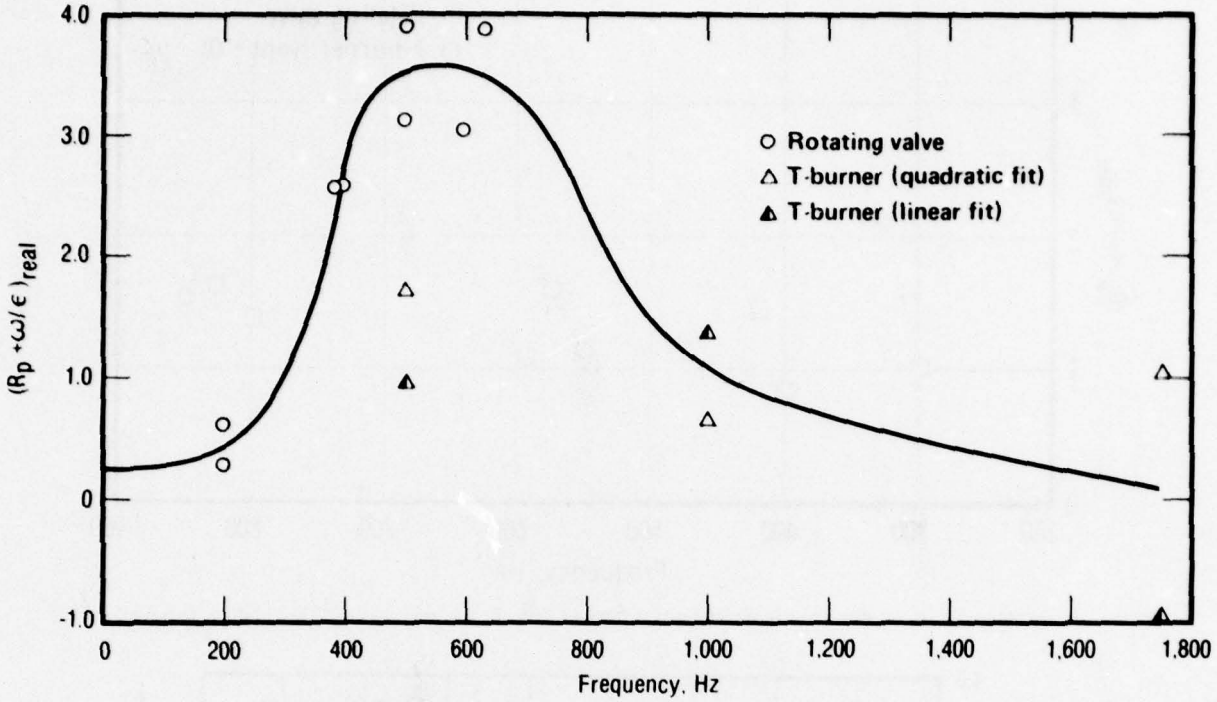

Figure 12. Pressure Coupled Combustion Response of Propellant E

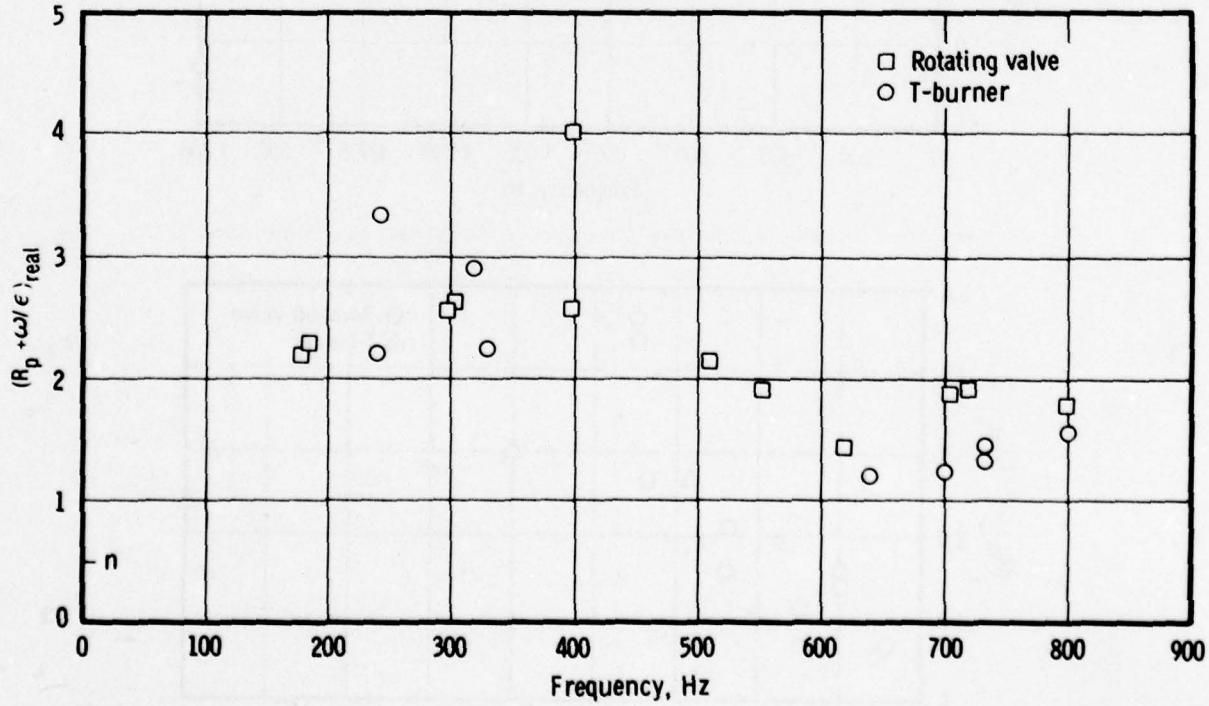

Figure 13. Pressure Coupled Combustion Response of Propellant F

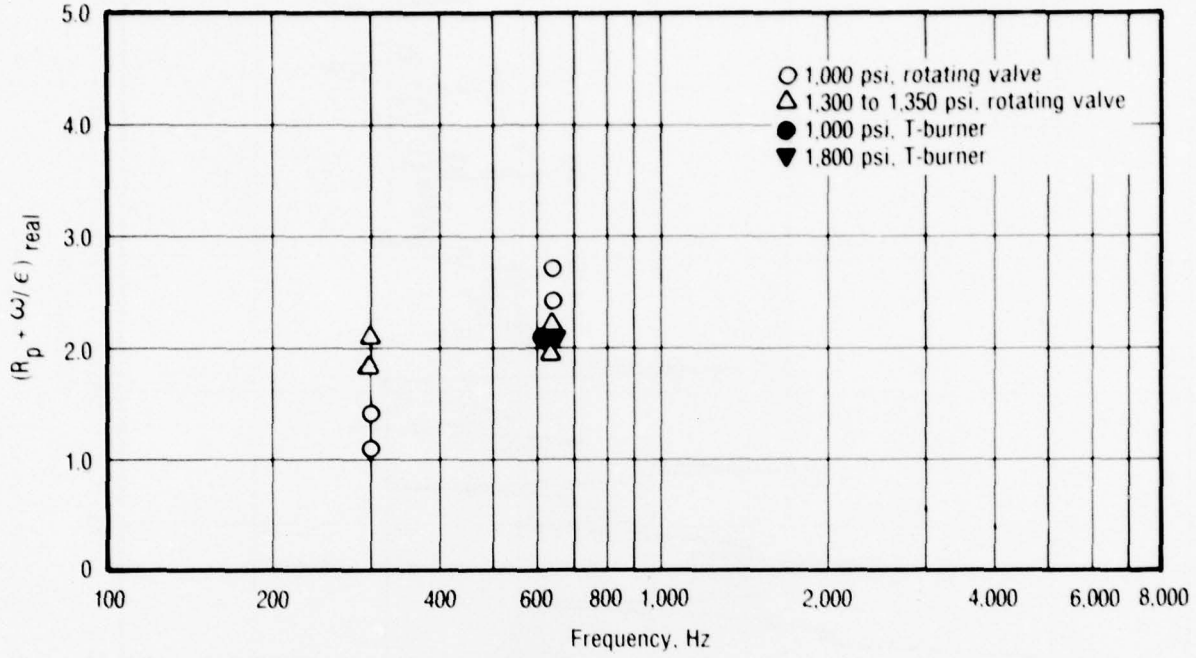

Figure 14. Combustion Response of Propellant G

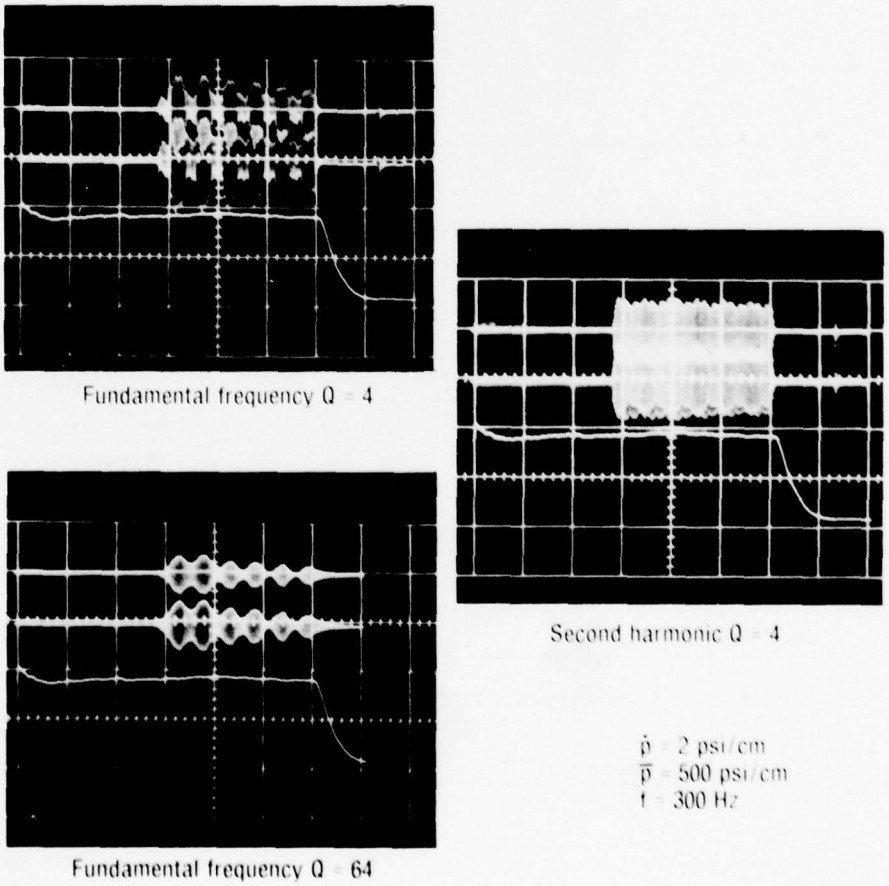

Figure 15. Velocity Coupled Test Results

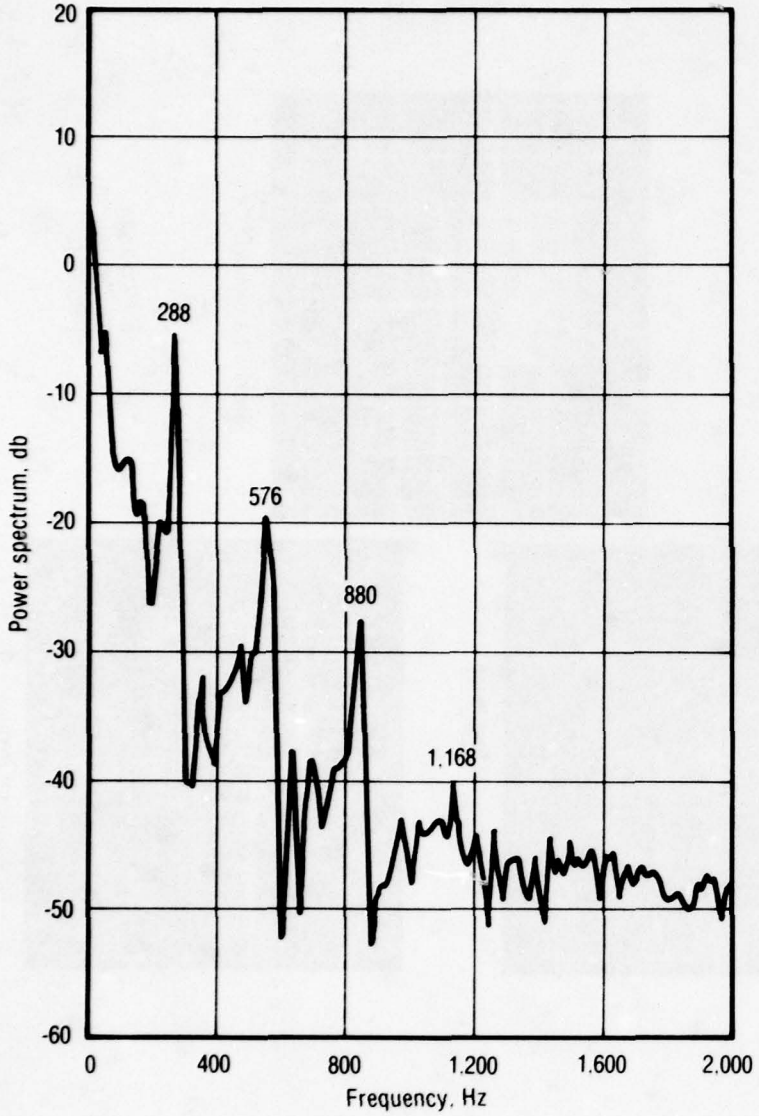

Figure 16. Harmonic Content of Pressure Oscillation

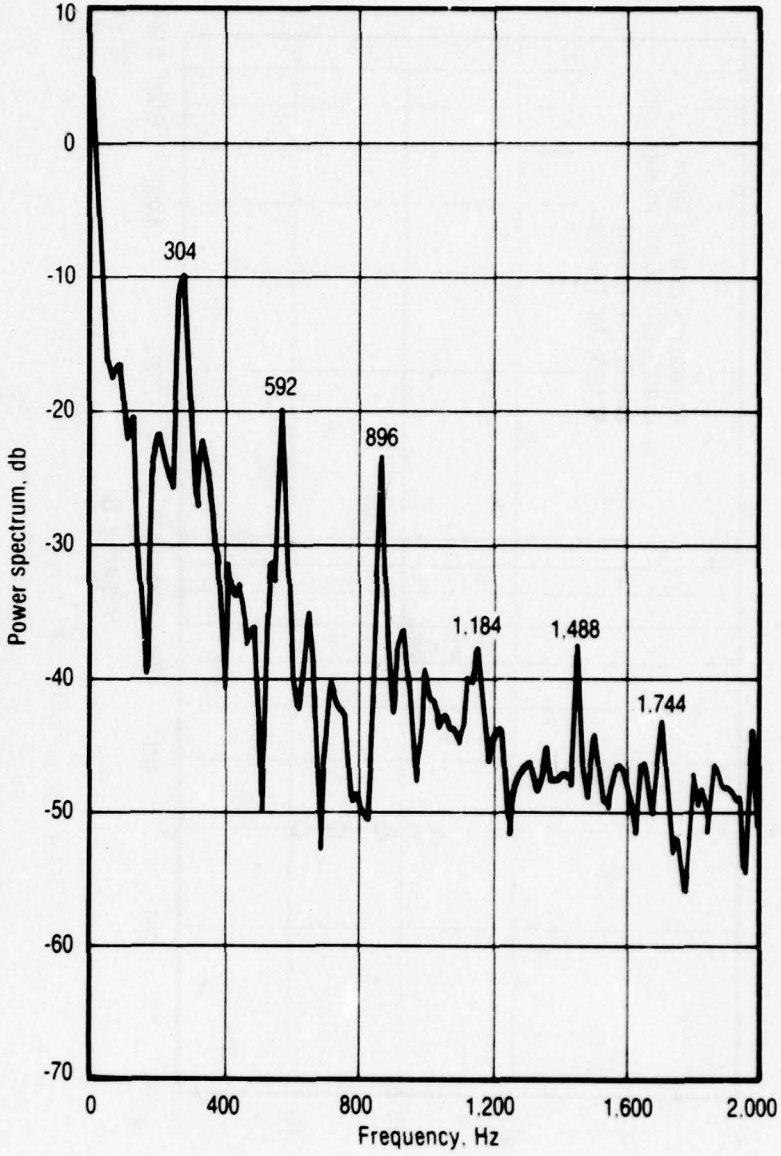

Figure 17. Harmonic Content of Pressure Oscillation

DISCUSSION

M.Barrere, ONERA, Fr

In your determination of the response function of the propellant, using the T-burner, did you take into account the thermal losses? For example as you decrease the frequency, you have to increase the length. This frequency-length variation affects thermal losses.

Author's Reply

We did not require to take account of these losses with the rotary valve technique because the propellant covers most of the length of the burner and length is invariable. This was the reason for using this burner and in fact our C* results were very good.

With the T-burner the thermal losses can be very significant and we tried to keep to the higher frequencies to minimise the losses. Our comparisons between the two techniques were made at the higher frequencies.

ULTRASONIC IMAGING AS APPLIED TO NON-DESTRUCTIVE TESTING OF ROCKET PROPELLANTS

by

D S Dean and D T Green

MOD PE
PERME
Westcott
Aylesbury
Buckinghamshire
HP18 ONZ
UK

SUMMARY

It is necessary to determine cracks, voids and other faults in solid propellant charges in order to assess the extent of their effect on design performance. Many such faults either cannot be detected radiographically at all or can only be found by taking a large number of radiographs from many different directions with consequent high inspection cost. Ultrasonic energy is very sensitive to discontinuities in solids but it is more difficult to use for the inspection of rocket motor charges because of the problems of coupling ultrasonic transducers to propellant and of interpreting signals transmitted through the charge. Presenting the results as a visual image of the interior of the propellant would lead to much easier determination and assessment of defects. A focused image of this nature may be obtained by holographic encoding or computational manipulation of the phase information of the ultrasonic field.

1. INTRODUCTION

Defects in or adjacent to propellant charges can produce undesirable burning characteristics such that the design performance of a motor may not be achieved or catastrophic failure may even occur. If the fault results in a reduction of the amount of material present along the viewing axis of more than about one percent then its outline may be determined radiographically. This, however, is not the case for many cracks, delaminations and bonding faults. In these cases ultrasonic inspection, which is interface sensitive rather than dependent upon the amount of material missing, is a potentially better technique.

To form a focused image from the ultrasonic field it is necessary to process and record ultrasonic signals transmitted through or reflected from within the propellant over a viewing aperture. Through-transmission is preferable because of the smaller range of signal attenuation involved. If the propellant can be immersed then a liquid acoustic couplant, for example water or a fluorinert liquid, can be used. Otherwise it is necessary to employ more difficult techniques such as the use of a rotating soft coupling medium to transfer energy from the ultrasonic transducers to the propellants (see Fig. 1). Transducers using this technique have been designed and used in rocket motor inspection facilities in the United Kingdom and in some industrial applications. An alternative, non-contacting, method is to use a scanning laser interferometer to measure surface displacement; but this is generally several orders of magnitude less sensitive than the use of solid or liquid coupled piezoelectrics. Any system which is to be applied to solid propellant rocket motor inspection needs to have good sensitivity (at least of the order of 10^{-7} W/m^2 for unity signal-to-noise ratio) because of the high attenuation of propellant at frequencies which allow the required minimum resolution. Piezoelectric detection is therefore nearly always necessary despite the advantages of many other methods.

The attenuation of ultrasound in propellant increases rapidly with frequency (see Fig. 2) and the shortest wavelength that can be utilised with sufficient received signal-to-noise ratio for subsequent data processing is generally of the order of 1-10 mm. Thus, as one would expect, one of the main characteristics of ultrasonic images is their inherently low resolution. They will also be very specular due to the relative smoothness of interfaces and boundaries compared to the wavelength and their high reflection coefficients. The ultrasonic image which is obtained has to be made acceptable within the constraints of its low resolution characteristics and therefore careful consideration should be given to definition, contrast, speckle etc. in the resultant display, bearing in mind that there is little margin for allowing the introduction of additional noise by the signal processing system.

An unfocused shadograph or "C-scan" picture can be obtained by measurement of the signal amplitudes; to obtain focused images and hence improved resolution and contrast it is necessary to use the phase information of the ultrasonic field as well. Ultrasonic lenses are very inconvenient and difficult to use in this application, particularly where liquids are inadmissible for providing coupling. Thus a two stage process using holographic encoding of the signal phases and subsequent optical reconstruction of the ultrasonic field or the use of phased array focusing with subsequent or real-time presentation of the data on a visual display unit are alternatives under investigation for ultrasonic imaging in propellants. In the former method focusing is obtained using optical components after the whole ultrasonic field has been reconstructed optically. In the latter method the ultrasonic wave itself may be focused using a transmitting array and the focusing of received energy achieved by electronic circuitry or computation.

2. ULTRASONIC IMAGING METHODS

2.1 Ultrasonic Holography

The holographic recording and reconstruction process may be used to record the wavefront of one form of energy propagated through an object and then reconstruct that wavefront using another type of energy (Fig. 3). Thus acoustic, microwave or other fields may be made visible using this process. Whatever radiation is used it must be sufficiently coherent, which is the case in most ultrasonic applications.

To form an acoustical hologram the phase and amplitude of the acoustical wavefront over an aperture must be recorded by means of interference, with an appropriate reference wavefront. Since a linear output is obtained from a piezoelectric detector which can be scanned across the aperture, a real, acoustical reference wave is not necessary because the phase of the sampled field is directly available. For example, interference with a plane reference wave may be simulated by sampling the field at temporally selected points which advance cyclically with respect to the phase of the transmission wave in linear fashion across the aperture (Fig. 4). Suitable circuitry will enable the angle of the "simulated reference" to be changed with respect to the aperture and wave propagation axes (Fig. 5).

The Fourier spectrum of such a "skewed" reference (Fig. 6) shows that the spatial frequencies about which the image information will be centred do not overlap with the aperture diffraction arms at zero-order light; the image information is therefore easily separated from these by spatial filtering.

Two conjugate images are formed, of course, and it is necessary to inform the circuitry which directions in space are the "forward" or "positive" directions of the aperture axes; otherwise, information for the real and virtual images will be ambiguous and may be wrongly assigned so that these images overlap with each other.

These complex functions have been reduced to one circuit module which can be incorporated in a suitable ultrasonic inspection system and is shown schematically in Figs. 7 and 8. The simple method of deriving the phase sampling points is independent of the transmission frequency. This facilitates operation and use of the system and also allows frequency-modulated holograms to be constructed which can reduce speckle noise in the subsequent reconstruction.

Operation of the unit is as follows. Transmitted signals are derived from a gated transmission carrier to permit subsequent time domain gating of the received signal and to reduce transmission power requirements. Sampling pulses of a few nanoseconds duration are generated at a selected phase angle of the transmission reference wave (Fig. 9). The phase angle selected is changed cyclically by appropriately changing the synthetic wave level which is compared with the rf ultrasonic wave to generate the sampling pulses. Logic circuitry corrects the selection sequence for spatial and temporal/magnitude ambiguities. The resulting sequence of pulses is then allowed to sample the received signal during the time corresponding to the required depth of field of view. The sampled level is held between each pulse to produce a "phase-amplitude profile" of the ultrasonic signal (Fig. 10). These "profiles" are then integrated to simulate the cw interference situation which occurs in optical holography (Fig. 11). (This is not essential if the transmission pulse is long enough to encompass the complete object depth.) If the receiving transducer is traversed in synchronism with the synthetic reference wave (or phase sampling increments) the output of the encoder, after suitable amplification and biasing, may be considered as a "cross-section" through a hologram when applied to a recording medium where the recording point also moves in synchronism with the receiving transducer. A hologram is thus obtained from the scan raster.

Having obtained the recording, or hologram, the ultrasonic wavefront may be reconstructed by diffraction of an optical reference wave by the hologram (as, for example, in Fig. 13). In order to do this the recording should first be spatially reduced. The simplest method is by photographic reduction to produce a transparency which may then be placed in the coherent reference beam of a viewing system. The reduction should be in the ratio of the optical to acoustic wavelengths used in order to prevent any aberration. However, a reduction of this magnitude is not usually possible resulting in depth distortion, which is not generally a problem, and some spherical aberration, which may have a small effect on resolution.

To obviate the photographic stage, and produce a real-time reconstruction system, the hologram can be written directly onto a photochromic film with a scanning laser beam which is modulated by the data from the encoder. These data may also be manipulated to enhance certain image characteristics. For example, the signal amplitudes may be logarithmically compressed which has the effect of enhancing the contribution of energy scattered from higher spatial frequencies in the object and hence intensifying image outlines.

An example showing a comparison between viewing different types of fault radiographically and ultrasonically is shown in Fig. 12.

2.2 Matrix image formation by multiple scan

The advent of mini- and micro-computers operating rapidly and with large storage capability has opened up techniques, in addition to holography, for producing ultrasonic images. The holographic technique can still use such computers for image forming and as its name implies, it stores the complete picture, but other simpler techniques may ease the problems of obtaining the primary ultrasonic information. One such technique is an ultrasonic adaptation of the method used by Hounsfield in the whole body X-ray scanner.

This assumes a narrow beam of radiation received by a detector after passing through the body. In one scanning method the source and detector are scanned linearly through a narrow slice across the body and the radiation intensity measured at intervals of approximately one beam width during the scan. At each sample point, therefore, the intensity is the result of the sum of the attenuation at all points in the passage of the beam. The source and detector are then rotated around the body to a new position but with the beam still passing through the same narrow slice one beam-width thick. A further linear scan is carried out with sampling as before. We can regard this slice through the body as divided into a matrix of cubes with sides equal to one beam width. Each of these cubes will have been scanned twice and will form part of the attenuating path traversed by the beam in two of its sampling positions. Typically 100 samples are taken per scan to give a 100 x 100 matrix of points. The source and scanner are then rotated to a multiplicity of other scan positions, typically 400 so that the computer will have 40,000 figures to process each of which is the total absorption along an individual path. The computer is required to identify the atenuation due to each individual cube in the section through the body and hence build up a picture of overall attenuation in the slice with a resolution of one beam width. As each slice of the body is dealt with the scan system moves laterally by one beam width and repeats the process for the next slice. In practice, by the use of shaped beams and multiple detectors, the total number of mechanical scans can be drastically reduced.

The computer carries out the calculations by successive approximation. The first attenuation reading obtained is assumed to be due to 100 equally attenuating elements in the path of the beam. As the scans progress, new values will be obtained for elements in the original path, which can then be inserted and the rest of the elements suitably adjusted. The process is repeated for all 40,000 beam positions until a distribution of attenuation values is found for all elements which agrees with all the recorded figures for beam attenuation.

The X-ray system produces greatly improved detailed images of the internal parts of the human body and its application to industrial problems, including rocket motor inspection, is currently being investigated. There seems no reason why other forms of radiation than X-ray should not be used and we have started a computer exercise to evaluate the use of ultrasound in a similar manner. There are many additional problems to be solved such as the finite beam spread at the frequencies needed to penetrate rocket motor propellant, which may be reduced by suitable design of receiver transducer. Ultrasound will also suffer refraction, reflection and mode conversion at boundaries which can confuse the result. This can be at least partially overcome by time gating. Coupling the energy into the motor and devising a scan which will permit each element to be irradiated by sufficient different beams is also difficult. The scan previously described is not however the only one used in the X-ray case and a wide variety is possible if the computer is suitably programmed.

An advantage with ultrasound is that attenuation is not the only quantity which can be measured, sound velocity measured by timing or phase being an alternative. This work is in too early a stage for its possibilities to be gauged, but it seems sufficiently promising to warrant investigation.

2.3 Phase delay focussing and arrays

The results obtained by holography could be equalled using an ultrasonic lens if it were not so difficult to employ in practice. The motor and lens would have to be immersed in a suitable fluid and internal reflections in the lens system would have to be suppressed. It has long been realised that a lens can be simulated by inserting controlled phase delays into signals from suitably placed transducers, equivalent to those introduced by a lens in the same positions. The technique has been used effectively in sonar but few attempts have been made to adapt it to ultrasonic inspection systems. Phase delay can also be used to deflect the polar diagram of an array of transducers, which may be transmitters, receivers or a combination of both. This can best be explained by considering each element of a linear array to be a source of spherical radiation in the manner of the Fresnel analysis of light from an aperture. For this to be valid, each element must be comparable with, or less than half a wavelength of the ultrasonic radiation used. If the phase and amplitude of the signals exciting each element are the same, a beam of radiation with plane wavefronts will be produced as in Fig. 14, the angle of deviation in the far field depending upon the combined aperture of all the elements. If the phase of the drive to each successive element across the array changes by a constant amount the plane wavefront will be tilted and the beam angled towards the side with maximum delay. Rapid scanning of the beam is thus possible without mechanical movement. In practice the individual wavelets will reinforce at angles other than along the axis of the beam, so that side lobes will be formed. This effect can be reduced by "shading" the drive, that is by varying the amplitude of the drive from element to element across the stack.

If the elements are arranged in concentric rings in one plane and maximum phase advance occurs at the outer ring of elements, with the phase progressively retarded towards the centre, the array acts as a concave transducer (Fig. 15). By suitably controlling the change of phase, the focus of the array can be adjusted as desired. If a progressive phase delay is superimposed on the focussing delays the focal point can be moved to one side. It is thus possible by programming the delays to scan a three dimensional space with the focal point of the beam. This technique offers particular advantages for examining bulk materials with poor surface finish as only one contact area needs to be prepared for good acoustic coupling. It is also of use on relatively soft materials, such as rocket propellants, where surface contours make mechanical scanning difficult.

Kino at Stanford University is developing a system using these principles operating at 3.8 MHz which will eventually use 180 elements in a linear array. This is carefully damped and matched into water, which will form the coupling material. Phase delay is used for scanning along the array and the complete array is moved mechanically in the other direction. Sampling and digitising is at 16 MHz into random access memories for each element. The outputs from each scan are added and fed to the display. The whole system is controlled from a mini-computer including adjustment of phase delays.

Our own approach, which is in a very early stage, has of necessity been a little different as we are unable to use water coupling. We are using an A/D converter with a 100 MHz sampling rate to feed signal information into store in a mini-computer. A manually operated scanner with a single transducer can be moved over the specimen to be examined so that the information is gathered point by point. The scanner feeds positional data for the transducer into the computer as well as signal data. Once all the information has been gathered the computer will be able to operate on it to simulate any focussed scan which we wish to make. Whilst this is possible in principle one must not minimise the formidable task involved in writing the programmes. The next step, for which an extramural research contract has been initiated, is to construct arrays which can be coupled to the complex shapes encountered in rocket motor conduits. It is hoped to scan electronically the critical areas at the ends of rocket motors, particularly those under expansion boots.

A 32 x 32 element array was developed under contract by Mullard in conjunction with PERME (Fig. 16). This was originally intended for use with the holographic system, but can be applied to any other system where rapid data gathering is required. This uses individual 3 mm piezoelectric cubes arranged in an "egg box" structure of thin insulating strips to reduce acoustic coupling between elements.

Behind these elements is a layer of photoconductive material followed by a transparent conducting layer. A light beam scanned by a rotating mirror switches each element on in turn to permit a fast scan. A problem with all multi-element switched systems is the shunting effect of and interfering signals from all the switched-off elements. This is overcome in this application by printing a series switch at each

element which is shunted by the photoconductor at the "on" element. In addition each adjacent element to the "on" element is connected to a shunt resistor incorporated in the area behind the "on" element. Thus if stray light falls on the adjacent elements any signal output is shunted. In practice it is found best to use a fan-shaped light beam to switch a complete row of elements at a time and to use electronic switches to select elements in the row.

3. CONCLUSION

Imaging systems offer a marked improvement over current conventional techniques in the delineation of defects, particularly in large volumes of material such as rocket propellant. The holographic method described in this paper has the advantage of parallel processing of information to produce a near real time image. Other techniques described permit processing of information in a variety of ways subsequent to the acquisition of the information. Arrays of transducers can permit the electronic scanning of complex shapes without the difficulties involved in mechanical scans, but it is likely that a combination of both will ultimately be the most satisfactory.

Although the principles of many of these techniques have been known for some time it is only in recent years that the advent of large scale integrated circuits and powerful mini- and micro-computers, at reasonable cost, has made them feasible.

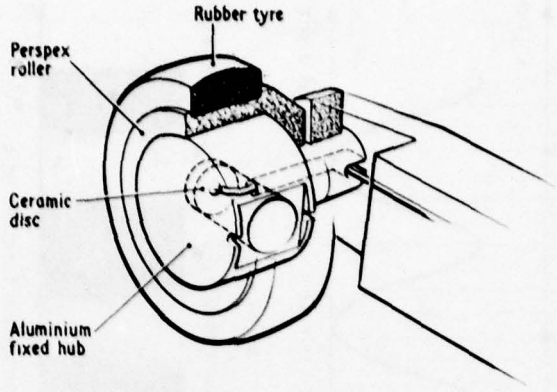

FIG.1 ULTRASONIC WHEEL PROBE

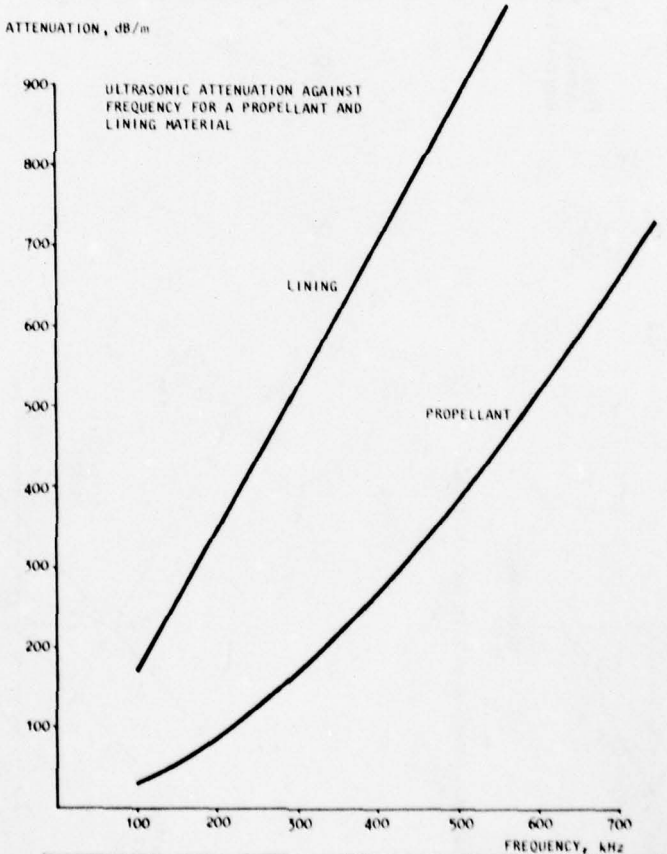

MATERIAL	VELOCITY (COMPRESSIONAL WAVE) m/s	DENSITY kg/m^3	ACOUSTIC IMPEDANCE kg m^{-2} s^{-1}
PROPELLANT	1740	1800	3.13_x10^6
LINER	1600	1320	2.11_x10^6

WAVELENGTH IN PROPELLANT AT 500 kHz = 3.48 mm)
CRITICAL ANGLE LINING/PROPELLANT = 67°) (COMPRESSIONAL WAVES)
TRANSMISSION COEFFICIENT PROPELLANT/LINER INTERFACE = 0.96

FIG. 2 ULTRASONIC PROPERTIES OF PROPELLANT AND HEAT RESISTANT LINER OF A ROCKET MOTOR

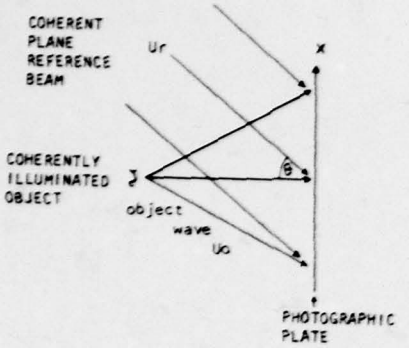

FIG. 3(a) HOLOGRAM FORMATION WITH OFF-AXIS REFERENCE

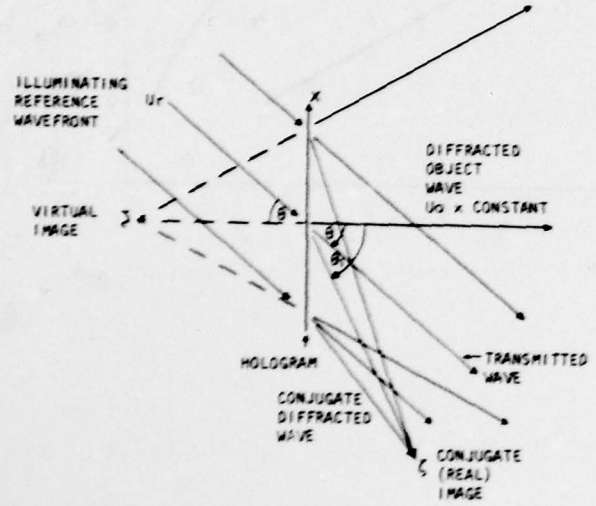

FIG. 3(b) RECONSTRUCTION FROM HOLOGRAM BY DIFFRACTION OF ORIGINAL REFERENCE

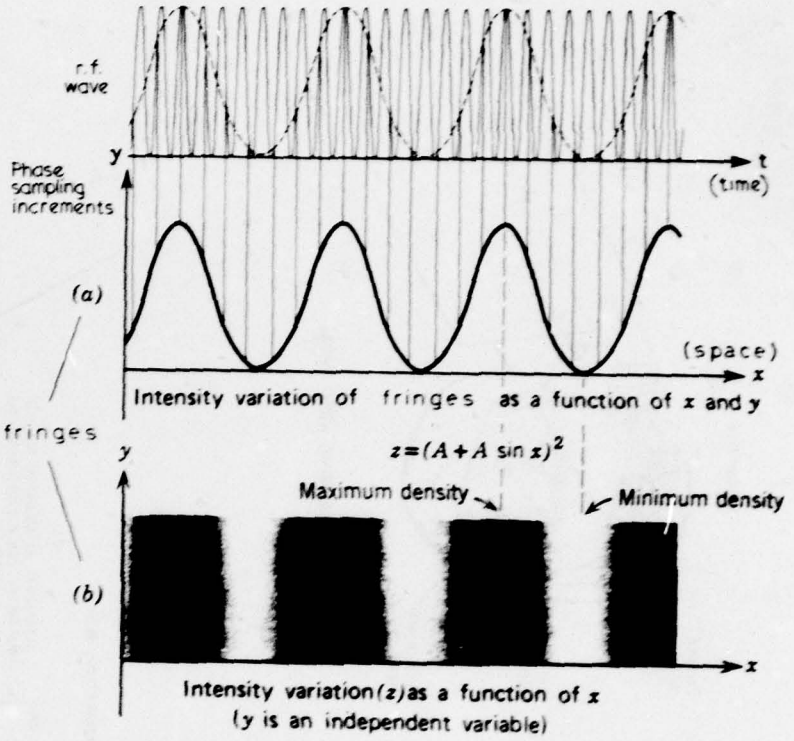

FIG. 4 PHASE ENCODING : Oscilloscope waveform and intensity displays.

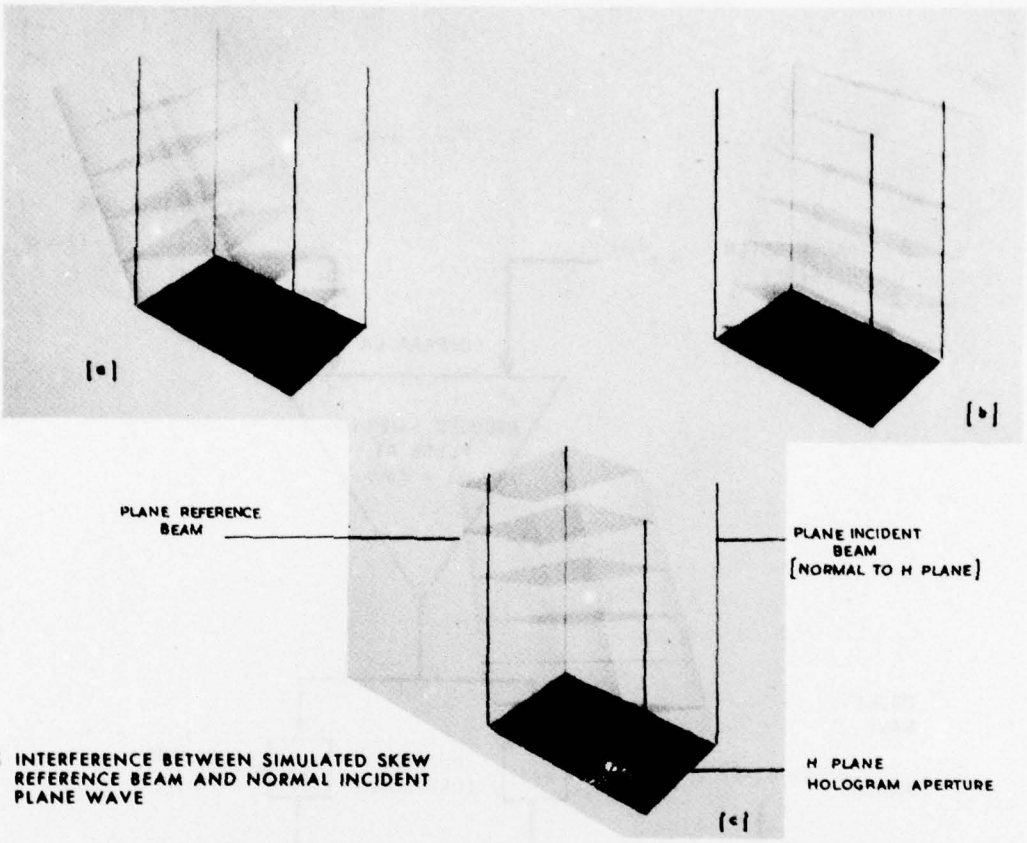

FIG. 5 INTERFERENCE BETWEEN SIMULATED SKEW REFERENCE BEAM AND NORMAL INCIDENT PLANE WAVE

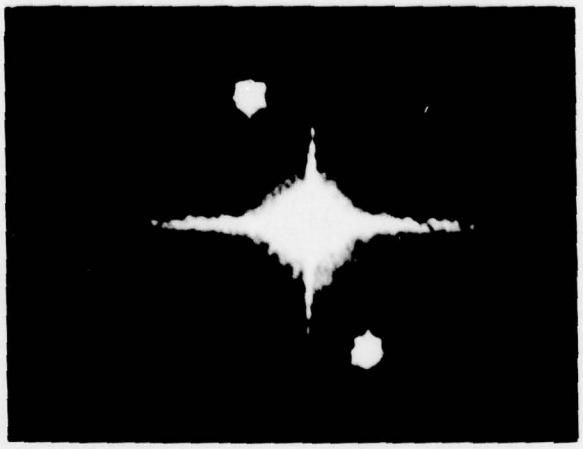

FIG. 6 FOURIER SPECTRUM OF RECTANGULAR APERTURE CONTAINING A HOLOGRAM CONSTRUCTED USING A REFERENCE BEAM AS IN FIG. 5 (c)

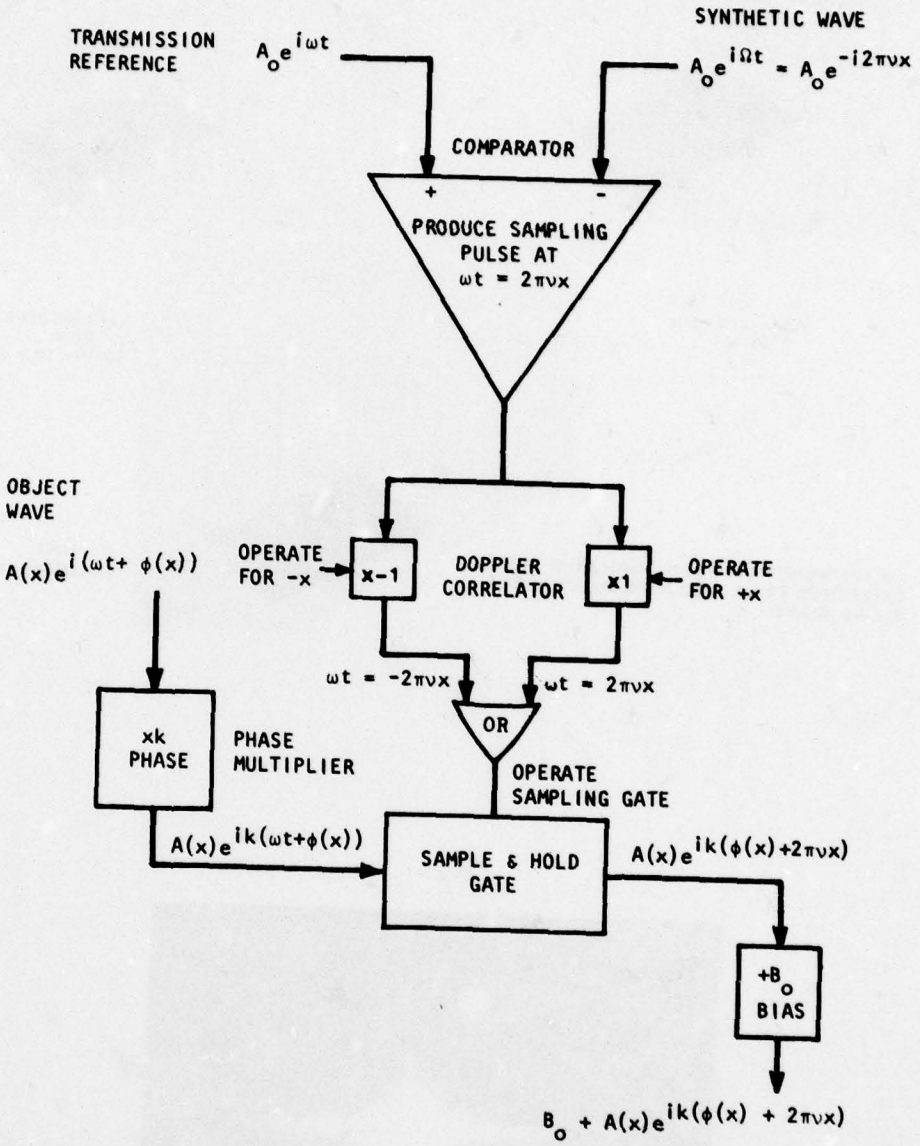

FIG. 7 SCHEMATIC DIAGRAM OF SYNTHETIC REFERENCE "PHASORAL" SAMPLING SYSTEM FOR THE HOLOGRAPHIC WAVE ENCODER

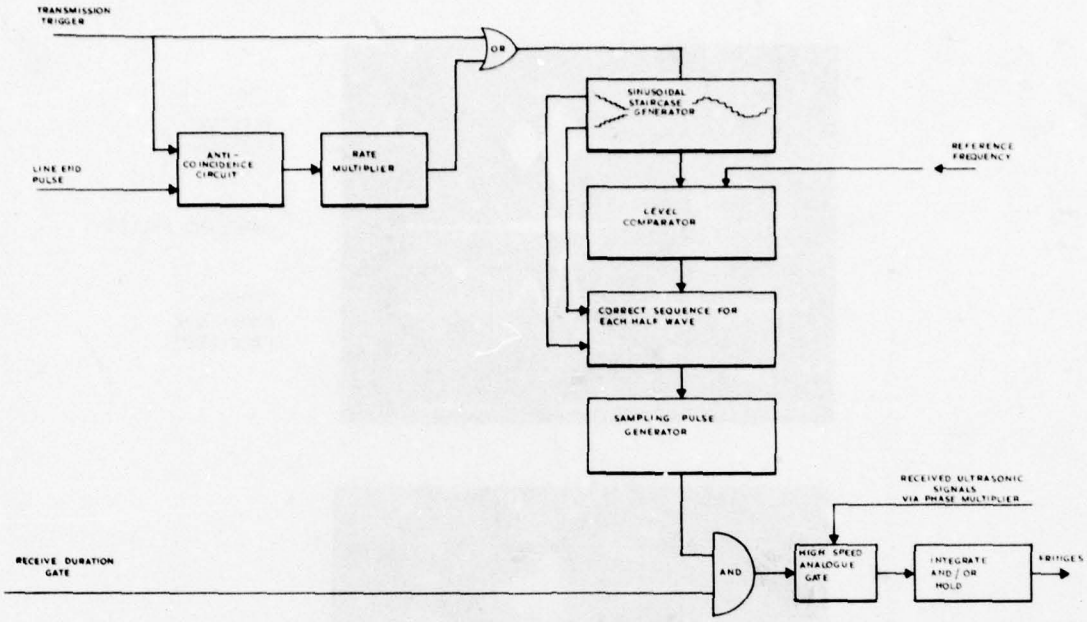

FIG. 8 HOLOGRAPHIC ULTRASONIC WAVE ENCODER (CIRCUIT SCHEMATIC)

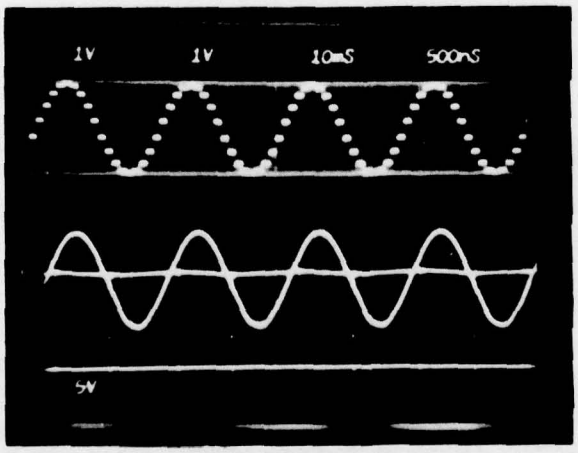

FIG. 9 SAMPLING PULSES (BOTTOM TRACE) GENERATED WHEN THE REFERENCE WAVE IS COMPARED WITH A VOLTAGE LEVEL. THE SINUSOIDAL SET OF VOLTAGE LEVELS IS SHOWN CYCLING ON THE LONGER TIME SCALE (TOP TRACE).

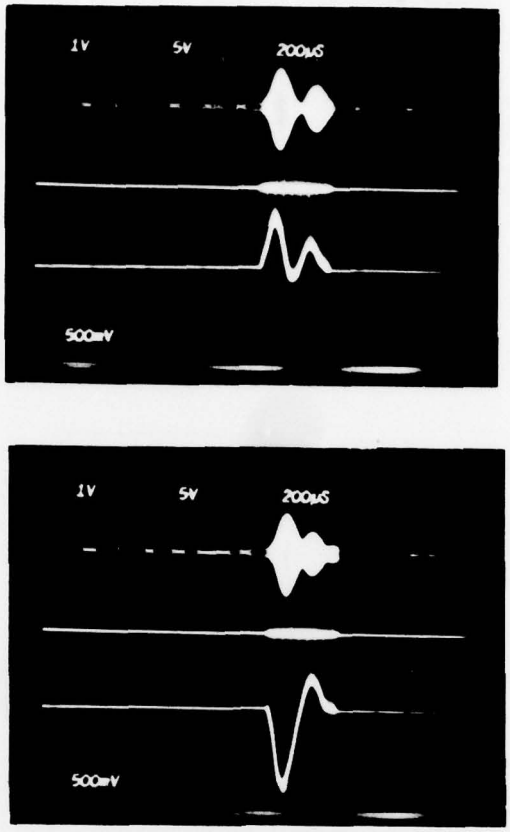

FIG. 10 RECEIVED SIGNALS, SAMPLING PULSES AND ASSOCIATED PHASE-AMPLITUDE PROFILES WITH THE TWO SELECTED SIGNALS (a) IN PHASE, AND (b) OUT OF PHASE WITH EACH OTHER

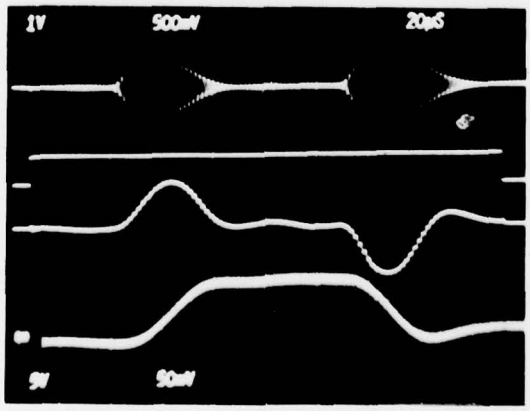

FIG. 11 ILLUSTRATION OF THE FUNCTION OF THE BIPOLAR INTEGRATOR FOR THE ADDITION OF THE PHASES AND AMPLITUDES OF TWO ULTRASONIC SIGNALS WHICH ARE OF SIMILAR AMPLITUDE BUT OUT OF PHASE WITH EACH OTHER

(a) RADIOGRAPH (b) ULTRASONIC "C-SCAN" (c) ULTRASONIC IMAGE BY HOLOGRAPHY

FIG. 12 COMPARISON OF DIFFERENT METHODS OF VIEWING THE INTERIOR OF AN OPTICALLY OPAQUE OBJECT. THE IMAGES SHOW BUBBLES AND A CRACK OF SQUARE OUTLINE INSIDE A 0.4 METRE THICK SLAB OF POLYTHENE

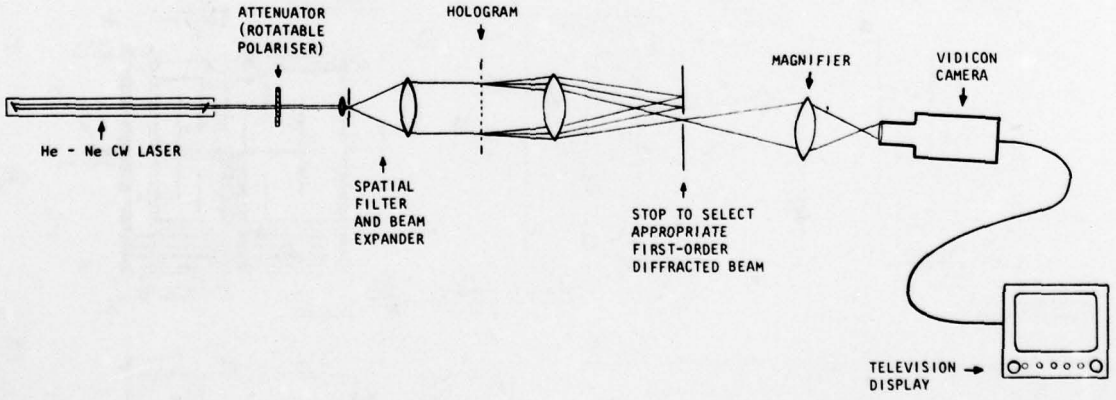

FIG. 13 OPTICAL SYSTEM USED TO VIEW RECONSTRUCTED WAVEFRONTS DIFFRACTED FROM THE HOLOGRAMS

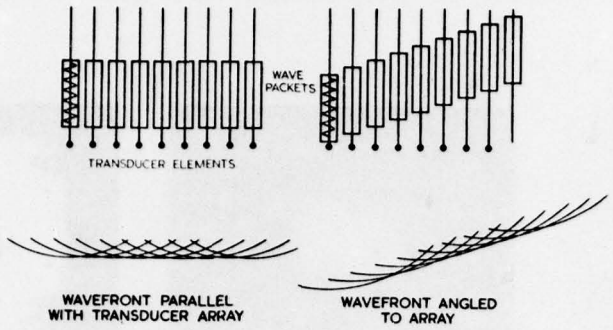

FIG.14 FRESNEL COMPOSITION OF LINEAR WAVEFRONTS

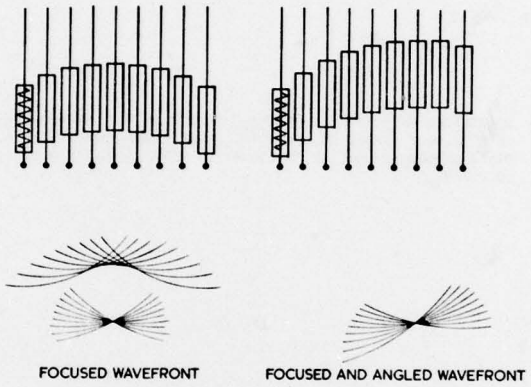

FIG.15 FRESNEL COMPOSITION OF FOCUSED WAVEFRONTS

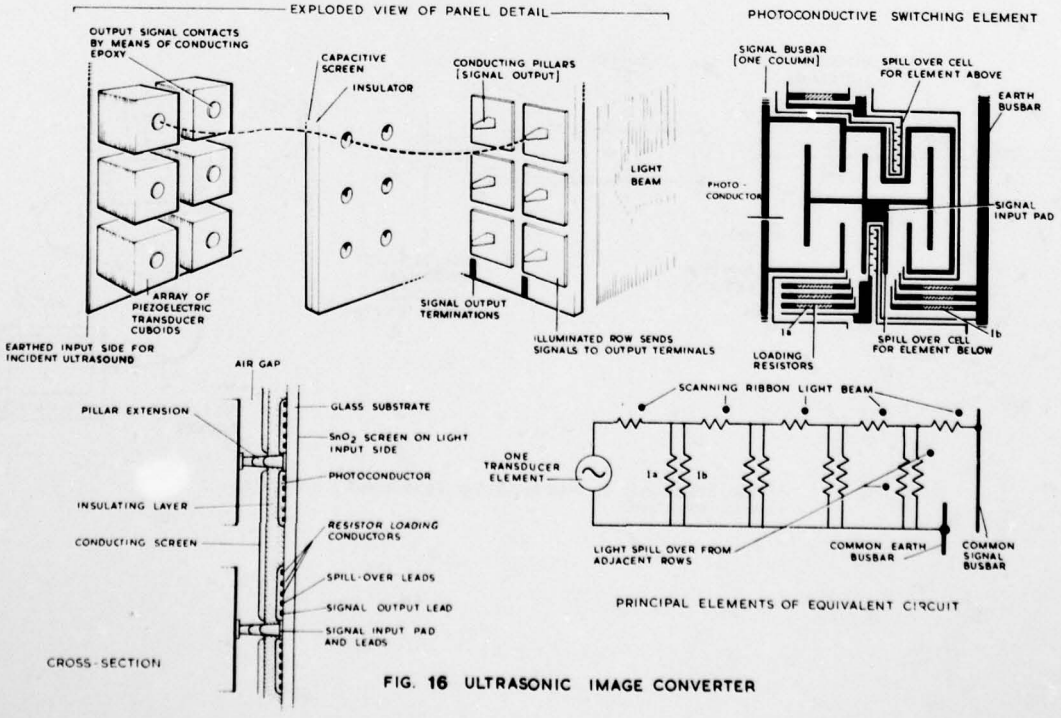

FIG. 16 ULTRASONIC IMAGE CONVERTER

DISCUSSION

R.L.Derr, Naval Weapons Centre, US

Using the ultrasonic imaging or holographic technique, what size of defect can be detected? What are the critical parameters that control resolution?

Author's Reply

The resolution depends upon the wavelength of ultrasound used, the effective size of transducer and area of the aperture. As a guide if one takes a motor of 500 mm diameter, then a frequency of 500 KHz can be used and a defect of 10 mm diameter can be readily detected.

A GENERALIZED SOLID MOTOR DEVELOPMENT TEST APPROACH WITH APPLICATION TO IUS

by

Ernst Stampfl
The Aerospace Corporation
P.O. Box 92957
Los Angeles, California
90009
U.S.A.

D. H. May, Major USAF
Space and Missile Systems Organization
P.O. Box 92960, Worldway Postal Center
Los Angeles, California
90009
U.S.A.

ABSTRACT

The generalized approach for solid motor development and qualification testing presented here relies on subjecting motor components and full-scale units to aggravated load conditions. Compared to conventional motor test methods, this approach offers improved schedules and more efficient utilization of program resources.

For a given technology level, development program costs and schedules are primarily dependent on the number of test units. Aggravated critical loads on a smaller number of motors and appropriate components can demonstrate equal or higher confidence in the operational design when compared with conventional methods employing nominal loads and large sample sizes.

The rationale leading from actual motor life-cycle requirements to development and qualification test requirements is presented. Aggravated load test conditions and their derivation from system requirements using state-of-the-art ballistic, thermochemical, and structural analysis techniques are discussed.

The application of the development test approach to the Inertial Upper Stage (IUS) program is described. IUS life cycle requirements and test conditions, which are in accordance with U.S. Air Force Directives, are discussed.

NOMENCLATURE

D	damage ratio	μ	distribution mean
I	motor total impulse, lb sec	ϵ	local induced strain, in/in
KSI	thousands of pounds per square inch	σ	distribution standard deviation
P	chamber pressure, lb/in^2	Subscripts	
R	reliability	A	allowable
T	temperature, °F	DF	design failure envelope
V	case volume, in^3	F	actual failure envelope
W	component weight, lb	OT	overtest envelope
X	grain response and failure properties	OTF	failure envelope deduced from overtests
Z	standardized normal variate	S	service envelope
a_T	time-temperature shift factor	SF	stress free
m	number of successful overtests	ST	storage
t	storage time, minutes		

INTRODUCTION

The major aspects of the Inertial Upper Stage (IUS) Solid Motor Propulsion Test Program are described, including the background and rationale leading to the baseline test approach that relies on overtesting. To establish the background for the test approach presented, a general description of IUS and its solid motors is given along with a delineation of system, motor, component, and material requirements.

An overall perspective of the various test phases and their integration with each other and with the design requirements is given. Objectives, test approaches, and a summary of available results of the various test phases are discussed, including their correlation with requirements.

INERTIAL UPPER STAGE

IUS DESCRIPTION AND REQUIREMENTS

The IUS is a two- or three-stage expendable solid motor vehicle designed to perform earth orbiting and planetary missions after deployment from either the Space Shuttle or an expendable launch vehicle (Figure 1). A large and a small solid motor with varying propellant loads and nozzle configurations are used as building blocks to configure various mission-unique vehicles to deliver, over a wide payload range, the necessary spectrum of energy requirements. The IUS can be used in a three-axis or spin-stabilized mode. Thrust vector control is provided by moveable motor nozzles; vernier velocity

corrections, roll control, and spinup are accomplished by a separate liquid monopropellant reaction control system.

The IUS is being designed to include a set of missions that includes existing as well as planned and projected payloads. The IUS design-driving missions are the 5000 lb geosynchronous and the outer planet missions. The IUS is required to be compatible with a 40-ft-long payload within the 60-ft-long Space Shuttle cargo bay and was designed to perform tandem Orbiter missions with payload lengths of 15 ft each within the Orbiter payload capability of 65,000 lb. The maximum allowable IUS steady-state free-flight acceleration for small payloads is 5 g; this is equal to the maximum acceleration incurred during Orbiter ascent. The IUS must withstand ascent loads of 6 g steady-state acceleration, and 1.1 g (rms) vibration when combined with thermal loads corresponding to temperatures between 43°F and 82°F and preceded by 5-year storage and handling loads. The overall IUS mission reliability is required to be 0.96 or greater. Payload and Orbiter contamination due to IUS operation is to be minimized.

The stage and motor designs which meet the foregoing system requirements were established in the IUS definition phase through a multiple variable optimization procedure subject to various system, program, and technology constraints. The solid motor test requirements were derived primarily from the IUS environmental, performance, and reliability requirements.

IUS SOLID MOTOR DESCRIPTION AND REQUIREMENTS

The principal IUS solid motor design features are short length, high mass fraction, high nozzle expansion ratio, long burning time, low thrust, and high total impulse flexibility (Figure 2). The designs incorporate current state-of-the-art design concepts and materials. The fully loaded large and small solid motors contain 21,400 lb and 6,000 lb of propellant, respectively. Both can be offloaded between 0 and 50 percent to comply with specific mission requirements within 60 days of the launch date. The nozzle expansion ratio for the large and small motor can be preselected between 28 and 59, and at 47 and 173, respectively. The large-motor expansion ratio variation is accomplished by truncating the long contoured nozzle. The small-motor expansion ratio variation is accomplished by the removal or adoption of a two-segment extendible carbon/carbon exit cone kit. Additional motor parameters are given in Table 1 (Ref. 1). The overall motor length for the large motor varies between 101 and 131 inches; the small motor is 76 inches long. The short motor lengths were achieved by incorporating low length-to-diameter cases (L/D = 0.86 and 0.78 for the large and small motor, respectively) and by submerging the high initial expansion angle nozzles to 18 and 16 percent of their total case lengths, respectively.

High performance materials were used to attain high motor mass fractions. The case, including skirts, is made of a high effective fiber strength (3.2×10^5 psi) Kevlar composite incorporating a rigid resin system. The nozzle consists of an integral three-dimensional carbon/carbon throat section and a two-dimensional carbon/carbon rosette exit cone. The insulation is a low-density, silica-loaded, ethylene propylene dimethyl monomer (EPDM) rubber. The propellant is a hydroxyl terminated polybutadiene (HTPB) formulation with 86 percent solids and a low burning rate (0.28 in/sec at 1000 psi). The propellant is common to both motors. The grains have large web thicknesses to provide the long burning times of 140 sec for the large motor and 96 sec for the small motor. To facilitate propellant offload flexibility, the grains have a simple tubular port which is machined to achieve the desired propellant weight. The corresponding pressure-time traces for both motors are progressive-regressive with a maximum expected operating pressure (MEOP) of 980 psi (Figure 3).

Aside from the noted nominal performance requirements, it is necessary that the total impulse uncertainty not exceed 0.7 percent of the nominal value over the required operating and qualification conditions. The motors must successfully perform with a reliability of 0.995 after exposure to complete life cycle loads which include; (a) manufacture; (b) 2,600 miles of overland transportation and handling; (c) long-term storage between 43° and 82°F; (d) short-term storage between 23° and 102°F; (e) ascent acceleration, vibration and shock; (f) exposure to space environment up to seven days in the Space Shuttle bay and 10 hr in free flight, and (g) fire in vacuum.

TEST PROGRAM

OVERVIEW

The overall IUS solid motor test program includes five test phases, each supporting a unique program milestone. The first, or definition, phase supported the IUS motor sizing and optimization; this was followed by the second, or validation, phase to support the preliminary design. Phase three, the development phase, currently under way, supports the final design. The motor qualification and operational phases will follow upon successful completion of the development phase.

Definition phase testing consisted of limited laboratory and subscale tests, the results of which, when augmented by related industry data, were used to establish the appropriate sensitivities and constraints in the motor sizing optimization. In addition, these early data were used to evaluate and rank the technical risk associated with various motor components and design features, and to plan subsequent risk reduction efforts.

The tests in support of the preliminary design, conducted during the validation phase, consisted of prototype case and nozzle tests and a prototype full-scale motor test.

During the development phase, the test program will consist of the final characterization of all materials, the testing of five large and eight small full-scale motors, including two small-motor spin firings, case burst tests, and nozzle overtests. One motor of each size will be subjected to overtest conditions. The overall objectives of this phase are to develop and demonstrate the final motor design and corresponding manufacturing approaches that will meet the motor qualification and subsequent operational requirements with high reliability.

The qualification test program will consist of six large-motor and seven small-motor tests, including one spin firing test. The qualification test articles will meet flight unit configuration and quality in all respects. Two motors of each size will be subjected to overtest loads. The overall objectives of the qualification test program are: (a) to demonstrate that nominal performance requirements are met; and (b) to show that the corresponding observed random variations are consistent with dispersed operational performance requirements. The qualification test program results must, in addition, allow the deduction of whether or not allocated reliabilities will be met.

The tests that are part of the operational phase consist of flight motor acceptance and flight readiness tests. The objectives of the operational tests are to ensure that: (a) at the time of delivery, acceptable units become part of the IUS motor inventory, and (b) at the time of launch, the units are flightworthy.

Because of the large potential payoff in cost and schedule through a reduced sample size, overtesting at the component and motor level is planned for the IUS. From the point of view of establishing motor performance, such a sample size reduction is tolerable. A general outline of the overtest approach to be implemented is as follows.

OVERTEST APPROACH

Overtests of various types are used in many fields to attain confidence in particular service units. Two generic overtest approaches, one which attempts to define the failure envelope and one which attempts to extend the non-failure envelope, are common. For IUS, the latter approach was chosen for the nozzle and motor overtests. This selection was made primarily because of the limitation of attribute testing, the large theoretical design margins (i.e., the failure envelope is significantly removed from the service envelope), and because of the large number and complexity of nozzle and solid motor failure modes. In such complex situations, it is necessary to pay special attention that, by aggravating in-service conditions, no new critical failure modes are introduced which are not pertinent to in-service application. By keeping overtest conditions to a minimum (i.e., restricting them to perturbations of the service loads), the risk of introducing irrelevant failure modes and the risk of accepting a false overtest hypothesis is minimized. For the motor case, since among other reasons it lends itself to variate testing, the failure envelope will be defined through conventional burst tests. A second criterion against which overtests must be evaluated is the condition that, by increasing test parameters, the probability of failure at least in the most critical failure mode is increased. Considering the above, it is apparent that a prerequisite for a good overtest is a good analysis.

The advantage of overtesting, when compared to conventional service level tests, is an increase in confidence in the allocated reliability at service life loads and an improvement of insight in the functioning of the unit itself at a reduced sample size and test period. The degree of this improvement is directly related to the number and degree of the overtests. Even though the selection of the overtest sample size and conditions is subjective, solid motor overtesting can yield significant schedule and cost payoffs. The specific overtest sample size, overtest conditions, and, therefore, in an indirect manner, the desired overtest payoff, are selected through statistical inferences considering the risk of false acceptance of a specific design and the risk of overtest failure. To accomplish the overtest selection for the simplest example, several assumptions are necessary. First, it is prudent to assume that all parameters pertinent to overtest response and failure are normally distributed. Based on historic data this assumption is not unreasonable for the principal parameters of concern. Second, it is assumed that the variances of the pertinent response and failure properties are given by the corresponding variances of appropriate subscale test devices. This assumption is reasonable since it has been demonstrated that the response and failure variances of special test specimens and subscale devices under the same failure modes are similar. Third, it is assumed that, in establishing an overtest, the uncertainties in analysis for simple loads with given material properties for the specific unit can be treated as a bias; for combined loads a weighted root mean square value is assumed to be appropriate. Fourth, it is necessary to assume that, because of the design factor of safety, a significant separation between service and actual failure envelopes exists. Finally it is assumed that one failure mode and criterion is dominant.

Under the foregoing conditions it is possible to estimate the expected reliability of service units, given a number of successful overtests. The lower bound of the probability of no failure indicated by m successful overtests, at overtest conditions, is (Ref. 2)

$$R = 1 - \frac{1}{m + 1} \tag{1}$$

Given this estimated reliability value, the standard deviation of the selected failure property, and the distribution function of the corresponding overtest response, the mean of the failure envelope that can be deduced from the overtests is estimated from the normal variate Z (Ref. 3).

$$Z = - \frac{\mu_{OTF} - 1.05\,\mu_{OT}}{\sqrt{\sigma^2_{OTF} + \sigma^2_{OT}}} \tag{2}$$

where the factor 1.05 accounts for the uncertainty in the response analysis. With the so determined failure envelope and the given service load envelope, the reliability for service units can be deduced as indicated by Eq. (2). The confidence in the deduced reliability can be improved by introducing statistics for small sample sizes, multiple failure modes, and improved estimates of the variances. The computational technique is illustrated in Figure 4. The estimated failure envelope, as deduced from three successful overtests and the given service load envelope of the example, yields a service unit reliability of 0.994. To demonstrate this value of reliability with tests at the

AD-A076 012 ADVISORY GROUP FOR AEROSPACE RESEARCH AND DEVELOPMENT--ETC F/G 21/8.2
SOLID ROCKET MOTOR TECHNOLOGY.(U)
JUL 79
UNCLASSIFIED AGARD-CP-259 NL

6 OF 6
AD
A076012

END
DATE
FILMED
12-79
DDC

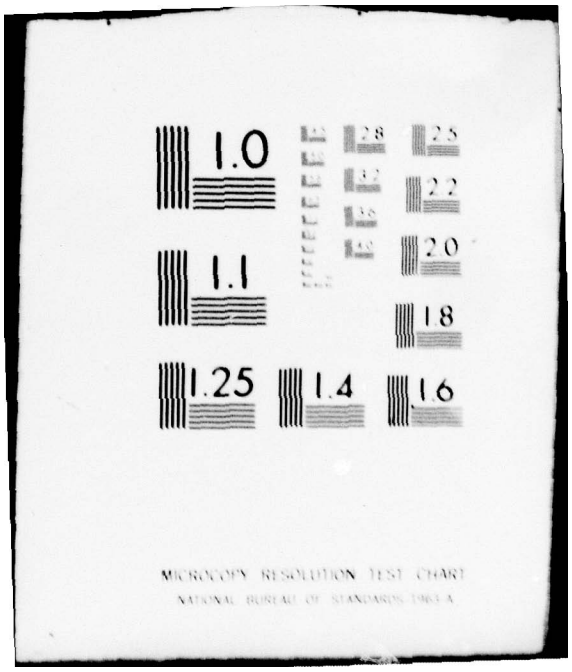
1.0
1.1
1.25
1.4
1.6
2.8
2.5
3.2
2.2
3.6
2.0
4.0
1.8
MICROCOPY RESOLUTION TEST CHART
NATIONAL BUREAU OF STANDARDS 1963-A

service stress level, 165 successful tests would be required. The potential therefore exists that three 18 percent overtests yield as much information as 165 nominal tests, significantly impacting cost and schedule. Although the indicated calculation can be refined by introducing small-number statistics, confidence levels, etc., which will reduce the indicated payoff, it is apparent that overtesting has a high potential solid-motor development payoff. It should be noted that the failure criterion can consist of a single variable, as in the above example, or of a multivariate, as in cumulative-damage theory.

DEFINITION PHASE TESTING

The test results of this IUS test phase, when combined with related industry data and experience at the same technology level, were used to establish sensitivities and constraints for use in sizing the IUS solid motors. The related industry data which played a significant role in establishing the IUS motor design point were obtained from advanced development programs funded by the Air Force Rocket Propulsion and Materials Laboratories.

To support nozzle sizing and performance, an abbreviated thermochemical characterization of two- and three-dimensional carbon/carbon materials was performed (Ref. 4). Samples of candidate carbon/carbon materials were subjected to plasma-arc-heated reactive gases (H_2, CO_2, H_2O, etc.) representative of propellant combustion products. From the measured specimen mass loss rate, surface temperature, and local plasma arc gas conditions, the necessary thermochemical parameters were obtained to allow computation of local carbon/carbon recession rate and in-depth heat conduction sensitivity to full-scale motor chamber pressure, burning time, and local aerothermal conditions used in motor sizing. Because of the expected long motor burning times, the lack of experience with nozzles having long burning times, and the relatively poor agreement between available nozzle erosion data and the predicted recession using the above indicated thermochemical data, the IUS nozzles were classified as the motor component having the highest technical risk. Mechanical properties used in the nozzle sizing effort were limited to nozzle substructure materials that were readily available. A nozzle weight efficiency goal of $I/W = 3.5 \times 10^4$ sec was established.

The motor-case sizing constraints and performance were established using Kevlar flat laminate and subscale pressure vessel data. Flat laminate test results primarily supplied Kevlar composite response properties; the 6-in. and 18-in. pressure vessels yielded Kevlar composite failure properties. The flat laminate and the 6-in. vessel specimens were standard American Society for Testing Materials (ASTM) specimens, while the 18-in. vessels exhibited anticipated full-scale case design features. Skirt failure properties were obtained from related program data. The data from the indicated tests, data from related programs, and data for conventional materials served to establish the necessary sensitivities and constraints. A case weight efficiency goal of $PV/W = 1.3 \times 10^6$ in. was established.

The propellant testing necessary to establish the required motor sizing parameters included determination of specific impulse, internal ballistics, and propellant and bond mechanical properties. The propellant specific impulse of the selected formulation was determined by firing standard Bates motors having a 2-in. throat and 20 lb of propellant. The result included propellant vacuum specific impulse at three expansion ratios. The necessary ballistic data were obtained by testing 4-lb ballistic test motors over the necessary pressure and temperature ranges. Finally, an abbreviated propellant and bond mechanical properties characterization was performed using standard Joint Army-Navy-NASA-Air Force (JANNAF) propellant and bond specimens. Typical mechanical property data used to establish grain, case, and nozzle design constraints are shown in Table 2.

VALIDATION PHASE TESTING

The testing during an 18-month validation phase was conducted to support the preliminary motor design. Tests were limited to (a) material tests necessary to support design analysis and (b) to prototype component and full-scale motor tests which were identified as requiring a reduction in technical risk before committing to full-scale development.

The material testing to support design analysis included a complete characterization of the propellant and abbreviated characterizations of case Kevlar composite, nozzle carbon/carbon, and insulation materials. The test specimens and the test data analysis generally reflected industry standards; test conditions spanned IUS requirements.

The propellant characterization included ballistic, performance, combustion stability, and thermal and mechanical properties testing. The ballistic tests consisted of 4-lb-burning-rate motor tests under spinning and non-spinning conditions. Liquid and solid-strand burning rate tests supplemented the ballistic motor tests. The performance tests included window bomb tests to determine aluminum aglomeration and Bates motor tests to determine vacuum specific impulse.

Standard T-burner and rotating valve tests were conducted from which the propellant combustion response function was derived. The thermal properties included specific heat, conductivity, and autoignition temperature. Propellant and bond failure properties under uniaxial, biaxial, and triaxial conditions were established over broad spectrum constant rate, constant load, and constant strain values. Through the use of the time-temperature shift criterion, failure properties over about ten decades in strain rate and time to failure were obtained. The response properties included broad-spectrum relaxation modulus, the coefficient of thermal expansion, and Poisson's ratio. The age-sensitivity of both failure and response properties was determined under accelerated and natural aging conditioning.

The abbreviated Kevlar composite and two- and three-dimensional carbon/carbon material characterization consisted of pertinent failure and response properties at ambient and elevated temperatures.

The characterization of insulation, in addition to parent material mechanical properties, also included insulation-to-case bond properties, thermal, and erosion properties. Insulation erosion data were obtained by subscale motor tests using the IUS propellant.

The prototype component and full-scale motor tests aimed at reducing the highest IUS propulsion development risks included four prototype full-scale sea level nozzle tests, burst test of one heavy-weight case, and the test of one full-scale prototype motor at vacuum.

The full-scale nozzle component test program consisted of two material evaluation tests and two nozzle design demonstration tests. The throat materials evaluated included pyrolytic graphite washers, high-density fine-weave carbon fiber carbon/carbon from two suppliers, and coarse-weave graphite fiber carbon/carbon. The exit cone material was a two-dimensional rosette lay-up carbon/carbon. The first two nozzle tests with primarily material evaluation objectives were conducted for about 50 percent of the required burning time. The next two tests were full-duration nozzle design demonstration tests which incorporated all critical aspects of the nozzle substructure. The overall results showed that the low-cost carbon fiber in a coarse weave meets IUS requirements.

The full-scale prototype motor and supporting case burst tests were conducted to demonstrate full-scale motor performance and ballistics, as well as case-grain and fixed nozzle-motor interactions. The results indicated good material, performance, and ballistic responses (Ref. 5). The case-grain and nozzle-motor interactions observed were acceptable but not predicted: the case growth in the dome shoulder region was less than predicted, and the nozzle nose erosion was greater than predicted. The principal test results are summarized in Table 3.

DEVELOPMENT PHASE TESTING

The testing of this phase is under way and is intended to support the final designs of the large and the small motor. The rationale leading to the overall development program was subject to several objectives and corresponding ground rules, the most pertinent of which are as follows.

The principal objective of the development program is to bring the motor designs to a level of maturity such that proceeding with the qualification program is low risk; this is to be accomplished at minimum cost. Aside from catastrophic failures or major design deficiencies, development cost is primarily dependent on the number of development test units; for this reason, the number of motor tests was kept to a minimum. However, in order to achieve development test and overall program objectives at an acceptable confidence, the overtest philosophy outlined earlier was adopted.

In the development motor test sequence, the early tests incorporate simple and milder loads, while the later tests involve combined and more severe loads. The stepwise approach is expected to allow more confident diagnosis and correction of design weaknesses.

Given the successful prototype nozzle and motor tests of the previous phase and the need to support the motor tests of this phase, early testing is concentrated on the motor case. A full Kevlar composite material characterization and subscale case test program preceded full-scale case proof, burst, and skirt tests. The proof and burst test apparatus allows for controlled hydraulic pressurization and thrust simulation. The instrumentation includes strain, deflection, acoustic emission measurements, and high-speed film coverage. The required proof and burst test factors are 1.05 and 1.25, respectively.

The case burst tests are, in effect, overtests which define the case failure envelope for pressure loads. The 1.25 safety factor is such that the probability of the operational motor chamber pressure exceeding the burst pressure is negligible. Case failure modes due to case-grain interaction during manufacture and operation are addressed at the motor level and not at the component level. The proof pressure tests, which on the small motor consist of two cycles to allow appropriate nozzle alignment, serve as case acceptance tests.

The skirt test apparatus allows for simultaneous application of axial, shear, and moment section loads. The level of instrumentation is comparable to that for the pressure tests. A total of three development burst tests and two skirt tests are planned for each motor.

Nozzle component tests are also planned for the full-scale development phase. The tests are planned as nozzle overtests, one each for the large and small motor to be conducted after about the second full-scale motor test. The nozzle component overtests are not tests to failure as in the case of motor cases, but are component margin limit tests which are intended to show that the non-failure envelope extends beyond the service envelope. Nozzle component overtests have, for various reasons, not been routinely performed in the past. However, the tests are warranted because the nozzle technical risk is significant and because, in the past, most solid motor failures in qualification and flight have resulted from nozzle failures.

The planned nozzle overtest approach specifically addresses thermal-load-induced structural failure modes early in the test, and failure modes late in the firing resulting primarily from combined thermal and pressure loads when material properties have degraded. The overtest conditions will be established from time-dependent finite element stress and strain responses and corresponding failure criteria using response and failure properties for the actual materials. The two specifically considered failure modes are the thermal-stress-induced cracking of the three-dimensional carbon/carbon material early in the firing, and the mechanical-stress-induced cracking near the two- and three-dimensional carbon/carbon interface late in the firing. The indicated overstress conditions will be generated by testing the nozzle in a test vehicle with IUS propellant that will generate a pressure time trace similar to that shown in Figure 5. The nozzle flow field will be simulated by retaining internal geometric similarity; vectoring conditions will be simulated by a constant cant angle. The projected best-estimate percent of overtest (i.e., the fraction of overtest load increase over the nominal service load) for the early throat insert failure mode is 20 percent and for the later interface failure mode is 25 percent. The potential payoff for IUS of one successful overtest is estimated to be equal to four nozzle tests at service conditions. Although only two failure modes are specifically considered, most other nozzle failure modes (including thermochemical modes) are also aggravated and will be evaluated. The extent to which confidence in

the nozzle design and nozzle reliability was improved can be determined by inspection of post-test hardware and comparison of actual temperature and strain measurements obtained from overtest and full-scale motor test data.

The full-scale motor development test program consists of a total of five large and eight small motor tests. Except for establishing motor spin capability on the small motor, the test sequence for both the large and small motor test programs is similar.

Conditions which specifically played a part in scheduling the full-scale development motor firings included use of heavyweight motor cases and insulation on early firings to reduce case-grain interaction and to account for potential ballistic, case, and insulation anomalies. The nozzle vectoring duty cycle was zero for the first test, was limited to one plane for the second test, and will be a full duty cycle for subsequent tests. This test sequence allows for a more confident determination of insulation and nozzle material performance and allows for better overall analytical tractability. The early development motors will be exposed to limited environmental loads; only the final development motor will be exposed to a full qualification test loads cycle including overtest conditions.

The specific development test order, conditions, objectives, and data are summarized in Table 4. The background and rationale which lead to the specific overtest test requirements were derived from qualification requirements and are discussed in the following section. All full-scale motor firing tests will be conducted in a test cell near vacuum. All test requirements except for the prolonged motor cold-soak and nozzle exit cone cold-soak are within the routine testing capability of the Arnold Engineering and Development Center (AEDC) (Ref. 6). Except for plume breakoff flow sampling, the instrumentation is standard consisting of temperature, high and low frequency pressure, strain, acceleration, and multicomponent thrust transducers. The exhaust will be sampled by special collectors to determine the plume contamination potential in flight.

QUALIFICATION PHASE TESTING

The motor qualification phase will consist of tests of six large and seven small motors. The test motors will in every way be configured, manufactured, and controlled like flight motors. All flight motor acceptance tests will be performed on qualification test units. The qualification test sequence is inverse to that of the development phase: motors with the most severe load life cycle are tested first; those with less aggressive conditions are tested last.

The principal qualification program performance objectives are to show that the delivered mean motor performance meets IUS requirements at the required confidence level and that the demonstrated variation is consistent with the design dispersion. From a reliability point of view, the qualification program is intended to show that flight motors will perform within the allocated reliability when subjected to service requirements which are less severe than qualification requirements.

The overtest conditions of particular interest are: the static testing of motors 20°F higher and lower than the operational temperatures; the prolonged storage at the upper and lower qualification temperature limits; the vibration at two times the flight vibration requirement; and, the transportation loads. Although the 20°F qualification temperature margin and the prolonged hot and cold soak times apply primarily to grain integrity, the nozzle and case simultaneously incur overtest loads. The vibration and transportation loads apply to all motor components.

The 20°F qualification test temperature margin first allows for errors in the predicted flight motor bulk temperature as required by Government guidelines (Ref. 7) but, just as important, it introduces overtest conditions. Grain integrity is the principally affected component. Grain integrity or reliability is typically determined by cumulative damage approaches, with the damage at failure taken as 100 percent (Refs. 8, 9). The overtesting for IUS is established and evaluated by the application of the linear strain-rate-dependent cumulative damage (i.e., the propellant and/or bond damage due to simultaneous and/or sequential loads at various strain rates are additive). The IUS grain geometry, propellant response properties, and propellant and bond failure properties are such that the motor is bond-stress-critical and the thermal and firing damages are monotonically increasing functions with decreasing temperature between 70° and 20°F. Motor tests at 23°F are therefore appropriate conditions for grain overtests of the most critical failure modes. For the tests at the upper temperature regime, analogous arguments apply but at a different location of the failure envelope. Best-estimate grain structural margin differences of motors tested at 23°F and 43°F show that the cold test reflects about a 5 percent overtest for otherwise identical conditions. Considering typical response and failure properties variations of about 10 percent coefficient of variation, this is not particularly significant.

A significant increase in the percent of overtest is achieved by subjecting the motor first to chemical aging through a prolonged hot soak period and then to mechanical aging by a prolonged cold soak period just before firing. The additional overtest conditions are achieved as a result of an upward shift in the stress-free temperature, a degradation in propellant properties, and an increased mechanical damage due to the prolonged storage at the low temperature. The upper temperature soak conditions, which include an eight-day exposure to humidity, were chosen as 120°F for five weeks plus heat-up and cool-down. The temperature was selected since it was shown that, up to this temperature, no significant new post-cure reactions are incurred when compared with those at ambient temperature. The time was selected based on the Arhenius reaction rate relation such that the test time would correspond to either overtest conditions of a new motor or to a near-nominal motor two years of age.

Similarly, the low temperature soak conditions of six weeks at 23°F were selected to reflect overtest conditions of a new motor or likely operational mechanical damage resulting from two years of storage. The specific overtest conditions were established by summing the damages for various loading conditions in the form of damage ratios, D,

$$D = \sum_{i=1}^{m} \Delta X_i / X_{iA} \qquad (3)$$

where i refers to a specific load condition over which the strain rate and temperature may be taken as constant. The appropriate response and failure properties needed to compute D are obtained from the aged propellant and bond data at the appropriate reduced strain rate, which for the cold soak condition is given by

$$da_T = \frac{\epsilon}{t\Delta T} \int_{T_{ST}}^{T_{SF}} a_T dT \qquad (4)$$

where t is the cold storage time, ϵ the induced strain, and a_T the time-temperature (WLF) shift factor. To attain the maximum damage, no temperature recovery will be allowed between the cold soak and the firing test. The percent of overtest condition induced when the motor is fired after exposure to the indicated hot and cold conditions is about 20 percent. The potential payoff for IUS of three successful overtests is estimated to be equal to ten successful tests at service level conditions. When other life cycle loads such as vibration, handling, and transportation are introduced between the hot- and cold-soak periods, additional overtest conditions are induced and can be accounted for in terms of permanent damage. Thermal cycling is not emphasized in the IUS test program; only one motor will be thermal cycled. Thermal cycling is: (a) not a significant load cycle of the total IUS life cycle; and (b) a meaningful number of thermal cycles are not consistent with the development schedule. As indicated earlier, the qualification motor test sequence was scheduled in the reverse sense when compared with the development program in that the motors with the most aggressive loads will be tested first and those with the less demanding environments will be tested last. With this schedule, the cost impact of a qualification failure and the probability of successfully completing qualification with detrimental motor design weaknesses is minimized. The two overtests of each motor are scheduled to be performed first, followed by the rest of the motors covering the remaining operational loads regime.

Although all full-scale motor tests are considered in projecting final flight motor performance, the qualification tests are the principal data base for motor performance. The primary performance objectives of the development and qualification testing are to establish, with high confidence, the mean total and specific impulse values for each motor and to show that their variations are consistent with the imposed requirement. The mean impulse values will be established as a function of the following motor parameters: propellant load, nozzle expansion ratio, propellant grain temperature, and throat diameter. A regression analysis similar to that described in Ref. 10 will be used to establish the necessary correlations and to show that the variances in the impulse values are consistent with requirements.

In addition to the full-scale motor tests, the qualification phase also includes laboratory acceptance tests for all major motor components. All cases are proof-tested to 1.05 MEOP for acceptance; in addition, a small witness bottle is burst for each delivered case. The propellant is subjected to ballistic and mechanical properties acceptance tests which cover various critical conditions to ascertain that specific batches meet requirements. The loaded motor is x-rayed and evaluated against ballistic and structural defect acceptance criteria. The acceptance tests for nozzle components will include three- and two-dimensional carbon/carbon tag end testing. The final motor assembly is leak-tested, and the moveable nozzle is actuated.

OPERATIONAL PHASE TESTING

Acceptance and preflight assurance tests are planned for the operational phase of the IUS program. Acceptance tests are planned at the material level, at the component level, and at the final assembly level. Preflight assurance tests are planned for the propellant, case, and for the final motor assembly.

The acceptance testing performed for flight units will be the same as that conducted for qualification units, with the data evaluated against the same accept/reject criteria.

The preflight assurance tests are limited to case, propellant and case-insulation-liner-propellant bond. Just prior to buildup of the stage small pressure vessels, bulk propellant, and bond materials are tested at conditions identical to those of the acceptance tests. The data are evaluated against criteria developed during the propellant characterization program conducted in the development phase and against design requirements.

SUMMARY

A five-phase solid motor test approach from definition to operational phase testing is presented. The various phases described support concept definition, preliminary design, final design, qualification, and flight readiness. IUS requirements and program milestones are discussed in relation to the indicated test approach.

A general overtest approach applicable to solid motor components and complete motors is outlined. Overtests of motor cases to failure serve to define the case failure envelope. Nozzle and motor overtest with no failure are proposed to extend the non-failure envelope beyond the service load envelope. The potential payoff of overtesting in terms of development cost and schedule is substantial, since the design margins of safety of solid motors is generally large relative to random variabilities.

The development schedule and cost payoff for IUS which can be deduced from the result of one 20 percent nozzle overtest is estimated to be equivalent to four nozzle tests at service load conditions. Similarly, three motor overtests are equivalent to ten motor tests at operational conditions.

Table 1

SRM-1 Ballistic Summary* (vacuum)

Action Time	24°F (-3σ)	60°F (nominal)	102°F (+3σ)
Time, sec	155.8	137.7	121.4
Average Pressure, psia	567	640	725
Average Thrust, lb_F	29,820	45,390	51,870
Duration			
Time, sec	156.4	138.3	122.1
Impulse, lb-sec x 10^{-6}	6.2086	6.2552	6.3021
Effective Delivered I_{sp}, sec	288.9	291.0	293.0
Maximum Pressure, psia	766	866	980
Time of Maximum Pressure, sec	98	86	76
Maximum Thrust, lb_F	54,670	62,370	71,140
Time of Maximum Thrust, sec	104	92	82
Maximum Acceleration, g	3.69	4.24	4.86
Time of Maximum Acceleration, sec	124	110	100

*Note: Effect of dilated case included. Nozzle length = 52.278 in.

SRM-2 Ballistic Summary* (vacuum)

Action Time	24°F (-3σ)	60°F (nominal)	102°F (+3σ)
Time, sec	105.99	94.16	83.08
Average Pressure, psia	568	642	729
Average Thrust, lb_F	16,318	18,498	21,110
Duration			
Time, sec	106.33	94.55	83.46
Impulse, lb-sec x 10^{-6}	1.7298	1.7420	1.7543
Effective Delivered I_{sp}, sec	286.54	288.56	290.60
Maximum Pressure, psia	761	866	980
Time of Maximum Pressure, sec	66.0	58.0	52.0
Maximum Thrust, lb_F	22,169	25,294	28,808
Time of Maximum Thrust, sec	66.0	60.0	52.0
Maximum Acceleration, g	3.77	4.33	4.98
Time of Maximum Acceleration, sec	84.0	74.0	66.0

*Note: Effect of dilated case included

Table 2

Typical IUS Solid Motor Material Characterization Data

Propellant Performance and Ballistic Data			
Standard Specific Impulse (15-lb Bates motor)	248 sec		
Burning Rate at 1000 psi, 70°F (4-lb motor)	0.28 in./sec		
Pressure Exponent	0.41		
Temperature Sensitivity	0.137 %/°F		
Propellant Mechanical Properties	28°F	70°F	120°F
Maximum Stress (2 in./min Crosshead)	255 psi	157 psi	135 psi
Strain at Maximum Stress (2 in./min Crosshead)	77%	73%	69%
Coefficient of Thermal Expansion	53.5×10^{-6} in./in.°F		
Equilibrium Modulus	60 psi		
Nozzle Three-Dimensional Carbon/Carbon Mechanical Properties	Ambient	2000°F	4000°F
Hoop ID Compressive Modulus, psi	4.5×10^{6}	5.1×10^{6}	4.1×10^{6}
Hoop ID Coefficient of Thermal Expansion, in./in.°F	-0.5×10^{-6}	0.18×10^{-6}	0.55×10^{-6}
Hoop OD Tensile Allowable Stress, psi	7.0×10^{3}	8.0×10^{3}	6.5×10^{3}
Case Composite Mechanical Properties			
Tensile Modulus in Fiber Direction, psi	11×10^{6}		
Tensile Modulus Normal to Fiber Direction, psi	0.75×10^{6}		
Coefficient of Thermal Expansion in Fiber Direction, in./in.°F	-3.0×10^{-6}		
Coefficient of Thermal Expansion Normal to Fiber Direction, in./in.°F	$+3.0 \times 10^{-6}$		
Vessel Ultimate Stress/Strain for Hoop Wrap, psi/%	3.5×10^{5}/1.9		
Vessel Maximum Stress/Strain for Polar Wrap Direction, psi/%	3.2×10^{5}/1.7		

Table 3

Validation Phase Test Data

	Char Motor No.1	Char Motor No.2	Super Hippo No.1	Super Hippo No.2	Full Scale Motor
Propellant Weight, lb	12,690	12,644	19,525	19,500	20,662
Burn Time, sec	86.0	87.0	135.6	135	150.7
Average Chamber Pressure, psia	650	643	596	615	549
Throat Material	Pyrolytic graphite throat pack	Pyrolytic graphite throat pack	Three-dimensional carbon-carbon fine weave	Three-dimensional carbon-carbon coarse weave	Three-dimensional carbon-carbon fine weave
Throat Erosion Rate, mils per sec, average	0.54	0.47	1.33	1.2	1.78
Exit Cone Material	Two-dimensional carbon-carbon rosette	Two-dimensional carbon-carbon rosette	Two-dimensional carbon-carbon rosette	Two-dimensional carbon-carbon rosette	Two-dimensional carbon-carbon rosette
Exit Cone Erosion Depth,* in. average	0.045	0.045	0.067	0.061	0.090

*At interface with three-dimensional carbon-carbon support.

Table 4

Specific Motor Development Tests

TEST NUMBER AND DESCRIPTION*	TEST OBJECTIVES	TEST DATA
TEST 1 • FULLY LOADED MOTOR • HEAVYWEIGHT NOZZLE AND CASE • HEAVYWEIGHT INSULATION (four candidates) • TVC IN ONE PLANE • TESTED AT AMBIENT TEMPERATURE WITH MINIMUM LIFE CYCLE LOADS	DEMONSTRATE: • OVERALL MOTOR DESIGN CONCEPT (component interaction) • AMBIENT PERFORMANCE AND BALLISTICS • TVC WITH PLANAR SYMMETRY • INSULATION SELECTION • COMBUSTION STABILITY • SELF-INDUCED VIBRATION	• THREE-AXIS THRUST • HIGH AND LOW FREQUENCY PRESSURE • VECTORING FORCE AND DISPLACEMENTS • TRI-AXIS ACCELEROMETERS • CASE AND NOZZLE TEMPERATURES • CASE STRAINS • PRE AND POST TEST CONDITION WEIGHT AND DIMENSIONAL MEASUREMENTS
TEST 2 • FULLY LOADED MOTOR • HEAVYWEIGHT NOZZLE, CASE AND FINAL INSULATION • TVC OMNIDIRECTIONAL • TESTED AT LOW TEMPERATURE AFTER EXPOSURE TO HANDLING AND TRANSPORTATION LOADS • NOZZLE EXIT CONE COOLED TO SPACE SOAK TEMPERATURES	DEMONSTRATE: • SAME AS TEST 1 EXCEPT • BALLISTICS AND PERFORMANCE AT LOW TEMPERATURE • ACTUAL TVC DUTY CYCLE • INSULATION PERFORMANCE • NOZZLE PERFORMANCE UNDER SIMULATED SPACE CONDITIONS	SAME AS FOR TEST 1 EXCEPT • NONOPERATING ACCELERATION • NONOPERATING NOZZLE TEMPERATURES
TEST 3 • 50% LOADED MOTOR • FLIGHT-WEIGHT NOZZLE AND CASE • HEAVYWEIGHT INSULATION • OMNIDIRECTIONAL TVC • TESTED AT LOW TEMPERATURE AFTER EXPOSURE TO TRANSPORT, HANDLING AND VIBRATION LOADS • NOZZLE EXIT CONE COOLED TO SPACE SOAK TEMPERATURES	DEMONSTRATE: • SAME AS TEST 2 EXCEPT FOR 50% PROPELLANT LOAD, FLIGHT-WEIGHT CASE AND NOZZLE, AND AFTER EXPOSURE TO VIBRATION LOADS	SAME AS FOR TEST 2
TEST 4 • FULLY LOADED MOTOR • FLIGHT-WEIGHT NOZZLE AND CASE • HEAVYWEIGHT INSULATION • OMNIDIRECTIONAL TVC • TESTED AT HIGH TEMPERATURE AFTER EXPOSURE TO TRANSPORT, HANDLING AND VIBRATION LOADS • NOZZLE EXIT CONE COOLED TO SPACE SOAK TEMPERATURES	DEMONSTRATE: • SAME AS TEST 3 EXCEPT FOR FULLY LOADED MOTOR AT HIGH TEMPERATURE	SAME AS FOR TEST 2
TEST 5 • SAME AS TEST 4 EXCEPT TESTED AT LOW TEMPERATURE AFTER EXPOSURE TO HOT AND COLD SOAK CONDITIONS, HUMIDITY, TRANSPORT, HANDLING AND VIBRATION LOADS	DEMONSTRATE: • SAME AS TEST 4 EXCEPT DESIGN MARGINS AT AGGRAVATED LIFE CYCLE CONDITIONS	SAME AS FOR TEST 2

*All tests at simulated vacuum

Figure 1

Inertial Upper Stage

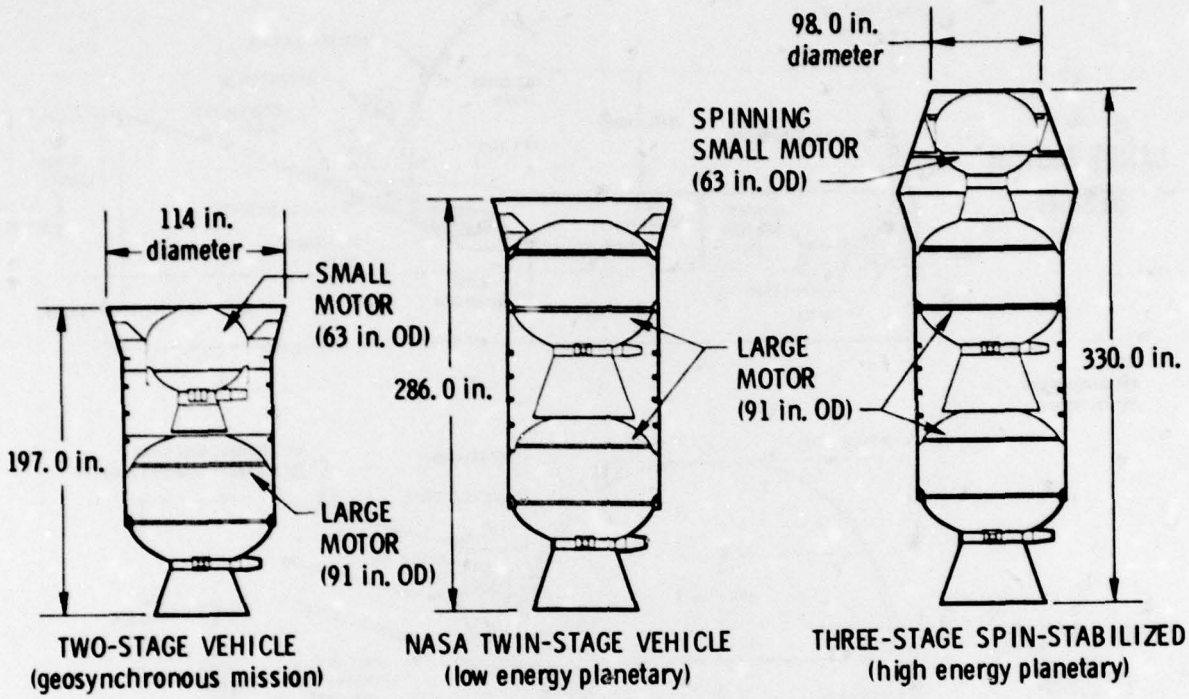

a. VEHICLE FAMILY

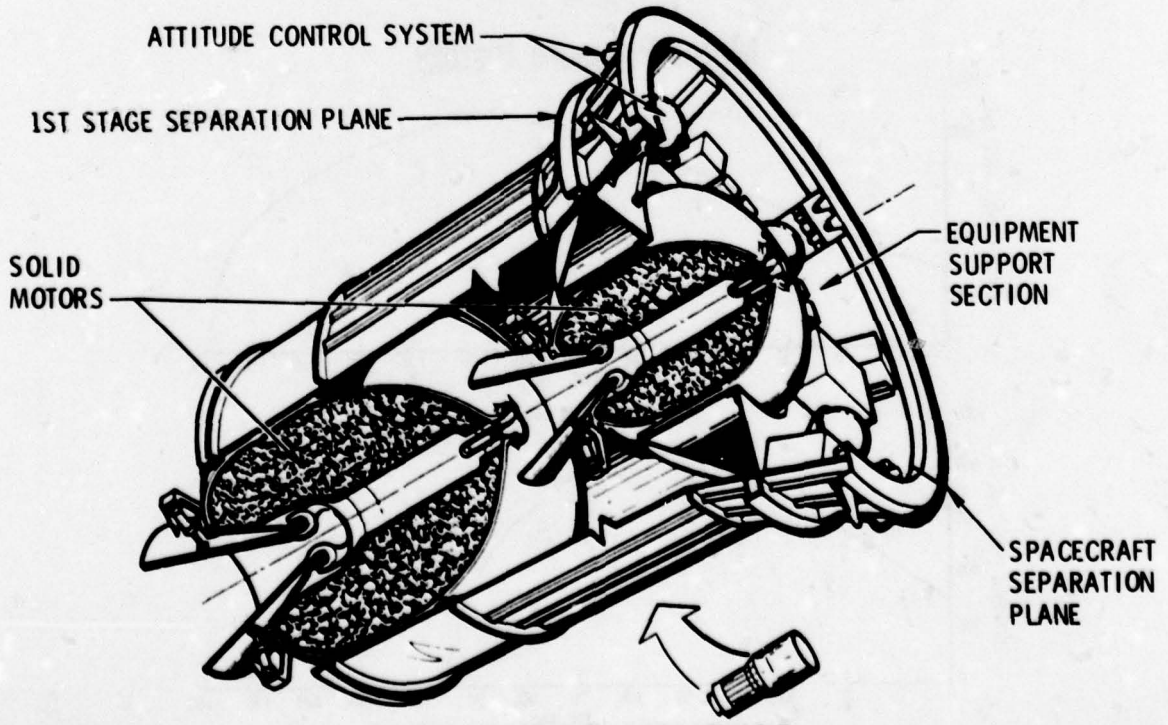

b. TWO-STAGE DoD, NASA VEHICLE

Figure 2

Inertial Upper Stage Motors

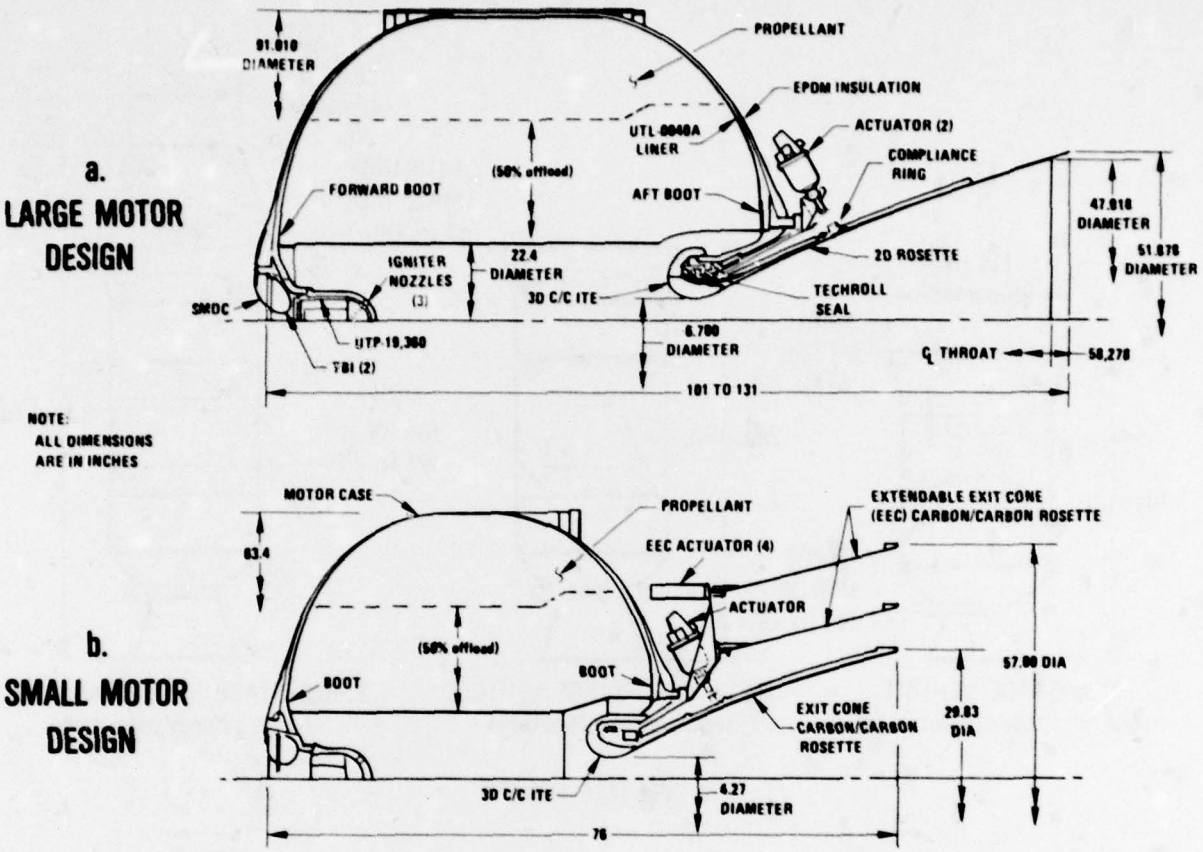

Figure 3

Motor Pressure History

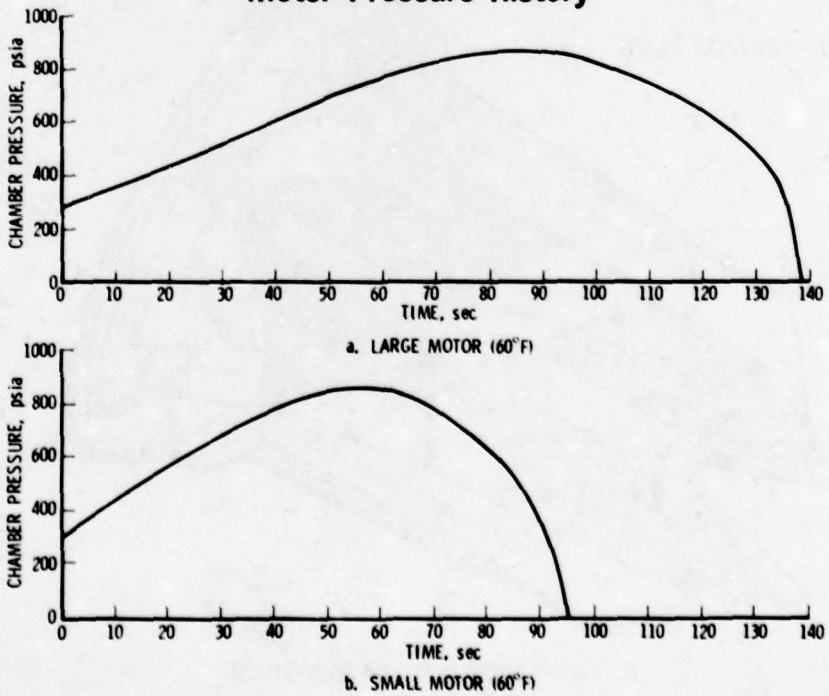

Figure 4

Example for Determining Overtest Conditions for Maximum Stress Failure Criterion

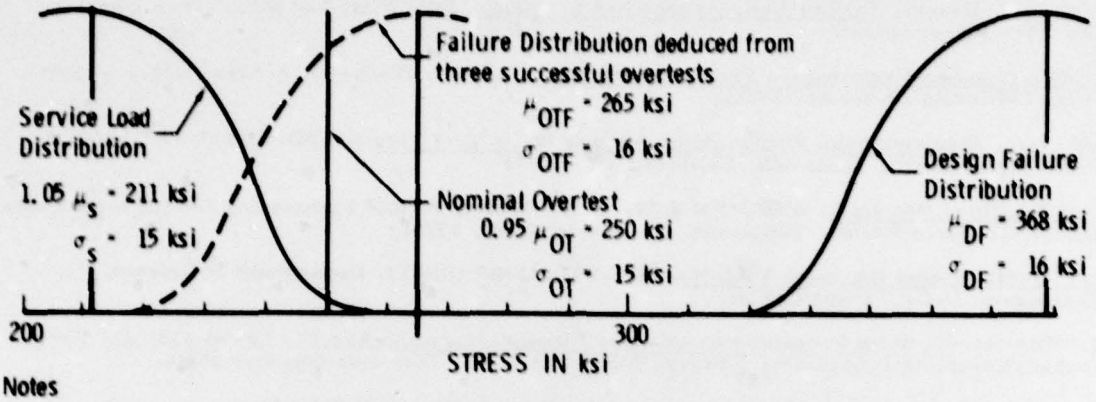

Notes

1. Minimum reliability estimate from three successful tests

$$R = 1 - \frac{1}{m+1} = 0.75$$

From cumulative normal distribution, $Z = 0.7$

2. Failure envelope mean deduced from three successful overtests

$$\mu_{OTF} = 0.7\sqrt{\sigma^2_{OT} + \sigma^2_{DF}} + 0.95\mu_{OT} = 265 \text{ ksi}$$

3. Service Unit Reliability

$$Z = \frac{0.95\mu_{OTF} - \mu_s}{\sqrt{\sigma^2_s + \sigma^2_{OTF}}} = 2.56$$

Distribution Function $R = 0.994$

4. Probability of false OT acceptance 3 percent

5. Probability of OT failure theoretically is negligible

Figure 5

Projected Pressure vs Time Trace for Nozzle Overtest

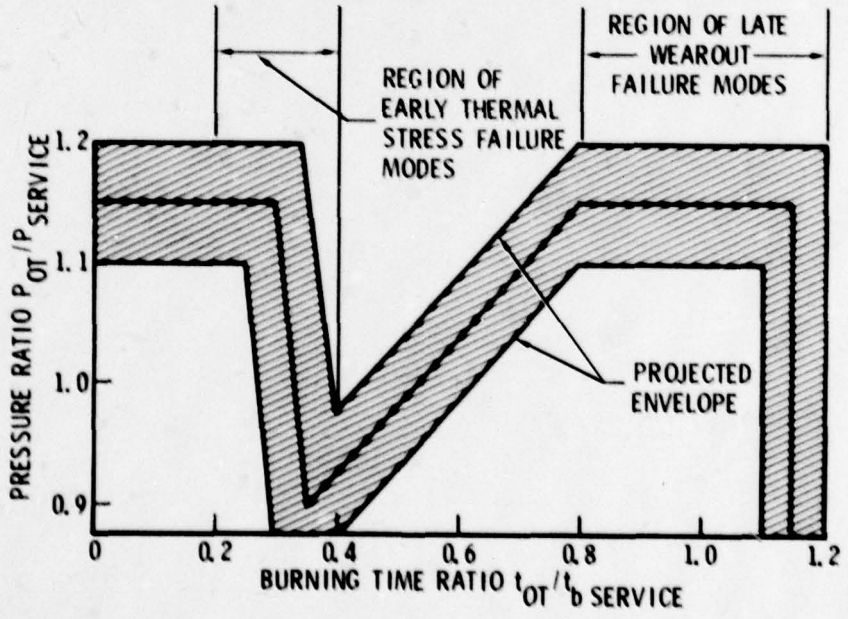

REFERENCES

1. IUS Motors Propulsion Subsystem Design Analysis Report, CSD-5001-77-9, United Technologies Corp., Sunnyvale, California (18 January 1979).

2. J. W. Duroux, Predictions of Operational Success, TR-0200(4306-01)-3, The Aerospace Corporation, El Segundo, California (June 1969).

3. Edward D. Haugen, Probabalistic Approaches to Design, John Wiley and Sons, Inc., London-New York-Sidney (1969).

4. AFRPL Graphite Performance Prediction Program, AFRPL TR-76-70, Acurex Corp., Mountain View, California (December 1976).

5. IUS 91-in. Diameter Solid Rocket Motor Altitude Static Test Firing, CSD-5001-78-7, United Technologies Corp., Sunnyvale, California (May 1978).

6. Test Facilities Handbook, AEDC/PM LTV, Tenth Edition, Arnold Engineering Development Center, Arnold Air Force Station, Tullahoma, Tennessee (8 July 1976).

7. Test Requirements for Space Vehicles, MIL-STD-1540A (USAF), Department of Defense, Washington, D.C. (15 April 1974).

8. K. Bills, et al., Solid Propellant Cumulative Damage Program, AFRPL-TR-68-131, Air Force Rocket Propulsion Laboratory, Edwards Air Force Base, California (October 1968).

9. Ernst Stampfl, Grain Integrity Evaluation of the Thiokol TE-M-521 Solid Motor, TOR-0059(6141-01)-3, The Aerospace Corporation, El Segundo, California (November 1970).

10. E. M. Landsbaum, Solid Propellant Specific Impulse Prediction, to be published, The Aerospace Corporation, El Segundo, California.

THE USE OF STANDARDIZED TEST MOTORS AND LABORATORY TOOLS IN THE DEVELOPMENT OF MISSILE PROPULSION TECHNOLOGY

by

RICHARD R. WEISS

Chief Scientist

Air Force Rocket Propulsion Laboratory

Edwards AFB, California

93523

USA

SUMMARY

Over the past twenty years, the Air Force Rocket Propulsion Laboratory (AFRPL) has devoted an extensive effort toward the development of standardized test motors and laboratory tools to enable evaluation of solid rocket motor component capabilities and propellant behavior. Although these standardized devices are used in a variety of ways, they can be grouped into two principal categories; either as an authority or as a basis of comparison in measuring or judging capacity, quantity, content, extent, value, quality, etc. Standard test motors and tools can be described by several characteristics, such as, heavy weight, reusable, versatile, common facility use, fixed operational procedures and consistent internal configurations.

The advantages offered by the use of standardized motors and laboratory tools are

- cost savings
- comparative evaluations
- survivability
- service for contractor developed products
- early development testing

The only major disadvantage is the somewhat questionable ability to reliably scale the results from test motors to the full scale motor of interest. This lack of credibility has led to the establishment of "families" of test motors and tools spanning a range of sizes to more nearly simulate full scale conditions.

Two primary motor families are used at the AFRPL. There is the "BATES" motor family used for propellant investigations and the "Super HIPPO" family used for component (e.g., nozzles, thrust vector control, insulations, etc.) evaluations. These motors are designed to accommodate a wide range of propellants and to simulate combustion chamber environments for a variety of large solid motors. These motors have proved very useful at the AFRPL. Descriptions and design rationale are provided which highlight the motor flexibility and reuse features.

The T-burner laboratory combustion tool is used principally to conduct comparative evaluations of propellant combustion stability characteristics. This device has received intensive study and development over the past ten years and is now in a status that permits credible evaluations to be made. It is used almost routinely in most Air Force sponsored programs leading to new propellant and/or motor developments. The devices most commonly used are the variable area T-burner, the slot vent T-burner and the rotating valve.

INTRODUCTION

Over the past twenty years the Air Force Rocket Propulsion Laboratory (AFRPL), in conjunction with the rocket propulsion industry, has developed and used a variety of standardized motors and tools to assist in the development of missile and space propulsion systems and technology. These devices are primarily used to aid in propellant and component development. Motors used at the AFRPL to investigate and/or verify new propellant developments are designated as the "BATES" motor family. Those used to evaluate component developments are designated as the "Super HIPPO" family.

In support of motor development programs, numerous laboratory tools are used to evaluate solid rocket motor behavior. Although these tools are too numerous to enumerate, the development of combustion stability tools is worthy of some note. These tools are represented by the many T-burner configurations and Combustion Window Bomb devices in use today. They are tools which have been designed specifically to address the combustion instability problems which are frequently encountered in motor development programs. Much progress in their development has resulted from intensive investigations over the past ten years. They are now used almost routinely as part of an overall motor development effort.

This paper briefly reviews the test motor families and combustion tools used at the AFRPL to assist missile propulsion technology development. The rationale for their selection, design and use is provided along with a description of the devices themselves.

DEFINITION

For lack of a better term, the devices around which this paper centers are referred to as "standardized." This term needs some explanation. Webster's dictionary defines "standardized" to mean, "to make to or regulate by a standard." It goes on to define standard in several ways, among which is "something established for use as a rule or basis of comparison in measuring or judging capacity, quantity, content, extent, value, quality, etc." The words "as a rule" imply a recognized criterion of excellence, accuracy or authority; something that can be taken as absolute. On the other hand, "basis of comparison" implies a method or technique in which there is sufficient consistency to permit comparisons to be made.

In interpreting the use of "standardized test motors and laboratory tools" in this paper, care needs to be exercised over which of the two above references apply. In discussing BATES motors, both apply. The BATES motors are often referred to as the "National Bureau of Standards for propellant performance." They can be used to provide authoritarian data as well as a basis for comparison. On the other hand, as will be discussed later, references to "HIPPO" motors can only be made as a basis for comparison. There is sufficient disparity between HIPPO test motor results and actual full-scale motor results to rule out any "absoluteness" between the two.

It will be shown later that the combustion tools also fall more along the "basis of comparison" interpretation.

With this exercise in language arts as a prelude, the following characteristics can best be used to describe the "standardized" devices in use at AFRPL today.

(1) They are heavyweight structures and, with slight refurbishment, can be reused indefinitely. This is different from the flightweight configuration motors which are essentially "used up" in each test.

(2) They are versatile and perform many functions. Segmented designs are used so that parts can be interchanged and technology components of various sizes and performance capabilities can be evaluated.

(3) Facility and motor operational procedures generally remain the same so as to enhance credibility and confidence in the test results.

(4) Within a motor family, key design parameters (e.g., internal configuration) are generally maintained the same so that scaling comparisons can be made.

To warrant the necessary investment in test hardware and facilities, there must be ample payoff from their use. Although difficult to quantitize in actual dollars saved, there are many aspects to their use that make the return on investment readily apparent. These advantages are itemized below and then discussed in subsequent paragraphs.

- Cost Savings
- Comparative Evaluations
- Survivability
- Service for Contractor Developed Products
- Early Development Testing

(1) Cost Savings - The availability of standard test motors and facilities offers major cost savings to both the Air Force and the rocket propulsion industry. Cost savings result both from the reusability aspects of major motor components as well as from having a common facility for motor test operations. The benefits derived from motor resuability are obvious; especially when considering large motors sized for evaluating ballistic missile and space motor components. If a new expendable motor were required each time a component - say a nozzle component - needed evaluation, the cost of doing business would be unacceptably high.

Similarly, with respect to the facility, major build-up costs for motor development programs are incurred in the design and fabrication of the thrust stand and thrust stand abutment. The design of these devices is very often sensitive to a given motor external geometry. If separate thrust stands and abutments were needed for each component or propellant demonstration test, costs would be prohibitive. Moreover, all contractors do not have the present facility capability to handle large scale, or hazardous motor tests. The capital investment required by either the industry or Air Force to facilitize the entire industry would be great and, based on the few number of large technology components, unwarranted as well. One facility, within the Air Force, to handle the test requirements for the industry in an objective and unbiased manner is a smart investment. Not only are test costs reduced by only investing in one major facility, but this approach also has advantages in reduced operational and maintenance costs. Handling equipment and personnel training costs are reduced.

When the AFRPL originally invested in its "Super HIPPO" capability (described later), it was estimated that investment costs would be amortised in 5 tests and each test thereafter would provide a cost savings of $300,000 to the Air Force. This was four years ago. At the present rate of inflation, this savings is undoubtedly even greater today.

(2) Comparative Evaluations - In general, standardized motors and tools provide an excellent "basis for comparison." Testing of several different propellant formulations or motor components in the same test motor under similar operating conditions provides an excellent basis for establishing trends and making comparative judgments on merit and value. In this regard, doing this testing in-house, within the Air Force, in an objective manner lends further credence to the use of the devices to establish these comparisons. The AFRPL can bring a high degree of objectivity to this type of testing because it seeks the "best" in terms of technology options and is not plagued by the "invented here" syndrome. The AFRPL has been asked often to serve as a "referee" on the ranking of various propellant formulations by use of the BATES motors.

There is another advantage to such a centralized concept of testing with standard devices. After a few years of gaining test experience on a variety of propellants and components in the same test motor, a data bank is developed that permits judgments to be made about propellant families without necessitating extensive testing. Thus tests can be more selective and fewer in number without introducing undue high risk into the final judgments.

(3) Survivability - The use of a heavy weight motor provides a high margin of safety to the motor and facility if the component (e.g., nozzle) fails during test. Flightweight motors generally would not be able to withstand the loads placed on the case when a nozzle component is ejected and thus would result in the loss of the test, the test motor and even perhaps the facility.

(4) Service for Contractor Developed Products - With today's austere budgets, companies often find it advantageous to spend their own funds, or government independent research and development funds on the engineering design and building aspects of a concept and then enter into a joint program with the Air Force to have the expensive testing done elsewhere - most frequently at AFRPL. That way, they get credible test results and an objective evaluation of their concept. The Air Force generally benefits bu gaining some data rights to the concept. This approach often provides an early evaluation of promising technology and the awareness on the part of the Air Force can ease the path toward eventual sponsorship. Thus the arrangement is mutually beneficial.

(5) Early Development Testing - The availability of test motors at the AFRPL makes it possible for the Air Force to enter into early "full-scale" developmental testing of propellant and components. Thus functional checks of propellant potential and component design can be evaluated early in a low risk environment. If the system developer were forced to delay such testing until the motor was designed and fabricated, there could be a considerable delay before initial data were obtained to see if it was designed "right." This introduces needless rick into a motor development program. The standard test motors and laboratory tools used to evaluate components and propellants make early testing and problem area identification possible.

DISADVANTAGE

The only real disadvantage is the lack of credibility associated with the use of some motors/tools in predicting full-scale results. This problem is associated with the unknowns about scaling solid rocket motor propellant and component behavior. More than any other known influence, the inability to accurately scale the results from the standard motors and tools to the actual, full-scale motor has led to the establishment of "families" of motors. These families are represented by motors of various sizes that permit testing at sizes that more truly represent the class of motors for which the component/propellant is designed, while retaining the advantages associated with a standard test motor approach. This approach has minimized the disparities but has not eliminated them. Thus when dealing with results from standardized devices, it is very important to understand their limitations and not expect absolute comparability. There will still need to be actual full-scale motor tests. Hopefully though, the trends will be proper and the problems properly identified so that the more expensive full-scale developmental testing can be kept to a minimum.

DESCRIPTION OF TEST MOTORS

The two primary families of test motors used at the AFRPL to evaluate solid propellants and solid rocket motor components are the "BATES" and the "Super HIPPO" families. The primary laboratory combustion tool is the T-burner. The remainder of this paper is devoted to providing a brief description of the motors and tools which comprise these families. Included are overall design data along with rationale and merits for their use. Detailed design information is not included. This information has been thoroughly described in several reference reports.

BATES MOTORS (References 1 - 5)

BATES is an acronym for BAllistic Test and Evaluation System. The initial BATES program was initiated at the AFRPL in 1960 to provide a tool for the comparison of state-of-the-art and advanced solid propellant performance. The program objectives were - and still are - to provide accurate, comparable, and unbiased ballistic performance data. This initial program resulted in two test motors: (1) the 70-pound-charge BATES test motor and the 15-pound-charge BATES test motor. In the early 1970s it was hypothesized that the smaller BATES motors were inadequate to provide for an accurate evaluation of solid propellants for ballistic missile or large space solid motor applications due to scaling uncertainties in performance corrections. Because a reusable test motor was not available to permit a full-scale evaluation of these propellants, a new BATES motor - termed "Super BATES" was created.

A schematic illustrating the 15-lbm and 70-lbm charge motors is shown in Figure 1. The dimensions of the two motors are:

	A (in)	B (in)	C (in)
15-lbm BATES	12.0	7.0	4.6
70-lbm BATES	20.0	12.0	8.0

Motor design and operating characteristics are provided in Table 1. The motors are designed for optimum ballistic parameters over a wide operating range. The motors have a short duration, neutral trace (constant burning area) and a fixed exposed area. They use a conventional nozzle and may be fired in a single or multiple segment configuration. Both motors use a double end-burning, center-perforated grain with a cylindrical bore. These grains are cartridge loaded because of operational and economical considerations. The ratio of propellant mass for the two motors is approximately five-to-one while the burning surface ratio is three-to-one. This gives a three-to-one mass discharge ratio between the two motors at equal burning rate. The motors have no insulation. This eliminates additional mass flow contributions. The motors are of a flanged construction and use high strength steel to prevent warping of the components.

Table 1

BATES MOTOR DESIGN AND OPERATING CAPABILITIES

	70-lbm Motors	15-lbm Motor
Propellant Weight (Nominal), lbm	75	15
Maximum Pressure, psi	1800	2000
Pressure Range, psi	100 to 1800	100 to 2000
Motor Weight, lbm	400	150
Nozzle Exit Half Angle, deg	15	10
Grain Configuration: Length, in	20	11.5
OD, in	11.75	6.6
ID, in	8	4.6
Web Thickness, in	1.9	1.0
Web Action Time, sec	2 to 10	1 to 6
Burn Surface, sq in	620	204
Mass Flow Rate, lbm/sec	18	5
Burning Rate, in/sec	0.15 to 1.0	0.15 to 1.0
Pressure Neutrality	1.08	1.10
Port/Throat Range	3 to 32	3 to 32
Igniter	15KS 1000 JATO	$BKNO_3$ Pellets
Nozzle Dimensions, in	1.0 to 4.0	0.3 to 3.0

The motors use a conventional, graphite nozzle which mates with the steel aft closure. The aft closure has a graphite insulator to avoid aft closure refurbishment from repeated testing. The 70-lbm charge can be used with nozzle throat sizes from 1.0 to 4.0 inches. The 15-lbm charge motor can be used with nozzle throat sizes from 0.3 to 3.0 inches. To adjust for nozzle expansion ratio variations, a removable steel divergence cone can be attached to the graphite nozzle.

Two thrust stands are used to conduct BATES motor tests. The design accuracy of the single-component, 70-lbm motor, thrust stand is ±0.1 percent of full-scale (0-10,000 lbf). The 15-lbm motor thrust stand is somewhat less accurate, being ±.25 percent of full-scale over load ranges of 0-1000 lbf, 0-2000 lbf, and 0-6000 lbf. Frequent end-to-end calibrations are conducted on the two systems to assure the accuracy of the test data.

Propellant performance capability is primarily assessed on a comparative basis with other propellants. For specific applications, tests are conducted at actual conditions of interest and compared with other propellants at the same conditions. For propellants having more general interest, the test data are normalized to standard conditions of 1000 psi corrected to sea level (14.7 psi). The normalization process involves taking the delivered impulse of the test and establishing the impulse efficiency at those conditions by comparing with theoretical, shifting equilibrium specific impulse values at the same conditions. Although some errors are introduced, it is then assumed that this efficiency is the same at the standard conditions and is used with the standard conditions theoretical impulse value to determine delivered Isp at those conditions.

Corrections are made to the delivered Isp numbers for both heat loss and nozzle divergence loss. To determine heat loss, an air calorimeter is used. This approach uses twelve thermocouples and they are placed as shown in Figure 1. The temperature difference for each position is determined during the test. Typical heat transfer for the 70-lbm motor and the 15-lbm motor is approximately 3400 BTUs and 600 BTUs, respectively. The motors have equal heat loss in terms of impulse efficiency because they are geometrically scaled to provide equal ratios of mass flow per unit of heat loss area.

If more quantitative performance values are required, a sophisticated approach is used which involves a computer prediction of performance, such as the Solid Motor Performance Prediction model (reference 6). This model accounts for other losses which cannot be experimentally determined at this time, such as the two-phase flow loss, kinetics loss and nozzle functional losses.

Of the two motors, the 70-lbm BATES motor is the workhorse. Its accuracy is better by virtue of having less scaling problems and longer burn durations. It has been found that the 15-lbm motor provides good ballistic properties, such as slope and burn rate, but does not provide credible impulse efficiency performance data for aluminized solid propellants. This is due to the reduced metal combustion efficiency resulting from shorter burn durations and less residence time. It is more difficult to determine the true expended weight of the 15-lbm grain due to unburned aluminum accumulation. Performance results from the 15-lbm BATES motor is still credible, however, for the non-metallized propellant performance, where the burn duration and residence time constraints are not severe. Thus the 15-lbm BATES motor is seeing less service with metallized propellants and is being used primarily as a screening device. Moreover, since tests are required in the 70-lbm BATES motor anyway for impulse performance, it is often more cost effective to go directly to this motor size for ballistic data as well.

To date there have been an approximate total of 1500 BATES tests for the two motors combined, on approximately 190 different propellant formulations. Numbers of tests per year have ranged as high as 300 but are generally more in the 100 to 200 range. Four tests are generally considered adequate for a valid, reproducible data point in the 70-lbm motor, whereby eight are generally required for the smaller 15-lbm motor.

SUPER BATES (References 7 - 8)

The purpose of the Super BATES is to test and compare solid rocket motor propellants in a motor large enough to accurately predict internal ballistic performance of full-scale missiles and boosters. A secondary purpose is to provide a test motor capable of providing accurate propellant performance data that can be compared to data obtained from the smaller 15-lbm and 70-lbm BATES motors. Using this comparison, it is hoped that a judgment can be made about the scalability of data obtained from the smaller motors. If such a scalability correlation can be obtained, then the smaller motors could confidently be used to provide propellant performance data for full scale applications. This would greatly reduce propellant and test costs for such data.

The AFRPL recognized a need for the Super BATES motor in the early 1970s. In 1974, a contract was awarded to Chemical Systems Division of United Technologies Corporation to analyze the requirements for such a motor and to generate motor and thrust stand designs. This work was followed by another effort to build the motor and thrust stand and demonstrate their operability at the AFRPL. This work was completed in 1976. The "system" delivered to AFRPL included motors and spare parts, handling and weighing equipment, and an accurate horizontal thrust stand.

The Super BATES motor is designed to accommodate a wide range of propellants and to simulate combustion chamber environments for a variety of large solid motors. Motor flexibility is achieved by using a segmented case approach. This permits great variation in propellant surface area without resulting in a large free chamber volume at low flow rate conditions. By using various combinations of segments with 60-inch and 30-inch long propellant grains, the motor can operate with propellants having burning rates from 0.3 to 1.0 inches/second. The maximum total combined propellant weight of the three 60-inch propellant grain segments is 2500-lbm with the standard 2.6-inch web. The motor case is designed to operate at pressures to 2200 psia with a design safety factor of 1.5 on yield. Maximum design thrust is 150,000 lbf. Table 2 provides a summary of the Super BATES motor design and operational characteristics. Figure 2 provides a schematic of the two and one-half segment configuration of the Super BATES motor with a submerged nozzle.

Table 2

SUPER BATES MOTOR DESIGN AND OPERATIONAL CAPABILITIES

Propellant Weight (Nominal)		800 lbs/segment
Maximum Pressure		2200 psi
Pressure Range		200 to 2200 psi
Maximum Thrust		150,000 lbf
Maximum Motor Weight		20,000 lbm
Nozzle Exit Half Angle		15°
Grain Configuration:	Length	60 inches
	OD	27.9 inches
	ID	22.7 inches
Web Thickness		2.6 inches
Web Action Time		2.8 seconds
Maximum Burn Surface		5600 sq inches/segment
Mass Flow Rate		322 lbm/sec
Burning Rate		0.3 to 1.0 inches/second
Pressure Neutrality		1.05
Igniter		Pyrogen
Nozzle Dimensions		4 to 10 inches

The motor grain design uses double end-burning, center-perforated grains with a cylindrical bore. Design simplicity and processing ease were primary design considerations. Propellant grain processing requirements had the greatest influence on selecting a motor case segmentation approach. In order to achieve a neutral trace the end burning, circular perforated grain must have the correct number of end burning surfaces; this is dependent upon the overall grain length. If a single, monolithic case design were selected, desired burning characteristics could only be achieved by casting or machining a slotted grain configuration; both of which are more costly and complicated. A segmented case allows the grain to be easily cast with two end burning faces.

Unlike the cartridge loaded smaller BATES motors, Super BATES propellant grains are case bonded to the motor case segments. This approach simplifies the motor design by avoiding the more difficult and costly tolerance and dimensional control problems that would be associated with a cartridge loaded motor for this application. Moreover, by using low cost commercially available, carbon steel pipe and providing for separate attach joints that are not part of the case segment design, the steel case segment is cost competitive to the glass cartridge and far more durable.

The motors are fully insulated with a designed reusability feature. Most components can be used three times before new insulation is required.

Motor case segments are joined with a pinned, double shear H-clevis. The segments have only male joints, thus substantially reducing manufacturing costs. All joints use conventional, elastomeric O-rings to maintain internal pressure during firing. The forward closure is fitted with a burst disc, used as a relief device to prevent overpressurization of the motor. The pressure relief passages are radially oriented so that overpressurization will not cause sudden large changes in motor axial thrust.

Flat plate closures are used for the motor to minimize fabrication costs and to simplify the closure-insulation interface. Both the forward and aft closures are 8 inches thick. The closures are fully insulated to minimize heat loss.

The system can be used with nozzle throat sizes from 4 to 10 inches with a conventional or submerged nozzle. Nozzle submergence can be varied from 3 to 18 inches. The nozzles consist of a graphite insert at the throat and a carbon phenolic laminate upstream and downstream of the throat with a silica phenolic divergence cone.

The thrust stand used for Super BATES motor tests is a single component, horizontal system capable of measuring axial thrust in ranges of 0 to 50,000 lbf, 0 to 100,000 lbf and 0 to 150,000 lbf. Thrust stand accuracy is within $\pm$0.15% over the full range. The stand includes a standard load cell with a jackscrew calibrator for accurate calibration of axial thrust measurements. The thrust stand design, fabrication, installation and checkout were done by Ormond, Inc of Santa Fe Springs, California.

To date the Super BATES motors have been tested only three times; all of which were highly successful. Preparation for more extensive use is underway in anticipated support of any advanced ballistic missile full scale development program. In support of the secondary objective of Super BATES to evaluate scalability correlations, additional tests are planned using four 70-lbm BATES motor segments connected together. This long configuration will provide additional combustion residence time to enable an assessment of that parameter's influence on propellant performance and the effect of the test motor used to determine same.

SUPER HIPPO MOTORS (References 9 - 12)

There are three motor configurations which make up the "Super HIPPO" family of motors. There is a standard configuration (Super HIPPO), an extended configuration (Extended Length Super HIPPO or ELSH) and a shortened configuration (Short Length Super HIPPO, or SLSH). Together they represent a family of workhorse, reusable solid propellant rocket test motors for evaluation of large solid rocket motor nozzles and associated components.

The need for this capability was first identified in the early 1970s. It was recognized that future ballistic missile motors would probably operate at high operating pressures, between 1000 psia to 2500 psia, where significant performance advantages were possible. Moreover, it was foreseen that these same missiles would require major nozzle component developments that were beyond the then current state-of-the-art. This created a need for a low-cost standard test motor that could deliver the full-scale motor environment for component demonstration. Test motors in use at that time were limited in both maximum pressure and mass flow capability and could not provide the desired conditions for large diameter nozzle hardware evaluation. Thus, the concepts of Super HIPPO and Extended Length Super HIPPO were born. The former being large enough to satisfy most upper stage ballistic missile requirements and the ELSH being capable of handling first stage applications. In 1972 a contract was given by AFRPL to Chemical Systems Division of United Technologies Corporation to design, fabricate, deliver to AFRPL and demonstrate the operational reasiness of the Super HIPPO and ELSH motors, along with a highly accurate six-component thrust stand for the motors.

The Short Length Super HIPPO motor was not born until much later in 1977. At that time a requirement was established for nozzle evaluations in support of the Air Force Space Shuttle Inertial Upper Stage (IUS) program. That requirement along with the additional advantage that such a motor would more realistically test components for future ballistic missile third stage motors, led to the birth of SLSH. The SLSH design evolved from the benefits that could be derived from commonality in design and components with the Super HIPPO and ELSH. All three motors are of the same diameter and use interchangeable parts.

Thus, the Super HIPPO motor system is actually a family of motors plus a facility for motor test. Maximum operating pressure is 2500 psi; and propellant grain weights from 8,000 to 90,000 lbm can be tested. The thrust stand provides a full six-component thrust resolution with 0.5% thrust accuracy, vector angle resolution accuracy of 20 minutes of arc at 15° deflection, and vertical centerline location

of 0.1 inch. The system is installed at AFRPL and includes all handling equipment for rapid test turnaround time.

The thrust stand consists of two subassemblies: the forward thrust unit which is permanently secured to the floor of the test bay, and the aft thrust unit which attaches to either of two stations on the thrust pad to accommodate at least two motor lengths. The thrust stand includes integrated calibration load trains, jackscrews, and hydraulic motors to provide calibration loads. The thrust stand was designed and fabricated by Ormond, Inc, Santa Fe Springs, California.

The standard Super HIPPO motor consists of a cylindrical case which is pinned to flat plate enclosures. The ELSH extension case pins to the top of the standard motor case to effectively become a double Super HIPPO, thus doubling the usable propellant volume.

The propellant grains are cartridge loaded for ease of handling and recharging. The motor can be assembled in a one-cartridge (SLSH), two-cartridge (Standard Super HIPPO), or four-cartridge (ELSH) configuration. (See Figure 3) Each cartridge contains up to 24,500 lbm of propellant. Inner diameter of the fiberglass cartridges is 80.6 inches, exclusive of insulation. Minimum bore is approximately 15 inches depending on physical properties of the propellant. Maximum grain length for each cartridge is 77 inches. The individual cartridge grains are essentially square so that the thrust can be progressive, regressive, or neutral with simple cylindrical ports. Standard grains have a cylindrical port with one end restricted for a reasonably neutral pressure - time trace. The two-cartridge configuration has approximately as much propellant capacity as the Minuteman first stage.

Design features of the Super HIPPO, ELSH and SLSH can be seen in figures 4 - 6. The motor cases are made of HY-130 steel to provide high strength and toughness. Closures are flat plate design of 4340 steel and are retained by clevis pins. Flat plate closures were selected to allow for economical flat insulators. The motor design goals were safety, minimum setup time, and minimum recurring test costs. The clevis pin type assembly was selected for holding the closures to the cylinders because clevis pins can be joined more rapidly than bolts. Since the closure insulators are flat and have no three-dimensional interfaces with the closures, they are relatively easy to install and economical to fabricate. The cartridge loaded propellant grains can be installed in the motor case rapidly and the cartridges are reusable.

Propellant cartridges for the standard Super HIPPO and ELSH are installed on spacers. Because of machining tolerances necessary for items of this size, a 1/4-inch gap results between the case ID and the propellant cartridge OD. This gap is pressurized from the forward end through holes in the spacer. O-ring seals between the cartridges and at the aft insulation prevent a flow-through of combustion gases. Additional insulation protects the case ID and provides protection at cartridge joints.

To date, the Super HIPPO has been tested once, the ELSH three times and the SLSH twice. In all cases, the motors and facility have performed successfully. There have been no comparable tests of the same components using actual flight configured motors. Therefore, the extent to which the test motor results simulated the full scale environment cannot be judged at this time. Previous experience with smaller test motors would indicate that some differences should result. However, these differences should play a secondary role on design evaluation. The test motors have been found to be excellent tools for comparative evaluations, relative rankings and concept screening.

LABORATORY COMBUSTION TOOLS (References 13-17)

Combustion instability is a complex phenomena that occurs in a great many solid rocket motors during the course of their development. Prior to 1970 there was very little help for the motor developer when this problem occurred. Analytical models to describe the phenomena were, at best, in an embryonic status. Laboratory tools to provide inexpensive means for examining the problem were still novelties of the research community. However, over the past ten years there has been a dedicated thrust on the part of the Air Force to develop a workable understanding of instability phenomena and how it influences solid rocket motor behavior. The goals have been to develop credible means to predict motor instability behavior and establish acceptable cures for the problem if it should occur. The emphasis has been clearly on the aspect of "build it right the first time."

The strategy of the Air Force in achieving these goals has been, and continues to be, one of encouraging an industrial-government recognition that the problem indeed exists, and that no manufacturer is more prone than others to incur the problem, and that it is in everybody's best interest to work together to achieve workable solutions that can be shared and standardized. To end this, the AFRPL extensively funded the industry so that a proper combustion stability scientific and engineering community could be developed. At the same time internal AFRPL expertise was developed to provide necessary guidance and leadership in the area.

Key in the approach toward achieving the goals stated above is the overall success of the T-burner, and to some extent, the Rotating Valve burner in gaining widespread use and acceptance as a standardized means for obtaining propellant combustion response. Currently, propellant combustion response can only be obtained experimentally and its value is an input must for stability prediction models.

In the past ten years, extensive work has been conducted with T-burners and other devices. Not only has this effort been directed at providing a data base for propellant stability characteristics but extensive effort has been done to further understand and develop the devices themselves. As a result these devices are seeing widespread use by government and industry as tools to support propellant and motor development programs. Their acceptability has progressed to the point that most AFRPL contracts with industry involving propellant and motor development now require T-burner or Rotating Valve characterization of stability behavior. As a result, most rocket motor contractors now have a qualified facility and necessary expertise to conduct the new tasks.

Table 3 provides a summary of the contractors and the type(s) of device(s) they use. The AFRPL is also included in this list for reference.

Table 3

COMBUSTION STABILITY LABORATORY TOOLS

USED BY THE USA SOLID ROCKET

PROPULSION INDUSTRY

CONTRACTOR	TOOL(S)
Aerojet Solid Propulsion Co.	VATB* Slot Vent T-Burner
Atlantic Research Corp	Slot Vent T-Burner
Chemical Systems Division	VATB Rotating Valve
Hercules (Bacchus Plant)	VATB
Hercules (ABL)	Slot Vent T-Burner VATB L* Burner
Hercules (McGregor)	VATB
Jet Propulsion Laboratory	VATB
Thiokol (Wasatch Division)	VATB
Thiokol (Huntsville Division)	Slot Vent T-Burner
Air Force Rocket Propulsion Laboratory	VATB Slot Vent T-Burner Rotating Valve L* Burner

*VATB: Variable Area T-Burner

From Table 3 it can be seen that there is more experience with the variable area T-burner concept than any other. This T-burner configuration is basically the same as that described in detail in reference 13 and will not be repeated here. The method of testing with the variable area T-burner is based on the hypothesis that the growth rate of unstable oscillations is proportional to the area of burning surface. The coefficient of proportionality is directly related to the response function for the surface. Tests are made for different propellant surface areas. Then a plot of the observed growth rates versus propellant surface area should be a straight line whose slope will be related to the response function. The value of the plot intercept with the ordinate (i.e., the point of zero surface area) should represent the damping associated with the system. By and large it has been found that results obtained from the variable area T-burner substantiate this hypothesis. Data from this T-burner generally show a good correlation with trends established by motor tests.

The disadvantages in use of the variable area T-burner center about the cost of its use and data reduction uncertainties. Data interpretation complexities are associated with substantial data scatter and uncertainty in defining the surface area at the time the oscillation growth takes place. The device requires a considerable amount of propellant to fully characterize its behavior. For propellants undergoing initial screening from small batch mixes, there may be insufficient propellant to conduct an adequate number of tests to establish the confidence in the results that one would desire.

Moreover, it is expensive to use a variable area T-burner. The cost per test (including test, data reduction, etc.) averages about $500. Ten tests are required per response function point at any given frequency. If data at six frequencies are required to fully map out the response function curve the cost somes to $30,000. This generally represents a substantial investment on the part of the rocket motor development program manager. Thus it is not likely that such full characterization will be made for each propellant formulation change introduced into a given program. Hence increased risk is introduced into the program.

The high costs and substantial propellant quantity required by the variable area T-burner is the major influence that drives the industry toward seeking alternate techniques to do the stability task. One such alternate technique is the Rotating Valve. This concept was first pursued in the United States by Chemical Systems Division of United Technologies Corporation and is illustrated in figure 7. The technique has been adequately described in references 14 - 16, and thus is only briefly summerized here.

Basically the method consists of a small rocket motor that employs a conventional nozzle to control combustion pressure and a secondary exhaust system which is periodically opened and closed to induce bulk mode pressure oscillations in the combustor while the propellant is burning. The pressure oscillations are induced by the use of a rotary valve with several equally spaced holes that traverse a slot type vent from the combustion chamber. The frequency of the induced oscillations is controlled by the rotational speed of the rotating valve. Measurements are made during tests with this device of both amplitude and phase which enable the determination of the real and imaginary part of the response function.

To date, experience with the rotating valve method indicates that the cost to characterize propellant stability behavior should be considerably less than that with the T-burner. This primarily results from a reduced number of tests needed with the rotating valve to get the same amount of data. For example, whereas ten tests per frequency are required with the T-burner, one should be sufficient with the rotating valve. However, the device cannot provide information on propellant damping behavior which is needed for stability prediction models. Test experience shows acceptable levels of correlation between the rotating valve data and the T-burner; particularly at low frequencies.

The slot vent T-burner is essentially the same configuration and principle as a conventional T-burner (see figure 8). The only difference is in the venting arrangement. Whereas the conventional T-burner uses a circular vent port, the slot vent T-burner, as the name implies, has a circular slot vent which has approximately the same cross-sectional area as the circular vent. By using a slot vent arrangement, the characteristic length of the device can be made much shorter than the conventional T-burner without introducing flow losses associated with a larger circular port and the uncertainties introduced in the data interpretation by same. Thus much higher frequencies can be tested with the slot vent T-burner than with the conventional T-burner. This is illustrated by figure 9 which summarizes the frequency regime for the slot vent T-burner as well as the variable area T-burner and the rotating valve device. The extended frequency range of the slot vent T-burner permits test evaluations to be made for propellants containing little or no metal, normally associated with reduced observable applications. These motors appear to be plagued with very high frequency instabilities associated with tangential modes or higher order axial modes. Although reliable results are obtained from the slot vent T-burner, it is plagued with the same high cost and data scatter disadvantages as the variable area T-burner.

CONCLUSION

Over the past twenty years, considerable progress has been made in the understanding and development of standard test motors and laboratory tools for use in the development of missile propulsion technology. The devices range in size and represent fairly sophisticated test capabilities used extensively by the United States Air Force for several purposes. They have gained in acceptability and credibility by the rocket propulsion community to the point where they are now considered to be an integral part of most propellant and motor development programs. Much of the credit for the successful development of the standard test motor and tool technologies goes to the Air Force Rocket Propulsion Laboratory's investments and guidance which brought it to its present favorable position of fruition.

References

1. H. W. Gale, 1st Lt, USAF, AFRPL, Development and Evaluation of the USAF Ballistic Test Evaluation System for Solid Rocket Propellants, 1962, SSD-TRD-62-45.

2. Ray G. Collins, AFRPL, Ballistic Test and Evaluation System (BATES), 1964, RPM Memorandum RPL-TM-64-13.

3. George A. Stetz, Laurice G. Altman, Charles W. Beckman, AFRPL, The AFRPL Ballistic Test, Evaluation, and Scaling Program (U) (BATES Program), 1968, TR AFRPL-TR-68-198.

4. Charles W. Beckman, AFRPL, Solid Propellant Impulse Scaling Prediction Techniques (U), 1971, AFRPL-TR-71-7.

5. Robert L. Geisler, Scott A. Kinkead, Charles W. Beckman, AIAA, The Relationship Between Solid Propellant Formulation Variables and Motor Performance, 1975, AIAA/SAE 11th Propulsion Conference, AIAA Paper No. 75-1199.

6. Coats, D. E., Nickerson, G. R., et al, Ultrasystems, Inc, A Computer Program for the Prediction of Solid Propellant Rocket Motor Performance, Vol. I, II & III, 1975, AFRPL-TR-75-36.

7. W. A. Stephen, T. C. Warren, J. M. Humphrey, United Technology Center, Ballistic Missile Propellant Evaluation Test Motor System - Super BATES, 1974, AFRPL-TR-74-70.

8. W. A. Stephen, T. C. Warren, P. R. Scannell, Chemical Systems Division, Ballistic Missile Propellant Evaluation Test Motor System - Super BATES, 1977, AFRPL-TR-77-5.

9. Paul R. Scannell, Chemical Systems Division, United Technologies Corporation, High Pressure Motors and Test Stand Super HIPPO and ELSH, Volume 1, Design , Fabrication, Demonstration, 1977, AFRPL-TR-77-24.

10. Paul R. Scannell, Chemical Systems Division, United Technologies Corporation, High Pressure Motors and Test Stand, Super HIPPO and ELSH, Volume II, Operations Manual, 1977, AFRPL-TR-77-24.

11. Paul R. Scannell, Chemical Systems Division, United Technologies Corporation, High Pressure Motors and Test Stand, Super HIPPO and ELSH, Volume III, Engineering Analysis, 1977, AFRPL-TR-77-24.

12. P. R. Scannell, W. A. Stephen, Chemical Systems Division, Short Length Super HIPPO Motor Assembly, 1978, AFRPL-TR-77-91.

13. Culick, F. E. C., California Institute of Technology, T-Burner Testing of Metallized Solid Propellants, 1974, AFRPL-TR-74-28.

14. Brown, R. S., Erickson, J. E., Babcock, W. R., Chemical Systems Division, United Technologies Corp, Combustion Instability Study of Solid Propellants, 1973, AFRPL-TR-73-42.

15. Brown, R. S., Chemical Systems Division, United Technologies Corp., Development and Evaluation of Rotating Valve Combustion Response Test Technique, 1976, AFRPL-TR-76-72.

16. Andrepont, W. C., Hewes, J. E., AFRPL, Combustion Response Measurements Using the Rotating Valve Burner, 1978, 15th JANNAF Combustion Meeting, Newport, R.I., 11-15 September 1978.

17. Andrepont, W. C., Lapora, D. J., Capt, USAF, AFRPL, High Frequency T-Burner Tests of Reduced Smoke Propellants, 1978, 15th JANNAF Combustion Meeting, Newport, R.I., 11-15 September 1978.

ACKNOWLEDGEMENT

I am particularly indebted to Mr C. W. Beckman, Mr J. G. Wanchek and Mr W. C. Andrepont for their contributions, their help and their cooperation. They all provided much information and insight on the techniques used and current status of the various motors and tools which are central to this paper.

I wish also to express my gratitude and appreciation to Mrs Dorothy Hummel who patiently and carefully did the necessary typing.

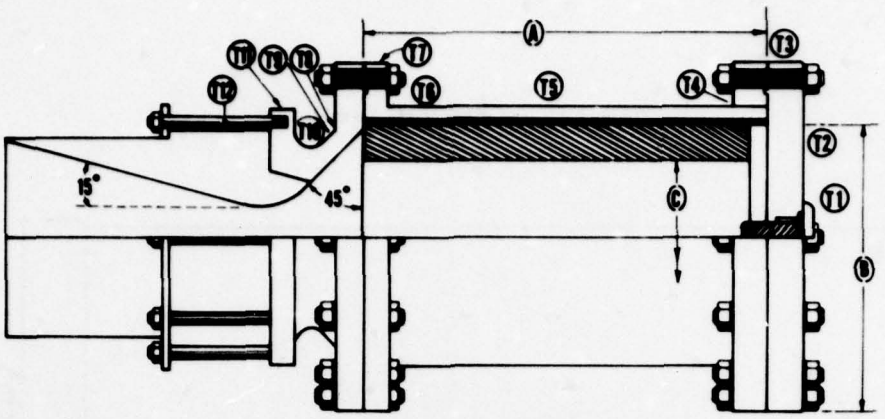

Figure 1. BATES Motor Schematic

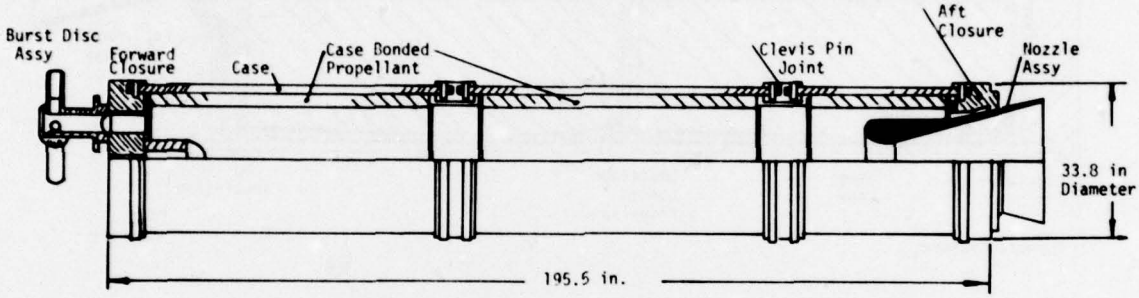

Figure 2 - Super BATES Motor Schematic (2-1/2 segments)

FIGURE 3.

SUPER HIPPO FAMILY OF TEST MOTORS

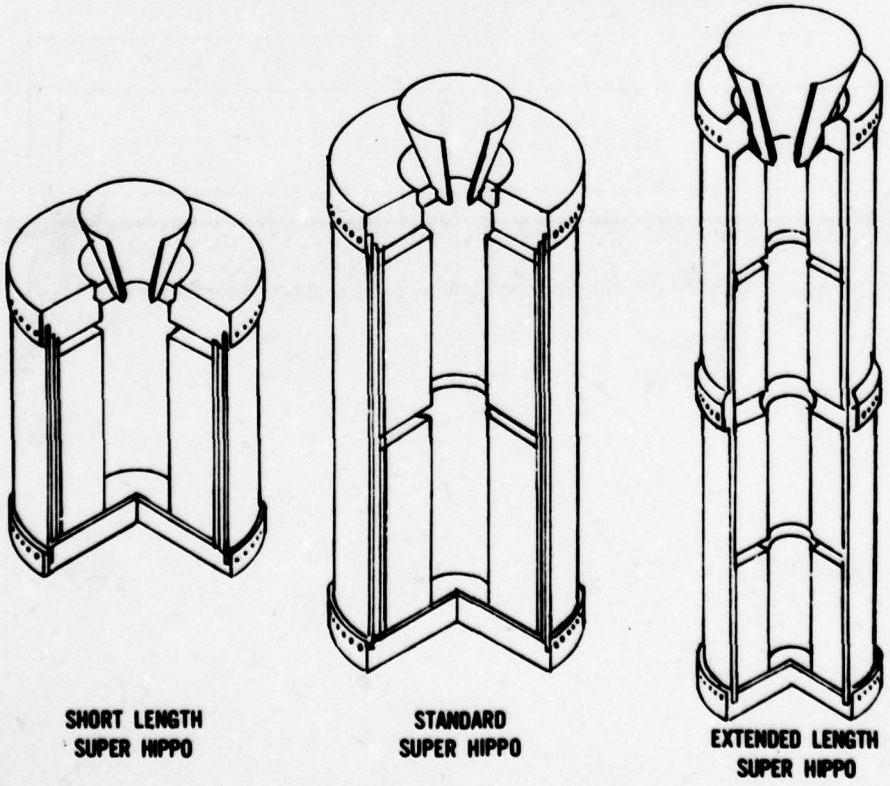

SHORT LENGTH SUPER HIPPO

STANDARD SUPER HIPPO

EXTENDED LENGTH SUPER HIPPO

Figure 4 - Super HIPPO Motor Assembly

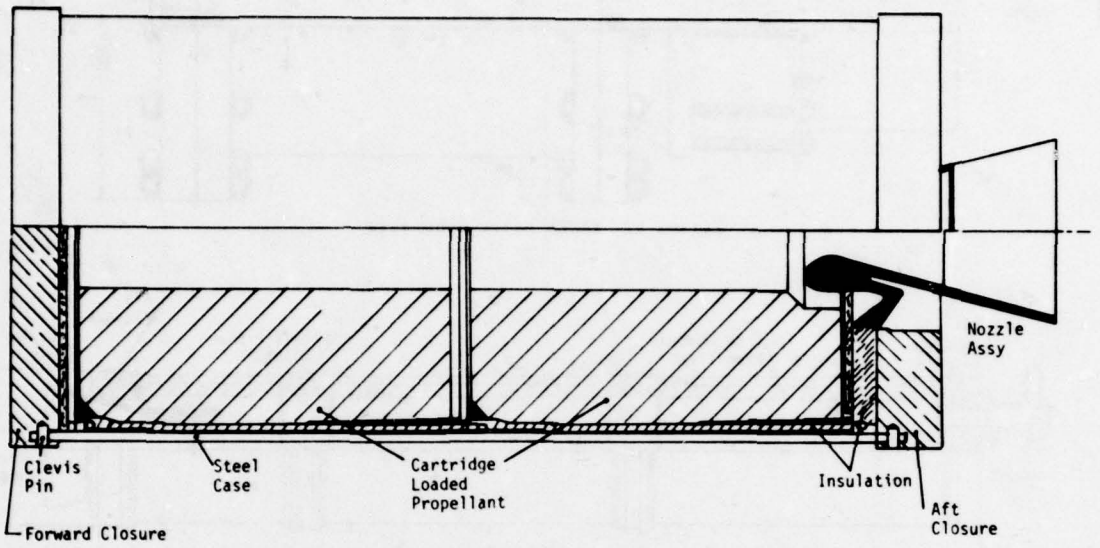

Figure 5 - Extended Length Super HIPPO (ELSH)

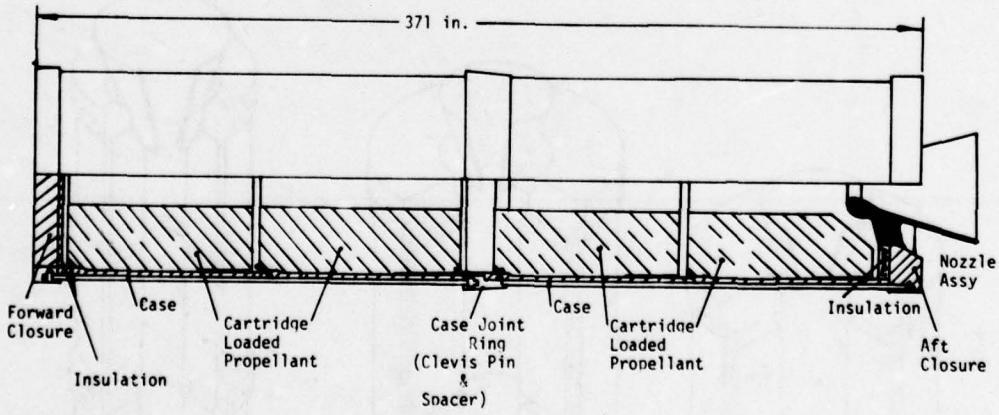

Figure 6 - Short Length Super HIPPO (SLSH)

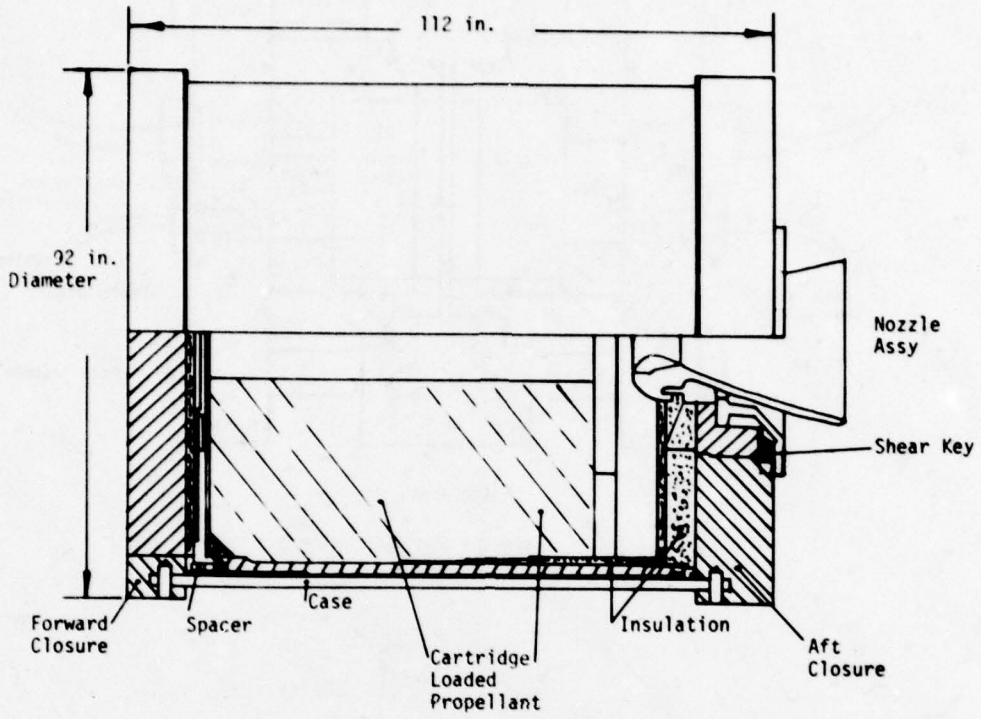

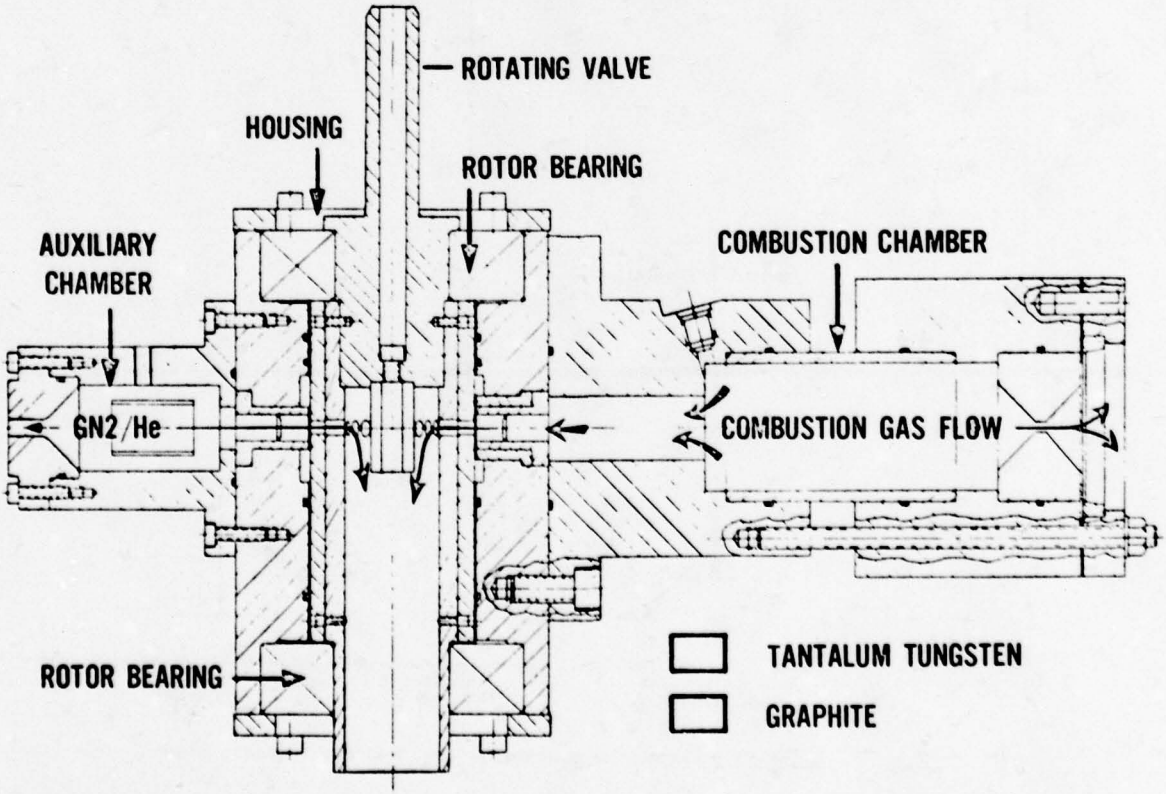

FIGURE 7. ROTATING VALVE BURNER - MAJOR COMPONENTS

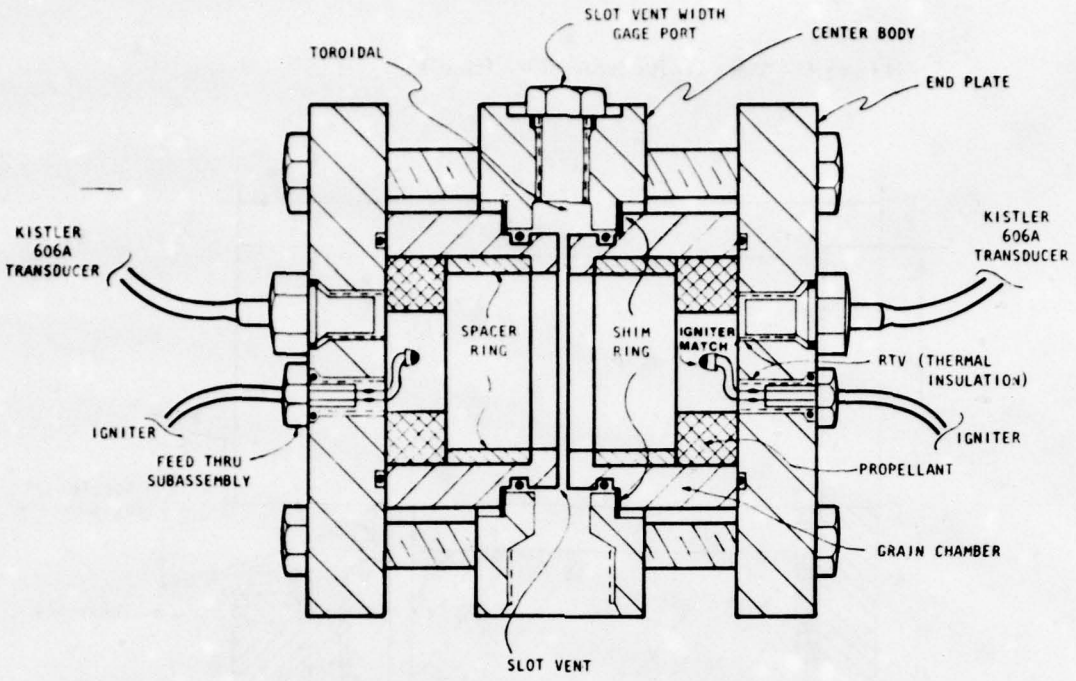

Figure 8 - Slot Vent T-Burner

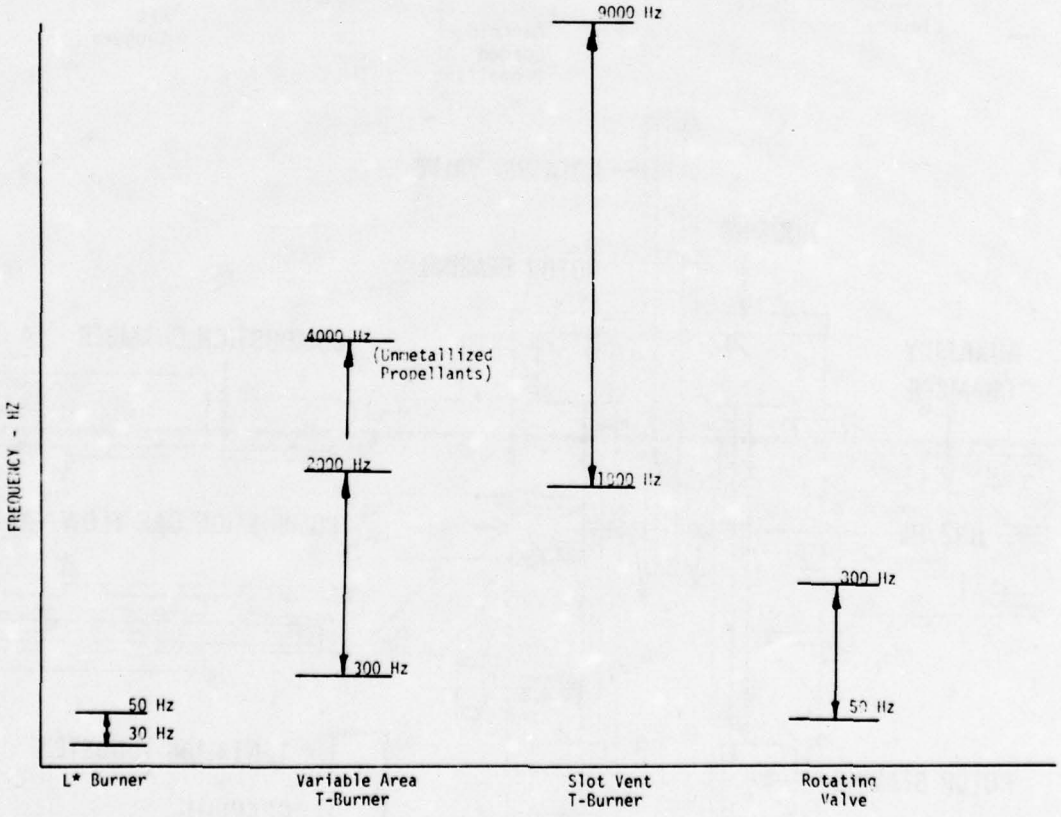

FIGURE 9 - Combustion Response Measuring Devices - Frequency Regime

MEASUREMENT OF THRUST TRANSIENTS IN ROCKET MOTORS

by

D S Dean

MOD PE
PERME
Westcott
Aylesbury
Buckinghamshire
HP18 ONZ
UK

SUMMARY

Any force measuring equipment can be represented by a system of masses and springs, or at its simplest by a single spring of stiffness, k and a mass, M, with damping, C, and displacement, x, such that $M\frac{d^2x}{dt^2} + C\frac{dx}{dt} + kx = T$, where T is the external force. Most systems measure only kx, which is adequate at low frequencies.

It is sometimes impractical to raise the rig natural frequency sufficiently above the frequency of thrust fluctuations for these to be recorded accurately. To overcome this two approaches have been used. The first combines all the terms of the equation of motion to give the external force to well above the rig natural frequency.

In the second a mass is freely accelerated by the motor on linear bearings, an accelerometer giving the thrust/time curve. Total impulse is obtained by integrating the force required to bring the mass to rest over a pre-selected longer period.

1. INTRODUCTION

Any force measuring system can be represented by a system of damped masses and springs interccupled so that its frequency response is far from linear. By careful design a rocket motor thrust measuring system can be made to approximate to a single mass attached to a damped spring. The mass, M, consists of the rocket motor and any part of the rig attached rigidly to it. The load measuring transducer can be regarded as a spring reacting against a rigid structure consisting of the thrust block. In practice there is compression of the flexures coupling the transducer and some compression of the thrust block. Any parasitic oscillation of the structure will have to be filtered in the signal conditioning equipment if it cannot be removed at source. The equation of motion of such a system may be written

$$T = M\frac{d^2x}{dt^2} + C\frac{dx}{dt} + kx \qquad (1)$$

where

- x is the displacement of the mass M
- C is the damping coefficient
- k is the stiffness of the system
- T is the external applied force.

To consider the response of the system, T may be replaced by an oscillatory force F sin ωt ($\omega = 2\pi$ frequency) and the natural frequency is given by

$$W_n = \sqrt{\frac{k}{M} - \left(\frac{C}{2M}\right)^2}$$

The second term, $\left(\frac{C}{2M}\right)^2$ is usually too small to have a significant effect on ω_n and can often be ignored. A set of graphs giving the natural frequency of a rig for a range of masses and stiffnesses is given in Fig. 1. Provided that ω is much less than ω_n, the first two terms in equation (1) can be ignored and kx gives a good representation of the applied force. Most firing rigs rely upon this and filter out electrically any components above about $\frac{\omega_n}{2}$. ω_n is raised to the highest practical value by keeping M to a minimum and k to a maximum. It is often impossible to raise ω_n sufficiently and it is then necessary to measure the other terms of the equation. The errors in amplitude and phase incurred by measuring only kx at various ratios of $\frac{\omega}{\omega_n}$ and at various damping ratios are shown in Fig. 2. The damping ratio, λ, is given by $\lambda = \frac{C}{C_c}$ where C_c is the critical damping coefficient at which oscillation just fails to occur when the system is shock excited. It can be seen that a reduced error in one results in an increased error in the other.

2. COMPLETE EVALUATION OF EQUATION OF MOTION

2.1 Practical rig construction and signal conditioning

Rigs have been constructed in which a load cell forms the spring, an accelerometer measures the $M\frac{d^2x}{dt^2}$ terms, and the force generated by two damper pistons is measured by load cells. The outputs of all these devices are summed by amplifiers and networks to give a true representation of T throughout the firing. The value of the term $C\frac{dx}{dt}$ measured by such a system may be in error if other damping is present and it may then be better to derive the term from another measured term.

If the system is oscillating

$$x = A \sin \omega t \quad \text{where } A \text{ is the amplitude of oscillation}$$

$$\frac{dx}{dt} = A\omega \cos \omega t$$

$$\frac{d^2x}{dt^2} = A\omega^2 \sin \omega t \quad .$$

$\frac{dx}{dt}$ can be obtained by differentiating x or by integrating $\frac{d^2x}{dt^2}$. In practice the latter course has been found preferable because any noise spike on the x signal results in a large value of $\frac{dx}{dt}$, whereas noise in $\frac{d^2x}{dt^2}$ is diminished by integration.

A block diagram of the signal conditioning equipment is shown in Fig. 3. The output from the load cell is buffered by an operational amplifier (No. 1) in which the gain may be varied between 0.1 and 10000. These amplifiers are used throughout and were chosen to have a high input impedance (100 MΩ), 140 db common mode rejection ratio and low offset drift of 1 $\mu V/^oC$. The output from the accelerometer goes to a similar amplifier (No. 3) and both amplifiers feed into opposite differential inputs of a further amplifier (No. 4) which adds them vectorially.

If the damping force is measured directly, the load cell which measures it feeds to a third amplifier (No. 2) and the outputs from this and from amplifier No. 4 are again mixed in amplifier No. 5. Resonance of the individual transducers may cause the combined output to contain unwanted high frequencies which limit the upper frequency response of the system. The final mixed signal is therefore fed via a buffer to a low pass filter stage which can be set to cut at any desired point in the frequency range of the equipment.

If damping force is not measured it is derived by feeding some of the $M\frac{d^2x}{dt^2}$ output from amplifier No. 3 to amplifier No. 6 which has a suitable integrating network operating over the frequency range 50 Hz to 1500 Hz. The low frequency response is limited to prevent the integrator from running out of range and in any case damping forces are expected to be low in this region. The output of amplifier No. 6 can be switched into the input of amplifier No. 4 in place of that from the damper amplifier, No. 2.

2.2 Calibration

The gains of the appropriate amplifiers must be adjusted to represent the values of k, C and M and it is possible, if tedious, to determine these individually and set up each amplifier. In practice this would be difficult and an empirical system based on the response of the rig to shock excitation is used. The shock is produced by striking the rig in an axial direction, preferably with an instrumented hammer containing a piezoelectric element which records the force and has a high natural frequency.

The kx channel is first calibrated and adjusted using static loads produced by deadweights or by methods described elsewhere in this report. The rig is then shock excited with the gain in the $C\frac{dx}{dt}$ channel set at zero. The gain of the $M\frac{d^2x}{dt^2}$ channel is adjusted to produce a minimum in the $M\frac{d^2x}{dt^2} + kx$ combined output. The $M\frac{d^2x}{dt^2}$ and kx signals are 180^o out of phase with each other and the minimum combined signal is at 90^o to each, as is the $C\frac{dx}{dt}$ signal. The $C\frac{dx}{dt}$ signal is now adjusted so that it just cancels out the remaining signal. The impulse recorded should now be a replica of that indicated by the instrumented hammer. Any higher frequency components present may now be filtered out by adjusting the cut-off point of the final filter circuit.

2.3 Practical problems and results

The practical problems in the use of such an arrangement are that rigs may have more than one resonant frequency, particularly when feed pipes and other connecting devices are required, and that few behave as a simple spring and mass system. Every attempt should be made to keep the rig simple to obviate these troubles, but if this is not possible the transfer function of the conditioner can be suitably adapted. In the simplest case, notch filters may be used to remove unwanted resonances and if they are sufficiently narrow they need not cause unacceptable distortion in the final output.

Fig. 4 shows the uncompensated response of a typical rig to an impulse, i.e. the signal produced by the load cell in the kx channel. Fig. 5 shows the response to the same impulse when both $M\frac{d^2x}{dt^2}$ and $c\frac{dx}{dt}$ channels are correctly adjusted.

Fig. 6 shows the results of a firing of a short burning time motor on a relatively undamped rig measuring only kx . Fig. 7 shows a similar firing in which full compensation was used, and reveals an unexpected, but real, negative kick in the rising part of the thrust curve. Comparison of the pressure and thrust curves indicates the effectiveness of the system.

3. BALLISTIC MEASUREMENT OF IMPULSE AND THRUST

3.1 Basis of the ballistic approach

An alternative to measuring or deriving all the terms of the equation of motion of a firing rig, when it is not possible to raise the natural frequency sufficiently, is to reduce the stiffness and damping to zero. The equation of motion of the previous section then reduces to $T = M\frac{d^2x}{dt^2}$ and it is necessary to measure only the acceleration of the motor and any mass attached to it. This is a practical solution only when the total impulse of the motor is small if the necessary mass to which the motor is attached is to be kept within practical limits. This constraint limits the usefulness of the technique to motors having burning times of tens of milliseconds at current thrust levels.

3.2 Ballistic pendulum system

Various ballistic measuring systems have been used to measure short duration forces, the most common being the ballistic pendulum. This was initially considered to be a solution to the problems of thrust measurement in motors with high thrust and short burning times. It depends upon the fact that in the absence of other forces:

$$\int_0^t F\,dt = MV$$

where F is the instantaneous thrust
t is the time for which the thrust acts
M is the moving mass
V is the final velocity assuming the mass to be initially at rest.

This is true if the mass and pendulum length are sufficient for the mass to move negligibly during the impulse. The impulse is deduced by measuring the final position of the mass at the peak of its swing. Usually its increase in height is measured directly or indirectly to give its gain in potential energy, which is equal to the initial kinetic energy and hence the impulse is known. A thrust/time curve may be obtained from an accelerometer mounted on the pendulum, but the accuracy is limited and calibration is difficult.

If displacement of the mass during the impulse is significant an allowance must be made. Its displacement must be measured at the end of thrust as well as at maximum swing. This assumes that the thrust can be considered to rise and fall instantaneously and remain at a constant value when applied. A real rocket motor is likely to generate a thrust which varies with time, so that F must be known as a function of displacement and measured with an accelerometer. Acceleration and velocity may also be derived by direct measurement or by appropriate differentiation of displacement along the arc of swing, but accuracy is not likely to be great.

The practical problems involved in the realisation of an accurate device are considerable. The mass of the pendulum, including anything attached to it must be known, and this changes with consumption of the motor charge. With a reasonable pendulum length the mass must be large (about 1000 kg with current motors) to minimise travel during the burning time. This involves a suspension having a substantial mass and this, with the finite size of the main mass, means that the moment of inertia of the combination about the pivot must be calculated or measured. A parallel motion suspension avoids the problem of the distributed mass of the pendulum, but the inertia of the suspension must be known.

Determination of the position of the centre of gravity of the mass at its maximum swing is difficult and allowance may be necessary for any motion in directions other than the intended direction of swing. This is particularly important if the measuring point on the mass is not at the centre of gravity and there is rotation about the centre of gravity. It is convenient to measure angular swing near the pivot, but there must be no bending or vibration in this region if errors are to be avoided. Frictional losses in the bearings needed to support the large mass may have to be evaluated, probably by measuring successive swings, and some means of arresting the pendulum must be provided.

Most of these problems can be overcome by allowing the mass to move horizontally after the impulse, and measuring the integral of the force required to bring it to rest.

3.3 Description of alternative system

The system finally selected is shown in Fig. 8. It consists of a mass M , the value of which need be known only approximately, supported on three low friction linear bearings sliding on horizontal rods. The motor to be tested is mounted on the rear face of the block so that it accelerates the mass along the rods for a short distance without resistance during the motor firing. An accelerometer mounted in the block on the motor axis near the front face produces a thrust/time curve since $F = Ma$, where a is

the acceleration. It is situated in this position to keep it as remote as possible from shock excitation from the rocket motor. The mass of the block is approximately 1000 kg to ensure reasonable lengths of travel during the firing time and reasonable final velocities with motors in the impulse range of 400 to 1500 Ns for which the equipment was designed. Since the block is approximately a 500 mm cube its lowest resonant frequency is such that $\lambda = 1$ m , i.e. 5 kHz. If this frequency is excited a low pass filter must be incorporated in the recording system to cut at a suitable frequency below this value. The accelerometer used in the initial experiments is an Endevco Model 2262-1000 piezo resistive type to match into existing instrumentation. It has an output of 0.5 mV per g and a natural frequency of 6 kHz, response being flat to within ±5% from 0 to 2000 Hz. This latter characteristic governs the cut-off frequency of the thrust measuring system in most cases.

After the end of motor burning the mass travels a short distance and is then brought to rest by a device which applies a constant decelerating force for a time which is inversely proportional to the magnitude of the force and is chosen to be such that normal recording and integrating systems can be used. A typical combination is 4000 N for 250 ms resulting from a motor impulse of 1000 Ns.

The initial decelerating device was designed as an oil filled piston and cylinder pressurised to a pre-selected value from a nitrogen gas reservoir large enough to prevent the pressure from altering significantly during the arresting period.

Subsequently, a commercial device was found to exist, in which the cylinder is perforated with a series of adjustable orifices which are closed in turn by the piston to achieve a similar effect. This is shown in Fig. 9. The device is mounted on the end of the frame carrying the rods which support the mass. The frame is supported by flexures and coupled by a rod flexure to a load cell and damper unit which measures the force applied to the decelerator. The time integral of this force is equal to the motor total impulse if there are no losses in the system.

3.4 System accuracy

Friction of the linear bearings could cause inaccuracy although their coefficient of friction is probably less than 0.005 when they are in good condition. To avoid such errors, whatever the condition of the bearings, the support rods are mounted on flexures so that the load cell measures the frictional forces generated in the bearings. Frictional forces in the retarding device are also measured by the cell so that losses from these effects are negligible.

The accuracy of measurement of total impulse depends on the load cell and recording devices. Since the retarding device gives rise to a sensibly constant decelerating force, the load cell may be operated close to its working maximum and should hence be capable of an accuracy of 0.1%. Digital recording and analysis devices used are capable of an accuracy of better than 0.1%. The cell is calibrated with a standard cell of 0.05% accuracy to achieve an overall accuracy of 0.2% in total impulse measurement.

Any stored elastic energy in the measuring system or retarding device may result in the mass acquiring a small velocity in the reverse direction after its arrest. If this is significant it is necessary to latch the mass to the arrester when it makes contact and to subtract from the integral any negative thrust produced during the final rebound.

The error in accelerometer measurement of thrust may be evaluated as follows. Let the permissible error be 1% and assume a coefficient of friction of 0.01. Since the mass is 1000 kg the frictional force is approximately 100 N, so that the minimum thrust is 10000 N to achieve 1% accuracy. If the total impulse is known to within 0.2% a greater error than 1% in thrust is probably acceptable as the shape of the thrust curve is usually more important than spot readings. Accuracy is probably limited by the accelerometer to ±5% for the higher Fourier components of the thrust transients, but can be shown to be within this limit provided that the rise time of the rocket motor thrust is not less than 2 ms. Except during the thrust transient an accuracy of ±2% is achieved.

Air drag is negligible since the force on the block at maximum velocity with the greatest total impulse envisaged is about 3 N, and since this acts for 20 ms at most the error in impulse is 0.06 Ns.

3.5 Use of the equipment

If it is assumed that a motor of total impulse I Ns and maximum thrust F Newtons is to be tested the thrust at the load cell must be spread over about 0.25 sec or longer to permit a sufficiently accurate integration of the thrust. The range of the load cell must thus be such that it can measure accurately a force, F_1 , where

$$F_1 = \frac{I}{0.25} \text{ N} \quad .$$

The linear decelerator must be adjusted to provide this decelerating force.

The maximum acceleration of the mass is given by

$$a = \frac{F}{10^3} \text{ m sec}^{-2}$$

so that the gain of the accelerometer amplifier must be set to accommodate the accelerometer output at this value.

The load cell must be calibrated in the usual manner with reference to the site standard.

The mass must be in its starting position and the motor attached to it firmly. To obtain an accurate thrust representation all mating surfaces must be machined flat to the best engineering tolerances and a film of grease may be applied to take up any remaining clearance between surfaces.

Recording of load cell output must be by a digital system with a resolution of better than 1 part in 1000, and a sampling rate of not less than 1 kHz and preferably above 5 kHz.

The accelerometer measurement must be recorded by a digital system with a sampling rate of at least 10 kHz or by an analogue system with a flat response to 2 kHz.

The thrust integral is obtained directly from the digital recording of the load cell output. The accelerometer recording can be integrated in terms of trace displacement, d, against time, t. Thus, for the accelerometer calibration constant, K:

$$K\int d\,dt = \int F dt = I$$

$$\therefore K = \frac{I}{\int d\,dt} .$$

3.6 Summary of advantages

This equipment permits measurement of the total impulse of motors with short burning times, with the same accuracy and using the same auxiliary equipment as for motors with long burning times. The thrust/time curve can be recorded using an accelerometer which need not be directly calibrated. It is easier to use and avoids most of the errors inherent in a ballistic pendulum. The mass must be known with only sufficient accuracy to permit adjustment of the range of the measuring systems, and only a static calibration of the load cell is required. It is capable of measuring total impulse with an accuracy of ±0.2% and instantaneous thrust, within frequency limitations, to ±2%.

4. CONCLUSION

Both these systems have performed satisfactorily and have their individual areas of application. The first is particularly suited to measuring starting transients of large motors, but it must be appreciated that any significant change in the mass, M will introduce an error in the compensation.

The second technique can only be used with short burning time motors if the moving mass and its distance of free travel are to be kept within practical bounds.

Future work is likely to make use of the high sampling rates of current digital recording and analysis systems, to process the signals after they have been recorded. This has advantages such as the ability to change coefficients progressively through the recorded firing.

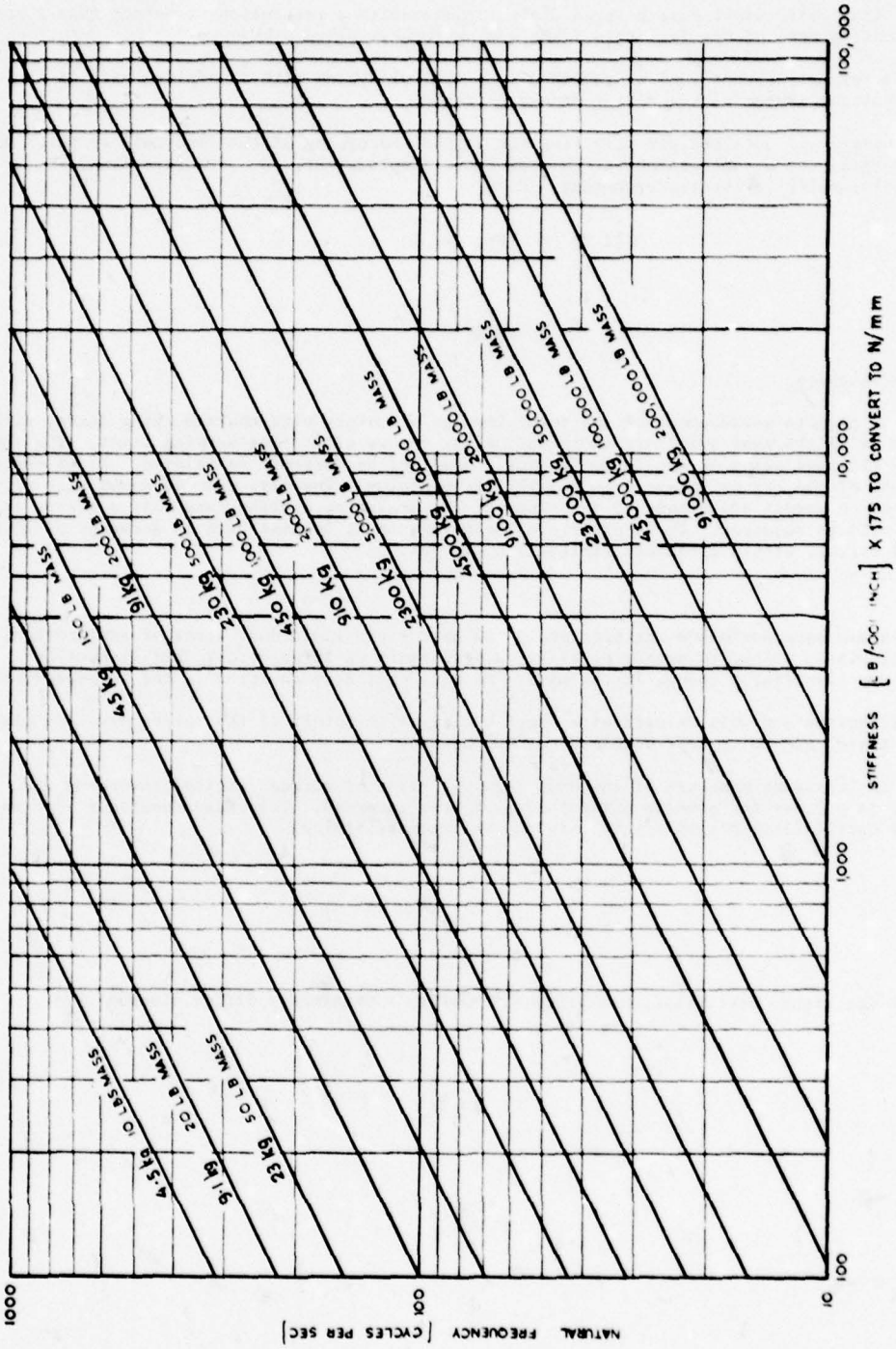

FIG. 1 NATURAL FREQUENCIES OF SPRING AND MASS SYSTEMS WITH ONE DEGREE OF FREEDOM

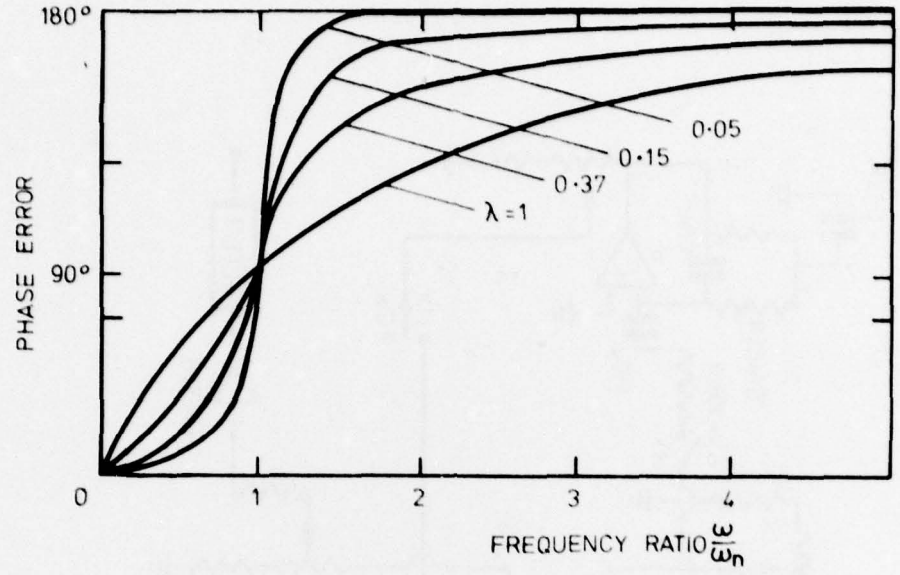

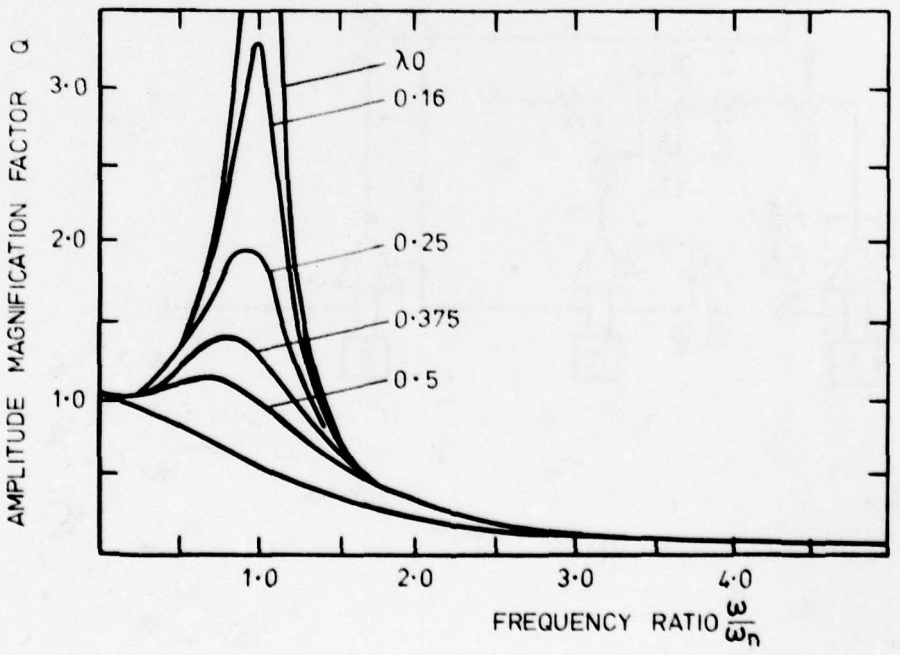

FIG. 2 PHASE AND AMPLITUDE ERRORS IN DAMPED RESONANT SYSTEM

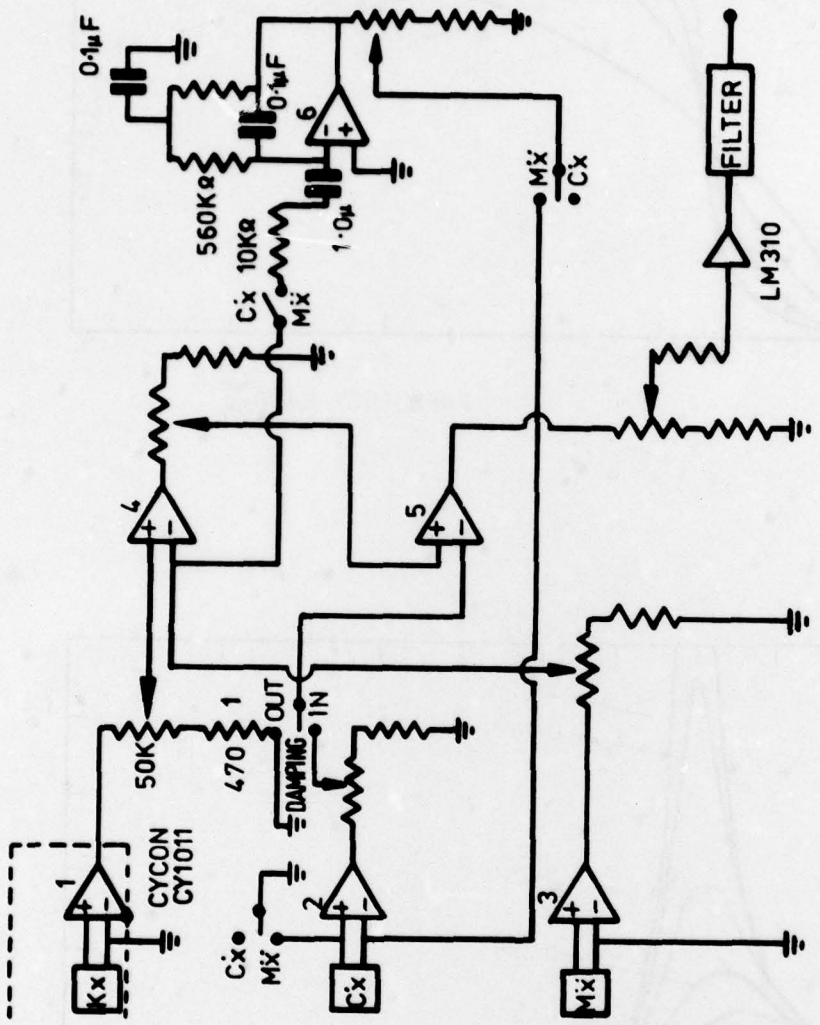

FIG. 3 BLOCK DIAGRAM OF SIGNAL CONDITIONING EQUIPMENT

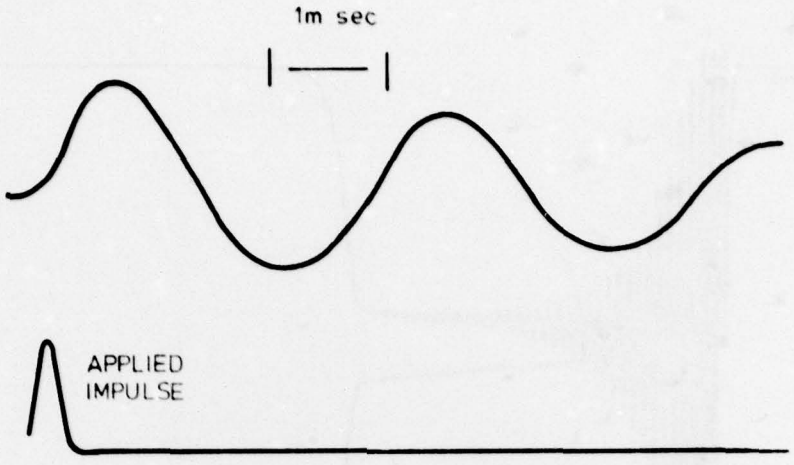

FIG. 4 UNCOMPENSATED RESPONSE OF THRUST RIG

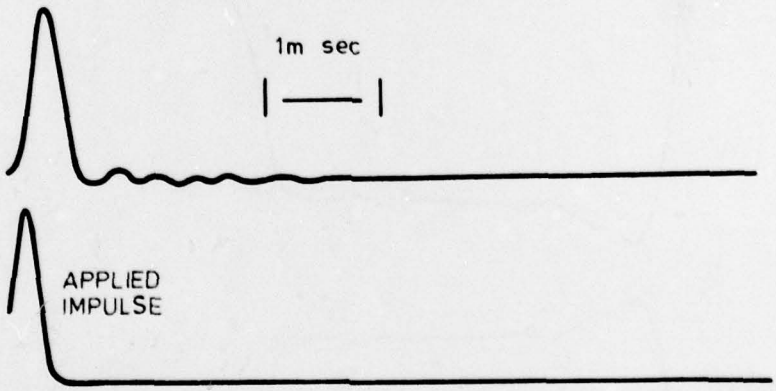

FIG. 5 COMPENSATED RESPONSE OF THRUST RIG

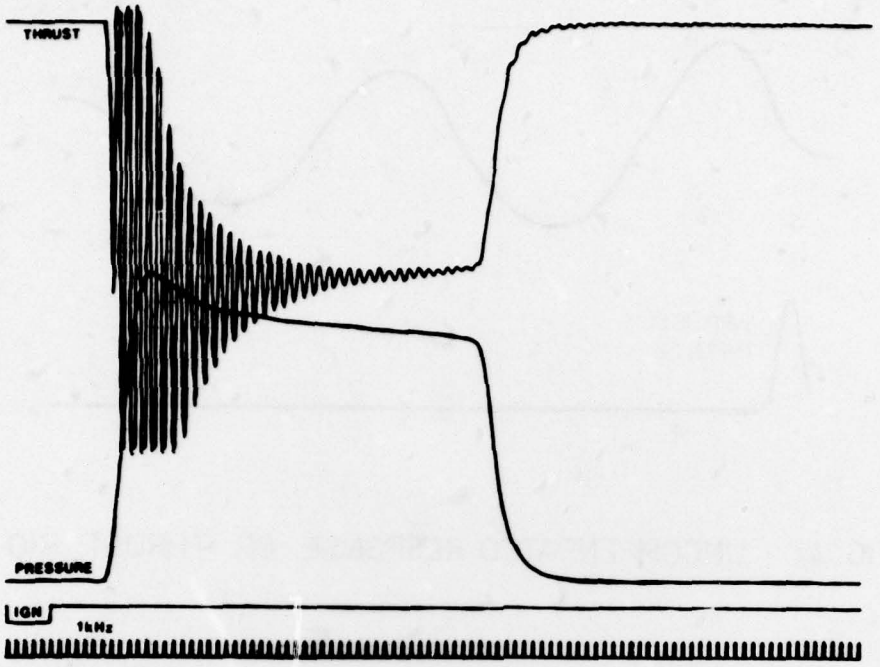

FIG.6 FIRING ON UNCOMPENSATED RIG

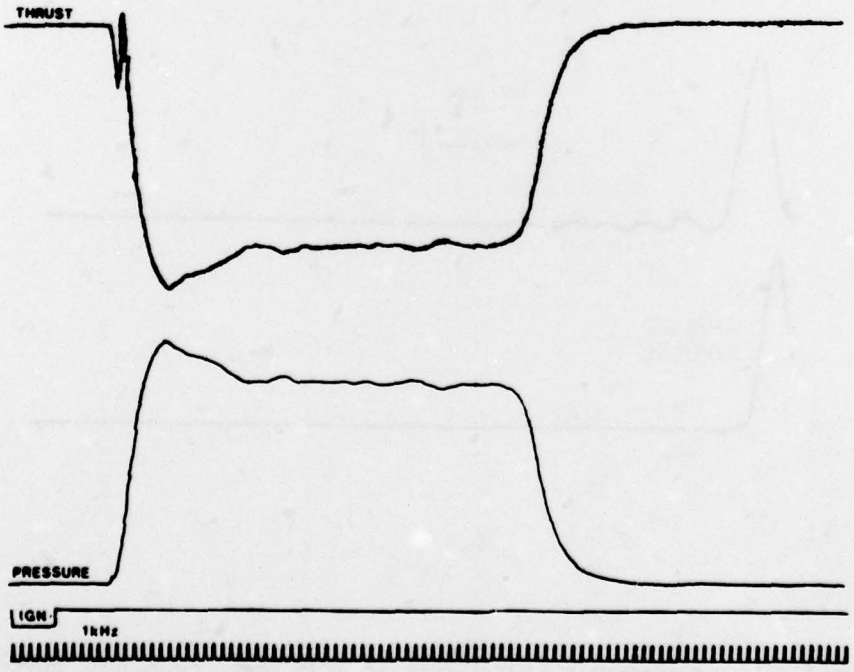

FIG.7 FIRING ON COMPENSATED RIG

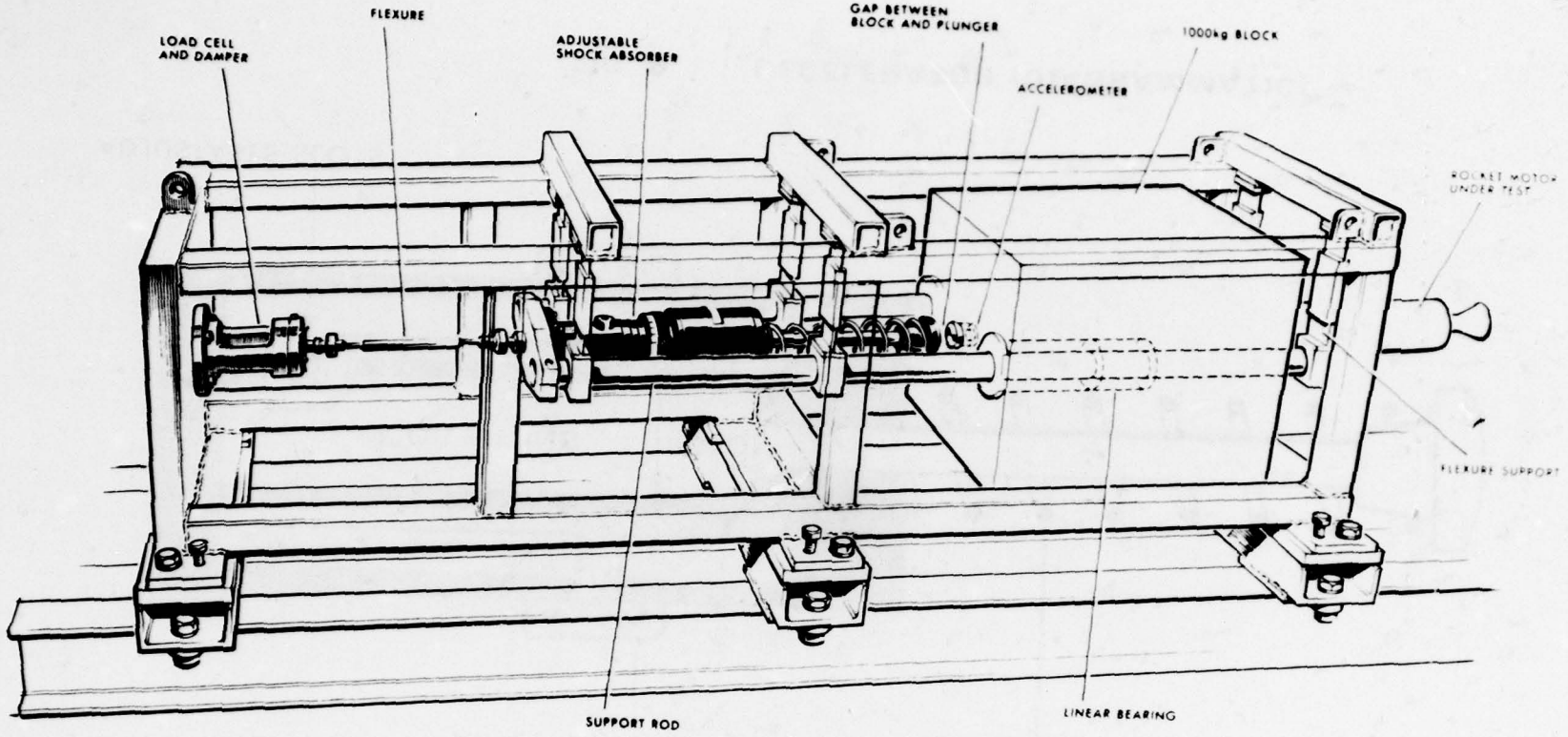

FIG. 8 BALLISTIC THRUST AND IMPULSE MEASURING DEVICE

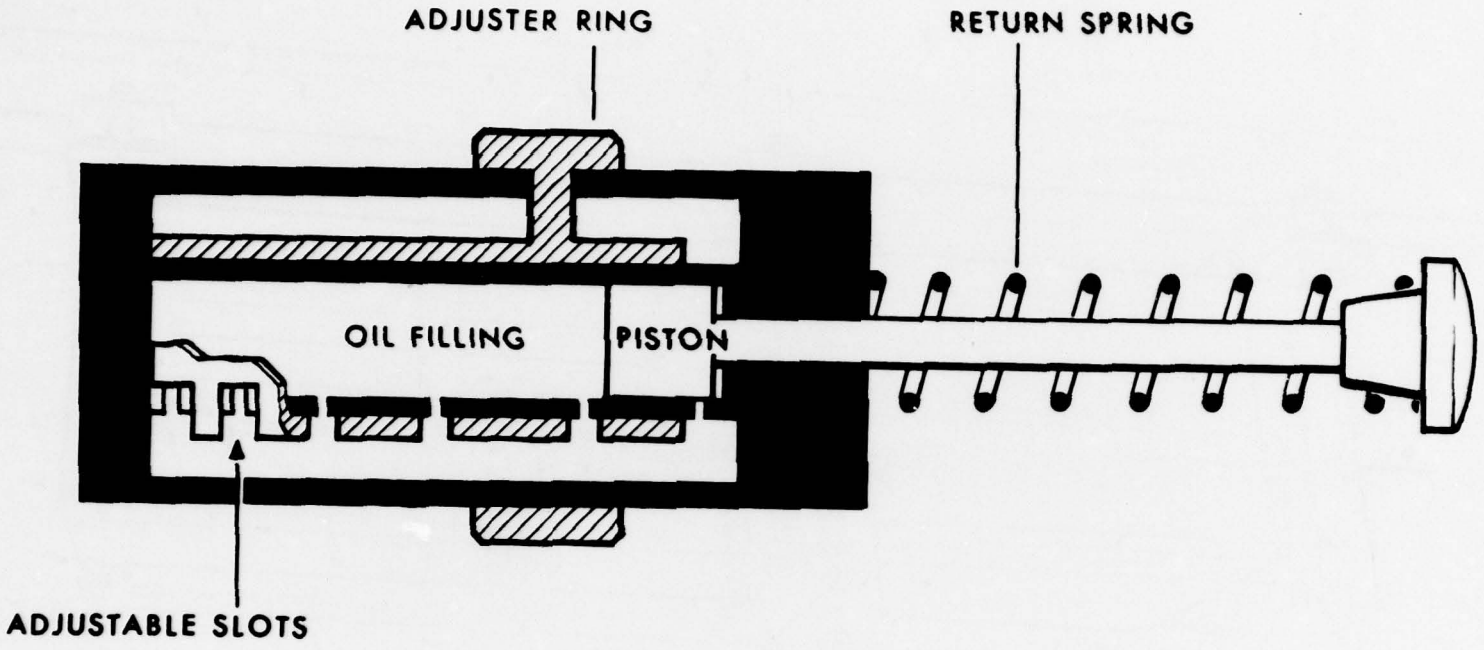

FIG. 9 DECELERATOR (DIAGRAMMATIC)

ROUND TABLE DISCUSSION

The Chairman, Professor Casci, opened the discussion by introducing the Round Table Panel Members:-

Prof. C.Casci	Italy (Chairman)
Mr R.Heron	UK
Dr R.Strecker	Germany
Mr M.Barrere	France
Prof. F.E.C.Culick	USA
Mr W.G.Haymes	USA

Professor Casci called upon Mr Barrere to review the work in Session V of the conference.

M.Barrere: In order to summarise the situation on combustion instability, I will ask you to consider three points. First of all there is the definition of the problem, secondly the advances given in this conference and thirdly the direction in which research and technology is moving in the future.

On the first point there are perhaps different ways of examining the problem. There are the progress aspects of basic research by which is inferred the analytical studies to enable us to better understand the phenomena. This enables one to try and construct a model by experimental or theoretical means so that we can proceed to verify the analysis. I think the first aim of the basic research should be the determination of the transfer function of the propellant under the imposed regime.

The program of research work involved setting up tests or synthesis, that is for example the design of a small scale motor duplicating the characteristics of a large motor. The small scale prototype is used to obtain basic data to enable the phenomenon to be modelled. Research and technology is aimed at obtaining information of direct interest and application for the motor constructor.

In considering the essence of the problem one must ask what are we seeking and what is the end objective? In this context there are a number of points I will try to summarise. One important objective is to predict whether a given motor design will be stable or exhibit combustion instability. This is of great importance to the motor manufacturer. Another important objective is to determine what remedies can be applied to existing motors which exhibit combustion instability. Research is necessary to find ways of suppressing the instability. A further desirable aim is to predict the pressure evolutions in the combustion chamber from the inception of ignition. For certain applications the variations in the rate of burning and pressure during transitory phase regimes is very important.

There is a need to co-ordinate this work more closely with the propellant formulation field. I would like to underline my impression that there is insufficient communication between combustion instability specialists and propellant formulators. It must be the role of AGARD to act as a communication forum, to establish the difficulties of the problem from the viewpoint of both specialities. AGARD must seek to give guidance to the propellant and motor manufacturer.

Let us consider what emerged at this conference. Many contributions were in the field of basic research, emphasising the problem of determining, as accurately as possible, the response function of the propellant. This function is very important, since an accurate knowledge of its value is fundamental to many of the other characteristics of instability including burning rate and pressure effects. The determination of the transfer function of the propellant under fluctuations of burning rate and pressure during the transitional phase was central to many of the contributions.

An exposition of fundamental research was given by Professor Culick on the acoustic mode wave propagation in the gas. Analytical methods were presented for modelling the mechanism with attention being given to the third order acoustics. Mr Luca discussed fundamental studies of the surface response, such as the time dependent variation of surface temperature. This is a very complicated and difficult area but there is a wealth of possibilities from such studies. The propagation of temperature in the solid substrate may be reduced to the resolution of differential equations but to do this requires more knowledge of the interfaces – the precise boundaries and a better knowledge of the surface reactions. It is important to determine the mechanisms of what happens at the surface. Mr Kuentzmann presented some of the work done at ONERA on combustion instability. He showed that in some cases there was correspondence whilst in others there was no good correspondence between theory and experience and between different scaled systems. The study of losses must be pursued further and the non-linearity of the phenomenon is important to analyse.

Does all this basic research interest the motor manufacturer? A paper by Derr et al. implies it does. The constructor can now predict with reasonable precision the occurrence of instability but progress is perhaps proceeding slowly in improving our understanding of the problem and its remedies.

We had an exposition on low frequency instability which is a special case where some rocket constructors are more worried about this region generally during the evolution at low pressure. Again a paper by Mr Hughes showed the importance of the study of the non-linearity of the instability.

Equally we had a paper by Mr Evans on the suppression of instability by inert particles. There were important experiments since the field of particle losses is still not well understood.

What can we conclude about the future from the results of this conference? All the fields previously mentioned are important and basic work although very costly is well justified. There is a need for the analytical and fundamental studies to continue on a theoretical and experimental plane. The theoretical plane should emphasise the study of non-linearity

and the experimental plane should aim at determining the propellant response function. The modelling of the combustion process must explain the effects of non-linearity and the prediction of losses is an important aim of research.

Professor Casci called on Professor Culick to comment on Session II of the Symposium.

F.E.C.Culick: Session II was concerned with ignition, extinction and internal ballistics. The first two topics are of course transient processes. Ignition can be considered in two aspects, firstly those areas concerned with hardware and practical technology are not in my field of experience. A number dealt with this aspect. The second aspect has to do with computations of criteria concerned with ignition and extinction to determine the conditions under which these transient processes perform their role.

In general, computations on these transient processes assume certain models of which a number of well known combustion models have been quoted in this session. All these models fall into the same class by making the basic assumptions that the gas phase behaves in a quasi steady manner. This assumption clearly fails during the ignition and extinction process. For example during ignition there is initially no flame whilst eventually there is flame and vice versa for extinction.

Therefore arguments which prove the virtues of one model versus another are somewhat superfluous since all have this same crucial assumption. All give the same results in form although numerically different, primarily because the only transient process considered explicitly in such computations only involve unsteady heat transfer in the solid phase. The time dependent processes in the gas phase are totally ignored. This problem has not been addressed in this session.

With regard to internal ballistics, we may be paying the penalty of having largely ignored this area for many years. In most cases very simple computations of one dimensional ballistics are adequate, but there are some crucial problems which have arisen in recent years. One of these is the heat transfer process in complicated grain geometries. This was not discussed at this session. However, another problem was discussed, namely erosive burning. I confess to a prejudice on this topic in that I favour the integral methods as having most promise. If the integrations can be properly done one can smear out errors and make good approximations more readily. The results are less costly. The erosive burning problem can in the main, be taken care of in practice by trial and error. However, in transient processes the time dependent counterpart of erosive burning i.e. velocity coupling has not had adequate treatment of its physical processes. The kinematics of velocity coupling has been well done but not the physical processes.

Until the steady state character of erosive burning has achieved greater understanding, I do not think that velocity coupling can be properly approached.

Finally on internal ballistics there is another subject which has not been treated in this session. More recently there have become real possibilities of 2 or 3 dimensional axisymmetric computations, to develop more detailed velocity field features in the motor. This study would be useful to the erosive burning and velocity coupling problems.

Mr Heron was called upon by Professor Casci to make some observations on Session III.

R.Heron: I make my comments as one who had left direct involvement in the scientific field for many years to be concerned with management and administration. My original special interest was the field of internal ballistics and when I started platonisation of double base propellants had only just been discovered and nobody knew how the additive worked. At that time aluminium had not been used in composite propellants. There were those who said aluminium could not work, it would not burn effectively and yield the expected performance.

From this vantage point I can say how impressed I am with the advance of understanding in the field of combustion. The paper given by Norman Cohen presented an excellent review of the state of the art. The papers in the session were an eloquent testimony of the role of aluminium and the interesting facets of its behaviour, illustrating the much greater insight since the early days of which I spoke. We witnessed in the paper by Dr Kraeutle et al. work aimed at tailoring aluminium combustion particles to suppress specific frequencies of acoustic instability.

All the sessions at this conference dealt with aspects of combustion, ignition, extinction which are really all related to the central aspect of combustion stability. In the context of many military applications we are frequently concerned with very small, very short burn motors. These present much greater problems for ignition and stable burning than the very large motor. Such small motors, burning for some millisecs present real problems of transient processes, where more fundamental research is required.

In the UK it has become fashionable for over a decade to demote the work in fundamental combustion analysis and modelling together with fundamental studies of propellant burning mechanisms. Superficially it is difficult to establish concrete returns particularly in competing for financial resources with other short term but pressing priorities. I believe this is a mistake, since, amongst other reasons, this kind of work generates the kind of people and attitudes of mind which can have marked beneficial effects on development work and on the propellant and rocket motor practical state of the art.

Some observations on Session IV were requested from Dr Strecker by Professor Casci.

R.Strecker: Three papers were presented on new propellants, one paper on a new technique of application and one on propellant ageing.

The paper on plastic screen structured propellants by Camp et al. showed a means for overcoming the debonding problem in short burning motors. It seems to me that the application of a lacquered or solution form of the smokeless double base propellants, enables more energetic propellants utilising higher nitroglycerine content to be facilitated. These

propellants are normally handled on hot rolls or mills which are limiting and they have inferior strength which is alleviated by the reinforcing plastic screen.

The second paper dealt with the use of ammonium nitrate in gas generator propellants. By using phase stablised ammonoum nitrate then the well known problems of this very useful oxidiser can be overcome.

The paper by Mr Gotzmer on a new binder system tackles the problem of ageing behaviour and mechanical properties of the binder. As long as double bonds occur in binders or the use of curing agents such as the aziridine type continue, then the binder will be susceptible to degradation by oxidation or thermal decomposition. The introduction of nitrile groups improves ageing character, an alternative is to saturate the double bonds, providing liquidity of the binder is maintained.

It was interesting to note the means of tailoring the low temperature properties of this binder by adjusting the nitrile content. Also the manufacturing method employed was of interest in reducing capital tooling costs. This involved the use of conventional vertical mixers to produce a liquid polymer propellant which was partially cured before proceeding to a conventional extrusion process.

The fourth paper dealt with new propellants of the composite smokeless double base kind. Mr Davenas spoke of the ways of increasing energy with nitramines as well as the improvement of mechanical properties at low temperature by the introduction of cross-link systems.

I must make some criticism of the under-representation in the conference of papers on new propellants for rocket motors. Propellants are the major part of the rocket and we know of the problems which still exist with propellants.

I would urge the PEP to organise a special meeting devoted to the subject of new propellants.

Professor Casci asked Mr Haymes to comment on Session VI.

W.G.Haymes: Session VI dealt with heat transfer and materials and was a small session, consisting of three papers which covered a wide scope. We had one paper by Mr Kampa dealing with jet vanes in TVC systems, one paper by Mr Parrat who speculated on the use of composite materials in rocket motors and a paper by Mr Bonnet on materials characterisation and methods of analysis.

Some comments I would make are more specific to tactical military applications. There is a need for research and development in new materials, particularly since we are increasingly becoming involved in environmental and health considerations. The latter affect materials used historically such as asbestos fillers, both as heat resistant and structural reinforcement. There is a real need for substitute materials to be evaluated, selected and characterised.

Also for tactical motors it is important to reduce weight and cost which present a continuing challenge to the materials specialist.

I would like to comment on the design and analysis area. Using finite element and finite difference techniques, that are applicable to transient heat flux problems, we have strong methods for predicting thermal history and distribution. I think this area is ahead of the material characterisation area. The analyst lacks sufficient data on materials to work with and make the best predictions with available analytical methods. This area can be improved with better and fuller material characterisation, even with existing materials under large temperature/pressure ranges and shear flow effects if these are applicable.

There is one analysis area to be improved on which is worthy of comment. Methods or models are used to predict the progressive ablation fronts of materials as a function of surface flow or energy fluxing into the surface. The techniques available are difficult to use and of questionable accuracy. These should be improved.

Professor Casci asked Mr Haymes to address himself to the next question submitted by G.I.Evans, IMI Summerfield, UK.

Question: "Could the panel comment on the direction in which propellants/rocket motors should proceed for future applications in the tactical missile field. In particular, commenting on the influence the following facets may have on such propellants – (1) Rocket exhaust properties of smokelessness and low signature in the visible to far infra-red. (2) Propellant mechanical properties, particularly strain capability at low temperatures. (3) Safety requirements such as fragment attack and the susceptibility of the motor/propellant to explosion or detonation."

W.G.Haymes: There has been an increasing emphasis, in the last few years, to develop propellants and motors which will display a reduced observable characteristic, to whatever sensing device is applicable to the mission. Usually we are concerned with visible smoke. This has led in the USA to the development of the so-called reduced smoke propellants. These involve elimination of aluminium and leaving only ammonium perchlorate. Our next objective is to further improve these by reducing the exhaust condensibles obtained from such composites.

This emphasis on such minimum smoke propellants will continue for the next few years. The emphasis will be on widening the useful range of burning rates, lower pressure exponent, better π_k to broaden their application.

This leads on to the last part of the question in that the propellant mechanical properties will be a big topic, if we are going to apply minimum smoke propellants to tactical missiles. Such missiles can have extreme environments such as wide temperature limits, high acceleration for air launch systems, shock and vibration for aircraft carrier systems and aerodynamic heating.

Composite propellants have been developed to meet these conditions but the minimum smoke propellants have yet to be fully developed to these rigours. Safety is a matter of policy for the system characteristics. It is a matter for the systems or user people to stipulate the safety requirements. If Class 7 (US classification) propellants are acceptable then these can be provided. However, if Class 2 is required then the reduced energy and other penalties or trade-offs have to be accepted.

M.Barrere commented further that for smokeless applications the igniter is an important area. Similarly the inhibitor can be the dominating influence in rocket smoke performance not least in the smoke emitted at motor all-burn.

Question and Answer Session

Professor Casci introduced a question by R.Lo of DFVLR and invited Mr Barrere to answer.

Question: "What is the future, if any, of liquid injection into solid rocket motors with respect to thrust modulation, specific impulse augmentation and extinction? What is the future for high energy ingredients such as hydrides, fluoramines etc?"

M.Barrere: Although thrust variation may be achieved, in my experience there is little to be gained in SI augmentation by liquid injection. By contrast there may be a useful field in extinction of rockets.

A lot of research has been done and I can summarise that done at ONERA, but I must emphasise that this has not led to any practical application. For example, the kind of modulation by liquid injection that one can practically and readily achieve gives pressure exponents of burning close to unity. If one does not stop the liquid one can even achieve a stable condition where the pressure exponent exceeds unity.

Equally from the point of view of modifying the combustion mechanism one generally finds the liquid in no way modifies the combustion of the solid. Both by calculation and experience one is able to determine that the useful range of SI augmentation is not great and in some cases the SI is lower.

With respect to extinction, the aim must be to minimise the amount of injected liquid necessary. According to research in the USA a very large mass of liquid is required for short duration times.

The modulation of thrust is a very desirable aim for solid propellant motors. A number of methods are possible with liquid injection, for example by using a mixture of very rich and deficient propellants.

With regard to high energy ingredients, it is important to emphasise that for military applications there are other, at least equally important, considerations that have to be weighed against specific impulse increase. The exotic ingredients for higher energy formulations can entrain serious practical difficulties such as storage and shelf life limitations. The requirements for smokelessness and other features may mitigate against most of the high energy ingredients. The essentials usually require a compromise which in itself is determined by the mission or application in the military field. These considerations are less restrictive with space application.

R.Heron commented further on this question: A solid propellant rocket motor is a very simple device in principle, made possible by the efforts of propellant chemists and design engineers. If you wish to impose on this device the capability of modulating the thrust on demand, extinguish the rocket on demand and render the exhaust smokeless with a low radar attenuation plume etc., then the result is much more complicated. I think that in this case then one might as well go for a wholly liquid propellant motor, possibly a packaged liquid motor.

Professor Casci requested Dr Strecker to comment on a question from Mr Korching of Prins Maurits Laboratory, Netherlands.

Question: "Can you comment on future trends in propellant formulation with respect to oxidiser type, binder, plasticiser, burning rate catalysts? In particular the influence of these on specific impulse, low smoke, burning rate extension, shelf life is of interest."

R.Strecker: Much of the euphoria in research and development with the more exotic oxidisers has declined or ceased. They are either too expensive or not compatible with the binder or unstable in themselves. In the latter case I am thinking of hydrazine diperchlorate. So in effect we are left for the foreseeable future with AP, RDX and HMX.

With regard to low smoke and the use of nitramines, we have to consider the requirements of the various services. It appears the air force and Navy will not allow propellants of Class 7 or NATO 1.1, so this leaves us with AP and the corresponding minimum smoke propellants.

For the binder type of HTPB polymer is becoming the work horse. It will replace increasingly the CTPB, PBAA, PBAN polymers. Nevertheless we do have some ageing problems due to the double bonds in HTPB and effort will be required to improve on this.

In commenting on plasticiser, I assume high energy plasticisers were the topic of the question. Despite considerable research effort we currently have to be content with nitroglycerine as the only accepted plasticiser. Others such as FIFO, TVOPA have problems in cost and production requiring further work.

The situation with respect to burning rate catalysts is well known. There are some which give high burning rates such as the carboranes, but we have to use a high concentration and the cost is too high.

R.Heron commented further: Anyone who looks at the propellant scene in the UK from the outside, may be surprised at first glance at the extensive use of double base systems for tactical applications. This is due to the emphasis we have always had to accept for low smoke. This has led to much concentration on inhibitors and igniters for low smoke performance. We have put priority in the UK into the development of elastomer modified double base. This enables us to case bond, without stress relief, over a wide operating temperature.

Professor Casci *summarised the discussions and the panel's sessions in his concluding remarks.*

Mr Barrere in his observations highlighted three areas namely steady state of burning of solid propellants, unsteady burning of solid propellants and rocket motor design.

For propellant steady state burning, contributions were given to the meeting on advances in propellant chemistry and combustion modelling. Some experimental evidence was given to further our understanding of aluminium combustion.

As for the status of unsteady burning, we had several experimental and theoretical contributions from a number of European and American sources. These were aimed at furthering our knowledge of this fundamental field. Of course a lot remains to be done.

The rocket motor design field offered the majority of contributions, again from European and American sources. In the main these papers offered a technical understanding of problems which were already solved empirically. They should allow a better overall design of rocket motor.

I would like to remark on the importance given to the problems of acoustic instability. On the other hand I regret the lack of attention given to the 2 phase flow with the combustion. Theoretical attention to a non-linear approach to the fluid dynamics and the combustion should be pursued.

The state of the art of rocket motor technology was reviewed by Mr Haymes. The user already has computer aided design facilities and the trend is towards such computer aids from the design through to machinery. This however is not likely to occur in Europe in the next few years and perhaps the European countries should pay more attention to this area.

We have now come to the end of this symposium meeting. I should like to thank all those who have contributed. I would like to thank the programme committee of Mr Barrere, Mr Crispin, Professors Culick, Hirch, Wazelt and the host nation co-ordinator Mr Kristofersen. Especial thanks are accorded to the interpreters and those who operated the visual and audio aids.

A special mention is made of Mr Krengel of our Panel Executive who will be leaving PEP next June. We wish to express our appreciation of his organising efforts and offer our best wished for his future.

REPORT DOCUMENTATION PAGE

1. Recipient's Reference	2. Originator's Reference	3. Further Reference	4. Security Classification of Document
	AGARD-CP-259	ISBN 92-835-0243-4	UNCLASSIFIED

5. Originator Advisory Group for Aerospace Research and Development
North Atlantic Treaty Organization
7 rue Ancelle, 92200 Neuilly sur Seine, France

6. Title

SOLID ROCKET MOTOR TECHNOLOGY

7. Presented at the 53rd Meeting of the AGARD Propulsion and Energetics Panel held at the Old War School, Oslo, Norway, 2–5 April 1979.

8. Author(s)/Editor(s)	9. Date
Various	July 1979
10. Author's/Editor's Address	**11. Pages**
Various	538

12. Distribution Statement This document is distributed in accordance with AGARD policies and regulations, which are outlined on the Outside Back Covers of all AGARD publications.

13. Keywords/Descriptors

Solid propellant rockets
Solid propellant rocket engines
Solid propellants
Ignition
Combustion stability
Burning rate
Interior ballistics

14. Abstract

These Conference Proceedings contain the 36 papers presented at the AGARD Propulsion and Energetics Panel 53rd Symposium on "Solid Rocket Motor Technology", which was held in Oslo, Norway, 2–5 April 1979. The questions and answers after the various presentations are included as well as the Round Table Discussion.

The Symposium was organized into seven sessions: Survey Papers (2); Ignition, Extinction and Internal Ballistics (8); Burn Rate Modelling and Combustion of Metal (5); New Propellants (5); Combustion Instability (7); Heat Transfer and Materials (3); and Testing and Instrumentation (6).

The Symposium provided a forum for discussion and exchange between research scientists, propellant formulators and motor technologists. Though main emphasis was placed on transient processes like ignition and extinction and on combustion instability with the various related aspects there were a number of papers dealing with propellants, their characteristics and their development.

Whether the symposium achieved its initial aim, i.e. furnishing a comprehensive survey of the technology available for solid propellant rocket motors and its further development capabilities, will be assessed in a Technical Evaluation Report, to be published as AGARD Advisory Report AR 151.

AGARD Conference Proceedings No.259 Advisory Group for Aerospace Research and Development, NATO SOLID ROCKET MOTOR TECHNOLOGY Published July 1979 538 pages These Conference Proceedings contain the 36 papers presented at the AGARD Propulsion and Energetics Panel 53rd Symposium on "Solid Rocket Motor Technology", which was held in Oslo, Norway, 2–5 April 1979. The questions and answers after the various presentations are included as well as the Round Table Discussion. The Symposium was organized into seven sessions: P.T.O.	AGARD-CP-259 Solid propellant rockets Solid propellant rocket engines Solid propellants Ignition Combustion stability Burning rate Interior ballistics	AGARD Conference Proceedings No.259 Advisory Group for Aerospace Research and Development, NATO SOLID ROCKET MOTOR TECHNOLOGY Published July 1979 538 pages These Conference Proceedings contain the 36 papers presented at the AGARD Propulsion and Energetics Panel 53rd Symposium on "Solid Rocket Motor Technology", which was held in Oslo, Norway, 2–5 April 1979. The questions and answers after the various presentations are included as well as the Round Table Discussion. The Symposium was organized into seven sessions: P.T.O.	AGARD-CP-259 Solid propellant rockets Solid propellant rocket engines Solid propellants Ignition Combustion stability Burning rate Interior ballistics
AGARD Conference Proceedings No.259 Advisory Group for Aerospace Research and Development, NATO SOLID ROCKET MOTOR TECHNOLOGY Published July 1979 538 pages These Conference Proceedings contain the 36 papers presented at the AGARD Propulsion and Energetics Panel 53rd Symposium on "Solid Rocket Motor Technology", which was held in Oslo, Norway, 2–5 April 1979. The questions and answers after the various presentations are included as well as the Round Table Discussion. The Symposium was organized into seven sessions: P.T.O.	AGARD-CP-259 Solid propellant rockets Solid propellant rocket engines Solid propellants Ignition Combustion stability Burning rate Interior ballistics	AGARD Conference Proceedings No.259 Advisory Group for Aerospace Research and Development, NATO SOLID ROCKET MOTOR TECHNOLOGY Published July 1979 538 pages These Conference Proceedings contain the 36 papers presented at the AGARD Propulsion and Energetics Panel 53rd Symposium on "Solid Rocket Motor Technology", which was held in Oslo, Norway, 2–5 April 1979. The questions and answers after the various presentations are included as well as the Round Table Discussion. The Symposium was organized into seven sessions: P.T.O.	AGARD-CP-259 Solid propellant rockets Solid propellant rocket engines Solid propellants Ignition Combustion stability Burning rate Interior ballistics

Survey Papers (2); Ignition, Extinction and Internal Ballistics (8); Burn Rate Modelling and Combustion of Metal (5); New Propellants (5); Combustion Instability (7); Heat Transfer and Materials (3); and Testing and Instrumentation (6).

The Symposium provided a forum for discussion and exchange between research scientists, propellant formulators and motor technologists. Though main emphasis was placed on transient processes like ignition and extinction and on combustion instability with the various related aspects there were a number of papers dealing with propellants, their characteristics and their development.

Whether the Symposium achieved its initial aim, i.e. furnishing a comprehensive survey of the technology available for solid propellant rocket motors and its further development capabilities, will be assessed in a Technical Evaluation Report, to be published as AGARD Advisory Report AR 151.

ISBN 92-835-0243-4

Survey Papers (2); Ignition, Extinction and Internal Ballistics (8); Burn Rate Modelling and Combustion of Metal (5); New Propellants (5); Combustion Instability (7); Heat Transfer and Materials (3); and Testing and Instrumentation (6).

The Symposium provided a forum for discussion and exchange between research scientists, propellant formulators and motor technologists. Though main emphasis was placed on transient processes like ignition and extinction and on combustion instability with the various related aspects there were a number of papers dealing with propellants, their characteristics and their development.

Whether the Symposium achieved its initial aim, i.e. furnishing a comprehensive survey of the technology available for solid propellant rocket motors and its further development capabilities, will be assessed in a Technical Evaluation Report, to be published as AGARD Advisory Report AR 151.

ISBN 92-835-0243-4

Survey Papers (2); Ignition, Extinction and Internal Ballistics (8); Burn Rate Modelling and Combustion of Metal (5); New Propellants (5); Combustion Instability (7); Heat Transfer and Materials (3); and Testing and Instrumentation (6).

The Symposium provided a forum for discussion and exchange between research scientists, propellant formulators and motor technologists. Though main emphasis was placed on transient processes like ignition and extinction and on combustion instability with the various related aspects there were a number of papers dealing with propellants, their characteristics and their development.

Whether the Symposium achieved its initial aim, i.e. furnishing a comprehensive survey of the technology available for solid propellant rocket motors and its further development capabilities, will be assessed in a Technical Evaluation Report, to be published as AGARD Advisory Report AR 151.

ISBN 92-835-0243-4

Survey Papers (2); Ignition, Extinction and Internal Ballistics (8); Burn Rate Modelling and Combustion of Metal (5); New Propellants (5); Combustion Instability (7); Heat Transfer and Materials (3); and Testing and Instrumentation (6).

The Symposium provided a forum for discussion and exchange between research scientists, propellant formulators and motor technologists. Though main emphasis was placed on transient processes like ignition and extinction and on combustion instability with the various related aspects there were a number of papers dealing with propellants, their characteristics and their development.

Whether the Symposium achieved its initial aim, i.e. furnishing a comprehensive survey of the technology available for solid propellant rocket motors and its further development capabilities, will be assessed in a Technical Evaluation Report, to be published as AGARD Advisory Report AR 151.

ISBN 92-835-0243-4

B658/4

AGARD
NATO OTAN
7 RUE ANCELLE · 92200 NEUILLY-SUR-SEINE
FRANCE
Telephone 745.08.10 · Telex 610176

DISTRIBUTION OF UNCLASSIFIED AGARD PUBLICATIONS

AGARD does NOT hold stocks of AGARD publications at the above address for general distribution. Initial distribution of AGARD publications is made to AGARD Member Nations through the following National Distribution Centres. Further copies are sometimes available from these Centres, but if not may be purchased in Microfiche or Photocopy form from the Purchase Agencies listed below.

NATIONAL DISTRIBUTION CENTRES

BELGIUM
Coordonnateur AGARD – VSL
Etat-Major de la Force Aérienne
Quartier Reine Elisabeth
Rue d'Evere, 1140 Bruxelles

CANADA
Defence Scientific Information Service
Department of National Defence
Ottawa, Ontario K1A 0Z2

DENMARK
Danish Defence Research Board
Østerbrogades Kaserne
Copenhagen Ø

FRANCE
O.N.E.R.A. (Direction)
29 Avenue de la Division Leclerc
92 Châtillon sous Bagneux

GERMANY
Zentralstelle für Luft- und Raumfahrt-
dokumentation und -information
c/o Fachinformationszentrum Energie,
Physik, Mathematik GmbH
Kernforschungszentrum
7514 Eggenstein-Leopoldshafen 2

GREECE
Hellenic Air Force General Staff
Research and Development Directorate
Holargos, Athens, Greece

ICELAND
Director of Aviation
c/o Flugrad
Reykjavik

ITALY
Aeronautica Militare
Ufficio del Delegato Nazionale all'AGARD
3, Piazzale Adenauer
Roma/EUR

LUXEMBOURG
See Belgium

NETHERLANDS
Netherlands Delegation to AGARD
National Aerospace Laboratory, NLR
P.O. Box 126
Delft

NORWAY
Norwegian Defence Research Establishment
Main Library
P.O. Box 25
N-2007 Kjeller

PORTUGAL
Direcção do Serviço de Material
da Forca Aerea
Rua da Escola Politecnica 42
Lisboa
Attn: AGARD National Delegate

TURKEY
Department of Research and Development (ARGE)
Ministry of National Defence, Ankara

UNITED KINGDOM
Defence Research Information Centre
Station Square House
St. Mary Cray
Orpington, Kent BR5 3RE

UNITED STATES
National Aeronautics and Space Administration (NASA)
Langley Field, Virginia 23365
Attn: Report Distribution and Storage Unit

THE UNITED STATES NATIONAL DISTRIBUTION CENTRE (NASA) DOES NOT HOLD STOCKS OF AGARD PUBLICATIONS, AND APPLICATIONS FOR COPIES SHOULD BE MADE DIRECT TO THE NATIONAL TECHNICAL INFORMATION SERVICE (NTIS) AT THE ADDRESS BELOW.

PURCHASE AGENCIES

Microfiche or Photocopy
National Technical
Information Service (NTIS)
5285 Port Royal Road
Springfield
Virginia 22161, USA

Microfiche
Space Documentation Service
European Space Agency
10, rue Mario Nikis
75015 Paris, France

Microfiche
Technology Reports
Centre (DTI)
Station Square House
St. Mary Cray
Orpington, Kent BR5 3RF
England

Requests for microfiche or photocopies of AGARD documents should include the AGARD serial number, title, author or editor, and publication date. Requests to NTIS should include the NASA accession report number. Full bibliographical references and abstracts of AGARD publications are given in the following journals:

Scientific and Technical Aerospace Reports (STAR)
published by NASA Scientific and Technical
Information Facility
Post Office Box 8757
Baltimore/Washington International Airport
Maryland 21240, USA

Government Reports Announcements (GRA)
published by the National Technical
Information Services, Springfield
Virginia 22161, USA

Printed by Technical Editing and Reproduction Ltd
Harford House, 7–9 Charlotte St, London W1P 1HD

ISBN 92-835-0243-4